Alaska Department of Transportation & Public Facilities

The Effects of Load History and Design Variables on Performance Limit States of Circular Bridge Columns Volume 2: Experimental Observations

Prepared By:
Jason Chad Goodnight
Yuhao Feng
Mervyn J. Kowalsky
James M. Nau
North Carolina State University

January 2015

Prepared For:

Alaska Department of Transportation and Public Facilities
Research, Development &Technology Transfer
P.O. Box 112500
3132 Channel Drive
Juneau, AK 99811-2500

4000(72)

REPORT DOCUMENTATION PAGE

Form approved OMB No. 298

1. AGENCY USE ONLY (LEAVE BLANK)	2. REPORT DATE	3. REPORT TYPE AND DATES COVERED
4000(72)	January 2015	FINAL, November 2008 through January 2015

4. TITLE AND SUBTITLE

The Effects of Load History and Design Variables on Performance Limit States of Circular Bridge Columns – Volume 2: Experimental Observations

5. FUNDING NUMBERS

AKSAS #60855/T2-08-02
Federal # HPR-4000(72)

6. AUTHOR(S)
Jason Chad Goodnight
Yuhao Feng
Mervyn J. Kowalsky
James M. Nau

7. PERFORMING ORGANIZATION NAME(S) AND ADDRESS(ES)
North Carolina State University

8. PERFORMING ORGANIZATION REPORT NUMBER

4000(72)

9. SPONSORING/MONITORING AGENCY NAME(S) AND ADDRESS(ES)

Alaska Department of Transportation and Public Facilities
Research, Development &Technology Transfer
P.O. Box 112500
3132 Channel Drive
Juneau, AK 99811-2500

10. SPONSORING/MONITORING AGENCY REPORT NUMBER

4000(72)

11. SUPPLEMENTARY NOTES

12a. DISTRIBUTION / AVAILABILITY STATEMENT

No restrictions.

12b. DISTRIBUTION CODE

13. ABSTRACT (Maximum 200 words)

This report is the second of three volumes and presents detailed data and test summaries of the experimental portion of the work. In total 30 large scale reinforced concrete bridge columns are reported in this volume. Recommendations for design and analysis can be found in Volumes 1 and 3 of this report.

14. KEYWORDS :
Seismic, reinforced concrete, strain limits, buckling, performance-based design, bridge design, plastic hinge lengths

15. NUMBER OF PAGES
748

16. PRICE CODE
N/A

17. SECURITY CLASSIFICATION OF REPORT	18. SECURITY CLASSIFICATION OF THIS PAGE	19. SECURITY CLASSIFICATION OF ABSTRACT	20. LIMITATION OF ABSTRACT
Unclassified	Unclassified	Unclassified	N/A

Notice

This document is disseminated under the sponsorship of the U.S. Department of Transportation in the interest of information exchange. The U.S. Government assumes no liability for the use of the information contained in this document.

The U.S. Government does not endorse products or manufacturers. Trademarks or manufacturers' names appear in this report only because they are considered essential to the objective of the document.

Quality Assurance Statement

The Federal Highway Administration (FHWA) provides high-quality information to serve Government, industry, and the public in a manner that promotes public understanding. Standards and policies are used to ensure and maximize the quality, objectivity, utility, and integrity of its information. FHWA periodically reviews quality issues and adjusts its programs and processes to ensure continuous quality improvement.

Author's Disclaimer

Opinions and conclusions expressed or implied in the report are those of the author. They are not necessarily those of the Alaska DOT&PF or funding agencies.

SI* (MODERN METRIC) CONVERSION FACTORS

APPROXIMATE CONVERSIONS TO SI UNITS

Symbol	When You Know	Multiply By	To Find	Symbol
		LENGTH		
in	inches	25.4	millimeters	mm
ft	feet	0.305	meters	m
yd	yards	0.914	meters	m
mi	miles	1.61	kilometers	km
		AREA		
in^2	square inches	645.2	square millimeters	mm^2
ft^2	square feet	0.093	square meters	m^2
yd^2	square yard	0.836	square meters	m^2
ac	acres	0.405	hectares	ha
mi^2	square miles	2.59	square kilometers	km^2
		VOLUME		
fl oz	fluid ounces	29.57	milliliters	mL
gal	gallons	3.785	liters	L
ft^3	cubic feet	0.028	cubic meters	m^3
yd^3	cubic yards	0.765	cubic meters	m^3
		NOTE: volumes greater than 1000 L shall be shown in m^3		
		MASS		
oz	ounces	28.35	grams	g
lb	pounds	0.454	kilograms	kg
T	short tons (2000 lb)	0.907	megagrams (or "metric ton")	Mg (or "t")
		TEMPERATURE (exact degrees)		
^oF	Fahrenheit	5 (F-32)/9 or (F-32)/1.8	Celsius	^oC
		ILLUMINATION		
fc	foot-candles	10.76	lux	lx
fl	foot-Lamberts	3.426	candela/m^2	cd/m^2
		FORCE and PRESSURE or STRESS		
lbf	poundforce	4.45	newtons	N
lbf/in^2	poundforce per square inch	6.89	kilopascals	kPa

APPROXIMATE CONVERSIONS FROM SI UNITS

Symbol	When You Know	Multiply By	To Find	Symbol
		LENGTH		
mm	millimeters	0.039	inches	in
m	meters	3.28	feet	ft
m	meters	1.09	yards	yd
km	kilometers	0.621	miles	mi
		AREA		
mm^2	square millimeters	0.0016	square inches	in^2
m^2	square meters	10.764	square feet	ft^2
m^2	square meters	1.195	square yards	yd^2
ha	hectares	2.47	acres	ac
km^2	square kilometers	0.386	square miles	mi^2
		VOLUME		
mL	milliliters	0.034	fluid ounces	fl oz
L	liters	0.264	gallons	gal
m^3	cubic meters	35.314	cubic feet	ft^3 m^3
	cubic meters	1.307	cubic yards	yd^3
		MASS		
g	grams	0.035	ounces	oz
kg	kilograms	2.202	pounds	lb
Mg (or "t")	megagrams (or "metric ton")	1.103	short tons (2000 lb)	T
		TEMPERATURE (exact degrees)		
^oC	Celsius	1.8C+32	Fahrenheit	^oF
		ILLUMINATION		
lx	lux	0.0929	foot-candles	fc
cd/m^2	candela/m^2	0.2919	foot-Lamberts	fl
		FORCE and PRESSURE or STRESS		
N	newtons	0.225	poundforce	lbf
kPa	kilopascals	0.145	poundforce per square inch	lbf/in^2

*SI is the symbol for the International System of Units. Appropriate rounding should be made to comply with Section 4 of ASTM E380.
(Revised March 2003)

ABSTRACT

This report discusses a research program aimed at defining accurate limit state displacements which relate to specific levels of damage in reinforced concrete bridge columns subjected to seismic hazards. Bridge columns are designed as ductile elements which form plastic hinges to dissipate energy in a seismic event. To satisfy the aims of performance based design, levels of damage which interrupt the serviceability of the structure or require more invasive repair techniques must be related to engineering criteria. For reinforced concrete flexural members such as bridge columns, concrete compressive and steel tensile strain limits are very good indicators of damage.

Serviceability limit states such as concrete cover crushing or residual crack widths exceeding 1mm may occur during smaller, more frequent earthquakes. While the serviceability limit states do not pose a safety concern, the hinge regions must be repaired to prevent corrosion of internal reinforcing steel. At higher ductility demands produced by larger less frequent earthquakes, reinforcing bar buckling may lead to permanent elongation in the transverse steel, which diminishes its effectiveness in confining the concrete core. Bar buckling and significant damage to the core concrete represent the damage control limit states, which when exceeded lead to significant repair costs. Furthermore, rupture of previously buckled bars during subsequent cycles of loading leads to rapid strength loss. The life safety or collapse prevention limit state is characterized by fracture of previously buckled bars.

The goal of the experimental program is to investigate the impact of load history and other design variables on the relationship between strain and displacement, performance strain limits, and the spread of plasticity. The main variables for the thirty circular bridge column tests included: lateral displacement history, axial load, longitudinal steel content, aspect ratio, and transverse steel detailing. A key feature of the experiments is the high fidelity strain data obtained through the use of an optical 3D position measurement system.

Column curvature distributions and fixed-end rotations attributable to strain penetration of reinforcement into the footing were quantified.

The following sequence of damage was observed in all of the cyclically loaded experiments: concrete cracking, longitudinal steel yielding, cover concrete crushing, confinement steel yielding, longitudinal bar buckling, and fracture of previously buckled reinforcement. The first significant loss in strength occurred when previously buckled reinforcement fractured. The measured data was used to refine strain limit recommendations. Particular attention was paid to the limit state of longitudinal bar buckling, since it limited the deformation capacity of all of the cyclically loaded specimens. Empirical expression were developed to predict the compressive strain at cover crushing, the compressive strain at spiral yielding, and the peak tensile strain prior to visible buckling after reversal of loading.

In design, limit state curvatures are converted to target displacements using an equivalent curvature distribution. The Modified Plastic Hinge Method was developed to improve the accuracy of strain-displacement predictions. Key aspects of the proposed model which differentiate it from the current method include: (1) a decoupling of column flexure and strain penetration deformation components, (2) a linear plastic curvature distribution which emulates the measured curvature profiles, and (3) separate plastic hinge lengths for tensile and compressive strain-displacement predictions.

In the experiments, the measured extent of plasticity was found to increase due to the combined effects of moment gradient and tension shift. The proposed tension hinge length was calibrated to match the upper bound of the measured spread of palsticity. The proposed compressive hinge length only contains a term related to the moment gradient effect. Expressions which describe the additional column deformation due to strain penetration of reinforcement into the adjoining member were developed. When compared to the current technique, the Modified Plastic Hinge Method improved the accuracy of both tensile and compressive strain-displacement predictions.

ACKNOWLEDGMENTS

The research work discussed in this dissertation was jointly funded by the Alaska DOT&PF (AKDOT&PF) and the Alaska University Transportation Center (AUTC) whom deserve primary acknowledgement for making the project possible. Special acknowledgement goes to Elmer Marx of the Alaska DOT&PF and Billy Connor of the AUTC who were closely involved in this research as the primary technical contacts between NCSU and AKDOT&PF/AUTC. In addition, acknowledgement should be given to the entire AKDOT/AUTC technical staff who was involved with this project.

The assistance of the entire staff and all graduate students of the Constructed Facilities Laboratory at NCSU is greatly appreciated. A special thanks is extended to Yuhao Feng, Steven Fulmer, Greg Lucier, Ty Rutledge, Nichole King, and Kelly Herrick all of whom helped extensively throughout the course of the project.

TABLE OF CONTENTS

LIST OF TABLES

LIST OF SELECTED NOTATIONS

A_{st} = Total Area of Longitudinal Steel in the Column Cross Section

A_g = Gross Area of the Column Cross Section

$\rho_l = A_{st}/A_g$ = Longituidnal Reinforcement Ratio

P = Compressive Axial Load Applied to the Specimen

f_c' = Measured Column Concrete Strength at the Day of Testing

f_{cf}' = Meausred Footing Concrete Strength at the Day of Testing

$P/(f_c'A_g)$ = Column Axial Load Ratio

L = Column Length from the Top of the Footing to the Center of the Applied Lateral Load

L_c = Column Cantilever Length, $L_c = L$ for Single Benidng, $L_c = L/2$ for Double Bending

D = Column Diameter

M = Moment in the Column, Specifically the Maximum Value at the Base Section

V = Shear Force in the Column

L/D = Column Aspect Ratio, Equivalent to $M/(VD)$

$f_y \; and \; \varepsilon_y$ = Yield Stress and Strain of Longituidnal Reinforcement

E_s = Elastic Modulus of Longitudinal Reinforcement

$f_h \; and \; \varepsilon_h$ = Stress and Strain at Strain Hardening of Longitudinal Reinforcement

$f_u \; and \; \varepsilon_u$ = Stress and Strain at Maximum Stress of Longituidnal Reinforcement

$d_{bl} \; and \; A_{bl}$ = Diameter and Area of the Longitudinal Bar

A_{sp} = Cross Sectional Area of a Single Spiral Trnasverse Steel Bar

s = Centerline Spacing between Transverse Steel Layers

D' = Diameter of the Confined Core Measured Between Spiral Centerlines

$\rho_s = \left(4A_{sp}\right)/(D's)$ = Transverse Volumetric Steel Ratio

$\rho_{eff} = \rho_s f_{yh}/f_c'$ = Effective Confinement Ratio

Δ = Column Displacement at the Center of the Applied Lateral Load

Δ_y' = Column Displacement at First Yield of Longitudinal Reinforcement

ϕ_y' = Base Section Curvature at First Yield of Longitudinal Reinforcement

F_y' and M_y' = Shear Force and Moment at First Yield of Longitudinal Reinforcement

L_{sp} = Equivalent Strain Penetration Length

L_{eff} = Effective Column Length

k = Moment Gradient Component of Plastic Hinge Length Expression

ε_s = Extreme Fiber Bar Longitudinal Steel Strain

ε_c = Extreme Fiber Cover Concrete Strain

ε_{core} = Core Concrete Strain Measured at the Centerline of the Transverse Steel

M_n = Nominal Moment Capacity Defined by First Occurance of Either $\varepsilon_s = 0.015$ or $\varepsilon_c = -0.004$

$\phi_y = \phi_y' M_n/M_y'$ = Equivalent Yield Curvature at the Base Section

$\Delta_y = \Delta_y' M_n/M_y'$ = Equivalent Yield Displacement of the Column

μ_Δ = Displacement Ductility

μ_ϕ = Curvature Ductility

$\phi_p = \phi - \phi'_y \, M/M'_y$ = Plastic Curvature at the base Section

Δ_p = Column Plastic Displacement

L_p = Equivalent Plastic Hinge Length from Priestley, Calvi, and Kowaksy (2007)

Δ_e = Elastic Column Displacement

Lpr = Extent of Plasticity, Measured at Intersection of Elastic and Plastic Curvature Profiles

Lpr_t = Tension Hinge Length Based on Triangular Distribution

Lpr_c = Compression Hinge Length Based on Triangular Distribution

Lp_t = Tension Hinge Length Based on Rectangular Distribution

Lp_c = Compression Hinge Length Based on Rectangular Distribution

Chapter 1: Experimental Observations

1.1 Load History Variable Tests 8-12

The load history variable specimens had nominally identical geometry and longitudinal steel content, and were subjected to different quasi-static unidirectional lateral displacement histories. The 24" (610mm) diameter bridge columns, Figure 1.2, contained 16 #6 (19mm) A706 bars for longitudinal reinforcement ($A_{st}/A_g = 1.6\%$) and a #3 (9.5mm) A706 spiral at 2" (51mm) ($4A_{sp}/(D's) = 1\%$) on center. The shear span for the cantilever columns was 8ft (244cm), and they had a moment to shear ratio of ($M/VD = 4$). The specimens were subjected to a constant axial load of 170kips (756kN), ($P/(f_c'A_g) \approx 5\%$) depending on the concrete compressive strength. The test matrix for the eight columns is shown in Table 1.1, and the material properties of the reinforcement appear in Table 1.2. Monotonic and cyclic stress-strain curves for the longitudinal steel appear in Figure 1.3 and Figure 1.4.

The specimens were subjected to various unidirectional top-column displacement histories including standardized laboratory reversed cyclic loading, and recreations of the displacement responses obtained from non-linear time history analysis of multiple earthquakes with distinct characteristics. The experiments utilized a quasi-static displacement controlled loading procedure. The symmetric three-cycle-set load history is commonly used to evaluate the seismic performance of structural components. The load history begins with elastic cycles to the following increments of the analytically predicted first yield force: ¼ F_y', ½ F_y', ¾ F_y', and F_y'. The experimental first yield displacement is then determined by taking the average of the recorded displacements during the first yield push and pulls cycles. The equivalent yield displacement, used to determine the displacement ductility levels ($\mu_{\Delta 1} = (1 * \Delta_y)$, is then calculated as $\Delta_y = \Delta_y' (M_n/M_y')$. The symmetric three-cycle-set load history resumes with three balanced cycles at each of the following displacement ductility levels: 1, 1.5, 2, 3, 4, 6, 8, 10, 12, etc.

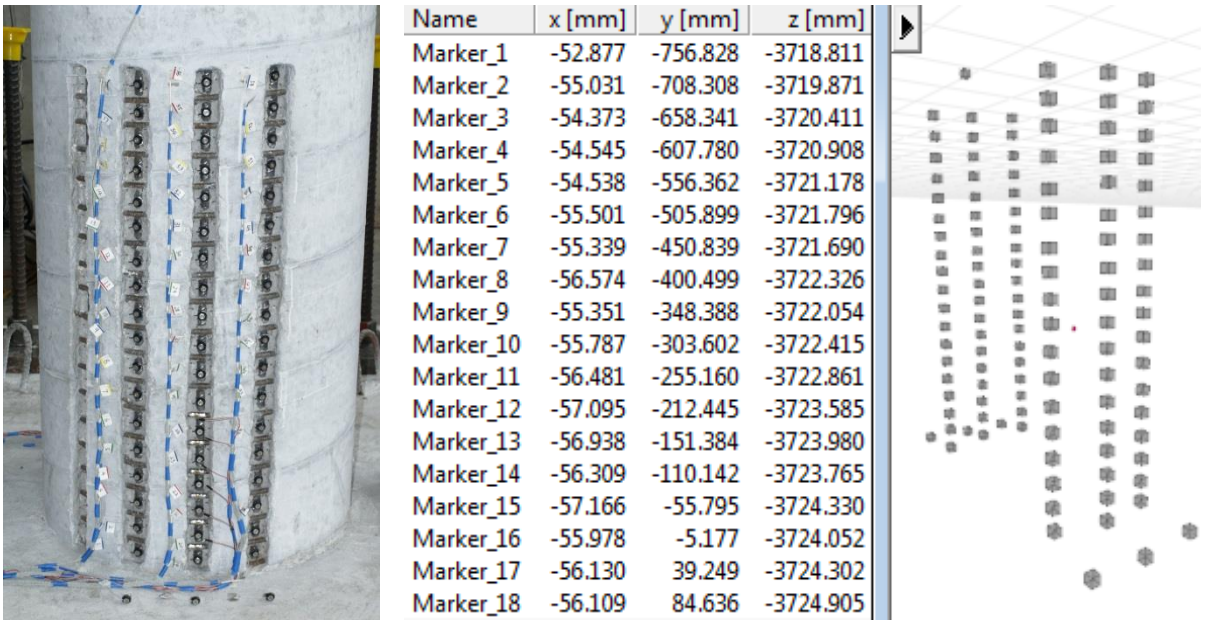

Name	x [mm]	y [mm]	z [mm]
Marker_1	-52.877	-756.828	-3718.811
Marker_2	-55.031	-708.308	-3719.871
Marker_3	-54.373	-658.341	-3720.411
Marker_4	-54.545	-607.780	-3720.908
Marker_5	-54.538	-556.362	-3721.178
Marker_6	-55.501	-505.899	-3721.796
Marker_7	-55.339	-450.839	-3721.690
Marker_8	-56.574	-400.499	-3722.326
Marker_9	-55.351	-348.388	-3722.054
Marker_10	-55.787	-303.602	-3722.415
Marker_11	-56.481	-255.160	-3722.861
Marker_12	-57.095	-212.445	-3723.585
Marker_13	-56.938	-151.384	-3723.980
Marker_14	-56.309	-110.142	-3723.765
Marker_15	-57.166	-55.795	-3724.330
Marker_16	-55.978	-5.177	-3724.052
Marker_17	-56.130	39.249	-3724.302
Marker_18	-56.109	84.636	-3724.905

Figure 1.1 Target Marker Application and Optotrak Spatial Coordinate Output

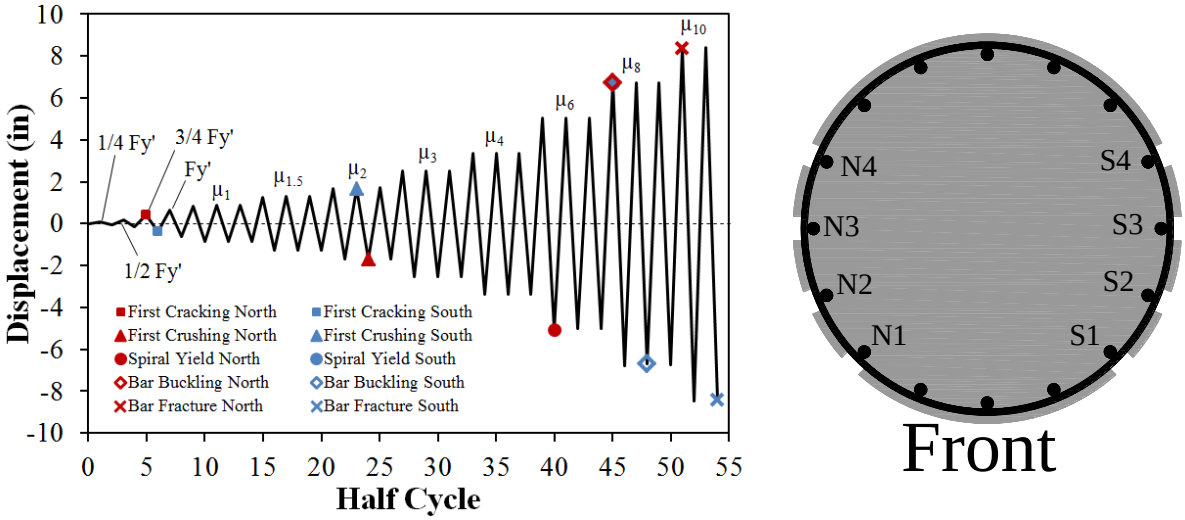

Figure 1.2 (Left) Symmetric Three Cycle Set Load History from Test 9 and (Right) Column Cross Section and Bar Designation

For earthquake time-history tests, the analytical top column displacement history is determined using non-linear time history analysis (NLTHA). The original acceleration input of the earthquake record is multiplied by a constant scale factor to produce a peak displacement response suitable for the experimental test. This is necessary because the amplitude of peak response is an important variable when comparing the performance of the columns subjected to different load histories. The goal of the experimental load history is not to re-produce the exact displacement response which the specific acceleration record may have created, but rather to compare the performance of columns subjected to specific characteristics in the displacement histories obtained from NLTHA. Specific earthquake top-column displacement response characteristics were chosen including: the number and amplitude of cycles prior to the peak, degree of symmetry, and peak displacement in each direction of loading.

The symmetric three-cycle-set experiment, Test 9, was conducted prior to earthquake tests to establish the displacement ductility levels. The scaling factors of the acceleration input used in NLTHA of the earthquake load histories were determined based on the displacement capacity of Test 9, which had bar buckling during displacement ductility eight. Two earthquake records (Tests 8 and 10) were scaled approximately displacement ductility nine while two records (Tests 11 and 12) were scaled to ductility ten. The strains at the first yield displacement of each earthquake test were verified to confirm that the ductility levels from Test 9 remained appropriate. Specimens which had un-buckled reinforcement during the earthquake load histories were subjected to a symmetric three-cycle-set displacement history to evaluate the columns post-earthquake performance, Tests 8b and 10b.

Table 1.1 Column Property Summary for Load History Variable Tests 8-12

Test	Load History	D (in)	L/D	Long. Steel (ρ_l)	Spiral Detailing (ρ_s)	f'c (psi)	P/f'c*Ag
8	Chile 2010	24	4	16 #6 bars (1.6%)	#3 at 2" (1%)	6988	5.4%
8b	Cyclic Aftershock	24	4	16 #6 bars (1.6%)	#3 at 2" (1%)	6988	5.4%
9	Three Cycle Set	24	4	16 #6 bars (1.6%)	#3 at 2" (1%)	6813	5.5%
10	Chichi 1999	24	4	16 #6 bars (1.6%)	#3 at 2" (1%)	5263	7.1%
10b	Cyclic Aftershock	24	4	16 #6 bars (1.6%)	#3 at 2" (1%)	5263	7.1%
11	Kobe 1995	24	4	16 #6 bars (1.6%)	#3 at 2" (1%)	6070	6.2%
12	Japan 2011	24	4	16 #6 bars (1.6%)	#3 at 2" (1%)	6100	6.2%

Table 1.2 Reinforcement Material Property Summary for Columns 8-12

Longitudinal Reinforcement	εy	fy (ksi)	εh	fh (ksi)	εu	fu (ksi)
Tests 8-12 (#6 Bar)	0.00235	68.1	0.0131	68.2	0.1189	92.8

Transverse Steel	Yield Stress, f_y (ksi)
Tests 8-12 (#3 Spiral)	74.1

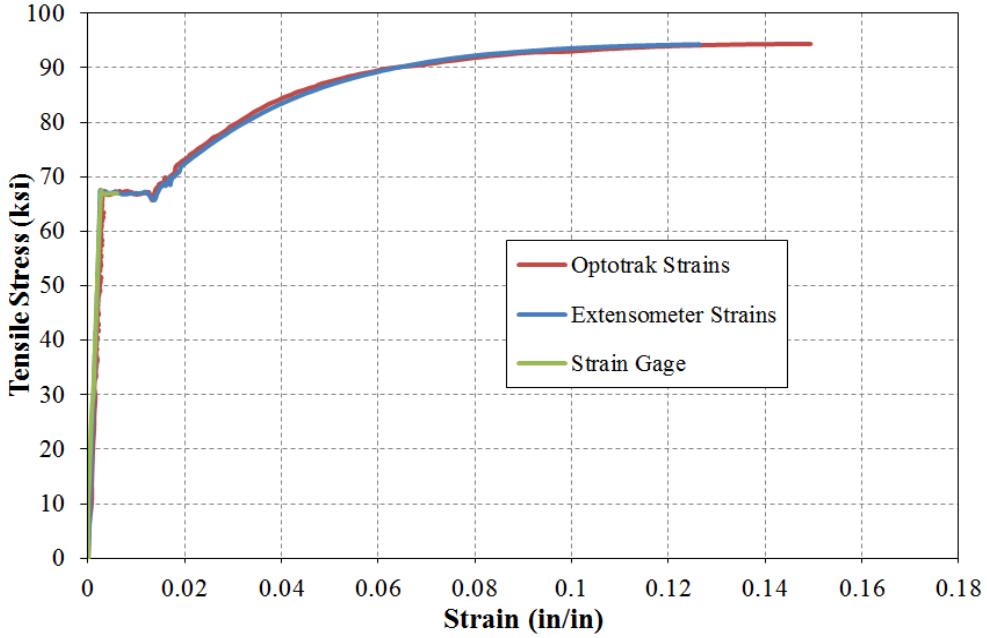

Figure 1.3 Long. Steel Stress-Strain Curve with Different Measurement Techniques

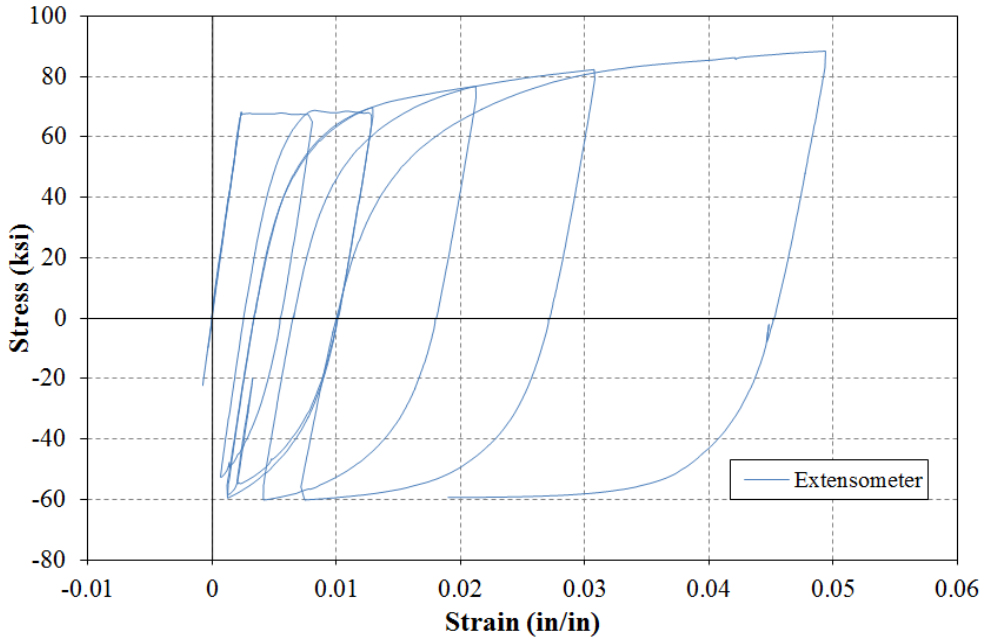

Figure 1.4 Cyclic Stress-Strain Curve for Longitudinal Reinforcement

1.1.1 Test 9 – Symmetric Three Cycle Set Load History

Table 1.3 Observational Summary for Test 9 – Symmetric Three Cycle Set LH

VALUES OF INTEREST:	
Concrete Compressive Strength:	$f_c' = 6814\ psi$
Axial Load:	$P = 170\ kips$
Analytical First Yield Force:	$F_y' = 46.9\ kips$
Experimental First Yield Displacement:	$\Delta_y' = 0.63"$
Analytical Nominal Moment Capacity:	$M_n = 503.6\ kip * ft$
Equivalent Yield Displacement:	$\Delta_y = 0.84"$
Maximum Lateral Force:	$70.3\ kips$
Failure Mode:	Fracture of Previously Buckled Reinforcement
DAMAGE OBSERVATIONS:	
First Cracking North:	$3/4Fy' = 0.40"$
First Cracking South:	$-3/4Fy' = -0.38"$
Cover Concrete Crushing North:	$\mu_2^{-2} = -1.67"$
Cover Concrete Crushing South:	$\mu_2^{+2} = 1.69"$
Transverse Steel Yield North:	At $-0.22"$ during pull to $\mu_6^{-1} = -5.05"$
Transverse Steel Yield South:	At $-3.69"$ during push to $\mu_8^{+1} = 6.72"$
Longitudinal Bar Buckling North:	Reversal from $\mu_8^{+1} = 6.72"$
Longitudinal Bar Buckling South:	Reversal from $\mu_8^{-2} = -6.70"$
Longitudinal Bar Fracture North:	At $5.18"$ during push to $\mu_{10}^{+1} = 8.38"$
Longitudinal Bar Fracture South:	At $-4.56"$ during pull to $\mu_{10}^{-2} = -8.42"$

*$\mu_8^{+1} = 6.64"$ represents the first push cycle of displacement ductility eight

Table 1.4 Strain Data Summary for Test 9 – Symmetric Three Cycle Set

MATERIAL STRAINS:	
Cover Concrete Crushing North:	$\varepsilon_s = 0.0041$ $(compression)$
Cover Concrete Crushing South:	$\varepsilon_s = 0.0032$ $(compression)$
Transverse Steel Yield North:	$\varepsilon_s = 0.0139$ $(compression)$
Transverse Steel Yield South:	$\varepsilon_s = 0.0163$ $(compression)$
Longitudinal Bar Buckling North:	$\varepsilon_s = 0.053$ $(peak\ tension\ prior\ to\ bb)$
	$\varepsilon_s = 0.018$ $(peak\ comp.\ prior\ to\ bb)$
Longitudinal Bar Buckling South:	$\varepsilon_s = 0.051$ $(peak\ tension\ prior\ to\ bb)$
	$\varepsilon_s = 0.015$ $(peak\ comp.\ prior\ to\ bb)$
Mander (1988) Ultimate Concrete Compression Strain, $\varepsilon_{cu} = 0.0175$	

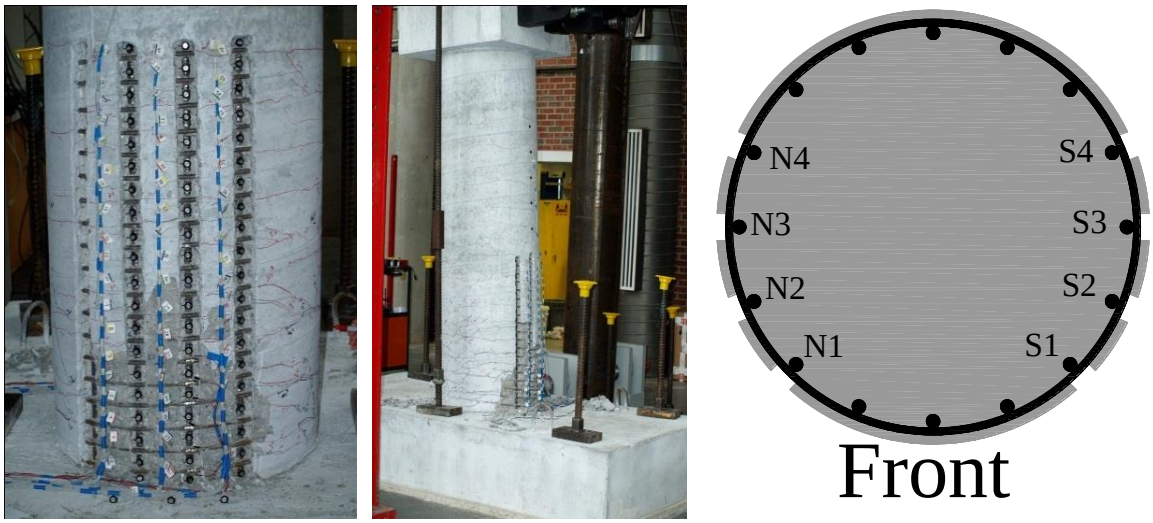

Figure 1.5 T9 – Cross Section Bar Designation – North in Tension for Push Cycles

*Note that push cycle black crack markings are on the North side while pull cycle red crack markings appear on the South side of the specimen

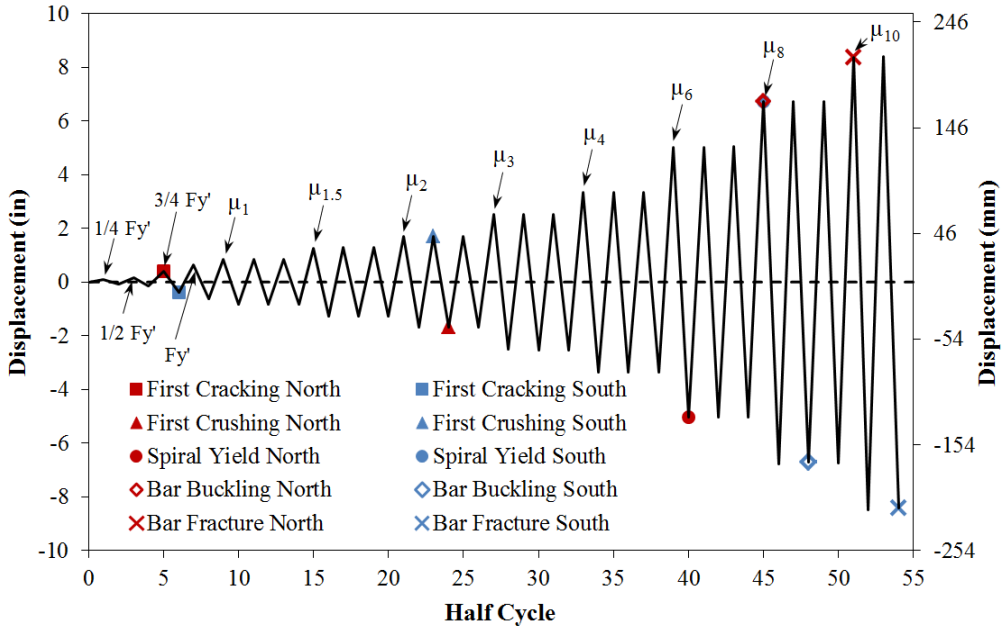

Figure 1.6 T9 – Symmetric Three Cycle Set Load History

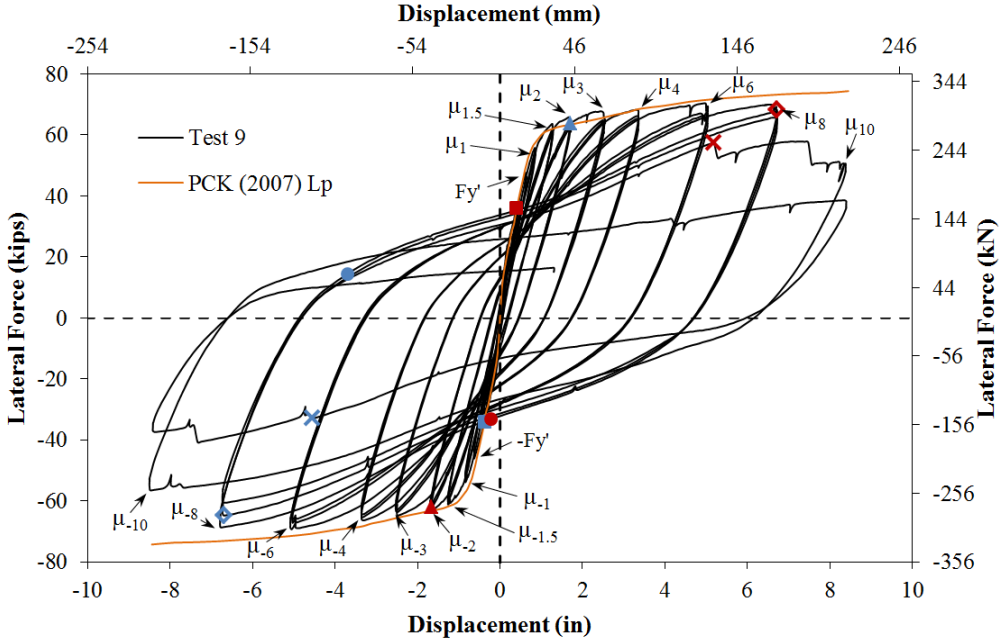

Figure 1.7 T9 – Force vs. Deformation Hysteretic Response

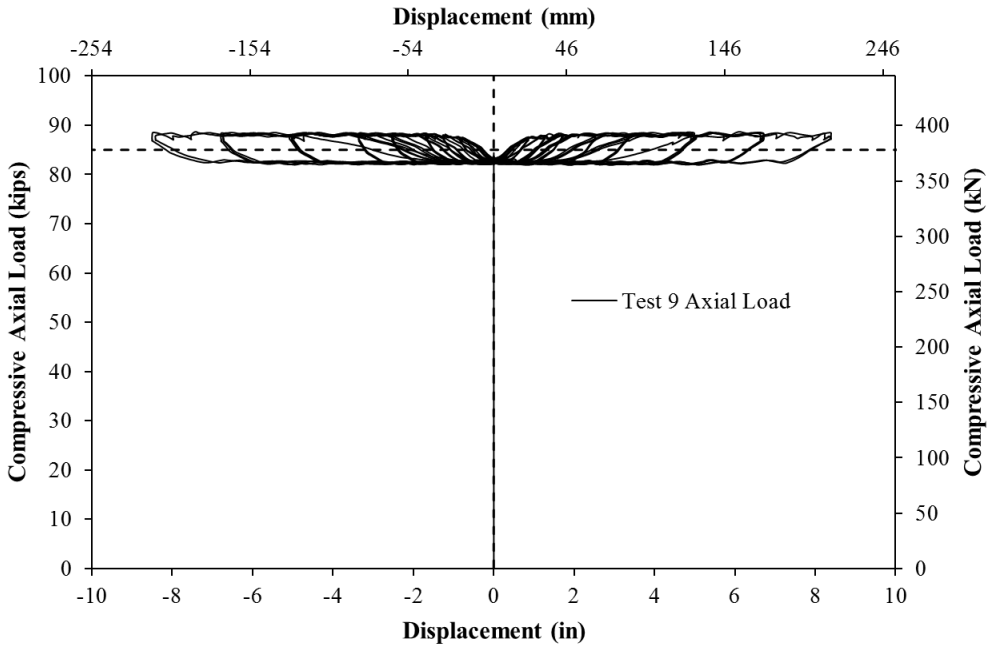

Figure 1.8 T9 – Compressive Axial Load from Each Jack, Total = 2xValue

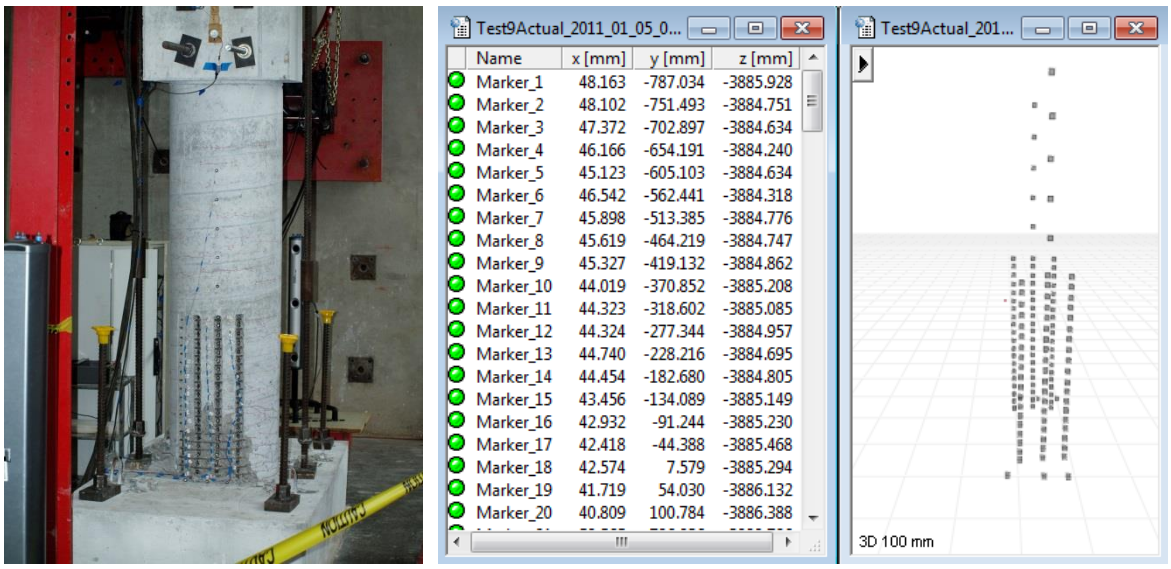

Figure 1.9 T9 – Two Optotrak Position Sensors with Vertical Cover Blockout Strips

Test 9 Symmetric Three Cycle Set – Experimental Observations:

The first yield force for the tested material and geometric properties was determined using moment curvature analysis (Cumbia $F_y' = 46.9\ kips$ with $f_c' = 6814\ psi$). The initial elastic portion of the symmetric three cycle set load history contains reversals of loading at ¼ Fy', ½ Fy', ¾ Fy', and Fy'. After the specimen has reached the first yield force in each direction, the first yield displacement is obtained as an average ($\Delta_y' = 0.63$"). The equivalent yield displacement, used to determine the displacement ductility levels ($\mu_{\Delta n} = \mathrm{n} * \Delta_y$), is then calculated as $\Delta_y = \Delta_y'(M_n/M_y') = 0.84$". The symmetric three cycle set load history continues with three complete cycles at each ductility level, as shown in Figure 1.6. The resulting lateral force vs. top column displacement response appears in Figure 1.7. The compressive axial load applied by one of the two self-regulating hydraulic jacks placed above the loading cap is shown in Figure 1.8. Since the pressure in the two jacks is equal, the total axial load (170 $kips$) is obtained by multiplying the recorded value by two. The extreme fiber vertical strain profiles for the initial elastic cycles appear in Figure 1.10.

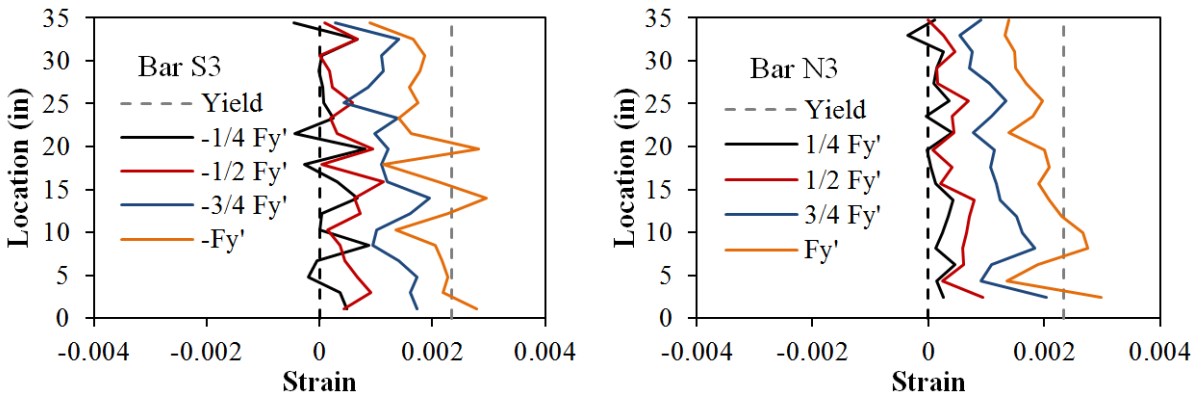

Figure 1.10 T9 – Vertical Strain Profiles to First Yield

The first cracks on the North side of the specimen appeared during the ($3/4Fy' = 0.40$") push cycle had a measured crack width of 0.1mm and were spaced at approximately 7", Figure 1.11. The first cracks on the on the South side of the specimen measured 0.2mm at approximate 8" spacing during ($-3/4Fy' = -0.38$"). During the first yield cycles the

cracks on the North side measured 0.3mm at 6" spacing and the cracks on the South side measured 0.35mm at 5". The vertical strain profiles in Figure 1.10 show that the yield strain, marked by the gray dashed line, was reached during the first yield push and pull cycles.

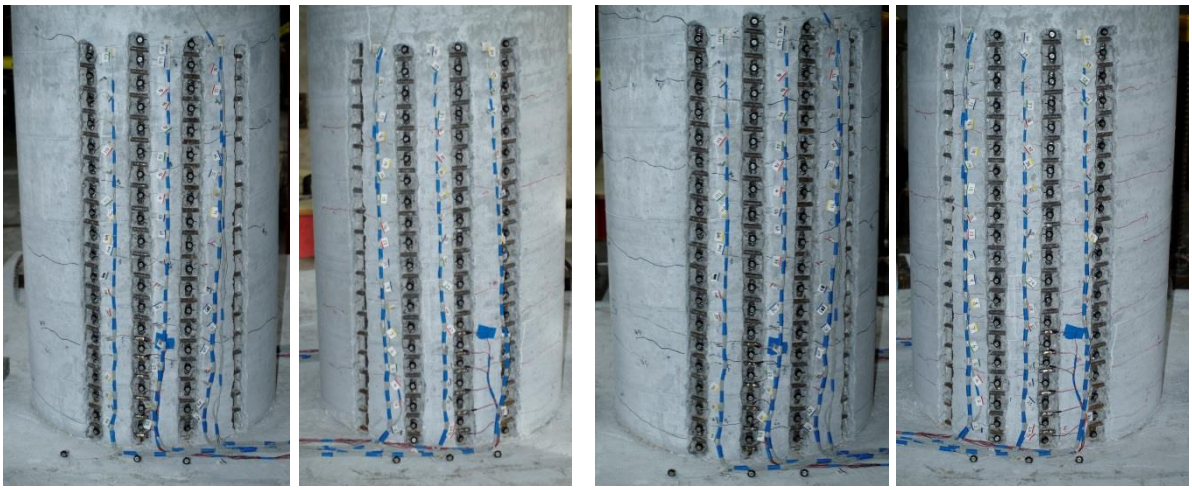

Figure 1.11 T9 – (Left) North and South Cracking during ¾ Fy' and (Right) during Fy'

At ($\mu_1^{+1} = 0.84"$) the cracks on the North side of the specimen measured 0.35mm at approximate 6" spacing. The cracks on the South side of the specimen expanded to 0.4mm at 5" during ($\mu_1^{-1} = -0.84"$). During ($\mu_{1.5}^{+1} = 1.26"$), the cracks on the North measured 0.5mm at 6" spacing. The cracks on the South side of the specimen reached 0.75mm at 5" spacing during ($\mu_{1.5}^{-1} = -1.26"$). The North cracks expanded to 1.6mm at 5" spacing during ($\mu_2^{+1} = 1.69"$) as shown in Figure 1.13. The cracks on the South side of the specimen measured 1.7mm at 5" spacing during ($\mu_2^{-1} = -1.68"$). The cover concrete on both sides of the specimen showed signs of visible flaking, which precedes crushing, during ($\mu_2^{+2} = 1.69"$) and ($\mu_2^{-2} = -1.67"$) as shown in Figure 1.12. During ($\mu_3^{+1} = 2.51"$), the extent of crushing on the South side of the column reached 17" above the footing and 2.5mm crack widths were measured on the North side of the column. The extent of crushing on the North side of the specimen reached 13" above the footing during ($\mu_3^{-1} = -2.51"$), as shown in Figure 1.14.

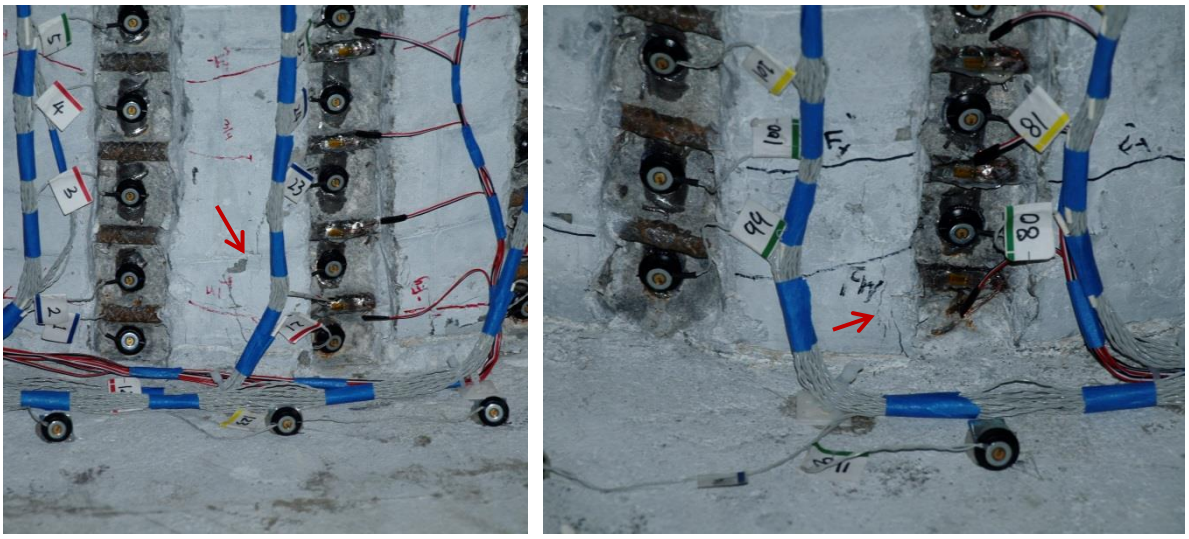

Figure 1.12 T9 – Cover Concrete Flaking (Left) South during ($\mu_2^{+2} = 1.69$") and (Right) North during ($\mu_2^{-2} = -1.67$")

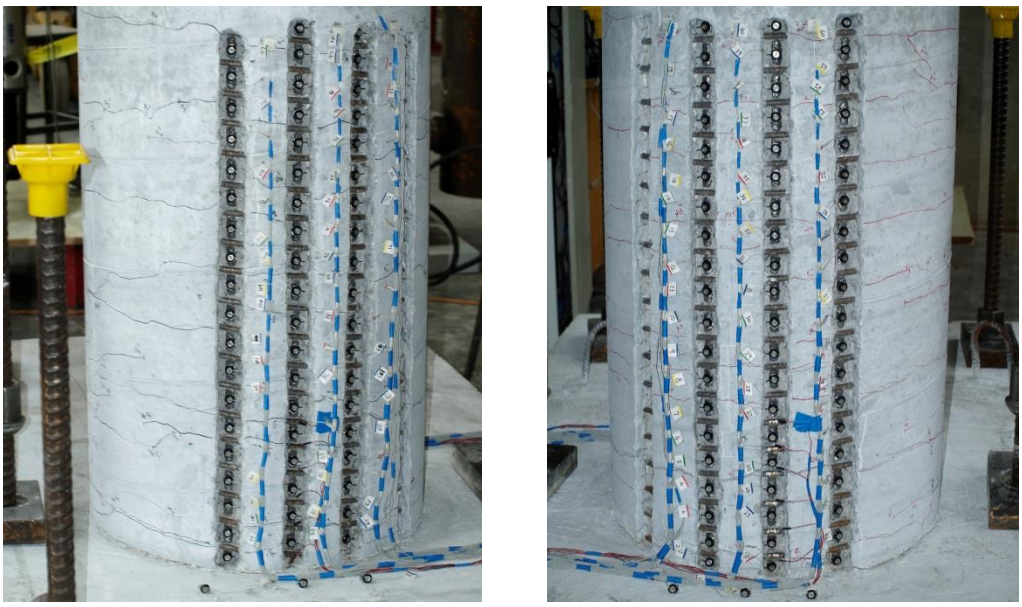

Figure 1.13 T9 – (Left) North Side during ($\mu_2^{+1} = 1.69$") and (Right) South Crack Pattern during ($\mu_2^{-1} = -1.68$")

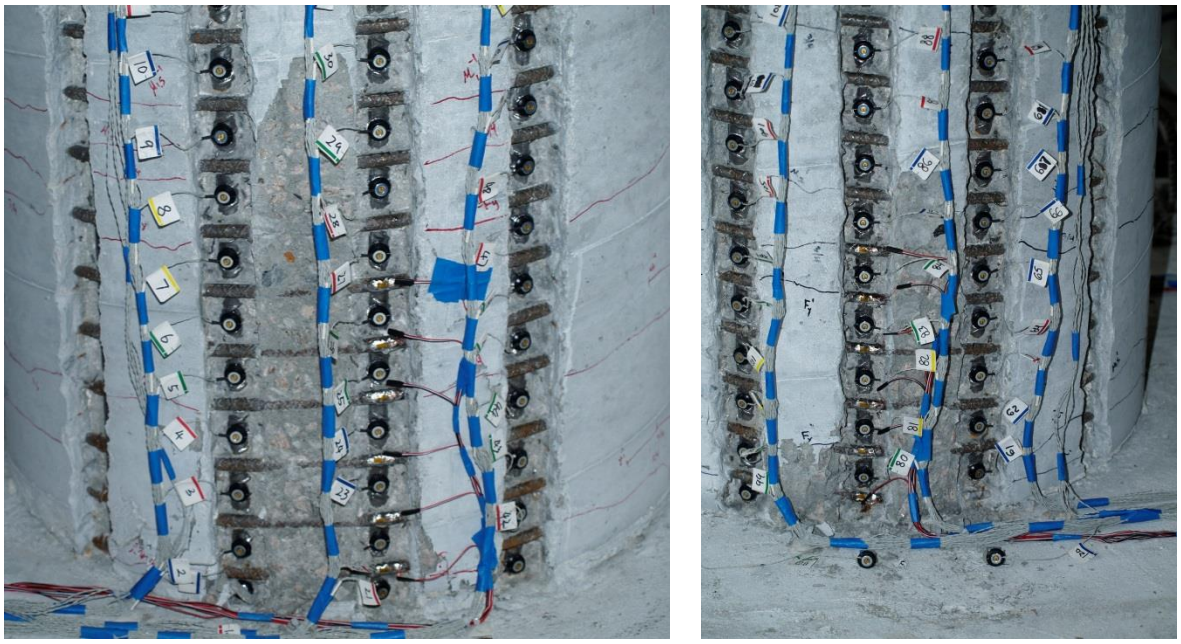

Figure 1.14 T9 – Cover Concrete Crushing (Left) South Side of the Specimen during ($\mu_3^{+1} = 2.51$") and (Right) North Side of the Specimen during ($\mu_3^{-1} = -2.51$")

The test progressed through ($\mu_8^{+1} = 6.72$") without incident. The progression of cracking on the shear faces of the column appears in Figure 1.15. As the ductility level increased, the cracks became more numerous, increased in inclination, and linked up with cracks formed during loading in the opposite direction. The North extreme fiber reinforcing bar buckled after reversal from ($\mu_8^{+1} = 6.72$"), as shown in Figure 1.16. Additional North reinfrocing bars N2 and N4 buckled after reversal from ($\mu_8^{+2} = 6.71$"). The extreme fiber South reinforcing bar S3 buckled after reversal from ($\mu_8^{-2} = -6.70$"), as shown in Figure 1.17. During ($\mu_{10}^{+1} = 8.38$"), prevously buckled bars N3 and N4 ruptured and bar S2 buckled as shown in Figure 1.18. Two additional North reinforcing bars outside of the instrumented region buckled during ($\mu_{10}^{-1} = -8.48$"). During ($\mu_{10}^{+2} = 8.39$"), previously buckled bar N2 ruptured and bars S1 and S4 buckled. The test was concluded after the pull cycle to ($\mu_{10}^{-2} = -8.42$") when previously buckled bars S3 and S2 ruptured. Rupture of previously buckled reinfrocing bars limited the displacement capacity of the bridge column as shown in Figure 1.20.

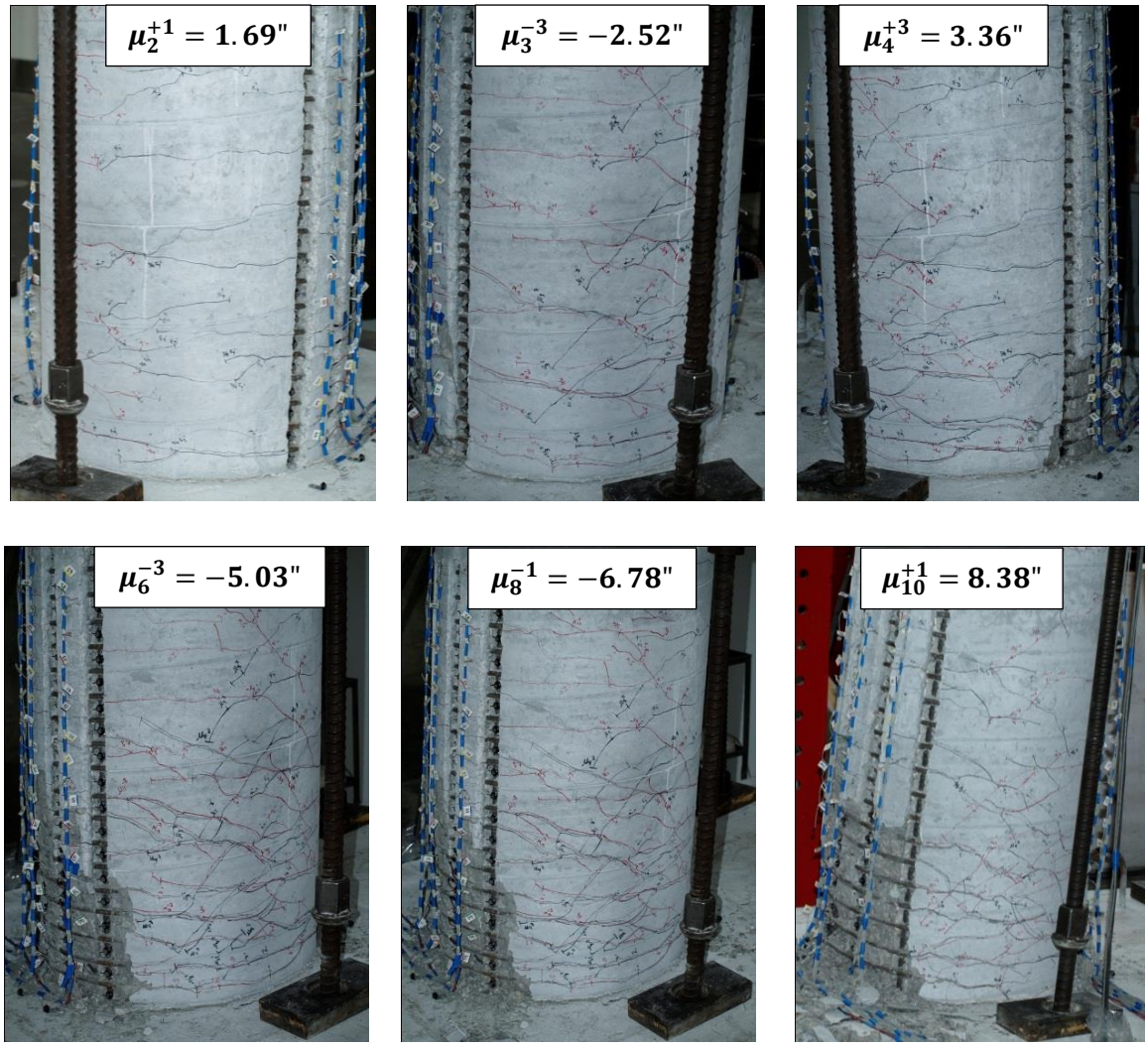

Figure 1.15 T9 – Crack Progression with Increasing Ductility Demands

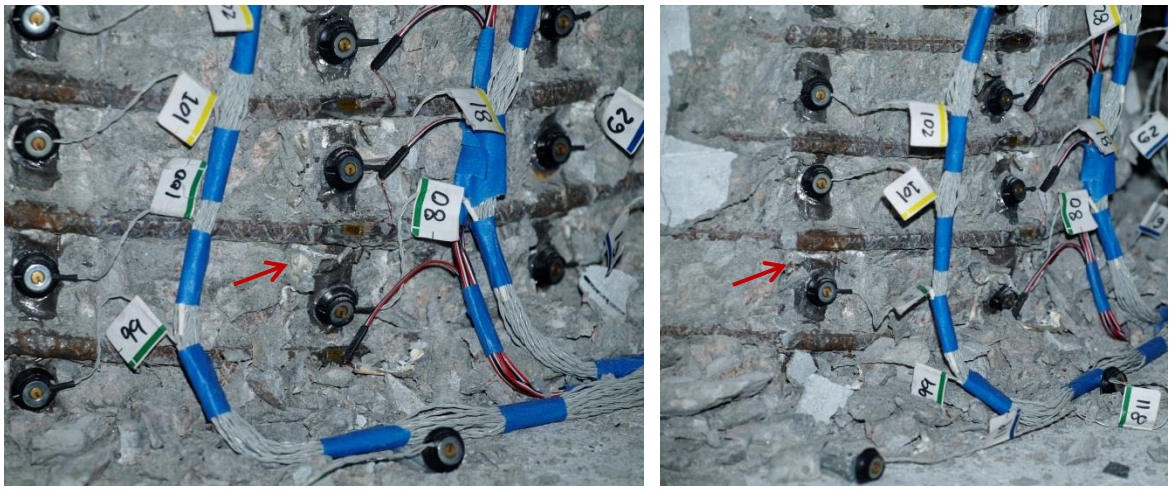

Figure 1.16 T9 – (Left) Buckling of Extreme Fiber Bar N3 during ($\mu_8^{-1} = 6.78$") and (Right) Additional Buckling of Bars N2 and N4 during ($\mu_8^{-2} = 6.70$")

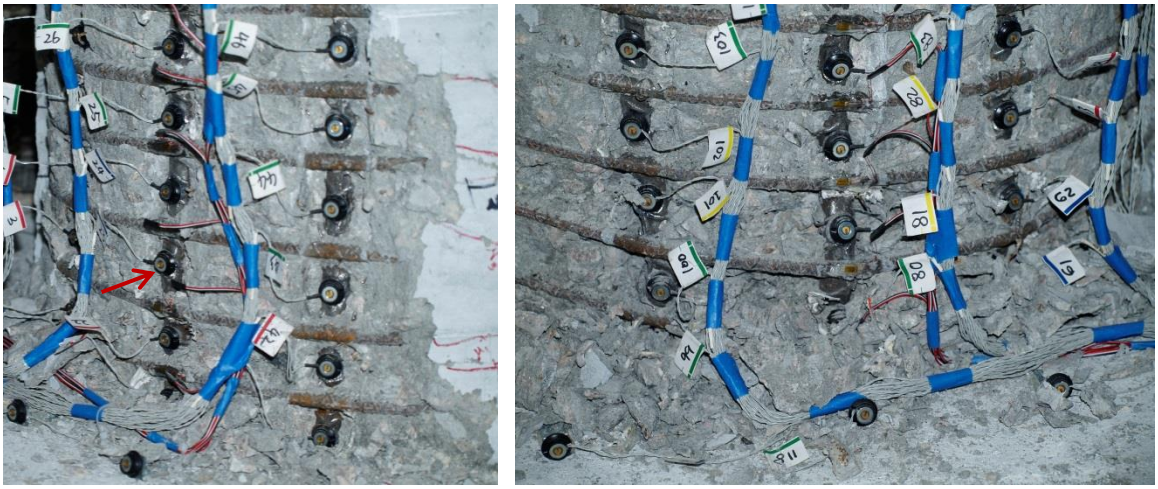

Figure 1.17 T9 – (Left) Buckling of Extreme Fiber Bar S3 after Reversal from ($\mu_8^{-2} = -6.70$") and (Right) Additional deformation in N2, N3, and N4 during ($\mu_8^{-3} = 6.73$")

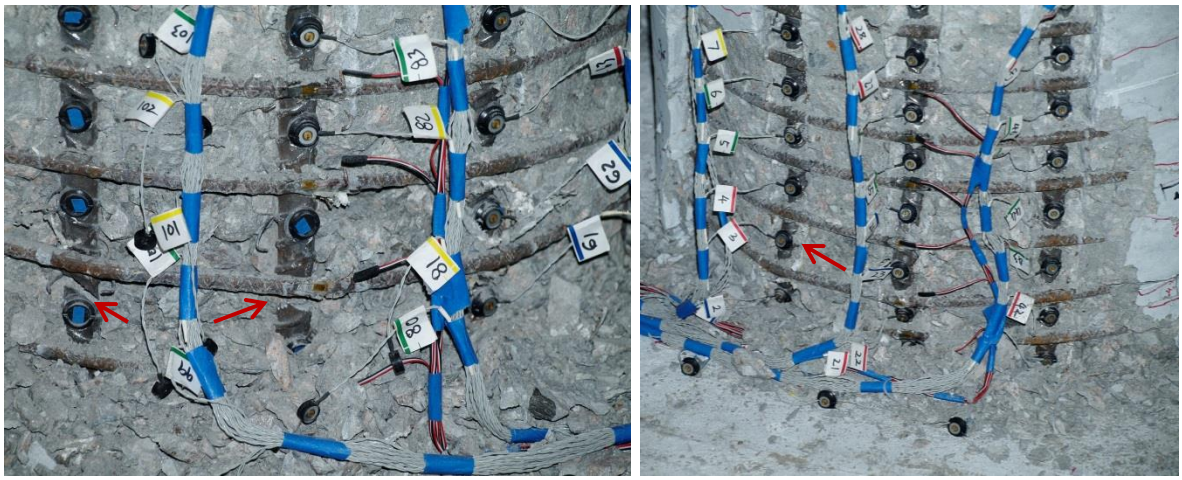

Figure 1.18 T9 – Photos during ($\mu_{10}^{+1} = 8.38$") (Left) Rupture of N3 and N4 and (Right) Buckling of S2 and Additional Deformation in Previously Buckled Bar S3

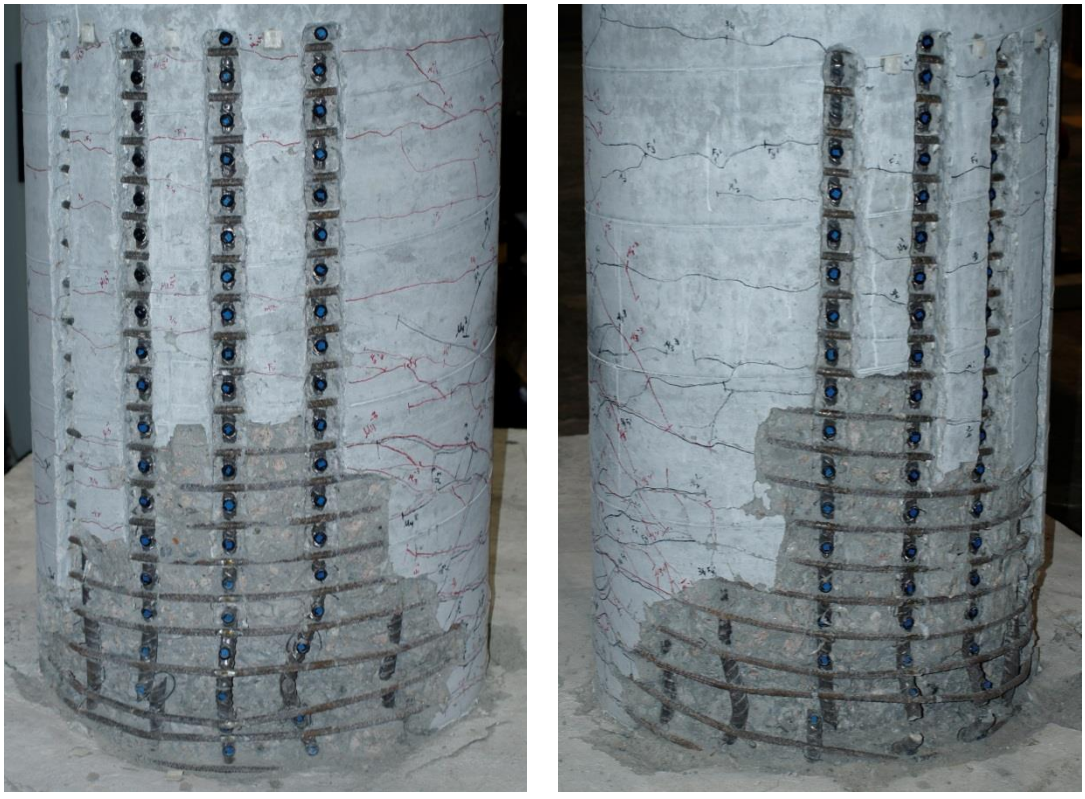

Figure 1.19 After the Test (Left) South Side and (Right) North Side

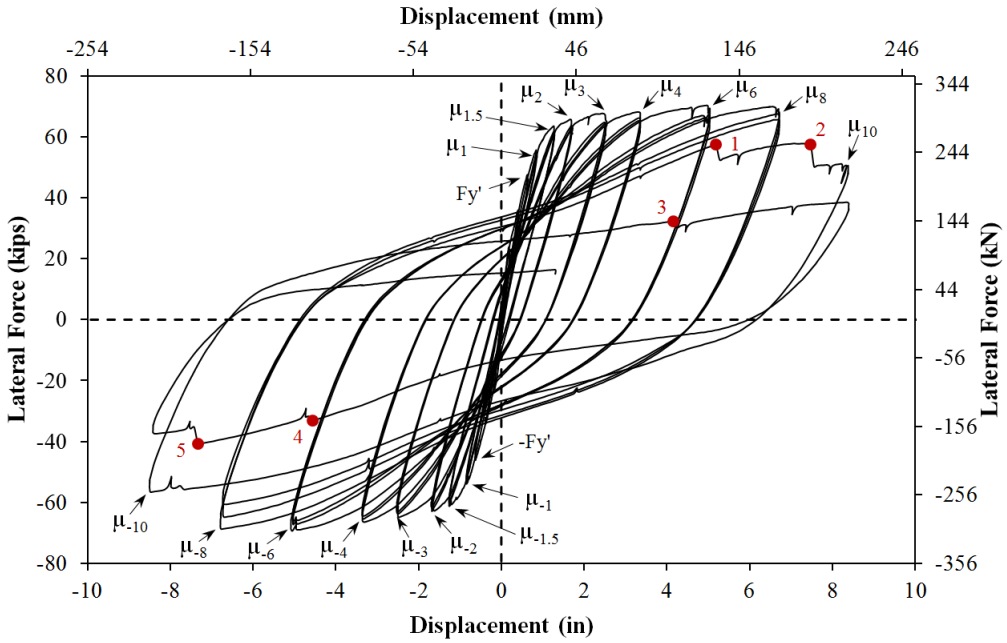

Figure 1.20 T9 – Rupture of Previously Buckled Longitudinal Reinforcement

Test 9 Symmetric Three Cycle Set – Strain Data Analysis:

South Reinforcement:

The vertical strain profile for north extreme fiber bar N3 placed into tension during push cycles appear in the right half of Figure 1.21. This figure shows both extreme fiber bars on the same graph to illustrate the effects of tension shift on strain profiles. As the hinge rotates about inclined flexural shear cracks, compressive strains are concentrated at the base and tensile strains are fanned out to a greater height following the crack distribution. Near the footing cracks remain effectively horizontal, but above this base section the flexural shear cracks are inclined as shown in Figure 1.15. The effects of tension shift increase as the cracks become more inclined at higher ductility levels. Due to the effects of tension shift, the tensile strains at the beginning of an inclined flexural shear crack do not coincide with the perceived moment demand at that location based on its height above the footing and the

applied lateral load. Since the tensile strains are fanned out over a greater distance, the measured tensile strains above the base section are increased. The initial vertical tensile strain profiles are highly influenced by individual crack locations, but later profiles past displacement ductility three are smoother. The compressive vertical strain profile for north extreme fiber bar N3 during pull cycles appears in the left half of Figure 1.22.

A peak tensile strain of 0.053 was measured 2.50" above the footing at ($\mu_8^{+1} = 6.72$"), before the North extreme fiber bar visibly buckled during the subsequent reversal of load. The relationship between tension strain and displacement for this gage length appears in Figure 1.23. Solid lines represent push cycles to the peak displacement while dashed lines correspond to the subsequent displacement reversal. The tensile strain-displacement relationship matches the moment curvature prediction well for cycles under displacement ductility three for the Priestley, Calvi, and Kowalsky (2007) plastic hinge method abbreviated as PCK (2007) Lp. As the displacement increases, moment curvature analysis begins to over predict the reinforcement tensile strains at an increasing rate. As part of this study, a new equivalent curvature distribution is recommended, the result of which is abbreviated Tensile Lpr in Figure 1.23. The intersection of the dashed unloading line with the vertical axis at zero displacement represents the residual growth strain measured over this gage length. The relationship between compression strain-displacement for the bar N3 gage length centered 4.38" above the footing appears in Figure 1.24. The recorded strains match the PCK (2007) Lp prediction well, with the exception of the second and third pull cycles of ductility six.

The compressive strain profile for bar N3, in Figure 1.25, shows that the compressive strains measured 4.38" above the footing increased with each additional cycle during displacement ductility six. This observation, combined with lower strains measured over the first gage length during these cycles suggests measurable deformation occurred before bar buckling. Six spiral layers closest to the footing-column interface were instrumented with strain gages at the location where they overlaid the extreme fiber reinforcement on each side of the specimen. The spiral strains measured on the North side of the specimen appear in

Figure 1.26. The spiral layer 3" above the footing entered the inelastic range during ($\mu_6^{-1} = -5.05"$). During the next two pull cycles of ductility six, the spiral strains continued to rise as the apparent measurable deformation increased. The North extreme fiber bar N3 visibly buckled after reversal from ($\mu_8^{+1} = 6.72"$) at the location of the previously inelastic spiral layer, as shown in Figure 1.16. The inelastic spiral layer, alone, did not lead to bar buckling during ductility six. Instead, the peak tensile strain of 0.053 sustained during ($\mu_8^{+1} = 6.72"$), combined with inelastic transverse steel restraint were sufficient to produce bar buckling upon reversal of load.

The strain hysteresis centered 2.50" above the footing on extreme fiber bar N3 appears in Figure 1.27 with a color bar that represents elapsed time while testing. During the first pull cycle of ductility eight, bar N3 begins to buckle at the location of the data label (X-Displacement, Y-Strain, and Z-Time). During pull cycles the strain in bar N3 should decrease, but the recorded strain begins increasing after the data label due to the outward deformation over the buckled region shown in Figure 1.16. The stain hysteresis also shows a small amount of deformation during each successive pull cycle of ductility six prior to visible buckling. The deformation over the first gage length above the footing causes an increase in strain with each successive cycle while the second gage length contracts causing larger compression strains, as shown in Figure 1.24.

The transverse steel strain hysteresis over the North buckled region appears in Figure 1.28. The transverse steel strain sharply increases upon reversal from the first push cycle of ductility eight, which is marked by the data label. The increase in transverse steel strain occurred before the increase in deformation of longitudinal bar N3 which signified the beginning of visible bar buckling. The measurable deformation in bar N3 during ductility six also caused small increases in the transverse steel strain prior to visible bar buckling.

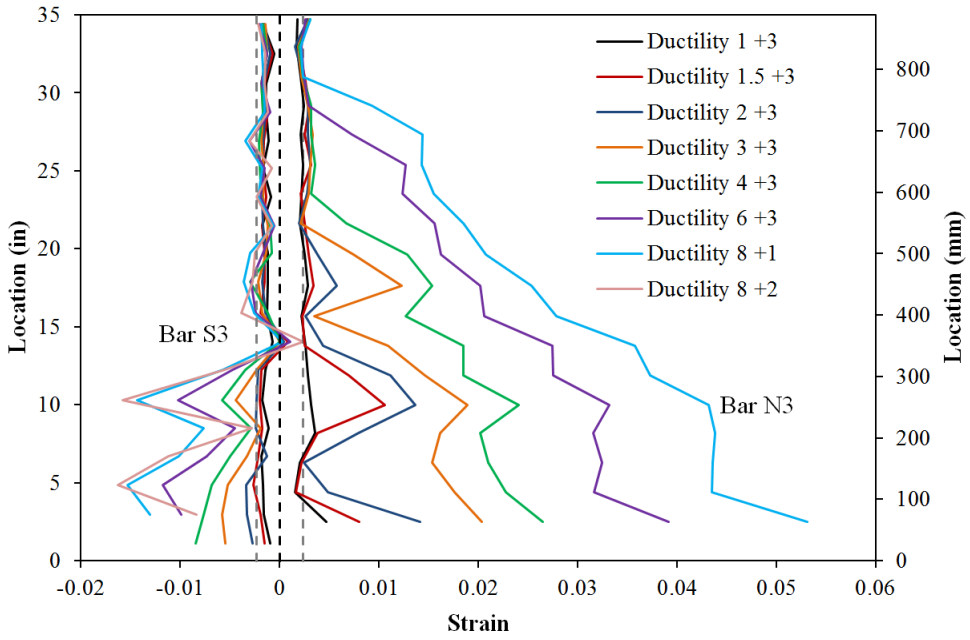

Figure 1.21 T9 – Extreme Fiber Vertical Strain Profiles During Push Cycles

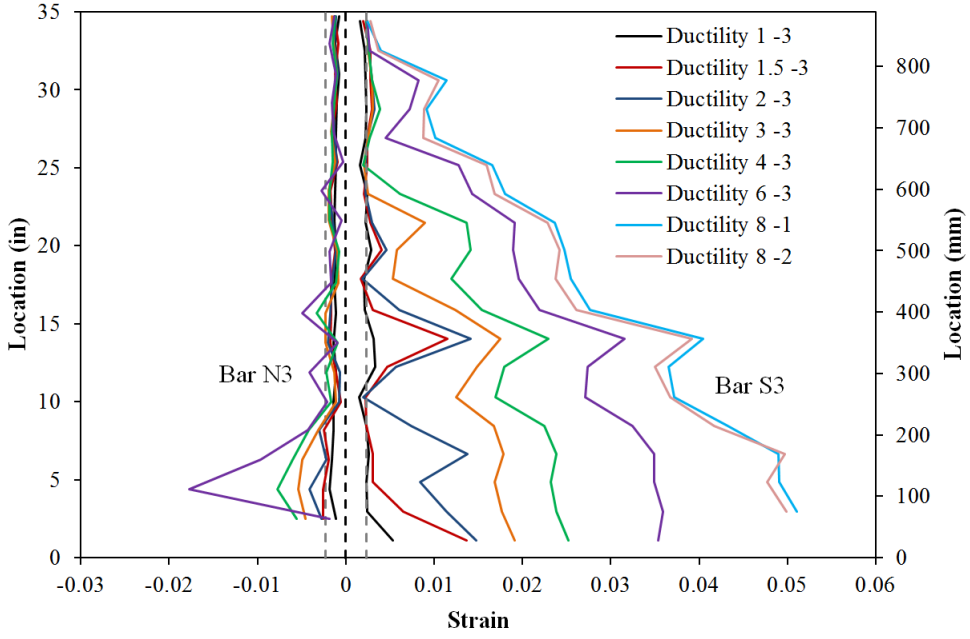

Figure 1.22 T9 – Extreme Fiber Vertical Strain Profiles During Pull Cycles

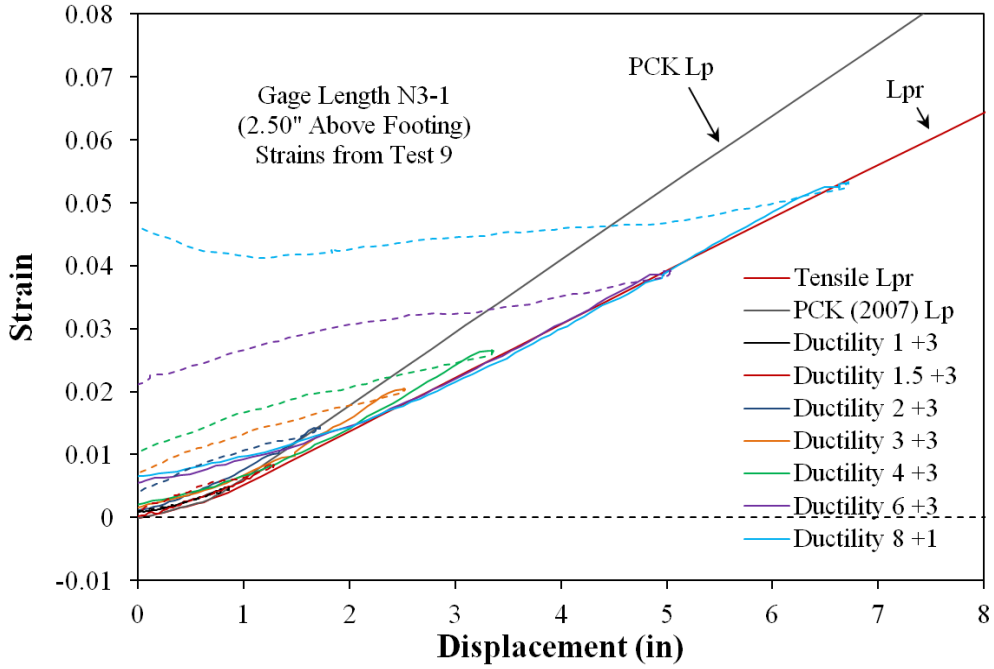

Figure 1.23 T9 – Tensile Strain-Displacement for Bar N3 during Push Cycles

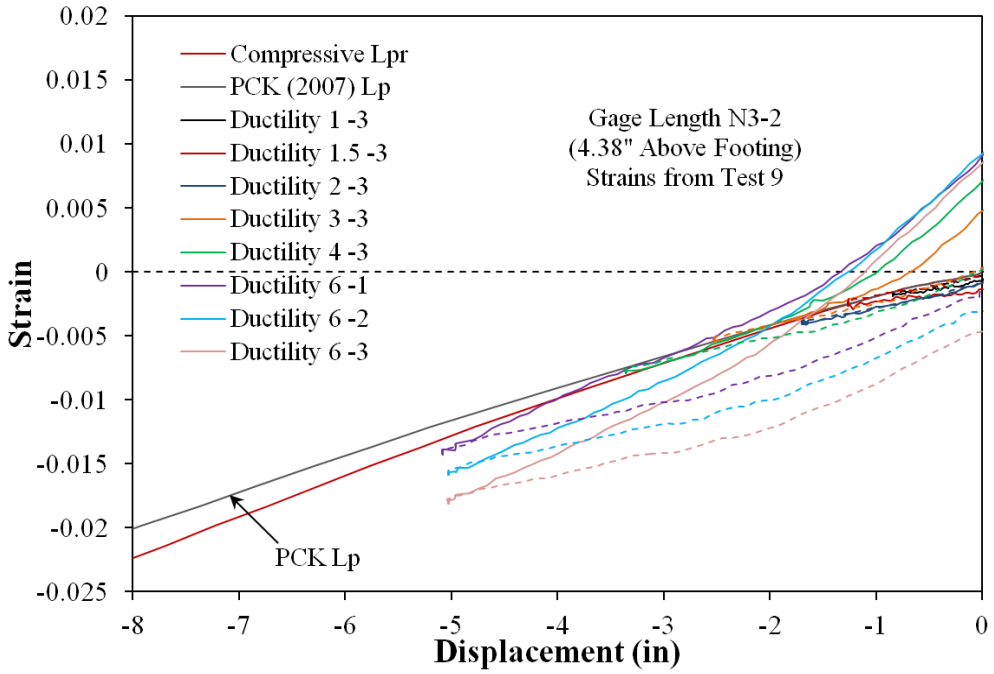

Figure 1.24 T9 – Compressive Strain-Displacement for Bar N3 during Pull Cycles

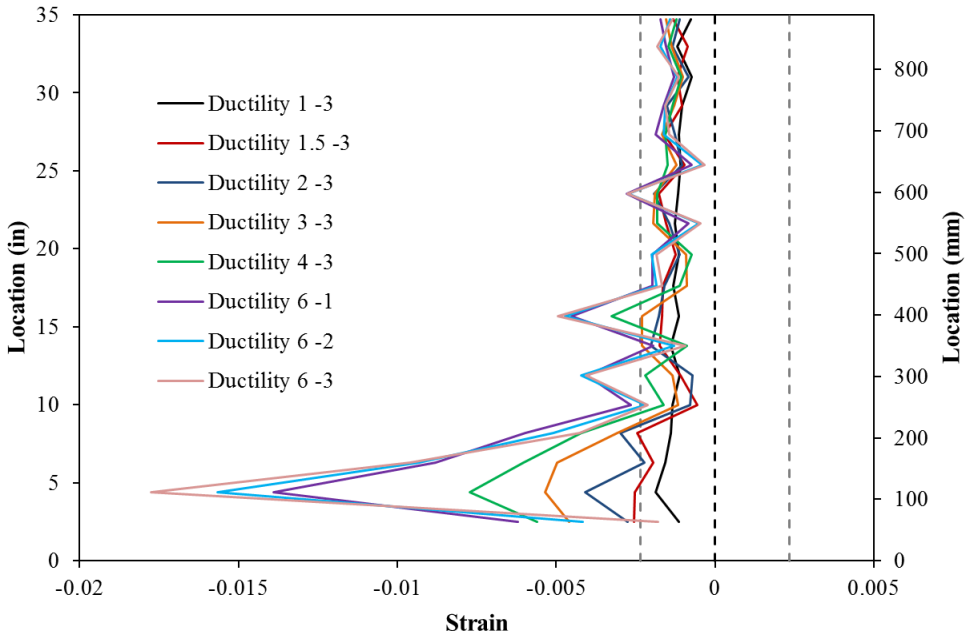

Figure 1.25 T9 – Vertical Strain Profile for Bar N3 with All Cycles during Ductility Six

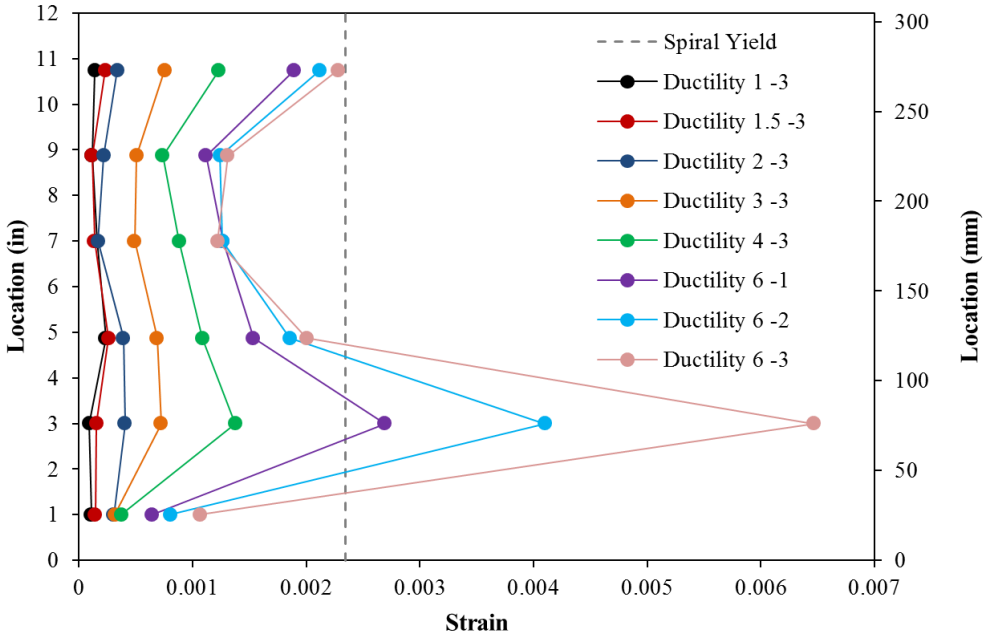

Figure 1.26 T9 – Transverse Steel Strain for the Lowest Six North Spiral Layers

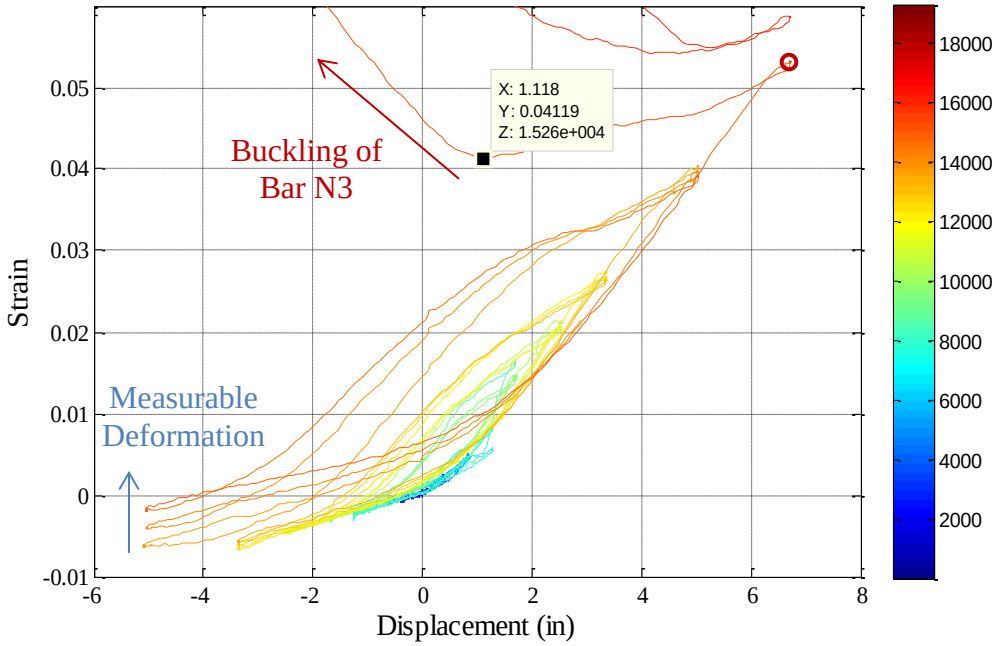

Figure 1.27 T9 – Bar N3 Strain Hysteresis, Gage Length Centered 2.50" above Footing

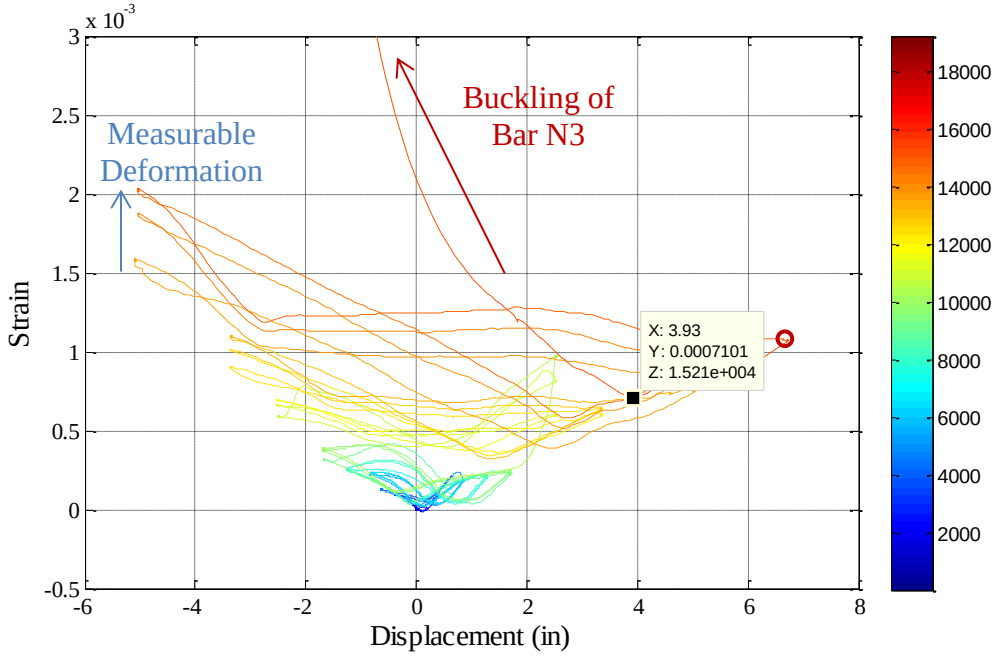

Figure 1.28 T9 – Spiral Strain Hysteresis for North Spiral Layer 4.88" Above Footing

South Reinforcement:

The vertical strain profile for south extreme fiber bar S3 which is placed into tension during pull cycles appears in the right half of Figure 1.22. The compressive strain profiles during push cycles are shown in the left half of Figure 1.21. The extreme fiber South reinforcing bar buckled during the third push cycle of ductility eight after sustaining a tension strain of 0.051 centered 2.95" above the footing at ($\mu_8^{-1} = -6.78"$). The tension strain over the same gage length during ($\mu_8^{-2} = -6.70"$) was 0.050. The compressive vertical strain profile for bar S3 during ($\mu_8^{+2} = 6.71"$) shows measurable deformation 2.95" and 8.47" above the footing before visible buckling occurred in the third push cycle. A peak compressive strain of -0.0177 was measured 4.38" above the footing on South extreme fiber bar S3 during ($\mu_6^{-3} = -5.03"$). The relationship between tension strain and displacement from when the column was vertical to the peak of significant pull cycles for bar S3, 2.95" above the footing, appears in Figure 1.29. The relationship between compression strain and displacement for push cycles 4.84" above the footing on bar S3 appears in Figure 1.30. Moment curvature analysis with the PCK (2007) Lp hinge method does a good job of predicting the compressive strains, but the tensile strains are over predicted.

The strain hysteresis 2.95" above the footing for extreme fiber south reinforcing bar S3 appears in Figure 1.32. The graph includes a color bar which represents elapsed time while testing to track the progression of the experiment. The strain hysteresis for bar S3 indicates that buckling occurred after reversal from ($\mu_8^{-2} = -6.70"$), which agrees with the test observations. While the South reinforcement should be in compression during the push cycle to ($\mu_8^{+3} = 6.71"$), the outward deformation of bar S3 during bar buckling causes elongation over the Optotrak gage length placed on the outside surface of the bar. The transverse steel strain hysteresis for the spiral layer overlaying the outward buckled region of bar S3 appears in Figure 1.33. Data labels in the longitudinal and transverse steel strain hystereses mark the initiation of bar buckling. As extreme fiber bar S3 began to visibly buckle, it placed a larger strain demand on the transverse steel. Measurable deformation occurred before visible buckling of bar S3 during ($\mu_8^{+2} = 6.71"$), resulting in increased transverse steel strains.

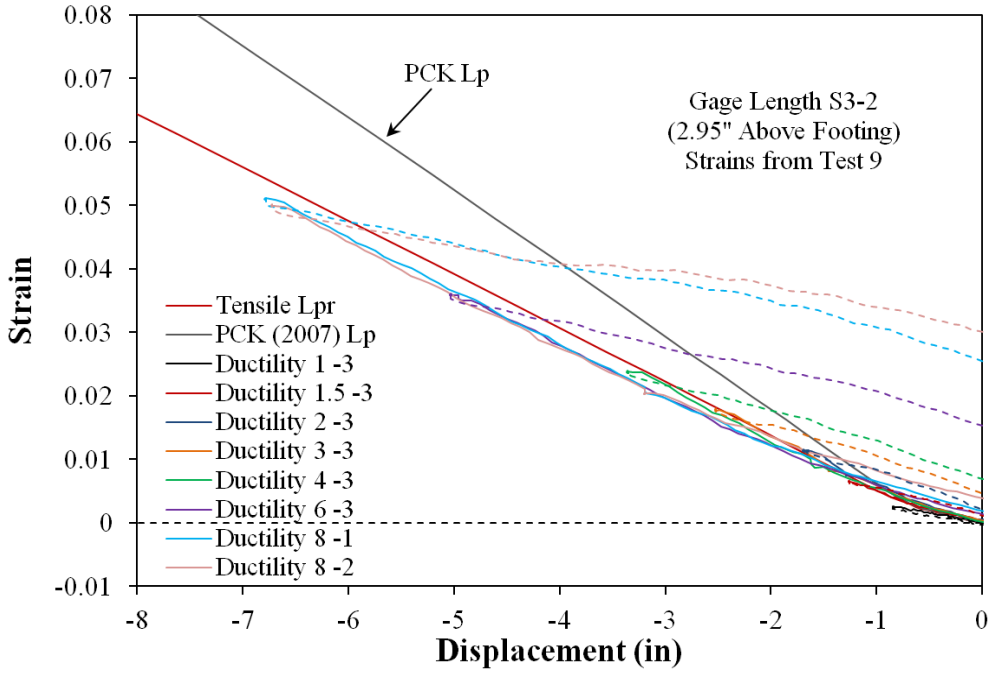

Figure 1.29 T9 – Tensile Strain-Displacement for Bar S3 during Pull Cycles

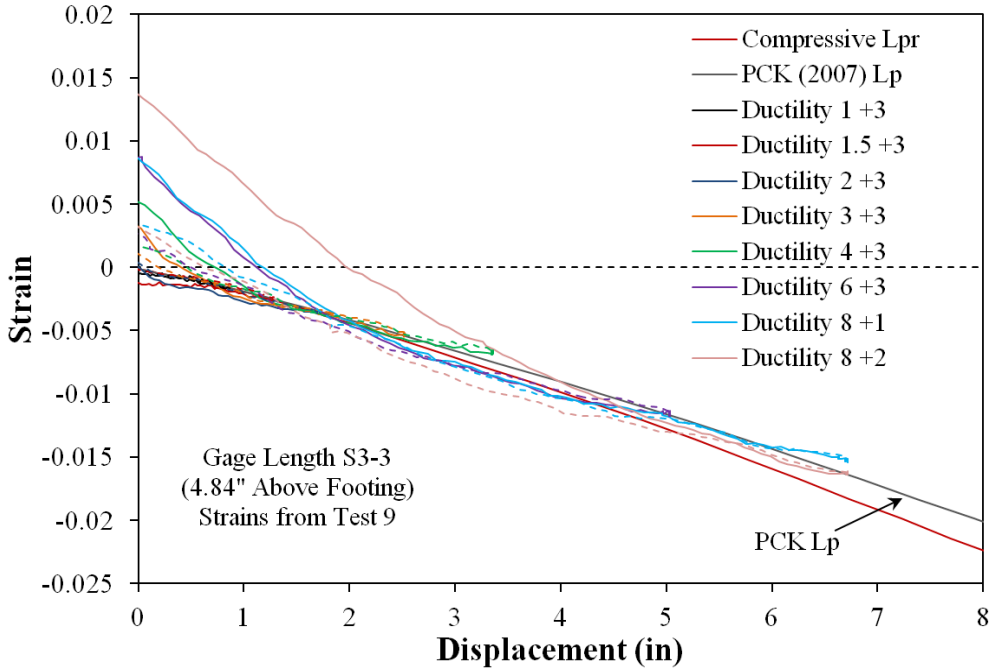

Figure 1.30 T9 – Compressive Strain-Displacement for Bar S3 during Push Cycles

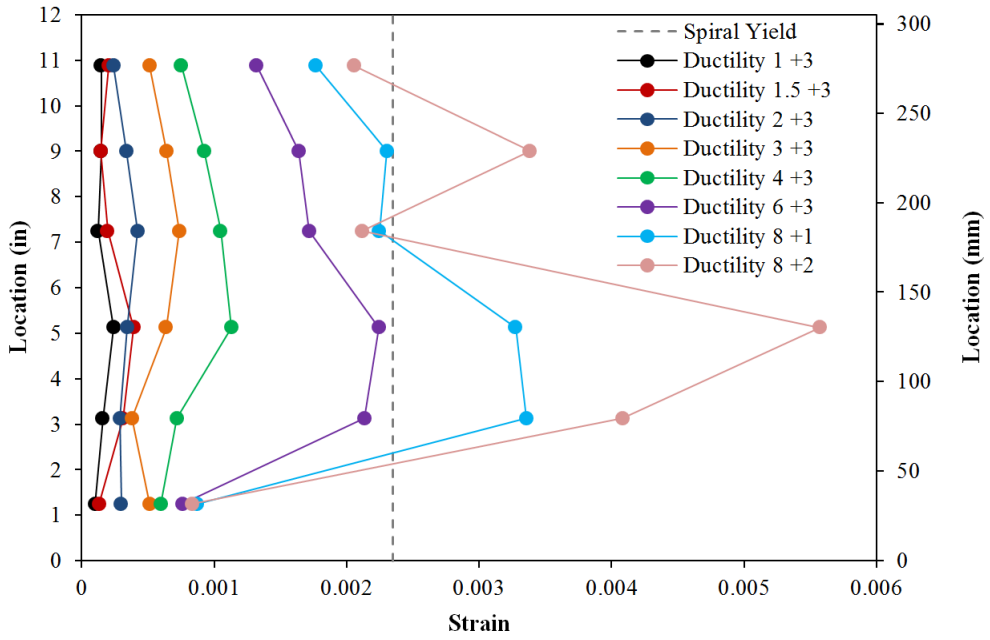

Figure 1.31 T9 – Transverse Steel Strain for the Lowest Six South Spiral Layers

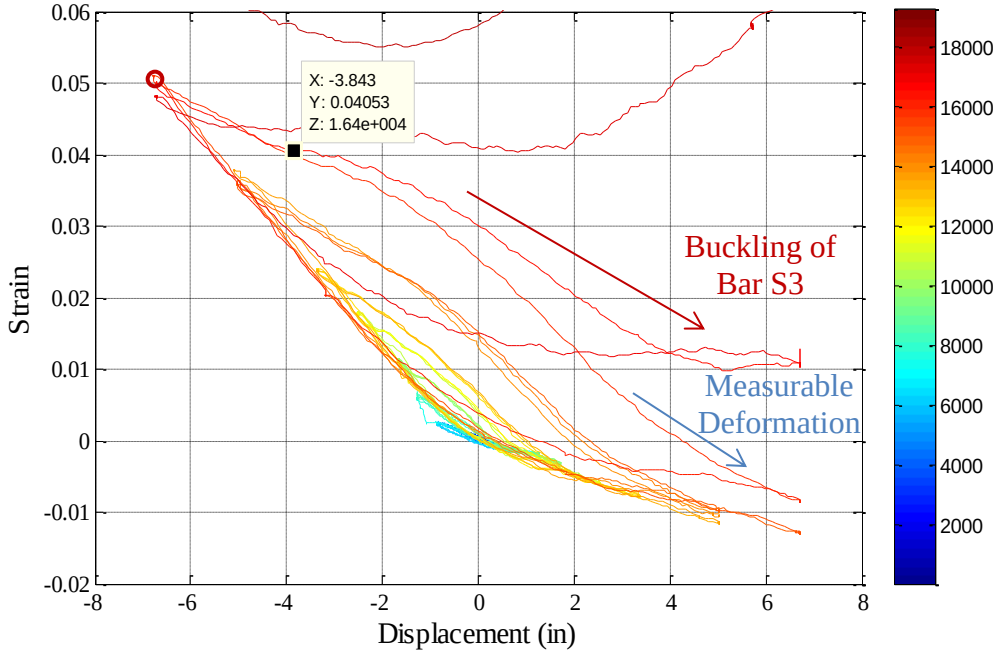

Figure 1.32 T9 – Bar S3 Strain Hysteresis, Gage Length Centered 2.95" above Footing

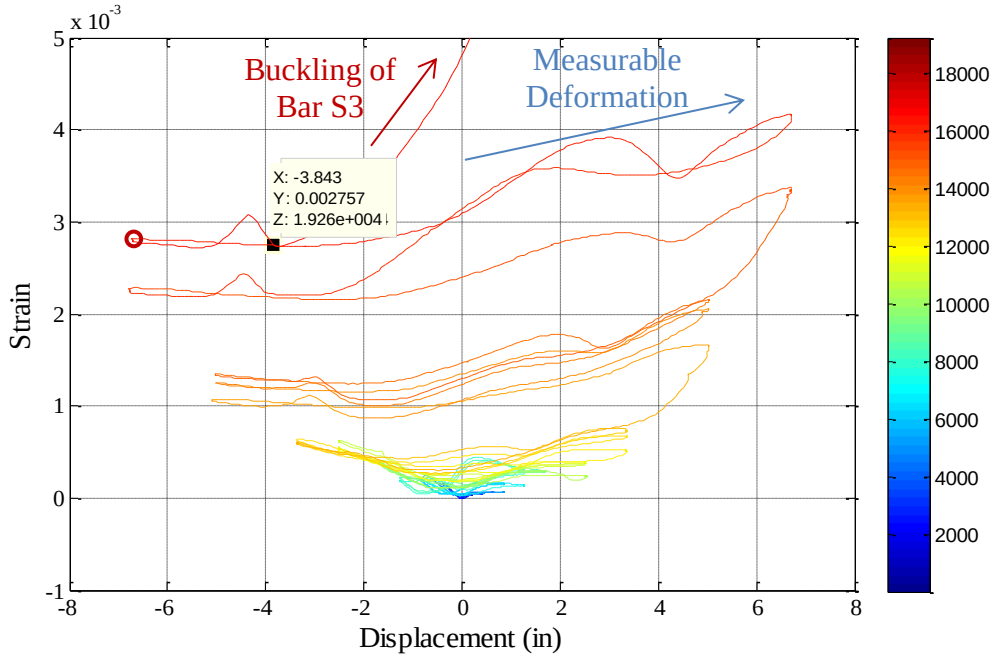

Figure 1.33 T9 – Spiral Strain Hysteresis for South Layer 3.13" Above the Footing

Test 9 – Curvature and Strain Penetration Data:

The cross section curvature profiles are plotted by connecting the measured strains from all six instrumented bars on a given horizontal cross section with a least squared error line. The curvature is then extracted from the slope of the least squared error line, see Figure 1.34. Vertical curvature profiles are plotted for push and pull cycles in Figure 1.35 and Figure 1.36 respectively. These figures show that plastic curvatures have a linear distribution at higher displacement ductility levels. The extent of plastic curvatures above the footing can be calculated by determining where the linear plastic curvature distribution intersects the triangular yield curvature distribution, shown as a grey dashed line. The dashed lines for each curvature distribution represent a least squared error linear fit to the plastic portion of the measured curvatures. The data points used to create the least squared error lines appear as circle data markers. The measured spread of plasticity for Test 9 is shown in Figure 1.44

as a function of base section curvature ductility. The extent of plasticity is computed as the intersection of the linear plastic curvature regression and the elastic curvature profile.

The target marker on each bar placed closest the footing-column interface can be used to create slip hysteresis and horizontal slip profiles attributable to strain penetration. The slip hysteresis for extreme fiber bars N3 and S3 appear in Figure 1.37 and Figure 1.38 respectively. The peak tensile slip of each bar exceeds 0.4in during ductility eight. If the measured slip of all of the instrumented bars is plotted along the cross section depth, the base rotation attributable to strain penetration may be calculated. The slip profiles for push and pull cycles appear in Figure 1.39 and Figure 1.40 respectively. The rotation of the base section can be extracted from the slope of the least squared error line connecting all six measured bar slips.

The displacement at the center of the lateral load may be calculated by combining the measured curvatures over the instrumented region (3ft above the footing), base rotation due to strain penetration, and an elastic curvature assumption above the instrumented region. This process is shown graphically in Figure 1.41. This integrated displacement calculated from the Optotrak system is compared to the measured string potentiometer displacement at the center of loading in Figure 1.42. The calculated displacements match well over the entire range of response indicating that shear displacements are negligible in comparison to flexural displacements for this column. A bar chart which plots the components of top column displacement for each displacement ductility level appears in Figure 1.43. Strain penetration accounts for between 25-35% of the top column displacement throughout the entire range of response.

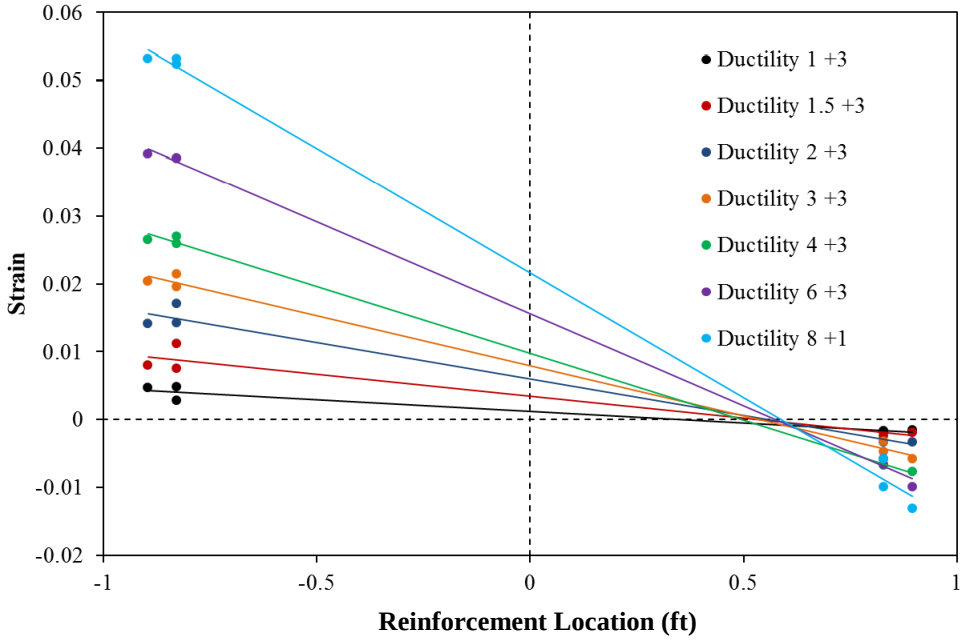

Figure 1.34 T9 – Base Section Curvature Profiles during Push Cycles

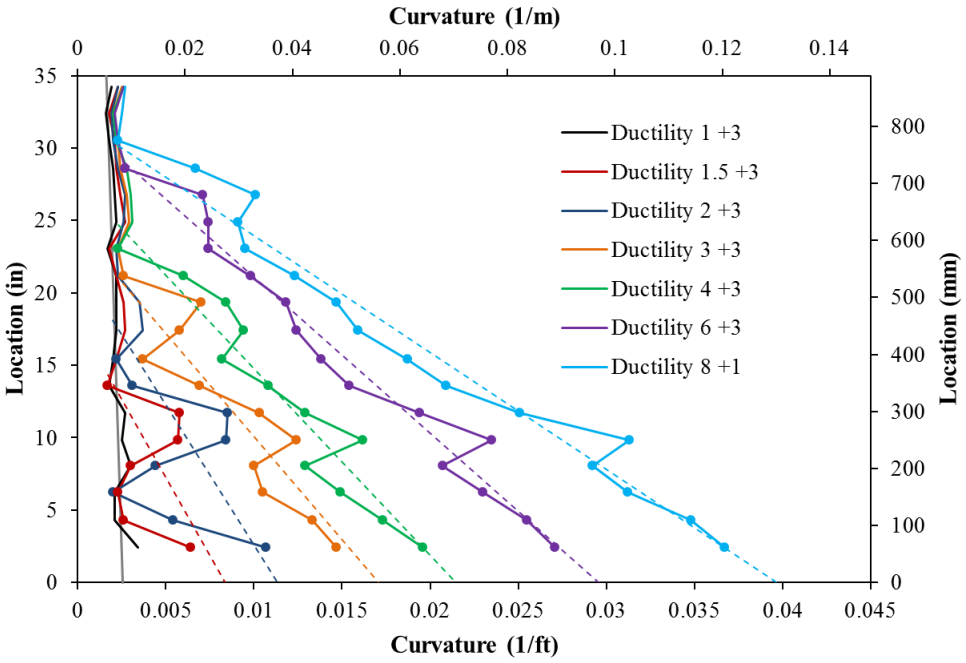

Figure 1.35 T9 – Push Cycle Curvature Profiles with Linear Plastic Dashed Regression

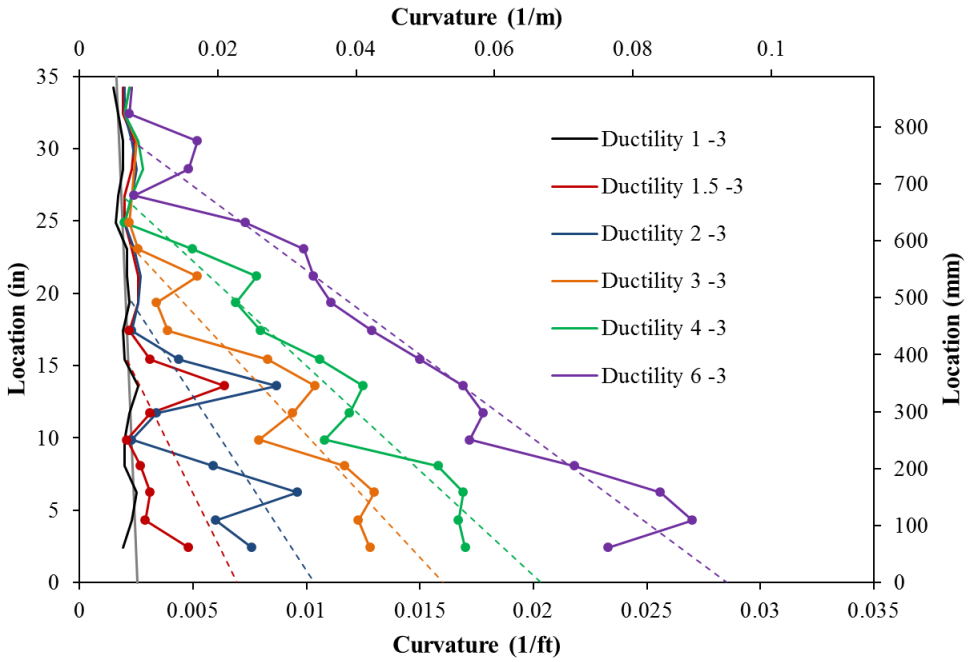

Figure 1.36 T9 – Pull Cycle Curvature Profiles with Linear Plastic Dashed Regression

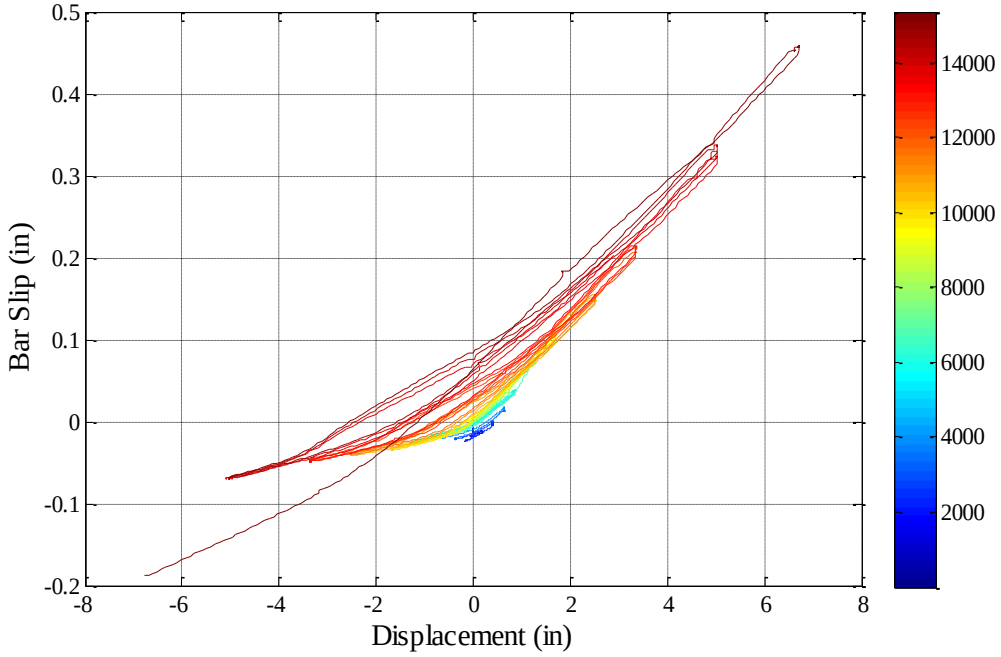

Figure 1.37 T9 – Bar N3 Base Section Slip Hysteresis due to Strain Penetration

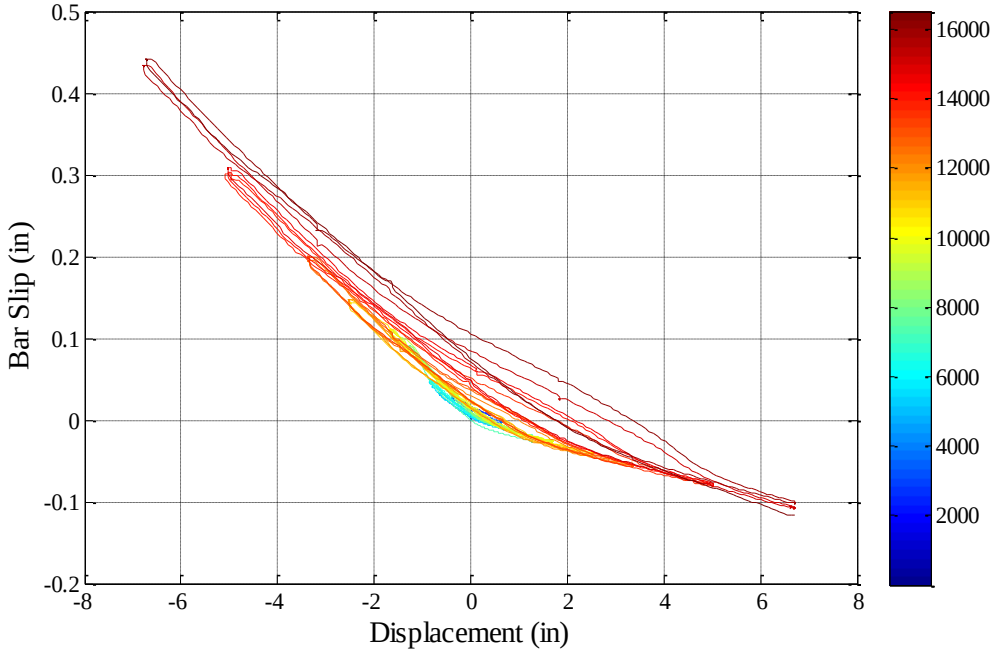

Figure 1.38 T9 – Bar S3 Base Section Slip Hysteresis due to Strain Penetration

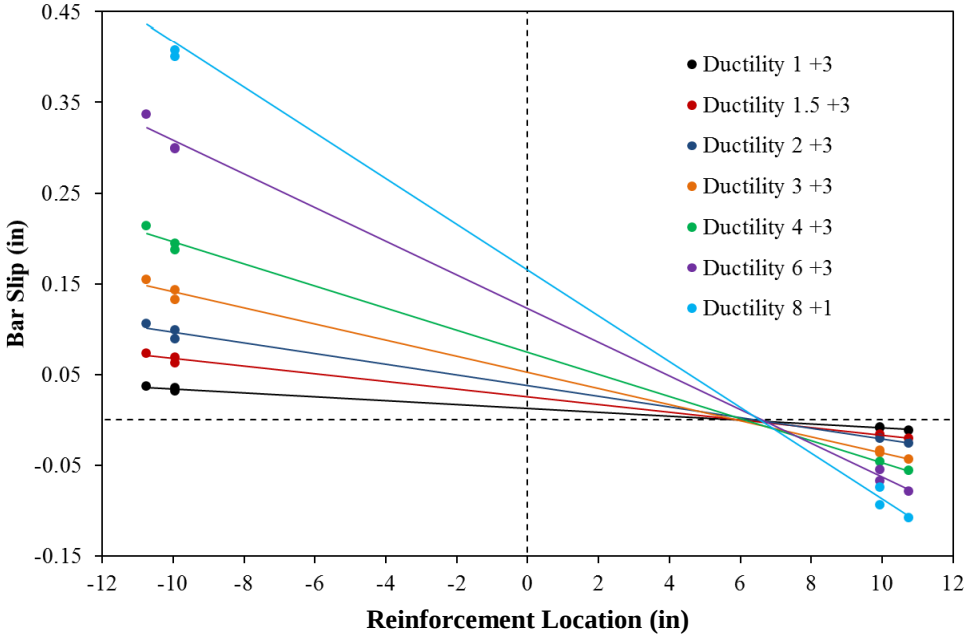

Figure 1.39 T9 – Base Section Rotation due to Strain Penetration during Push Cycles

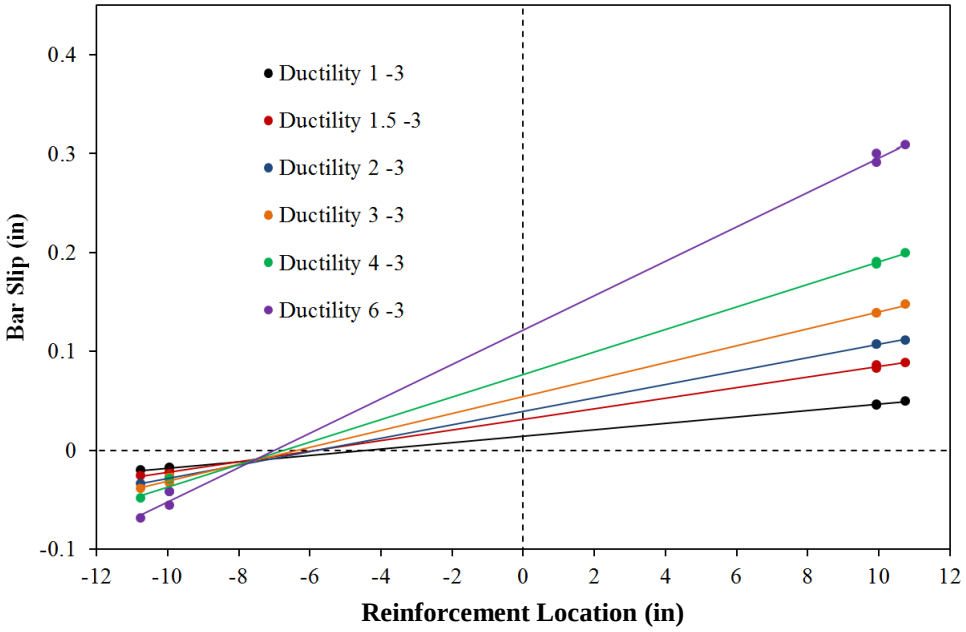

Figure 1.40 T9 – Base Section Rotation due to Strain Penetration during Pull Cycles

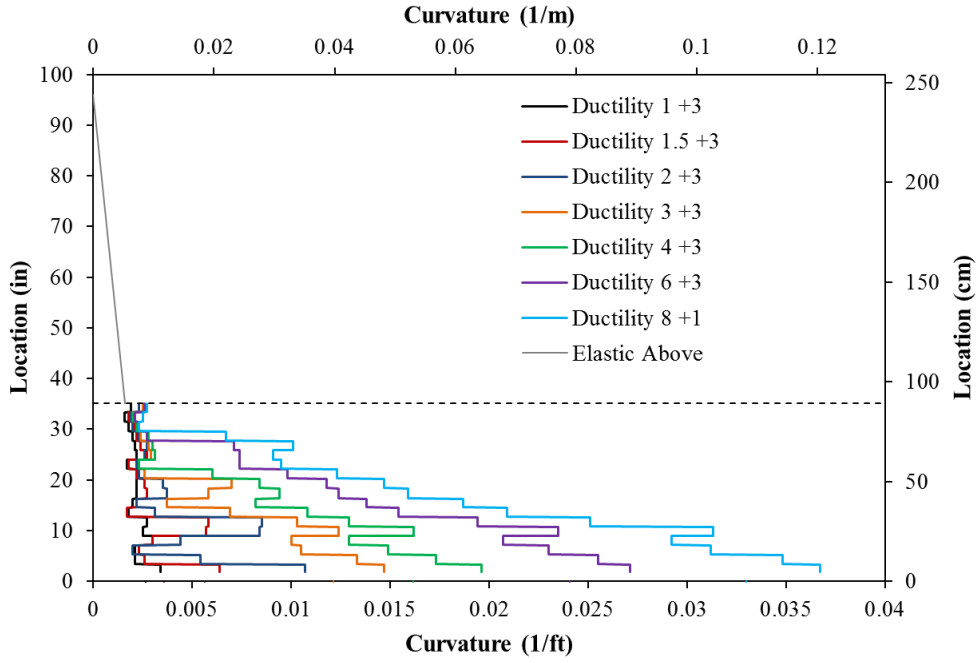

Figure 1.41 T9 – Integration Method for Flexural Displacements

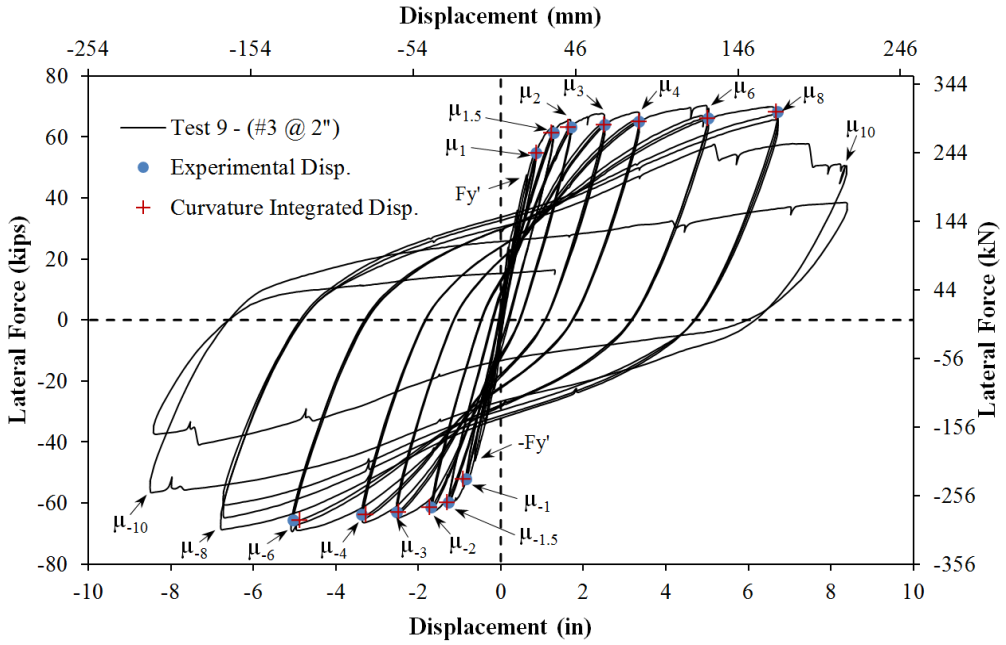

Figure 1.42 T9 – Comparison of String Potentiometer and Integrated Displacements

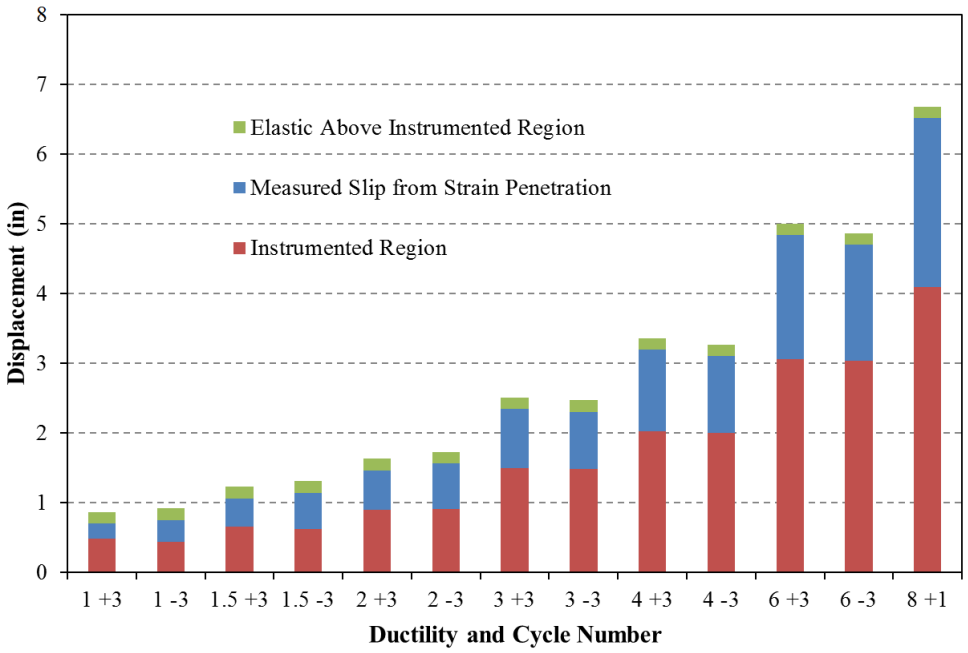

Figure 1.43 T9 – Components of Integrated Deformation

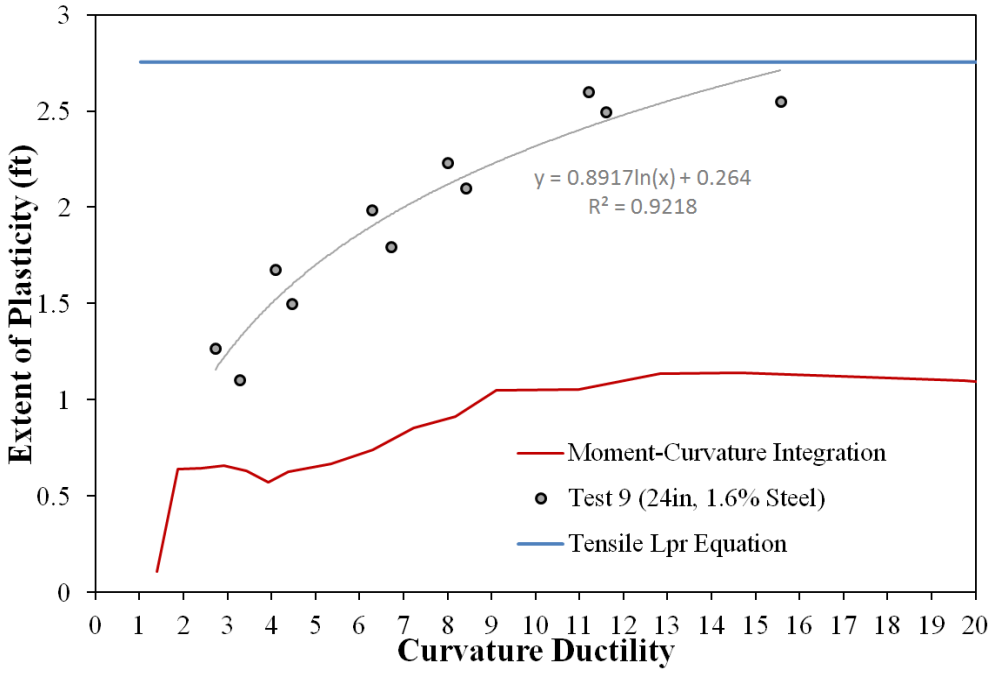

Figure 1.44 T9 – Measured Spread of Plasticity (Circle Data Points)

1.1.2 Tests 8 and 8b – Chile 2010 Earthquake and Cyclic Aftershock LH

Table 1.5 Observational Summary for Test 8 – Chile 2010 Earthquake Load History

VALUES OF INTEREST:	
Concrete Compressive Strength:	$f_c' = 6988\ psi$
Axial Load:	$P = 170\ kips$
Analytical First Yield Force:	$F_y' = 47.0\ kips$
Experimental First Yield Displacement:	$\Delta_y' = 0.63"$
Analytical Nominal Moment Capacity:	$M_n = 503.8\ kip * ft$
Equivalent Yield Displacement:	$\Delta_y = 0.84"$
Maximum Lateral Force:	$69.2\ kips$
Maximum Lateral Displacement:	$\mu_{8.7}^{26.34\ sec} = 7.25"$
Failure Mode:	No Significant Damage from Earthquake LH
DAMAGE OBSERVATIONS: During Chile 2010 Earthquake LH	
First Cracking North:	$\mu_{0.3}^{6.95\ sec} = 0.21"$
First Cracking South:	$\mu_{-0.2}^{7.14\ sec} = -0.20"$
Cover Concrete Crushing North:	*During cycle to $\mu_{-4.0}^{9.69\ sec} = -4.03"$
Cover Concrete Crushing South:	$\mu_{2.92}^{9.17\ sec} = 2.42"$
Transverse Steel Yield North:	At $-0.34"$ otwt $\mu_{-3.2}^{26.90\ sec} = -2.65"$
Transverse Steel Yield South:	At $5.98"$ otwt $\mu_{8.7}^{26.34\ sec} = 7.25"$

*$\mu_{8.7}^{26.34\ sec} = 7.25"$ represents a push cycle 26.34 seconds into the earthquake load history which reached a peak displacement of 7.25” and a displacement ductility of 8.7

Table 1.6 Observational Summary for Test 8b – Symmetric Three Cycle Set Aftershock LH

DAMAGE OBSERVATIONS: During Symmetric Three Cycle Set Post Earthquake LH	
Longitudinal Bar Buckling North:	Reversal from $\mu_8^{+1} = 6.64"$
Longitudinal Bar Buckling South:	Reversal from $\mu_8^{-1} = -6.65"$
Failure Mode:	Specimen Saved as a Repair Candidate after Each Extreme Fiber Longitudinal Bar Buckled

$*\mu_8^{+1} = 6.64"$ represents the first push cycle of displacement ductility eight

Table 1.7 Strain Data Summary for Test 8 and 8b – Chile 2010 Earthquake and Cyclic Aftershock LH

MATERIAL STRAINS:	
Cover Concrete Crushing North:	N/A, During cycle to $\mu_{-4.0}^{9.69\,sec} = -4.03"$
Cover Concrete Crushing South:	$\varepsilon_s = 0.006\ (compression)$
Transverse Steel Yield North:	N/A, Spiral Yielded during reversal from peak tensile. Not a function of compression strain.
Transverse Steel Yield South:	$\varepsilon_s = 0.0183\ (compression)$
Longitudinal Bar Buckling North:	$\varepsilon_s = 0.051\ (peak\ tension\ prior\ to\ bb)$
	$\varepsilon_s = 0.013\ (peak\ comp.\ prior\ to\ bb)$
Longitudinal Bar Buckling South:	$\varepsilon_s = 0.048\ (peak\ tension\ prior\ to\ bb)$
	$\varepsilon_s = 0.032\ (peak\ comp.\ prior\ to\ bb)$
Mander (1988) Ultimate Concrete Compression Strain, $\varepsilon_{cu} = 0.0172$	

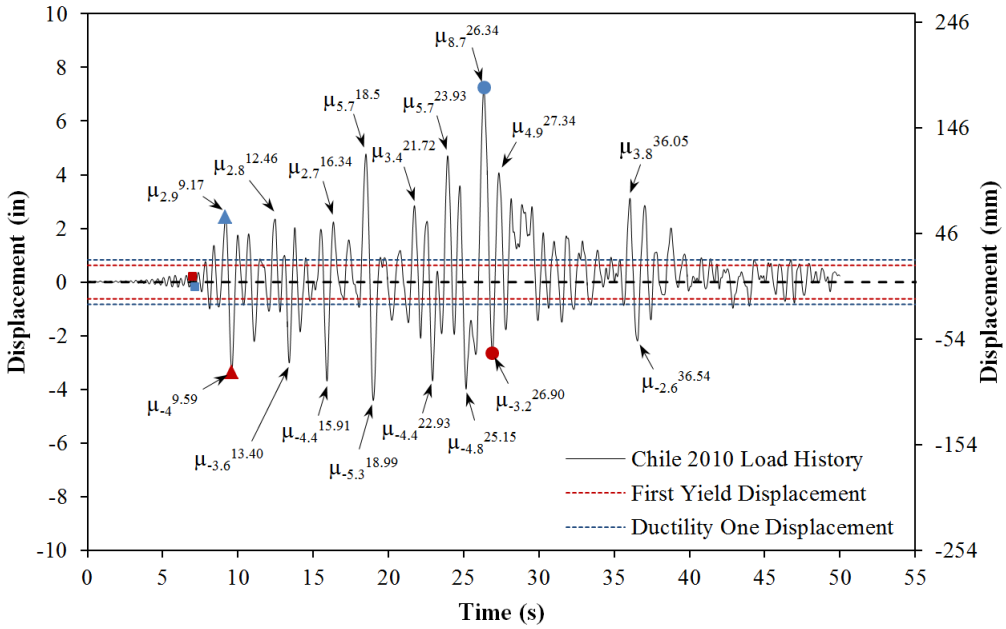

Figure 1.45 T8 – Chile 2010 Earthquake Load History

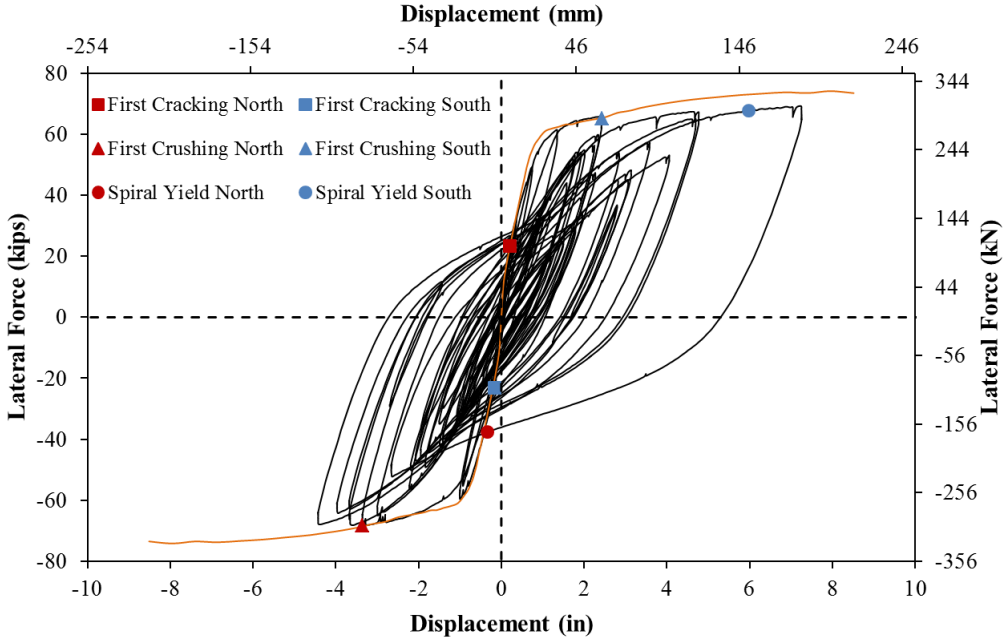

Figure 1.46 T8 – Chile 2010 Lateral Force vs. Top Column Displacement Response

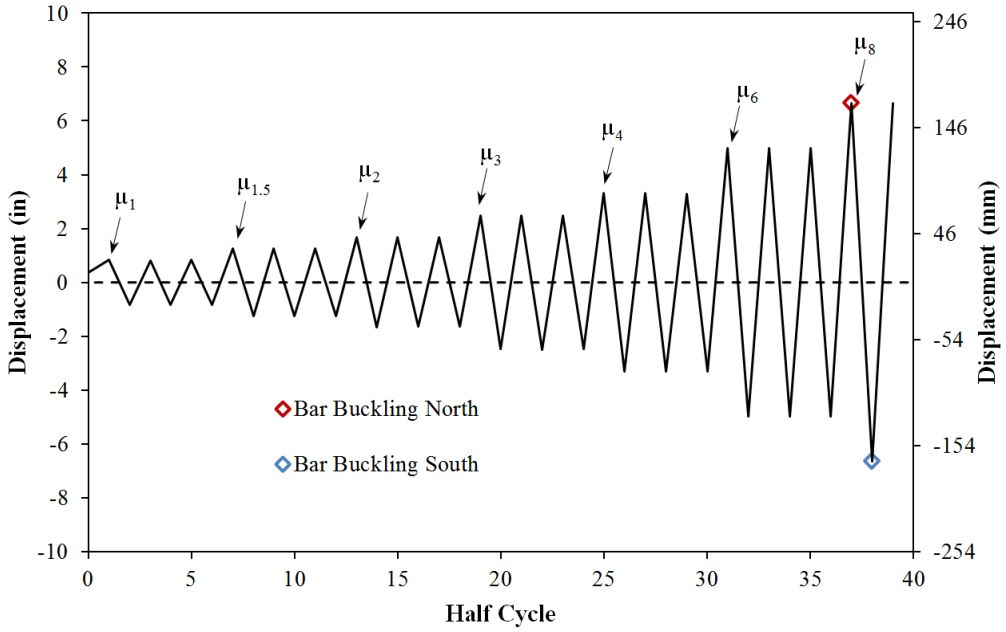

Figure 1.47 T8b – Symmetric Three Cycle Set Aftershock Load History

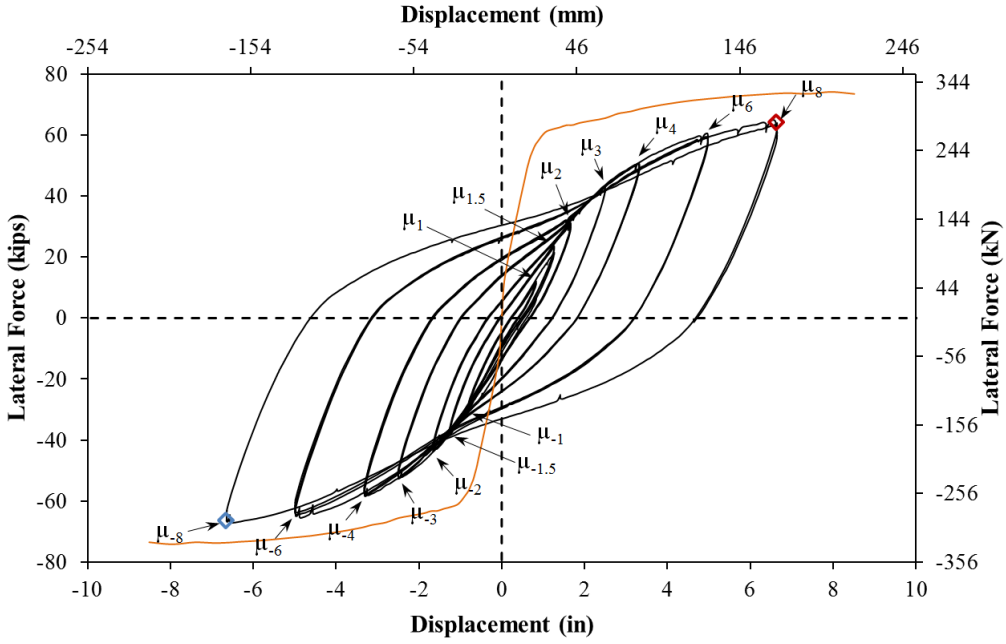

Figure 1.48 T8b – Cyclic Aftershock Hysteretic Response

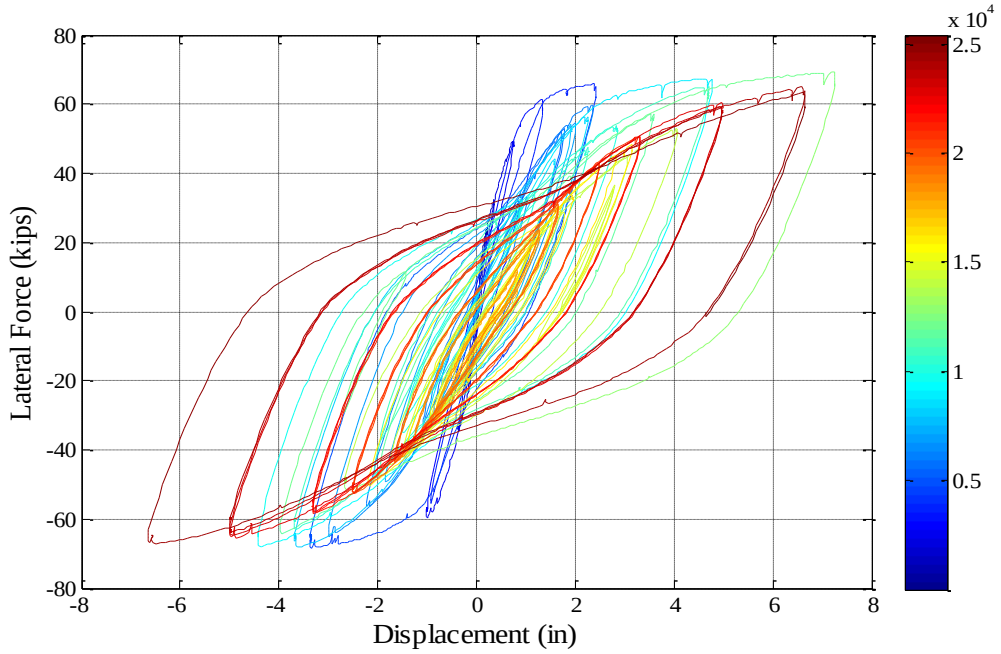

Figure 1.49 T8 and T8b – Hysteretic Response with Elapsed Time Color Bar

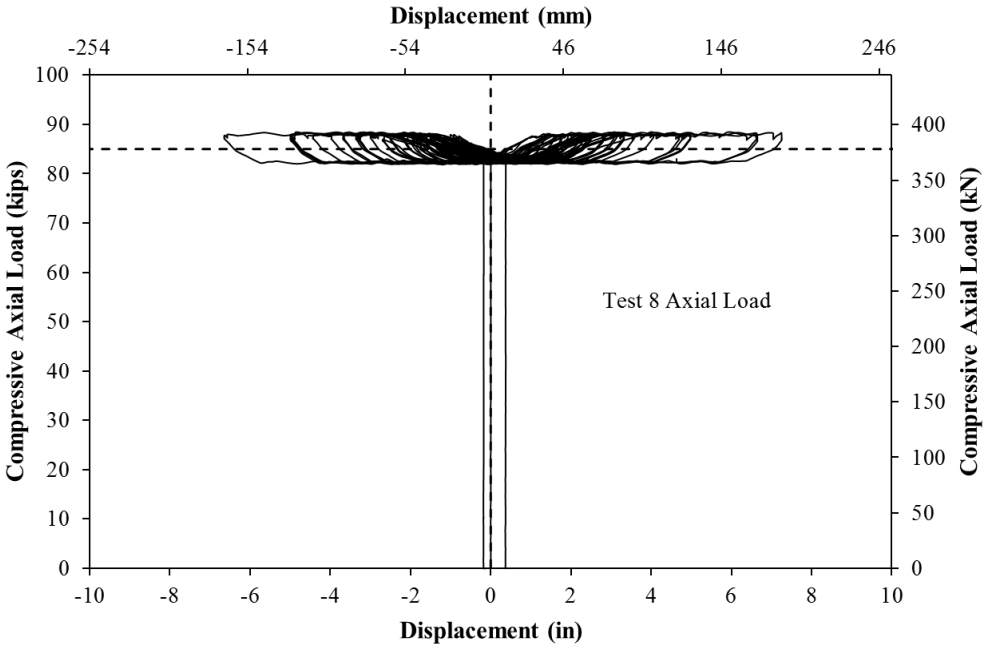

Figure 1.50 T8 and T8b – Compressive Axial Load from One Jack (Total = 2*Value)

Test 8 Chile 2010 Earthquake Load History:

Fiber based analytical modeling in OpenSees was used to determine the top column displacement history using a scaled version of the 2010 Chile earthquake. The acceleration values from the Chile time history were scaled until the peak displacement was equal to 7.25" as shown in Figure 1.45. This peak displacement was chosen based on engineering judgment and the results of the first six specimens. For the first six tests, a displacement ductility of ten produced buckling for specimens with transverse steel spacing in the plastic hinge region closest to 2". The Chile displacement history includes a large amount of high ductility reversals before the peak cycle. With the exception of the peak displacement cycle, the load history is symmetric with similar ductility demands in each direction.

The analytical displacement history has a series of small cycles within the first eight seconds. The experimental load history began during the first cycle which exceeded the displacement at half yield from Test 7 (same as Test 9). Since the concrete begins to crack around half yield, leaving out smaller cycles at the beginning of the load history should not impact the response. Every intermediate cycle in the analytical displacement history was matched in the experimental test from 6.95sec to 39.24sec when the last meaningful cycle past ductility one was concluded. The displacement history was recreated in the lab using a displacement controlled quasi-static loading procedure with displacement rates below 6 in/min.

The resulting experimental lateral force vs. displacement response for the Chile 2010 earthquake record appears in Figure 1.46. The Chile load history scaled to a peak displacement of 7.25" was concluded without buckling of reinforcement on either side of the specimen and without any loss of strength. A symmetric three cycle set aftershock study was then conducted to determine when reinforcement buckling would occur in a column with degraded stiffness and strain accumulation, but without loss of strength. The cyclic aftershock load history and hysteretic response appear in Figure 1.47 and Figure 1.48 respectively. The entire response for the column including both load histories is shown in Figure 1.49 with an elapsed time colorbar to track the progression of the experiment.

Test 8 Chile 2010 Earthquake Load History – Experimental Observations:

The first cracks on the North side of the specimen were measured at 0.1mm during ($\mu_{0.3}^{6.95\,sec} = 0.21"$). The cycle annotation represents a push cycle 6.95 second into the Chile load history to 0.21", which is equivalent to displacement ductility 0.3. During the next cycle, the South side of the specimen had cracks measuring 0.1mm at ($\mu_{-0.2}^{7.14\,sec} = -0.17"$). Cracks on the South side of the specimen measured 0.75mm at approximate 6" spacing during ($\mu_{-1.2}^{8.12\,sec} = -1.00"$), see Figure 1.51. Cracks on the North side of the specimen measured 1mm at approximate 5" spacing during ($\mu_{1.6}^{8.40\,sec} = 1.35"$). The first signs of cover concrete crushing over the bottom 5" of the South side of the column occurred during ($\mu_{2.9}^{9.17\,sec} = 2.42"$), as shown in Figure 1.52, while cracks on the tension side of the column were measured at 1/8" with approximate 4" spacing. Crushing of the cover concrete on the North side of the specimen extended 15" above the top of the footing during ($\mu_{-4.0}^{9.59\,sec} = -3.35"$) while cracks on the tension side measured 1/8", Figure 1.52. Crushing on the south side of the specimen reached 12" above the footing during ($\mu_{2.2}^{14.13\,sec} = -1.84"$), Figure 1.53. The crack Distribution on the front shear face of the specimen during the largest pull cycle to ($\mu_{5.3}^{18.99\,sec} = -4.43"$) appears in Figure 1.53.

The peak displacement of ($\mu_{8.7}^{26.34\,sec} = 7.25"$) from the scaled Chile 2010 load history was reached with a lateral force of 69.18 kips. Photos of extreme fiber regions of the column at the peak displacement are shown in Figure 1.54. During subsequent reversals of loading the reinforcement remained visibly straight. Bar buckling or rupture did not occur, therefore, the load history was completed with degraded stiffness but no large losses in strength.

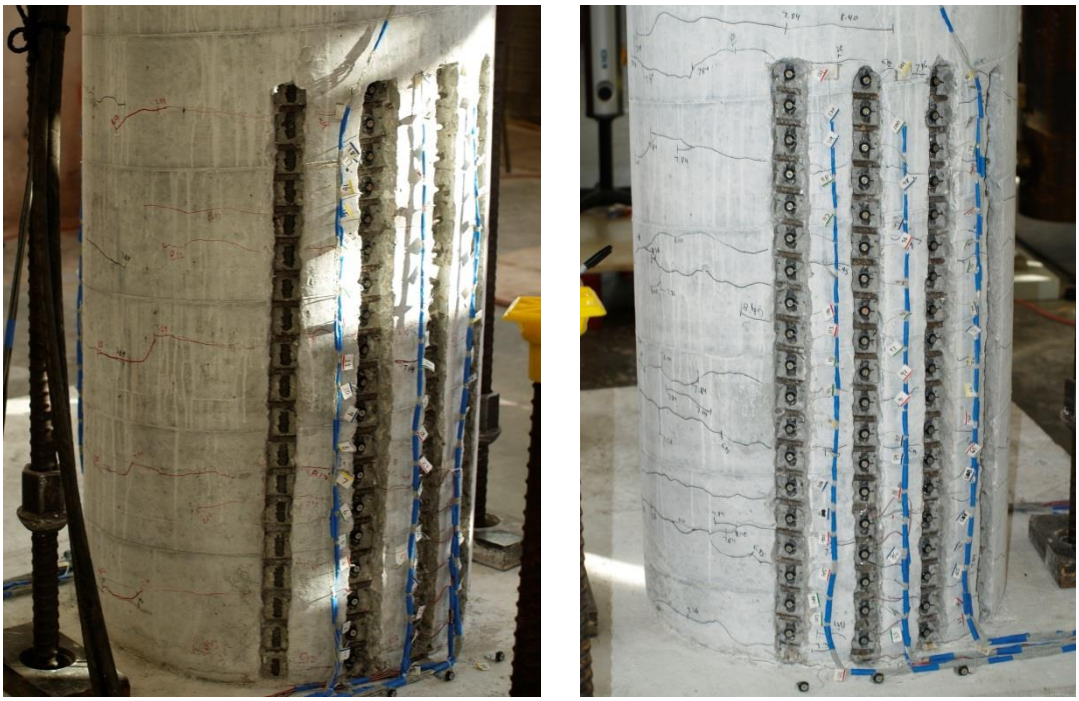

Figure 1.51 T8 – Crack Patterns on the (Left) South Side at ($\mu_{-1.2}^{8.12\,sec} = -1.00$") and (Right) North Side at ($\mu_{1.6}^{8.40\,sec} = 1.35$")

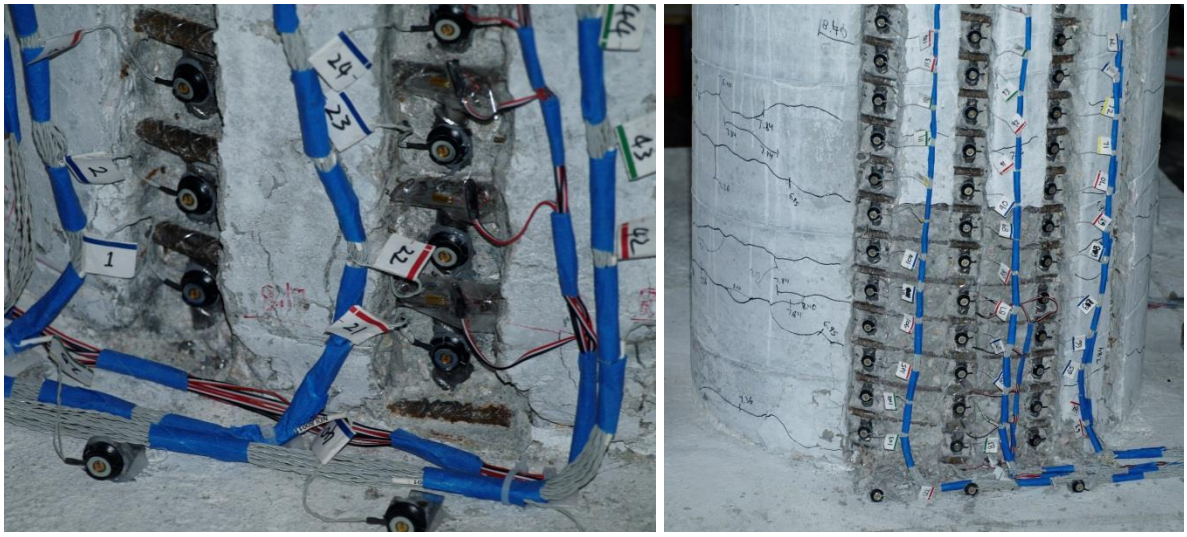

Figure 1.52 T8 – Crushing on the (Left) South Side at ($\mu_{2.9}^{9.17\,sec} = 2.42$") and (Right) North Side at ($\mu_{-4.0}^{9.59\,sec} = -3.35$")

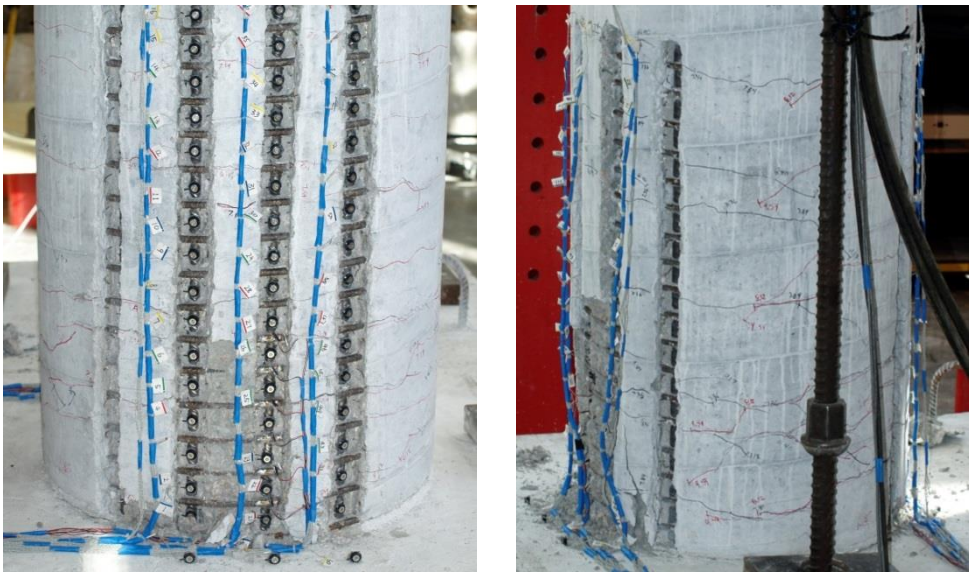

Figure 1.53 T8 – (Left) South Crack Distribution at ($\mu_{2.2}^{14.13\ sec} = -1.84$") and (Right) Front of the Specimen during ($\mu_{5.3}^{18.99\ sec} = -4.43$")

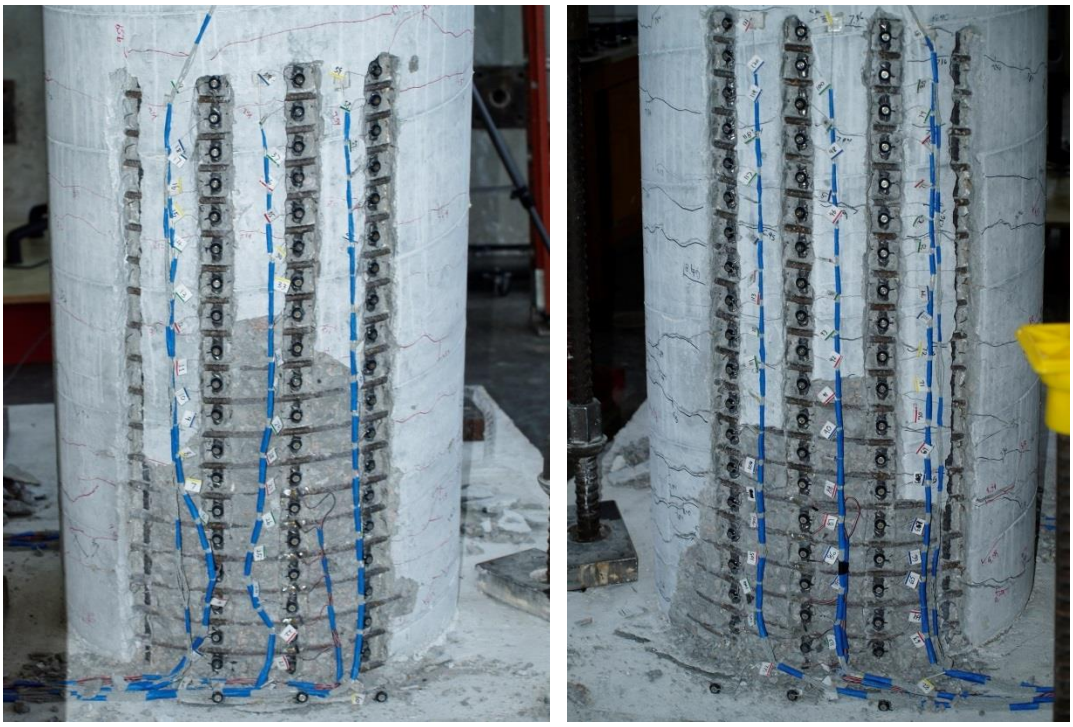

Figure 1.54 T8 – Peak Displacement ($\mu_{8.7}^{26.34\ sec} = 7.25$") (Left) South & (Right) North

Test 8 Chile 2010 Earthquake Load History – Strain Data Analysis:

Due to the random cyclic nature of the earthquake load histories, specific observation points along the backbone curve of cyclic response were chosen for data analysis in Figure 1.55. The tensile and compressive vertical strain profiles for bar S3 appear in the right half of Figure 1.57 and the left half of Figure 1.56 respectively. The transverse steel strains in the lowest six spiral layers for the South and North extreme fiber regions in compression appear in Figure 1.58 and Figure 1.59. A peak tension strain of 0.031 was measured 2.02" above the footing on bar S3 during ($\mu_{-5.3}^{18.99\,sec} = -4.42"$). The relationship between tensile strain and displacement for this gage length appears in Figure 1.62. The maximum compression strain of -0.02 in reinforcing bar S3 occurred 5.75" above the footing during ($\mu_{8.7}^{26.34\,sec} = 7.25"$). The relationship between compression strain and displacement for bar S3 for this gage length appears in Figure 1.63.

Vertical strain profiles for extreme fiber bar N3 appear in Figure 1.56 and Figure 1.57 for push tension strains and pull compression strains respectively. The largest tensile strain of 0.051, located 2.09" above the footing, was measured on bar N3 at ($\mu_{8.7}^{26.34\,sec} = 7.25"$). The relationship between tensile strain and displacement for this gage length appears in Figure 1.60. The error in strain prediction by moment curvature analysis with the PCK (2007) hinge method becomes larger with increasing displacement. The largest compression strain value of -0.013 for extreme fiber bar N3 occurred 5.85" above the footing at ($\mu_{-5.3}^{18.99\,sec} = -4.42"$). The relationship between compression strain and displacement for significant pull cycles, 5.85" above the footing, for bar N3 appears in Figure 1.61.

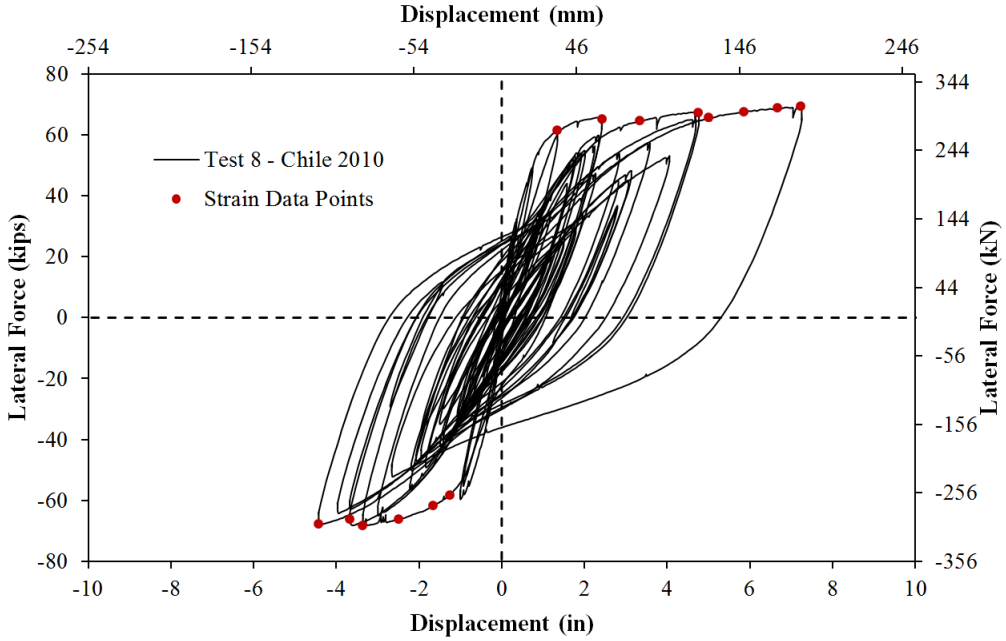

Figure 1.55 T8 – Strain Data Observation Points along the Envelope Curve

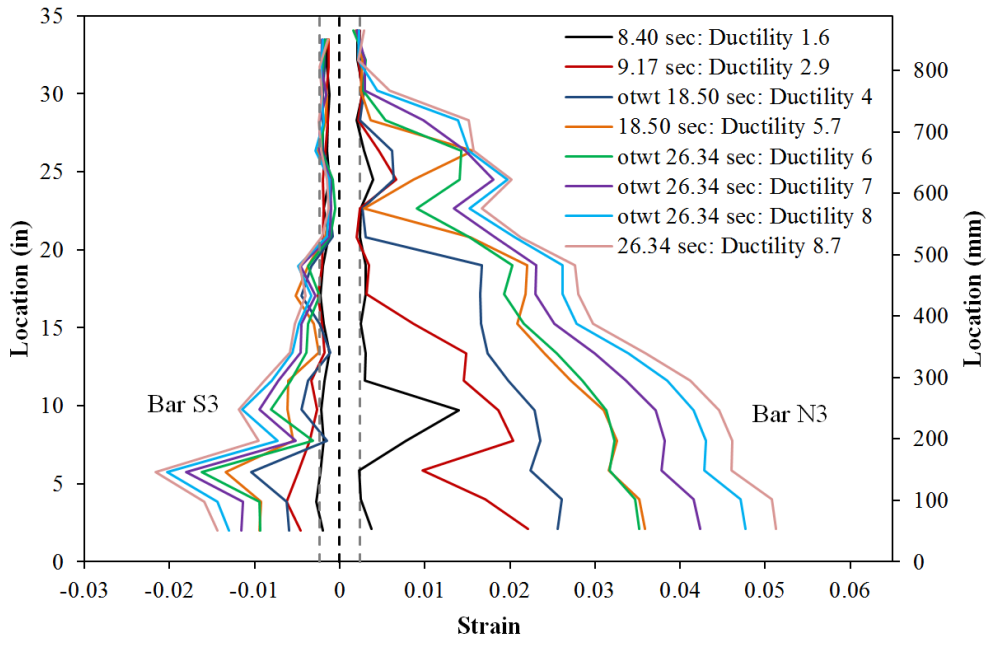

Figure 1.56 T8 – Extreme Fiber Vertical Strain Profiles during Push Cycles

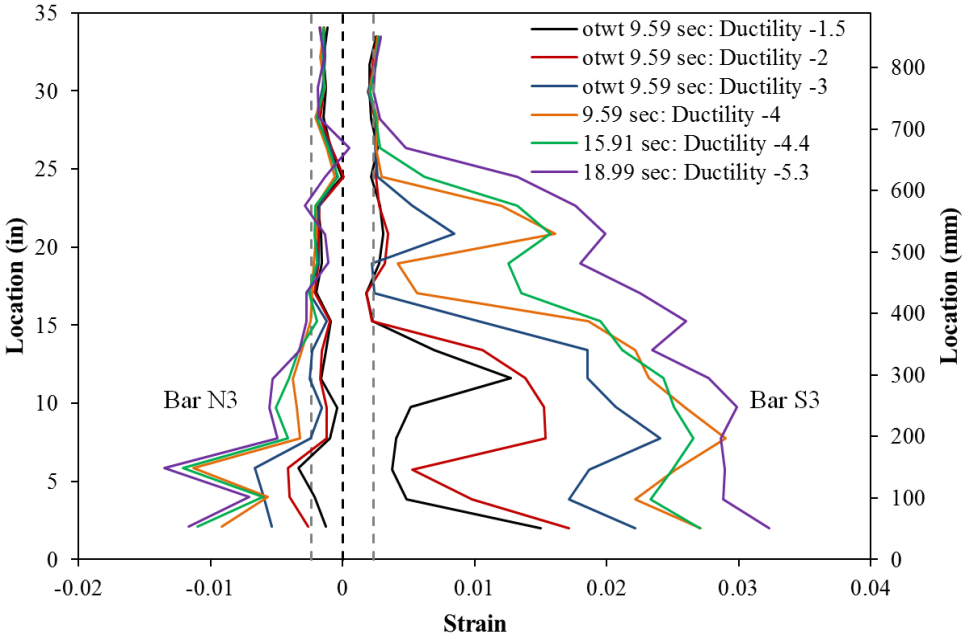

Figure 1.57 T8 – Extreme Fiber Vertical Strain Profiles during Pull Cycles

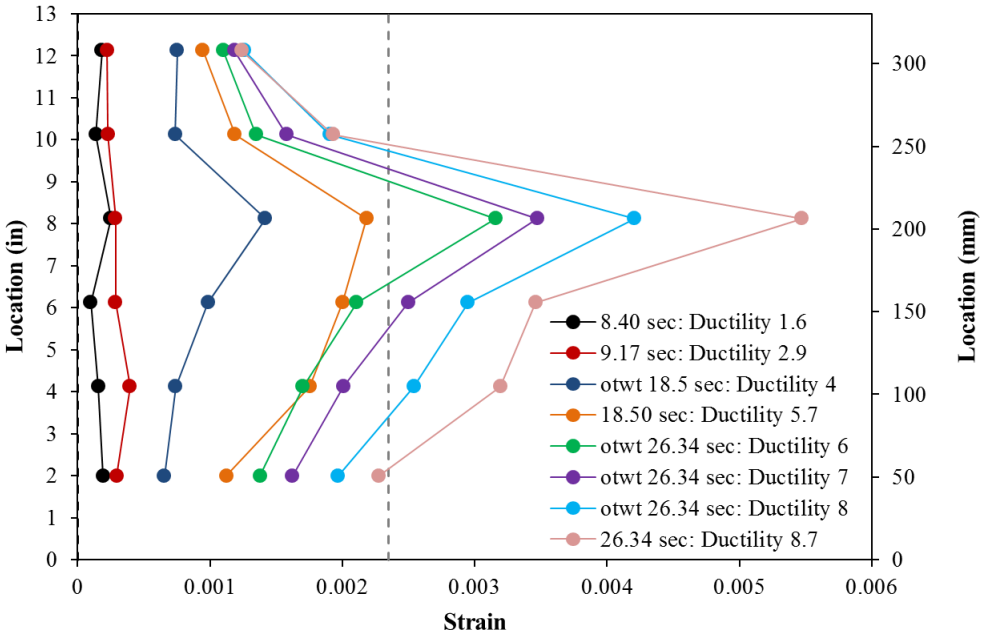

Figure 1.58 T8 – Transverse Steel Strains over the South Extreme Fiber Bar S3

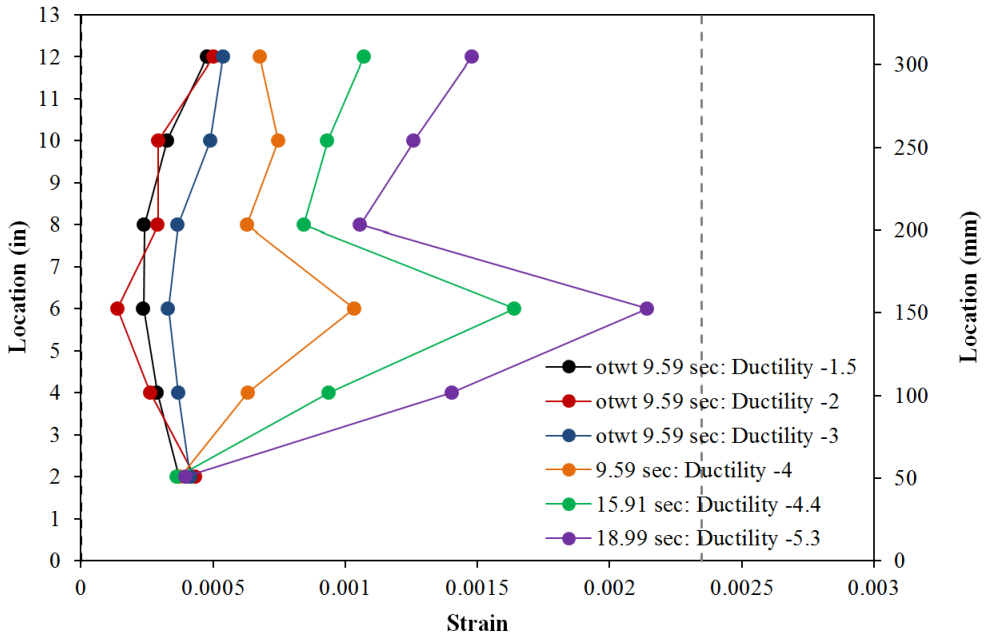

Figure 1.59 T8 – Transverse Steel Strains over the North Extreme Fiber Bar N3

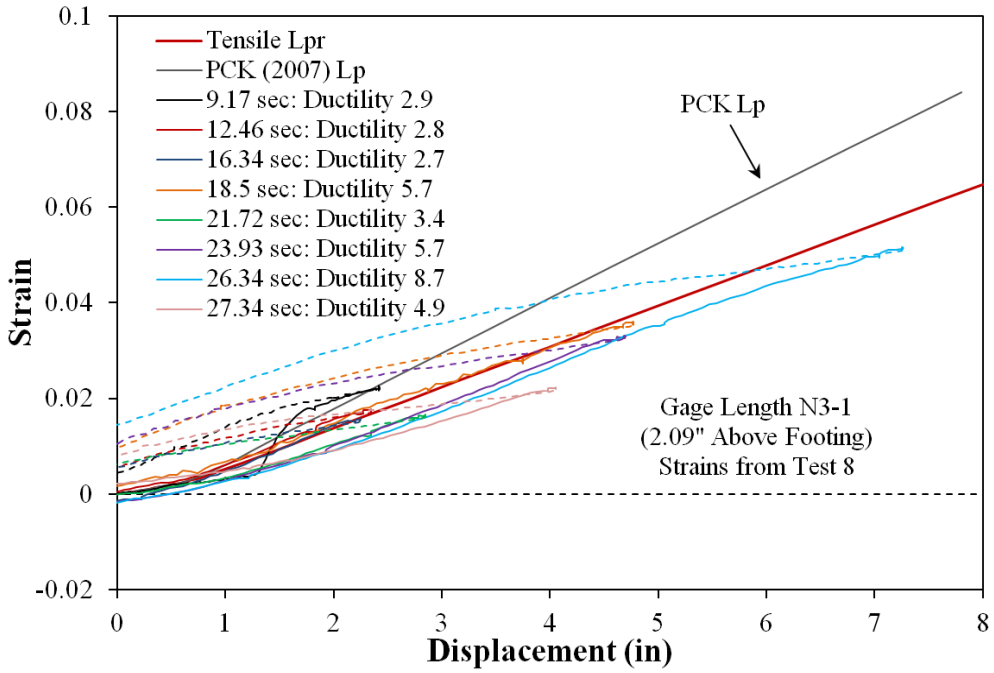

Figure 1.60 T8 – Tension Strain-Displacement for Bar N3 during Push Cycles

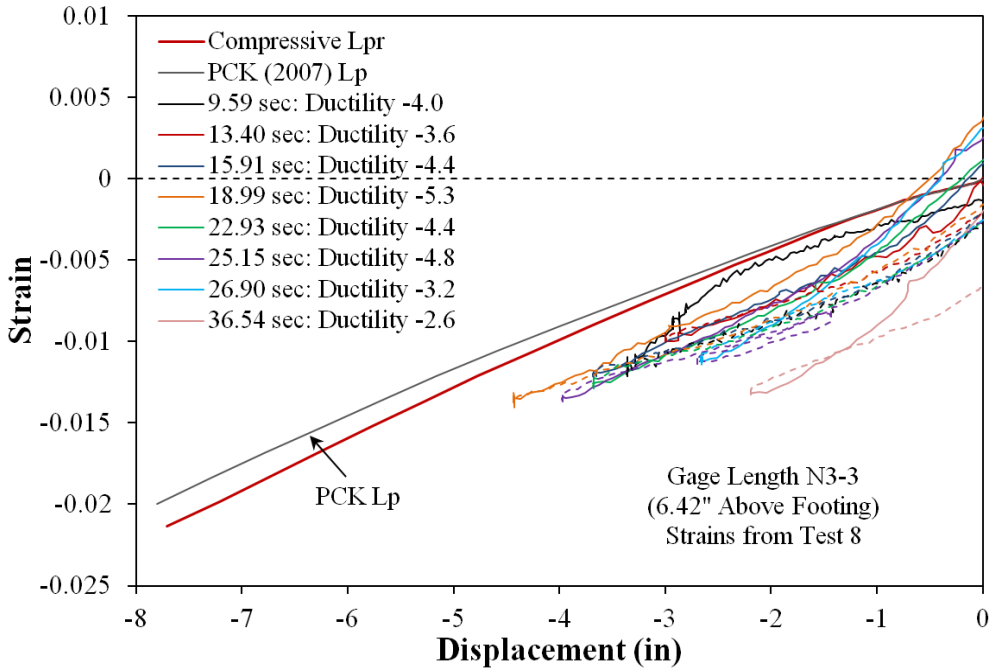

Figure 1.61 T8 – Compression Strain-Displacement for Bar N3 during Pull Cycles

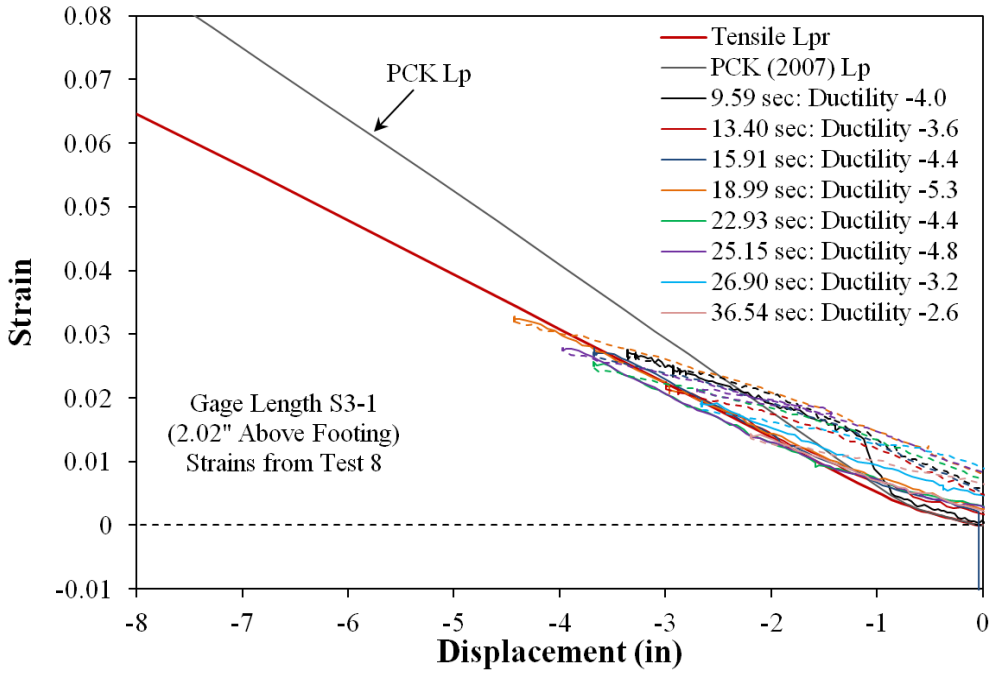

Figure 1.62 T8 – Tensile Strain-Displacement for Bar S3 during Pull Cycles

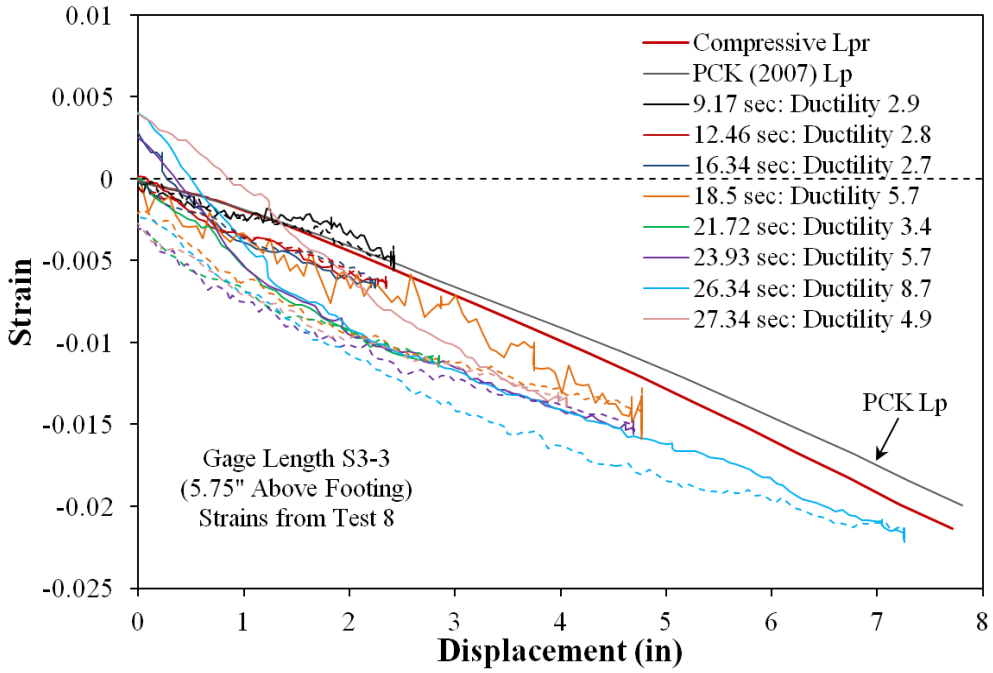

Figure 1.63 T8 – Compressive Strain-Displacement for Bar S3 during Push Cycles

Test 8 Chile 2010 Earthquake Load History – Strain Penetration and Curvature Data:

The vertical strain profiles for observation points along the backbone curve of cyclic response, see Figure 1.55, for push and pull cycles appear in Figure 1.64 and Figure 1.65. The slip hysteresis for extreme fiber bars N3 and S3 due to strain penetration of the reinforcement into the footing appear in Figure 1.78 and Figure 1.79 respectively. The slip hystereses contained data from the Chile and Cyclic Aftershock load histories up until each reinforcing bar buckled. The base section rotation attributable to strain penetration of reinforcing bars appears in Figure 1.66 and Figure 1.67 for push and pull cycles respectively. The total deformation calculated by integrating the measured curvature profiles and extrapolating the base section rotation to the center of loading appear in Figure 1.68. The integrated curvatures match well throughout the entire range of response. Circle data points in Figure 1.69 track the spread of plasticity as a function of curvature ductility for the measured curvature profiles.

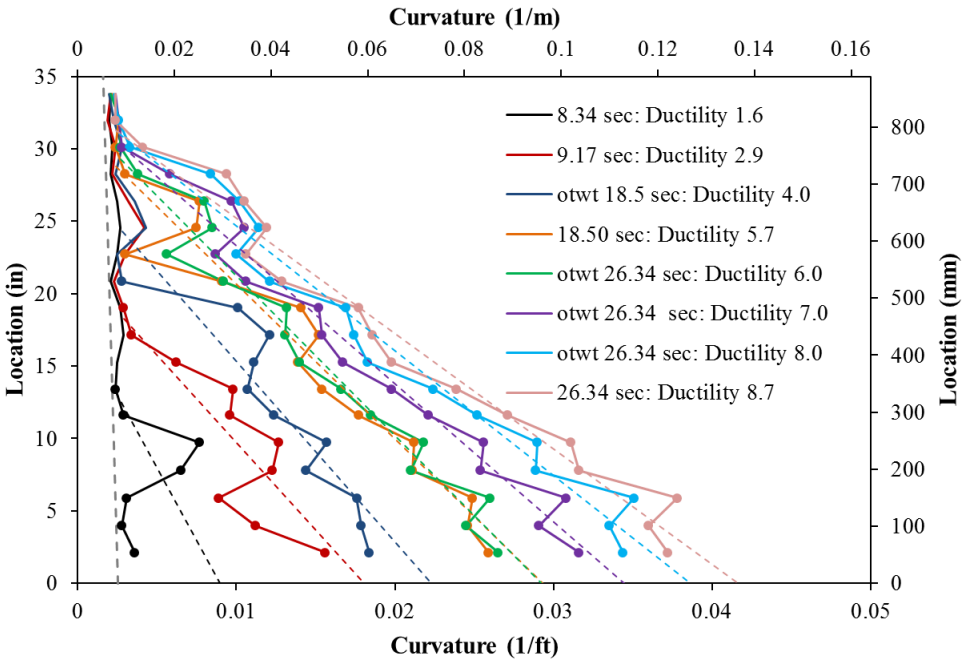

Figure 1.64 T8 – Push Cycle Curvature Profiles with Linear Plastic Dashed Regression

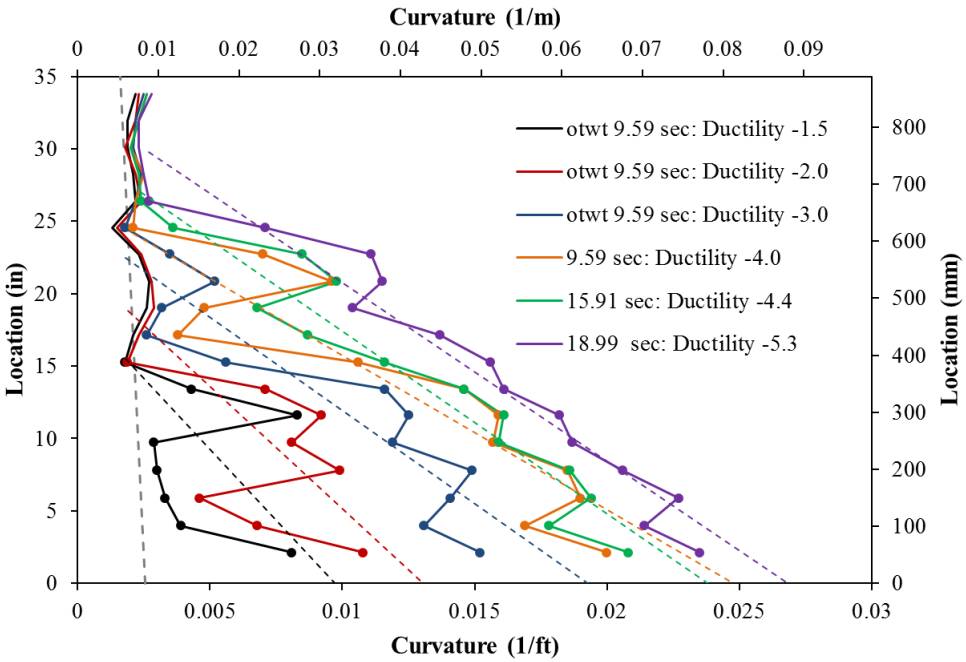

Figure 1.65 T8 – Pull Cycle Curvature Profiles with Linear Plastic Dashed Regression

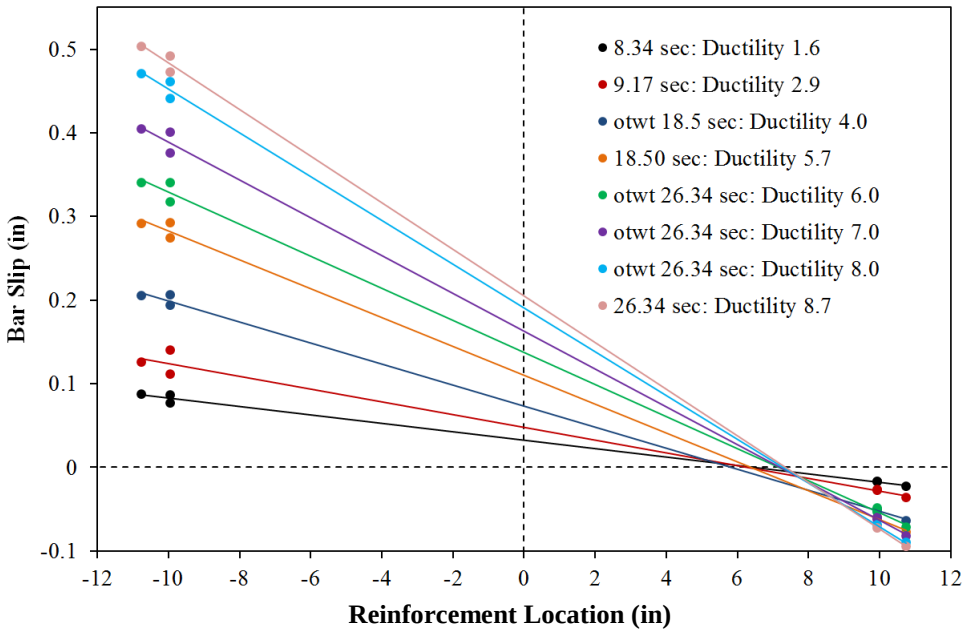

Figure 1.66 T8 – Base Section Rotation due to Strain Penetration during Push Cycles

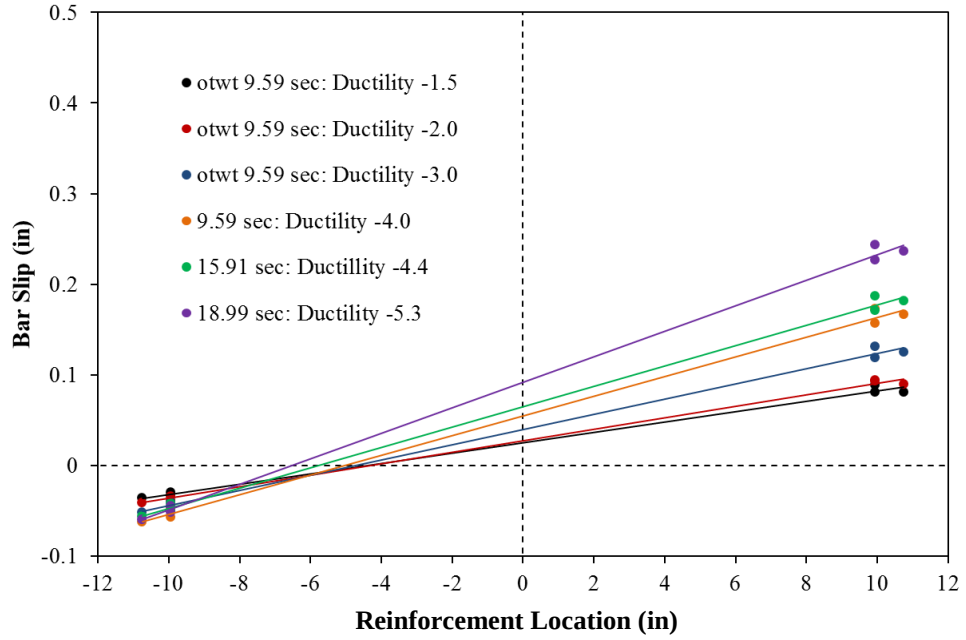

Figure 1.67 T8 – Base Section Rotation due to Strain Penetration during Pull Cycles

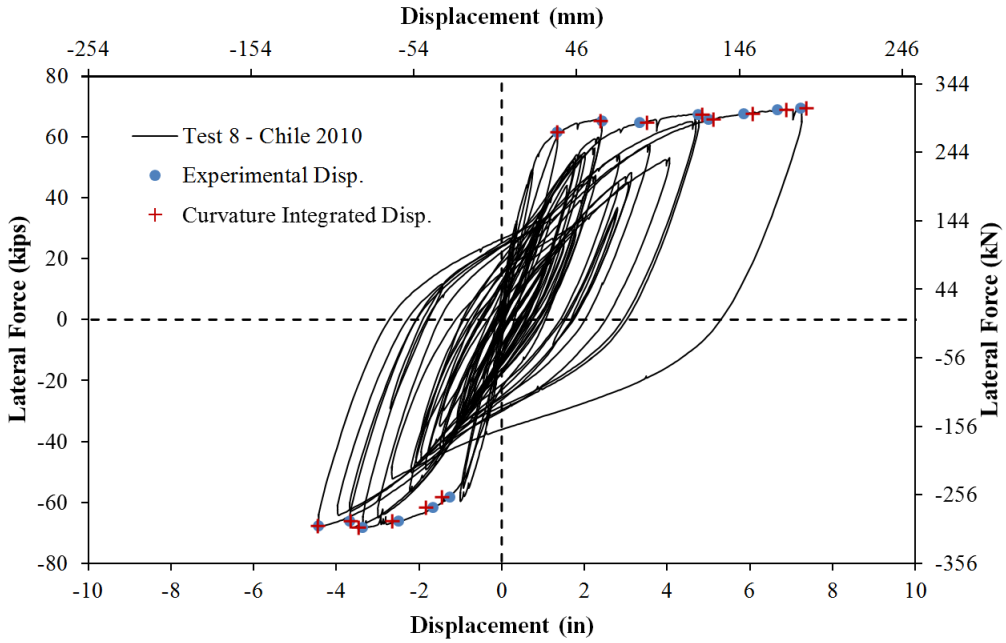

Figure 1.68 T8 – Comparison of Integrated and Measured Lateral Displacements

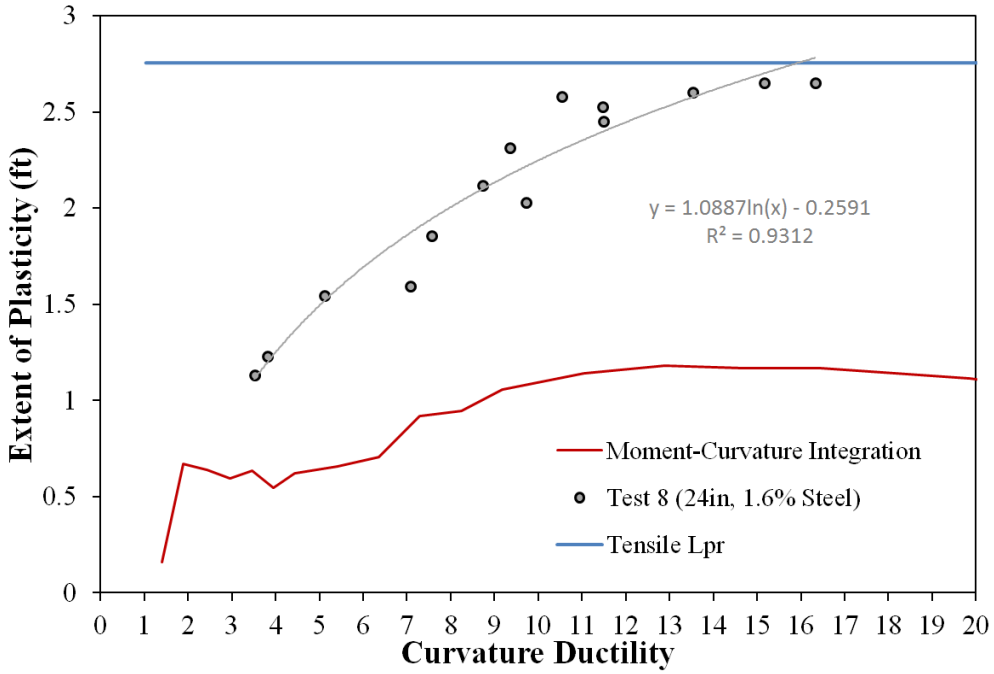

Figure 1.69 T8 – Measured Spread of Plasticity (Circle Data Points)

Test 8b Symmetric Three-Cycle-Set Aftershock LH – Experimental Observations:

Since the Chile load history scaled to a peak displacement of 7.25" was concluded without buckling reinforcement on either side of the specimen, a symmetric three-cycle-set aftershock study was then conducted to determine when buckling would occur to the column with degraded stiffness and accumulated strains. The top column displacement history and resultant force vs. displacement response for the cyclic aftershock study appear in Figure 1.47 and Figure 1.48 respectively. The complete hysteretic response for Tests 8 and 8b appears in Figure 1.49 with a color bar which represents elapsed time during the experiment. Since the largest cycle in the Chile load history exceeded the peak displacement of the aftershock study in the push direction, there is more strength degradation in the push direction of loading.

The symmetric three-cycle-set load history progressed through ductility six without incident. After the North reinforcement was exposed to tension during ($\mu_8^{+1} = 6.64"$), the extreme fiber bar N3 buckled over the first and second gage lengths during the subsequent reversal, as shown in Figure 1.70. Remember that the North reinforcement had already been subjected to larger displacements placing the bars in tension during ($\mu_{8.7}^{26.34} = 7.25"$) in the Chile load history. After being exposed to tension during ($\mu_8^{-1} = -6.65"$), extreme fiber bar S3 buckled over the first and fourth gage lengths as shown in Figure 1.70. The experiment was concluded with buckled reinforcement on each side of the specimen to save the column as a repair candidate. A photo of the damaged regions of the column after removal of the instrumentation appears in Figure 1.71.

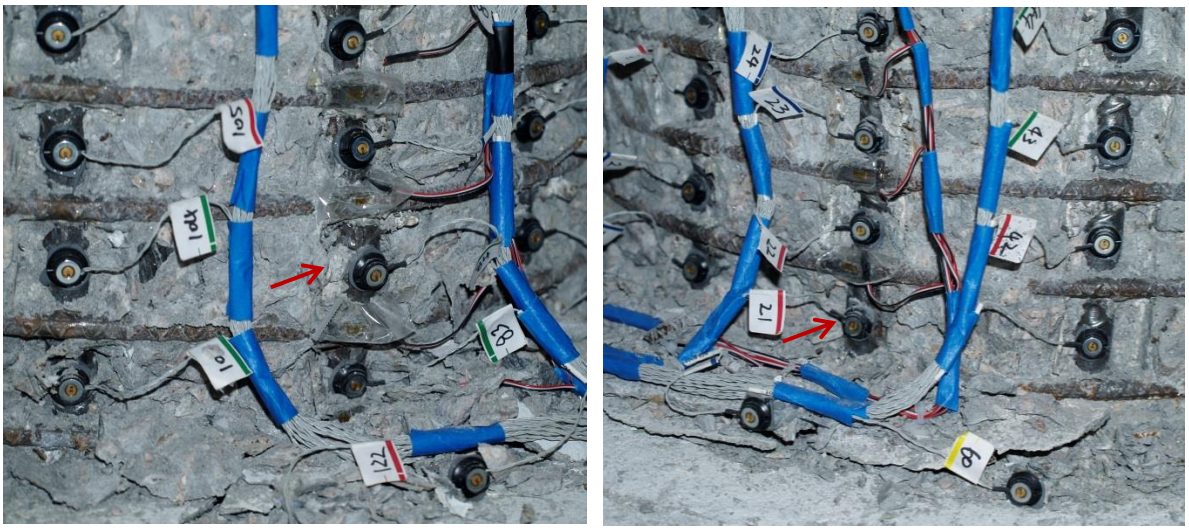

Figure 1.70 T8b – (Left) Buckling of Bar N3 after Reversal from ($\mu_8^{+1} = 6.64$") and (Right) Buckling of Bar S3 after Reversal from ($\mu_8^{-1} = 6.65$")

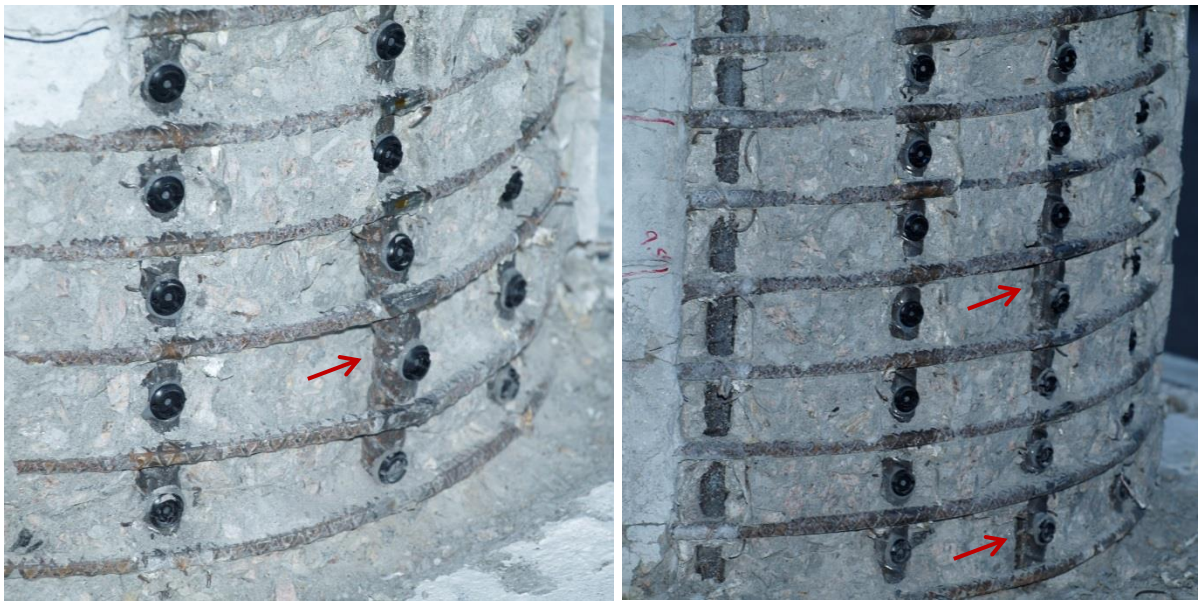

Figure 1.71 T8b – (Left) Buckling of N3 after Experiment and (Right) Buckling of S3

Test 8b Symmetric Three-Cycle-Set Aftershock LH – Strain Data Analysis:

Extreme fiber vertical strain profiles for push and pull cycles of the symmetric three cycle set aftershock load history are shown in Figure 1.72 and Figure 1.73 respectively. The strain profiles shape is controlled by the crack distribution set in place during high ductility cycles of the original Chile load history. The compressive vertical strain profiles for each extreme fiber reinforcing bar show significant deformation prior to visible bar buckling. If the reinforcing bar where to outwardly deform, the gage length over the deformation would increase in tensile strain while the gage lengths above and below would further increase in compressive strain. The strain values measured when this deformation occurred do not represent engineering strains, but they are shown to highlight the progression of damage.

South Reinforcement:

Visible buckling of Bar S3 was not observed until the second push cycle of ductility eight. The South reinforcing bar buckled over the first and fourth gage lengths, see Figure 1.71, which matches the problematic areas of the compressive vertical strain profile in Figure 1.72. The tension strain sustained by bar S3 prior to visible buckling during the aftershock study was 0.048, for the gage length 2.02" above the footing, during ($\mu_8^{-1} = 6.65"$). The largest strain sustained by bar S3 during the Chile load history was 0.032 located 2.02" above the footing at ($\mu_{-5.3}^{18.99\,sec} = -4.42"$).

The complete strain hysteresis for extreme fiber bar S3 appears in Figure 1.76 for the gage length 7.76" above footing in the upper buckled region. The strain hysteresis obtained from a strain gage located on the transverses steel overlaying the upper buckled region of bar S3 appears in Figure 1.77. The strains in bar S3 increase during each successive push cycle of ductility six during the aftershock study even though visible buckling was not observed. For the second and third push cycles of ductility six the peak strain increases with each successive cycle indicating measureable deformation prior to buckling. The trend continues as the first push cycle of ductility eight produces an even larger tensile strain in the South reinforcement even though this region should be in compression during push cycles. The

tension strain during push cycles becomes much larger after reversal from ($\mu_8^{-1} = 6.65$"), which coincides with visible buckling of bar S3. When buckling occurs, the reinforcing bar places additional demand on the transverse steel, which can be seen in Figure 1.77. During each successive cycle of ductility six the measured strains on the transverse steel in the upper buckled region of bar S3 become larger. During the first push cycle of ductility eight, prior to visible buckling, the strain in the transverse steel sharply increases to the point where the strain gage goes off scale preventing further measurement. The longitudinal and transverse strain hystereses show that buckling may be a more gradual process with measurable deformation prior to visible buckling.

North Reinforcement:

The extreme fiber bar N3 was exposed to 0.043 during ($\mu_8^{+1} = 6.64$") which is less than the strain which occurred during the largest cycle of the Chile load history 0.051 at ($\mu_{8.7}^{26.34\,sec} = 7.25$"). The compressive strain vertical profile in Figure 1.73 for bar N3 during pull cycles shows measurable deformation during ($\mu_6^{-3} = -4.99$") before visible buckling. The complete strain hysteresis, for the same gage length 4.02" above the footing on bar N3 is shown in Figure 1.74. After each successive pull cycle of ductility six the deformation in the buckled region of bar N3 increases, as indicated by positive strain when the reinforcement should be in compression. Similarly, the strain rises sharply after reversal from ($\mu_8^{+1} = 6.64$") when visible buckling was observed. The transverse steel strain hysteresis over the buckled region of bar N3 is shown in Figure 1.75. Again, each cycle of ductility six produces a greater strain demand on the transverse steel which is restraining bar N3. After reversal from ($\mu_8^{+1} = 6.64$"), when the bar visibly buckled, the transverse steel strain gage goes off scale preventing further measurement.

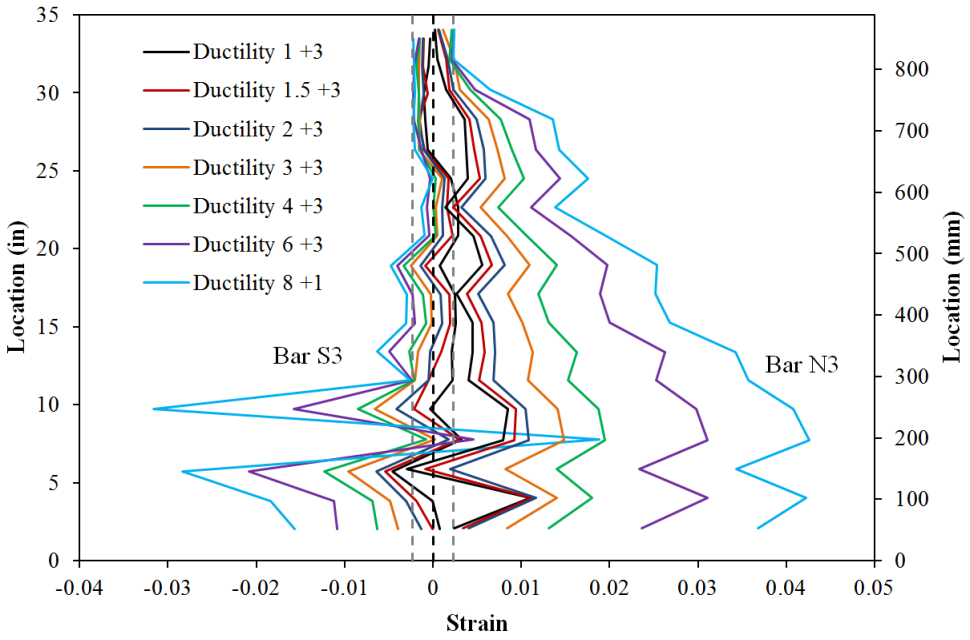

Figure 1.72 T8b – Cyclic Aftershock Vertical Strain Profiles during Push Cycles

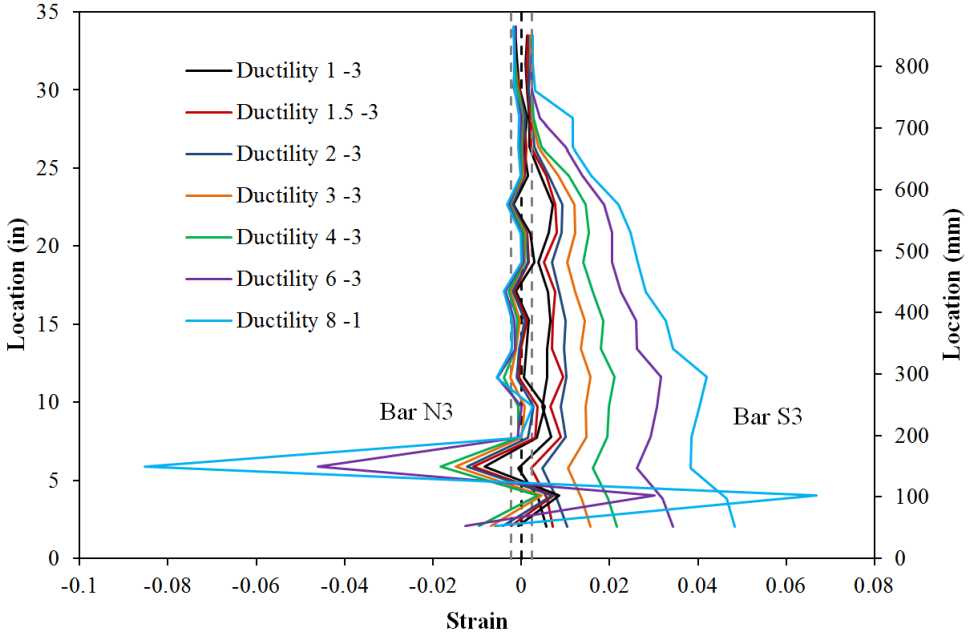

Figure 1.73 T8b – Cyclic Aftershock Vertical Strain Profiles during Pull Cycles

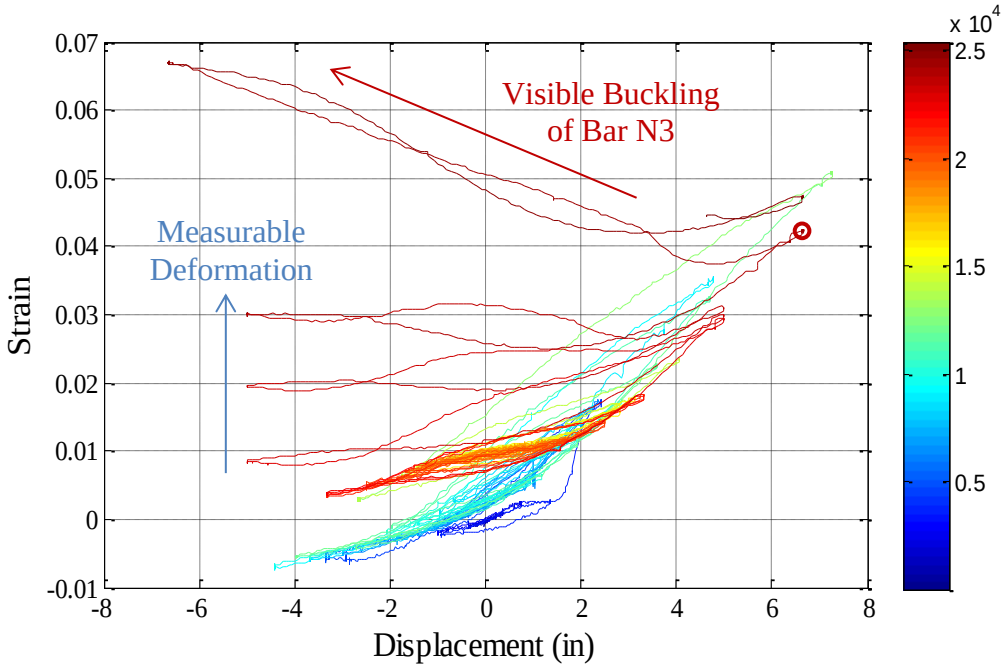

Figure 1.74 T8 and T8b – Bar N3 Strain Hysteresis (4.02" Above Footing)

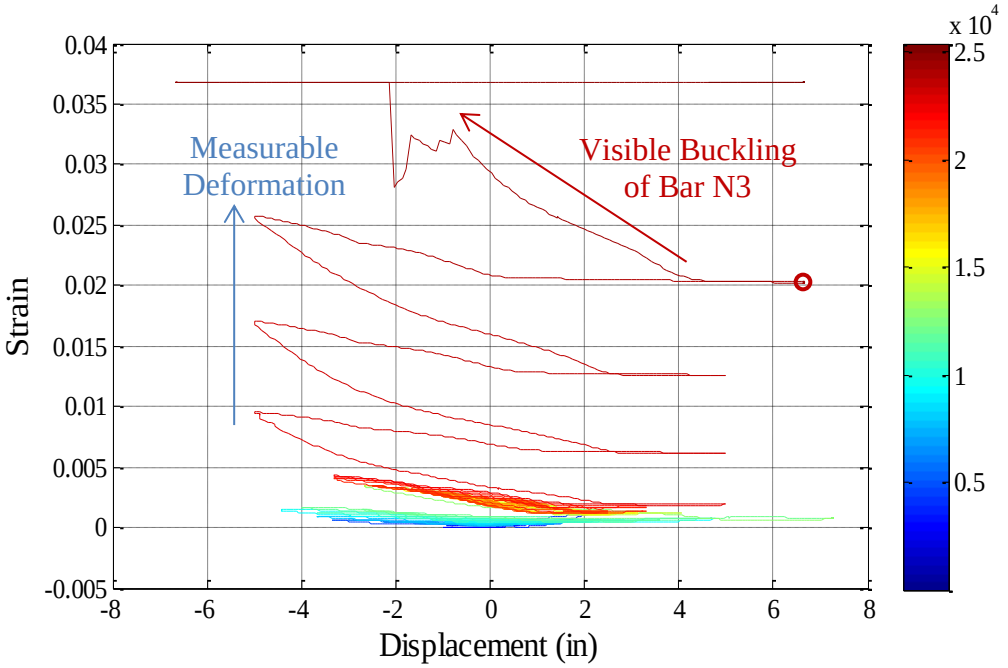

Figure 1.75 T8 and T8b – Spiral Strain Hysteresis over North Buckled Region

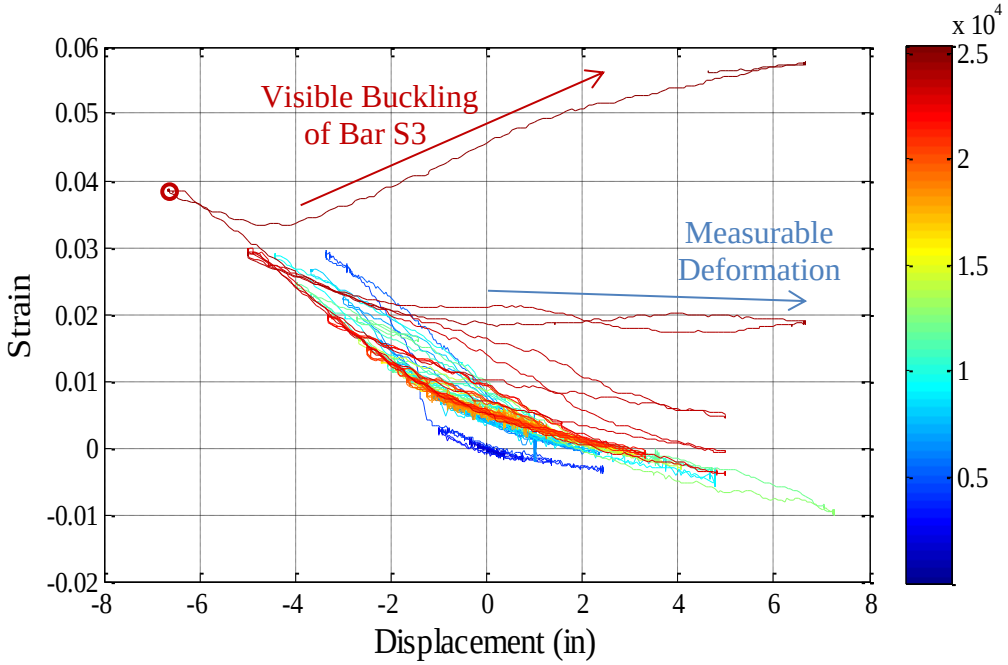

Figure 1.76 T8 and T8b – Bar S3-4 Strain Hysteresis (7.76" Above Footing)

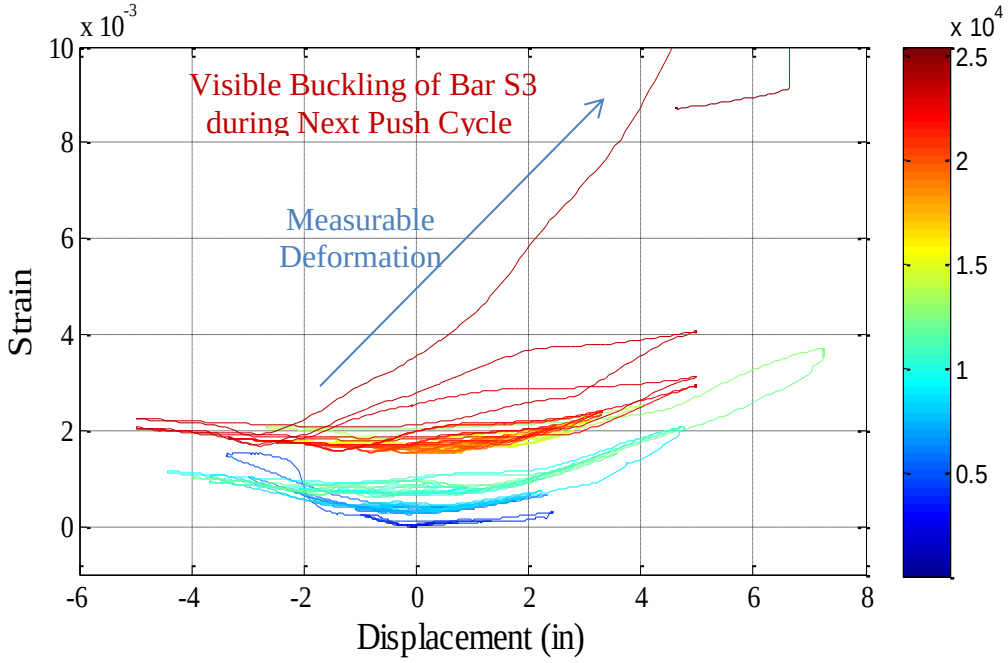

Figure 1.77 T8 and T8b – Spiral Strain Hysteresis over South Buckled Region

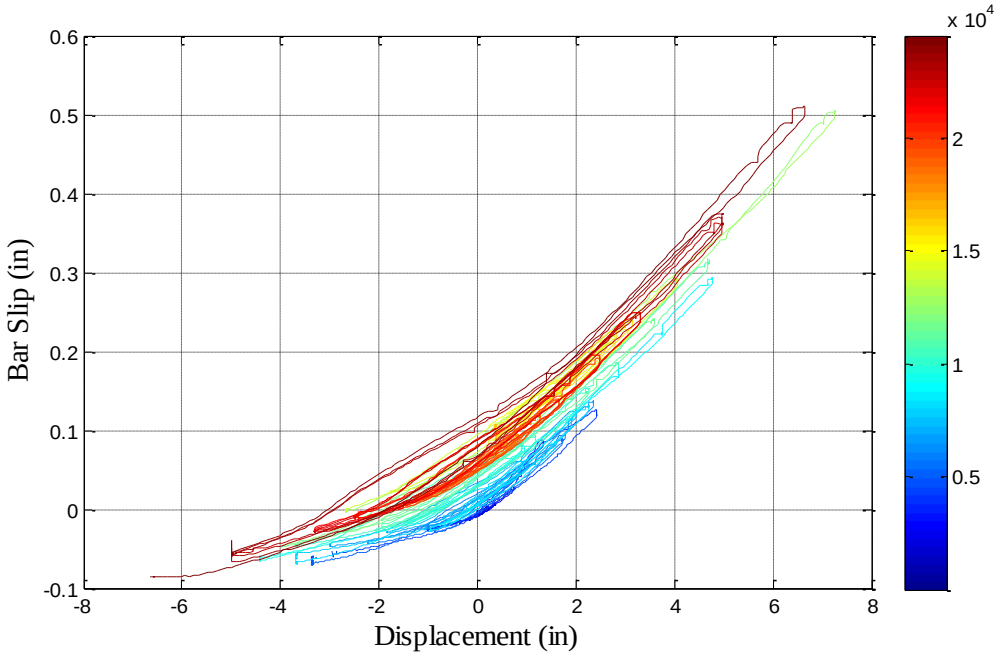

Figure 1.78 T8 and T8b – North Extreme Fiber Bar N3 Slip Hysteresis

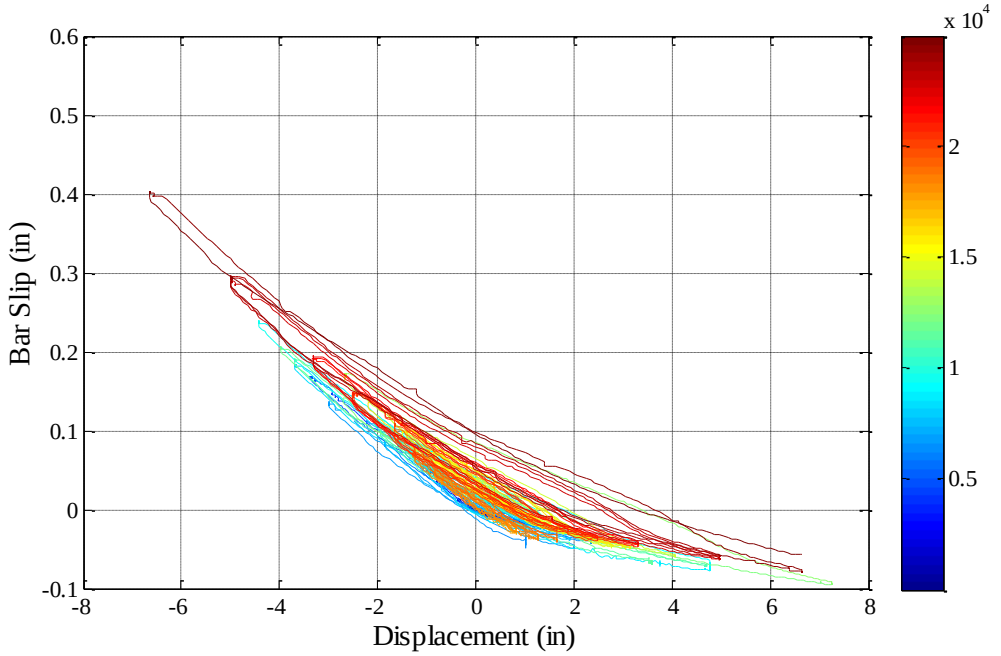

Figure 1.79 T8 and T8b – South Extreme Fiber Bar S3 Slip Hysteresis

1.1.3 Tests 10 and 10b – Chichi Earthquake and Cyclic Aftershock LH

Table 1.8 Observational Summary for Test 10 – Chichi Earthquake Load History

VALUES OF INTEREST:	
Concrete Compressive Strength:	$f_c' = 5263\ psi$
Axial Load:	$P = 170\ kips$
Analytical First Yield Force:	$F_y' = 45.9\ kips$
Experimental First Yield Displacement:	$\Delta_y' = 0.62"$ (Same as Test 9)
Analytical Nominal Moment Capacity:	$M_n = 505.6\ kip * ft$
Equivalent Yield Displacement:	$\Delta_y = 0.84"$
Maximum Lateral Force:	$70.6\ kips$
Maximum Lateral Displacement:	$\mu_{8.9}^{17.31\ sec} = 7.40"$
Failure Mode:	No Significant Damage from Earthquake LH
DAMAGE OBSERVATIONS: During Chichi Earthquake LH	
First Cracking North:	$\mu_{0.3}^{7.02\ sec} = 0.25"$
First Cracking South:	$\mu_{-0.27}^{6.80\ sec} = -0.22"$
Cover Concrete Crushing North:	$\mu_{-1.7}^{13.72\ sec} = -1.39"$
Cover Concrete Crushing South:	$\mu_{2}^{13.40\ sec} = 1.70"$
Transverse Steel Yield South:	At 4.47" otwt $\mu_{8.9}^{17.31\ sec} = 7.40"$

*$\mu_{8.9}^{17.31\ sec} = 7.40"$represents a push cycle 17.31 seconds into the earthquake load history which reached a peak displacement of 7.40" and a displacement ductility of 8.9

Table 1.9 Observational Summary for Test 8b – Symmetric Three Cycle Set Aftershock LH

DAMAGE OBSERVATIONS: During Symmetric Three Cycle Set Post Earthquake LH	
Transverse Steel Yield North:	At $-4.57"$ otwt $\mu_6^{-3} = -4.98"$
Longitudinal Bar Buckling North:	No Visible Buckling Observed
Longitudinal Bar Buckling South:	Reversal from $\mu_6^{-1} = -5.01"$
Failure Mode:	Specimen Saved as a Repair Candidate with Buckled South Reinforcement

$*\mu_6^{-1} = -5.01"$ represents the first pull cycle of displacement ductility six

Table 1.10 Strain Data Summary for Test 8 and 8b – Chile 2010 Earthquake and Cyclic Aftershock LH

MATERIAL STRAINS:	
Cover Concrete Crushing North:	$\varepsilon_s = 0.0026$ $(compression)$
Cover Concrete Crushing South:	$\varepsilon_s = 0.0039$ $(compression)$
Transverse Steel Yield North:	$\varepsilon_s = 0.0092$ $(compression)$
Transverse Steel Yield South:	$\varepsilon_s = 0.0151$ $(compression)$
Longitudinal Bar Buckling North:	No Visible Buckling Observed
Longitudinal Bar Buckling South:	$\varepsilon_s = 0.038$ $(peak\ tension\ prior\ to\ bb)$
	$\varepsilon_s = 0.045$ $(peak\ comp.\ prior\ to\ bb)$
Mander (1988) Ultimate Concrete Compression Strain, $\varepsilon_{cu} = 0.0204$	

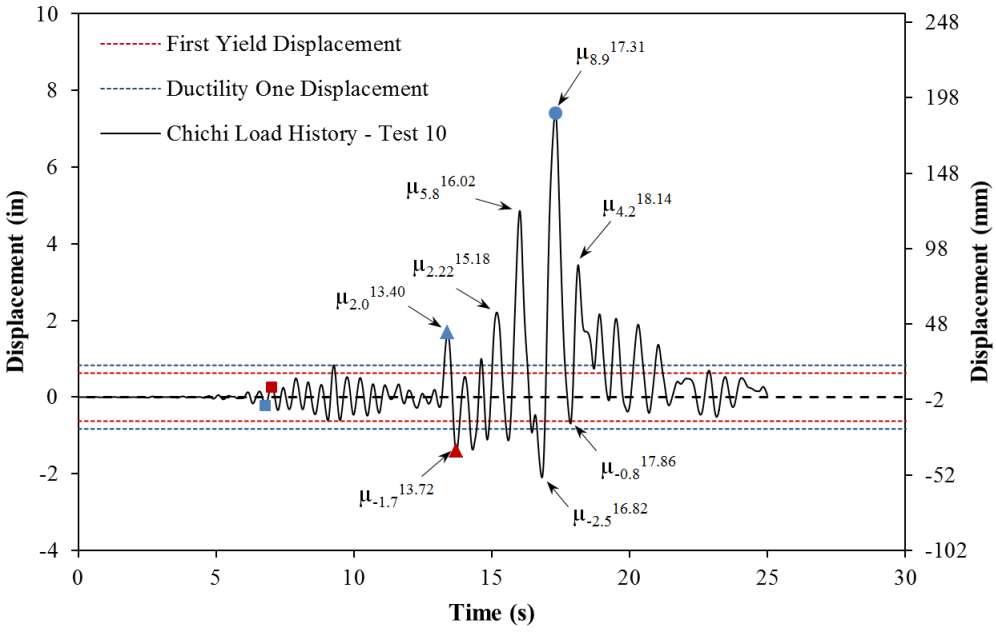

Figure 1.80 T10 – Chichi Earthquake Displacement History

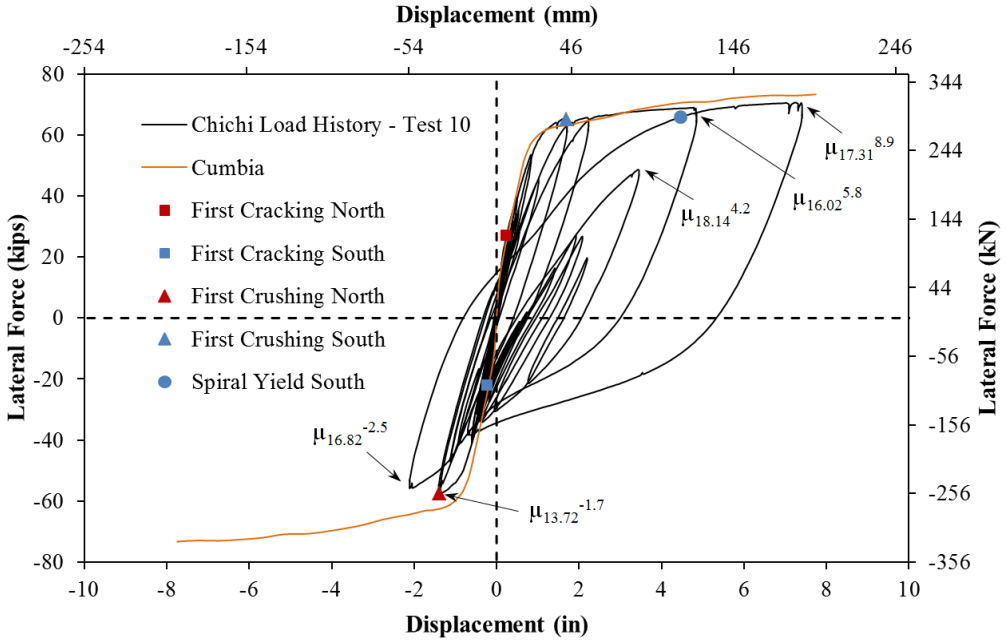

Figure 1.81 T10 – Hysteretic Response for the Chichi Earthquake Load History

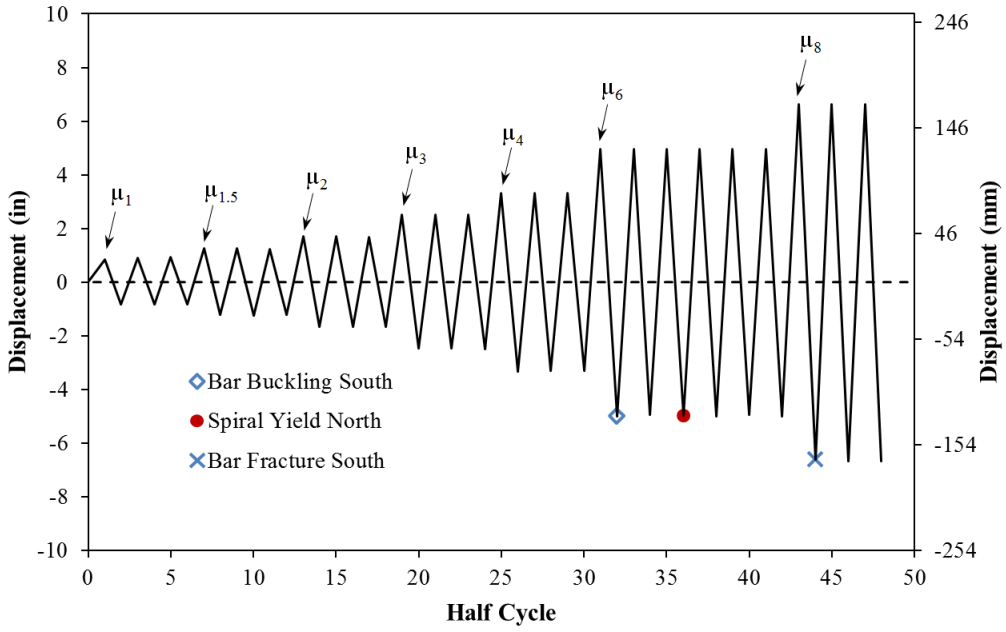

Figure 1.82 T10b – Symmetric Three Cycle Set Aftershock Load History

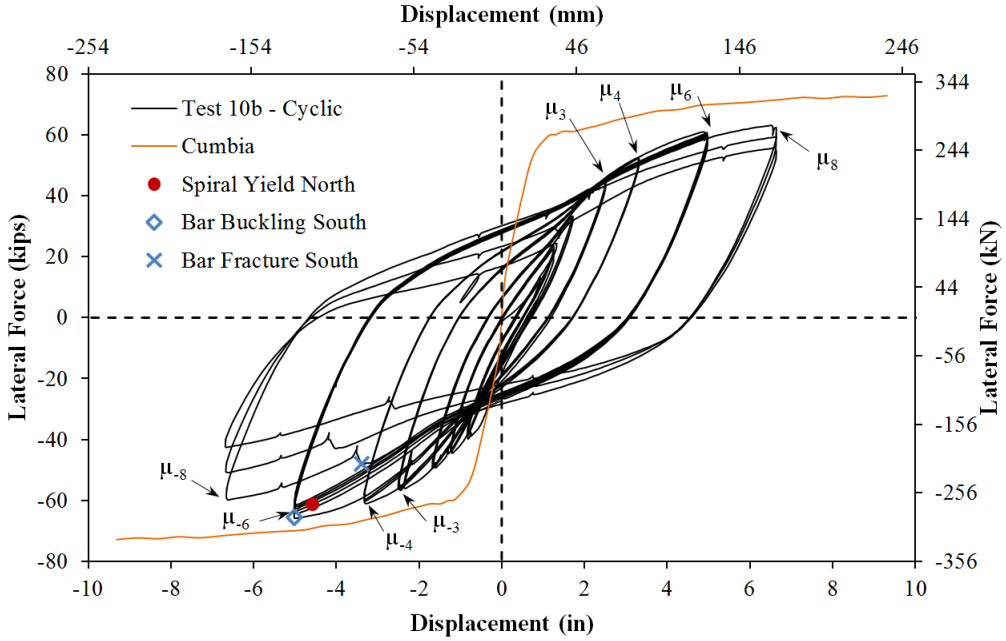

Figure 1.83 T10b – Symmetric Three Cycle Set Aftershock Hysteretic Response

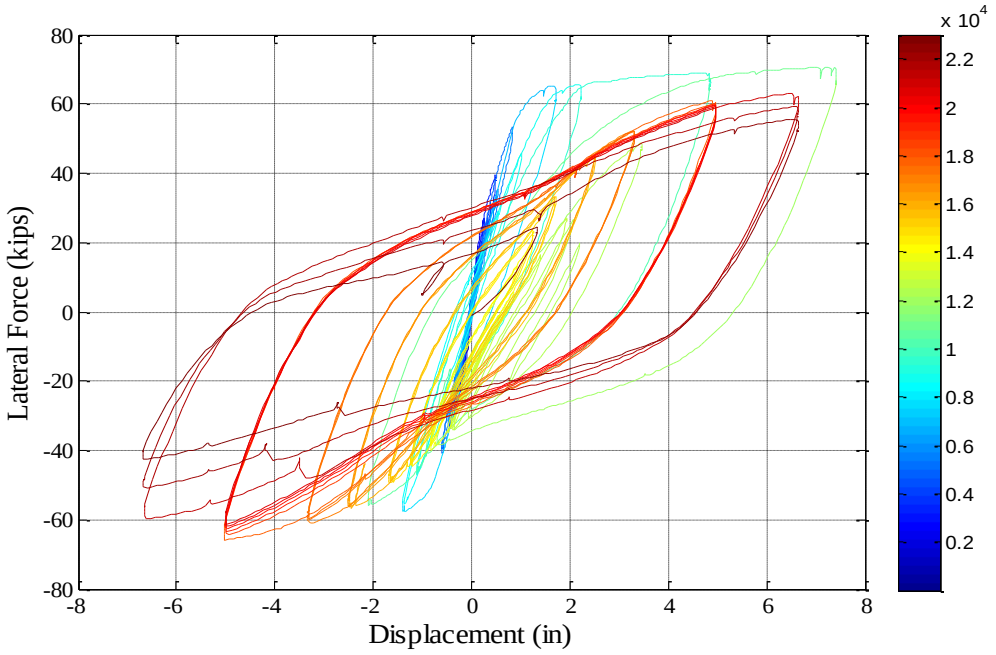

Figure 1.84 T10 and T10b – Complete Response with an Elapsed Time Color Bar

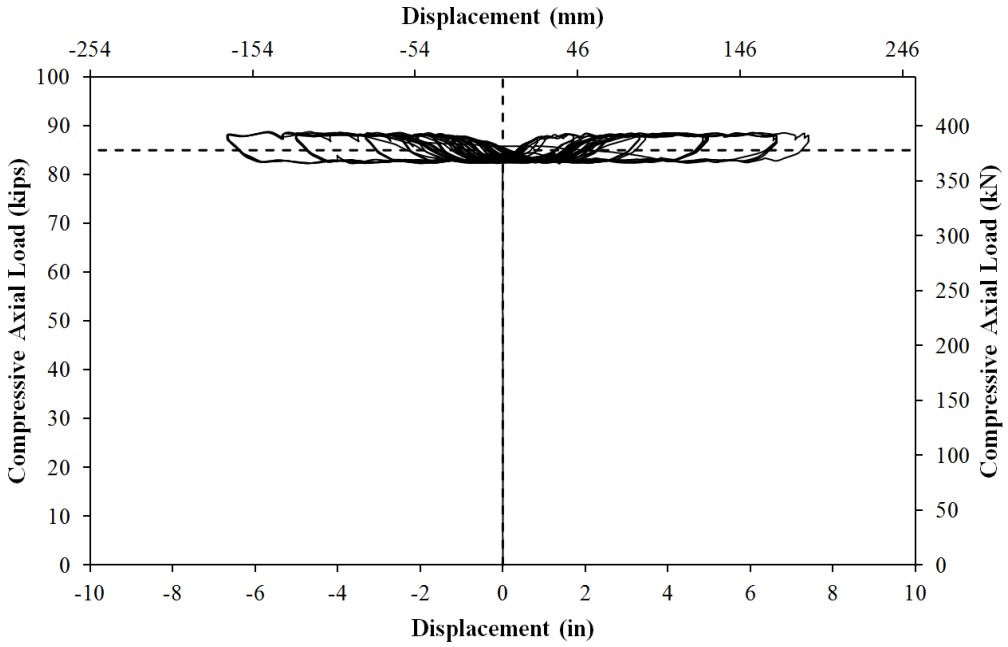

Figure 1.85 T10 and T10b – Compressive Axial Load from One Jack (Total = 2*Value)

Test 10 Chichi Earthquake Load History – Experimental Observations:

To determine possible effects of different load history characteristics on the relationship between strain and displacement, an asymmetric displacement history from the 1999 Chichi Earthquake in Taiwan was used. The Chichi record, see Figure 1.80, produced a one sided response with a displacement ductility demand of 8.9 in one direction of loading and a ductility demand of only 2.5 in the opposing direction. The resulting lateral force vs. top column displacement response appears in Figure 1.81. Buckling did not occur during the Chile or Chichi load histories even though the peak displacements exceeded ductility eight which produced buckling during the symmetric three cycle set load history of Test 9. The purpose of running the Chichi load history was to determine if the asymmetric characteristic has an impact on the relationship between strain and displacement. The asymmetric load history produces significantly different tensile demands on the North and South sides of the specimen.

Cracks measuring 0.1mm at approximate 6" spacing on the South side of the specimen first occurred at ($\mu_{-0.3}^{6.80\,sec} = -0.22"$). On the North side of the specimen cracks measuring 0.1mm at approximate 9" spacing where observed at ($\mu_{0.3}^{7.02\,sec} = 0.25"$). The cracks on the North side of the specimen increased to 0.3mm at approximate 8" spacing during ($\mu_{0.6}^{7.90\,sec} = 0.49"$). The cracks on the South side of the specimen increased to 0.3mm at approximate 5" spacing during ($\mu_{-0.7}^{9.06\,sec} = 0.60"$). Crushing of the cover concrete 8" above the footing on the South side of the specimen began during ($\mu_{2.0}^{13.40\,sec} = 1.70"$) while cracks on the North side of the specimen measured 1.25mm at approximate 4" spacing, Figure 1.86. The cover concrete on the North side of the specimen crushed 5" above the footing during ($\mu_{-1.7}^{13.72\,sec} = -1.39"$), as shown in Figure 1.87. The extent of crushing on the South side of the specimen extended 15" above the footing during ($\mu_{2.6}^{15.18\,sec} = 2.20"$), Figure 1.88. The peak cycle of the load history at ($\mu_{8.9}^{17.31\,sec} = 7.40"$), with a lateral force of 69.98 kips, was completed without additional visible damage, Figure 1.89 and Figure 1.90. Bar Buckling did not occur in subsequent cycles of the Chichi earthquake load history.

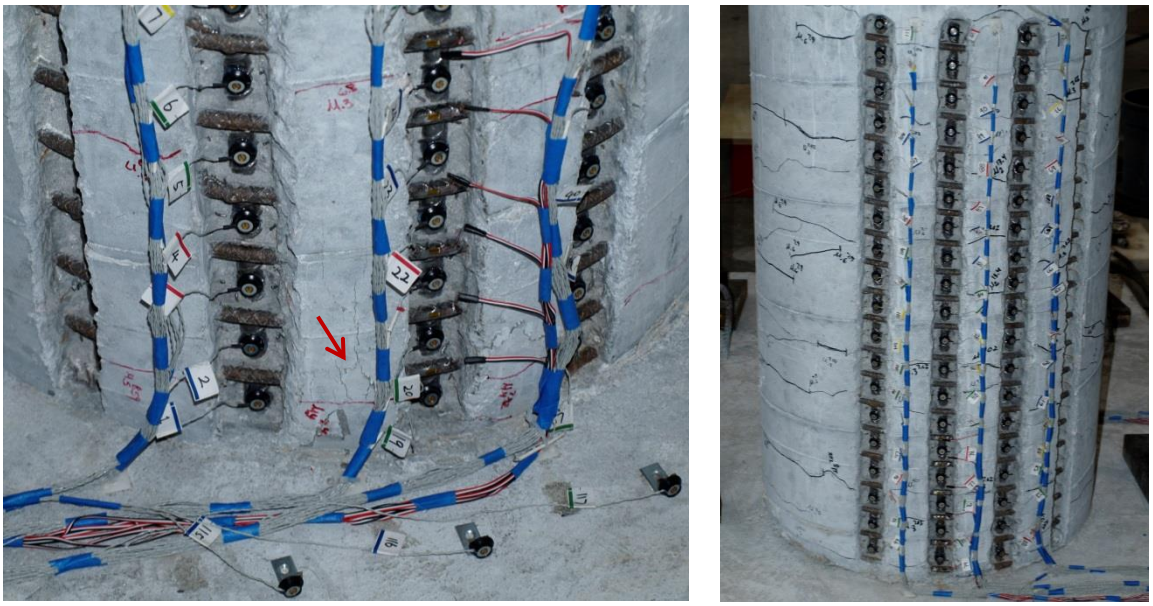

Figure 1.86 T10 – (Left) South Concrete Crushing ($\mu_{2.0}^{13.40\ sec} = 1.70$"), (Right) North

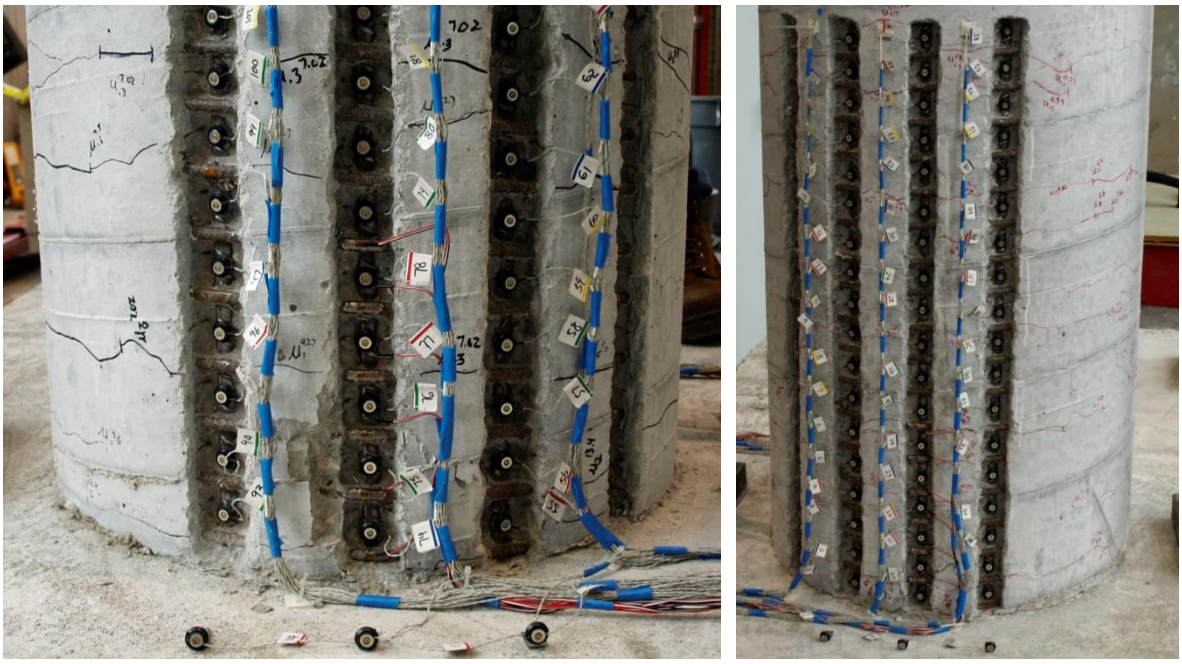

Figure 1.87 T10 – (Left) North Crushing ($\mu_{-1.7}^{13.72\ sec} = -1.39$"), (Right) South Side

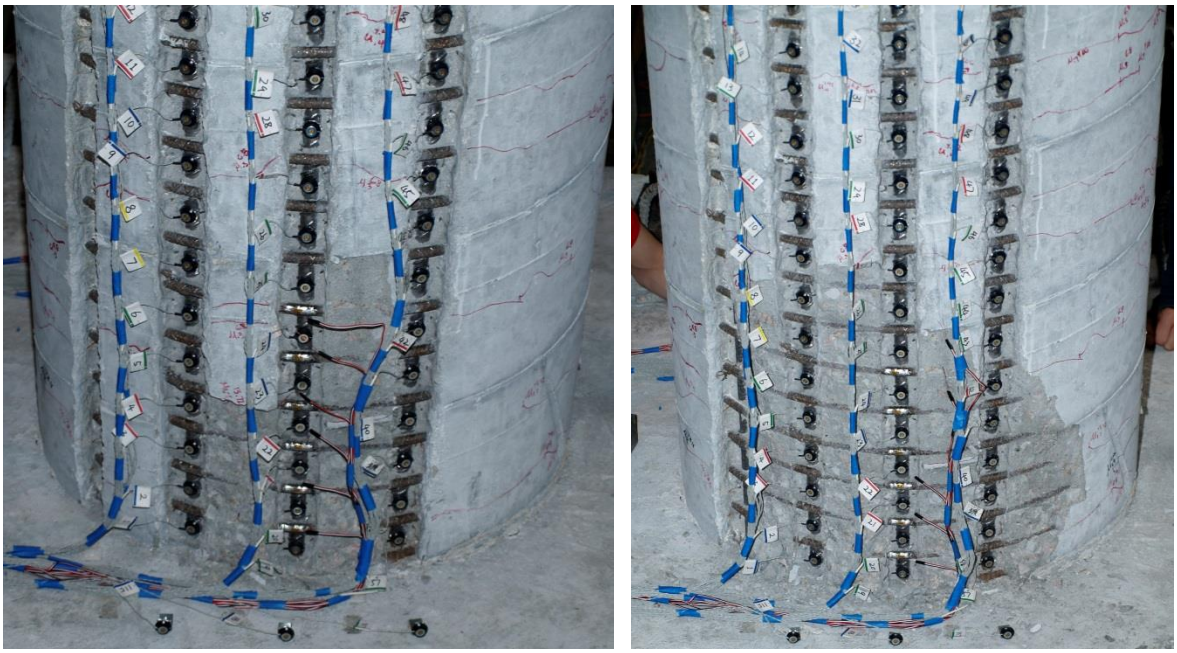

Figure 1.88 T10 – (Left) South ($\mu_{2.7}^{15.18\,sec} = 2.23$"), (Right) ($\mu_{5.8}^{16.02\,sec} = 4.85$")

Figure 1.89 T10 – Specimen at the Peak Disp. of the Chichi EQ ($\mu_{8.9}^{17.31\,sec} = 7.40$")

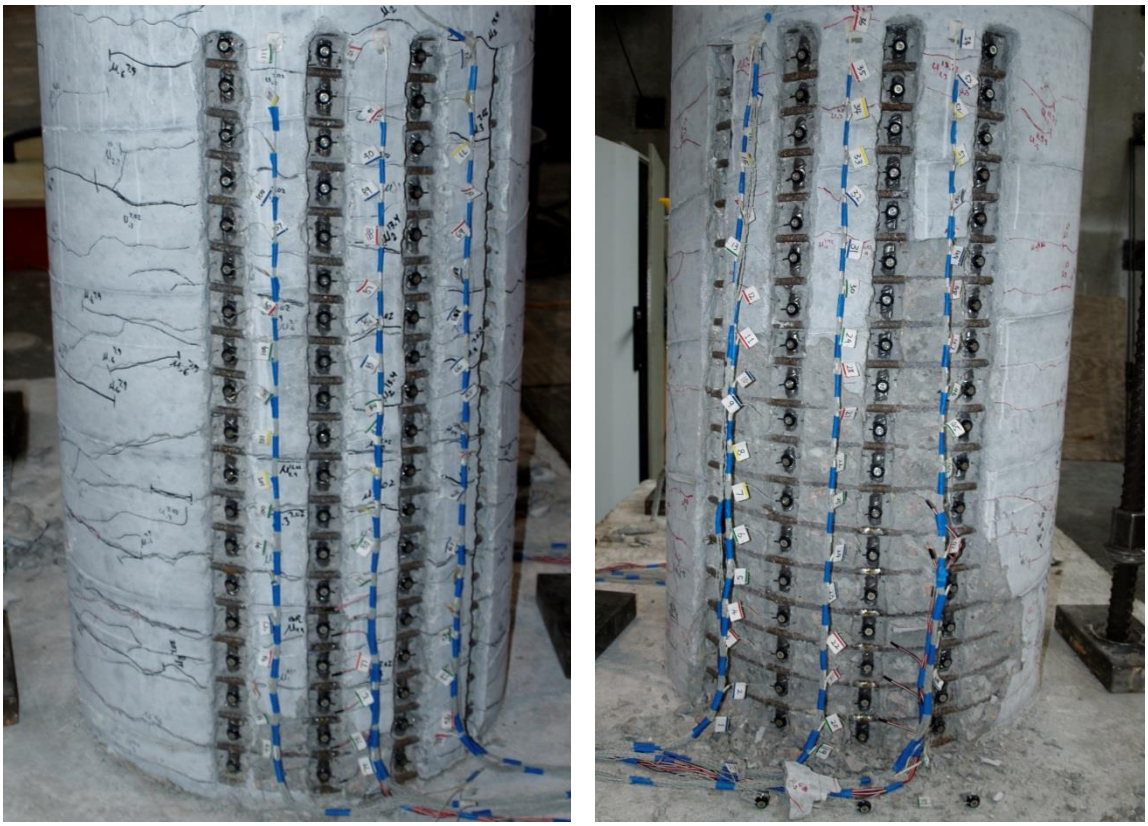

Figure 1.90 T10 – (Left) North and (Right) South at ($\mu_{8.9}^{17.31\,sec} = 7.40$")

Test 10 Chichi Earthquake Load History – Strain Data Analysis:

Due to the random cyclic nature of the Chichi earthquake load history, specific data observation points along the backbone curve of cyclic response were chosen in Figure 1.91. The vertical strain profiles for each extreme fiber bar during push and pull cycles are shown in Figure 1.92 and Figure 1.93. The strain profiles for cycles exceeding displacement ductility three are smoother and are influenced less by individual crack locations. The maximum recorded compression strain in the extreme fiber bar S3 during ($\mu_{8.9}^{17.31\,sec} =$ 7.40") was 0.032 measured 7.64" above the footing. A peak tensile strain of 0.052, centered 4.33" above the footing, was measured on bar N3 during the push cycle to ($\mu_{8.9}^{17.3\,sec1} =$ 7.40"). Tests 8, 9, and 10 (Chile 2010, Symmetric Three Cycle Set, and Chichi) were

subjected to similar values of peak tensile strain (0.051, 0.053, and 0.052 respectively) at different levels of displacement ductility (8.7, 8, and 8.9 respectively), but buckling only occurred during the Symmetric Three Cycle Set load history of Test 9.

The relationship between tensile strain and displacement for North extreme fiber bar N3, centered 4.33" above the footing, appears in Figure 1.94. The Cumbia moment curvature analysis with the PCK (2007) Lp hinge method prediction significantly over predicts the tensile strains at higher displacements. The relationship between compressive strain and displacement for extreme fiber bar N3 during significant pull cycles appears in Figure 1.95. The ductility demands in the pull direction after the peak cycle were not large enough to place the North reinforcement back into compression due to the large residual growth strains.

The relationship between compressive strain and displacement, for gage length centered 1.82" above the footing on extreme fiber bar S3, from when the column was vertical to the peak of significant push cycles appears in Figure 1.97. The moment curvature prediction with the PCK (2007) Lp hinge method for compressive strains matches the recorded strains well. The graph shows compressive strains over the first gage length above the footing, even though measured strains in the fourth gage length were larger. The recorded strains during the ($\mu_{8.9}^{17.31\,sec} = 7.40"$) push cycle exceed the moment curvature prediction. Strains recorded during later cycles of the load history are similarly under predicted by moment curvature analysis. The relationship between tensile strain and displacement for extreme fiber bar S3 placed into tension during pull cycles appears in Figure 1.96.

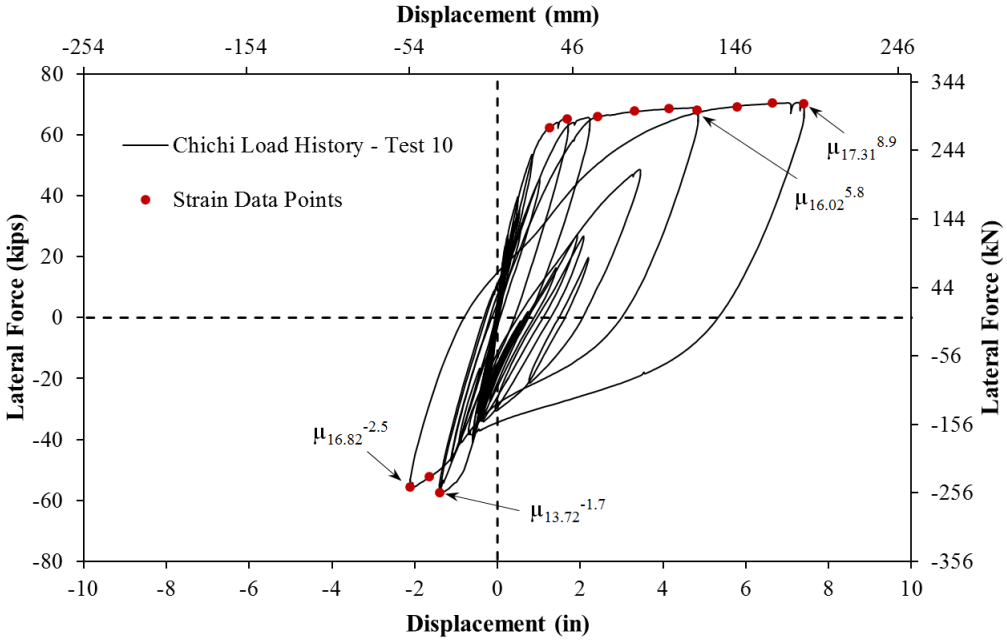

Figure 1.91 T10 – Strain Data Observation Points along the Backbone Curve

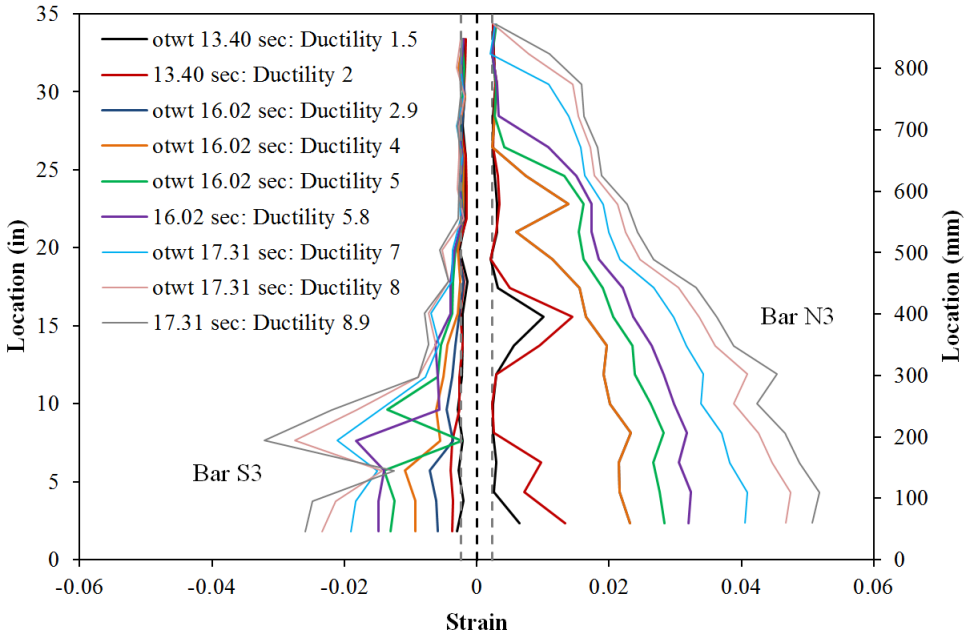

Figure 1.92 T10 – Extreme Fiber Vertical Strain Profiles During Push Cycles

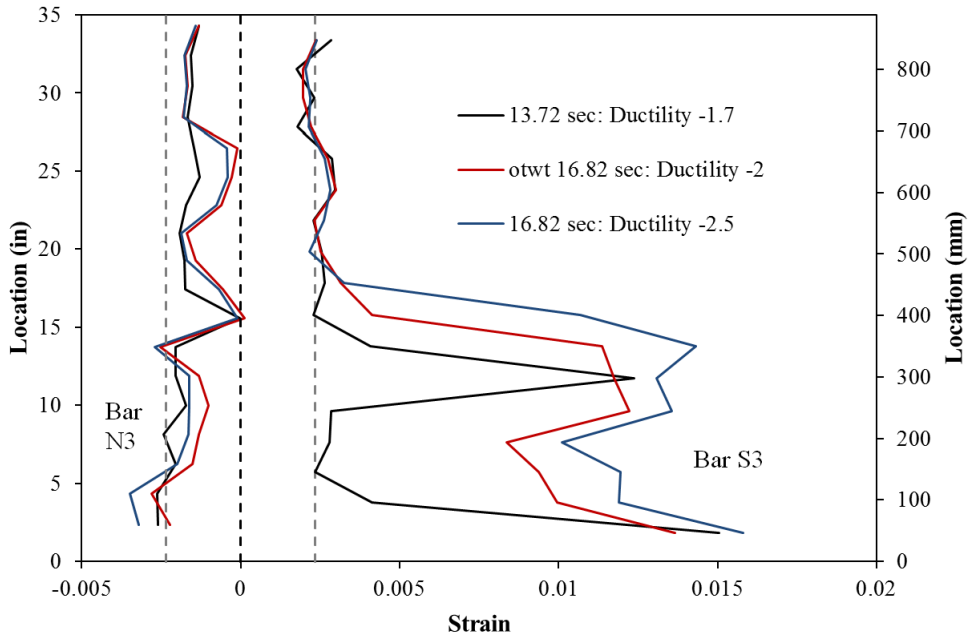

Figure 1.93 T10 – Extreme Fiber Vertical Strain Profiles During Pull Cycles

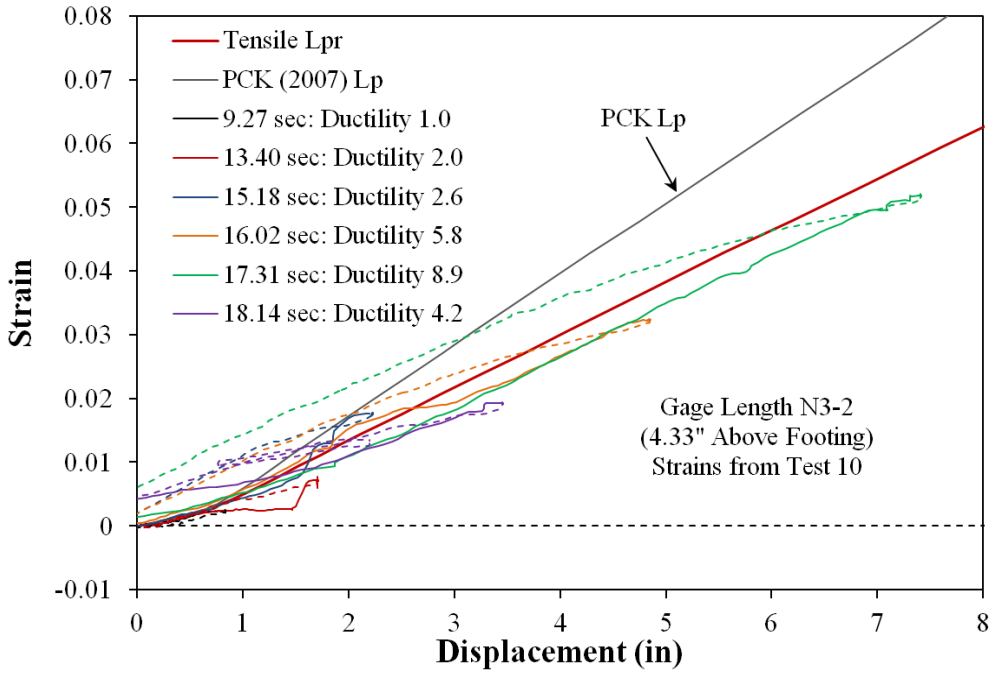

Figure 1.94 T10 – Tensile Strain-Displacement for Bar N3 during Push Cycles

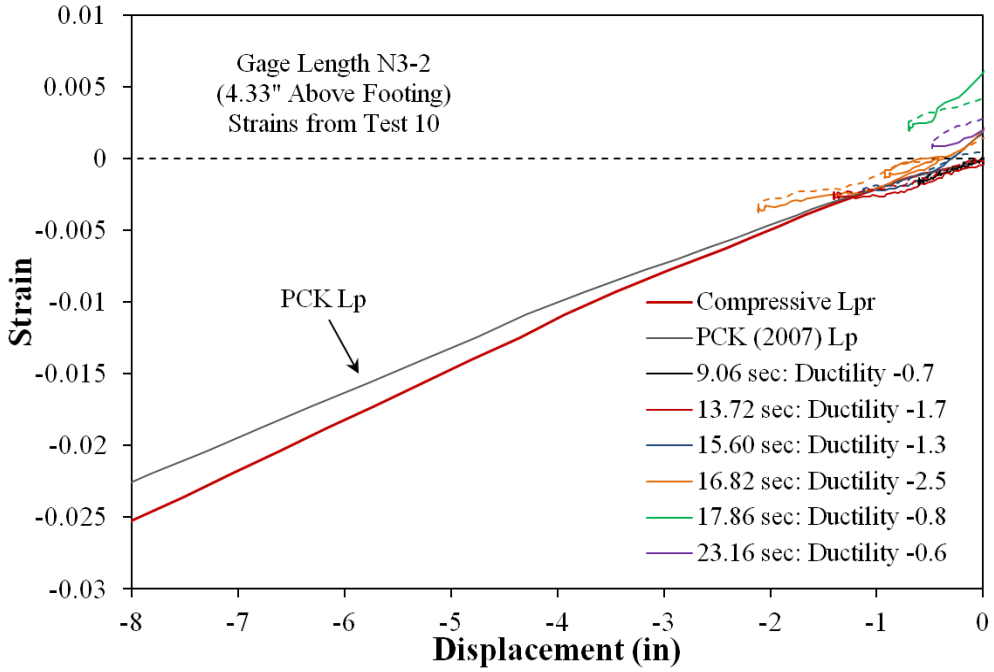

Figure 1.95 T10 – Compressive Strain-Displacement for Bar N3 during Pull Cycles

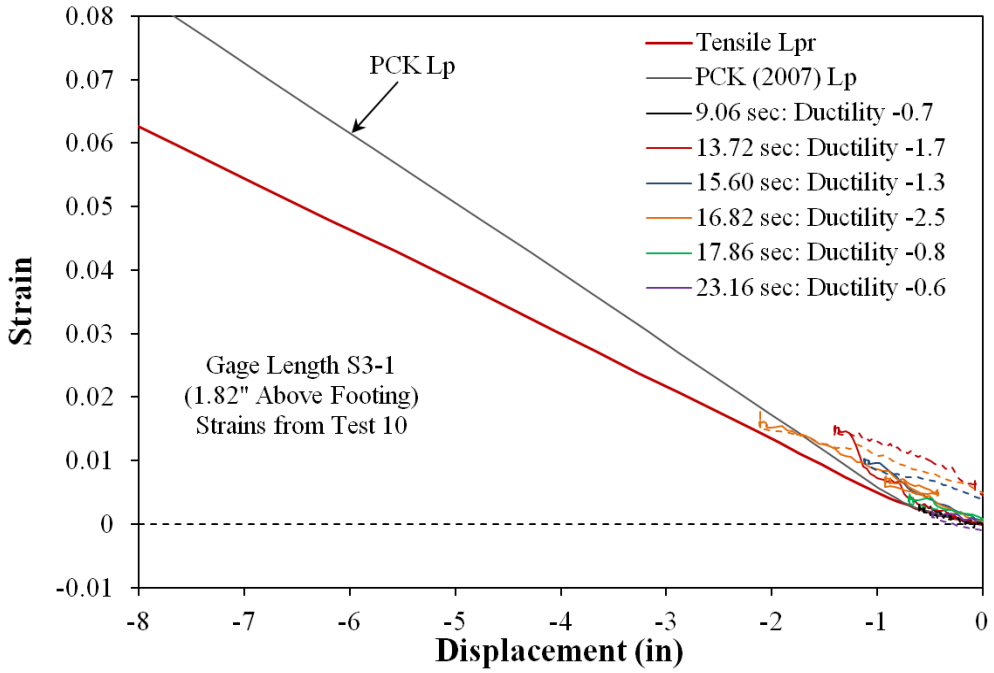

Figure 1.96 T10 – Tensile Strain-Displacement for Bar S3 during Pull Cycles

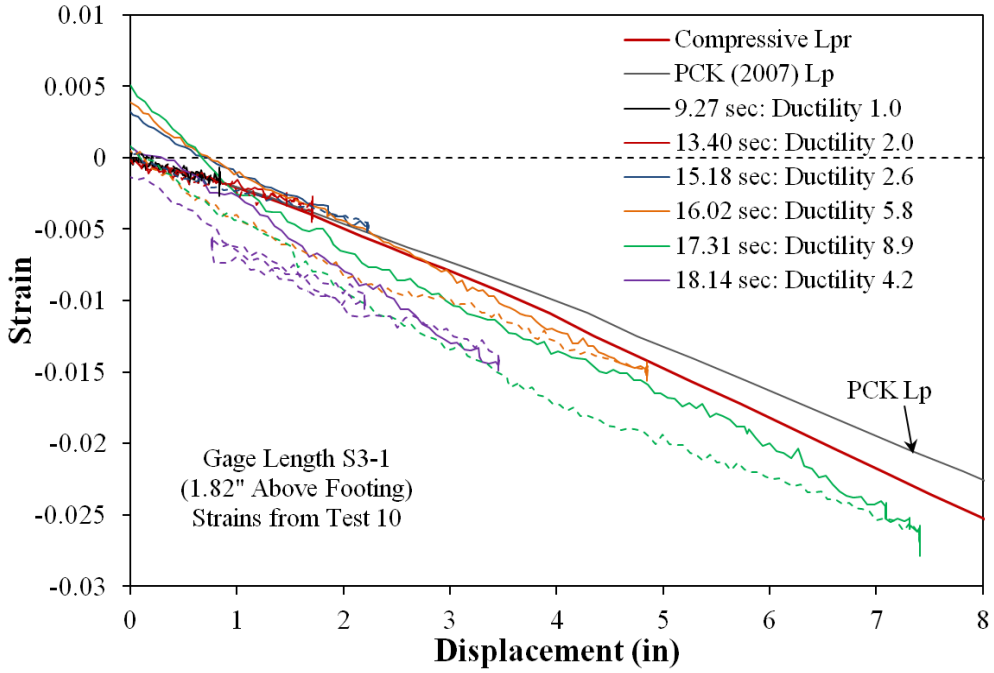

Figure 1.97 T10 – Compressive Strain-Displacement for Bar S3 during Push Cycles

Test 10 Chichi Earthquake Load History – Strain Penetration and Curvature Data:

Vertical curvature profiles obtained for points along the backbone curve of cyclic response during push and pull cycles appear in Figure 1.98 and Figure 1.99 respectively. Linear plastic curvature least squared error lines show that the curvatures are linearly distributed after displacement ductility three when the profiles smooth out. Initial cycles below ductility three are highly influenced by individual crack locations. The base section rotation attributable to strain penetration of reinforcing bars appears in Figure 1.100 and Figure 1.101 for push and pull cycles respectively. The total deformation calculated by integrating the measured curvature profiles and extrapolating the base section rotation to the center of loading appear in Figure 1.102. The integrated curvatures match well throughout the entire range of displacements. The measured spread of plasticity as a function of curvature ductility appears in Figure 1.103.

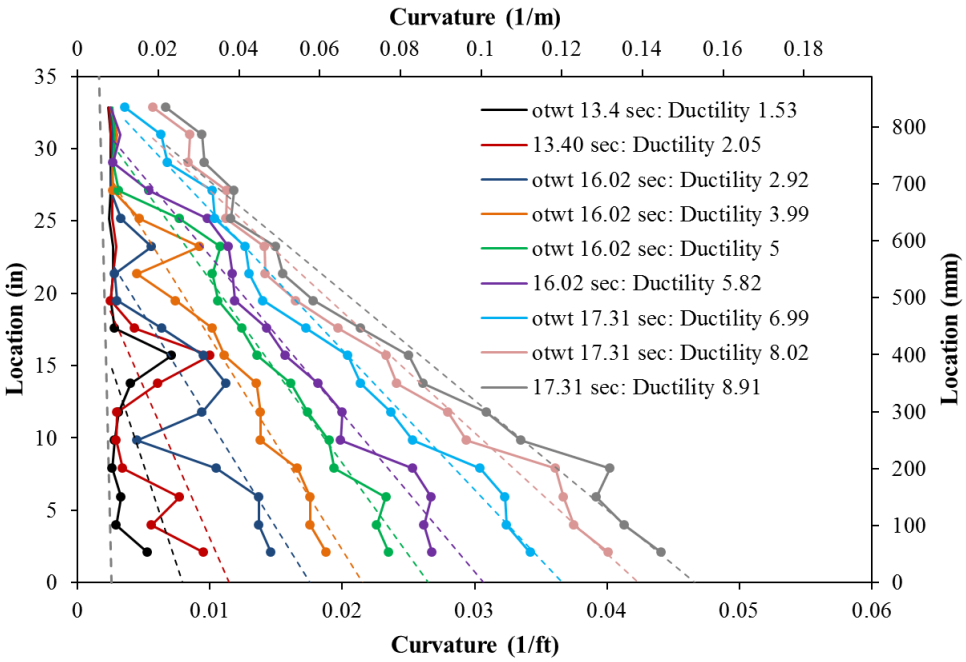

Figure 1.98 T10 – Vertical Curvature Profiles during Push Cycles

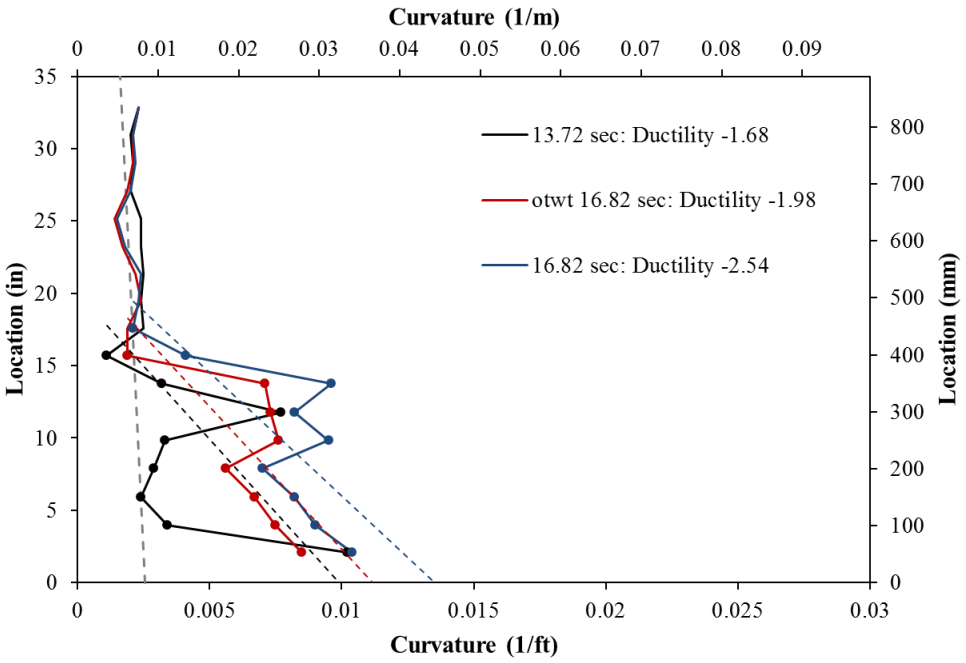

Figure 1.99 T10 – Vertical Curvature Profiles during Pull Cycles

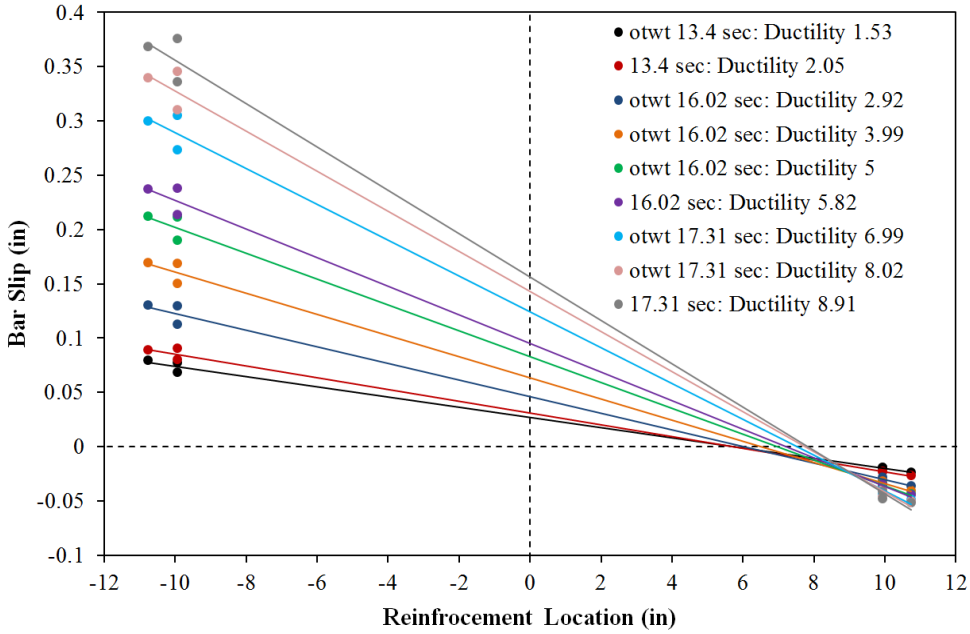

Figure 1.100 T10 – Base Section Rotation due to Strain Penetration during Push Cycles

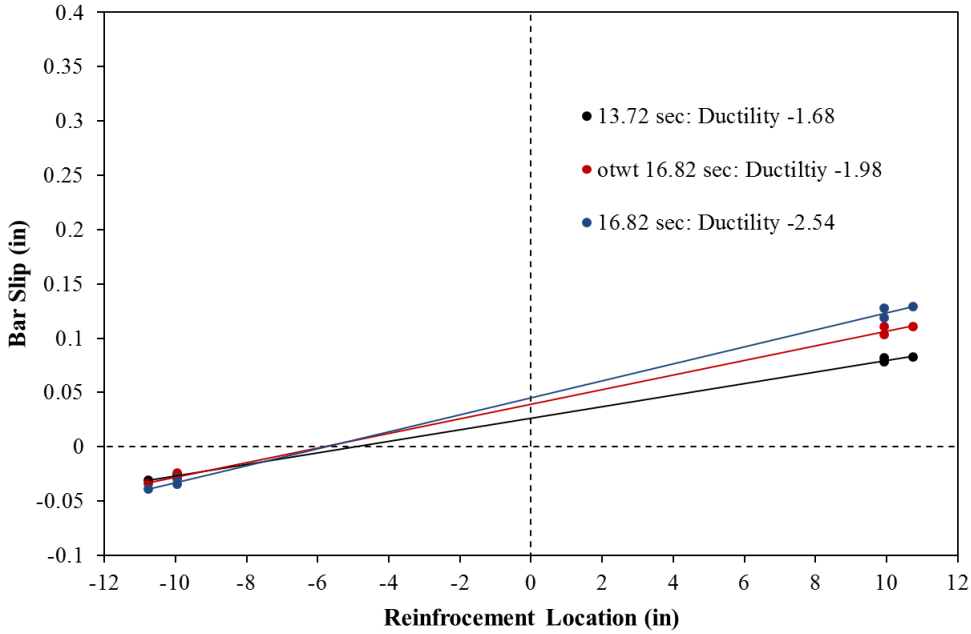

Figure 1.101 T10 – Base Section Rotation due to Strain Penetration during Pull Cycles

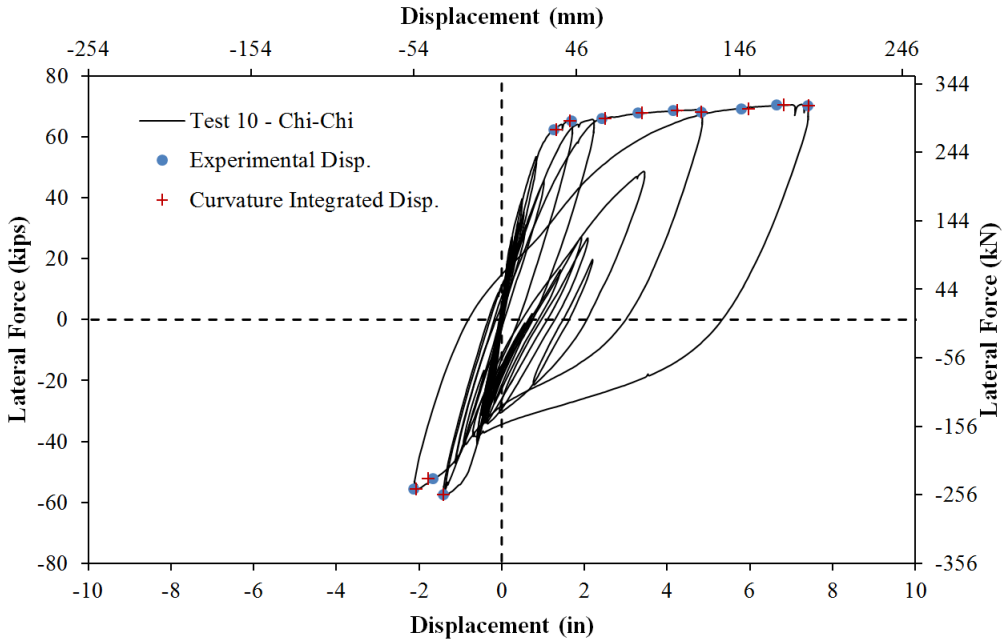

Figure 1.102 T10 – Comparison of Measured and Optotrak Integrated Displacements

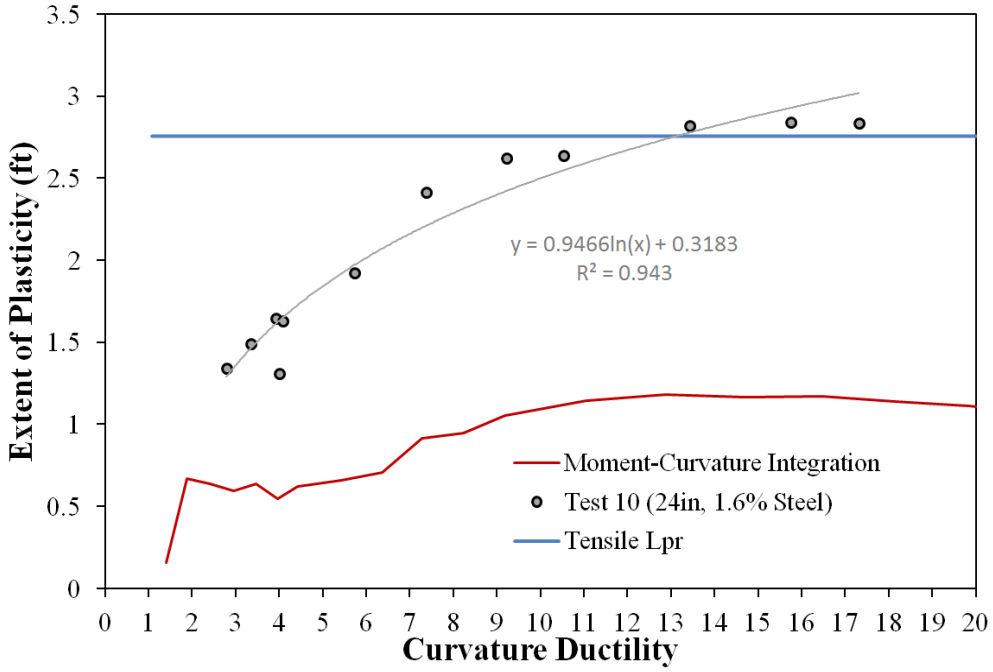

Figure 1.103 T10 – Measured Spread of Plasticity (Circle Data Points)

Test 10b Symmetric Three-Cycle-Set Aftershock LH – Experimental Observations:

Since buckling did not occur during the Chichi load history, a second symmetric three cycle set load history was conducted on the specimen with degraded stiffness but no losses in strength, similar to Test 8b conducted after the Chile 2010 load history. The extreme fiber South reinforcement bar S3 buckled after reversal from ($\mu_6^{-1} = -5.01$"), Figure 1.104. Due to the asymmetric nature of the Chichi load history, the South side of the specimen was subjected to low tensile demands but high compressive demands during the peak displacement cycle to ($\mu_{8.9}^{17.31\,sec} = 7.40$"). The purpose of the cyclic aftershock study shifted to determine if continued cycling at ductility six would rupture the previously buckled South reinforcement. After reversal from ($\mu_6^{-3} = -4.98$"), bar S2 buckled as shown in Figure 1.104. Six complete cycles of ductility six where completed without rupturing previously buckled reinforcement on the South side of the specimen, so the load history continued to ductility eight as shown in Figure 1.82. As the load history progressed, visible deterioration of the core concrete on the South side of the specimen over the buckled region occurred due to loss of confinement, which is evident in the left photo in Figure 1.105 taken at ($\mu_8^{+1} = 6.64$").

Additionally, South reinforcement bar S4 buckled during ($\mu_8^{+1} = 6.64$"). Previously buckled reinforcing bar S3 ruptured in tension during ($\mu_8^{-1} = -6.63$"). Bar S1 buckled during ($\mu_8^{+2} = 6.62$"), and previously buckled Bar S2 ruptured during ($\mu_8^{-2} = -6.67$"). At ($\mu_8^{+3} = 6.63$"), the fifth reinforcing bar on the South side of the specimen buckled. Previously buckled reinforcing bar S4 ruptured during ($\mu_8^{-3} = -6.67$"). . The test was concluded with five buckled bars on the South side of the specimen and intact reinforcing bars on the North side of the specimen, see Figure 1.106 and Figure 1.105 for photos of South and North sides of the specimen after testing.

The complete hysteretic response for Tests 10 and 10b is shown in Figure 1.84 with an elapsed time color bar to track the progression of the response through both load histories. Buckling of multiple bars during ductility six produced minimal losses in strength during pull

cycles when previously buckled reinforcement was placed into tension, but push cycles of ductility six did not suffer from losses in strength. During each pull cycle of ductility eight, a previously buckled bar on the South side of the specimen ruptured leading to losses of strength in both the push and pull directions of loading. When the response from Test 10b is compared to the moment curvature prediction, in Figure 1.83, it is clear that there is a larger amount of stiffness degradation at lower ductility cycles in the push direction of loading due to the original asymmetric Chichi load history. The hysteretic response for Tests 9 and 10b are shown in Figure 1.107, and the response for Tests 8b and 10b are compared in Figure 1.108. The hysteretic response for Tests 8b and 10b are similar up to ductility six except test 10b has larger forces in the pull direction due to lower stiffness degradation during the asymmetric Chichi load history compared to the symmetric Chile 2010 load history of Test 8.

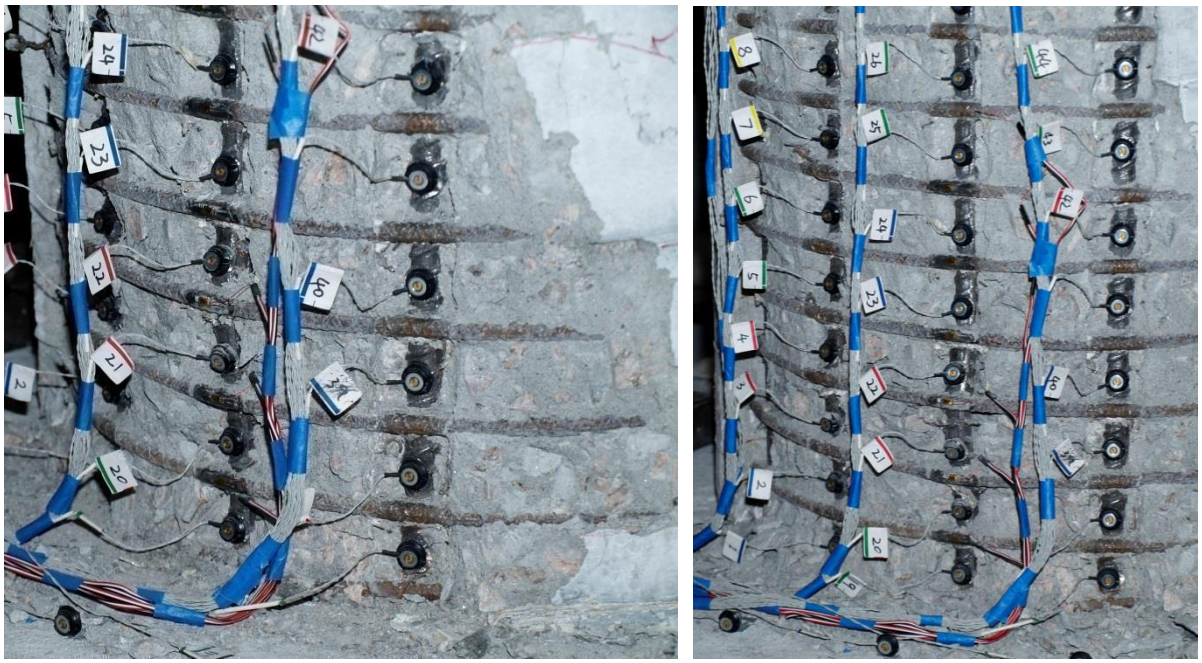

Figure 1.104 T10b – (Left) Buckling of Bar S3 after Reversal from ($\mu_6^{-1} = -5.01$") and (Right) Buckling of S2 after Reversal from ($\mu_6^{-3} = -4.98$")

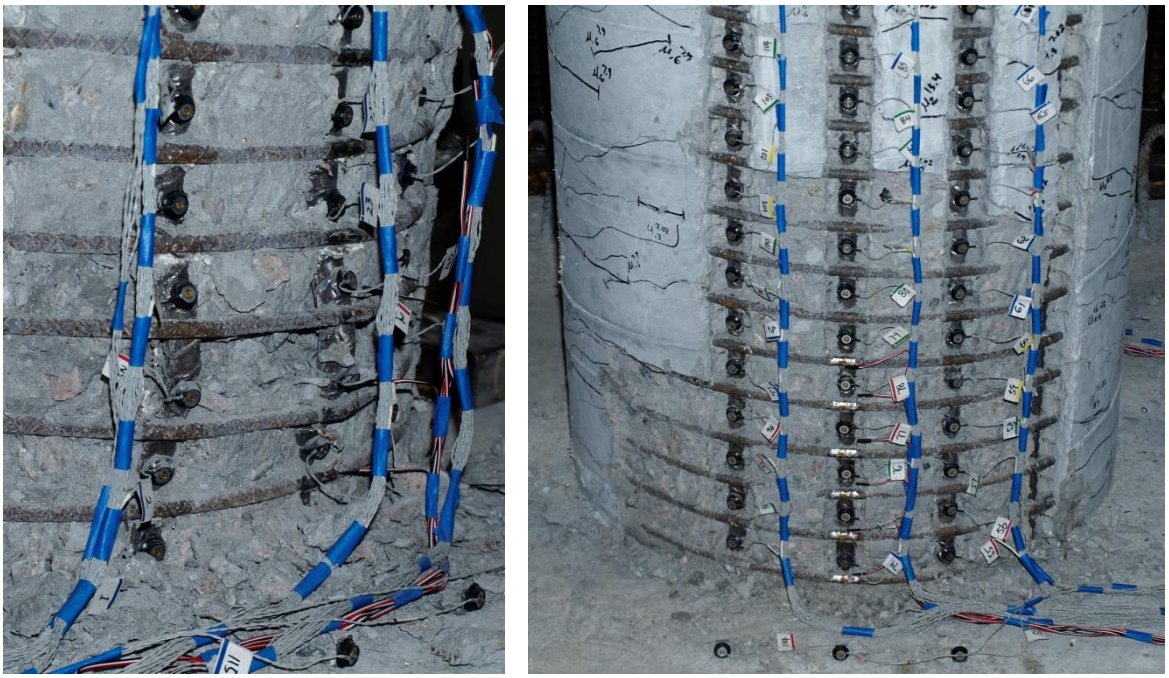

Figure 1.105 T10b – (Left) South at ($\mu_8^{+1} = 6.64$") and (Right) North Side after Test

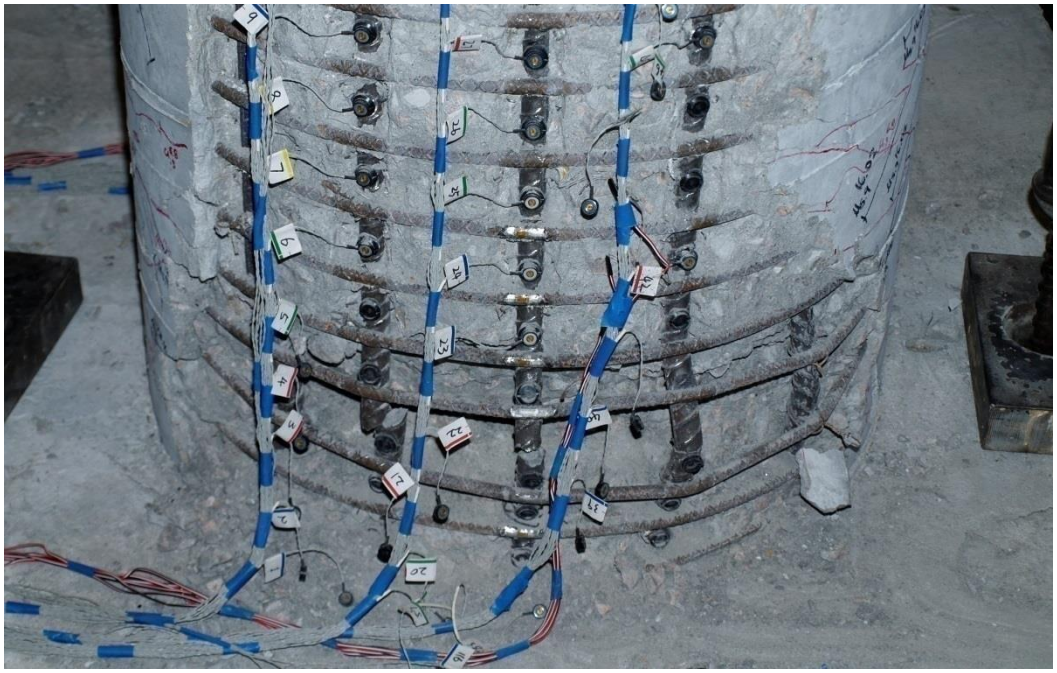

Figure 1.106 T10b – South Side after the Test (5 Buckled and 3 Ruptured Bars)

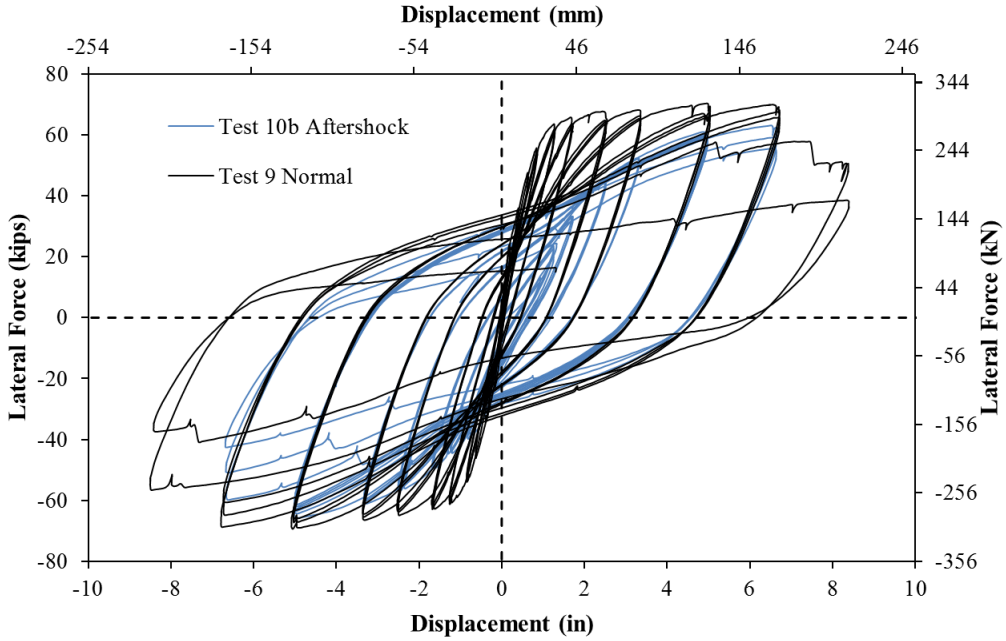

Figure 1.107 T10b – Cyclic Aftershock Response Compared to Initially Undamaged T9

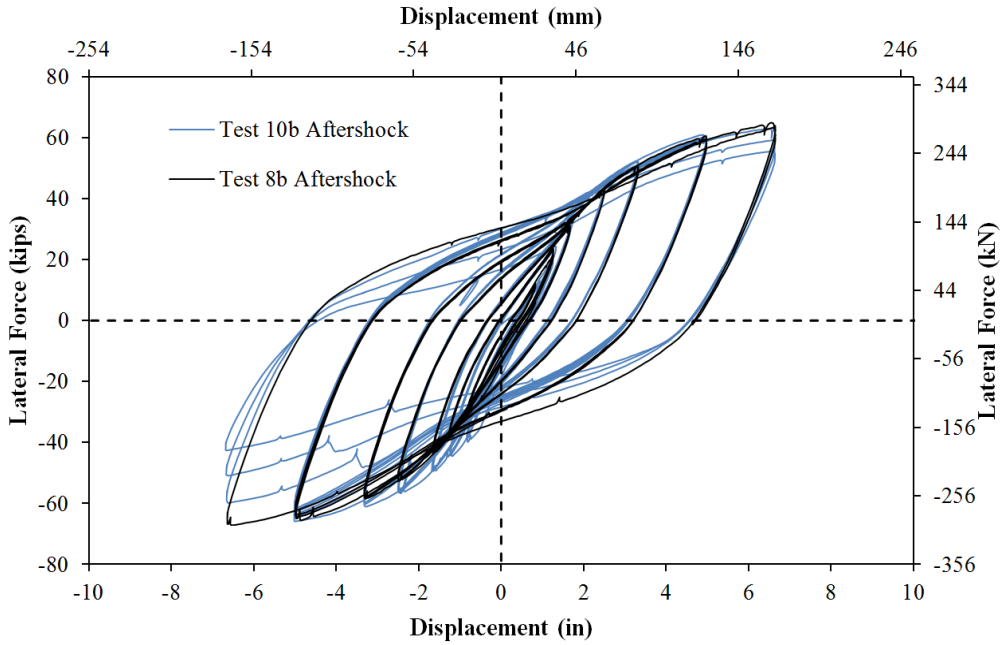

Figure 1.108 Comparison of Post-Earthquake Cyclic Response of T8b and T10b

Test 10b Symmetric Three-Cycle-Set Aftershock LH – Strain Data Analysis:

South Reinforcement:

The extreme fiber vertical strain profiles for push and pull cycles of the cyclic aftershock load history are shown in Figure 1.109 and Figure 1.110 respectively. The compressive vertical strain profiles for Bar S3, left half of Figure 1.109, indicate a large amount of measurable deformation prior to visible buckling occurred after reversal from ($\mu_6^{-1} = -5.01"$). Tensile strains were measured in the third gage length above the footing, while large compression strains were recorded over adjacent gage lengths above and below, which indicates outward deformation of the reinforcement. Visually, this is supported by the left photo in Figure 1.104 that shows outward deformation over the third gage length when visible buckling was observed during the second push cycle of ductility six. The vertical strain profile shows that measurable deformation over second, third, and fourth gage lengths were recorded over the entire cyclic aftershock test. The measured deformation increased during the fourth ductility level before visible buckling was observed. Once outward deformation of the longitudinal steel occurs, the magnitude of recorded strains is no longer representative of engineering strain. Instead, the vertical strain profiles are shown until visible buckling to highlight the location and propagation of damage.

The complete strain hysteresis for South extreme fiber bar S3 for the gage length centered 5.72" above the footing for Tests 10 and 10b appear in Figure 1.113. This particular gage length captures the outwards deformation of the buckled bar which increases the distance between target markers. The strain hysteresis shows the peak cycle of the Chichi load history with bar S3 in compression, and upon reversal many small ductility cycles failed to place the gage length back into large compression due to the effects of small deformation prior to visible buckling. The recorded strains over the South reinforcement gage length should be in compression after reversal from pull cycles; instead the apparent strain increases as the column is pushed due to the outward deformation. The opposite phenomenon was observed over adjacent gage lengths where increasing compression strains were observed at locations where the bar begins to straighten back out. The final push cycle in Figure 1.113

represents the push to ($\mu_6^{+2} = 4.97"$) when visible buckling occurred. The recorded data at this stage of the strain hysteresis is affected by measurable deformations prior to buckling.

The strain gage hysteresis for the transverse steel layer overlaying the portion of the extreme fiber south reinforcing bar that later buckled outwards appears in Figure 1.114. After reversal from the peak cycle, the transverse steel maintained a large residual strain over 0.01, even during low ductility cycles. The increased residual strain in the transverse steel affects the column behavior in two distinct ways: (1) Inelastic strains in the transverse steel decrease its effectiveness as a boundary condition restraining buckling of the longitudinal steel, which explains small measurable deformation prior to visible buckling, and (2) Large residual strains in the transverse steel result in reduced confinement of the core concrete which concentrates further damage at that location. Presumably, if the effectiveness of the transverse steel in confining the core concrete was reduced, repeated cycles could lead to deterioration of the core concrete in the localized region critical to reinforcement buckling. If even small regions of the confined core were to crush, the effect of this crushing is analogous to increasing the demand on the longitudinal steel while cracks are closing since the longitudinal steel would be required to maintain compression zone stability until portions of the core concrete were engaged at potentially greater displacements.

North Reinforcement:

The tensile and compressive vertical strain profiles for extreme fiber bar N3 during push and pull cycles appear in Figure 1.109 and Figure 1.110 respectively. A peak tensile strain of 0.048 was measured 4.33" above the footing on bar N3 during ($\mu_8^{+3} = 6.63"$). This value is lower than the peak tensile strain of 0.052 measured over the same gage length during the original Chichi record at ($\mu_{8.9}^{17.31\,sec} = 7.40"$). Initial strain profiles at low ductility levels are strongly influenced by residual tension strains from previous high ductility cycles during the Chichi record. The compression strains for bar N3 up to ductility six follow the same trend with increasing strain at greater displacements with no sign of measurable deformation.

The complete strain hysteresis for extreme fiber north reinforcing bar N3 appears in Figure 1.111 with an elapsed time color bar to follow the test progression. Since the North reinforcement did not buckle during either load history, stable hysteretic loops were observed for the gage length centered 4.33" above the footing. The transverse steel strain gage hysteresis for the spiral layer which experienced the highest tensile strains overlaying the North unbuckled region appears in Figure 1.112. Large transverse steel strains were not recorded until displacement ductility eight of the cyclic aftershock study.

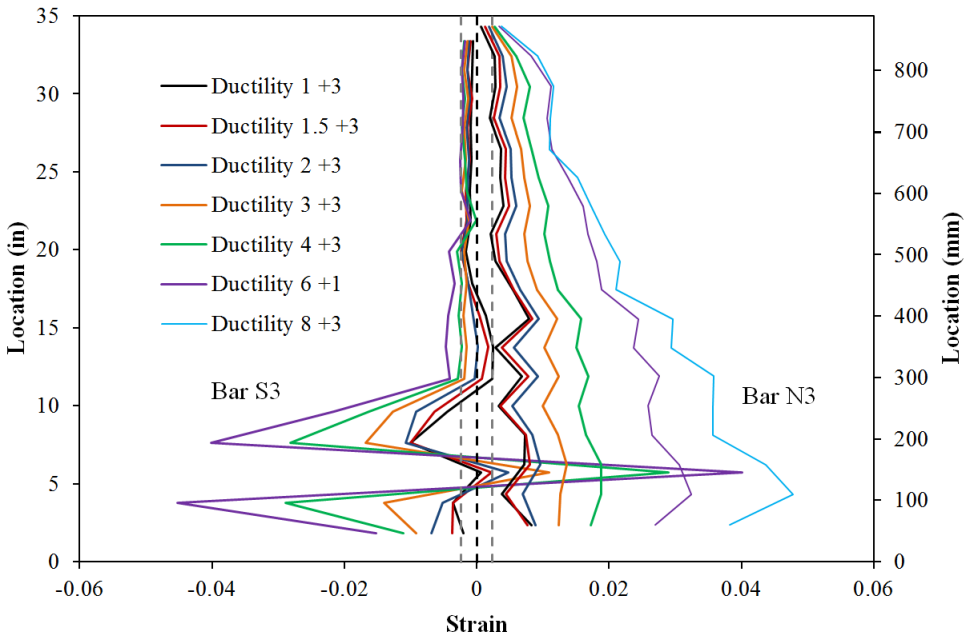

Figure 1.109 T10b – Extreme Fiber Vertical Strain Profiles during Push Cycles (Significant Measurable Deformation in Bar S3)

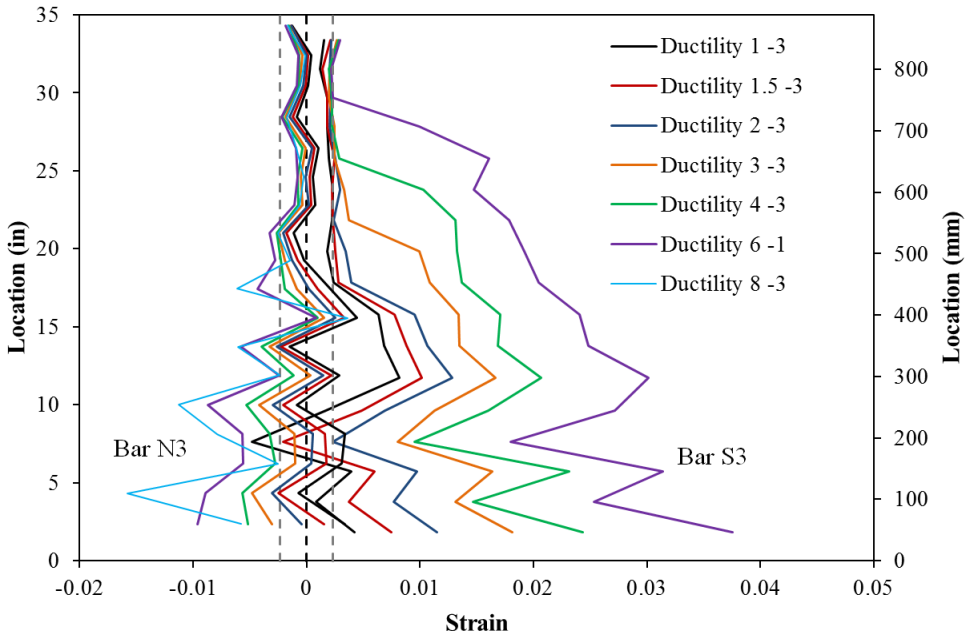

Figure 1.110 T10b – Extreme Fiber Vertical Strain Profiles during Pull Cycles

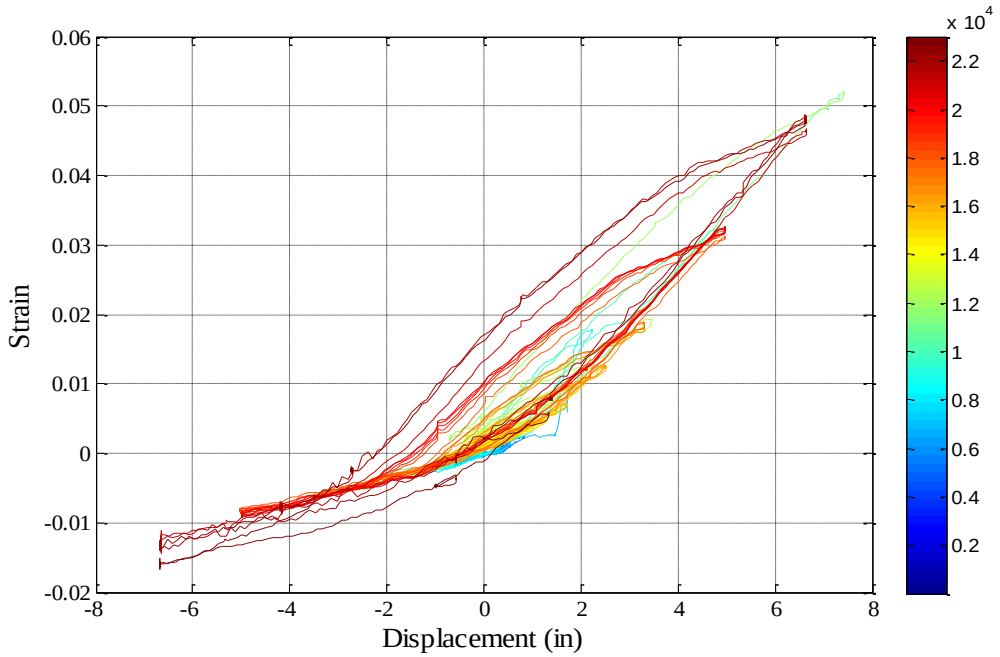

Figure 1.111 T10 and T10b – Bar N3 Strain Hysteresis for Gage Length (4.33" Above)

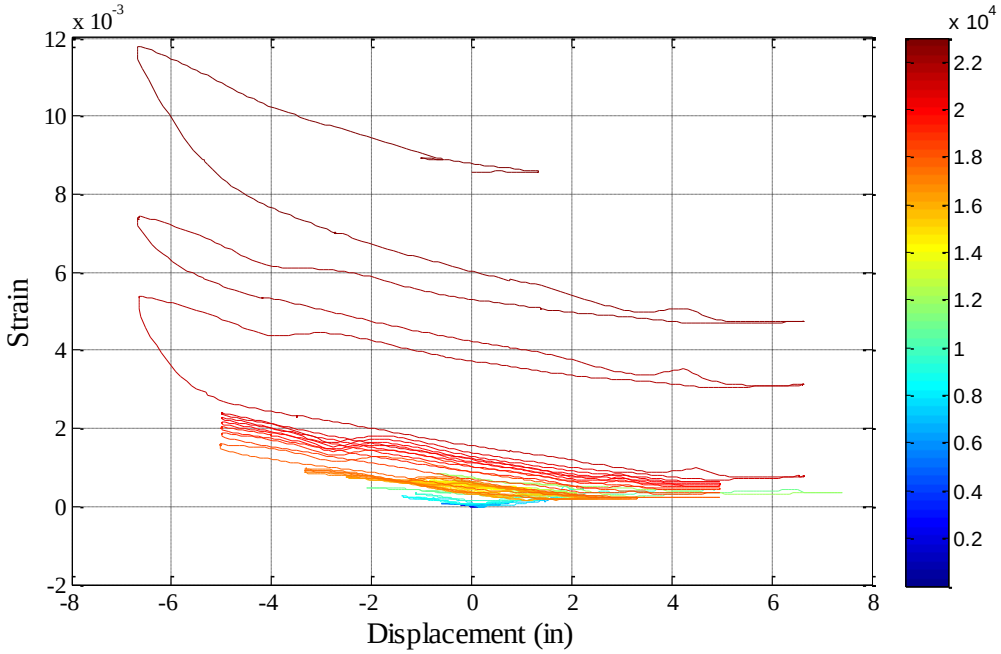

Figure 1.112 T10 and T10b – Spiral Strain Hysteresis over North "Unbuckled" Region

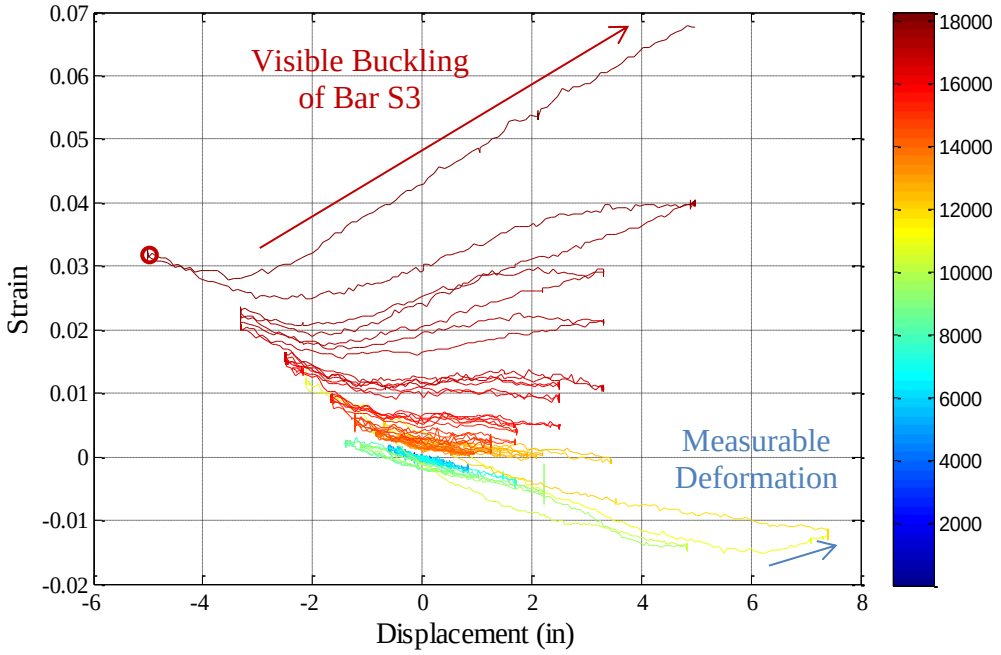

Figure 1.113 T10 and T10b – Bar S3 Strain Hysteresis for Gage Length 5.72" Above

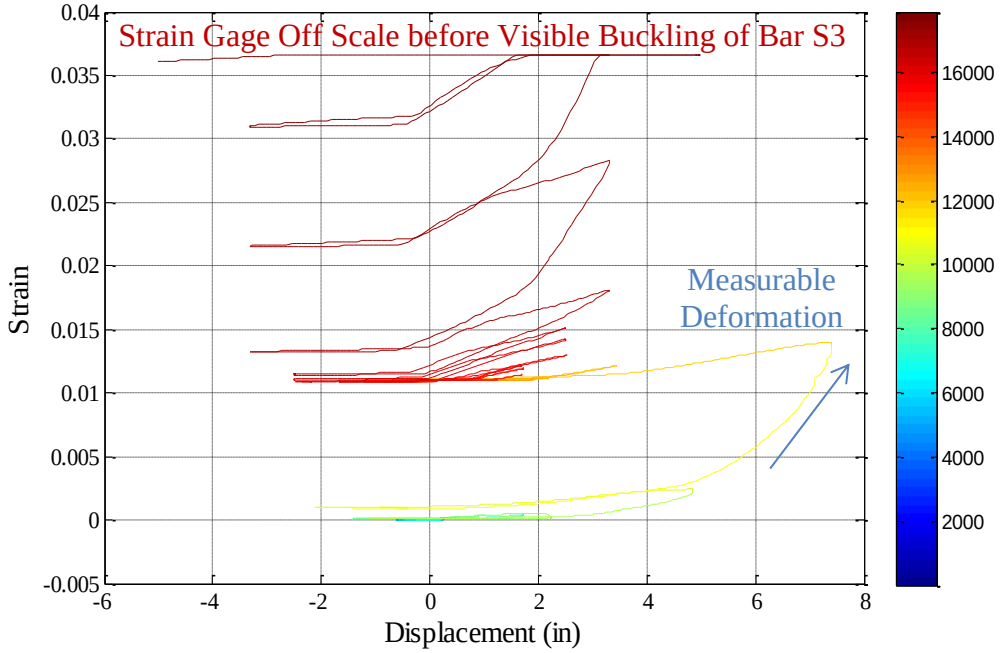

Figure 1.114 T10 and T10b – Spiral Strain Hysteresis over South Buckled Region

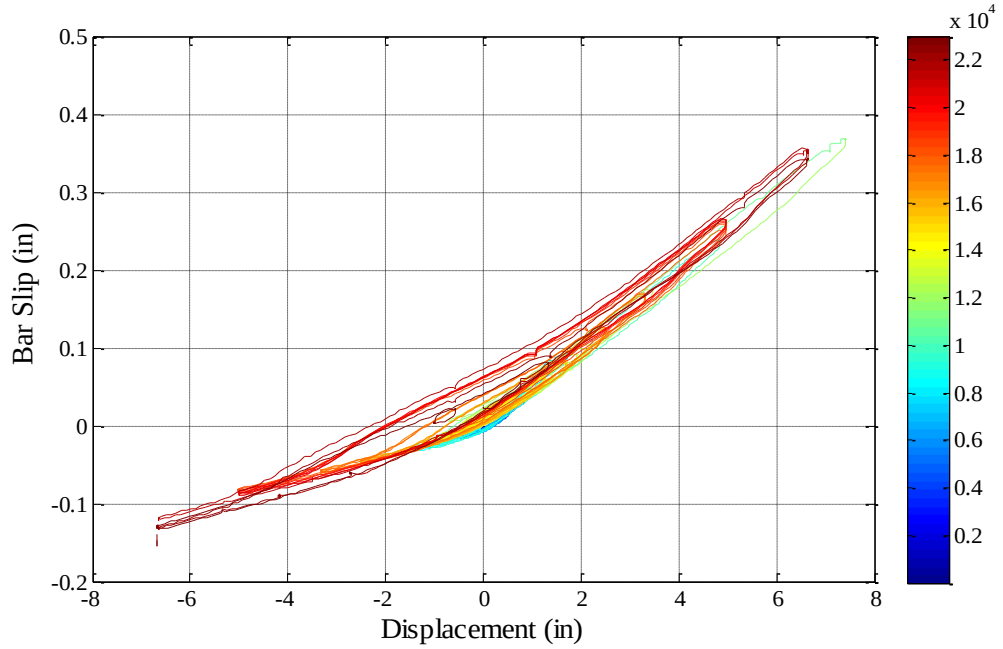

Figure 1.115 T10 and T10b – Bar N3 Base Section Slip Hysteresis

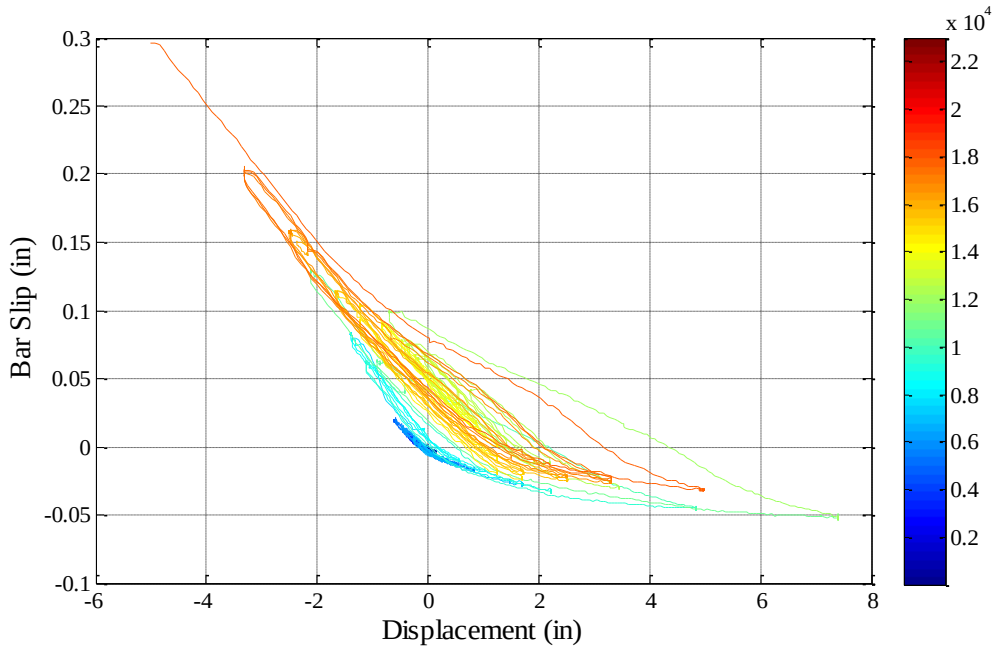

Figure 1.116 T10 and T10b – Bar S3 Base Section Slip Hysteresis

1.1.4 Test 11 – Kobe 1995 Earthquake Load History

Table 1.11 Observational Summary for Test 11 – Kobe 1995 Earthquake Load History

VALUES OF INTEREST:	
Concrete Compressive Strength:	$f_c' = 6070\ psi$
Axial Load:	$P = 170\ kips$
Analytical First Yield Force:	$F_y' = 46.5\ kips$
Experimental First Yield Displacement:	$\Delta_y' = 0.62"$
Analytical Nominal Moment Capacity:	$M_n = 495.58\ kip * ft$
Equivalent Yield Displacement:	$\Delta_y = 0.83"$
Maximum Lateral Force:	$68.0\ kips$
Maximum Lateral Displacement:	$\mu_{10}^{3.86\ sec} = 8.28"$
Failure Mode:	Specimen Saved as a Repair Candidate
DAMAGE OBSERVATIONS:	
First Cracking North:	Unknown Δ during Push to $\mu_{10}^{3.86sec} = 8.28"$
First Cracking South:	Unknown Δ during Pull to $\mu_{-1.5}^{3.44sec} = -1.24"$
Cover Concrete Crushing North:	Unknown Δ during Pull to $\mu_{-6.1}^{4.42sec} = -5.08"$
Cover Concrete Crushing South:	Unknown Δ during Push to $\mu_{10}^{3.86sec} = 8.28"$
Transverse Steel Yield North:	At 1.47" during pull to $\mu_{-2.7}^{7.16sec} = -2.22"$
Transverse Steel Yield South:	At 3.96" during push to $\mu_{10}^{3.86sec} = 8.28"$
Longitudinal Bar Buckling North:	Reversal from $\mu_{9.3}^{6.56sec} = 7.75"$
Longitudinal Bar Buckling South:	Reversal from $\mu_{-6.1}^{4.42sec} = -5.08"$

*$\mu_{10}^{3.86sec} = 8.28"$ represents a ductility ten push cycle 3.86 seconds into the Kobe EQ LH

Table 1.12 Strain Data Summary for Test 11 – Kobe 1995 Earthquake Load History

MATERIAL STRAINS:	
Cover Concrete Crushing North:	N/A, During cycle to $\mu_{-6.1}^{4.42sec} = -5.08"$
Cover Concrete Crushing South:	N/A, During cycle to $\mu_{10}^{3.86sec} = 8.28"$
Transverse Steel Yield North:	N/A, Due to Reversal From Tensile Strain
Transverse Steel Yield South:	$\varepsilon_s = 0.0163$ $(compression)$
Longitudinal Bar Buckling North:	$\varepsilon_s = 0.059$ $(peak\ tension\ prior\ to\ bb)$
	$\varepsilon_s = 0.012$ $(peak\ comp.\ prior\ to\ bb)$
Longitudinal Bar Buckling South:	$\varepsilon_s = 0.033$ $(peak\ tension\ prior\ to\ bb)$
	$\varepsilon_s = 0.037$ $(peak\ comp.\ prior\ to\ bb)$
Mander (1988) Ultimate Concrete Compression Strain, $\varepsilon_{cu} = 0.0187$	

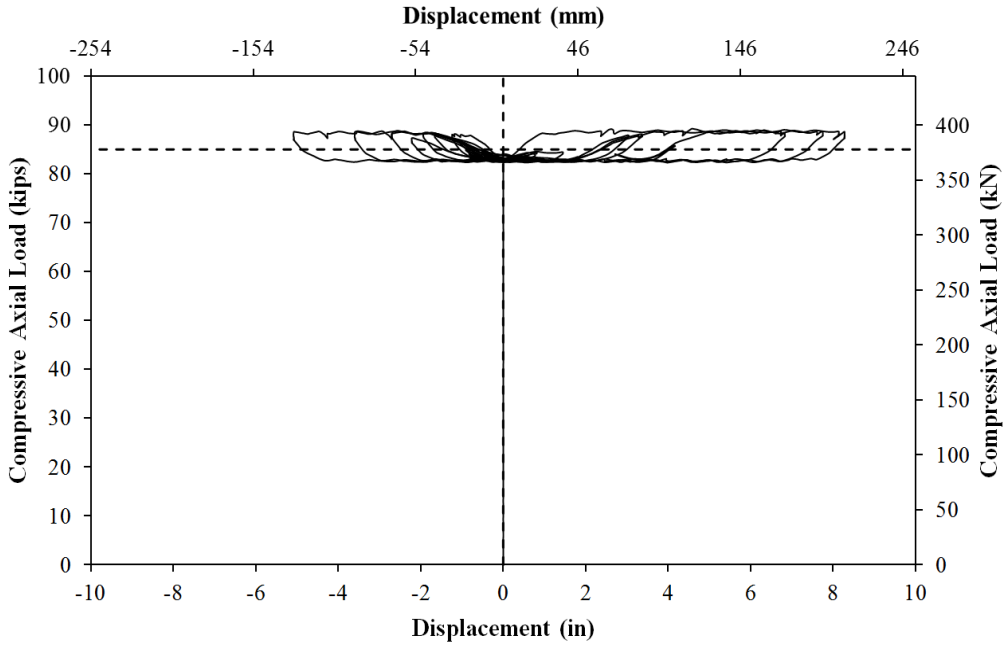

Figure 1.117 T11 – Compressive Axial Load from One Jack (Total = 2*Value)

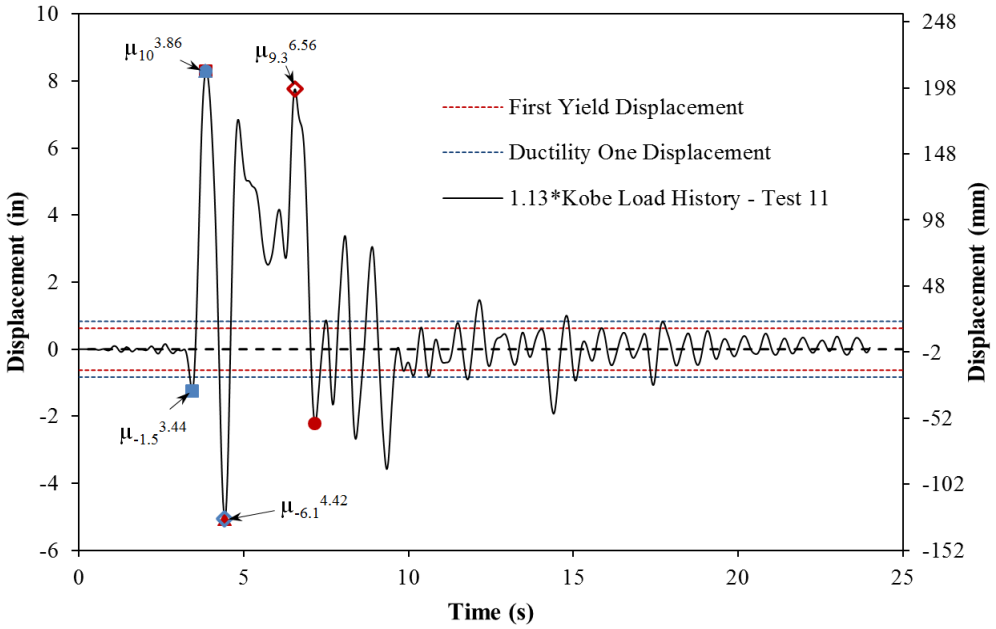

Figure 1.118 T11 – Kobe 1995 Earthquake Load History

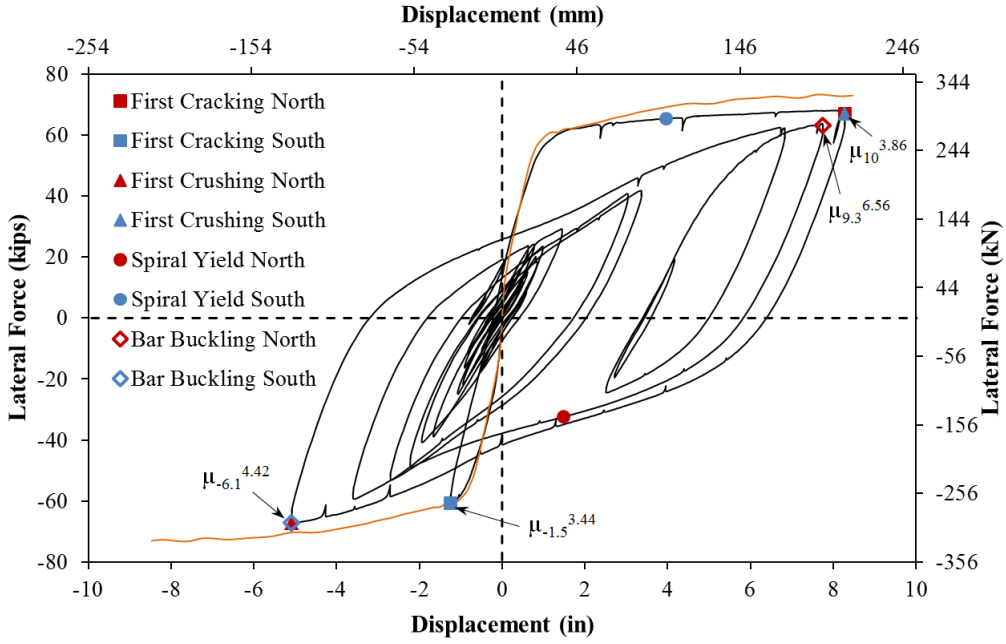

Figure 1.119 T11 – Kobe Earthquake Hysteretic Response

Test 11 – Kobe Earthquake Load History:

The analytical top column displacement history for the scaled Kobe earthquake, see Figure 1.118, was determined using fiber-based numerical simulation in OpenSees. A 1.13x scaled version of the 1995 Kobe Japan earthquake was selected because it contains a near monotonic cycle to the peak displacement ductility of ten in one direction followed by the largest reversal to the peak cycle in the opposing direction of loading. In previous time history based tests, buckling did not occur during the Chile or Chichi records scaled to displacement ductility 8.7 and 8.9 respectively. The results from the asymmetric Chichi record suggest that high ductility cycles can decrease the effectiveness of transverse steel as a boundary condition restraining the longitudinal steel. A peak displacement level consistent with ductility ten was chosen to increase the level of tension strain in the steel to evaluate the steel tensile strain limit. The Kobe displacement history is unique since the peak cycle occurs early, without previous cyclic ramp up in a near monotonic fashion. The resulting lateral force vs. top column displacement history for the Kobe earthquake is shown in Figure 1.119.

The North reinforcement was exposed to a tensile strain of 0.059 during the peak cycle, but did not initially buckle after the first large reversal of loading. Instead, the North extreme fiber bar buckled after the second largest push cycle with elastic transverse steel restraint prior to bar buckling. The transverse steel on the South side of the specimen experienced inelastic strains over 0.015 during the largest push cycle of the load history. Since the transverse steel was less effective as a boundary condition restraining buckling, the South reinforcement buckled after reversal from the largest pull cycle with a tensile strain of only 0.033. The Kobe earthquake points out the effects of load history on the longitudinal steel buckling mechanism.

Test 11 – Kobe Earthquake Load History Experimental Observations:

The first cycle of loading consisted a of small pull cycle to ductility 1.5, where cracks were measured at 0.75mm at approximate 5" spacing on the South side of the specimen. The Chile and Chichi records contained a cyclic ramp up to the peak cycle in contrast to the near monotonic push cycle to the peak displacement in the Kobe load history ($\mu_{10}^{3.86\,sec} = 8.28"$). The crack distribution on the North side of the specimen can be seen in the left photo of Figure 1.121, while the extent of crushing on the South side of the specimen appears in the middle photo. During the largest pull cycle at ($\mu_{-6.1}^{4.42\,sec} = -5.08"$), the concrete on the North side of the specimen crushed and the reinforcement did not show signs of visible buckling even though large tensile strains occurred during the near monotonic push cycle, Figure 1.121.

The South side of the specimen was exposed to large compressive strains during ($\mu_{10}^{3.86\,sec} = 8.28"$). The dilation of the core concrete caused large strains in the transverse steel which decrease its effectiveness as a boundary condition restraining longitudinal bar buckling during subsequent push cycles. The extreme fiber South reinforcing bar buckled after reversal from the peak cycle in the pull direction ($\mu_{-6.1}^{4.42\,sec} = -5.08"$), as shown in the left photo of Figure 1.122. Buckling on the South side of the specimen after reversal from such a low level of displacement required diminished lateral restraint from the transverse steel and sufficient tensile strains to induce buckling upon reversal. The extreme fiber North reinforcing bar visibly buckled after reversal from the second largest push cycle at ($\mu_{9.3}^{6.56\,sec} = 7.75"$), as shown in the right photo of Figure 1.122. Additional deformation in previously buckled bars S3 and N3 occurred during the remainder of the load history as shown in Figure 1.123. The specimen was saved as a repair candidate with a single buckled extreme fiber bar on each side of the specimen, but without significant loss in strength.

Figure 1.120 T12 – Crack Distribution at Peak Displacement ($\mu_{10}^{3.86\,sec} = 8.28$")

Figure 1.121 T11 – (Left and Middle) North and South Sides of Specimen during ($\mu_{10}^{3.86\,sec} = 8.28$") and (Right) North Side of the Specimen during ($\mu_{-6.1}^{4.42\,sec} = -5.08$")

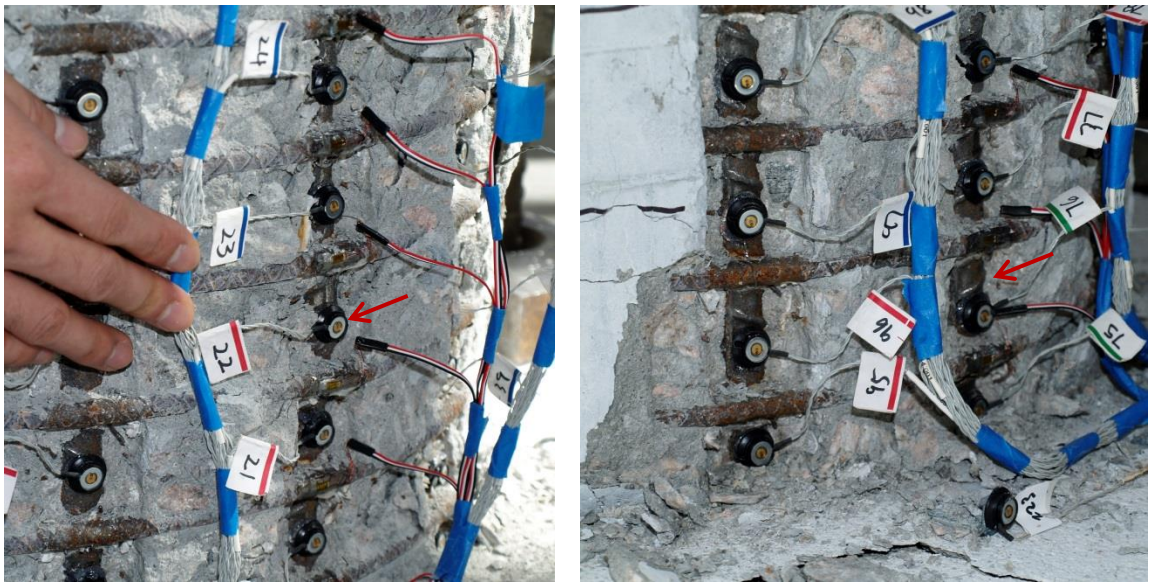

Figure 1.122 T11 – (Left) Buckling of Bar S3 after Reversal from ($\mu_{-6.1}^{4.42\ sec} = -5.08$") and (Right) Buckling of Bar N3 after Reversal from ($\mu_{9.3}^{6.56\ sec} = 7.75$")

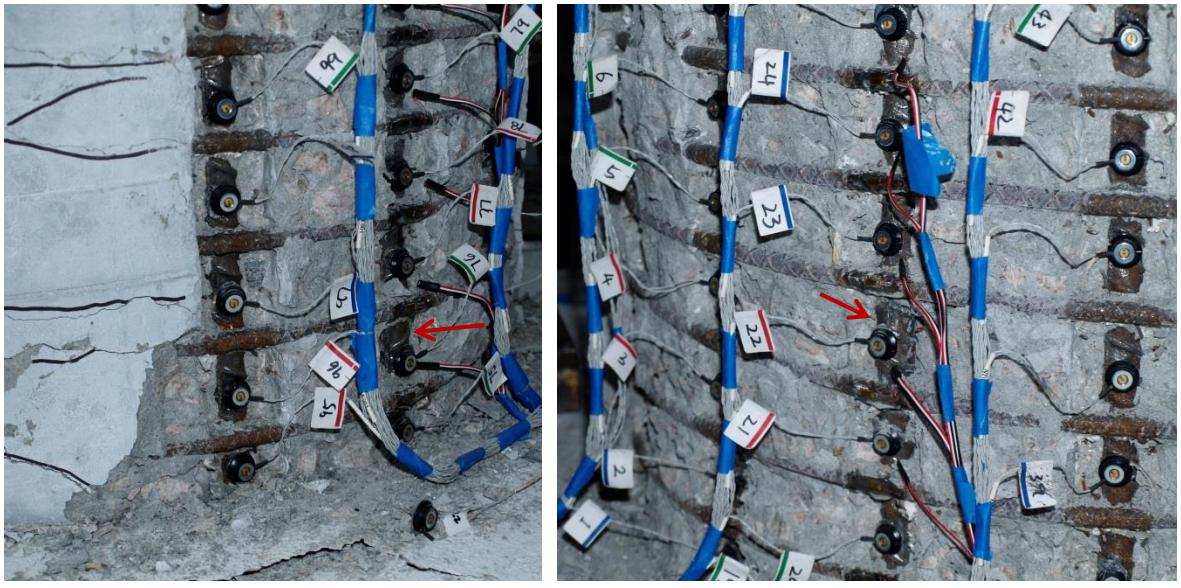

Figure 1.123 T11 – Additional Deformation in the (Left) North and (Right) South Buckled Regions

Test 11 – Kobe Earthquake Load History Strain Data Analysis

North Reinforcement

The extreme fiber vertical strain profiles for push and pull cycles appear in Figure 1.124 and Figure 1.125. The vertical strain profiles in the push direction are all from the backbone curve of the near monotonic push cycle which occurred 3.86 seconds into the Kobe load history, the data observation points appear in Figure 1.140. The lowest gage lengths on each side of the specimen were blocked by debris for most of the push cycle. The pull cycle vertical strain profiles mainly show the reversal from the peak displacement, and are therefore highly influenced by residual strains. The spiral layer placed closed to the footing-column interface remained elastic due to the additional confinement provided by the footing. The spiral strains on the North side of the specimen, see Figure 1.127, remained elastic during the peak pull cycle to ($\mu_{-6.1}^{4.42\,sec} = -5.08$").

Since bar buckling happened so early into the load history, only a few cycles contain usable strain data. The relationship between tensile strain and displacement for Bar N3 during push cycles before bar buckling is shown in Figure 1.128. Moment curvature analysis with the PCK (2007) Lp hinge method significantly over predicts the measured tensile strains at higher displacements. The relationship between compression strain and displacement for the gage length centered 3.33" above the footing appears in Figure 1.129.

The strain hysteresis for the buckled region of the North extreme fiber bar, 3.33" above the footing, appears in Figure 1.134. The peak tensile strain over the North buckled region is slightly lower than the maximum tensile strain sustained by bar N3 since they occur over different gage lengths. The strain values after reversal from ($\mu_{9.3}^{6.56\,sec} = 7.75$") no longer represent engineering strain since visible bar buckling occurred. After this point, the reinforcement is never placed back into compression, indicating an outward deformation of the reinforcement over this location which matches test observations. The transverse steel strain gage hysteresis for the spiral layer overlaying the North buckled region appears in Figure 1.135. The transverse steel restraining the North reinforcement did not yield until

reversal from ($\mu_{9.3}^{6.56\,sec} = 7.75"$), which was when visible buckling was observed in the test. Since the transverse steel on the North side of the specimen did not yield during the largest pull cycle, the inelastic spiral layers are attributed to bar buckling.

South Reinforcement

The measured compressive strains in bar S3 during the peak cycle, see Figure 1.131, are under predicted by moment curvature analysis with the PCK (2007) Lp hinge method. This is likely due to the inelastic layers of transverse steel in this region. The measured strains in the lowest six spiral layers on the South side of the specimen during the push cycle to ($\mu_{10}^{3.86\,sec} = 8.28"$) are shown in Figure 1.126. A single layer of transverse steel entered the inelastic range at a displacement ductility of five. The compressive demand continued to increase during the push to ($\mu_{10}^{3.86\,sec} = 8.28"$) until five layers of transverse steel were inelastic.

The longitudinal steel strain hysteresis over the South buckled region, 7.13" above the footing, appears in Figure 1.132. While the entire strain hysteresis is shown, only the data before buckling occurred, upon reversal from ($\mu_{-6.1}^{4.42\,sec} = -5.08"$), represents engineering strains. This particular gage length was over the outward buckled region of the bar that expands during buckling. This explains the erroneous tensile strains measured during a cycle which should have placed the reinforcement in compression. The transverse steel strain gage hysteresis over the South buckled region appears in Figure 1.133. Transverses steel strains over 0.015 were measured during the peak push cycle to ($\mu_{10}^{3.86\,sec} = 8.28"$). The measured spiral strains sharply increase after reversal from ($\mu_{-6.1}^{4.42\,sec} = -5.08"$) when visible buckling was observed. The strain gage quickly goes off scale and no longer provides meaningful data.

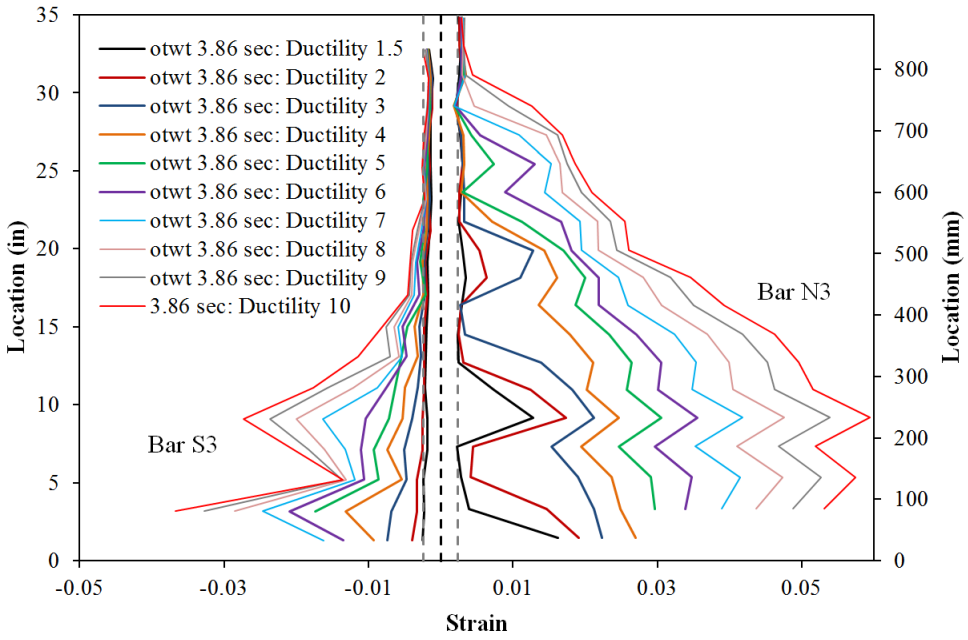

Figure 1.124 T11 – Extreme Fiber Vertical Strain Profiles during Push Cycles

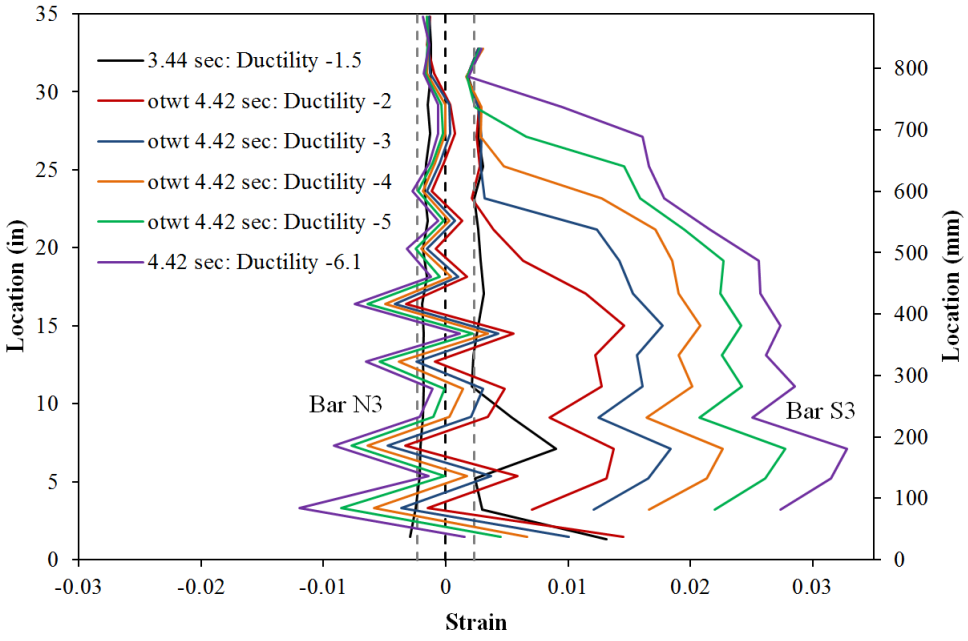

Figure 1.125 T11 – Extreme Fiber Vertical Strain Profiles during Pull Cycles

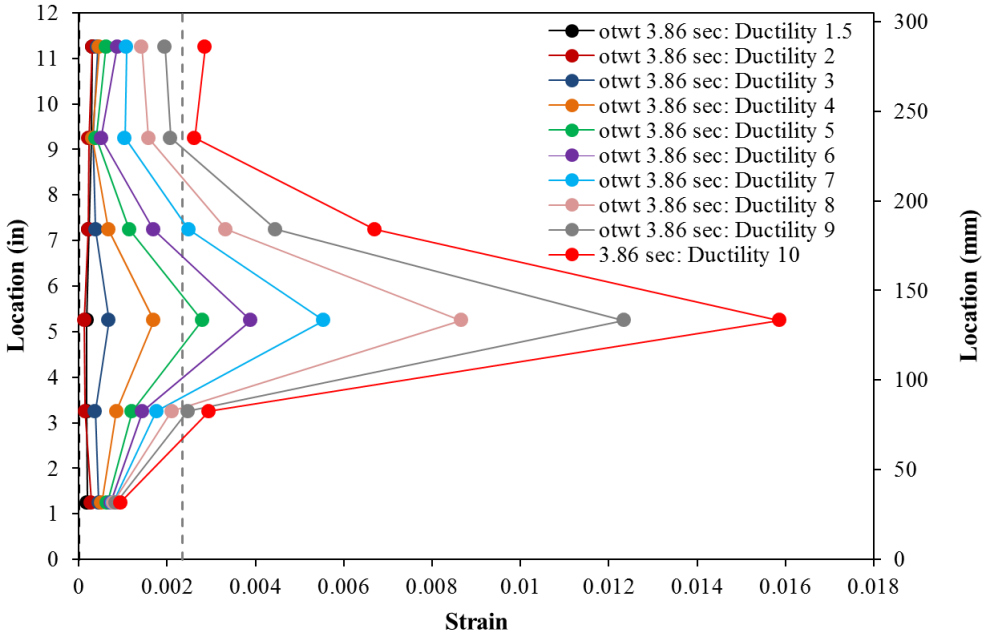

Figure 1.126 T11 – Spiral Strains for Lowest Six Spiral Layers on the South Side

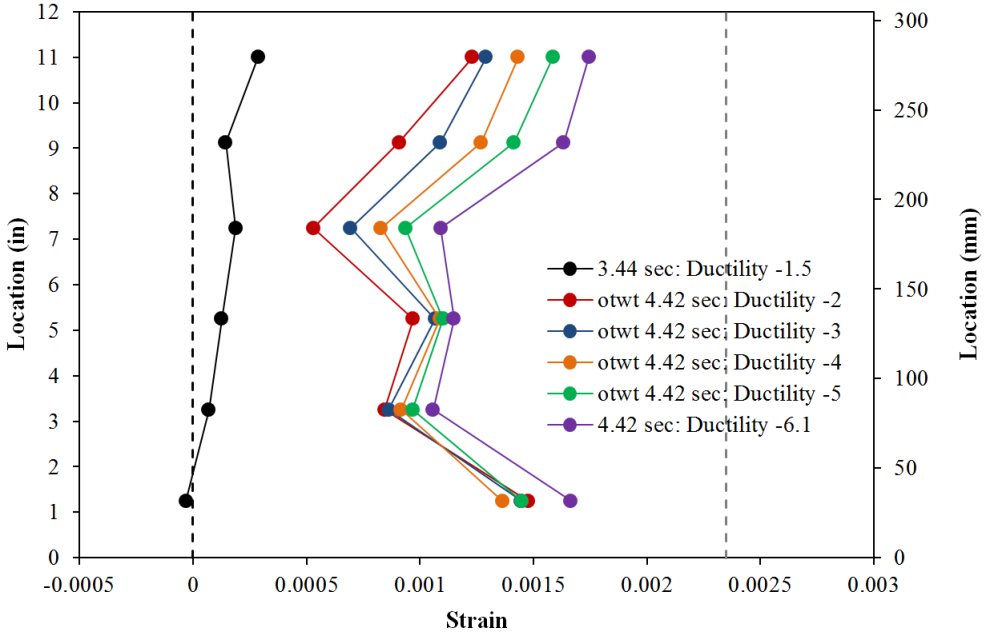

Figure 1.127 T11 – Spiral Strains for Lowest Six Spiral Layers on the North Side

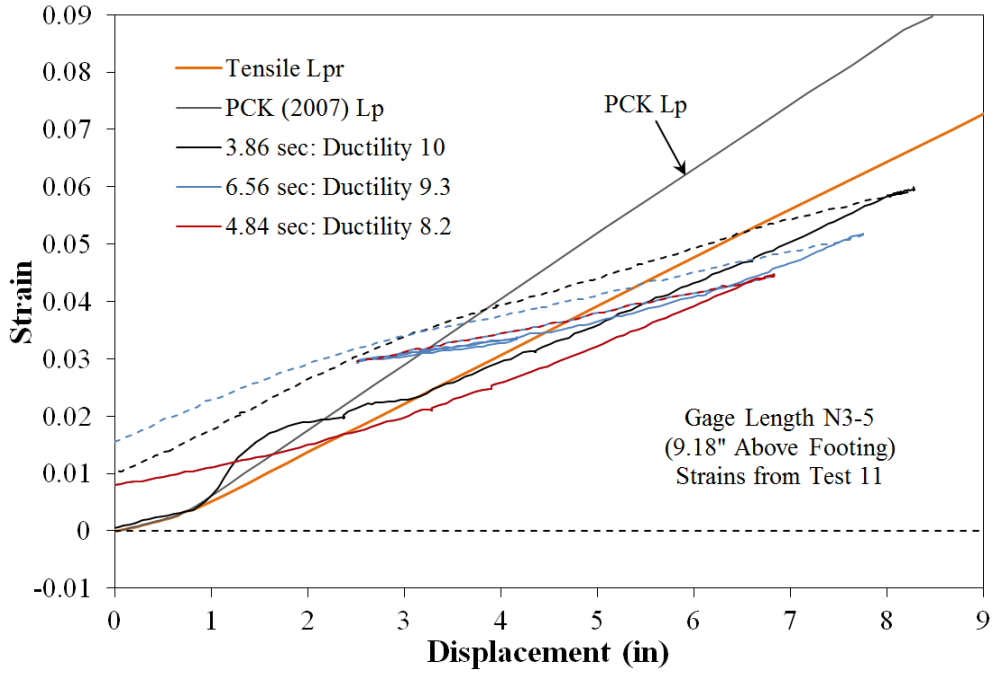

Figure 1.128 T11 – Tensile Strain-Displacement for Bar N3 during Push Cycles

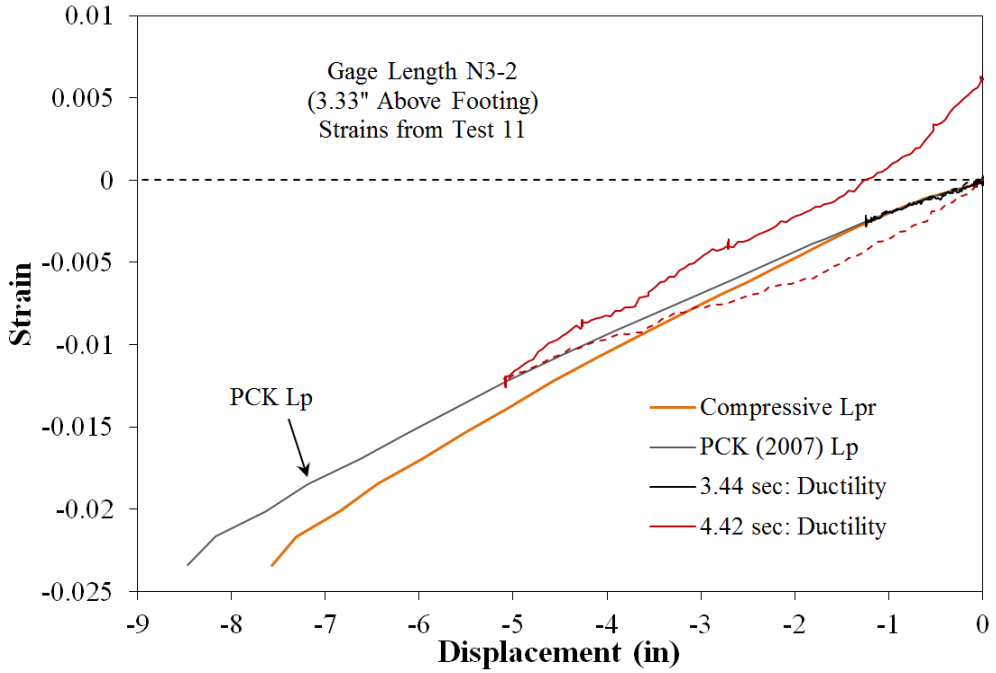

Figure 1.129 T11 – Compressive Strain-Displacement for Bar N3 during Pull Cycles

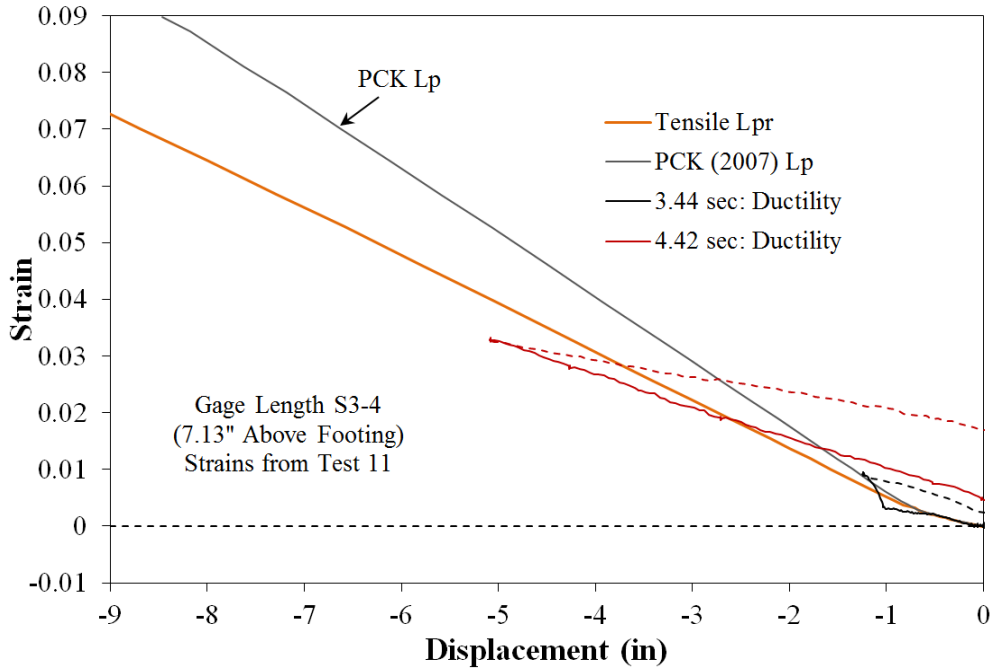

Figure 1.130 T11 – Tensile Strain-Displacement for Bar S3 during Pull Cycles

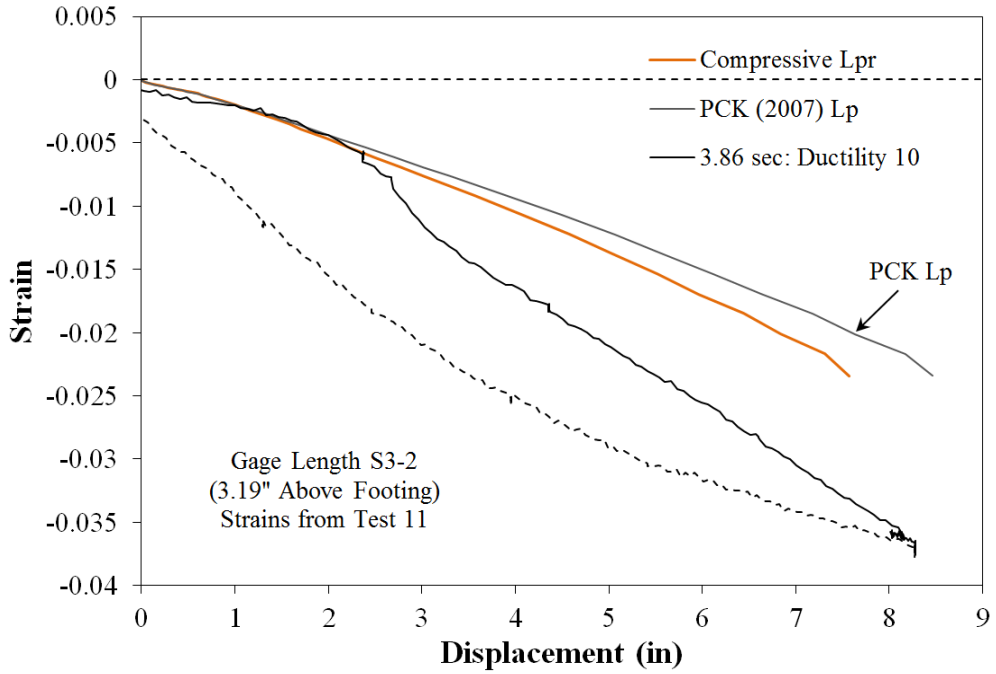

Figure 1.131 T11 – Compressive Strain-Displacement for Bar S3 during Push Cycles

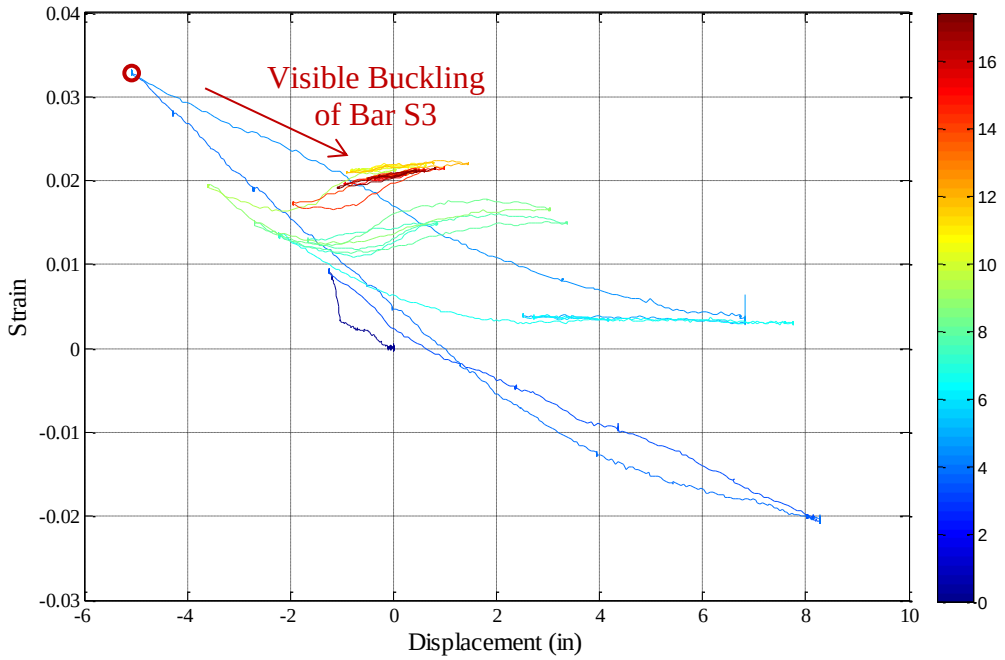

Figure 1.132 T11 – Bar S3 Strain Hysteresis over South Buckled Region (7.13" Above)

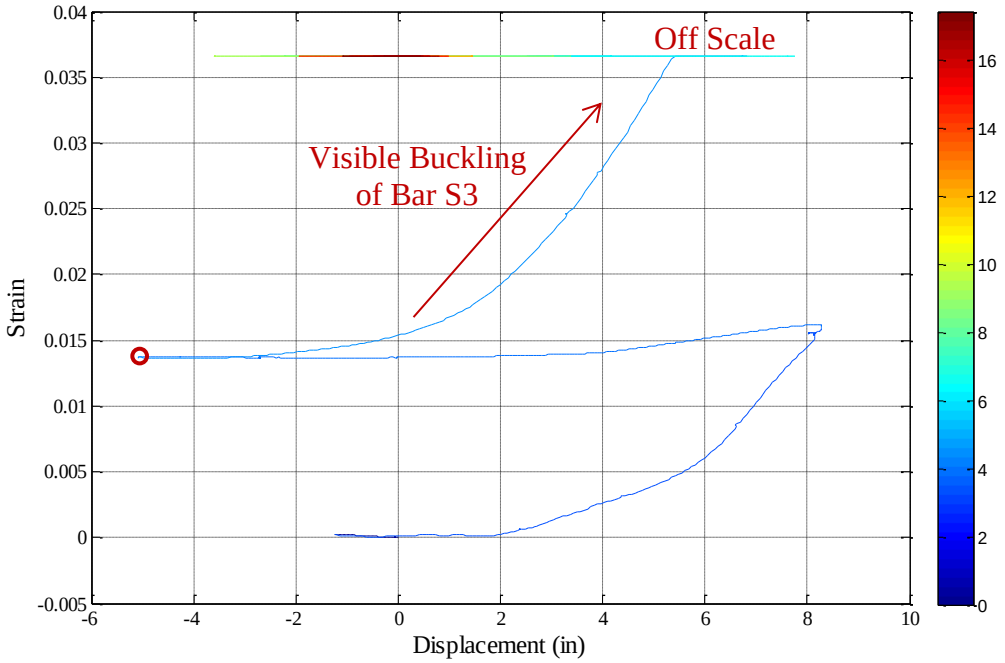

Figure 1.133 Test 11 – Transverse Steel Strain Hysteresis over South Buckled Region

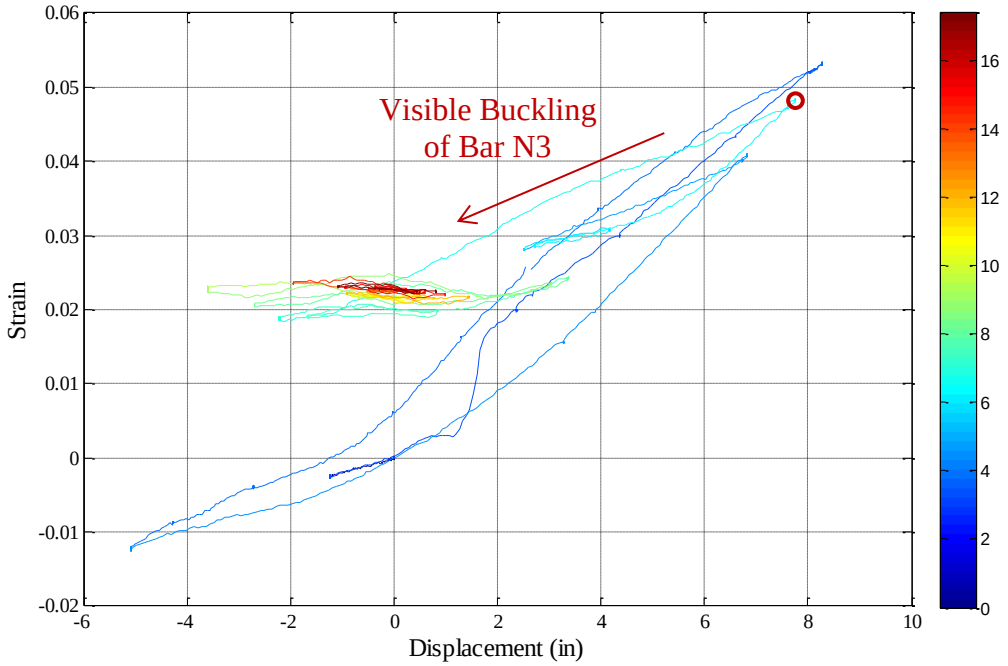

Figure 1.134 T11 – Bar N3 Strain Hysteresis over North Buckled Region (3.33" Above)

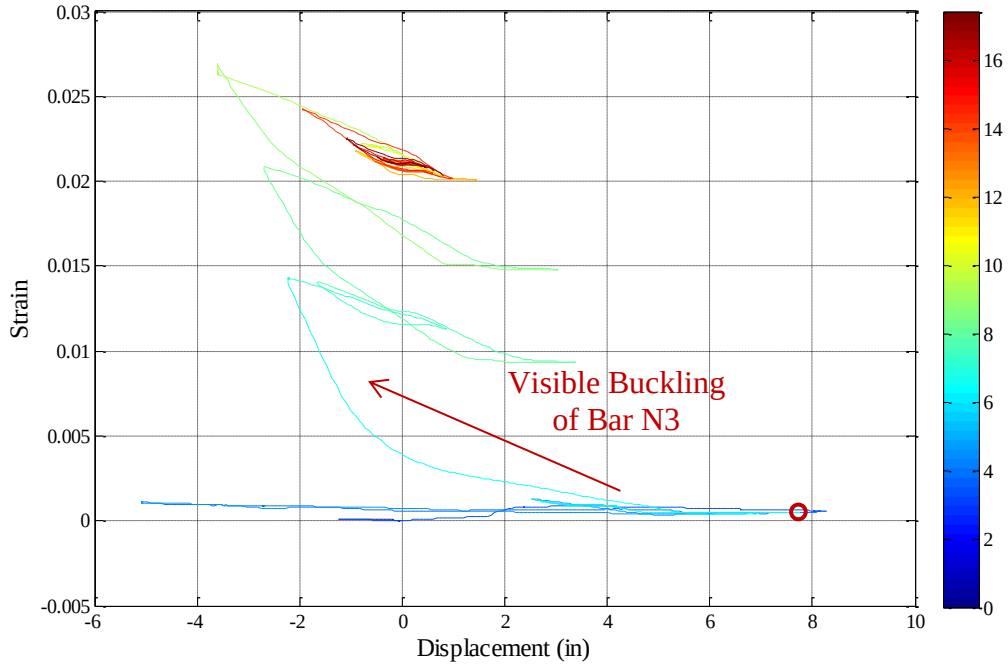

Figure 1.135 T11 – Transverse Steel Strain Hysteresis over North Buckled Region

Test 11 – Kobe Earthquake Load History Curvature and Strain Penetration Data

Vertical curvature profiles for push and pull cycles before bar buckling appear in Figure 1.136 and Figure 1.137. The curvature profiles during pull cycles seem to be affected by residual strains from the peak displacement cycle to ($\mu_{10}^{3.86\,sec} = 8.28$"). The plastic portions of the curvature profiles during pull cycles are less linear when compared to profiles in other tests. The curvatures measured in the lowest 18" above the footing remained effectively constant during the pull cycle to ($\mu_{-6.1}^{4.42\,sec} = -5.08$"). The base section rotations attributable to strain penetration during push and pull cycles appear in Figure 1.138 and Figure 1.139 respectively. A comparison of the measured top column displacements and the integrated displacements from the curvature data and base rotation profiles appear in Figure 1.140. The Optotrak integrated displacements match the measured string potentiometer displacements well throughout the entire range of response. Circle data points in Figure 1.141 plot the measured spread of plasticity as a function of base section rotation.

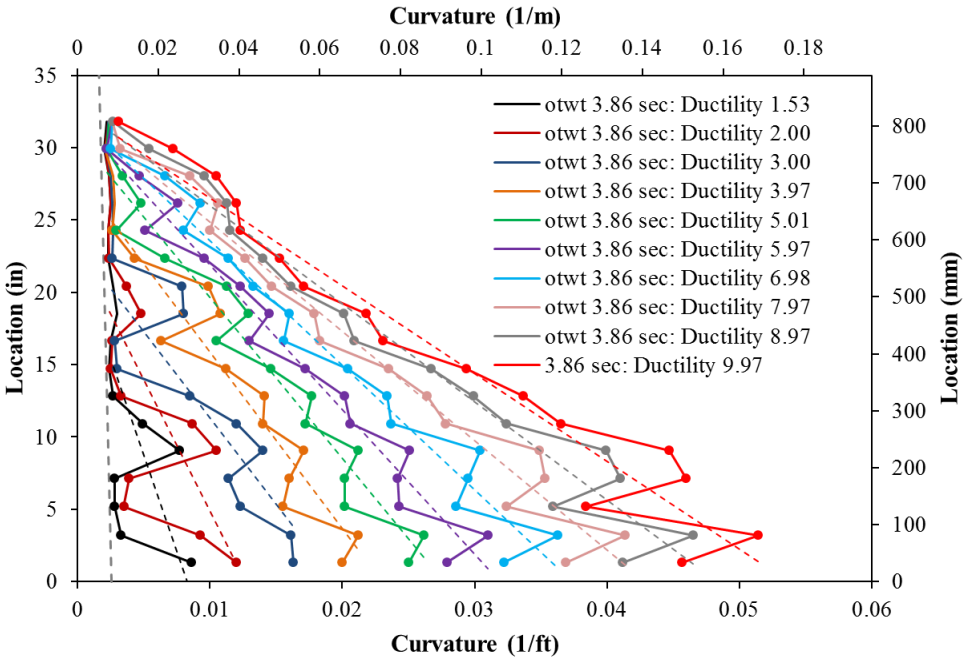

Figure 1.136 T11 – Vertical Curvature Profiles during Push Cycles

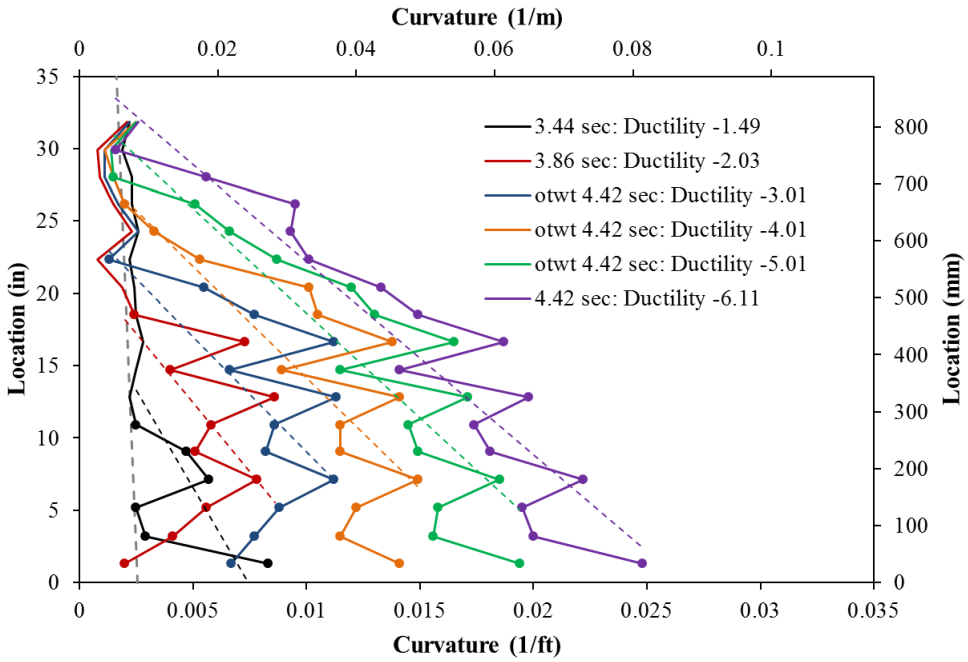

Figure 1.137 T11 – Vertical Curvature Profiles during Pull Cycles

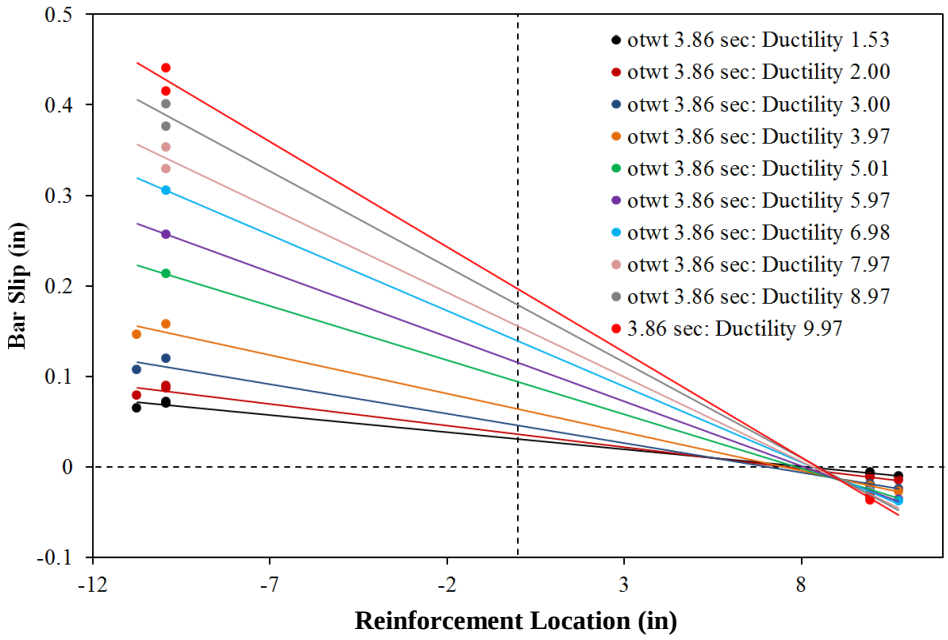

Figure 1.138 T11 – Base Rotation due to Strain Penetration during Push Cycles

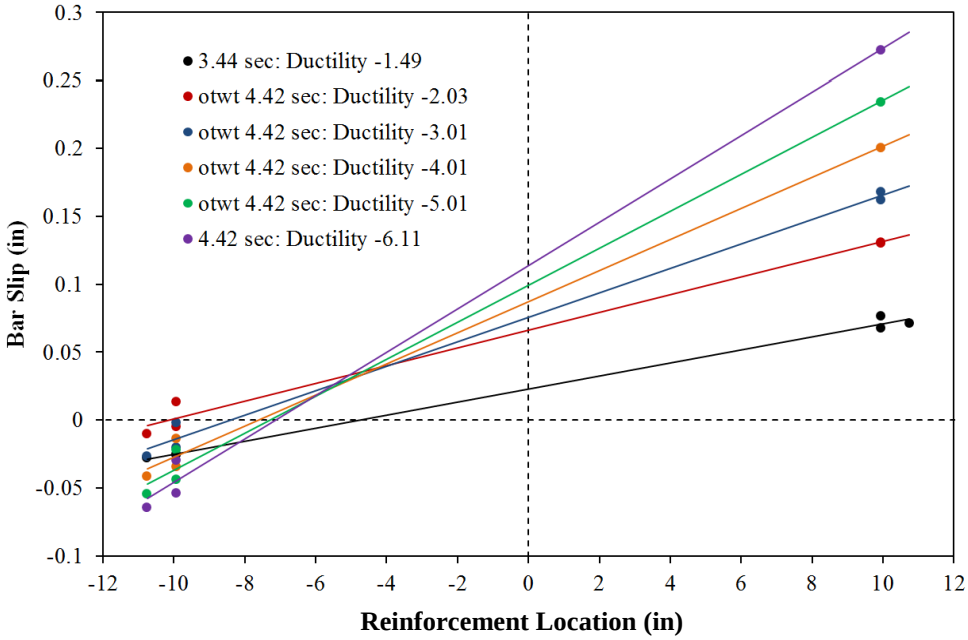

Figure 1.139 T11 – Base Rotation due to Strain Penetration during Pull Cycles

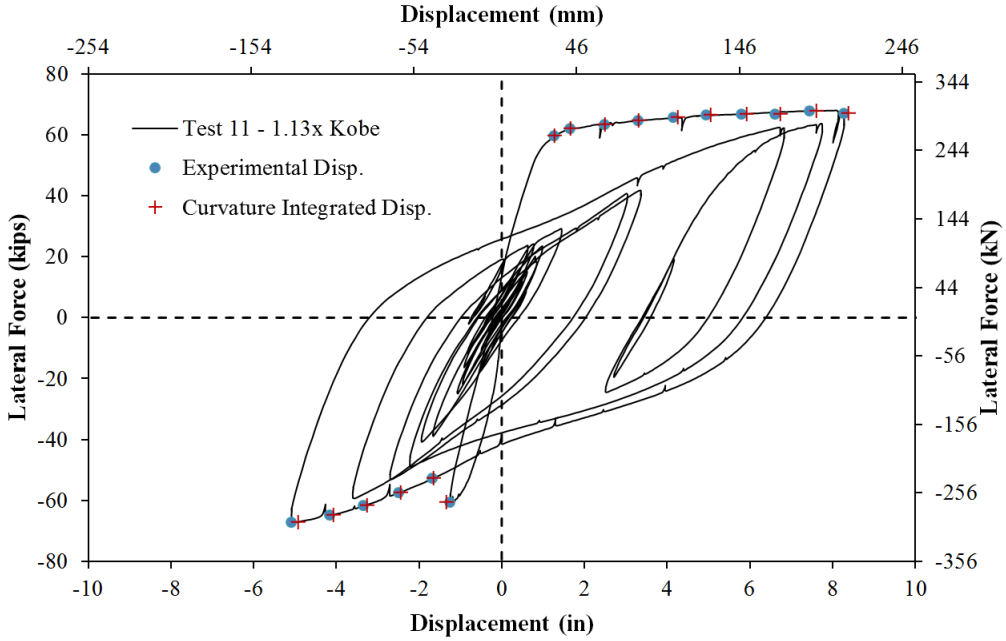

Figure 1.140 T11 – Comparison of Measured and Integrated Displacements

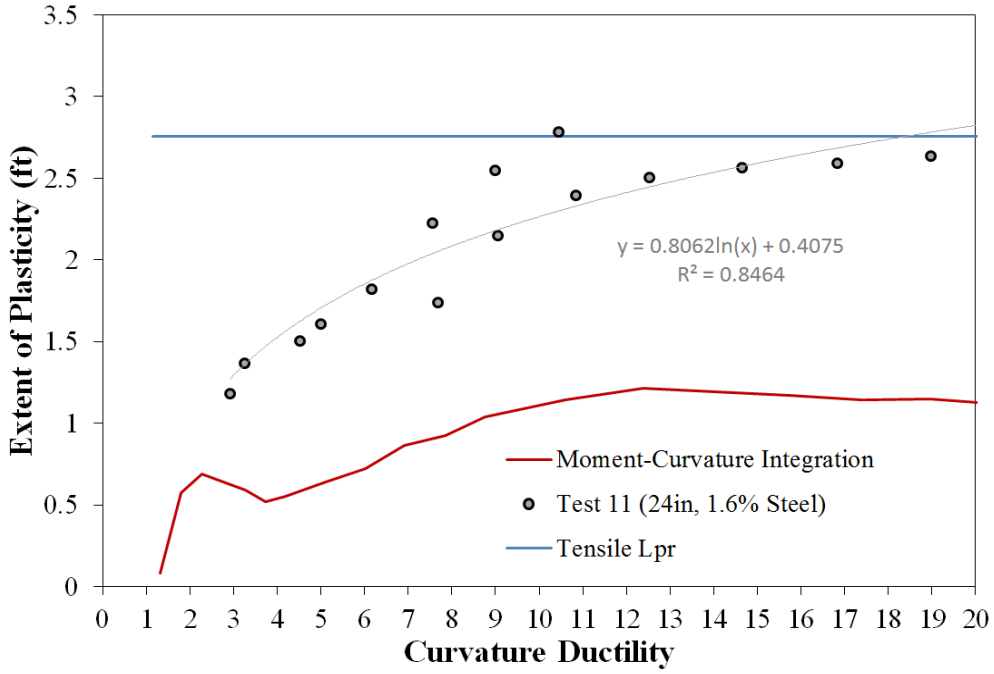

Figure 1.141 T11 – Measured Spread of Plasticity (Circle Data Points)

1.1.5 Test 12 – Japan 2011 Earthquake Load History

Table 1.13 Observational Summary for Test 12 – Japan 2011 Earthquake Load History

VALUES OF INTEREST:	
Concrete Compressive Strength:	$f_c' = 6100\ psi$
Axial Load:	$P = 170\ kips$
Analytical First Yield Force:	$F_y' = 46.5\ kips$
Experimental First Yield Displacement:	$\Delta_y' = 0.62"$
Analytical Nominal Moment Capacity:	$M_n = 494.5\ kip * ft$
Equivalent Yield Displacement:	$\Delta_y = 0.83"$
Maximum Lateral Force:	$72.6\ kips$
Maximum Lateral Displacement:	$\mu_{9.9}^{68.62sec} = 8.22"$
Failure Mode:	Specimen Saved as a Repair Candidate with Buckled Reinforcement
DAMAGE OBSERVATIONS:	
First Cracking North:	$\mu_{0.5}^{44.26sec} = 0.39"$
First Cracking South:	$\mu_{-0.3}^{43.98sec} = -0.26"$
Cover Concrete Crushing North:	$\mu_{-2.2}^{61.80sec} = -1.85"$
Cover Concrete Crushing South:	$\mu_{2.1}^{48.83sec} = 1.77"$
Transverse Steel Yield North:	At $-5.02"$ during pull to $\mu_{-7.9}^{66.88sec} = -6.53"$
Transverse Steel Yield South:	At $5.70"$ during push to $\mu_{9.9}^{68.62sec} = 8.22"$
Longitudinal Bar Buckling North:	Reversal from $\mu_{9.9}^{68.62sec} = 8.22"$
Longitudinal Bar Buckling South:	*Deformation during $\mu_{-5.1}^{70.55sec} = -4.17"$

*$\mu_{9.9}^{68.62sec} = 8.22"$ represents a ductility 9.9 push cycle 68.62 seconds into the Japan EQ LH

Table 1.14 Strain Data Summary for Test 12 – Japan 2011 Earthquake Load History

MATERIAL STRAINS:	
Cover Concrete Crushing North:	$\varepsilon_s = 0.0047$ $(compression)$
Cover Concrete Crushing South:	$\varepsilon_s = 0.0044$ $(compression)$
Transverse Steel Yield North:	$\varepsilon_s = 0.0165$ $(compression)$
Transverse Steel Yield South:	$\varepsilon_s = 0.0176$ $(compression)$
Longitudinal Bar Buckling North:	$\varepsilon_s = 0.058$ $(peak\ tension\ prior\ to\ bb)$
	$\varepsilon_s = 0.021$ $(peak\ comp.\ prior\ to\ bb)$
Longitudinal Bar Buckling South:	$*\varepsilon_s = 0.044$ $(peak\ tension\ prior\ to\ bb)$
*Deformation, No Visible Buckling	$*\varepsilon_s = 0.032$ $(peak\ comp.\ prior\ to\ bb)$
Mander (1988) Ultimate Concrete Compression Strain, $\varepsilon_{cu} = 0.0187$	

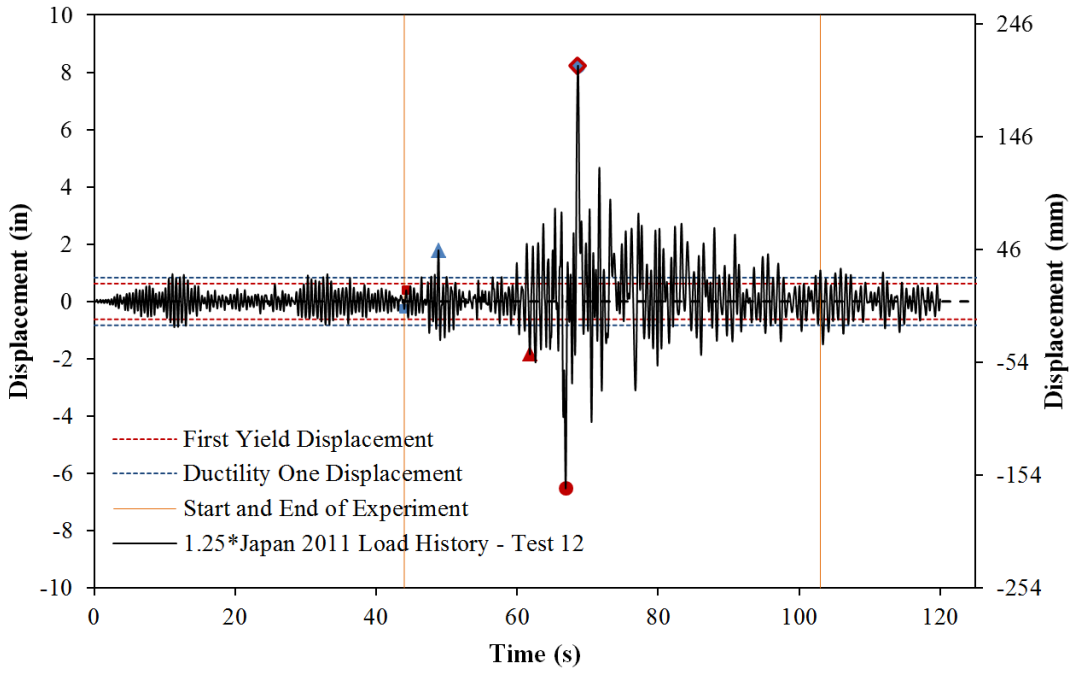

Figure 1.142 T12 – Test 12 – Complete Japan 2011 Load History and Exp. Portion

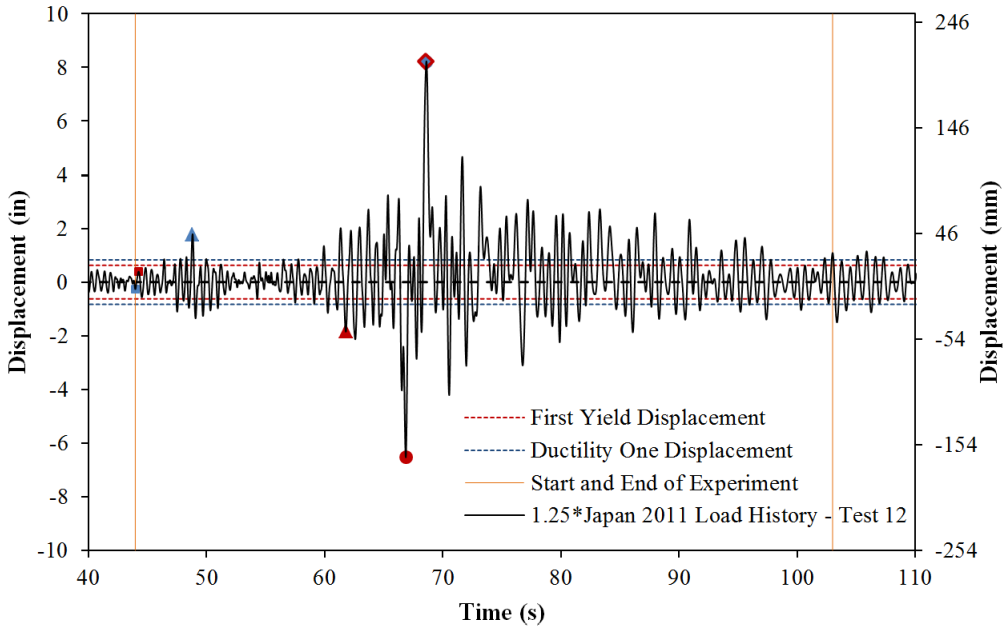

Figure 1.143 T12 – Experimental Portion of the Japan 2011 Earthquake Load History

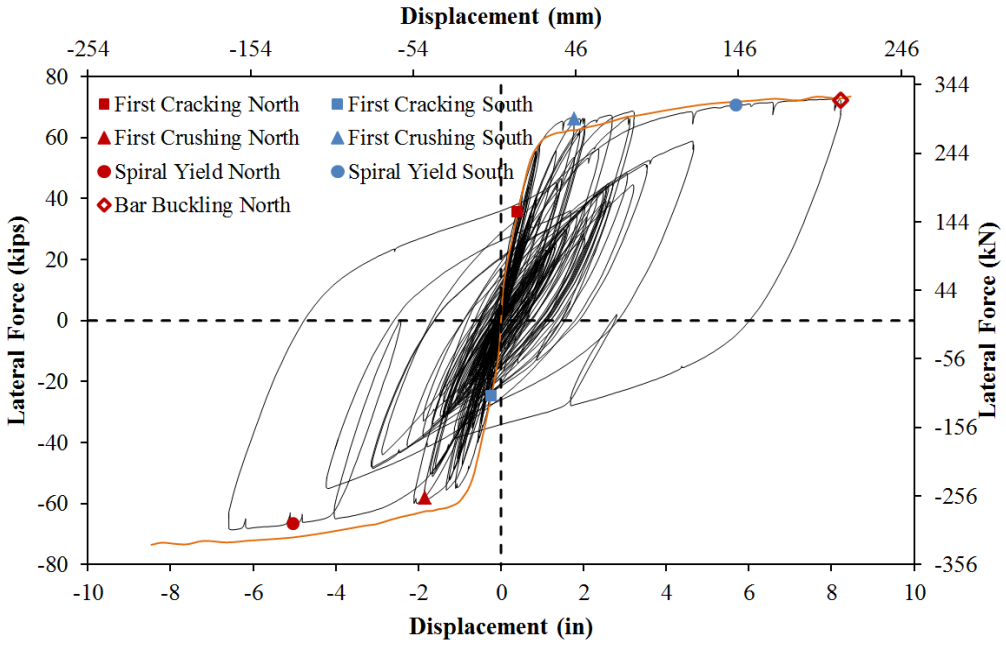

Figure 1.144 T12 – Japan 2011 Lateral Force vs. Top Column Displacement Response

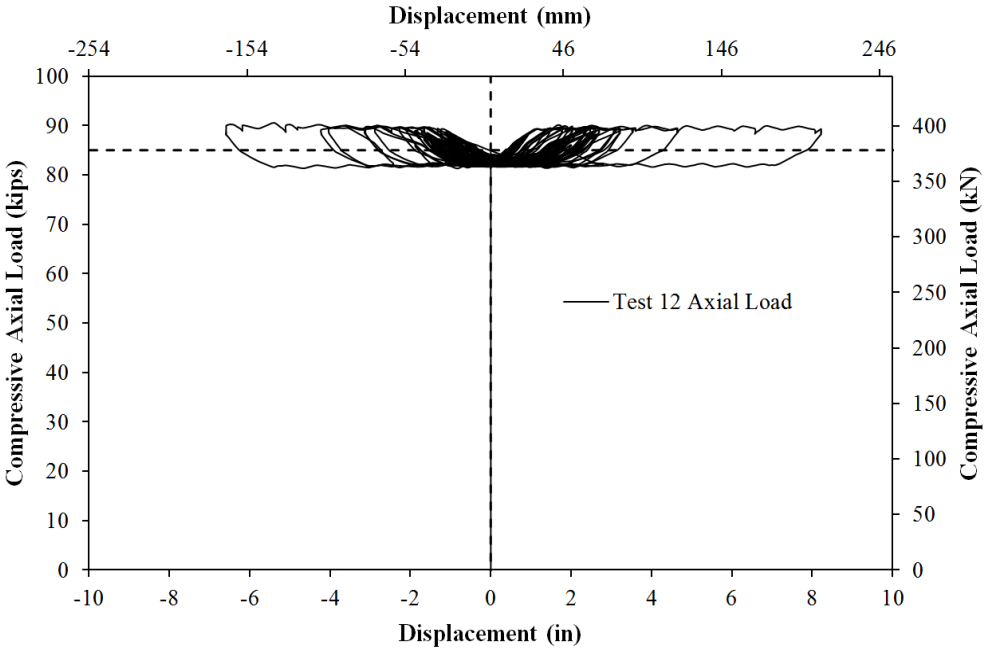

Figure 1.145 T12 – Compressive Axial Load from One Jack (Total = 2*Value)

Test 12 – Japan 2011 Earthquake Load History Experimental Observations:

The analytical top column displacement history for the scaled Japan 2011 earthquake, which appears in Figure 1.142, was determined using fiber-based numerical simulation in OpenSees. A 1.25x scaled version of the 2011 Japan earthquake was selected to reach a displacement ductility of ten during the largest cycle. In previous time history based tests, buckling did not occur during the Chile or Chichi records scaled to displacement ductility 8.7 and 8.9 respectively. The results from the Chichi and Kobe records suggest that high ductility cycles can decrease the effectiveness of transverse steel as a boundary condition restraining the longitudinal steel. A peak displacement ductility level of ten was chosen to increase the level of tension strain in the steel to evaluate the steel tensile strain limit which leads to buckling of longitudinal steel upon reversal of loading. The initial portion of the Japan 2011 earthquake contained reversals around ductility one which have little large impact on the remainder of the test. The portion of the load history recreated in the

experiment is shown in Figure 1.143. The resulting lateral force vs. top column displacement response for the Japan 2011 record appears in Figure 1.144.

The first cycle for the experimental test reached ($\mu_{-0.3}^{43.98sec} = -0.26$"), as shown in Figure 1.143. The first cracks on the South side of the specimen measured 0.1mm at a lateral force of -24.63 kips which is over half of the first yield force. The load history prior to this point contained many cycles of loading around a displacement ductility of one, which were not included in the experimental test. The beginning cycles omitted from the experimental displacement history should not have a large impact on the relationship between strain and displacement or damage within the section. Cracks measuring 0.2mm on the North side of the specimen occurred during ($\mu_{0.5}^{44.26sec} = 0.39$"), which had a lateral force of 35.69 kips. This equates to around 75% of the analytical first yield force.

Cracks on the South side of the specimen were measured at 0.4mm during ($\mu_{-1.3}^{47.53\ sec} = -1.10$") as shown in Figure 1.146. The crack distribution on the North side of the specimen during ($\mu_{2.1}^{48.83\ sec} = 1.77$") appears in the middle and right photos of Figure 1.146. Crack widths on the North side of the specimen measured 2mm and the cover concrete on the South side of the specimen began to crush as shown in the left photo of Figure 1.147. Crushing on the South side of the specimen extended 10" above the footing during ($\mu_{2.4}^{61.36sec} = 2.02$"), while crack widths on the North side of the column measured 2.5mm. In previous tests, cover crushing began after visual flaking. This flaking was observed on the North side of the specimen during ($\mu_{-2.2}^{61.80\ sec} = -1.85$"), as shown in the right photo of Figure 1.147. The extent of crushing on the North side of the specimen extended 7" above the footing during ($\mu_{-2.1}^{65.83\ sec} = -1.71$") as shown in the right photo of Figure 1.148.

The largest cycle in the pull direction of loading occurred during ($\mu_{-7.9}^{66.88\ sec} = -6.53$") with additional crushing on the North side of the specimen, see Figure 1.149. The peak cycle in the push direction at ($\mu_{9.9}^{68.62\ sec} = -8.22$") was concluded without visible buckling on the South side of the specimen, Figure 1.150. A peak lateral load of 72.1 kips was recorded during the largest cycle of the Japan 2011 load history. Upon reversal of loading from

($\mu_{9.9}^{68.62\,sec} = 8.22$"), which placed the North side of the specimen under large tensile strains, the extreme fiber North reinforcing bar N3 buckled on the way to ($\mu_{2.0}^{68.95\,sec} = 1.68$"), Figure 1.151. Even though the reversal only brought the specimen to a lower ductility in the same direction of loading as the peak cycle, a lateral load of -27.40 kips was recorded due to hysteretic offset from the peak displacement cycle. Therefore, visible buckling was observed while the cracks on the North side of the specimen remained open and the North reinforcement was the sole source of compression zone stability. After a small push cycle to ($\mu_{3.4}^{69.12\,sec} = 2.80$"), a second reinforcing bar N4 on the North side of the specimen buckled on the way to ($\mu_{-1.4}^{69.41\,sec} = -1.14$"), as shown in the right photo of Figure 1.151. The rest of the load history progressed without any additional buckled reinforcement or rupture of buckled reinforcement. The deformation in the previously buckled bars increased and the core concrete over the North buckled region began to deteriorate as the load history progressed, see Figure 1.152. Visible buckling of the South reinforcement was never observed, although very slight deformation over the bottom three transverse steel spacing was noticed. This deformation never visibly increased with additional cycles.

Figure 1.146 T12 – (Left) South Crack Distribution during ($\mu_{-1.3}^{47.53\,sec} = -1.10$") and (Middle & Right) North Crack Distribution during ($\mu_{2.1}^{48.83\,sec} = 1.77$")

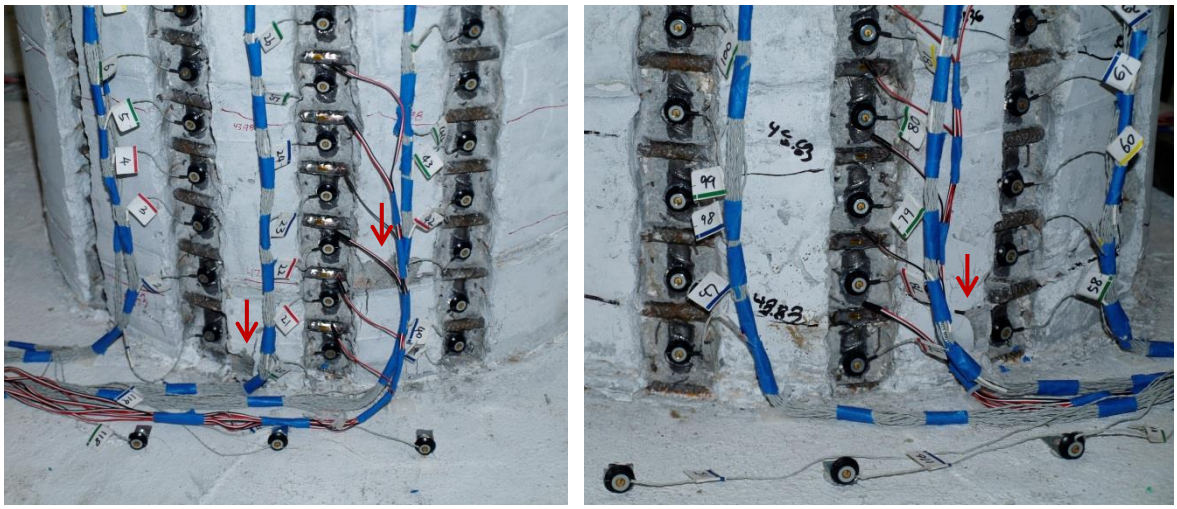

Figure 1.147 T12 – First Signs of Crushing (Left) South Side at ($\mu_{2.1}^{48.83\ sec} = 1.77$") and (Right) North Side at ($\mu_{-2.2}^{61.80\ sec} = -1.85$")

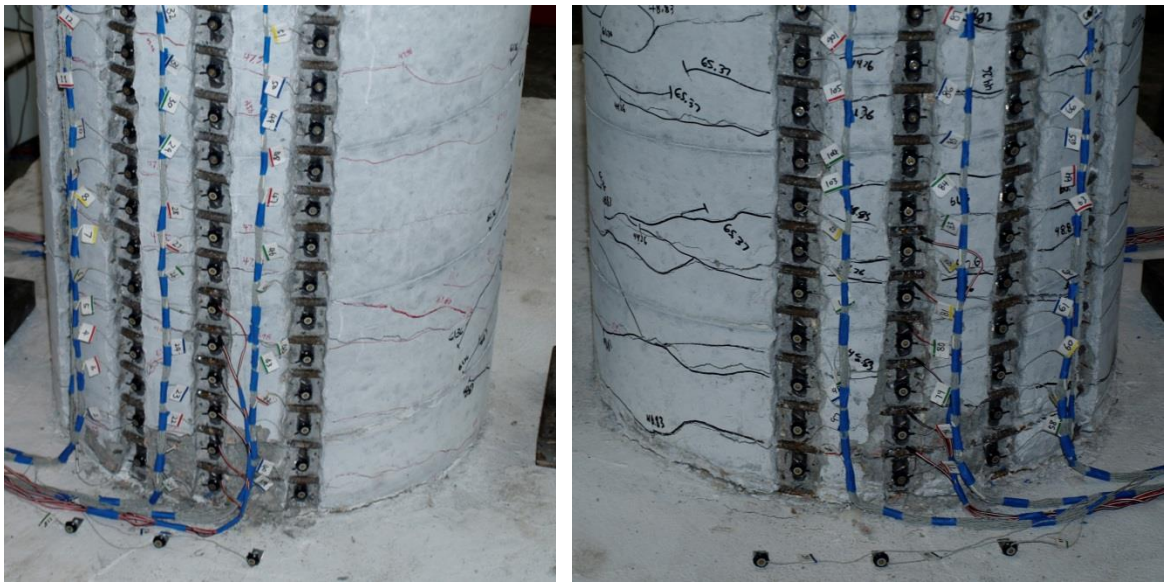

Figure 1.148 T12 – (Left) South side at ($\mu_{2.4}^{61.36\ sec} = 2.02$") and (Right) North side at ($\mu_{-2.1}^{65.83\ sec} = -1.71$")

Figure 1.149 T12 – Peak Pull Cycle at ($\mu_{-7.9}^{66.88\,sec} = -6.53$") – (Left) Back Side of the Specimen, (Middle) South Side, and (Right) North Side

Figure 1.150 T12 – Peak Push Cycle in the Japan 2011 Load History ($\mu_{9.9}^{68.62sec} = 8.22$")

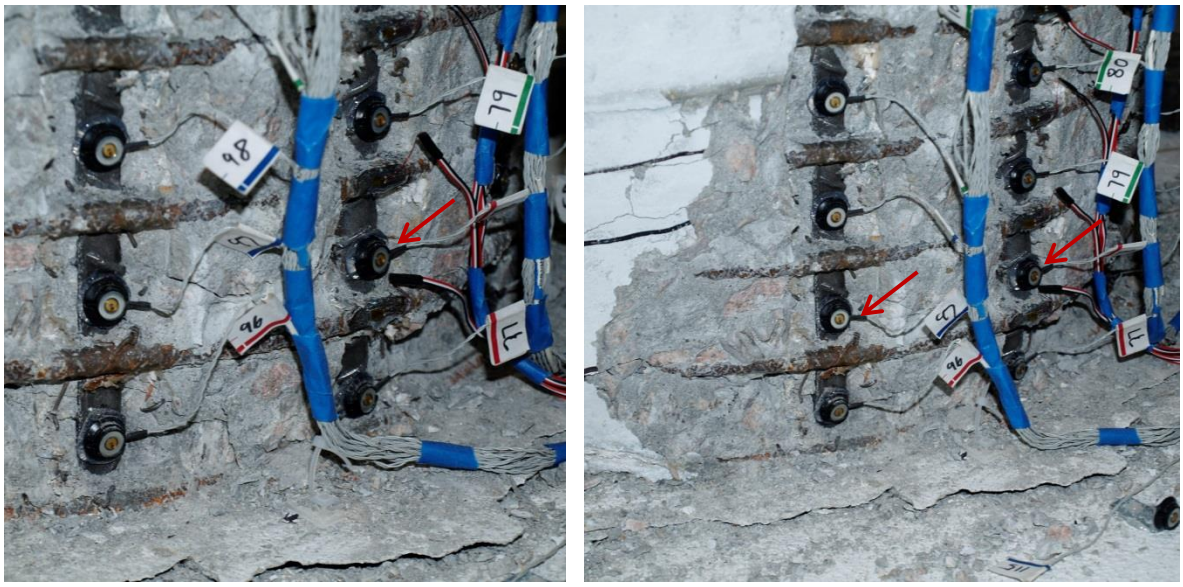

Figure 1.151 T12 – (Left) Buckling of Extreme Fiber Bar N3 after Reversal from ($\mu_{9.9}^{68.62\ sec} = 8.22$") and (Right) Buckling of Bar N4 at ($\mu_{-1.4}^{69.41\ sec} = -1.14$")

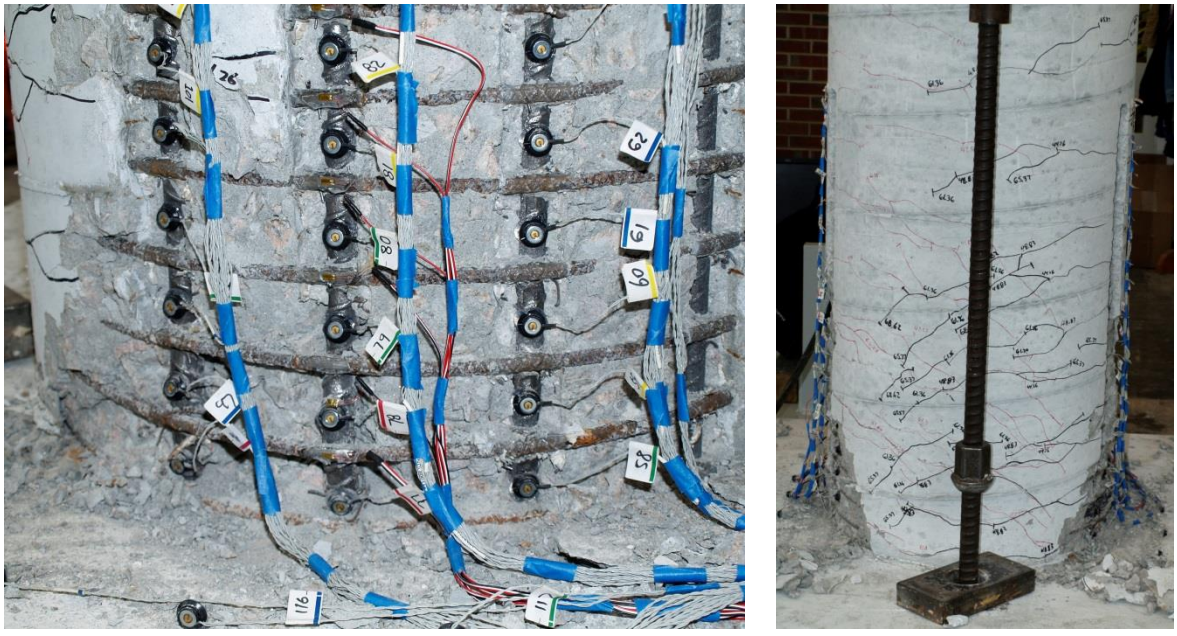

Figure 1.152 T12 – Increased Deformation in the Buckled bars toward the End of LH

Test 12 – Japan 2011 Earthquake Load History Strain Data Analysis:

North Reinforcement

Specific strain data observation points along the backbone curve of cyclic response were chosen for analysis, see Figure 1.153. The extreme fiber vertical strain profiles for push and pull cycles appear in Figure 1.154 and Figure 1.155 respectively. Transverse steel strains for the lowest six spiral layers on the North side of the column appear in Figure 1.157 for compressive pull cycles.

Bar N3 buckled after reversal from a peak tensile strain of 0.058, measured 3.57" above the footing, during the peak push cycle ($\mu_{9.9}^{68.62\,sec} = 8.22"$). The peak compressive strain of -0.021 measured 3.57" above the footing in bar N3 during ($\mu_{-7.9}^{66.88\,sec} = -6.53"$) preceded the peak tensile cycle which caused buckling upon reversal of loading. The location of the largest tensile and compressive strains coincides with the location of outward buckling later in the test. The relationship between tensile strain and displacement from when the column was vertical to the peak of push cycles for extreme fiber bar N3 appears in Figure 1.158. The relationship between compressive strain and displacement for bar N3 appears in Figure 1.159. During initial pull cycles, the moment curvature prediction with the PCK (2007) Lp Hinge Method matches the recorded compressive strains well, but during the peak pull cycle to ($\mu_{-7.9}^{66.88\,sec} = -6.53"$) the recorded strains begin to exceed the prediction at an increasing rate.

The strain hysteresis for the buckled region of bar N3, 3.57" above the footing, appears in Figure 1.163 with an earthquake time color bar to track the progression of the test. The peak tensile and compressive strains for bar N3 were measured over this gage length during the largest push and pull cycles respectively. The transverse steel strain gage hysteresis for the spiral layer overlaying the North buckled region appears in Figure 1.164. The strain in the transverse steel went into the inelastic range during the largest pull cycle to ($\mu_{-7.9}^{66.88\,sec} = -6.53"$). A data marker was placed at the location when the transverse steel strain began to sharply increase during the reversal from ($\mu_{9.9}^{68.62\,sec} = 8.22"$), indicating outward

deformation over the buckled extreme fiber bar. A similar data label is shown on the bar N3 strain hysteresis. Measured strains past this point no longer represent engineering strain, but are included to illustrate the progression of damage. Similarly, the strain gage placed over the transverse steel quickly debonds, preventing further measurement.

South Reinforcement

A peak compressive strain of -0.032 was measured 7.88" above the footing for extreme fiber bar S3. The relationship between compressive strain and displacement from when the column was vertical to the peak of push cycles appears in Figure 1.161 for bar S3. The recorded compressive strains exceed the moment curvature prediction with the PCK (2007) Lp Hinge Method during the peak cycle at ($\mu_{9.9}^{68.62\,sec} = 8.22"$). The relationship between tensile strain and displacement is shown in Figure 1.160.

The strain hysteresis for extreme fiber bar S3 appears in Figure 1.165 with an earthquake time color bar to track the progression of the test. The transverse steel strain hysteresis for the spiral layer restraining the potential outward deformed region of bar S3 is shown in Figure 1.166. The transverse steel strain sharply increased during the peak push cycle at ($\mu_{9.9}^{68.62\,sec} = 8.22"$). Since visible buckling was not observed for the South reinforcement, this sharp increase is largely attributed to compressive demand in the region. The strain hysteresis in Figure 1.165 would suggest that measurable deformation occurred after the second largest pull cycle. This particular gage length was never placed back into compression due to outward deformation during push cycles. The potential deformation cannot be visually verified by test results since bar buckling on the South side of the specimen was not observed. In previous tests, the measurable deformation was verified by buckling in the same region later in the test.

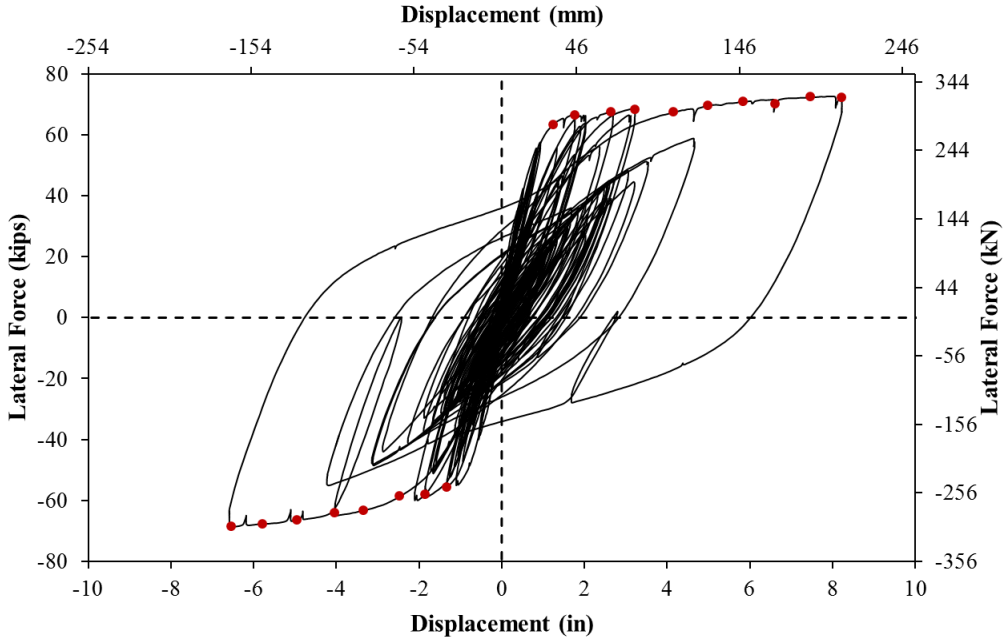

Figure 1.153 T12 – Strain Data Observation Points along the Backbone Curve

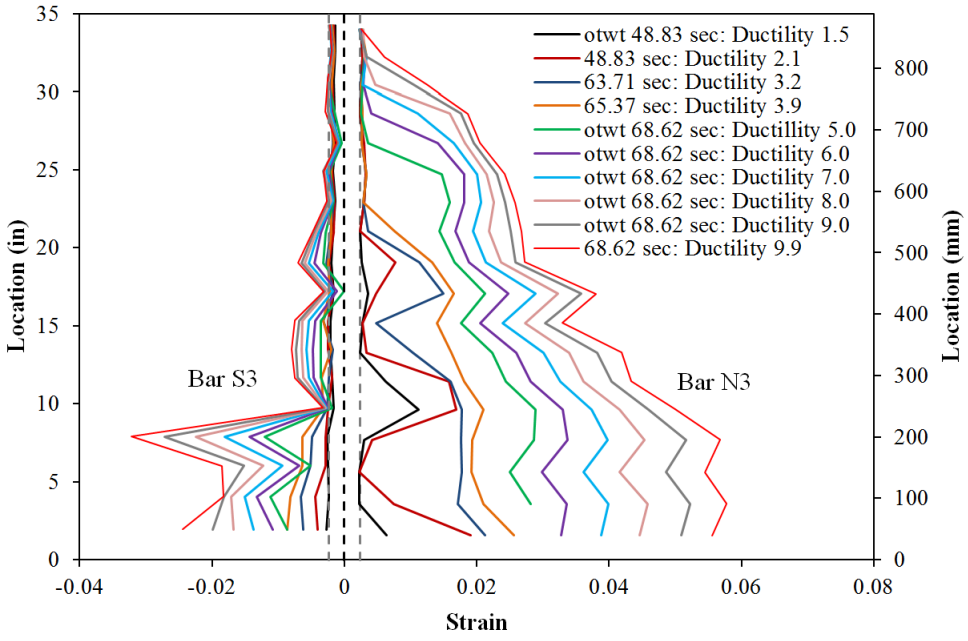

Figure 1.154 T12 – Extreme Fiber Vertical Strain Profiles during Push Cycles

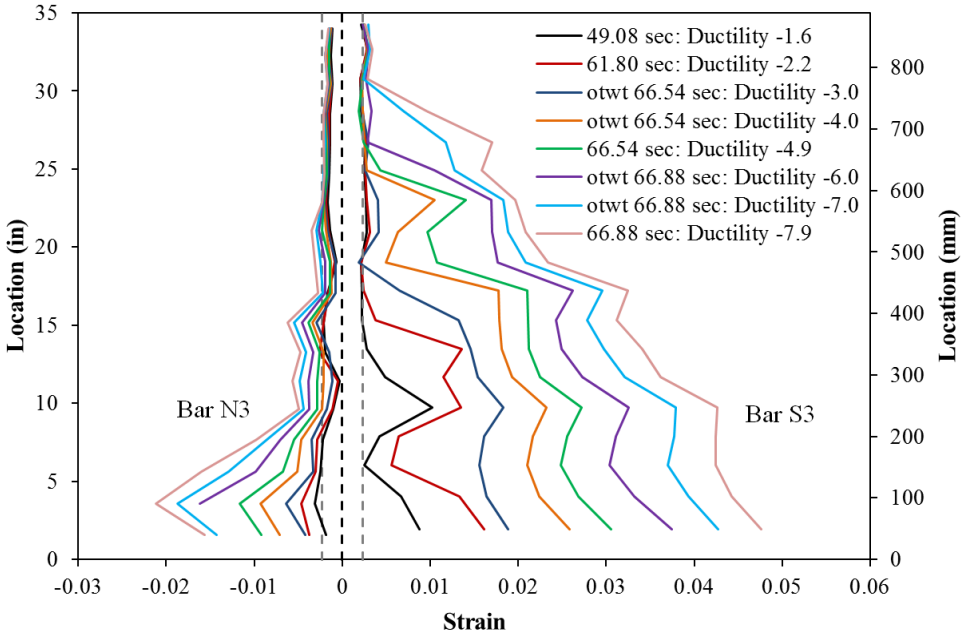

Figure 1.155 T12 – Extreme Fiber Vertical Strain Profiles during Pull Cycles

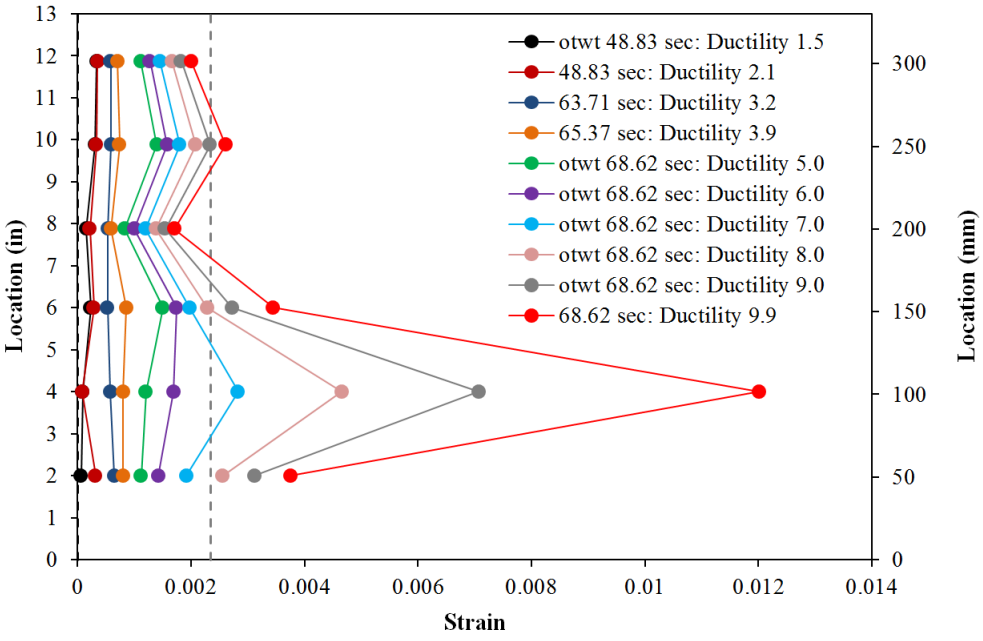

Figure 1.156 T12 – Spiral Strains for Six Lowest Spiral Layers on the South Side

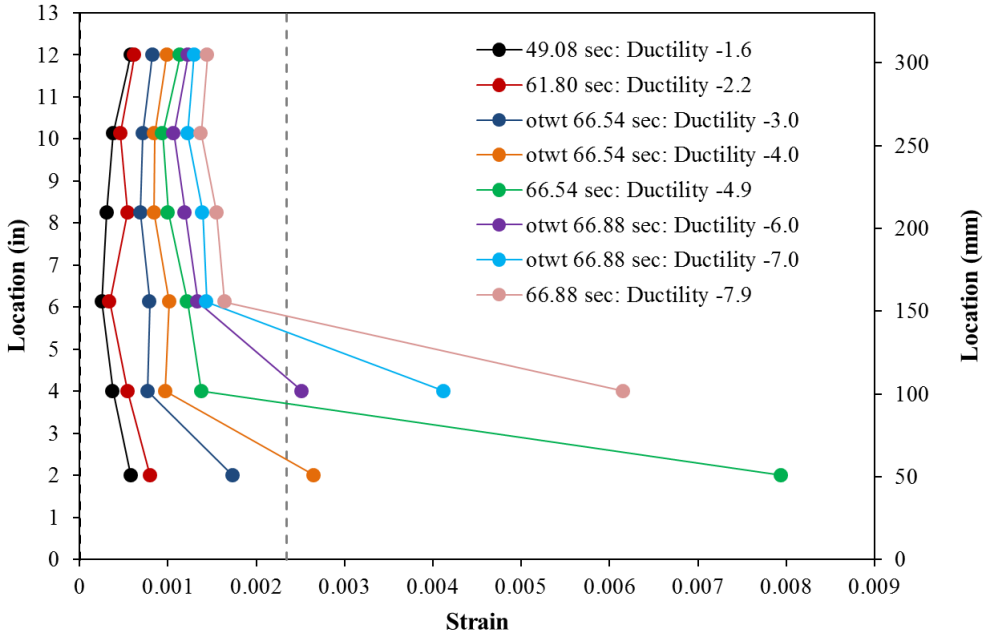

Figure 1.157 T12 – Spiral Strains for Six Lowest Spiral Layers on the North Side

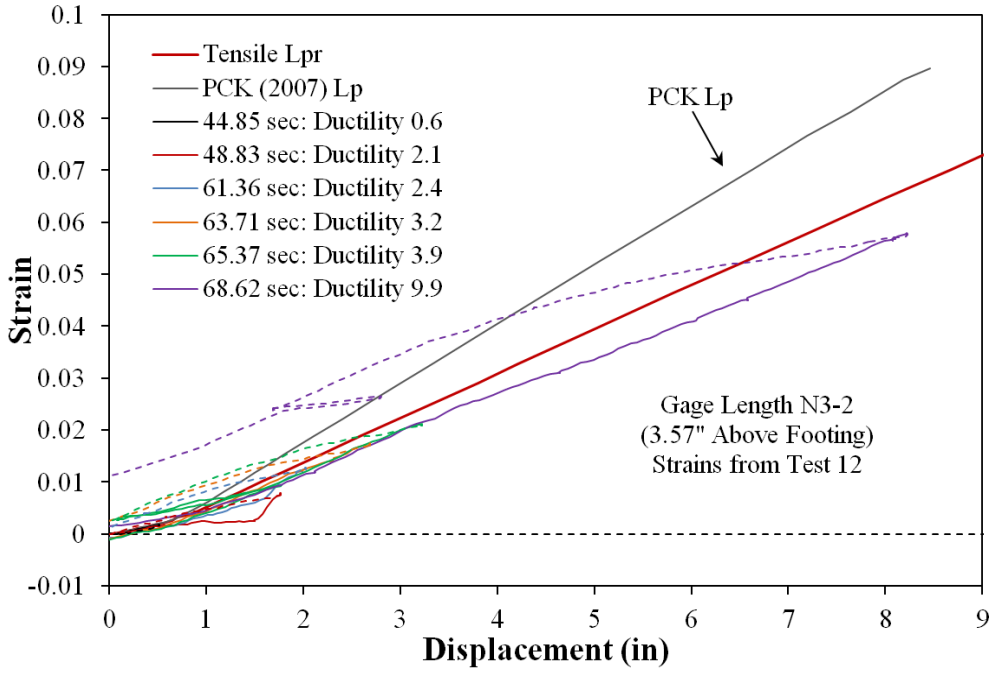

Figure 1.158 T12 – Tensile Strain-Displacement for Bar N3 during Push Cycles

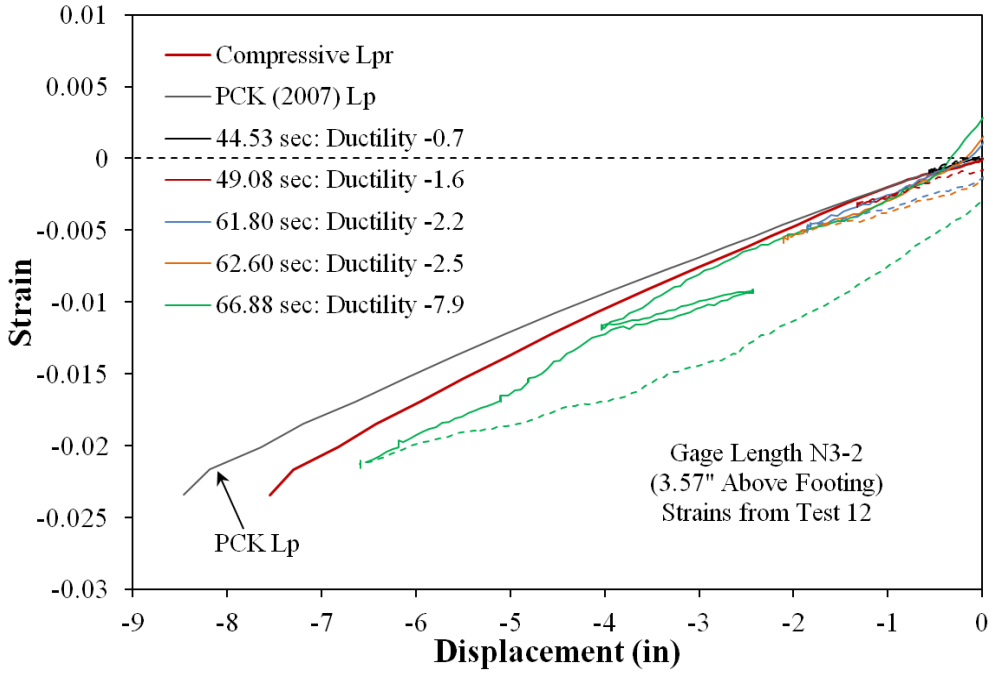

Figure 1.159 T12 – Compressive Strain-Displacement for Bar N3 during Pull Cycles

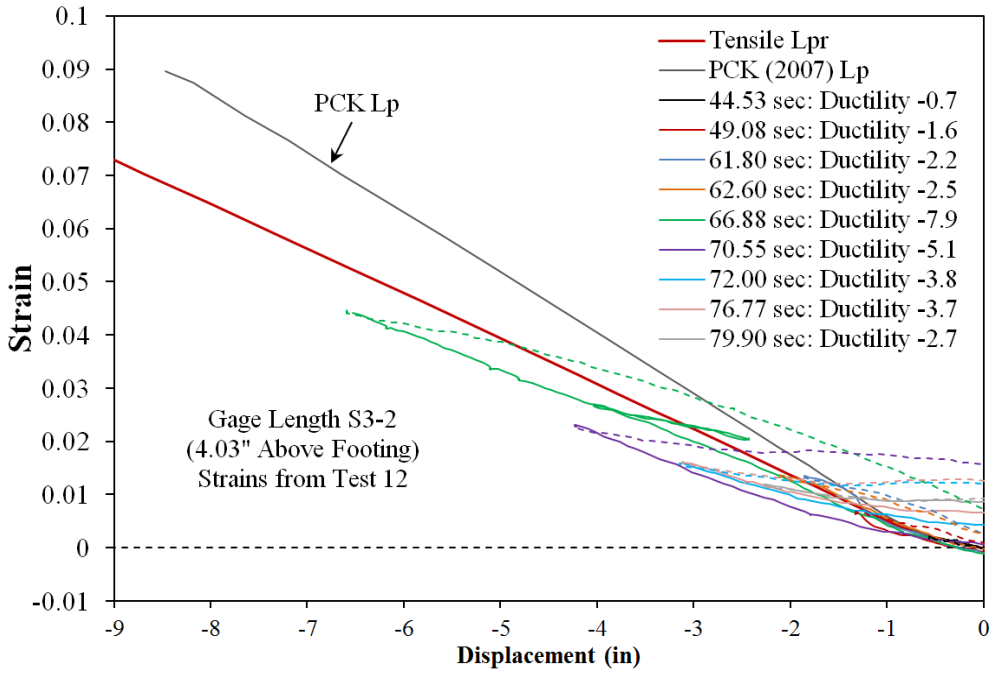

Figure 1.160 T12 – Tensile Strain-Displacement for Bar S3 during Pull Cycles

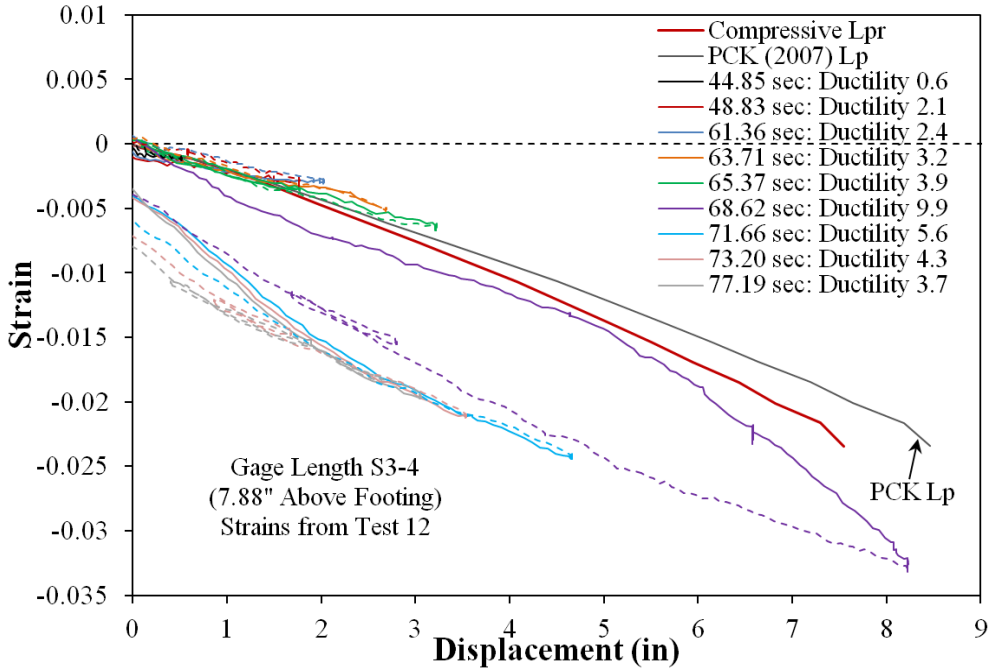

Figure 1.161 T12 – Compressive Strain-Displacement for Bar S3 during Push Cycles

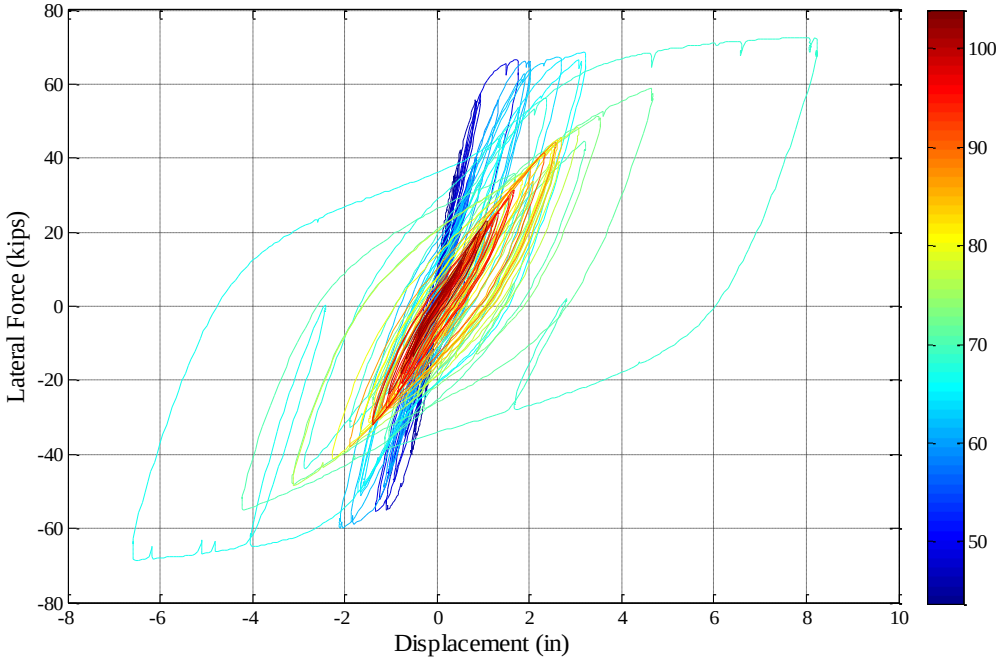

Figure 1.162 T12 – Hysteretic Response Japan 2011 Record with an EQ Time Colorbar

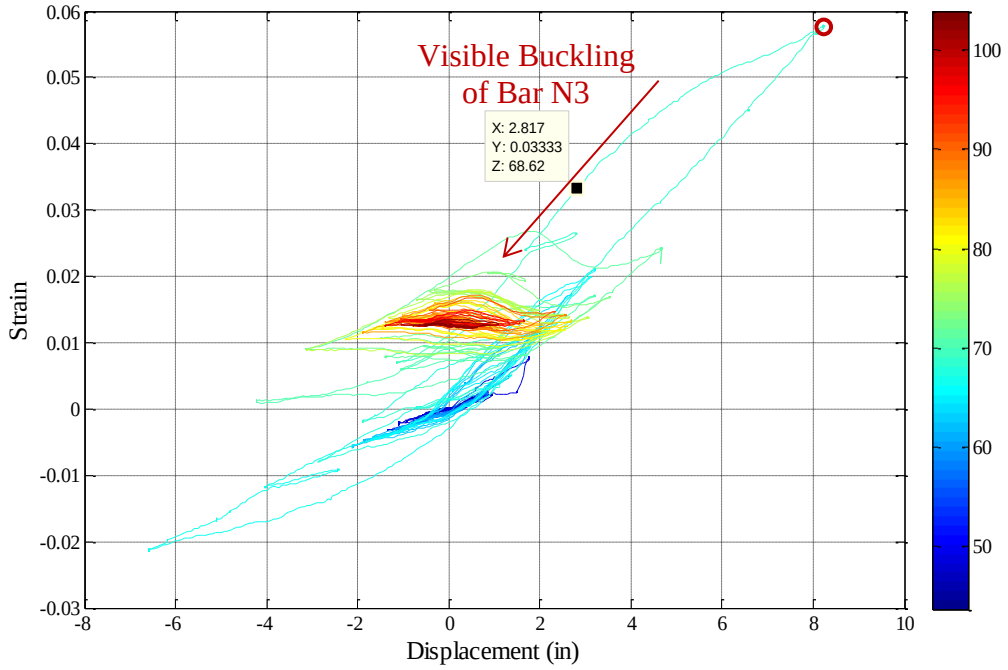

Figure 1.163 T12 – North Extreme Fiber Bar N3 Strain Hysteresis (3.57" Above)

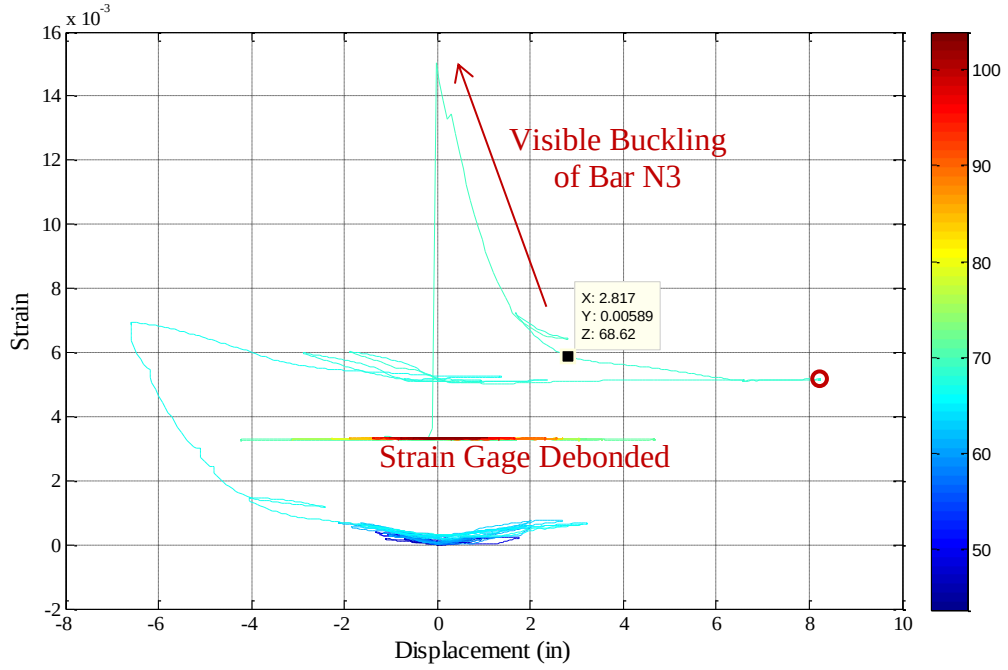

Figure 1.164 T12 – Transverse Steel Strain Hysteresis over North Buckled Region

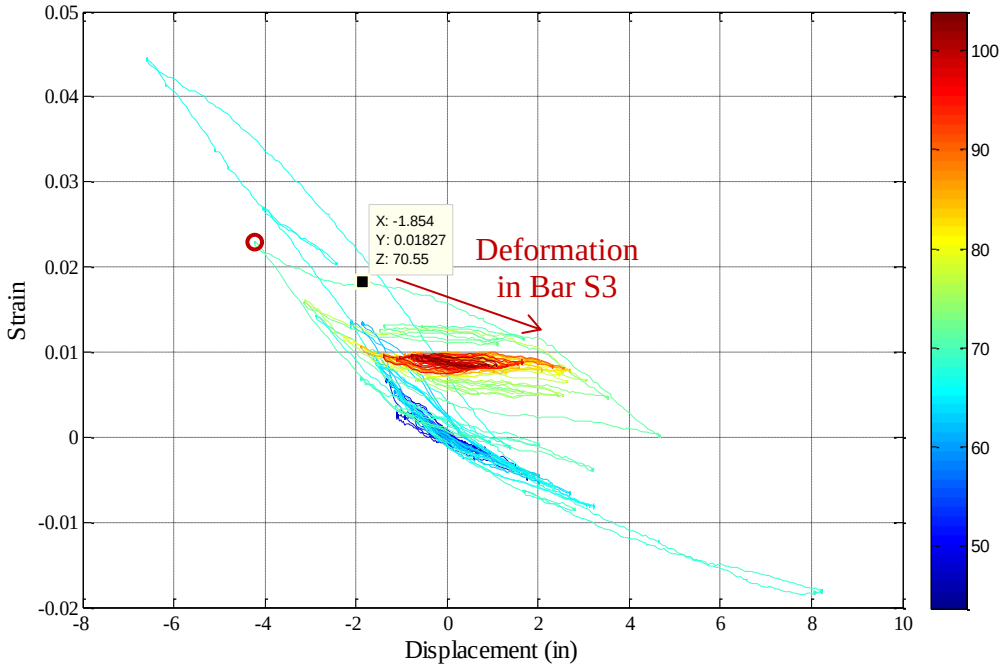

Figure 1.165 T12 – South Extreme Fiber Bar S3 Strain Hysteresis (4.03" Above)

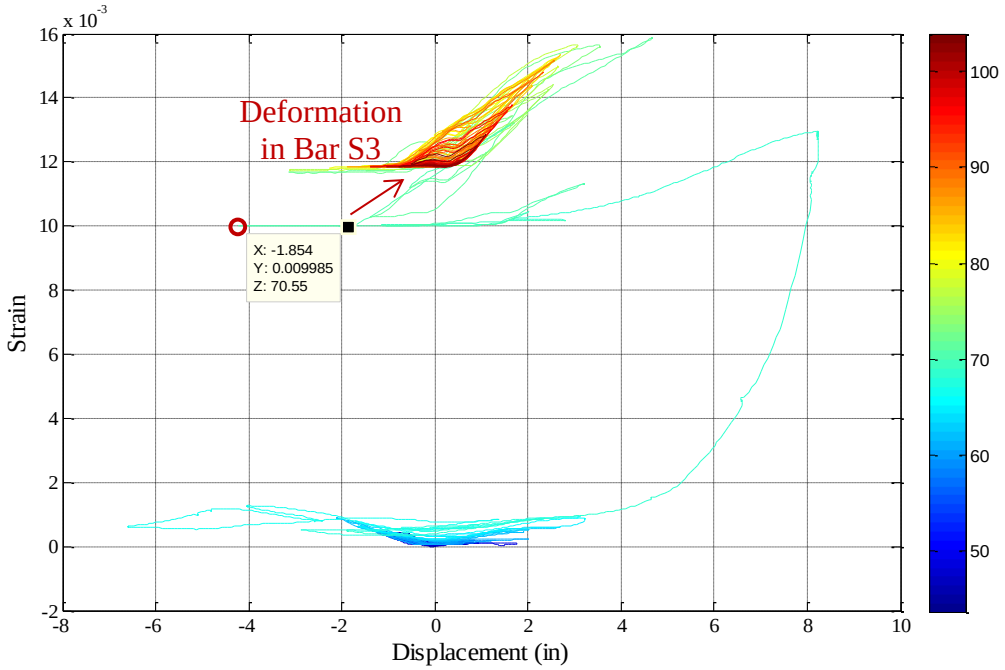

Figure 1.166 T12 – Spiral Strain Hysteresis for South "Measurable Deformation"

Test 12 – Japan 2011 Earthquake LH - Strain Penetration and Curvature Data:

Vertical curvature profiles for push and pull cycles along the backbone curve of cyclic response appear in Figure 1.167 and Figure 1.168. The least squared error lines show that higher ductility cycles have a linear distribution of plastic curvature similar to previous tests. The base rotations attributable to strain penetration of longitudinal reinforcement into the footing are shown in Figure 1.169 and Figure 1.170 respectively. The measured displacement of the base section was obtained from the LED placed closest to the footing-column interface. The slip hysteresis for extreme fiber bars N3 and S3 appear in Figure 1.171 and Figure 1.172 respectively. The top column displacement from the Optotrak may be determined by integrating the measured curvature distribution, extrapolating the base rotation to the center of loading, and assuming a linear distribution of curvature above the instrumented region which aligns the equivalent yield curvature at the base section. A comparison of the Optotrak integrated and measured top column displacements, in Figure 1.173, shows that the two methods agree throughout the entire range of displacements. The measured spread of plasticity as a function of base section curvature ductility appears in Figure 1.174. The extent of plasticity is computed as the intersection of the linear plastic curvature regression and the elastic curvature profile.

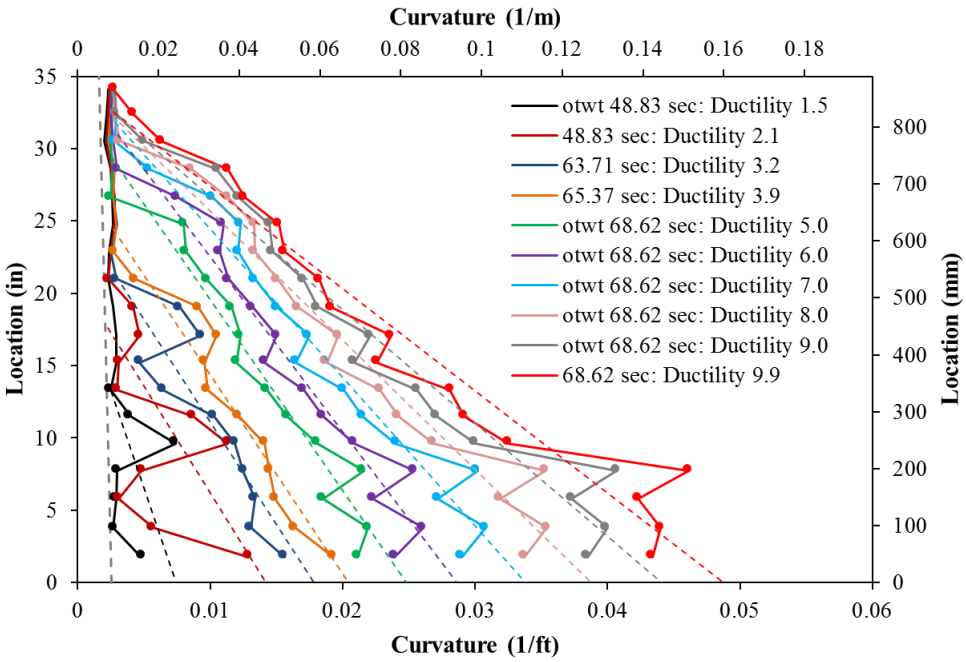

Figure 1.167 T12 – Vertical Curvature Profiles during Push Cycles

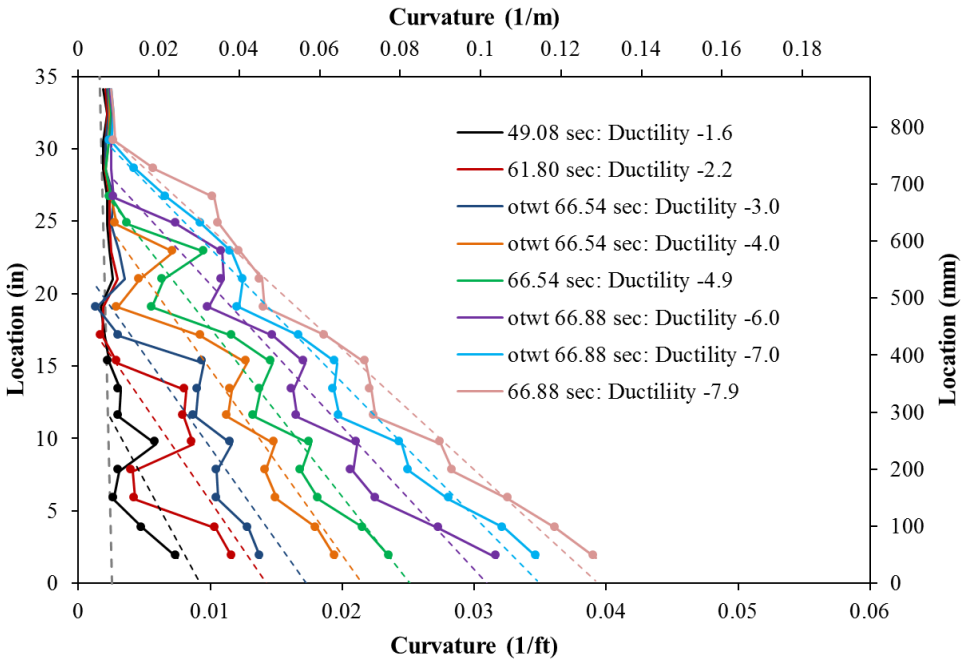

Figure 1.168 T12 – Vertical Curvature Profiles during Pull Cycles

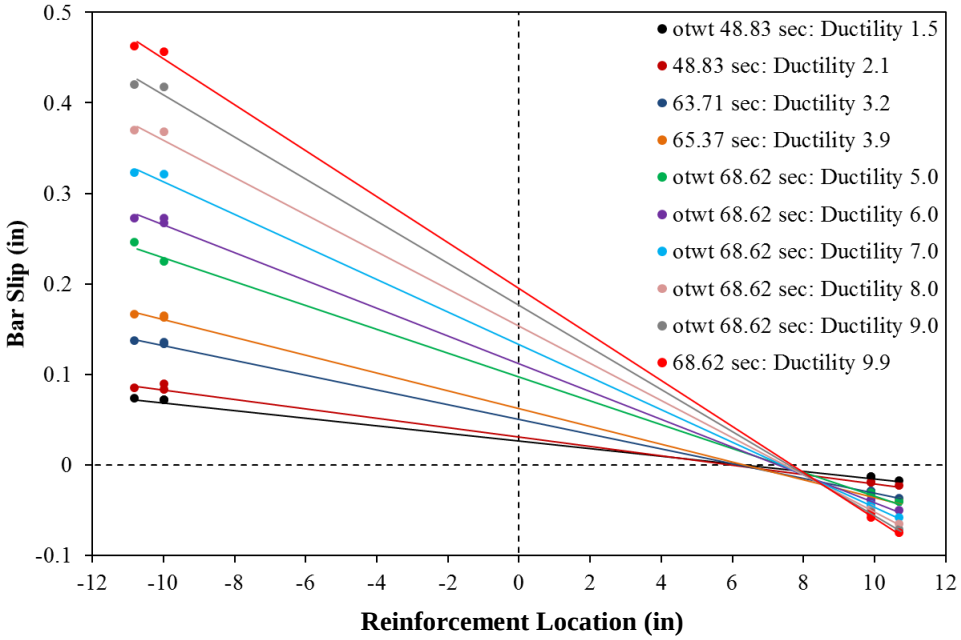

Figure 1.169 T12 – Base Rotation due to Strain Penetration during Push Cycles

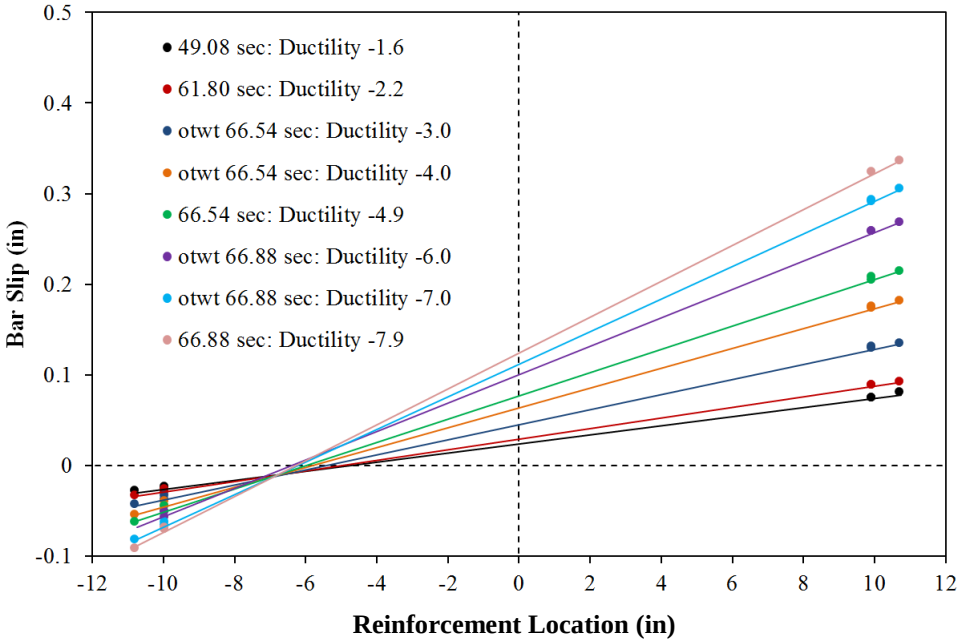

Figure 1.170 T12 – Base Rotation due to Strain Penetration during Pull Cycles

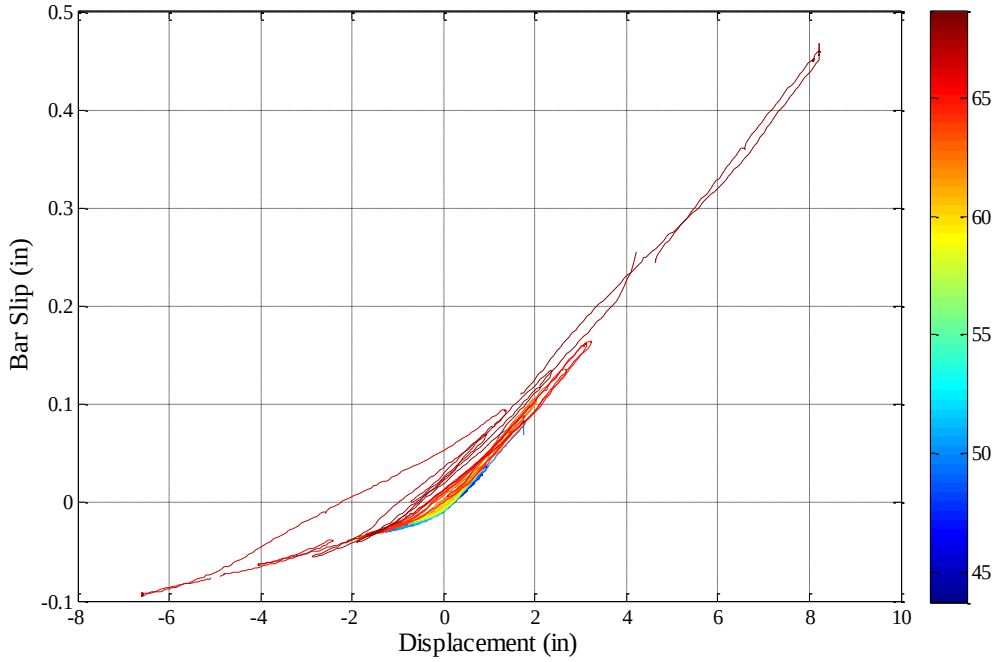

Figure 1.171 T12 – Bar N3 Base Section Slip Hysteresis due to Strain Penetration

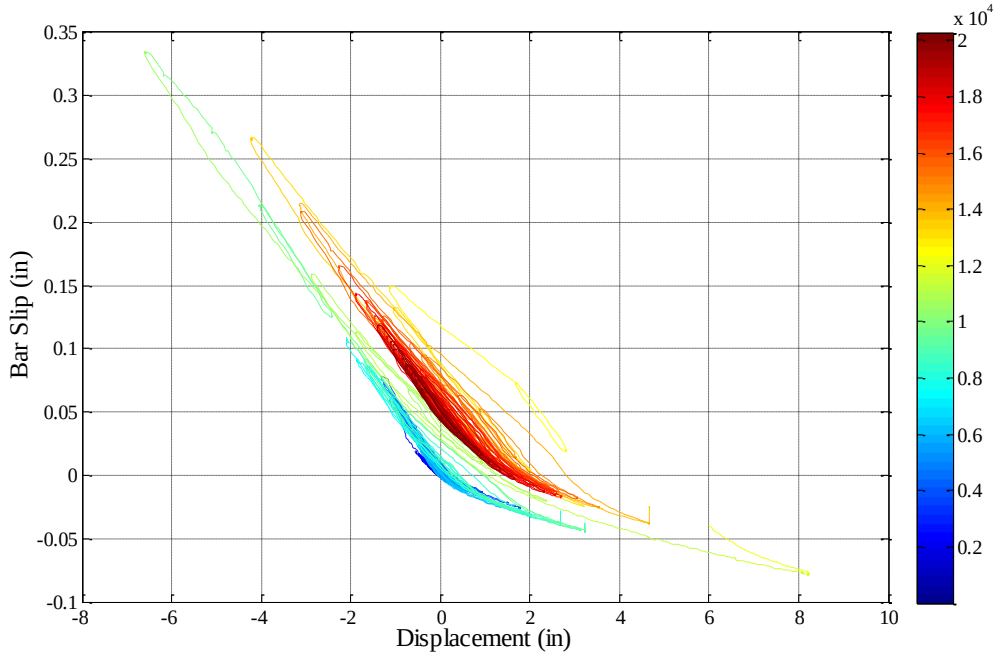

Figure 1.172 T12 – Bar S3 Base Section Slip Hysteresis due to Strain Penetration

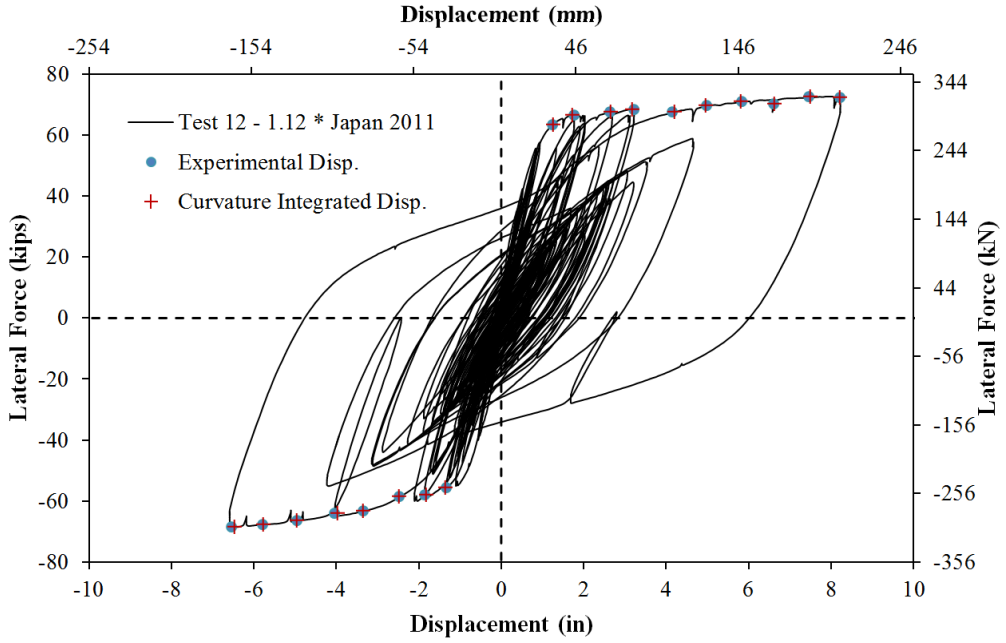

Figure 1.173 T12 – Comparison of Measured and Optotrak Integrated Displacements

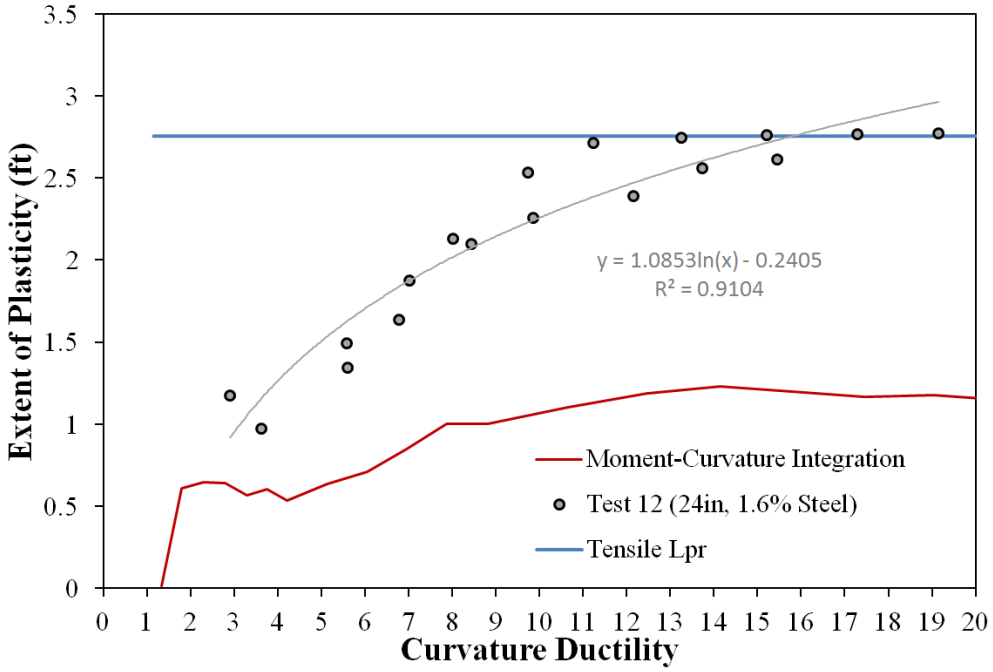

Figure 1.174 T12 – Measured Spread of Plasticity (Circular Data Points)

1.2 Load History and Transverse Steel Variable Tests 13-18

The effect of transverse steel detailing on restraint of longitudinal bars was the main variable for Tests 13-18. The test matrix for the eight columns is shown in Table 1.15, and the material properties of the reinforcement appear in Table 1.16. The 24" (610mm) diameter bridge columns, Figure 1.178, contained 16 #6 (19mm) A706 bars for longitudinal reinforcement ($A_{st}/A_g = 1.6\%$) and either a #3 (9.5mm) or #4 (12.7mm) A706 spiral at variable spacing. The shear span for the cantilever columns was 8ft (244cm), and they had a moment to shear ratio of ($M/VD = 4$). The specimens were subjected to a constant axial load of 170kips (756kN), ($P/(f_c' A_g) \approx 5\%$) depending on the concrete compressive strength. Load history was maintained as a variable for Tests 16-18 which had the same transverse steel detailing. The following transverse volumetric steel ratios were investigated: ($4A_{sp}/(D's)) = 0.5\%$ ($6d_{bl}$ spacing), 0.7%, 1% (previous test series), and two separate detailing arrangements for 1.3%. Both the volumetric ratio and spacing of the transverse steel are important when describing confinement and bar buckling restraint. Two columns were tested with 1.3% transverse steel, one with a #3 spiral at 1.5" spacing and another with a #4 spiral at 2.75" spacing. For comparison, a specimen was tested with a #3 spiral at 2.75" spacing.

An engineer has the most control over the size and spacing of transverse steel to improve buckling resistance. Previously tested specimens 8-12 utilized a #3 spiral at 2" pitch ($4A_{sp}/(D's) = 1\%$). During the Kobe and Japan 2011 load histories, a peak displacement ductility of ten was necessary to produce sufficient tensile strain to buckle reinforcement upon reversal in an earthquake load history. The compressive demand at ductility ten resulted in server layers of inelastic transverse steel, which decreased their effectiveness in restraining the longitudinal reinforcement during the remainder of the load history. Even though this side of the specimen was subjected to lower levels of tensile strain, the reinforcement still buckled due to the inelastic transverse steel.

Table 1.15 Column Property Summary for Load History Variable Tests 13-18

Test	Load History	D (in)	L/D	Long. Steel (ρ_l)	Spiral Detailing (ρ_s)	f'c (psi)	P/f'c*Ag
13	Three Cycle Set	24	4	16 #6 bars (1.6%)	#4 at 2.75" (1.3%)	6097	6.2%
14	Three Cycle Set	24	4	16 #6 bars (1.6%)	#3 at 4" (0.5%)	6641	5.7%
15	Three Cycle Set	24	4	16 #6 bars (1.6%)	#3 at 2.75" (0.7%)	7232	5.2%
16	Three Cycle Set	24	4	16 #6 bars (1.6%)	#3 at 1.5" (1.3%)	6711	5.6%
17	Llolleo 1985	24	4	16 #6 bars (1.6%)	#3 at 1.5" (1.3%)	7590	5.0%
17b	Cyclic Aftershock	24	4	16 #6 bars (1.6%)	#3 at 1.5" (1.3%)	7590	5.0%
18	Darfield 2010	24	4	16 #6 bars (1.6%)	#3 at 1.5" (1.3%)	7807	4.8%
18b	Cyclic Aftershock	24	4	16 #6 bars (1.6%)	#3 at 1.5" (1.3%)	7807	4.8%

Table 1.16 Reinforcement Material Property Summary for Columns 13-18

Longitudinal Reinforcement	εy	fy (ksi)	εh	fh (ksi)	εu	fu (ksi)
Tests 8-12 (#6 Bar)	0.00235	68.1	0.0131	68.2	0.1189	92.8
Tests 13-18 (#6 Bar)	0.00235	68.1	0.0146	68.2	0.1331	94.8

Transverse Steel	Yield Stress, f_y (ksi)
Tests 8-12 (#3 Spiral)	74.1
Tests 13-18 (#3 Spiral)	64.6
Tests 13-18 (#4 Spiral)	69.9

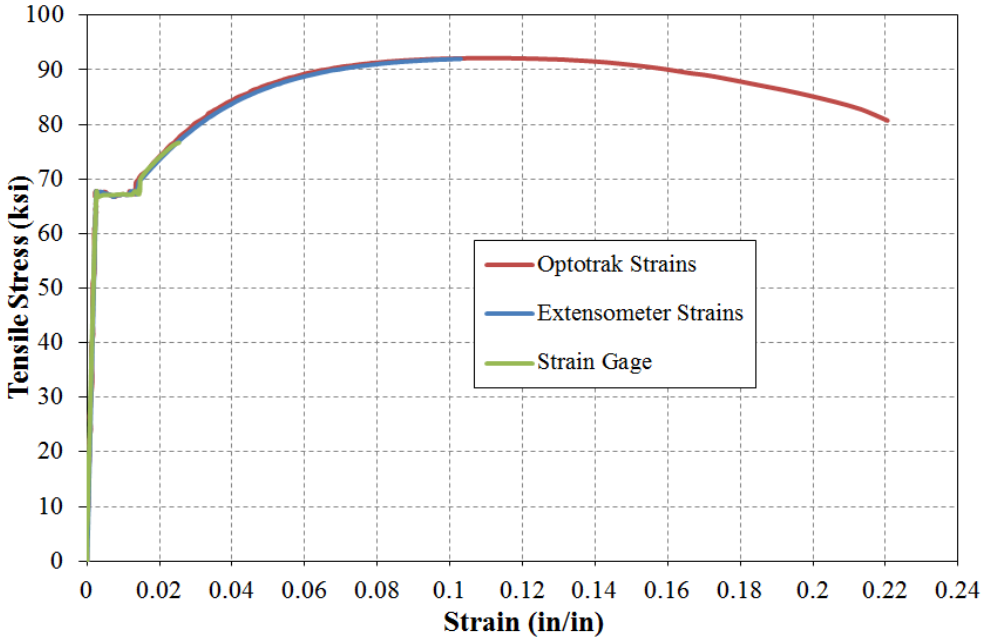

Figure 1.175 Long. Steel Stress-Strain Response with Three Measurement Methods

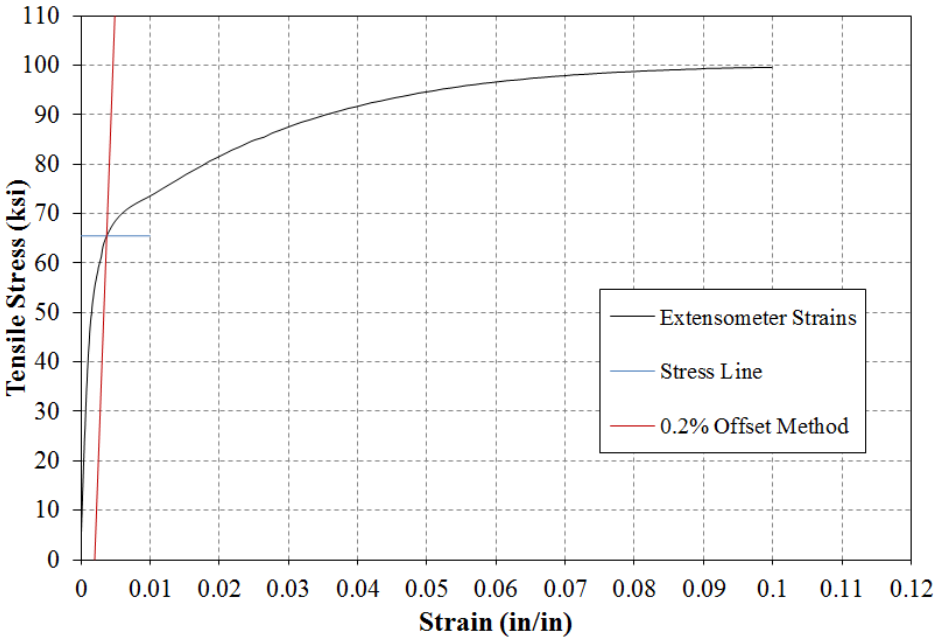

Figure 1.176 #3 Bar Transverse Steel Stress-Strain Response and 0.2% Offset Method

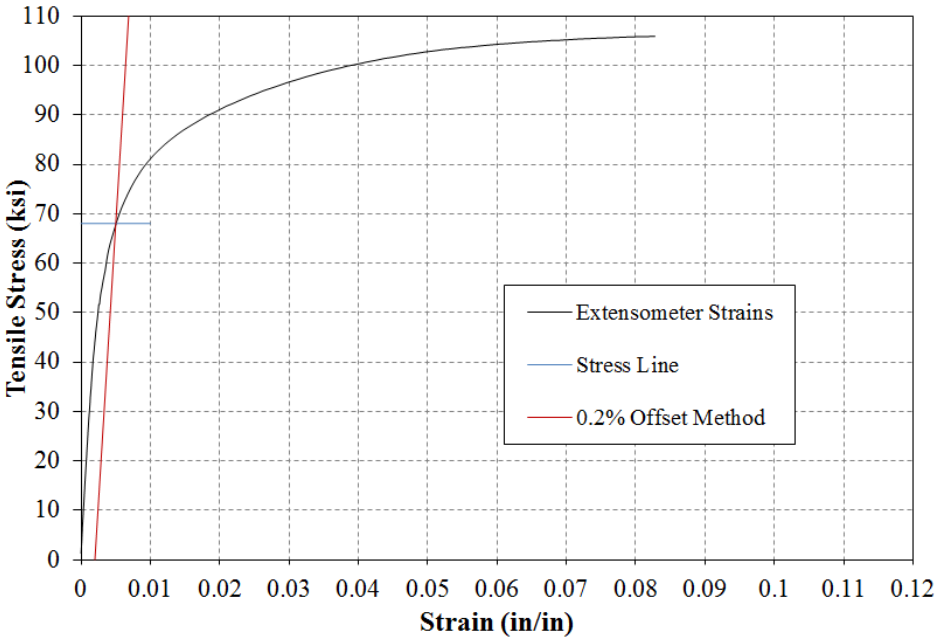

Figure 1.177 #4 Bar Transverse Steel Stress-Strain Response and 0.2% Offset Method

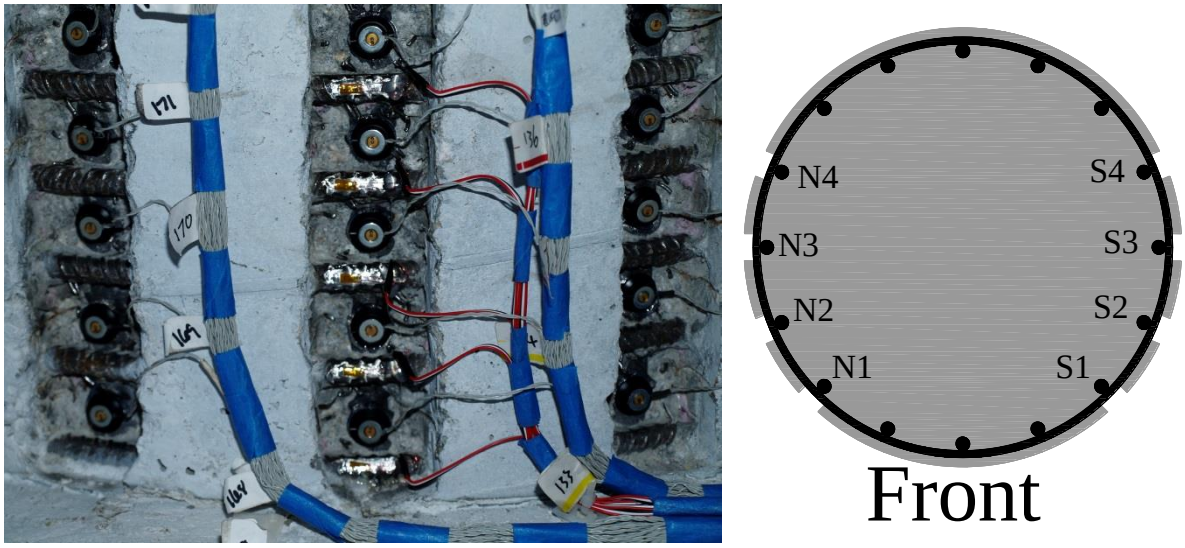

Figure 1.178 (Left) Vertical Cover Concrete Blockout Strips and Target Marker Application, (Right) Cross Section Bar Designation

1.2.1 Test 13 –Three Cycle Set Load History with #4 Spiral at 2.75" (1.3%)

Table 1.17 Observational Summary for Test 13 – Cyclic with #4 Spiral at 2.75" (1.3%)

VALUES OF INTEREST:	
Concrete Compressive Strength:	$f_c' = 6097\ psi$
Axial Load:	$P = 170\ kips$
Analytical First Yield Force:	$F_y' = 46.5\ kips$
Experimental First Yield Displacement:	$\Delta_y' = 0.60"$
Analytical Nominal Moment Capacity:	$M_n = 498.7\ kip * ft$
Equivalent Yield Displacement:	$\Delta_y = 0.81"$
Maximum Lateral Force:	$70.9\ kips$
Failure Mode:	Fracture of Previously Buckled Reinforcement
DAMAGE OBSERVATIONS:	
First Cracking North:	$1/2Fy' = 0.17"$
First Cracking South:	$-1/2Fy' = -0.16"$
Cover Concrete Crushing North:	$\mu_2^{-1} = -1.61"$
Cover Concrete Crushing South:	$\mu_2^{+1} = 1.60"$
Transverse Steel Yield North:	At $-4.78"$ during pull to $\mu_6^{-3} = -4.85"$
Transverse Steel Yield South:	At $4.17"$ during push to $\mu_8^{+2} = 6.46"$
Longitudinal Bar Buckling North:	Reversal from $\mu_8^{+1} = 6.46"$
Longitudinal Bar Buckling South:	Reversal from $\mu_8^{-1} = 6.48"$
Longitudinal Bar Fracture North:	At $-0.79"$ during push to $\mu_{10}^{+1} = 8.06"$
Longitudinal Bar Fracture South:	At $-2.51"$ during pull to $\mu_{10}^{-2} = -8.12"$

*$\mu_8^{-1} = 6.48"$ represents the first pull cycle of displacement ductility eight

Table 1.18 Strain Data Summary for Test 13 – Cyclic with #4 Spiral at 2.75" (1.3%)

MATERIAL STRAINS:	
Cover Concrete Crushing North:	$\varepsilon_s = 0.046\ (compression)$
Cover Concrete Crushing South:	$\varepsilon_s = 0.036\ (compression)$
Transverse Steel Yield North:	$\varepsilon_s = 0.0166\ (compression)$
Transverse Steel Yield South:	$\varepsilon_s = 0.0162\ (compression)$
Longitudinal Bar Buckling North:	$\varepsilon_s = 0.047\ (peak\ tension\ prior\ to\ bb)$
	$\varepsilon_s = 0.017\ (peak\ comp.\ prior\ to\ bb)$
Longitudinal Bar Buckling South:	$\varepsilon_s = 0.047\ (peak\ tension\ prior\ to\ bb)$
	$\varepsilon_s = 0.017\ (peak\ comp.\ prior\ to\ bb)$
Mander (1988) Ultimate Concrete Compression Strain, $\varepsilon_{cu} = 0.0211$	

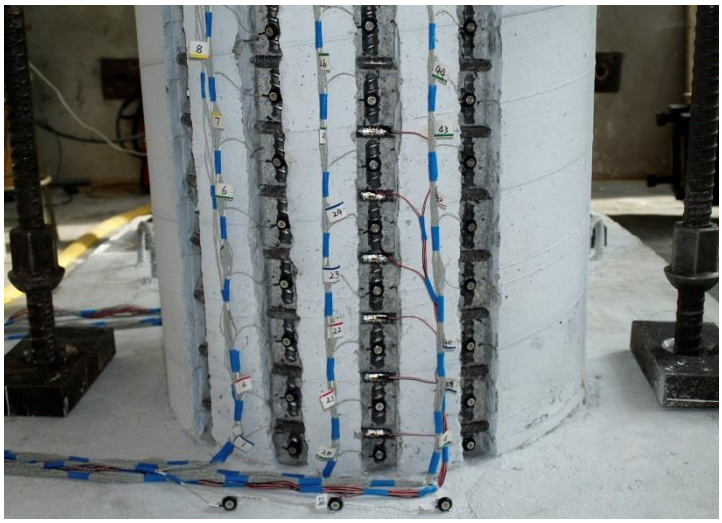

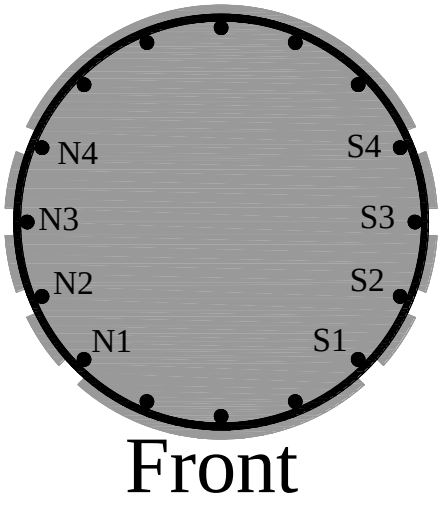

Figure 1.179 Cross Section Bar Designation for Tests 13-18

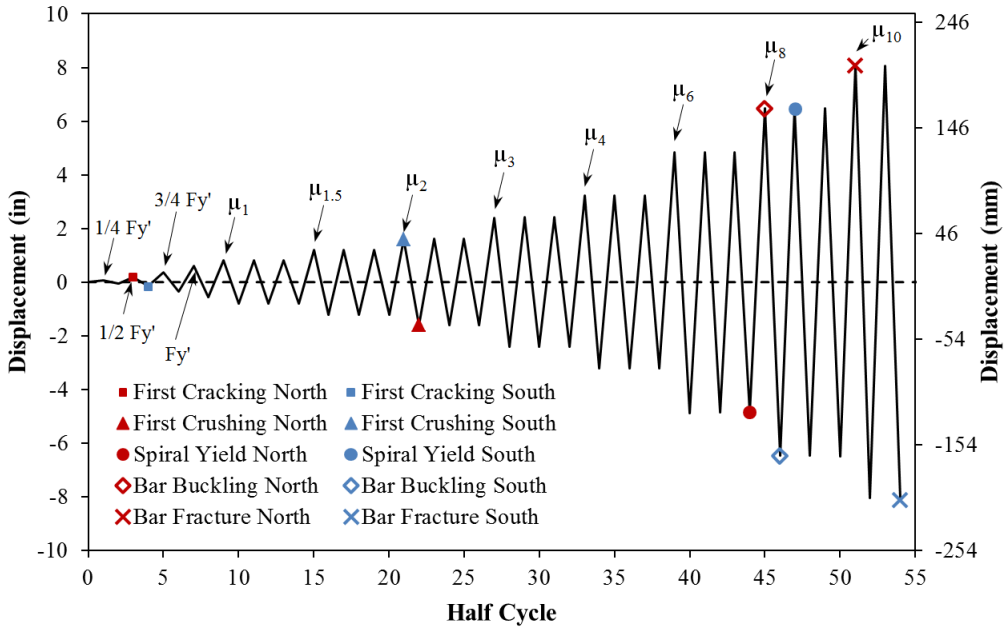

Figure 1.180 T13 – Symmetric Three Cycle Set Load History

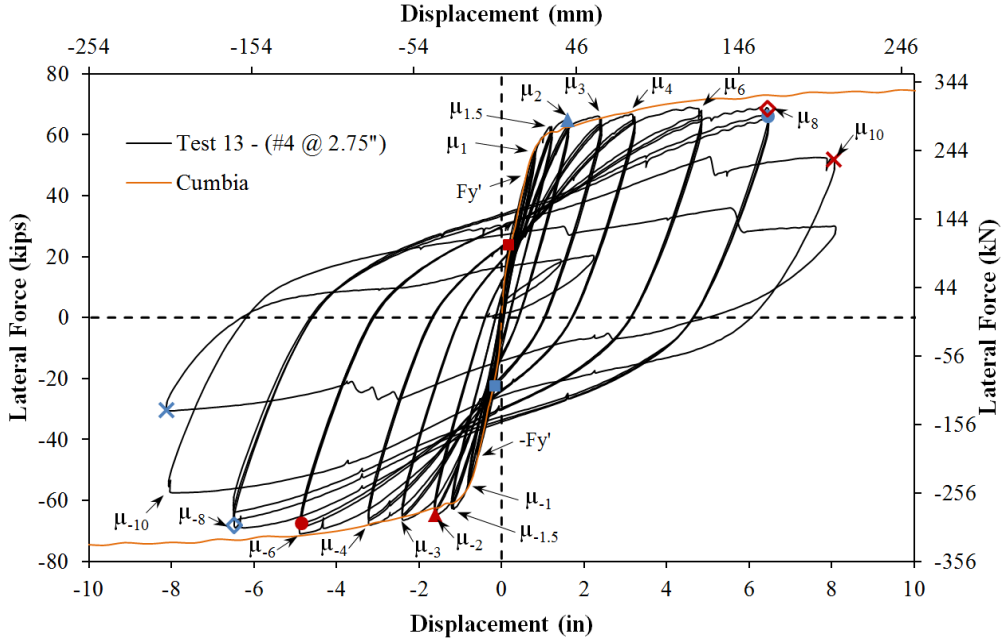

Figure 1.181 T13 – Hysteretic Response with PCK (2007) Lp Prediction

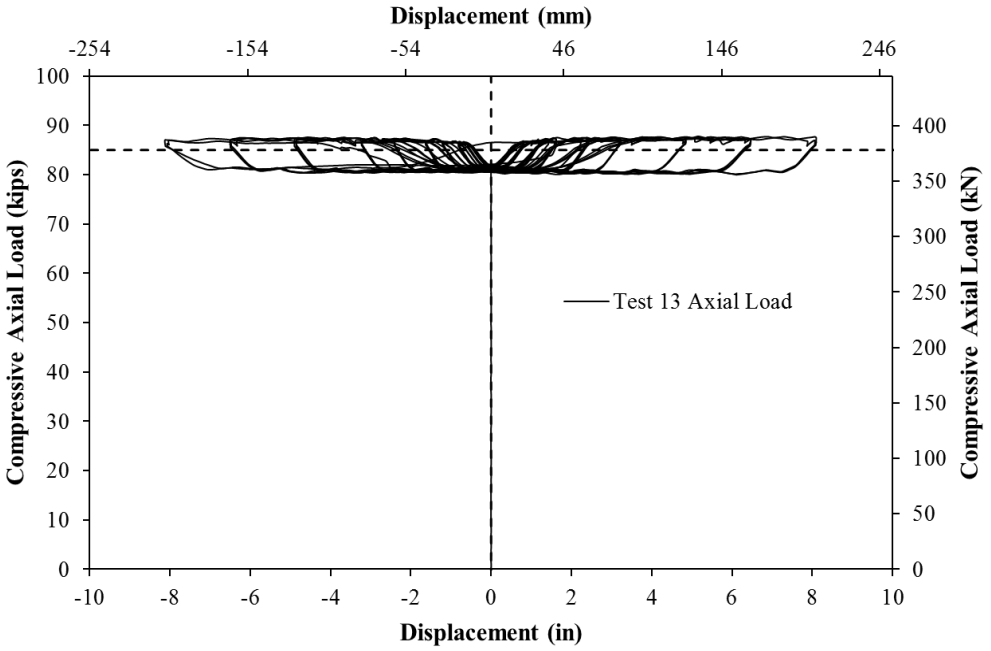

Figure 1.182 T13 – Compressive Axial Load from One Jack (Total = 2*Value)

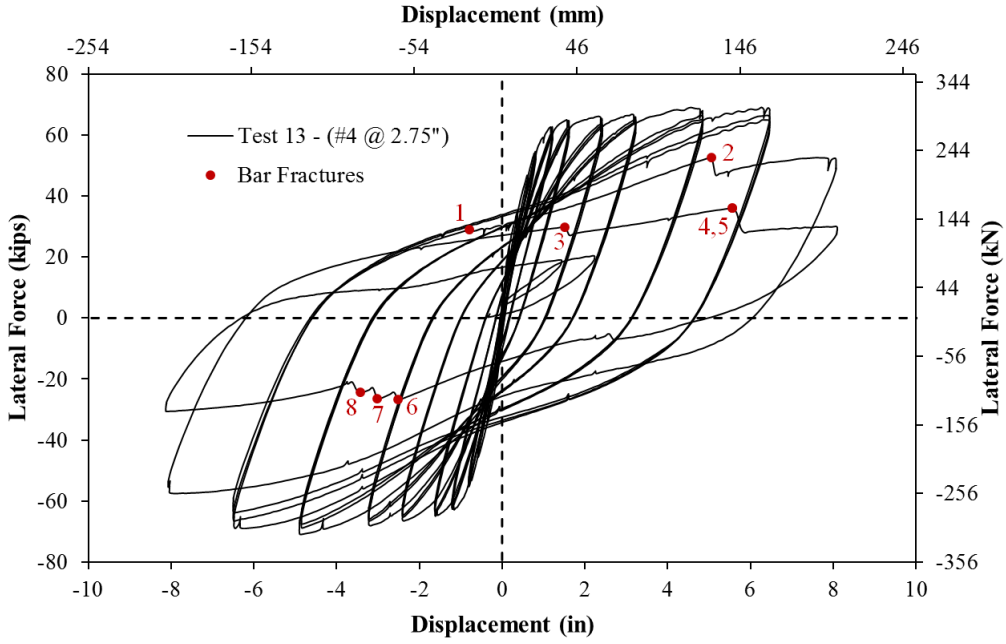

Figure 1.183 T13 – Bar Fracture History of Previously Buckled Reinforcement

Test 13 – Symmetric Three Cycle Set (#4 @ 2.75") Experimental Observations

The first yield force for the tested material and geometric properties was determined using moment curvature analysis (Test 13: Cumbia Fy' = 46.5 kips with f'c = 6097 psi) compared to (Test 9: Cumbia Fy' = 46.9 kips with f'c = 6814 psi). The predicted first yield force for both test series, 7-12 and 13-18, are remarkably similar due to the near identical longitudinal reinforcement properties for both batches of steel. The first yield displacement for the thirteenth test was obtained as an average for the first yield push and pull cycles ($\Delta'_y = 0.60$") compared to ($\Delta'_y = 0.63$") for the ninth test. Vertical strain profiles for both push and pull cycles up to the first yield force appear in Figure 1.184 with a dashed line representing the yield strain of the longitudinal reinforcement. The equivalent yield displacement, used to determine the displacement ductility levels ($\mu_{\Delta 1} = 1 * \Delta_y$), is then calculated as $\Delta_y = \Delta'_y(M_n/M'_y) = 0.81$" for Test 13 compared to $\Delta_y = 0.84$" for Test 9. The full symmetric three-cycle-set load history appears in Figure 1.180 and the resulting lateral force vs. top column displacement hysteresis is shown in Figure 1.181.

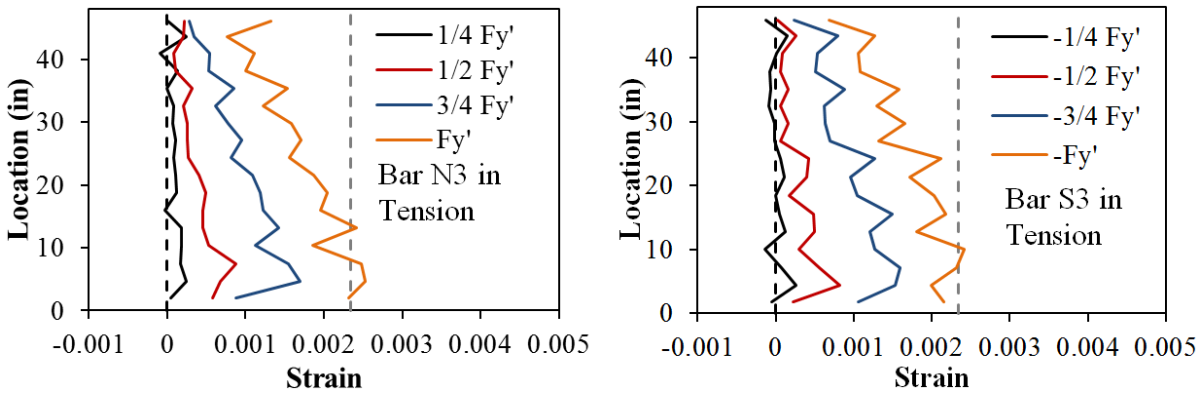

Figure 1.184 T13 – Vertical Strain Profiles for Extreme Fiber Bars (Dashed Yield Line)

The first cracks on the North side of the specimen where measured at 0.1mm at approximate 8" spacing during the push cycle to ½Fy'. Cracks of the same width and approximate spacing where measured on the South side of the specimen during the -½Fy' pull cycle. The cracks on the North side of the specimen increased to 0.2mm at 4" spacing

during the push cycle to ¾Fy'. Larger 0.3mm crack widths at a greater spacing of 8" were measured on the South side of the specimen during -¾Fy'. Up until the first yield force was reached, the cracks were all horizontal without any inclination on the sides of the specimen with greater shear stress. The change in orientation of flexural shear cracks with increased ductility demands appears in Figure 1.190. Cracks on the North side of the specimen increased to 0.3mm width at approximate 4" spacing during the first yield push cycle. During the first yield pull cycle cracks increased to 0.4mm width at 5" spacing.

During ($\mu_1^{+3} = 0.81"$), crack widths measured 0.4mm at 4" spacing on the North side of the specimen. On the opposite side of the specimen crack widths were measured at 0.5mm at 5" spacing during ($\mu_1^{-3} = -0.80"$). Visible flaking which occurs just before cover concrete crushing was apparent on both sides of the specimens after the first push and pull cycles of ductility 1.5. This flaking did not lead to crushing during subsequent cycles at displacement ductility 1.5. Cracks on the North side of the specimen measured 1.1mm, while the South side measured 1.25mm during the third push and pull cycles of ductility 1.5 respectively. Concrete cover crushing 2" above the footing occurred on the South side of the specimen during ($\mu_2^{+1} = 1.60"$). Similarly, crushing over 2" on the North side of the specimen was observed during the ($\mu_2^{-1} = -1.61"$). Cracks on the North and South sides of the specimens measured 1.5mm and 2mm during the third push and pull cycles of ductility two respectively. After three complete cycles at ductility three, the extent of crushing increased to 10" on the North and 7" on the South side of the specimen. The load history continued through ductility six with additional inclined flexural shear cracks and increased extent of crushing, but without buckling of the longitudinal steel.

After reversal from ($\mu_8^{+1} = 6.46"$), extreme fiber bar N3 and adjacent bar N2 buckled as shown in the left photo of Figure 1.187. During the second push cycle of ductility eight, South reinforcing bar S4 visibly buckled, see the left photo of Figure 1.188. The South extreme fiber bar S3 did not show signs of visible buckling while adjacent bar S4 deformed out of plane at the location where more prominent buckling later occurred. During the second and third pull cycles of ductility eight the deformation in the North buckled bars

increased and an additional bar N4 buckled as shown in the right photo of Figure 1.187. The buckled deformation of both the North and South reinforcement occurred between layers of transverse steel (#4 at 2.75" spacing). Buckling over two to three layers of transverse steel was observed in previous tests with a #3 spiral at 2" spacing.

During ($\mu_{10}^{+1} = 8.07"$), two of the previously buckled North reinforcing bars ruptured and South reinforcing bars S2 and S3 buckled, see Figure 1.188 and Figure 1.189. Rupture of the North reinforcing bar N3 occurred before the bar straightened out in tension. While this has never been observed in previous tests, it is likely a consequence of the more severe buckled profile between layers of transverse reinforcement, see Figure 1.187. Losses in strength from reinforcement ruptures are shown in Figure 1.183 on the hysteretic response. Three additional North reinforcing bars ruptured during the ($\mu_{10}^{+2} = 8.06"$). Three previously buckled reinforcing bars on the South side of the specimen ruptured during ($\mu_{10}^{-2} = -8.12"$). The test was concluded with a total of eight ruptured reinforcing bars and a considerable loss of strength in each direction of loading.

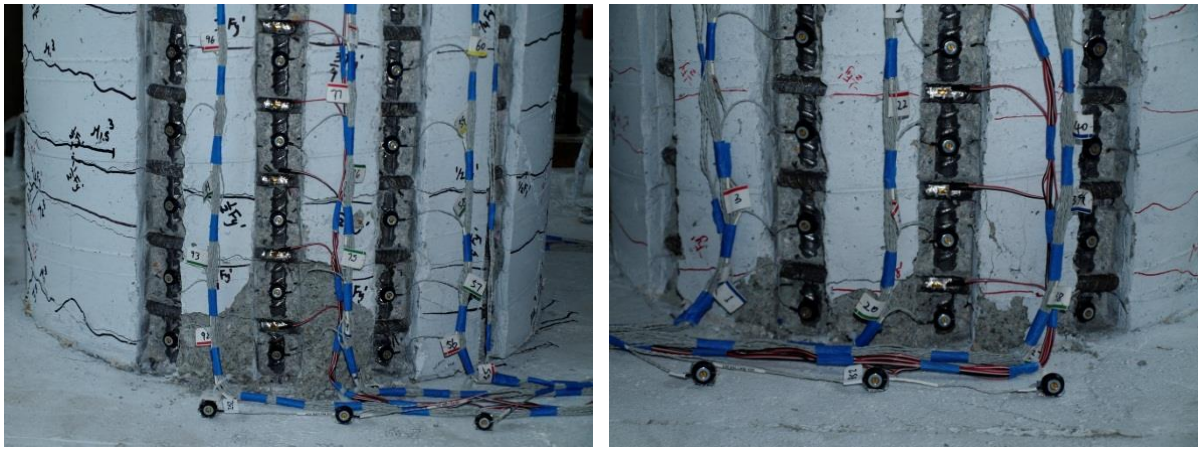

Figure 1.185 T13 – Concrete Cover Crushing at the End of Ductility Two (Left) North and (Right) South

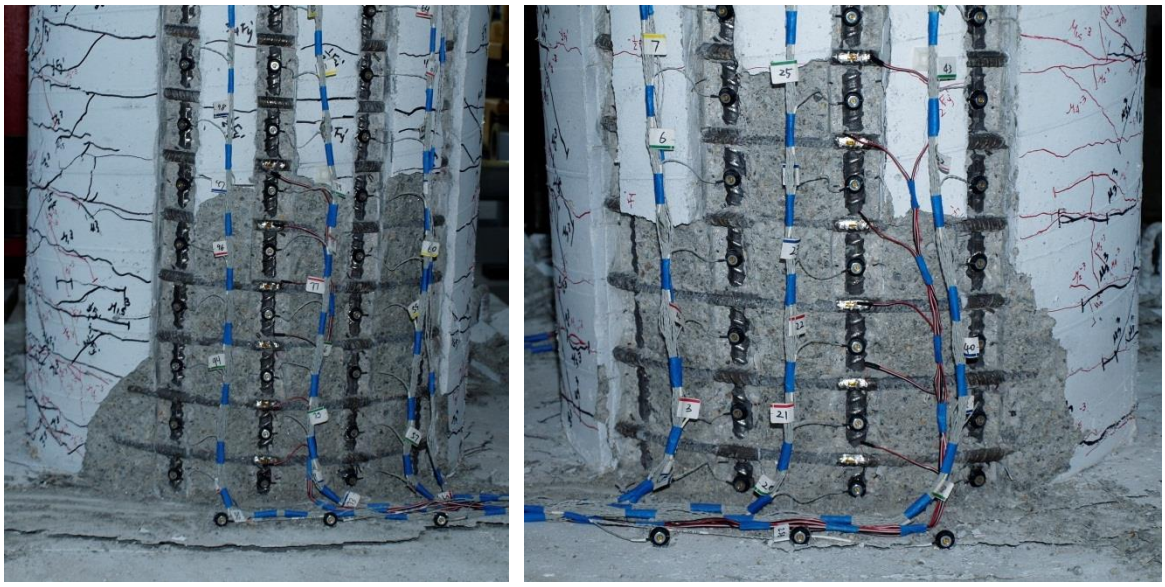

Figure 1.186 T13 – Crushing at the End of Ductility Six (Left) North and (Right) South

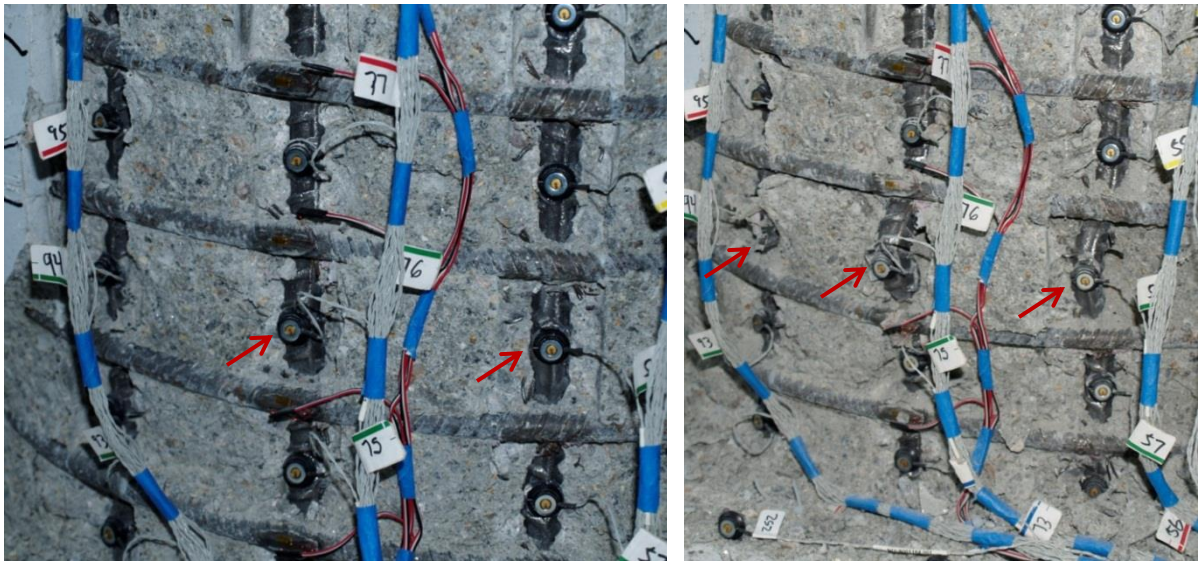

Figure 1.187 T13 – (Left) Buckling of Reinforcing Bars N2 and N3 during ($\mu_8^{-1} = -6.48$") and (Right) Increased deformation in North Buckled Bars ($\mu_8^{-3} = -6.50$")

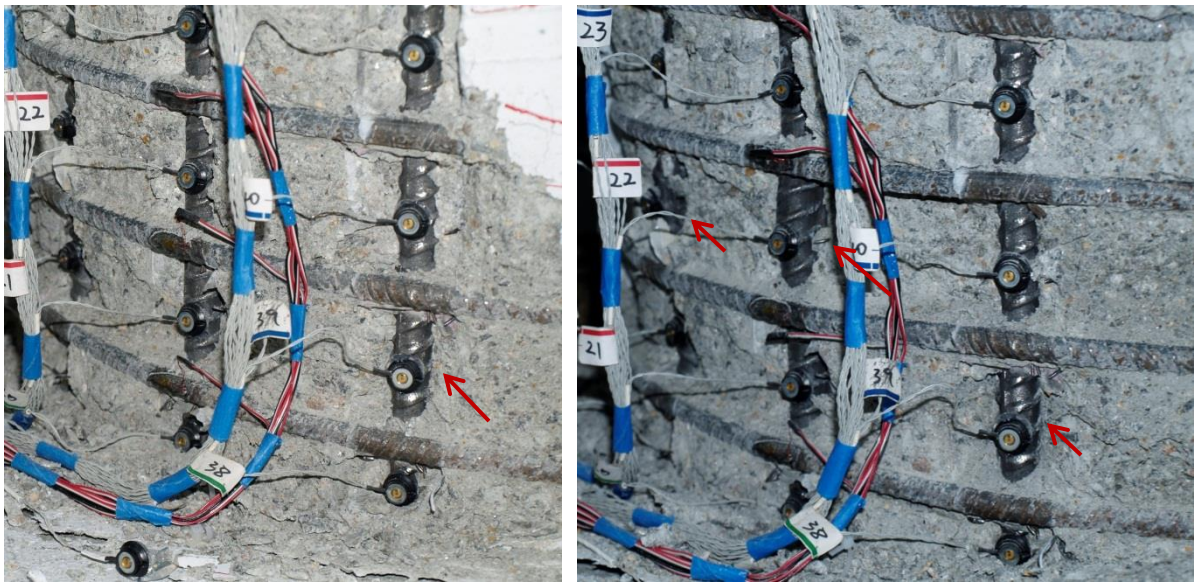

Figure 1.188 T13 – Buckling of South Reinforcing Bar S4 during ($\mu_8^{+2} = 6.46$") and (Right) Buckling of Bar S2 and S3 during ($\mu_{10}^{+1} = 8.07$")

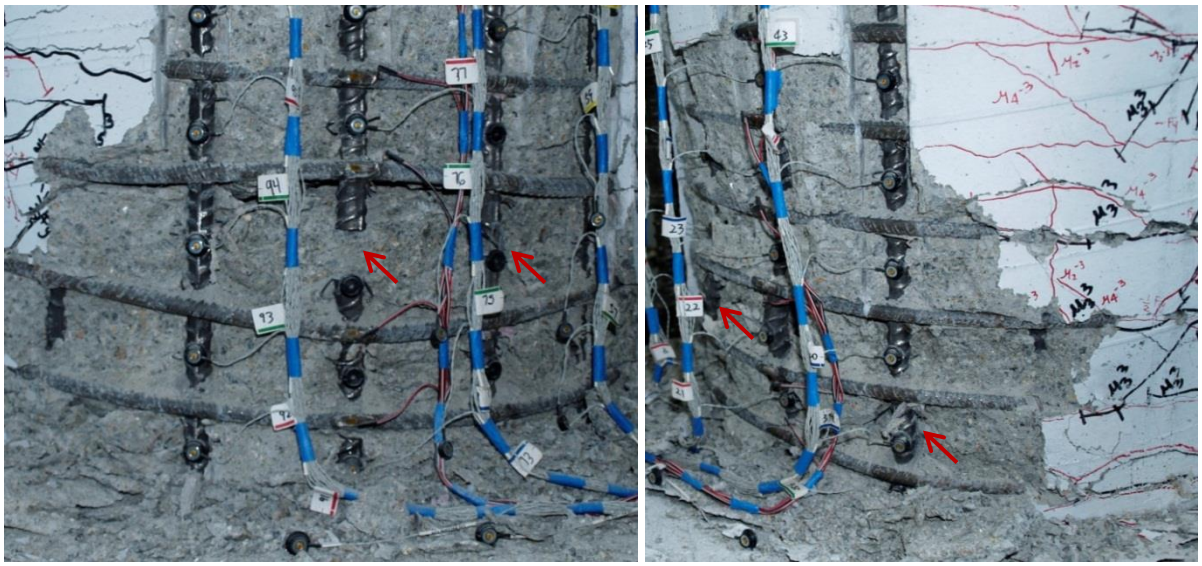

Figure 1.189 T13 – (Left) Rupture of North Reinforcement Bars N2 and N3 during ($\mu_{10}^{+1} = 8.07$") and (Right) Additional Deformation in South Bars during ($\mu_{10}^{+2} = 8.06$")

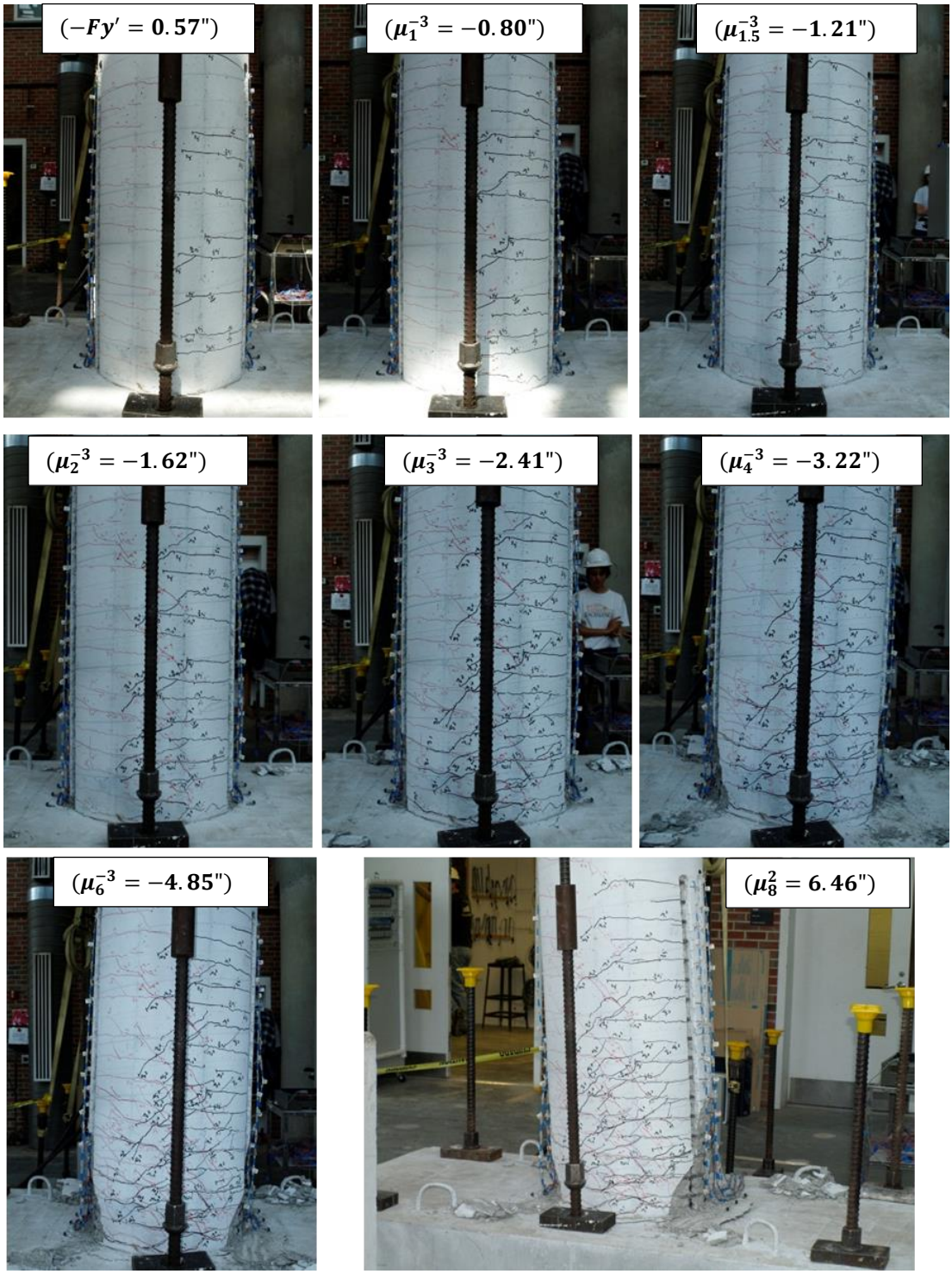

Figure 1.190 T13 – Crack Progression on the Back Side of the Specimen

Test 13 – Symmetric Three Cycle Set (#4 @ 2.75") Strain Data Analysis

North Reinforcement

Extreme fiber vertical strain profiles during push and pull cycles appear in Figure 1.191 and Figure 1.192 respectively. These figures show both extreme fiber bars on the same graph to illustrate the effects of tension shift on strain profiles. As the hinge rotates about inclined flexural shear cracks, compressive strains are concentrated at the base and tensile strains are fanned out to a greater height following the crack distribution. Just above the footing cracks remain horizontal, but above this base section the flexural shear cracks are inclined as shown in Figure 1.190. Due to the effects of tension shift, the tensile strains at the beginning of an inclined flexural shear crack do not coincide with the perceived moment demand at that location based on its height above the footing and the applied lateral load.

A peak tensile strain of 0.047, at a height of 2.03" above the footing, was measured in North extreme fiber bar N3 during ($\mu_8^{+1} = 6.46"$). It is notable that a higher peak tensile strain of 0.050 was measured 2.2" above the footing in the adjacent North reinforcement bar N4. Bar N2 and N3 visually buckled after reversal from ($\mu_8^{+1} = 6.46"$), leaving bar N4 intact. During the next pull cycle bar N4 visually buckled. The largest compressive strain in bar N3 of -0.017, located 2.03" above the footing, was measured during ($\mu_6^{+3} = 4.85"$). The relationship between tensile strain and displacement for bar N3 appears in Figure 1.195 for the largest tensile gage length 2.03" above the footing. Each curve in the graph represents the tensile strains measured from when the column was vertical to the peak of the given cycle of the load history. The gray line represents the moment curvature prediction for the relationship between strain and displacement from using the PCK (2007) Lp Hinge Method. During higher displacement ductility cycles, the measured tensile strains are significantly lower than the moment curvature prediction. The relationship between compressive strain and displacement for bar N3 appears in Figure 1.196. Buckling of bar N3 during the first pull cycle of ductility eight did not have a large impact on the relationship between compressive strain and displacement for this gage length, see the left photo of Figure 1.187.

The strain hysteresis for the buckled region of extreme fiber north reinforcing bar N3 appears in Figure 1.199. The transverse steel strain hysteresis for a layer of transverse steel close to the buckled region is shown in Figure 1.200. The peak displacement cycle at ($\mu_8^{+1} = 6.46"$), which preceded visible buckling, appears as a small red circle in both figures. A data label at the same displacement appears in both figures which represents the time when the buckled bar began to rapidly increase the tensile strain in the transverse steel restraint. The compressive demand during ($\mu_6^{+3} = 4.85"$) was not enough to cause the transverse steel to enter the nonlinear range.

South Reinforcement

The peak compressive strain in bar S3 of -0.0174 was measured 1.82" above the footing during ($\mu_8^{+1} = 6.46"$). A peak tensile strain of 0.047, centered 7.18" above the footing, was measured in bar S3 at ($\mu_8^{-1} = 6.48"$). The lowest tensile gage length for bar S3 was blocked by debris during ductility eight, so larger tensile strains may have occurred over this region. To illustrate this point, the vertical strain profile for adjacent bar S4 appears in Figure 1.201. The largest tensile strain in bar S4 of 0.051 was measured 1.82" above the footing during ($\mu_8^{-1} = 6.48"$). Bar S4 was the first South reinforcement to visibly buckle after reversal from ($\mu_8^{-1} = 6.48"$). The strain hysteresis for the buckled region of bar S4 can be seen in Figure 1.202. Buckling of the extreme fiber south bar S3 was delayed until ($\mu_{10}^{+1} = 8.07"$), which is confirmed by the measured longitudinal and transverse steel strain hysteresis in Figure 1.203 and Figure 1.204. The relationship between strain and displacement for push and pull cycles for extreme fiber bar S3 appears in Figure 1.198 and Figure 1.197 respectfully.

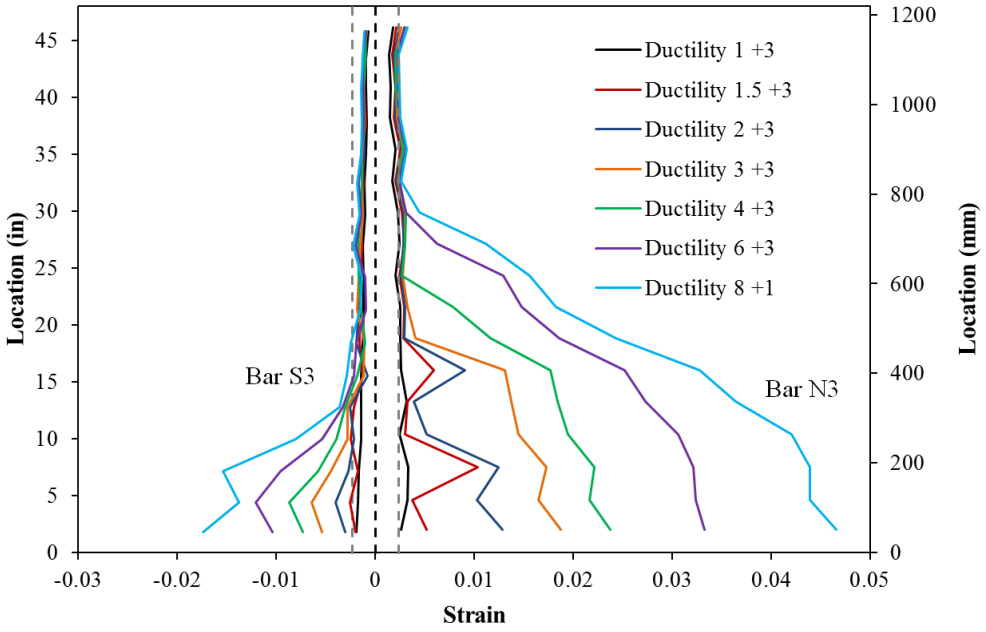

Figure 1.191 T13 – Extreme Fiber Vertical Strain Profiles during Push Cycles

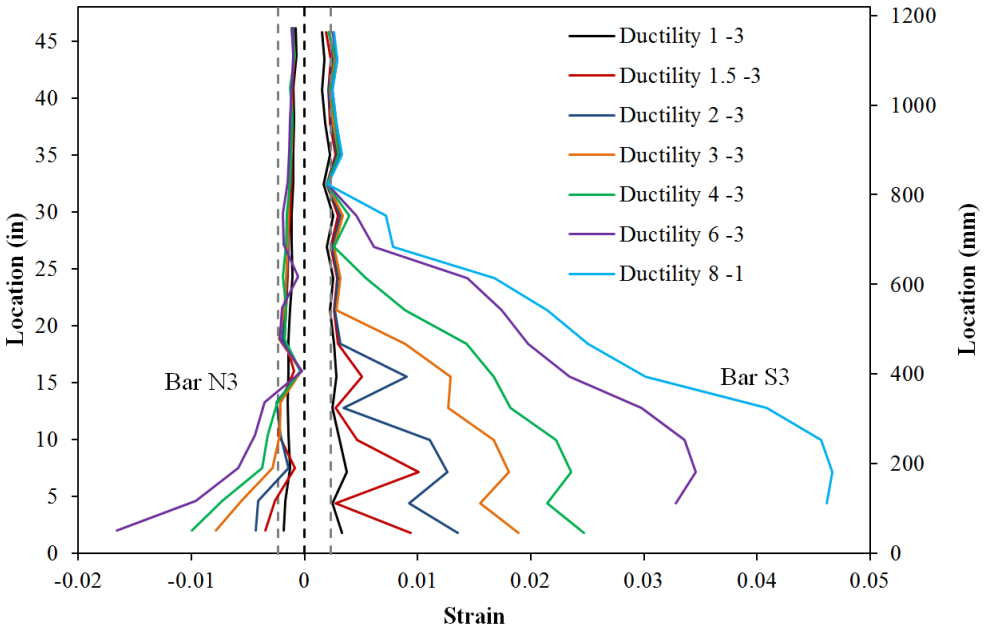

Figure 1.192 T13 – Extreme Fiber Vertical Strain Profiles during Pull Cycles

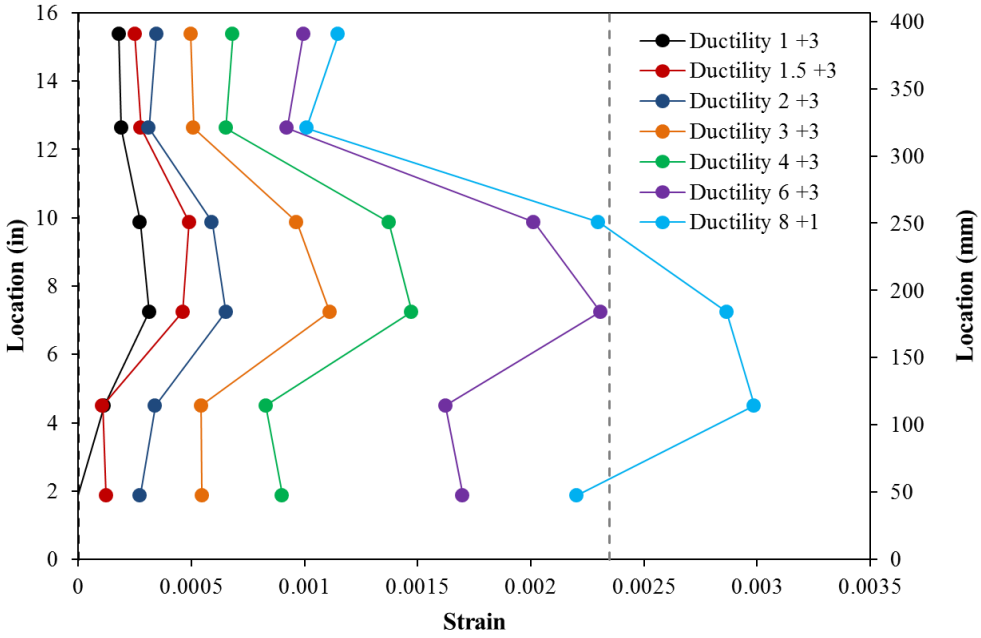

Figure 1.193 T13 – Spiral Strains for the Lowest Six Layers on the South Side

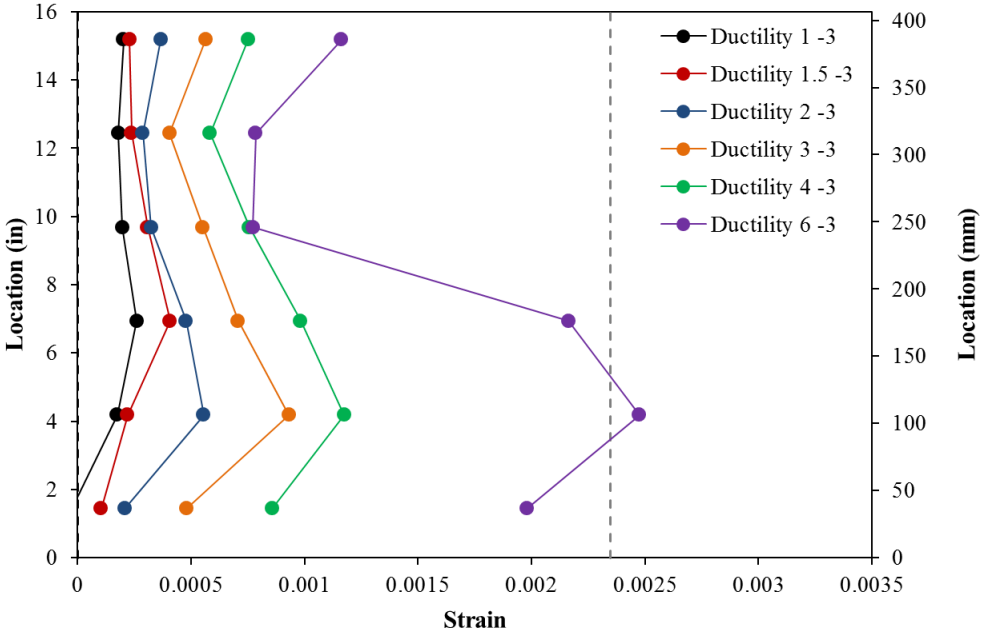

Figure 1.194 T13 – Spiral Strains for the Lowest Six Layers on the North Side

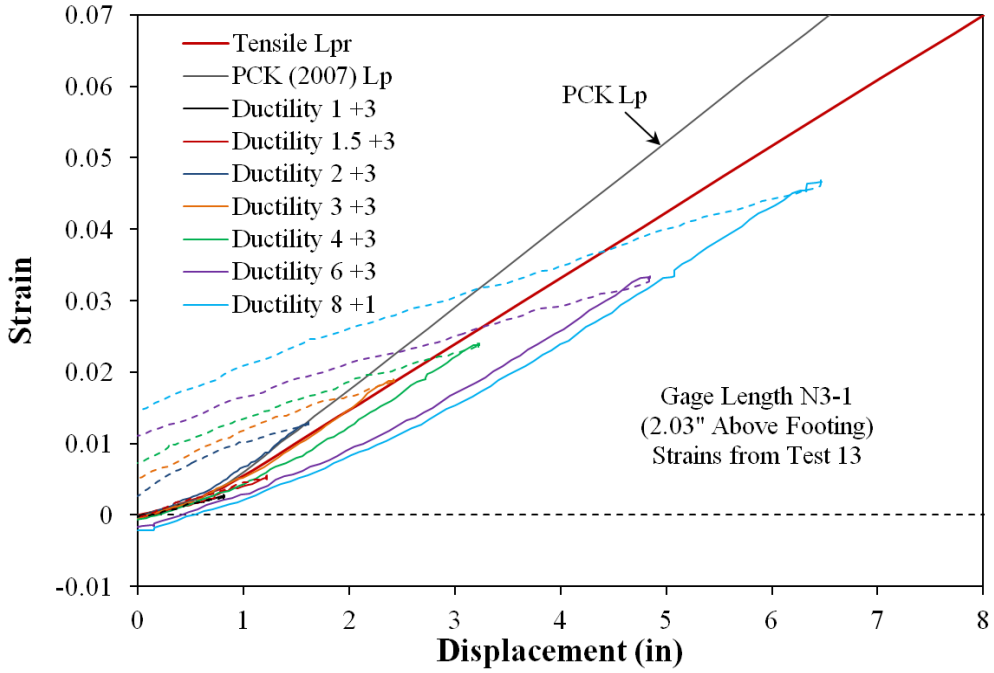

Figure 1.195 T13 – Tensile Strain-Displacement for Bar N3 during Push Cycles

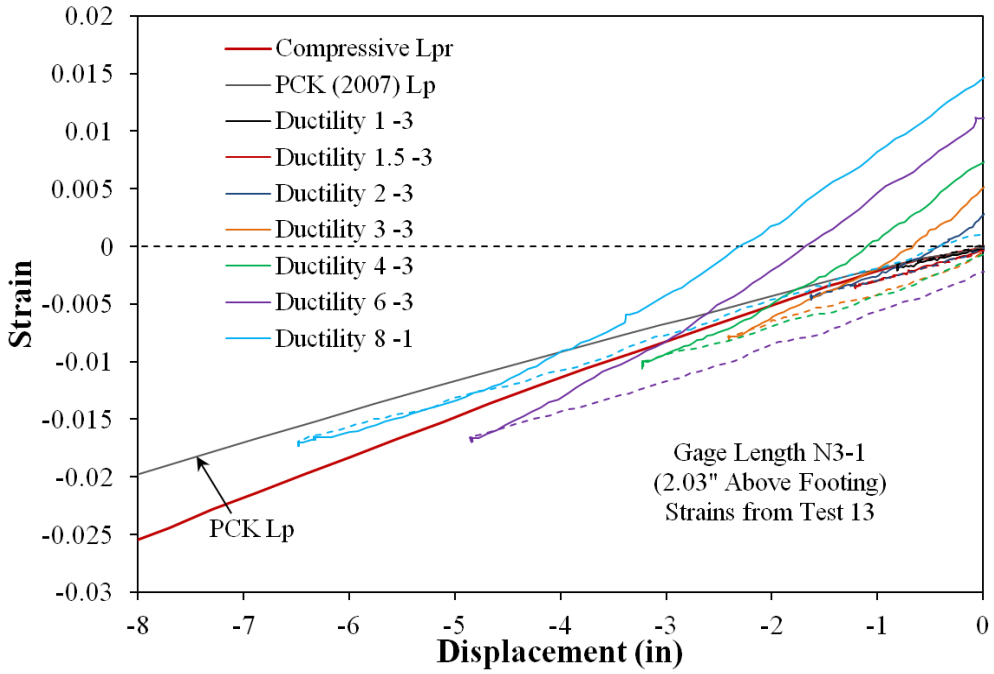

Figure 1.196 T13 – Compressive Strain-Displacement for Bar N3 during Pull Cycles

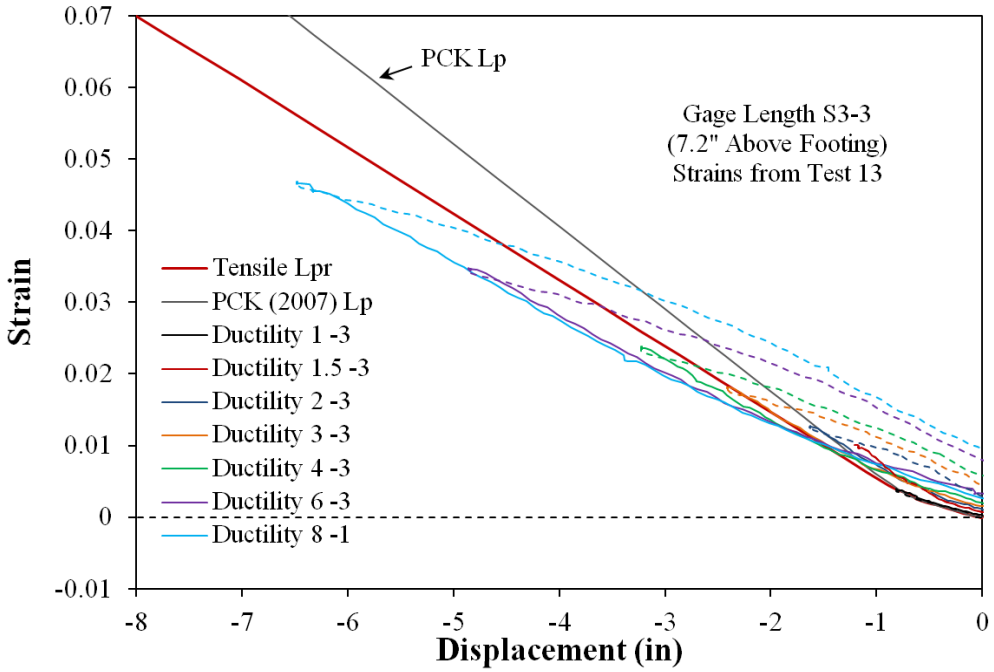

Figure 1.197 T13 – Tensile Strain-Displacement for Bar S3 during Pull Cycles

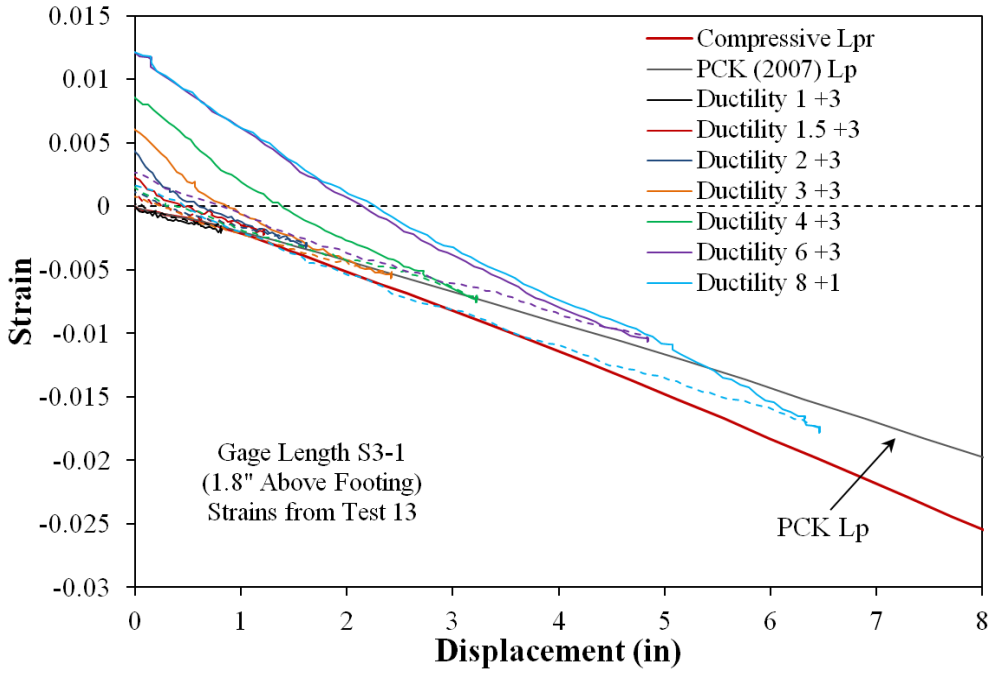

Figure 1.198 T13 – Compressive Strain-Displacement for Bar S3 during Push Cycles

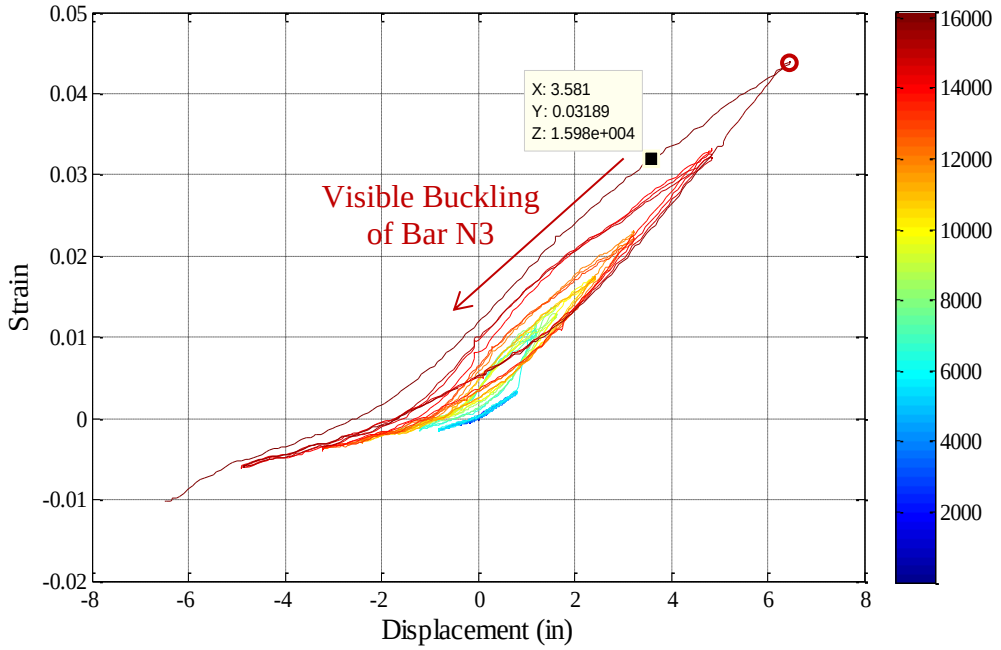

Figure 1.199 T13 – Bar N3 Strain Hysteresis for Buckled Region (7.48" Above Footing)

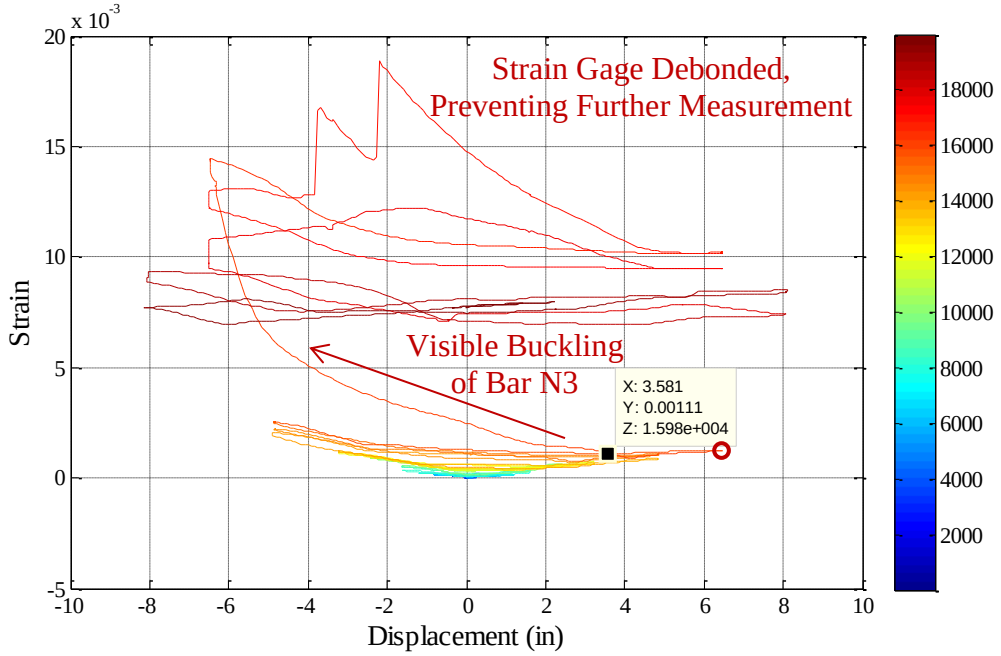

Figure 1.200 T13 – Spiral Strain Hysteresis for Layer over the North Buckled Region

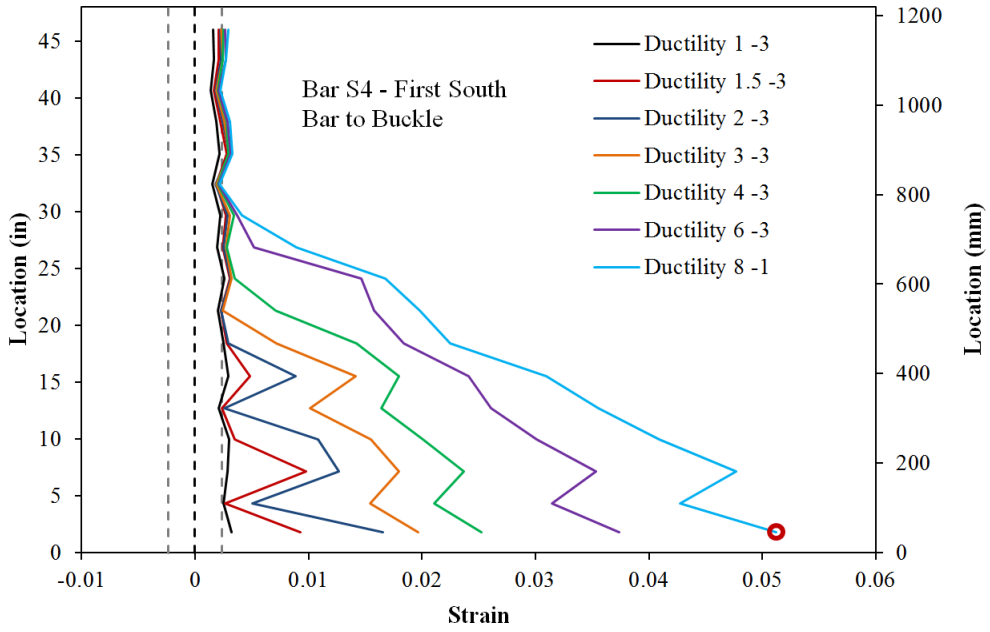

Figure 1.201 T13 – Tensile Strain Profile for Bar S4 (First South Bar to Buckle)

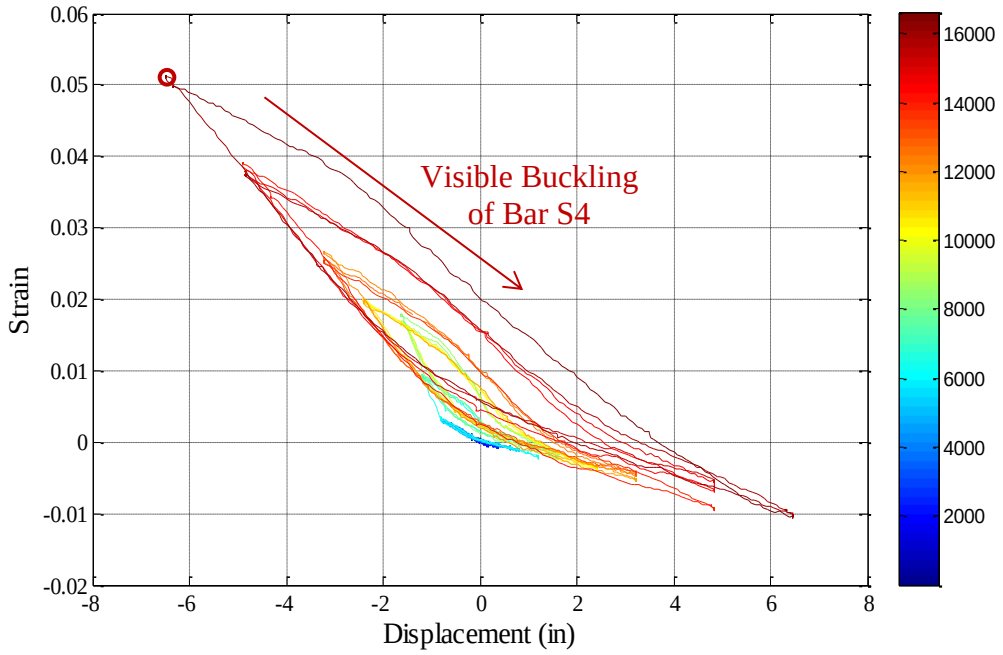

Figure 1.202 T13 – Bar S4 Strain Hysteresis for Buckled Region (1.82" Above Footing)

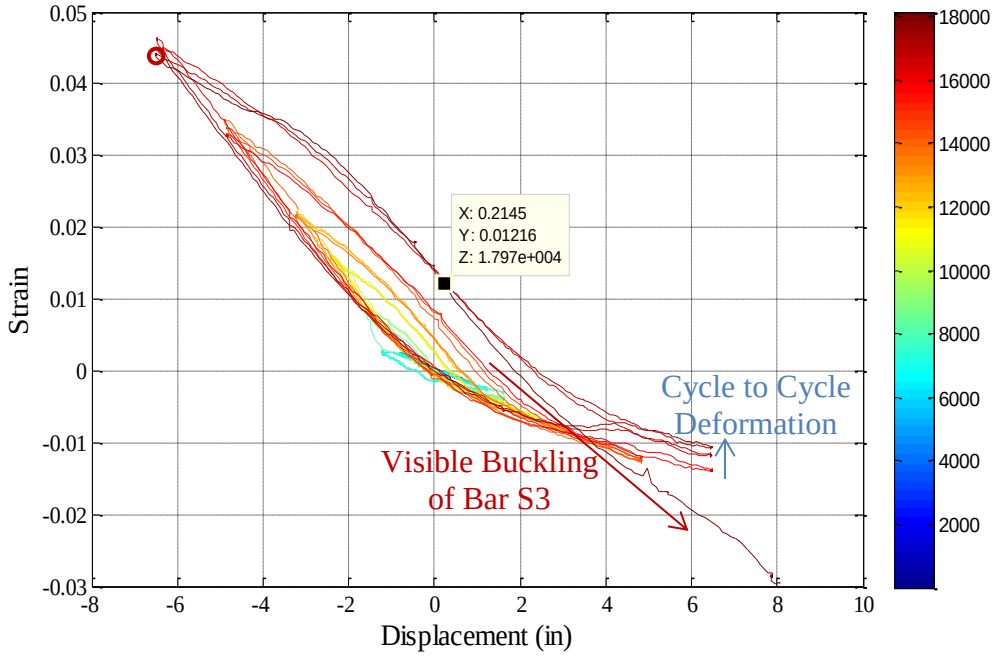

Figure 1.203 T13 – Bar S3 Strain Hysteresis for Buckled Region (4.41" Above Footing)

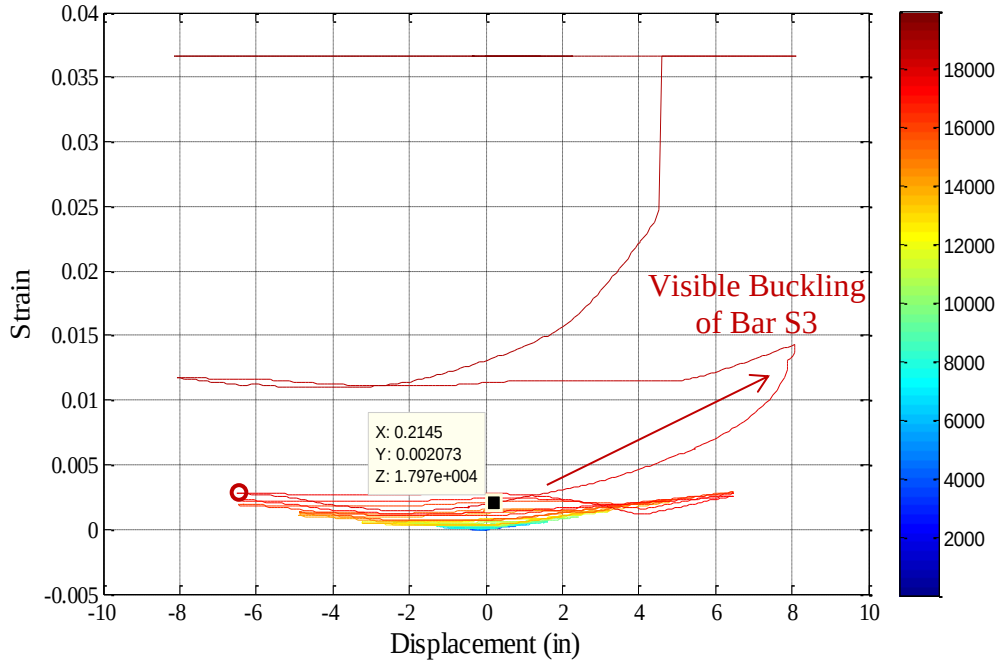

Figure 1.204 T13 – Spiral Strain Hysteresis for Layer over the South Buckled Region

Test 13 – Three Cycle Set (#4 @ 2.75") Curvature and Strain Penetration Data:

The cross section curvature for each horizontal section above the footing is determined by connecting the strain measurements from all six instrumented bars with a least squared error line. The curvature is then extracted from the slope of the least squared error line as shown in Figure 1.205. Vertical curvature profiles are plotted for push and pull cycles as shown in Figure 1.206 and Figure 1.207 respectively. These figures show that plastic curvatures have a linear distribution at higher displacement ductility levels. The extent of plastic curvatures above the footing can be calculated by determining where the linear plastic curvature distribution intersects the triangular yield curvature shown as a grey dashed line. The dashed lines for each curvature distribution represent a least squared error linear fit to the plastic portion of the measured curvatures. The data points used to create the least squared error lines appear as circle data markers.

LEDs placed closest to the footing-column interface on the six reinforcing bars can track the base section rotation due to strain penetration of longitudinal reinforcement into the footing. The measured base rotations for push and pull cycles appear in Figure 1.210 and Figure 1.211 respectively. Compared to previous tests, the bar slip profiles are shifted down slightly. Inspection of the measured slip hysteresis for extreme fiber bars N3 and S3 in Figure 1.208 and Figure 1.209 shows that each bar shifted downwards after the tests began. A possible explanation for why this occurred is not available, since this was not observed in any of the other experiments. A comparison of the measured top column displacement and the Optotrak integrated displacements appear in Figure 1.212. The Optotrak displacement was obtained by integrating the measured curvature profile, extrapolating the base rotation to the center of loading, and assuming an elastic curvature distribution above the instrumented region. The measured spread of plasticity as a function of base section curvature ductility is shown in Figure 1.213. The extent of plasticity is calculated as the intersection of the linear plastic curvature regression with the elastic curvature profile, Figure 1.206.

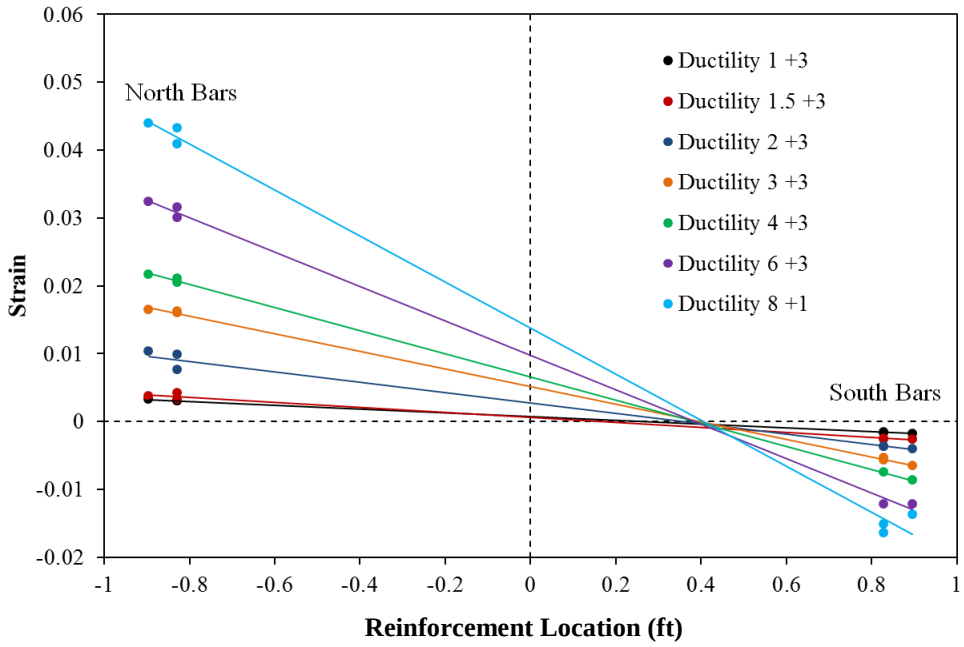

Figure 1.205 T13 – Push Cycle Strain Profiles Used to Find Cross Section Curvatures

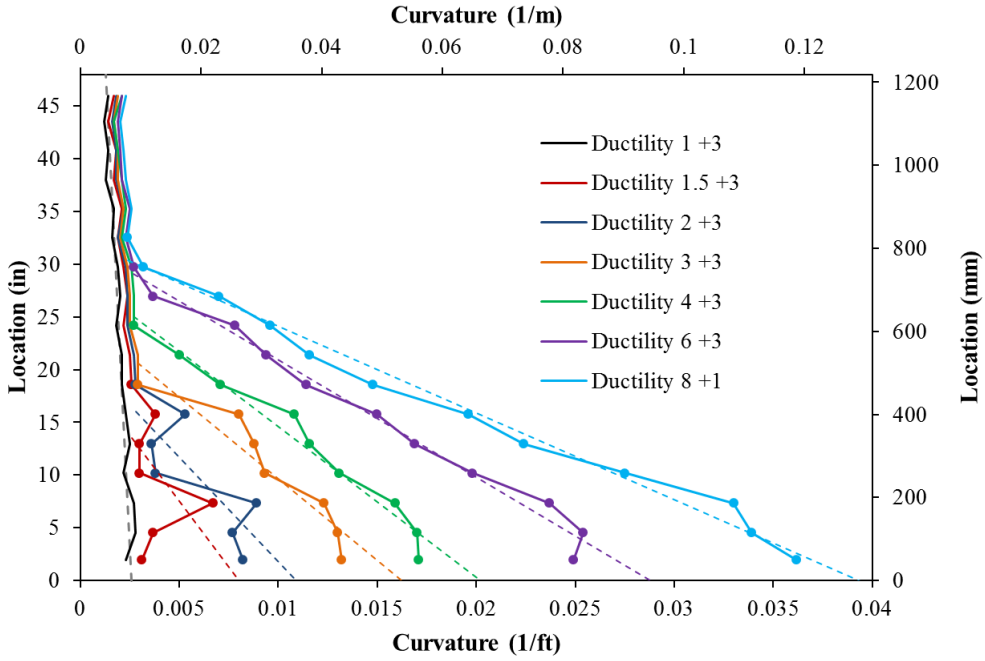

Figure 1.206 T13 – Vertical Curvature Profiles for Push Cycles with Plastic Regression

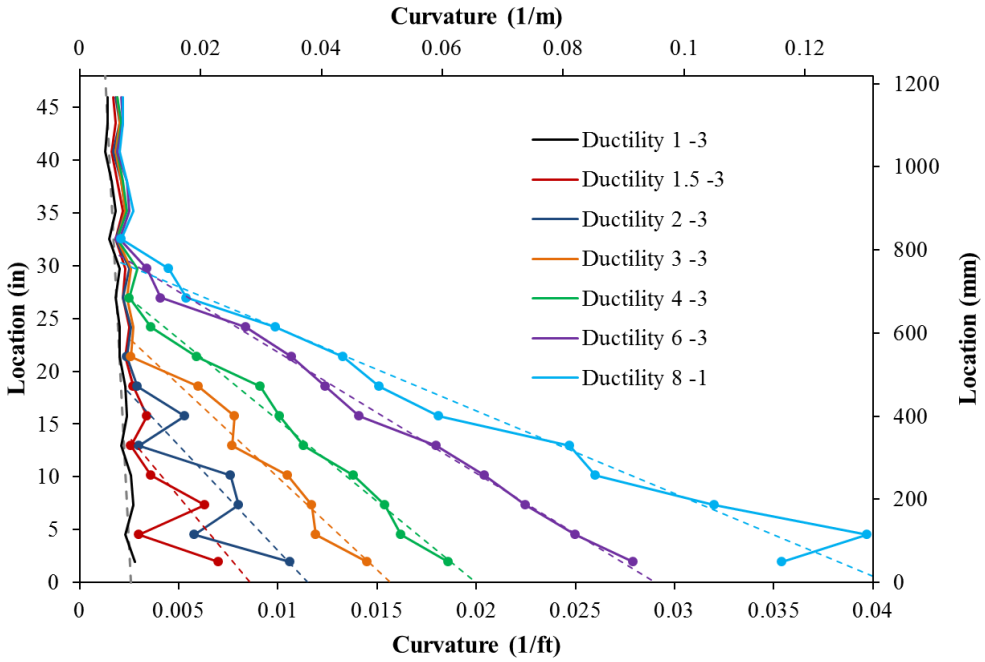

Figure 1.207 T13 – Vertical Curvature Profiles for Pull Cycles with Plastic Regression

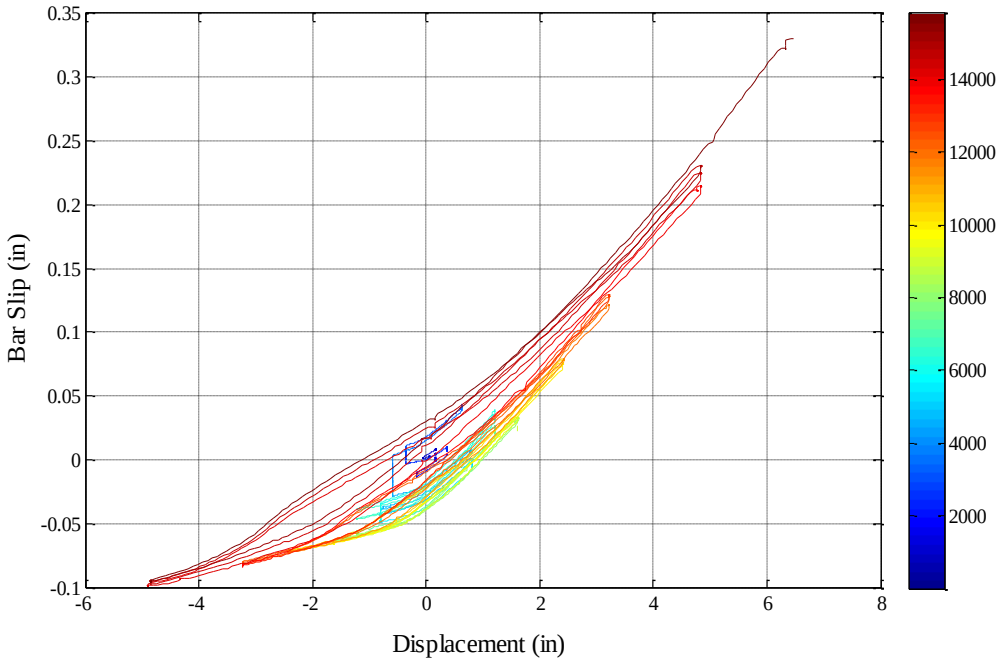

Figure 1.208 T13 – Bar N3 Base Section Slip Hysteresis due to Strain Penetration

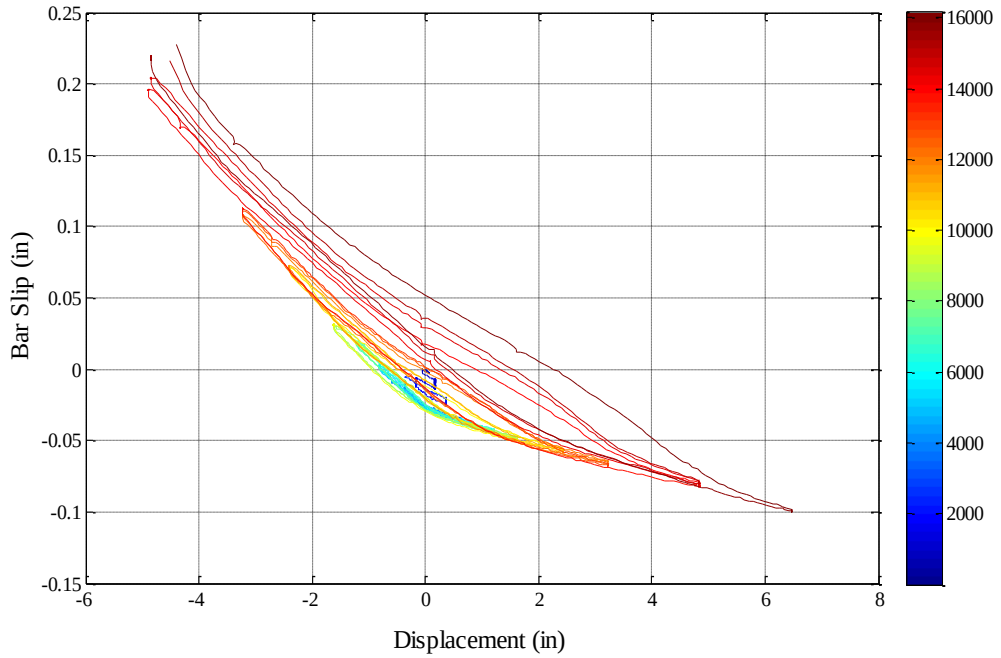

Figure 1.209 T13 – Bar S3 Base Section Slip Hysteresis due to Strain Penetration

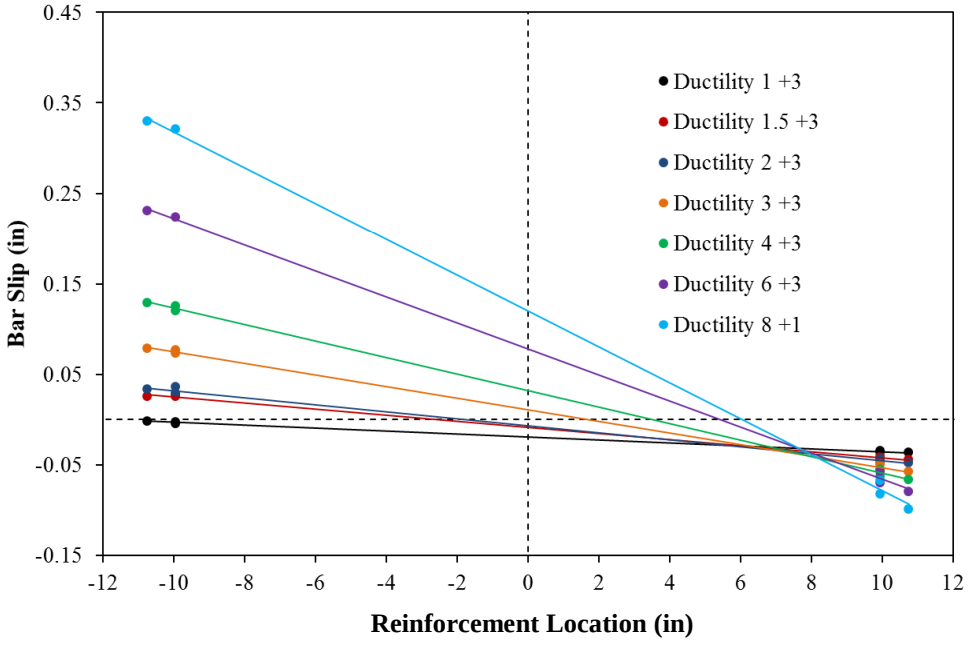

Figure 1.210 T13 – Base Rotations during Push Cycles due to Strain Penetration

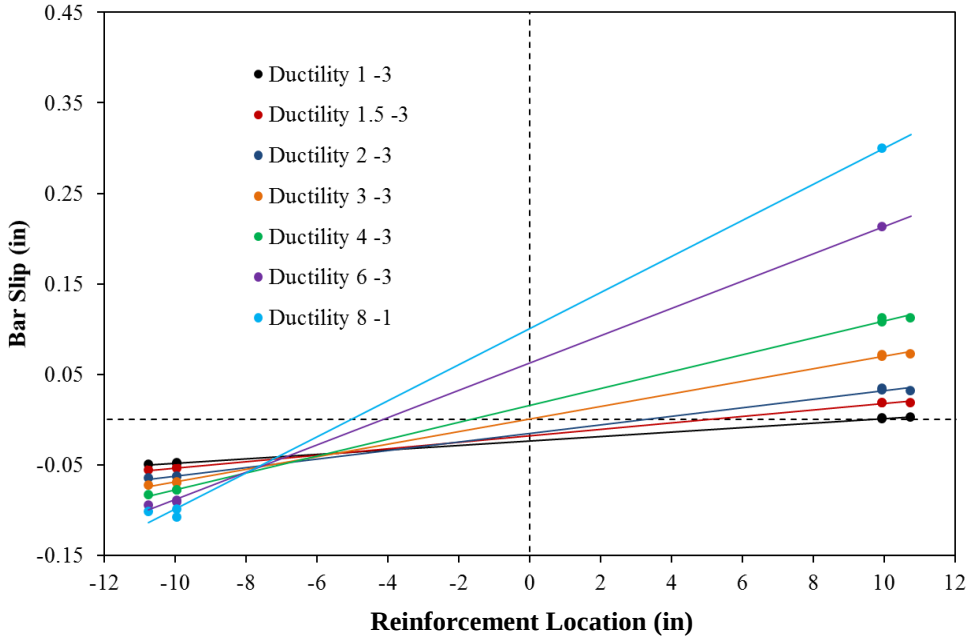

Figure 1.211 T13 – Base Rotations during Pull Cycles due to Strain Penetration

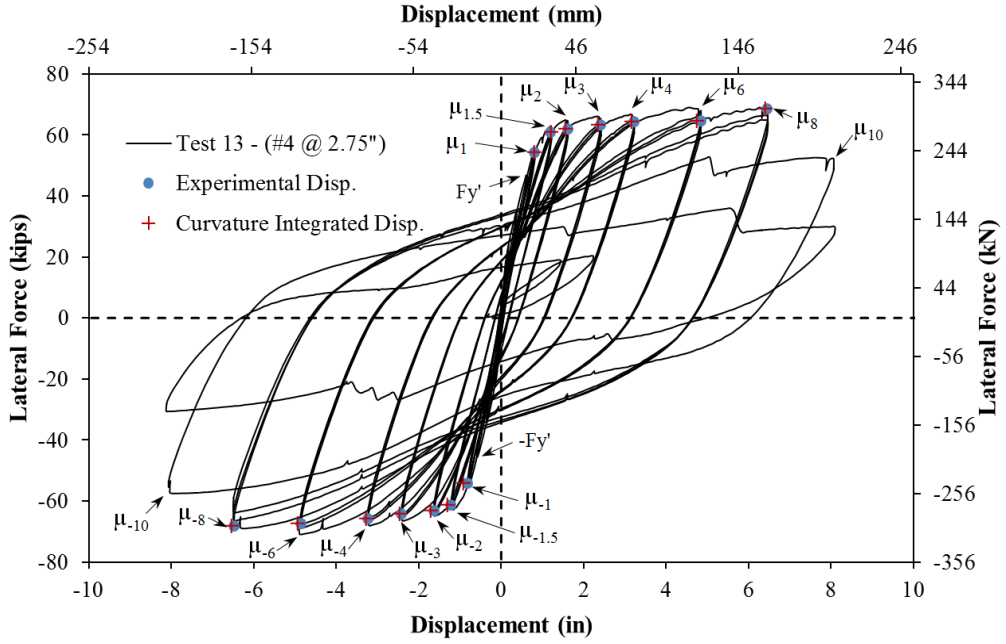

Figure 1.212 T13 – Comparison of Measured and Optotrak Integrated Displacements

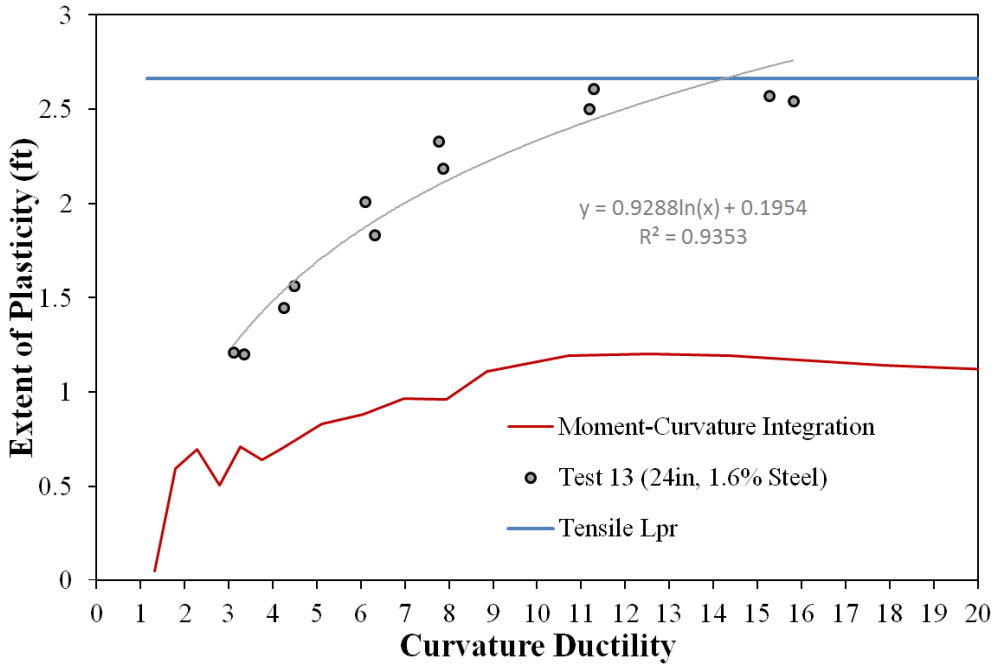

Figure 1.213 T13 – Measured Spread of Plasticity (Circular Data Points)

1.2.2 Test 14 –Three Cycle Set Load History with #3 Spiral at 4" (0.5%)

Table 1.19 Observational Summary for Test 14 – Cyclic with #3 Spiral at 4" (0.5%)

VALUES OF INTEREST:	
Concrete Compressive Strength:	$f_c' = 6641\ psi$
Axial Load:	$P = 170\ kips$
Analytical First Yield Force:	$F_y' = 47.0\ kips$
Experimental First Yield Displacement:	$\Delta_y' = 0.60"$ *From Test 13, See Discussion
Analytical Nominal Moment Capacity:	$M_n = 499.7\ kip * ft$
Equivalent Yield Displacement:	$\Delta_y = 0.80"$
Maximum Lateral Force:	$69.1\ kips$
Failure Mode:	Fracture of Previously Buckled Reinforcement
DAMAGE OBSERVATIONS:	
First Cracking North:	**Intended Cycle to $1/2Fy' = 0.42"$
First Cracking South:	**Intended Cycle to $-1/2Fy' = -0.45"$
Cover Concrete Crushing North:	$\mu_{1.5}^{-3} = -1.19"$
Cover Concrete Crushing South:	$\mu_{1.5}^{+3} = 1.20"$
Transverse Steel Yield North:	At $-0.25"$ during pull to $\mu_6^{-1} = -4.80"$
Transverse Steel Yield South:	At 3.84" during push to $\mu_6^{+1} = 4.80"$
Longitudinal Bar Buckling North:	Reversal from $\mu_6^{+1} = 4.80"$
Longitudinal Bar Buckling South:	Reversal from $\mu_6^{-1} = -4.80"$
Longitudinal Bar Fracture North:	At $-3.46"$ during push to $\mu_8^{+2} = 6.40"$
Longitudinal Bar Fracture South:	At $-2.81"$ during pull to $\mu_8^{-1} = -6.39"$

*$\mu_6^{-1} = -4.80"$ represents the first pull cycle of displacement ductility six

Table 1.20 Strain Data Summary for Test 14 – Cyclic with #3 Spiral at 4" (0.5%)

MATERIAL STRAINS:	
Cover Concrete Crushing North:	$\varepsilon_s = 0.0029\ (compression)$
Cover Concrete Crushing South:	$\varepsilon_s = 0.003\ (compression)$
Transverse Steel Yield North:	N/A, Due to Reversal From Tensile Strain
Transverse Steel Yield South:	$\varepsilon_s = 0.0152\ (compression)$
Longitudinal Bar Buckling North:	$\varepsilon_s = 0.035\ (peak\ tension\ prior\ to\ bb)$
	$\varepsilon_s = 0.011\ (peak\ comp.\ prior\ to\ bb)$
Longitudinal Bar Buckling South:	$\varepsilon_s = 0.035\ (peak\ tension\ prior\ to\ bb)$
	$\varepsilon_s = 0.015\ (peak\ comp.\ prior\ to\ bb)$
Mander (1988) Ultimate Concrete Compression Strain, $\varepsilon_{cu} = 0.0109$	

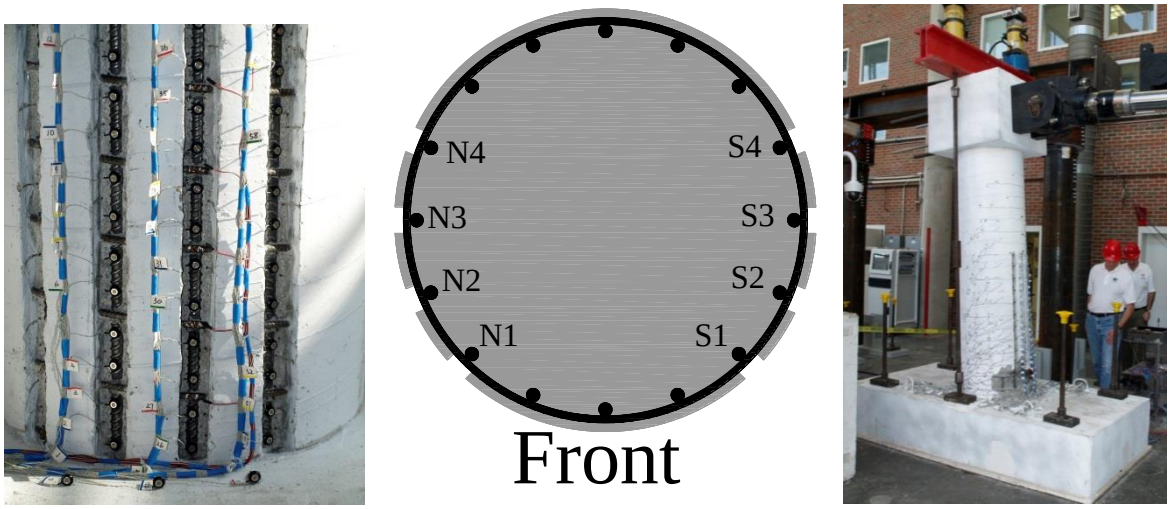

Figure 1.214 T14 – Cross Section Bar Designation and Target Marker Application

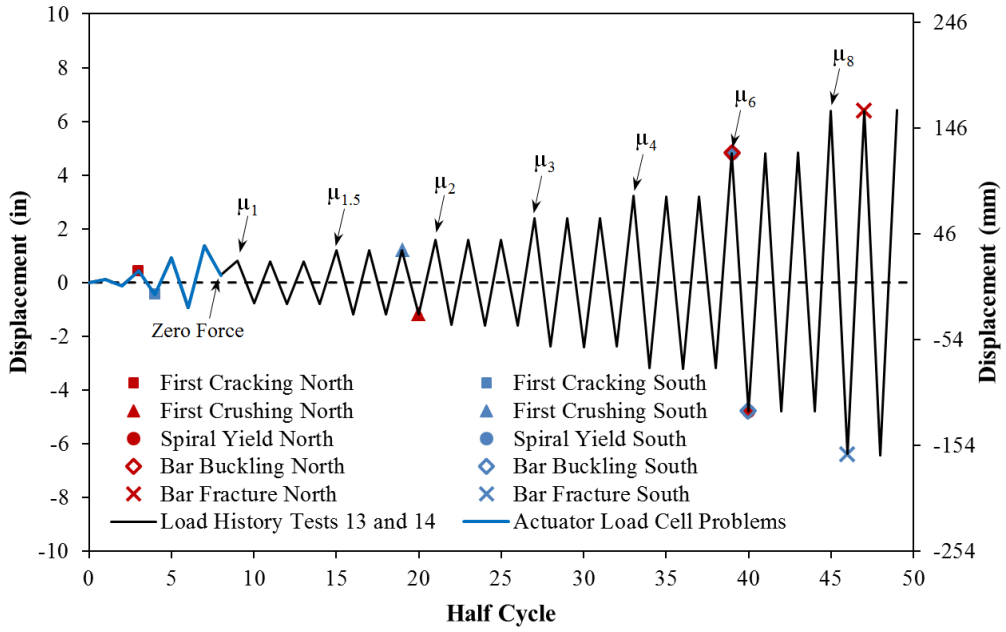

Figure 1.215 T14 – Cyclic Load History (Initial Cycles Influenced by Load Cell Error)

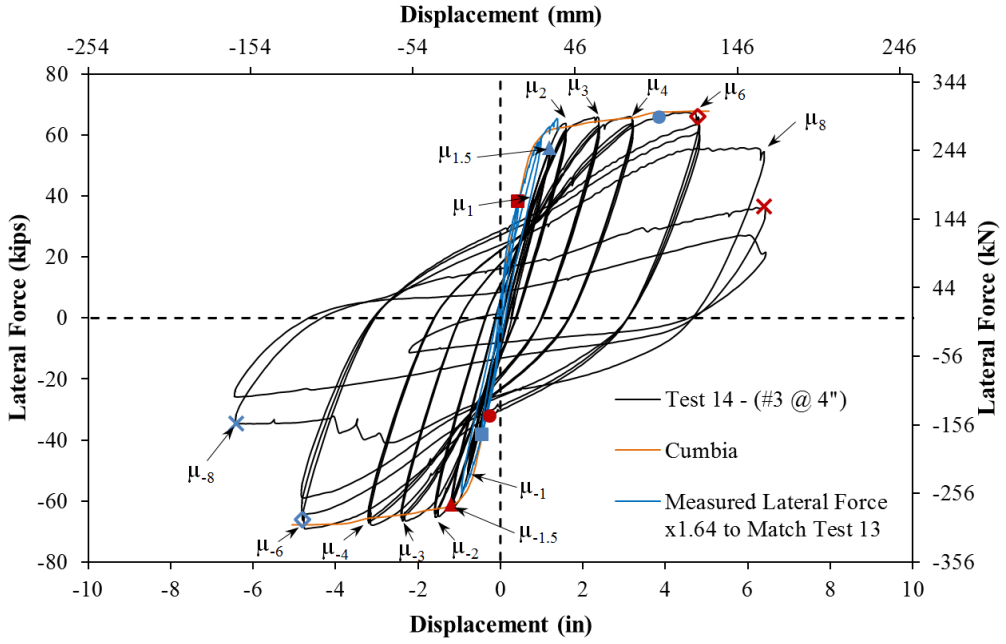

Figure 1.216 T14 – Lateral Force vs. Top Column Displacement Response

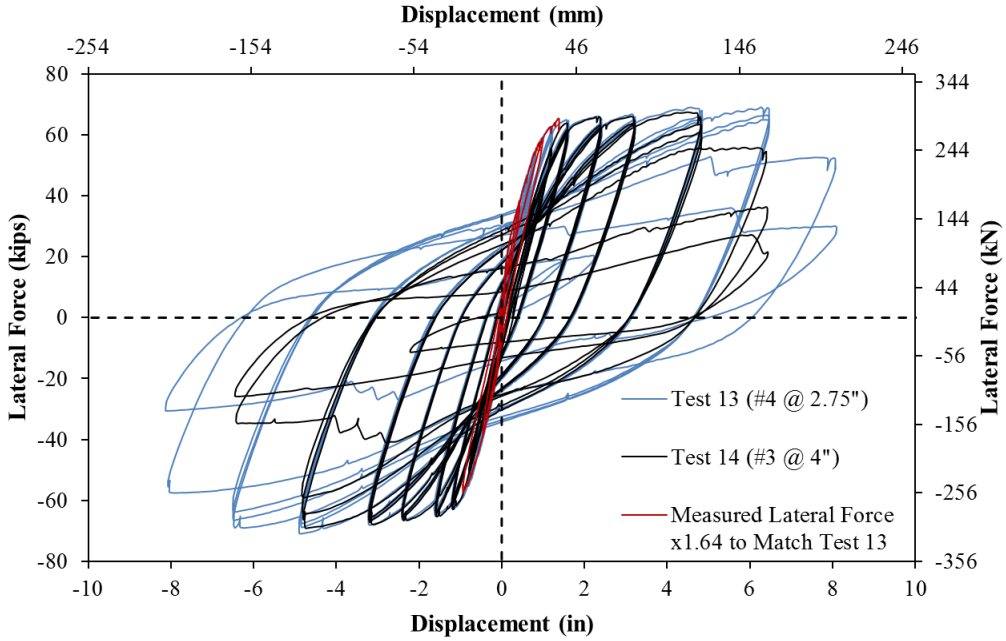

Figure 1.217 T14 – Appropriate Scale Factor for Initial Cycles with Load Cell Error

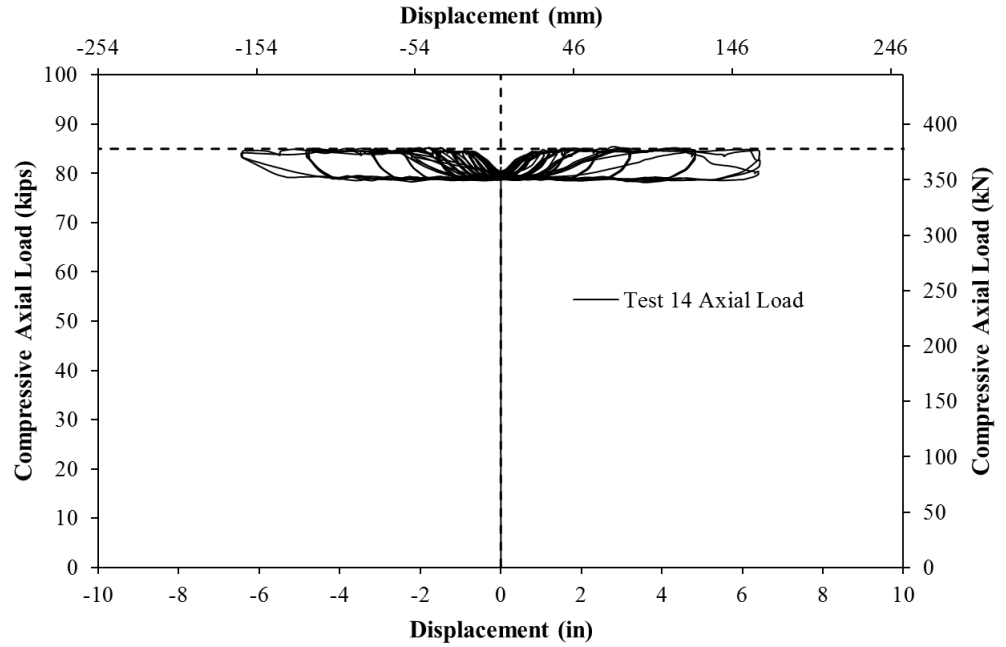

Figure 1.218 T14 – Compressive Axial Load from One Jack (Total = 2*Value)

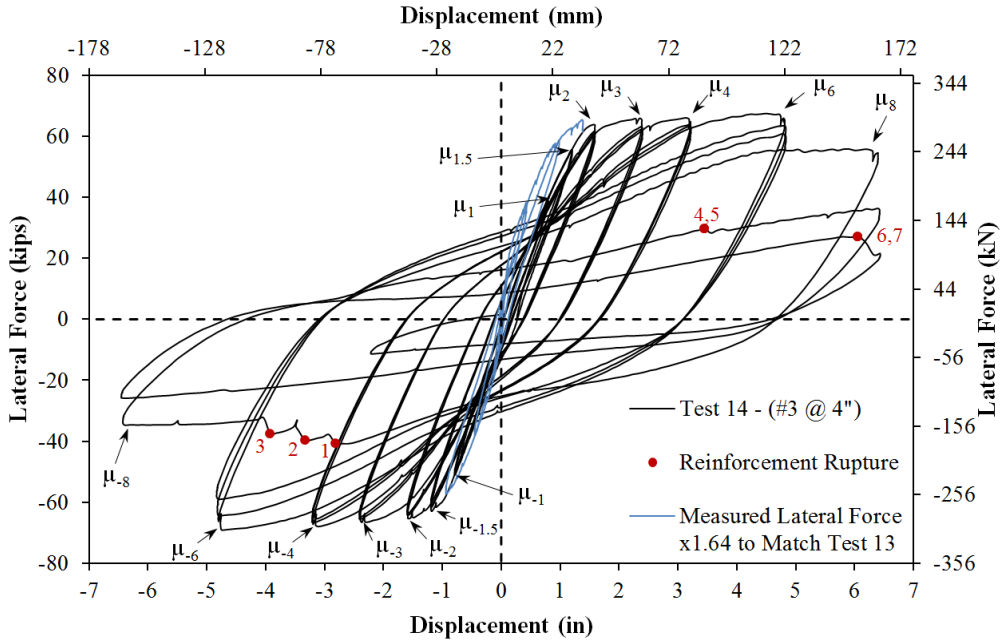

Figure 1.219 Test 14 – Rupture History of Previously Buckled Reinforcement

Test 14 – Symmetric Three Cycle Set (#3 @ 4") Experimental Observations

The first yield force for the tested material and geometric properties was determined using moment curvature analysis (Test 14: Cumbia Fy' = 46.97 kips with f'c = 6641 psi) compared to (Test 13: Cumbia Fy' = 46.48 kips with f'c = 6097 psi). During the early cycles of the Test 14 load history, it became apparent that the actuator load cell was not functioning properly. This was noticed because the forces were considerably lower than expected at small displacements. Initially, this problem was not attributed to the actuator load cell and several small cycles were conducted to try and pin down the specific cause of the problem. During these cycles, the specimen was pushed past the first and equivalent yield displacements in both directions of loading, see Figure 1.215. In the push direction of loading the specimen went past displacement ductility 1.5 and in the pull direction the displacement was just past ductility one. It was determined that the only thing that could have caused this issue is an incorrect actuator load cell reading, and upon inspection a

damaged cable connection was found. The cable was replaced and the actuator load cell began recording the correct lateral force for the remainder of the test.

At this point of the test, there was no way to go back and redo the elastic cycles to the first yield displacement due to the slight stiffness degradation from inelastic cycles in each direction of loading. For this reason, the first yield displacement from Test 13 was used for Test 14. The first yield displacement for the thirteenth test was obtained as an average for the first yield push and pull cycles ($\Delta_y' = 0.60"$). Extreme fiber vertical strain profiles, for Test 14, at the first yield displacement appear in Figure 1.220 for push and pull cycles respectively. The first yield displacement from Test 13 is also appropriate for Test 14 based on the vertical strain profiles which have strains just past yield at large crack locations.

The equivalent yield displacement, used to determine the displacement ductility levels ($\mu_{\Delta n} = \mathrm{n} * \Delta_y$), is then calculated as $\Delta_y = \Delta_y'(M_n/M_y') = 0.80"$ for Test 14 compared to $\Delta_y = 0.81"$ for Test 13. The full symmetric three-cycle-set load history appears in Figure 1.215 and the resulting lateral force vs. top column displacement hysteresis is shown in Figure 1.216. Past tests in the load history research program suggest that cycles at lower displacement ductility levels, such as those prior to fixing lateral load issue, should not have an impact on later cycles at larger displacements. The concrete cover on the South side of the specimen remained intact during the largest overload cycle, Figure 1.221. These initial cycles caused stiffness degradation which decreased the force during lower displacement ductility levels in the three cycle set load history.

Since the actuator load is calibrated based on a linear curve relating voltage to lateral force which passes through the origin, a constant scale factor can be used to transform the incorrect data to a better approximation of the actual lateral force. The backbone curves of reinforced concrete bridge columns with similar material properties should remain similar, so this was used to calibrate the scale factor to relate the incorrect lateral force of Test 14 to the backbone curve of Test 13. As shown in Figure 1.217, a constant scale factor of 1.64 gave

the best approximation of the actual lateral force during early cycles affected by the damaged load cell cable.

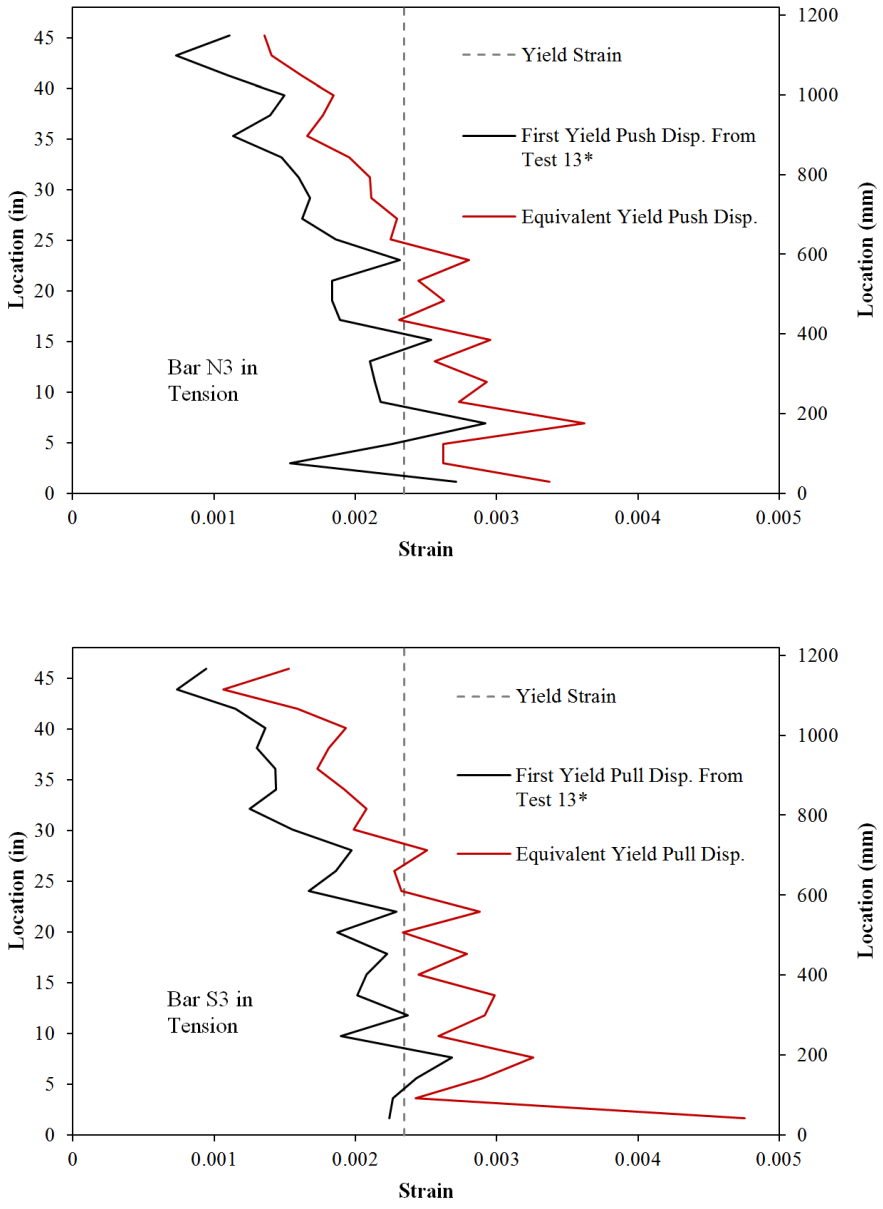

Figure 1.220 T14 – North and South Bar Strain Profiles during Δ'_y (Test 13) and Δ_y

Even though the initial cycles were did not reach the proper level of force expected in a symmetric three-cycle-set load history, information on the crack location, width, and orientation were still taken at the peak of each cycle. The first half cycle was intended to reach ¼ Fy', but since the actuator load cell cable was damaged, the actual displacement at this intended lateral force was greater. This initial cycle and the subsequent reversal to -¼ Fy' were not large enough to cause cracking in the specimen. The third half cycle intended to reach ½ Fy' pushed the specimen to 0.42" and 0.3mm cracks at 8" spacing were observed. As expected, the cracks occurred at the level of the transverse steel. The same crack width and spacing was observed during the pull cycle to -½ Fy'. The cycle intended for ¾ Fy' reached a displacement of 0.91". Note that this is larger than the equivalent yield displacement of 0.80". The largest crack width measured 0.6mm at 4" spacing which followed the locations of transverse steel. During the intended pull cycle to -¾ Fy' at -0.94", 0.75mm crack widths were measured at 4" spacing.

The next cycle was intended to reach Fy', but the specimen was paused and the actuator load cell connection problem was determined. The peak displacement reached prior to pausing and reversing the load to zero force was 1.38". Note that this is equal to a displacement ductility of 1.73, therefore latter cycles in the load history to ductility 1 and 1.5 in the push direction have a loss of stiffness due to this overload. In the pull direction of loading only the ductility one cycles are affected by stiffness degradation from the displacement ductility -1.13 cycle.

During ($\mu_1^{+3} = 0.79"$), 0.75mm crack widths at 4" spacing were measured. This is very similar to the crack widths and spacing observed during the intended ¾ Fy' cycle earlier in the load history to ductility 1.13. The same crack width and spacing were measured during ($\mu_1^{-3} = -0.79"$). At ($\mu_{1.5}^{+1} = 1.19"$) visible flaking of the cover concrete was observed on the South side of the specimen which usually occurs just before crushing. Crushing over the bottom two inches of the cover concrete on the south side occurred during ($\mu_{1.5}^{+3} = 1.20"$), as shown in the left photo of Figure 1.222. During this same cycle cracks on the North side of the specimen were measured at 1.25mm at 4" spacing. The extent of crushing on the North

side of the specimen reached 7" above the footing during ($\mu_{1.5}^{-3} = 1.19$"), see the right photo of Figure 1.222. Here, the cracks on the South side of the specimen increased to 1.5mm width at 4" spacing. Cracks on the North side of the specimen measured 1.5mm at 4" spacing at ($\mu_2^{+3} = 1.58$") while the extent of crushing on the South side of the specimen reached 7" above the footing. The extent of crushing on the North side of the specimen did not increase during ductility two, but it spread to other uncrushed locations near the base of the column. The extent of crushing on the South side of the specimen increased to 10" above the footing and widened during ($\mu_3^{+3} = 2.40$"). The crushing on North side of the specimen widened, but did not increase in height during ductility three.

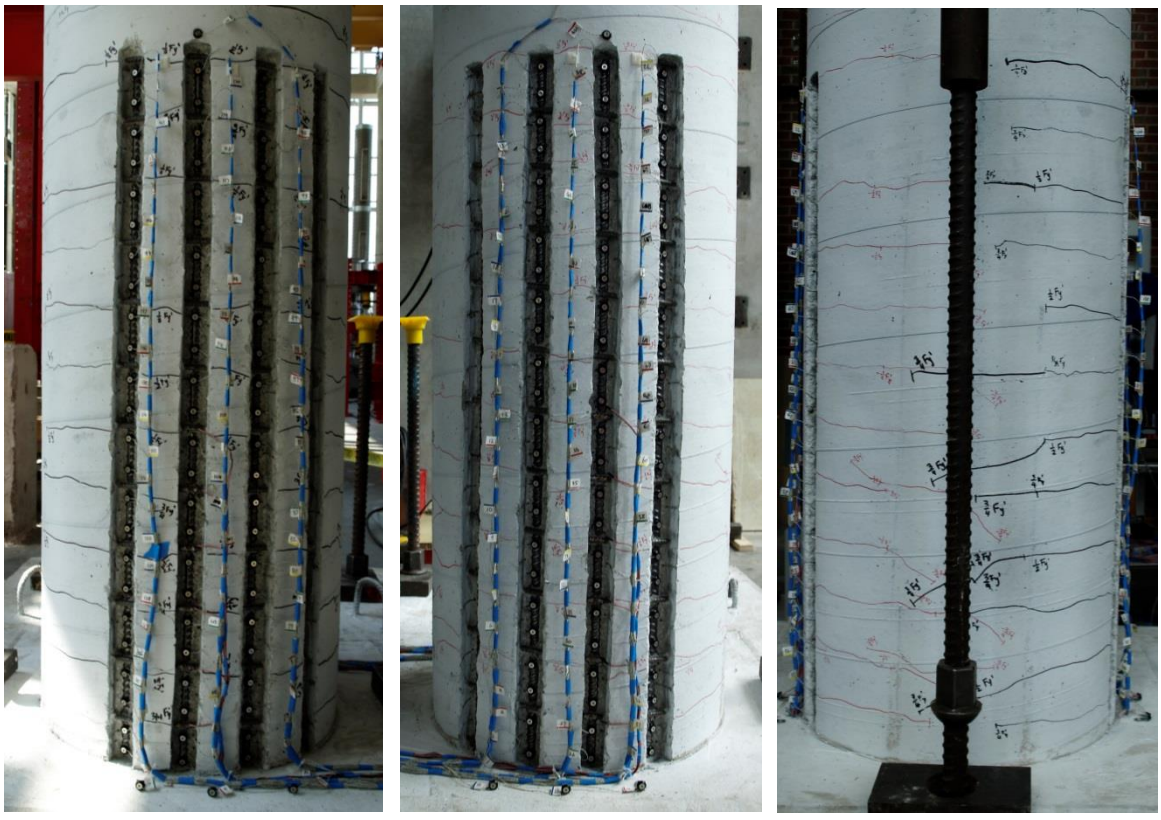

Figure 1.221 T14 – Crack Distribution after All Cycles with Actuator Load Cell Errors (No Notable Limit States Reached)

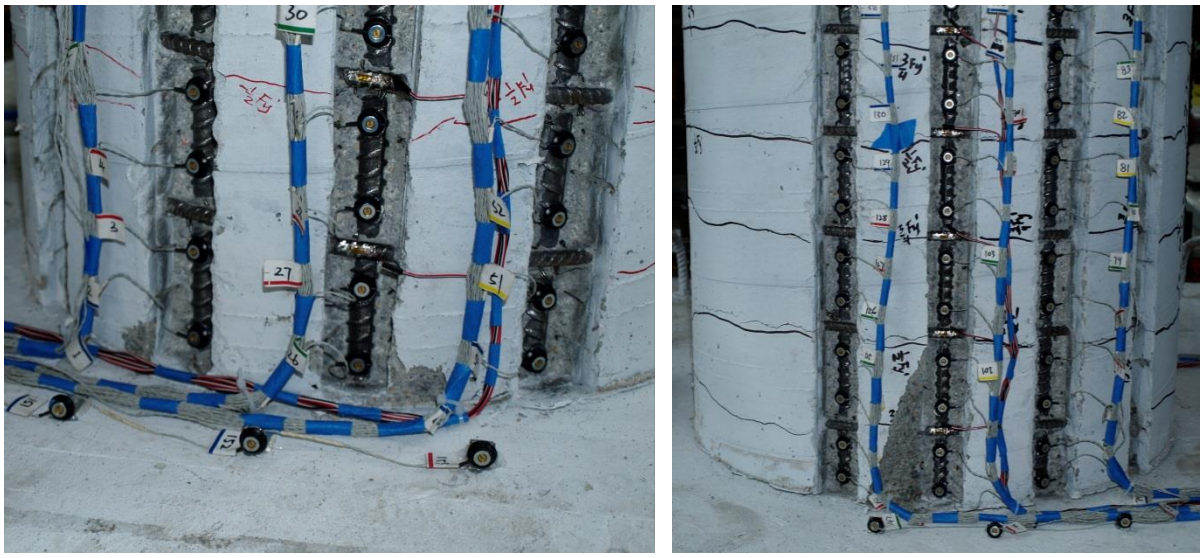

Figure 1.222 T14 – (Left) South Cover Crushing during ($\mu_{1.5}^{+3} = 1.20$") and (Right) Cover Crushing on the North Side of the Specimen at ($\mu_{1.5}^{-3} = 1.19$")

The extent of crushing on the North and South sides of the specimen during the third cycle of ductility four is shown in Figure 1.223. Extreme fiber North reinforcing bar N3 buckled after reversal from ($\mu_6^{+1} = 4.80$"), see the left photo of Figure 1.224. All three instrumented bars on the South side of the specimen (S2, S3, and S4) buckled after reversal from ($\mu_6^{-1} = -4.80$"), as shown in the right photo of Figure 1.224. During the reversal from ($\mu_6^{+2} = 4.82$"), additional North reinforcement bars N2 and N4 buckled, Figure 1.225. North reinforcing bars N1 and N5 buckled during ($\mu_6^{-3} = -4.80$"). At the end of ductility six there was 9% strength loss in the push direction of loading and 12% strength loss in the pull direction due to buckled reinforcing bars and loss of confinement prior to rupture. On the way to ($\mu_8^{+1} = 6.40$"), South reinforcing bar S1 buckled. Separation of the deformed spiral North reinforcing bars, while they were in tension, is shown in Figure 1.226. During ($\mu_8^{-1} = -6.39$"), previously buckled South reinforcing bars S2, S3, and S4 ruptured causing a 48% loss in strength, Figure 1.227. On the way to ($\mu_8^{+2} = 6.40$"), previously buckled North reinforcing bars N2 and N3 ruptured causing a 45% loss in strength, as shown in the left photo of Figure 1.228. North reinforcement bars N4 and N5 ruptured on the way to ($\mu_8^{+2} = 6.40$") causing a 67% loss in strength. The test was concluded at this time and

photos which show the specimen after instrumentation and debris were removed appear in Figure 1.228. A photo progression of the crack propagation on the back side of the specimen is shown in Figure 1.229.

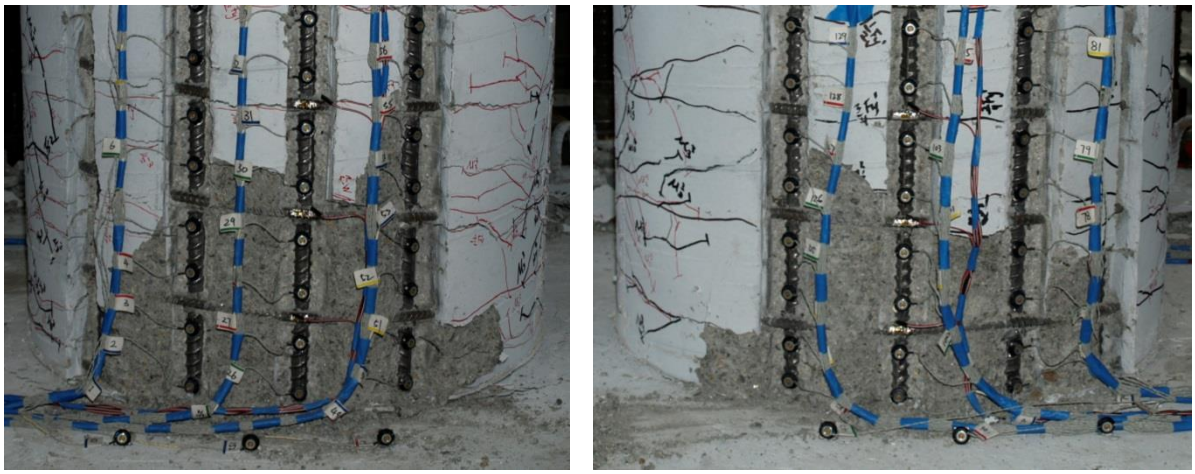

Figure 1.223 T14 – (Left) Extent of Crushing on the South Side of the Specimen during ($\mu_4^{+3} = 3.19$") and (Right) Extent of Crushing on the North Side during ($\mu_4^{-3} = 3.20$")

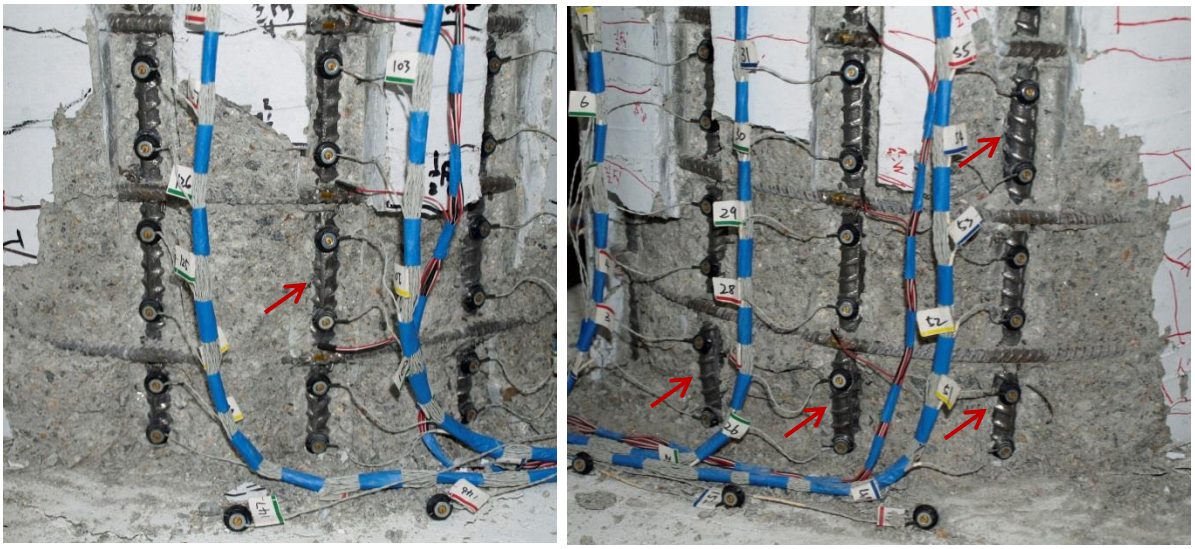

Figure 1.224 T14 – (Left) Buckling of Bar N3 during ($\mu_6^{-1} = -4.80$") and (Right) Buckling of South Reinforcing Bars S2, S3, and S4 during ($\mu_6^{+2} = 4.82$")

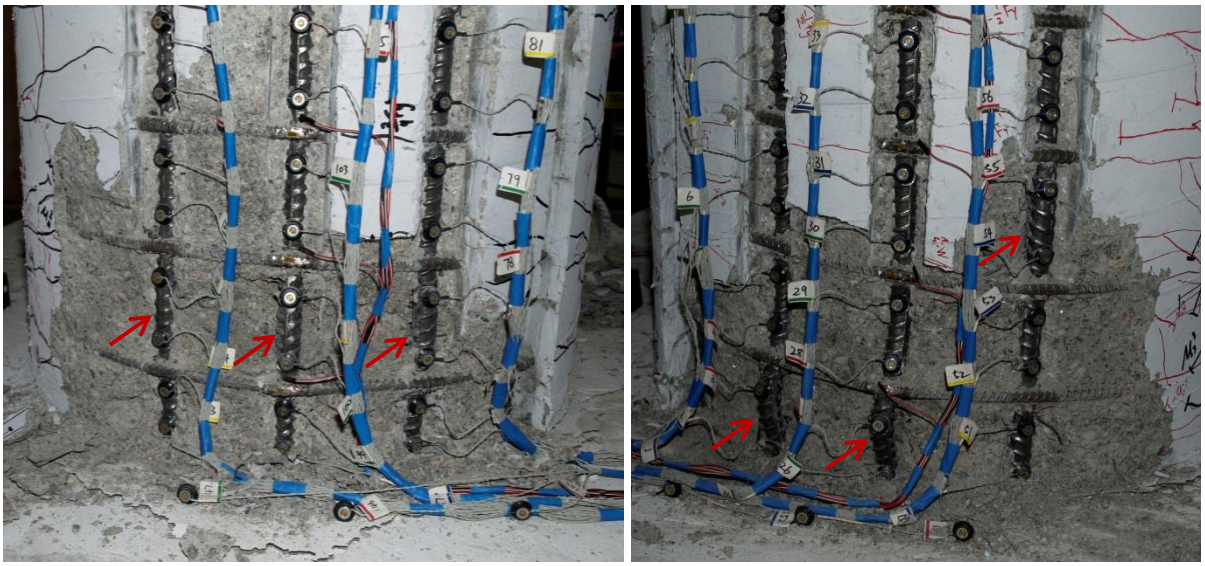

Figure 1.225 T14 – (Left) Buckling of North Bars N2 and N4 during ($\mu_6^{-2} = -4.80$") and (Right) Deformation in Buckled Bars S2, S3, and S4 during ($\mu_6^{+3} = 4.83$")

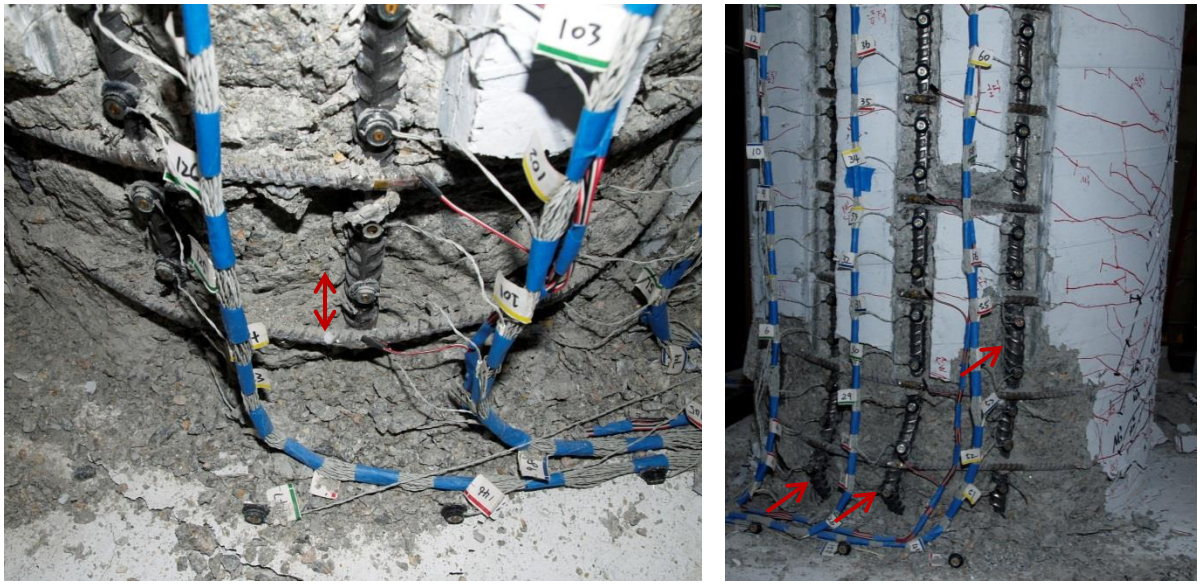

Figure 1.226 T14 – (Left) Separation of Deformed Spiral Layer from Buckled Bar N3 at ($\mu_8^{+1} = 6.40$") and (Right) Additional Deformation in Buckled South Bars S1, S2, S3, and S4 during ($\mu_8^{+1} = 6.40$")

Figure 1.227 T14 – (Left) Deformation in North Buckled Bars during ($\mu_8^{-1} = -6.39$") and (Right) Rupture of South Buckled Bars S2, S3, and S4 during ($\mu_8^{-1} = -6.39$")

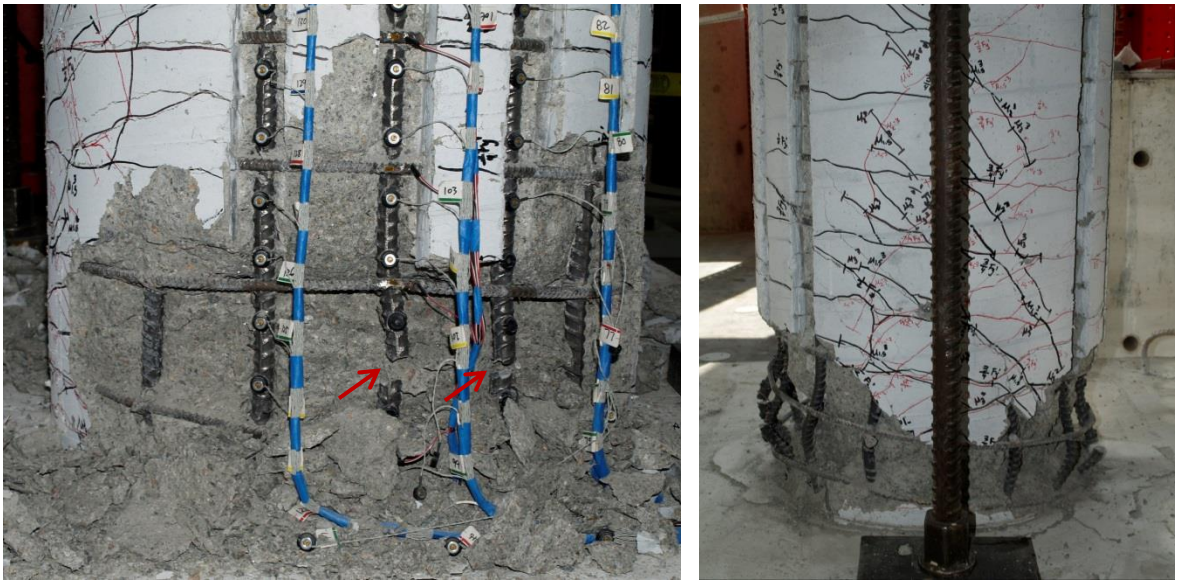

Figure 1.228 T14 – (Left) Rupture of North Buckled Bars N2 and N3 during ($\mu_8^{+2} = 6.40$") and (Right) Front of the Specimen after the Conclusion of the Test

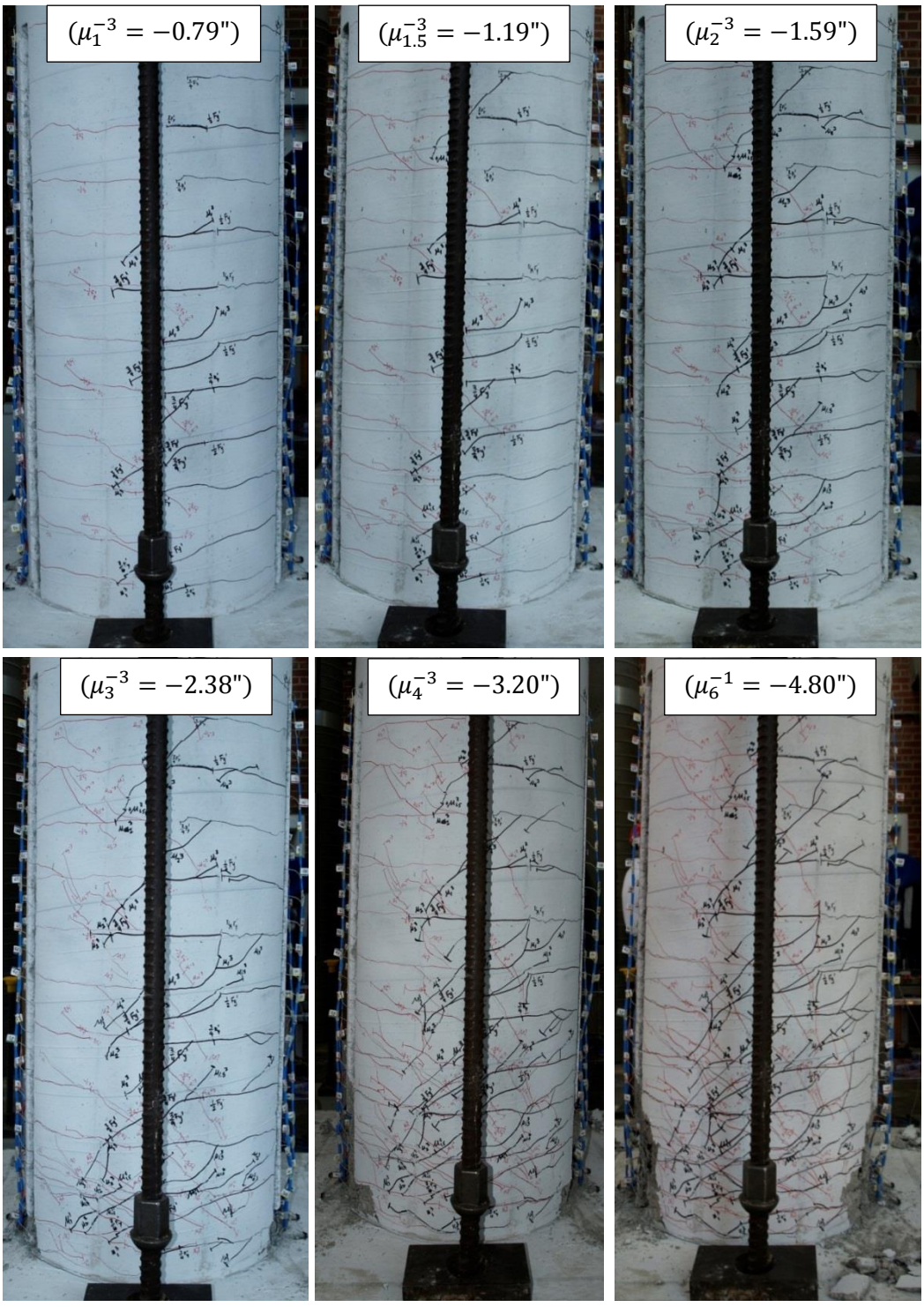

Figure 1.229 T14 – Crack Propagation and Orientation on the Back of the Specimen

Test 14 – Symmetric Three Cycle Set (#3 @ 4") Strain Data Analysis

North Reinforcement

Vertical strain profiles for each extreme fiber bar during push and pull cycles appear in Figure 1.230 and Figure 1.231 respectively. Measured strains at the first occurrence of ductility 1 and 1.5 are also shown due to the initial overload cycles while the actuator load cell problems were being resolved. A peak tensile strain of 0.0348, at a height of 6.95" above the footing, was measured for extreme fiber bar N3 during ($\mu_6^{+1} = 4.80"$) before the bar buckled after reversal of load. The relationship between tensile strain and displacement for this gage length appears in Figure 1.234. Similar to previous tests, the moment curvature prediction with the PCK (2007) Lp Hinge Method begins to over predict the measured tensile strains at higher displacements at an increasing rate. The largest compressive strain of -0.011, located 4.92" above the footing, was measured during ($\mu_4^{-3} = -3.20"$). The relationship between compressive strain and displacement for bar N3 during pull cycles appears in Figure 1.235 for the gage length 4.92" above the footing. Here the measured compressive strains are slightly larger than the moment curvature prediction, but the overall trend is captured through displacement ductility three.

The strain hysteresis for the largest tensile gage length on extreme fiber bar N3 is shown in Figure 1.238 with a color bar to track the progression of the test. The strain hysteresis is plotted through ($\mu_6^{-1} = -4.80"$) when the bar buckled. Prior to bar buckling, the spiral layers on the North side of the specimen remained elastic, as shown in Figure 1.233. After reversal from ($\mu_6^{+1} = 4.80"$), the relationship between strain and displacement begins to break away from the trend at around 1", which coincides with the visual buckling observation. This gage length is centered over a layer of transverse steel with the largest tensile crack. Since the outward buckling of bar N3 occurred between layers of transverse steel, this particular gage length just above the outward buckled region shortens as the deformation increases. To illustrate this point, the strain hysteresis over the outward buckled region of bar N3, located 4.92" above the footing, appears in Figure 1.239. The transverse

steel strain gage hysteresis for a spiral layer restraining buckled bar N3 is shown in Figure 1.240. In all three graphs, buckling looks like it occurred between 0-1" of displacement after reversal from ($\mu_6^{+1} = 4.80"$). Here the gage length over the outward buckled region begins to rapidly elongate and the transverse steel restraint tensile strain sharply increases.

South Reinforcement

A peak tensile strain of 0.035 in extreme fiber bar S3 was measured 3.61" above the footing during ($\mu_6^{-1} = -4.80"$). Debris was blocking the lowest gage length of bar S3 during this cycle, so it is unclear whether higher strains occurred. The relationship between tensile strain and displacement for bar S3 is shown in Figure 1.236 for the gage length located 3.61" above the footing. A peak compression strain of -0.0152 was measured 7.62" above the footing during ($\mu_6^{+1} = 4.80"$). This particular gage length did not have the largest compressive strains during earlier cycles. The relationship between compressive strain and displacement for the gage length 3.61" above the footing appears in Figure 1.237. The measured strains match the moment curvature prediction with the PCK (2007) Lp Hinge Method. For the gage length 7.62" above the footing, the compression strain sharply increased during the first push cycle of ductility six.

Transverse steel strains in the lowest six spiral layers on the South side of the specimen are shown in Figure 1.232. During ($\mu_6^{+1} = 4.80"$), compressive demands the South side of the specimen caused the transverse steel to enter the inelastic range. The strain hysteresis for the gage length overlaying the outward buckled region of bar S3, 3.61" above the footing, appears in Figure 1.241. After reversal from a peak tensile strain of 0.035 at ($\mu_6^{-1} = -4.80"$), the relationship between strain and displacement begins to break from the trend around 1" which agrees with visible buckling observations during the test. The transverse steel strain gage hysteresis for a spiral layer over the South buckled region is shown in Figure 1.242.

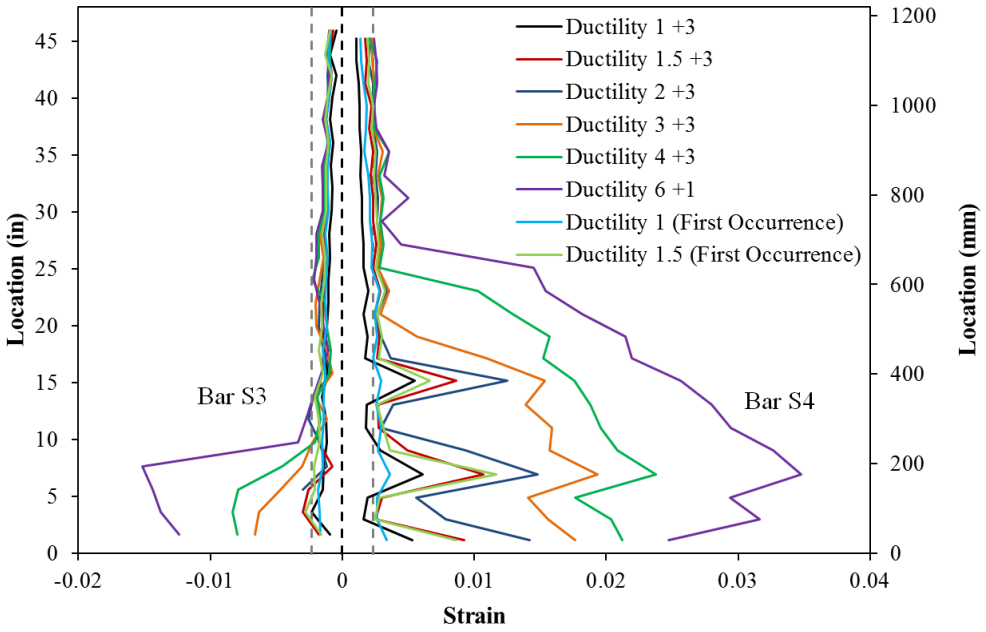

Figure 1.230 T14 – Extreme Fiber Vertical Strain Profiles for Push Cycles

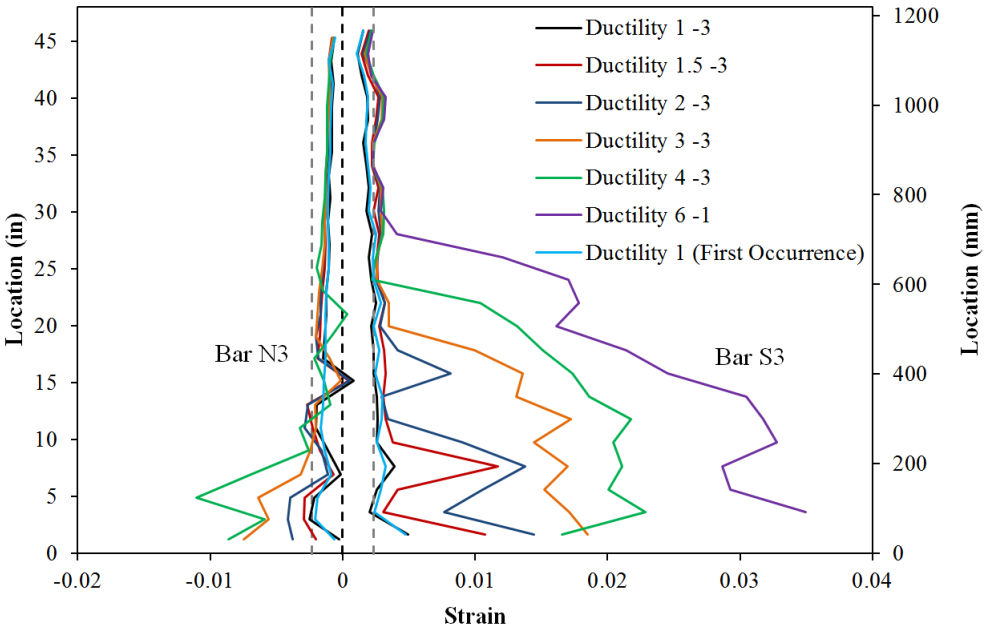

Figure 1.231 T14 – Extreme Fiber Vertical Strain Profiles during Pull Cycles

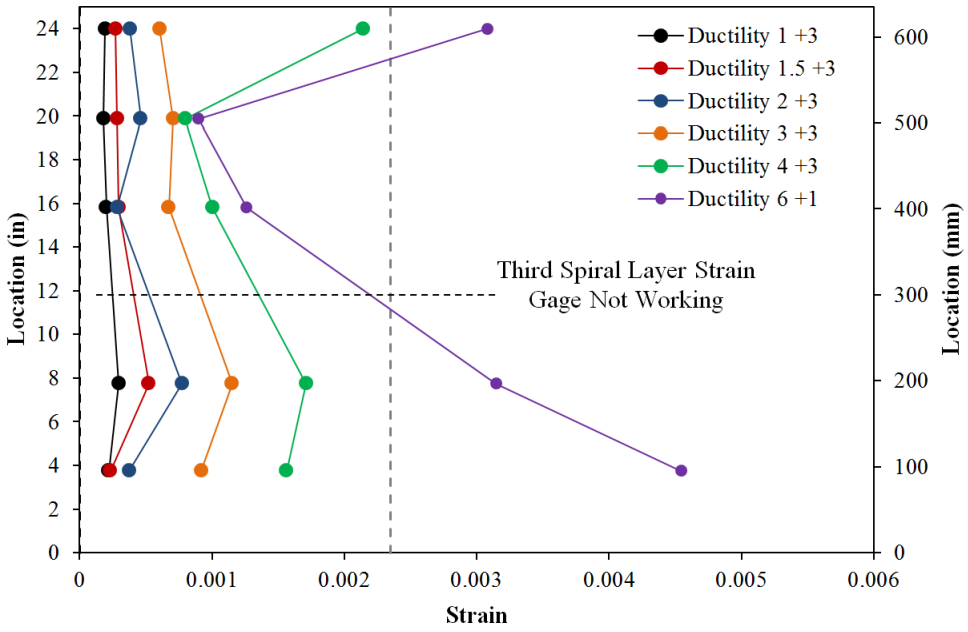

Figure 1.232 T14 – Spiral Strains for the Lowest Six Layers on the South Side

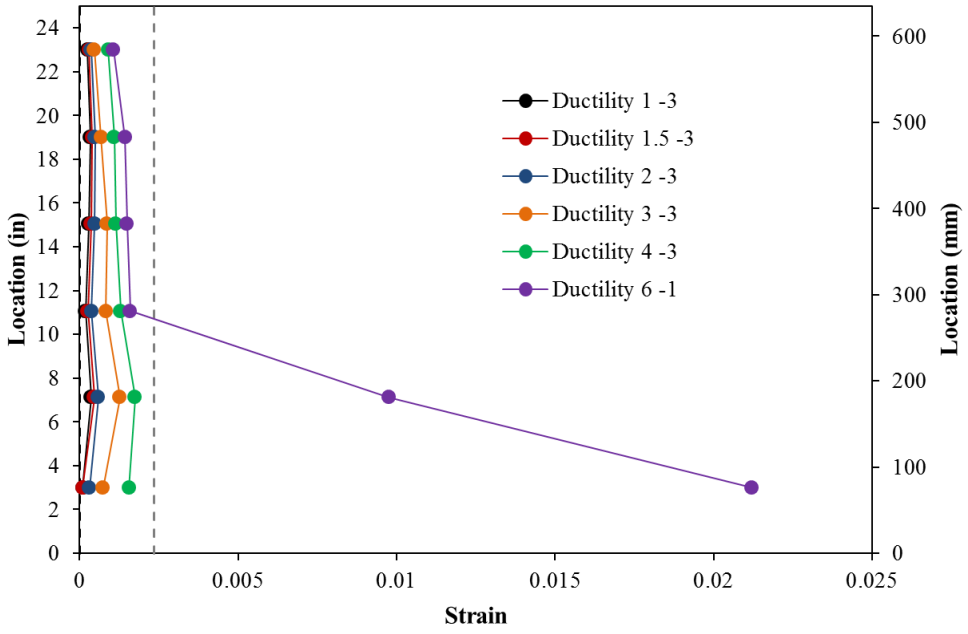

Figure 1.233 T14 – Spiral Strains for the Lowest Six Layers on the North Side

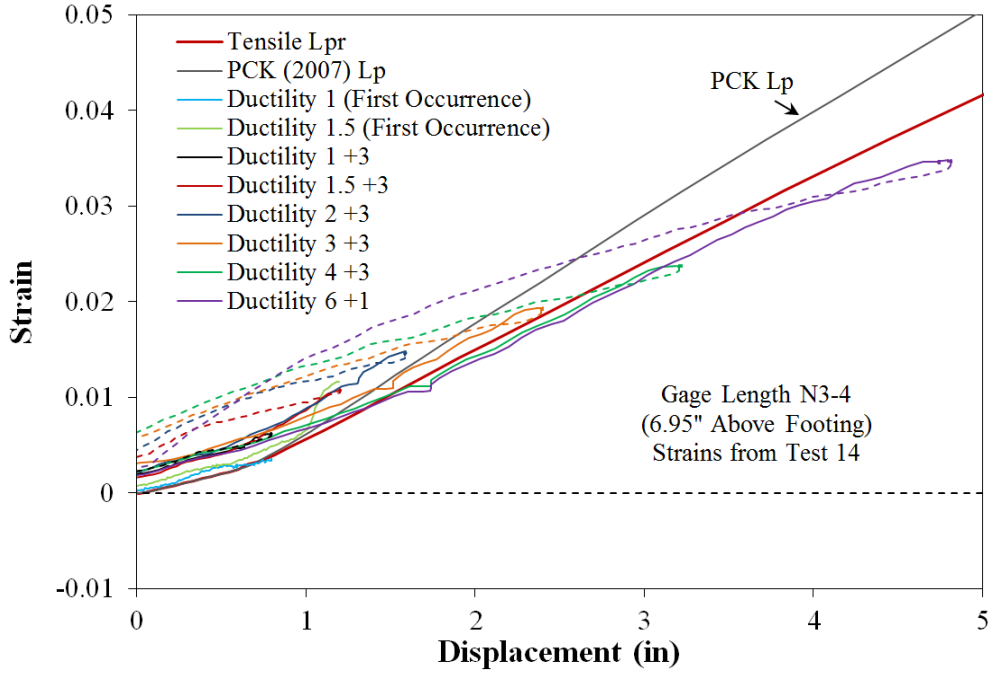

Figure 1.234 T14 – Tensile Strain-Displacement for Bar N3 during Push Cycles

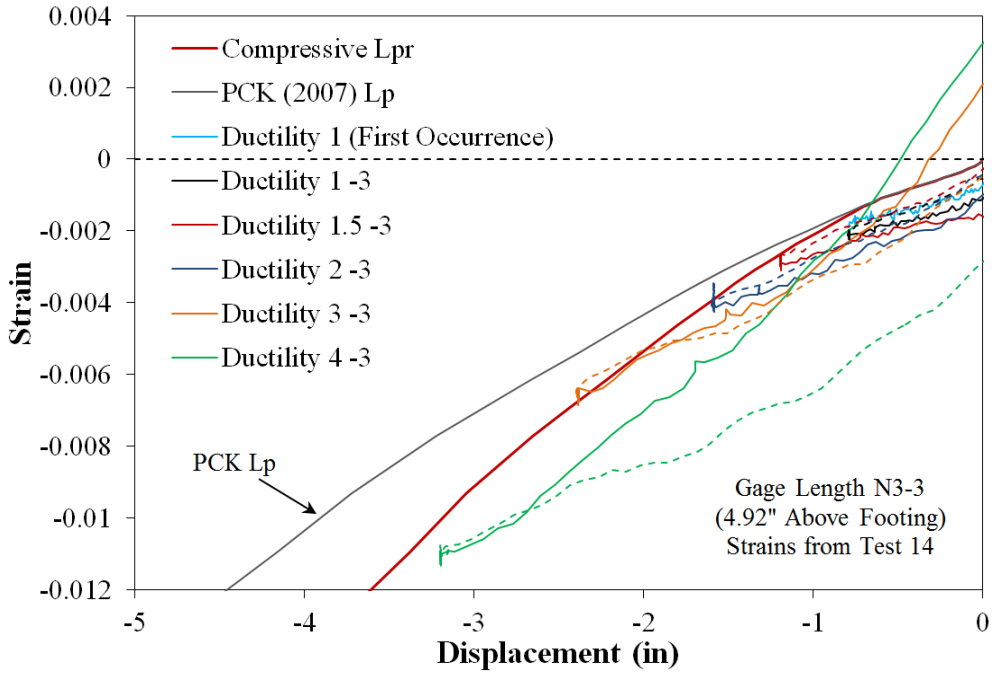

Figure 1.235 T14 – Compressive Strain-Displacement for Bar N3 during Pull Cycles

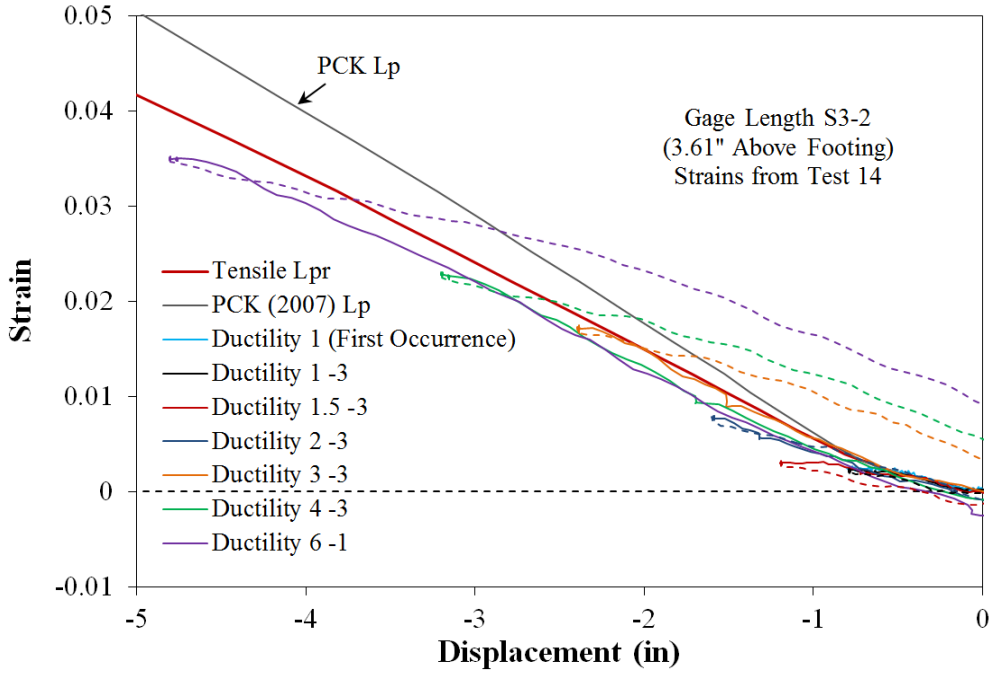

Figure 1.236 T14 – Tensile Strain-Displacement for Bar S3 during Pull Cycles

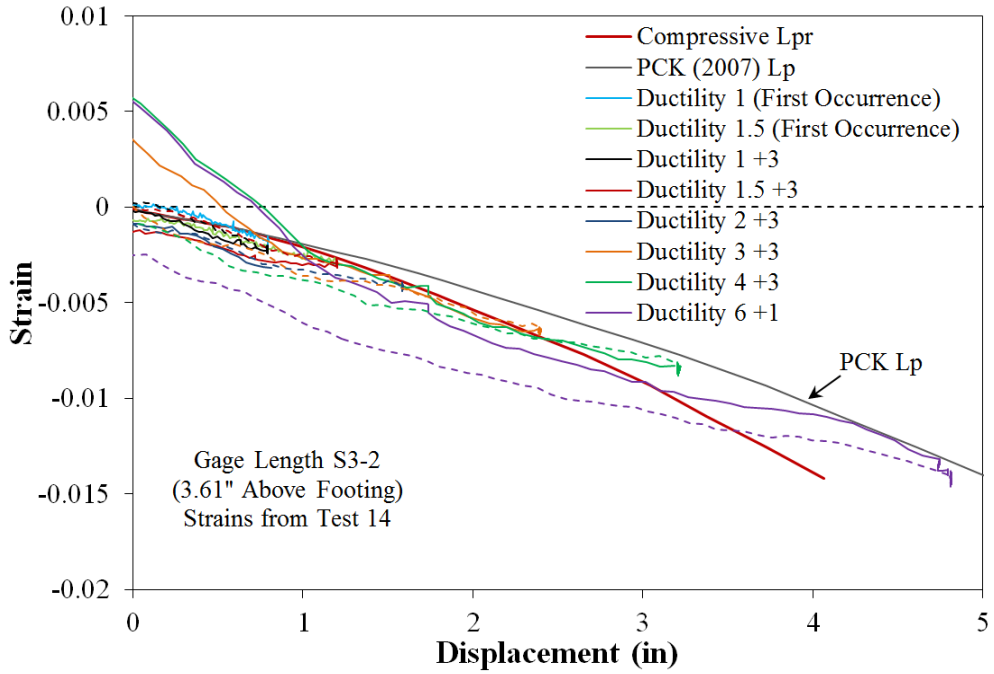

Figure 1.237 T14 – Compressive Strain-Displacement for Bar S3 during Push Cycles

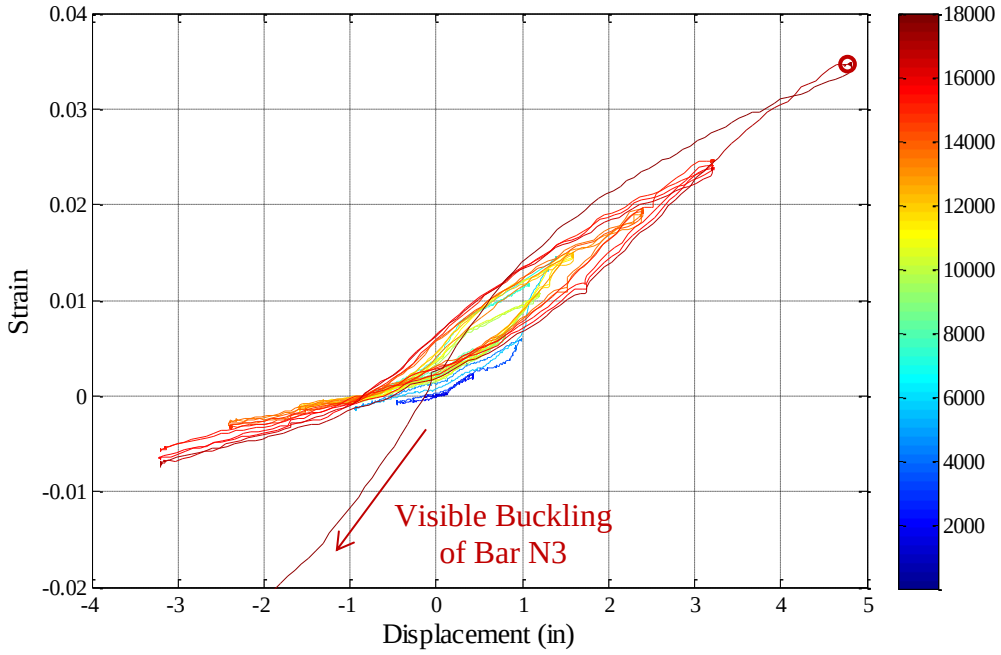

Figure 1.238 T14 – Bar N3 Strain Hysteresis (6.95" Above Footing)

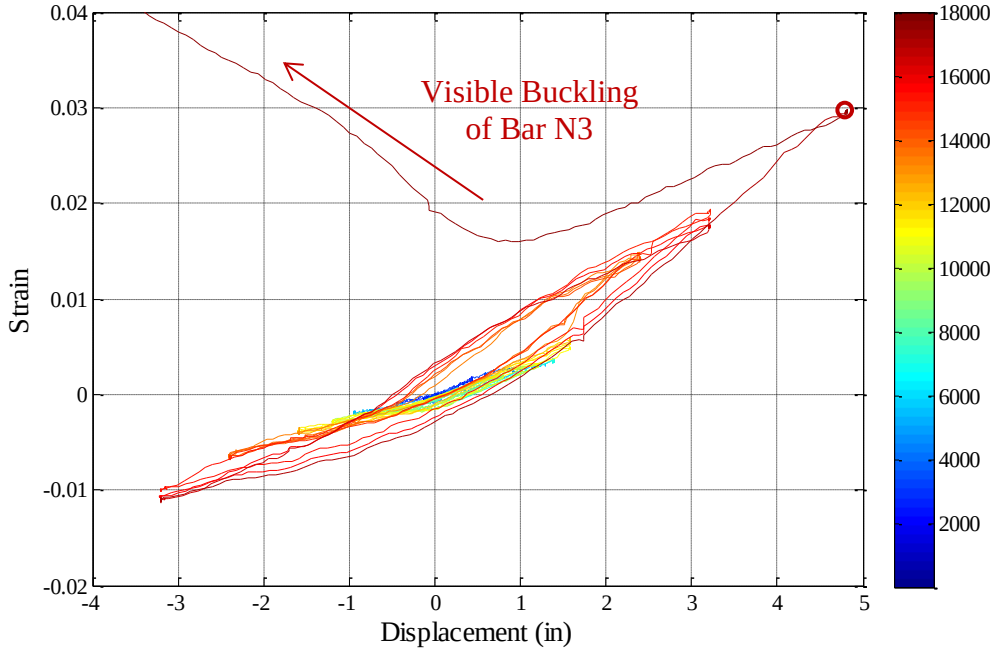

Figure 1.239 T14 – Bar N3 Strain Hysteresis (4.92" Above Footing)

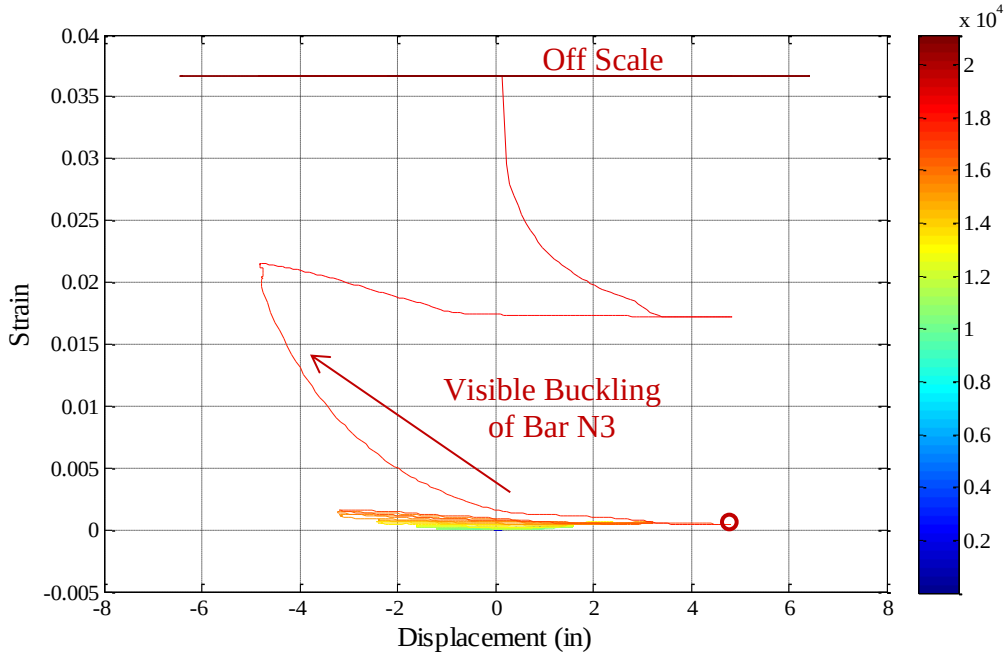

Figure 1.240 T14 – Spiral Strain Gage Hysteresis over North Buckled Region

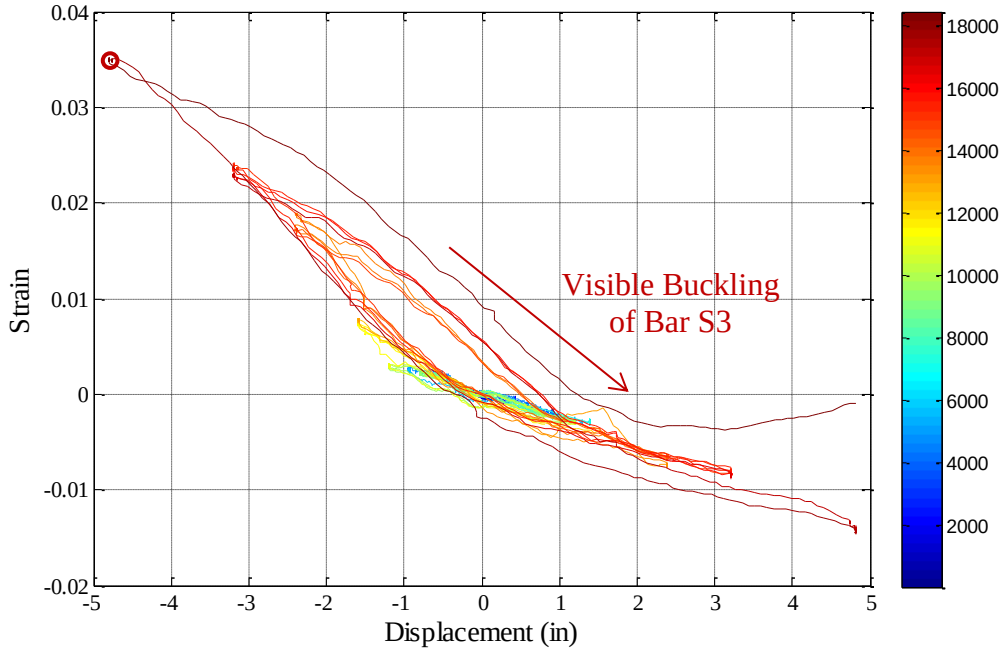

Figure 1.241 T14 – Bar S3 Strain Hysteresis (3.61" Above Footing)

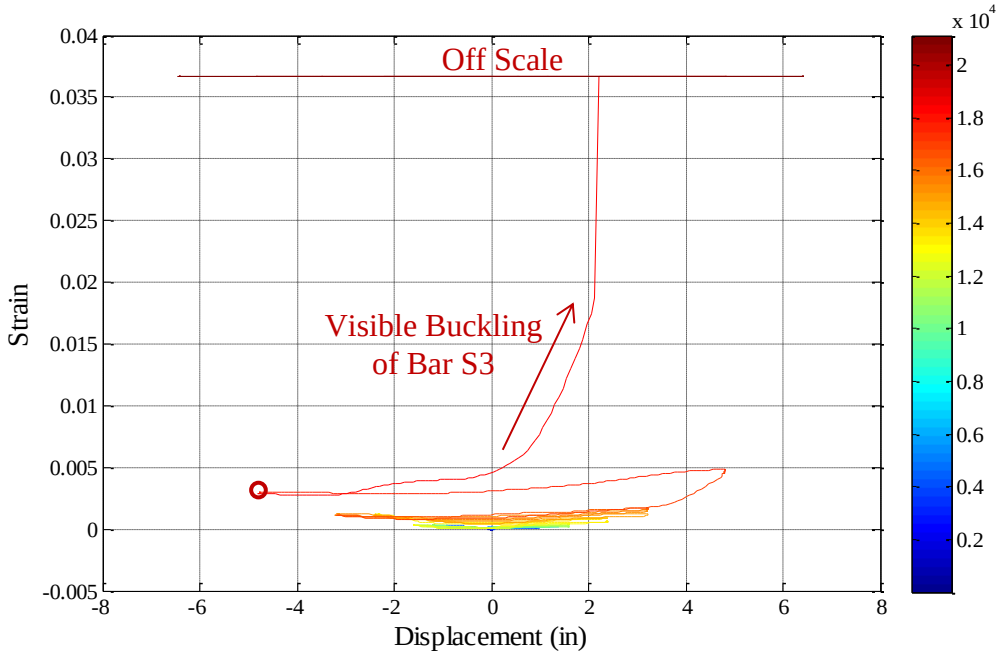

Figure 1.242 T14 – Spiral Strain Gage Hysteresis over South Buckled Region

Test 14 – Symmetric Three Cycle Set (#3 @ 4") Curvature and Strain Penetration Data

Vertical curvature profiles for push and pull cycles appear in Figure 1.243 and Figure 1.244 respectively. Plastic curvatures at higher ductility levels have a linear distribution as shown by the linear least squared error lines. The base section reinforcement slip measured at the footing-column interface can be monitored using the Optotrak system. The slip hysteresis for North and South extreme fiber bars appears in Figure 1.245 and Figure 1.246. The base section rotation due to strain penetration during push and pull cycles is shown in Figure 1.247 and Figure 1.248 respectively. The top column displacement can be calculated by integrating the measured curvature profiles, extrapolating the base section rotation to the center of loading, and assuming an elastic curvature distribution above the instrumented region. A comparison of measured and integrated top column displacements appears in Figure 1.249. The measured spread of plasticity for Test 14 is shown in Figure 1.250. The extent of plasticity is the intersection of the plastic regression and elastic curvature profiles.

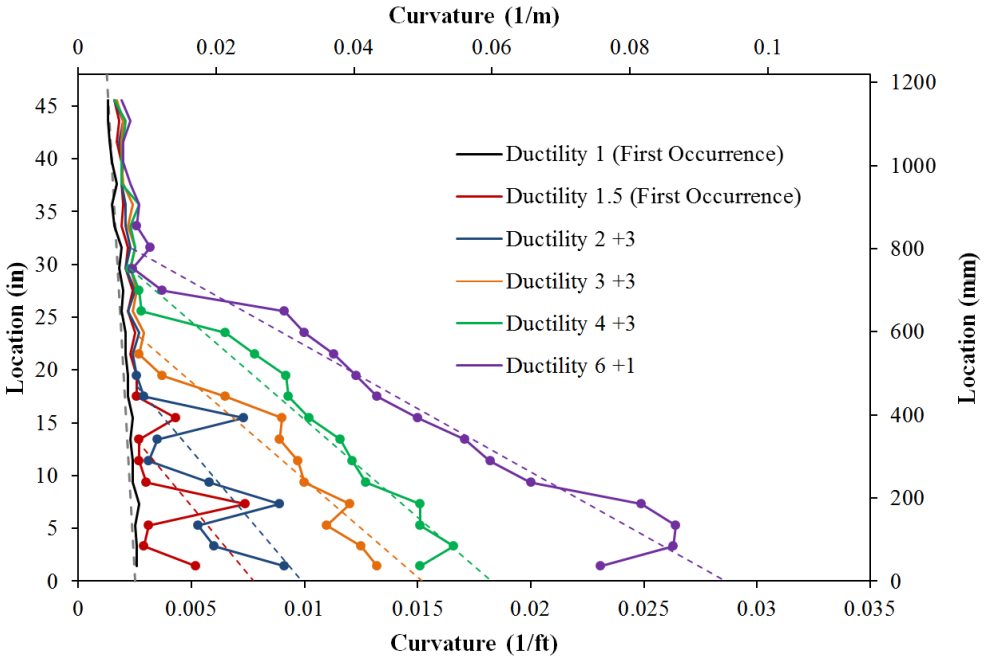

Figure 1.243 T14 – Vertical Curvature Profiles during Push Cycles

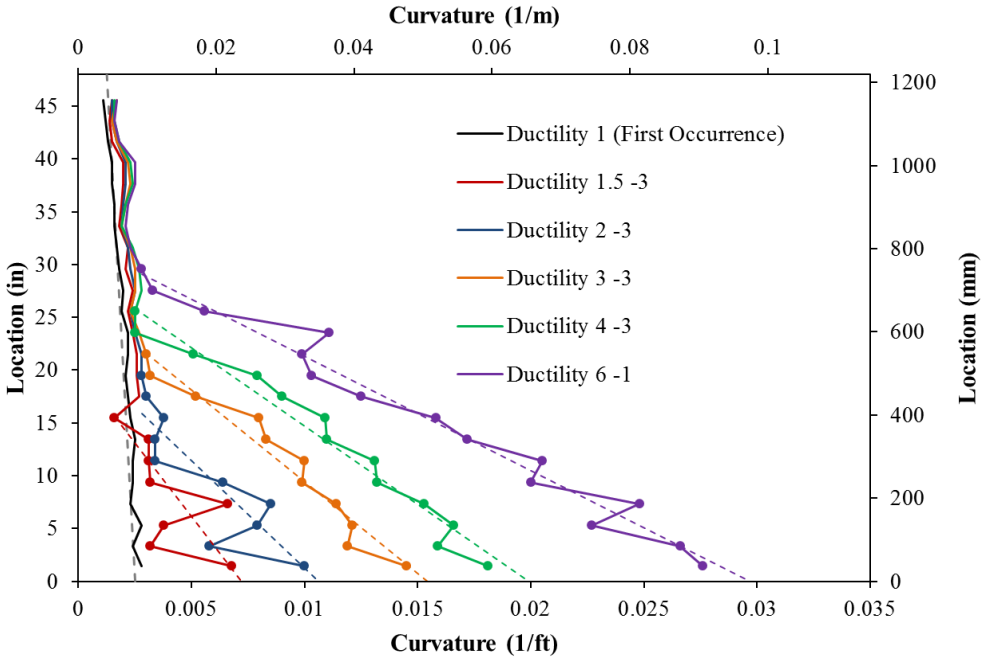

Figure 1.244 T14 – Vertical Curvature Profiles during Pull Cycles

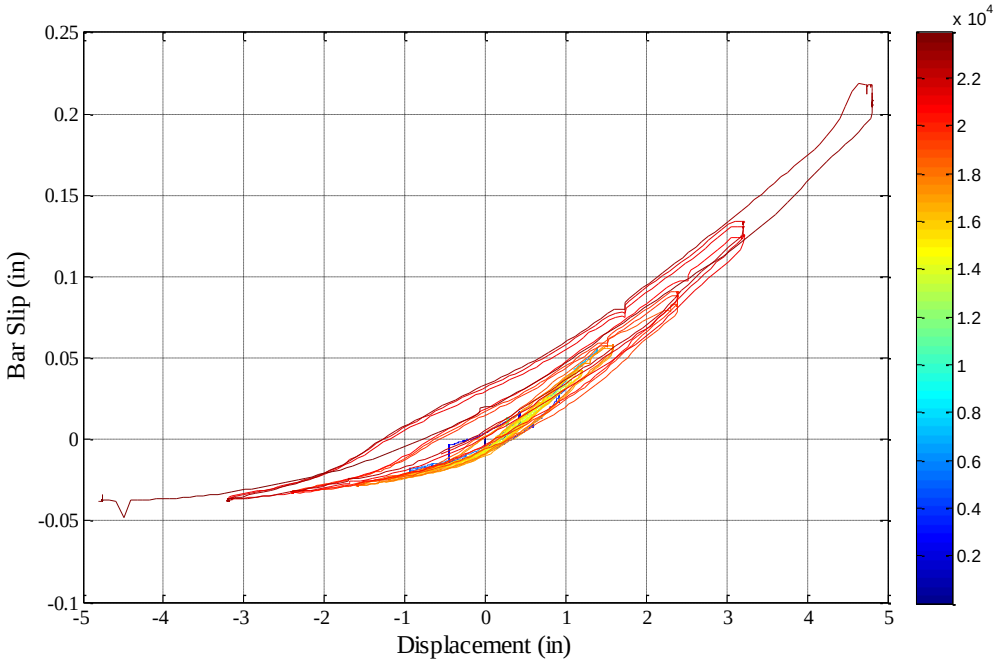

Figure 1.245 T14 – Bar N3 Base Section Slip Hysteresis due to Strain Penetration

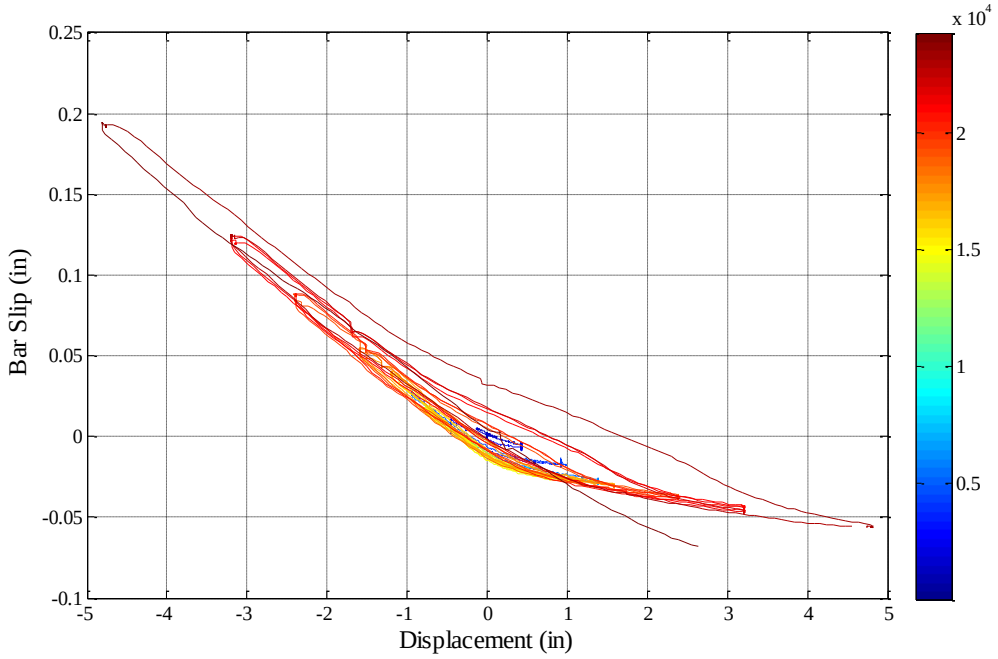

Figure 1.246 T14 – Bar S3 Base Section Slip Hysteresis due to Strain Penetration

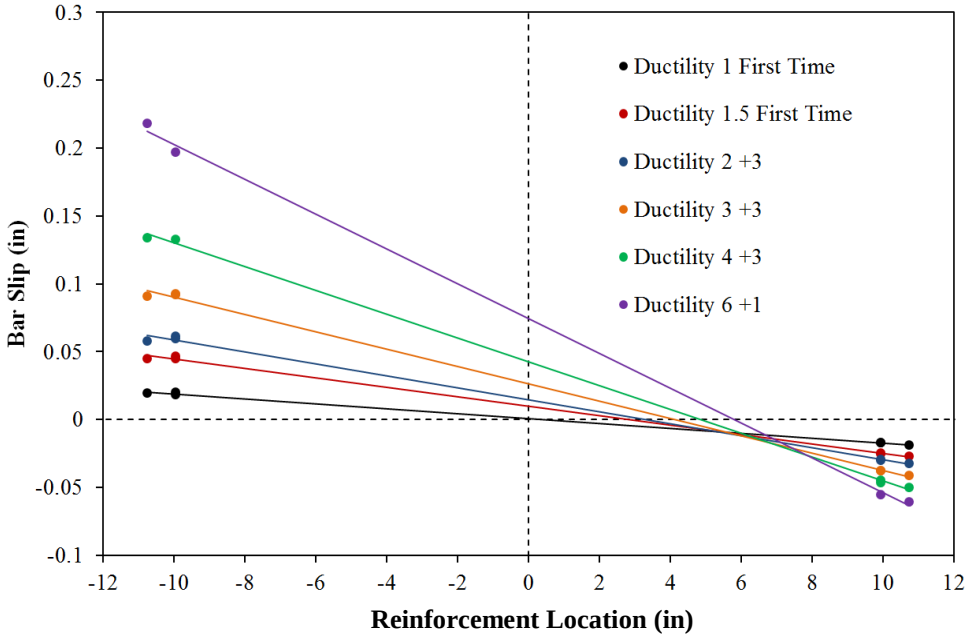

Figure 1.247 T14 – Base Section Rotation due to Strain Penetration during Push Cycles

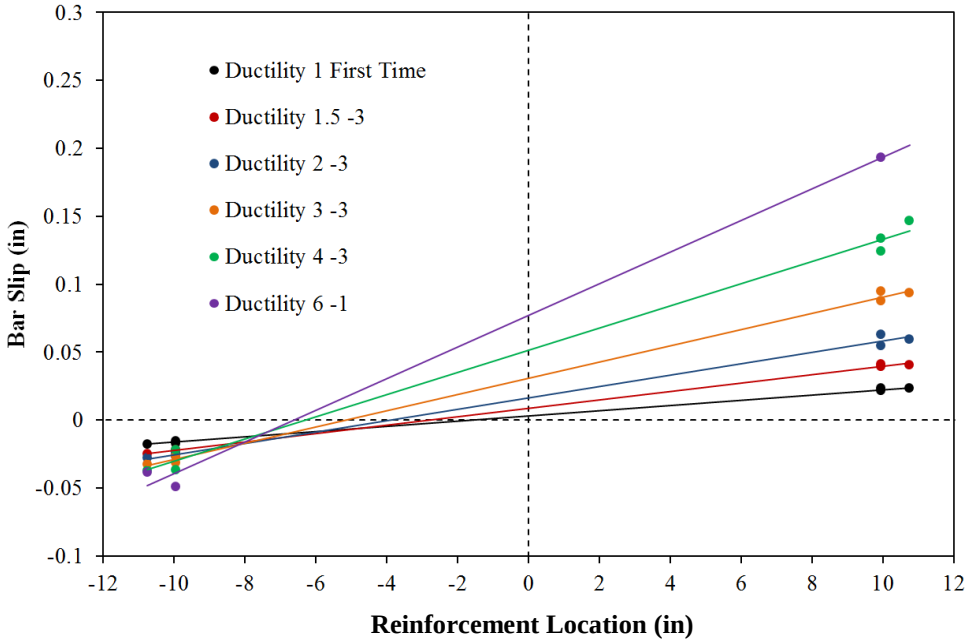

Figure 1.248 T14 – Base Section Rotation due to Strain Penetration during Pull Cycles

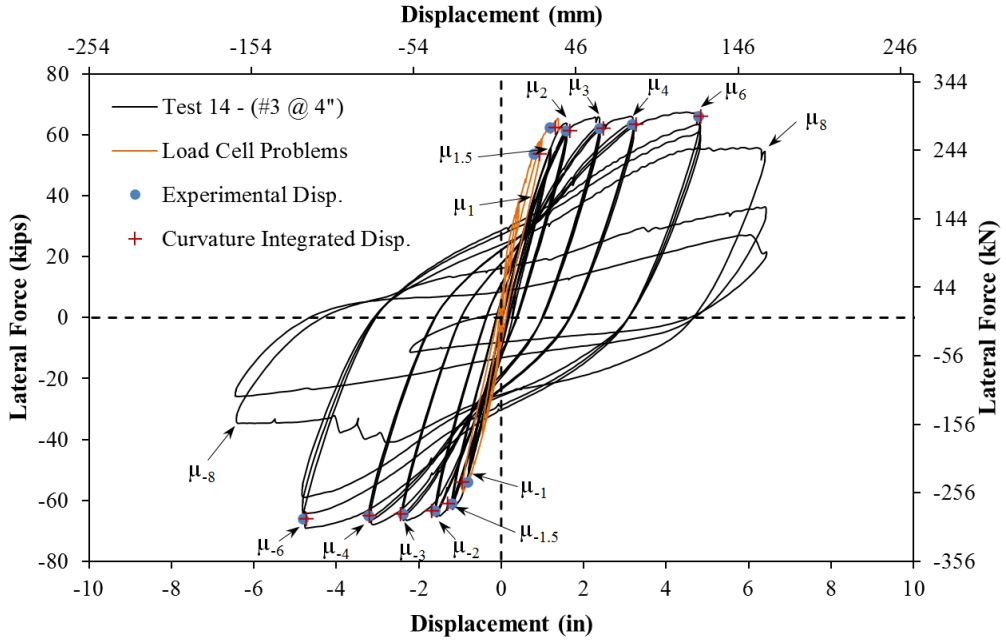

Figure 1.249 T14 – Comparison of Measured and Optotrak Integrated Displacements

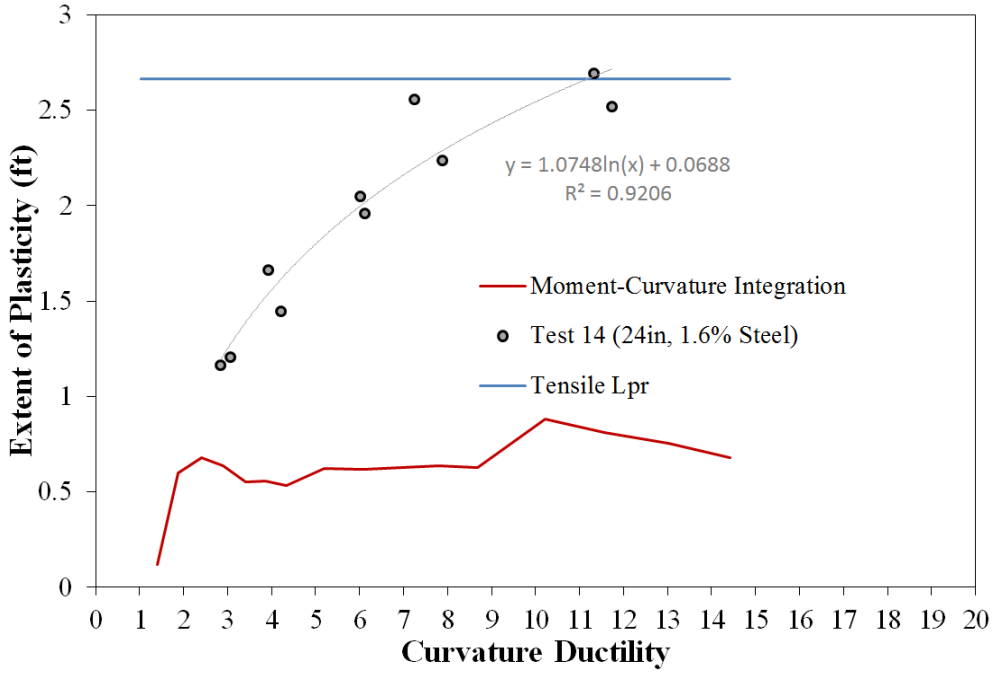

Figure 1.250 T14 – Measured Spread of Plasticity (Circular Data Points)

1.2.3 Test 15 – Three Cycle Set Load History with #3 Spiral at 2.75" (0.7%)

Table 1.21 Observational Summary for Test 15 – Cyclic with #3 Spiral at 2.75" (0.7%)

VALUES OF INTEREST:	
Concrete Compressive Strength:	$f_c' = 7232\ psi$
Axial Load:	$P = 170\ kips$
Analytical First Yield Force:	$F_y' = 47.1\ kips$
Experimental First Yield Displacement:	$\Delta_y' = 0.62"$
Analytical Nominal Moment Capacity:	$M_n = 506.9\ kip * ft$
Equivalent Yield Displacement:	$\Delta_y = 0.84"$
Maximum Lateral Force:	$68.6\ kips$
Failure Mode:	Fracture of Previously Buckled Reinforcement
DAMAGE OBSERVATIONS:	
First Cracking North:	$1/2Fy' = 0.16"$
First Cracking South:	$-1/2Fy' = -0.20"$
Cover Concrete Crushing North:	$\mu_{1.5}^{-3} = -1.25"$
Cover Concrete Crushing South:	$\mu_2^{+1} = 1.68"$
Transverse Steel Yield North:	At $-1.89"$ during pull to $\mu_6^{-1} = -5.00"$
Transverse Steel Yield South:	At $2.08"$ during push to $\mu_4^{+2} = 3.33"$
Longitudinal Bar Buckling North:	Reversal from $\mu_6^{+2} = 5.00"$
Longitudinal Bar Buckling South:	Reversal from $\mu_6^{-1} = -5.00"$
Longitudinal Bar Fracture North:	At $3.91"$ during push to $\mu_8^{+2} = 6.67"$
Longitudinal Bar Fracture South:	At $-2.54"$ during pull to $\mu_8^{-1} = -6.69"$

*$\mu_6^{-1} = -5.00"$ represents the first pull cycle of displacement ductility six

Table 1.22 Strain Data Summary for Test 15 – Cyclic with #3 Spiral at 2.75" (0.7%)

MATERIAL STRAINS:	
Cover Concrete Crushing North:	$\varepsilon_s = 0.0027\ (compression)$
Cover Concrete Crushing South:	$\varepsilon_s = 0.0041\ (compression)$
Transverse Steel Yield North:	$\varepsilon_s = 0.0199\ (compression)$
Transverse Steel Yield South:	$\varepsilon_s = 0.0125\ (compression)$
Longitudinal Bar Buckling North:	$\varepsilon_s = 0.037\ (peak\ tension\ prior\ to\ bb)$
	$\varepsilon_s = 0.020\ (peak\ comp.\ prior\ to\ bb)$
Longitudinal Bar Buckling South:	$\varepsilon_s = 0.038\ (peak\ tension\ prior\ to\ bb)$
	$\varepsilon_s = 0.023\ (peak\ comp.\ prior\ to\ bb)$
Mander (1988) Ultimate Concrete Compression Strain, $\varepsilon_{cu} = 0.0129$	

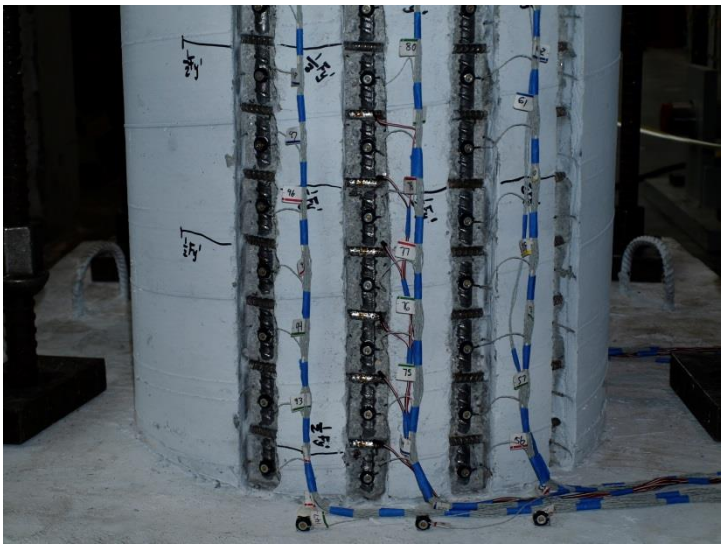

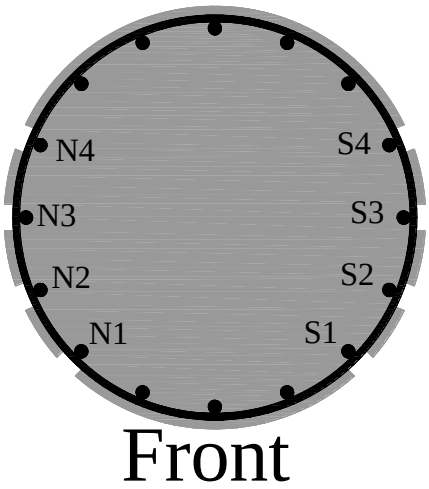

Figure 1.251 T15 – Cross Section Bar Designation and Target Marker Application

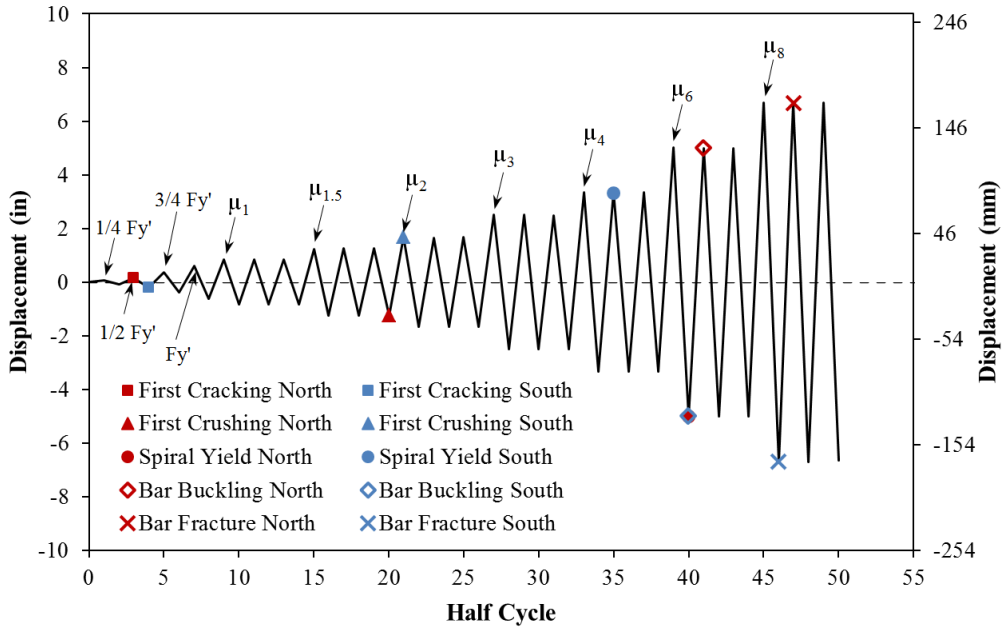

Figure 1.252 T15 – Symmetric Three Cycle Set Load History

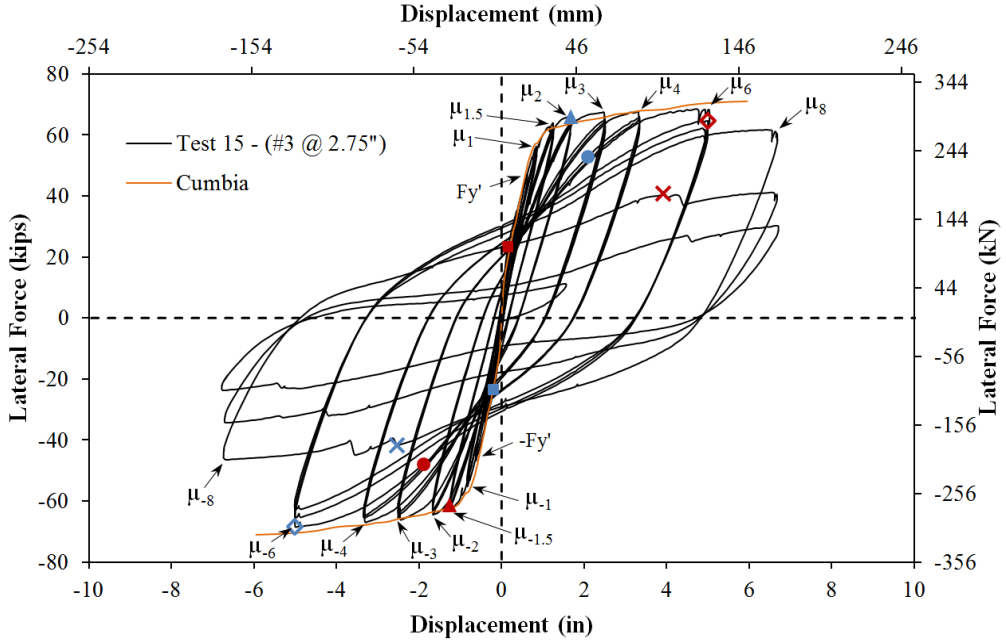

Figure 1.253 T15 – Lateral Force vs. Top Column Displacement Response

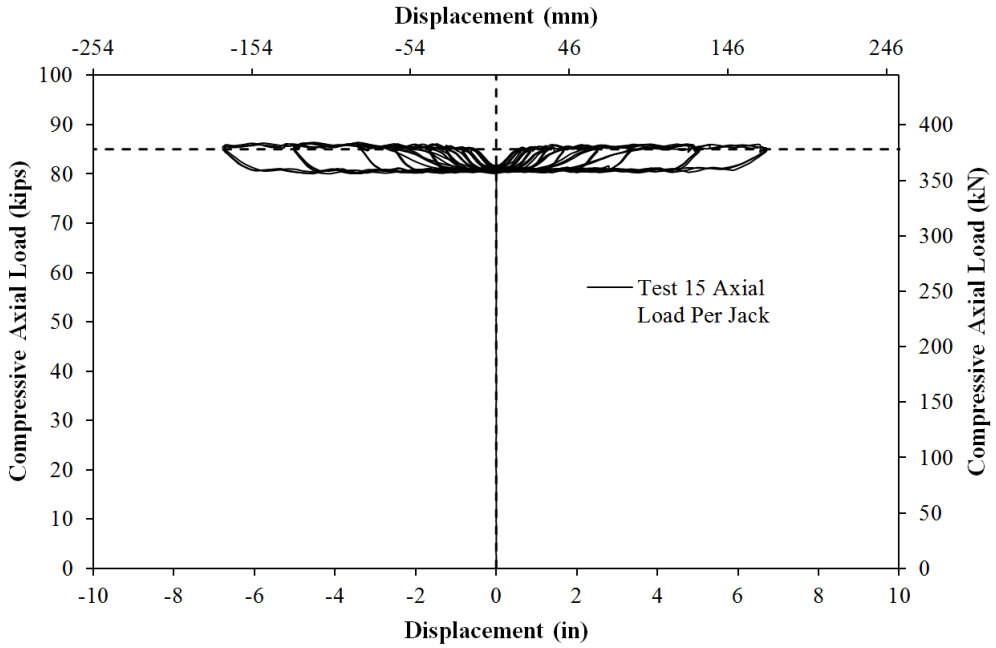

Figure 1.254 T15 – Compressive Axial Load from One Jack (Total = 2*Value)

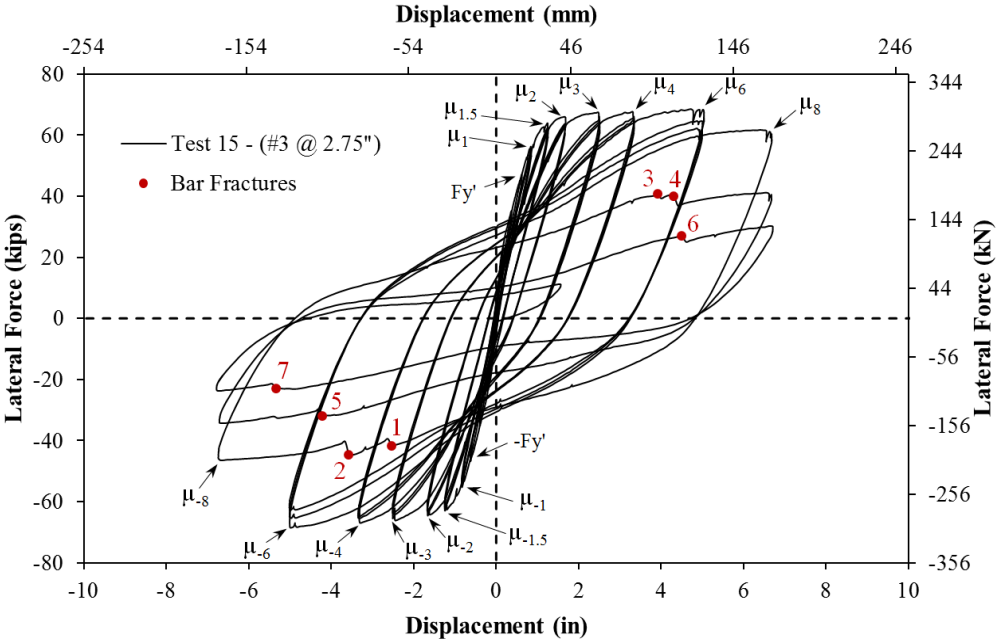

Figure 1.255 T15 – Rupture History of Previously Buckled Reinforcement

Test 15 – Symmetric Three Cycle Set (#3 @ 2.75") Experimental Observations

The first yield force for the tested material and geometric properties was determined using moment curvature analysis (Test 15: Cumbia Fy' = 47.11 kips with f'c = 7232 psi). The first yield displacement was obtained as an average for the first yield push and pull cycles ($\Delta'_y = 0.62$"). Vertical strain profiles for both extreme fiber bars during push and pull cycles up to the first yield force appear in Figure 1.256 with a dashed line representing the yield strain of the longitudinal reinforcement. The equivalent yield displacement, used to determine the displacement ductility levels ($\mu_{\Delta n} = \mathrm{n} * \Delta_y$), is then calculated as $\Delta_y = \Delta'_y(M_n/M'_y) = 0.84$" for Test 15. The full symmetric three-cycle-set load history appears in Figure 1.252 and the resulting lateral force vs. top column displacement hysteresis is shown in Figure 1.253.

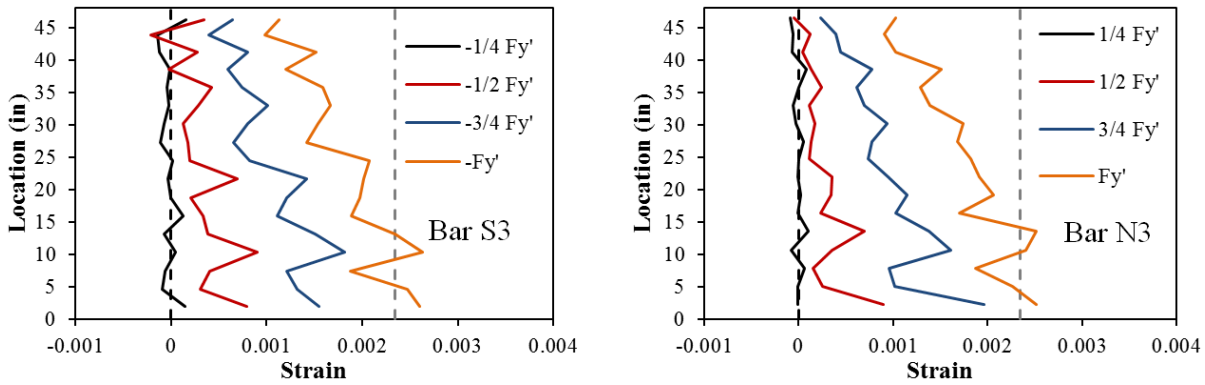

Figure 1.256 T15 – Vertical Strain Profiles (Dashed Yield Strain Line)

The test began with cycles in ¼ Fy' (first yield force) increments in each direction of loading until the first yield force was reached. The first cracks on the North side of the specimen measured 0.1mm at approximate 10" spacing at $(1/2Fy' = 23.27kips)$. Cracks on the South Side of the specimen measured 0.1mm at approximate 10" spacing during $(-1/2Fy' = -23.47kips)$. The largest crack widths on the North side of the specimen reached 0.2mm at approximate 5" spacing at $(3/4Fy' = 35.23kips)$. Cracks measured at 0.3mm with 5" spacing were observed on the South side of the specimen during $(-3/$

$4Fy' = -35.16kips$). During the first yield push cycle ($Fy' = 47.13kips$, 0.62"), the largest crack widths measured 0.35mm at approximate 5" spacing. During the subsequent pull cycle ($-Fy' = -46.81kips, -0.63$"), crack widths reached 0.4mm on the South side of the specimen. The crack distribution at first yield is shown in Figure 1.257. The progression of the crack distribution on the back side of the specimen is shown in Figure 1.267. Cracks on the North side of the specimen measured 0.5mm at approximate 4" spacing during ($\mu_1^3 = 0.85$"). After reversal, cracks on the South side reached 0.55mm at 5" spacing during ($\mu_1^{-3} = -0.84$"). Visible flaking of the cover concrete in compression, which is a precursor to crushing, was observed on the South side of the specimen during ($\mu_{1.5}^{+1} = 1.24$"). A similar observation on the North side of the specimen occurred during ($\mu_{1.5}^{-1} = -1.24$").

Cracks on the North side of the specimen measured 1mm during ($\mu_{1.5}^{+3} = 1.25$"). Crushing of the cover concrete on the North side of the specimen was observed during ($\mu_{1.5}^{-3} = -1.25$"), see the left photo of Figure 1.258. Here, the largest crack width on the South side of the specimen reached 1.25mm. Crushing on the South side of the specimen did not occur until ($\mu_2^{+1} = 1.68$"), as shown in the right photo of Figure 1.258. The largest crack width on the North side of the specimen measured 1.25mm during ($\mu_2^{+3} = 1.66$"). The extent of crushing on the South side of the specimen increased to 13" above the footing during ($\mu_3^{+3} = 2.49$"), as shown in the right photo of Figure 1.259. On the North side of the specimen, the extent of crushing reached 10 ¾" above the footing during ($\mu_3^{-3} = -2.51$"). The extent of crushing on the South side of the specimen reached 24 ½" above the footing during ($\mu_6^{+1} = 5.01$"). Crushing on the North side of the specimen reached 16 ¼" above the footing at ($\mu_6^{-1} = -5.00$"), as shown in the left photo of Figure 1.260. The first push and pull cycles of ductility six were concluded without visible buckling on either side of the specimen.

South reinforcing bars S2 and S3 visibly buckled on the way to ($\mu_6^{+2} = 5.00$"), as shown in Figure 1.261. Buckling of the two South bars caused a 5.5% loss of strength from the peak load of 68.37 kips measured during ($\mu_6^{+1} = 5.01$"). North reinforcing bars N2 and N3

visibly buckled on the way to ($\mu_6^{-2} = -5.01$"), as shown in Figure 1.262. Buckling of the two North bars caused a 5% loss of strength from the peak load of -68.51 kips, which occurred during ($\mu_6^{-1} = -5.00$"). An additional South reinforcing bar S4 buckled during ($\mu_6^{+3} = 4.99$) and the outward deformation in bars S2 and S3 increased, which lead to a 9.3% loss in strength. North reinforcing bar N4 buckled during ($\mu_6^{-3} = -5.00$") causing an 8.1% loss in strength relative to the peak load in the pull direction. During the first push cycle of ductility eight, an 11.75% loss of strength was observed without additional buckling or rupture of reinforcement. The effect of buckling on confinement loss is highlighted by observed permanent deformation in spiral layers over the North reinforcement when the bar was placed back into tension, see Figure 1.263.

Previously buckled bars S2 and S3 ruptured in tension during ($\mu_8^{-1} = -6.69$"), see Figure 1.264. Rupture of the two South bars lead to a 32.2% total loss in strength, as shown in Figure 1.255 on the force vs. displacement response. During ($\mu_8^{+2} = 6.67$"), South bars S1 and S5 buckled and previously buckled North reinforcing bars N2 and N3 ruptured in tension, as shown in Figure 1.265. This caused a 40.72% total loss of strength in the push direction of loading. During ($\mu_8^{-2} = -6.71$"), North bars N1 and N5 buckled and an additional bar S4 ruptured in tension leading to a 50.1% loss in strength. North bar N4 ruptured during ($\mu_8^{+3} = 6.70$") causing a 55.9% loss in strength. During the final cycle of the load history ($\mu_8^{-3} = -6.66$"), South bar S1 ruptured leading to a total loss in strength of 65.4%. Photos of the specimen after the test was concluded appear in Figure 1.266.

Figure 1.257 T15 – Crack Distribution at First Yield (Left) North and (Right) South

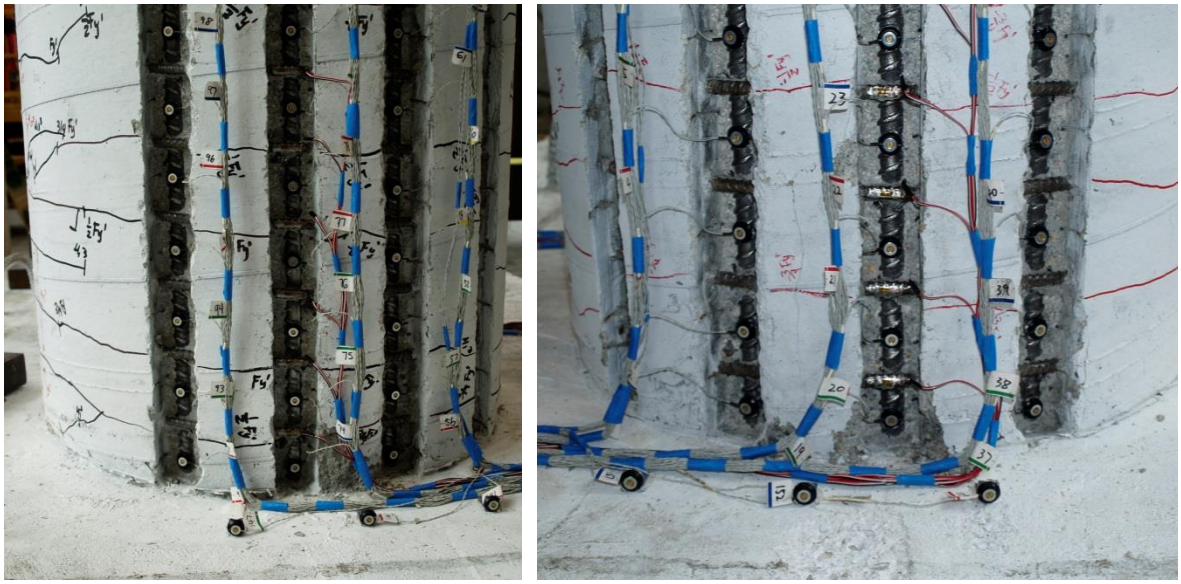

Figure 1.258 T15 – (Left) Crushing on the North Side of the Specimen during ($\mu_{1.5}^{-3} = -1.25$") and (Right) Crushing on the South Side during ($\mu_{2}^{+1} = 1.68$")

Figure 1.259 T15 – (Left) Crushing on the North Side of the Specimen during ($\mu_3^{-3} = -2.51$") and (Left) Crushing on the South Side during ($\mu_3^{+3} = 2.49$")

Figure 1.260 T15 – (Left) Extent of Crushing on the North Side of the Specimen during ($\mu_6^{-1} = -5.00$") and (Right) Crushing on the South Side during ($\mu_6^{+1} = 5.01$")

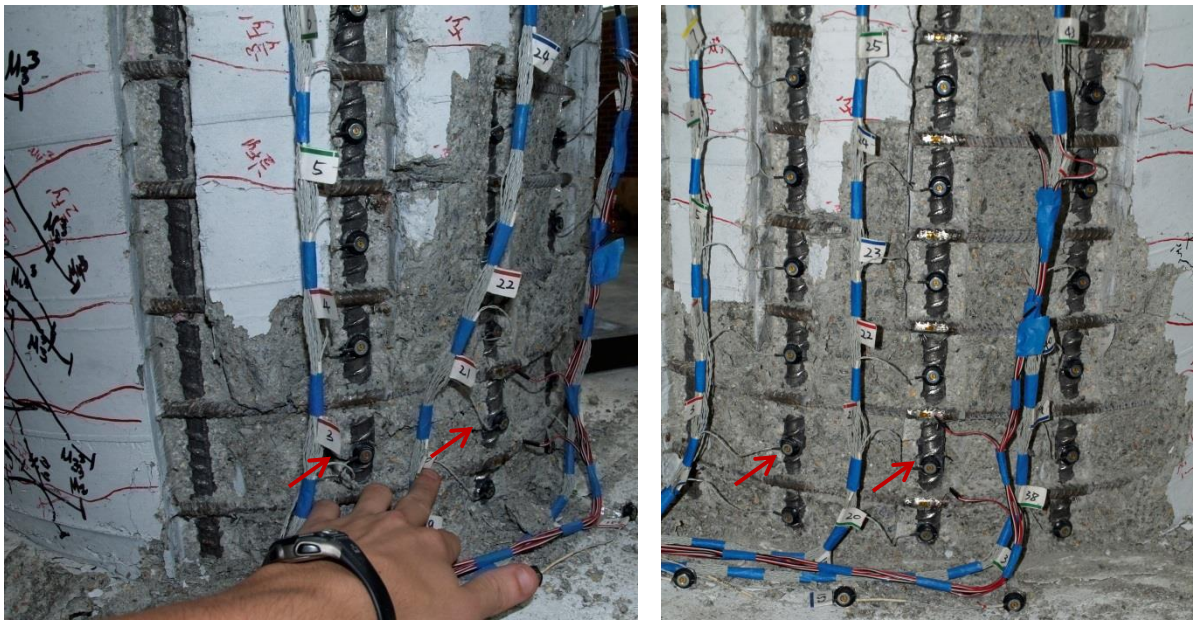

Figure 1.261 T15 – Buckling of Reinforcing Bars S2 and S3 during ($\mu_6^{+2} = 5.00$")

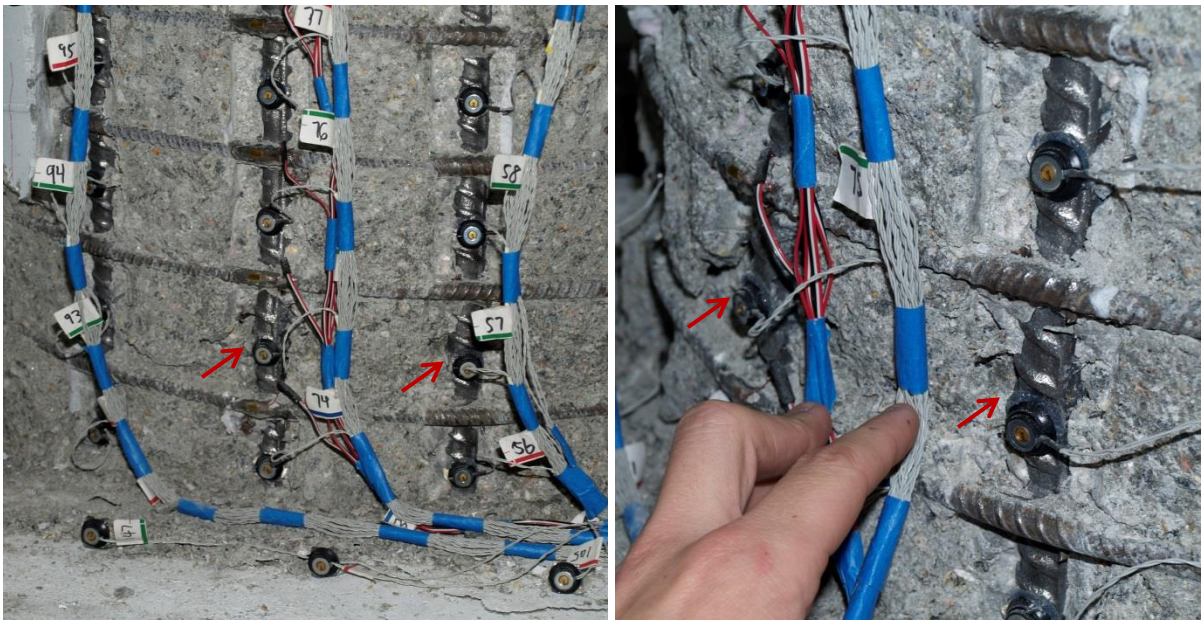

Figure 1.262 T15 – Buckling of Bars N2 and N3 during ($\mu_6^{-2} = -5.01$")

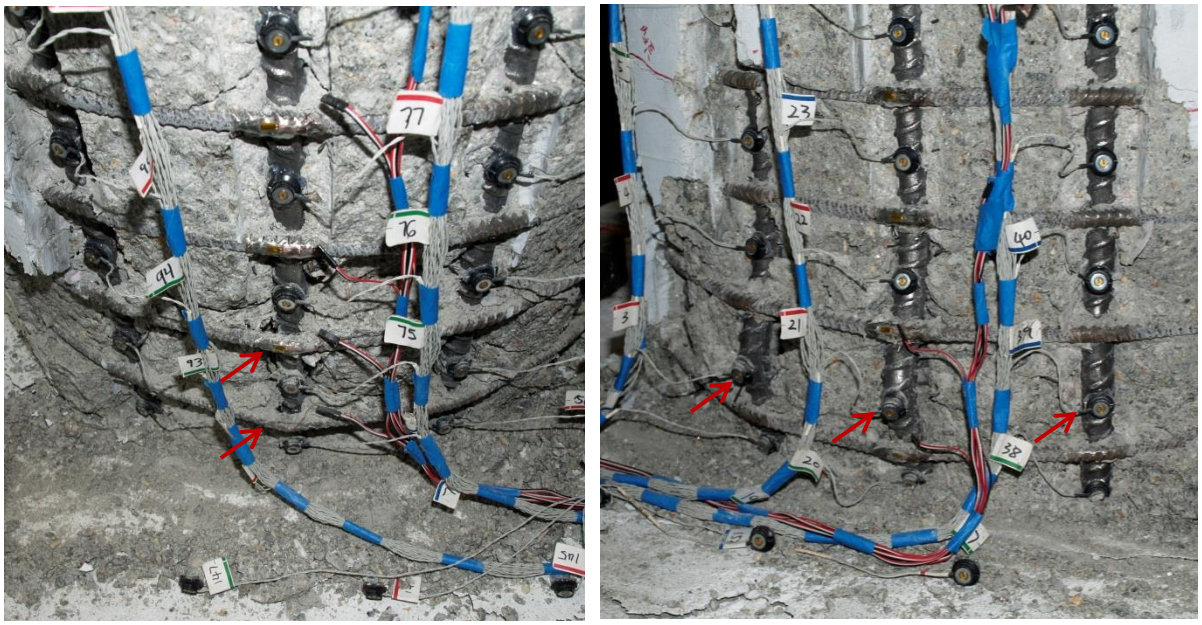

Figure 1.263 T15 – (Left) Permanent Deformation in North Spiral Layers at ($\mu_8^{+1} = 6.68$") and (Right) Deformation of Buckled Bars S2, S3, and S4 during ($\mu_8^{+1} = 6.68$")

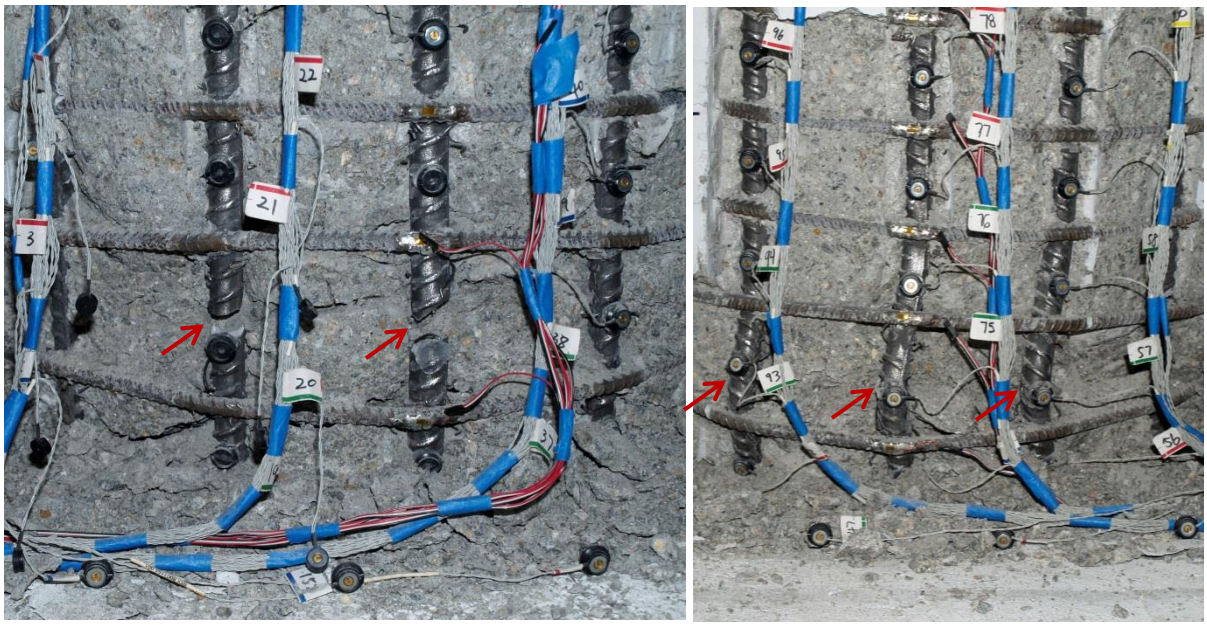

Figure 1.264 T15 – (Left) Rupture of Previously Buckled Bars S2 and S3 during ($\mu_8^{-1} = -6.69$") and (Right) Deformation in Bars N2, N3, and N4 at ($\mu_8^{-1} = -6.69$")

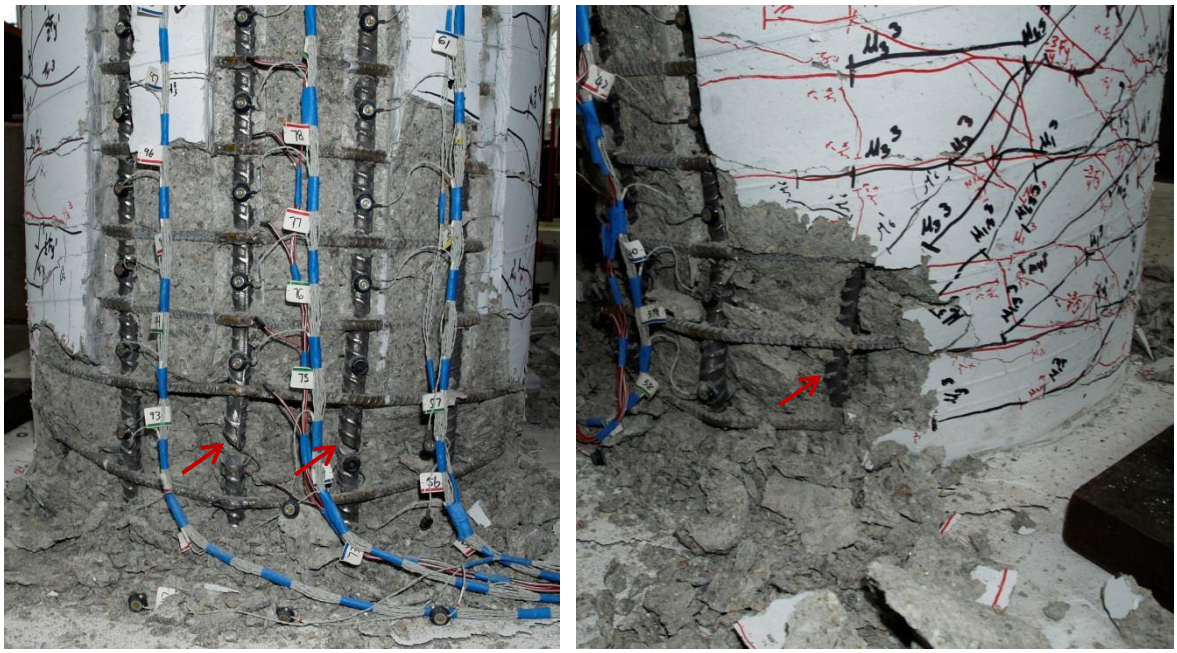

Figure 1.265 T15 – (Left) Rupture of Previously Buckled Bars N2 and N3 during ($\mu_8^{+2} = 6.67$") and (Right) Buckling of Bar S1 and S5 during ($\mu_8^{+2} = 6.67$")

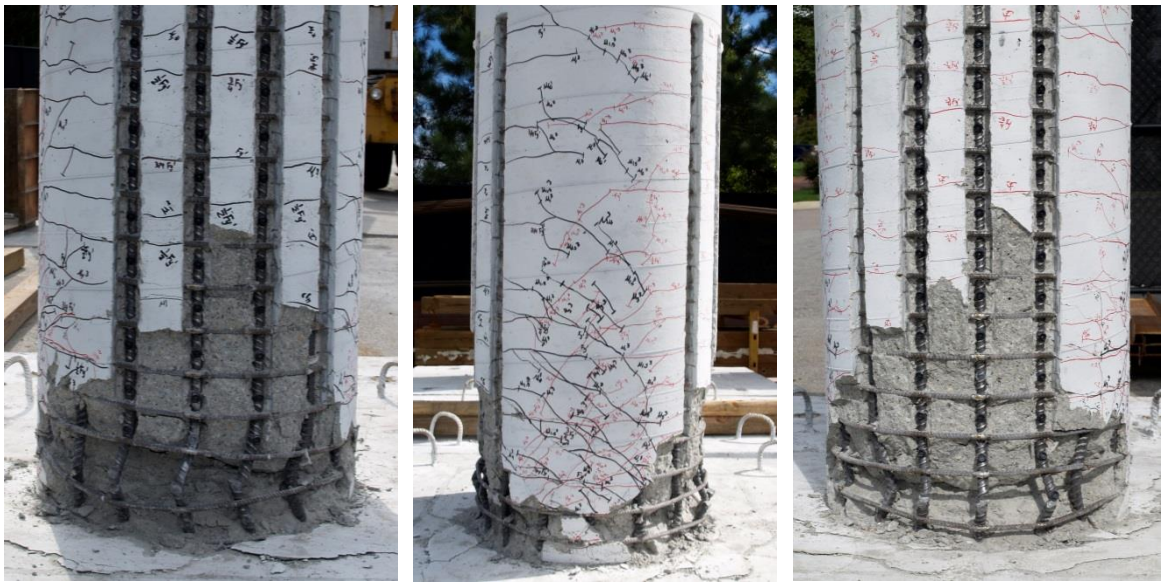

Figure 1.266 T15 – After the Test (Left) North, (Middle) Front, and (Right) South Side

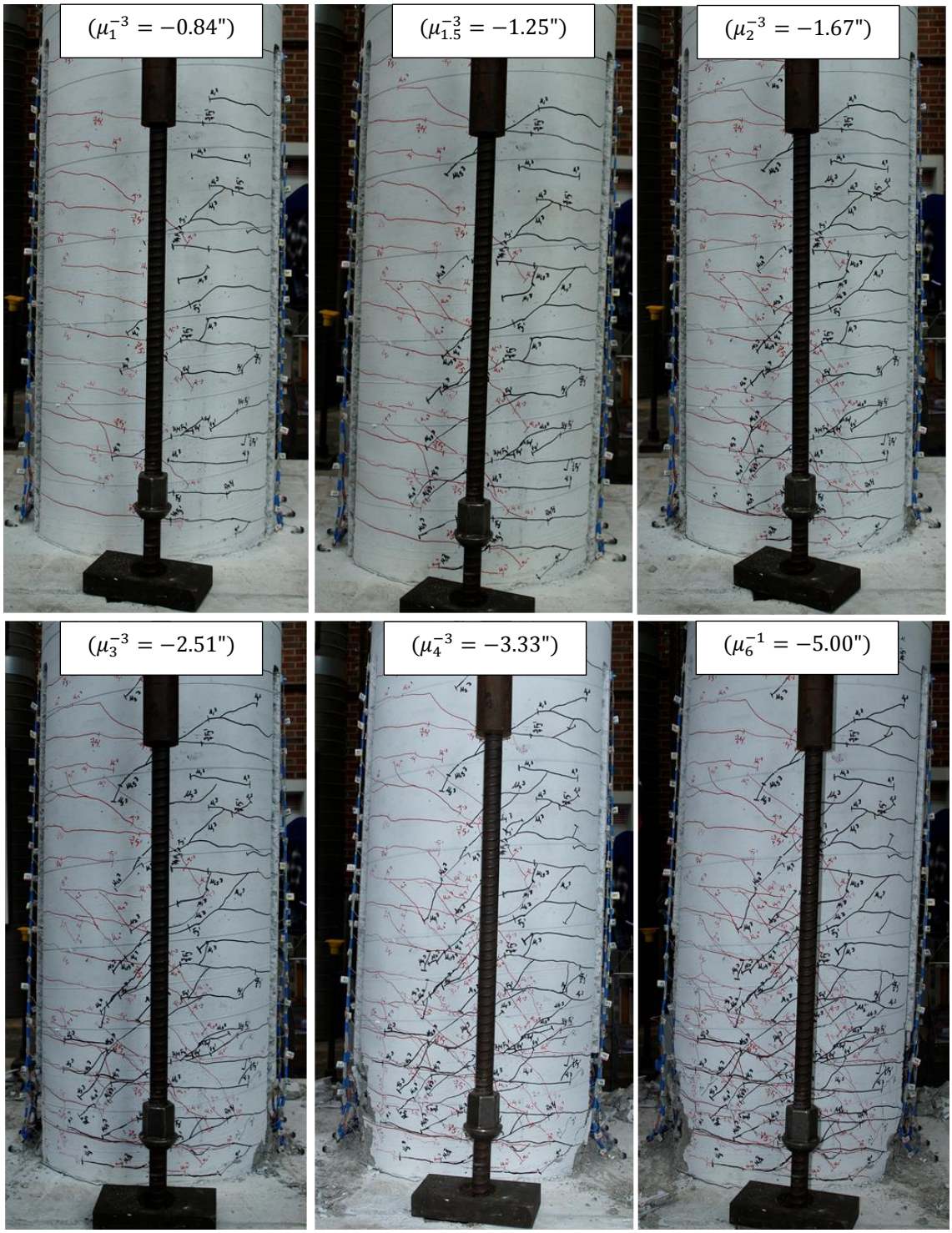

Figure 1.267 T15 – Crack Progression on the Back Side of the Specimen

Test 15 – Symmetric Three Cycle Set (#3 @ 2.75") Strain Data Analysis

North Reinforcement

Extreme fiber vertical strain profiles for push and pull cycles appear in Figure 1.268 and Figure 1.269 respectively. As the hinge rotates about inclined flexural shear cracks, compressive strains are concentrated at the base and tensile strains are fanned out to a greater height following the inclined crack distribution. Near the footing cracks remain effectively horizontal, but above the base section flexural shear cracks are inclined as shown in Figure 1.267. The effects of tension shift increase as the cracks become more inclined at higher ductility levels. A peak tensile strain of 0.0372 was measured 2.31" above the footing for bar N3 during ($\mu_6^{+1} = 5.01"$). Bar N3 did not buckle until reversal from ($\mu_6^{+2} = 5.00"$), when the peak tensile strain was 0.0365. The relationship between tensile strain and displacement for this gage length appears in Figure 1.272. The solid line contains data during the push cycle loading up to the peak displacement and the dashed line represents the subsequent reversal of load. Similar to previous tests, the moment curvature prediction with the PCK (2007) Lp Hinge Method over predicts the tensile strain-displacement relationship at an increasing rate. The largest compressive strain of -0.0199, located 7.89" above the footing, was measured during ($\mu_6^{-1} = -5.00"$). The peak compressive strain of -0.0199 measured in bar N3 is 54.3% larger than the original Mander ultimate concrete compressive strain of -0.0129. The relationship between compressive strain and displacement for bar N3, gage length centered 2.31" above the footing, during pull cycles appears in Figure 1.273. Here the measured compressive strains are slightly larger than the moment curvature prediction with the PCK (2007) Lp Hinge Method, but the overall trend is captured. At the section 7.89" above the footing, the relationship between strain and displacement does not match as well at higher ductility levels.

The strain hysteresis for the largest tensile gage length, 2.31" above the footing, on extreme fiber bar N3 is shown in Figure 1.276 with an elapsed time color bar to track the progression of the test. The strain hysteresis is plotted through ($\mu_6^{-2} = -5.01"$) when the bar

visibly buckled. After reversal from ($\mu_6^{+2} = 5.00$"), the relationship between strain and displacement begins to break away from the trend at around zero displacement. This gage length is centered over a layer of transverse steel where the largest crack was located. Since the outward buckled deformation of bar N3 occurred between layers of transverse steel, this particular gage length just below the outward buckled region shortens with increased deformation. To illustrate this point, the strain hysteresis over the outward buckled region of bar N3, located 5.11" above the footing, appears in Figure 1.277. The transverse steel strain gage hysteresis for a spiral layer restraining buckled bar N3 is shown in Figure 1.278. In all three graphs, buckling looks like bar buckling occurred between 0-2" of displacement after reversal from ($\mu_6^{+2} = 5.00$"). Here the gage length over the outward buckled region begins to elongate as the overlaying spiral strain increases. The transverse steel restraint on the North side of the specimen went into the inelastic range during ($\mu_6^{-1} = -5.00$"), as shown in Figure 1.271. Even though the transverse steel was inelastic during this cycle, visibly buckling was not observed. The strain hysteresis for the gage length located 5.11" above the footing on bar N3, in Figure 1.277, shows that some measurable deformation occurred during ($\mu_6^{-1} = -5.00$"). The curve which represents the reversal from μ_6^{+1} to μ_6^{-1} breaks away from the trend set by previous cycles.

South Reinforcement

A peak tensile strain of 0.0347 was measured 4.64" above the footing on bar S3 during ($\mu_6^{-1} = -5.00$"). When the loading of the specimen was paused at μ_6^{-1}, debris was removed and the peak tensile strain over the base gage length measured 0.0378. The relationship between tensile strain and displacement for bar S3 is shown in Figure 1.274 for the gage length located 4.64" above the footing. A peak compression strain of -0.0233 was measured 7.47" above the footing on bar S3 during ($\mu_6^{+1} = 5.01$"). The peak value is 80.6% larger than the original Mander (1988) ultimate concrete compressive strain of -0.0129. The relationship between compressive strain and displacement for the gage length 2.03" above the footing on bar S3 during push cycles appears in Figure 1.275. This gage length

represents the base section, where a peak compression strain of -0.0115 was measured during ($\mu_6^{+1} = 5.01$").

The strain hysteresis for the gage length overlaying the outward buckled region of bar S3, 4.64" above the footing, appears in Figure 1.279. After reversal from a peak tensile strain of 0.0378 at ($\mu_6^{-1} = -5.00$"), the relationship between strain and displacement begins to break from the trend at around -3", which agrees with the visible buckling observation. The transverse steel strain gage hysteresis for a spiral layer restraining the top portion of the outward buckled region is shown in Figure 1.280. The strain hysteresis for the spiral layer restraining the lower portion of the outward buckled region appears in Figure 1.281. The second spiral layer above the footing was inelastic by the time the specimen reached ($\mu_6^{+1} = 5.01$"), see Figure 1.270. The South reinforcing bars S2 and S3 buckled during the push cycle to ($\mu_6^{+2} = 5.00$"). The measured strain in the upper spiral layer continued to rapidly increase while the lower spiral layer entered the inelastic range for the first time. The data suggests that buckling of bar S3 began at around -3".

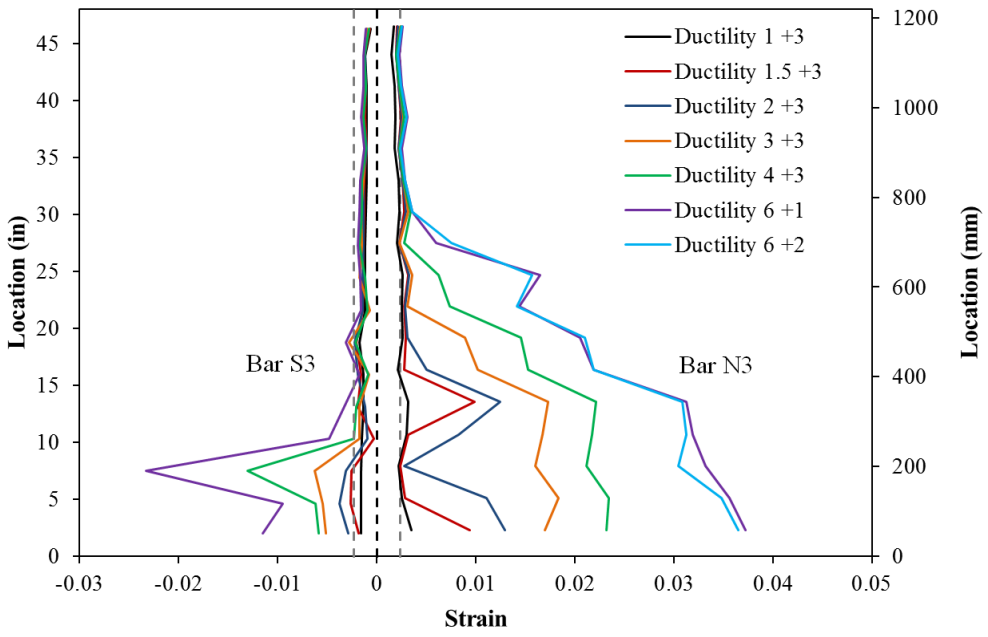

Figure 1.268 T15 – Extreme Fiber Vertical Strain Profiles during Push Cycles

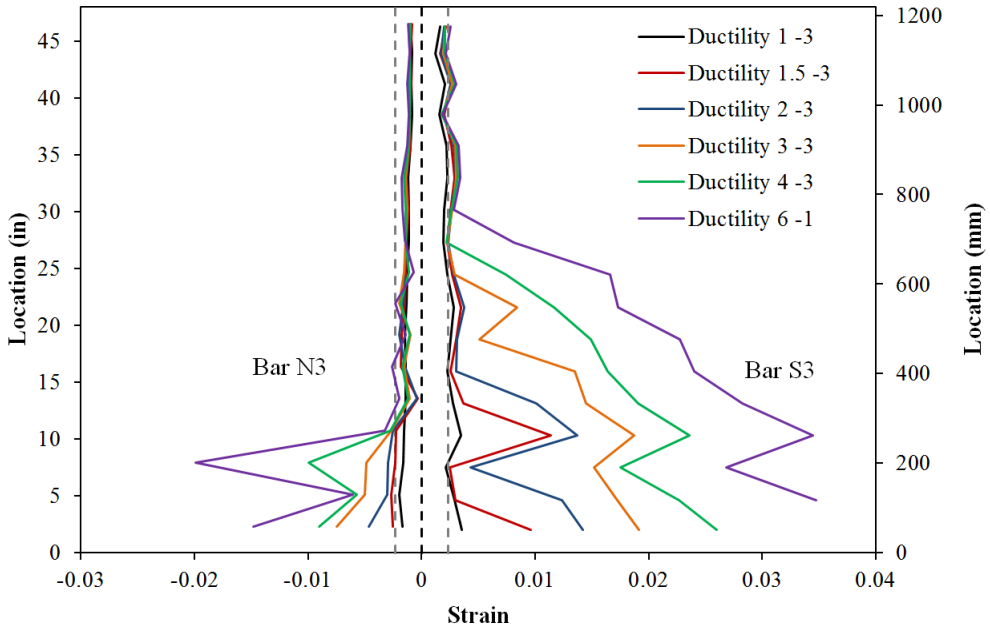

Figure 1.269 T15 – Extreme Fiber Vertical Strain Profiles during Pull Cycles

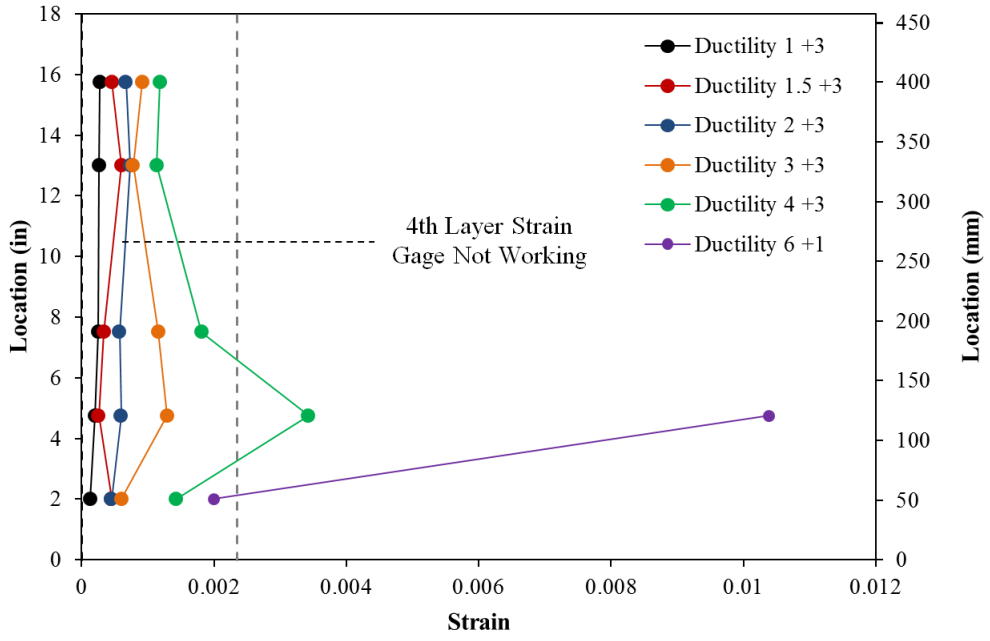

Figure 1.270 T15 – Spiral Strains on the South Side during Push Cycles

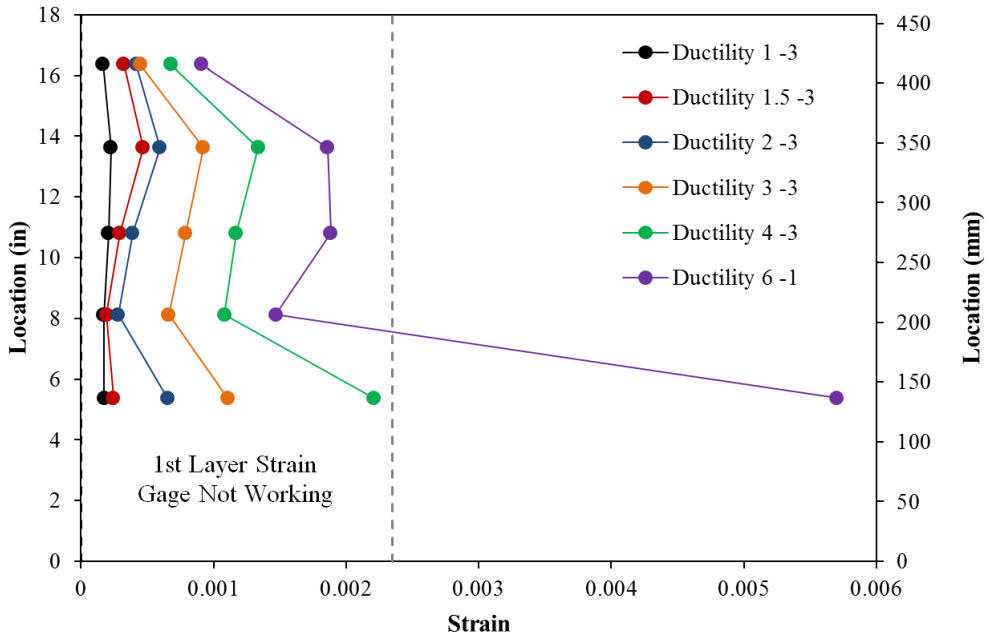

Figure 1.271 T15 – Spiral Strains on the North Side during Pull Cycles

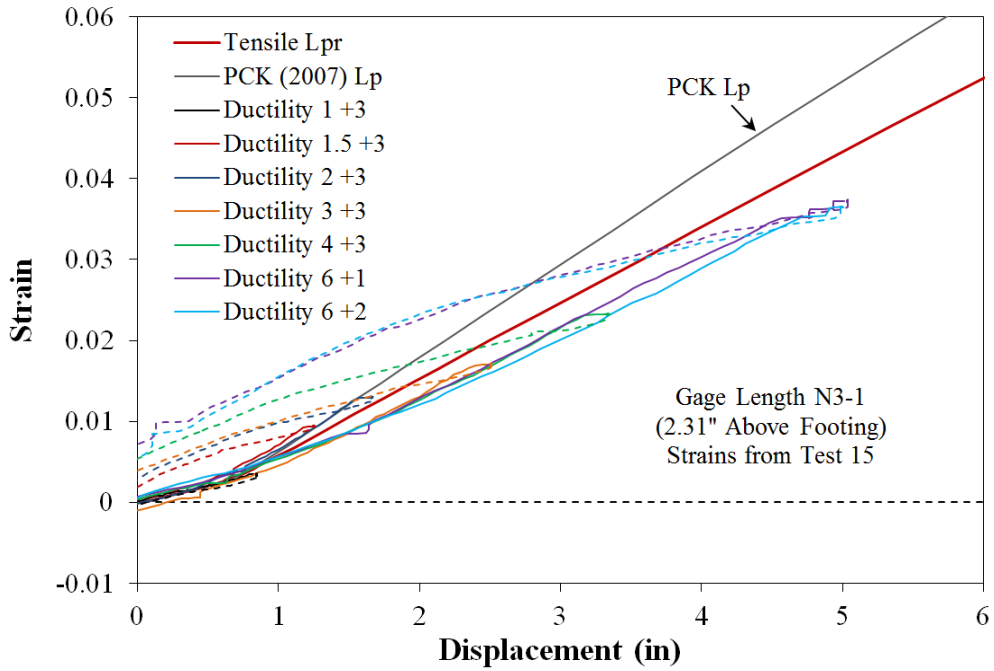

Figure 1.272 T15 – Tensile Strain-Displacement for Bar N3 during Push Cycles

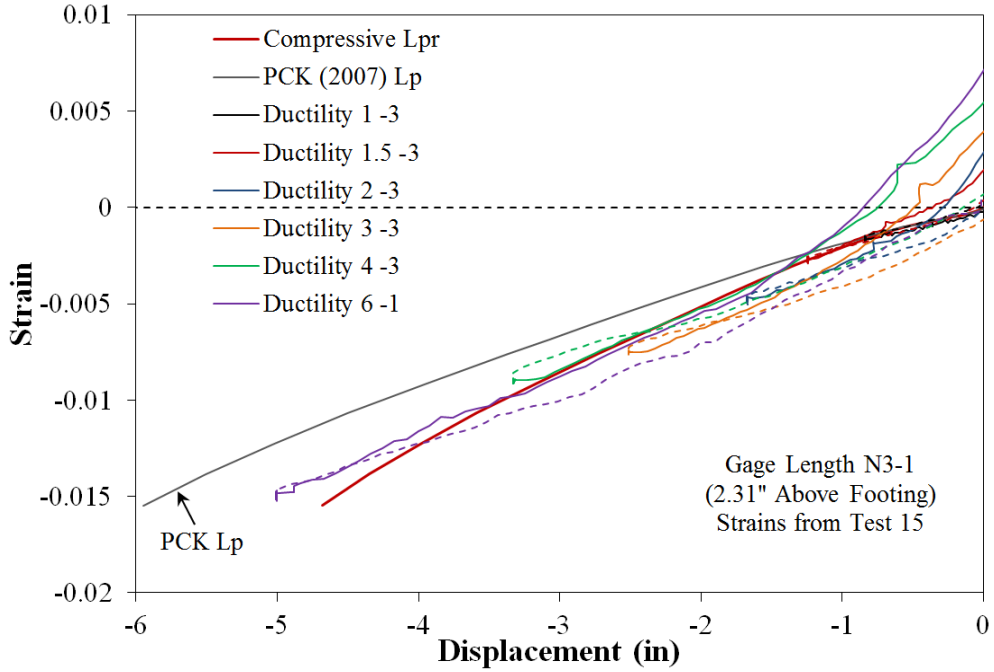

Figure 1.273 T15 – Compressive Strain-Displacement for Bar N3 during Pull Cycles

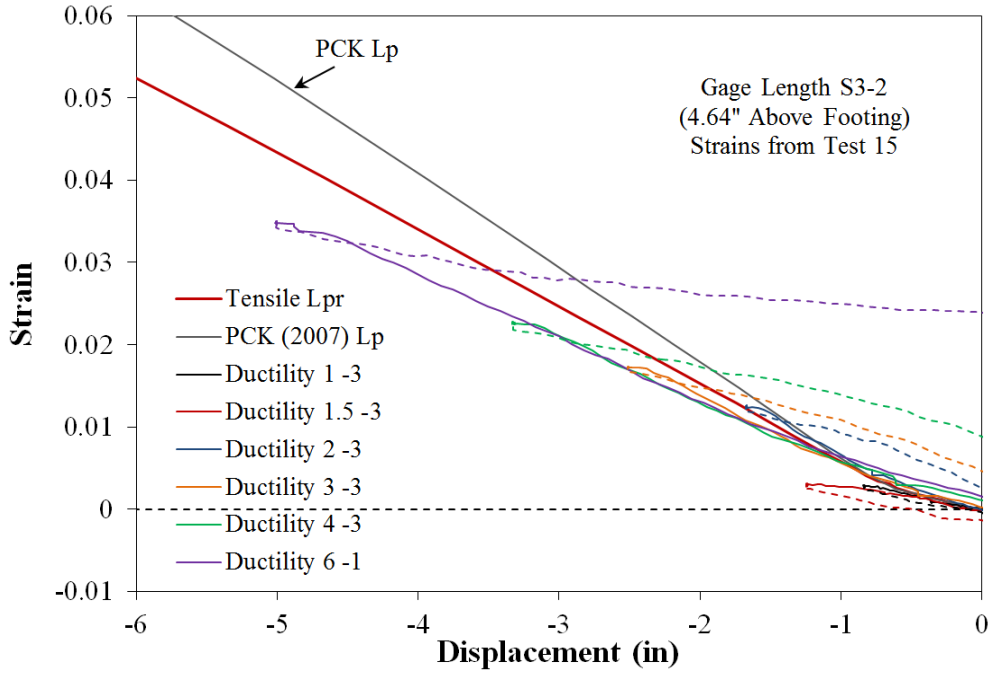

Figure 1.274 T15 – Tensile Strain-Displacement for Bar S3 during Pull Cycles

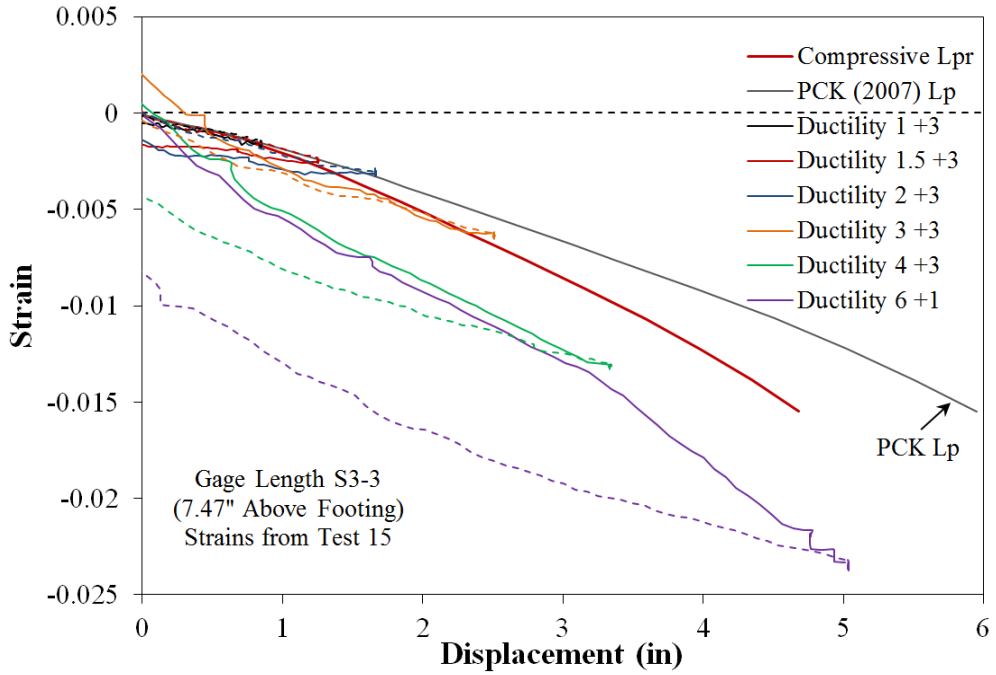

Figure 1.275 T15 – Compressive Strain-Displacement for Bar S3 during Push Cycles

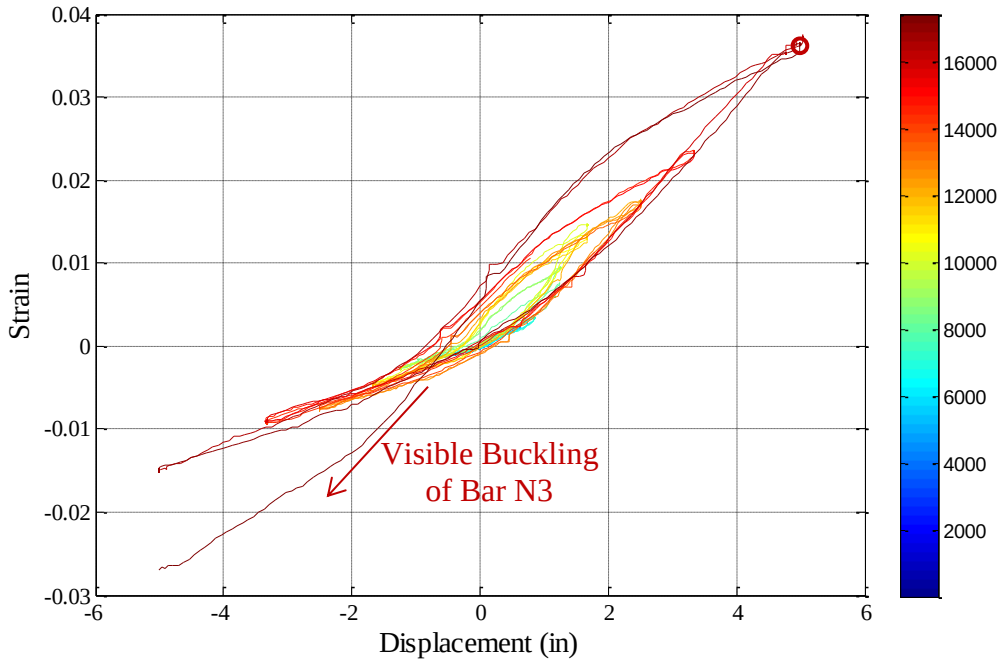

Figure 1.276 T15 – Strain Hysteresis over the Buckled Region of Bar N3 (2.31” Above)

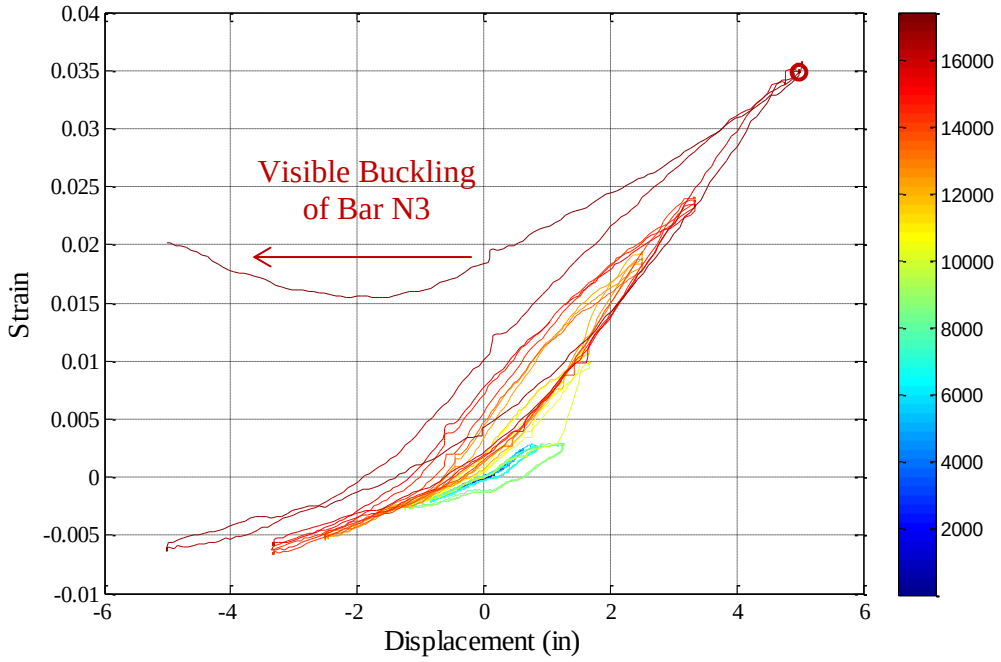

Figure 1.277 T15 – Strain Hysteresis over the Buckled Region of Bar N3 (5.11" Above)

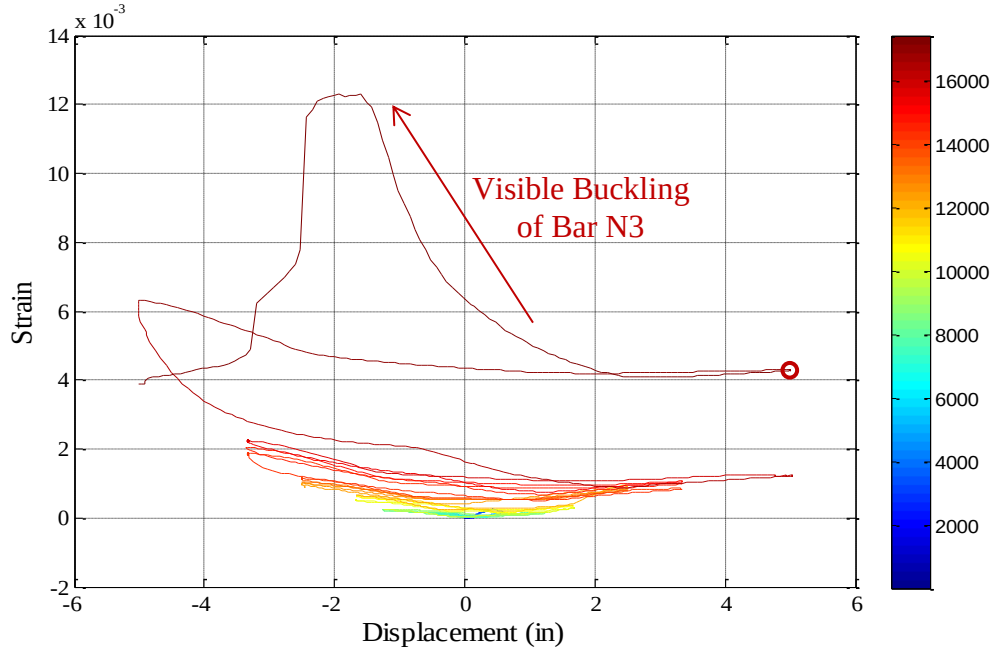

Figure 1.278 T15 – Spiral Strain Hysteresis over the Buckled Region of Bar N3

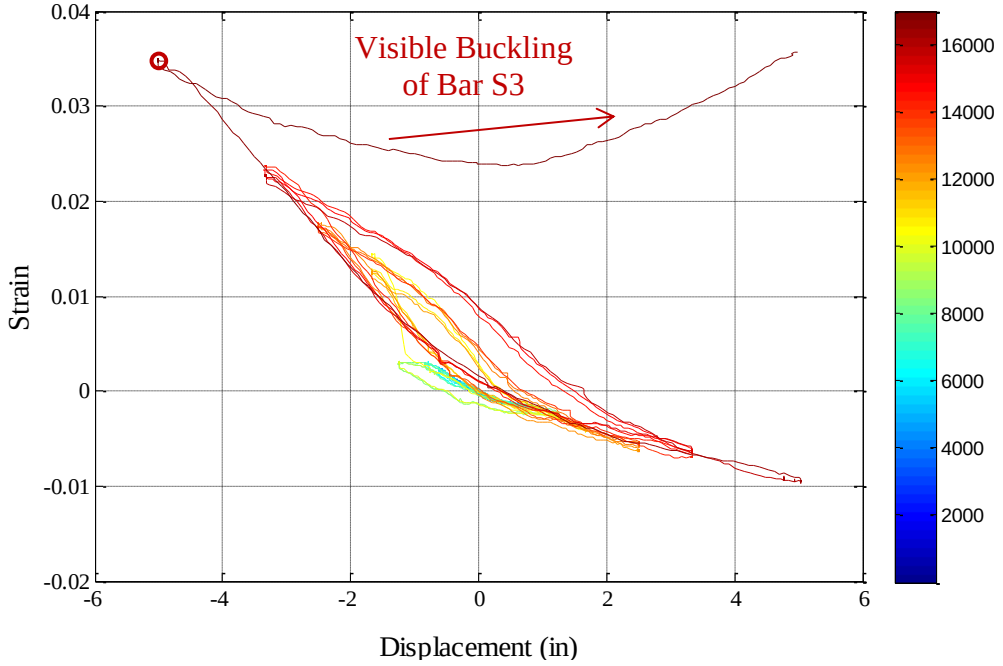

Figure 1.279 T15 – Strain Hysteresis over the Buckled Region of Bar S3 (4.64" Above)

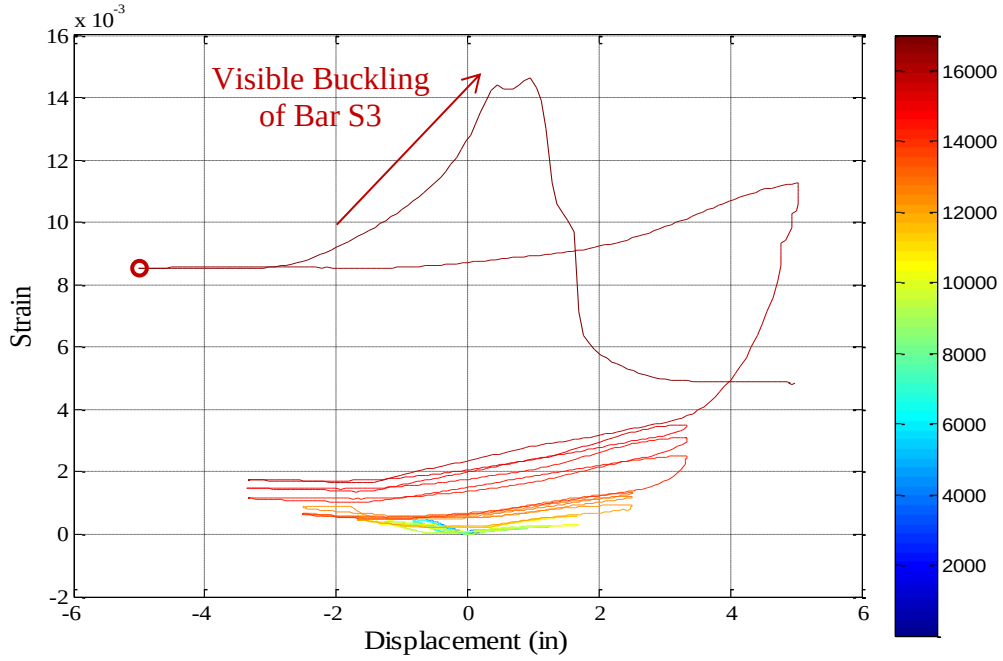

Figure 1.280 T15 – Spiral Strains over the Buckled Region of Bar S3 (2nd Layer)

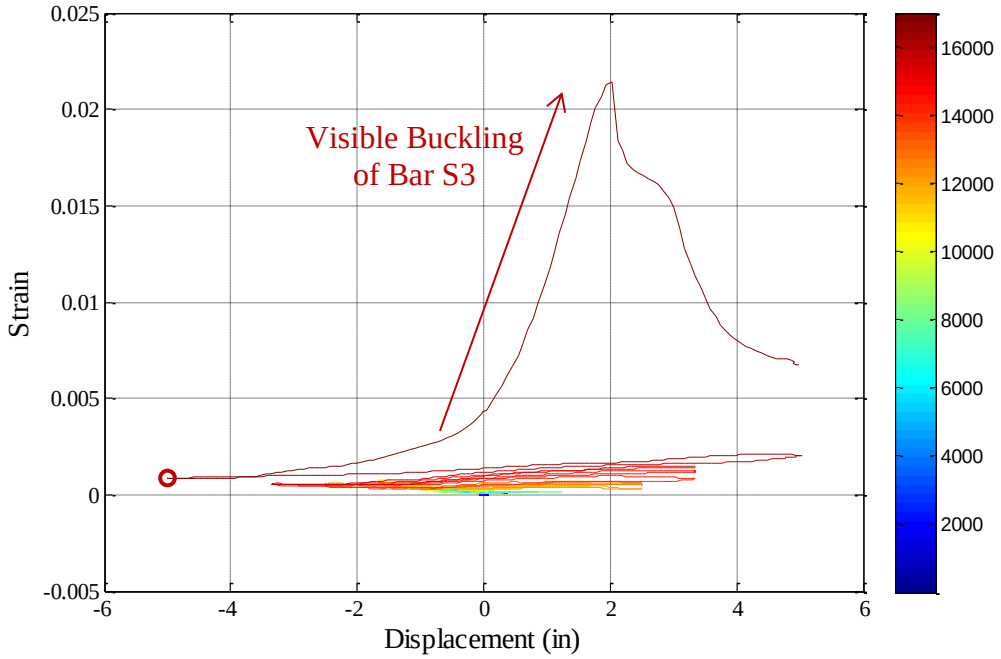

Figure 1.281 T15 – Spiral Strains over the Buckled Region of Bar S3 (1st Layer)

Test 15 – Cyclic Load History (#3 @ 2.75") Curvature and Strain Penetration Data

Vertical curvature profiles are plotted for push and pull cycles as shown in Figure 1.282 and Figure 1.283 respectively. These figures show that plastic curvatures have a linear distribution at higher displacement ductility levels. As the displacements increase, the base curvatures become larger and the extent of plastic curvatures reach higher above the footing. The effects of strain penetration of longitudinal reinforcement into the footing can be measured with the LEDs placed closest to the footing-column interface. The slip hysteresis for the North and South extreme fiber bars appear in Figure 1.284 and Figure 1.285. The base rotation attributable to strain penetration is obtained by looking at the measured slip of all six instrumented bars, as shown in Figure 1.286 and Figure 1.287 for push and pull respectively. The base rotation is equal to the slop of the least squared error line connecting the measured values.

The top column displacement can be determined using the Optotrak system by integrating the measured curvatures, extrapolating the base rotation to the center of loading, and assuming an elastic distribution of curvature above the instrumented region. A comparison of the measured top column displacements and the Optotrak integrated displacements appears in Figure 1.288. The two methods agree well throughout the entire test. The measured spread of plasticity for Test 14 is shown in Figure 1.289 as a function of base section curvature ductility. The extent of plasticity is the intersection of the linear regression for the plastic curvature profile and the elastic curvature distribution.

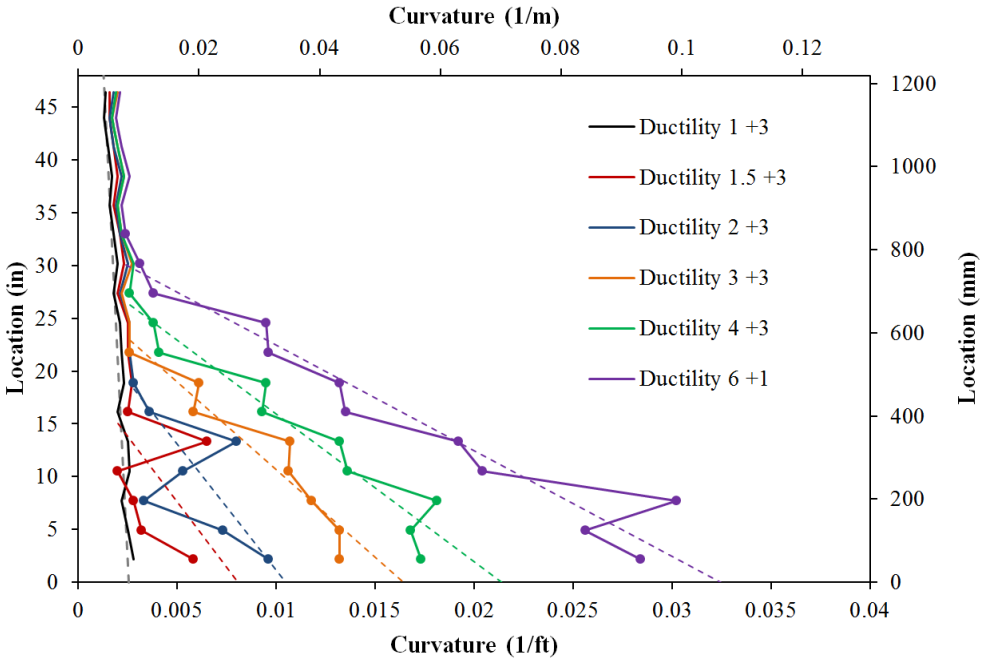

Figure 1.282 T15 – Vertical Curvature Profiles during Push Cycles

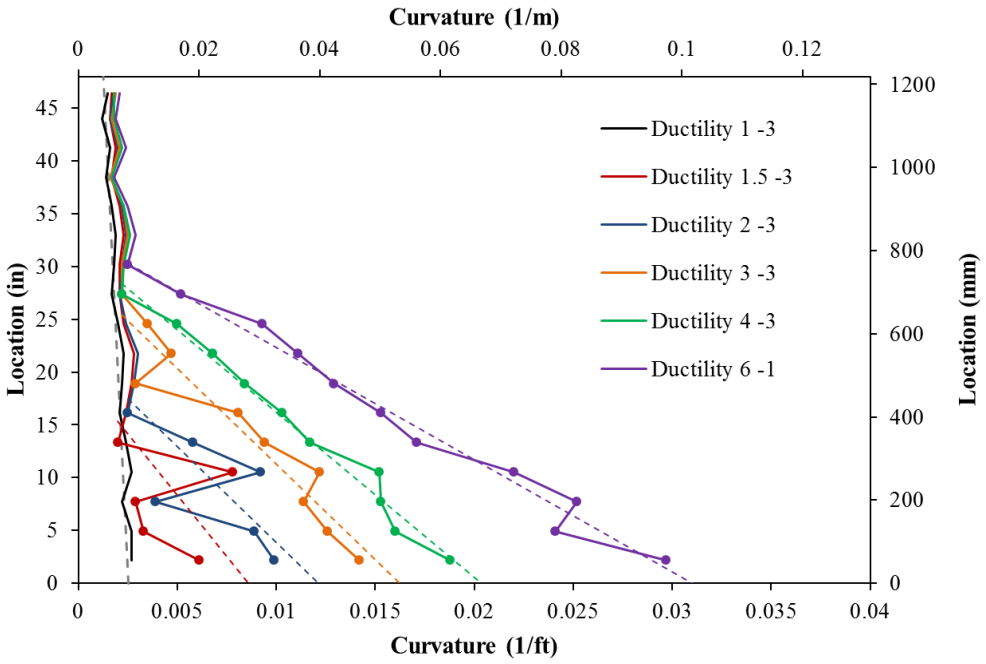

Figure 1.283 T15 – Vertical Curvature Profiles during Pull Cycles

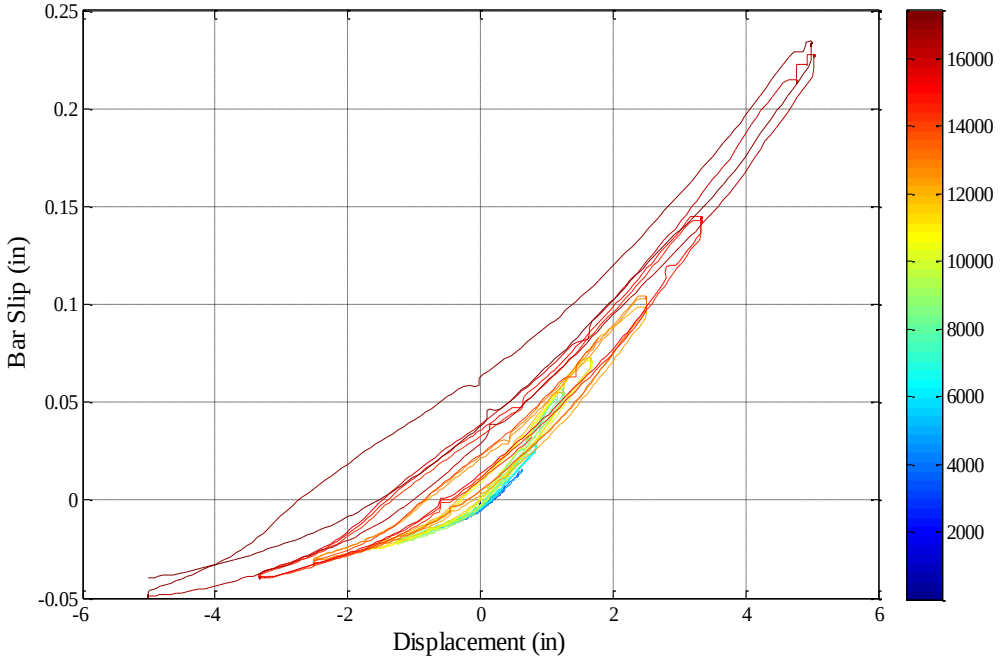

Figure 1.284 T15 – Bar N3 Base Section Slip Hysteresis due to Strain Penetration

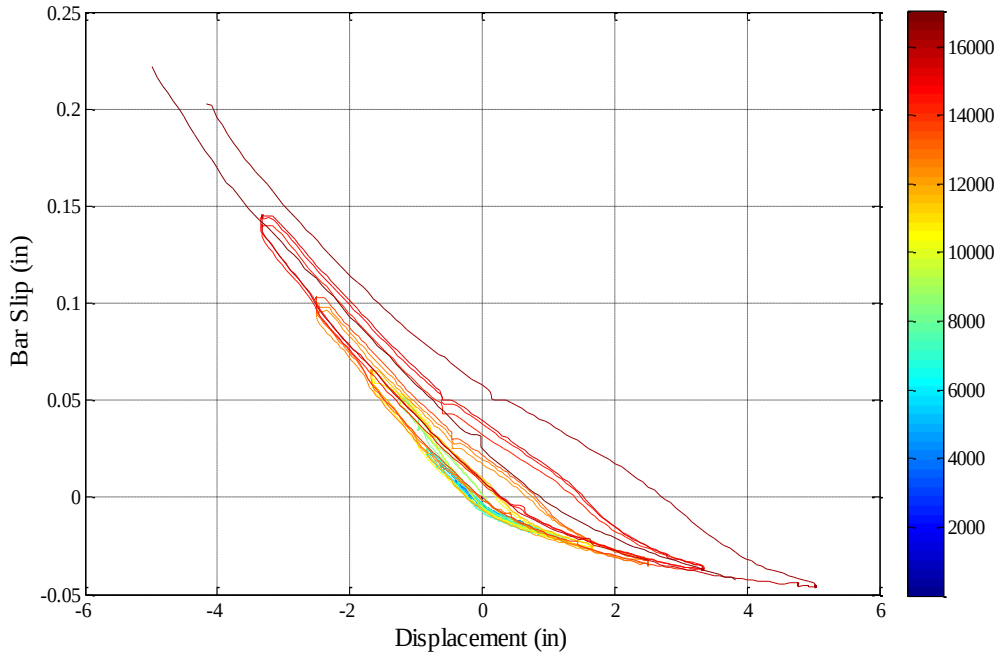

Figure 1.285 T15 – Bar S3 Base Section Slip Hysteresis due to Strain Penetration

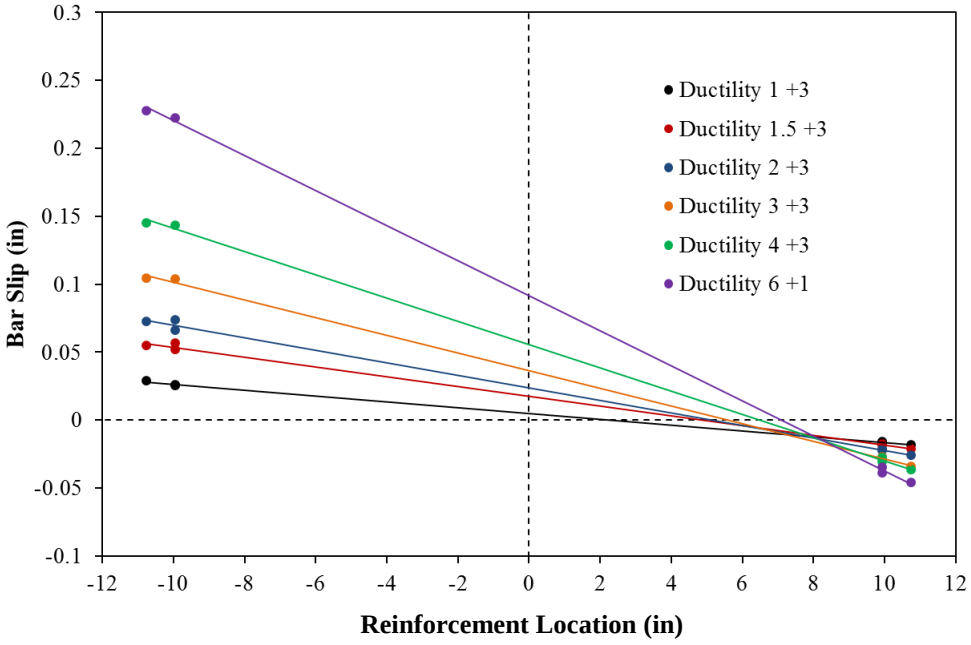

Figure 1.286 T15 – Base Rotation due to Strain Penetration during Push Cycles

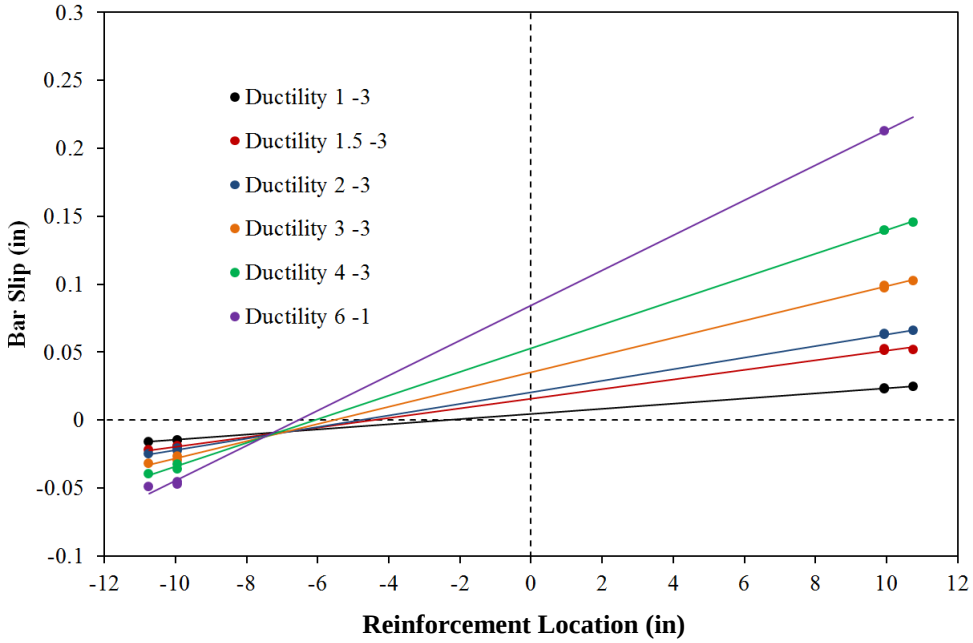

Figure 1.287 T15 – Base Rotation due to Strain Penetration during Pull Cycles

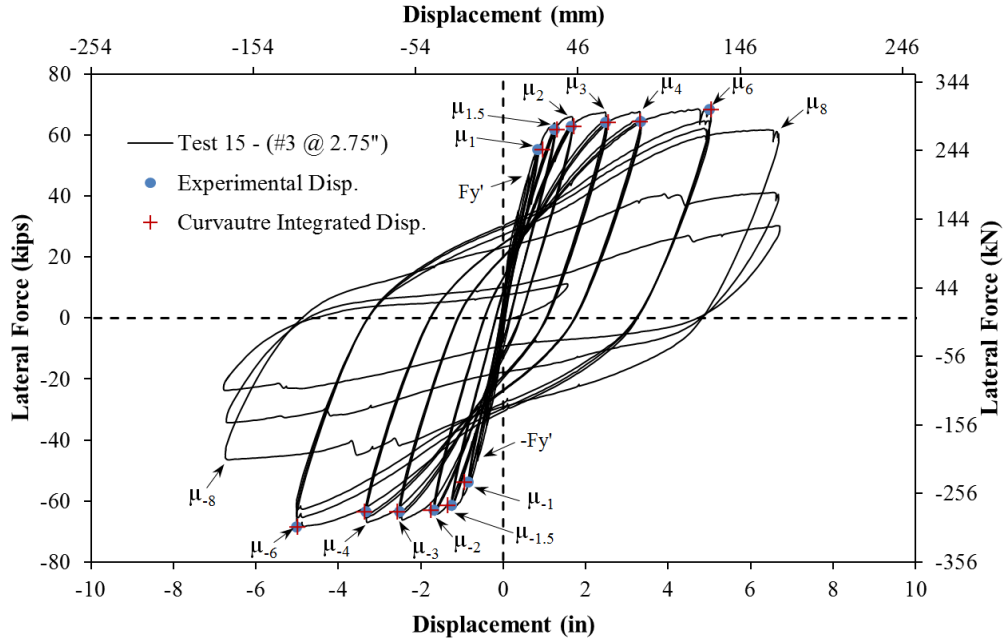

Figure 1.288 T15 – Comparison of Measured and Optotrak Integrated Displacements

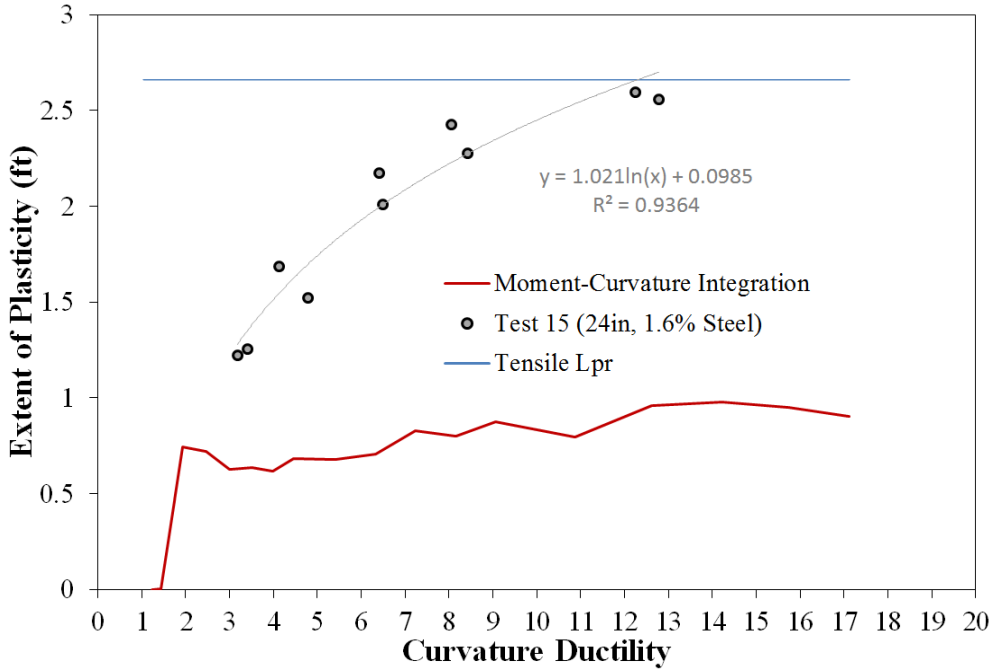

Figure 1.289 T15 – Measured Spread of Plasticity (Circular Data Points)

1.2.4 Test 16 – Three Cycle Set Load History with #3 Spiral at 1.5" (1.3%)

Table 1.23 Observational Summary for Test 16 – Cyclic with #3 Spiral at 1.5" (1.3%)

VALUES OF INTEREST:	
Concrete Compressive Strength:	$f_c' = 6711\ psi$
Axial Load:	$P = 170\ kips$
Analytical First Yield Force:	$F_y' = 46.8\ kips$
Experimental First Yield Displacement:	$\Delta_y' = 0.62"$
Analytical Nominal Moment Capacity:	$M_n = 503.2\ kip * ft$
Equivalent Yield Displacement:	$\Delta_y = 0.83"$
Maximum Lateral Force:	$70.7\ kips$
Failure Mode:	Fracture of Previously Buckled Reinforcement
DAMAGE OBSERVATIONS:	
First Cracking North:	$1/2Fy' = 0.17"$
First Cracking South:	$-1/2Fy' = -0.19"$
Cover Concrete Crushing North:	$\mu_2^{-3} = -1.65"$
Cover Concrete Crushing South:	$\mu_2^{+1} = 1.66"$
Transverse Steel Yield North:	At $-4.98"$ during pull to $\mu_6^{-1} = -4.98"$
Transverse Steel Yield South:	At $3.80"$ during push to $\mu_6^{+1} = 4.99"$
Longitudinal Bar Buckling North:	Reversal from $\mu_6^{+2} = 5.00"$
Longitudinal Bar Buckling South:	Reversal from $\mu_6^{-1} = -4.98"$
Longitudinal Bar Fracture North:	At $3.68"$ during push to $\mu_{10}^{+2} = 8.32"$
Longitudinal Bar Fracture South:	At $-2.64"$ during pull to $\mu_{10}^{-1} = -8.34"$

$*\mu_6^{-1} = -4.98"$ represents the first pull cycle of displacement ductility six

Table 1.24 Strain Data Summary for Test 16 – Cyclic with #3 Spiral at 1.5" (1.3%)

MATERIAL STRAINS:	
Cover Concrete Crushing North:	$\varepsilon_s = 0.0048\ (compression)$
Cover Concrete Crushing South:	$\varepsilon_s = 0.0038\ (compression)$
Transverse Steel Yield North:	$\varepsilon_s = 0.0120\ (compression)$
Transverse Steel Yield South:	$\varepsilon_s = 0.0152\ (compression)$
Longitudinal Bar Buckling North:	$\varepsilon_s = 0.056\ (peak\ tension\ prior\ to\ bb)$
	$\varepsilon_s = 0.019\ (peak\ comp.\ prior\ to\ bb)$
Longitudinal Bar Buckling South:	$\varepsilon_s = 0.052\ (peak\ tension\ prior\ to\ bb)$
	$\varepsilon_s = 0.030\ (peak\ comp.\ prior\ to\ bb)$
Mander (1988) Ultimate Concrete Compression Strain, $\varepsilon_{cu} = 0.0193$	

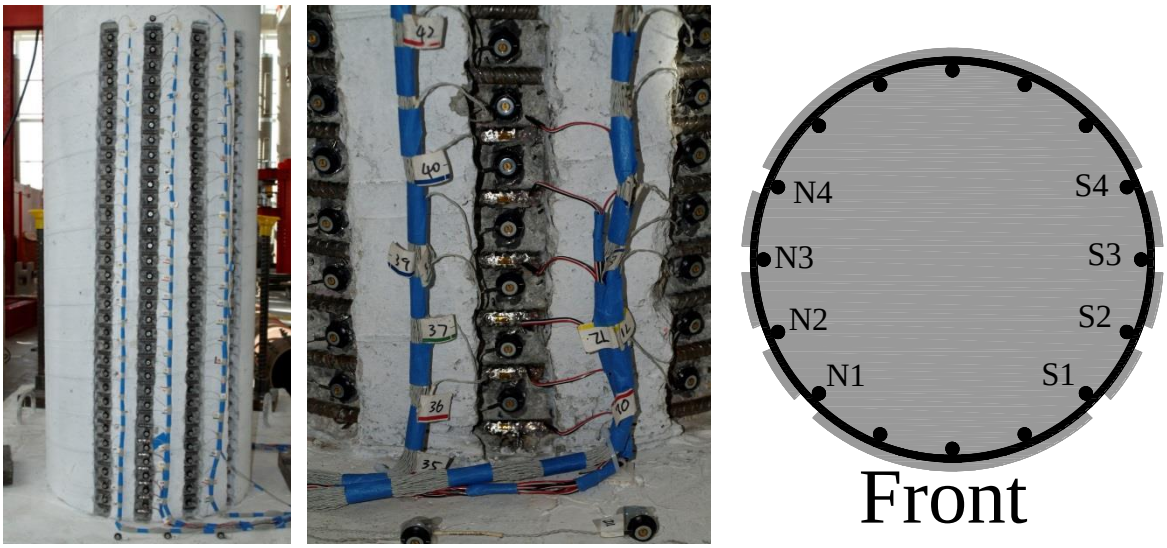

Figure 1.290 T16 – Cross Section Bar Designation and Target Marker Application

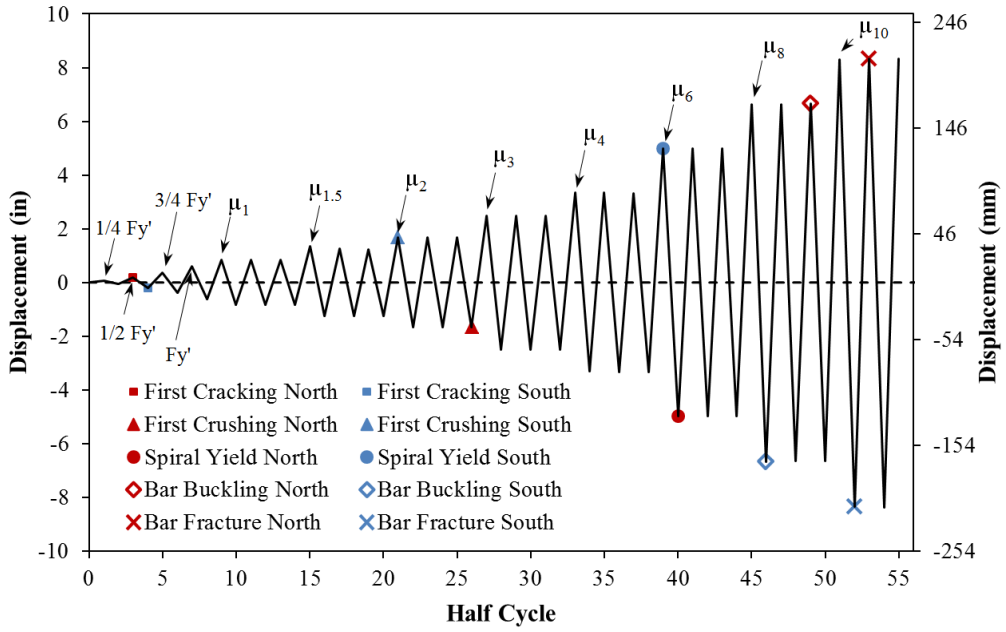

Figure 1.291 T16 – Symmetric Three Cycle Set Load History

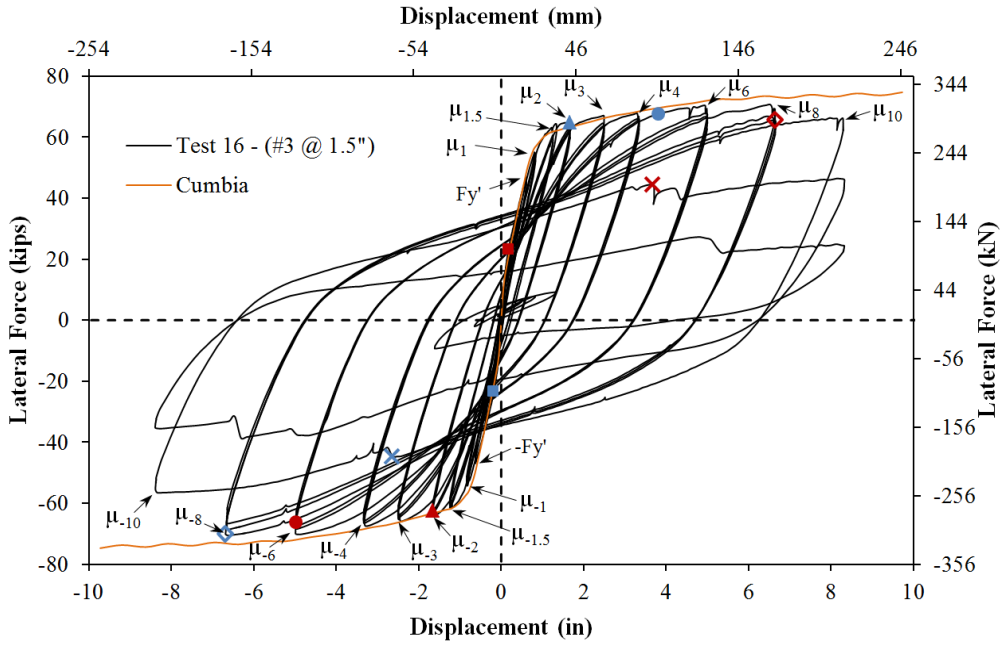

Figure 1.292 T16 – Lateral Force vs. Top Column Displacement Response

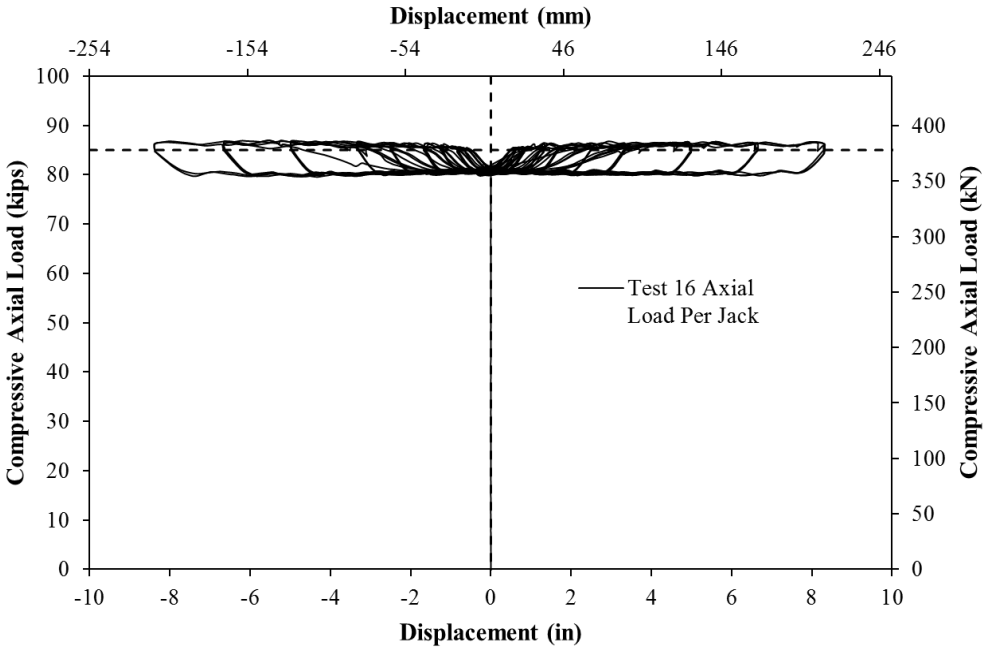

Figure 1.293 T16 – Compressive Axial Load from One Jack (Total = 2*Value)

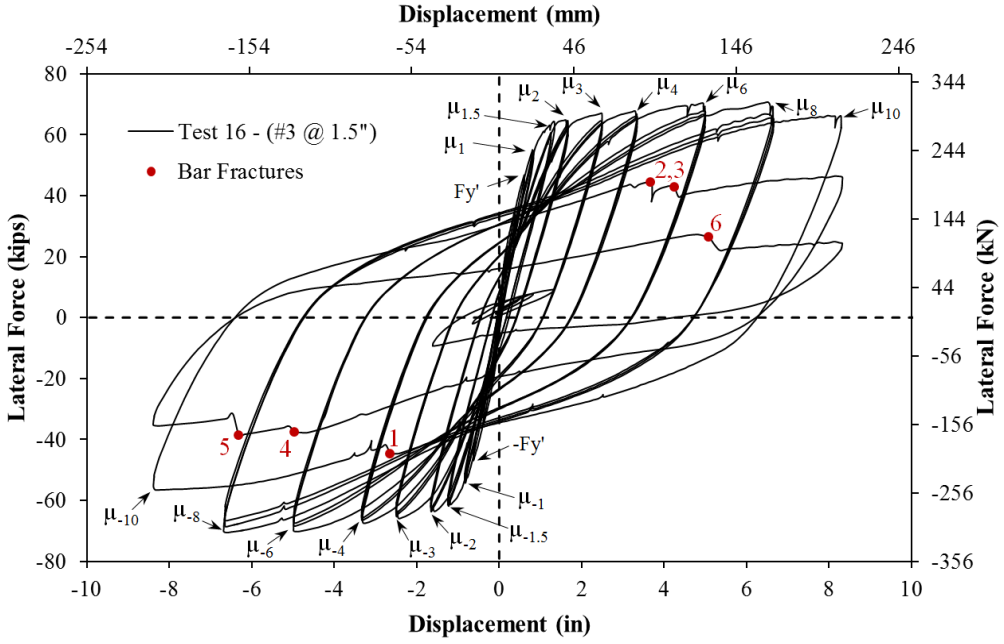

Figure 1.294 T16 – Bar Fracture History of Previously Buckled Reinforcement

Test 16 – Symmetric Three Cycle Set (#3 @ 1.5") Experimental Observations

The test began with cycles in ¼ Fy' (first yield force) increments in each direction of loading until the first yield force was reached. The first cracks on the North side of the specimen measured 0.1mm at approximate 9" spacing at $(1/2Fy' = 23.30\ kips)$. Cracks on the South Side of the specimen measured 0.1mm at approximate 7" spacing during $(-1/2Fy' = -23.40\ kips)$. The largest crack widths on the North side of the specimen reached 0.2mm at approximate 6" spacing at $(3/4Fy' = 35.06\ kips)$. Crack widths measuring 0.3mm with 6" spacing were observed on the South side of the specimen during $(-3/4Fy' = -34.46\ kips)$. During the first yield push cycle $(Fy' = 46.85\ kips,\ 0.61")$, the largest crack widths measured 0.3mm at approximate 6" spacing. During the subsequent pull cycle $(-Fy' = -46.92\ kips, -0.63")$, crack widths reached 0.4mm at approximate 5" spacing on the South side of the specimen. The crack distribution at first yield is shown in Figure 1.295. The progression of the crack distribution on the back side of the specimen is shown in Figure 1.303. Cracks on the North side of the specimen measured 0.6mm at approximate 4" spacing during $(\mu_1^{+3} = 0.83")$. After reversal, cracks on the South side reached 0.6mm at 6" spacing at $(\mu_1^{-3} = -0.84")$.

Visible flaking of the cover concrete in compression, which is a precursor to crushing, was observed on the South side of the specimen during $(\mu_{1.5}^{+1} = 1.34")$. While the displacement for this cycle was intended to reach 1.25", a slight overload to 1.34" occurred. The largest crack width on the North side of the specimen measured 0.9mm, located 10" above the footing, during $(\mu_{1.5}^{+3} = 1.24")$. Crushing on the South side of the specimen 2" above the footing was observed during $(\mu_2^{+1} = 1.66")$, see the left photo of Figure 1.296. Visible cover concrete flaking on the North side of the specimen did not occur until $(\mu_2^{-1} = -1.66")$. During $(\mu_2^{-3} = -1.65")$, the largest crack width on the South side of the specimen measured 1.5mm and cover concrete crushing on the North side of the specimen reached 5" above the footing as shown in the right photo of Figure 1.296. The extent of crushing on the South side of the specimen reached 15" above the footing during $(\mu_3^{+3} = 2.50")$, as shown in the left photo of Figure 1.297. Crushing on the North side of the specimen extended 11"

above the footing during ($\mu_3^{-3} = -2.50$"), see the right photo of Figure 1.297. During ($\mu_4^{+3} = 3.33$") and ($\mu_4^{-3} = -3.33$") the extent of crushing on the South and North side of the specimen reached 15" and 13" above the footing respectively.

Crushing on the North and South sides of the specimen both reached 25" above the footing during ($\mu_6^{+3} = 5.00$") and ($\mu_6^{-3} = -4.99$"), as shown in Figure 1.298. After reversal from ($\mu_8^{-1} = -6.68$"), south extreme fiber bar S3 buckled as shown in the left and middle photos of Figure 1.299. After reversal from ($\mu_8^{+3} = 6.65$"), north extreme fiber bar N3 and adjacent bar N2 buckled, see the right photo of Figure 1.299. Even though rupture of the North reinforcement did not occur during ($\mu_{10}^{+2} = 8.32$"), a 5.7% loss in strength was observed due only to buckled bars on each side of the specimen during ($\mu_{10}^{+1} = 8.29$"). An additional South reinforcing bar S2 buckled during ($\mu_{10}^{+1} = 8.29$"), as shown in the left photo of Figure 1.300.

During ($\mu_{10}^{-1} = 8.34$"), previously buckled South reinforcing bar S3 ruptured causing a 19.5% loss in strength, see the right photo of Figure 1.300. North reinforcing bars N1 and N4 also buckled during ($\mu_{10}^{-1} = 8.34$"), see the left photo of Figure 1.301. Previously buckled North bars N2 and N3 ruptured during ($\mu_{10}^{+2} = 8.32$"), leading to a 33.4% total loss in strength, see the right photo of Figure 1.301. Additional South reinforcing bars S1 and S4 buckled during ($\mu_{10}^{+2} = 8.32$"), as shown in Figure 1.302. Previously buckled South bars S2 and S4 ruptured during ($\mu_{10}^{-2} = -8.39$"), causing a 49.7% total loss in strength. During ($\mu_{10}^{+3} = 8.32$"), North bars N1 and N5 ruptured leading to a total 64.7% loss in strength. At this time the test was concluded. A graph plotting the rupture locations and corresponding losses in strength on the hysteretic response appears in Figure 1.294.

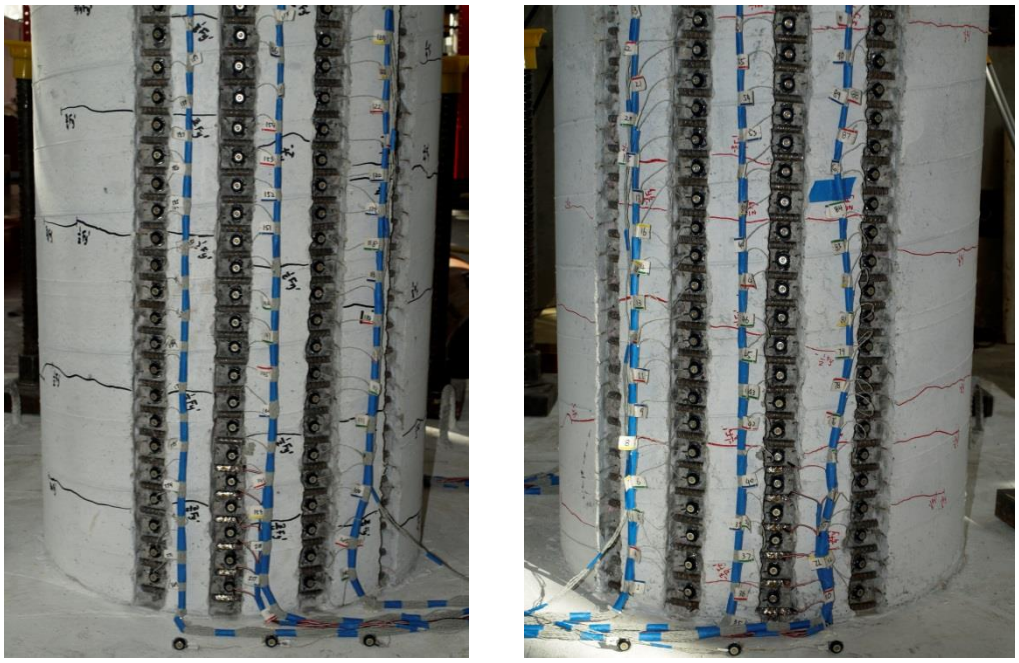

Figure 1.295 T16 – Crack Distribution at First Yield (Left) North and (Right) South

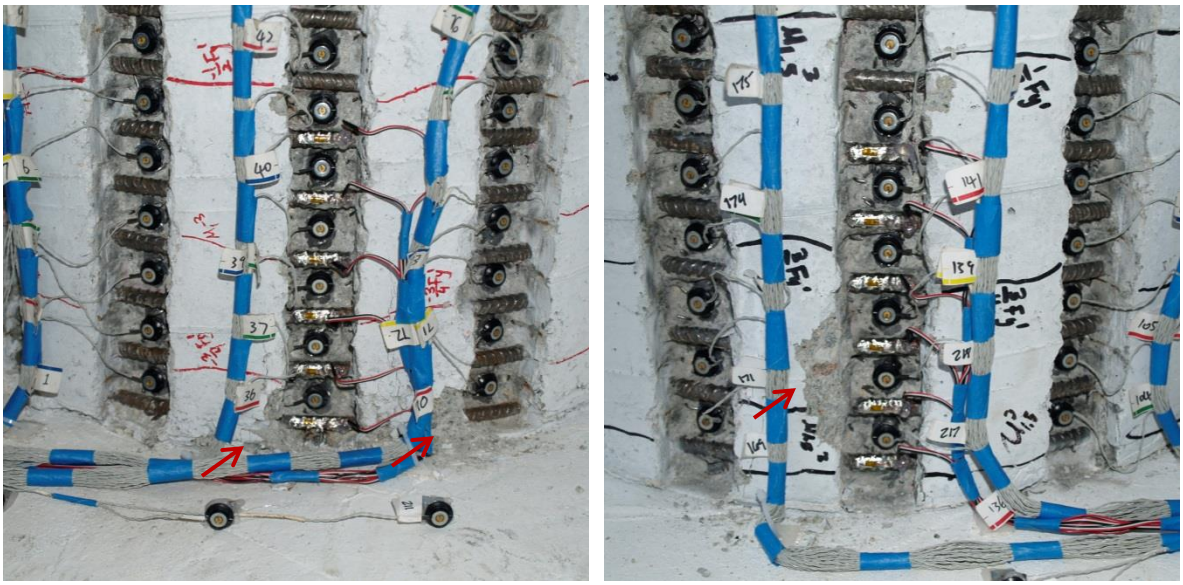

Figure 1.296 T16 – (Left) South Crushing during ($\mu_2^{+1} = 1.66$") and (Right) North Crushing during ($\mu_2^{-3} = -1.65$")

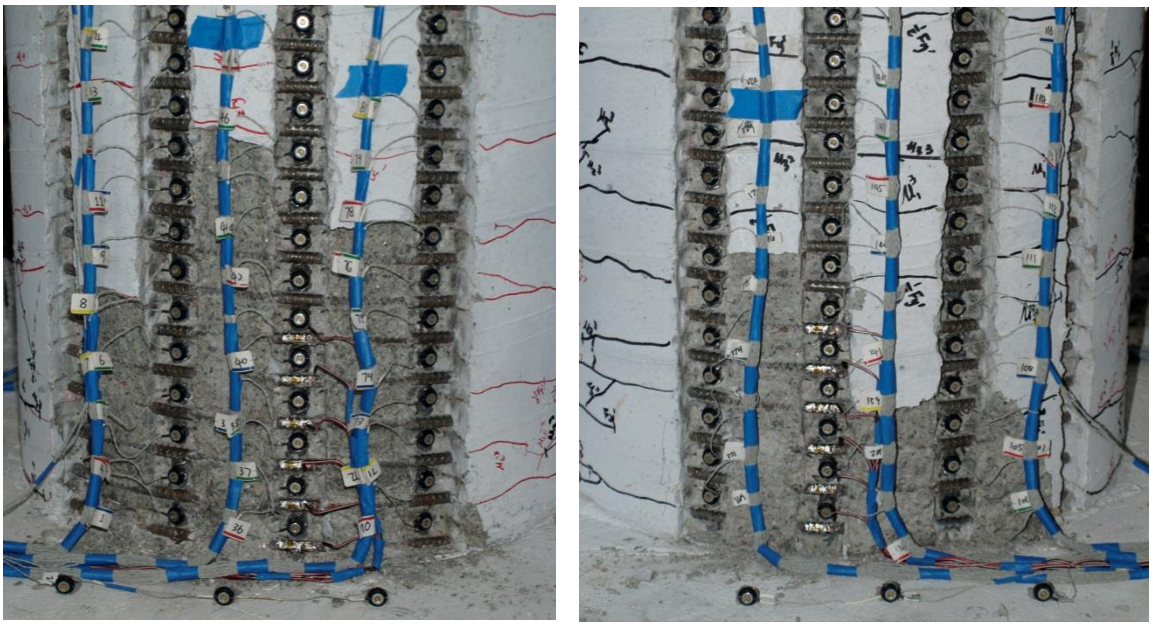

Figure 1.297 T16 – (Left) South Side at ($\mu_3^{+3} = 2.50$"), (Right) North at($\mu_3^{-3} = -2.50$")

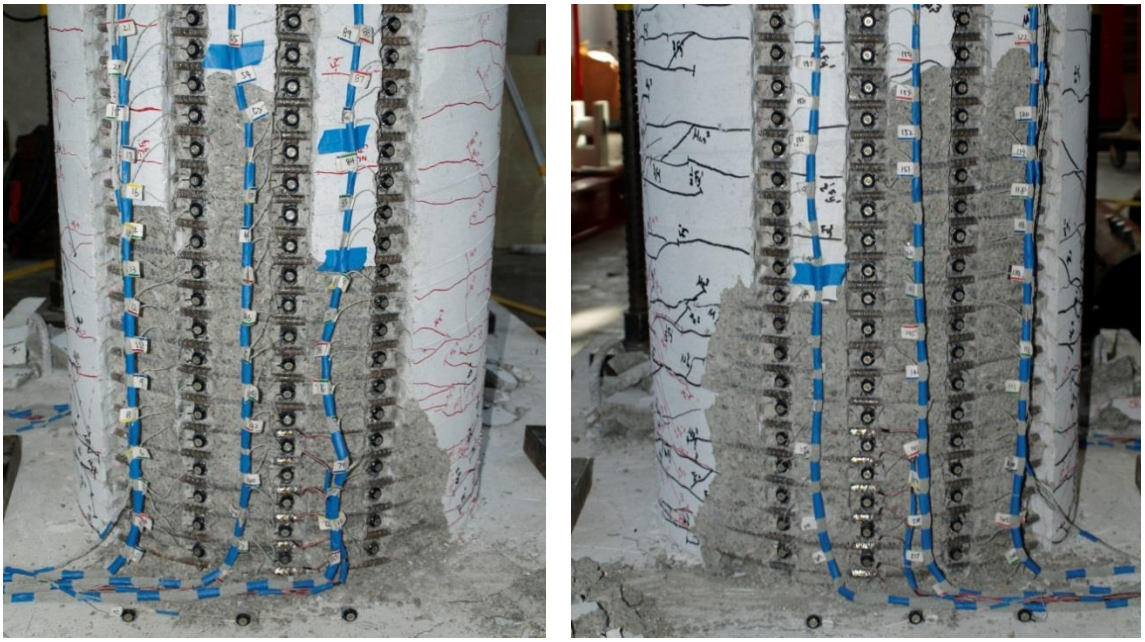

Figure 1.298 T16 – (Left) South Crushing during ($\mu_6^{+3} = 5.00$") and (Right) North Crushing during ($\mu_6^{-3} = -4.99$")

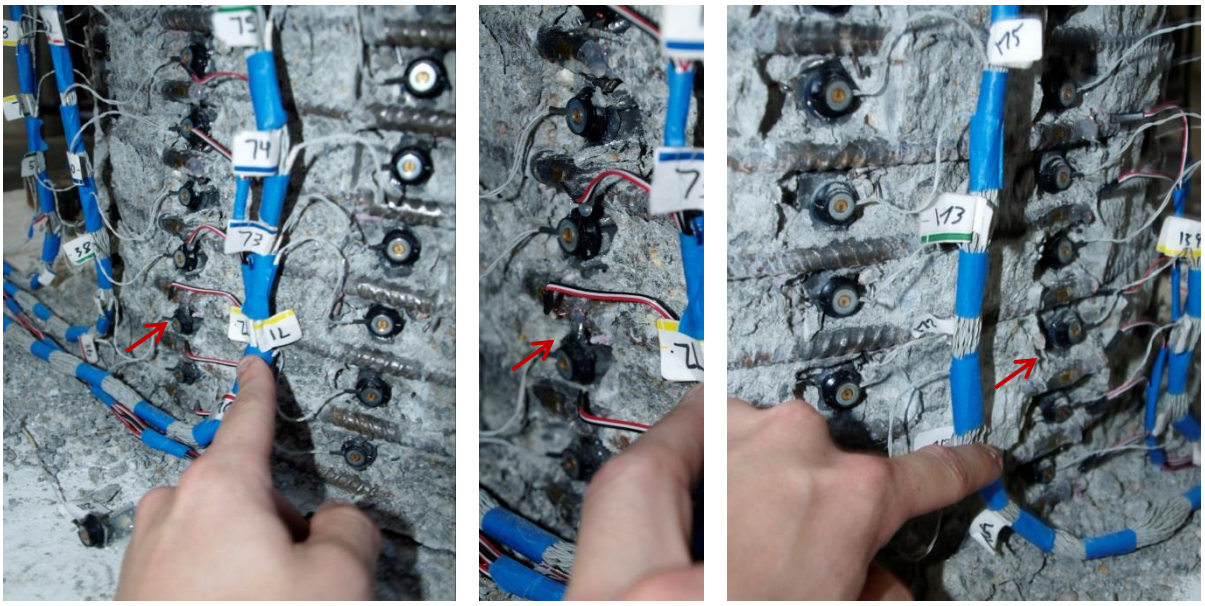

Figure 1.299 T16 – (Left and Middle) Buckling of Bar S3 during ($\mu_8^{+2} = 6.64$") and (Right) Buckling of Bar N2 and N3 during ($\mu_8^{-3} = 6.66$")

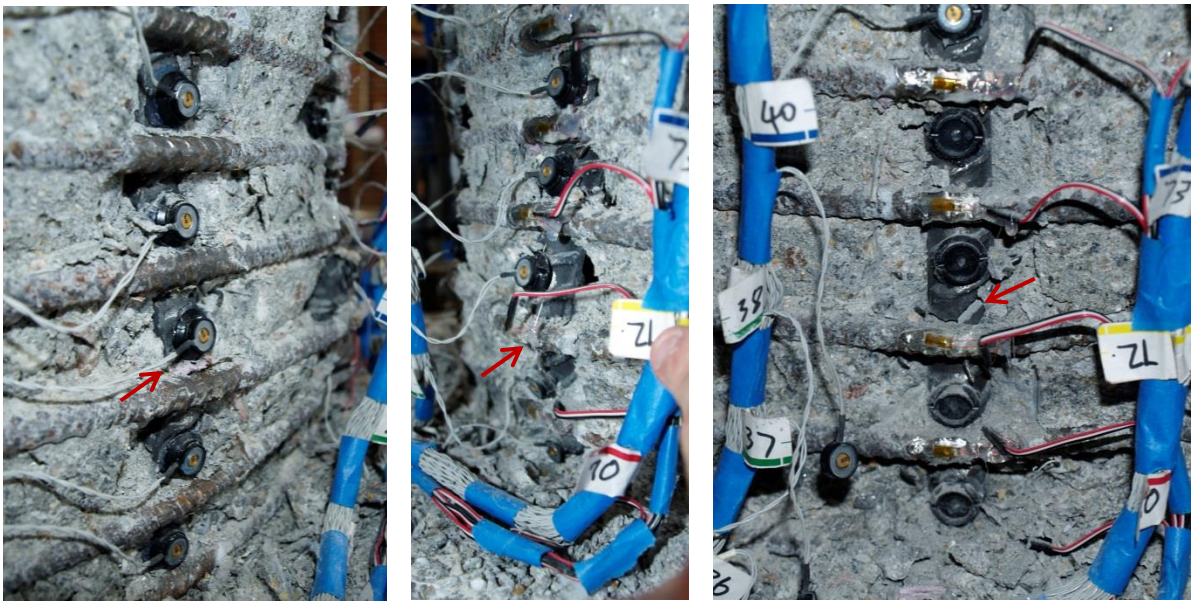

Figure 1.300 T16 – (Left) Buckling of Bar S2 during ($\mu_{10}^{+1} = 8.29$"), (Middle) Deformation in Bar S3 at ($\mu_{10}^{+1} = 8.29$"), and (Right) Rupture of Bar S3 during ($\mu_{10}^{-1} = -8.34$")

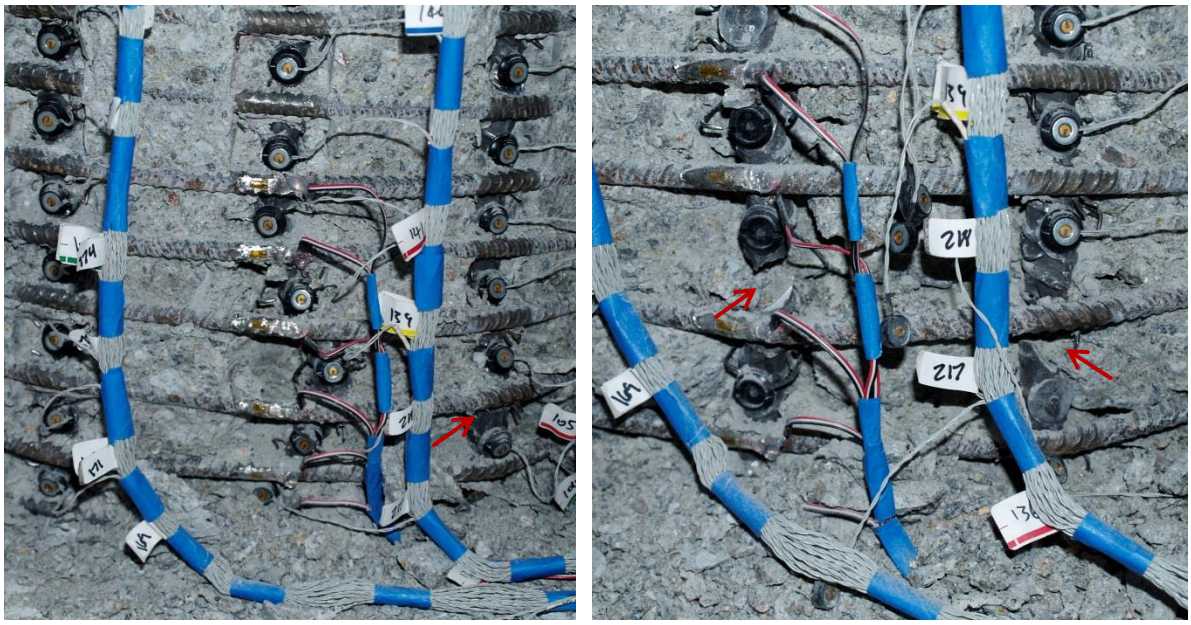

Figure 1.301 T16 – (Left) Buckling of N1 and N4 during ($\mu_{10}^{-1} = -8.34$") and (Right) Rupture of N2 and N3 during ($\mu_{10}^{+2} = 8.32$")

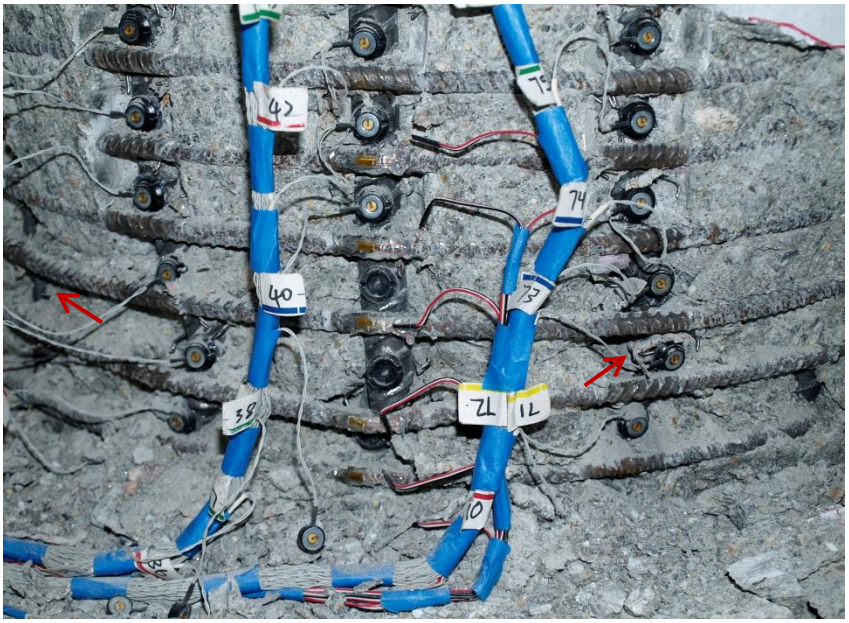

Figure 1.302 T16 – Buckling of S1 and S4 during ($\mu_{10}^{+2} = 8.32$")

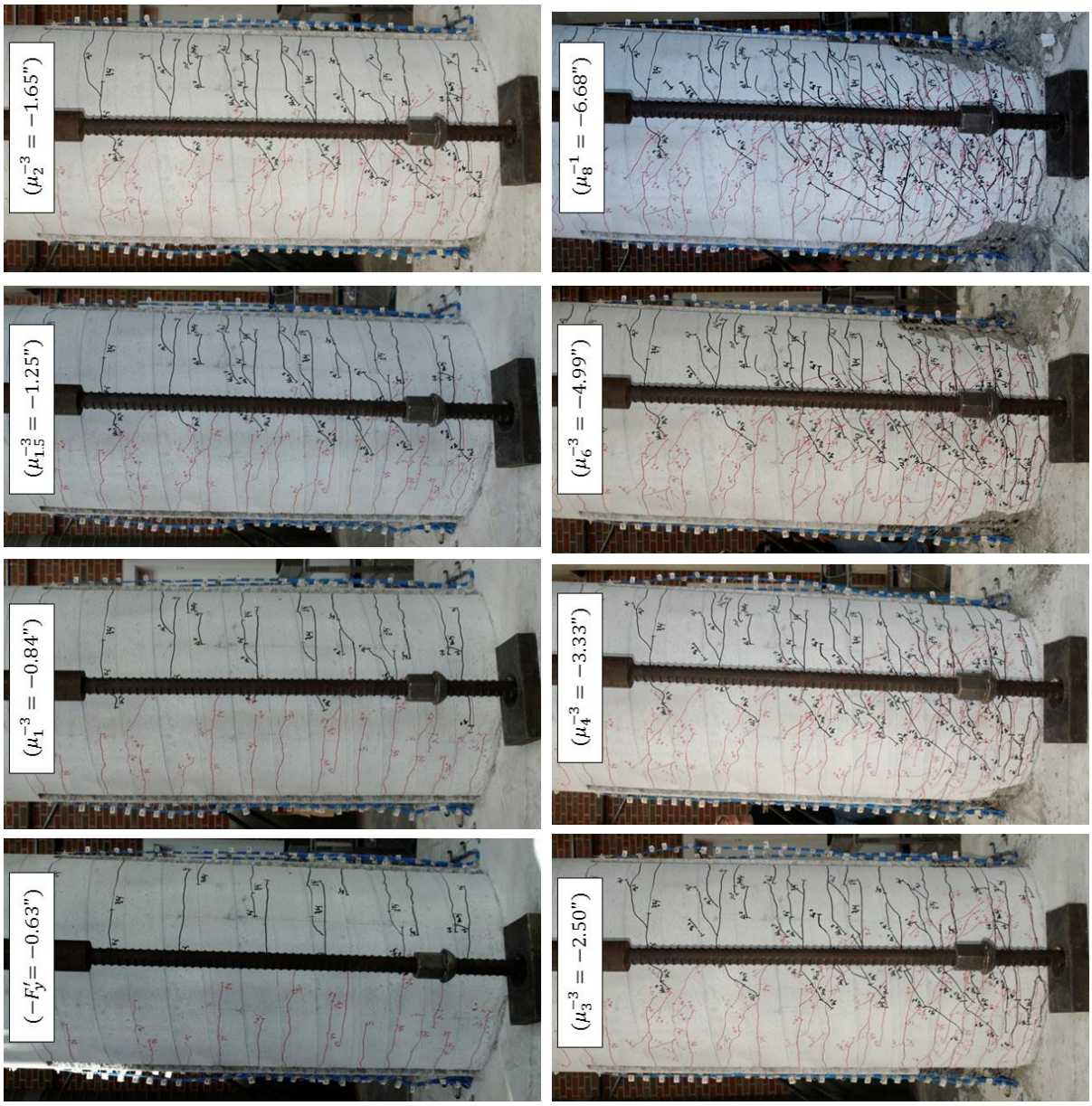

Figure 1.303 T16 – Crack Progression on the Back Side of the Specimen (North has Black Crack Markings while South has Red)

Test 16 – Symmetric Three Cycle Set (#3 @ 1.5") Strain Data Analysis

North Reinforcement

Extreme fiber vertical strain profiles for push and pull cycles appear in Figure 1.304 and Figure 1.305 respectively. These figures show both extreme fiber bars on the same graph to illustrate the effects of tension shift on strain profiles. Compressive strains are concentrated near the base of the column while tensile strains are fanned out to a greater height above the footing following the inclined crack distribution shown in Figure 1.303. The compressive vertical strain profile for north extreme fiber bar N3 during pull cycles appears in the left half of Figure 1.305. While the overall shape of the compressive strain profile matches past observations, a single gage length located 14.8" above the footing shows tensile strains during compressive cycles. The calculations for this gage length have been checked, and an explanation for why this may occur is not available. At this same height on adjacent bars N2 and N4, compressive strains were measured as expected.

A peak tensile strain of 0.056, located 3.40" above the footing, was measured for North extreme fiber bar N3 during ($\mu_8^{+3} = 6.65"$). Bar N3 buckled after reversal from this peak tensile strain. The relationship between tensile strain and displacement for this gage length appears in Figure 1.308. The solid line contains data during the push cycle loading up to the peak and the dashed line represents the subsequent reversal of load. Similar to previous tests, the moment curvature prediction for the relationship between strain and displacement using the PCK (2007) Lp Plastic Hinge Method begins to over predict the tensile strains at higher displacements at an increasing rate. The largest compressive strain of -0.0187, located 7.70" above the footing, was measured during ($\mu_8^{-1} = -6.68"$). The relationship between compressive strain and displacement for bar N3, gage length centered 3.4" above the footing, during pull cycles appears in Figure 1.309. Here the measured compressive strains deviate above or below the prediction depending on the displacement range, but the overall trend is captured.

The strains in the lowest six transverse steel layers restraining North extreme fiber bar N3 are plotted in Figure 1.307. The individual data points are from strain gages attached to each spiral layer at a specific height above the footing. The data points are connected with lines only to show trends for the particular displacement level. The vertical grey dashed line represents the yield strain of the transverse reinforcement. A single transverse steel layer, located 3.5" above the footing, entered the inelastic range during ($\mu_6^{-3} = -4.99$"). Compressive demands during ($\mu_8^{-1} = -6.68$") led to three layers of transverse steel going into the inelastic range. Prior to buckling, the strain in the three inelastic spiral layers increased during ($\mu_8^{-2} = -6.64$"), even though the displacement level remained the same. When bar N3 latter buckled during ($\mu_8^{-3} = -6.66$") the tensile strain for these spiral layers rapidly increased as they accommodated the outward deformation of the bar.

The strain hysteresis over the outward buckled region of bar N3, gage length located 3.40" above the footing, appears in Figure 1.312. It is clear that there was some measurable outward deformation during ($\mu_8^{-2} = -6.64$"), as shown by the blue arrow in Figure 1.312. Visible Buckling occurred after reversal from ($\mu_8^{+3} = 6.65$"), here the outward deformation begins to rapidly increase as indicated by the red arrow. The transverse steel strain gage hysteresis for the layer over the outward buckled region of bar N3 appears in Figure 1.313. The measurable deformation during ($\mu_8^{-2} = -6.64$"), shown by the blue arrow, increases the inelastic tensile strain in the spiral layer. Visible bar buckling after reversal from ($\mu_8^{+3} = 6.65$") leads to a rapid increase in the spiral strain causing the gage to go beyond its measurable range.

South Reinforcement

A peak tensile strain of 0.052 on bar S3 was measured 7.76" above the footing during ($\mu_8^{-1} = -6.68$"). The relationship between tensile strain and displacement for bar S3 is shown in Figure 1.310 for the gage length located 7.75" above the footing. The same comments on the accuracy of the moment curvature prediction with the PCK (2007) Lp Hinge Method for the North reinforcement bar N3 also apply to bar S3. A peak compression

strain of -0.0303 was measured 4.89" above the footing during ($\mu_8^{+1} = 6.64"$). The relationship between compressive strain and displacement for the gage length 4.89" above the footing on bar S3 during push cycles appears in Figure 1.311. The measured strains match the moment curvature prediction with the PCK (2007) Lp Hinge Method well through ductility two, but at higher ductility levels the measured compressive strains are significantly larger than the prediction. The peak compressive strain of -0.0303 measured in bar S3 is 57% larger than the original Mander (1988) ultimate concrete compressive strain of -0.0193.

The strains in the lowest six transverse steel layers restraining south extreme fiber bar S3 are plotted in Figure 1.306. Compressive demands during ($\mu_6^{+3} = 6.64"$), led to two layers of transverse steel exceeding the yield strain. Prior to buckling, the strain in the two inelastic spiral layers increased and a third layer entered the inelastic range during ($\mu_8^{+1} = 6.64"$). The strain hysteresis for the outward buckled region of extreme fiber bar S3, gage length located 3.37" above the footing, appears in Figure 1.314. The strain gage hysteresis for the spiral layer overlaying the outward buckled region of bar S3 appears in Figure 1.315. Visible buckling of bar S3 occurred after reversal from ($\mu_8^{-1} = -6.68"$). During this reversal, measurable outward deformation over bar S3 occurred as shown by the increased tensile strains in Figure 1.314. As the bar deformed outwards, the spiral restraint tensile strain began to rapidly increase until the strain gage exceeded its maximum value by going off scale.

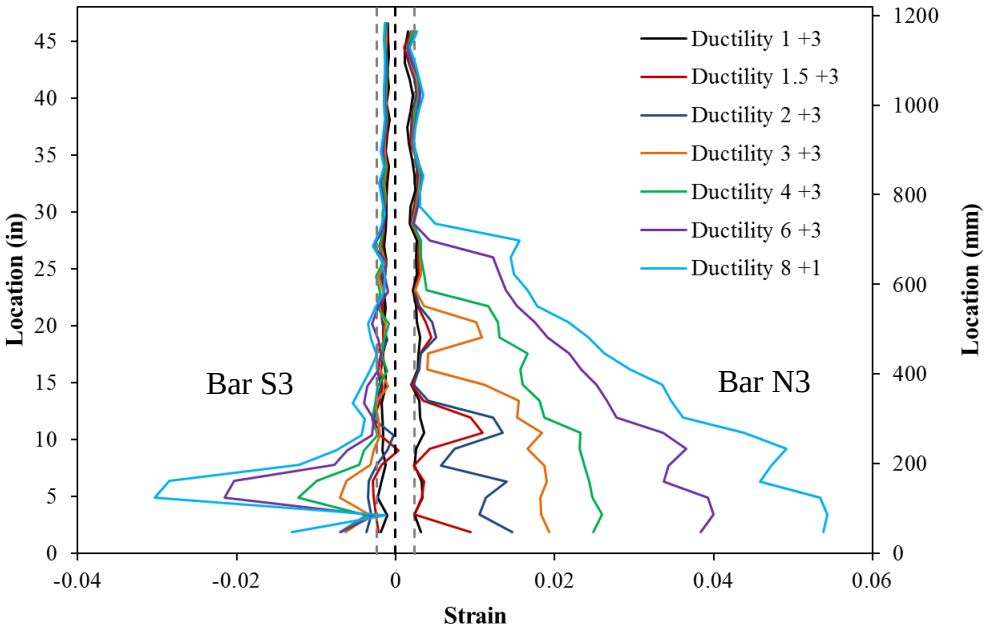

Figure 1.304 T16 – Extreme Fiber Vertical Strain Profiles during Push Cycles

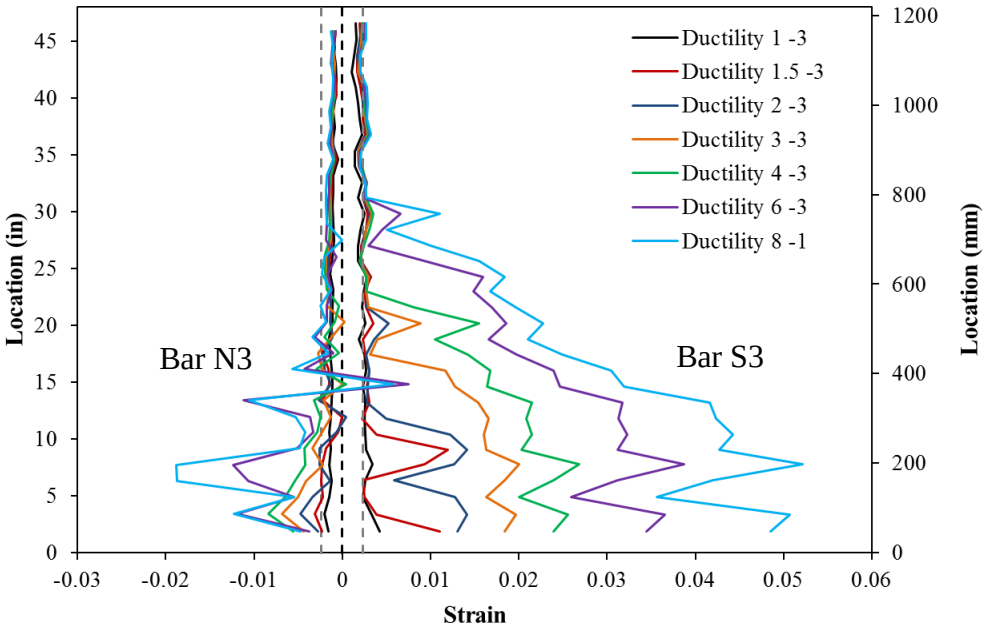

Figure 1.305 T16 – Extreme Fiber Vertical Strain Profiles during Pull Cycles

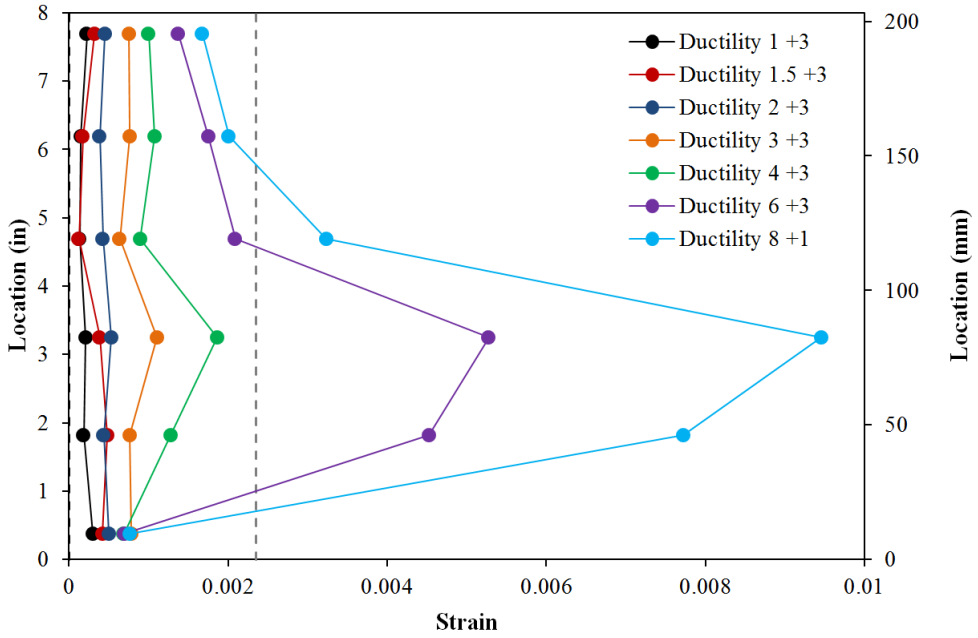

Figure 1.306 T16 – Transverse Steel Strains on the South Side during Push Cycles

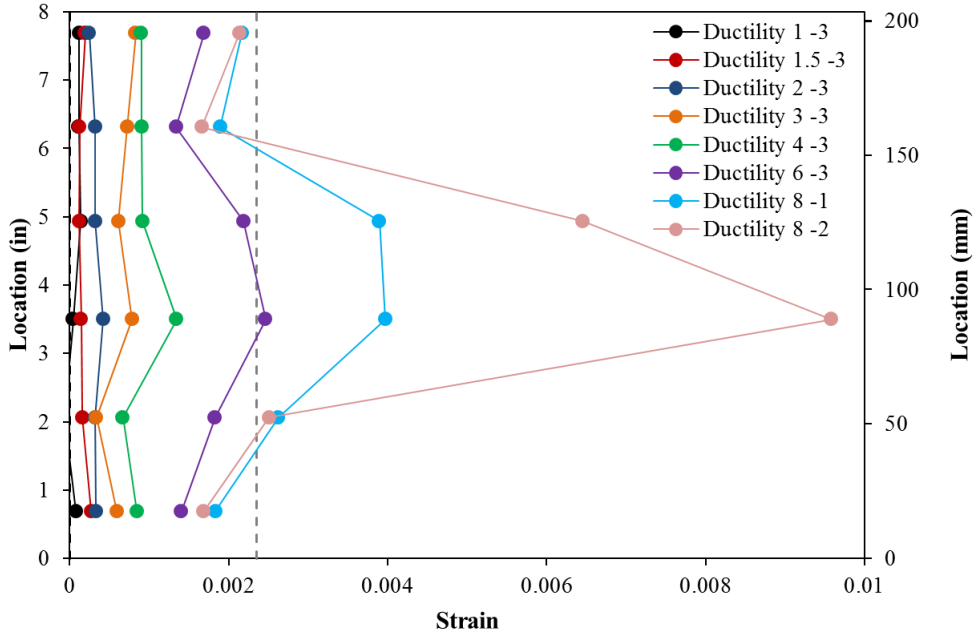

Figure 1.307 T16 – Transverse Steel Strains on the North Side during Pull Cycles

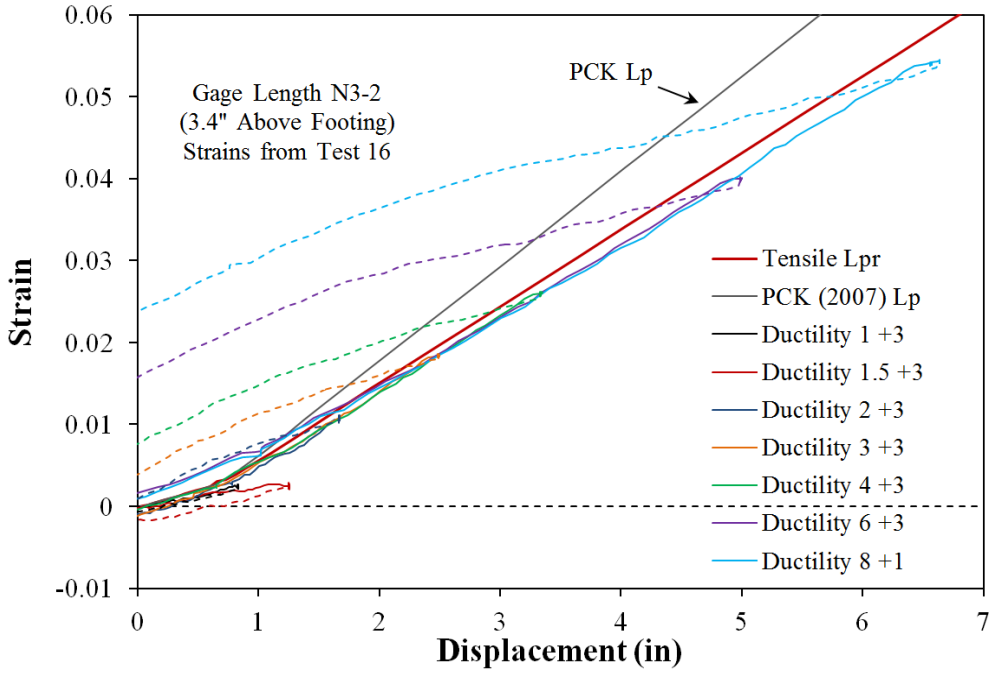

Figure 1.308 T16 – Tensile Strain-Displacement for Bar N3 during Push Cycles

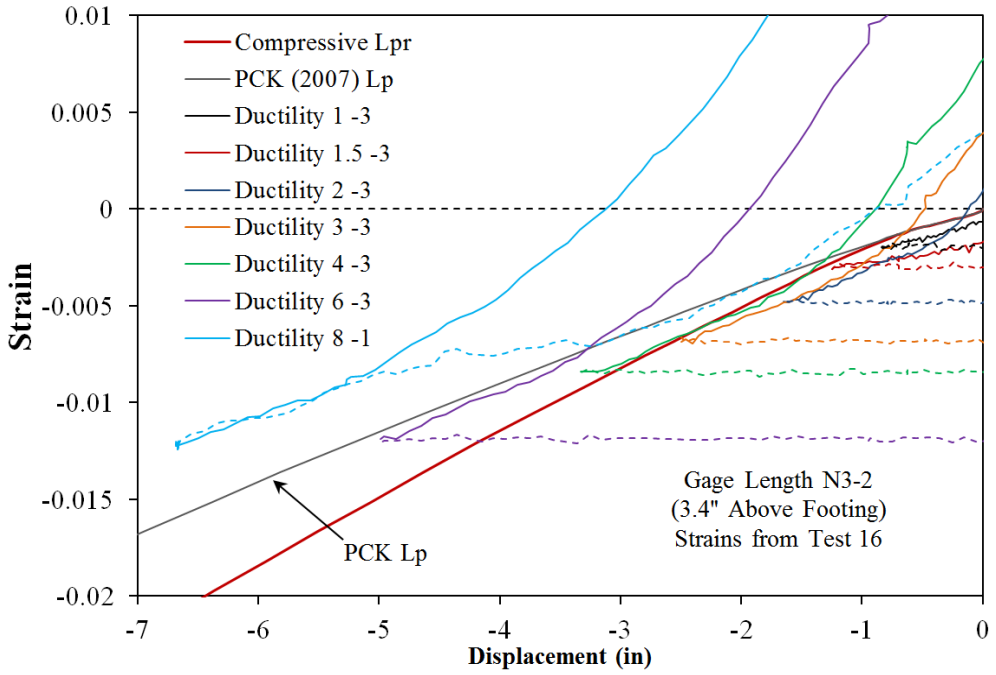

Figure 1.309 T16 – Compressive Strain-Displacement for Bar N3 during Pull Cycles

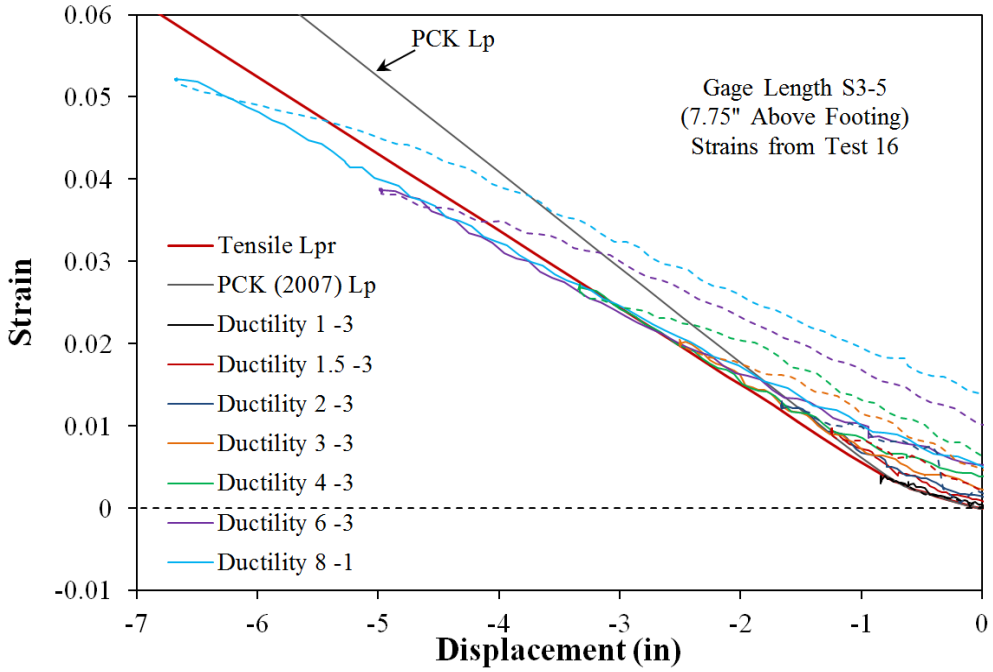

Figure 1.310 T16 – Tensile Strain-Displacement for Bar S3 during Pull Cycles

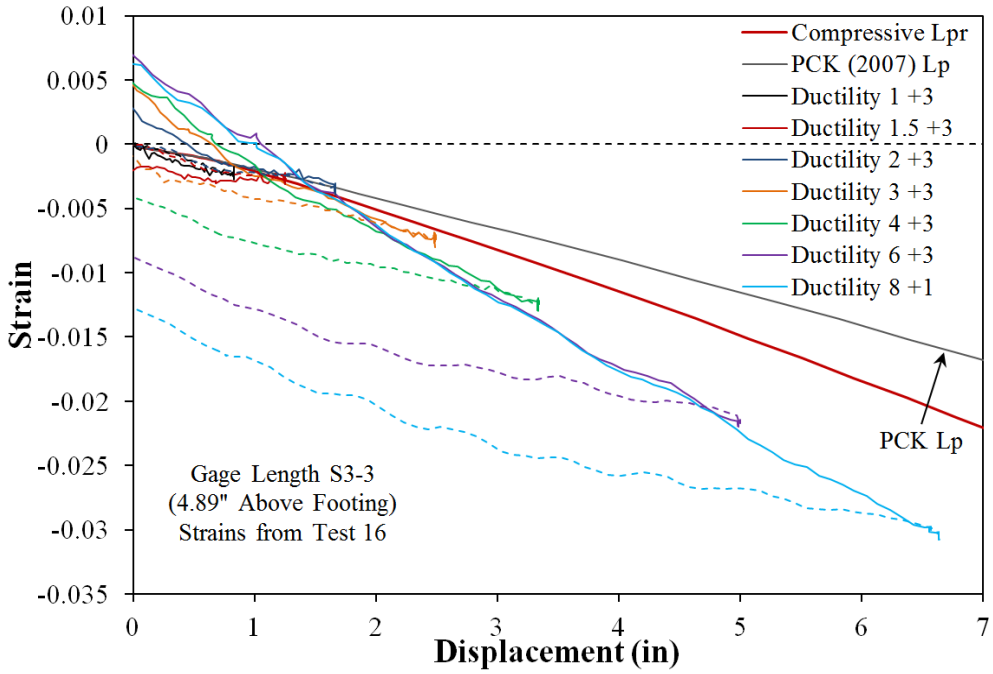

Figure 1.311 T16 – Compressive Strain-Displacement for Bar S3 during Push Cycles

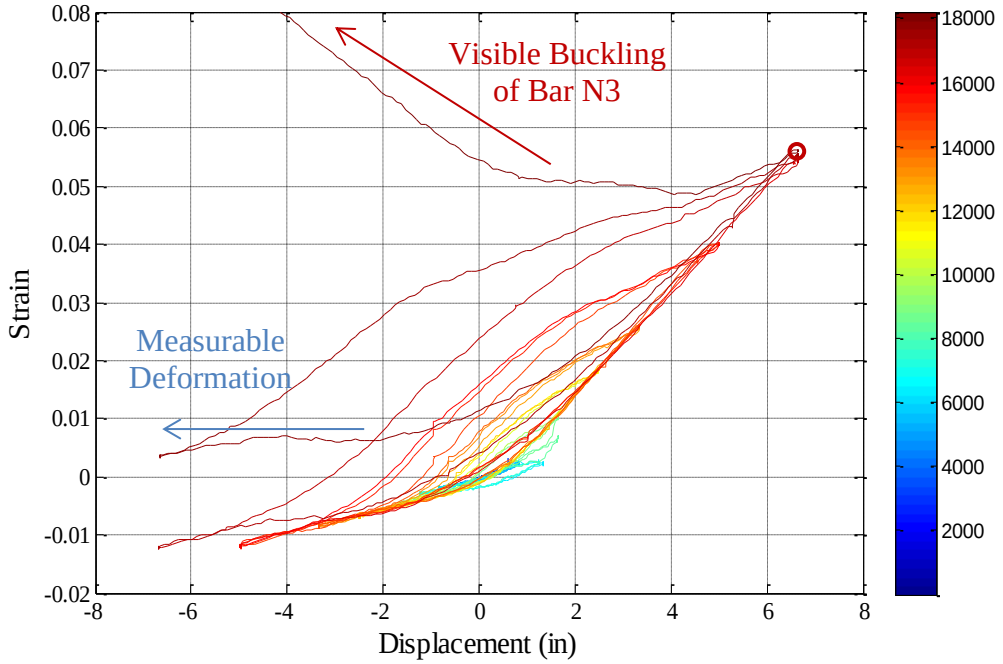

Figure 1.312 T16 – Strain Hysteresis over the Buckled Region of Bar N3 (3.4" Above)

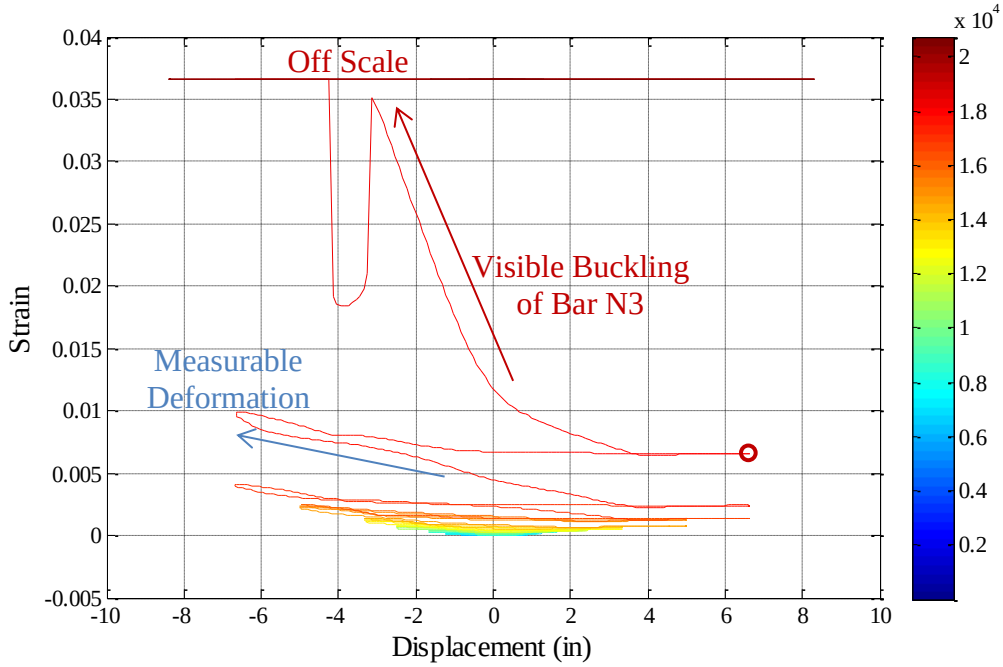

Figure 1.313 T16 – Spiral Strain Gage Hysteresis over the Buckled Region of Bar N3

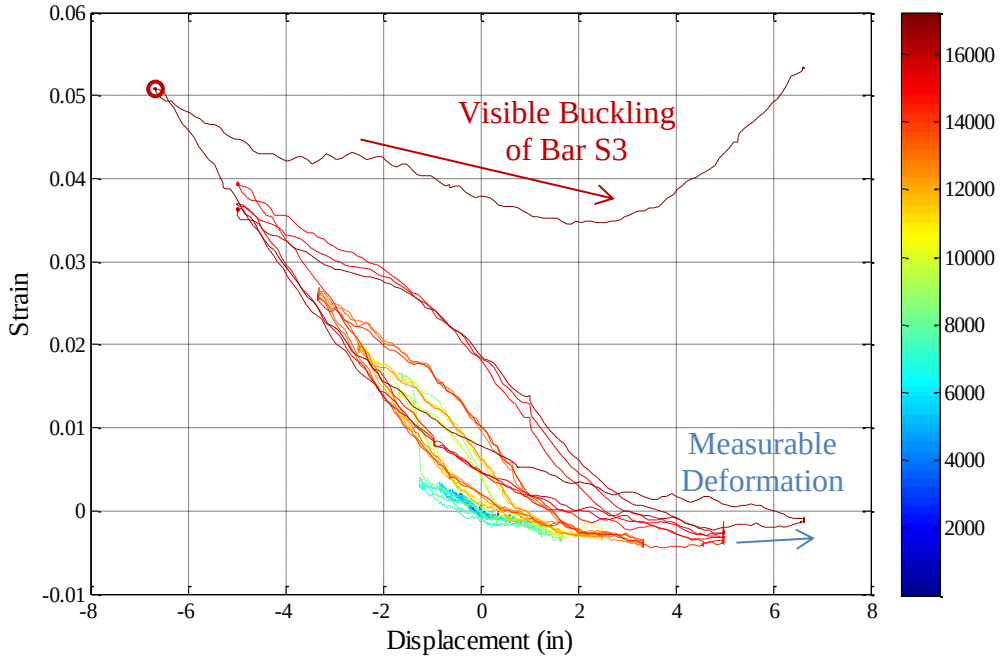

Figure 1.314 T16 – Strain Hysteresis over the Buckled Region of Bar S3 (3.37" Above)

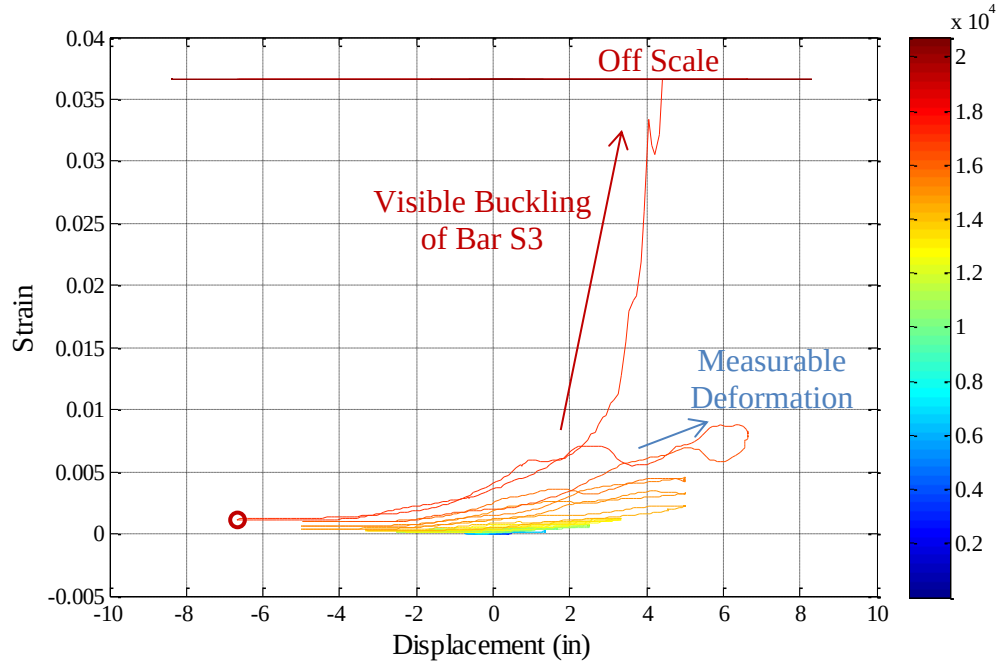

Figure 1.315 T16 – Spiral Strain Gage Hysteresis over the Buckled Region of Bar S3

Test 16 – Cyclic Load History (#3 @ 1.5") Curvature and Strain Penetration Data

The cross section curvature for each horizontal section above the footing is determined by connecting the strain measurements from all six instrumented bars with a least squared error line. The curvature is then extracted from the slope of the least squared error line, see Figure 1.316. Vertical curvature profiles are plotted for push and pull cycles as shown in Figure 1.317 and Figure 1.318 respectively. These figures show that plastic curvatures have a linear distribution at higher displacement ductility levels. The extent of plastic curvatures above the footing can be calculated by determining where the linear plastic curvature distribution intersects the triangular yield curvature distribution, shown as a grey dashed line. The dashed lines for each curvature distribution represent a least squared error linear fit to the plastic portion of the measured curvatures. The measured spread of plasticity as a function of curvature ductility appears in Figure 1.121.

The target marker on each bar placed closest the footing-column interface can be used to create slip hysteresis and horizontal slip profiles attributable to strain penetration. The slip hysteresis for extreme fiber bars N3 and S3 appear in Figure 1.319 and Figure 1.320 respectively. If the tensile and compressive slip of all of the instrumented bars is plotted along the cross section depth, the base rotation attributable to strain penetration may be calculated. The slip profiles for push and pull cycles appear in Figure 1.321 and Figure 1.322 respectively. The rotation of the base section can be extracted from the slope of the least squared error line connecting all six measured bar slips.

Combining the curvatures over the instrumented region (4ft above the footing), bar slip profiles, and an elastic curvature assumption above the instrumented region, the top column displacement can be calculated. This top column displacement calculated from the Optotrak system is compared to the top column displacement measured with a string potentiometer at the center of loading in Figure 1.323. The calculated displacements match well over the entire range of response indicating that shear displacements are negligible in comparison to flexural displacements.

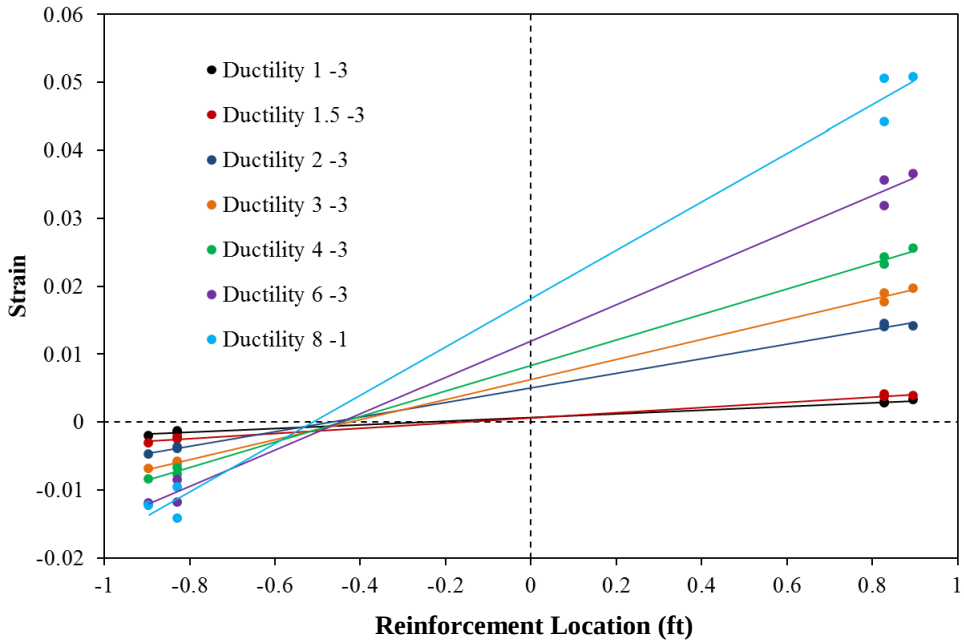

Figure 1.316 T16 – Cross Section Curvature from Slope of Regression Line

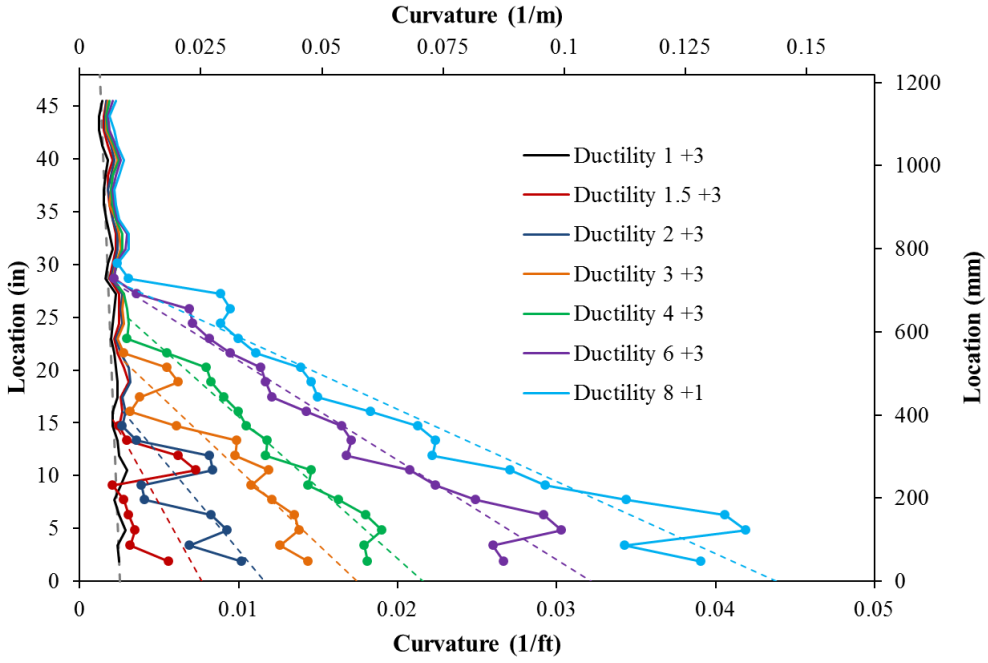

Figure 1.317 T16 – Curvature Profiles during Push Cycles with Plastic Regression

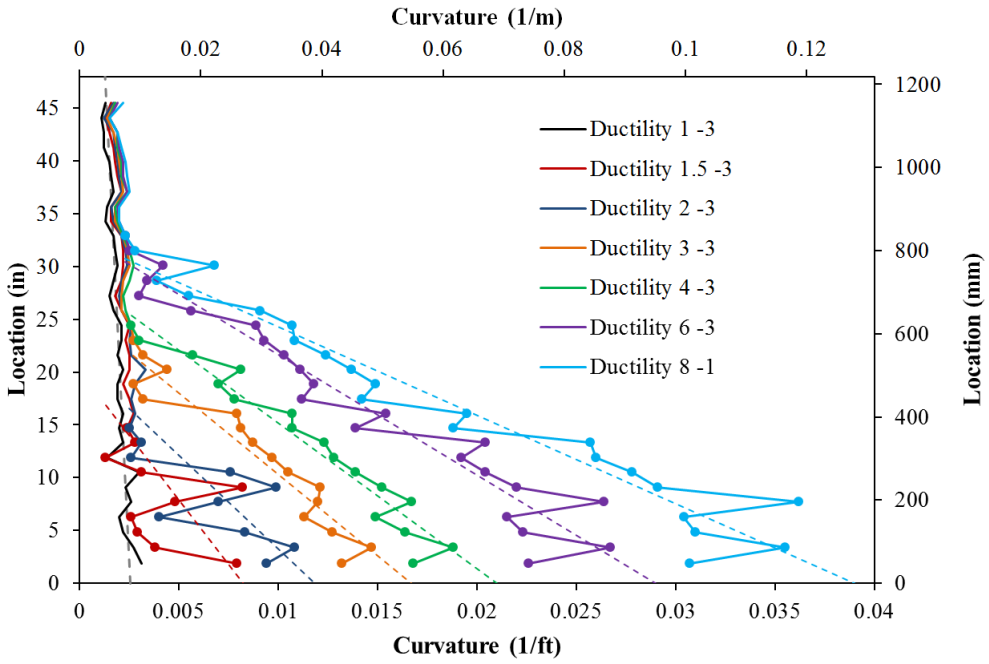

Figure 1.318 T16 – Curvature Profiles during Pull Cycles with Plastic Regression

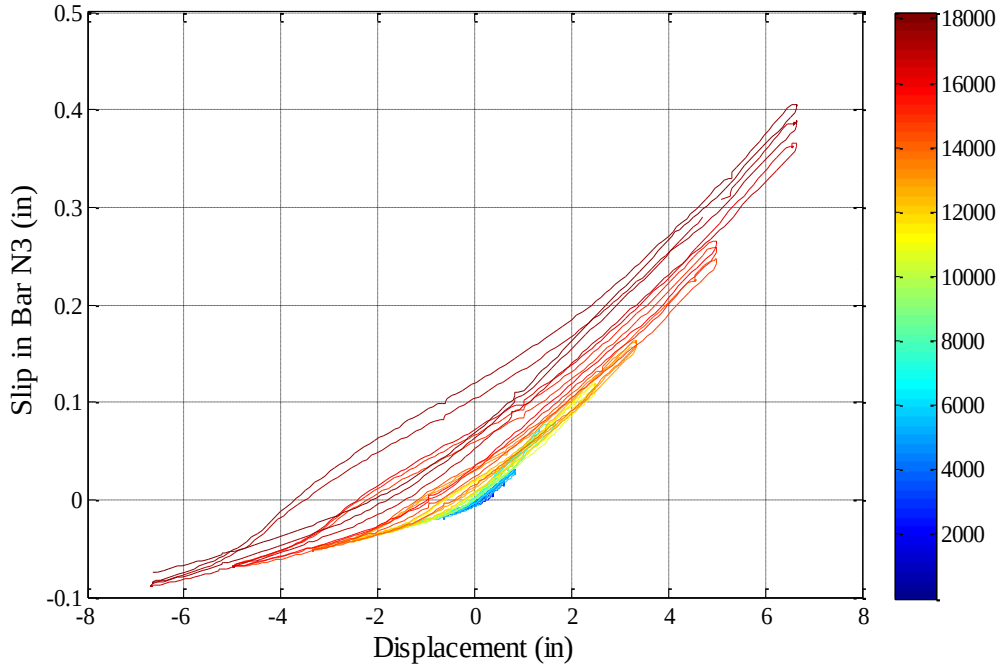

Figure 1.319 T16 – Extreme Fiber Bar N3 Slip Hysteresis due to Strain Penetration

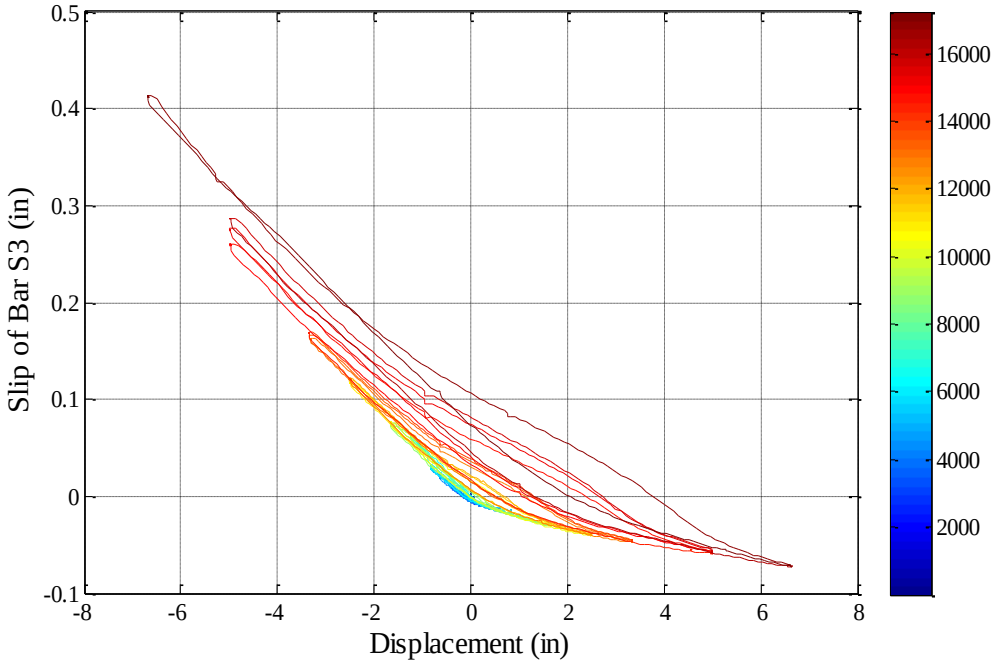

Figure 1.320 T16 – Extreme Fiber Bar S3 Slip Hysteresis due to Strain Penetration

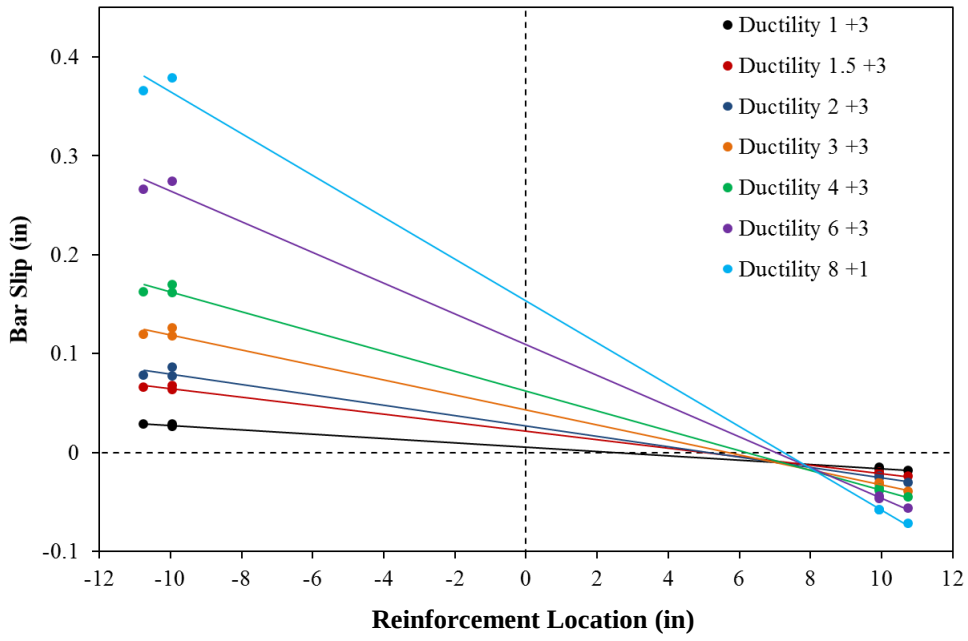

Figure 1.321 T16 – Fixed End Rotation due to Strain Penetration during Push Cycles

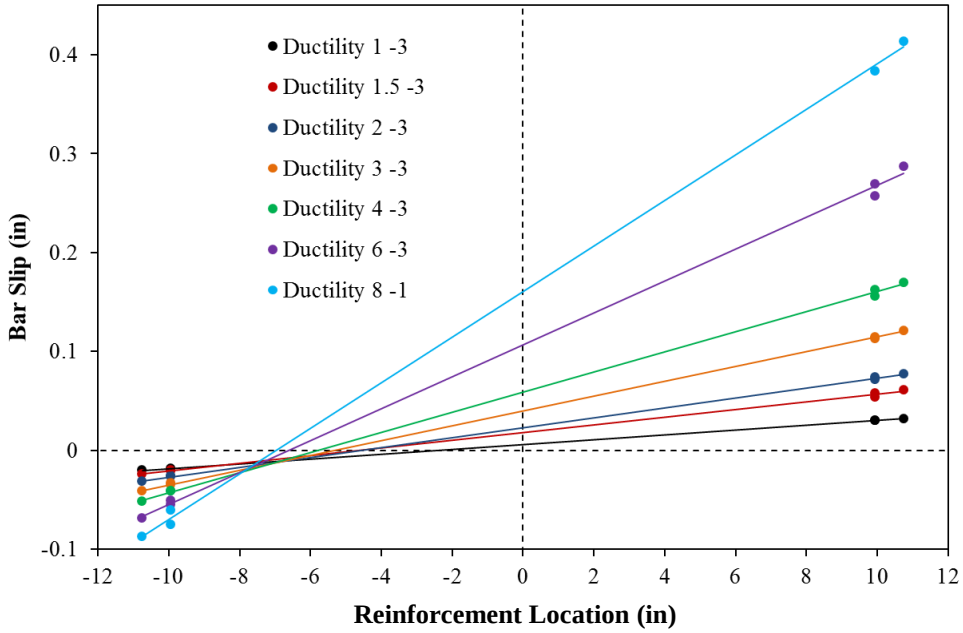

Figure 1.322 T16 – Fixed End Rotation due to Strain Penetration during Pull Cycles

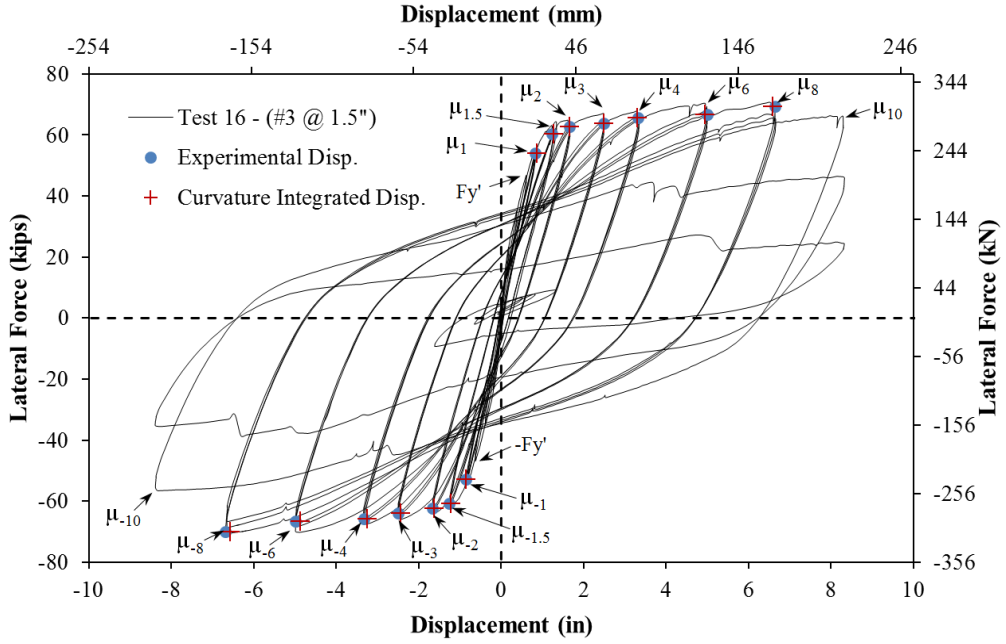

Figure 1.323 T16 – Comparison of Measured and Optotrak Integrated Displacements

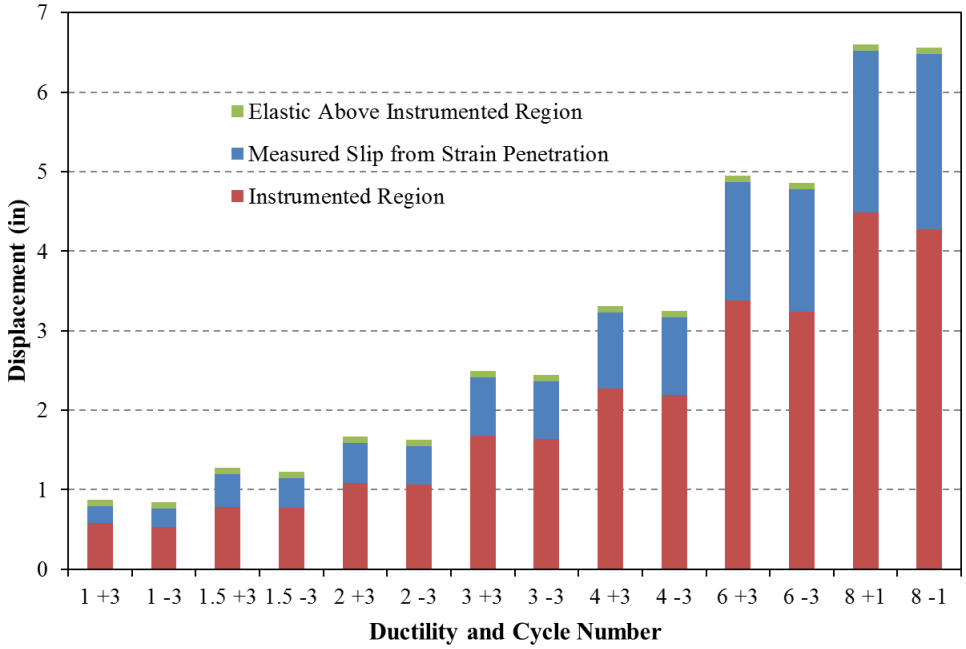

Figure 1.324 T16 – Optotrak Integrated Deformation Components

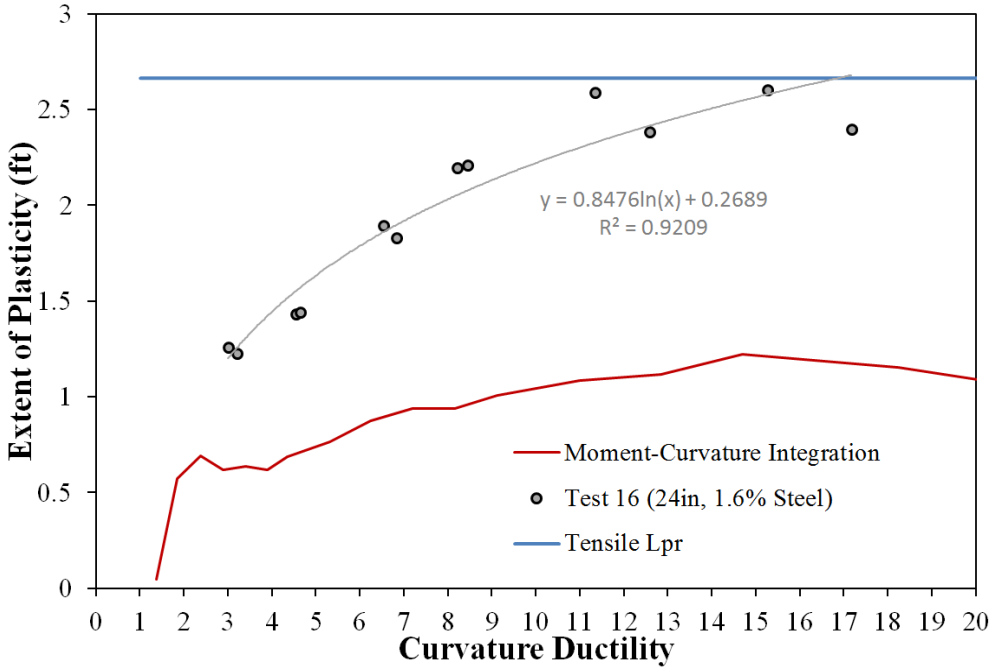

Figure 1.325 T16 – Measured Spread of Plasticity (Circular Data Points)

1.2.5 Test 17 – Chile 1985 Earthquake LH with #3 Spiral at 1.5" (1.3%)

Table 1.25 Observational Summary for Test 17 – Chile 1985 Earthquake LH with #3 Spiral at 1.5" (1.3%)

VALUES OF INTEREST:	
Concrete Compressive Strength:	$f_c' = 7590\ psi$
Axial Load:	$P = 170\ kips$
Analytical First Yield Force:	$F_y' = 47.5\ kips$
Experimental First Yield Displacement:	$\Delta_y' = 0.62"$ *From Test 16
Analytical Nominal Moment Capacity:	$M_n = 509.2\ kip * ft$
Equivalent Yield Displacement:	$\Delta_y = 0.83"$
Maximum Lateral Force:	$72.0\ kips$
Maximum Lateral Displacement:	$\mu_{9.0}^{32.76\ sec} = 7.49"$
Failure Mode:	No Significant Damage from Earthquake LH.
DAMAGE OBSERVATIONS:	
First Cracking North:	During cycle to $\mu_{1.0}^{10.50\ sec} = 0.84"$
First Cracking South:	During cycle to $\mu_{-0.6}^{10.29\ sec} = -0.49"$
Cover Concrete Crushing North:	$\mu_{-1.9}^{16.27\ sec} = -1.60"$
Cover Concrete Crushing South:	$\mu_{2.0}^{15.32\ sec} = 1.67"$
Transverse Steel Yield North:	At $-4.02"$ otwt $\mu_{-5.4}^{18.52\ sec} = -4.49"$
Transverse Steel Yield South:	At 4.5" otwt $\mu_{9.0}^{32.76\ sec} = 7.49"$

*$\mu_{9.0}^{32.76\ sec} = 7.49"$ represents a push cycle 32.76 seconds into the earthquake load history which reached a peak displacement of 7.49" and a displacement ductility of 9.0

Table 1.26 Observational Summary for Test 17b – Symmetric Three Cycle Set Aftershock LH

DAMAGE OBSERVATIONS: During Symmetric Three Cycle Set Post Earthquake LH	
Longitudinal Bar Buckling North:	Reversal from $\mu_6^{+2} = 4.99"$
Longitudinal Bar Buckling South:	Reversal from $\mu_6^{-2} = -5.00"$
Failure Mode:	Specimen Saved as a Repair Candidate after Each Extreme Fiber Longitudinal Bar Buckled

$*\mu_6^{-2} = -5.00"$ represents the second pull cycle of displacement ductility six

Table 1.27 Strain Data Summary for Test 17 and Test 17b – Chile 1985 EQ LH and Cyclic Aftershock LH

MATERIAL STRAINS:	
Cover Concrete Crushing North:	$\varepsilon_s = 0.0043\ (compression)$
Cover Concrete Crushing South:	$\varepsilon_s = 0.0043\ (compression)$
Transverse Steel Yield North:	$\varepsilon_s = 0.0148\ (compression)$
Transverse Steel Yield South:	$\varepsilon_s = 0.0168\ (compression)$
Longitudinal Bar Buckling North:	$\varepsilon_s = 0.055\ (peak\ tension\ prior\ to\ bb)$
	$\varepsilon_s = 0.039\ (peak\ comp.\ prior\ to\ bb)$
Longitudinal Bar Buckling South:	$\varepsilon_s = 0.039\ (peak\ tension\ prior\ to\ bb)$
	$\varepsilon_s = 0.043\ (peak\ comp.\ prior\ to\ bb)$
Mander (1988) Ultimate Concrete Compression Strain, $\varepsilon_{cu} = 0.0179$	

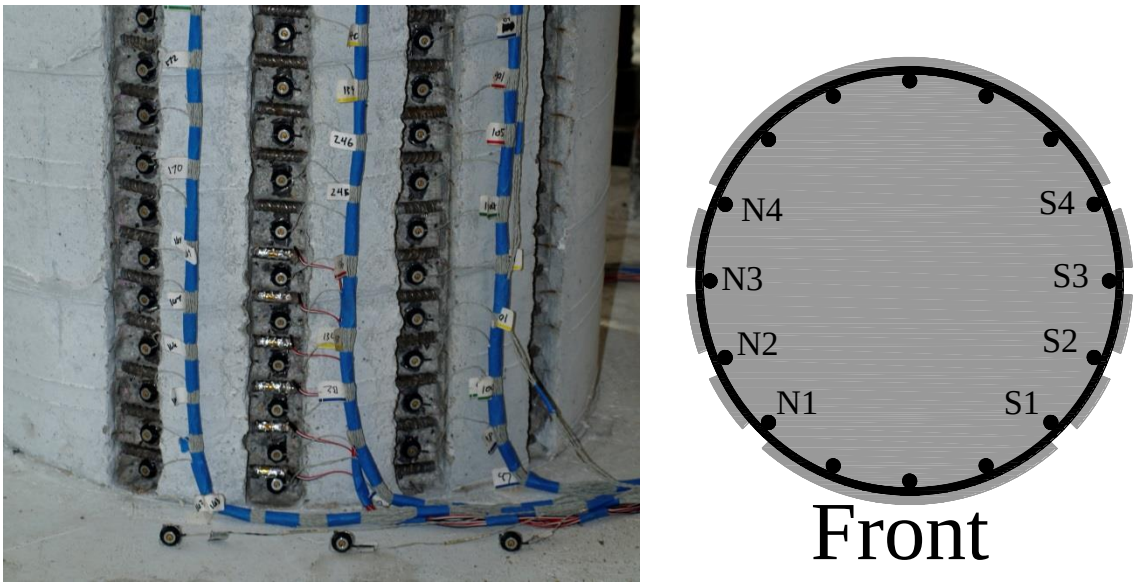

Figure 1.326 T17 – Cross Section Bar Designation and Target Marker Application

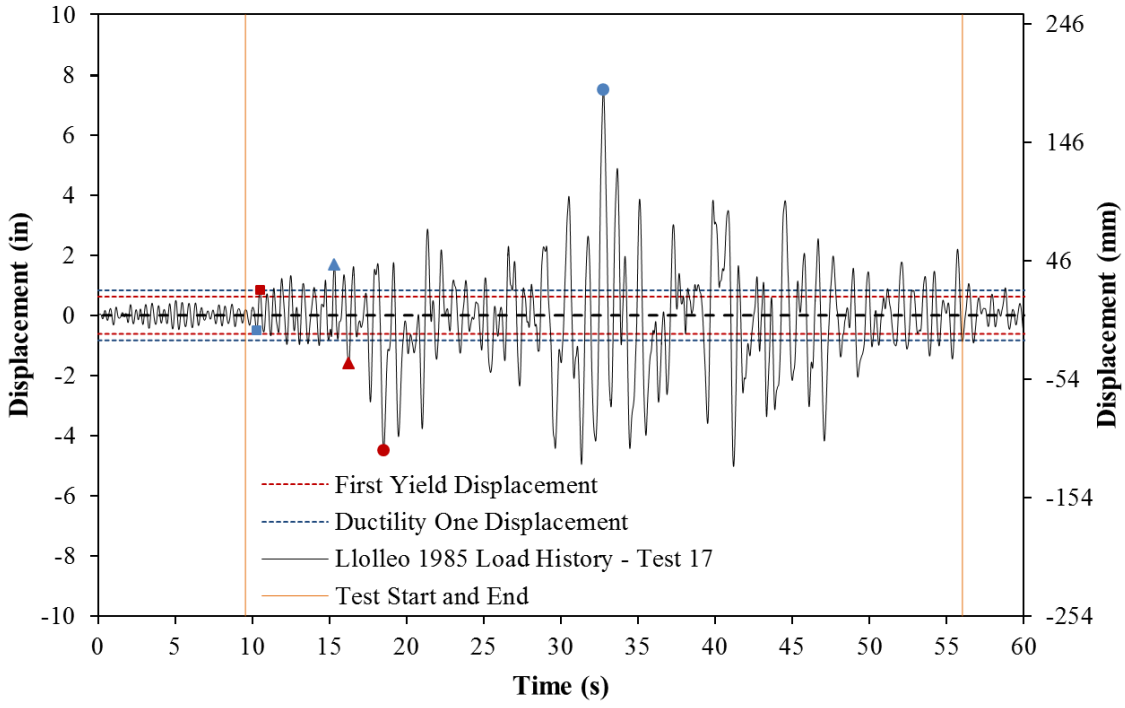

Figure 1.327 T17 – Llolleo Chile 1985 Earthquake Load History

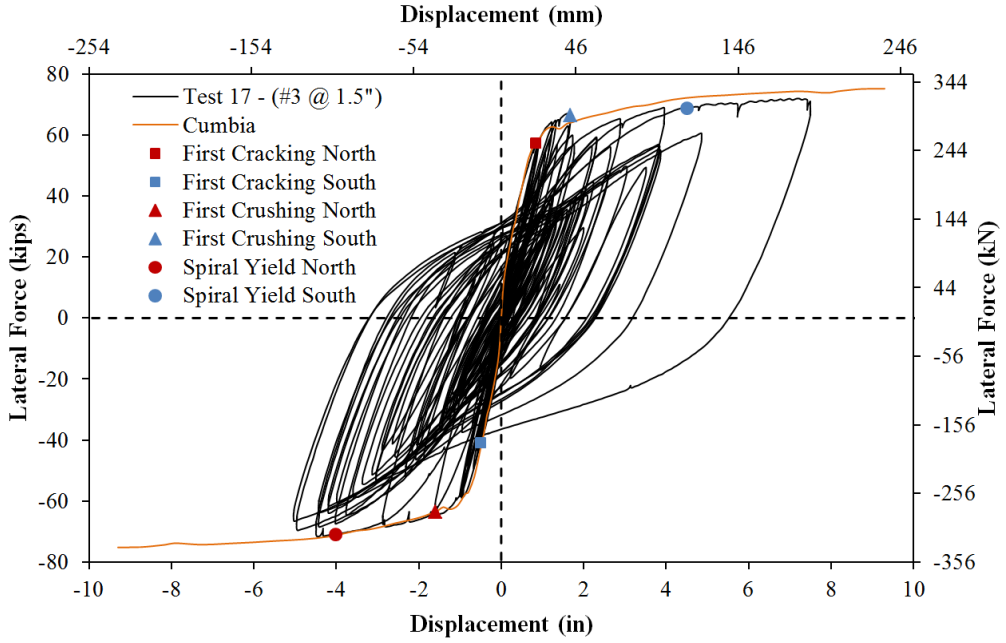

Figure 1.328 T17 – Lateral Force vs. Top Column Displacement Hysteretic Response

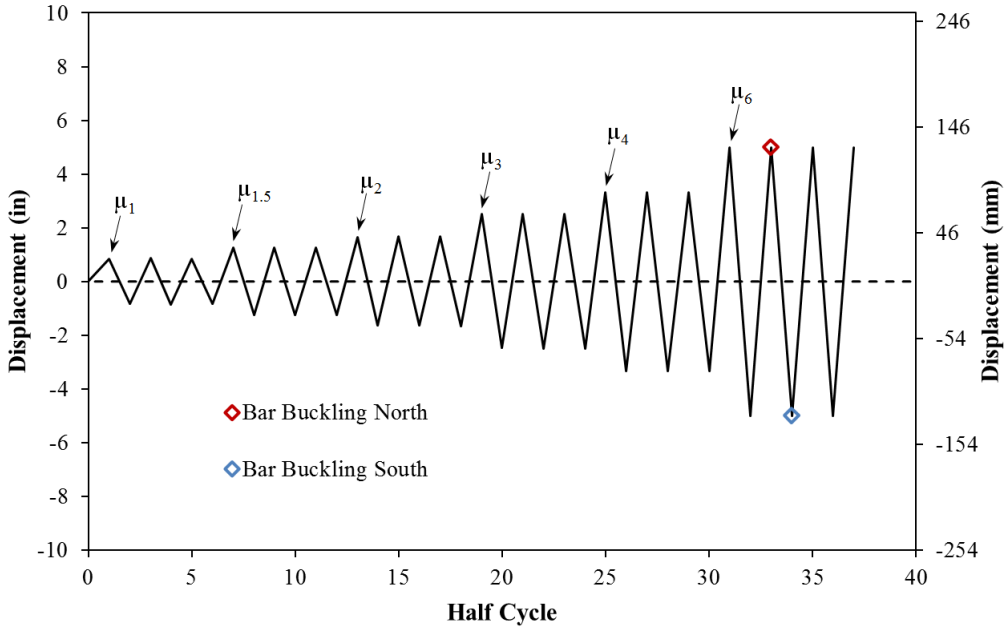

Figure 1.329 T17b – Symmetric Three Cycle Set Aftershock Load History

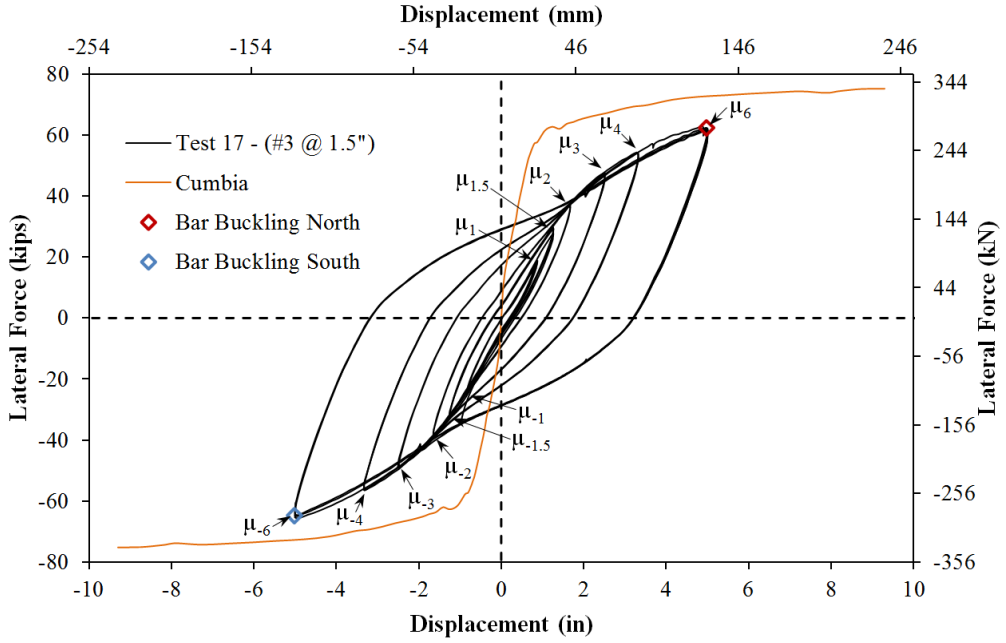

Figure 1.330 T17b – Lateral Force vs. Top Column Displacement Hysteretic Response

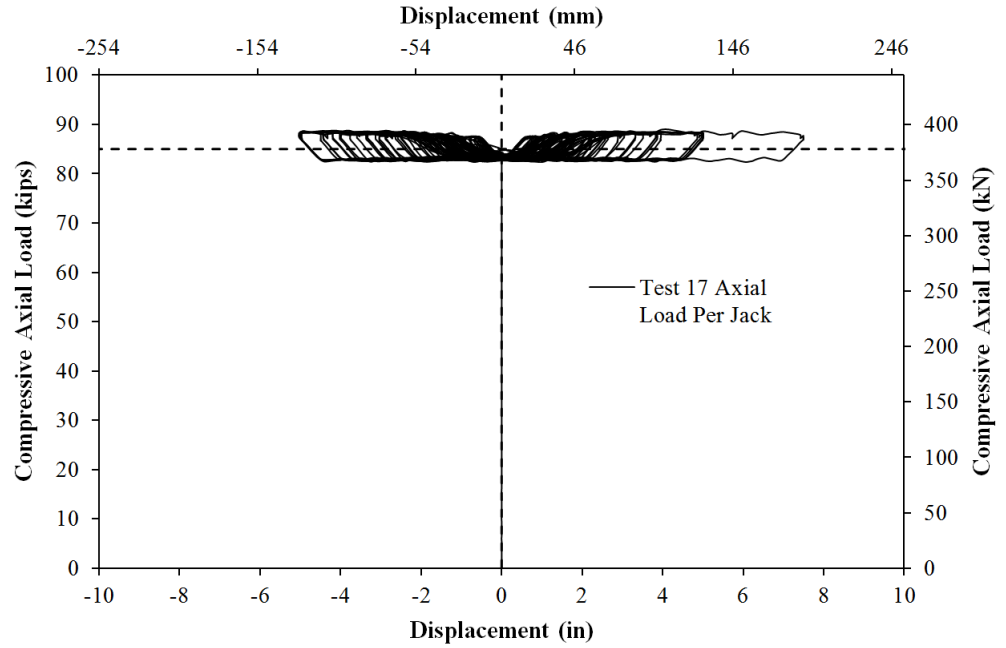

Figure 1.331 T17 – Compressive Axial Load from One Jack (Total = 2*Value)

Test 17 – Llolleo Chile 1985 Earthquake Load History (#3 @ 1.5")

A scaled version of the Llolleo 1985 Chile earthquake load history, with a peak displacement ductility of nine, was chosen for Test 17. The top column displacement history, in Figure 1.327, was obtained using numerical analysis in OpenSees with a force-based fiber element to model the column and a zero-length strain penetration element to model the effects of strain penetration. The acceleration input of the Llolleo 1985 Chile earthquake was multiplied by 2.16 to produce a peak displacement ductility of nine. The resulting experimental lateral force vs. top column displacement response for the Llolleo 1985 Chile earthquake load history appears in Figure 1.328. The first yield displacement for Test 16, which contained the same spiral detailing as Test 17, was obtained as an average of the experimental first yield push and pull cycles ($\Delta'_y = 0.62"$). To determine if this first yield displacement is applicable to Test 17, the tensile strain profile at ($\Delta'_y = 0.62"$) for each extreme fiber bar appears in Figure 1.332. At the first yield displacement, the tensile strains in both extreme fiber reinforcing bars reached yield. The equivalent yield displacement, used to determine the displacement ductility levels ($\mu_{\Delta n} = \mathrm{n} * \Delta_y$), was then calculated as $\Delta_y = \Delta'_y(M_n/M'_y) = 0.84"$ for Test 16. The displacement ductility levels for Test 16, see Figure 1.332, are also applicable for Test 17.

Previous Tests 8-12 focused on the effects of load history on reinforcement buckling. For the detailing of Tests 8-12 (#3 @ 2", 1% volumetric ratio), it was found that reinforcement bar buckling occurred during displacement ductility eight of a three cycle set laboratory load history. Subsequent earthquake load history based tests scaled to displacement ductility (Test 8 - Chile 2010, 8.7) and (Test 10 - Chi-Chi 1999, 8.9) did not produce buckling of longitudinal steel. Instead, earthquake load histories scaled to ductility ten (Test 11 - Kobe 1995, 10) and (Test 12 – Japan 2011, 9.9) buckled reinforcing bars. The balanced repeated cycles of increasing ductility of the symmetric three-cycle-set load history appear to be more damaging than the load histories produced by historical earthquake records. To buckle reinforcing bars, the earthquake load histories were required to reach larger peak displacement ductility.

For the previous Test 16 (also #3 @ 1.5", 1.3% volumetric ratio), a column with the same transverse steel detailing produced bar buckling during ductility eight of a symmetric three cycle set load history. The Llolleo 1985 Chile load history for Test 17 was scaled to displacement ductility nine to further evaluate the effect of load history on accumulated strains in the longitudinal and transverse steel. Based on previous test observations, an earthquake load history scaled to ductility nine is not expected to produce bar buckling. The Llolleo 1985 Chile top column displacement history contains a large number of inelastic reversals of generally high amplitude both before and after the peak displacement. The push direction of loading is dominated by a single large push cycle to ductility nine with many smaller reversals which range between ductility four and six. In the opposing direction of loading, there are a large number of reversals within the range of ductility four to six which appear both before and after the peak displacement.

After conclusion of the Llolleo 1985 Chile load history, the specimen had crushed cover concrete and degraded stiffness, but the longitudinal steel had not visibly buckled. The state of the specimen resembled Tests 8 and 10 where the reinforcement did not visibly buckle during the earthquake load history. Specimens 8, 10, and now 17 were subjected to a symmetric three cycle set aftershock to study the effect of degraded stiffness and strain accumulation on post-earthquake performance during a controlled load history. The displacement history and hysteretic response for the symmetric three-cycle-set aftershock study for Test 17 appear in Figure 1.329 and Figure 1.330 respectively. Visible bar buckling was observed on both sides of the specimen during ductility six of the cyclic aftershock study of Test 17b.

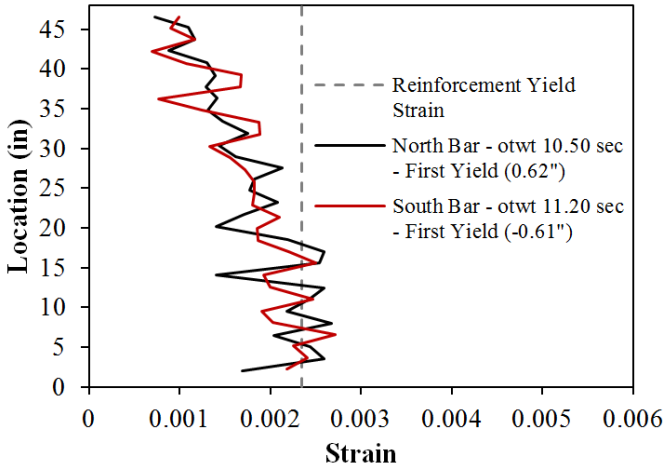

Analytical Fy'	46.80	kips
Experimental Δy'	0.62	in
Analytical My'	374.44	kip-ft
Analytical Mn	503.19	kip-ft
μ1	0.83	in
μ1.5	1.25	in
μ2	1.66	in
μ3	2.50	in
μ4	3.33	in
μ6	4.99	in
μ8	6.65	in
μ10	8.32	in
μ12	9.98	in

Figure 1.332 T17 – (Left) Tensile Strain Profiles at the First Yield Displacement of Test 16 and (Right) Displacement Ductility Levels from Test 16 (Also Apply for Test 17)

Test 17 – Llolleo Chile 1985 Earthquake (#3 @ 1.5") Experimental Observations

The Llolleo 1985 Chile earthquake load history begins with a series of cycles below the first yield displacement, followed by cycles below ductility two as shown in Figure 1.327. Since the initial elastic cycles are not expected to affect the relationship between strain and displacement during later inelastic cycles, they were excluded from the experimental load history to save time. Crack widths on the North side of the specimen reached 0.45mm at approximate 6" spacing during ($\mu_{1.0}^{10.50\,sec} = 0.84$"), as shown in the left photo of Figure 1.333. The format for the cycle naming system is as follows: ($\mu_{1.0}^{10.50\,sec} = 0.84$") represents the peak of the push cycle 10.50 seconds into the Llolleo earthquake load history which reached a displacement of 0.84" and a displacement ductility of 1.0. During ($\mu_{1.5}^{11.91\,sec} = 1.22$"), the largest crack width on the North side of the specimen increased to 1mm. Crack widths on the South side of the specimen reached 0.5mm in width and approximate 6" spacing at ($\mu_{-1.2}^{12.25\,sec} = -0.96$"), see the right two photos of Figure 1.333.

Visible flaking of cover concrete, which precedes crushing, was observed on the South side of the specimen during ($\mu_{1.6}^{12.50\,sec} = 1.32"$), as shown in the left photo of Figure 1.334. Cover concrete crushing over the lowest 5" of the South side of the column occurred during ($\mu_{2.0}^{15.32\,sec} = 1.67"$), see the right photo of Figure 1.334. Also during this cycle, crack widths on the North side of the specimen reached 1.5mm at approximate 6" spacing. Cover concrete crushing on the North side of the specimen over 3.5" occurred during ($\mu_{-1.9}^{16.27\,sec} = -1.60"$), see the left photo of Figure 1.335. The extent of crushing on the North side increased to 18.5" above the footing during ($\mu_{-3.5}^{17.66\,sec} = -2.87"$), as shown in the right photo of Figure 1.335. The extent of crushing on the North side of the specimen reached 24" above the footing during ($\mu_{-5.4}^{18.52\,sec} = -4.49"$), see the left photo of Figure 1.336. The extent of crushing on the South side of the specimen reached 21.5" above the footing during ($\mu_{3.5}^{21.36\,sec} = 2.89"$). The crack distribution on the South and back sides of the specimen appear in the middle and right photos of Figure 1.336.

During ($\mu_{4.7}^{30.52\,sec} = 3.95"$) and ($\mu_{-6.0}^{31.34\,sec} = -4.96"$) crushing on the South and North sides of the specimen did not increase in height, but rather widened to previously uncrushed areas around the column base as shown in Figure 1.337. At the peak cycle of the load history ($\mu_{9.0}^{32.76\,sec} = 7.49"$), the extent of crushing on the South side of the specimen reached 25" above the footing. Photos of each side of the specimen during the peak cycle of the Llolleo earthquake load history appear in Figure 1.338. The remainder of the earthquake load history contained a large number of cycles below ductility six. Visible bar buckling was not observed during the remainder of the load history.

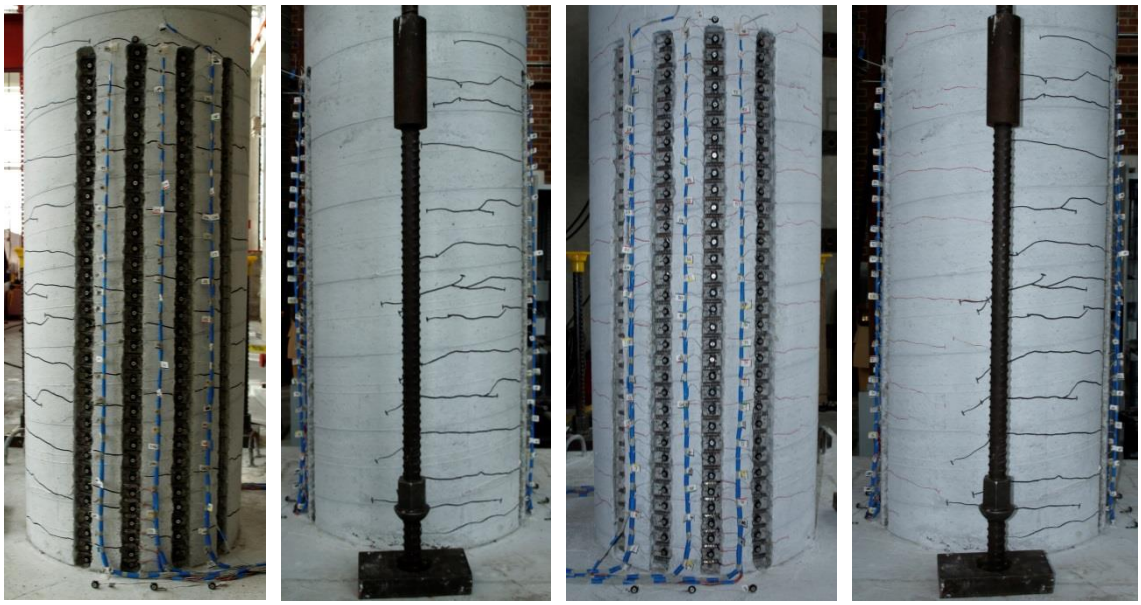

Figure 1.333 T17 – (Left) North Crack Distribution during ($\mu_{1.0}^{10.50\ sec} = 0.84$"), (Mid-Left) Back Side during ($\mu_{1.5}^{11.91\ sec} = 1.22$"), (Mid-Right) South Side during ($\mu_{-1.2}^{12.25\ sec} = -0.96$"), and (Right) Back Side during ($\mu_{-1.2}^{12.25\ sec} = -0.96$")

Figure 1.334 T17 – (Left) Cover Concrete Flaking Preceding Crushing on the South Side during ($\mu_{1.6}^{12.50\ sec} = 1.32$"), (Right) Cover Concrete Crushing on the South Side at ($\mu_{2.0}^{15.32\ sec} = 1.67$")

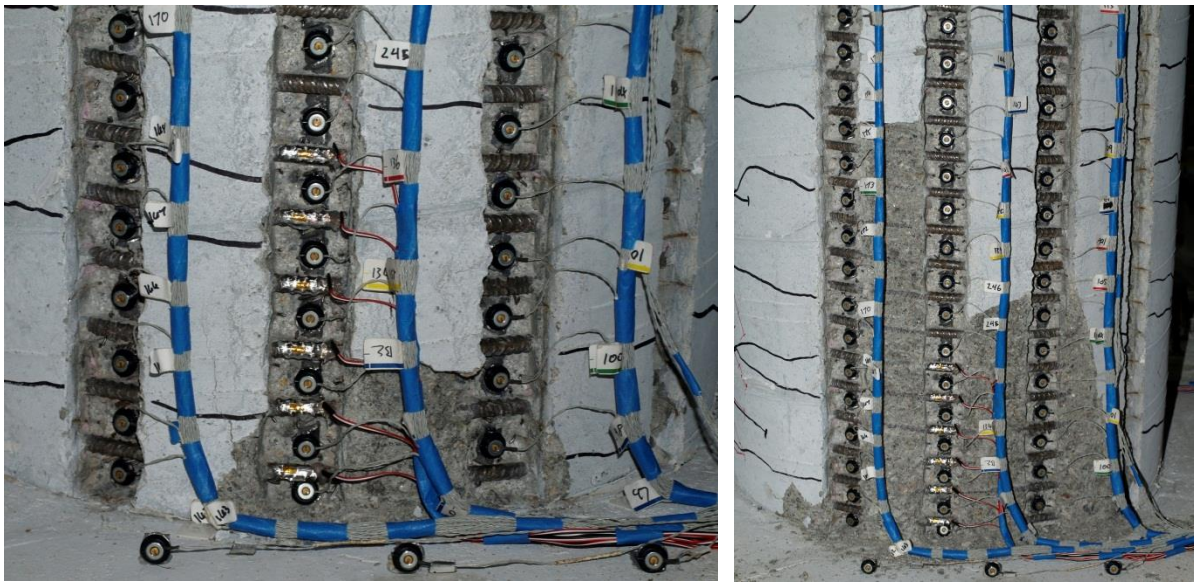

Figure 1.335 T17 – (Left) North Cover Concrete Crushing during ($\mu_{-1.9}^{16.27\,sec} = -1.60$") and (Right) Extent of Crushing on the North Side during ($\mu_{-3.5}^{17.66\,sec} = -2.87$")

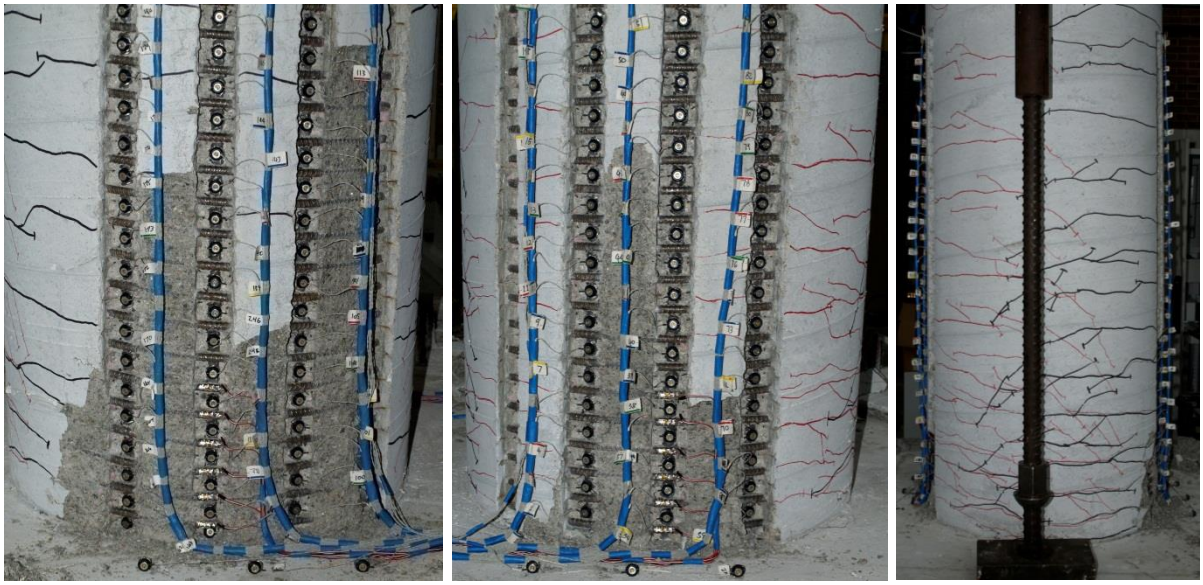

Figure 1.336 T17 – (Left) Extent of Crushing on the North Side during ($\mu_{-5.4}^{18.52\,sec} = -4.49$"), (Middle) Extent of Crushing on the South Side during ($\mu_{3.5}^{21.36\,sec} = 2.89$"), and (Right) Crack Distribution on the Back Side during ($\mu_{3.5}^{21.36\,sec} = 2.89$")

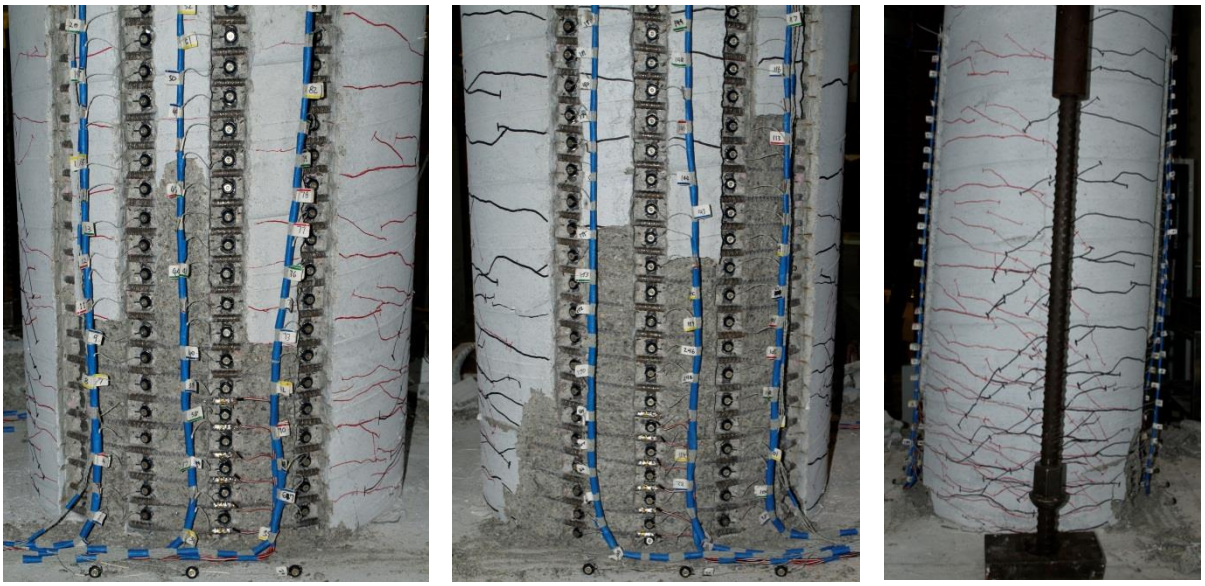

Figure 1.337 T17 – (Left) Extent of Crushing on the South during ($\mu_{4.7}^{30.52\ sec} = 3.95$"), (Middle) Crushing on the North Side during ($\mu_{-6.0}^{31.34\ sec} = -4.96$"), and (Right) Crack Distribution on the Back Side during ($\mu_{-6.0}^{31.34\ sec} = -4.96$")

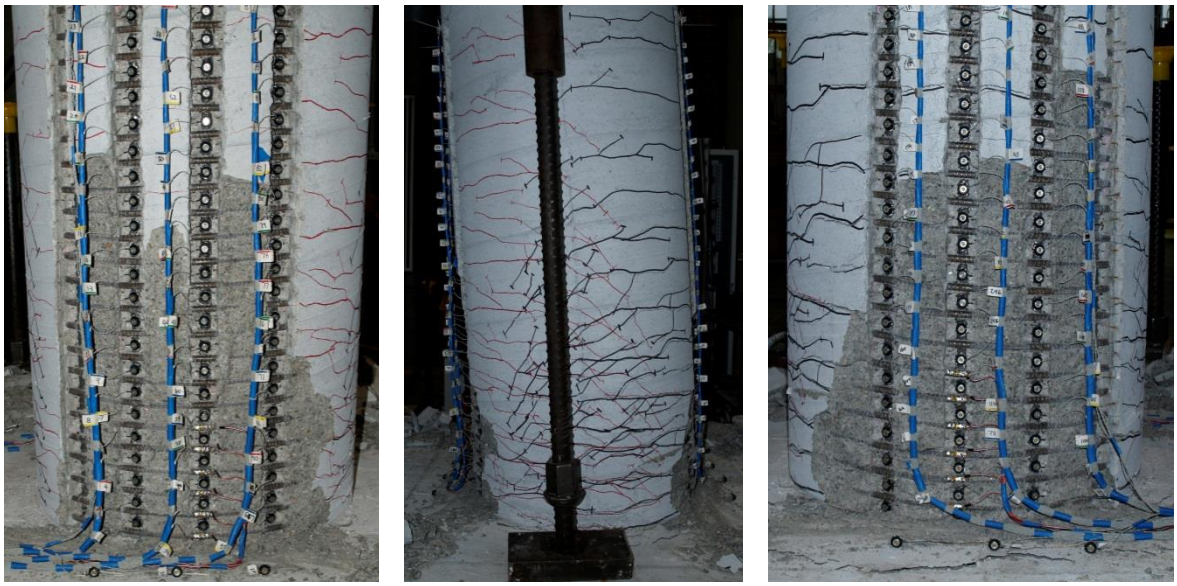

Figure 1.338 T17 – (Left, Middle, and Right) South, Back, and North Side of the Specimen during ($\mu_{9.0}^{32.76\ sec} = 7.49$") Respectively

Test 17b – Cyclic Aftershock Load History (#3 @ 1.5") Experimental Observations

Since bar buckling did not occur during the earthquake record, a symmetric three cycle set load history was conducted to determine the effect of degraded stiffness and strain accumulation on column behavior. The displacement ductility levels for the cyclic aftershock matched those from the symmetric three cycle set load history of Test 16. No notable damage was observed during cycles from displacement ductility one to four. The extreme fiber reinforcement remained visibly straight without noticeable outward deformation. Visible buckling of the North extreme fiber bar N3 occurred during ($\mu_6^{-2} = -5.00"$), as shown in Figure 1.339. Visible outward deformation was observed 3.5" above the footing on bar N3 as well as slight rotation of LEDs above and below where the bar begins to straighten back out.

During the subsequent push cycle to ($\mu_6^{+3} = 5.00"$), the South extreme fiber bar S3 visibly buckled as shown in Figure 1.340. Outward deformation was observed 8" above the footing over the highest transverse steel layer instrumented with a strain gage. During the next pull cycle to ($\mu_6^{-3} = -5.00"$), the deformation in buckled bar N3 increased as shown in the left photo of Figure 1.341. Permanent deformation in spiral layers overlaying bar N3 was observed during ($\mu_6^{+4} = 5.00"$), see the middle photo of Figure 1.341. During this cycle, the outward deformation in buckled bar S3 increased as shown in the right photo of Figure 1.341. A fourth cycle at ductility six was conducted to verify that the outward deformation in bar S3 would increase over the same location giving a stronger indication of observable bar buckling during the previous cycle. After this cycle, the test was concluded with buckling of each extreme fiber bar, but without any strength loss or rupture of reinforcement. The specimen was saved as a repair candidate.

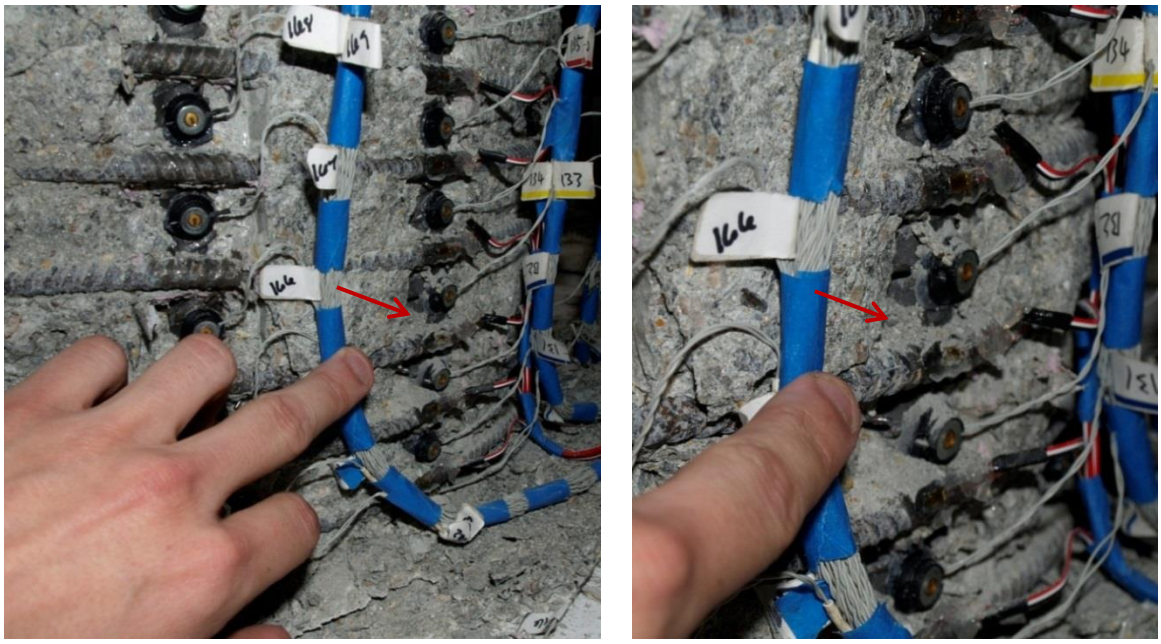

Figure 1.339 T17b – (Left and Right) Buckling of North Reinforcing Bar N3 during ($\mu_6^{-2} = -5.00$") of the Cyclic Aftershock Load History

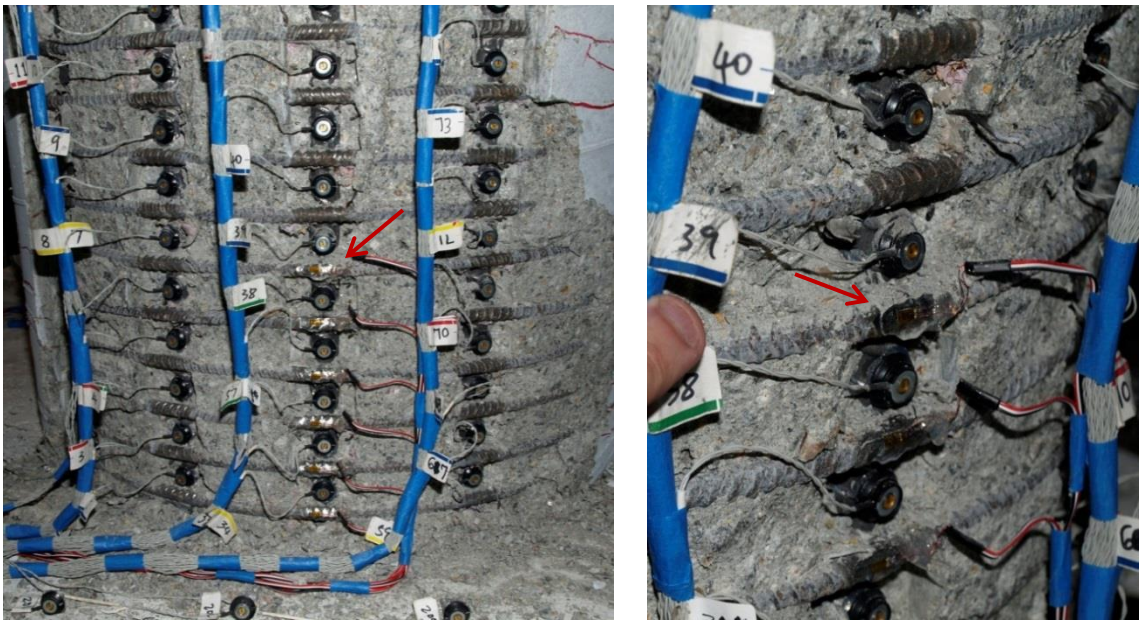

Figure 1.340 T17b – (Left and Right) Buckling of South Reinforcing Bar S3 during ($\mu_6^{+3} = 5.00$") of the Cyclic Aftershock

Figure 1.341 T17 – (Left) Additional Deformation in Buckled Bar N3 during ($\mu_6^{-3} = -5.00$"), (Middle) Spiral Deformation over North Buckled Region at ($\mu_6^{+4} = 5.00$"), and (Right) Additional Deformation in Buckled Bar S3 during ($\mu_6^{+4} = 5.00$")

Test 17 – Llolleo Chile 1985 Earthquake (#3 @ 1.5") Strain Data Analysis

North Reinforcement

Since the peaks of cycles during the earthquake load history do not align with the ductility levels of a traditional three cycle set load history, intermediate cycles along the backbone curve were selected for strain data analysis, see Figure 1.342. Extreme fiber vertical strain profiles for push and pull cycles appear in Figure 1.343 and Figure 1.344 respectively. A peak tensile strain of 0.055, located 3.56" above footing, was measured for Bar N3 during ($\mu_{9.0}^{32.76\,sec} = 7.49$"). The relationship between tensile strain and displacement for this gage length appears in Figure 1.347. Each line represents a single push cycle which began with the column at zero displacement and ended at the peak during a continuous push cycle. The solid line contains data during the push cycle loading up to the peak displacement and the dashed line represents the subsequent reversal of load. The peak tensile strain of

0.055 was not sufficient to produce visible bar buckling after reversal of load. Similar to previous tests, the moment curvature prediction for the relationship between strain and displacement using the PCK (2007) Lp Hinge Method begins to over predict the tensile strains at higher displacements at an increasing rate. The largest compressive strain of -0.023 was measured over the bar N3 gage length 2.05" above the footing during ($\mu_{-6.0}^{41.20\ \mathrm{sec}} = -5.02"$). The relationship between compressive strain and displacement for this gage length appears in Figure 1.348. The recorded strains match the trend predicted by moment curvature analysis and the PCK (2007) Lp Hinge Method through ($\mu_{-3.5}^{17.66\ sec} = -2.87"$), but during later cycles the measured strains are larger than expected.

The transverse steel strains measured over the lowest six spiral layers overlaying the North reinforcement were plotted in Figure 1.346. Even though the peak compressive strains were measured 2.05" and 6.45" above the footing, the layer of transverse steel located 3.6" above the footing went furthest into the inelastic range during the Llolleo load history. The outward buckled region of bar N3 latter formed at this location during the ductility six of the cyclic aftershock, as shown in Figure 1.339. The peak tensile strains for bar N3 were located 3.56" above the footing. As previously mentioned, the residual growth strains measured for this gage were large, as shown in Figure 1.347. One possible explanation for the observations noted above is that measureable outward deformation occurred over the gage length 3.56" above the footing on bar N3 prior to visible bar buckling. It is not immediately obvious that this occurred because a large amount of growth strain could, perhaps, outweigh future compressive strains during subsequent cycles. Some amount of measureable outward deformation would increase the residual growth strain, increase the demand on the layer of transverse steel overlaying the bar, and agree with the location of visible bar buckling observations during the cyclic aftershock study.

South Reinforcement

A peak tensile strain of 0.0387 on bar S3 was measured 2.26" above the footing during ($\mu_{-6.0}^{41.20\,\mathrm{sec}} = -5.02"$). The relationship between tensile strain and displacement for this gage length is shown in Figure 1.349. The same comments on the accuracy of the moment curvature prediction for bar N3 also apply to bar S3. A peak compression strain of -0.0392 on bar S3 was measured 9.53" above the footing during ($\mu_{9.0}^{32.76\,sec} = 7.49"$). The measured peak compression strain is 2.2 times the calculated Mander (1988) ultimate concrete compressive strain of -0.0179. The relationship between compressive strain and displacement for the gage length 5.12" above the footing on bar S3 during push cycles appears in Figure 1.350. The measured compressive strains begin to deviate away from the prediction after a displacement ductility of 3.5. The gage length centered 9.53" above the footing with the largest compressive strain during ($\mu_{9.0}^{32.76\,sec} = 7.49"$) appears in Figure 1.351. The relationship between compressive strain and displacement matches well until 5" of displacement during the push cycle to ($\mu_{9.0}^{32.76\,sec} = 7.49"$), when the measured compression strains begin to sharply increase. Closer inspection of the transverse steel strains for spiral layers restraining the South bar during push cycles, in Figure 1.345, provides an explanation for measured increase in compressive strains. The transverse steel layer 8" above the footing first goes inelastic during ductility six, at approximately 5", during the push cycle to ($\mu_{9.0}^{32.76\,sec} = 7.49"$). It appears that the transverse steel layer entering the inelastic range influenced the relationship between compressive strain and displacement for the gage length 9.53" above the footing, localizing further compressive demand at this location.

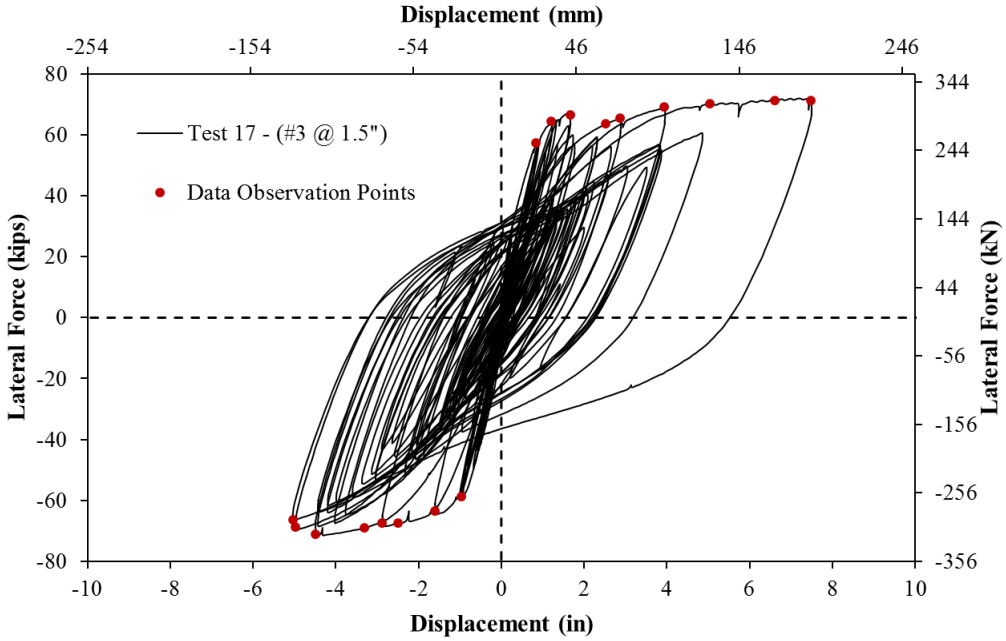

Figure 1.342 T17 – Strain Data Observation Points on the Hysteretic Response

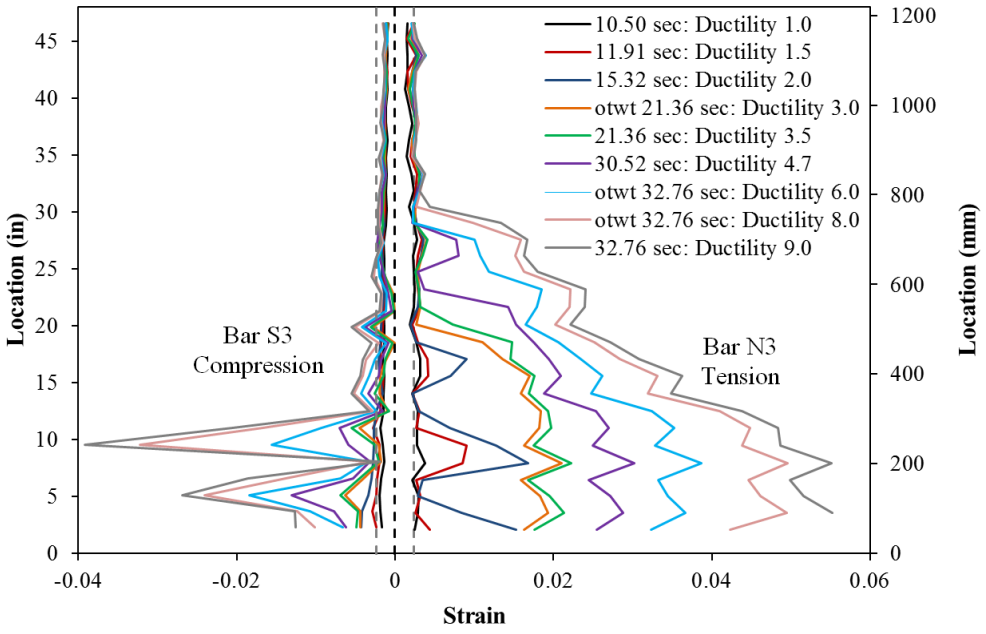

Figure 1.343 T17 – Extreme Fiber Vertical Strain Profiles during Push Cycles

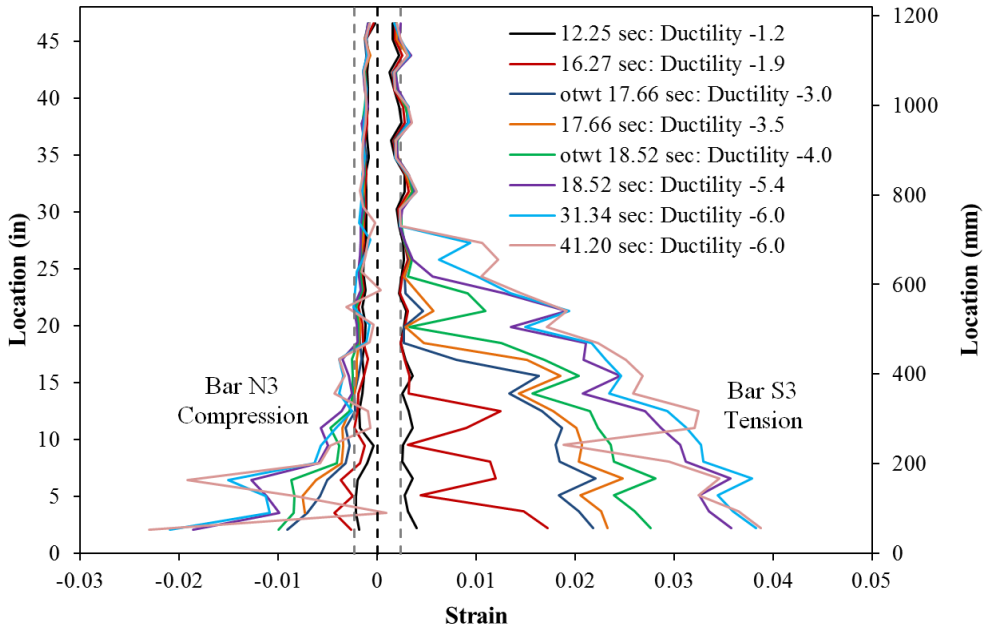

Figure 1.344 T17 – Extreme Fiber Vertical Strain Profiles during Pull Cycles

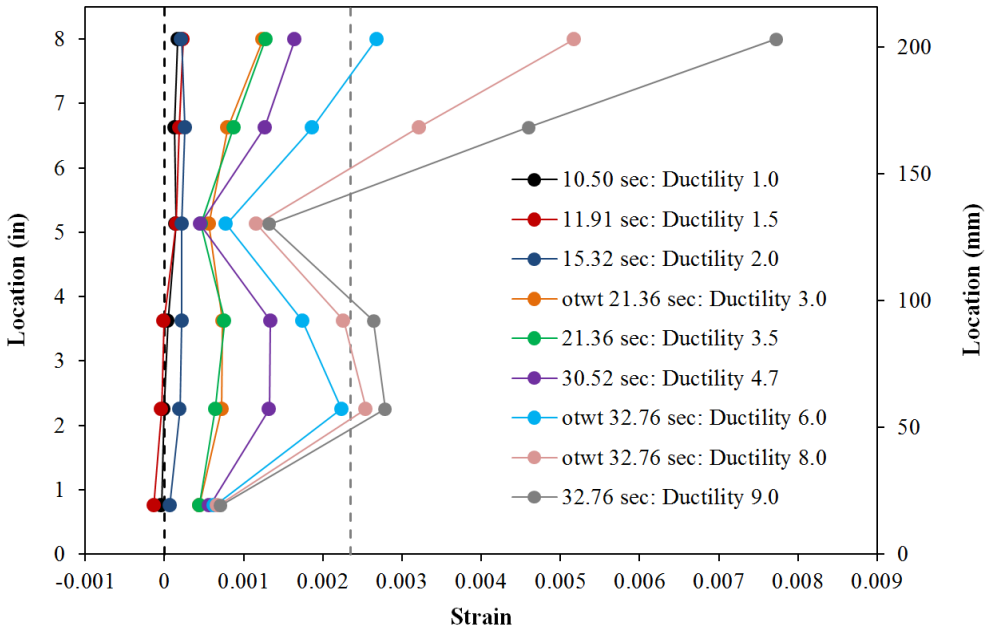

Figure 1.345 T17 – Transverse Steel Strains on the South Side during Push Cycles

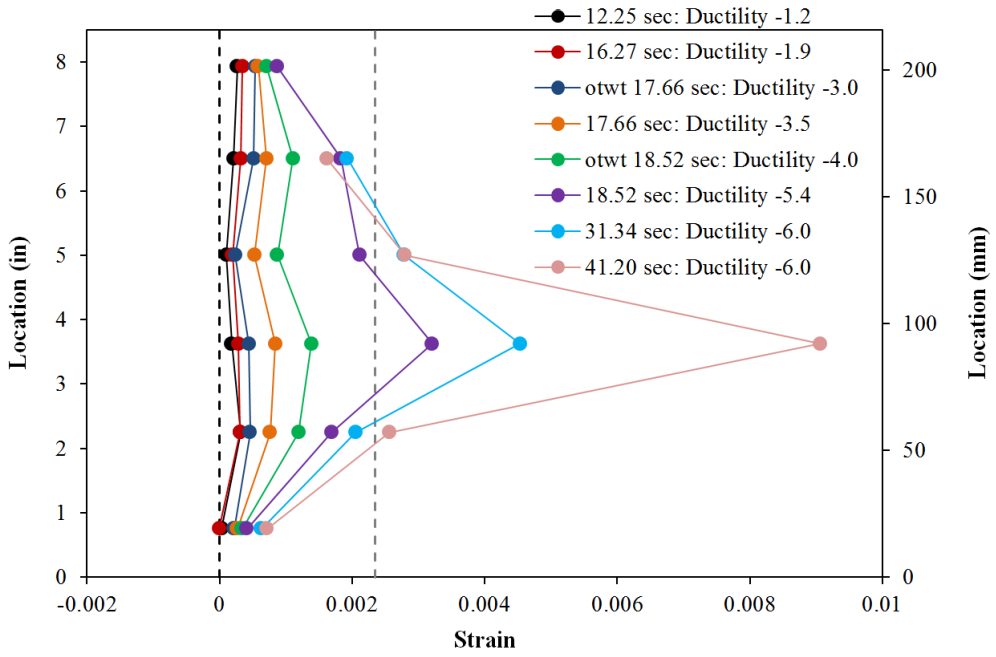

Figure 1.346 T17 – Transverse Steel Strains on the North Side during Pull Cycles

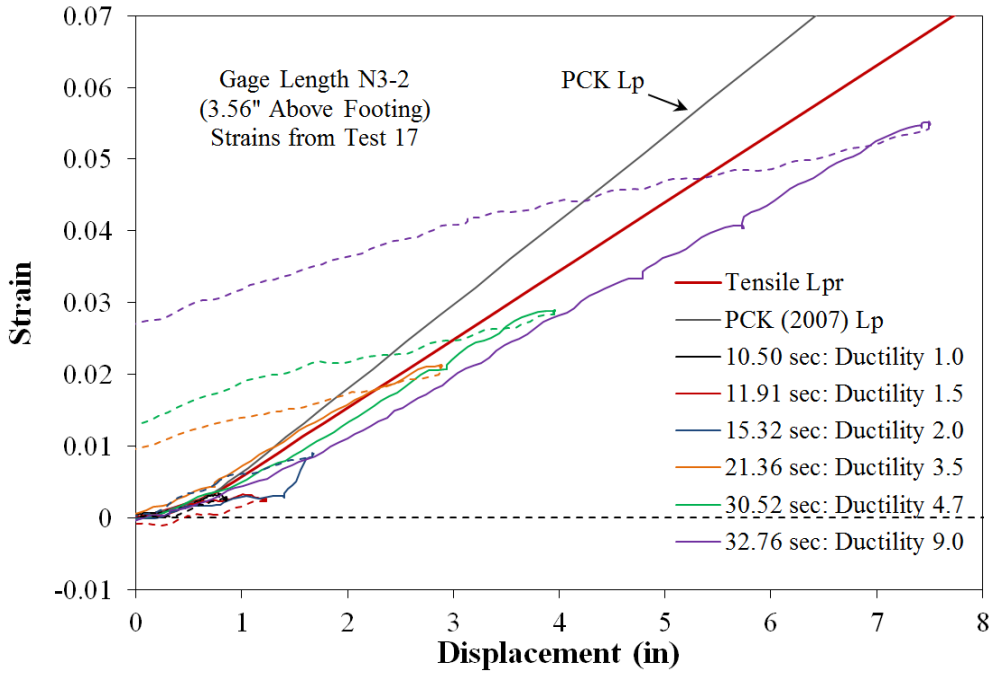

Figure 1.347 T17 – Tensile Strain-Disp. during Push Cycles (Bar N3, 3.56" Above)

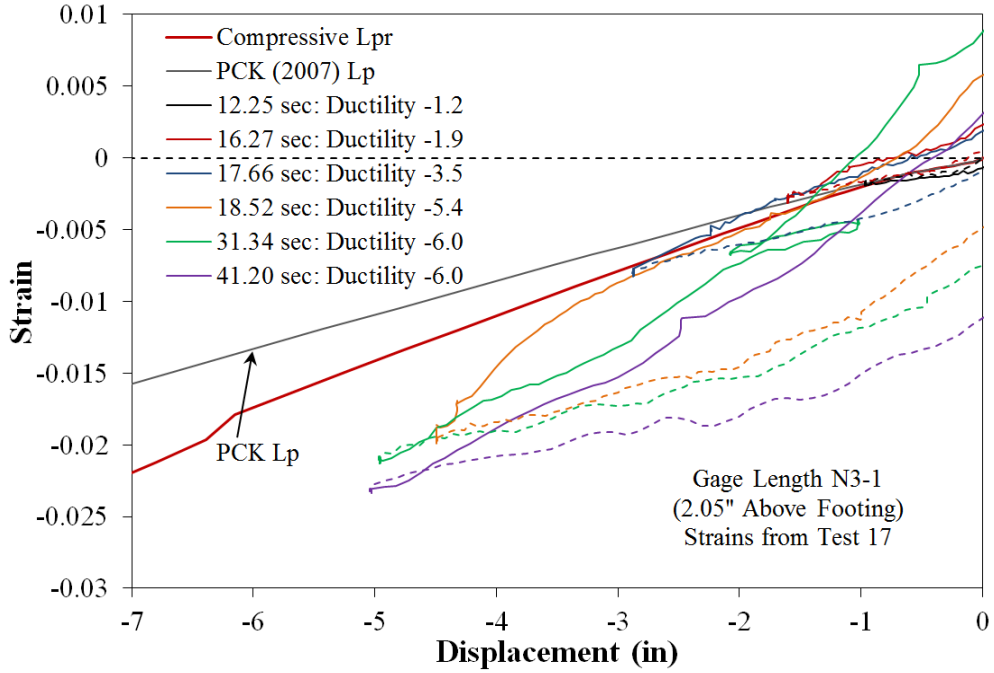

Figure 1.348 T17 – Compressive Strain-Disp. for Pull Cycles (Bar N3, 2.05" Above)

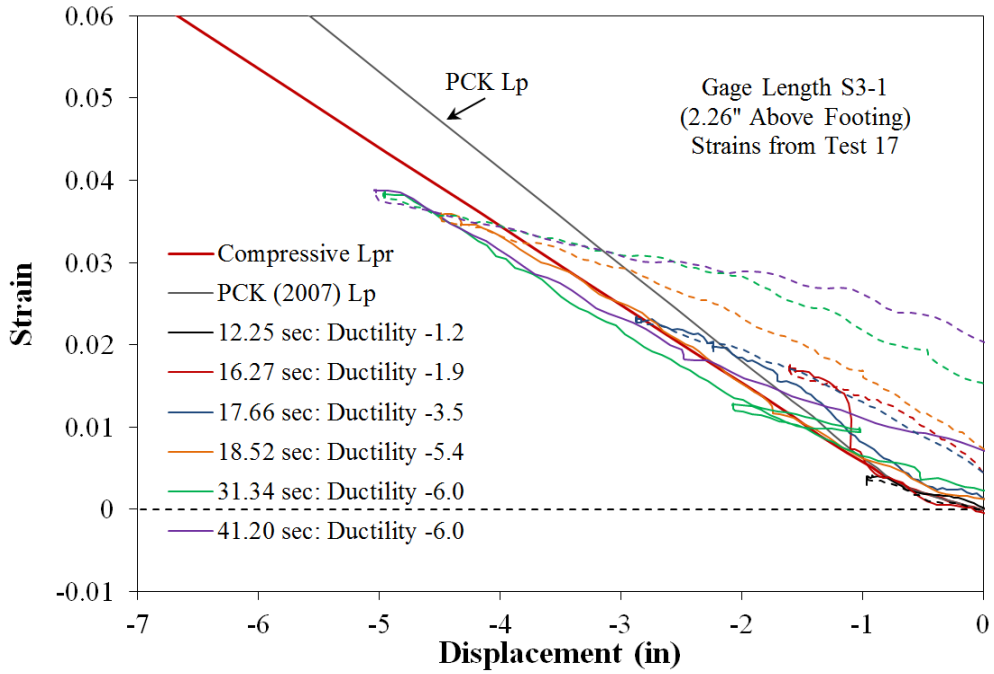

Figure 1.349 T17 – Tensile Strain-Disp. during Pull Cycles (Bar S3, 2.26" Above)

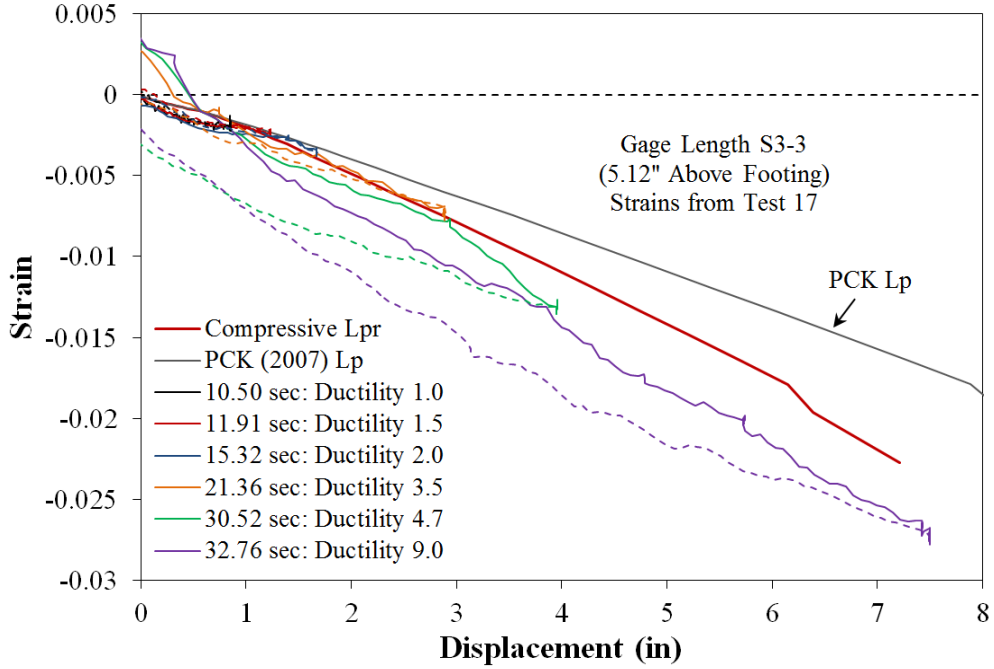

Figure 1.350 T17 – Compressive Strain-Disp. for Push Cycles (Bar S3, 5.12” Above)

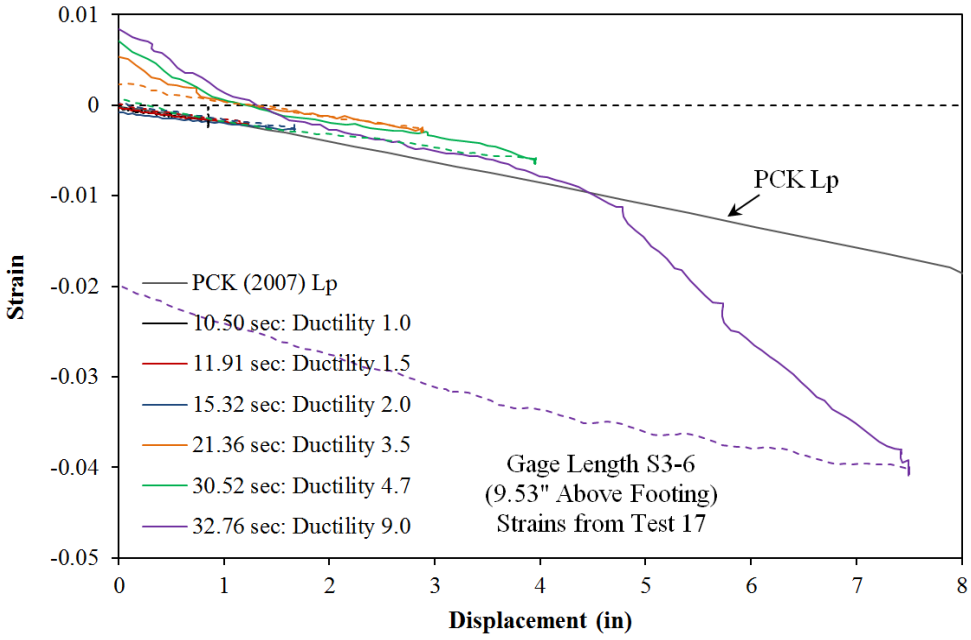

Figure 1.351 T17 – Compressive Strain-Disp. for Push Cycles (Bar S3, 9.53” Above)

Test 17 – Llolleo Chile 1985 (#3 @ 1.5") Curvature and Strain Penetration Data

Vertical curvature profiles are plotted for push and pull cycles in Figure 1.352 and Figure 1.353 respectively. These figures show that plastic curvatures have a linear distribution at higher displacement ductility levels. The dashed lines for each curvature distribution represent a least squared error linear fit to the plastic portion of the measured curvatures. The data points used to create the least squared error lines appear as circle data markers. The target marker on each bar placed closest the footing-column interface can be used to create slip hysteresis and horizontal slip profiles attributable to strain penetration. The slip hysteresis for extreme fiber bars N3 and S3 appear in Figure 1.354 and Figure 1.355 respectively. The peak tensile slip of North extreme fiber bar N3 exceeds 0.45" during displacement ductility nine.

If the tensile and compressive slip of all of the instrumented bars is plotted along the cross section depth, the base rotation attributable to strain penetration may be calculated. The slip profiles for push and pull cycles appear in Figure 1.356 and Figure 1.357 respectively. The rotation of the base section can be extracted from the slope of the least squared error line connecting all six measured bar slips. The total displacement could be calculated as the addition of the column flexure, strain penetration, and shear displacement components. The measured string potentiometer displacements from Test 17 were compared to the displacements obtained from curvature diagram integration and slip profile extrapolation to the center of loading in Figure 1.358. The measured and integrated top column displacements match well throughout the entire range of displacements indicating that shear displacements, which were not directly accounted for, must be small and thus negligible. The measured spread of plasticity as a function of base section curvature ductility appears in Figure 1.359. The circular data points represent the measured extent of plasticity, determined as the intersection of the linear plastic regression and the elastic curvature profile.

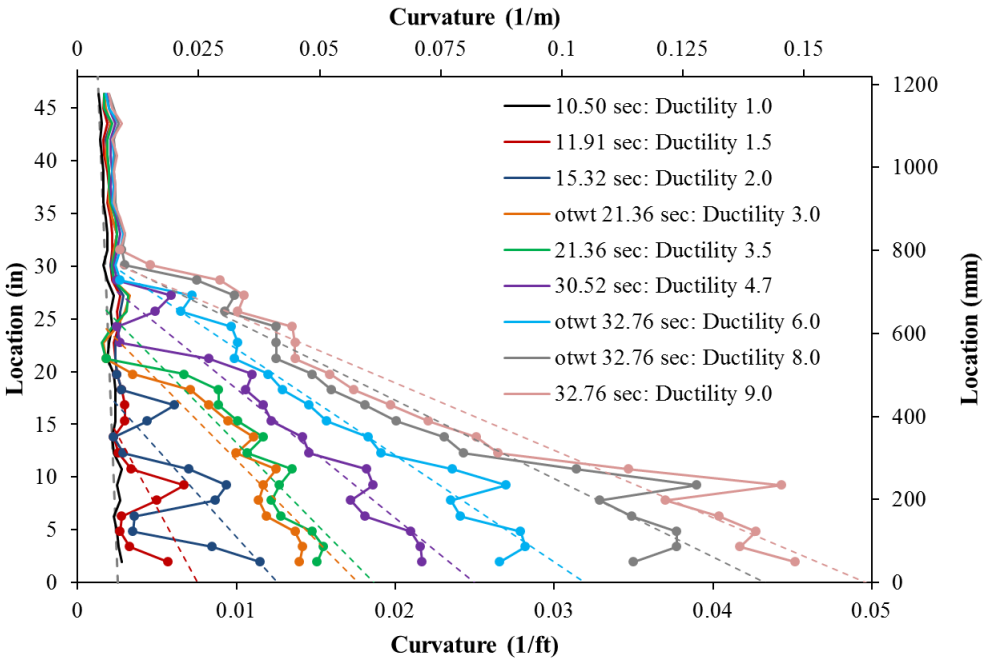

Figure 1.352 T17 – Curvature Profiles during Push Cycles with Plastic Regression

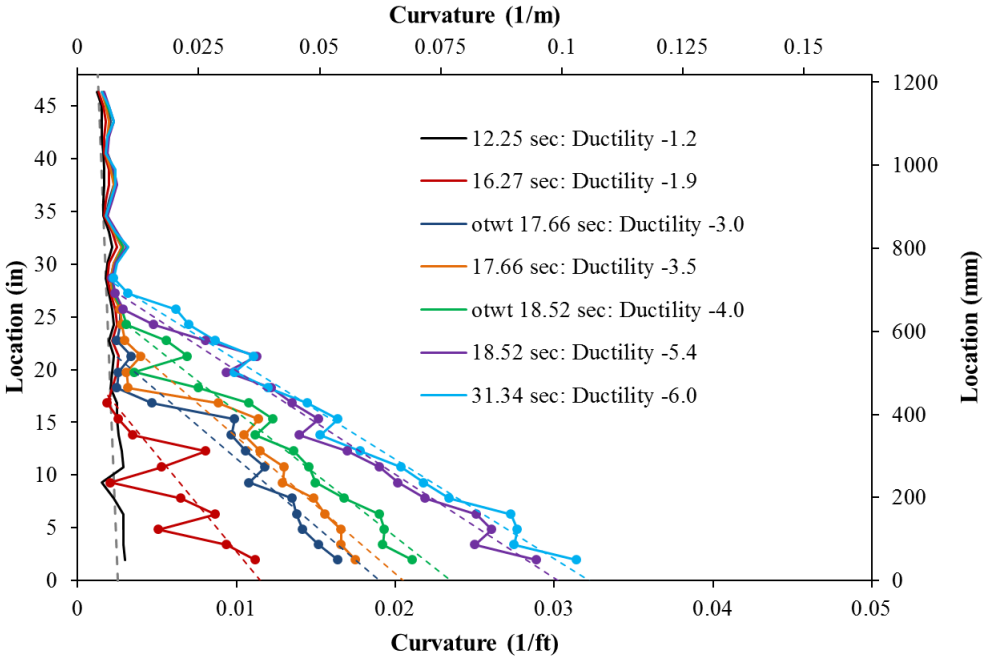

Figure 1.353 T17 – Curvature Profiles during Pull Cycles with Plastic Regression

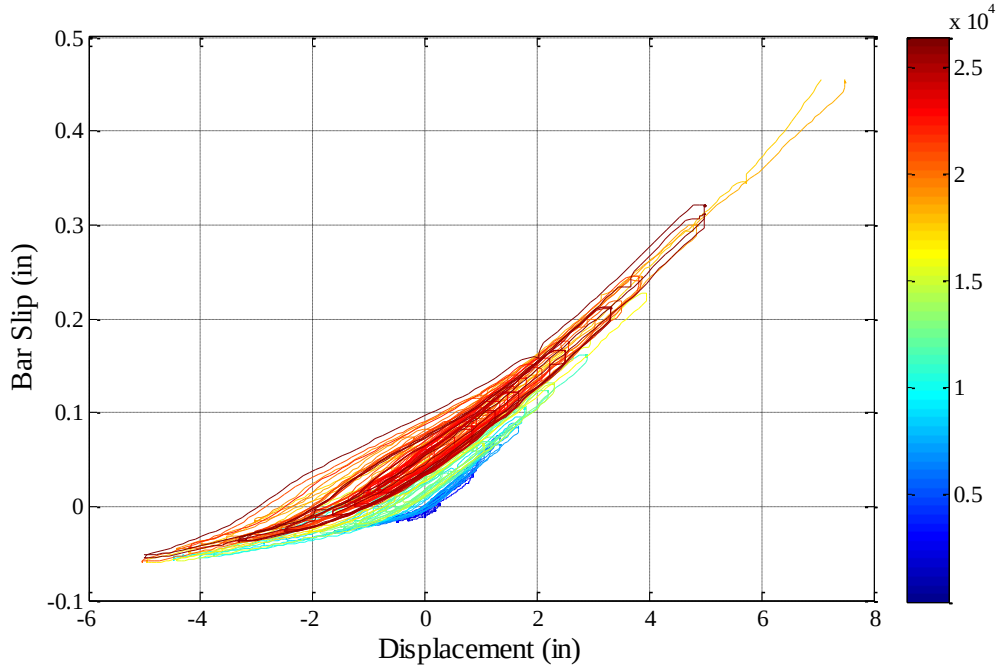

Figure 1.354 T17 and T17b – Bar N3 Slip Hysteresis at the Footling-Column Interface

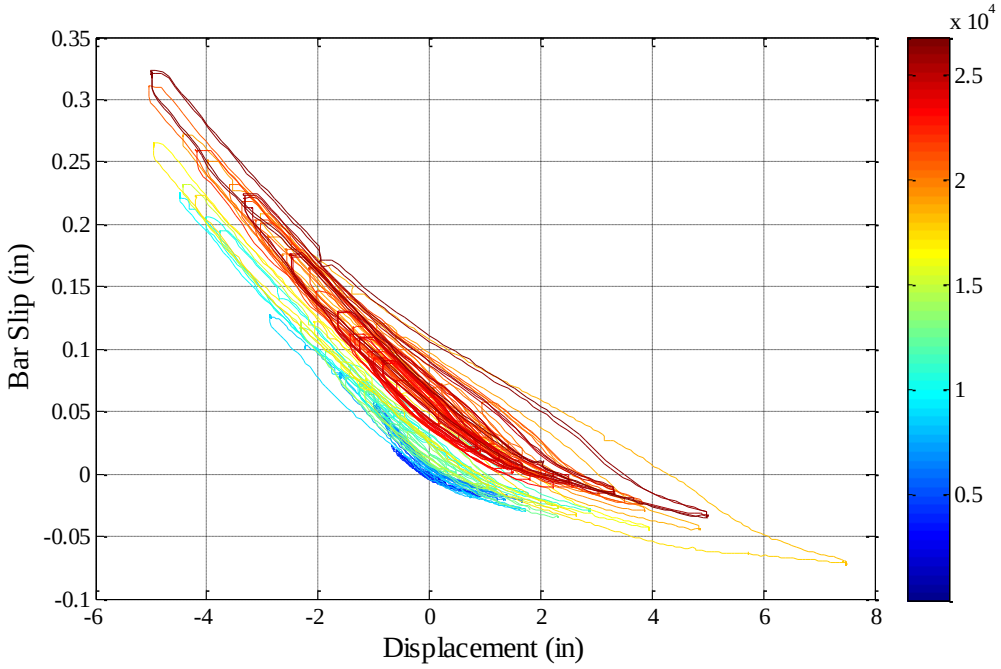

Figure 1.355 T17 and T17b – Bar S3 Slip Hysteresis at the Footling-Column Interface

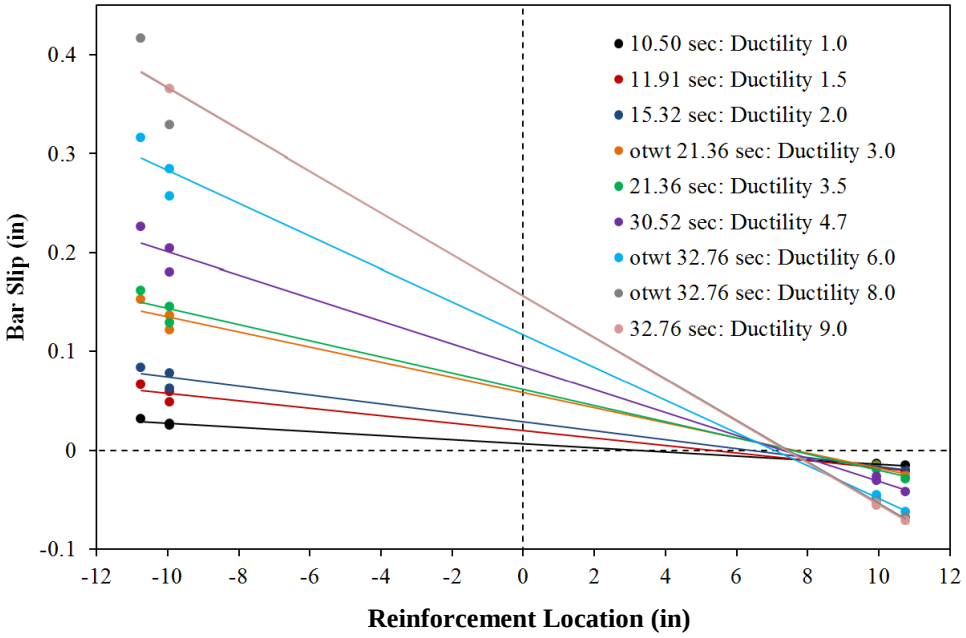

Figure 1.356 T17 – Base Rotation due to Strain Penetration during Push Cycles

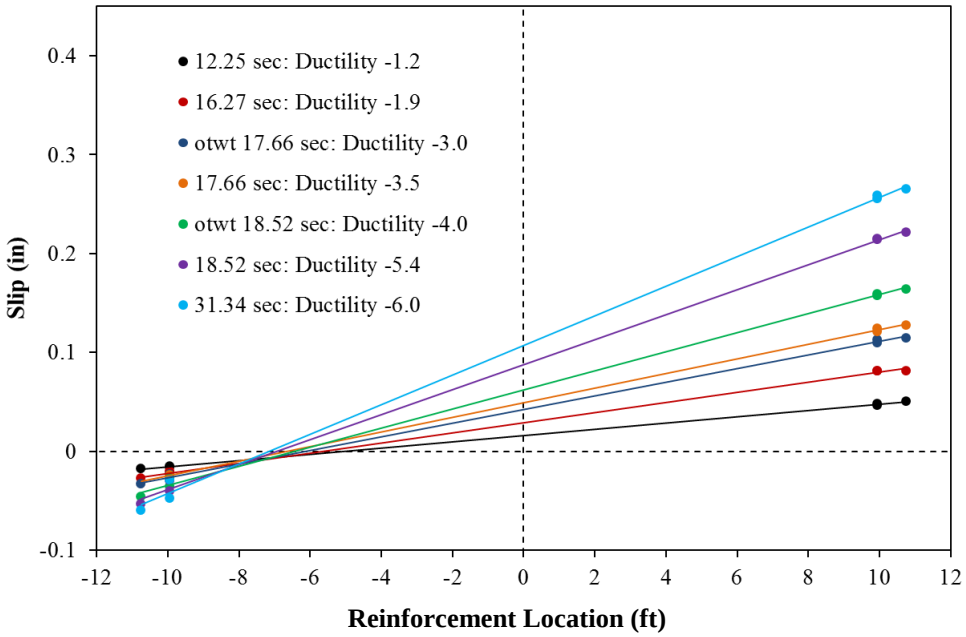

Figure 1.357 T17 – Base Rotation due to Strain Penetration during Pull Cycles

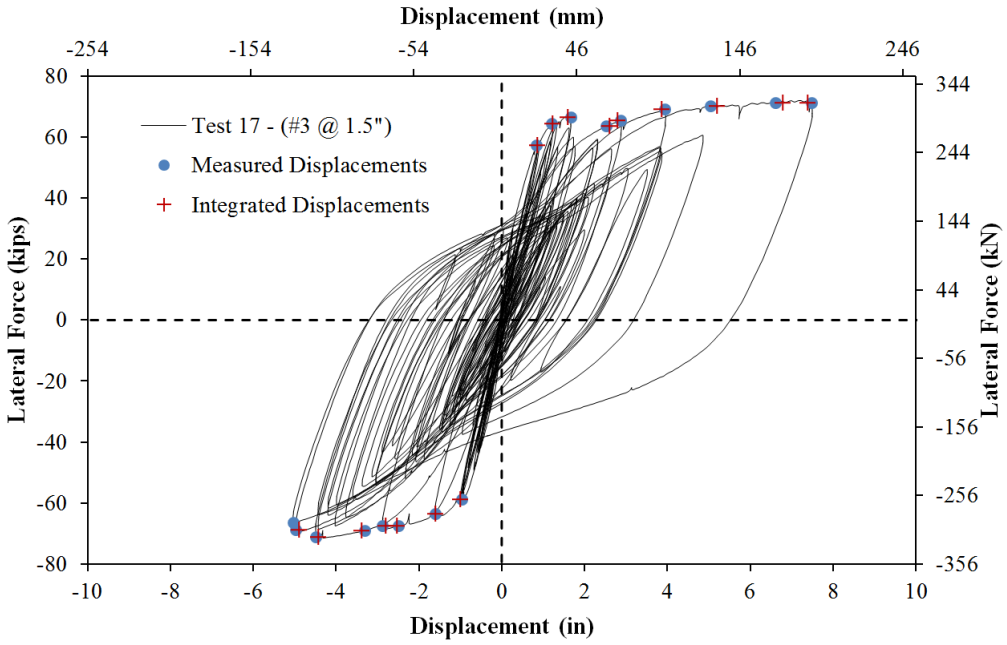

Figure 1.358 T17 – Comparison of Measured and Optotrak Integrated Displacements

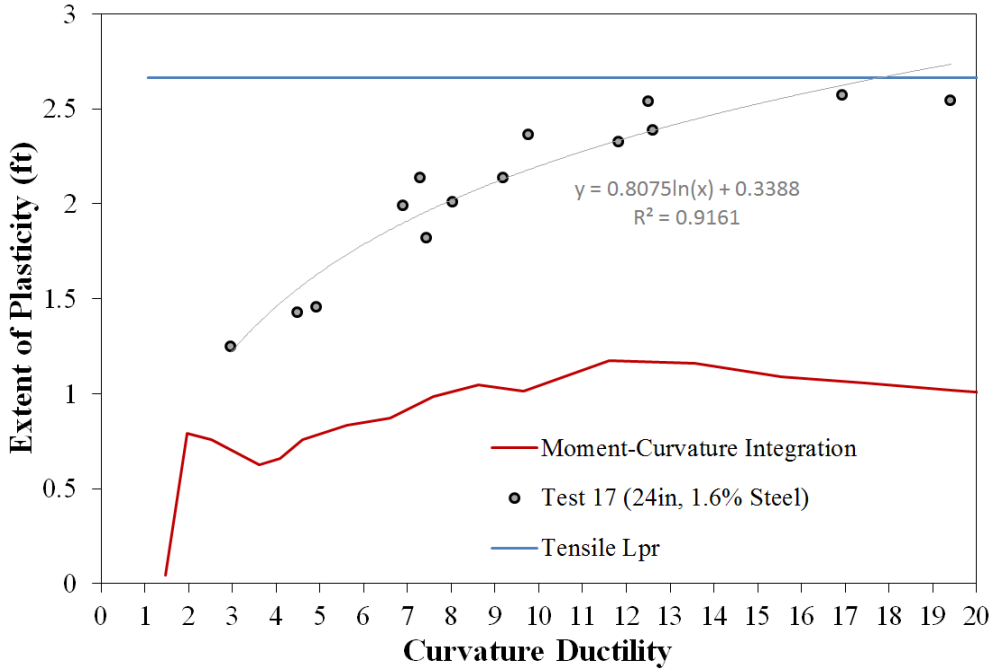

Figure 1.359 T17 – Measured Spread of Plasticity (Circular Data Points)

Test 17b – Cyclic Aftershock Load History (#3 @ 1.5") Strain Data Analysis

North Reinforcement

Extreme fiber vertical strain profiles for the cyclic aftershock load history appear in Figure 1.360 and Figure 1.361 for push and pull cycles respectively. The shape of the tensile strain profiles during the cyclic aftershock resemble each other since the specimen rotates about crack profiles induced during higher ductility cycles of the Llolleo load history. The compressive vertical strain profiles are highly influenced by the measureable outward deformation 3.56" above the footing. The height of potential outward deformation coincides with the location where the bar later visually buckled. The gage lengths above and below 3.56" show greater compressive strains at the location where the bar begins to straighten back out. The recorded strains over these gage lengths are not accurate representations of engineering strains due to the deformation. The graphs are plotted in order to show the location and severity of the deformation.

The complete strain hysteresis for the outward buckled region of bar N3 appears in Figure 1.362 for the gage length 3.56" above the footing. A peak tensile strain of 0.055, located 3.56" above footing, was measured for North extreme fiber bar N3 during ($\mu_{9.0}^{32.76\,sec} = 7.49"$). The peak tensile strain is marked by a small blue circle along with a blue arrow after reversal which represents the beginning of the measurable outward deformation. The transverse steel strain gage hysteresis for the spiral layer over the outward buckled region of bar N3 appears in Figure 1.363. After reversal from the peak displacement, while the cracks on the north side still remained open, the transverse steel strain starts to increase indicating additional demand caused by restraint of bar N3. The peak displacement prior to reinforcement buckling during the cyclic after shock study of ($\mu_6^{-2} = -5.00"$) is marked by a small red circle on the longitudinal and transverse steel strain hysteresis. Following the red arrow in both hystereses, the measured strains in the longitudinal steel deviate further deviate from prior trends, at the same time the measured transverse steel restraint strain increased rapidly.

South Reinforcement

The compressive strain profiles for bar S3 indicate measurable outward deformation 8.06” above the footing. At this height the outward deformation increased the measured tensile strain during cycles where the South reinforcing bar should be placed into compression. Gage lengths above and below the outward deformations reached higher compressive strains where the bar straightens back out. The longitudinal steel strain hysteresis for bar S3, over the outward buckled region 8.06" above the footing, appears in Figure 1.364. A strain hysteresis for the gage length above the outward buckled region 9.5” above the footing is shown in Figure 1.365. The transverse steel strain hysteresis, 8” above the footing, for the spiral layer over the outward buckled region of bar S3 appears in Figure 1.366. A blue data point marker on all three hysteresis marks the point at which the measured compression strain 9.5” above the footing started to rapidly increase during the push to ($\mu_{9.0}^{32.76\,sec} = 7.49"$). As the gage length at 9.5” increased in compressive strain, the measured strains for the gage length below at 8.06” decreased. Coinciding with these two observations the transverse steel layer 8” above the footing entered the inelastic range. The strain hysteresis for the gage length 9.5” above the footing, in Figure 1.365, operates about a permanent downward shift decreasing the strain at a given displacement for the remainder of the test. Deviation after the blue data point for the gage length 8.06” above the footing, in Figure 1.364, indicates some measurable outward deformation. For the portion of the load history between ($\mu_{9.0}^{32.76\,sec} = 7.49"$) of the Llolleo earthquake and ($\mu_{6}^{+1} = 4.99"$) of the cyclic aftershock, the strain in the transverse steel layer 8” above the footing in Figure 1.366 did not sharply increase indicating that the measurable deformation remained small prior to visible bar buckling. Over multiple cycles at ductility six the transverse steel strain gradually increased during each cycle, before rapidly increasing during ($\mu_{6}^{+3} = 5.00"$) when the bar visibly buckled.

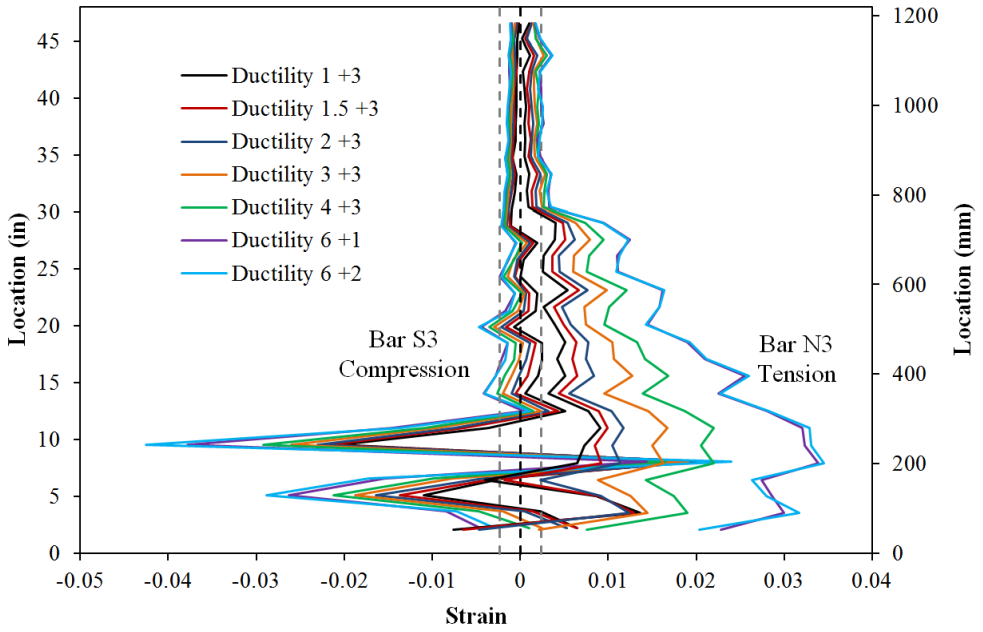

Figure 1.360 T17b – Extreme Fiber Vertical Strain Profiles during Push Cycles

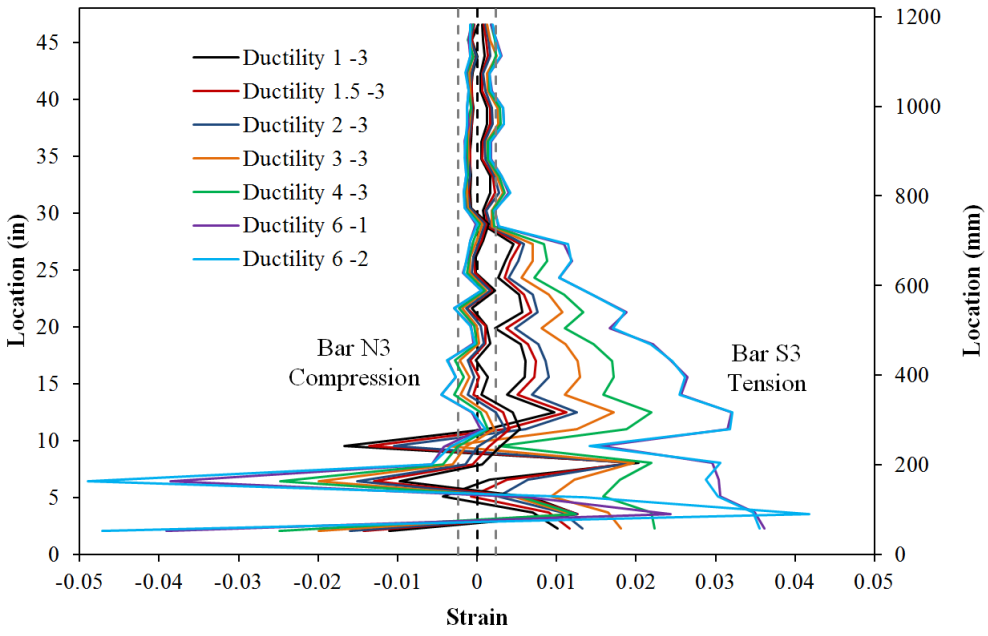

Figure 1.361 T17b – Extreme Fiber Vertical Strain Profiles during Pull Cycles

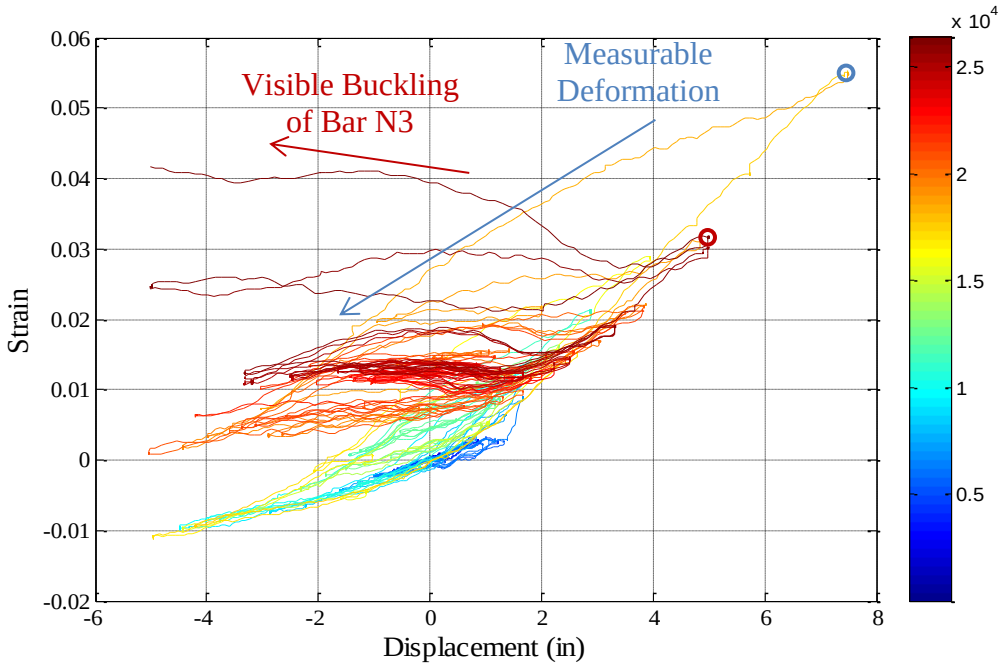

Figure 1.362 T17 and T17b – Bar N3 Strain Hysteresis Located 3.56" Above Footing

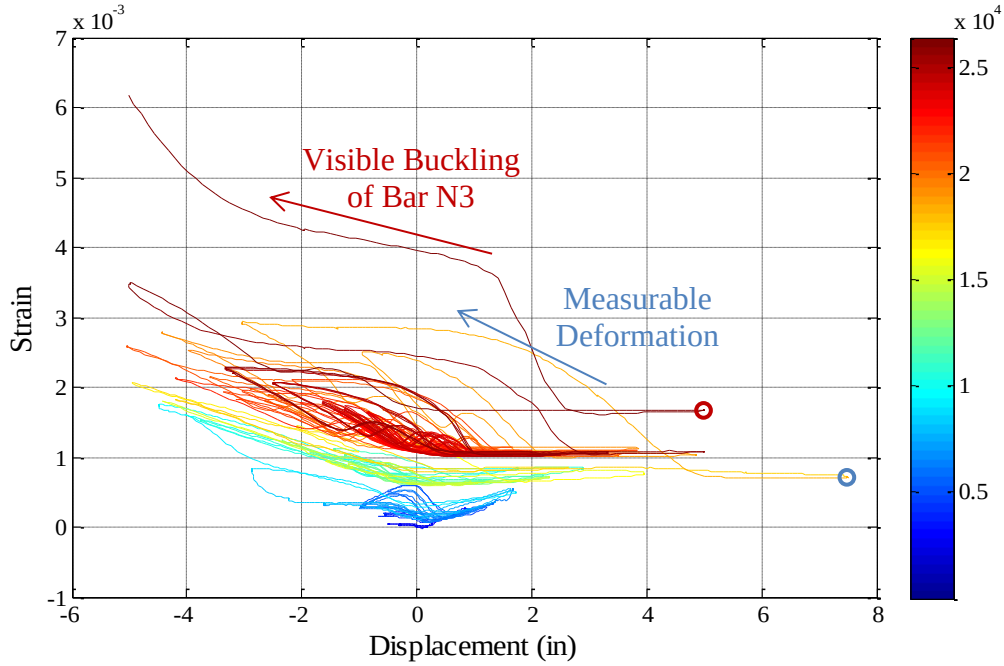

Figure 1.363 T17 and T17b – Spiral Strain Hysteresis over North Buckled Region

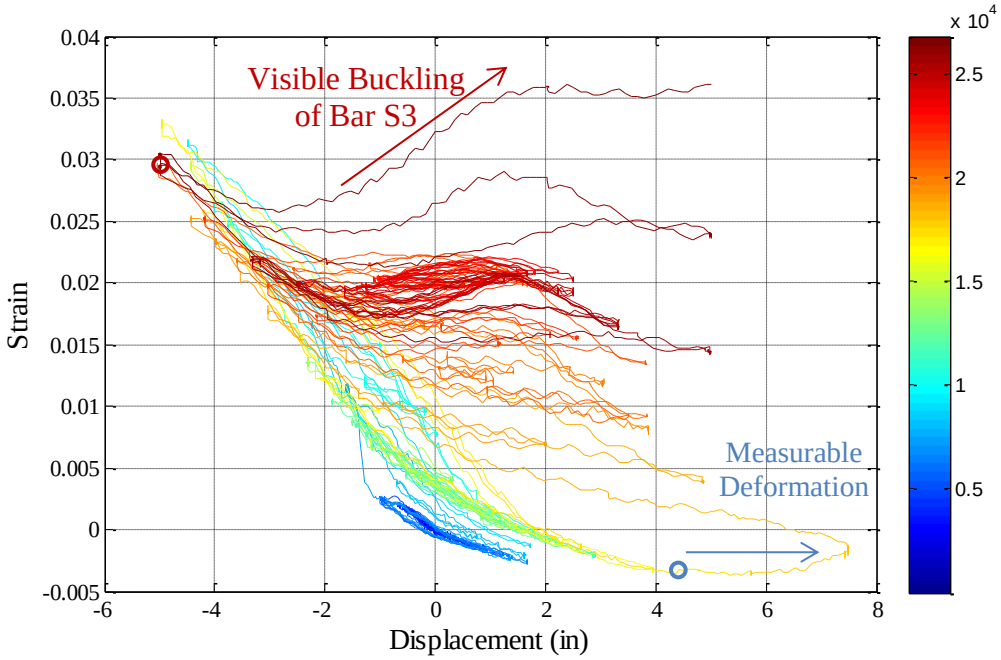

Figure 1.364 T17 and T17b – Bar S3 Strain Hysteresis Located 8.06" Above Footing

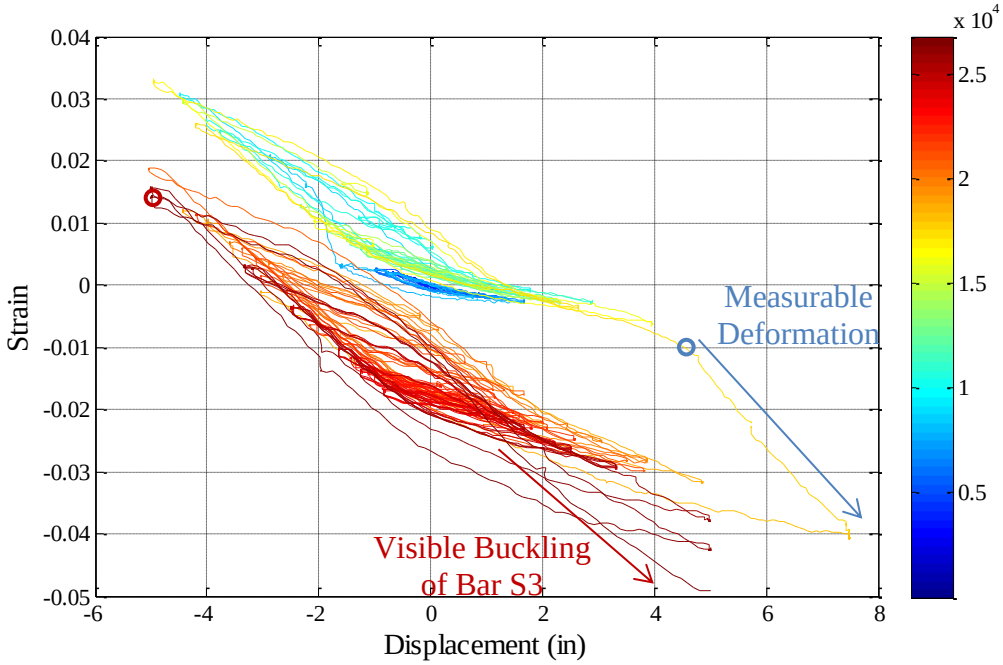

Figure 1.365 T17 and T17b – Bar S3 Strain Hysteresis Located 9.53" Above Footing

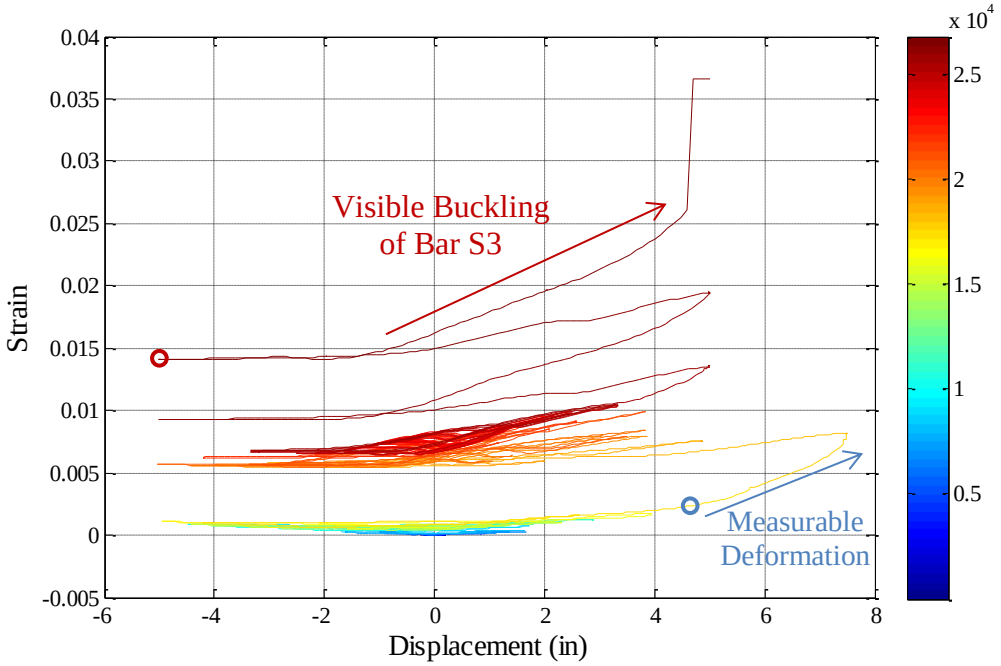

Figure 1.366 T17 and T17b – Spiral Strain Hysteresis over South Buckled Region

1.2.6 Test 18 – Darfield NZ 2010 EQ LH with #3 Spiral at 1.5" (1.3%)

Table 1.28 Observational Summary for Test 17 – Darfield NZ Earthquake LH with #3 Spiral at 1.5" (1.3%)

VALUES OF INTEREST:	
Concrete Compressive Strength:	$f_c' = 7807\ psi$
Axial Load:	$P = 170\ kips$
Analytical First Yield Force:	$F_y' = 47.6\ kips$
Experimental First Yield Displacement:	$\Delta_y' = 0.62"$ *From Test 16
Analytical Nominal Moment Capacity:	$M_n = 510.4\ kip * ft$
Equivalent Yield Displacement:	$\Delta_y = 0.83"$
Maximum Lateral Force:	$72.7\ kips$
Maximum Lateral Displacement:	$\mu_{9.0}^{24.40\ sec} = 7.46"$
Failure Mode:	Single Buckled Bar during Earthquake LH
	No significant Strength Loss Observed
DAMAGE OBSERVATIONS:	
First Cracking North:	$\mu_{0.2}^{18.12\ sec} = 0.17"$
First Cracking South:	$\mu_{-0.3}^{18.12\ sec} = -0.23"$
Cover Concrete Crushing North:	During the pull to $\mu_{-2.7}^{23.72\ sec} = -2.21"$
Cover Concrete Crushing South:	During the push to $\mu_{9.0}^{24.40\ sec} = 7.46"$
Transverse Steel Yield North:	At $-5.49"$ otwt $\mu_{-7.3}^{25.00\ sec} = -6.05"$
Transverse Steel Yield South:	At $3.70"$ otwt $\mu_{9.0}^{24.40\ sec} = 7.46"$
Bar Buckling South:	After Reversal from $\mu_{-7.3}^{25.00\ sec} = -6.05"$

$*\mu_{9.0}^{24.40\ sec} = 7.46"$ represents a push cycle 24.40 seconds into the earthquake load history which reached a peak displacement of 7.46" and a displacement ductility of 9.0

Table 1.29 Observational Summary for Test 17b – Symmetric Three Cycle Set Aftershock LH

DAMAGE OBSERVATIONS: During Symmetric Three Cycle Set Post Earthquake LH	
Longitudinal Bar Fracture South:	Reversal from $\mu_6^{-2} = -4.99"$
Failure Mode:	Fracture of Previously Buckled Reinforcement

$*\mu_6^{-2} = -4.99"$ represents the second pull cycle of displacement ductility six

Table 1.30 Strain Data Summary for Test 17 and Test 17b – Darfield NZ EQ LH and Cyclic Aftershock

MATERIAL STRAINS:	
Cover Concrete Crushing North:	$\varepsilon_s = 0.068\ (compression)$
Cover Concrete Crushing South:	N/A, During the push to $\mu_{9.0}^{24.40\ sec} = 7.46"$
Transverse Steel Yield North:	$\varepsilon_s = 0.0147 (compression)$
Transverse Steel Yield South:	$\varepsilon_s = 0.0136\ (compression)$
Longitudinal Bar Buckling North:	North Bar Never Visibly Buckled
Longitudinal Bar Buckling South:	$\varepsilon_s = 0.047\ (peak\ tension\ prior\ to\ bb)$
	$\varepsilon_s = 0.048\ (peak\ comp.\ prior\ to\ bb)$
Mander (1988) Ultimate Concrete Compression Strain, $\varepsilon_{cu} = 0.0176$	

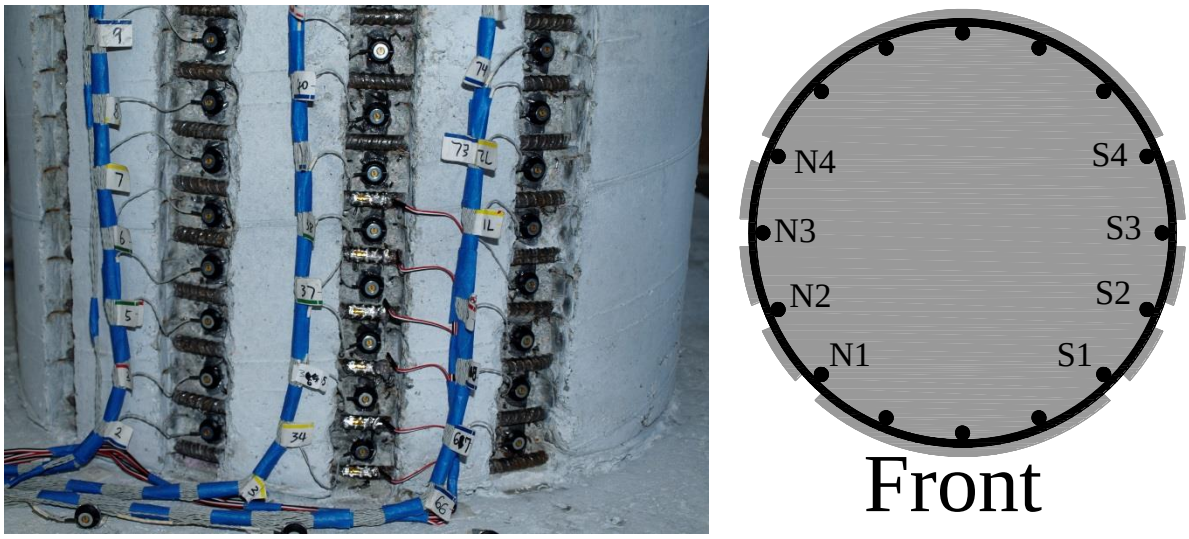

Figure 1.367 T18 – Cross Section Bar Designation and Target Marker Application

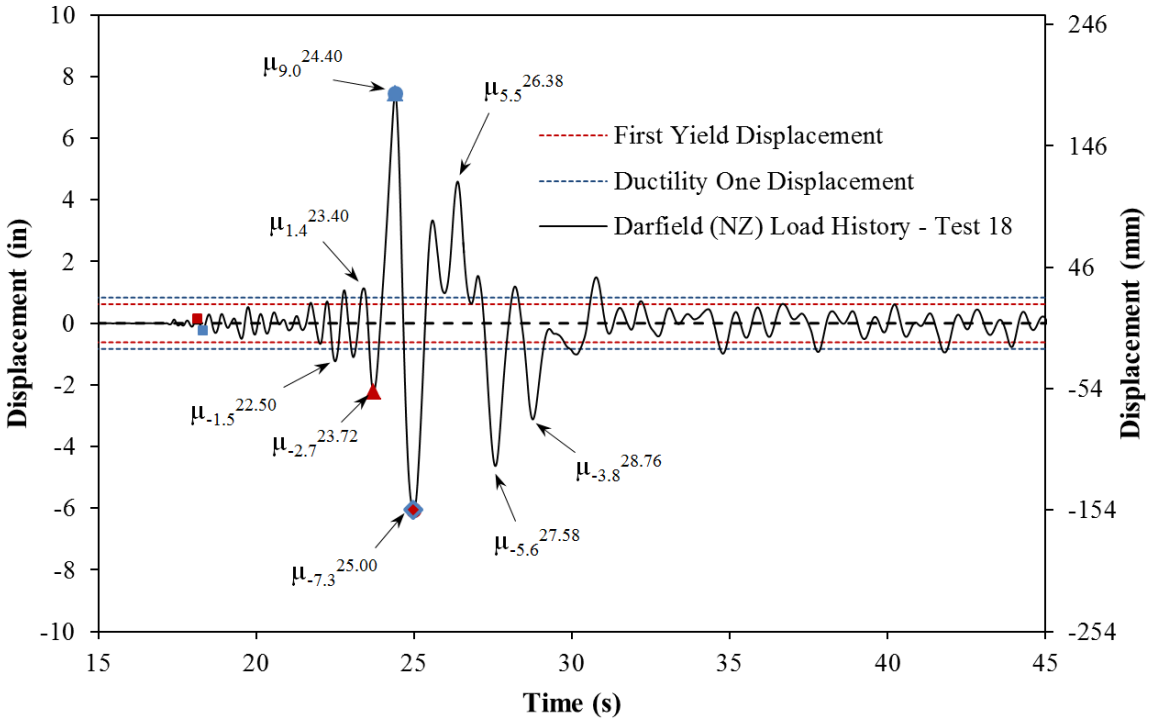

Figure 1.368 T18 – Darfield NZ 2010 Earthquake Load History

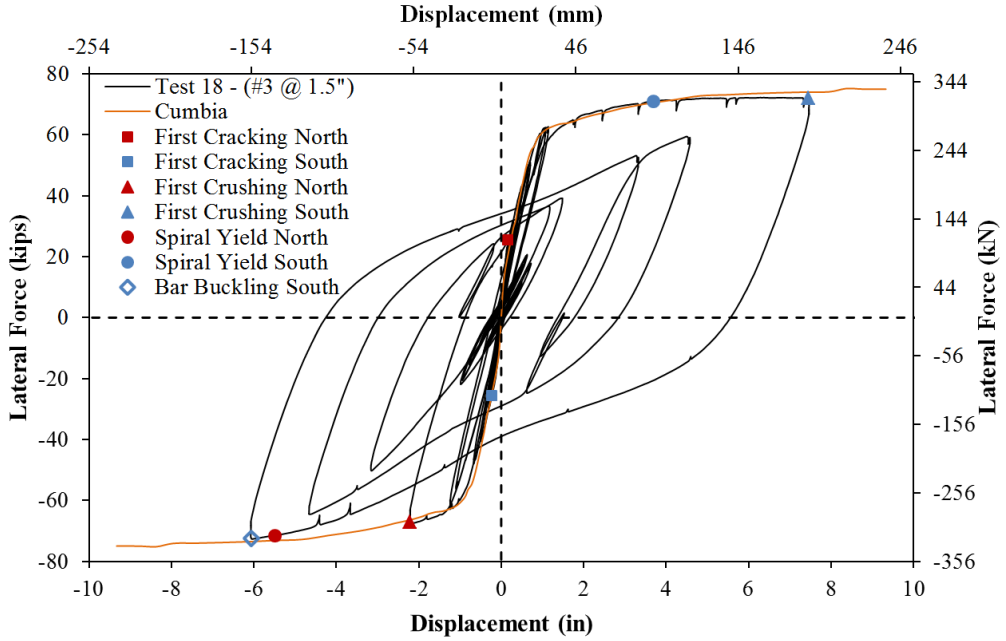

Figure 1.369 T18 – Darfield NZ Lateral Force vs. Top Column Displacement Response

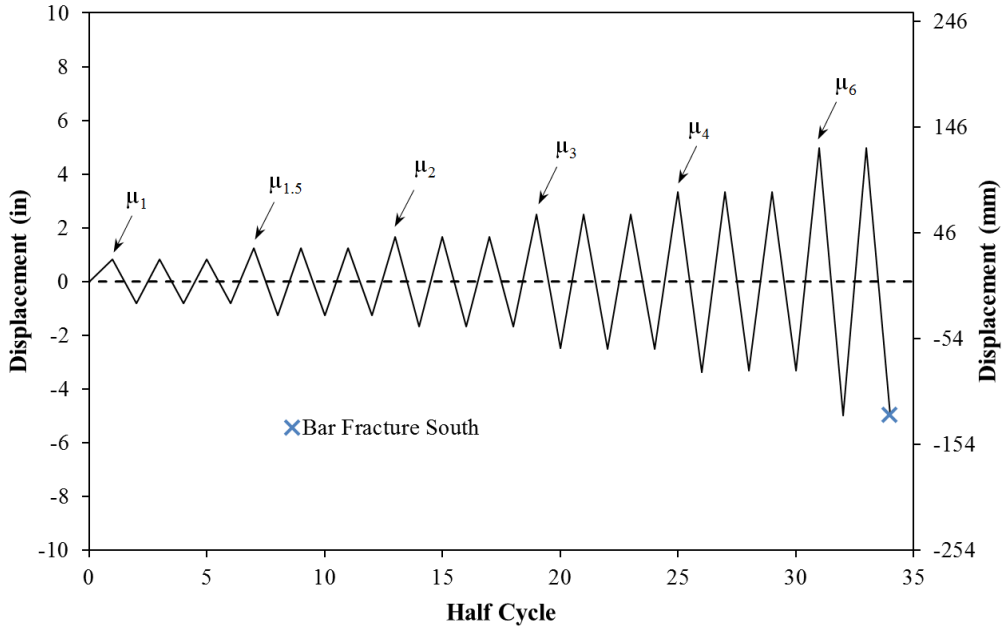

Figure 1.370 T18b – Symmetric Three Cycle Set Aftershock Load History

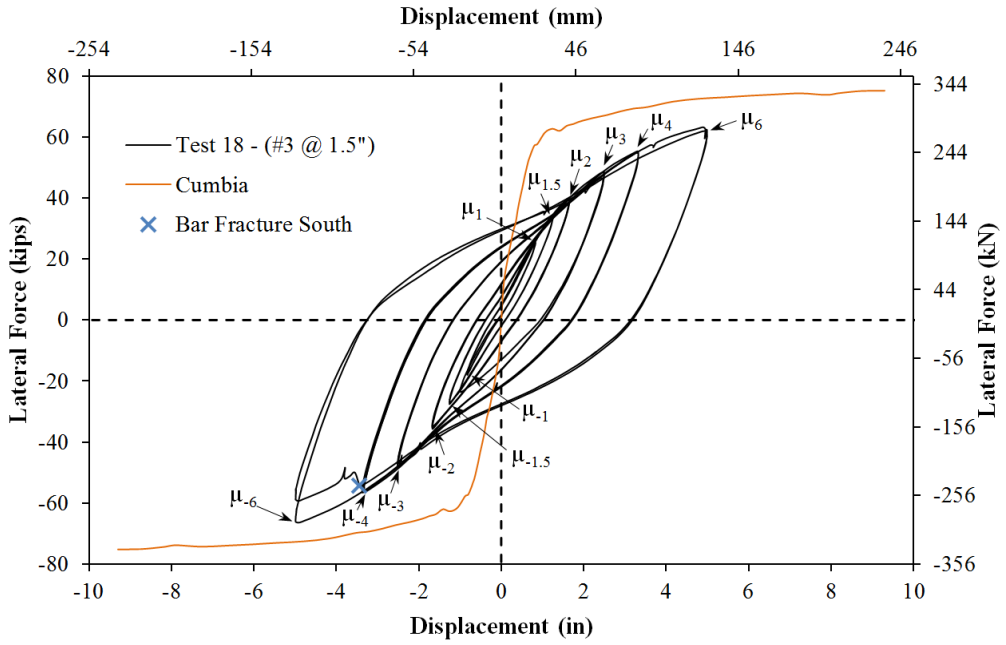

Figure 1.371 T18b – Cyclic Aftershock Lateral Force vs. Displacement Response

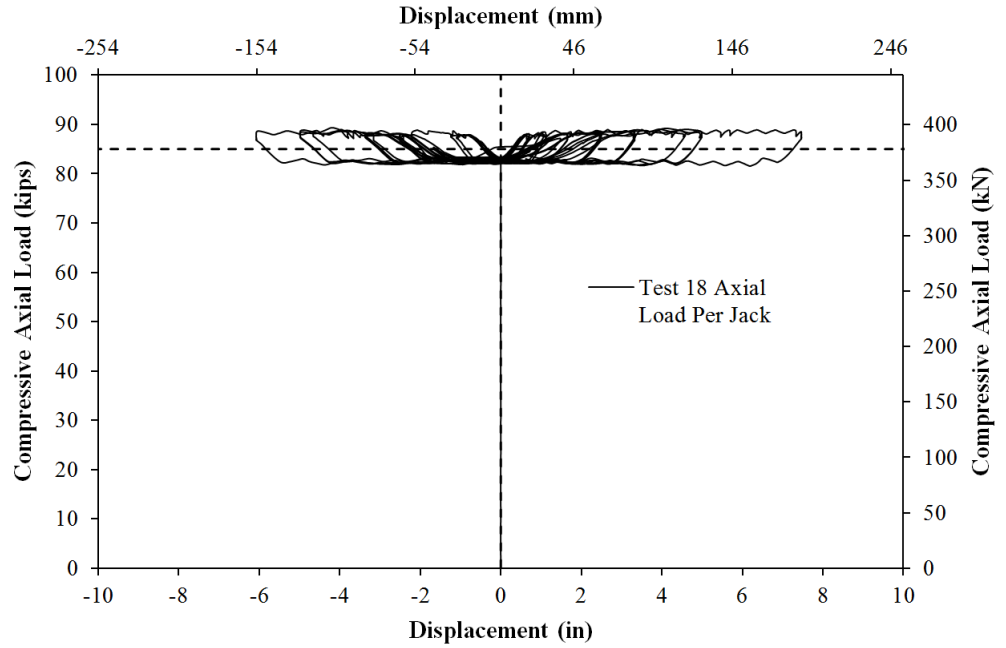

Figure 1.372 T18 – Compressive Axial Load from One Jack (Total = 2*Value)

Test 18 – Darfield NZ 2010 Earthquake Load History (#3 @ 1.5")

A scaled version of the Darfield 2010 New Zealand earthquake load history, with a peak displacement ductility of nine, was chosen for Test 18. The top column displacement history, in Figure 1.368, was obtained using numerical analysis in OpenSees with a force-based fiber element to model the column and a zero-length strain penetration element. The acceleration input of the Darfield 2010 earthquake record was multiplied by 0.97 to produce a peak displacement ductility of nine. The analytical top column displacement history was recreated in the lab with a quasi-static loading procedure. The resulting experimental lateral force vs. top column displacement response for the Darfield 2010 load history appears in Figure 1.369. The first yield displacement for Test 16, which had same detailing as Tests 17 and 18, was obtained as an average for the experimental first yield push and pull cycles ($\Delta'_y = 0.62"$). To determine if this first yield displacement is applicable to Test 18, the tensile strain profile at ($\Delta'_y = 0.62"$) for each extreme fiber bar appears in Figure 1.373. At the first yield displacement, the tensile strains in both extreme fiber reinforcing bars reached yield. The equivalent yield displacement, used to determine the displacement ductility levels ($\mu_{\Delta n} = \mathrm{n} * \Delta_y$), was then calculated as $\Delta_y = \Delta'_y(M_n/M'_y) = 0.83"$. The displacement ductility levels for Test 16, see Figure 1.373, are also applicable for Tests 17 and 18.

Three columns detailed with a #3 spiral at 1.5" spacing ($4A_{sp}/(D's) = 1.3\%$) were chosen for Tests 16-18. Reinforcement buckling occurred during ductility eight of a symmetric three cycle set load history in Test 16. A scaled version of the 1985 Llolleo Chile earthquake record did not produce bar buckling even though the peak response reached displacement ductility nine. The Llolleo 1985 Chile top column displacement history contains a large number of inelastic reversals of high amplitude both before and after the peak displacement. The top column displacement history for Test 18, which utilized a scaled version of the Darfield 2010 New Zealand record, appears in Figure 1.368. In comparison, the Darfield load history contains only a few high ductility cycles. The peak cycle in the opposing direction of the maximum response reaches displacement ductility 7.3. Bar buckling is not expected to occur after reversal from the peak displacement ductility of 9.0,

however, it offers the opportunity to study the influence of inelastic transverse steel restraint on potential buckling of longitudinal steel placed into tension during the ductility 7.3 reversal.

After conclusion of the Darfield 2010 New Zealand load history, the specimen had crushed cover concrete, degraded stiffness, and a single buckled reinforcing bar on the South side of the specimen. The specimen was subjected to a symmetric three cycle set load history to evaluate the effect of additional cycles on the buckled region on the South side of the column, and to determine what level of displacement is required to induce buckling of the North reinforcement. During ductility six, two additional South reinforcing bars buckled. The tensile demand sustained during repeated cycles at displacement ductility six was sufficient to rupture the extreme fiber South reinforcing bar which buckled during the Darfield load history. The test was concluded with three buckled bars and a single ruptured bar on the South side and unbuckled reinforcement on the North. The specimen was saved as a repair candidate.

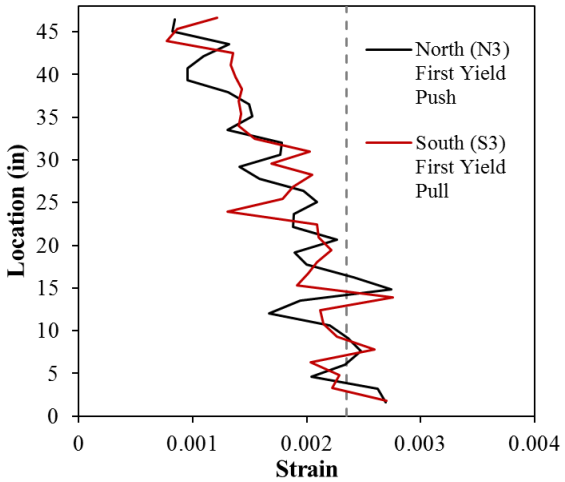

Analytical Fy'	46.80	kips
Experimental Δy'	0.62	in
Analytical My'	374.44	kip-ft
Analytical Mn	503.19	kip-ft
μ1	0.83	in
μ1.5	1.25	in
μ2	1.66	in
μ3	2.50	in
μ4	3.33	in
μ6	4.99	in
μ8	6.65	in
μ10	8.32	in
μ12	9.98	in

Figure 1.373 T18 – (Left) Tensile Strain Profiles at the First Yield Displacement of Test 16 and (Right) Displacement Ductility Levels from Test 16 (Also Apply for Test 17)

Test 18 – Darfield NZ 2010 Earthquake (#3 @ 1.5") Experimental Observations

The beginning of the Darfield 2010 New Zealand load history contains a large number of elastic reversals. The first cracks on the North side of the specimen measured 0.1mm at approximate 9" spacing during ($\mu_{0.2}^{18.12\,sec} = 0.17"$), as shown in the left photo of Figure 1.374. Crack widths reached 0.1mm at approximate 9" spacing on the South side of the specimen during ($\mu_{-0.3}^{18.30\,sec} = -0.23"$), see the middle photo of Figure 1.374. During the pull cycle to ($\mu_{-0.6}^{19.54\,sec} = -0.50"$), in the right photo of Figure 1.374, crack widths on the South side reached 0.3mm at approximate 5" spacing. Cracks on the North side reached 0.4mm at 5" spacing during the pull cycle to ($\mu_{0.6}^{19.74\,sec} = 0.51"$), see the left photo of Figure 1.375. The first cycles exceeding yield for the Darfield load history occurred during ($\mu_{0.8}^{21.72\,sec} = 0.66"$), when cracks on the North side of the specimen increased to 0.45mm at approximate 5" spacing. Crack widths reached 0.5mm at 5" spacing on the South side of the specimen during ($\mu_{-0.8}^{22.02\,sec} = -0.66"$), see the right two photos of Figure 1.375.

The first cycle exceeding the equivalent yield displacement in the push direction occurred during ($\mu_{-1.5}^{22.50\,sec} = -1.24"$), where crack widths reached 0.8mm at approximate 3-4" spacing. The crack distribution on the front side of the specimen at ($\mu_{1.3}^{22.78\,sec} = 1.04"$) appears in the left photo of Figure 1.376. During the pull cycle to ($\mu_{-2.7}^{23.72\,sec} = -2.21"$), crushing on the North side of the specimen extended 16" above the footing. Crack widths on the South side of the specimen reached 2.5mm at 3-4" spacing, as shown in Figure 1.376. The displacement when crushing first occurred was not recorded. The following reversal of loading pushed the specimen to the peak displacement of ($\mu_{9.0}^{24.40\,sec} = 7.46"$). The extent of crushing on the South side of the specimen reached 21" above the footing, see the middle photo of Figure 1.377. Additional photos of the specimen at the peak displacement appear in Figure 1.378. Crushing on the North side of the specimen reached 22" above the footing during the pull cycle to ($\mu_{-7.3}^{25.00\,sec} = -6.05"$), Figure 1.379.

North reinforcement exposed to tension during ($\mu_{9.0}^{24.40\,sec} = 7.46"$) did not visibly buckle during the large reversal to ($\mu_{-7.3}^{25.00\,sec} = -6.05"$). Large compressive demand during

($\mu_{9.0}^{24.40\,sec} = 7.46$") caused several layers of transverse steel on the South side of the specimen to enter the inelastic range. Inelastic transverse steel layers combined with large tensile strains during ($\mu_{-7.3}^{25.00\,sec} = -6.05$") buckled the extreme fiber South reinforcing bar during the following reversal of load. Visible buckling of Bar S3 is shown in the right two photos of Figure 1.379 at ($\mu_{4.0}^{25.58\,sec} = 3.32$"). Outward bar buckling occurred over the second and third transverse steel spacings above the footing. The remainder of the Darfield load history contained lower ductility cycles which did not produce any notable damage beyond increasing the buckled deformation in Bar S3.

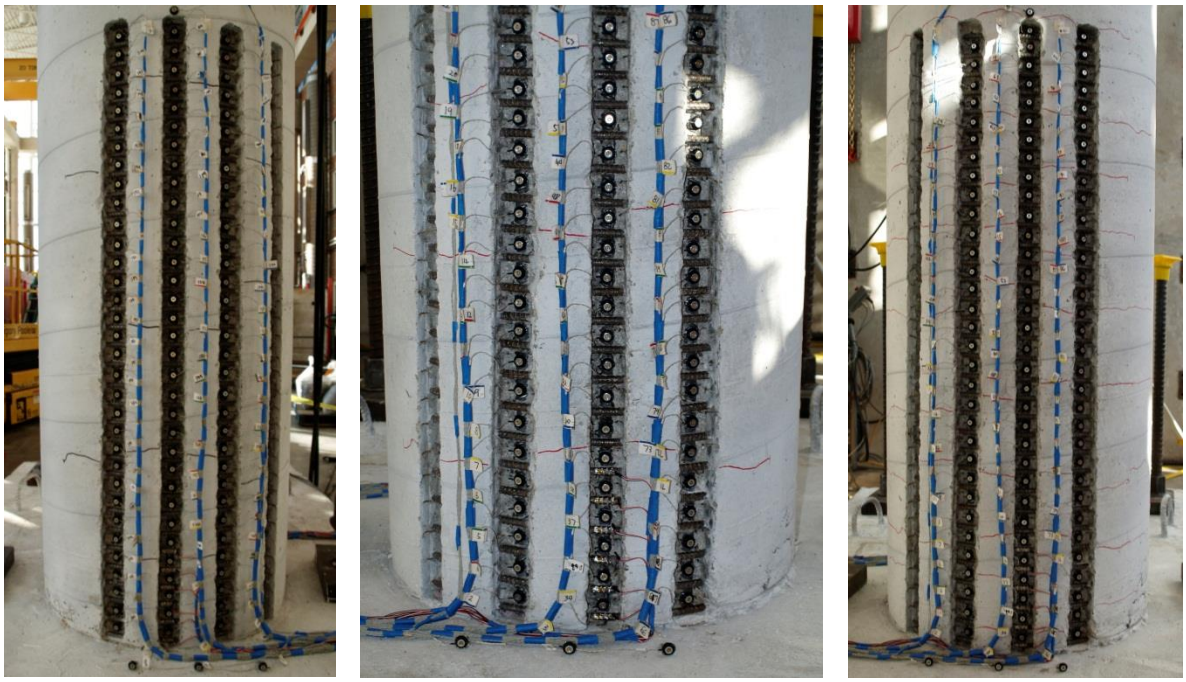

Figure 1.374 T18 – (Left) First Cracking on the North Side during ($\mu_{0.2}^{18.12\,sec} = 0.17$"), (Middle) First Cracking on the South Side during ($\mu_{-0.3}^{18.30\,sec} = -0.23$"), and (Right) South Crack Distribution during ($\mu_{-0.6}^{19.54\,sec} = -0.50$")

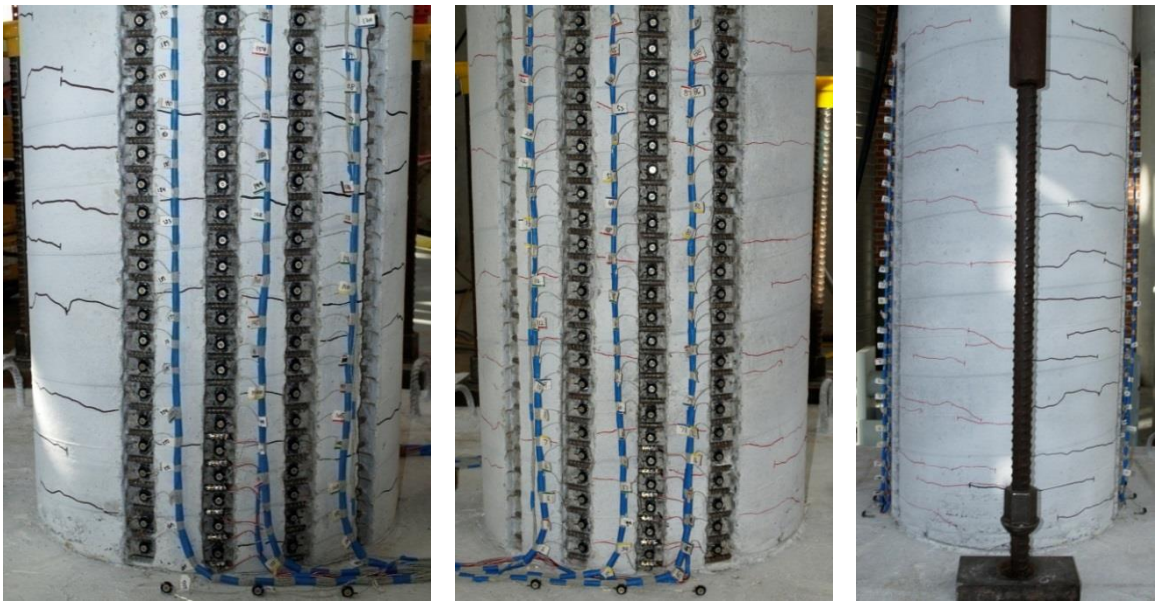

Figure 1.375 T18 – (Left) Cracks on the North Side at ($\mu_{0.6}^{19.74\,sec} = 0.51$"), (Middle and Right) Crack Distribution on the South and Back Sides at ($\mu_{-0.8}^{22.02\,sec} = -0.66$")

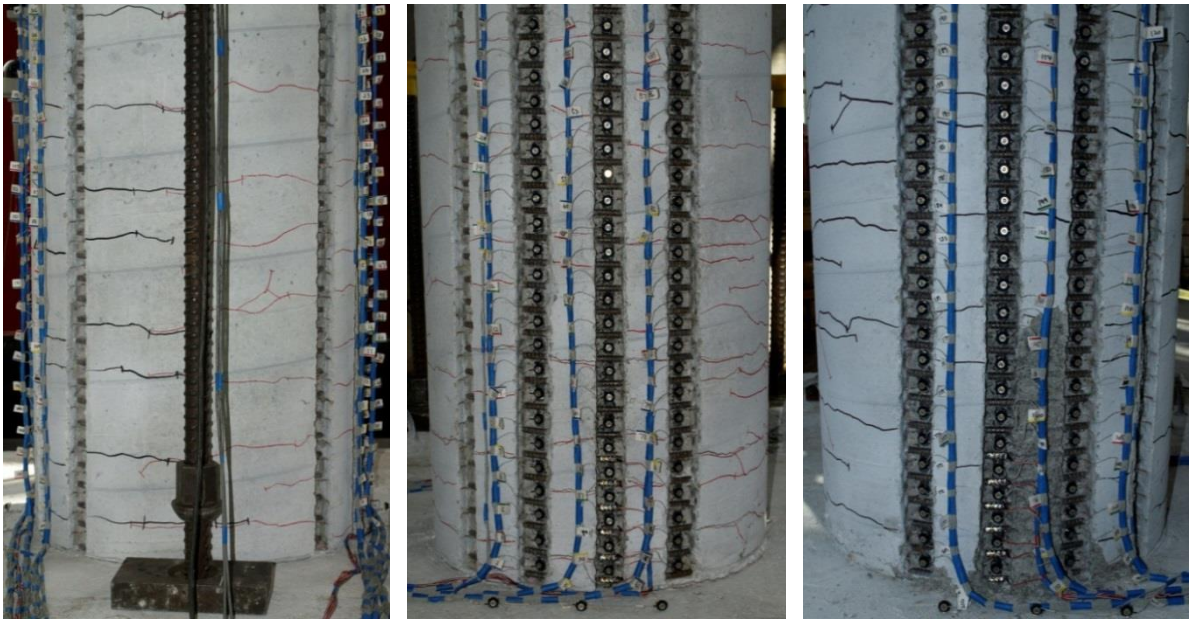

Figure 1.376 T18 – (Left) Crack Distribution on the Front Side during ($\mu_{1.3}^{22.78\,sec} = 1.04$"), (Middle) Cracking on the South Side during ($\mu_{-2.7}^{23.72\,sec} = -2.21$"), and (Right) Extent of Cover Concrete Crushing on the North Side at ($\mu_{-2.7}^{23.72\,sec} = -2.21$")

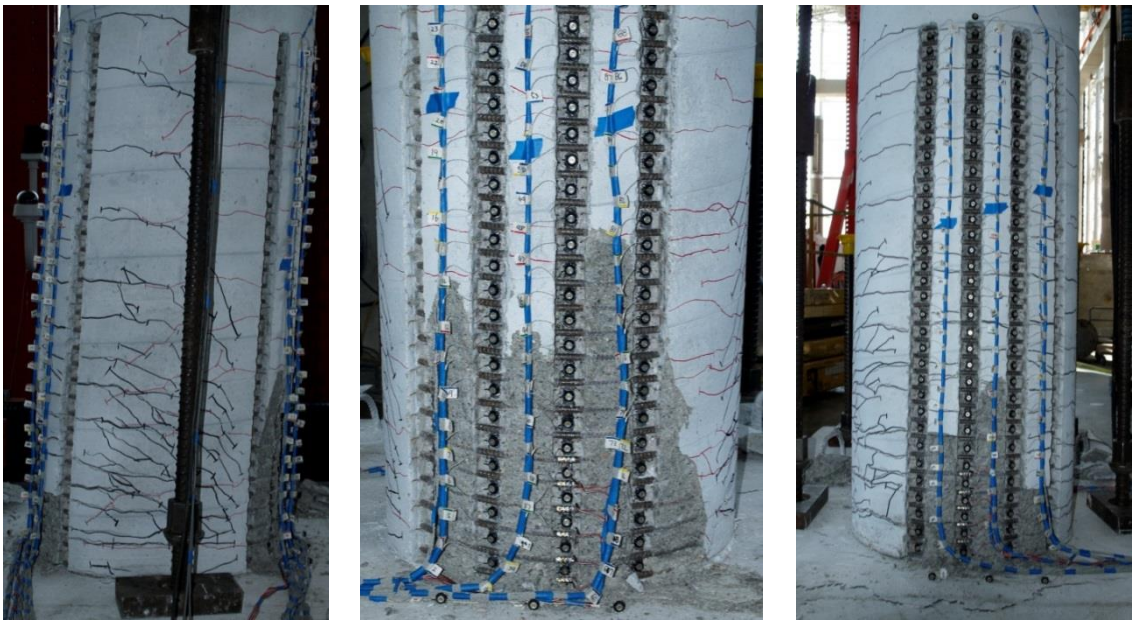

Figure 1.377 T18 – (Left) Crack Distribution on the Front Side during the Peak Cycle to ($\mu_{9.0}^{24.40\,sec} = 7.46$"), (Middle) Crushing on the South Side, and (Right) Crack on the Top of the Footing on the North Side of the Column

Figure 1.378 T18 – Crack Distribution at Peak Displacement ($\mu_{9.0}^{24.40\,sec} = 7.46$")

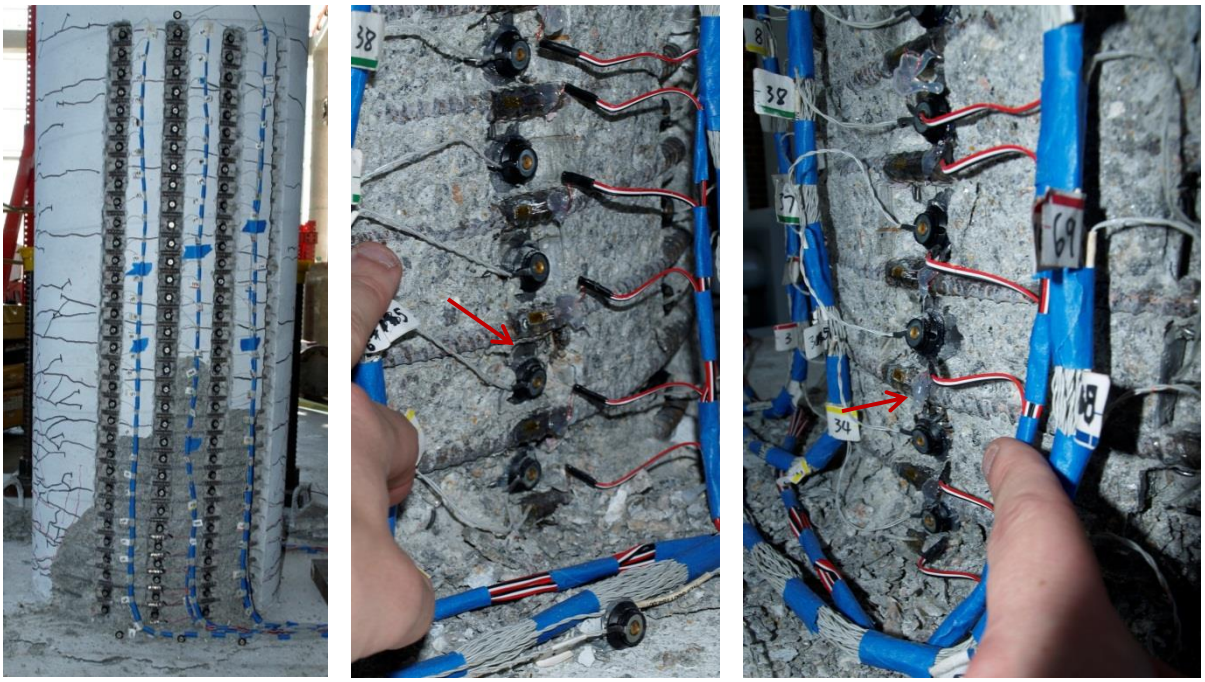

Figure 1.379 T18 – (Left) Extent of Crushing on the North Side during ($\mu_{-7.3}^{25.00\ sec} = -6.05$"), (Middle and Right) Visible Buckling of Bar S3 at ($\mu_{4.0}^{25.58\ sec} = 3.32$")

Test 18b – Cyclic Aftershock Load History (#3 @ 1.5") Experimental Observations:

After conclusion of the Darfield 2010 New Zealand load history, the specimen had crushed cover concrete, degraded stiffness, and a single buckled reinforcing bar on the South side of the specimen. Previous earthquake load histories scaled to approximately ductility nine failed to produce visible buckling. The specimen was subjected to a symmetric three cycle set load history, see Figure 1.370, to evaluate the effect of additional cycles on the buckled region on the South side of the column, and to determine what level of displacement is required to induce buckling of the North reinforcement. No notable damage occurred through ductility four of the cyclic aftershock study.

During the first push cycle of displacement ductility six, ($\mu_6^{+1} = 4.99$"), additional South reinforcing bars S2 and S4 buckled as shown in the left photo of Figure 1.380. The

outward deformation of previously buckled bar S3 was more severe than at any other point of the load history. On the way to ($\mu_6^{-2} = -4.99$"), previously buckled South reinforcing bar S3 ruptured in tension. The ruptured bar and deformations in several spiral layers is shown in Figure 1.380. The test was concluded with three buckled bars and a single ruptured bar on the South side and unbuckled reinforcement on the North. Cross section equilibrium was distorted beyond the use of additional buckling data for North reinforcement if test were to continue. The specimen was saved as a repair candidate.

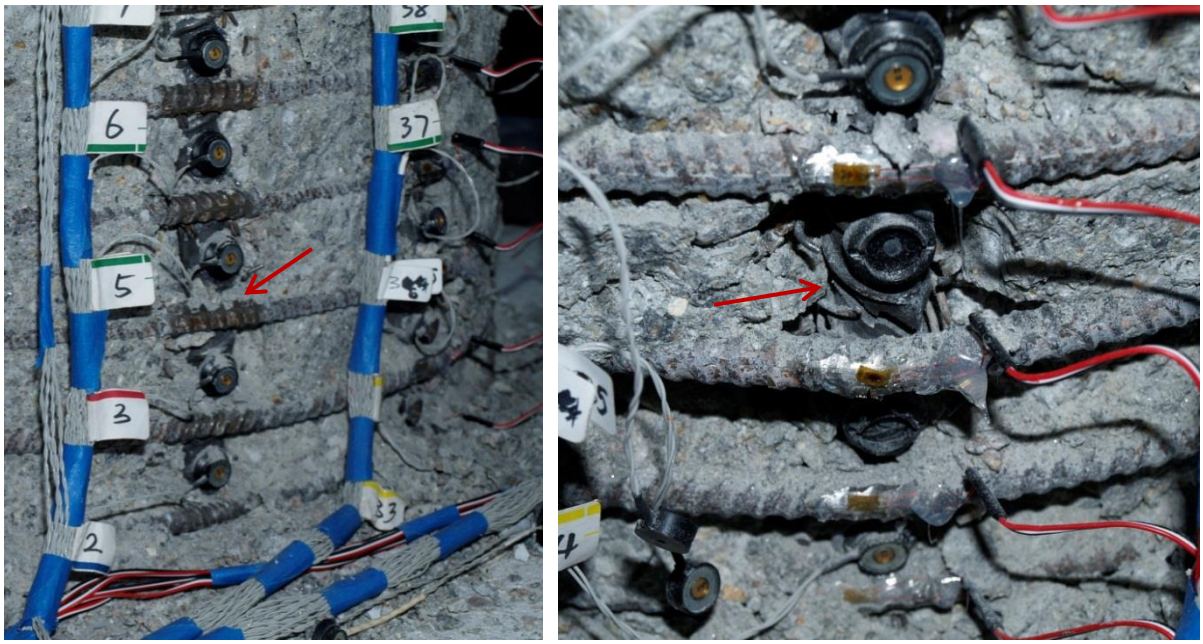

Figure 1.380 T18 – (Left) Buckling of Bars S2 and S4 during ($\mu_6^{+1} = 4.99$") and (Right) Rupture of Previously Buckled Bar S3 during ($\mu_6^{-2} = -4.99$")

Test 18 – Darfield NZ 2010 Earthquake Load History (#3 @ 1.5") Strain Data Analysis

North Reinforcement

Since the peaks of cycles during the earthquake load history do not align with the ductility levels of a traditional three cycle set load history, intermediate cycles along the backbone curve were selected for strain data analysis, see Figure 1.382. Extreme fiber vertical strain profiles for push and pull cycles appear in Figure 1.383 and Figure 1.384 respectively. A peak tensile strain of 0.062, located 3.19" above footing, was measured for extreme fiber bar N3 during ($\mu_{9.0}^{24.40\,sec} = 7.46"$). The relationship between tensile strain and displacement for this gage length appears in Figure 1.387. The solid line contains data during the push cycle loading up to the peak displacement and the dashed line represents the subsequent reversal of load. The peak tensile strain of 0.062 was not sufficient to produce visible bar buckling after reversal of load. The peak tensile gage length overlaid the largest crack on the north side of the specimen in Figure 1.381. Similar to previous tests, the moment curvature prediction for the relationship between strain and displacement using the PCK (2007) Lp Hinge Method begins to over predict the tensile strains at higher displacements at an increasing rate.

The largest compressive strain of -0.021 was measured in bar N3 for the gage length located 1.63" above the footing during ($\mu_{-7.3}^{25.00\,sec} = -6.05"$). The relationship between compressive strain and displacement for the gage length 1.63" above the footing appears in Figure 1.388. The transverse steel strains measured for the lowest six spiral layers overlaying the North reinforcement are plotted in Figure 1.386. The figure depicts tensile strains in the spiral layers on the North side of the specimen placed into compression during pull cycles. During the peak pull cycle to ($\mu_{-7.3}^{25.00\,sec} = -6.05"$), two spiral layers entered the inelastic range. The strain data for the North reinforcement does not give any indication of measurable deformation during the Darfield load history.

South Reinforcement

A peak tensile strain of 0.0466 on bar S3 was measured 3.31" above the footing during ($\mu_{-7.3}^{25.00\,sec} = -6.05"$). The relationship between tensile strain and displacement for this gage length is shown in Figure 1.389. The same comments on the accuracy of the moment curvature prediction for the North reinforcement also apply to bar S3. The blue dashed line, after reversal from ($\mu_{-7.3}^{25.00\,sec} = -6.05"$), no longer represents engineering strain due to the observed outward buckling over the gage length depicted in Figure 1.379. A peak compression strain of -0.0481 was measured 1.78" above the footing during ($\mu_{9.0}^{24.40\,sec} = 7.46"$). The relationship between compressive strain and displacement for this gage length appears in Figure 1.390. At large displacements, the measured compressive strains are significantly larger than the moment curvature prediction. The measured compression strain of -0.0481 is 2.7 times larger than the Mander ultimate concrete compressive strain of -0.0176. The effect of the large compressive demand on the South side of the specimen can be seen in the transverse steel layers overlaying the extreme fiber bar in Figure 1.385. Two layers of transverse steel enter the inelastic range at displacement ductility six during the push cycle to ($\mu_{9.0}^{24.40\,sec} = 7.46"$). By displacement ductility eight, four transverse steel layers went into the inelastic range. The strain gage on the spiral layer 3.56" above the footing went off scale during ($\mu_{9.0}^{24.40\,sec} = 7.46"$).

The strain hysteresis for extreme fiber Bar S3 appears in Figure 1.391 for the gage length 3.31" above the footing which outwardly deformed as the bar buckled. The strain hysteresis for the gage length located 4.83" above the footing appears in Figure 1.392. This gage length coincides with the region where the bar begins to straighten back out. Both graphs are shown to illustrate the effect compressive localization over inelastic spiral layers. The transverse steel strain hysteresis for the spiral layers located 2.06" and 3.56" above the footing appear in Figure 1.393 and Figure 1.394 respectively. During ($\mu_{9.0}^{24.40\,sec} = 7.46"$), the strain in the transverse steel layer 3.56" above the footing increased beyond 0.016, where the strain gages goes off scale. As this occurred, the instrumentation indicated measurable deformation in bar S3, leading to higher compressive strains in the gage length 4.83" above

the footing and lower compressive strains 3.31" above the footing. This location agrees with the location of bar buckling observed in the test.

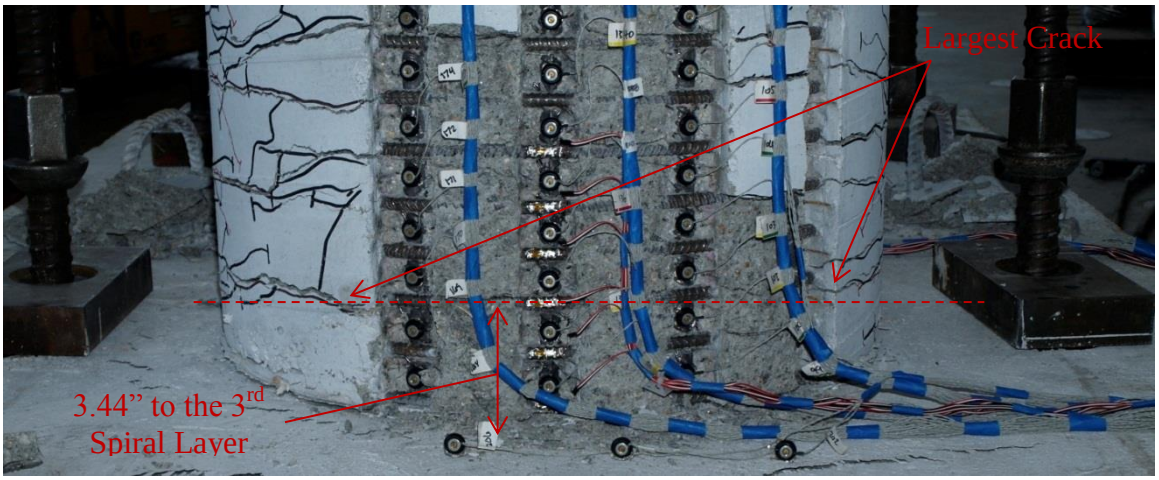

Figure 1.381 T18 – Largest Cracks on North Side at ($\mu_{9.0}^{24.40\ sec} = 7.46$")

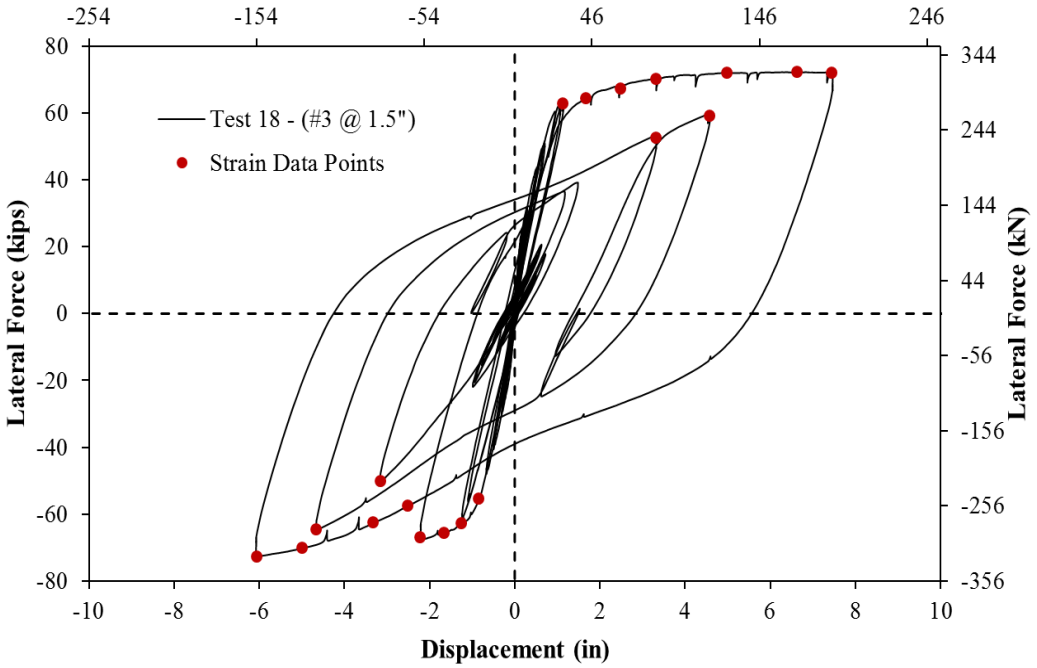

Figure 1.382 T18 – Strain Data Observation Points along the Backbone Curve

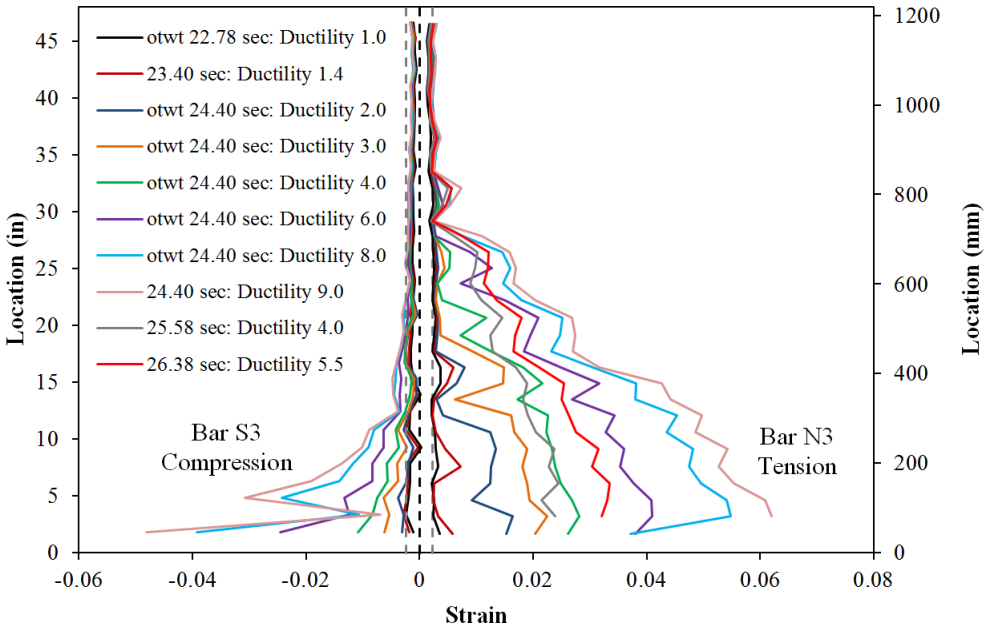

Figure 1.383 T18 – Extreme Fiber Vertical Strain Profiles during Push Cycles

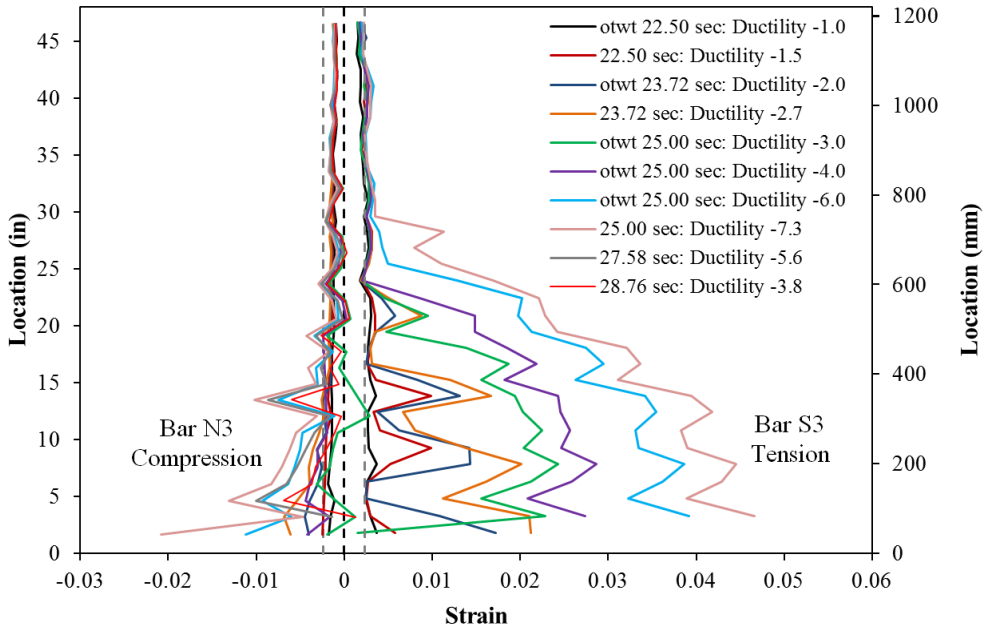

Figure 1.384 T18 – Extreme Fiber Vertical Strain Profiles during Pull Cycles

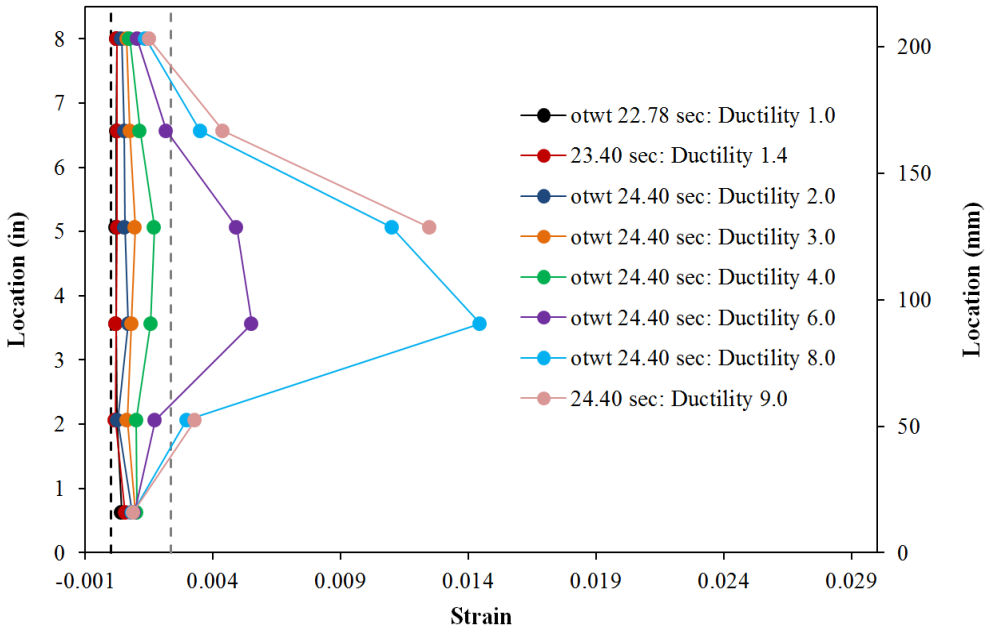

Figure 1.385 T18 – Transverse Steel Strains on the South Side during Push Cycles

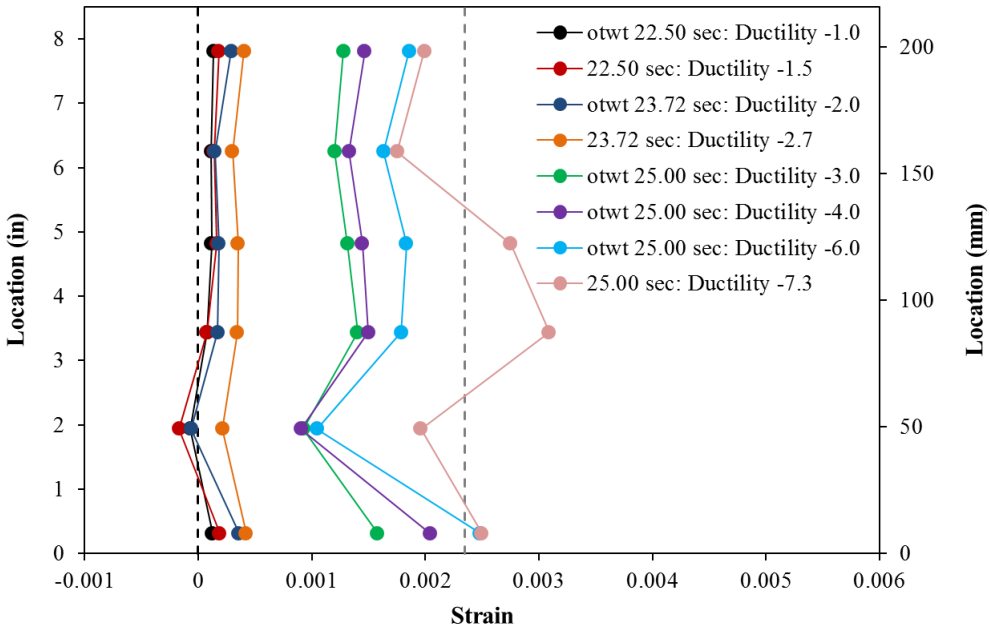

Figure 1.386 T18 – Transverse Steel Strains on the North Side during Pull Cycles

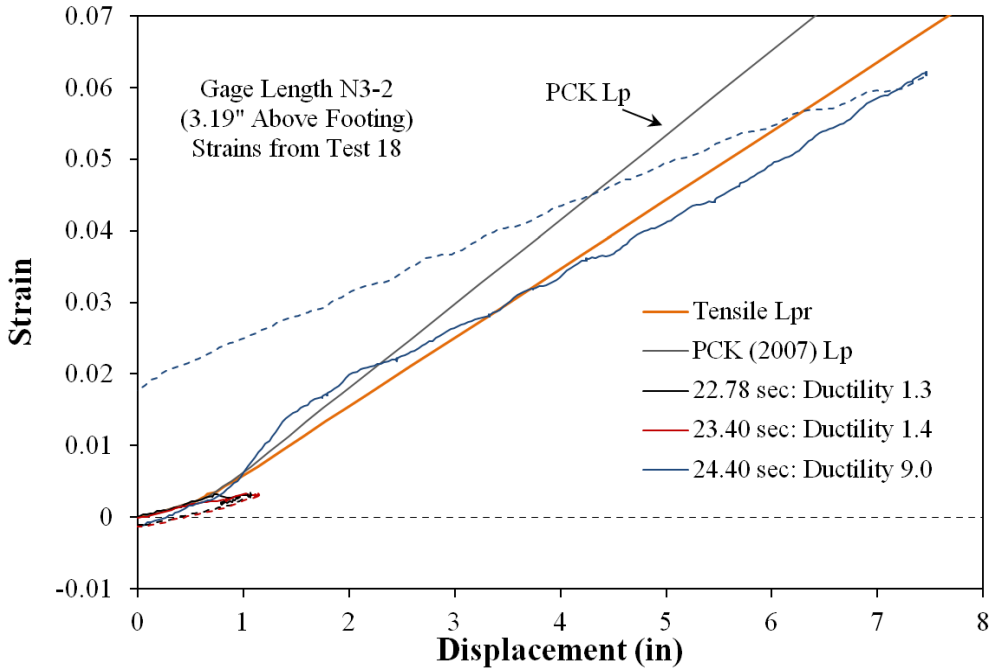

Figure 1.387 T18 – Tensile Strain-Displacement for Bar N3 (3.19" Above Footing)

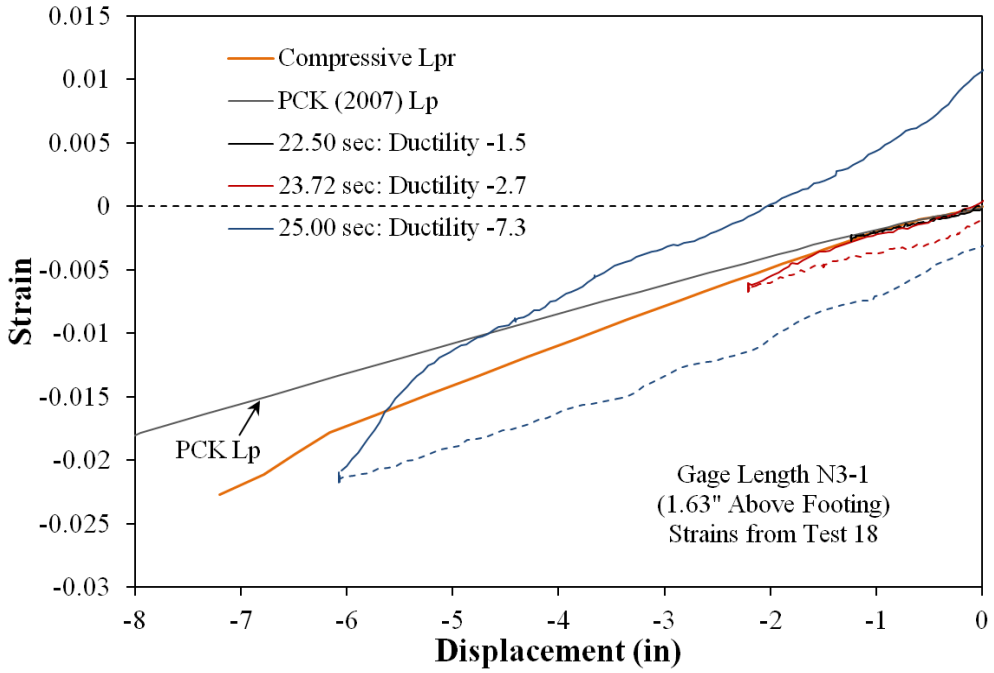

Figure 1.388 T18 – Compressive Strain-Displacement for Bar N3 (1.63" Above)

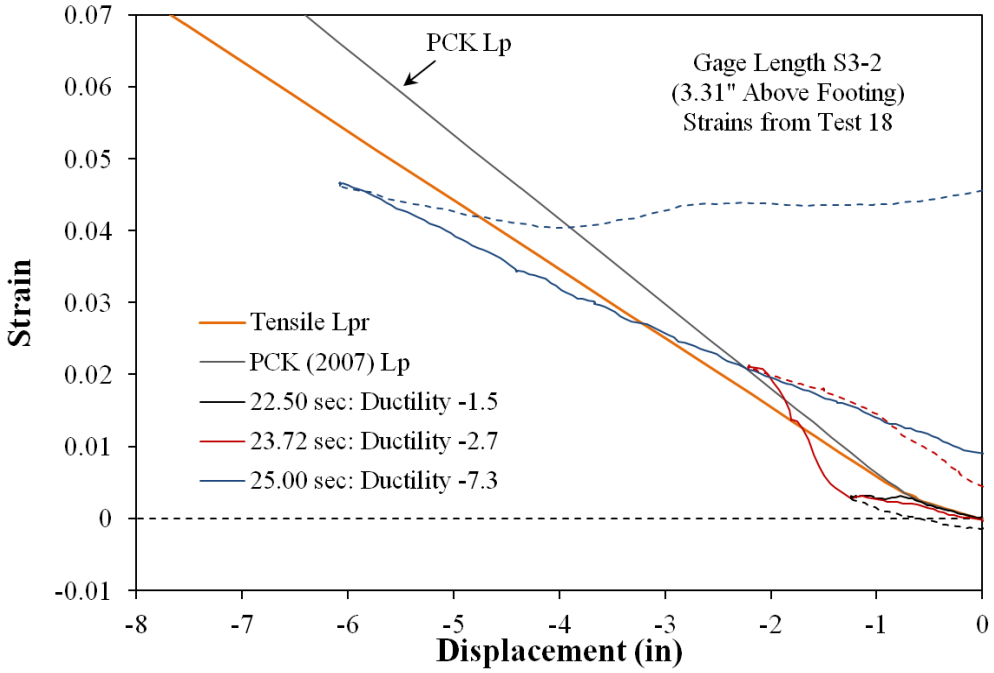

Figure 1.389 T18 – Tensile Strain-Displacement for Bar S3 (3.31" Above Footing)

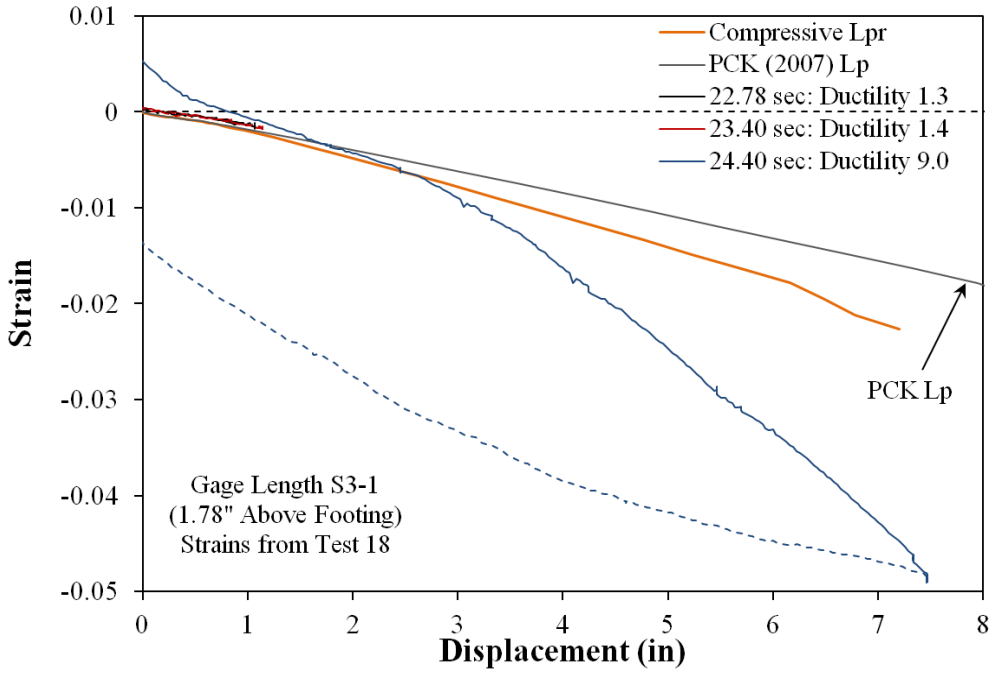

Figure 1.390 T18 – Compressive Strain-Displacement for Bar S3 (1.78" Above)

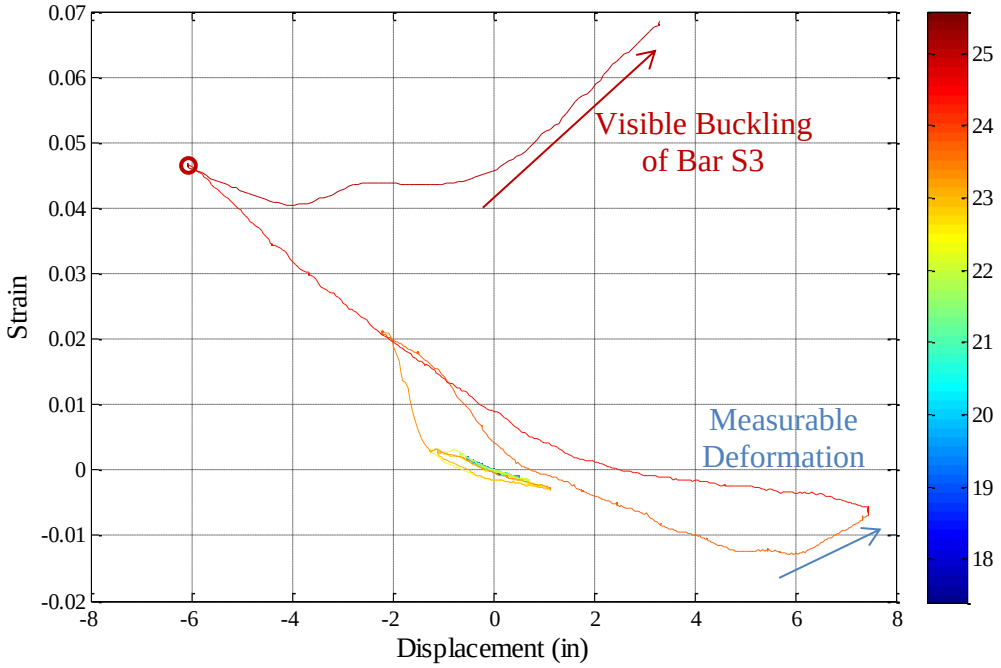

Figure 1.391 T18 – Bar S3 Strain Hysteresis for the Gage Length 3.31" Above Footing

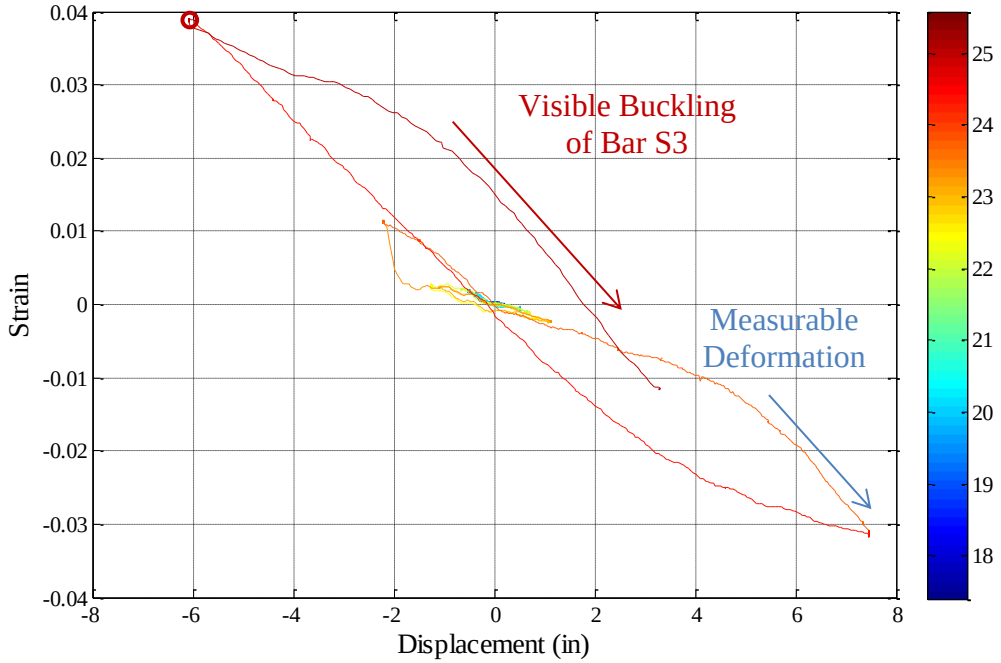

Figure 1.392 T18 – Bar S3 Strain Hysteresis for the Gage Length 4.83" Above Footing

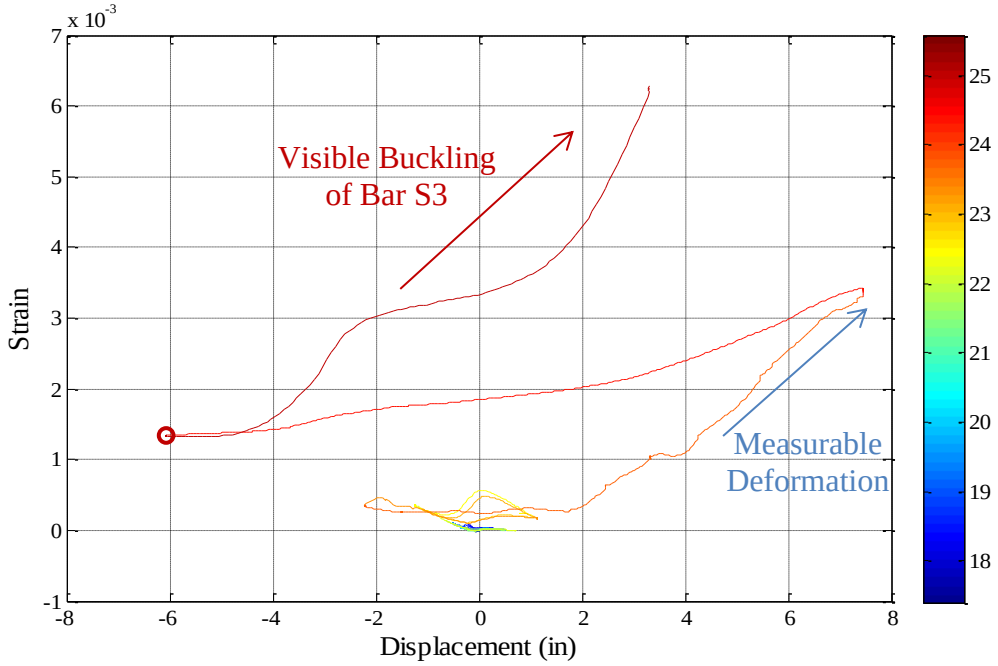

Figure 1.393 T18 – Spiral Strain Hysteresis over Buckled Bar S3 (Layer 2.06" Above)

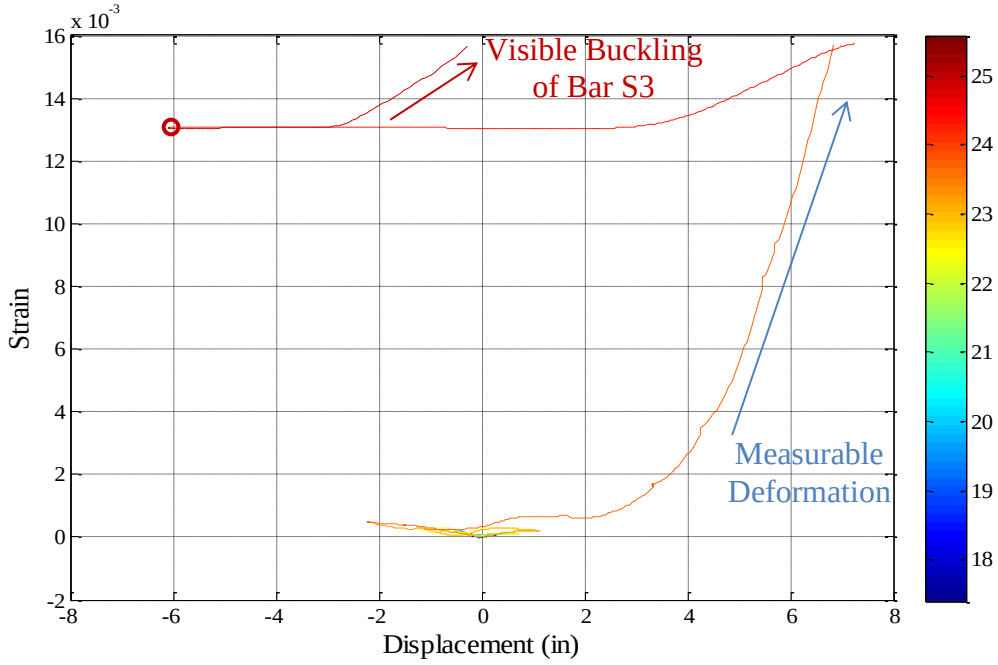

Figure 1.394 T18 – Spiral Strain Hysteresis over Buckled Bar S3 (Layer 3.56" Above)

Test 18 – Darfield NZ 2010 EQ LH (#3 @ 1.5") Curvature and Strain Penetration Data

Vertical curvature profiles are plotted for push and pull cycles in Figure 1.395 and Figure 1.396 respectively. These figures show that plastic curvatures have a linear distribution at higher displacement ductility levels. As the displacements increase, the base curvatures become larger and the extent of plastic curvatures reach higher above the footing. The target marker on each reinforcing bar placed closest the footing-column interface can be used to create slip hysteresis and horizontal slip profiles attributable to strain penetration. The slip hysteresis for North extreme fiber bar N3 appears in Figure 1.399. The peak tensile slip bar N3 exceeded 0.34" at ($\mu_{9.0}^{24.40\,sec} = 7.46"$). If the tensile and compressive slip of all of the instrumented bars is plotted along the cross section depth, the base rotation attributable to strain penetration may be calculated. The slip profiles for push and pull cycles appear in Figure 1.397 and Figure 1.398 respectively.

The measured string potentiometer displacements from Test 18 were compared to the displacement obtained from curvature diagram integration and slip profile extrapolation to the center of loading in Figure 1.400. The measured and integrated top column displacements match well with the exception of high ductility data points near ($\mu_{-7.3}^{25.00\,sec} = -6.05"$). The measured spread of plasticity as a function of base section curvature ductility appears in Figure 1.401. The circular data points plot the measured extent of plasticity, obtained as the intersection of the linear plastic curvature regression and the elastic curvature profiles.

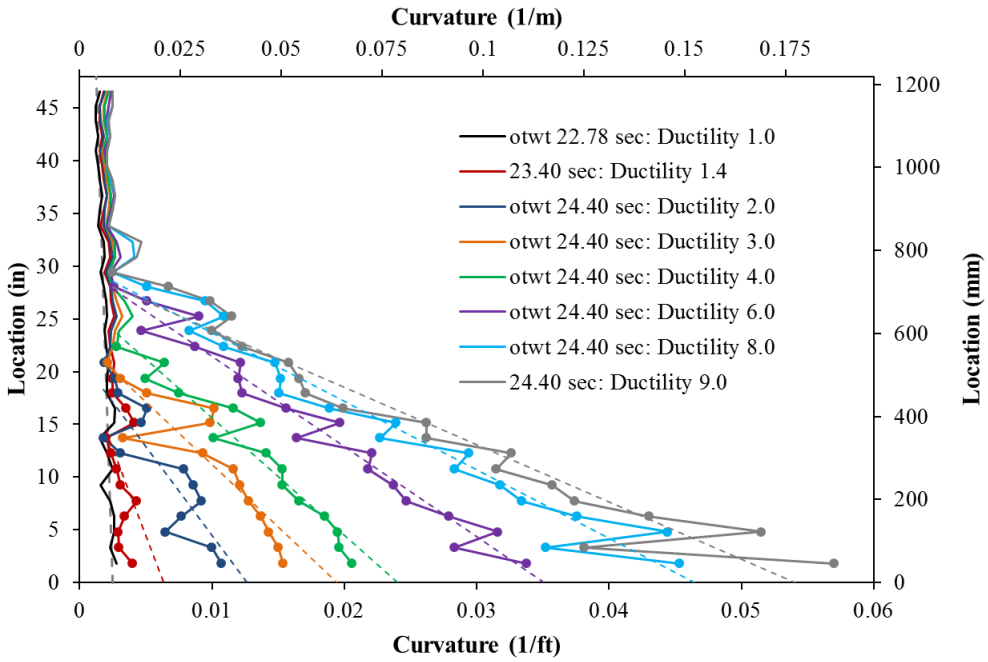

Figure 1.395 T18 – Curvature Profiles during Push Cycles with Plastic Regression

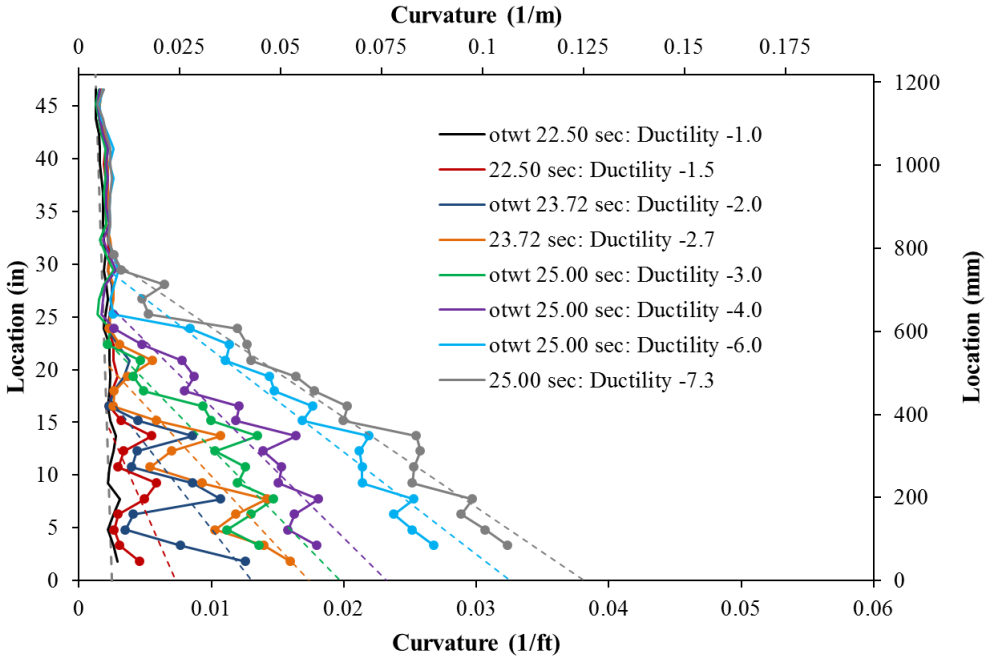

Figure 1.396 T18 – Curvature Profiles during Pull Cycles with Plastic Regression

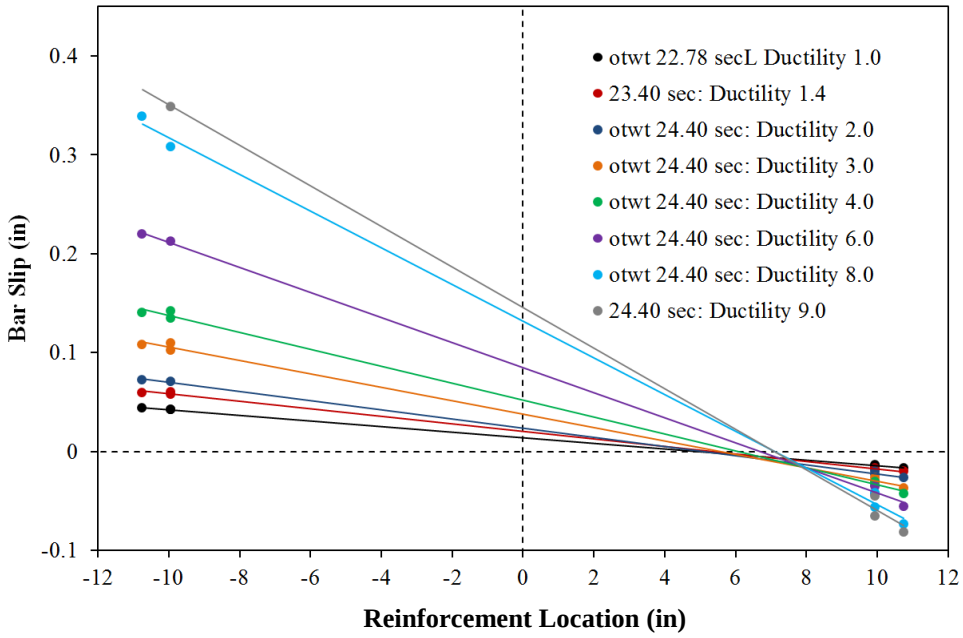

Figure 1.397 T18 – Base Rotation during Push Cycles due to Strain Penetration

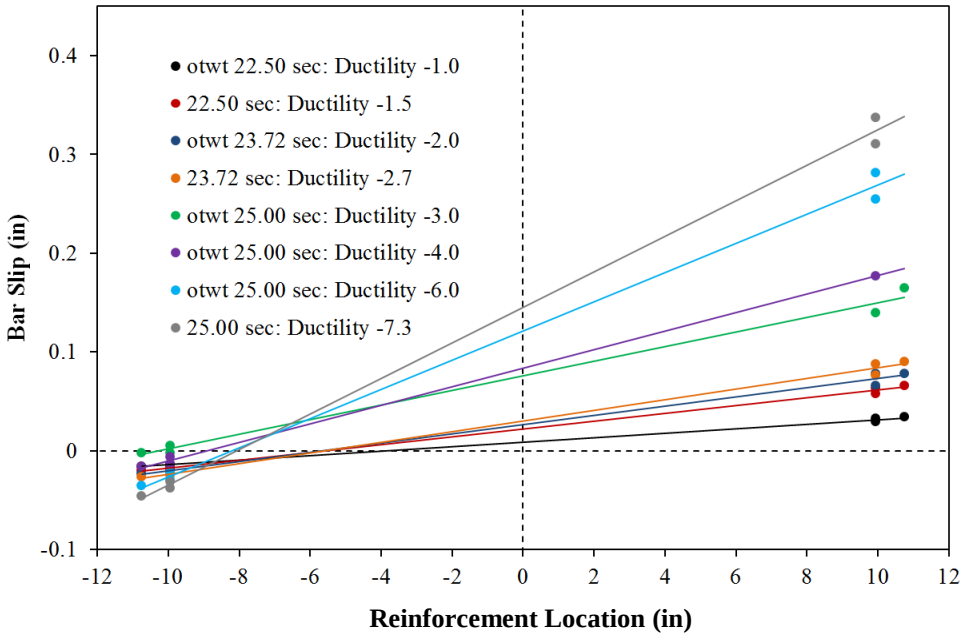

Figure 1.398 T18 – Base Rotation during Pull Cycles due to Strain Penetration

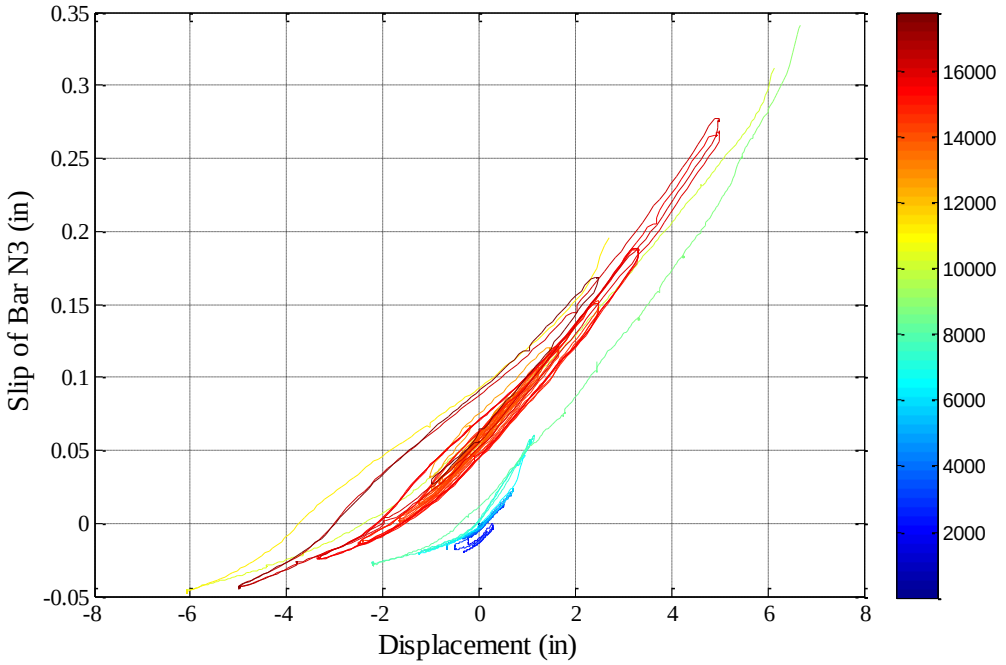

Figure 1.399 Test 18 – Bar N3 Slip Hysteresis at the Footing-Column Interface

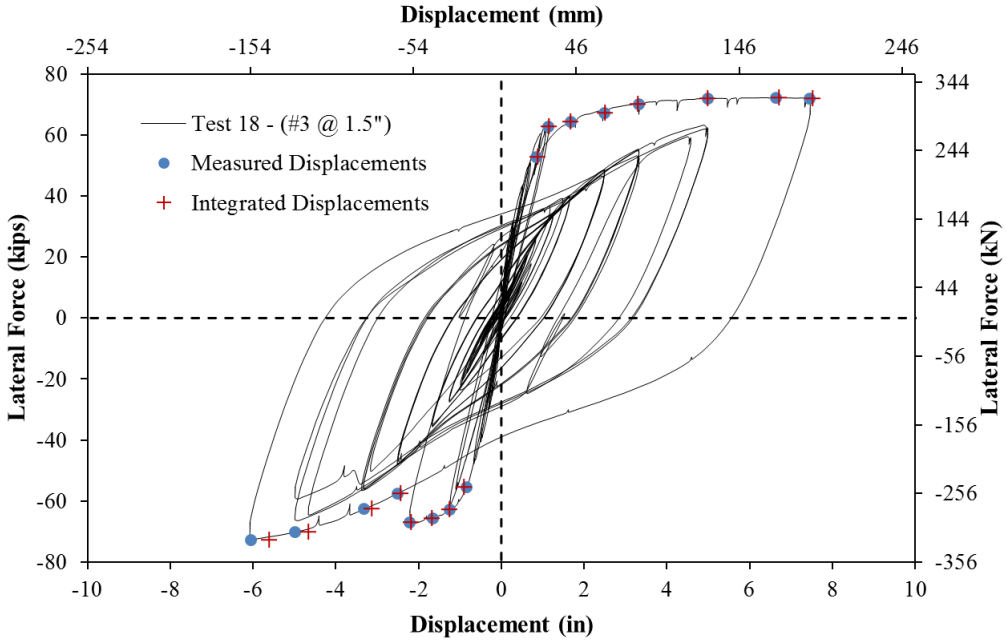

Figure 1.400 T18 – Comparison of Measured and Optotrak Integrated Displacements

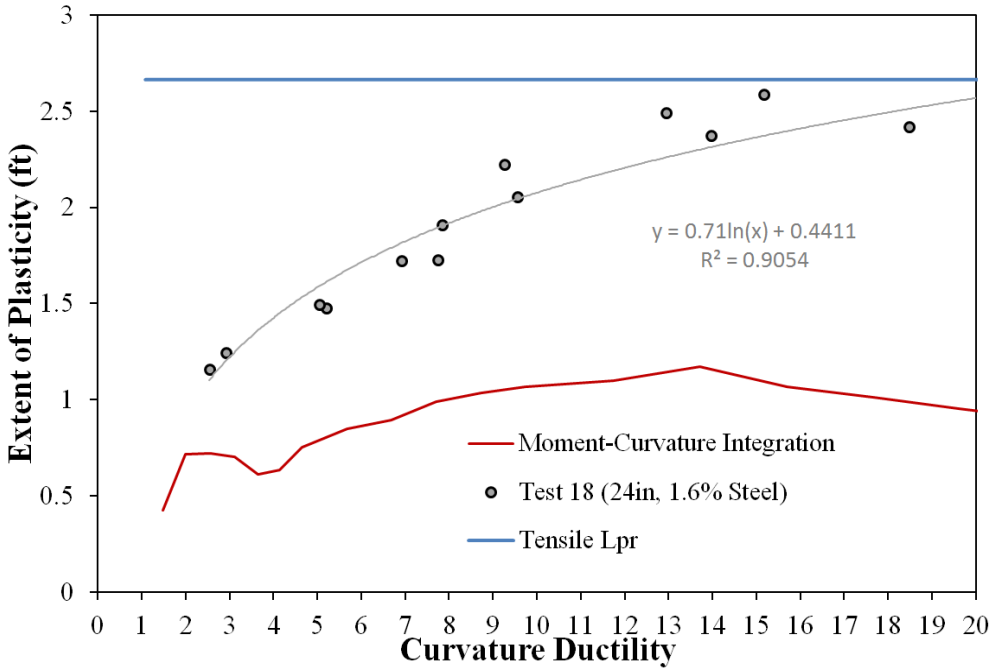

Figure 1.401 T18 – Measured Spread of Plasticity (Circular Data Point Markers)

Test 18b – Cyclic Aftershock Load History (#3 @ 1.5") Strain Data Analysis:

Vertical strain profiles for extreme fiber Bar N3 during push and pull cycles of the cyclic aftershock load history appear in Figure 1.402 and Figure 1.403 respectively. The strain profiles for bar N3 follow a similar shape because the crack distribution was previously set in place during peak cycles of the Darfield load history. The transverse steel strains measured over the lowest six spiral layers overlaying the North reinforcement are plotted in Figure 1.404. During the first and second pull cycles of ductility six, transverse steel strains reached 0.0038 and 0.0039 respectively. The complete strain hysteresis for bar N3, for the gage length 3.19" above the footing, appears in Figure 1.405. A similar strain hysteresis for the gage length 4.63" above the footing is shown in Figure 1.406. The gage length 3.19" above the footing is directly crossed by the largest crack on the North side of the specimen as shown in Figure 1.381. This explains the larger residual strain after the peak cycle evident in the gage length 3.19" above the footing.

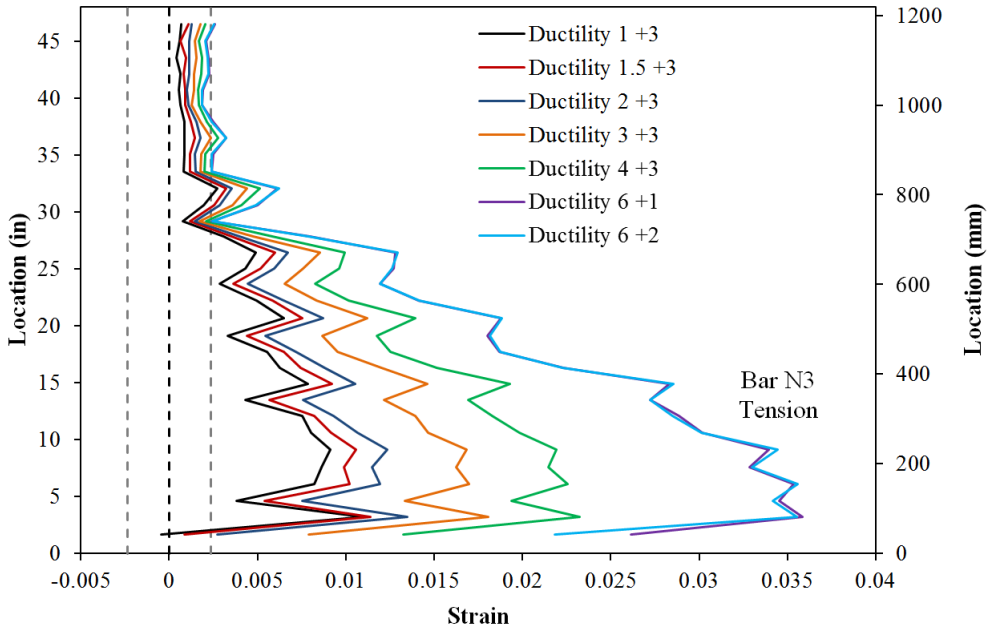

Figure 1.402 T18b – Vertical Strain Profiles for Bar N3 during Push Cycles

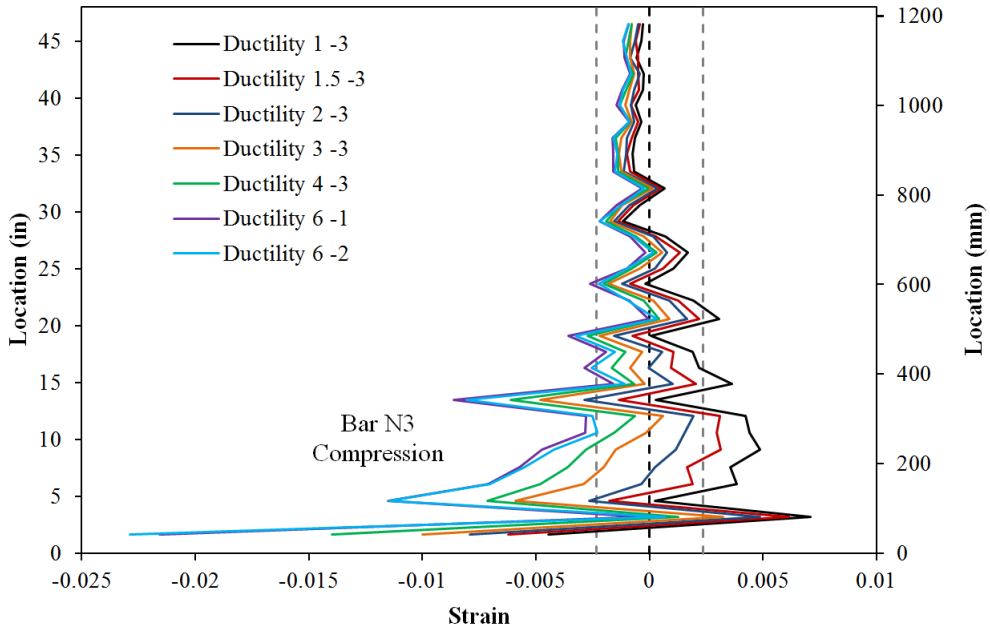

Figure 1.403 T18b – Vertical Strain Profiles for Bar N3 during Pull Cycles

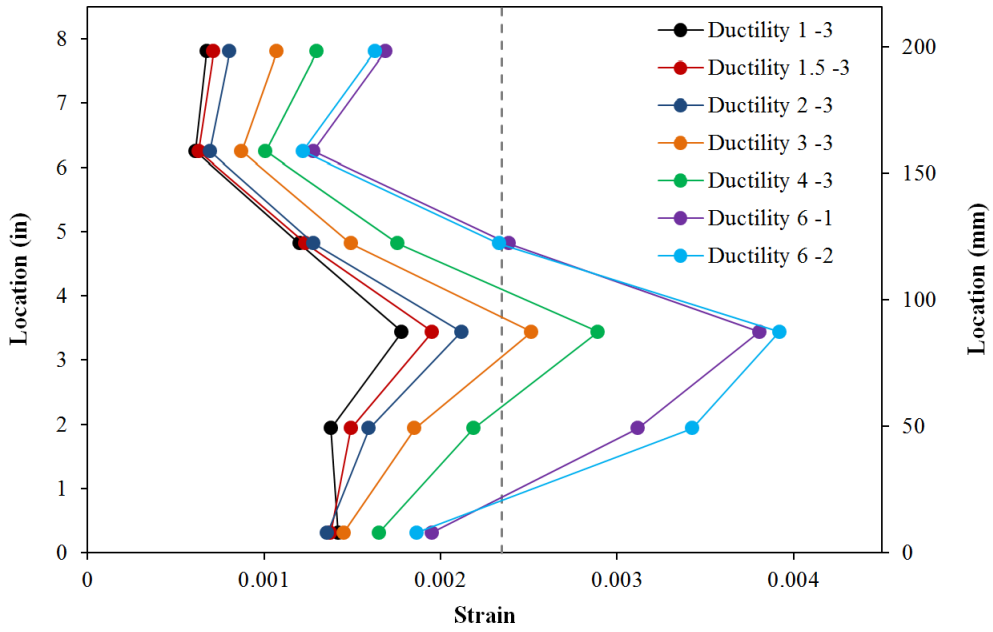

Figure 1.404 T18b – Spiral Strains for Layers overlaying Bar N3 during Pull Cycles

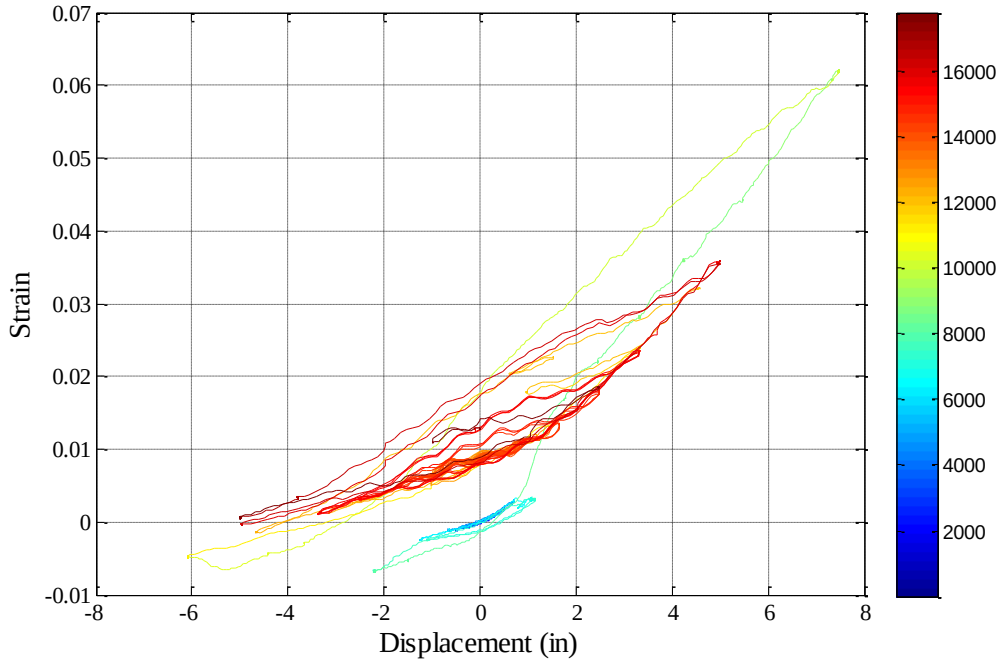

Figure 1.405 T18 and T18b – Bar N3 Strain Hysteresis 3.19" Above the Footing

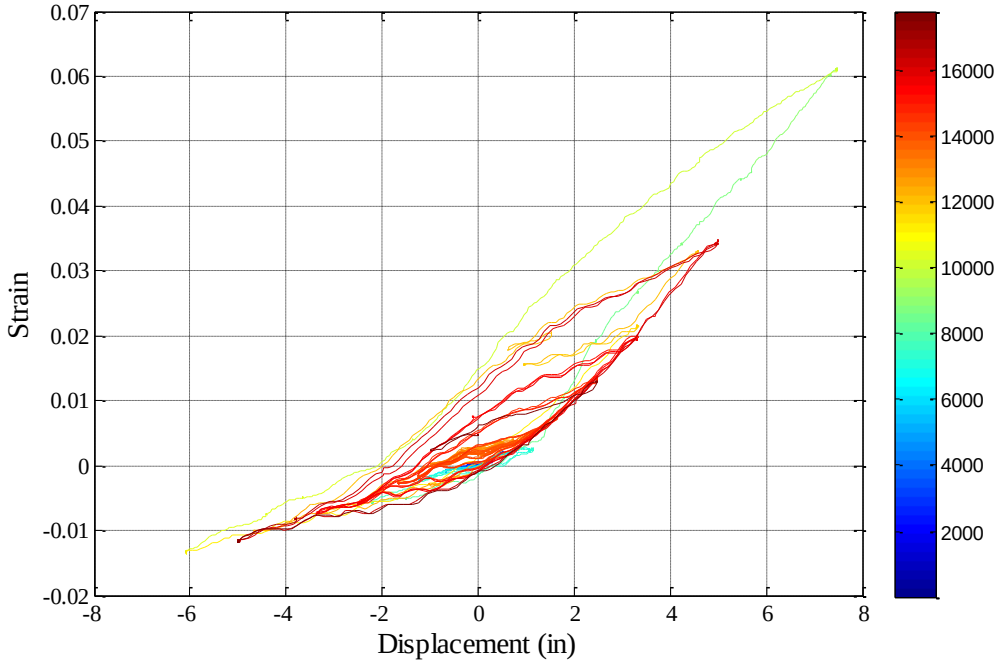

Figure 1.406 T18 and T18b – Bar N3 Strain Hysteresis 4.63" Above the Footing

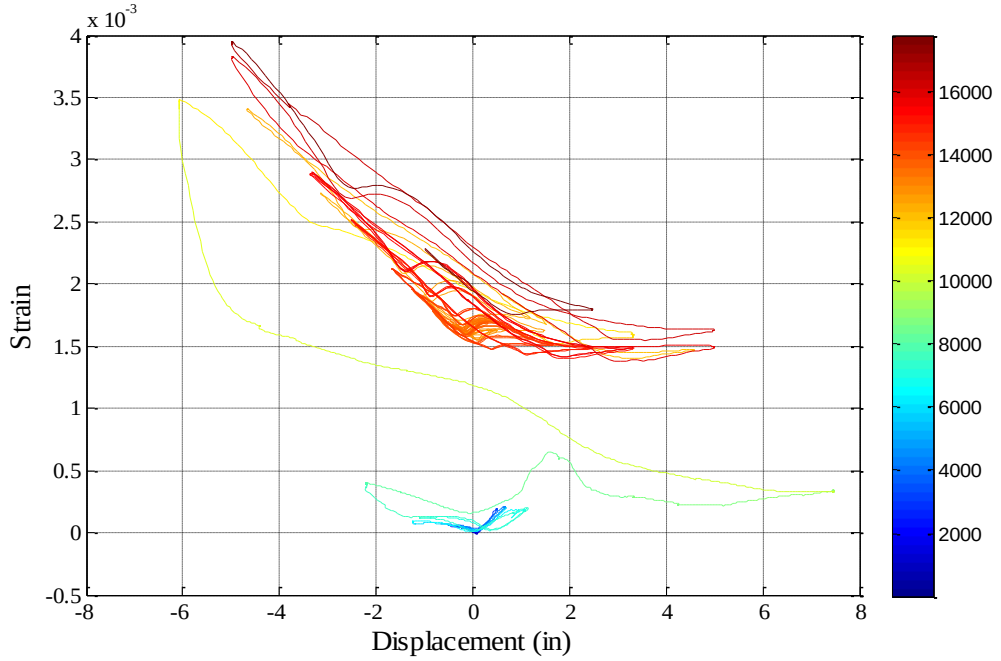

Figure 1.407 Spiral Strain Hysteresis for the Layer over Bar N3 (3.44" Above)

1.3 Aspect Ratio and Axial Load Variable Tests 19-24

The effects of aspect ratio and axial load ratio on column performance were the main variables for Tests 19-24. The test matrix for the eight columns is shown in Table 1.31, and the material properties of the reinforcement appear in Table 1.32. The 18" (457mm) diameter bridge columns, Figure 1.410, contained 10 #6 (19mm) A706 bars for longitudinal reinforcement ($A_{st}/A_g = 1.7\%$) and a #3 (9.5mm) A706 spiral at 2" spacing ($4A_{sp}/D's = 1.3\%$). The shear span for the cantilever columns was either 8ft (244cm), 11ft (335cm), or 13ft (396cm), resulting in moment to shear ratios of ($M/VD = 5.33,\ 7.33,\ or\ 8.67$). For each aspect ratio, one specimen was subjected to ($P/(f_c'A_g) = 5\%$) and the other was subjected to 10% axial load. Photos of the test setup for the tallest aspect ratio columns appear in Figure 1.411. Stress-strain curves for the longitudinal and transverse steel are shown in Figure 1.408 and Figure 1.409. The test series used the full cover concrete blockout method with target markers applied to both longitudinal and transverse steel, Figure 1.410.

In design, an equivalent curvature distribution such as the Plastic Hinge Method from Priestley, Calvi, and Kowalsky (2007) is used to translate the curvature at specific material strain limits to column deformations. The moment gradient component of the plastic hinge length is dependent on the column length. Aspect ratio also influences shear in the column, which impacts the additional spread in plasticity due to tension shift. Aspect ratio is not expected to influence bar buckling behavior, but the tests are included to evaluate its effect on the spread of plasticity.

Axial load influences the distribution of forces within the cross section. Columns with higher levels of axial load are expected to have a reduced deformation capacity but higher lateral forces. Limit states governed by compression are influenced by the increased axial load. Tests 19-24 evaluate columns subjected to 5% and 10% axial load, while future specimens are subjected to 15% and 20% axial load.

Table 1.31 Column Summary for Aspect Ratio and Axial Load Variable Tests 19-24

Test	Load History	D (in)	L/D	Long. Steel (ρ_l)	Spiral Detailing (ρ_s)	f'c (psi)	P/f'c*Ag
19	Three Cycle Set	18	5.33	10 #6 bars (1.7%)	#3 at 2" (1.3%)	6334	10%
20	Three Cycle Set	18	5.33	10 #6 bars (1.7%)	#3 at 2" (1.3%)	6467	5%
21	Three Cycle Set	18	7.33	10 #6 bars (1.7%)	#3 at 2" (1.3%)	6390	5%
22	Three Cycle Set	18	7.33	10 #6 bars (1.7%)	#3 at 2" (1.3%)	6530	10%
23	Three Cycle Set	18	8.67	10 #6 bars (1.7%)	#3 at 2" (1.3%)	6606	5%
24	Three Cycle Set	18	8.67	10 #6 bars (1.7%)	#3 at 2" (1.3%)	6473	10%

Table 1.32 Reinforcement Material Property Summary for Columns 19-24

Longitudinal Reinforcement	εy	fy (ksi)	εh	fh (ksi)	εu	fu (ksi)
Tests 19-24 (#6 Bar)	0.00250	68.1	0.0153	68.1	0.1208	92.4

Transverse Steel	εy (0.2% offset)	fy (ksi)	εu	fu (ksi)
Tests 19-24 (#3 Spiral)	0.00465	65.6	0.1181	100.0

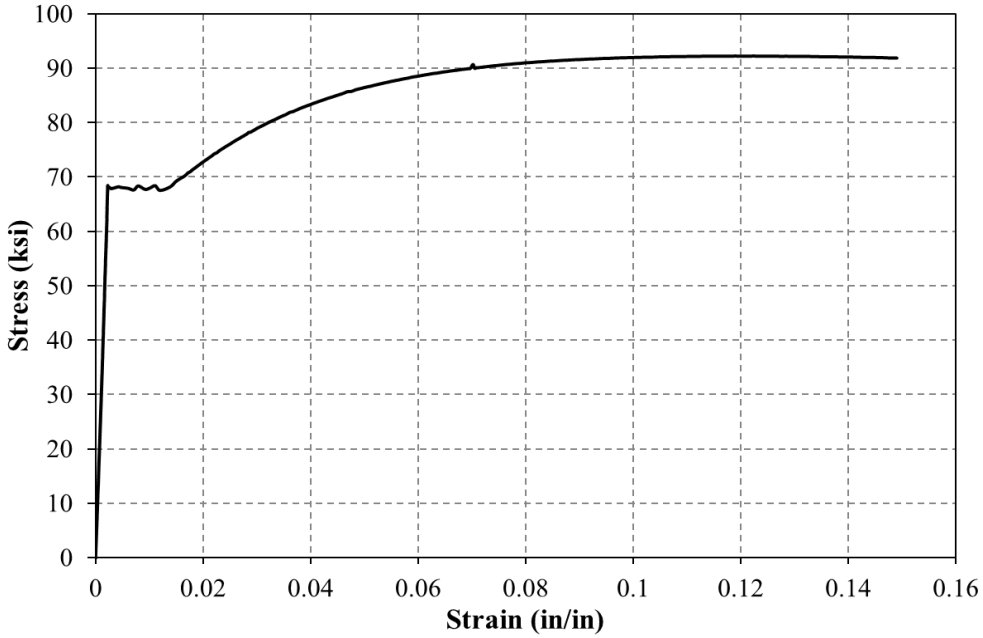

Figure 1.408 Test 19-24 – Longitudinal Steel Tensile Test Results

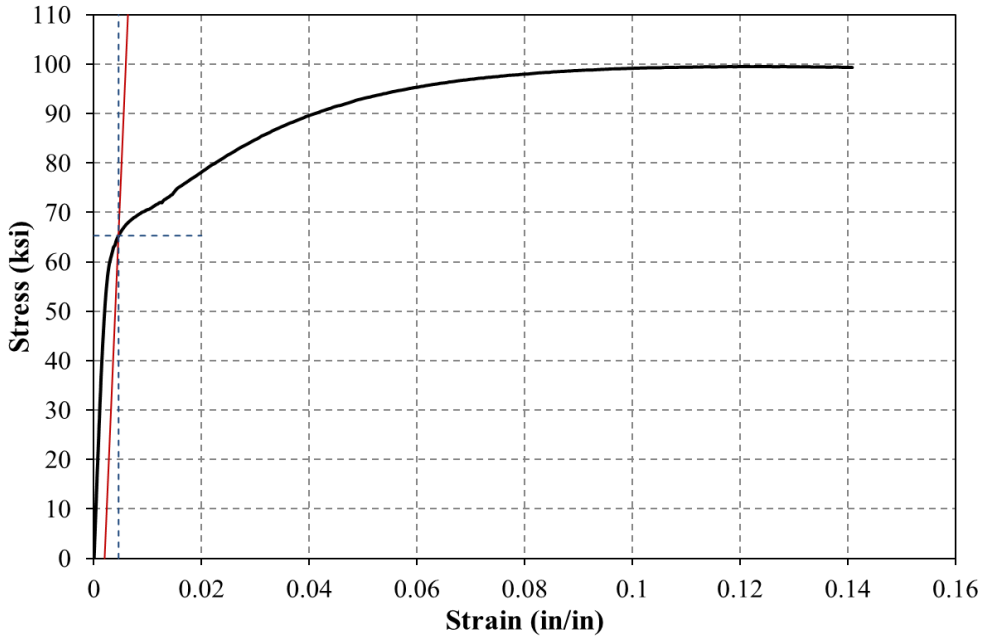

Figure 1.409 Test 19-24 – Transverse Steel Tensile Test Results

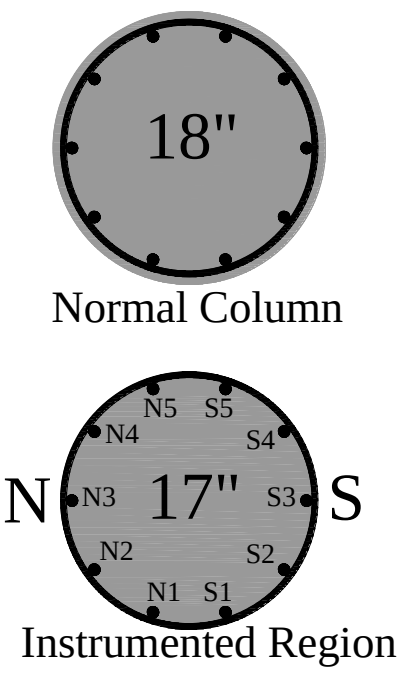

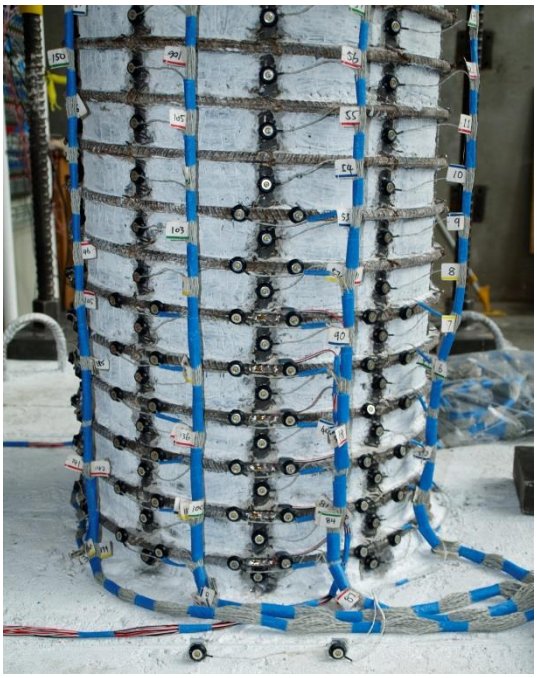

Figure 1.410 Tests 19-24 Cross Section and Bar Designation for Smaller Section

Figure 1.411 Test Setup for 11' and 13' Cantilever Length Specimens

1.3.1 Test 19 – Aspect Ratio of 5.33 and 10% Axial Load

Table 1.33 Observations for Test 19 – Aspect Ratio of 5.33 and 10% Axial Load

VALUES OF INTEREST:	
Concrete Compressive Strength:	$f_c' = 6334\ psi$
Axial Load:	$P = 144\ kips\ \ (P/(f_c' A_g) = 10\%)$
Column Length and Aspect Ratio:	$8ft\ \ (L/D = 5.33)$
Analytical First Yield Force:	$F_y' = 21.90\ kips$
Experimental First Yield Displacement:	$\Delta_y' = 0.87"$
Analytical Nominal Moment Capacity:	$M_n = 230.93\ kip * ft$
Equivalent Yield Displacement:	$\Delta_y = 1.15"$
Maximum Lateral Force:	$29.81\ kips$
DAMAGE OBSERVATIONS:	
First Cracking North:	$3/4Fy' = 0.48"$
First Cracking South:	$-3/4Fy' = -0.58"$
Cover Concrete Crushing North:	$\mu_3^{-2} = -3.44"$
Cover Concrete Crushing South:	$\mu_3^{+2} = 3.43"$
Transverse Steel Yield North:	At $-3.17"$ during pull to $\mu_3^{-1} = -3.42"$
Transverse Steel Yield South:	At $0.23"$ during push to $\mu_3^{+3} = 3.43"$
Longitudinal Bar Buckling North:	Reversal from $\mu_5^{+3} = 5.74"$
Longitudinal Bar Buckling South:	Reversal from $\mu_5^{-2} = -5.71"$
Longitudinal Bar Fracture North:	At $4.10"$ during push to $\mu_6^{+4} = 6.89"$
Longitudinal Bar Fracture South:	At $-4.22"$ during pull to $\mu_6^{-3} = -6.88"$

*$\mu_5^{+3} = 5.74"$ represents the third push cycle of displacement ductility five

Table 1.34 Strain Data Summary for Test 19 – Aspect Ratio of 5.33 and 10% Axial

MATERIAL STRAINS:	
Cover Concrete Crushing North:	$\varepsilon_s = 0.0060\ (compression)\ \ ^*\mu_{\Delta 2} = -2.29"$
Cover Concrete Crushing South:	$\varepsilon_s = 0.0065\ (compression)\ \ ^*\mu_{\Delta 2} = 2.29"$
Transverse Steel Yield North:	$\varepsilon_s = 0.0103\ (compression)$
Transverse Steel Yield South:	$\varepsilon_s = 0.0119\ (compression)$
Longitudinal Bar Buckling North:	$\varepsilon_s = 0.037\ (peak\ tension\ prior\ to\ bb)$
	$\varepsilon_s = 0.024\ (peak\ comp.\ prior\ to\ bb)$
Longitudinal Bar Buckling South:	$\varepsilon_s = 0.032\ (peak\ tension\ prior\ to\ bb)$
	$\varepsilon_s = 0.022\ (peak\ comp.\ prior\ to\ bb)$
Mander (1988) Ultimate Concrete Compression Strain, $\varepsilon_{cu} = 0.0205$	

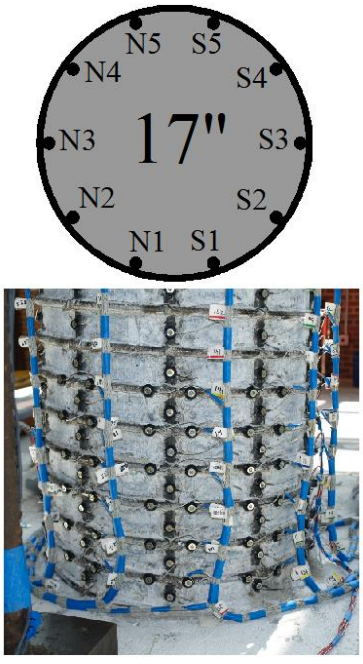

Name	x [mm]	y [mm]	z [mm]
Marker_1	227.837	-743.247	-2675.236
Marker_2	229.260	-693.387	-2674.606
Marker_3	228.326	-642.646	-2674.488
Marker_4	228.043	-590.826	-2673.867
Marker_5	228.387	-541.593	-2673.530
Marker_6	227.853	-491.590	-2673.371
Marker_7	226.511	-440.457	-2672.473
Marker_8	228.167	-392.557	-2673.159
Marker_9	227.752	-342.702	-2672.750
Marker_10	227.643	-292.833	-2672.577
Marker_11	227.504	-243.686	-2672.421
Marker_12	228.426	-196.037	-2672.781
Marker_13	227.467	-146.911	-2672.133
Marker_14	227.595	-98.260	-2672.066
Marker_15	228.140	-49.702	-2672.101
Marker_16	227.980	-1.470	-2671.947
Marker_17	227.540	46.859	-2671.635
Marker_18	227.851	95.893	-2671.769
Marker_19	227.814	146.163	-2671.750
Marker_20	227.959	191.979	-2671.589
Marker_21	228.480	243.329	-2671.532
Marker_22	228.617	292.777	-2671.523
Marker_23	229.119	342.149	-2671.766
Marker_24	228.974	390.922	-2671.644
Marker_25	229.632	439.316	-2671.782
Marker_26	229.537	488.376	-2671.803
Marker_27	228.086	534.668	-2671.403
Marker_28	229.304	583.947	-2672.205
Marker_29	229.900	633.784	-2672.513
Marker_30	230.140	683.750	-2672.778
Marker_31	230.841	732.312	-2673.176

Figure 1.412 T19 – Target Marker Application and Optotrak Rendering

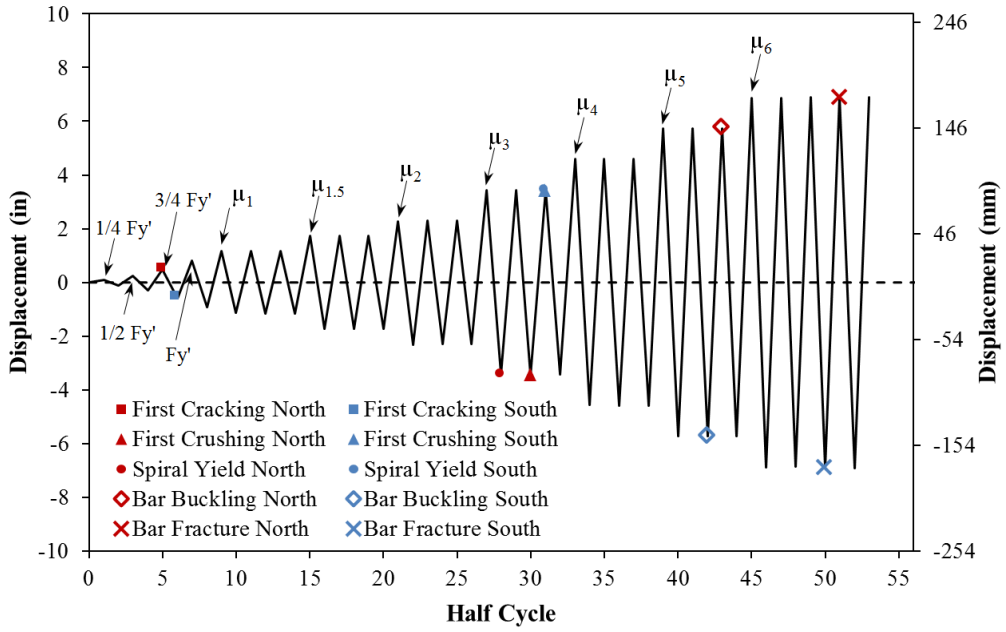

Figure 1.413 T19 – Symmetric Three Cycle Set Load History

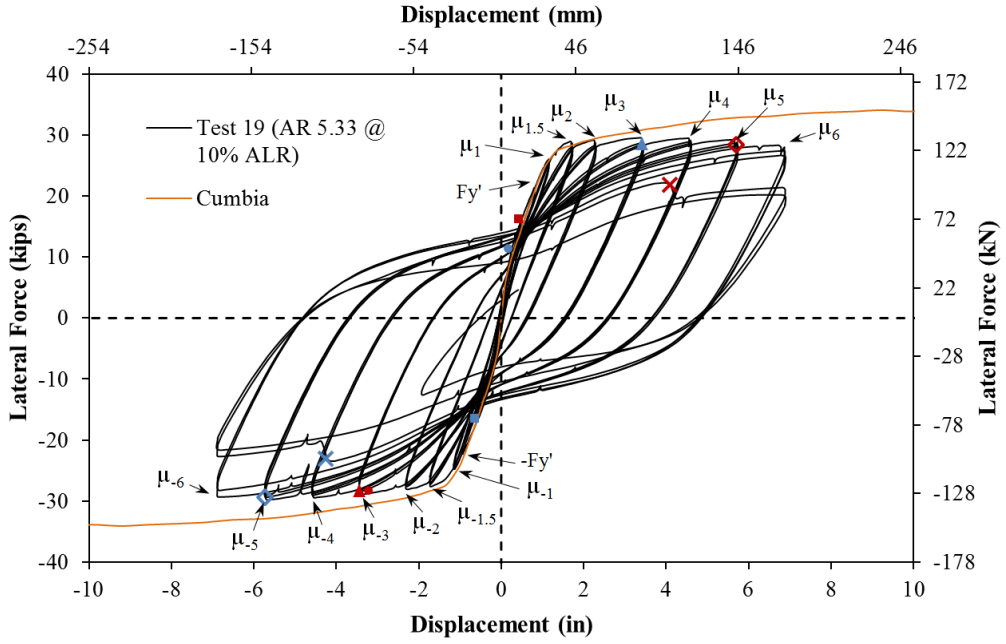

Figure 1.414 T19 – Lateral Force vs. Top Column Displacement Response

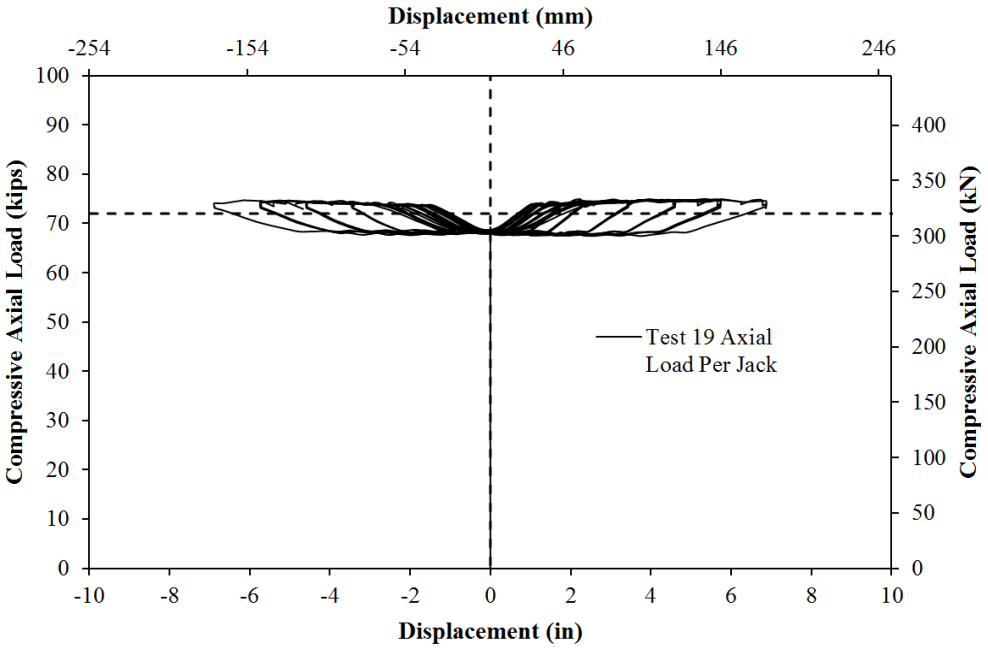

Figure 1.415 T19 – Compressive Axial Load from One Jack (Total = 2*Value)

Test 19 Aspect Ratio of 5.33 and 10% Axial Load – Experimental Observations

Specimens 19-24 focus on the effects of axial load and aspect ratio on column behavior. The 18" diameter columns contain 10 #6 (A706) bars for longitudinal reinforcement ($A_{st}/A_g = 1.7\%$) and a #3 A706 spiral at 2" on center ($4A_{sp}/(D's) = 1.3\%$). The specific specimen chosen for Test 19 has an 8ft cantilever length ($L/D = 5.33$), and was subjected to ($P/(f_c'A_g) = 10\%$) axial load. The symmetric three-cycle-set laboratory load history was used for Tests 19-24. The load history begins with elastic cycles to the following increments of the analytically predicted first yield force: ¼ Fy', ½ Fy', ¾ Fy', and Fy'. The first yield force for the tested material and geometric properties was determined using moment curvature analysis (Test 19: Cumbia Fy' = 21.90 kips with f'c = 6334 psi). The first yield displacement for the nineteenth test was obtained as an average for the experimental first yield push and pull cycles ($\Delta_y' = 0.87$"). Vertical strain profiles for both push and pull

cycles up to the first yield force appear in Figure 1.416 with a dashed line representing the yield strain of the longitudinal reinforcement. The equivalent yield displacement, used to determine the displacement ductility levels ($\mu_{\Delta 1} = 1 * \Delta_y$), is then calculated as $\Delta_y = \Delta'_y(M_n/M'_y) = 1.15"$ for Test 19. The symmetric three-cycle-set load history resumes with three balanced cycles at each of the following ductility levels: 1, 1.5, 2, 3, 4, 5, 6, 7, 8, etc. The full symmetric three-cycle-set load history appears in Figure 1.413 and the resulting lateral force vs. top column displacement hysteresis is shown in Figure 1.414. The monotonic moment curvature prediction does not include P-Δ effects.

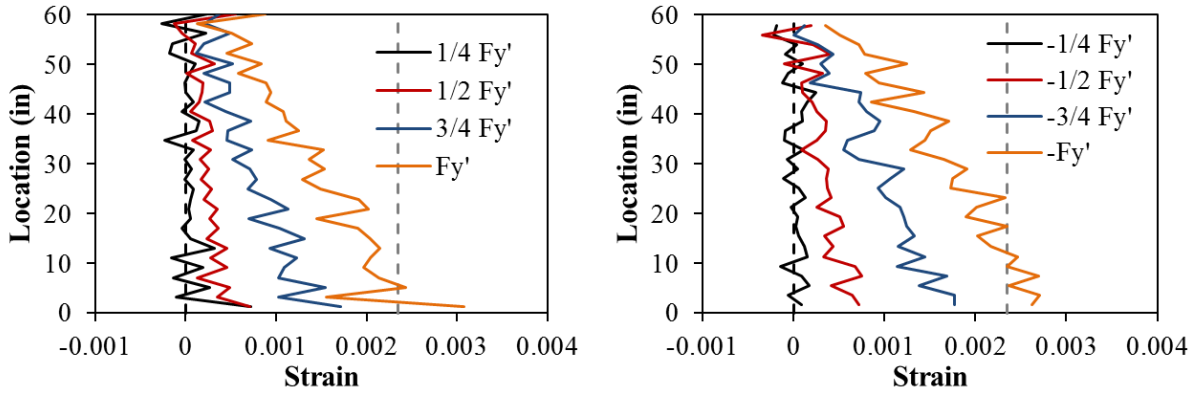

Figure 1.416 T19 – Strain Profiles before Yield (Left) Bar N3 and (Right) Bar S3

The test began with cycles in ¼ Fy' (first yield force) increments in each direction of loading until the first yield force was reached. The first cracks on the North and South sides of the specimen were observed during $(3/4Fy' = 15.95\,kips)$ and $(-3/4Fy' = -16.96\,kips)$ respectively. The first cracks appeared at the location of the spirals, therefore they were difficult to locate and measure. Crack widths measured on the outside surface of the concrete core have little meaning when describing a serviceability limit state which applies to columns with cover concrete. The crack distribution on all sides of the specimen at first yield, $(Fy' = 21.39\,kips)$ and $(-Fy' = -22.29\,kips)$, appears in Figure 1.417. Similarly, the crack progression at displacement ductility 1, 1.5, and 2 appear in Figure 1.418, Figure 1.419, and Figure 1.420 respectively. During these cycles the cracks became more numerous and increased in inclination on the shear faces of the specimen. A small

amount of core concrete crushed on the North side of the specimen during ($\mu_3^{-2} = -3.44$), as shown in the left photo of Figure 1.421. A similar observation was made, see the right photo of Figure 1.421, on the South side of the specimen during ($\mu_3^{+3} = 3.43$"). The crushing on each side of the specimen during ductility three was not severe, and it appeared that only a thin layer of concrete flaked off between spiral layers. The crack distribution on the front side of the specimen during ($\mu_3^{-3} = -3.43$") and ($\mu_4^{-3} = -4.59$") appears in the left and right photos of Figure 1.422.

The South extreme fiber bar S3 visibly buckled after reversal from ($\mu_5^{-2} = -5.71$"), as shown in Figure 1.423. After reversal from ($\mu_5^{+3} = 5.74$"), the North extreme fiber bar N3 visibly buckled as shown in Figure 1.424. The additional deformation in previously buckled bars S3 during ($\mu_6^{+1} = 6.86$") and N3 during ($\mu_6^{-1} = -6.88$") is shown in Figure 1.425. The deformed spiral layers over the outward buckled region of bars S3 and N3 allow for further cycle to cycle degradation of the core concrete. Previously buckled South extreme fiber bar S3 ruptured during the pull cycle to ($\mu_6^{-3} = -6.88$"), as shown in the left photo of Figure 1.426. During this same cycle two additional North reinforcing bars buckled, N2 and N4, as shown in the right photo of Figure 1.426 and the left photo of Figure 1.427. Rupture of bar S3 lead to a 24% loss in strength measured at ($\mu_6^{-3} = -6.88$") relative to the peak load in the pull direction of loading. During the push cycle to ($\mu_6^{+4} = 6.89$"), previously buckled extreme fiber North reinforcement bar N3 ruptured as shown in the right photo of Figure 1.427. Rupture of bar N3 lead to a 29% loss in strength measured at ($\mu_6^{+4} = 6.89$") relative to the peak load in the push direction of loading. Normally a fourth cycle at displacement ductility six would not appear within the load history, but it was apparent that it would not take additional displacement to rupture the North reinforcement. After reaching ($\mu_6^{+5} = 6.90$"), the test was concluded. Photos of the specimen after removal of all of the instrumentation appear in Figure 1.428.

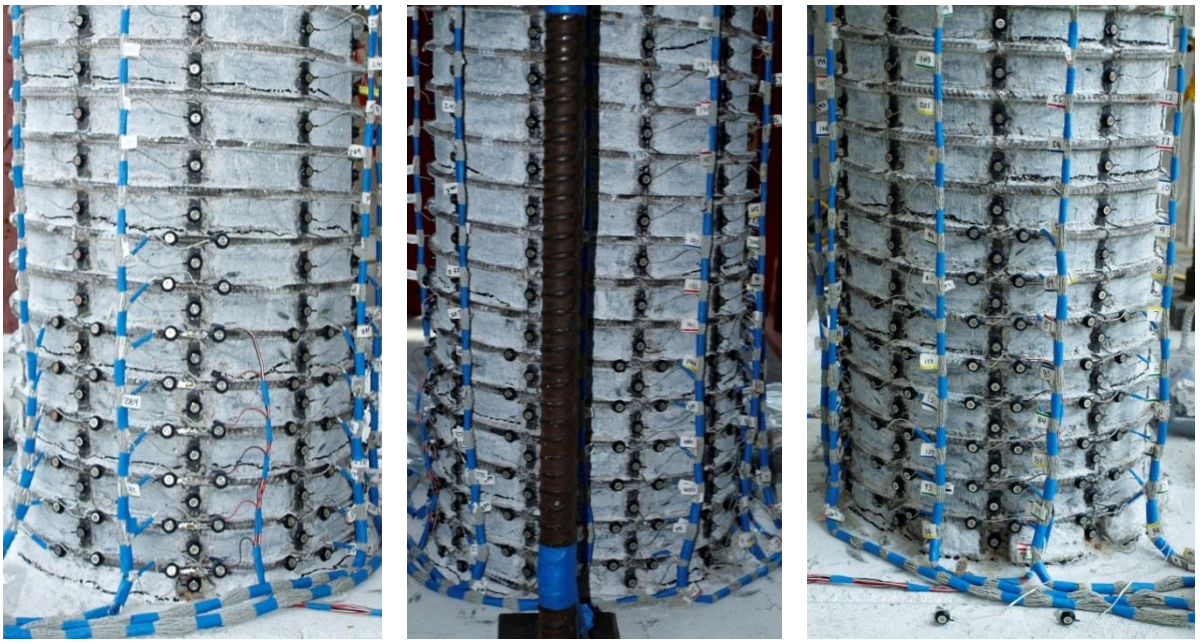

Figure 1.417 T19 – (Left) North at Fy', (Mid) Front at -Fy', and (Right) South at -Fy'

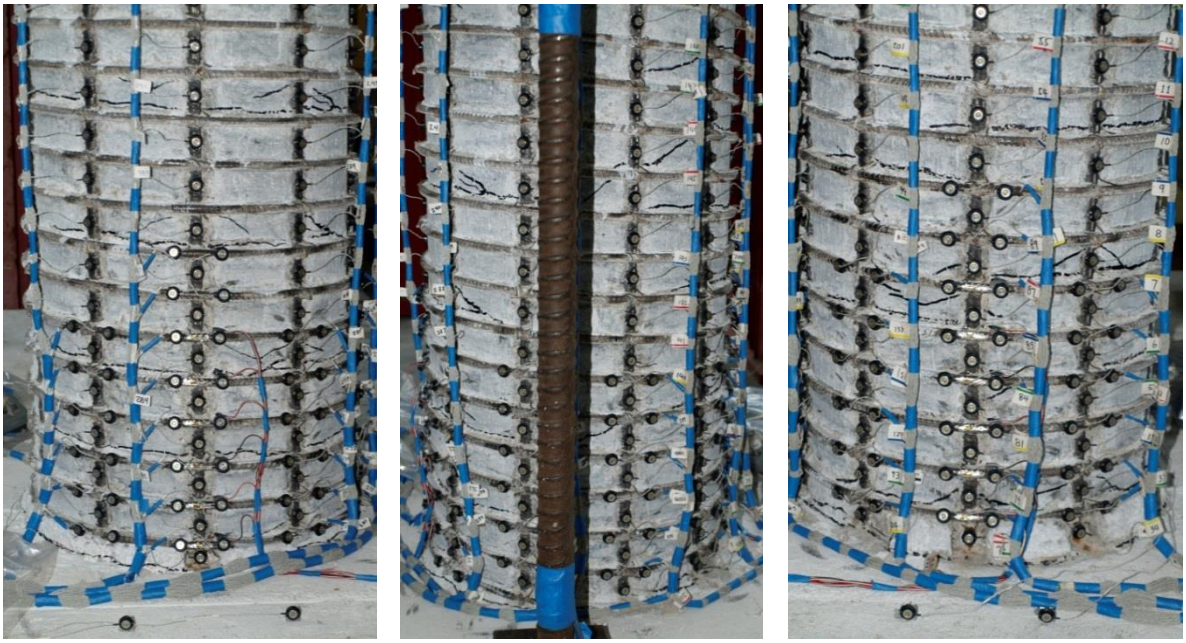

Figure 1.418 T19 – (Left) North at μ_1^{+3}, (Mid) Front at μ_1^{-3}, and (Right) South at μ_1^{-3}

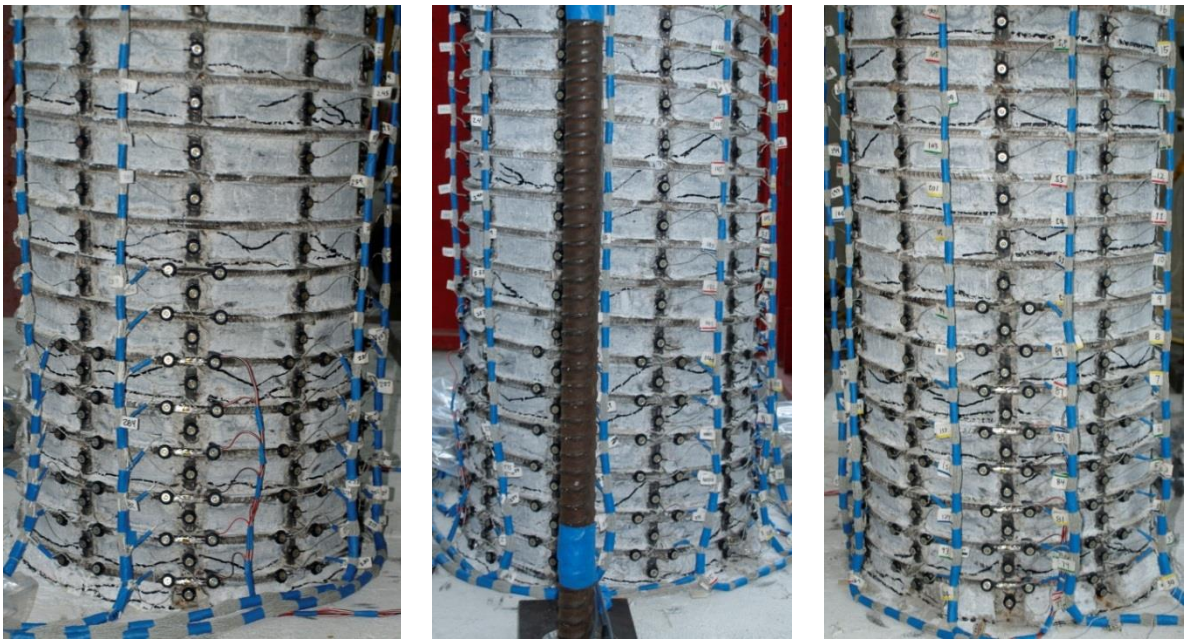

Figure 1.419 T19 – (Left) North at $\mu_{1.5}^{+3}$, (Mid) Front at $\mu_{1.5}^{-3}$, and (Right) South at $\mu_{1.5}^{-3}$

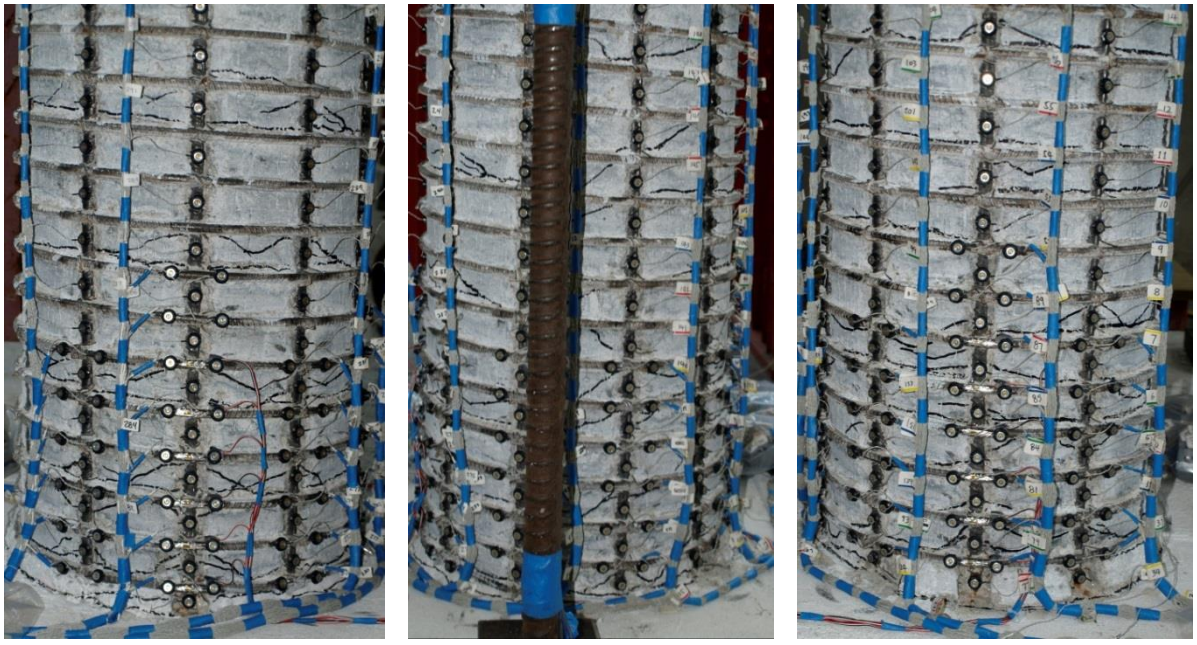

Figure 1.420 T19 – (Left) North at μ_{2}^{+3}, (Mid) Front at μ_{2}^{-3}, and (Right) South at μ_{2}^{-3}

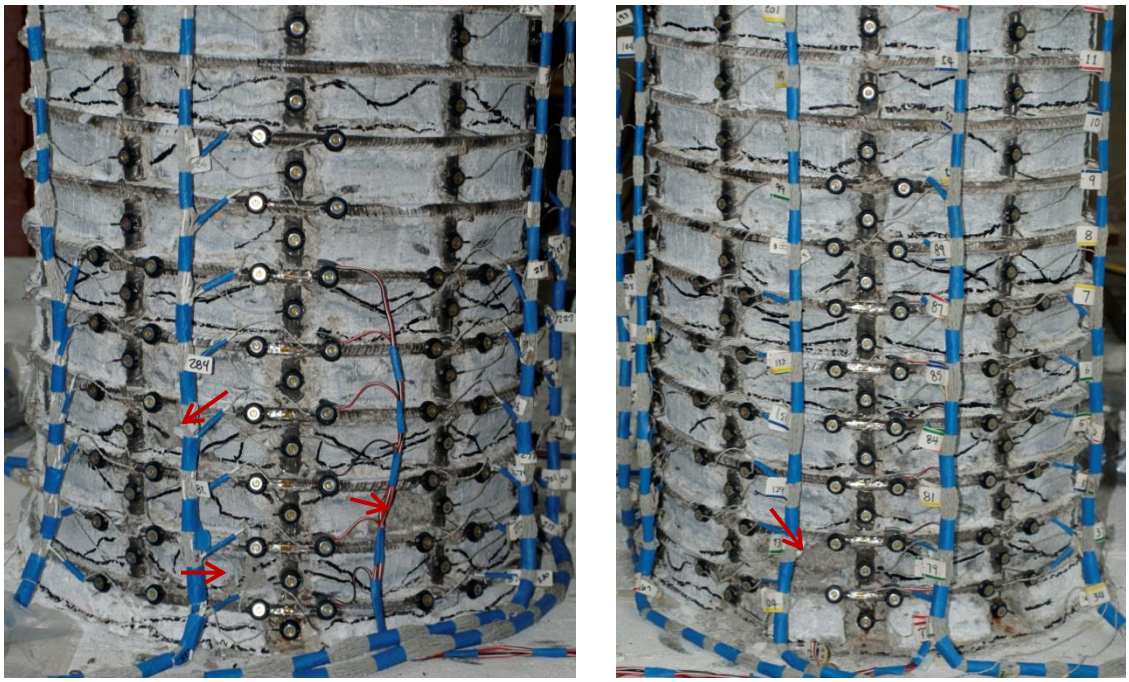

Figure 1.421 T19 – (Left) North Crushing at (μ_3^{-2}) and (Right) South Side at (μ_3^{+3})

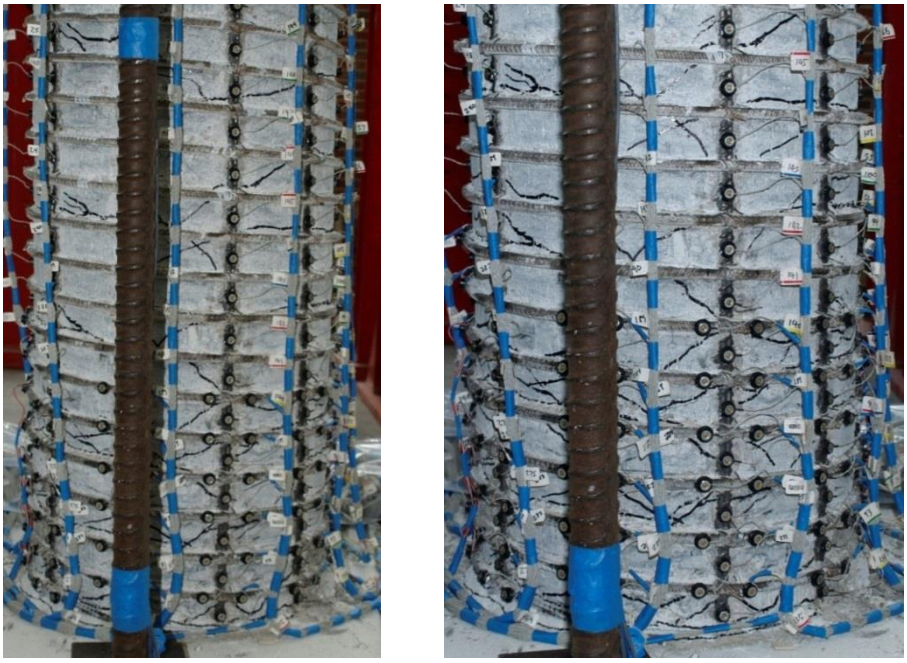

Figure 1.422 T19 – (Left) Front Crack Distribution at (μ_3^{-3}) and (Right) Front at (μ_4^{-3})

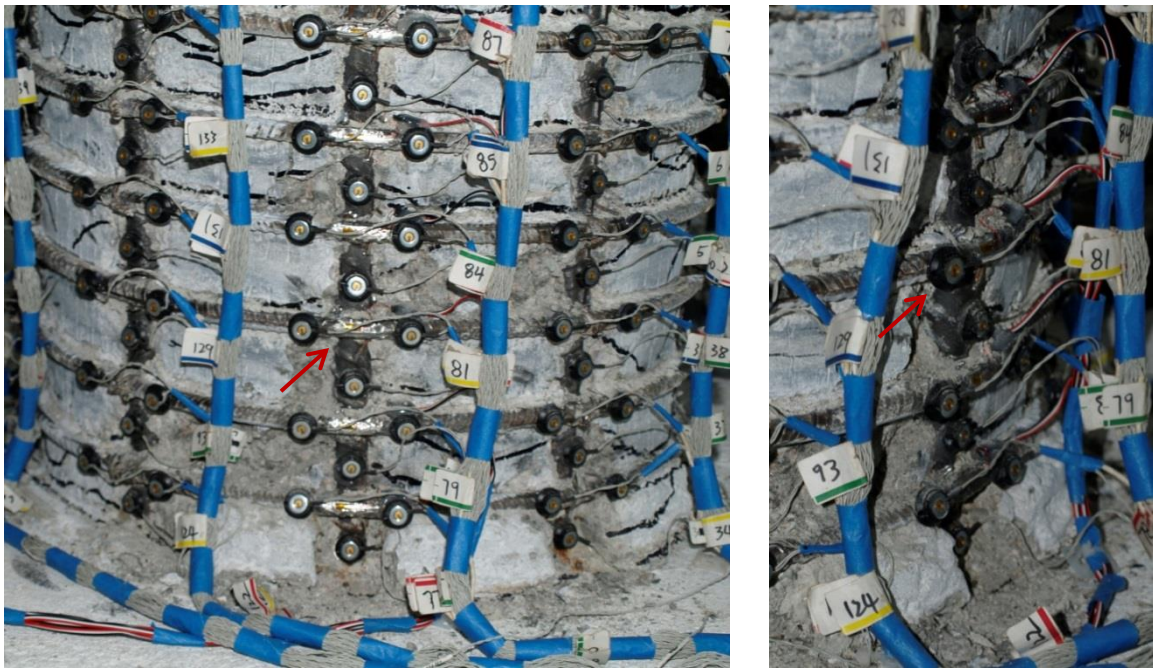

Figure 1.423 T19 – Buckling of the South Bar S3 after Reversal from (μ_5^{-2})

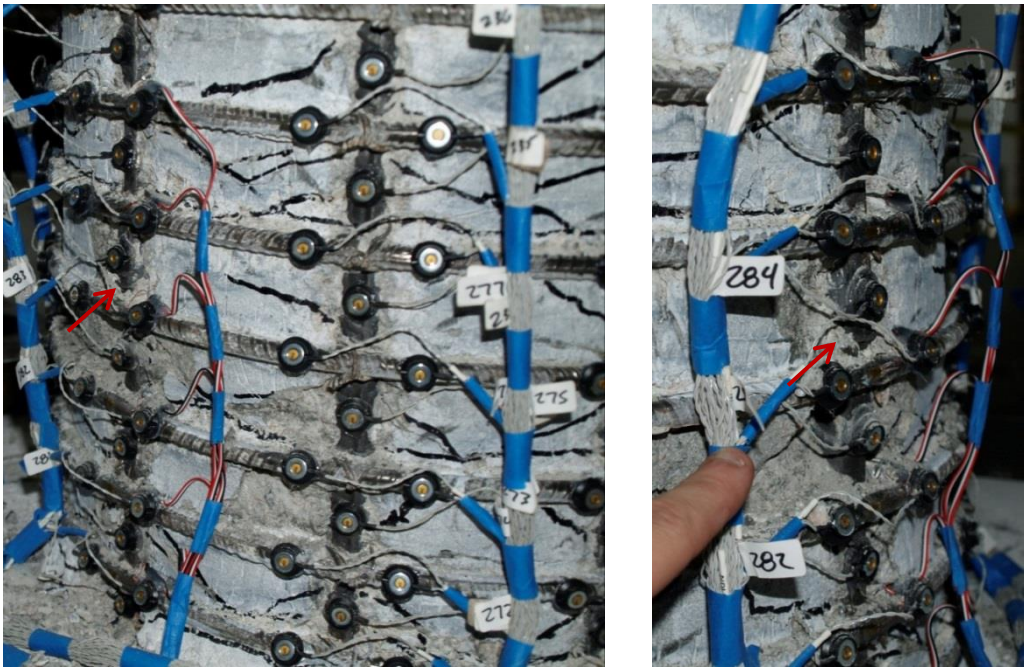

Figure 1.424 T19 – Buckling of the North Bar N3 after Reversal from (μ_5^{+3})

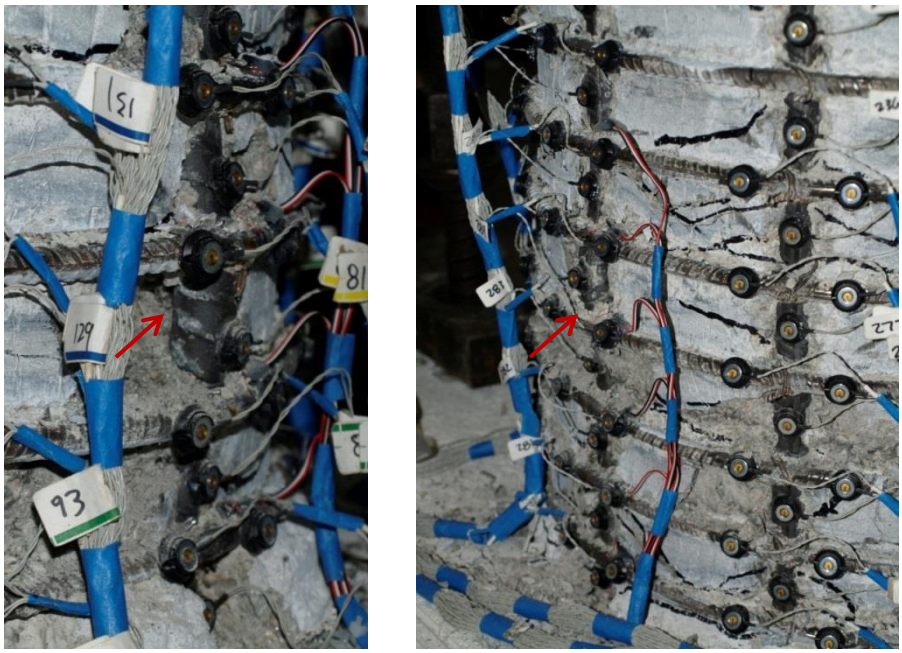

Figure 1.425 T19 – Deformation in (Left) Bar S3 at (μ_6^{+1}) and (Right) Bar N3 at (μ_6^{-1})

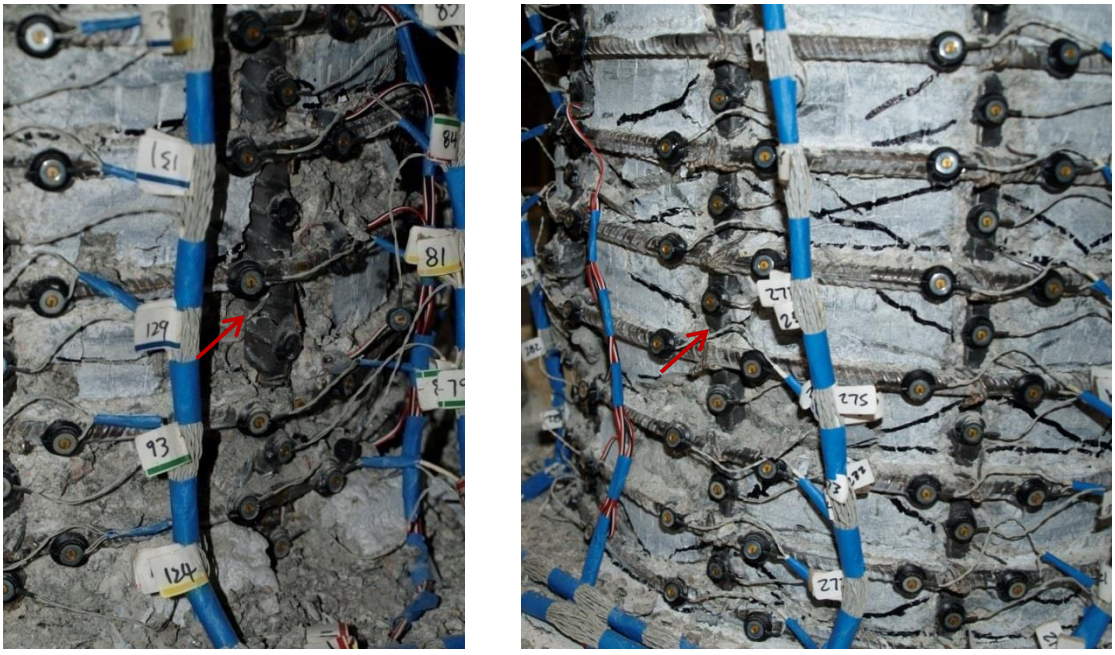

Figure 1.426 T19 – (Left) Rupture of Previously Buckled Bar S3 during (μ_6^{-3}) and (Right) Buckling of Bar N2 at (μ_6^{-3})

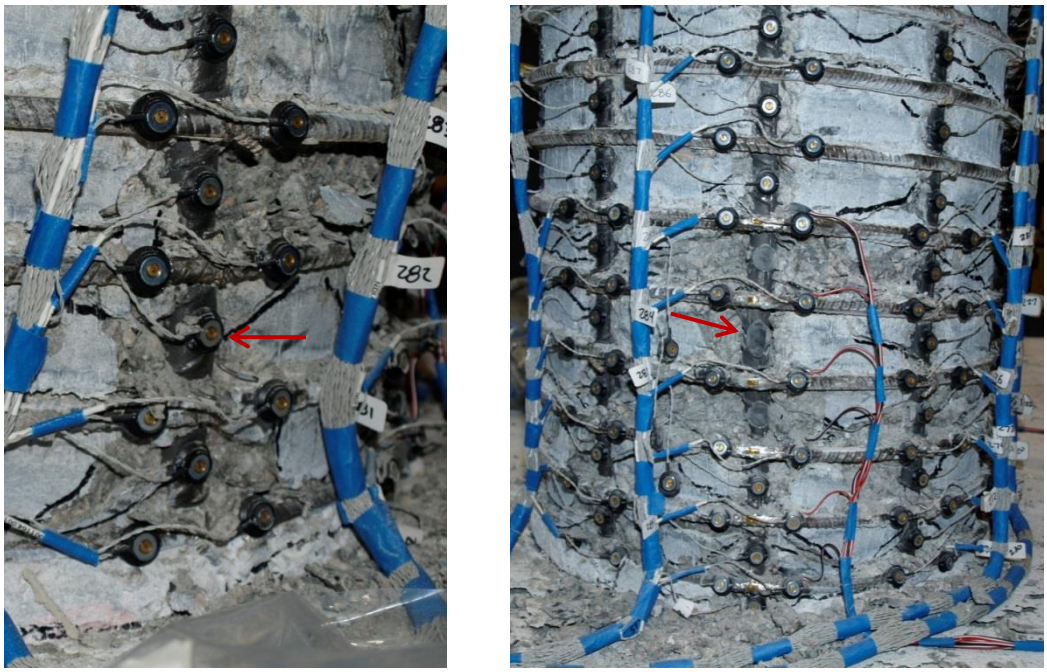

Figure 1.427 T19 – (Left) Buckling of Bar N4 at (μ_6^{-3}) and (Right) Rupture of Previously Buckled Bar N3 during (μ_6^{+4})

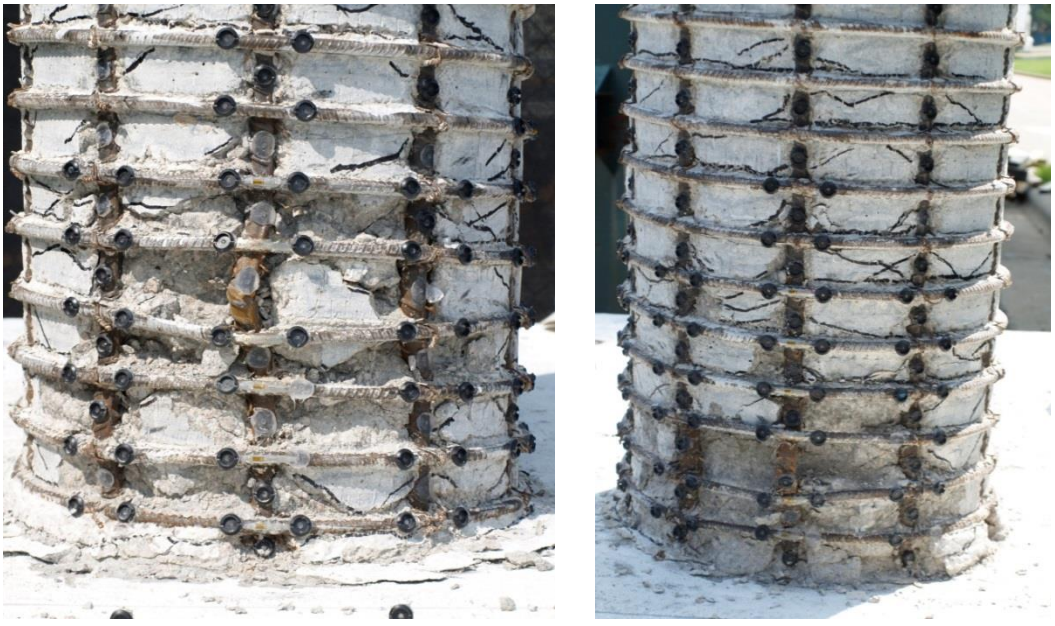

Figure 1.428 T19 – After the Conclusion of the Test (Left) North and (Right) South

Test 19 Aspect Ratio of 5.33 and 10% Axial Load – Strain Data Analysis

North Reinforcement

The vertical strain profile for North extreme fiber bar N3 placed into tension during push cycles appears in the right half of Figure 1.429. This figure shows both extreme fiber bars on the same graph to illustrate the effects of tension shift on strain profiles. As the hinge rotates about inclined flexural shear cracks, compressive strains are concentrated at the base and tensile strains are fanned out to a greater height following the crack distribution. Near the footing cracks remain effectively horizontal, but above this base section the flexural shear cracks are inclined as shown in Figure 1.422.

The compressive vertical strain profile for North extreme fiber bar N3 during pull cycles appears in the left half of Figure 1.430. From displacement ductility four and onwards, two adjacent gage lengths on bar N3, located 5.17" and 7.15" above the footing, were combined into a single gage length centered 6.17" above the footing. The common LED for the two original gage lengths was partially debonded affecting its spatial readings. Similarly, the common LED for gage lengths centered 11.18" and 13.13" above the footing was not allowed to move freely by a piece of steel tie wire. These two gage lengths were also combined into a single gage length for cycles after displacement ductility four. These are the only two locations that were affected by this phenomenon.

A peak tensile strain of 0.0366, located 1.38" above the footing, was measured for North extreme fiber bar N3 during ($\mu_5^{+1} = 5.72"$). The relationship between tensile strain and displacement for this gage length appears in Figure 1.433. Each line represents a single push cycle which began with the column at zero displacement and ended at the peak during a continuous push cycle. The solid line contains data during the push cycle loading up to the peak displacement, and the dashed line represents the subsequent reversal of load. This is the first gage length in which moment curvature prediction for the relationship between tensile strain and displacement using the PCK (2007) Lp Hinge Method matches the test results. Even though this gage length sustained the highest tensile strains, bar buckling occurred 8"

above the footing where multiple spiral layers yielded. The lowest spiral layer, which crossed the peak tensile gage length, remained elastic due to the additional confinement and restraint provided by the footing.

The largest compressive strain of -0.0243, located 9.16" above the footing, was measured during ($\mu_5^{-2} = -5.71$"). The peak compressive strain of -0.0243 in bar N3 exceeds the Mander ultimate concrete compressive strain of -0.0205. The relationship between compressive strain and displacement for bar N3, gage length centered 9.16" above the footing, appears in Figure 1.435. Here the measured compressive strains are significantly larger than the moment curvature prediction with the PCK (2007) Lp Hinge Method. As a comparison, compressive strains measured 6.17" above the footing are shown in Figure 1.434. For both gage lengths, the measured compressive strains match the prediction up until displacement ductility two, but at larger displacements the measured strains are greater than the moment curvature prediction.

The strains in the lowest six transverse steel layers restraining North extreme fiber bar N3 are plotted in Figure 1.432. The individual data points are from strain gages attached to each spiral layer at a specific height above the footing. The vertical grey dashed line represents a fictitious spiral yield strain of fy/Es, see Figure 1.409, that approximates the point at which permanent deformation in the spiral layer begins. The strain gage on the spiral layer 3.18" above the footing stopped functioning after displacement ductility two. This is of little consequence, since bar buckling occurred 8" above the footing over spiral layers which went inelastic during displacement ductility three. After reversal from ($\mu_5^{+3} = 5.74$"), the tensile strain for these spiral layers rapidly increased as they accommodated the outward deformation of the buckled extreme fiber bar.

The strain hysteresis over the buckled region of bar N3, gage length located 6.17" above the footing, appears in Figure 1.438. Visible Buckling occurred after reversal from ($\mu_5^{+3} = 5.74$"), here the deformation shown in Figure 1.424 does not have a large influence on the measured strains. The transverse steel strain gage hysteresis for the layer over the outward

buckled region of bar N3 appears in Figure 1.439. Outward deformation during visible buckling leads to an increase in the spiral strain, causing the gage to go beyond its measurable range. A similar increase in the measured spiral strains occurred during ($\mu_5^{-2} = -5.71"$), but this was not accompanied by visible bar buckling.

South Reinforcement

The vertical strain profile for South extreme fiber bar S3 placed into tension during pull cycles appears in the right half of Figure 1.430. A peak tensile strain of 0.0322 was measured 3.63" above the footing during ($\mu_5^{-1} = -5.72"$). The relationship between tensile strain and displacement for this gage length is shown in Figure 1.436. The same comments on the accuracy of the moment curvature prediction for the North reinforcement bar N3 also apply to bar S3.

Vertical strain profiles for bar S3 in compression during push cycles appear in the left half of Figure 1.429. A peak compression strain of -0.0224 was measured 3.63" above the footing during ($\mu_5^{+1} = 5.72"$). The relationship between compressive strain and displacement for this gage length appears in Figure 1.437. The measured strains match the moment curvature prediction with the PCK (2007) LP Hinge Method well through ductility two, but exceed the prediction at higher ductility levels. The peak compressive strain of -0.0224 measured in bar S3 is larger than the Mander ultimate concrete compressive strain of -0.0205.

The strains in the lowest six transverse steel layers restraining South extreme fiber bar S3 are plotted in Figure 1.431. Compressive demands during displacement ductility three led to two layers of transverse steel entering the inelastic range. Prior to buckling, the strain in the two inelastic spiral layers increased and a third layer entered the inelastic range during ($\mu_5^{+1} = 5.72"$). The strain hysteresis for the outward buckled region of extreme fiber bar S3, gage length located 5.59" above the footing, appears in Figure 1.440. The strain gage hysteresis for the spiral layer overlaying the outward buckled region of bar S3 appears in Figure 1.441. Visible buckling of bar S3 occurred after reversal from ($\mu_5^{-2} = -5.71"$), but

the data suggests that significant outward deformation occurred after reversal from ($\mu_5^{-1} = -5.72$"). During this reversal outward deformation over bar S3 occurred as shown by the increased tensile strains measured in Figure 1.440. This coincides with a spike in the measured tensile strains in the spiral restraint, in Figure 1.441, which caused the strain gage to go off scale preventing further measurement.

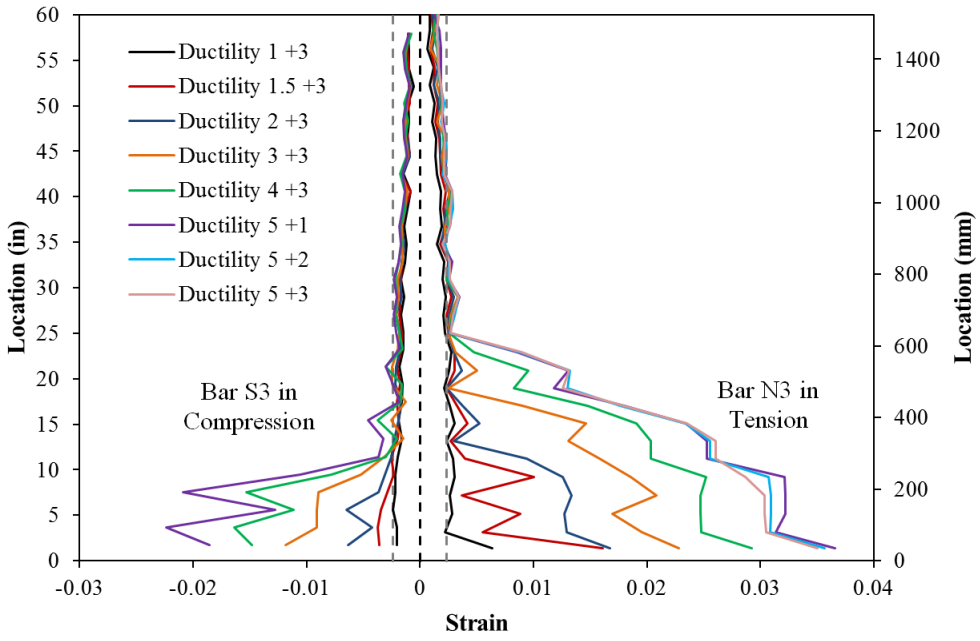

Figure 1.429 T19 – Extreme Fiber Vertical Strain Profiles during Push Cycles

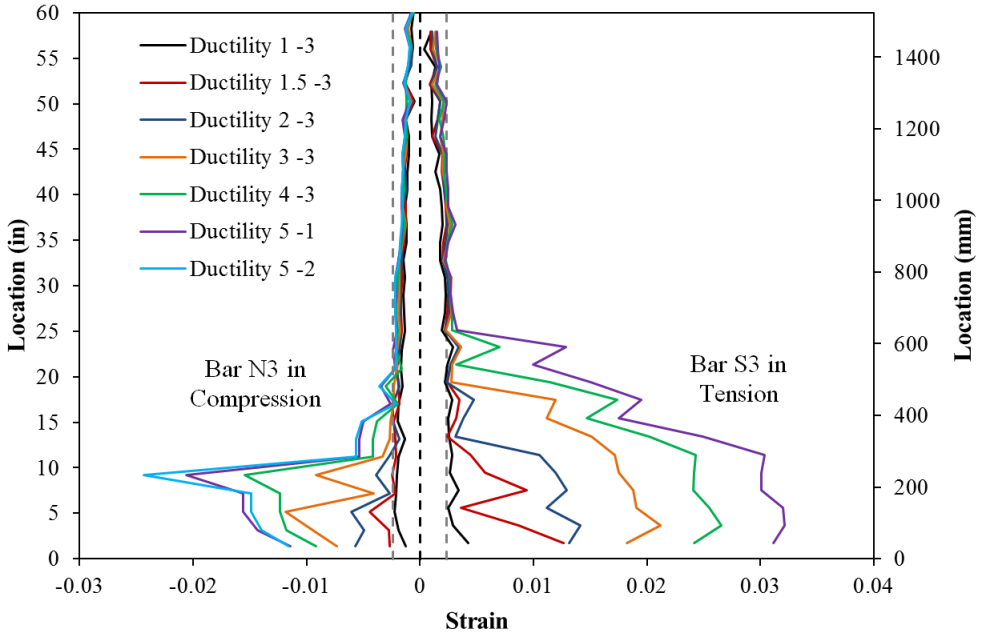

Figure 1.430 T19 – Extreme Fiber Vertical Strain Profiles during Pull Cycles

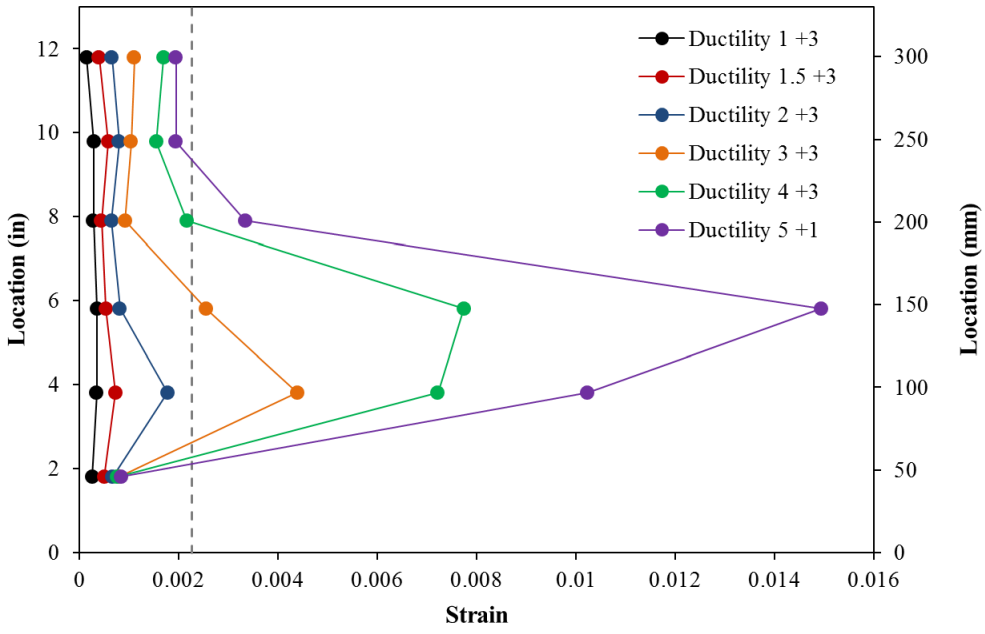

Figure 1.431 T19 – Spiral Strains on the South Side during Push Cycles

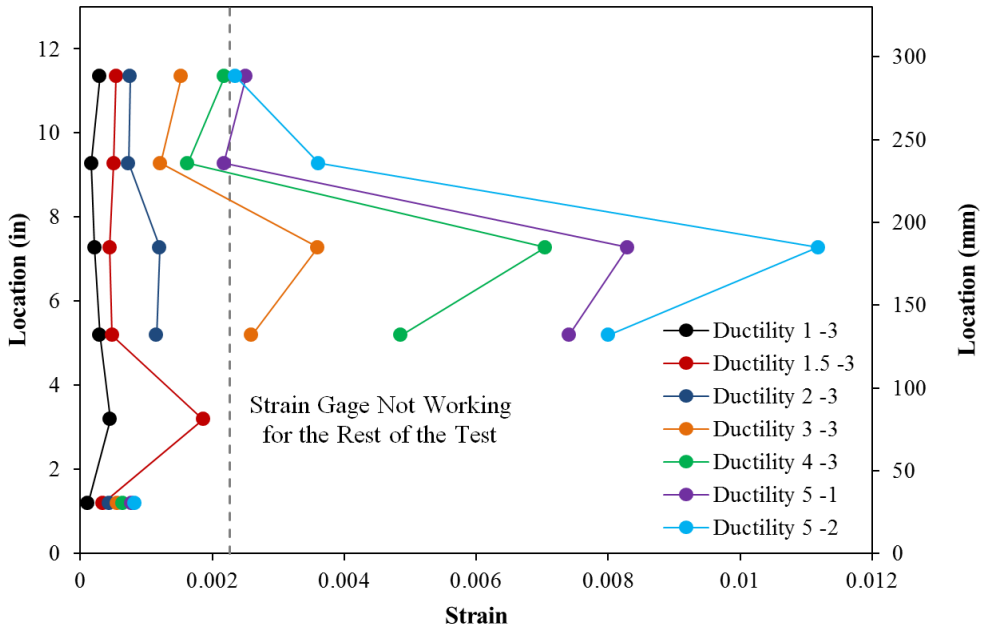

Figure 1.432 T19 – Spiral Strains on the North Side during Pull Cycles

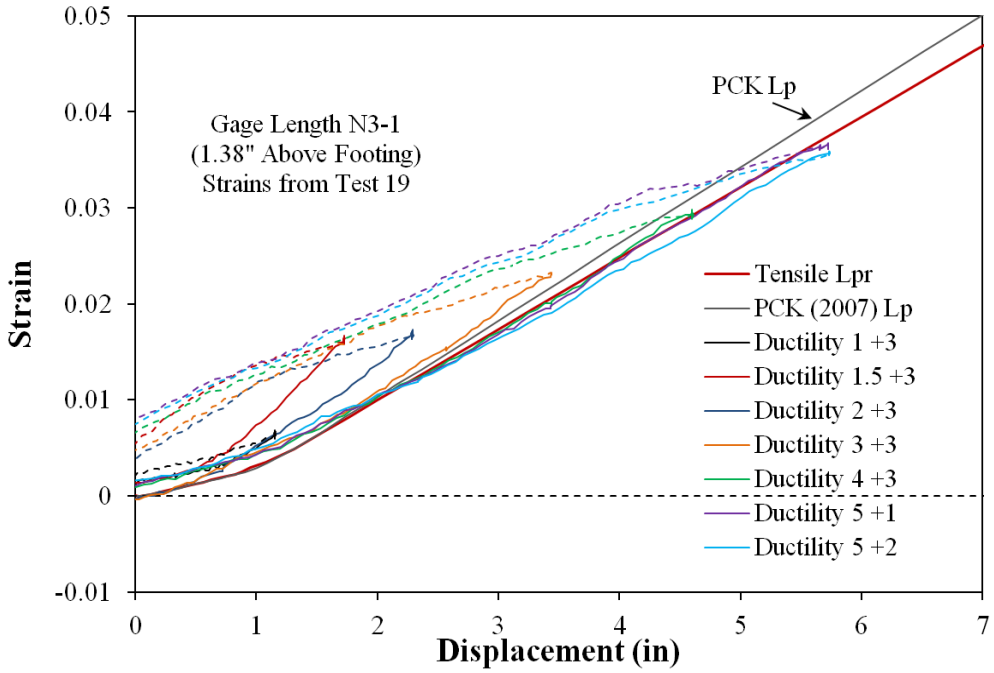

Figure 1.433 T19 – Tensile Strain-Displacement for Bar N3 during Push Cycles

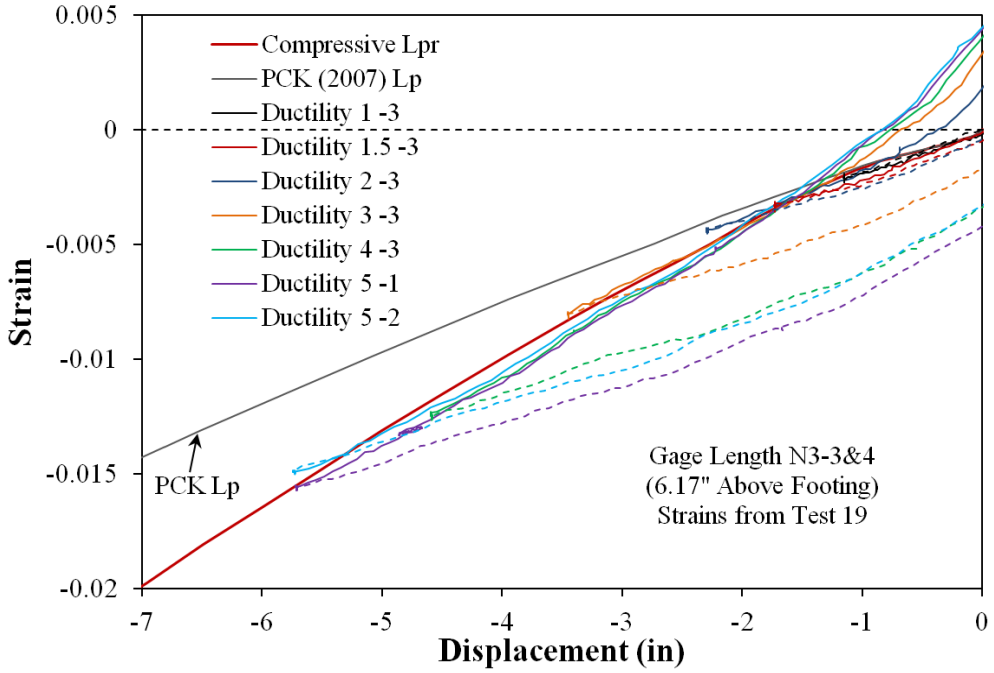

Figure 1.434 T19 – Compressive Strain-Displacement for Bar N3 during Pull Cycles

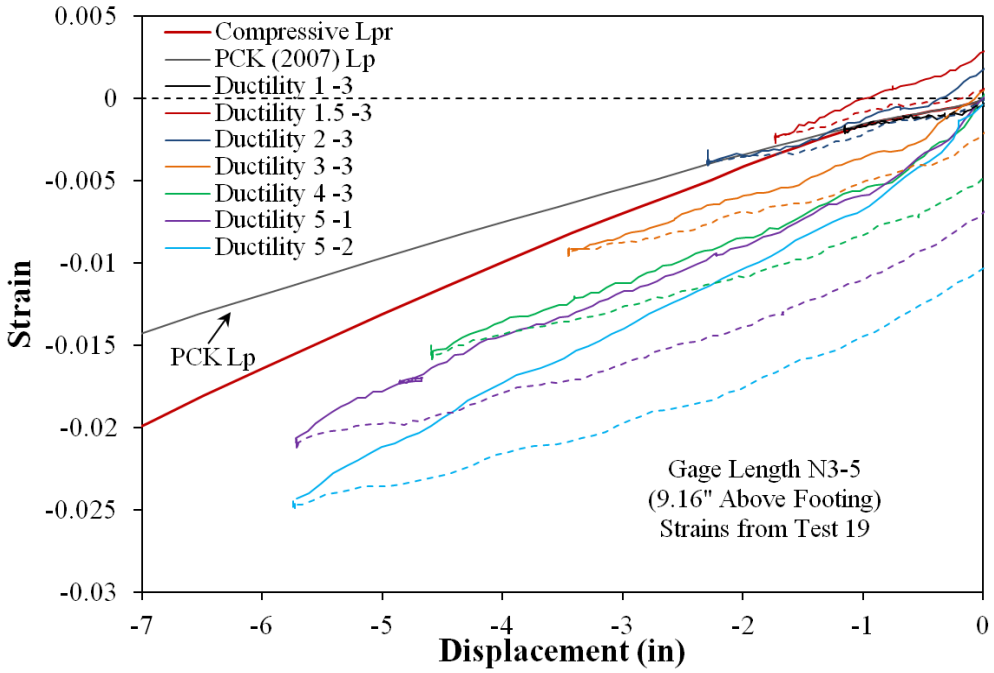

Figure 1.435 T19 – Compressive Strain-Displacement for Bar N3 during Pull Cycles

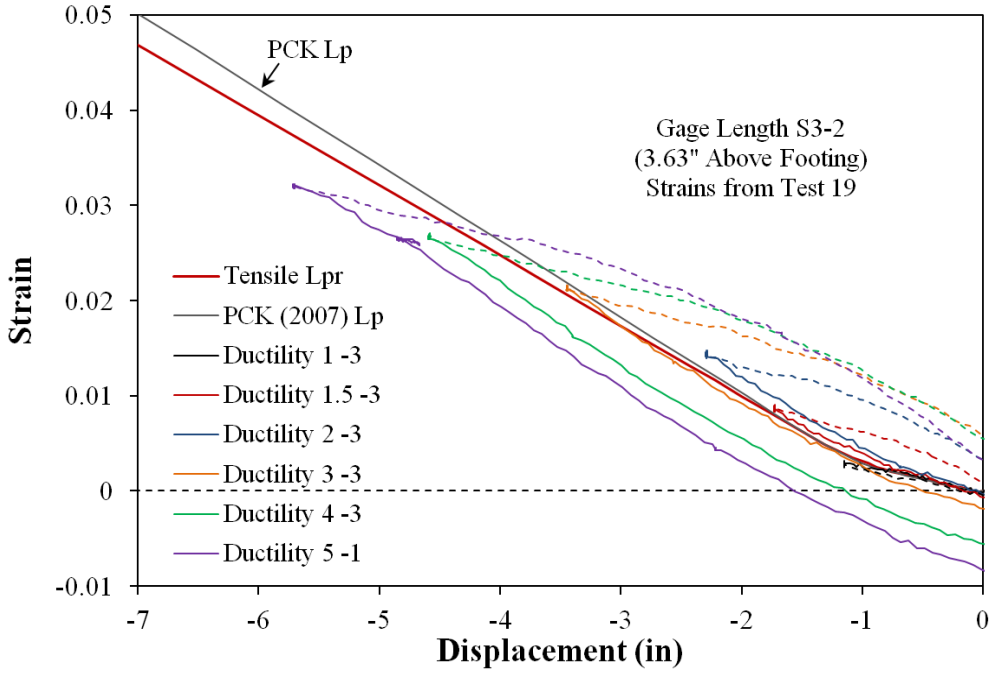

Figure 1.436 T19 – Tensile Strain-Displacement for Bar S3 during Pull Cycles

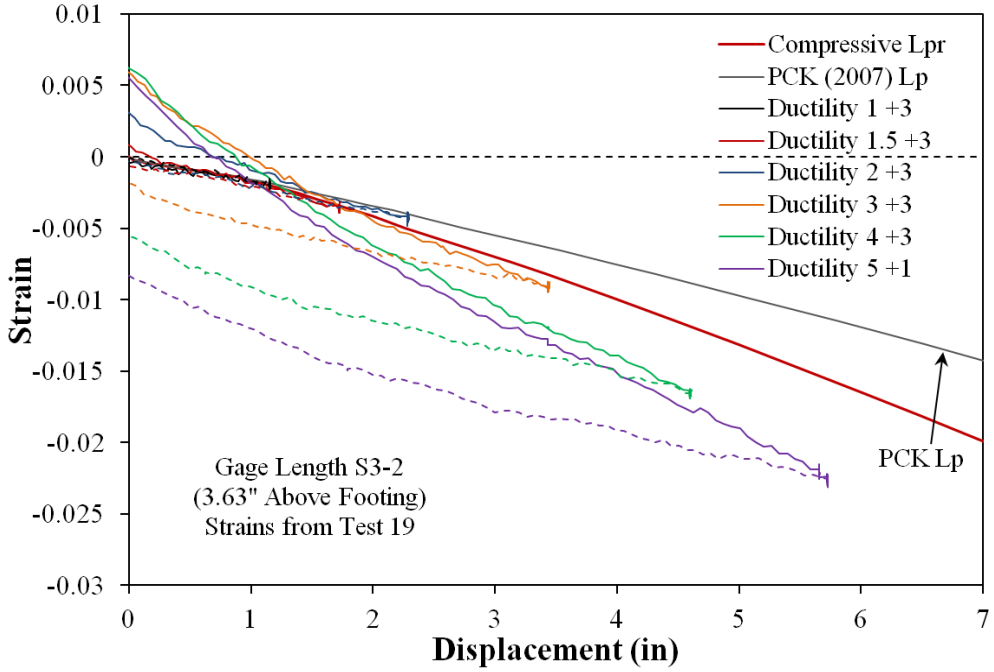

Figure 1.437 T19 – Compressive Strain-Displacement for Bar S3 during Push Cycles

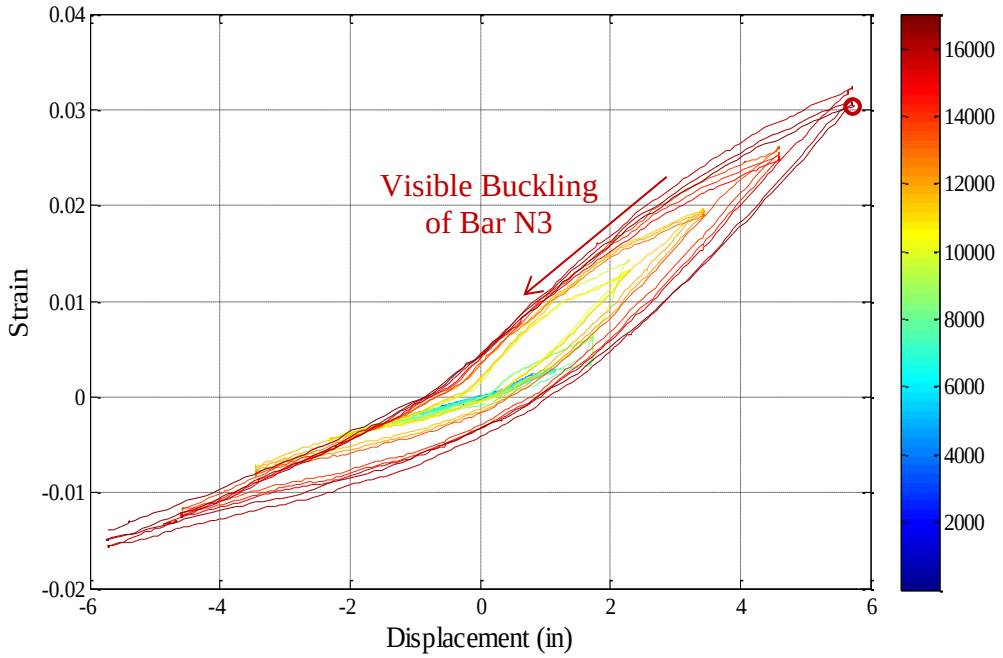

Figure 1.438 T19 – Bar N3 Strain Hysteresis to Buckling (Gage Length 6.17" Above)

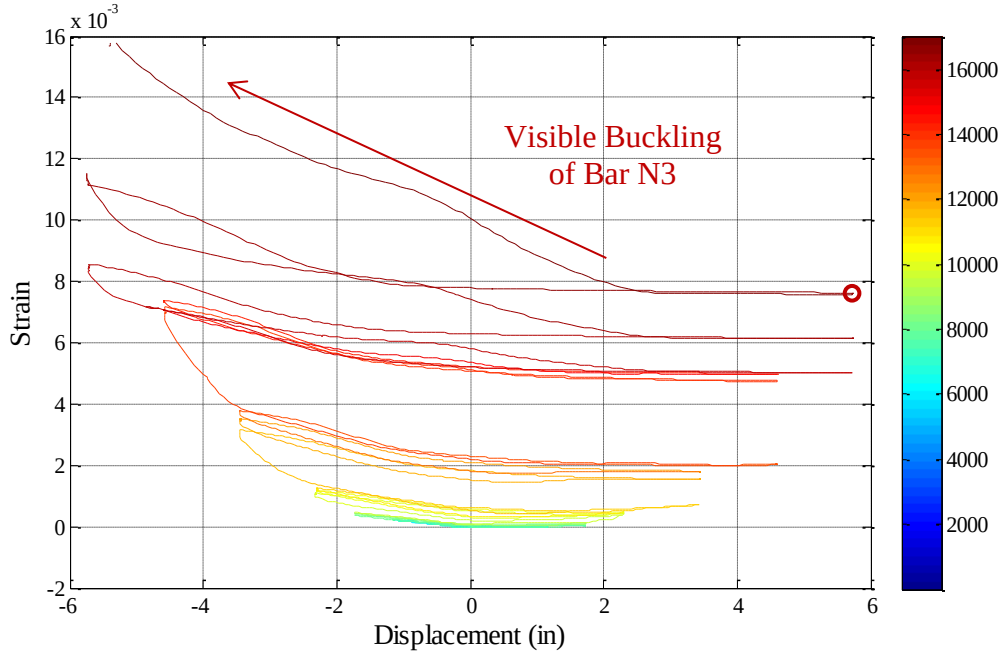

Figure 1.439 T19 – Spiral Strain Hysteresis for the Layer over North Buckled Region

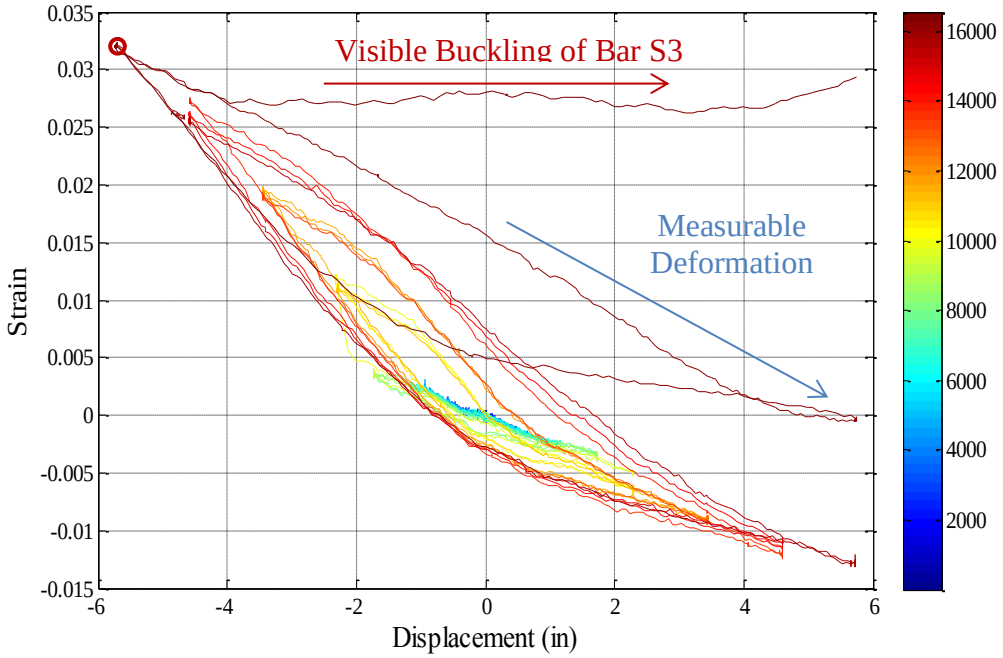

Figure 1.440 T19 – Bar S3 Strain Hysteresis to Buckling (Gage Length 5.59" Above)

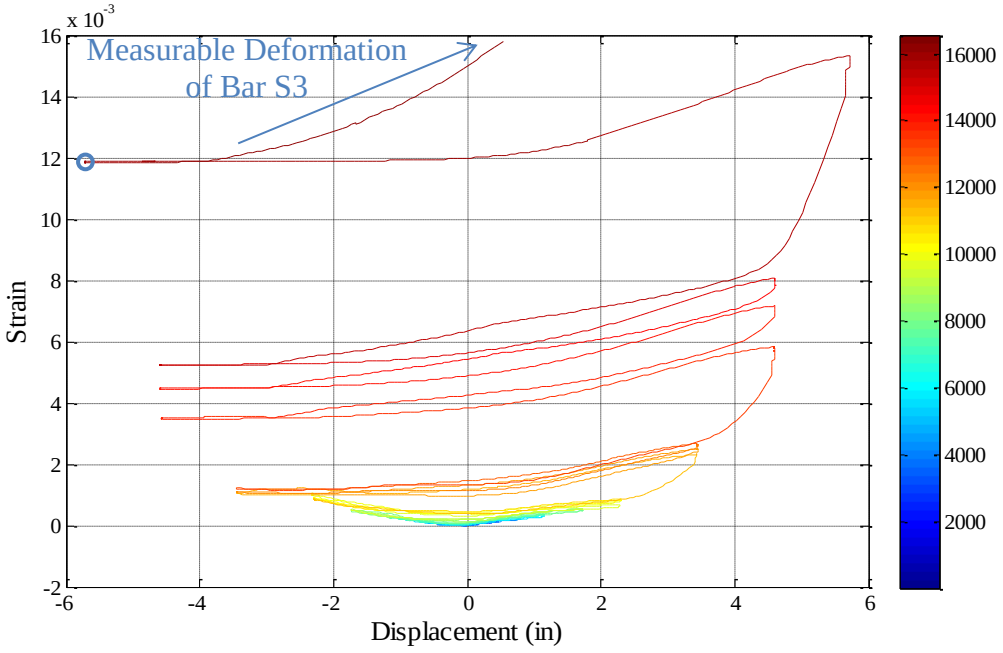

Figure 1.441 T19 – Spiral Strain Hysteresis for the Layer over South Buckled Region

Test 19 – Curvature and Strain Penetration Data

The cross section curvature for each horizontal section above the footing is determined by connecting the strain measurements from all eight instrumented bars with a least squared error line. The curvature is then extracted from the slope of the least squared error line, see Figure 1.442 and Figure 1.443. The cross section curvature profiles in these figures are shown for the horizontal section closest to the footing-column interface. For these sections, it appears that the plane sections hypothesis is appropriate. Vertical curvature profiles are plotted for push and pull cycles as shown in Figure 1.444 and Figure 1.445 respectively. These figures show that plastic curvatures have a linear distribution at higher displacement ductility levels. The extent of plastic curvatures above the footing can be calculated by determining where the linear plastic curvature regression intersects the triangular yield curvature distribution, shown as a grey dashed line. Circular data points in Figure 1.451 plot the measured spread of plasticity as a function of base section curvature ductility.

The target marker on each bar placed closest the footing-column interface can be used to create slip hysteresis and horizontal slip profiles attributable to strain penetration. The slip hysteresis for extreme fiber bars N3 and S3 appear in Figure 1.448 and Figure 1.449 respectively. If the tensile and compressive slip of all of the instrumented bars is plotted along the cross section depth, the base rotation attributable to strain penetration may be calculated. The slip profiles for push and pull cycles appear in Figure 1.446 and Figure 1.447 respectively. The rotation of the base section can be extracted from the slope of the least squared error line connecting all six measured bar slips. Combining the curvatures over the instrumented region (5ft above the footing), bar slip profiles, and an elastic curvature assumption above the instrumented region, the top column displacement can be calculated. This top column displacement calculated from the Optotrak system is compared to the top column displacement measured with a string potentiometer at the center of loading in Figure 1.450. The Optotrak integrated displacements match well in the push direction of loading, but they are uniformly over predicting the pull displacements by a small margin.

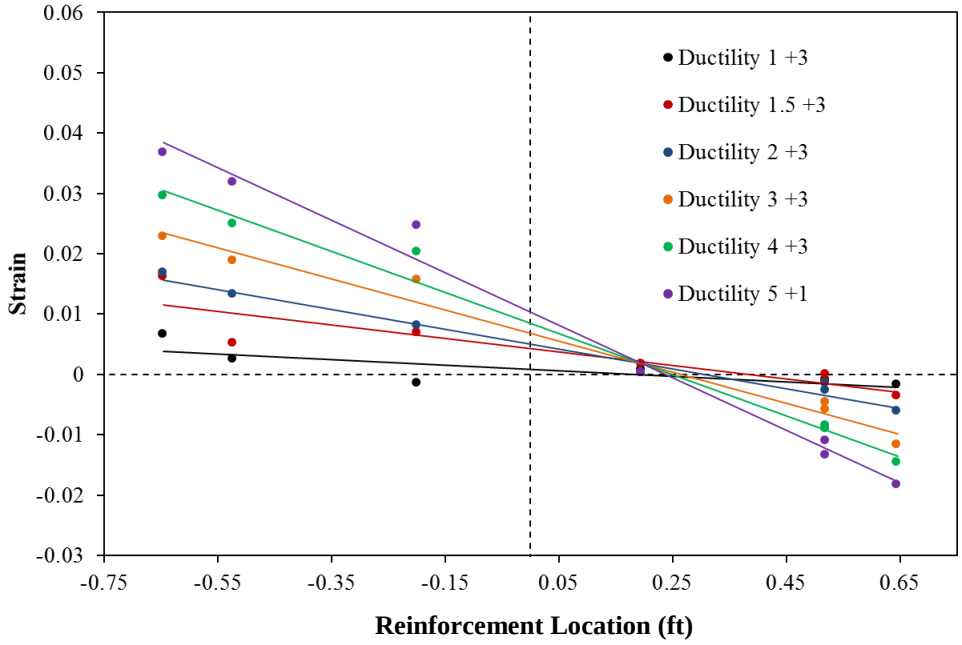

Figure 1.442 T19 – Lowest Horizontal Section Strain Profiles during Push Cycles

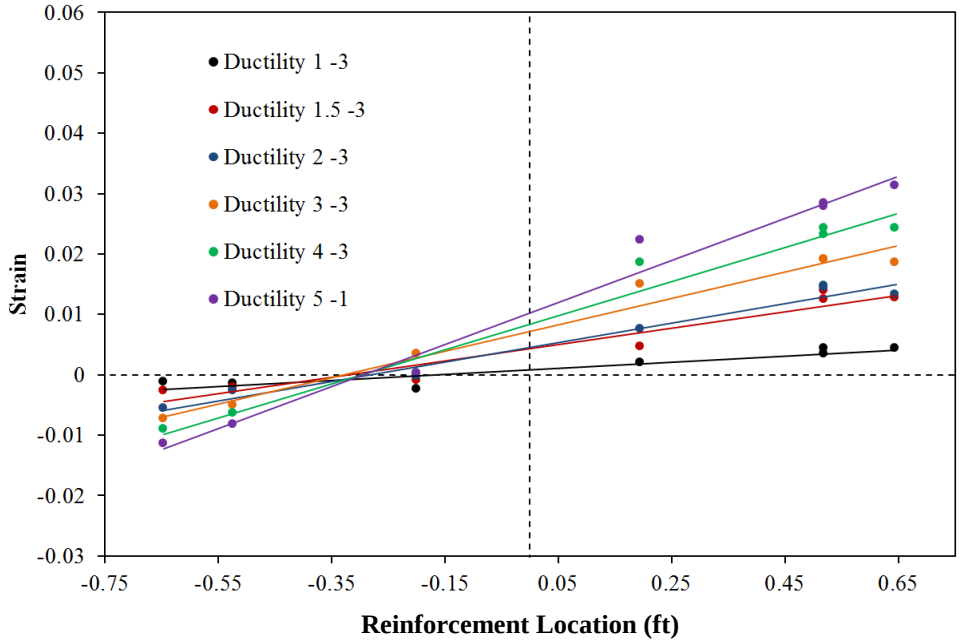

Figure 1.443 T19 – Lowest Horizontal Section Strain Profiles during Pull Cycles

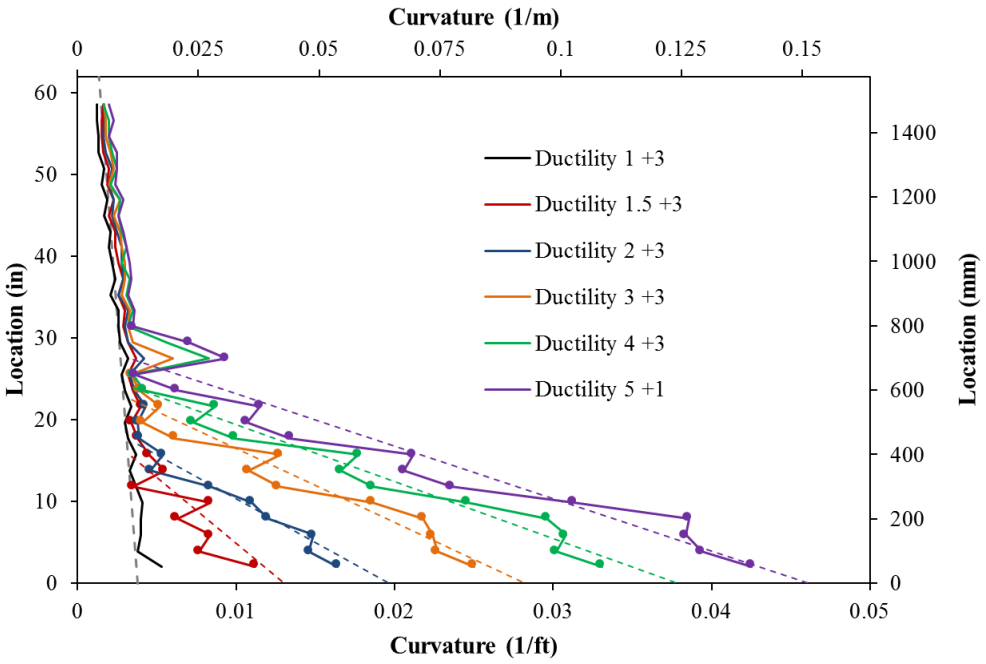

Figure 1.444 T19 – Push Cycle Curvature Profiles with Plastic Regression

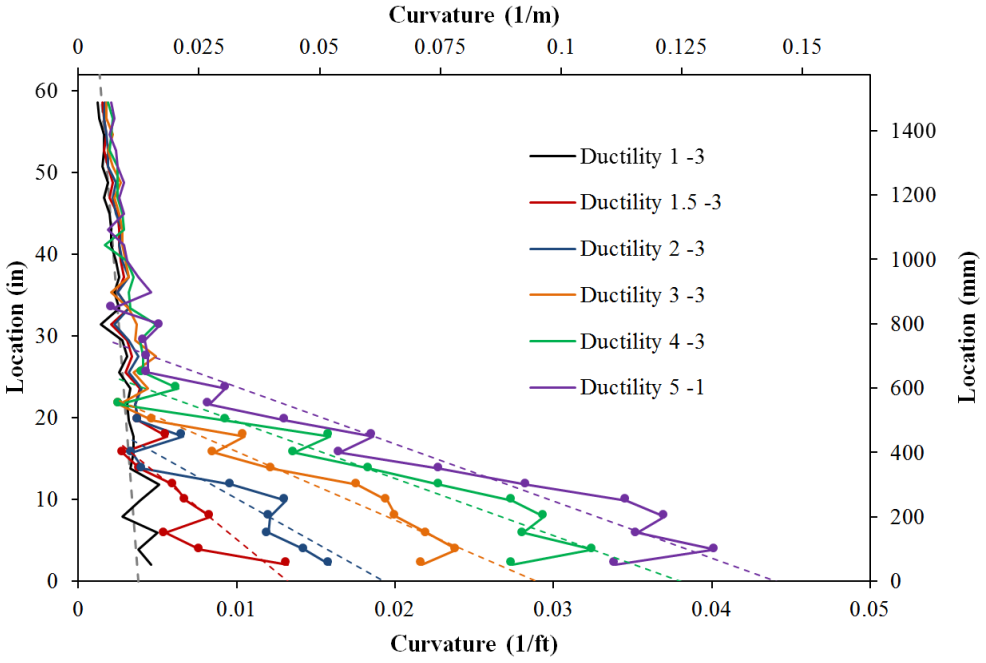

Figure 1.445 T19 – Pull Cycle Curvature Profiles with Plastic Regression

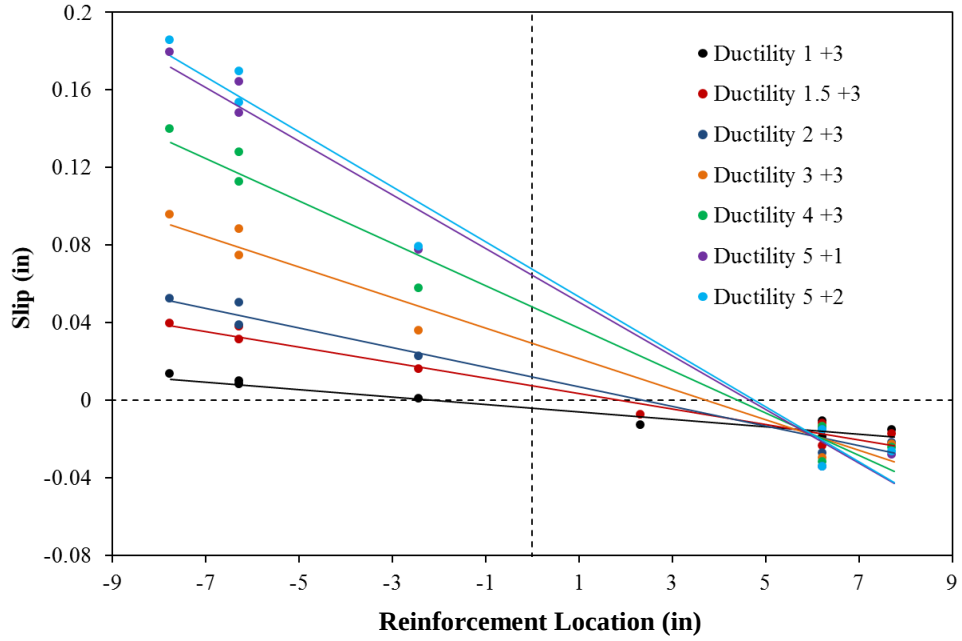

Figure 1.446 T19 – Base Rotation due to Strain Penetration during Push Cycles

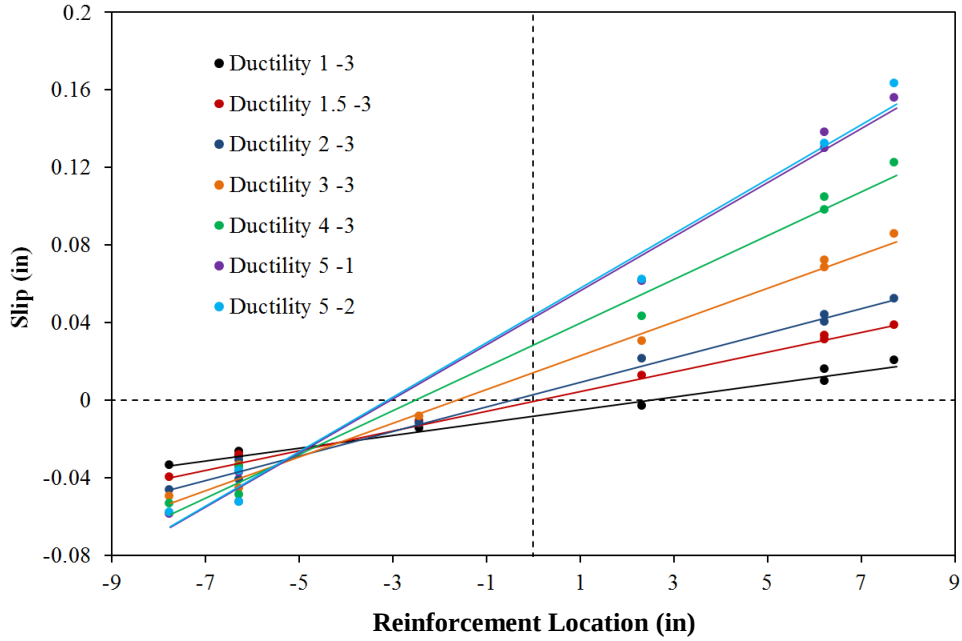

Figure 1.447 T19 – Base Rotation due to Strain Penetration during Pull Cycles

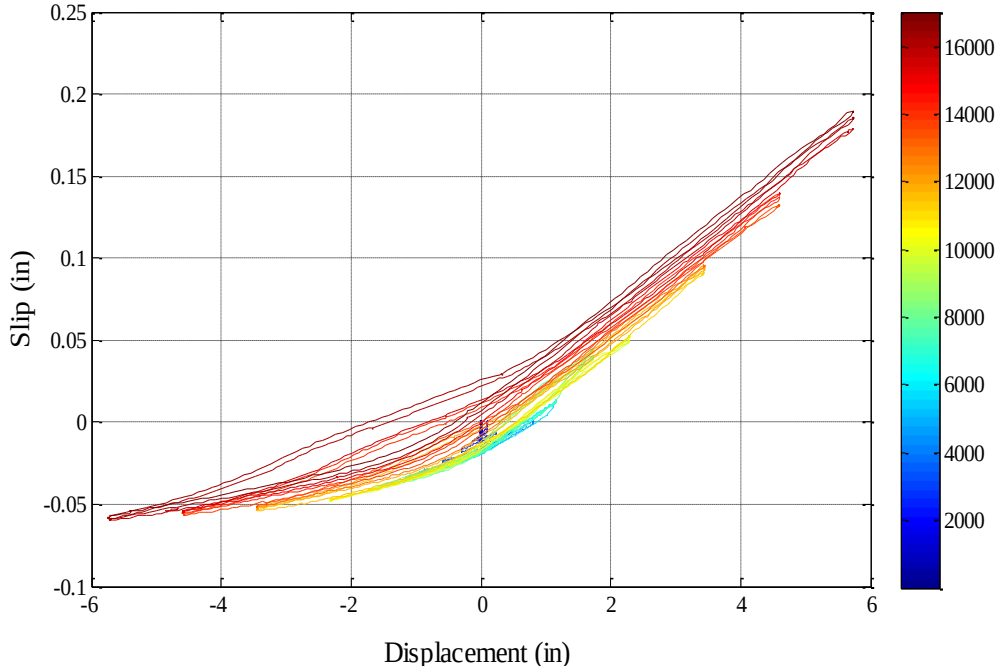

Figure 1.448 T19 – Base Section Slip Hysteresis for North Extreme Fiber Bar N3

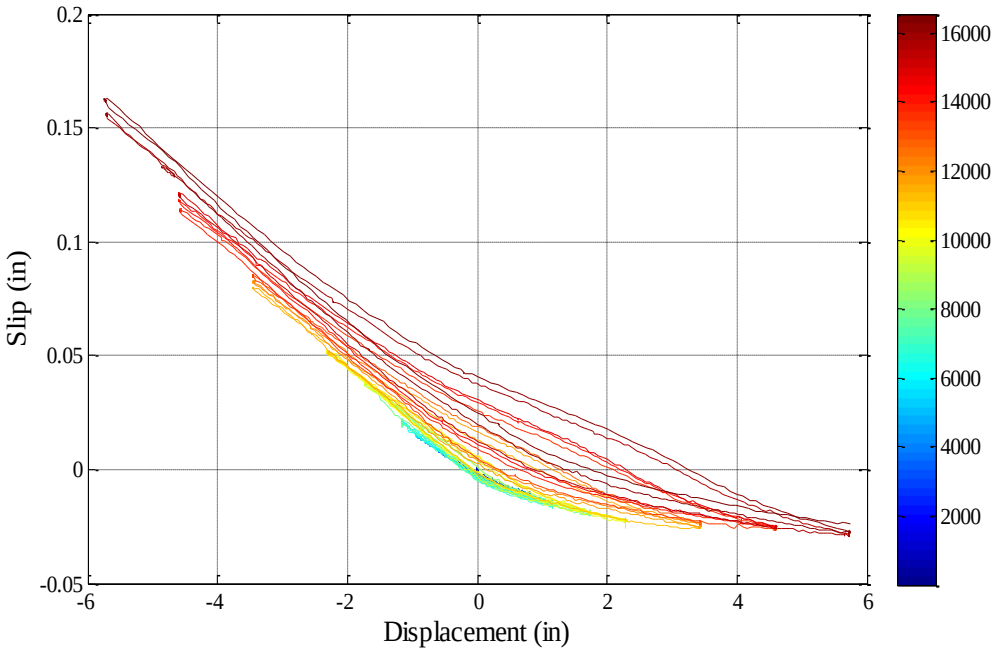

Figure 1.449 T19 – Base Section Slip Hysteresis for South Extreme Fiber Bar S3

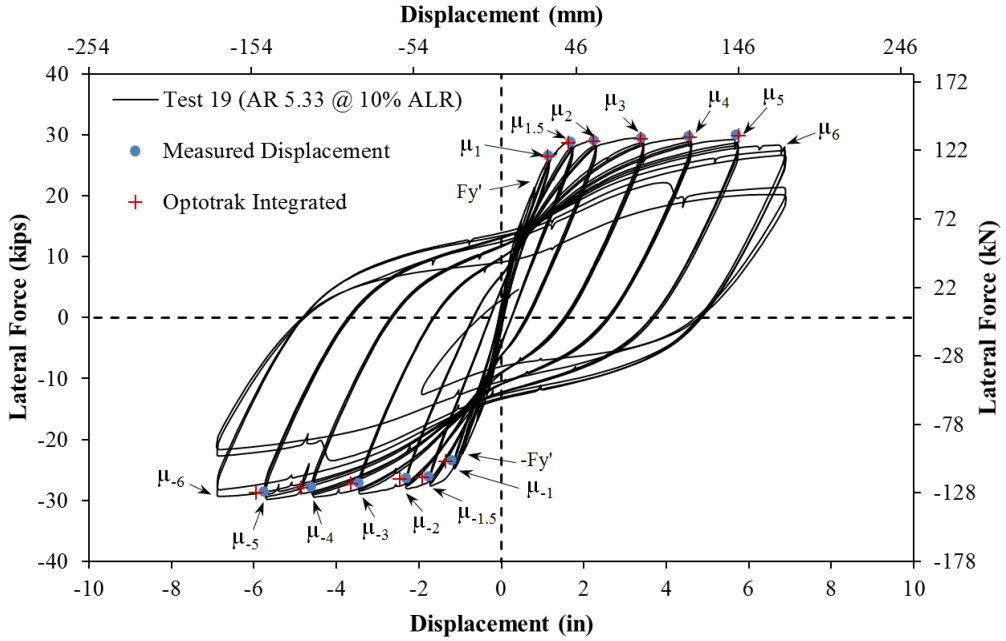

Figure 1.450 T19 – Comparison of Measured and Optotrak Integrated Displacements

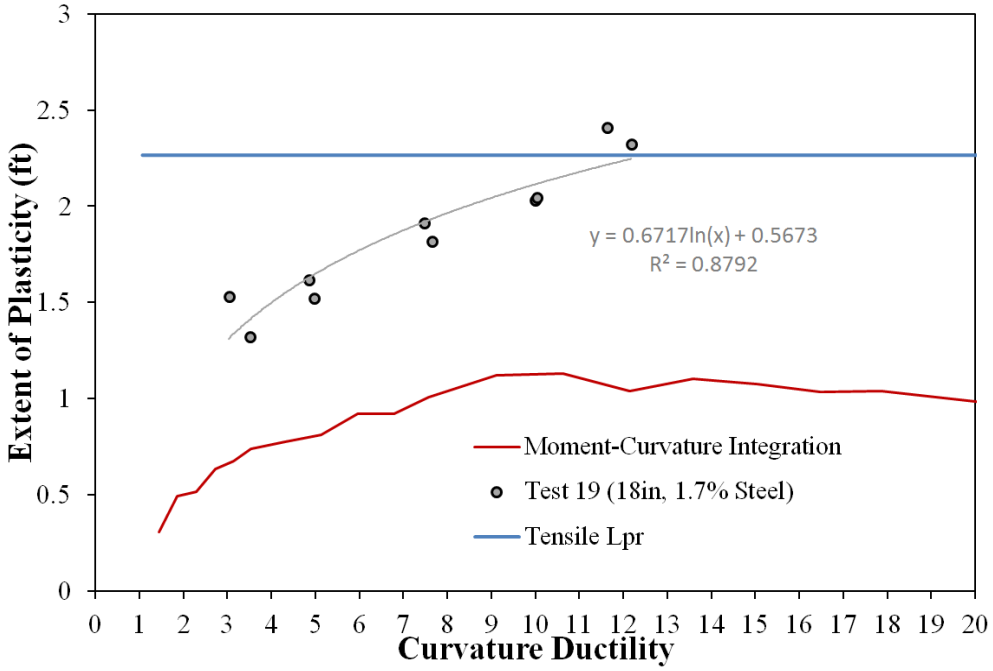

Figure 1.451 T19 – Measured Spread of Plasticity (Circular Data Points)

1.3.2 Test 20 – Aspect Ratio of 5.33 and 5% Axial Load

Table 1.35 Observations for Test 20 – Aspect Ratio of 5.33 and 5% Axial Load

VALUES OF INTEREST:	
Concrete Compressive Strength:	$f_c' = 6467\ psi$
Axial Load:	$P = 73.4\ kips\ \ (P/(f_c' A_g) = 5\%)$
Column Length and Aspect Ratio:	$8ft\ \ (L/D = 5.33)$
Analytical First Yield Force:	$F_y' = 18.58\ kips$
Experimental First Yield Displacement:	$\Delta_y' = 0.86"$
Analytical Nominal Moment Capacity:	$M_n = 205.63\ kip * ft$
Equivalent Yield Displacement:	$\Delta_y = 1.18"$
Maximum Lateral Force:	$27.3\ kips$
DAMAGE OBSERVATIONS:	
First Cracking North:	$3/4Fy' = 0.53"$
First Cracking South:	$-3/4Fy' = -0.56"$
Cover Concrete Crushing North:	$\mu_3^{-2} = -3.56"$
Cover Concrete Crushing South:	$\mu_3^{+1} = 3.55"$
Transverse Steel Yield North:	At $-4.04"$ during pull to $\mu_4^{-1} = -4.72"$
Transverse Steel Yield South:	At $3.54"$ during push to $\mu_3^{+1} = 3.55"$
Longitudinal Bar Buckling North:	*Deformation after Reversal from $\mu_6^{+4} = 7.10"$
Longitudinal Bar Buckling South:	Reversal from $\mu_5^{-2} = -5.93"$
Longitudinal Bar Fracture South:	At $-5.43"$ during pull to $\mu_6^{-3} = -7.01"$

*$\mu_5^{-2} = -5.93"$represents the second pull cycle of displacement ductility five

Table 1.36 Strain Data Summary for Test 20 – Aspect Ratio of 5.33 and 5% Axial Load

MATERIAL STRAINS:	
Cover Concrete Crushing North:	$\varepsilon_s = 0.0065\ (compression)\ \ ^*\mu_{\Delta 2} = -2.36"$
Cover Concrete Crushing South:	$\varepsilon_s = 0.0046\ (compression)\ \ ^*\mu_{\Delta 2} = 2.36"$
Transverse Steel Yield North:	$\varepsilon_s = 0.0114\ (compression)$
Transverse Steel Yield South:	$\varepsilon_s = 0.0109\ (compression)$
Longitudinal Bar Buckling North:	$\varepsilon_s = 0.046\ (peak\ tension\ prior\ to\ bb)$
*(Measurable Deformation in N3)	$\varepsilon_s = 0.016\ (peak\ comp.\ prior\ to\ bb)$
Longitudinal Bar Buckling South:	$\varepsilon_s = 0.037\ (peak\ tension\ prior\ to\ bb)$
	$\varepsilon_s = 0.016\ (peak\ comp.\ prior\ to\ bb)$
Mander (1988) Ultimate Concrete Compression Strain, $\varepsilon_{cu} = 0.0202$	

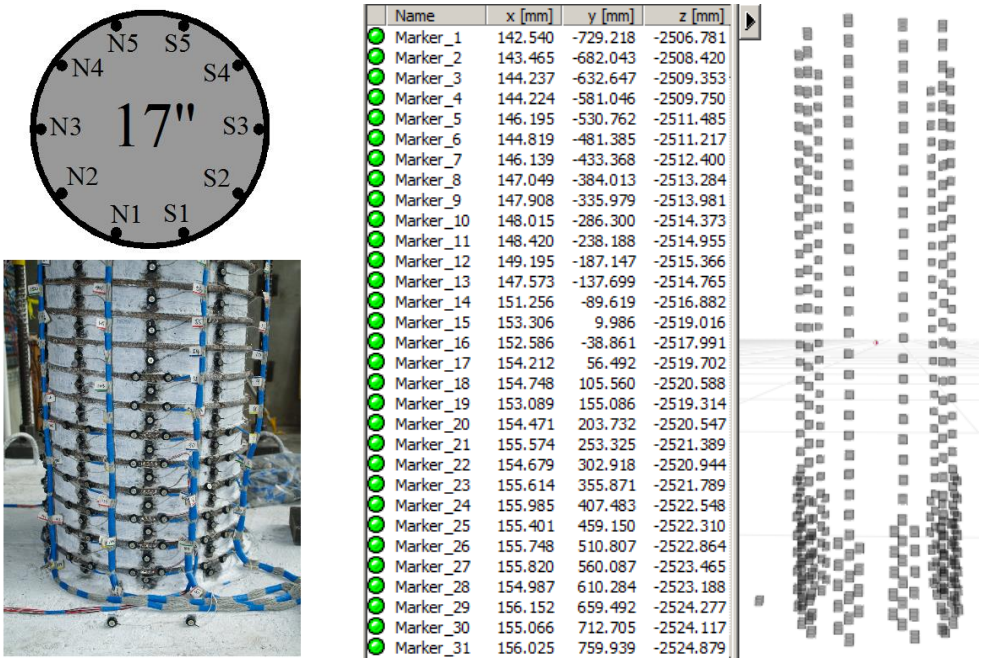

Name	x [mm]	y [mm]	z [mm]
Marker_1	142.540	-729.218	-2506.781
Marker_2	143.465	-682.043	-2508.420
Marker_3	144.237	-632.647	-2509.353
Marker_4	144.224	-581.046	-2509.750
Marker_5	146.195	-530.762	-2511.485
Marker_6	144.819	-481.385	-2511.217
Marker_7	146.139	-433.368	-2512.400
Marker_8	147.049	-384.013	-2513.284
Marker_9	147.908	-335.979	-2513.981
Marker_10	148.015	-286.300	-2514.373
Marker_11	148.420	-238.188	-2514.955
Marker_12	149.195	-187.147	-2515.366
Marker_13	147.573	-137.699	-2514.765
Marker_14	151.256	-89.619	-2516.882
Marker_15	153.306	9.986	-2519.016
Marker_16	152.586	-38.861	-2517.991
Marker_17	154.212	56.492	-2519.702
Marker_18	154.748	105.560	-2520.588
Marker_19	153.089	155.086	-2519.314
Marker_20	154.471	203.732	-2520.547
Marker_21	155.574	253.325	-2521.389
Marker_22	154.679	302.918	-2520.944
Marker_23	155.614	355.871	-2521.789
Marker_24	155.985	407.483	-2522.548
Marker_25	155.401	459.150	-2522.310
Marker_26	155.748	510.807	-2522.864
Marker_27	155.820	560.087	-2523.465
Marker_28	154.987	610.284	-2523.188
Marker_29	156.152	659.492	-2524.277
Marker_30	155.066	712.705	-2524.117
Marker_31	156.025	759.939	-2524.879

Figure 1.452 T20 – Cross Section Bar Designation and Target Marker Application

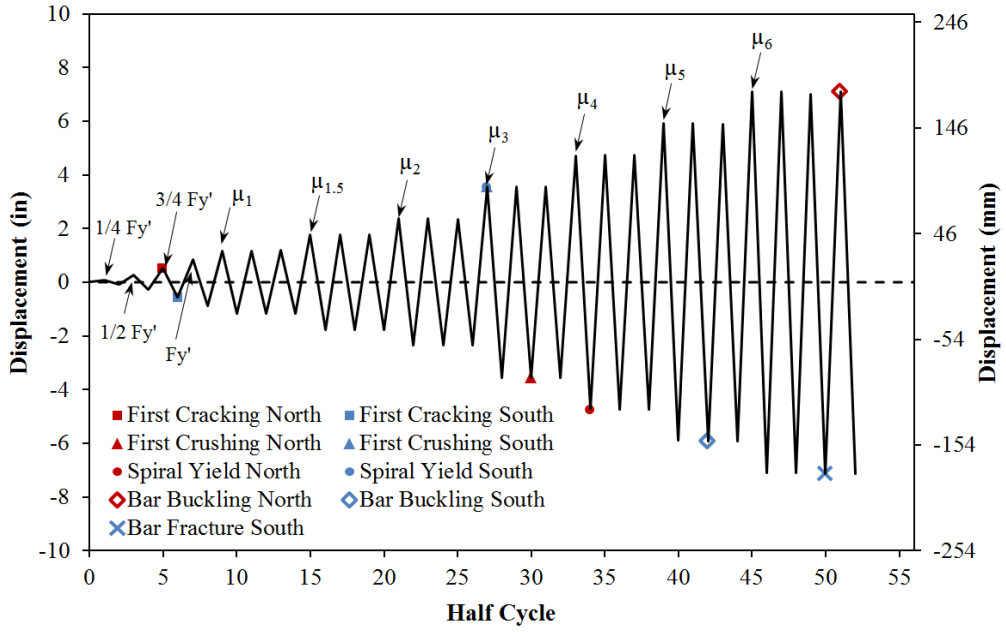

Figure 1.453 T20 – Symmetric Three Cycle Set Load History

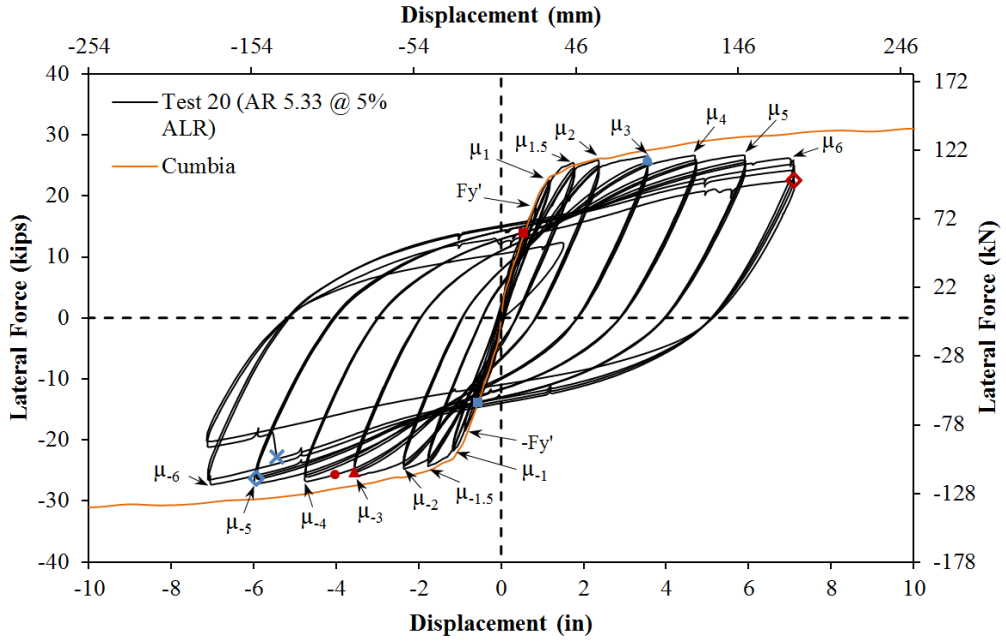

Figure 1.454 T20 – Lateral Force vs. Top Column Displacement Response

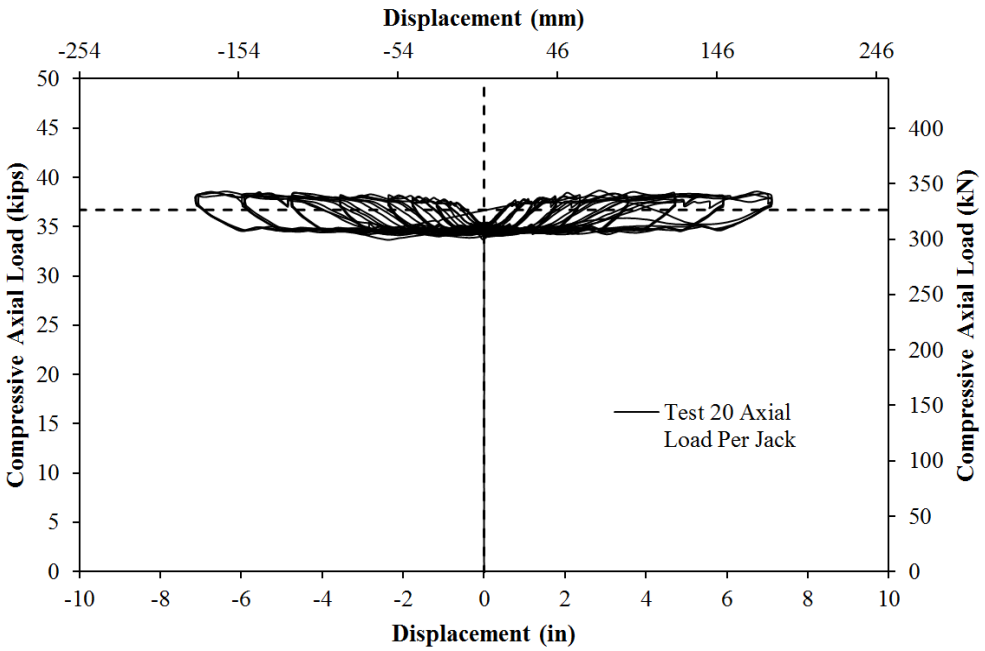

Figure 1.455 T20 – Compressive Axial Load from One Jack (Total = 2*Value)

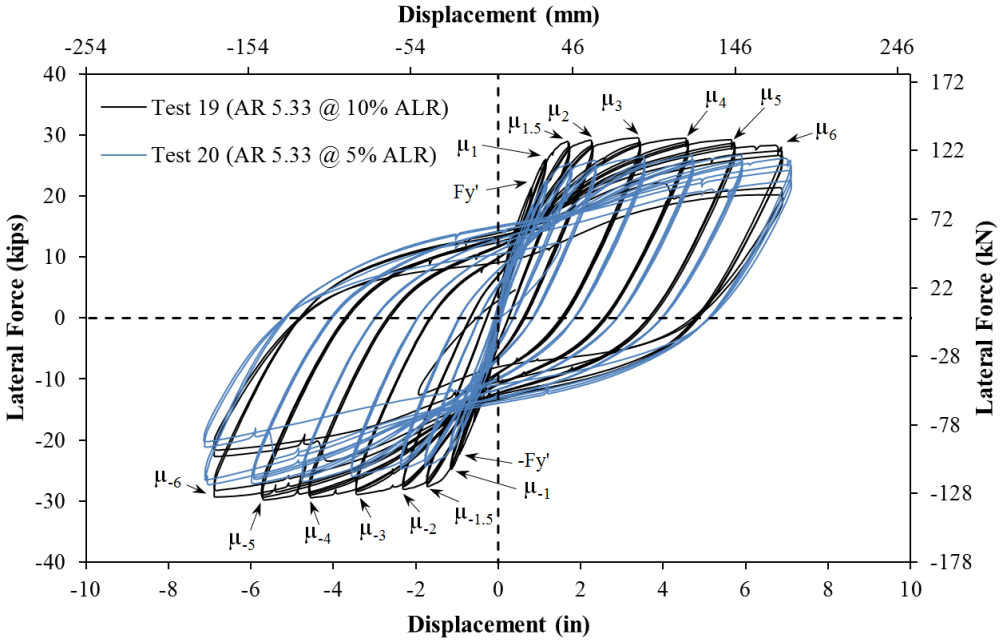

Figure 1.456 T19 and T20 Hysteretic Comparison with Different Axial Loads

Test 20 Aspect Ratio of 5.33 and 5% Axial Load – Experimental Observations

The transverse steel detailing, longitudinal reinforcement content, and material properties remain constant for Tests 19-24. The 18" diameter columns contain 10 #6 (A706) bars for longitudinal reinforcement ($A_{st}/A_g = 1.7\%$) and a #3 A706 spiral at 2" on center ($4A_{sp}/(D's) = 1.3\%$). The specific specimen chosen for Test 20 has an 8ft cantilever length ($L/D = 5.33$), and was subjected to ($P/(f_c'A_g) = 5\%$) axial load. The symmetric three-cycle-set laboratory load history is used to evaluate the seismic performance of structural components. The load history begins with elastic cycles to the following increments of the analytically predicted first yield force: ¼ Fy', ½ Fy', ¾ Fy', and Fy'. The first yield force for the tested material and geometric properties was determined using moment curvature analysis (Test 20: Cumbia Fy' = 18.58 kips with f'c = 6467 psi). The first yield displacement was obtained as an average for the experimental first yield push and pull cycles ($\Delta_y' = 0.86$").

Vertical strain profiles for both push and pull cycles up to the first yield force appear in Figure 1.457 with a dashed line representing the yield strain of the longitudinal reinforcement. The equivalent yield displacement, used to determine the displacement ductility levels ($\mu_{\Delta 1} = 1 * \Delta_y$), is then calculated as $\Delta_y = \Delta_y'(M_n/M_y') = 1.18$" for Test 20. The symmetric three-cycle-set load history resumes with three balanced cycles at each of the following ductility levels: 1, 1.5, 2, 3, 4, 5, 6, 7, 8, etc. The full symmetric three-cycle-set load history appears in Figure 1.453 and the resulting lateral force vs. top column displacement hysteresis is shown in Figure 1.454. The monotonic moment curvature prediction does not include P-Δ effects. A comparison of the measured hysteretic response for Tests 19 and 20 is shown in Figure 1.456. The strength of Test 19 was higher due to the larger axial load, but the deformation capacity for the two specimens remained similar.

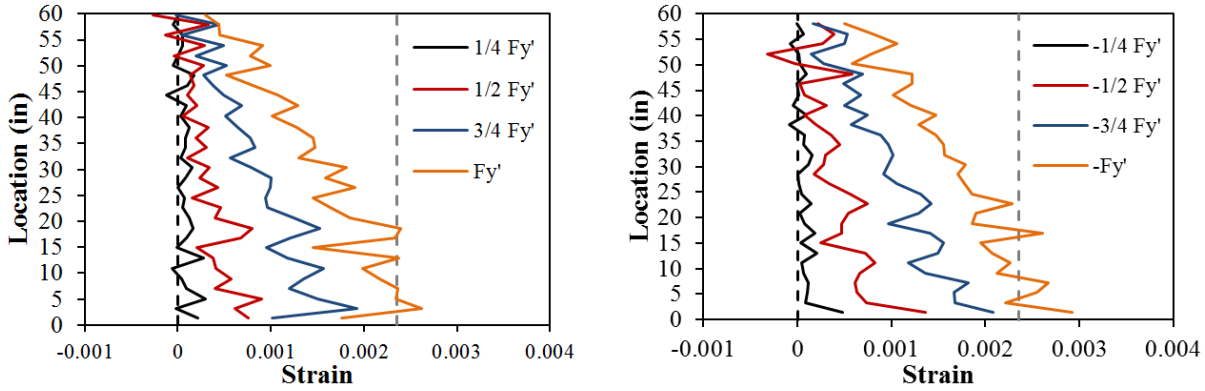

Figure 1.457 T20 – Strain Profiles before Yield (Left) Bar N3 and (Right) Bar S3

The test began with cycles in ¼ Fy' (first yield force) increments in each direction of loading until the first yield force was reached. The first cracks on the North and South sides of the specimen were observed during $(3/4Fy' = 13.94\,kips)$ and $(-3/4Fy' = -13.83\,kips)$ respectively. The first cracks appeared at the location of the spirals, therefore they were difficult to locate and measure. Crack widths measured on the outside surface of the concrete core have little meaning when describing a serviceability limit state which applies to columns with cover concrete. The crack distribution on all sides of the specimen at first yield, $(Fy' = 18.61\,kips)$ and $(-Fy' = -18.51\,kips)$, appears in Figure 1.458. Similarly, the crack progression at displacement ductility 1, 1.5, and 2 appear in Figure 1.459, Figure 1.460, and Figure 1.461 respectively. During these cycles the cracks became more numerous and increased in inclination on the shear faces of the specimen. A small amount of core concrete crushed on the South side of the specimen during ($\mu_3^{+1} = 3.55$"), as shown in the left photo of Figure 1.462. A similar observation was made, see the right photo of Figure 1.462, on the North side of the specimen during ($\mu_3^{-2} = -3.56$"). The crushing on each side of the specimen during ductility three was not severe, and it appeared that only a thin layer of concrete flaked off between spiral layers. Photos of the crack distributions during displacement ductility three and four appear in Figure 1.463 and Figure 1.464 respectively.

The South extreme fiber bar S3 visibly buckled after reversal from ($\mu_5^{-2} = -5.93$"), as shown in Figure 1.465. Photos of the crack distribution during displacement ductility five appear in Figure 1.466. Permanent deformation in spiral layers restraining the outward buckled region of bar S3 allows for further cycle to cycle degradation of the core concrete, see the left photo of Figure 1.468. An additional South reinforcing bar S4 buckled after reversal from ($\mu_6^{-2} = -7.10$"), as shown in the right photo of Figure 1.468. Previously buckled South extreme fiber bar S3 ruptured during the pull cycle to ($\mu_6^{-3} = -7.12$"), as shown in the right photo of Figure 1.469. Rupture of bar S3 lead to a 23% loss in strength measured at ($\mu_6^{-3} = -7.12$") relative to the peak load in the pull direction of loading. A fourth cycle at displacement ductility six was conducted. Although North bar buckling was not observed in the test, subsequent analysis of the strain data suggest that significant measurable deformation occurred in Bar N3 upon reversal from ($\mu_6^{+4} = 7.10$"). Photos of the specimen after removal of the instrumentation appear in Figure 1.470.

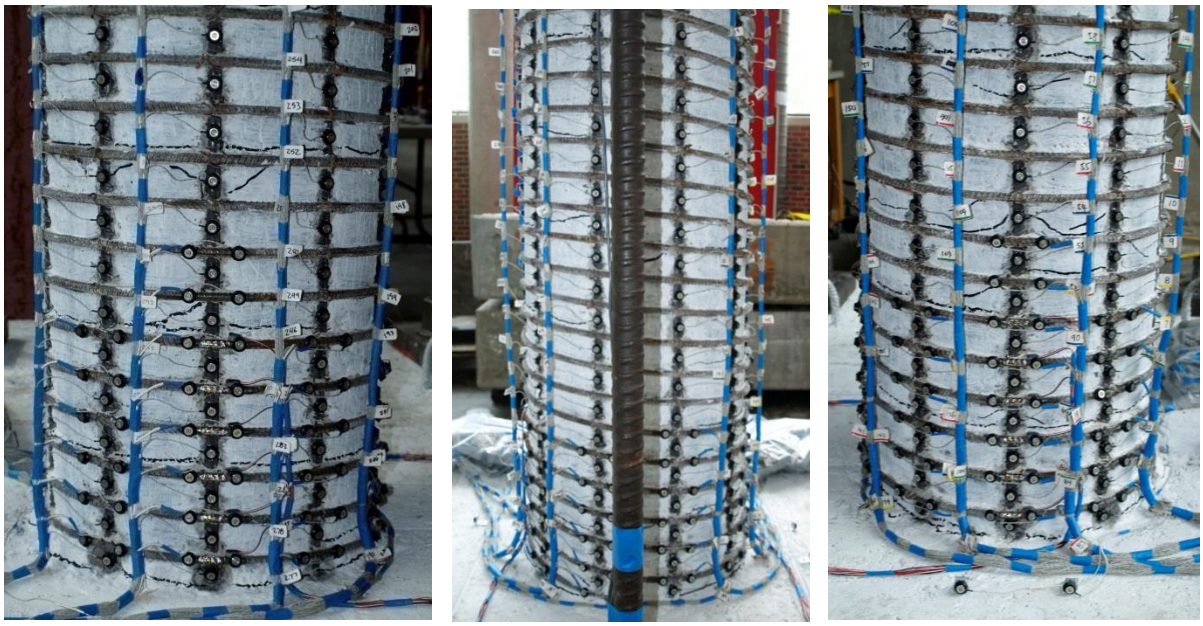

Figure 1.458 T19 – (Left) North at Fy', (Mid) Front at -Fy', and (Right) South at -Fy'

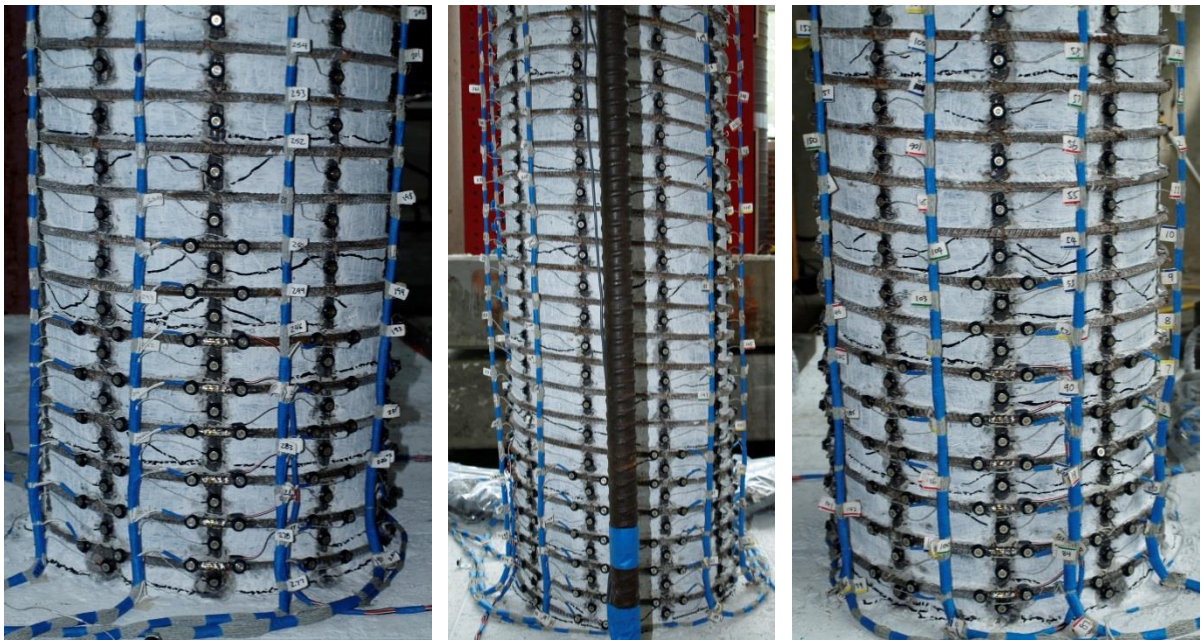

Figure 1.459 T20 – (Left) North at μ_1^{+3}, (Mid) Front at μ_1^{-3}, and (Right) South at μ_1^{-3}

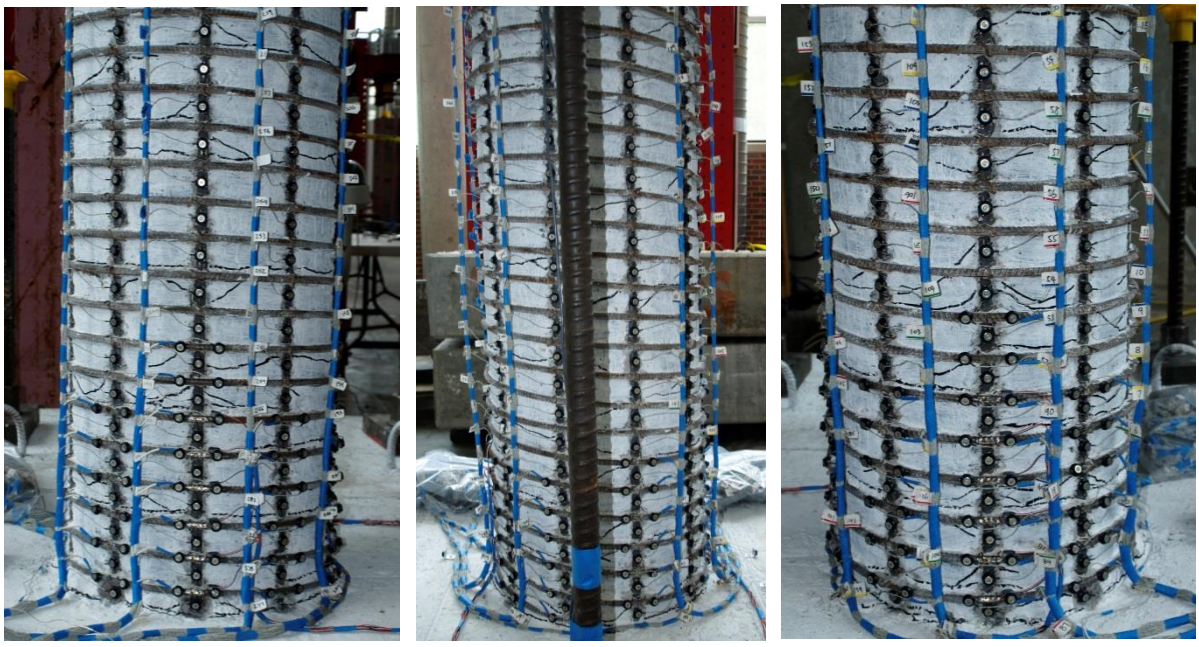

Figure 1.460 T20 – (Left) North at $\mu_{1.5}^{+3}$, (Mid) Front at $\mu_{1.5}^{-3}$, and (Right) South at $\mu_{1.5}^{-3}$

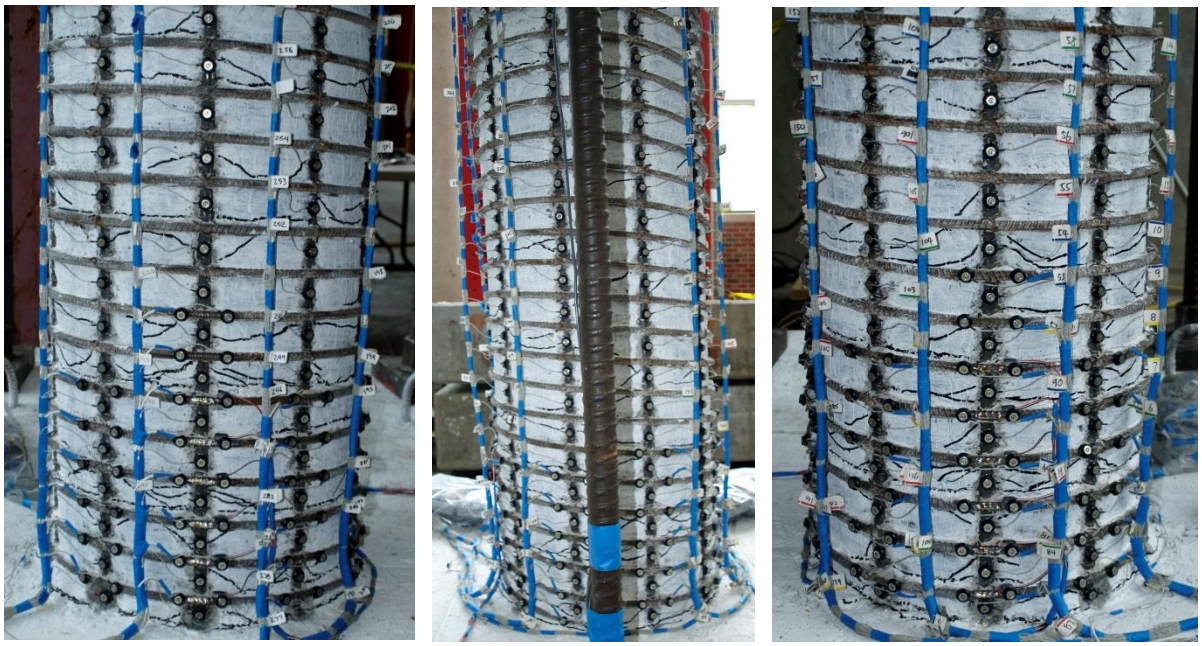

Figure 1.461 T20 – (Left) North at μ_2^{+3}, (Mid) Front at μ_2^{-3}, and (Right) South at μ_2^{-3}

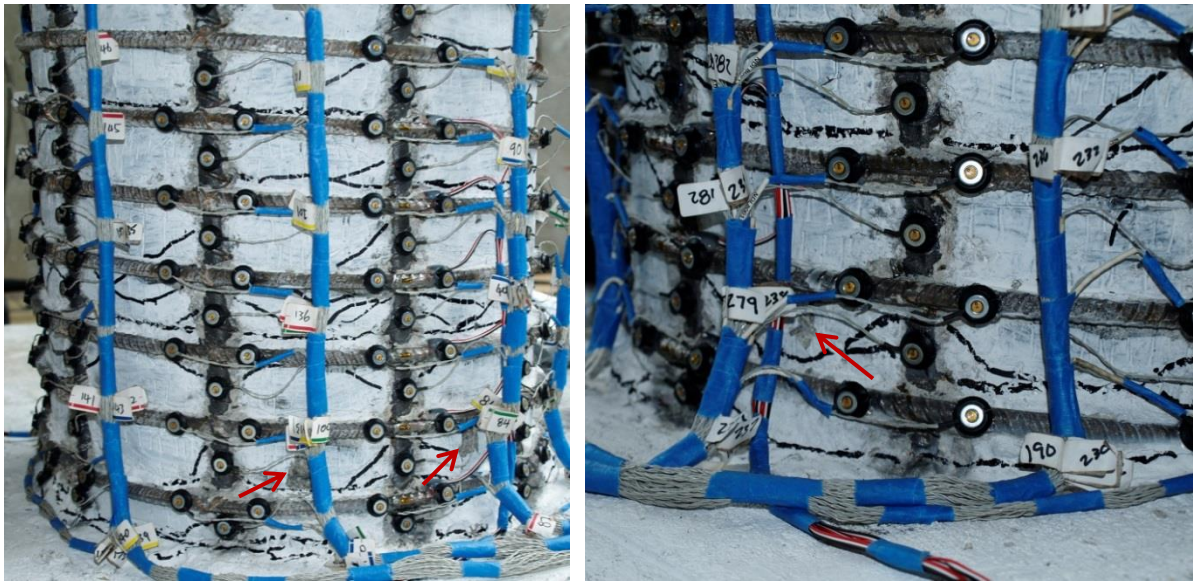

Figure 1.462 T20 – (Left) Cover Concrete Crushing on the South Side at μ_3^{+1} and (Right) Crushing on the North Side during μ_3^{-2}

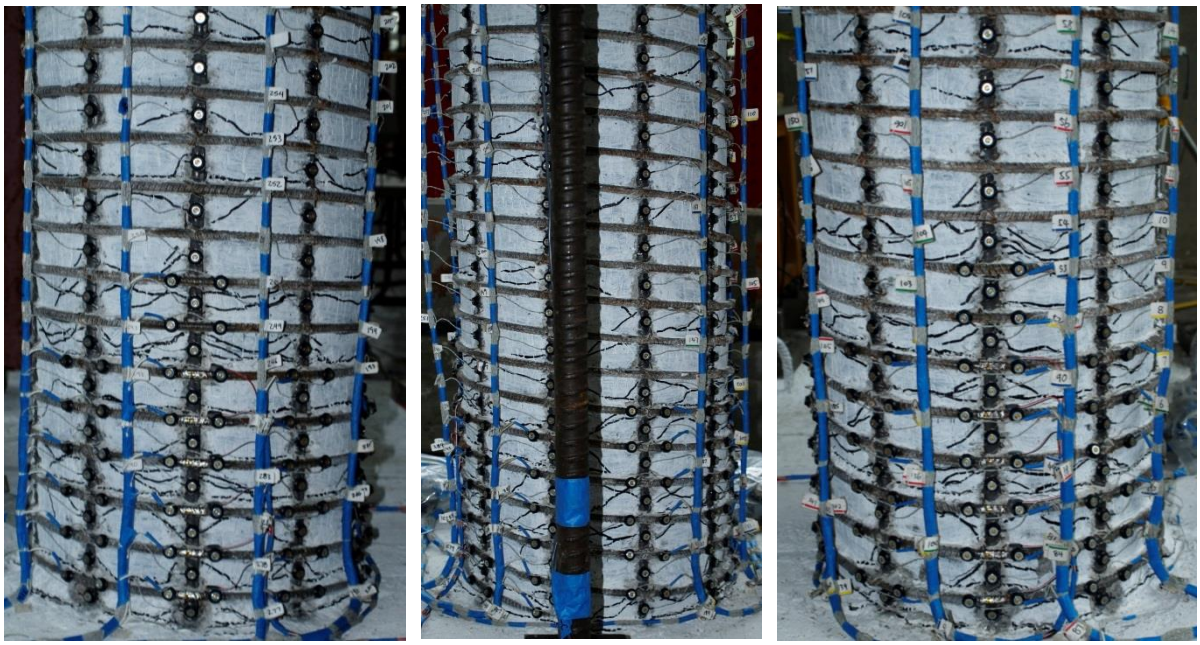

Figure 1.463 T20 – (Left) North at μ_3^{+3}, (Mid) Front at μ_3^{-3}, and (Right) South at μ_3^{-3}

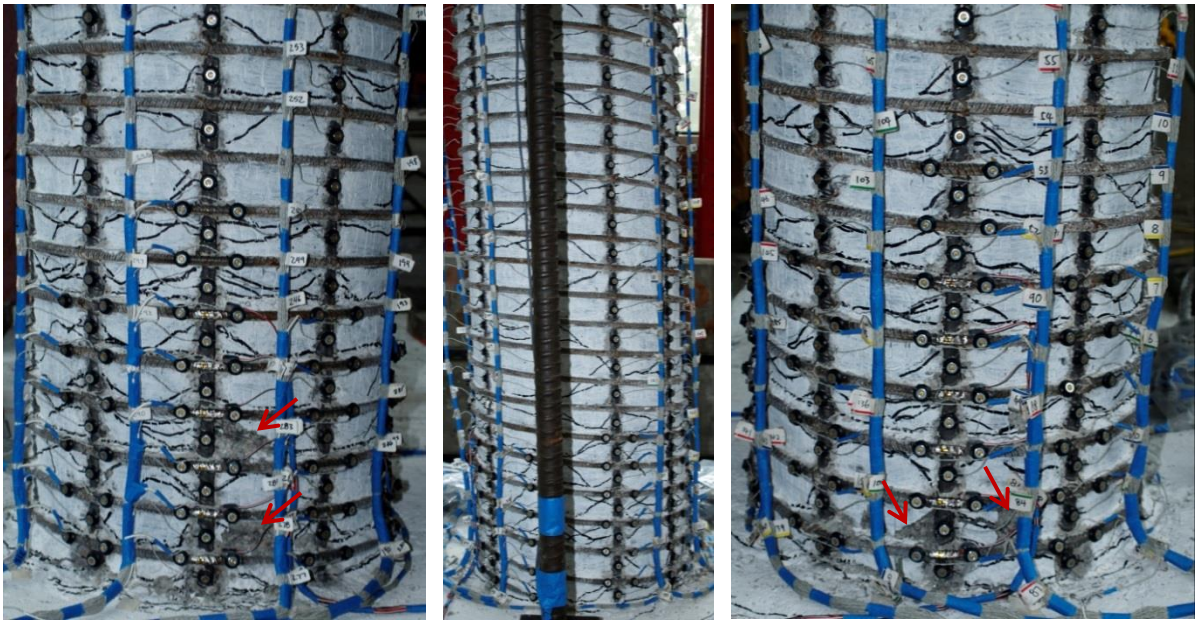

Figure 1.464 T20 – (Left) North at μ_4^{+3}, (Mid) Front at μ_4^{-3}, and (Right) South at μ_4^{-3}

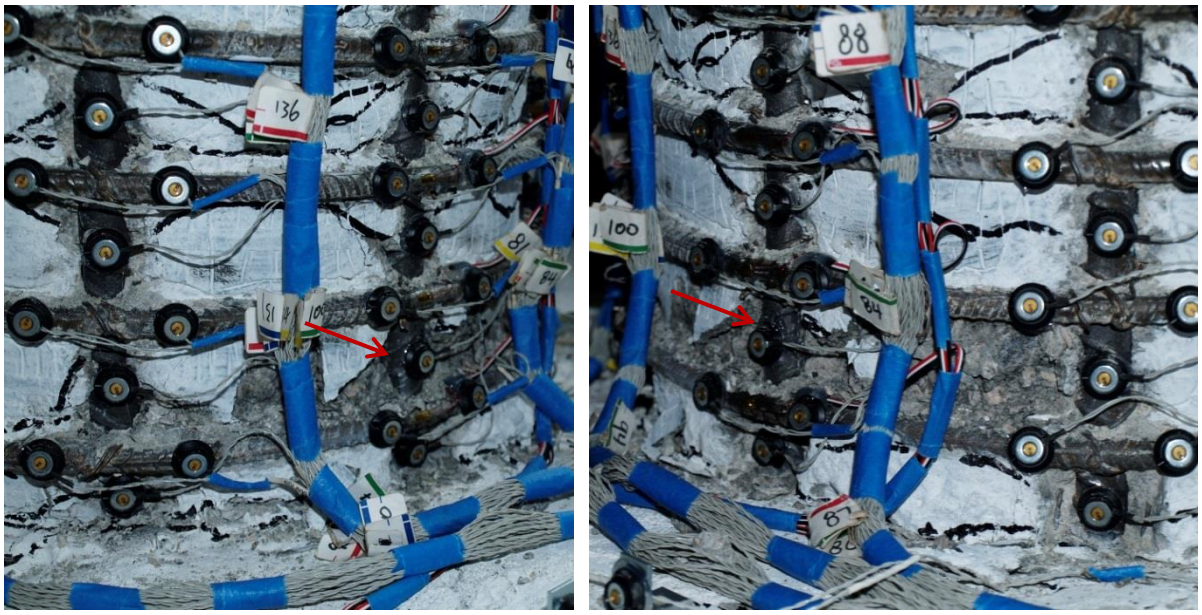

Figure 1.465 T20 – Buckling of Bar S3 after Reversal from ($\mu_5^{-2} = -5.93$")

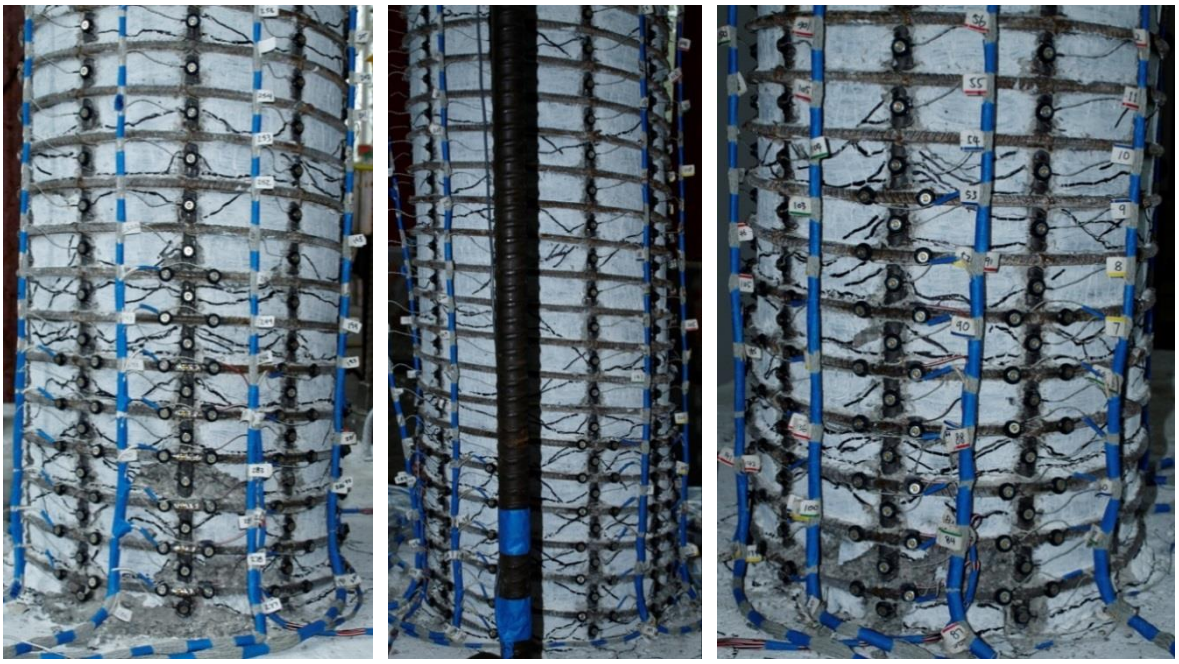

Figure 1.466 T20 – (Left) North at μ_5^{+3}, (Mid) Front at μ_5^{-3}, and (Right) South at μ_5^{-3}

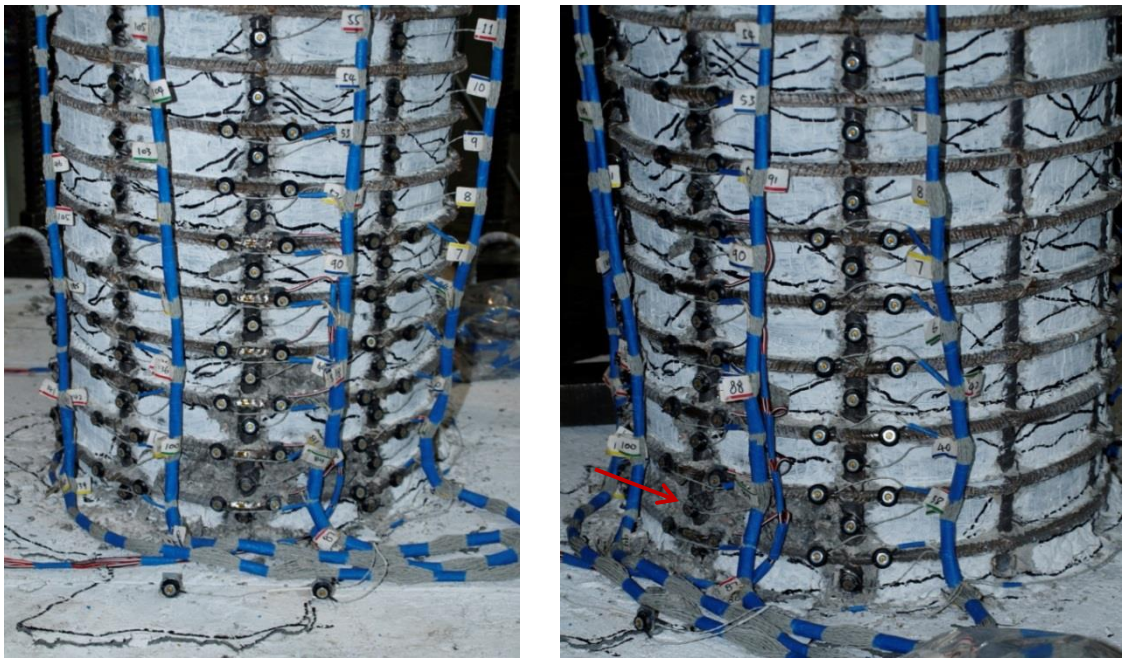

Figure 1.467 T20 – (Left) North Side at μ_6^{+2} and (Right) Deformation in Bar S3 at μ_6^{+2}

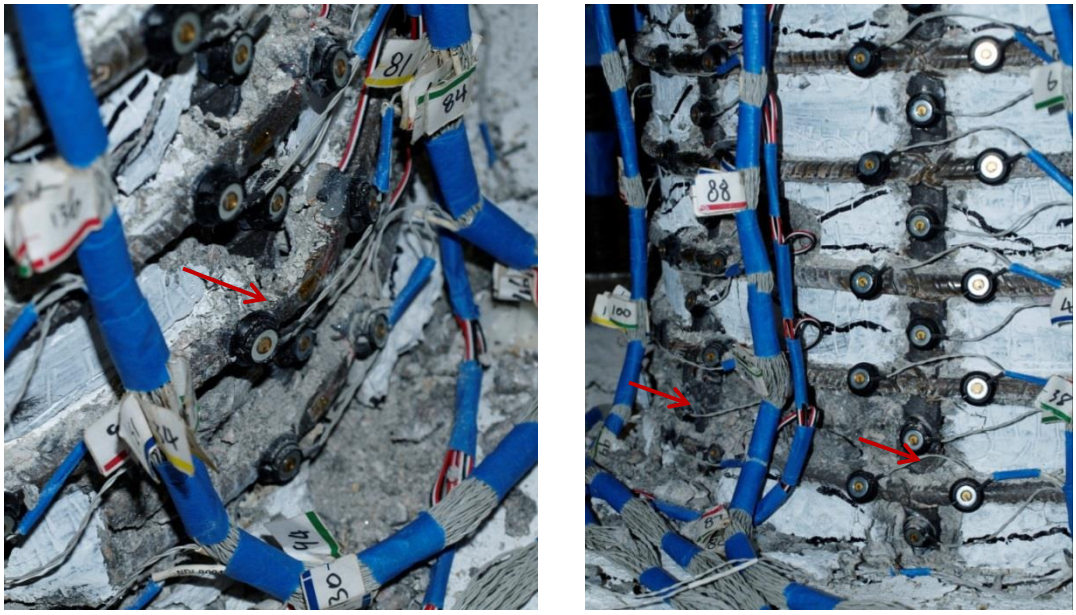

Figure 1.468 T20 – (Left) Deformation in Spiral Layers over Buckled Bar S3 during μ_6^{-2} and (Right) Buckling of Bar S4 after Reversal from μ_6^{-2}

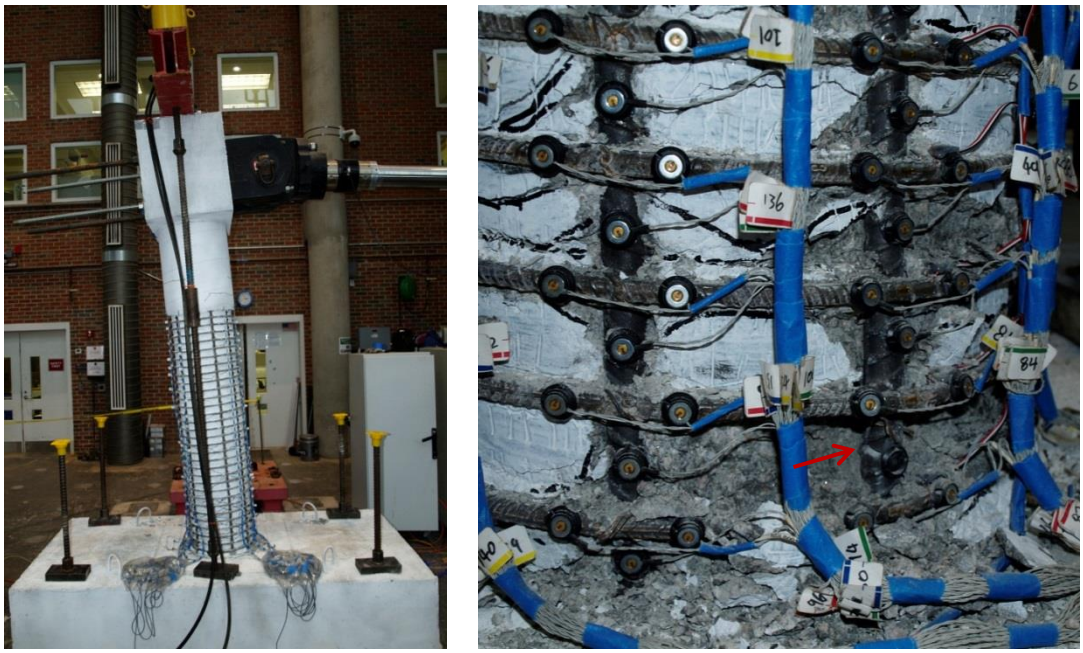

Figure 1.469 T20 – (Left) Lateral Displacement at ($\mu_6^{+3} = 7.01$") and (Right) Fracture of Previously Buckled Bar S3 during μ_6^{-3}

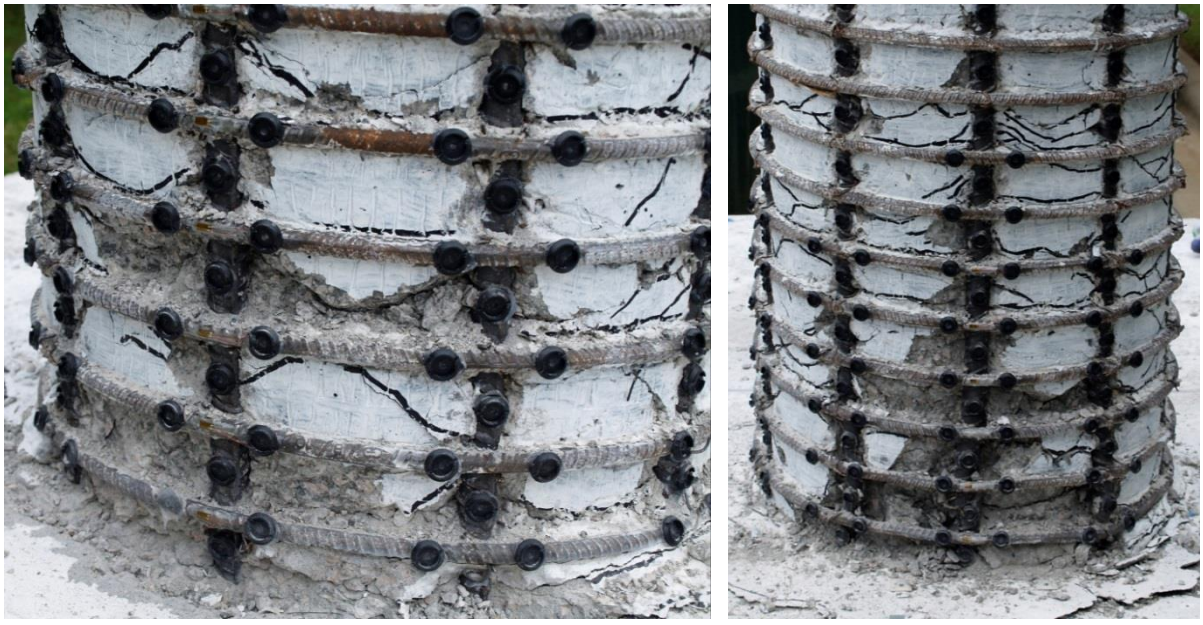

Figure 1.470 T20 – After Testing (Left) North Side and (Right) South Side

Test 20 Aspect Ratio of 5.33 and 5% Axial Load – Strain Data Analysis

North Reinforcement

Vertical strain profiles for north extreme fiber bar N3 placed into tension during push cycles appear in the right half of Figure 1.471. This figure shows both extreme fiber bars on the same graph to illustrate the effects of tension shift on strain profiles. Compressive vertical strain profiles for North extreme fiber bar N3 during pull cycles appear in the left half of Figure 1.472. As the hinge rotates about inclined flexural shear cracks, compressive strains are concentrated at the base and tensile strains are fanned out to a greater height following the crack distribution.

A peak tensile strain of 0.0458, located 1.38" above the footing, was measured for North extreme fiber bar N3 during ($\mu_6^{+4} = 7.10"$). The largest tensile strain in bar N3 measured during cycles at displacement ductility five was 0.0372 for the gage length 7.06" above the footing. The relationship between tensile strain and displacement for the gage length 3.17" above the footing appears in Figure 1.475. Each line represents a single push cycle which began with the column at zero displacement and ended at the peak during a continuous push cycle. The solid line contains data during the push cycle loading up to the peak displacement, and the dashed line represents the subsequent reversal of load. This gage length follows trends observed in the previous specimens. The moment curvature prediction with the PCK (2007) Lp Hinge Method matches well through displacement ductility three, but at larger displacements it begins to over predict the measured strains at an increasing rate.

The largest compressive strain of -0.0198, located 3.17" above the footing, was measured during ($\mu_6^{-1} = -7.09"$). The peak compressive strain of -0.0198 in bar N3 is lower the Mander ultimate concrete compressive strain of -0.0202. The relationship between compressive strain and displacement for bar N3 appears in Figure 1.476, for the gage length centered 3.17" above the footing. Here the measured compressive strains are significantly larger than the moment curvature prediction with the PCK (2007) Lp Hinge Method.

The strains in the lowest six transverse steel layers restraining North extreme fiber bar N3 are plotted in Figure 1.474. The individual data points are from strain gages attached to each spiral layer. The vertical grey dashed line represents a spiral yield strain of fy/Es, see Figure 1.409, which approximates the point at which permanent deformation in the spiral layer begins. Two adjacent spiral layers, 5.22" and 7.28" above the footing, entered the inelastic range during displacement ductility four. While the spiral strains over these layers marginally increased during displacement ductility five, it appears that the largest increases in spiral demand occurred over the layers 1.31" and 3.31" above the footing during displacement ductility six. The spiral strains in the lowest two transverse steel layers sharply increased during ($\mu_6^{+4} = 7.10"$), which suggests that measurable outward deformation of Bar N3 is present. The strain hysteresis for bar N3, gage length located 3.17" above the footing, appears in Figure 1.479. While visible buckling was not observed during the load history, measurable deformation occurred after reversal from ($\mu_6^{+4} = 7.10"$). The transverse steel strain gage hysteresis for the layer in the region of Bar N3 outward deformation appears in Figure 1.480. Larger cycle to cycle increases in the transverse steel demand were observed during ductility six as the apparent measurable deformation increased.

South Reinforcement

Vertical strain profiles for south extreme fiber bar S3 placed into tension during pull cycles appear in the right half of Figure 1.472. A peak tensile strain of 0.0367 was measured 5.29" above the footing during ($\mu_5^{-1} = -5.89"$). The relationship between tensile strain and displacement for this gage length is shown in Figure 1.477. The same comments on the accuracy of the moment curvature prediction for the North reinforcement bar N3 also apply to bar S3. Vertical strain profiles for bar S3 in compression during push cycles appear in the left half of Figure 1.471. A peak compression strain of -0.0155 was measured 1.45" above the footing during ($\mu_5^{+2} = 5.92"$). The relationship between compressive strain and displacement for the gage length 3.30" above the footing appears in Figure 1.478. The measured strains match the moment curvature prediction with the PCK (2007) Lp Hinge Method well through ductility 1.5, but at higher ductility levels the measured compressive

strains are larger than the moment curvature prediction. The peak compressive strain of -0.0155 measured in bar S3 is larger than the Mander ultimate concrete compressive strain of -0.0202.

The strains in the lowest six transverse steel layers restraining south extreme fiber bar S3 are plotted in Figure 1.473. The strain gage attached to the spiral layer 7.31" above the footing stopped functioning after displacement ductility two. A single spiral layer, located 3.31" above the footing, entered the inelastic range during displacement ductility three. The measured strain in the spiral layer 3.31" above the footing increased during ($\mu_5^{+2} = 5.92"$) relative to the values measured during the previous push cycle. The South extreme fiber bar S3 visibly buckled after reversal from ($\mu_5^{-2} = -5.93"$), as shown in Figure 1.465. The outward buckled region occurred over the previously inelastic spiral layer 3.31" above the footing. The strain hysteresis for the outward buckled region of bar S3 appears in Figure 1.481. The strain hysteresis for the spiral layer overlaying the outward buckled region of bar S3 is shown in Figure 1.482. Cycle to cycle increases in the measured spiral strains were observed during displacement ductility five, and a sharp increase occurred after reversal from ($\mu_5^{-2} = -5.93"$) when visible bar buckling was observed.

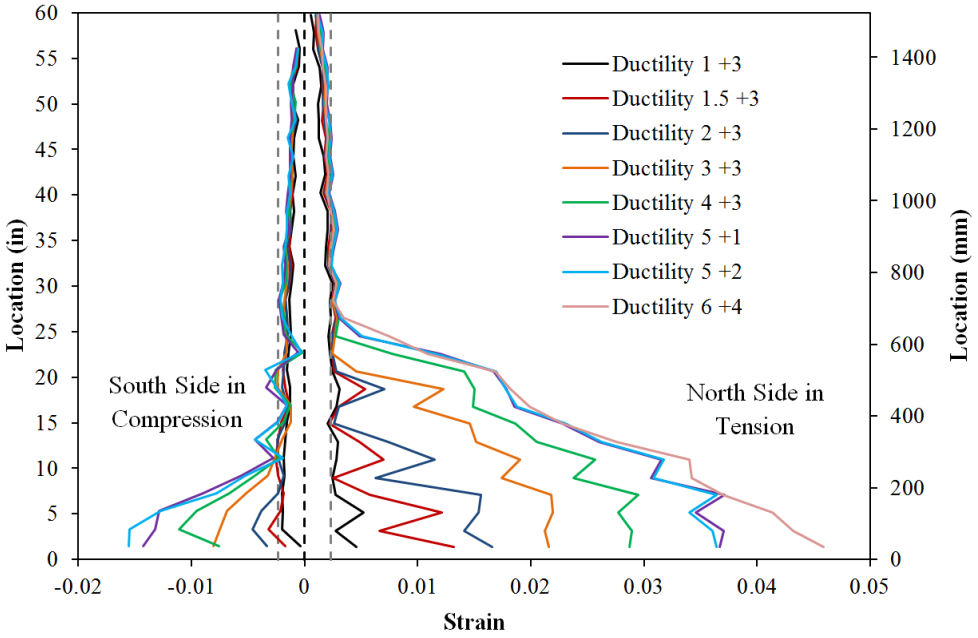

Figure 1.471 T20 – Extreme Fiber Vertical Strain Profiles during Push Cycles

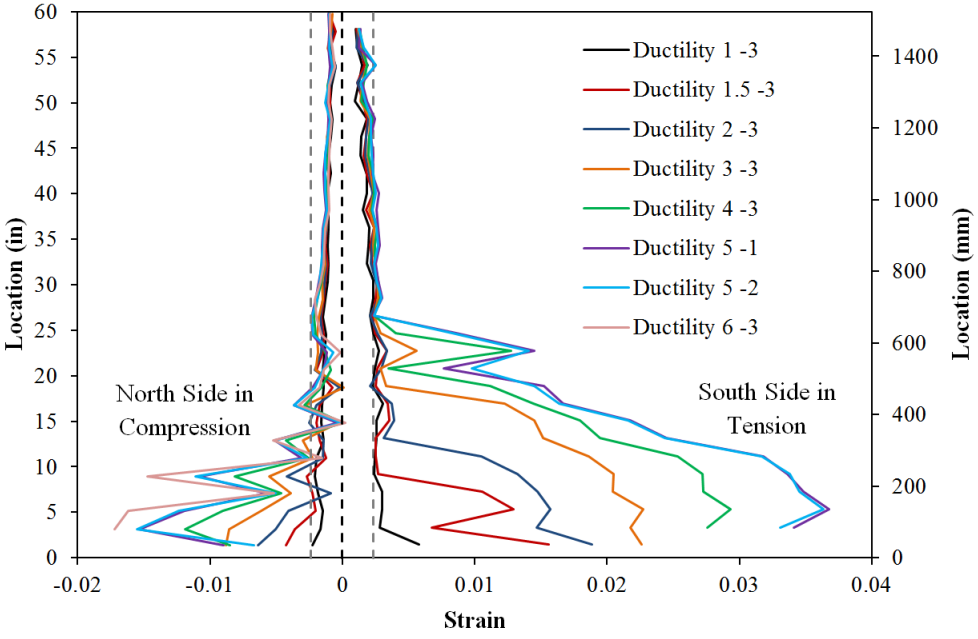

Figure 1.472 T20 – Extreme Fiber Vertical Strain Profiles during Pull Cycles

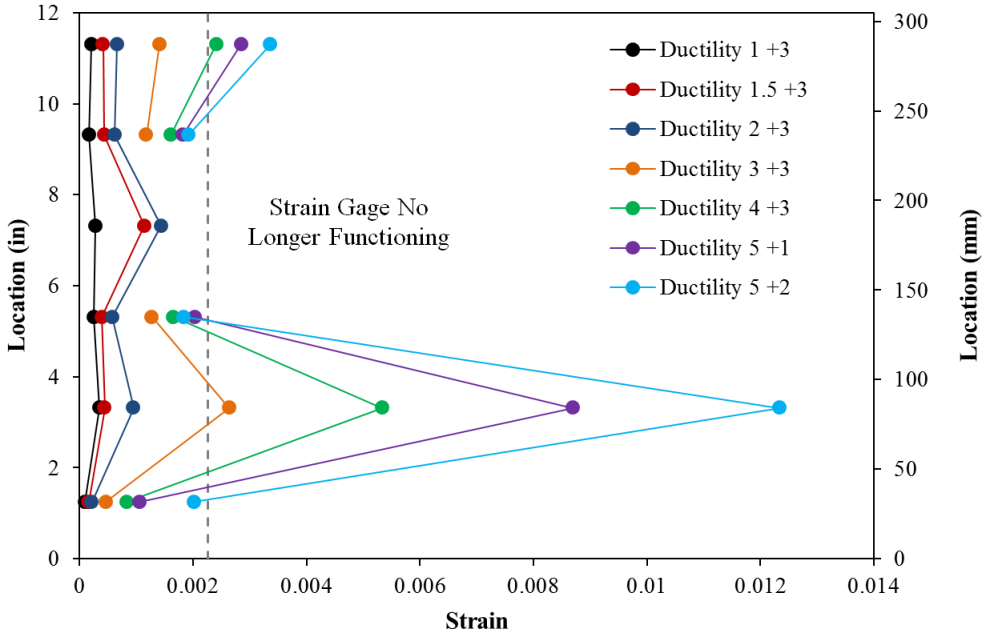

Figure 1.473 T20 – Spiral Strains on the South Side during Push Cycles

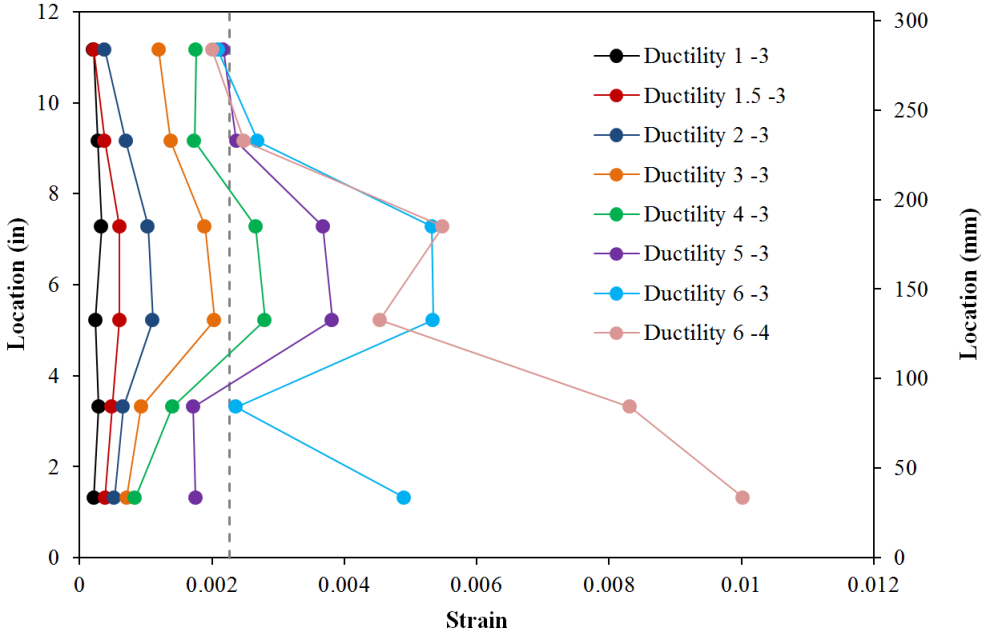

Figure 1.474 T20 – Spiral Strains on the North Side during Pull Cycles

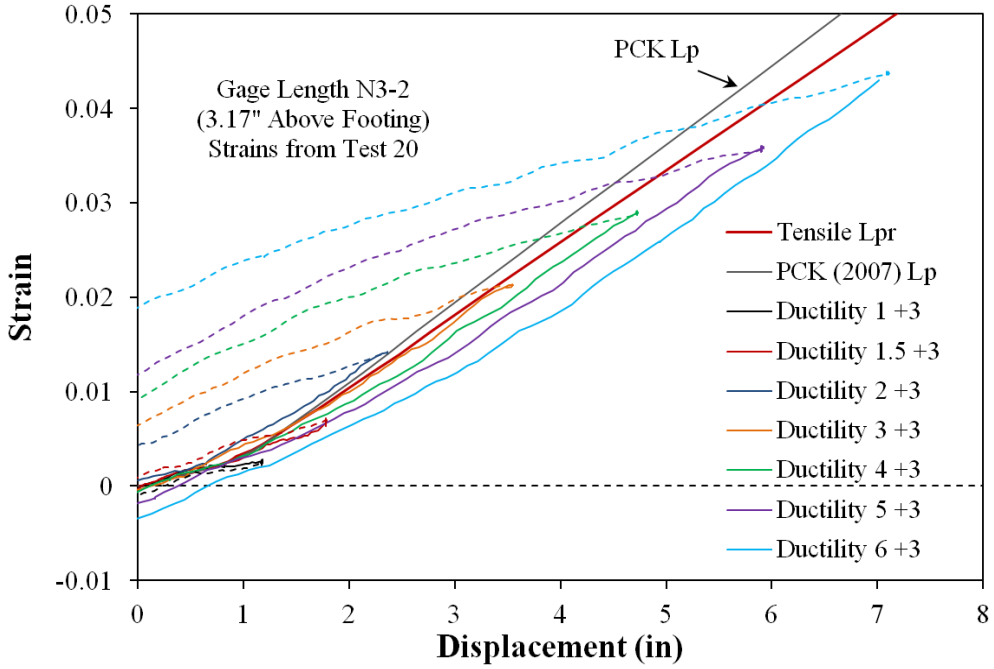

Figure 1.475 T20 – Tensile Strain-Displacement for Bar N3 during Push Cycles

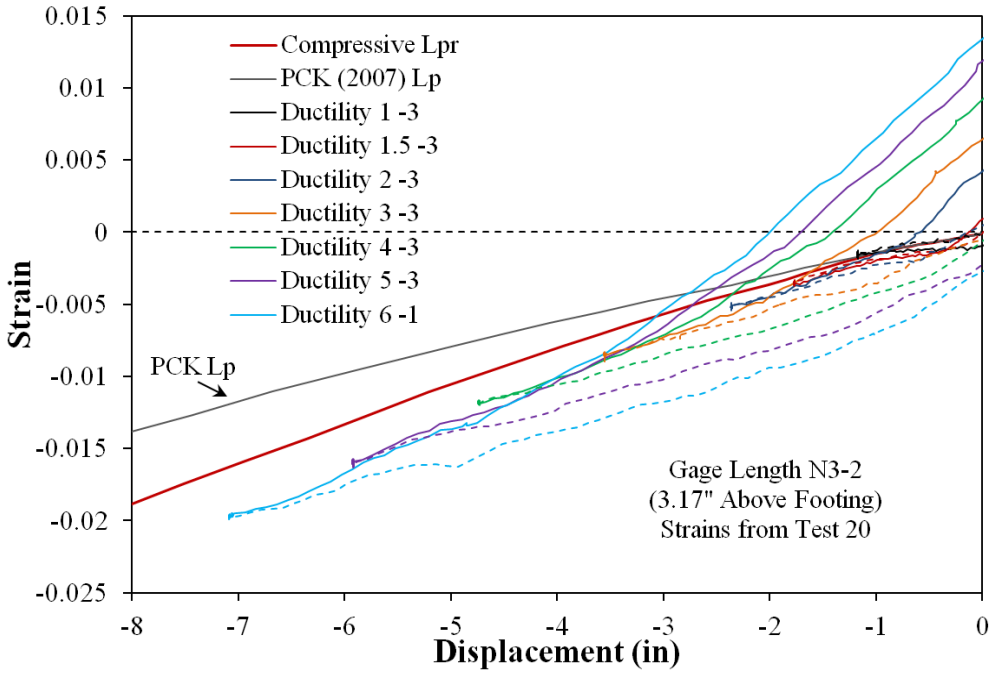

Figure 1.476 T20 – Compressive Strain-Displacement for Bar N3 during Pull Cycles

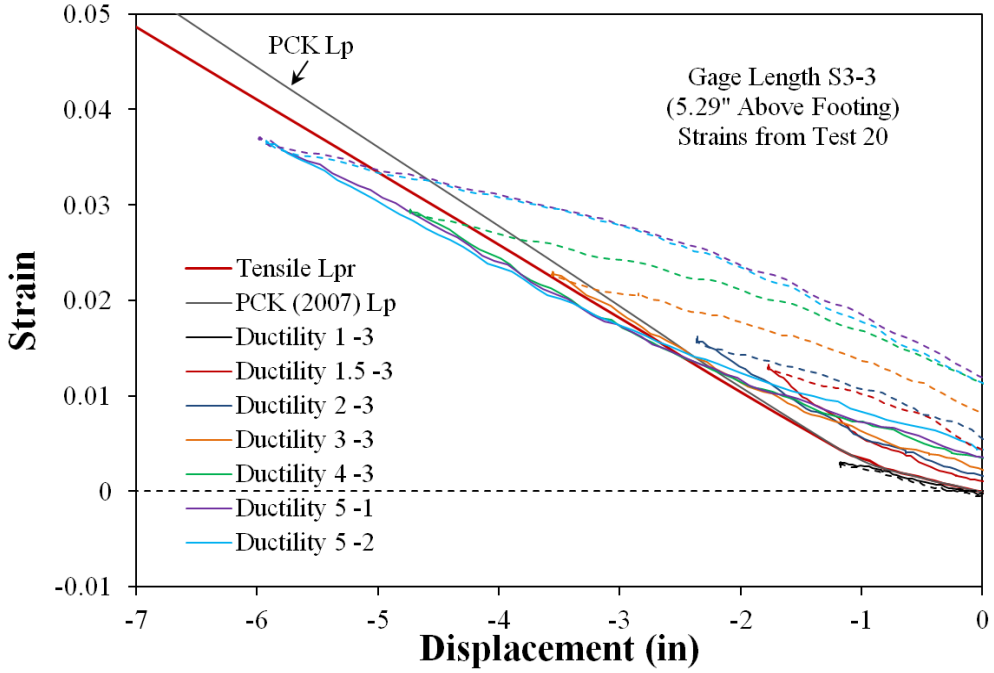

Figure 1.477 T20 – Tensile Strain-Displacement for Bar S3 during Pull Cycles

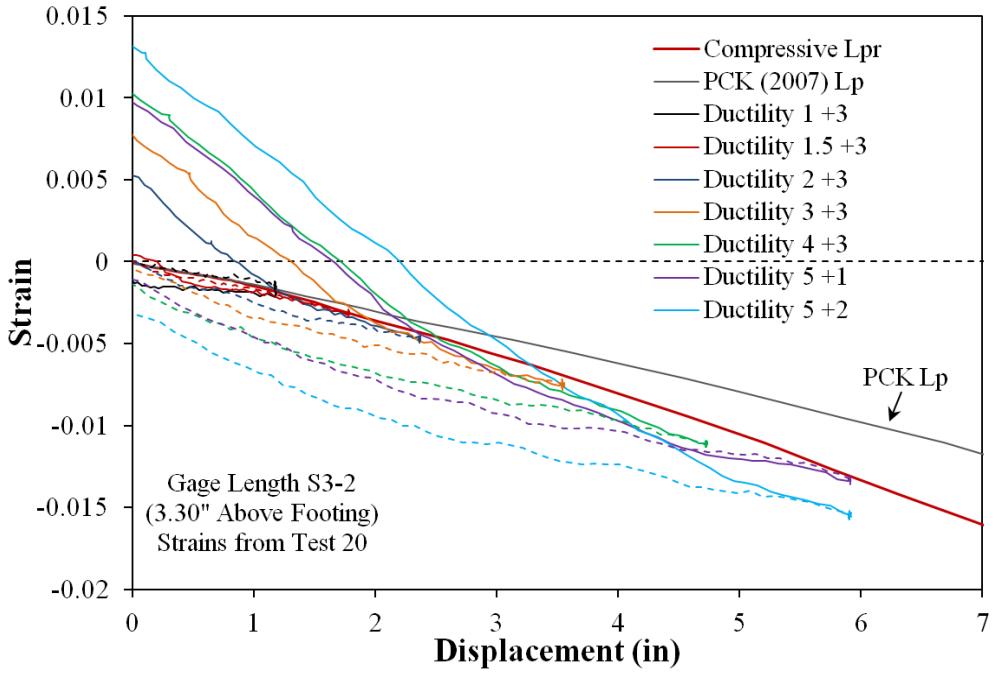

Figure 1.478 T20 – Compressive Strain-Displacement for Bar S3 during Push Cycles

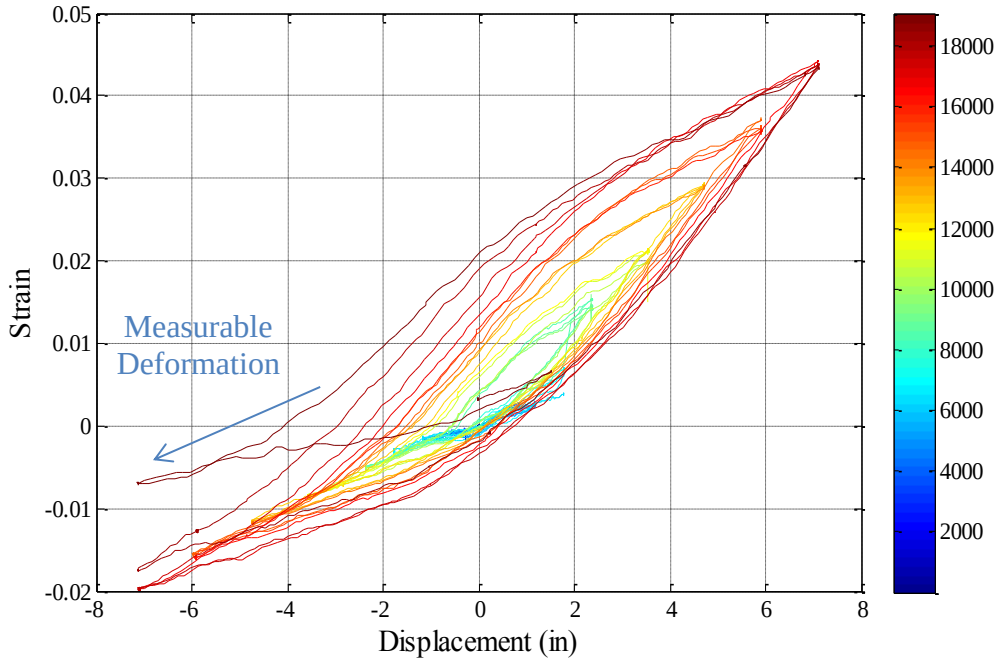

Figure 1.479 T20 – Extreme Fiber Bar N3 Strain Hysteresis (3.17" above the Footing)

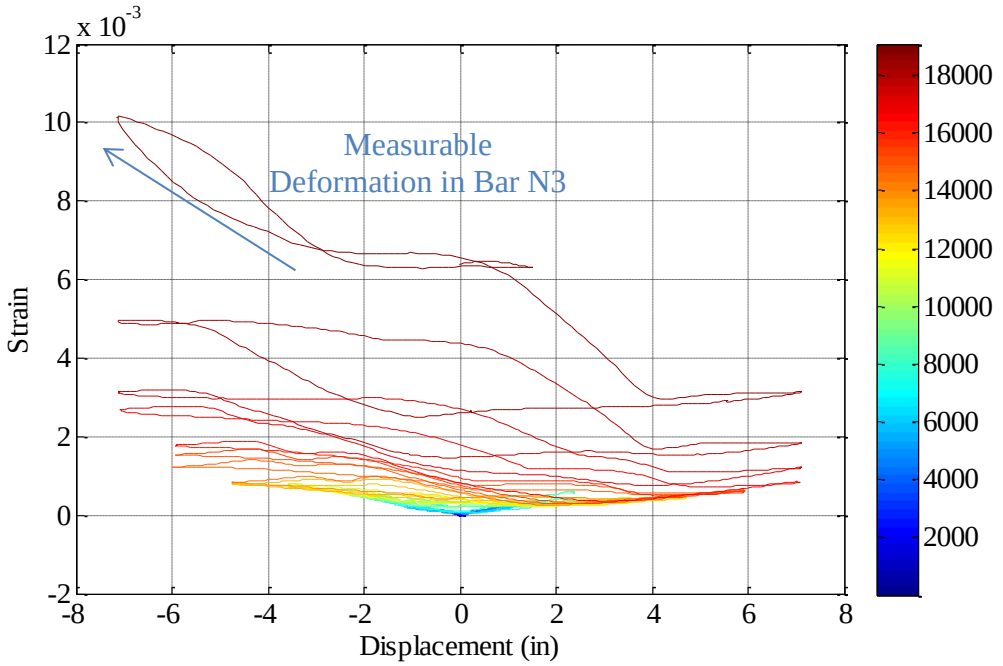

Figure 1.480 T20 – Spiral Strain Hysteresis 1.31" Above the Footing on North Side

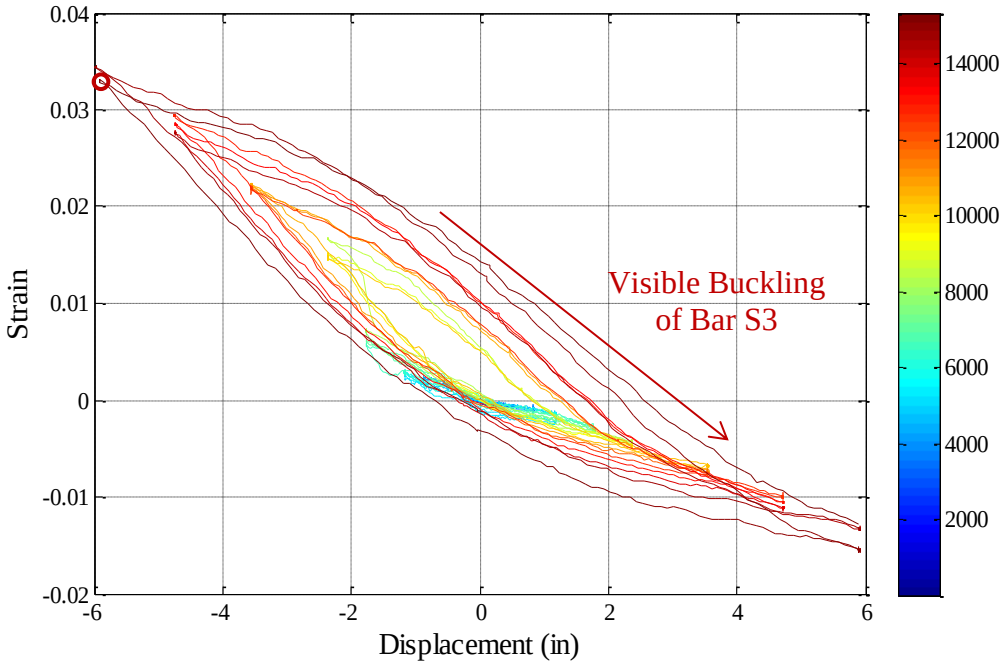

Figure 1.481 T20 – Extreme Fiber Bar S3 Strain Hysteresis (5.29" above the Footing)

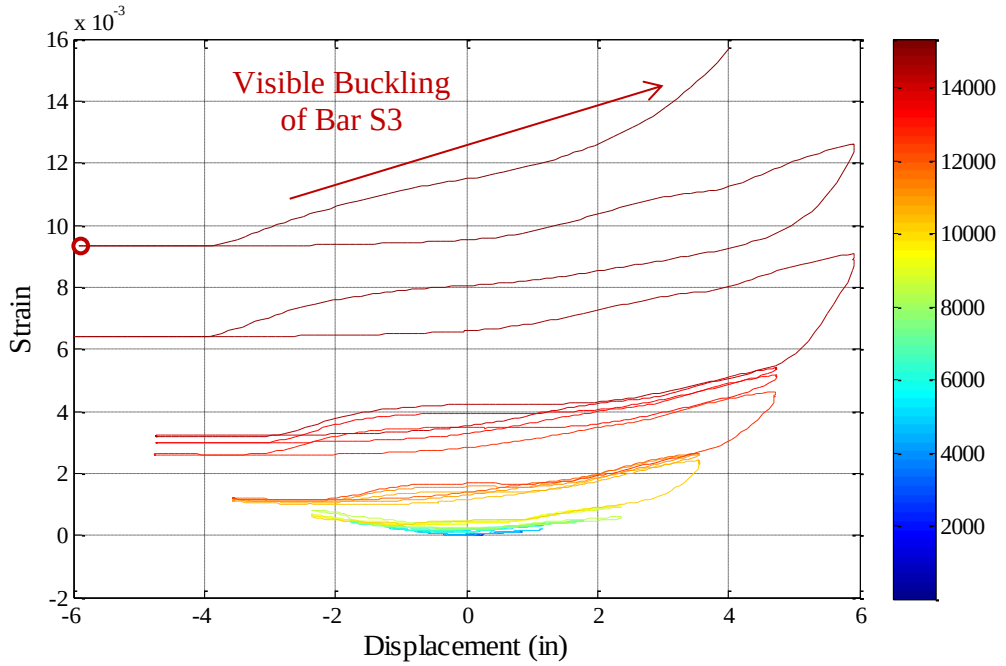

Figure 1.482 T20 – Spiral Strain Hysteresis 3.31" Above the Footing on South Side

Test 20 – Curvature and Strain Penetration Data

The cross section curvature for each horizontal section above the footing is determined by connecting the strain measurements from all eight instrumented bars with a least squared error line. The curvature is then extracted from the slope of the least squared error line, see Figure 1.483 and Figure 1.484. The cross section curvature profiles in these figures are shown for the second horizontal section above the footing-column interface. This is because the target markers in the lowest gage lengths for bars near the middle of the column were not visible to the Optotrak position monitor. For these sections, it appears that the plane sections hypothesis is appropriate. Vertical curvature profiles are plotted for push and pull cycles in Figure 1.485 and Figure 1.486 respectively. These figures show that plastic curvatures have a linear distribution at higher displacement ductility levels. The extent of plasticity is determined by the intersection of the linear plastic curvature regression and the triangular yield curvature profile, shown as a grey dashed line. The dashed lines for each curvature distribution represent a least squared error linear fit to the plastic portion of the measured curvatures. The measured spread of plasticity as a function of base section curvature ductility is shown in Figure 1.493.

The target marker on each bar placed closest the footing-column interface can be used to create slip hysteresis and horizontal slip profiles attributable to strain penetration. The slip hysteresis for extreme fiber bars N3 and S3 appear in Figure 1.487 and Figure 1.488 respectively. If the tensile and compressive slip of all of the instrumented bars is plotted along the cross section depth, the base rotation attributable to strain penetration may be calculated. The slip profiles for push and pull cycles appear in Figure 1.489 and Figure 1.490 respectively. The rotation of the base section can be extracted from the slope of the least squared error line connecting all six measured bar slips.

Combining the curvatures over the instrumented region (5ft above the footing), bar slip profiles, and an elastic curvature assumption above the instrumented region, the top column displacement can be calculated by integrating the curvature distributions and extrapolating the fixed-end rotations to the center of loading. The top column displacements calculated

from the Optotrak system are compared to displacements measured with a string potentiometer at the center of loading in Figure 1.491. The Optotrak integrated displacements match well throughout the entire range of response. A closer look at the deformation components from the Optotrak integrated displacements appear in Figure 1.492.

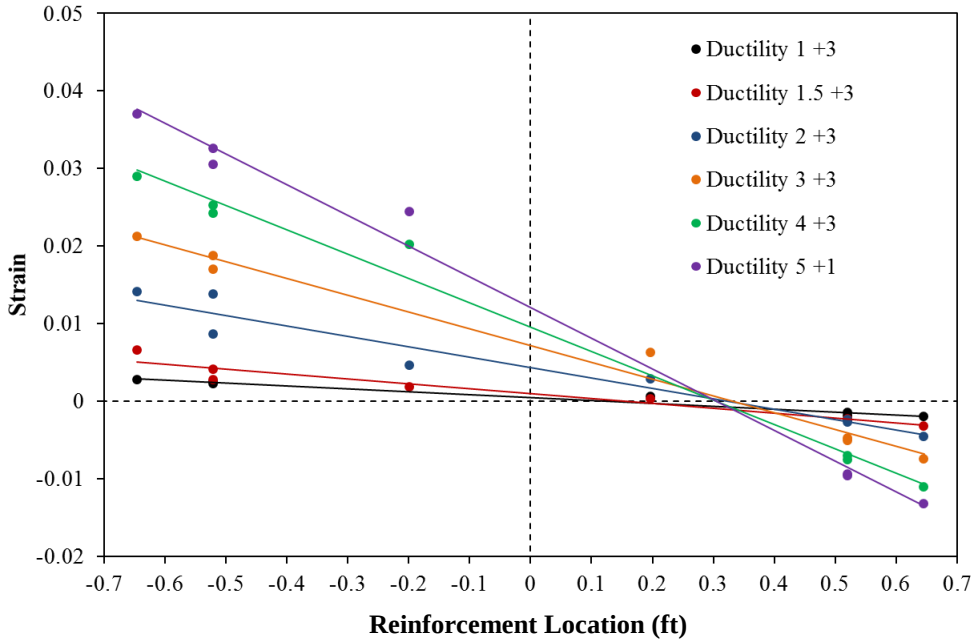

Figure 1.483 T20 – Sample Cross Section Strain Profiles during Push Cycles

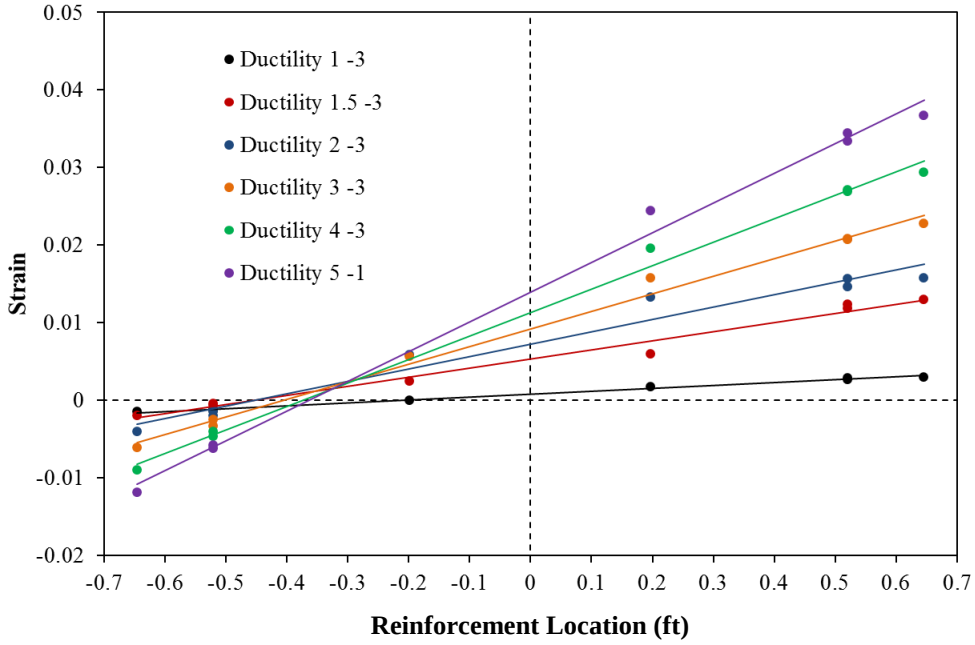

Figure 1.484 T20 – Sample Cross Section Strain Profiles during Pull Cycles

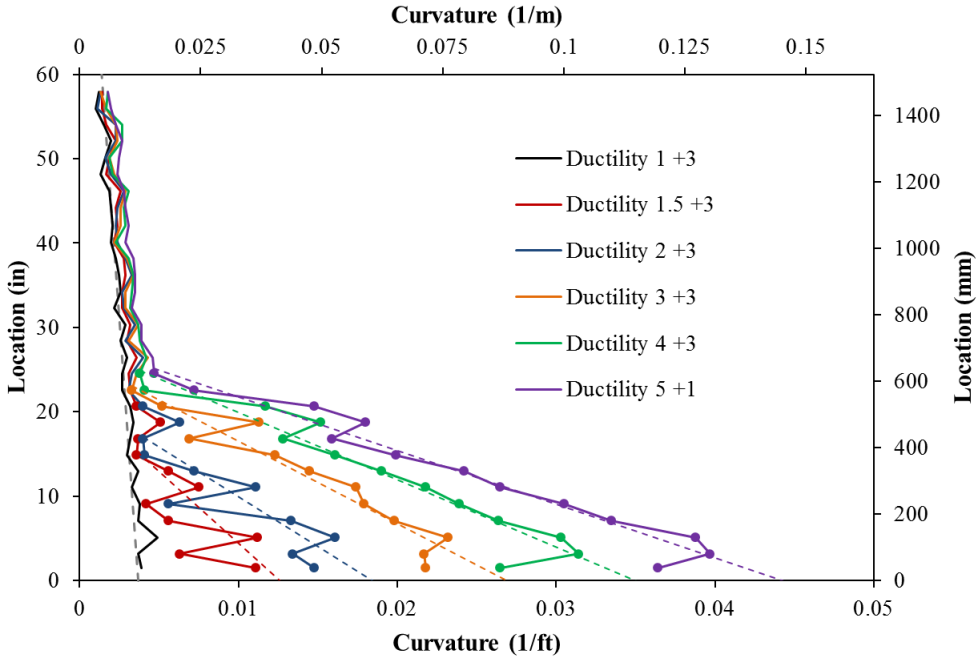

Figure 1.485 T20 – Push Cycle Curvature Profiles with Plastic Regression

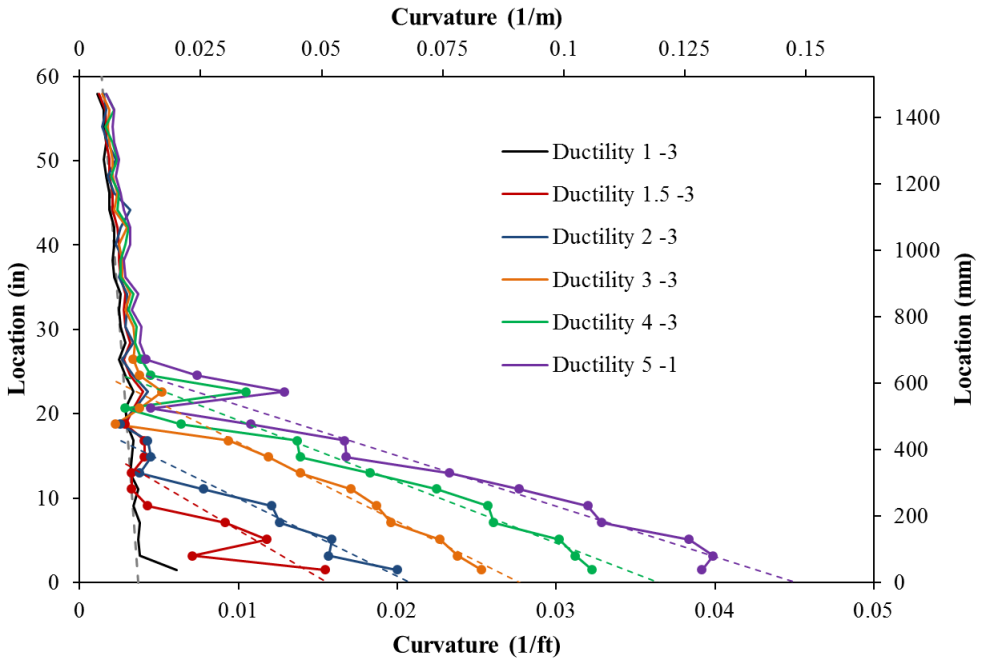

Figure 1.486 T20 – Pull Cycle Curvature Profiles with Plastic Regression

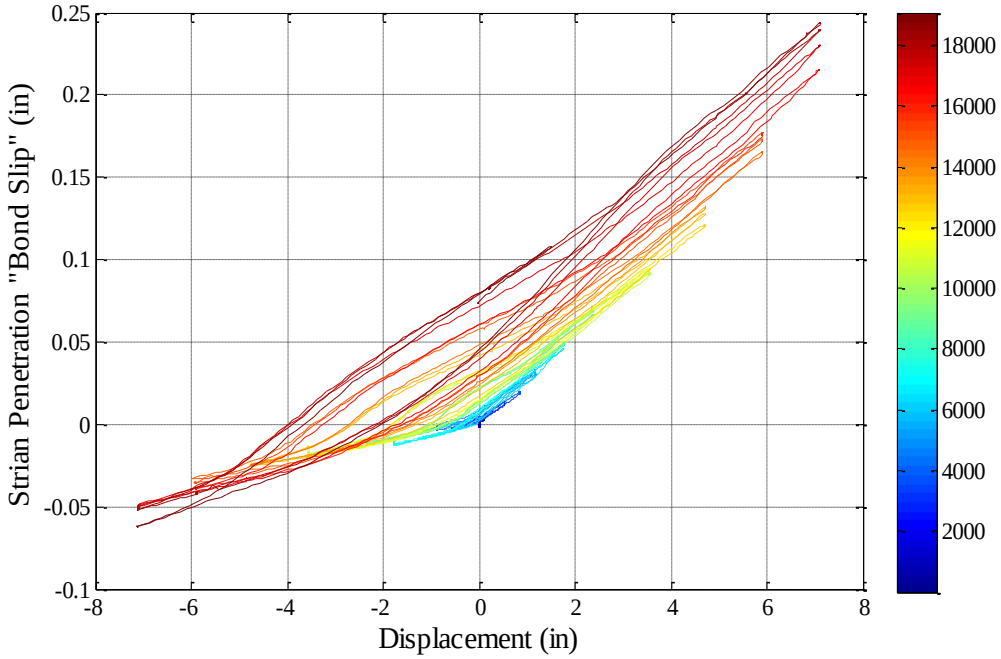

Figure 1.487 T20 – Strain Penetration Bond Slip Hysteresis for Bar N3

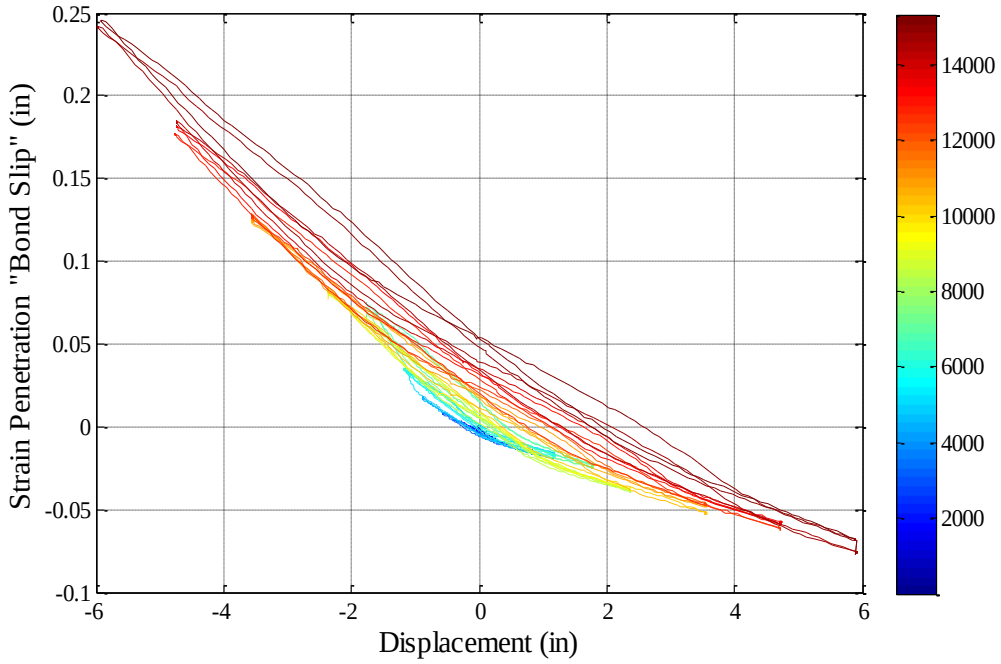

Figure 1.488 T20 – Strain Penetration Bond Slip Hysteresis for Bar S3

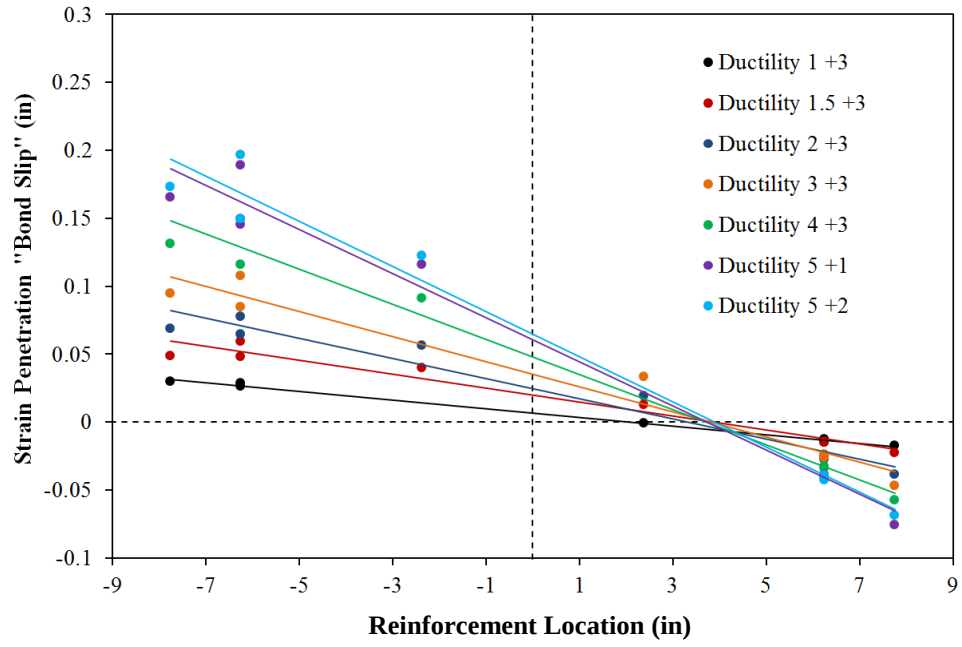

Figure 1.489 T20 – Base Rotation due to Strain Penetration during Push Cycles

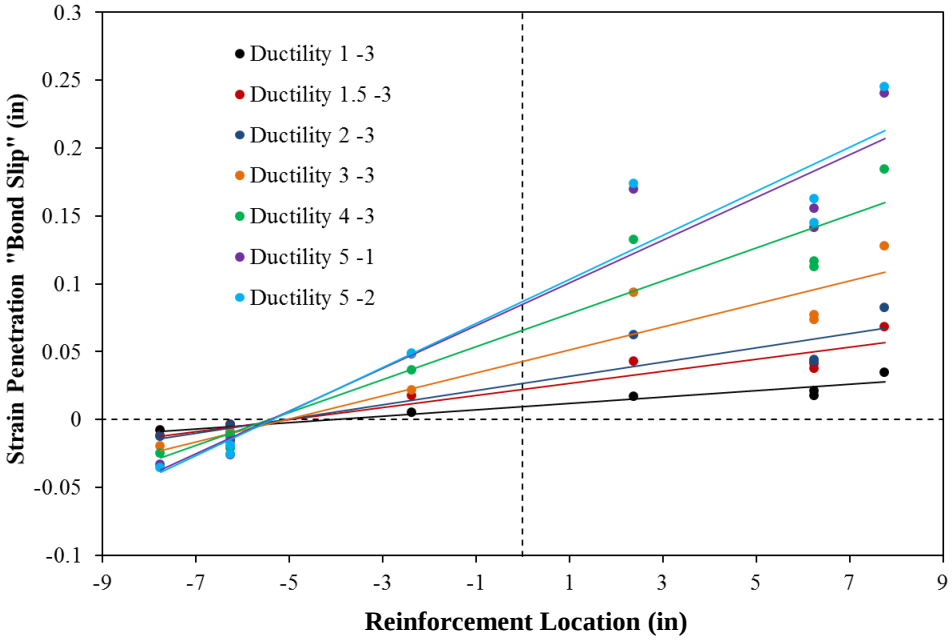

Figure 1.490 T20 – Base Rotation due to Strain Penetration during Pull Cycles

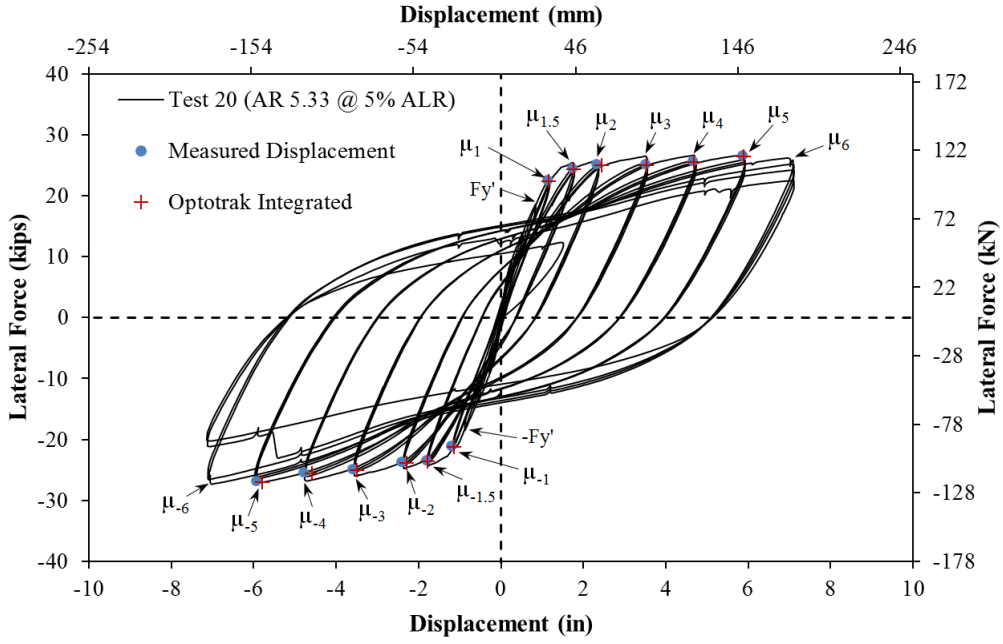

Figure 1.491 T20 – Comparison of Measured and Optotrak Integrated Displacements

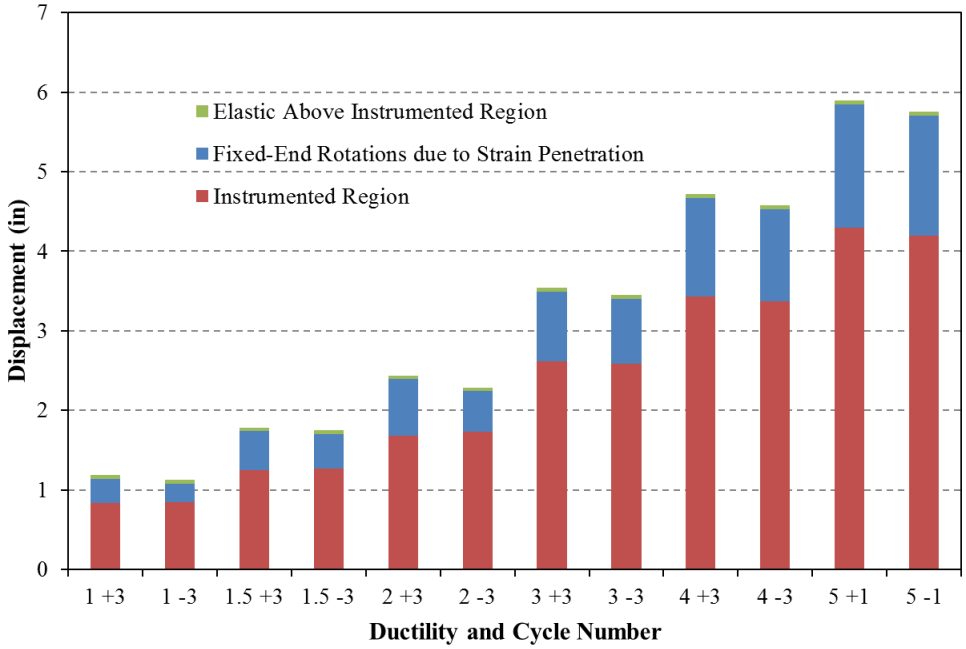

Figure 1.492 T20 – Components of the Optotrak Integrated Deformation

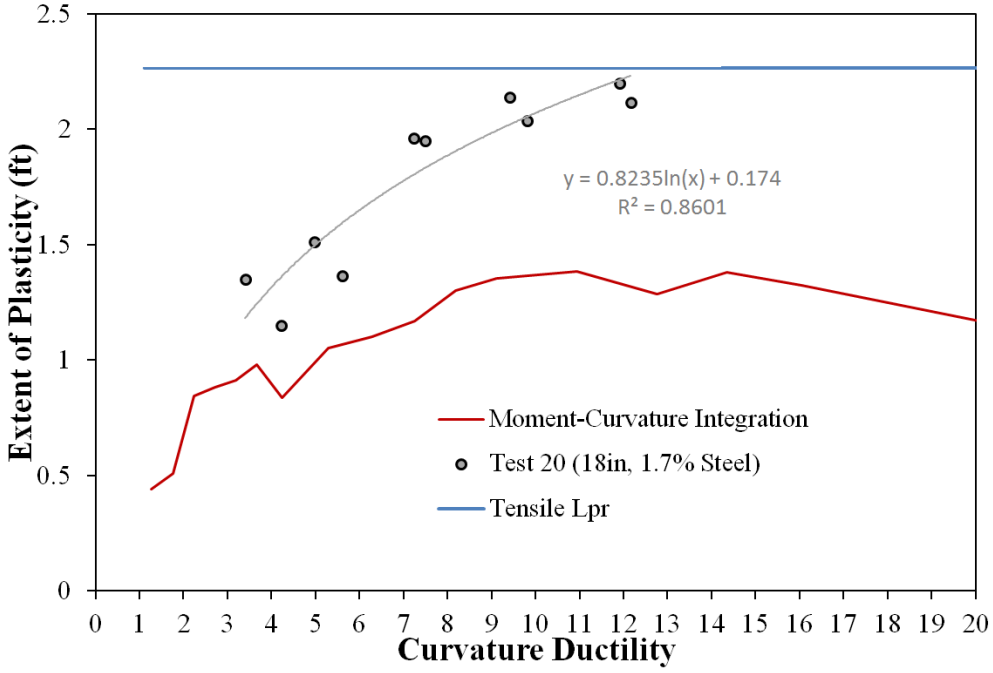

Figure 1.493 T20 – Measured Spread of Plasticity (Circular Data Points)

1.3.3 Test 21 – Aspect Ratio of 7.33 and 5% Axial Load

Table 1.37 Observations for Test 21 – Aspect Ratio of 7.33 and 5% Axial Load

VALUES OF INTEREST:	
Concrete Compressive Strength:	$f_c' = 6390\ psi$
Axial Load:	$P = 72.5\ kips\ \ (P/(f_c' A_g) = 5\%)$
Column Length and Aspect Ratio:	$11ft\ \ (L/D = 7.33)$
Analytical First Yield Force:	$F_y' = 13.50\ kips$
Experimental First Yield Displacement:	$\Delta_y' = 1.43"$
Analytical Nominal Moment Capacity:	$M_n = 205.5\ kip * ft$
Equivalent Yield Displacement:	$\Delta_y = 1.98"$
Maximum Lateral Force:	$19.34\ kips$
DAMAGE OBSERVATIONS:	
First Cracking North:	$1/2Fy' = 0.40"$
First Cracking South:	$-1/2Fy' = -0.45"$
Cover Concrete Crushing North:	$\mu_3^{-1} = -5.94"$
Cover Concrete Crushing South:	$\mu_2^{+3} = 3.97"$
Transverse Steel Yield North:	At $-6.50"$ during pull to $\mu_4^{-1} = -7.91"$
Transverse Steel Yield South:	At $5.67"$ during push to $\mu_3^{+1} = 5.94"$
Longitudinal Bar Buckling North:	Reversal from $\mu_6^{+1} = 11.86"$
Longitudinal Bar Buckling South:	Reversal from $\mu_5^{-2} = -9.88"$
Longitudinal Bar Fracture North:	At $7.59"$ during push to $\mu_6^{+4} = 11.88"$
Longitudinal Bar Fracture South:	At $-2.81"$ during pull to $\mu_6^{-4} = -11.86"$

*$\mu_5^{-2} = -9.88"$represents the second pull cycle of displacement ductility five

Table 1.38 Strain Data Summary for Test 21 – Aspect Ratio of 7.33 and 5% Axial Load

MATERIAL STRAINS:	
Cover Concrete Crushing North:	$\varepsilon_s = 0.0046\ (compression)\ \ ^*\mu_{\Delta 2} = -3.95"$
Cover Concrete Crushing South:	$\varepsilon_s = 0.0048\ (compression)$
Transverse Steel Yield North:	$\varepsilon_s = 0.0146\ (compression)$
Transverse Steel Yield South:	$\varepsilon_s = 0.0102\ (compression)$
Longitudinal Bar Buckling North:	$\varepsilon_s = 0.051\ (peak\ tension\ prior\ to\ bb)$
	$\varepsilon_s = 0.024\ (peak\ comp.\ prior\ to\ bb)$
Longitudinal Bar Buckling South:	$\varepsilon_s = 0.036\ (peak\ tension\ prior\ to\ bb)$
	$\varepsilon_s = 0.034\ (peak\ comp.\ prior\ to\ bb)$
Mander (1988) Ultimate Concrete Compression Strain, $\varepsilon_{cu} = 0.0203$	

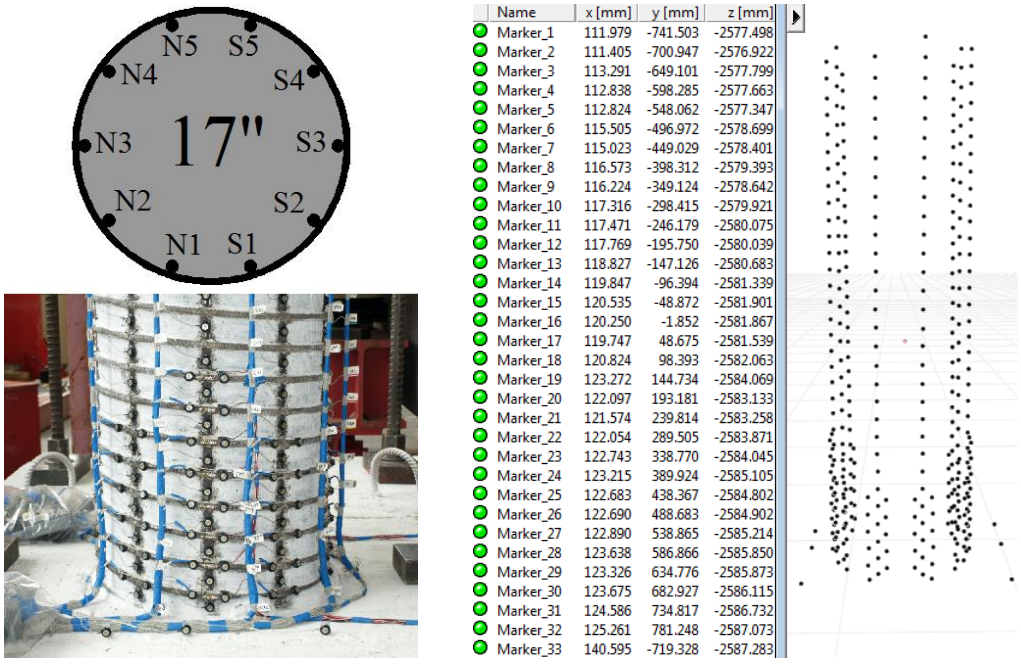

Name	x [mm]	y [mm]	z [mm]
Marker_1	111.979	-741.503	-2577.498
Marker_2	111.405	-700.947	-2576.922
Marker_3	113.291	-649.101	-2577.799
Marker_4	112.838	-598.285	-2577.663
Marker_5	112.824	-548.062	-2577.347
Marker_6	115.505	-496.972	-2578.699
Marker_7	115.023	-449.029	-2578.401
Marker_8	116.573	-398.312	-2579.393
Marker_9	116.224	-349.124	-2578.642
Marker_10	117.316	-298.415	-2579.921
Marker_11	117.471	-246.179	-2580.075
Marker_12	117.769	-195.750	-2580.039
Marker_13	118.827	-147.126	-2580.683
Marker_14	119.847	-96.394	-2581.339
Marker_15	120.535	-48.872	-2581.901
Marker_16	120.250	-1.852	-2581.867
Marker_17	119.747	48.675	-2581.539
Marker_18	120.824	98.393	-2582.063
Marker_19	123.272	144.734	-2584.069
Marker_20	122.097	193.181	-2583.133
Marker_21	121.574	239.814	-2583.258
Marker_22	122.054	289.505	-2583.871
Marker_23	122.743	338.770	-2584.045
Marker_24	123.215	389.924	-2585.105
Marker_25	122.683	438.367	-2584.802
Marker_26	122.690	488.683	-2584.902
Marker_27	122.890	538.865	-2585.214
Marker_28	123.638	586.866	-2585.850
Marker_29	123.326	634.776	-2585.873
Marker_30	123.675	682.927	-2586.115
Marker_31	124.586	734.817	-2586.732
Marker_32	125.261	781.248	-2587.073
Marker_33	140.595	-719.328	-2587.283

Figure 1.494 T21 – Cross Section Bar Designation and Target Marker Application

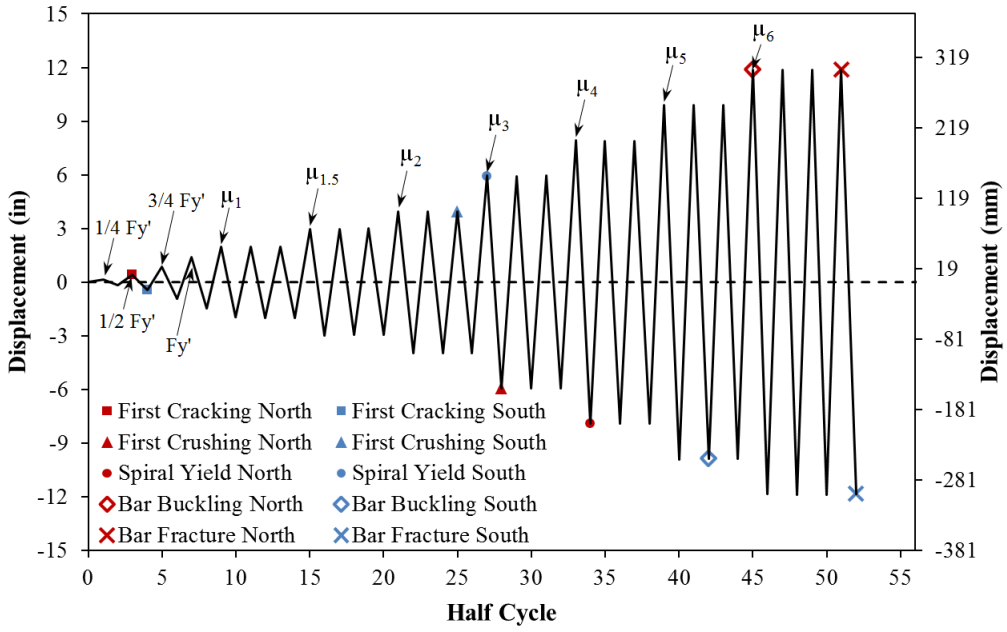

Figure 1.495 T21 – Symmetric Three Cycle Set Load History

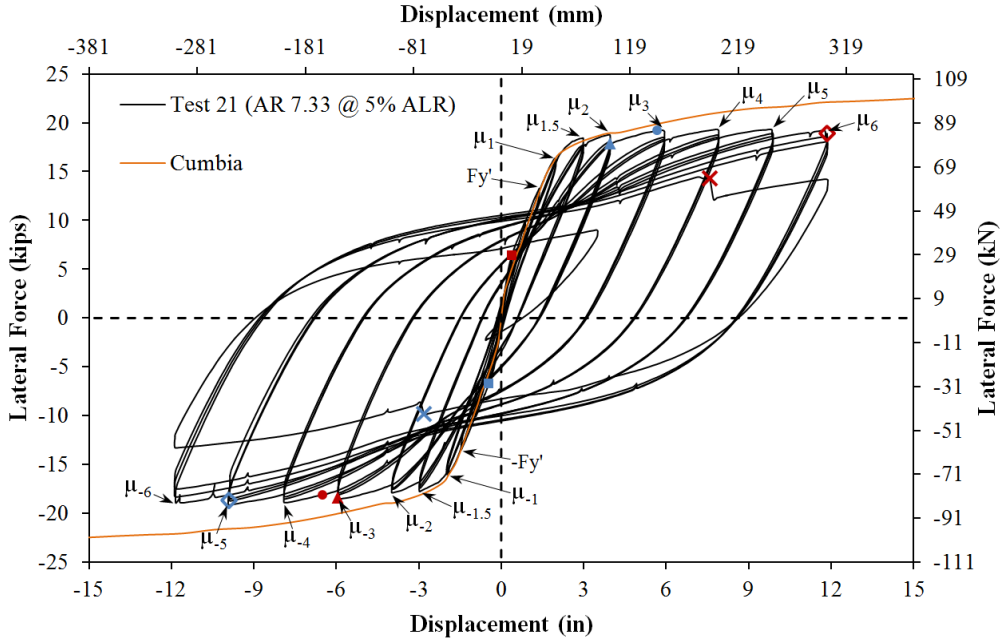

Figure 1.496 T21 – Lateral Force vs. Top Column Displacement Response

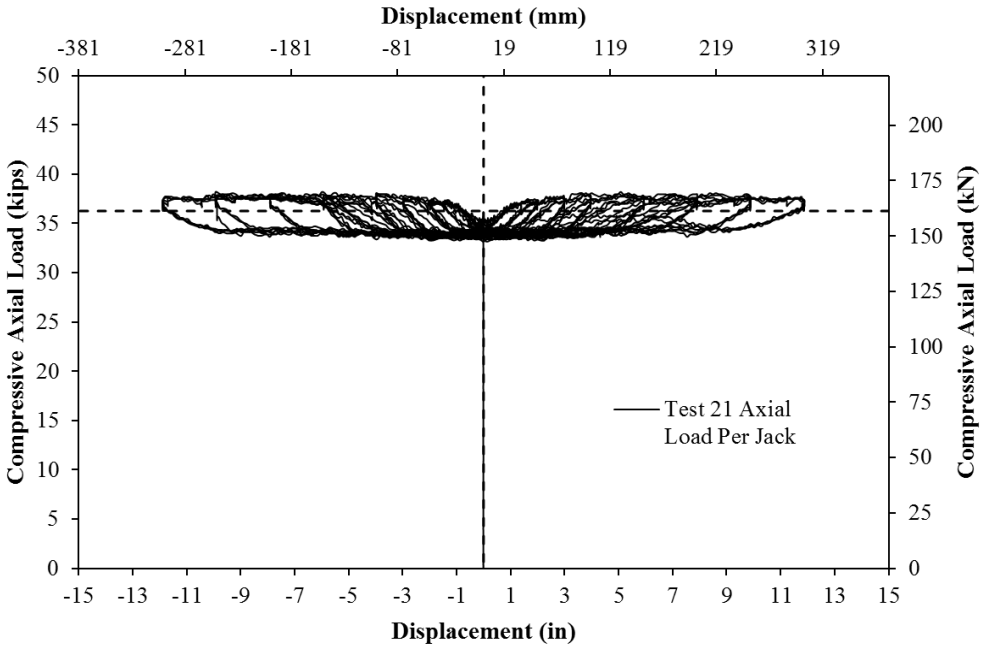

Figure 1.497 T21 – Compressive Axial Load from One Jack (Total = 2*Value)

Test 21 Aspect Ratio of 7.33 and 5% Axial Load – Experimental Observations

Specimens 19-24 focus on the effects of axial load and aspect ratio on column behavior. The 18" diameter columns contain 10 #6 (A706) bars for longitudinal reinforcement ($A_{st}/A_g = 1.7\%$) and a #3 A706 spiral at 2" on center ($4A_{sp}/(D's) = 1.3\%$). The specific specimen chosen for Test 21 has an 11ft cantilever length ($L/D = 7.33$), and was subjected to ($P/(f_c'A_g) = 5\%$) axial load. The symmetric three-cycle-set laboratory load history is used to evaluate the seismic performance of structural components. The load history begins with elastic cycles to the following increments of the analytically predicted first yield force: ¼ Fy', ½ Fy', ¾ Fy', and Fy'. The first yield force for the tested material and geometric properties was determined using moment curvature analysis (Test 21: Cumbia Fy' = 13.50 kips with f'c = 6390 psi). The first yield displacement was obtained as an average for the experimental first yield push and pull cycles ($\Delta_y' = 1.43"$). Vertical strain profiles for both

push and pull cycles up to the first yield force appear in Figure 1.498 with a dashed line representing the yield strain of the longitudinal reinforcement. The equivalent yield displacement, used to determine the displacement ductility levels ($\mu_{\Delta 1} = 1 * \Delta_y$), is then calculated as $\Delta_y = \Delta'_y(M_n/M'_y) = 1.98$" for Test 21. The symmetric three-cycle-set load history resumes with three balanced cycles at each of the following ductility levels: 1, 1.5, 2, 3, 4, 5, 6, 7, 8, etc. The full symmetric three-cycle-set load history appears in Figure 1.495 and the resulting lateral force vs. top column displacement hysteresis is shown in Figure 1.496. The monotonic moment curvature prediction does not include P-Δ effects.

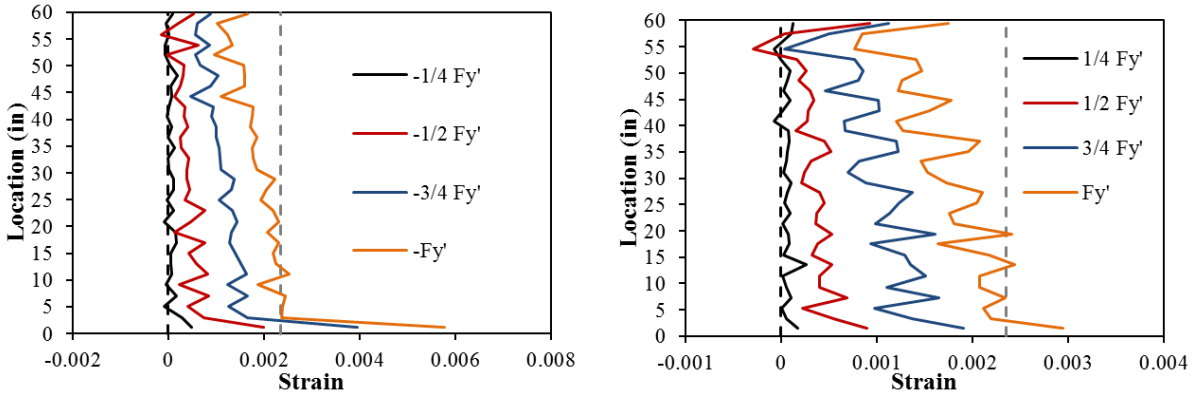

Figure 1.498 T21 – Strain Profiles before Yield (Left) Bar N3 and (Right) Bar S3

The test began with cycles in ¼ Fy' (first yield force) increments in each direction of loading until the first yield force was reached. The first cracks on the North and South sides of the specimen were observed during $(1/2Fy' = 6.42\,kips)$ and $(-1/2Fy' = -6.75\,kips)$ respectively. The first crack occurred at the footing column interface. Crack widths measured on the outside surface of the concrete core have little meaning when describing a serviceability limit state which applies to columns with cover concrete. Cracking in the column occurred during $(3/4Fy' = 9.95\,kips)$ and $(-3/4Fy' = -10.10\,kips)$. The crack distribution on all sides of the specimen at first yield, $(Fy' = 13.28\,kips)$ and $(-Fy' = -13.50\,kips)$, appears in Figure 1.499.

Similarly, the crack progression at displacement ductility 1, 1.5, and 2 appear in Figure 1.500, Figure 1.501, and Figure 1.502 respectively. During these cycles the cracks became more numerous and increased in inclination on the shear faces of the specimen. A small amount of core concrete crushed on the South side of the specimen during ($\mu_2^{+3} = 3.97"$), as shown in the left photo of Figure 1.503. A similar observation was made, see the right photo of Figure 1.503, on the North side of the specimen during ($\mu_3^{-1} = -5.94"$). The crushing on each side of the specimen during ductility three was not severe, and it appeared that only a thin layer of concrete flaked off between spiral layers. Photos of the crack distributions during displacement ductility three and four appear in Figure 1.504 and Figure 1.505 respectively.

The South extreme fiber bar S3 visibly buckled after reversal from ($\mu_5^{-2} = -9.88"$), as shown in Figure 1.506. Photos of the crack distribution during displacement ductility five appear in Figure 1.507. The North extreme fiber bar N3 visibly buckled after reversal from ($\mu_6^{+1} = 11.86"$), as shown in the right photo of Figure 1.508. Additional deformation in the previously buckled bar S3 appears in the left photo of Figure 1.508 and Figure 1.509. An additional North reinforcing bar buckled after reversal from ($\mu_6^{+3} = 11.87"$), as shown in Figure 1.509. The previously buckled North extreme fiber bar N3 ruptured during ($\mu_6^{+4} = 11.88"$), see Figure 1.510. Similarly, previously buckled bar S3 ruptured during ($\mu_6^{-4} = -11.86"$). A photo of the south ruptured bar and lateral displacement at ($\mu_6^{-4} = -11.86"$) appears in Figure 1.510 and Figure 1.511.

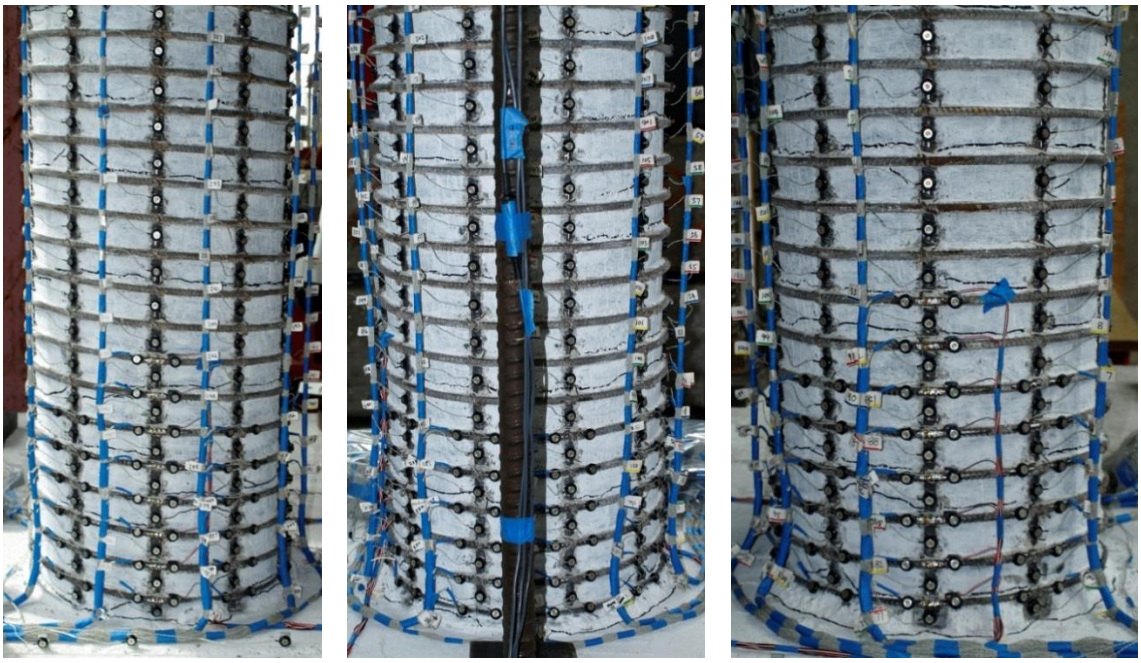

Figure 1.499 T21 – (Left) North at Fy', (Mid) Front at -Fy', and (Right) South at -Fy'

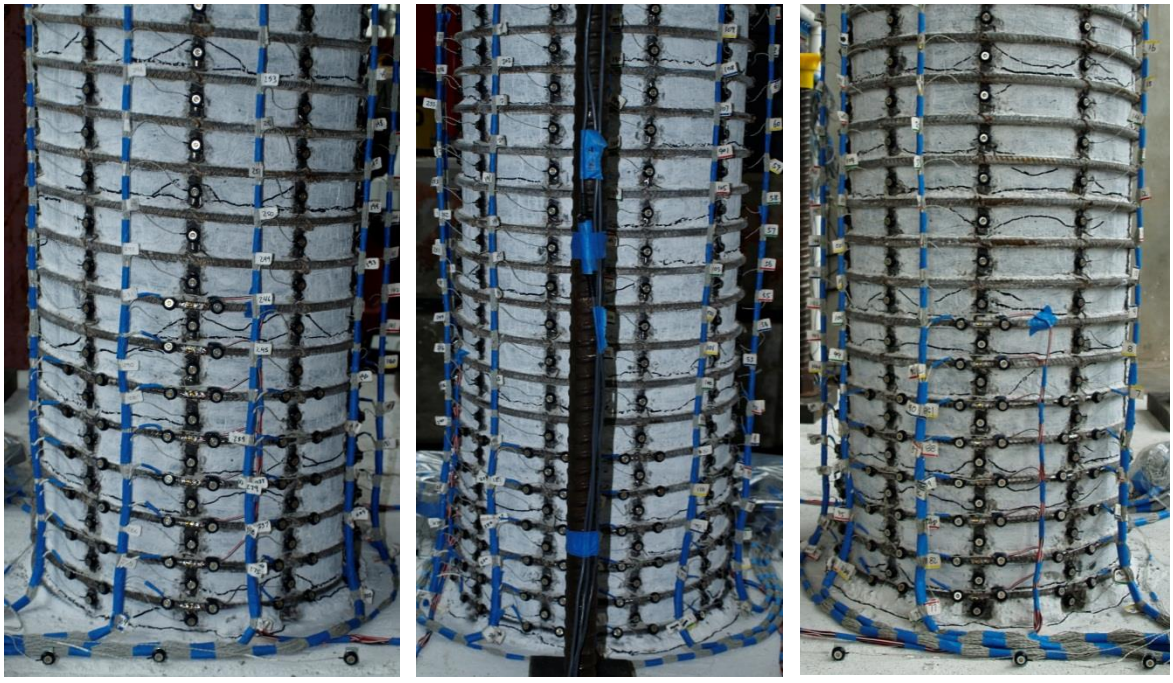

Figure 1.500 T21 – (Left) North at μ_1^{+3}, (Mid) Front at μ_1^{-3}, and (Right) South at μ_1^{-3}

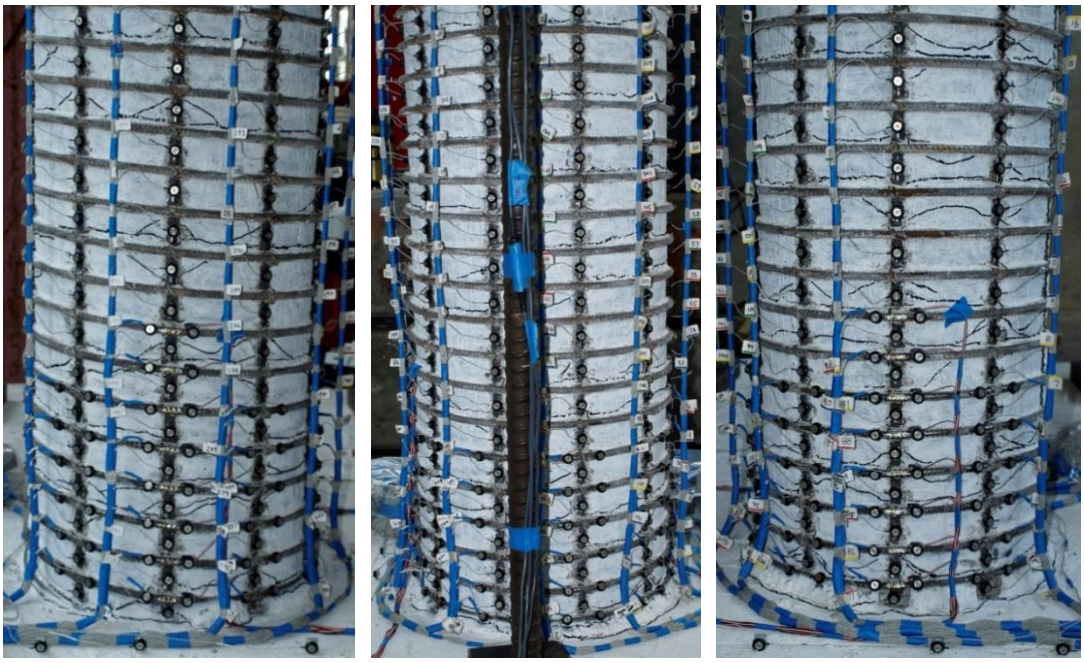

Figure 1.501 T21 – (Left) North at $\mu_{1.5}^{+3}$, (Mid) Front at $\mu_{1.5}^{-3}$, and (Right) South at $\mu_{1.5}^{-3}$

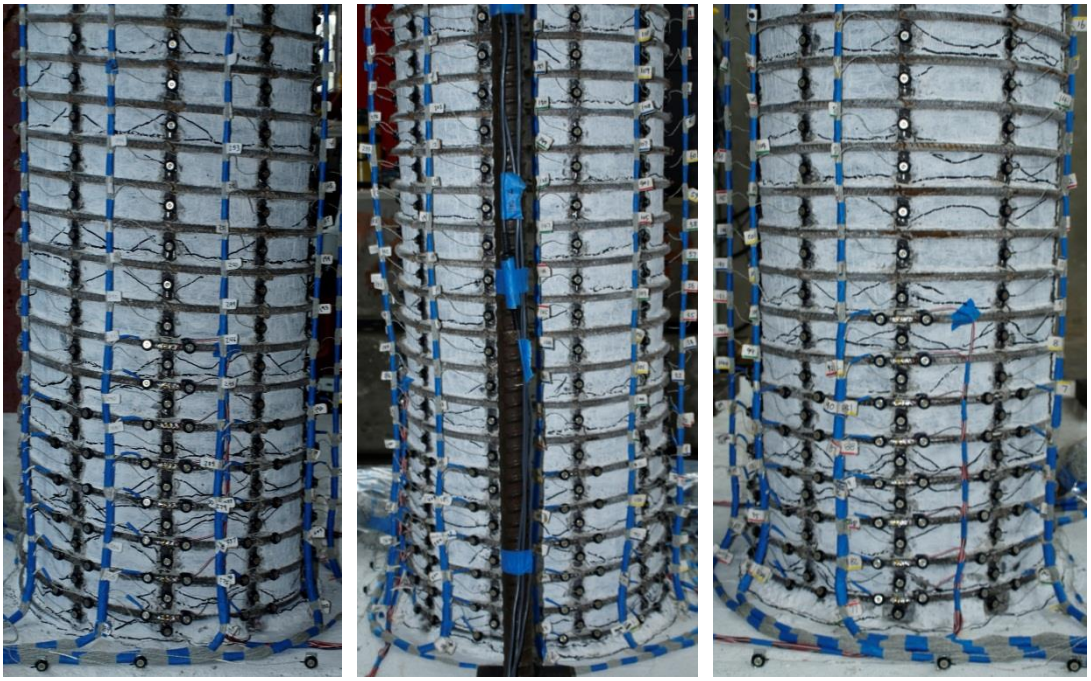

Figure 1.502 T21 – (Left) North at μ_{2}^{+3}, (Mid) Front at μ_{2}^{-3}, and (Right) South at μ_{2}^{-3}

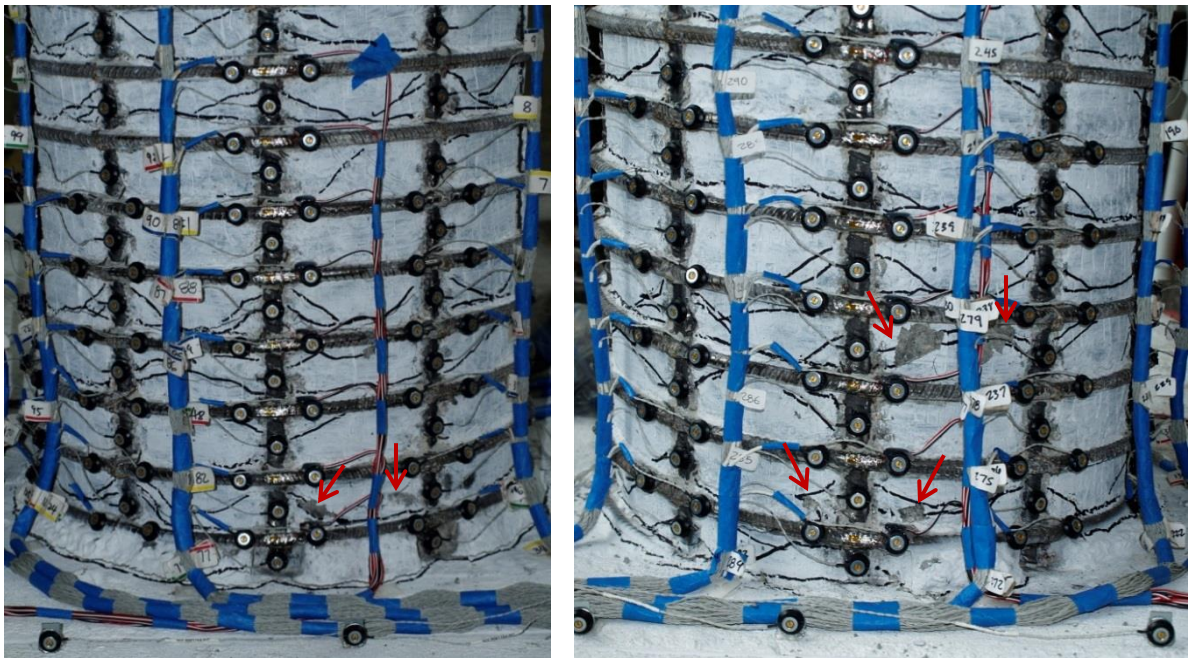

Figure 1.503 T21 – (Left) South Crushing at μ_2^{+3} and (Right) North Crushing at μ_3^{-1}

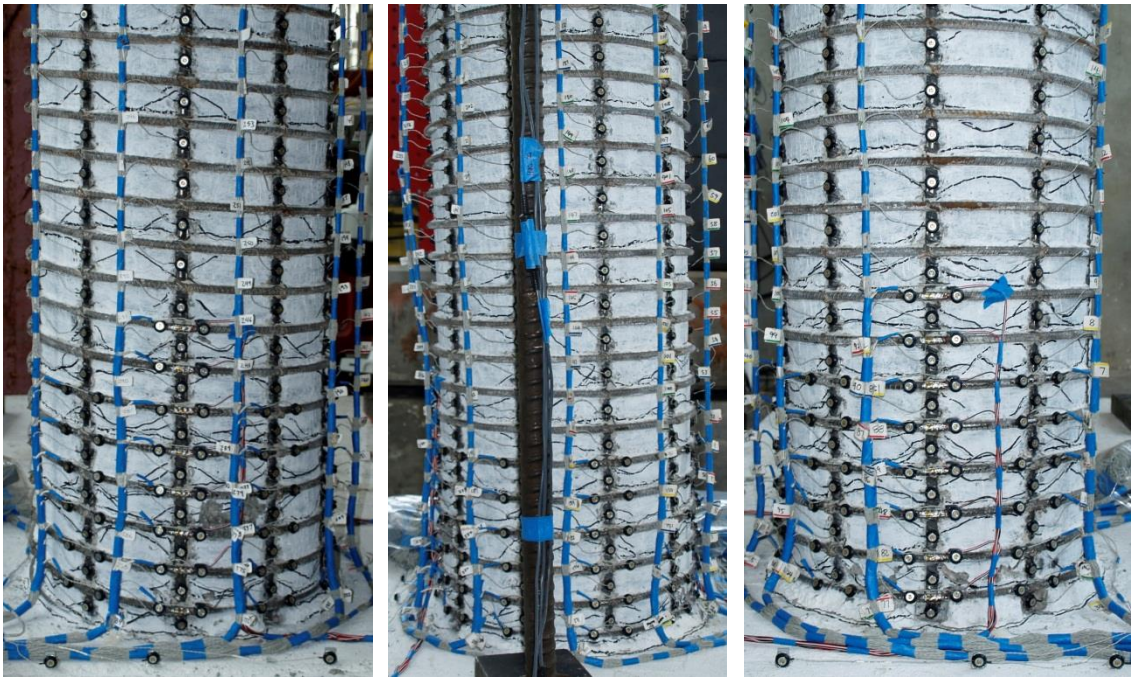

Figure 1.504 T21 – (Left) North at μ_3^{+3}, (Mid) Front at μ_3^{-3}, and (Right) South at μ_3^{-3}

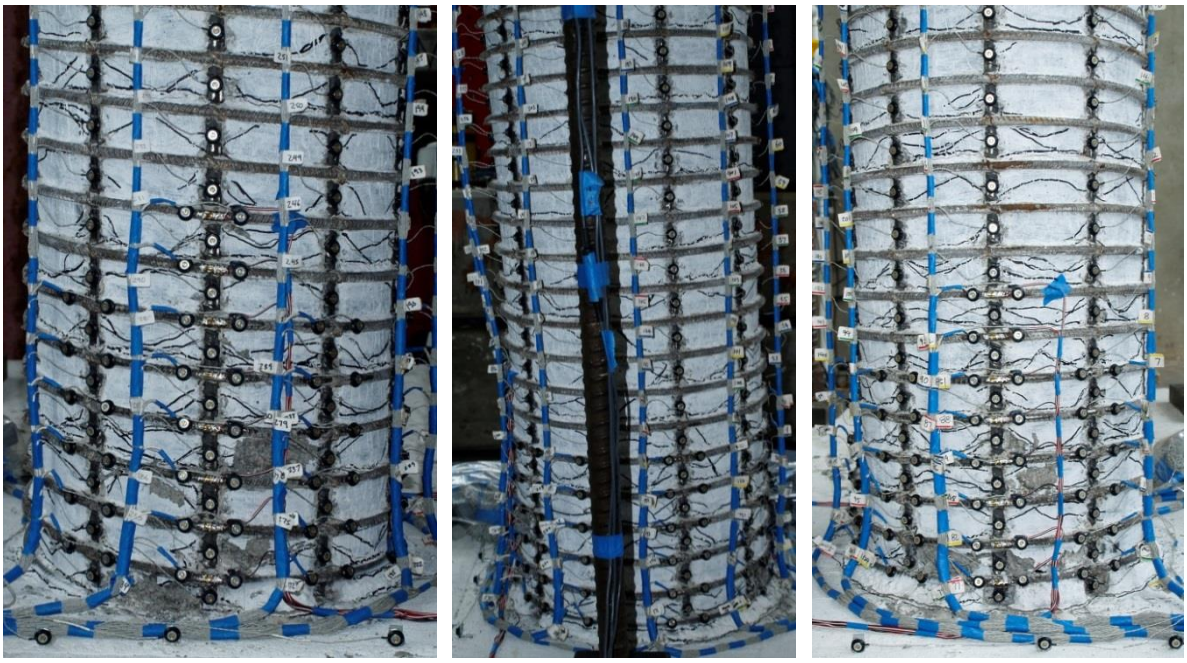

Figure 1.505 T21 – (Left) North at μ_4^{+3}, (Mid) Front at μ_4^{-3}, and (Right) South at μ_4^{-3}

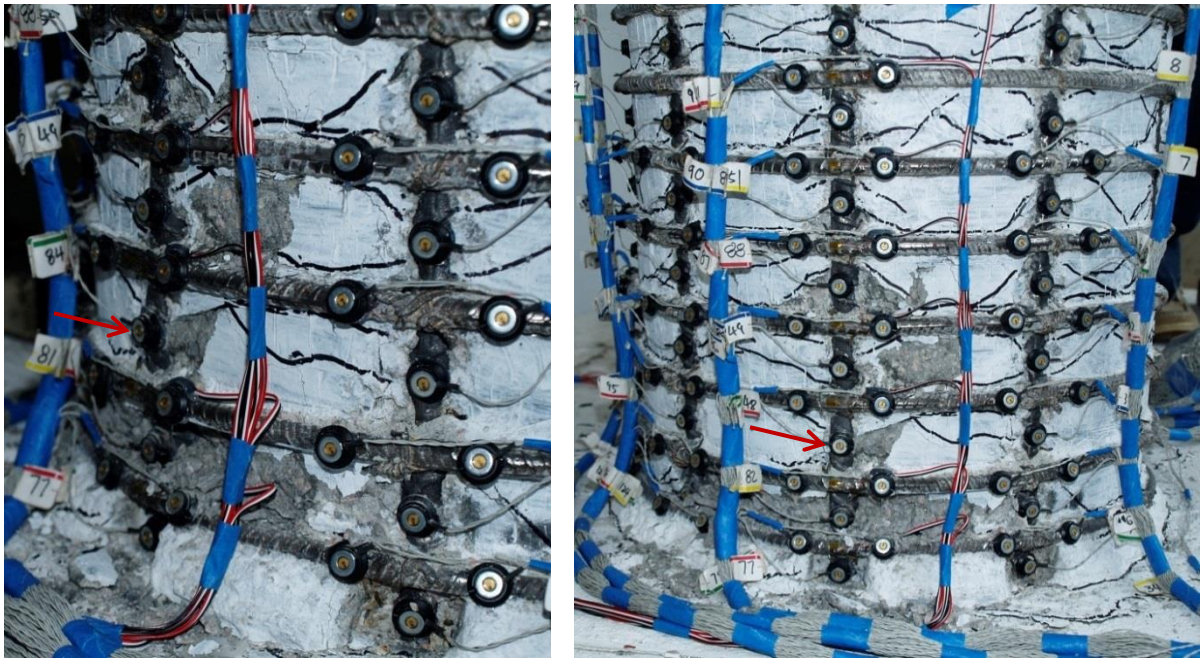

Figure 1.506 T21 – Buckling of South Bar S3 after Reversal from ($\mu_5^{-2} = -9.88$")

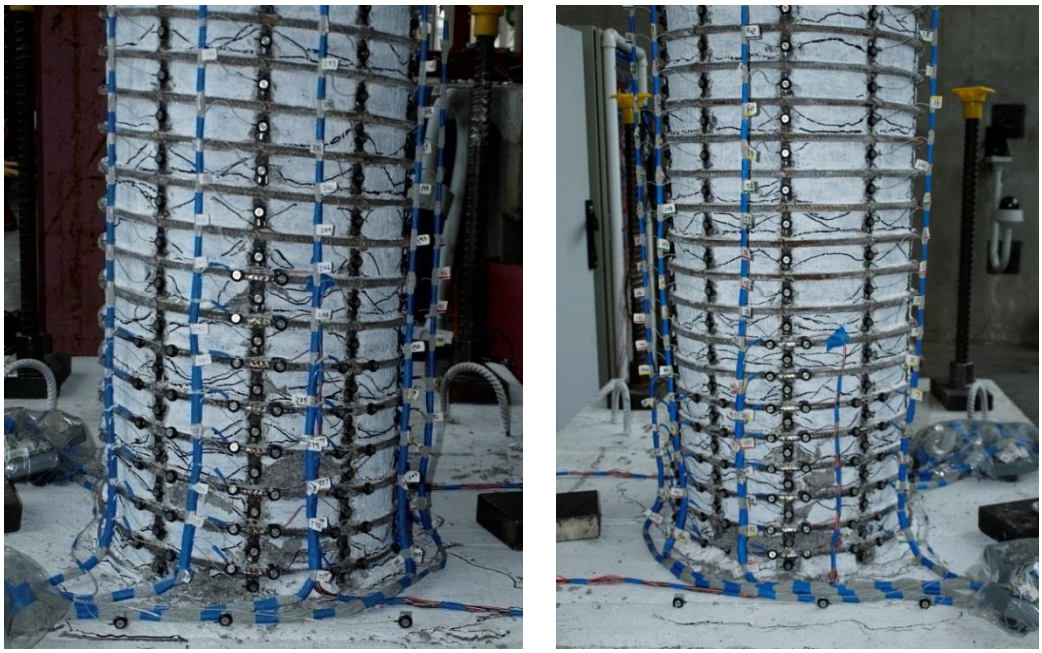

Figure 1.507 T21 – (Left) North Side at μ_5^{+3} and (Right) South Side at μ_5^{-3}

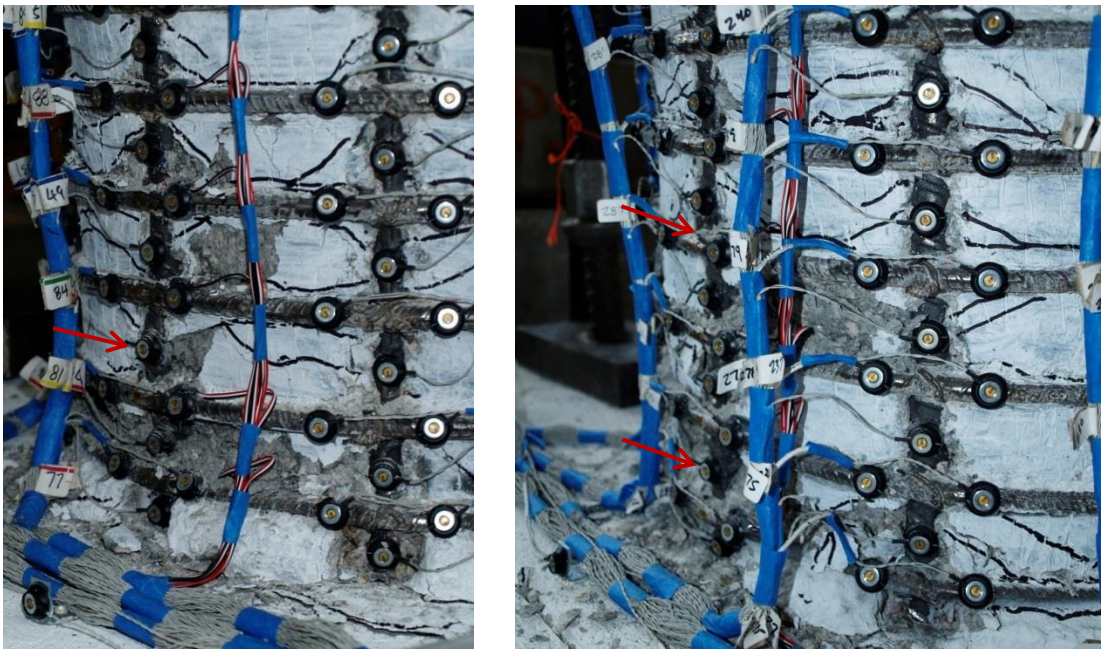

Figure 1.508 T21 – (Left) Deformation in Bar S3 at μ_6^{+1} and (Right) Buckling of Bar N3 after reversal from μ_6^{+1}, Note the Two Outward Deformed Regions

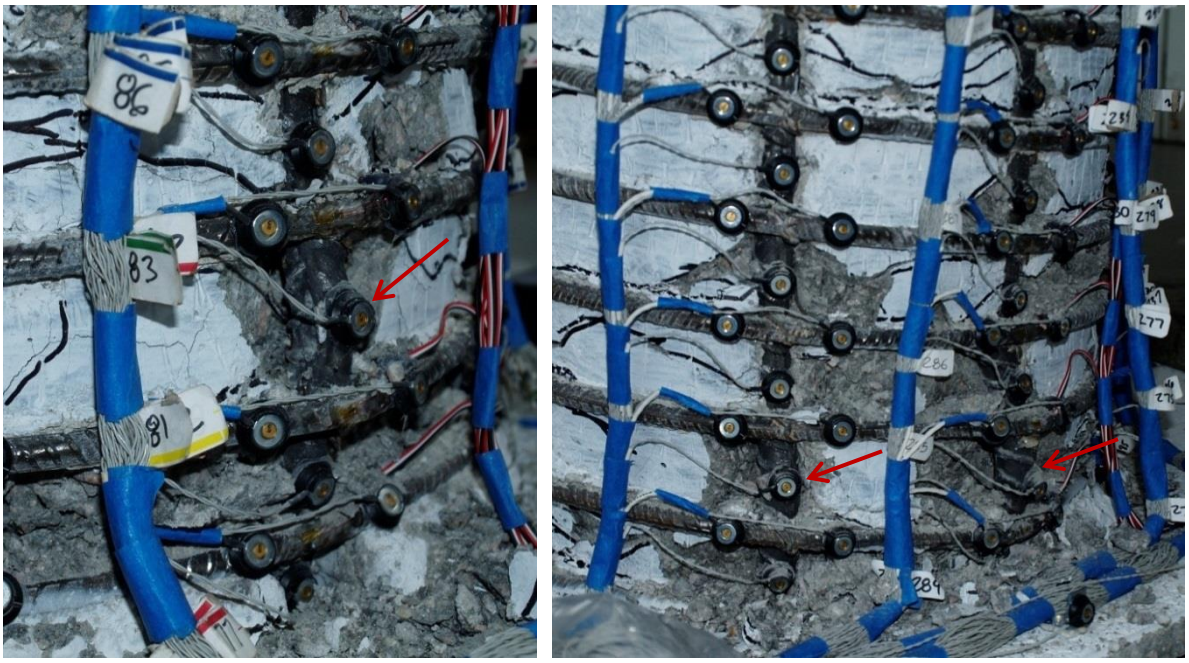

Figure 1.509 T21 – (Left) Deformation in Bar S3 at μ_6^{+3} and (Right) Buckling of Bar N4 during μ_6^{-3} and Additional Deformation in Bar N3

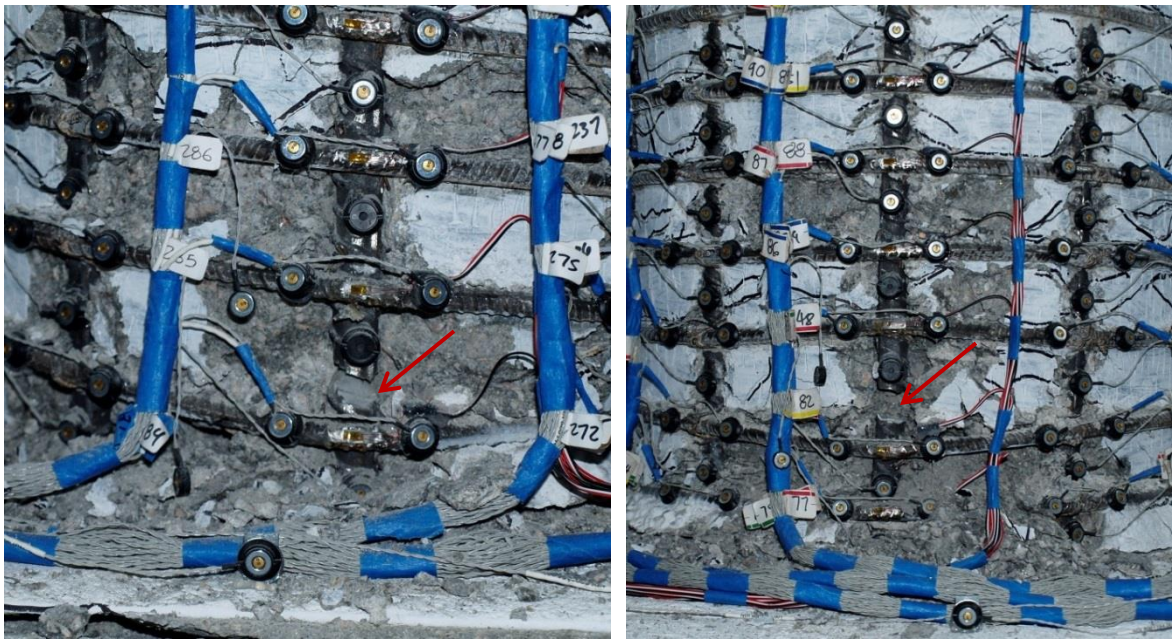

Figure 1.510 T21 – Fracture of (Left) Bar N3 at μ_6^{+4} and (Right) Bar S3 during at μ_6^{-4}

Figure 1.511 T21 – Lateral Displacement at ($\mu_6^{-4} = -11.86$")

Test 21 Aspect Ratio of 7.33 and 5% Axial Load – Strain Data Analysis

North Reinforcement

Vertical strain profiles for north extreme fiber bar N3 placed into tension during push cycles appear in the right half of Figure 1.512. This figure shows both extreme fiber bars on the same graph to illustrate the effects of tension shift on strain profiles. Each reinforcing bar contains thirty separate ≈2" gage lengths which appear as a single data point at its center linked to adjacent gage lengths with straight lines. Compressive vertical strain profiles for North extreme fiber bar N3 during pull cycles appear in the left half of Figure 1.513. As the hinge rotates about inclined flexural shear cracks, compressive strains are concentrated at the base and tensile strains are fanned out to a greater height following the crack distribution. Near the footing cracks remain effectively horizontal, but above this base section the flexural shear cracks are inclined on the shear faces of the column.

A peak tensile strain of 0.051, located 1.49" above the footing, was measured for North extreme fiber bar N3 during ($\mu_6^{+1} = 11.86"$). The largest tensile strain in bar N3 measured during cycles at displacement ductility five was 0.0437 for the gage length 1.49" above the footing. The relationship between tensile strain and displacement for this gage length appears in Figure 1.516. Each line represents a single push cycle which began with the column at zero displacement and ended at the peak during a continuous push cycle. The solid line contains data during the push cycle loading up to the peak displacement, and the dashed line represents the subsequent reversal of load. This gage length matches the moment curvature prediction well when the PCK (2007) Lp Hinge Method is used.

The largest compressive strain of -0.0237, located 3.37" above the footing, was measured during ($\mu_5^{-3} = -9.89"$). This value exceeds the Mander ultimate concrete compressive strain of -0.0203. The relationship between compressive strain and displacement for bar N3 appears in Figure 1.517, for the gage length centered 3.37" above the footing. The measured compressive strains are significantly larger than the moment curvature prediction with the PCK (2007) Lp Hinge Method.

The strains in the lowest six transverse steel layers restraining North extreme fiber bar N3 are plotted in Figure 1.515. The individual data points are from strain gages attached to each spiral layer. The data points are connected with lines only to show trends for the particular displacement level. The vertical grey dashed line represents a spiral yield strain of fy/Es, see Figure 1.409, which approximates the point at which permanent deformation in the spiral layer begins. The spiral layer located 7.22" above the footing went into the inelastic range during at -6.49" during the pull cycle to ($\mu_4^{-1} = -7.91"$). The lowest two spiral layers, 1.22" and 3.28" above the footing, went inelastic during ($\mu_5^{-1} = -9.93"$). Cycle to cycle increases in the spiral strains were observed over these gage lengths during displacement ductility five.

The strain hysteresis for bar N3, gage length located 7.27" above the footing, appears in Figure 1.521. This gage length coincides with the upper buckled region of bar N3 shown in

Figure 1.508. During later cycles of the load history the buckled deformation increased significantly over the lower buckled region. The transverse steel strain hysteresis for the spiral layer overlaying the upper buckled region appears in Figure 1.522. The strain hysteresis for the lower buckled region of bar N3 appears in Figure 1.523 for the gage length located 3.37" above the footing. The corresponding spiral strain hysteresis for the lowest spiral layer is shown in Figure 1.524. Over both buckled regions, the spiral strains spiked after reversal from ($\mu_6^{+1} = 11.86$") when visible bar buckling was observed.

South Reinforcement

Vertical strain profiles for south extreme fiber bar S3 placed into tension during pull cycles appear in the right half of Figure 1.513. A peak tensile strain of 0.0360 was measured 7.05" above the footing during ($\mu_5^{-2} = -9.88$"). The relationship between tensile strain and displacement for this gage length is shown in Figure 1.518. The moment curvature analysis with the PCK (2007) Lp Hinge Method over predicts the measured tensile strains at an increasing rate at higher ductility levels. Vertical strain profiles for bar S3 in compression during push cycles appear in the left half of Figure 1.512. A peak compression strain of -0.0335 was measured 1.23" above the footing during ($\mu_5^{+1} = 9.88$"). This gage length was obstructed by debris during ($\mu_5^{+2} = 9.89$"). A strain of -0.0235 was measured over the second largest compressive gage length, located 5.02" above the footing, during ($\mu_5^{+2} = 9.89$"). The relationships between compressive strain and displacement for these gage lengths appear in Figure 1.519 and Figure 1.520. Again, the measured compressive strains are significantly larger than the moment curvature prediction with the PCK (2007) Lp Hinge Method. The peak compressive strains for these two gage lengths are also larger than the Mander ultimate concrete compressive strain value of -0.0203.

The strains in the lowest six transverse steel layers restraining south extreme fiber bar S3 are plotted in Figure 1.514. A single spiral layer located 5.16" above the footing entered the inelastic range at 5.67" during the push cycle to ($\mu_3^{+1} = 5.94$"). The measured spiral strains in the layers located 3.09" and 5.16" above the footing increased significantly during

($\mu_5^{+2} = 9.89$") compared to the valued measured at ($\mu_5^{+1} = 9.88$"). The South extreme fiber bar S3 visibly buckled after reversal from ($\mu_5^{-2} = -9.88$"), as shown in Figure 1.506. The strain hysteresis for the outward buckled region of bar S3, gage length located 3.02" above the footing, appears in Figure 1.525. A transverse steel strain hysteresis for the spiral layer overlaying the outward buckled region is shown in Figure 1.526. The data suggests that measurable deformation was present after reversal from ($\mu_5^{-1} = -9.93$"), even though visible bar buckling was not observed until the following cycle. The measurable deformation decreased the apparent compressive strains measured during the push to ($\mu_5^{+2} = 9.89$"), and lead to an increase in the spiral restraint strain. Visible bar buckling occurred after reversal from ($\mu_5^{-2} = -9.88$"), leading to an elongation of the gage length over the outward buckled region and a spike in the transverse steel strain.

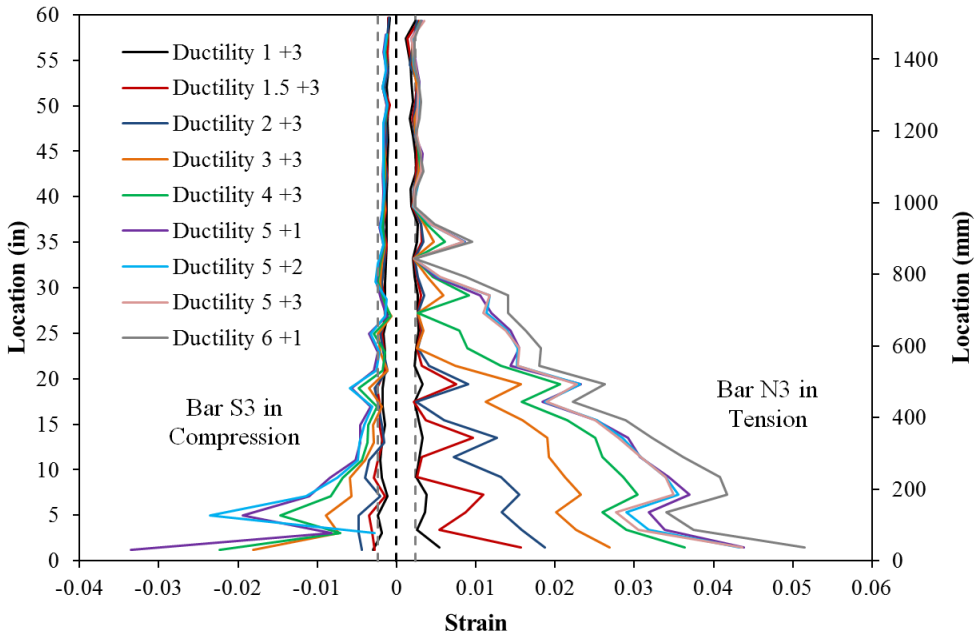

Figure 1.512 T21 – Extreme Fiber Vertical Strain Profiles during Push Cycles

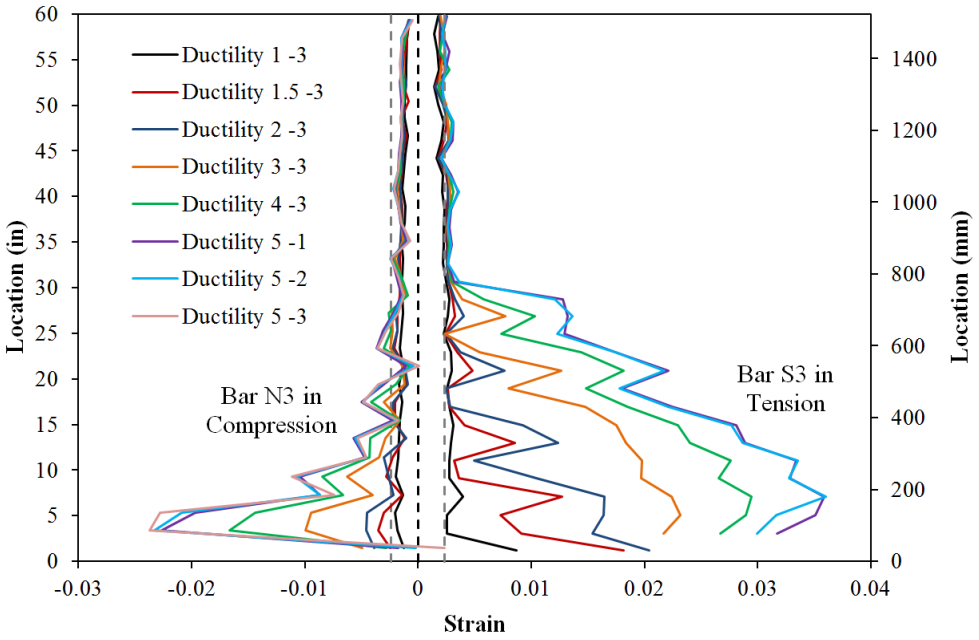

Figure 1.513 T21 – Extreme Fiber Vertical Strain Profiles during Pull Cycles

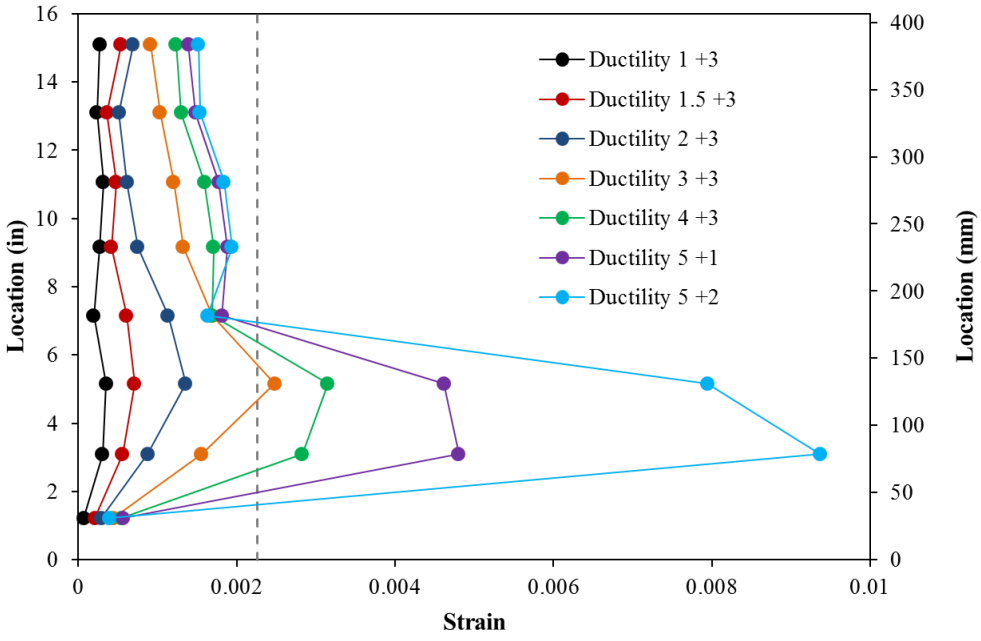

Figure 1.514 T21 – Spiral Strains on the South Side during Push Cycles

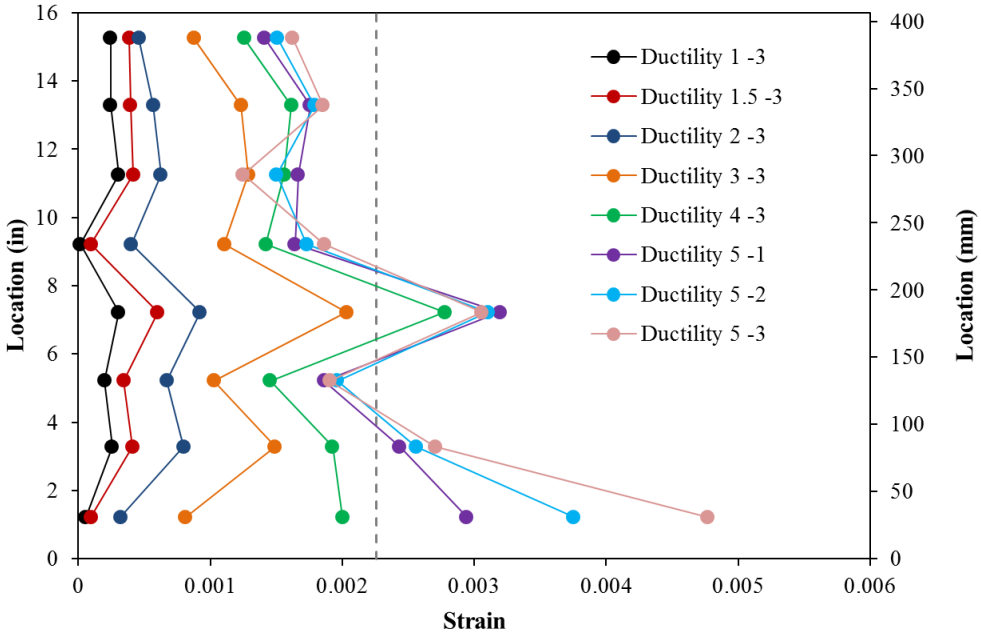

Figure 1.515 T21 – Spiral Strains on the North Side during Pull Cycles

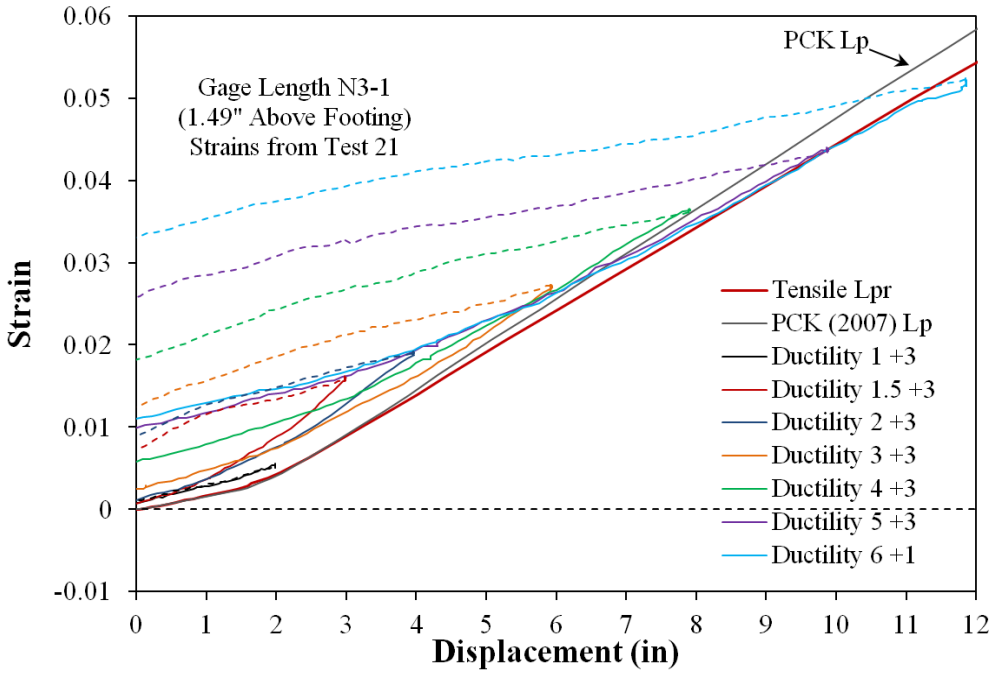

Figure 1.516 T21 – Tensile Strain-Displacement for Bar N3 during Push Cycles

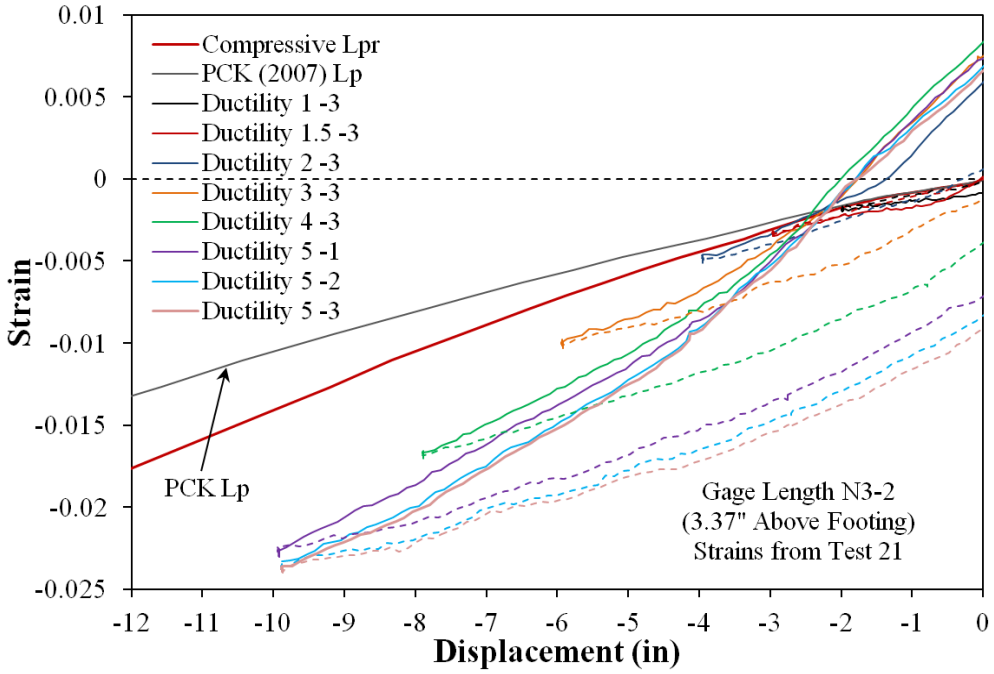

Figure 1.517 T21 – Compressive Strain-Displacement for Bar N3 during Pull Cycles

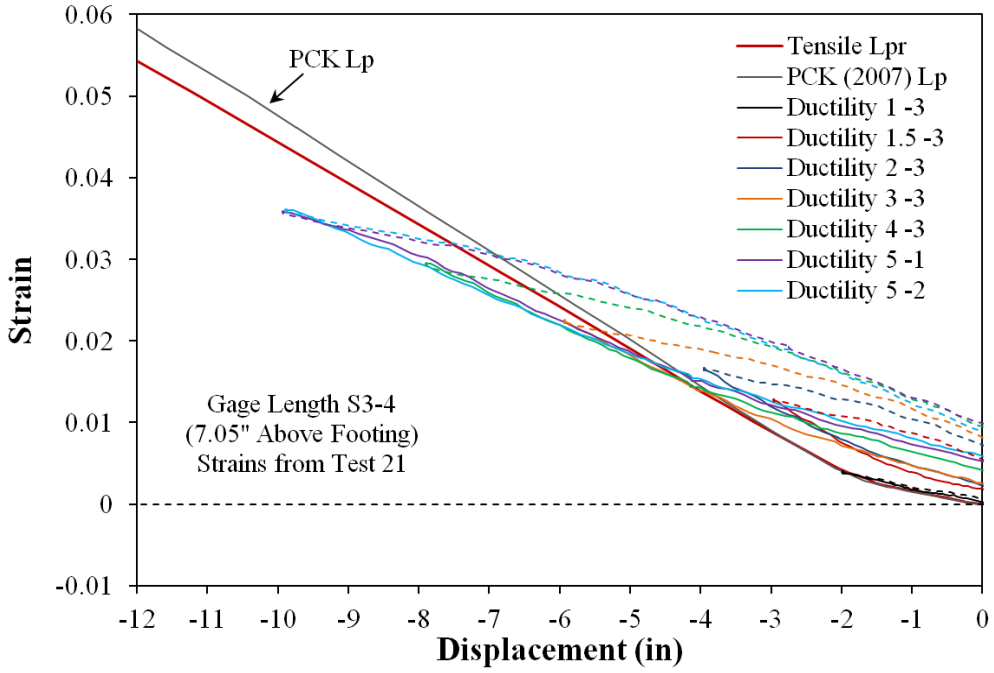

Figure 1.518 T21 – Tensile Strain-Displacement for Bar S3 during Pull Cycles

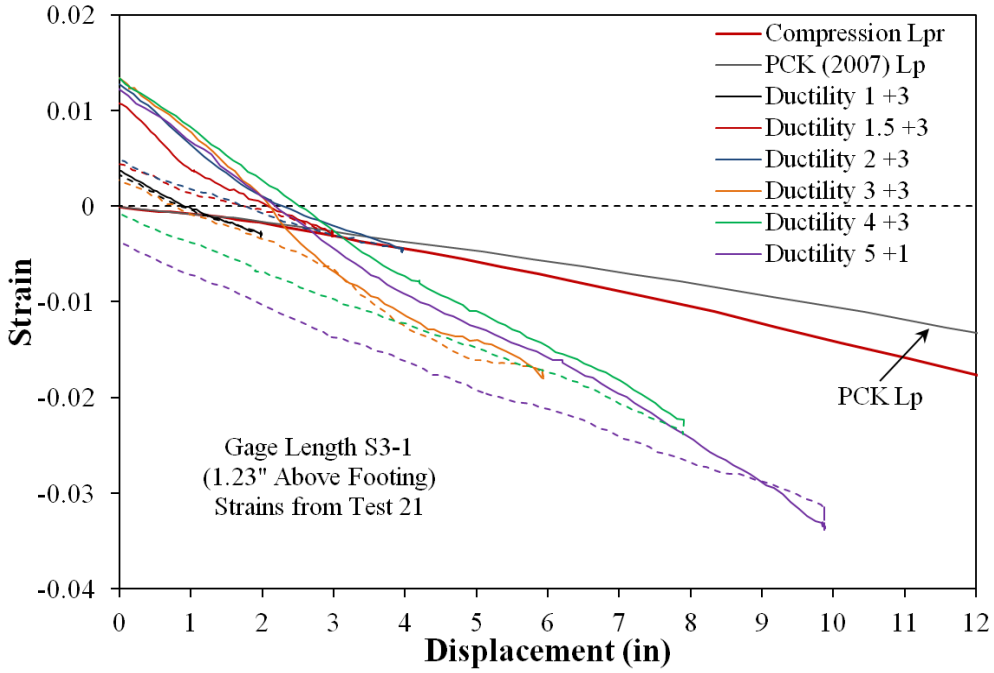

Figure 1.519 T21 – Compressive Strain-Displacement for Bar S3 during Push Cycles

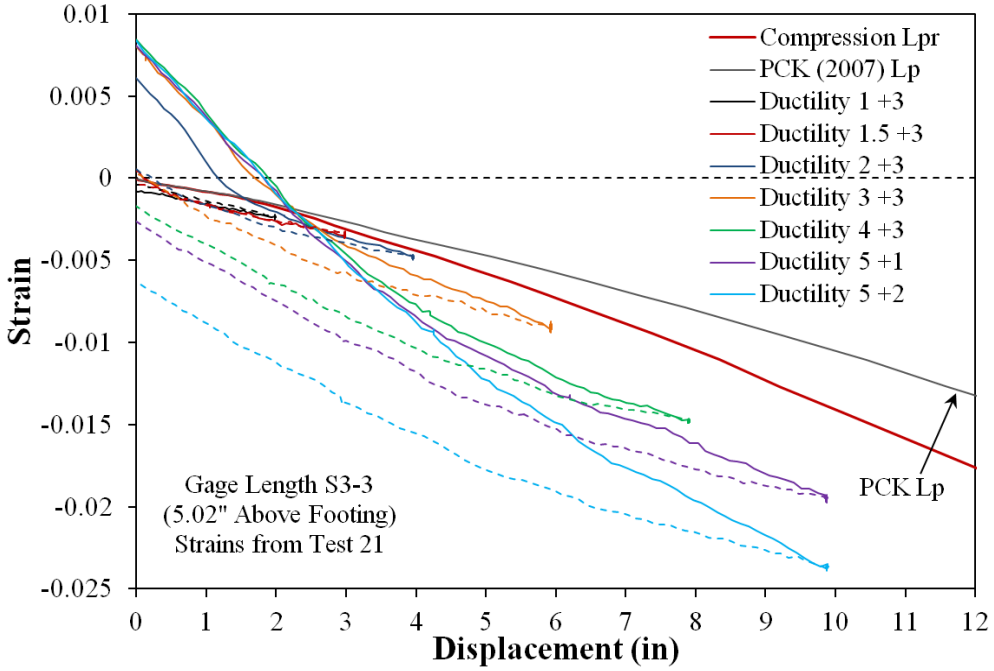

Figure 1.520 T21 – Compressive Strain-Displacement for Bar S3 during Push Cycles

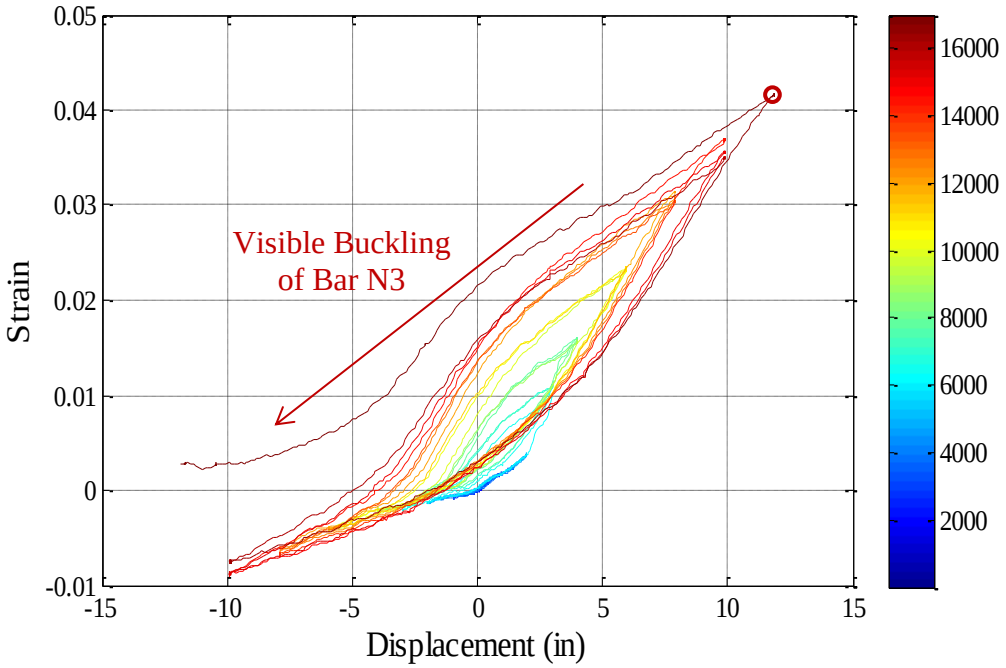

Figure 1.521 T21 – Extreme Fiber Bar N3 Strain Hysteresis to Buckling (7.27" Above)

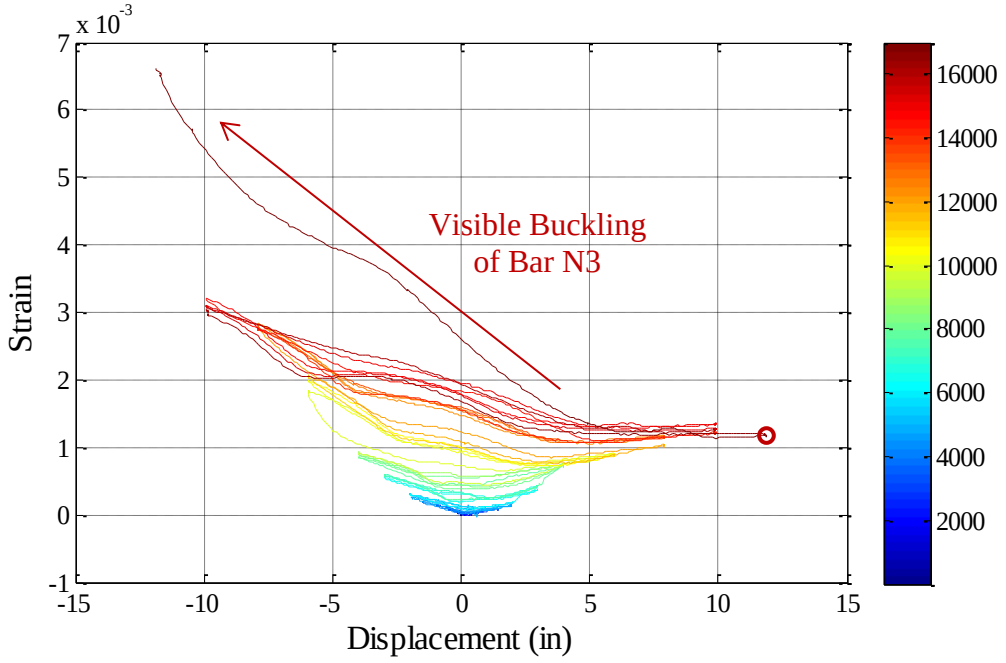

Figure 1.522 T21 – Spiral Strain Hysteresis over North Buckled Region (7.22" Above)

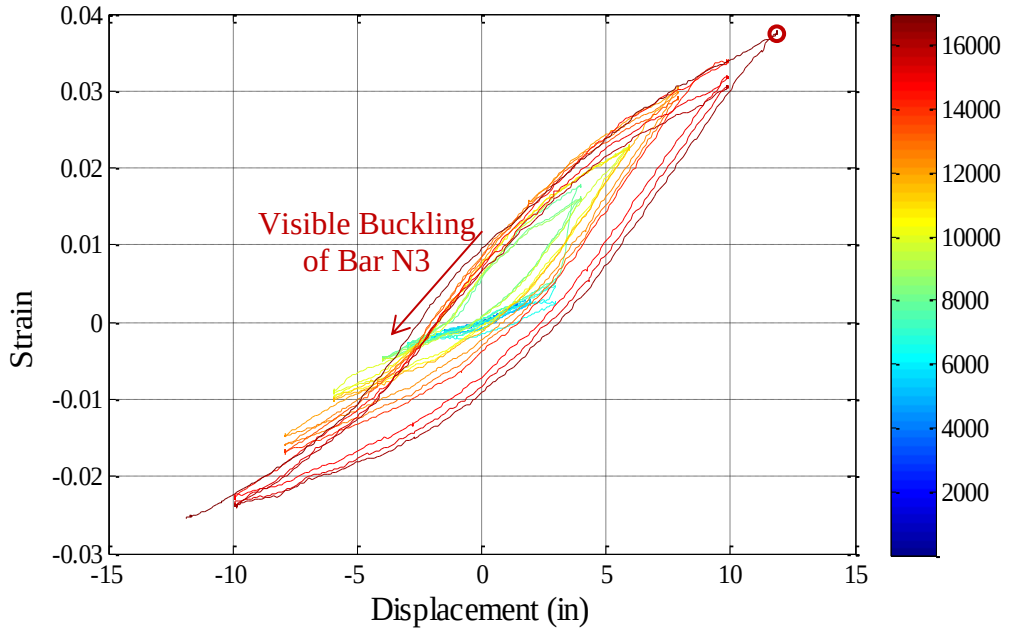

Figure 1.523 T21 – Extreme Fiber Bar N3 Strain Hysteresis to Buckling (3.37" Above)

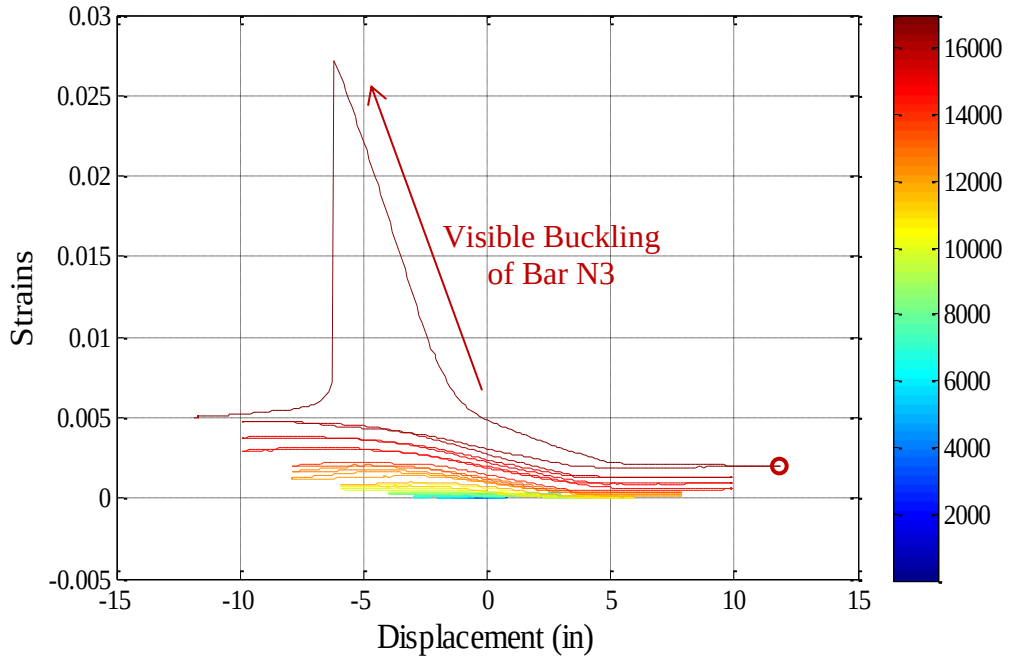

Figure 1.524 T21 – Spiral Strain Hysteresis over North Buckled Region (1.22" Above)

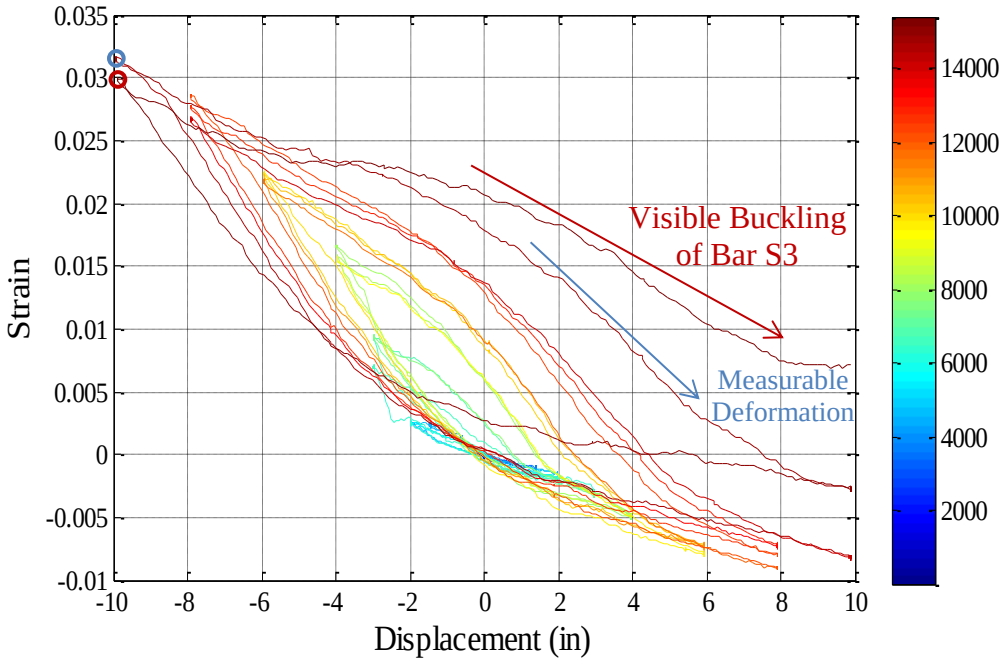

Figure 1.525 T21 – Extreme Fiber Bar S3 Strain Hysteresis to Buckling (3.02" Above)

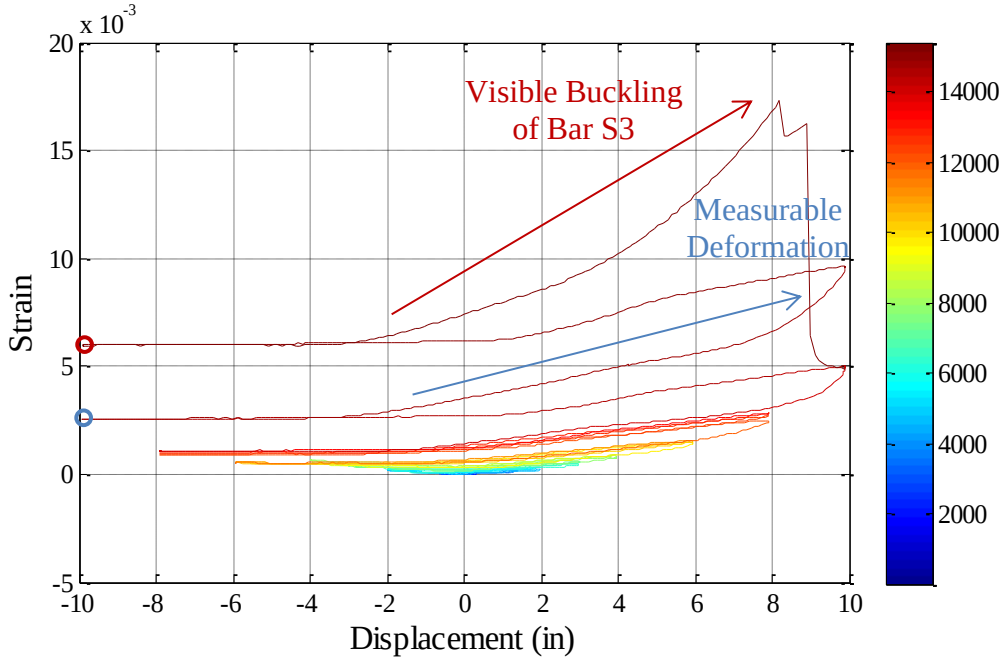

Figure 1.526 T21 – Spiral Strain Hysteresis over South Buckled Region (3.09" Above)

Test 21 Aspect Ratio of 7.33 and 5% Axial Load – Curvature and Strain Penetration

The cross section curvature for each horizontal section above the footing is determined by connecting the strain measurements from all eight instrumented bars with a least squared error line. The curvature is then extracted from the slope of the least squared error line, see Figure 1.527 and Figure 1.528. The cross section curvature profiles in these figures are shown for the first horizontal section above the footing-column interface. This is because the target markers in the lowest gage lengths for bars near the middle of the column were not visible to the Optotrak position monitor. For these sections, it appears that the plane sections hypothesis is appropriate. Vertical curvature profiles are plotted for push and pull cycles in Figure 1.529 and Figure 1.530 respectively. These figures show that plastic curvatures have a linear distribution at higher displacement ductility levels. The extent of plastic curvatures above the footing can be calculated by determining where the linear plastic curvature distribution intersects the triangular yield curvature profile, shown as a grey dashed line. The dashed lines for each curvature distribution represent a least squared error linear fit to the plastic portion of the measured curvatures. The data points used to create the least squared error lines appear as circle data markers. The extent of plastic curvature vs. base curvature ductility is shown graphically in Figure 1.536.

The target marker on each bar placed closest the footing-column interface can be used to create slip hysteresis and horizontal slip profiles attributable to strain penetration. The slip hysteresis for bars N3 and S2 appear in Figure 1.531 and Figure 1.532 respectively. Bar S2 is shown since the lowest LED in extreme fiber bar S3 was obstructed by debris. If the tensile and compressive slip of all of the instrumented bars is plotted along the cross section depth, the base rotation attributable to strain penetration may be calculated. The slip profiles for push and pull cycles appear in Figure 1.533 and Figure 1.534 respectively. The rotation of the base section can be extracted from the slope of the least squared error line connecting all six measured bar slips.

Combining the curvatures over the instrumented region (5ft above the footing), bar slip profiles, and an elastic curvature assumption above the instrumented region, the top column

displacement can be calculated by integrating the curvature distributions and extrapolating the fixed-end rotations to the center of loading. The top column displacements calculated from the Optotrak system are compared to displacements measured with a string potentiometer at the center of loading in Figure 1.535. The Optotrak integrated displacements match well throughout the entire range of response, implying that the shear displacement component is small.

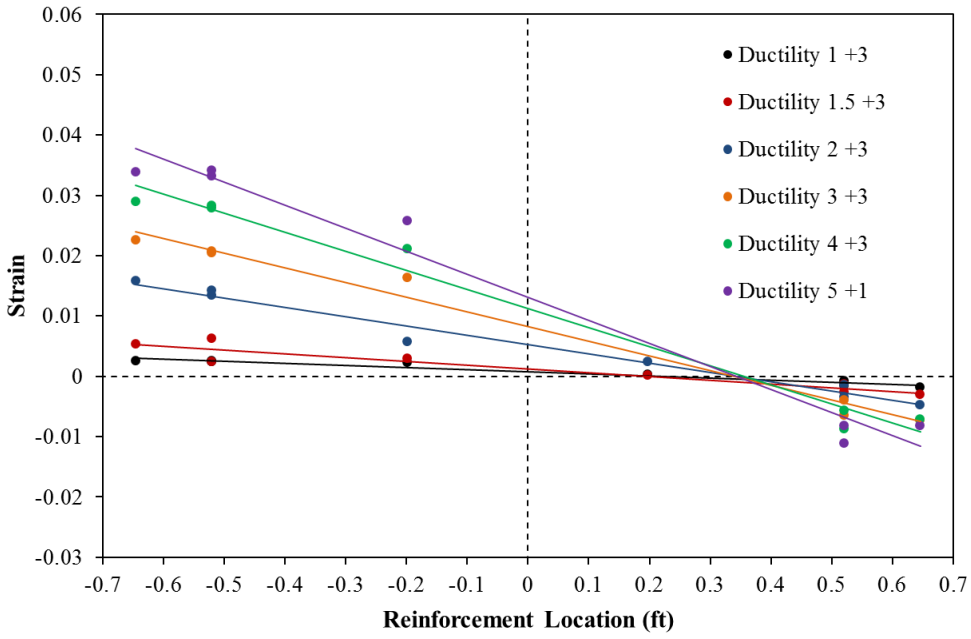

Figure 1.527 T21 – Sample Cross Section Strain Profiles during Push Cycles

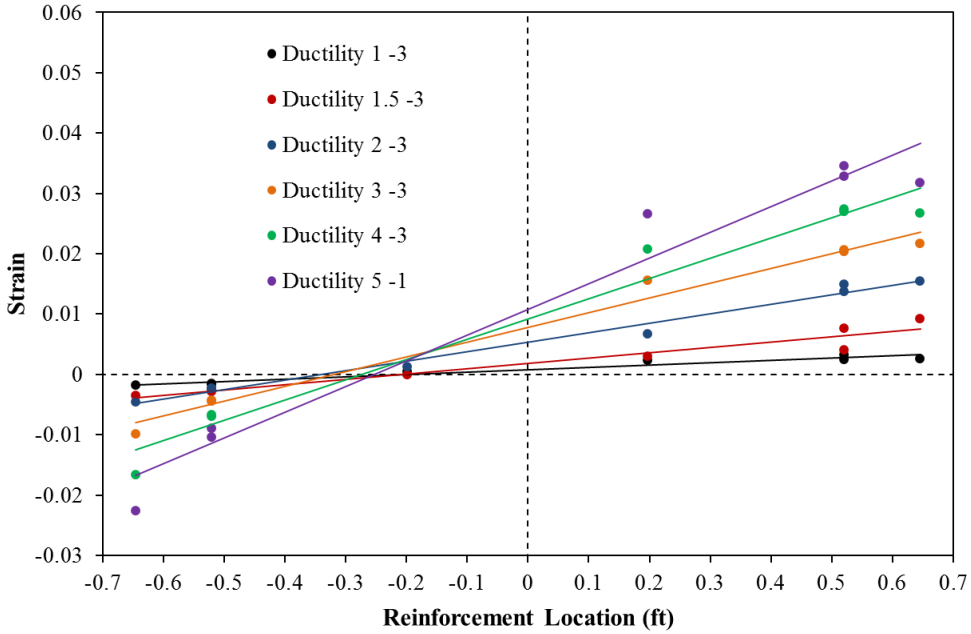

Figure 1.528 T21 – Sample Cross Section Strain Profile during Pull Cycles

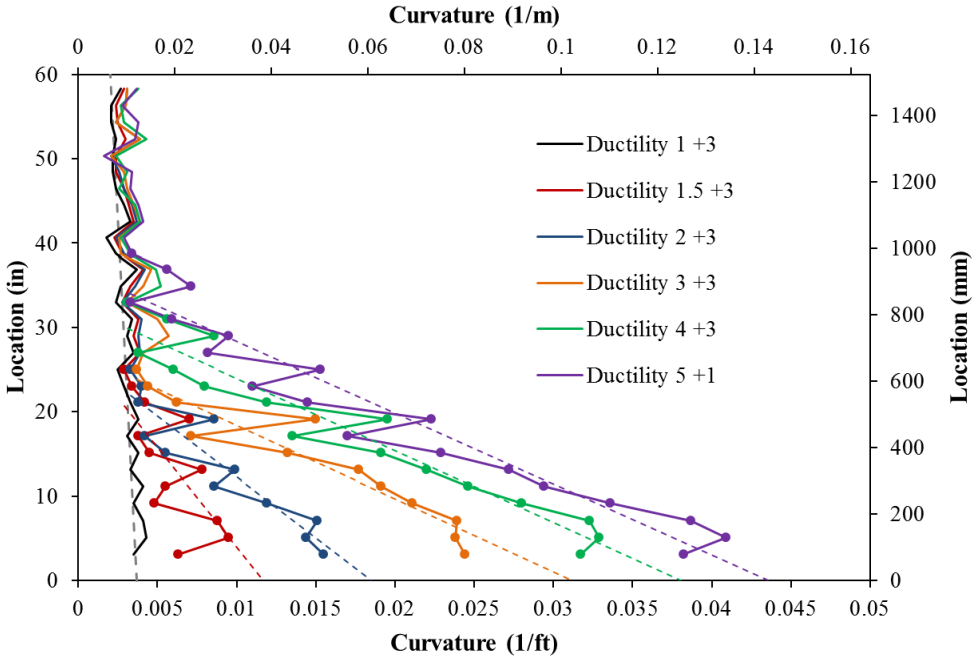

Figure 1.529 T21 – Curvature Profiles during Push Cycles with Plastic Regression

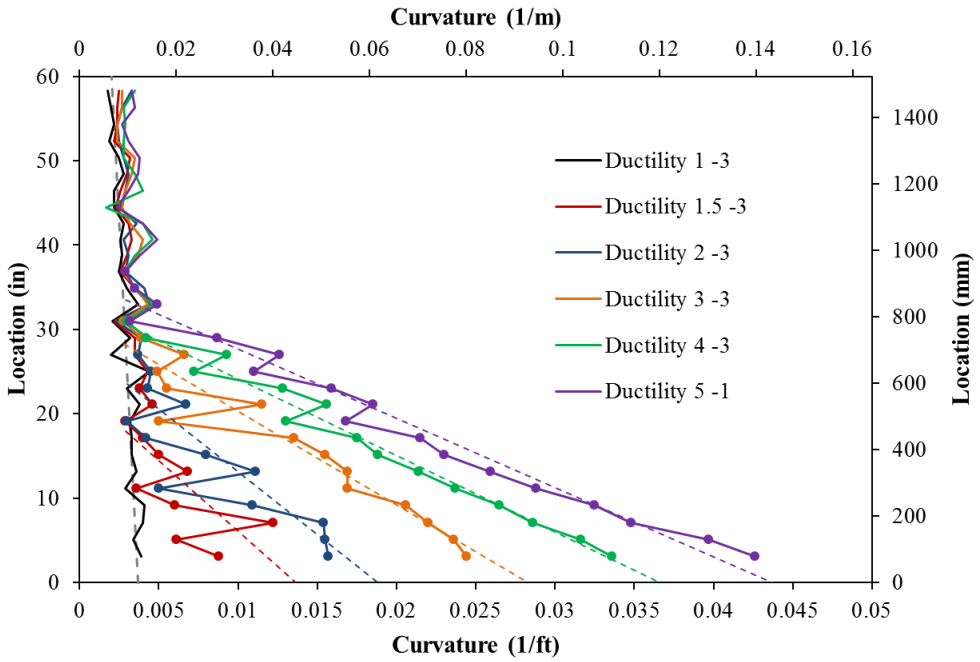

Figure 1.530 T21 – Curvature Profiles during Pull Cycles with Plastic Regression

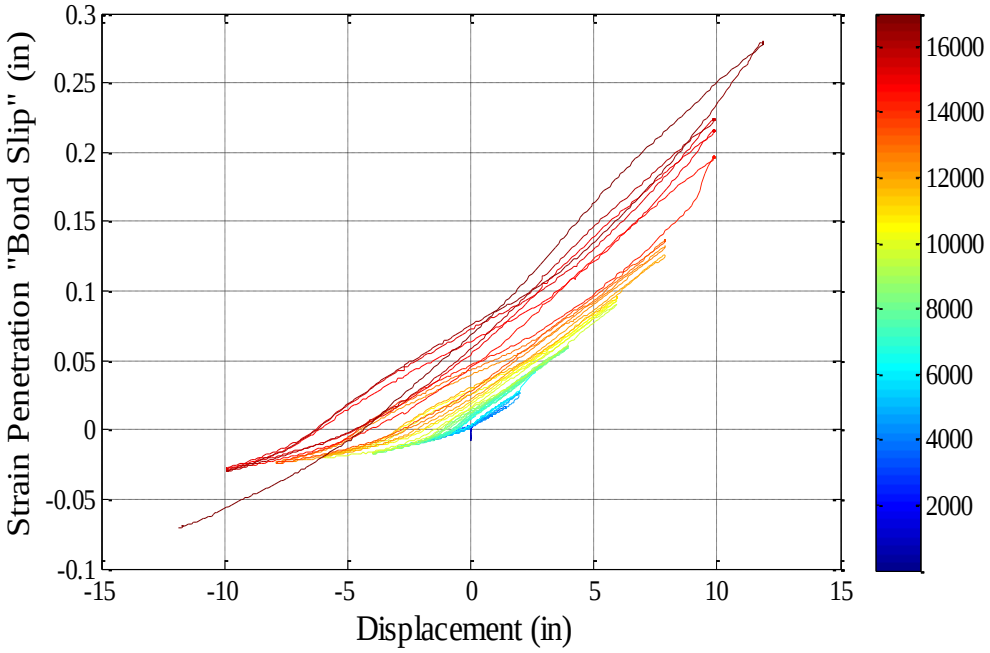

Figure 1.531 T21 – Bond Slip Hysteresis for Bar N3 due to Strain Penetration

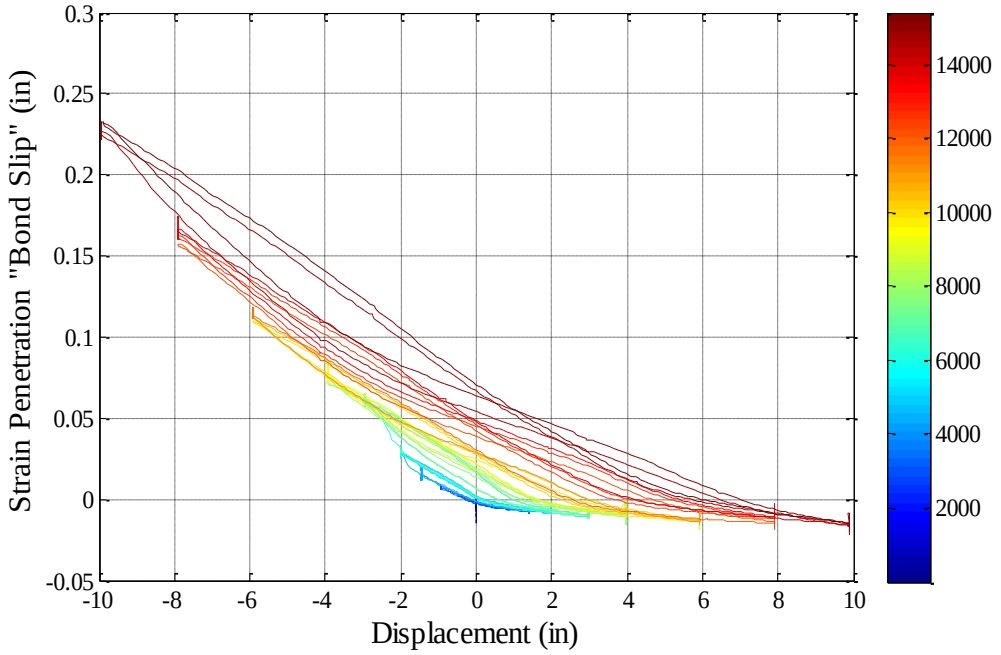

Figure 1.532 T21 – Bond Slip Hysteresis for Bar S4 due to Strain Penetration

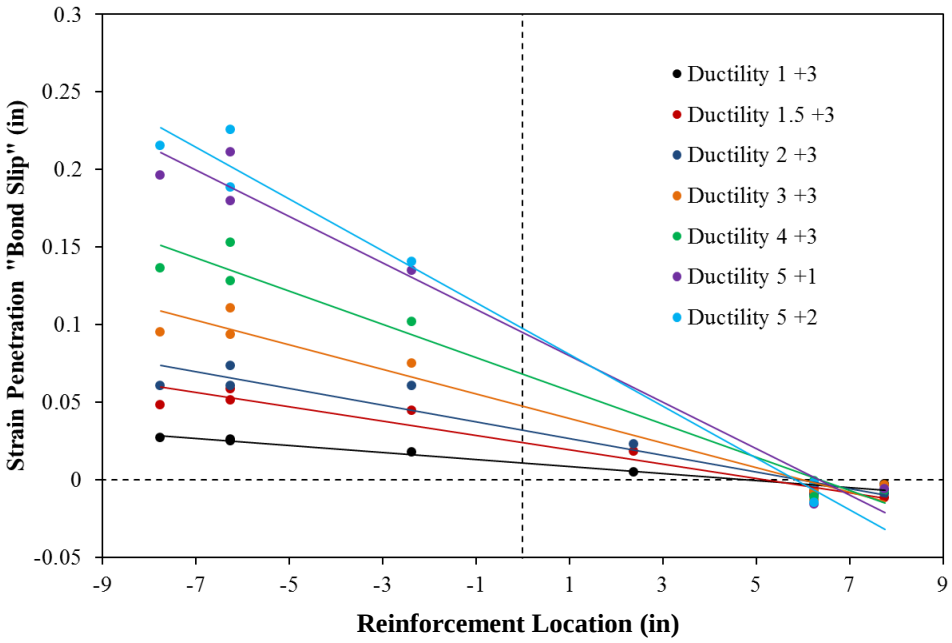

Figure 1.533 T21 – Base Rotation due to Strain Penetration during Push Cycles

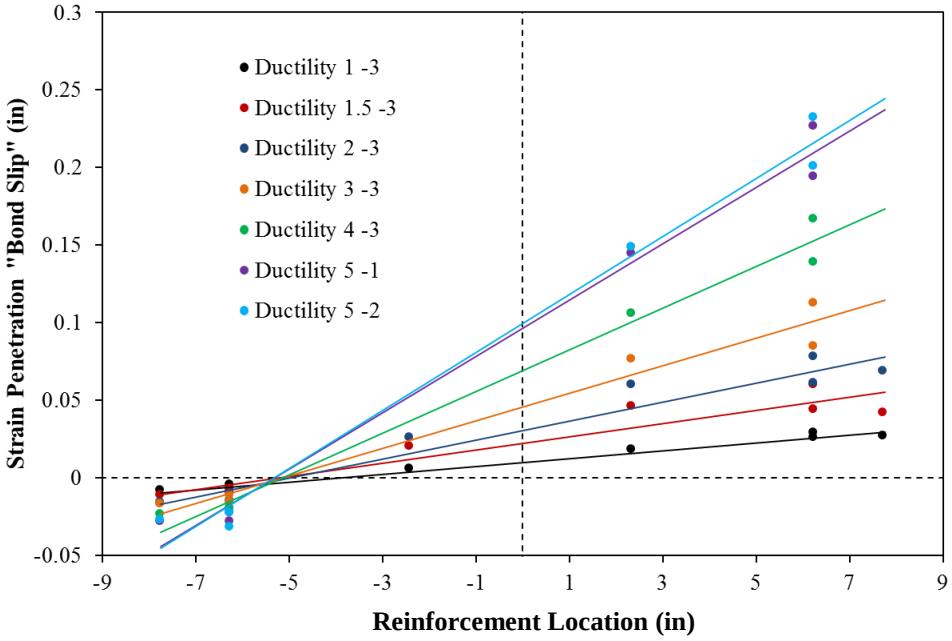

Figure 1.534 T21 – Base Rotation due to Strain Penetration during Pull Cycles

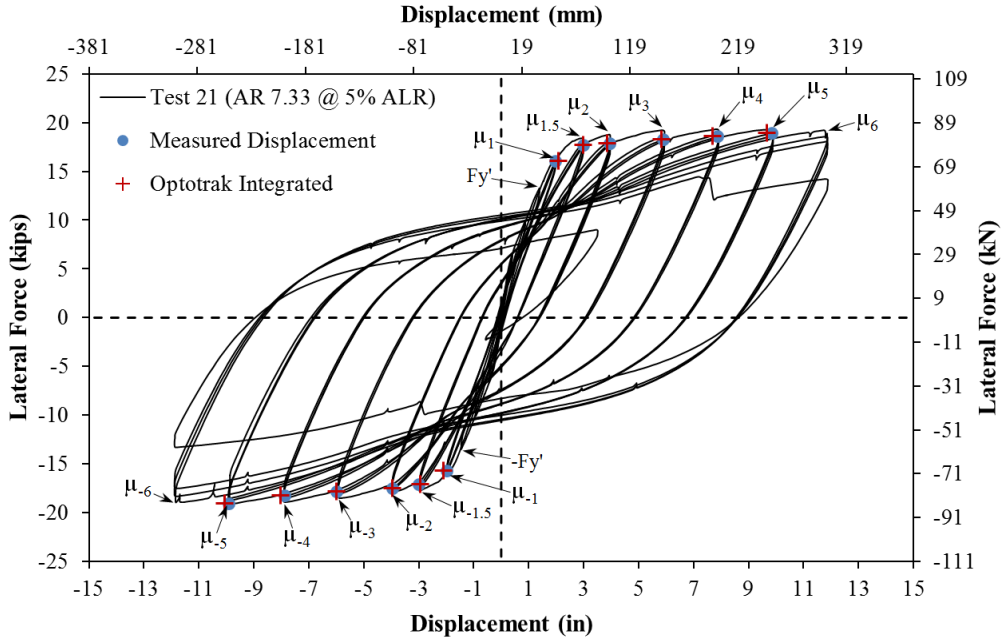

Figure 1.535 T21 – Comparison of Measured and Optotrak Integrated Displacements

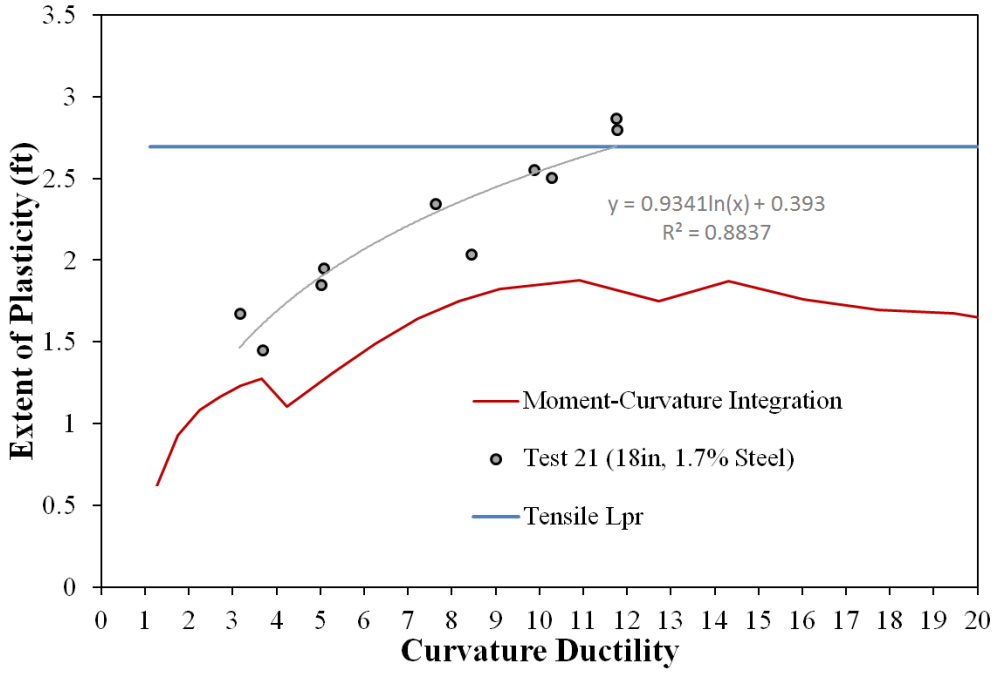

Figure 1.536 T21 – Measured Spread of Plasticity (Circular Data Points)

1.3.4 Test 22 – Aspect Ratio of 7.33 and 10% Axial Load

Table 1.39 Observations for Test 22 – Aspect Ratio of 7.33 and 10% Axial Load

VALUES OF INTEREST:	
Concrete Compressive Strength:	$f_c' = 6530\ psi$
Axial Load:	$P = 148\ kips\ \ (P/(f_c' A_g) = 10\%)$
Column Length and Aspect Ratio:	$11ft\ \ (L/D = 7.33)$
Analytical First Yield Force:	$F_y' = 16.1\ kips$
Experimental First Yield Displacement:	$\Delta_y' = 1.59"$
Analytical Nominal Moment Capacity:	$M_n = 233.3\ kip * ft$
Equivalent Yield Displacement:	$\Delta_y = 2.09"$
Maximum Lateral Force:	$21.9\ kips$
DAMAGE OBSERVATIONS:	
First Cracking North:	$3/4Fy' = 0.90"$
First Cracking South:	$-1/2Fy' = -0.52"$
Cover Concrete Crushing North:	$\mu_3^{-1} = -6.27"$
Cover Concrete Crushing South:	$\mu_3^{+1} = 6.26"$
Transverse Steel Yield North:	At $-6.07"$ during pull to $\mu_3^{-1} = -6.27"$
Transverse Steel Yield South:	At $6.17"$ during push to $\mu_3^{+1} = 6.26"$
Longitudinal Bar Buckling North:	Reversal from $\mu_5^{+1} = 10.45"$
Longitudinal Bar Buckling South:	Reversal from $\mu_6^{-1} = -12.53"$
Longitudinal Bar Fracture North:	At $4.81"$ during push to $\mu_6^{+2} = 12.56"$
Longitudinal Bar Fracture South:	Test Concluded without Fracture of South Bars

$*\mu_6^{-1} = -12.53"$represents the first pull cycle of displacement ductility six

Table 1.40 Strain Data Summary for Test 22 – Aspect Ratio of 7.33 and 10% Axial

MATERIAL STRAINS:	
Cover Concrete Crushing North:	$\varepsilon_s = 0.0063\ (compression)\ \ ^*\mu_{\Delta 2} = -4.17"$
Cover Concrete Crushing South:	$\varepsilon_s = 0.0085\ (compression)\ \ ^*\mu_{\Delta 2} = 4.17"$
Transverse Steel Yield North:	$\varepsilon_s = 0.0103\ (compression)$
Transverse Steel Yield South:	$\varepsilon_s = 0.0124\ (compression)$
Longitudinal Bar Buckling North:	$\varepsilon_s = 0.041\ (peak\ tension\ prior\ to\ bb)$
	$\varepsilon_s = 0.016\ (peak\ comp.\ prior\ to\ bb)$
Longitudinal Bar Buckling South:	$\varepsilon_s = 0.053\ (peak\ tension\ prior\ to\ bb)$
	$\varepsilon_s = 0.035\ (peak\ comp.\ prior\ to\ bb)$
Mander (1988) Ultimate Concrete Compression Strain, $\varepsilon_{cu} = 0.0201$	

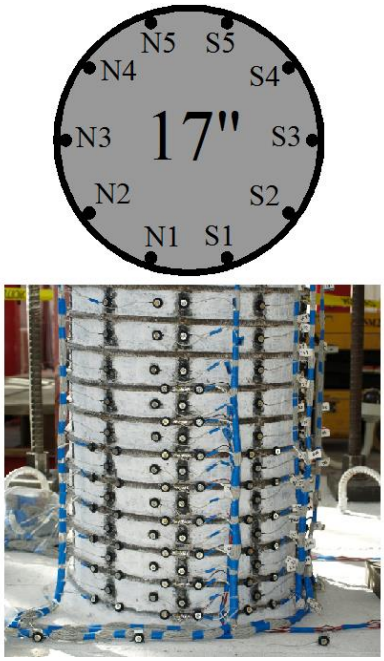

Name	x [mm]	y [mm]	z [mm]
Marker_1	172.315	-723.685	-2801.723
Marker_2	171.154	-675.587	-2801.432
Marker_3	169.830	-625.366	-2801.183
Marker_4	169.013	-573.645	-2801.472
Marker_5	167.165	-525.109	-2801.045
Marker_6	166.562	-474.515	-2800.538
Marker_7	165.978	-426.779	-2800.954
Marker_8	165.483	-376.275	-2801.550
Marker_9	164.655	-323.989	-2802.073
Marker_10	163.951	-270.572	-2802.734
Marker_11	162.581	-219.058	-2802.898
Marker_12	162.803	-169.941	-2804.069
Marker_13	161.318	-120.298	-2804.295
Marker_14	160.949	-72.587	-2804.906
Marker_15	159.355	-21.391	-2805.421
Marker_16	159.433	26.972	-2806.501
Marker_17	157.203	76.304	-2806.586
Marker_18	157.713	126.238	-2807.946
Marker_19	157.017	177.399	-2808.800
Marker_20	156.113	224.792	-2809.343
Marker_21	156.148	278.130	-2810.953
Marker_22	153.280	329.896	-2810.607
Marker_23	152.511	382.595	-2811.395
Marker_24	151.853	432.209	-2812.414
Marker_25	149.168	484.050	-2812.132
Marker_26	150.181	535.773	-2813.438
Marker_27	149.953	586.160	-2814.322
Marker_28	150.357	637.588	-2815.779
Marker_29	149.092	685.654	-2816.174
Marker_30	149.553	735.809	-2817.577

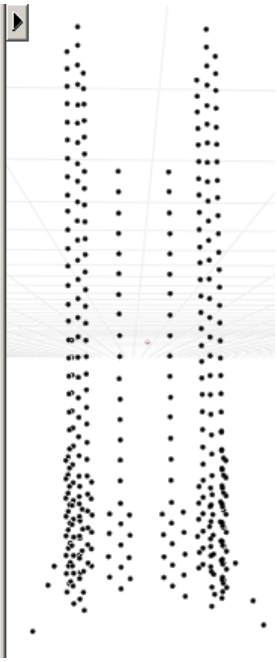

Figure 1.537 T22 – Cross Section Bar Designation and Target Marker Application

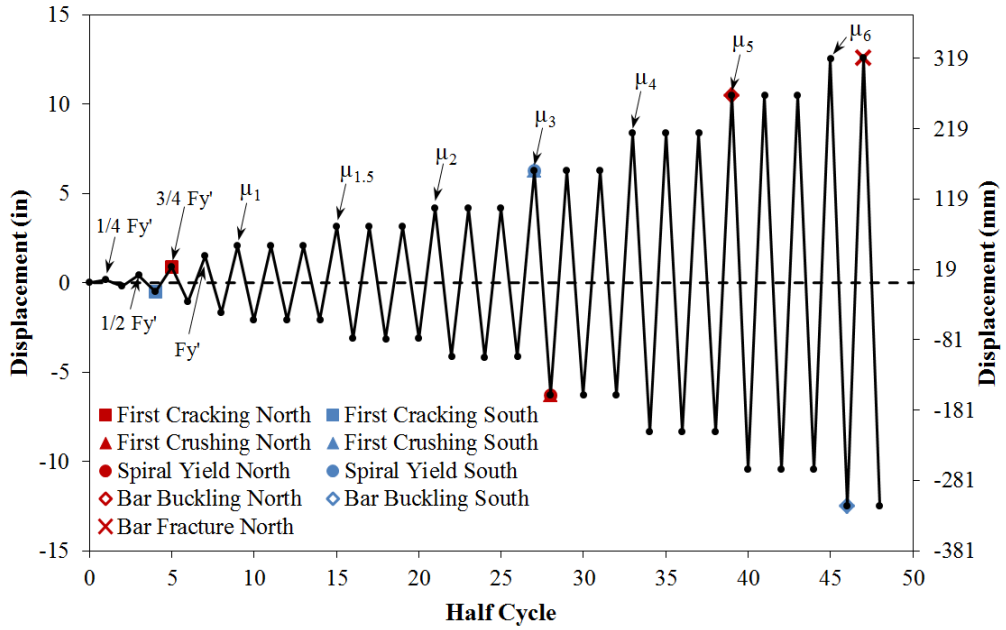

Figure 1.538 T22 – Symmetric Three Cycle Set Load History

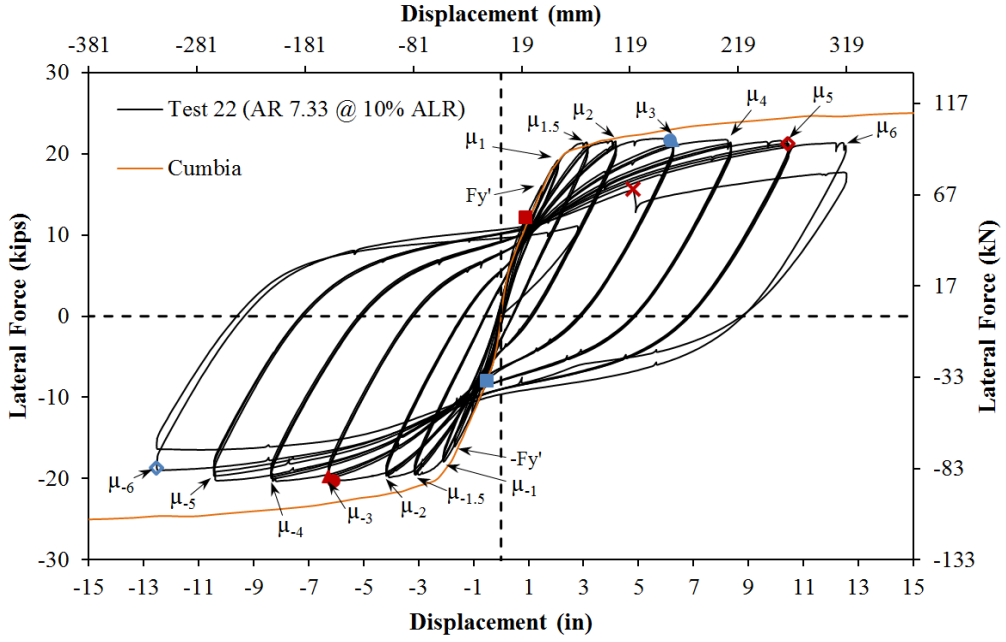

Figure 1.539 T22 – Lateral Force vs. Displacement Response

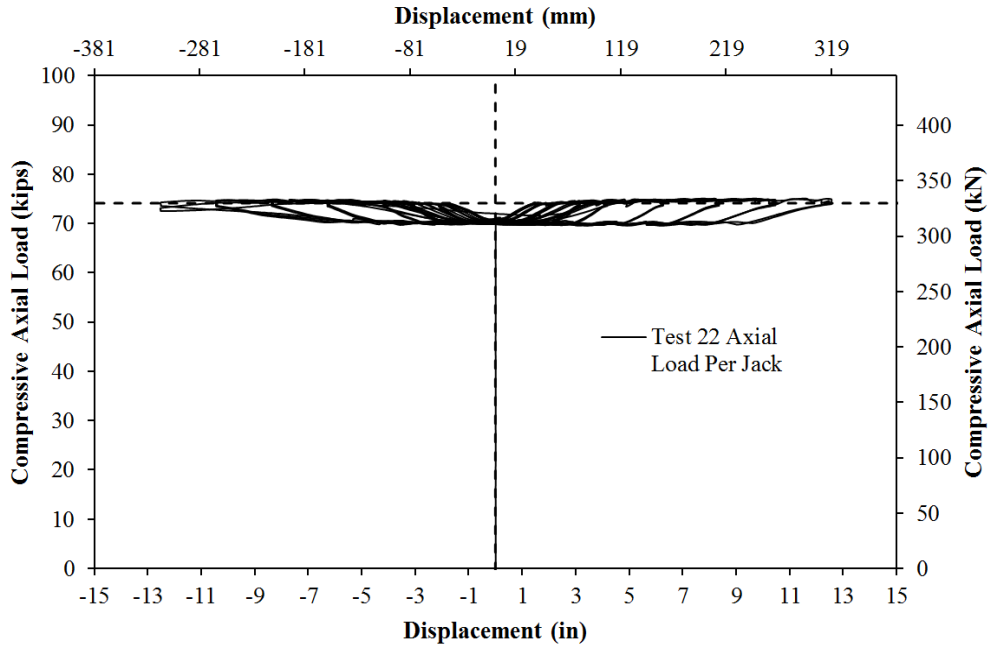

Figure 1.540 T22 – Compressive Axial Load from One Jack (Total = 2*Value)

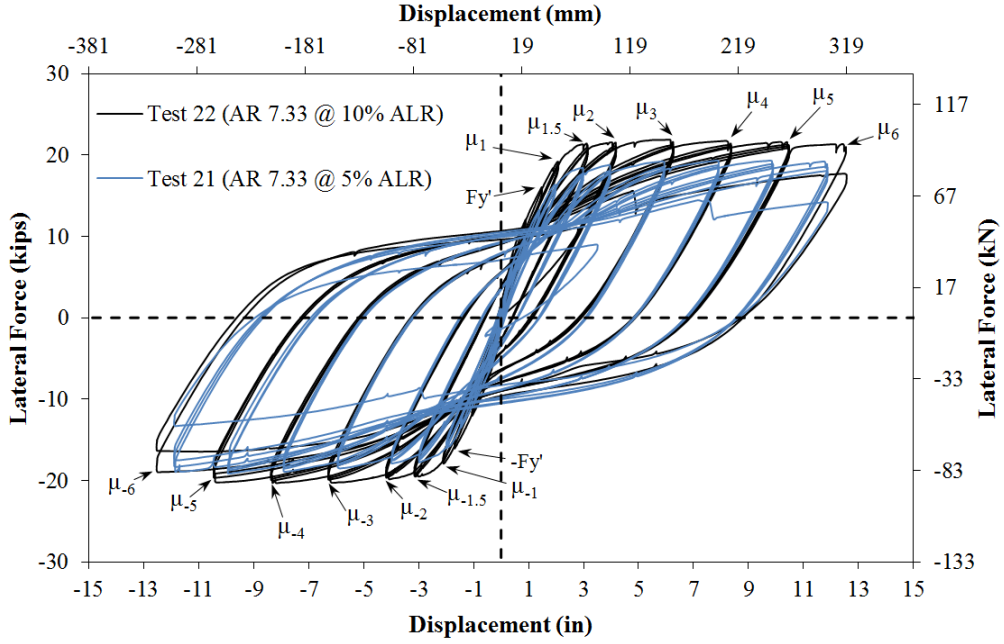

Figure 1.541 T20 and T21 Hysteretic Comparison with Different Axial Load Levels

Test 22 Aspect Ratio of 7.33 and 10% Axial Load – Experimental Observations

The symmetric three-cycle-set laboratory load history is typically used to evaluate the seismic performance of structural components. The load history begins with elastic cycles to the following increments of the analytically predicted first yield force: ¼ Fy', ½ Fy', ¾ Fy', and Fy'. The first yield force for the tested material and geometric properties was determined using moment-curvature analysis (Test 22: Cumbia Fy' = 16.1 kips with f'c = 6530 psi). The first yield displacement was obtained as an average for the experimental first yield push and pull cycles ($\Delta'_y = 1.59"$). Vertical strain profiles for both push and pull cycles up to the first yield force appear in Figure 1.542 with a dashed line representing the yield strain of the longitudinal reinforcement. The equivalent yield displacement, used to determine the displacement ductility levels ($\mu_{\Delta 1} = 1 * \Delta_y$), is then calculated as $\Delta_y = \Delta'_y(M_n/M'_y) = 2.09"$ for Test 22. The symmetric three-cycle-set load history resumes with three balanced cycles at each of the following displacement ductility levels: 1, 1.5, 2, 3, 4, 5, 6, 7, 8, etc. The full symmetric three-cycle-set load history appears in Figure 1.538, and the resulting lateral force versus top column displacement hysteresis is shown in Figure 1.539. The monotonic moment-curvature prediction does not include P-Δ effects.

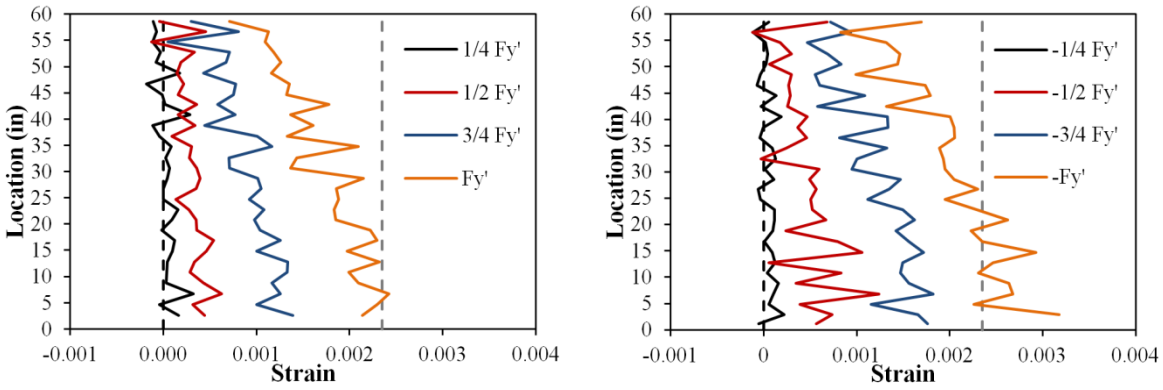

Figure 1.542 T22 – Strain Profiles before Yield (Left) Bar N3 and (Right) Bar S3

The test began with cycles in ¼ Fy' (first yield force) increments in each direction of loading until the first yield force was reached. The first cracks on the North and South sides of the specimen were observed during $(3/4Fy' = 0.90")$ and $(-1/2Fy' = -0.52")$ respectively. The crack distribution on all sides of the specimen at first yield, $(Fy' = 1.48")$ and $(-Fy' = -1.69")$, appears in Figure 1.543. Similarly, the crack progression at displacement ductility 1, 1.5, and 2 appear in Figure 1.544, Figure 1.545, and Figure 1.546 respectively. During these cycles the cracks became more numerous and increased in inclination on the shear faces of the specimen. A small amount of core concrete crushed on the South side of the specimen during $(\mu_3^{+1} = 6.26")$, as shown in the left photo of Figure 1.547. A similar observation was made on the North side of the specimen during $(\mu_3^{-1} = -6.27")$, see the right photo of Figure 1.547. The crushing on each side of the specimen during ductility three was not severe, and it appeared that only a thin layer of concrete flaked off between spiral layers. Photos of the crack distributions during displacement ductility three and four appear in Figure 1.548 and Figure 1.549 respectively.

The North extreme fiber bar N3 visibly buckled under compressive stress during the reversal from $(\mu_5^{+1} = 10.45")$, as shown in Figure 1.550. At this time the buckled deformation was small. Additional outward deformation was observed in buckled bar N3 at $(\mu_5^{-2} = -10.45")$, see the left photo of Figure 1.551. The South reinforcing bars remained intact during ductility five, and additional crushing of the core concrete was observed up to 20" above the footing (right photo of Figure 1.551). A photo of the specimen at $(\mu_6^{+1} = 12.54")$ and additional deformation in previously buckled bar N3 during $(\mu_6^{-1} = -12.53")$ appears in Figure 1.552. The previously buckled North extreme fiber bar N3 fractured at 4.81" during the push cycle to $(\mu_6^{+2} = 10.45")$, Figure 1.553. Visible buckling of the South extreme fiber bar was observed 17" above the footing at $(\mu_6^{+2} = 10.45")$, as shown in the right photo of Figure 1.553. Buckling of adjacent North reinforcing bars N2 and N4 was observed during the final pull cycle to $(\mu_6^{-2} = -12.53")$. Photos of the specimen after the test are shown in Figure 1.554.

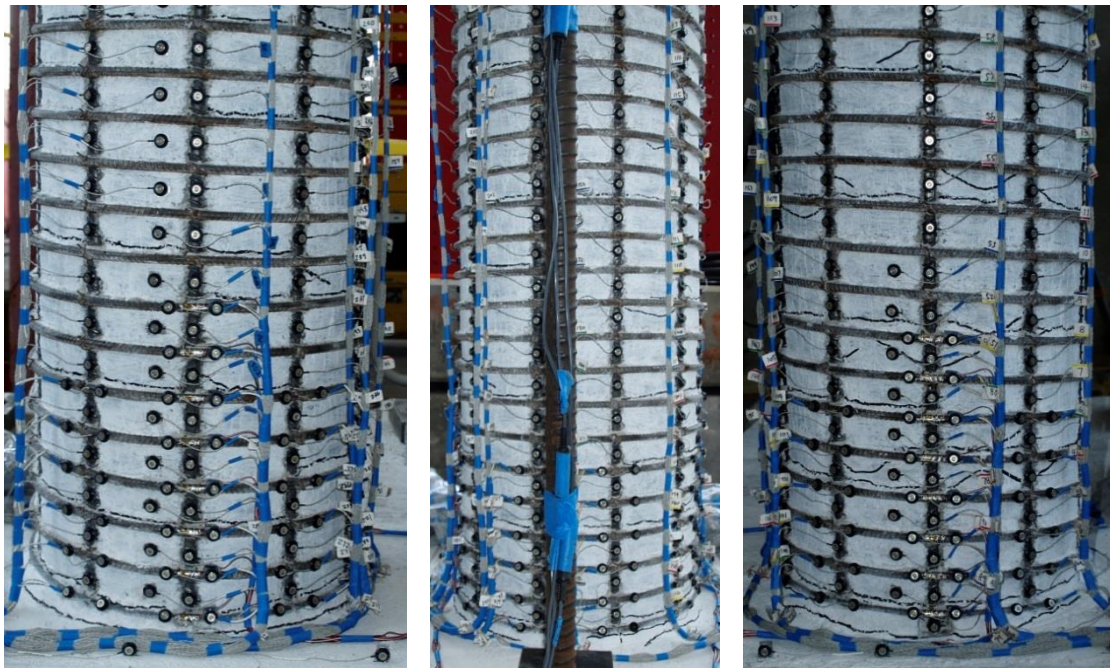

Figure 1.543 T22 – (Left) North at Fy', (Mid) Front at -Fy', and (Right) South at -Fy'

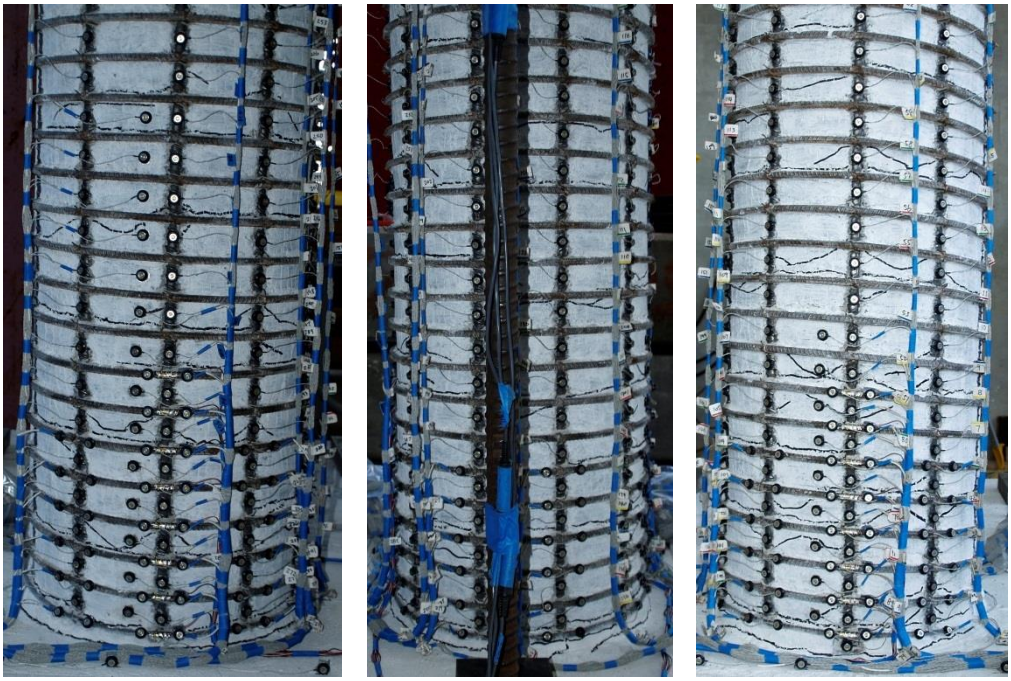

Figure 1.544 T22 – (Left) North at μ_1^{+3}, (Mid) Front at μ_1^{-3}, and (Right) South at μ_1^{-3}

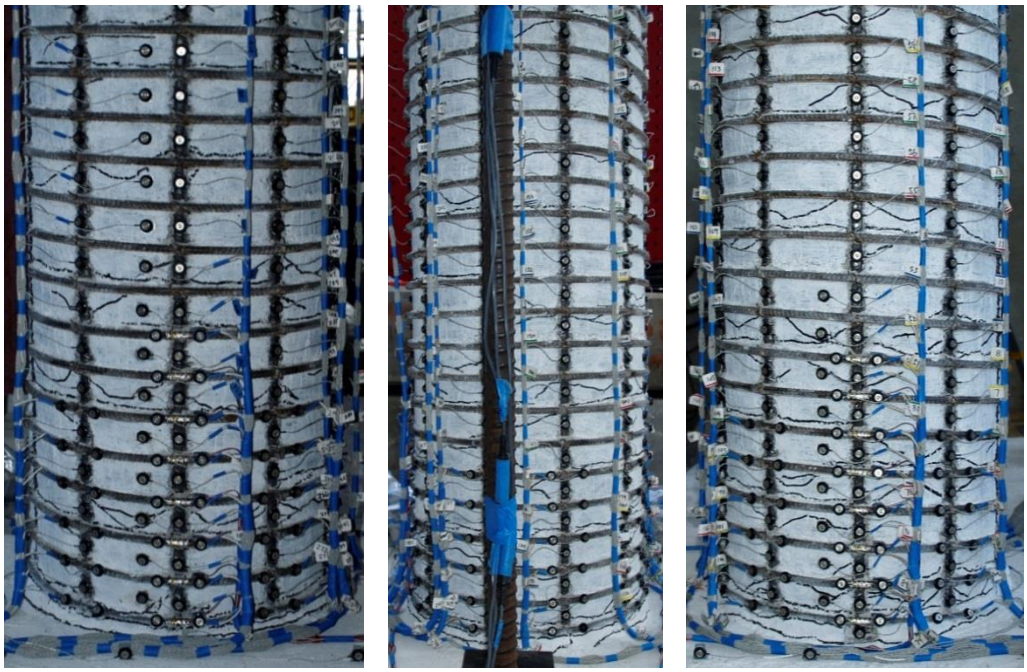

Figure 1.545 T22 – (Left) North at $\mu_{1.5}^{+3}$, (Mid) Front at $\mu_{1.5}^{-3}$, and (Right) South at $\mu_{1.5}^{-3}$

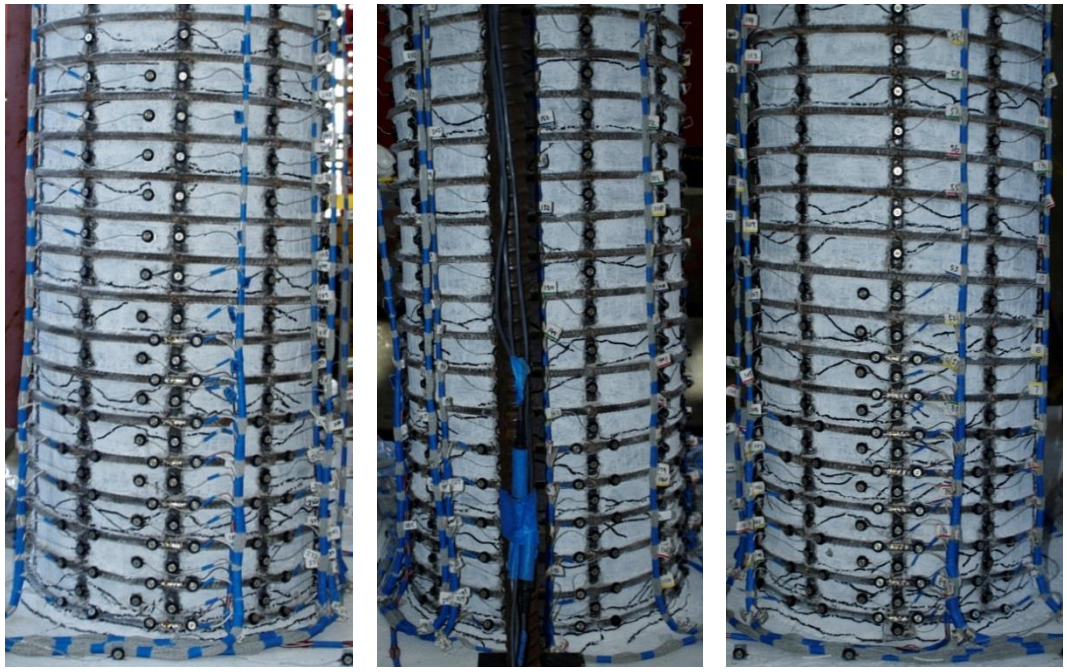

Figure 1.546 T22 – (Left) North at μ_{2}^{+3}, (Mid) Front at μ_{2}^{-3}, and (Right) South at μ_{2}^{-3}

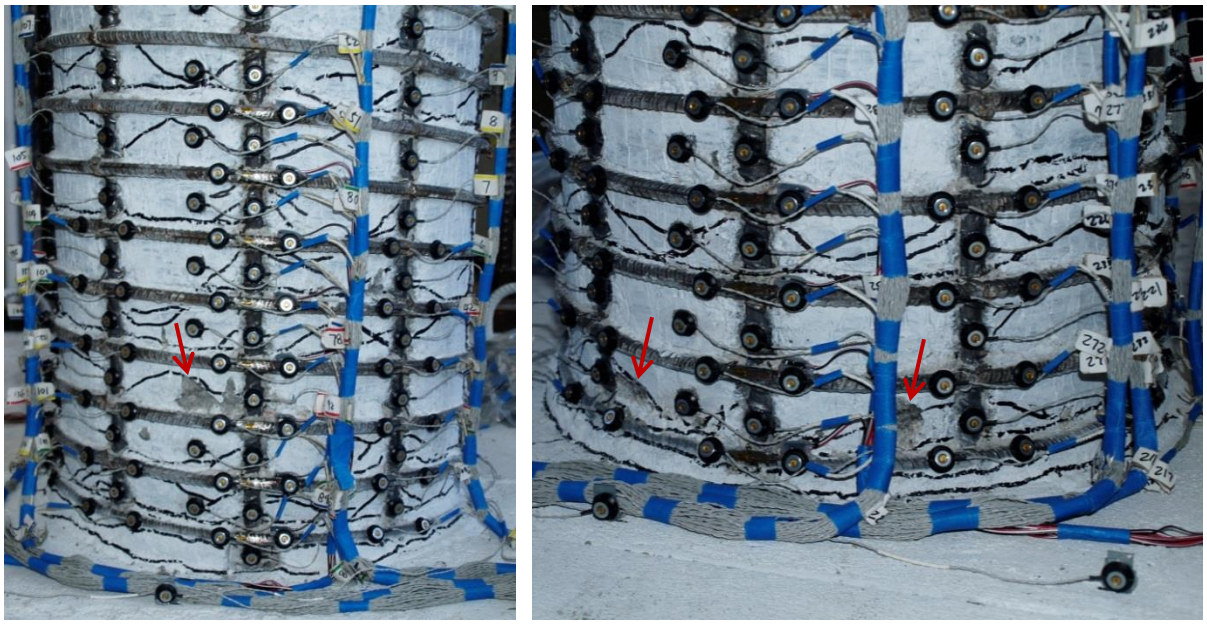

Figure 1.547 T22 – (Left) Concrete Crushing on the South Side at μ_3^{+1} and (Right) Concrete Crushing on the North Side at μ_3^{-1}

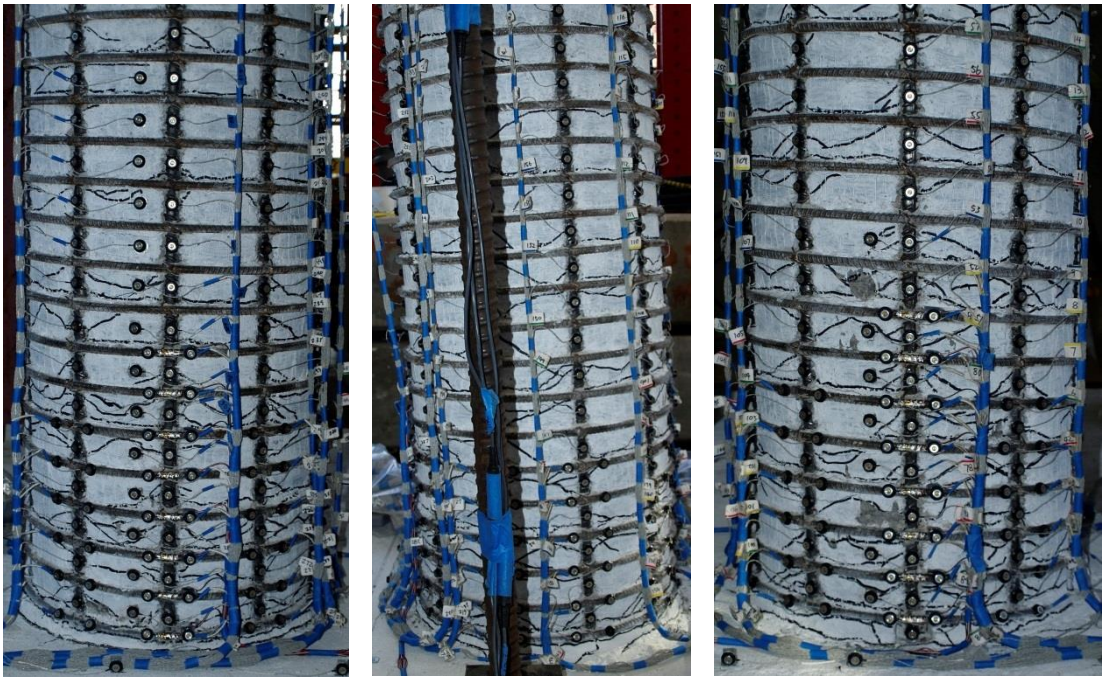

Figure 1.548 T22 – (Left) North at μ_3^{+3}, (Mid) Front at μ_3^{-3}, and (Right) South at μ_3^{-3}

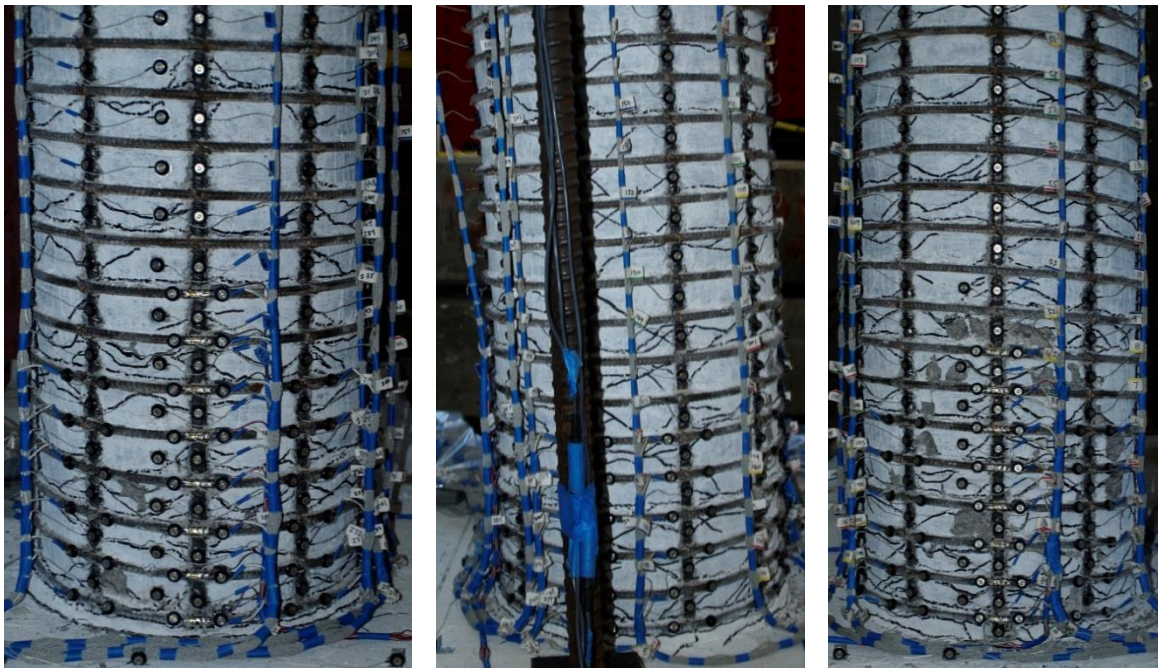

Figure 1.549 T22 – (Left) North at μ_4^{+3}, (Mid) Front at μ_4^{-3}, and (Right) South at μ_4^{-3}

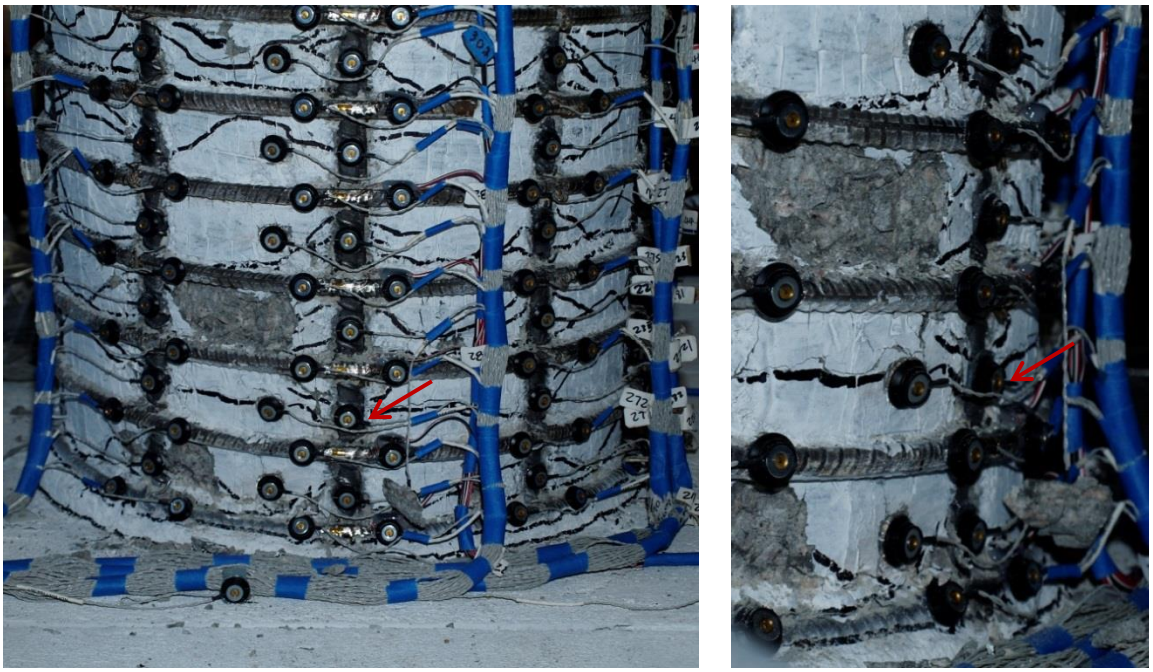

Figure 1.550 T22 – Buckling of Bar N3 after Reversal from ($\mu_5^{+1} = 10.45$")

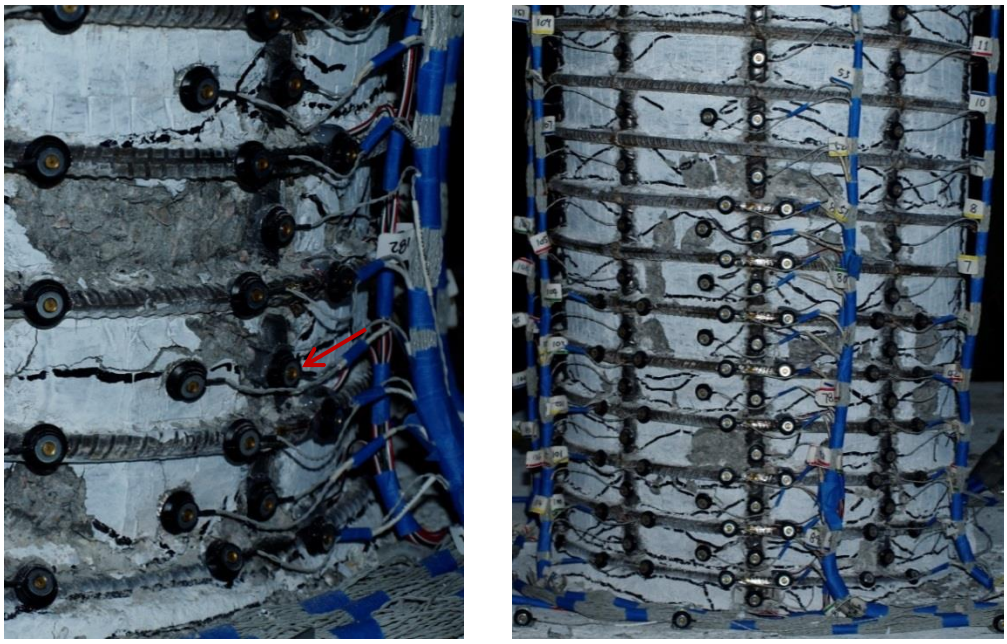

Figure 1.551 T22 – (Left) Deformation in Buckled Bar N3 at ($\mu_5^{-2} = -10.45$") and (Right) South Side of the Specimen at ($\mu_5^{+3} = 10.46$")

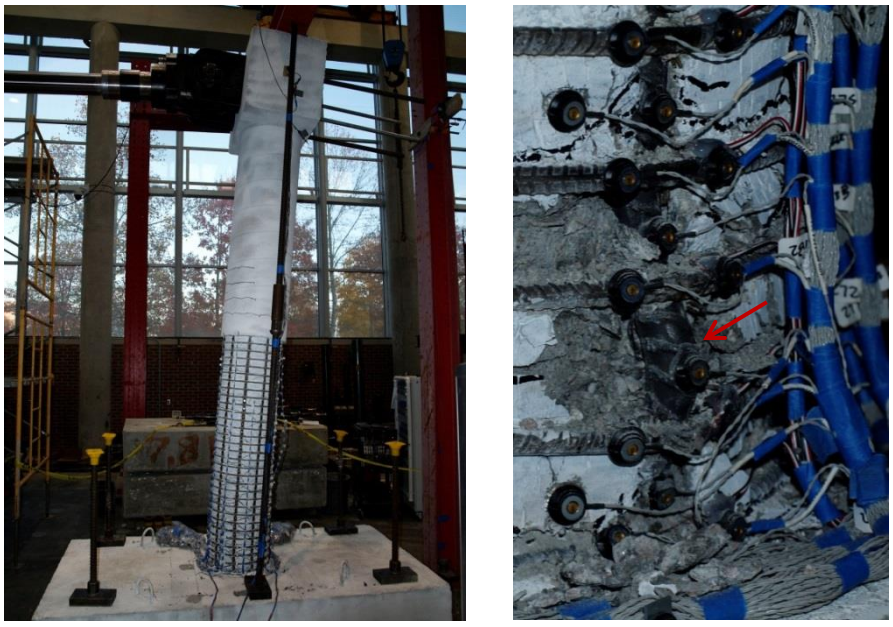

Figure 1.552 T22 – (Left) Specimen at ($\mu_6^{+1} = 12.54$") and (Right) Additional Deformation in Buckled Bar N3 at ($\mu_6^{-1} = -12.53$")

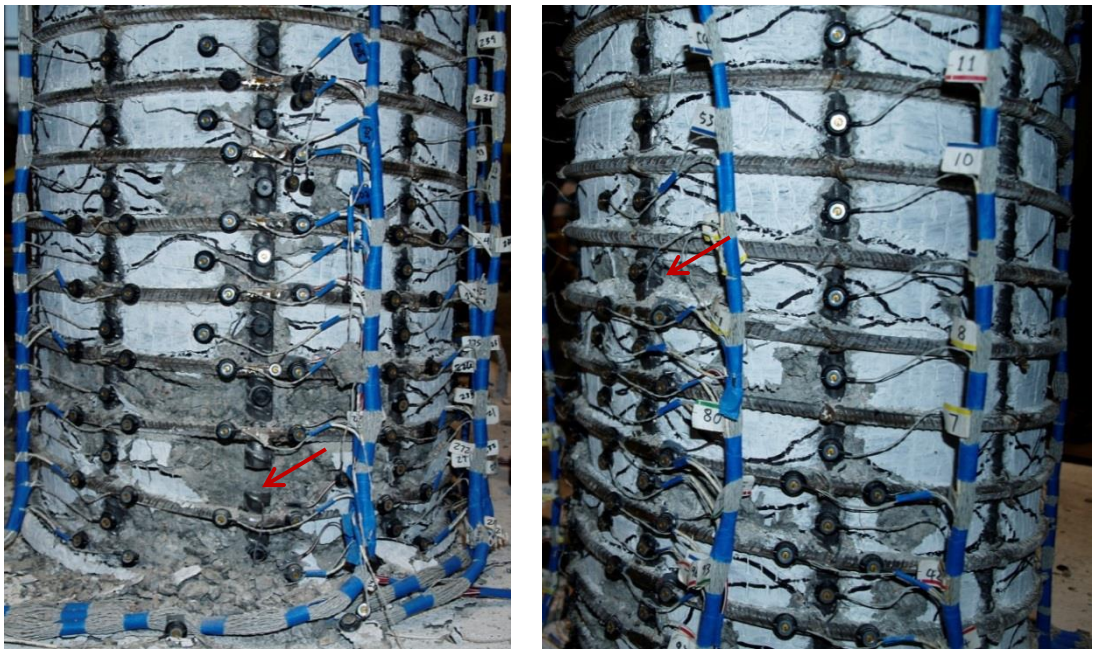

Figure 1.553 T22 – (Left) Fracture of Previously Buckled Bar N3 during ($\mu_6^{+2} = 12.56$") and (Right) Buckling of Extreme Fiber Bar S3 at ($\mu_6^{+2} = 12.56$")

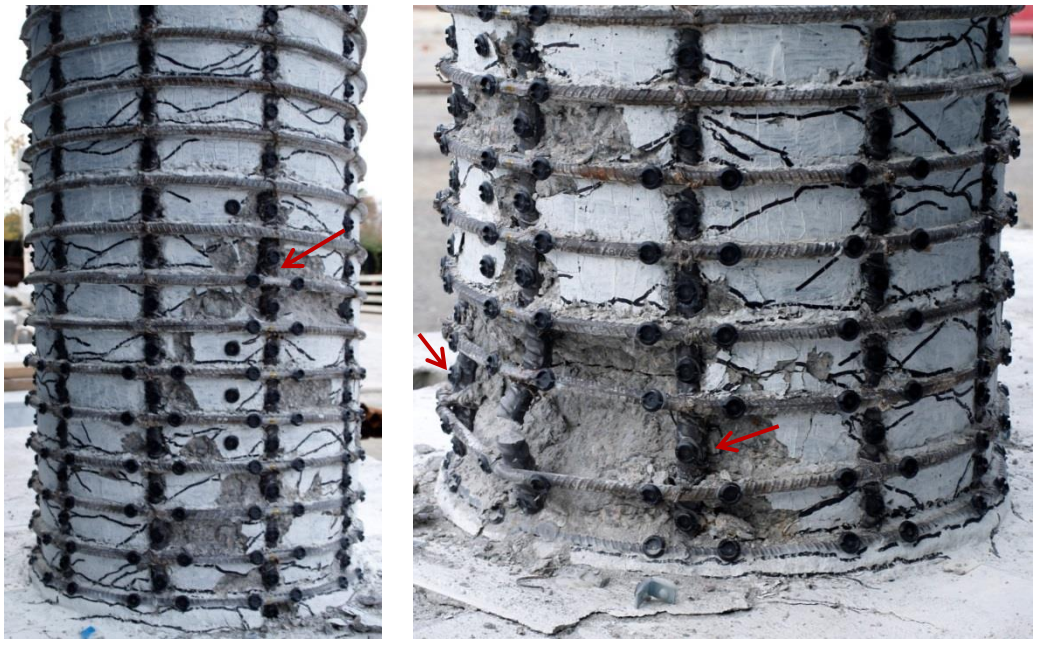

Figure 1.554 T22 – After the Test (Left) South Side and (Right) North Side

Test 22 Aspect Ratio of 7.33 and 10% Axial Load – Strain Data Analysis

North Reinforcement

Vertical strain profiles for the North extreme fiber bar N3 placed into tension during push cycles appear in the right half of Figure 1.555. This figure shows both extreme fiber bars on the same graph to illustrate the effects of tension shift on strain profiles. Compressive vertical strain profiles for North extreme fiber bar N3 during pull cycles appear in the left half of Figure 1.556.

A peak tensile strain of 0.041, located 6.73" above the footing, was measured for North extreme fiber bar N3 during ($\mu_5^{+1} = 10.45"$). The largest tensile strain in bar N3 measured during cycles at displacement ductility four was 0.033 for the gage length 4.61" above the footing. The relationship between tensile strain and displacement for the gage length 6.73" above the footing appears in Figure 1.559. Each line represents a single push cycle which began with the column at zero displacement and ended at the peak of a continuous push cycle. The solid line contains data during the push cycle loading up to the peak displacement, and the dashed line represents the subsequent reversal of load. The monotonic moment-curvature prediction, with the PCK (2007) Lp Hinge Method, matches well until displacement ductility two, when it begins to over predict the measured tensile strains.

The largest compressive strain of -0.020, located 2.54" above the footing, was measured during ($\mu_5^{-1} = -10.43"$). It is important to note that visible bar buckling occurred during this cycle, see Figure 1.550, but the outward deformation was small enough to barely affect the strains measured over the lowest gage lengths. This value is equal to the Mander ultimate concrete compressive strain of -0.020. The relationship between compressive strain and displacement for bar N3 appears in Figure 1.560, for the gage length centered 2.54" above the footing. The monotonic moment-curvature prediction with the PCK (2007) Lp Hinge Method matches well until ductility two, when the measured strains begin to exceed the prediction at an increasing rate. The effect of the compressive demand on the North side of the specimen on eight spiral layers near the footing-column interface is shown in Figure

1.558. Two layers of transverse steel entered the inelastic range during displacement ductility three, which coincides with the region were the moment-curvature analysis begins to under predict the measured response. By displacement ductility four, four layers of transverse steel had entered the inelastic range. At ($\mu_5^{-1} = -10.43"$), the peak spiral strain measured 0.022 for the layer 2.72" above the footing at the location of slight visible bar buckling.

North extreme fiber bar N3 visibly buckled during the reversal from ($\mu_5^{+1} = 10.45"$), as depicted in Figure 1.550. The previous peak compressive strain and tensile strain in the transverse steel measured over this region were -0.016 and 0.009 respectively. The strain hysteresis for the outward buckled region of bar N3 appear in Figure 1.564 and Figure 1.565 for gage lengths located 2.54" and 4.61" above the footing respectively. The gage length normally increases in the outward buckled region during the compressive cycle since the target markers are applied to the convex side of the longitudinal bar undergoing outward deformation. The effect of outward bar buckling on the transverse steel restraint is shown in Figure 1.566 for spiral layer 2.72" above the footing. Outward deformation of the longitudinal bar caused the spiral strain to increase during the reversal from ($\mu_5^{+1} = 10.45"$) when visible bar buckling was observed. Transverse steel in this region yielded during displacement ductility three, see Figure 1.558. Cycle to cycle increases in the transverse steel strain during displacement ductility three and four were observed. Presumably, this explains the cycle to cycle change in hysteretic loop shape for the longitudinal steel after spiral yielding. This implies that some level of measurable deformation took place before visible bar buckling.

South Reinforcement

Vertical strain profiles for the South extreme fiber bar S3 placed into tension during pull cycles appear in the right half of Figure 1.556. A peak tensile strain of 0.053, located 2.88" above the footing, was measured in the South extreme fiber bar S3 during ($\mu_6^{-1} = -12.53"$). The relationship between tensile strain and displacement for this gage length appears in

Figure 1.561. The moment-curvature prediction matches well until displacement ductility three, when the PCK (2007) Lp Hinge Method begins to over predict the measured tensile strains.

Compressive vertical strain profiles for the South extreme fiber bar S3 during push cycles appear in the left half of Figure 1.555. The region under high compressive demands extends higher up the column than previous tests. The visible effects of the compressive demand can be seen in the right photo of Figure 1.551. In this photo it is clear that crushing of the core concrete occurred over the regions of the column where the largest compressive demand was measured. A peak compressive strain of -0.035 was measured 16.74" above the footing on bar S3 during ($\mu_6^{+1} = 12.54$"). This exceeds the Mander ultimate concrete compressive strain of -0.020. A second peak compressive strain of -0.025 was measured 6.81" above the footing during the same cycle. The relationship between compressive strain and displacement on bar S3 for gage lengths 6.81" and 16.74" above the footing appear in Figure 1.562 and Figure 1.563 respectively. The relationship between compressive strain and displacement for the gage length 6.81" above the footing begins to exceed the moment-curvature prediction with the PCK (2007) Lp Hinge Method after displacement ductility two. Similarly, measured strains 16.74" above the footing are significantly under predicted after displacement ductility three. It is apparent that measurable deformation occurred over the gage length 16.74" above the footing, which aligns with the location of later visible bar buckling.

The effects of compressive demand on spiral strains in transverse steel layers overlaying bar S3 are shown in Figure 1.557. A single layer of transverse steel yielded during displacement ductility three, while three other layers had strains just below yield. The regions of heightened compressive demand shown in the left half of Figure 1.555 also produced the largest transverse steel strains. A peak transverse steel strain of 0.0124 was measured in the spiral layer 14.81" above the footing during ($\mu_6^{+1} = 12.54$"). It is apparent that there was a cycle to cycle increase in the transverse steel strains measured 14.81" above

the footing during displacement ductility five, indicating some level of measurable deformation.

A peak tensile strain of 0.053, located 2.88" above the footing, was measured in the South extreme fiber bar S3 during ($\mu_6^{-1} = -12.53"$). Visible bar buckling occurred during the following reversal, but not at the location of previous peak tensile strains. Instead, visible bar buckling occurred over the region of heightened compressive demand and large inelastic spiral strains approximately 14-17" above the footing, as shown in the right photo of Figure 1.553. The strain hysteresis for the outward buckled region of bar S3 appears in Figure 1.567 for the gage length 14.72" above the footing. The effect of outward visible bar buckling of spiral restraint strain hysteresis is shown in Figure 1.569 for the layer located 14.81" above the footing. Vertical strain profiles in the right half of Figure 1.556 and the strain hysteresis in Figure 1.567 both indicate that tensile demand over the region 14-17" above the footing is significantly lower than regions of the column closer to the footing-column interface. The strain hysteresis for the peak tensile gage length, located 6.81" above the footing (Figure 1.568), appears to be unaffected by visible bar buckling higher up the column. Even though bar buckling did not happen over the peak tensile gage length, it is important to note that tensile strains sustained during ($\mu_6^{-1} = -12.53"$) were required to initiate visible bar buckling during ($\mu_6^{+2} = 12.56"$). The measured spiral strains did not spike on the South side of the specimen until the initial compressive cycle of ($\mu_6^{+1} = 12.54"$). This implies that the previous compressive demand and multiple layers of inelastic transverse steel lowered the magnitude of the peak tensile strains required to initiate bar buckling during the following reversal of load.

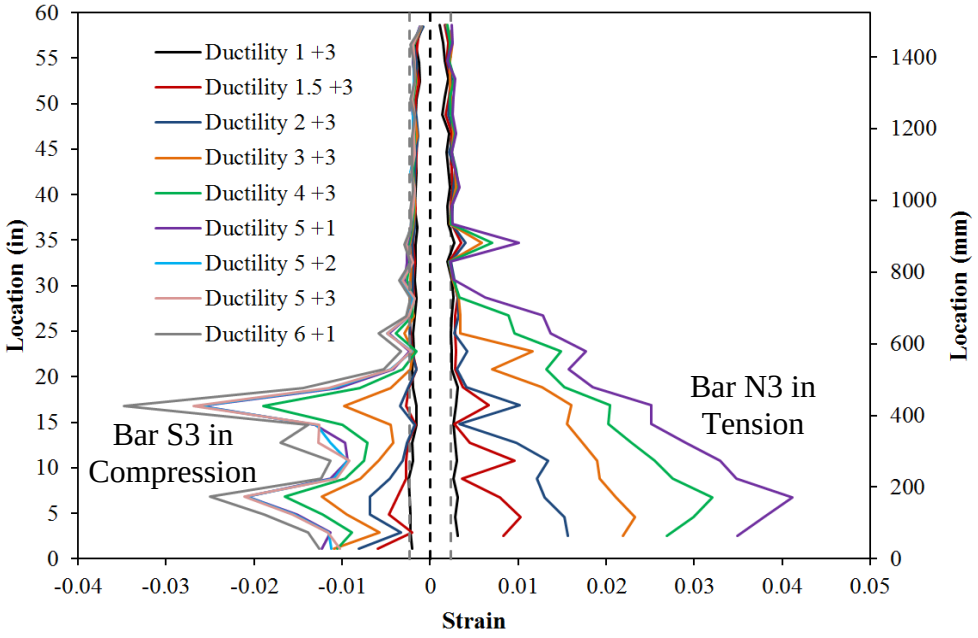

Figure 1.555 T22 – Extreme Fiber Bar Vertical Strain Profiles during Push Cycles

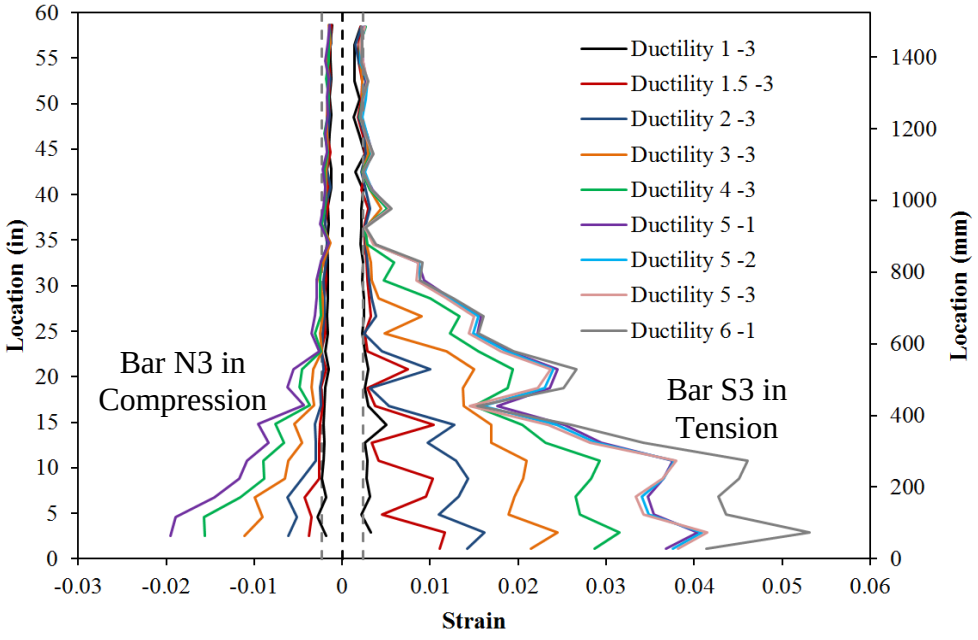

Figure 1.556 T22 – Extreme Fiber Bar Vertical Strain Profiles during Pull Cycles

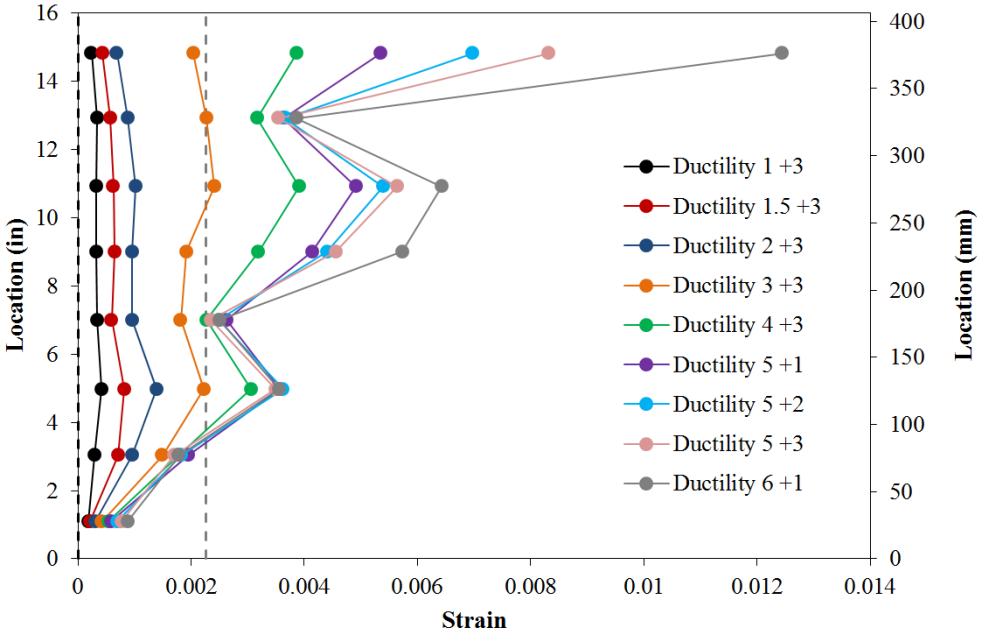

Figure 1.557 T22 – Spiral Strains on the South Side during Push Cycles

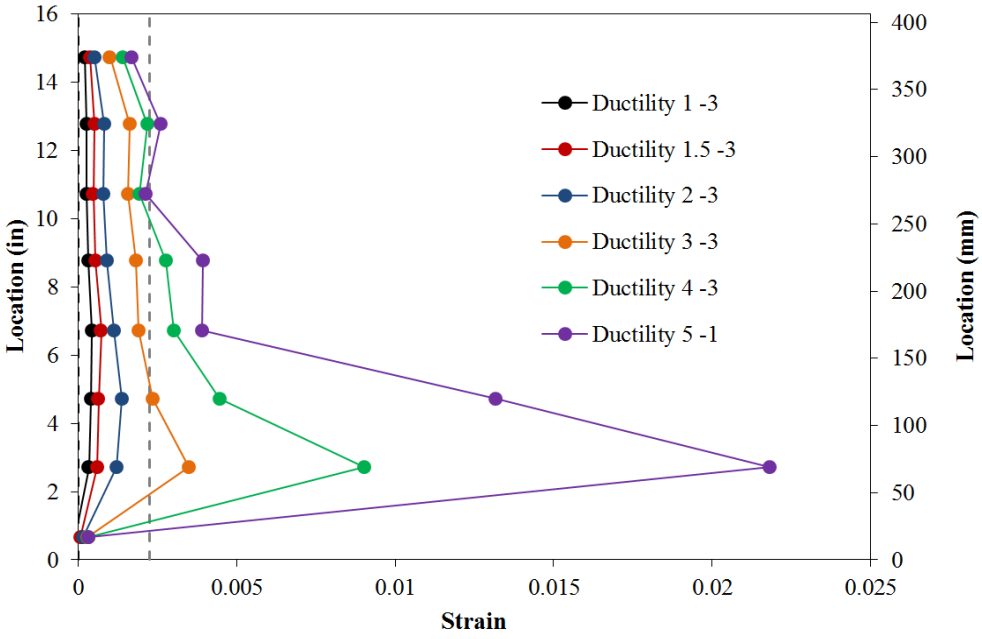

Figure 1.558 T22 – Spiral Strains on the North Side during Pull Cycles

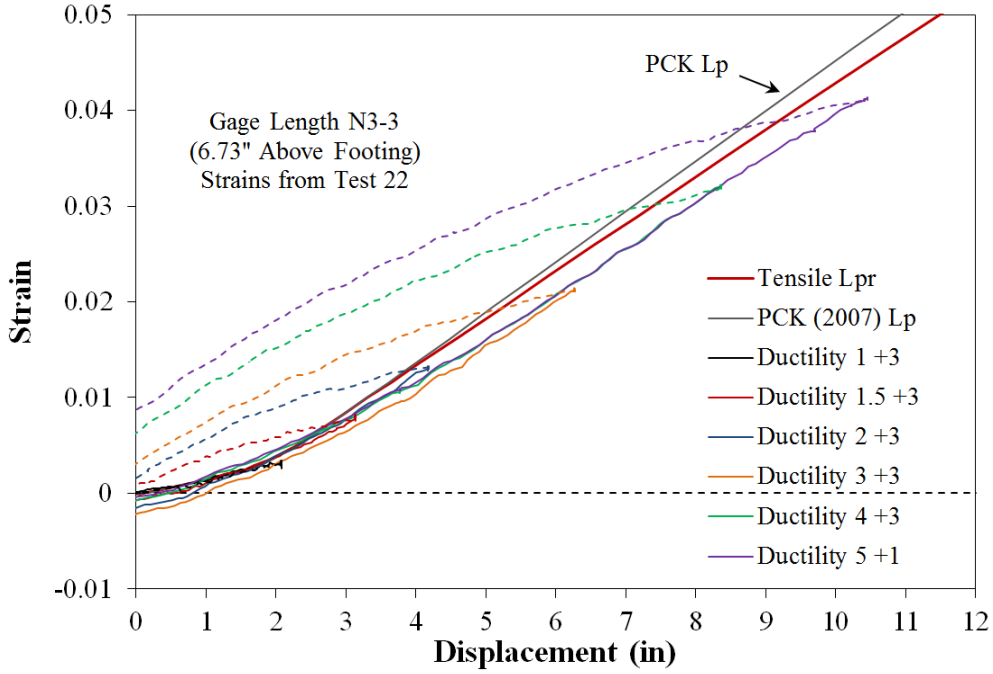

Figure 1.559 T22 – Tensile Strain-Displacement for Bar N3 during Push Cycles

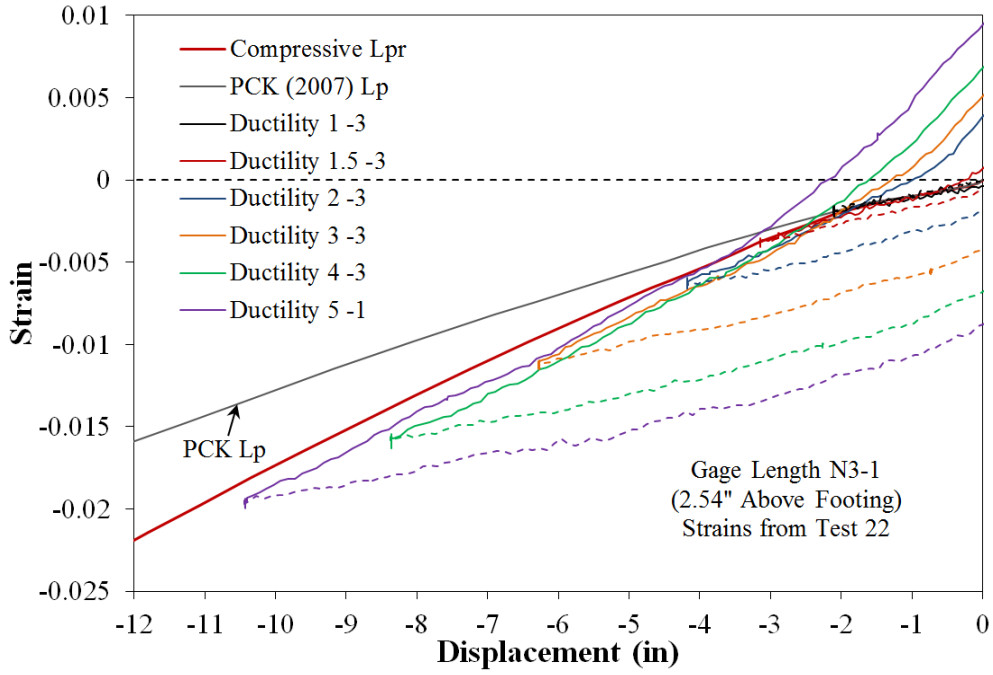

Figure 1.560 T22 – Compressive Strain-Displacement for Bar N3 during Pull Cycles

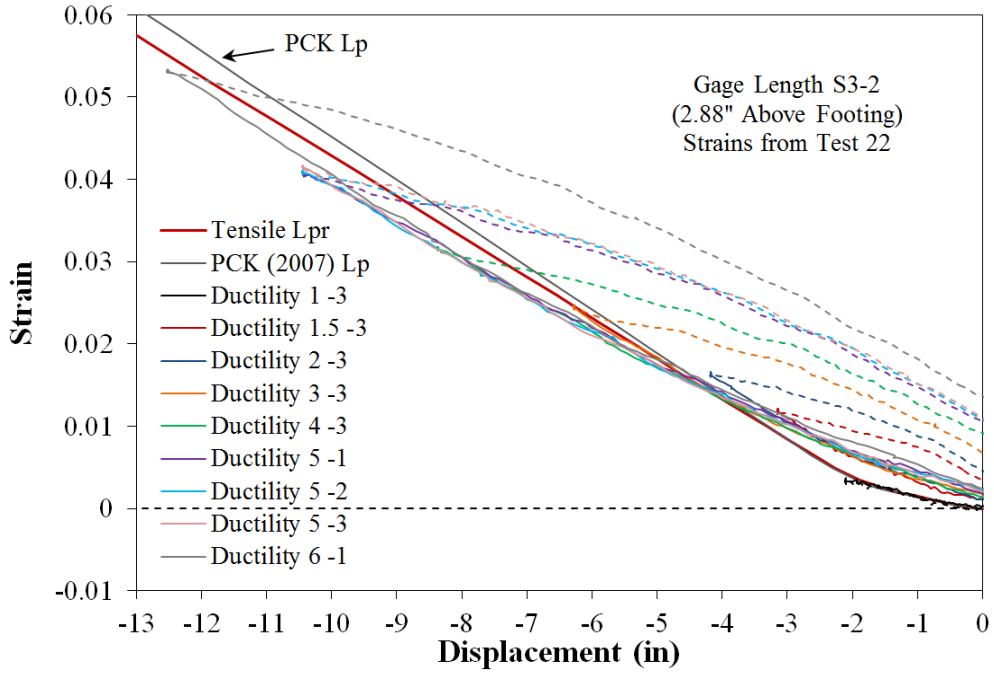

Figure 1.561 T22 – Tensile Strain-Displacement for Bar S3 during Pull Cycles

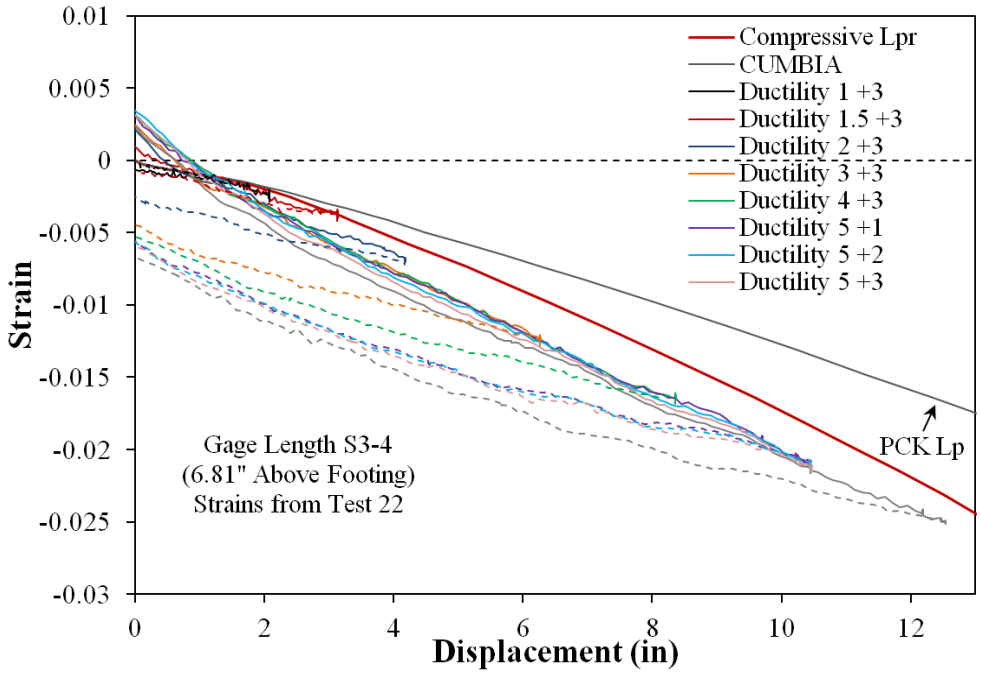

Figure 1.562 T22 – Compressive Strain-Displacement for Bar S3 during Push Cycles

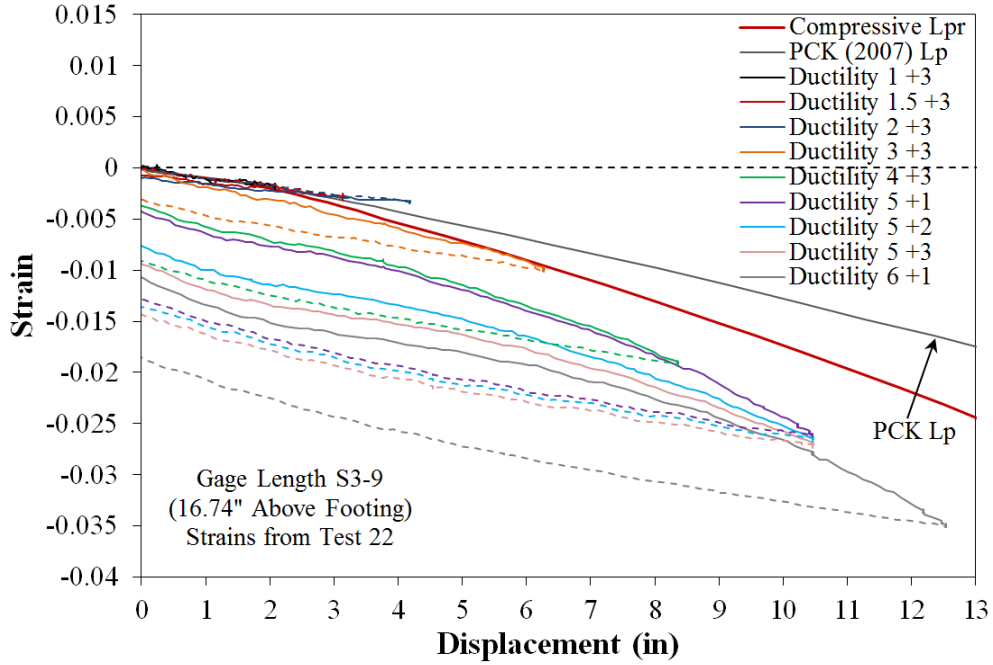

Figure 1.563 T22 – Compressive Strain-Displacement for Bar S3 during Push Cycles

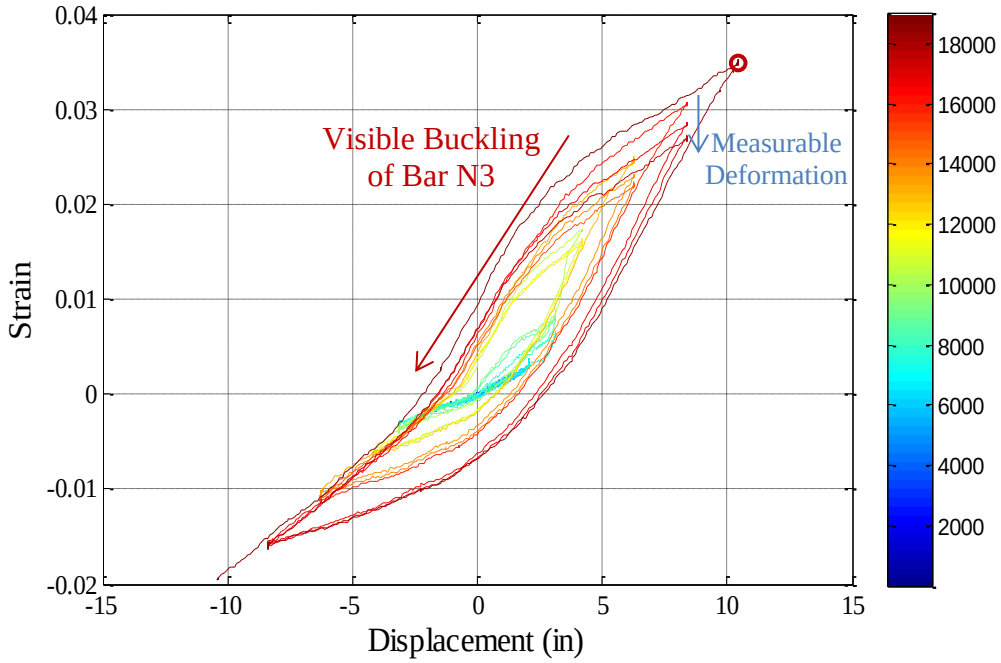

Figure 1.564 T22 – Strain Hysteresis for Bar N3 to Buckling (2.54" above the Footing)

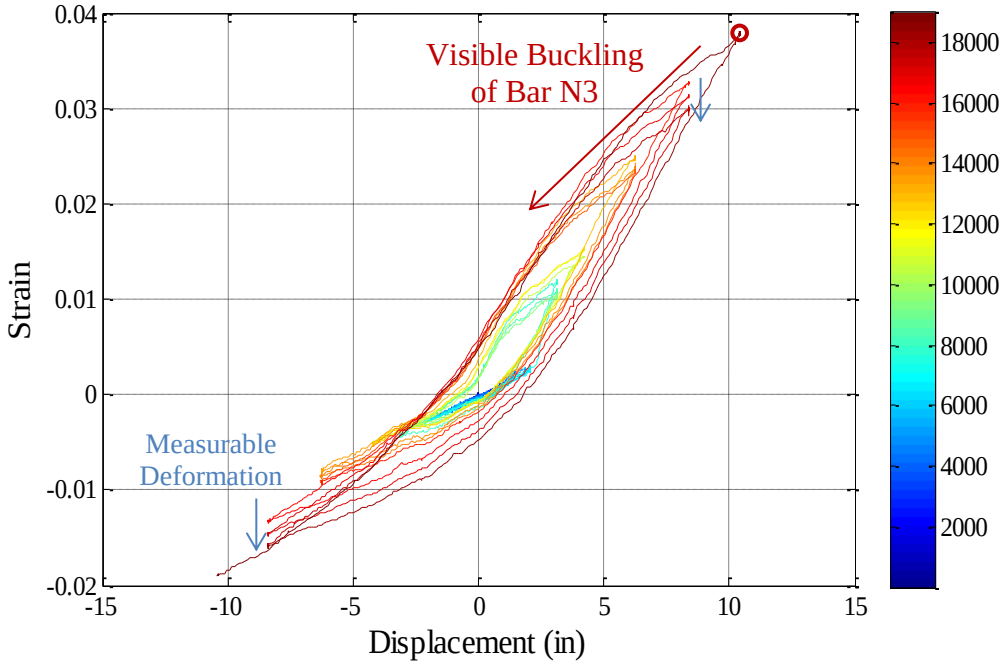

Figure 1.565 T22 – Strain Hysteresis for Bar N3 to Buckling (4.61" above the Footing)

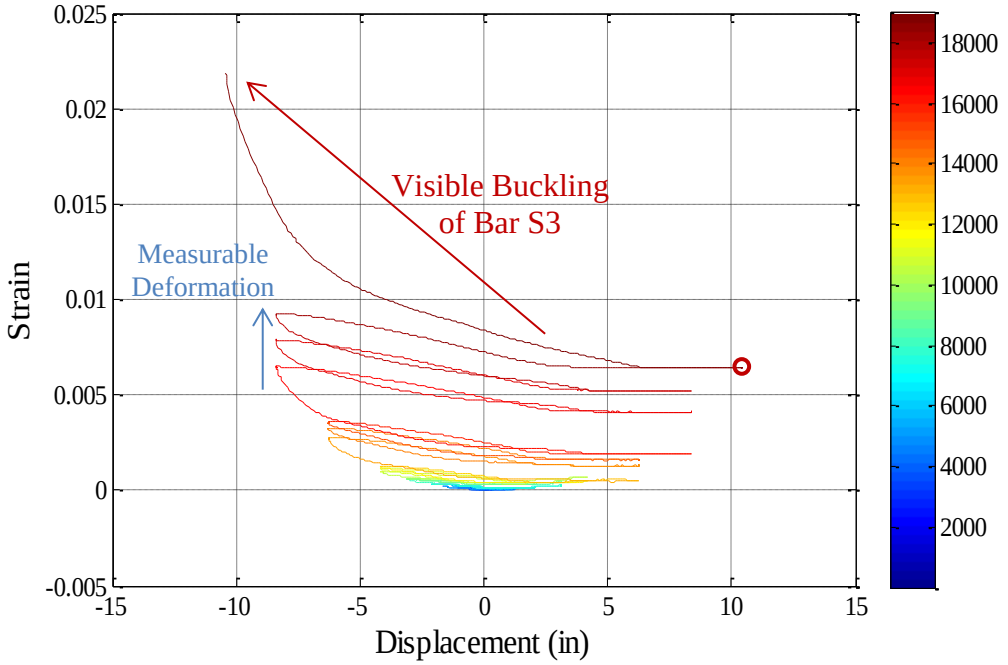

Figure 1.566 T22 – Spiral Strain Hysteresis over North Bucked Region (2.72" Above)

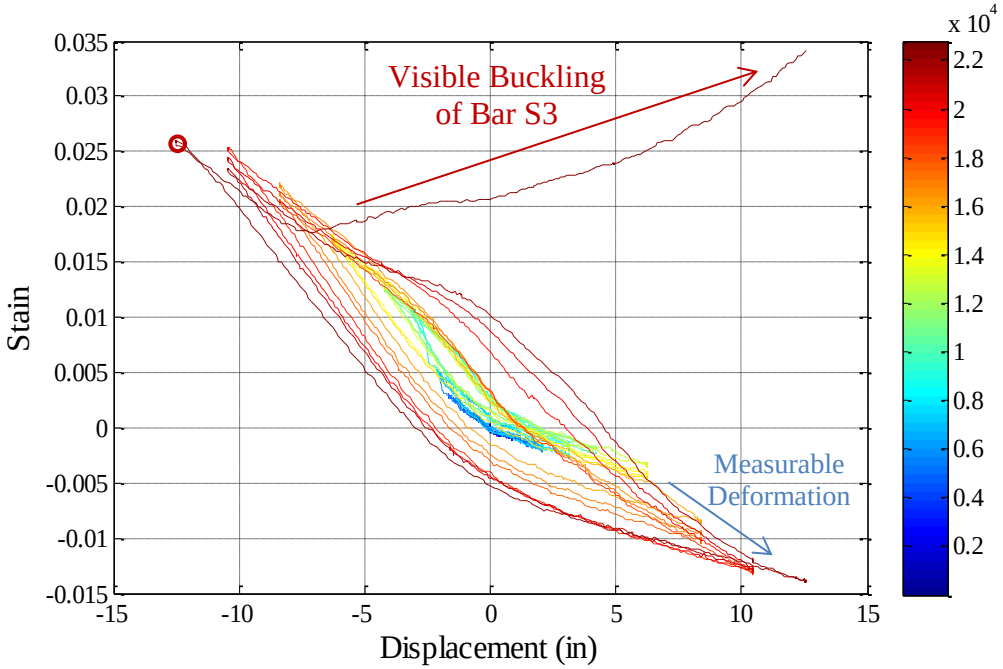

Figure 1.567 T22 – Strain Hysteresis for Bar S3 to Buckling (14.72" above the Footing)

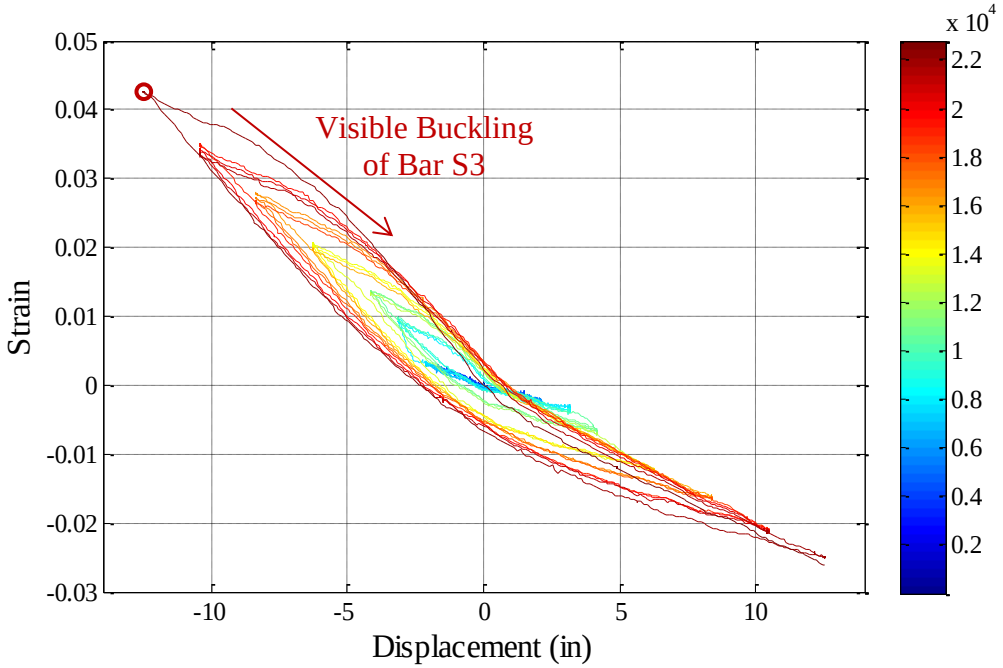

Figure 1.568 T22 – Strain Hysteresis for Bar S3 to Buckling (6.81" above the Footing)

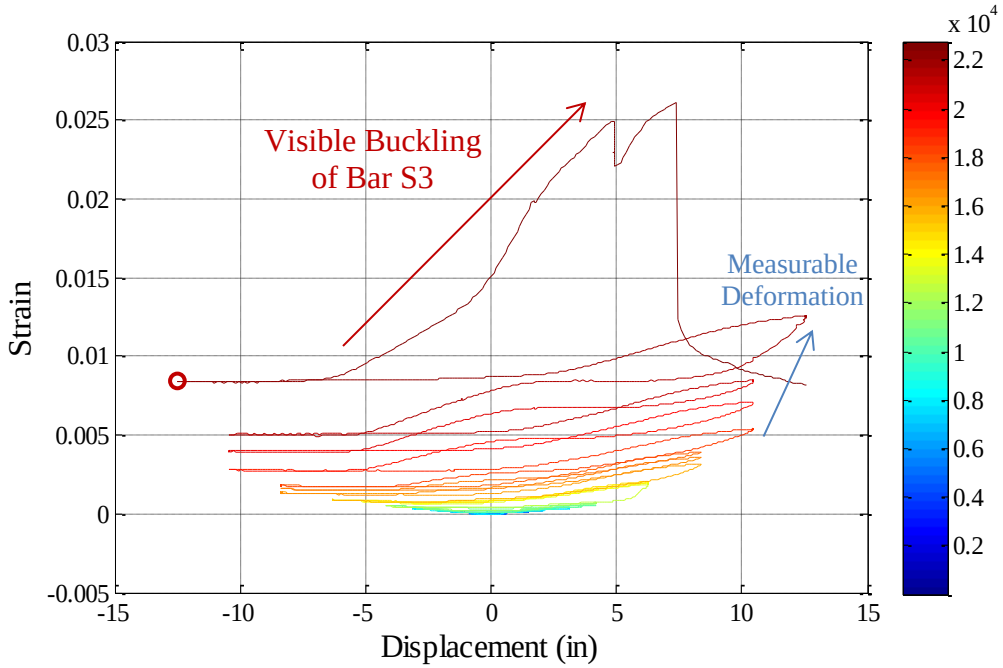

Figure 1.569 T22 – Spiral Strain Hysteresis over South Bucked Region (14.81" Above)

Test 22 Aspect Ratio of 7.33 and 10% Axial Load – Curvature and Strain Penetration

The cross section curvature for each horizontal section above the footing is determined by connecting the strain measurements from all eight instrumented bars with a least squared error line. The curvature is then extracted from the slope of the least squared error line, see Figure 1.570 and Figure 1.571. The cross section curvature profiles in these figures are shown for the first horizontal section above the footing-column interface which had measurements for all six instrumented bars. This is because the target markers in the lowest gage lengths for bars near the middle of the column were not visible to the Optotrak position monitor. For these sections, it appears that the plane sections hypothesis is appropriate. Vertical curvature profiles are plotted for push and pull cycles in Figure 1.572 and Figure 1.573 respectively. These figures show that plastic curvatures have a linear distribution at higher displacement ductility levels. The extent of plastic curvatures above the footing can be calculated by determining where the linear plastic curvature distribution intersects the

triangular yield curvature profile, shown as a grey dashed line. The measured spread of plasticity is depicted by circular data points in Figure 1.579 as a function of base section curvature ductility.

The target marker on each bar placed closest the footing-column interface can be used to create bond slip hysteresis and horizontal bond slip profiles attributable to strain penetration. The bond slip hysteresis for bars N3 and S3 appear in Figure 1.574 and Figure 1.575 respectively. If the tensile and compressive bond slips of the instrumented bars are plotted along the cross section depth, the base rotation attributable to strain penetration may be calculated. The slip profiles for push and pull cycles appear in Figure 1.576 and Figure 1.577 respectively. The rotation of the base section can be extracted from the slope of the least squared error line connecting all of the measured bar slips.

Combining the curvatures over the instrumented region (5ft above the footing), bar slip profiles, and an elastic curvature assumption above the instrumented region, the top column displacement can be calculated by integrating the curvature distributions and extrapolating the fixed-end rotations to the center of loading. The top column displacements calculated from the Optotrak system are compared to displacements measured with a string potentiometer at the center of loading in Figure 1.578. The Optotrak integrated displacements match well throughout the entire range of response, implying that the shear displacement component is small.

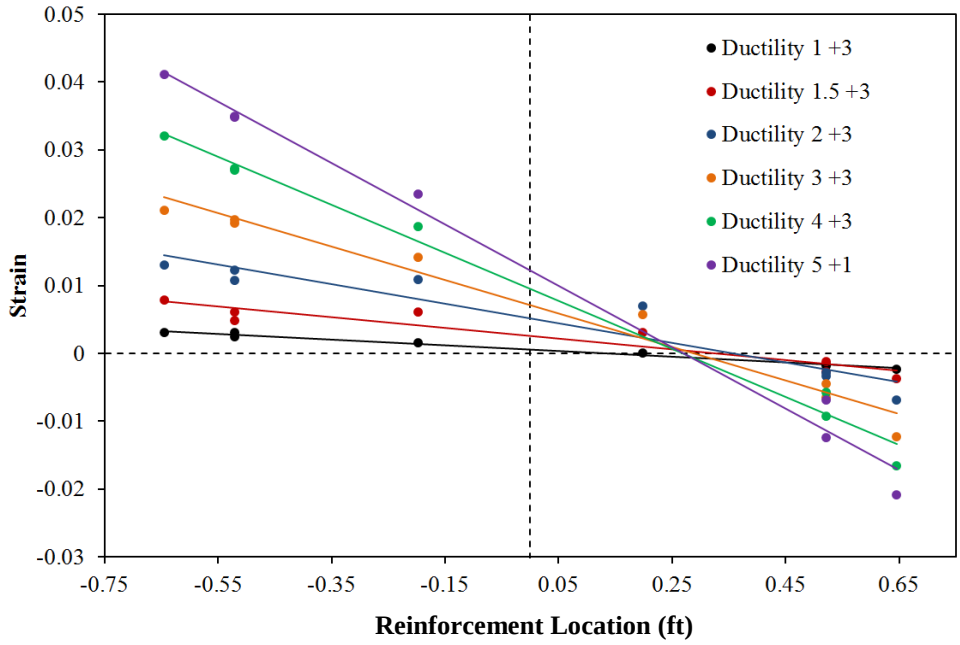

Figure 1.570 T22 – Cross Section Curvatures during Push Cycles (6.78" above Footing)

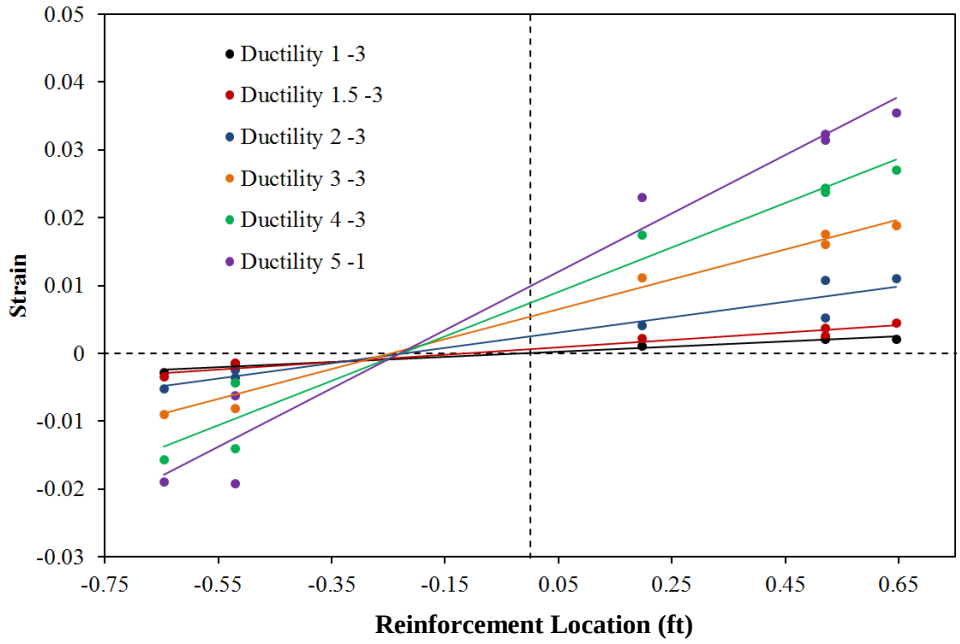

Figure 1.571 T22 – Cross Section Curvatures during Pull Cycles (4.76" above Footing)

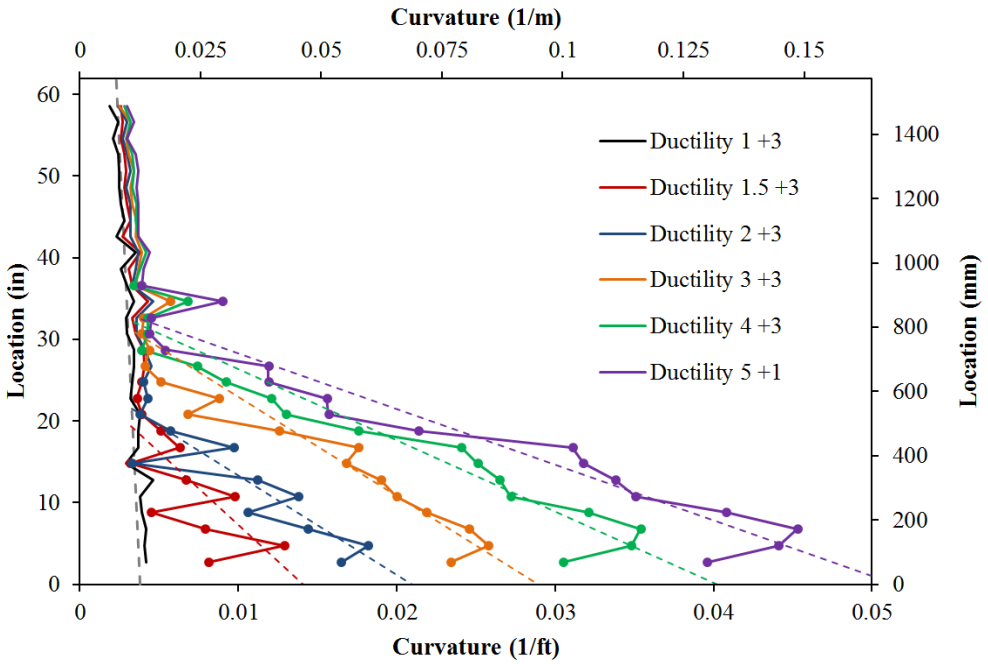

Figure 1.572 T22 – Push Cycle Curvature Profiles with Plastic Regression

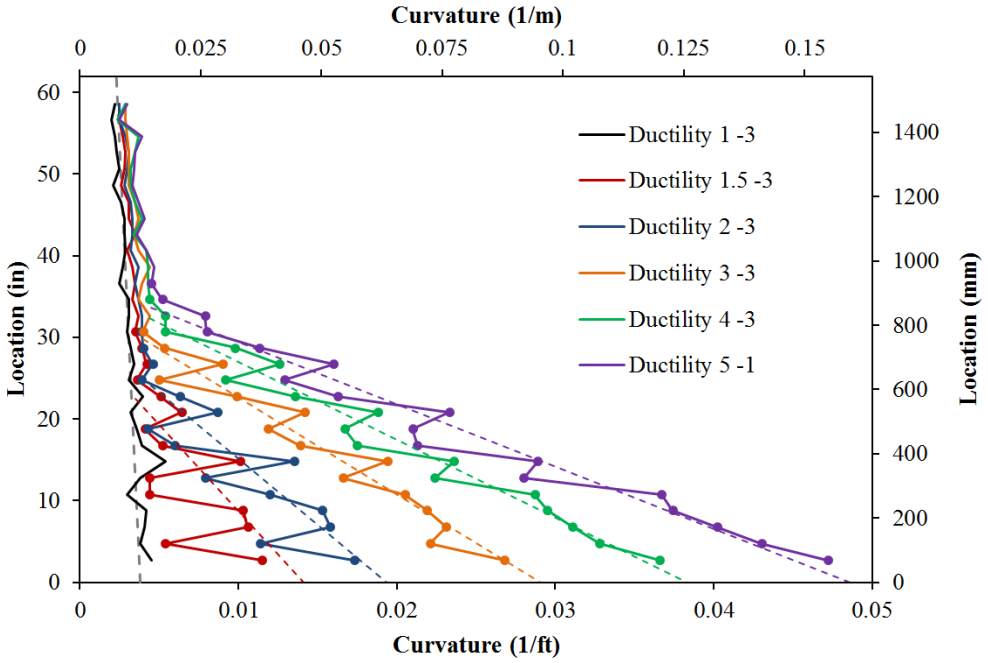

Figure 1.573 T22 – Pull Cycle Curvature Profiles with Plastic Regression

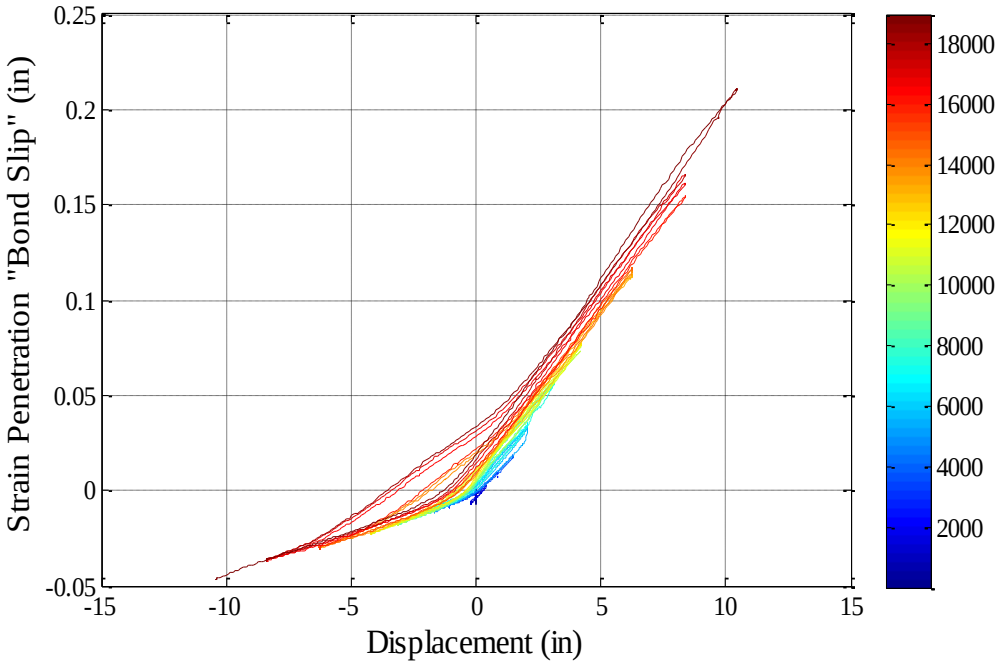

Figure 1.574 T22 – Bar N3 Bond Slip Hysteresis due to Strain Penetration

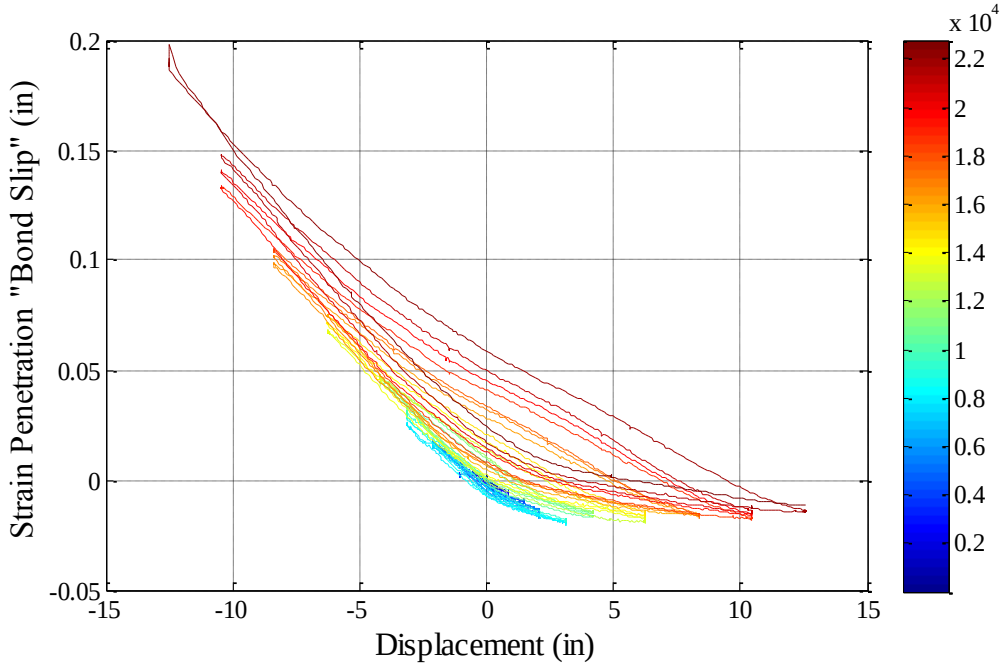

Figure 1.575 T22 – Bar S3 Bond Slip Hysteresis due to Strain Penetration

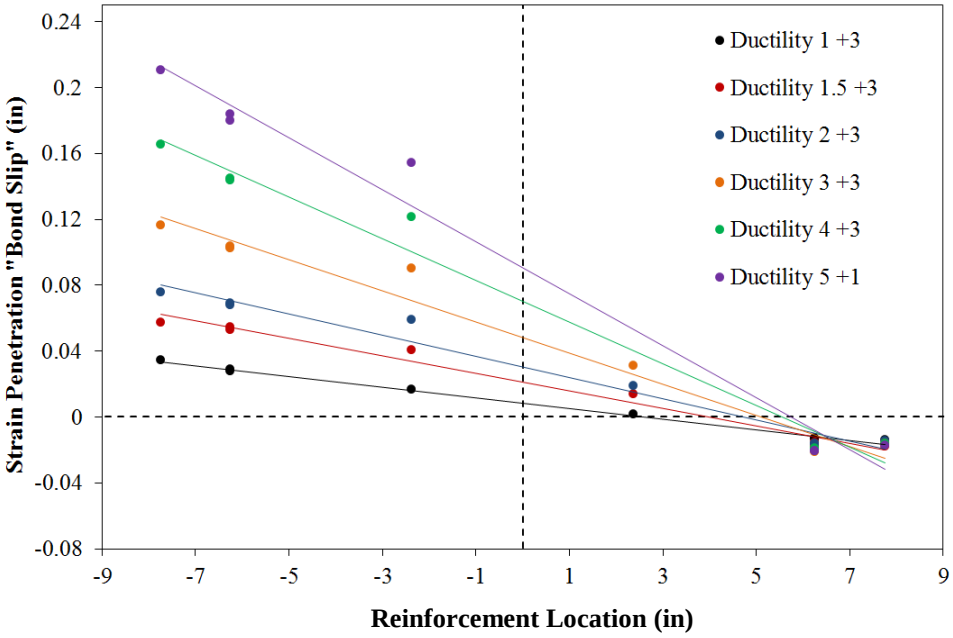

Figure 1.576 T22 – Bond Slip Profiles during Push Cycles due to Strain Penetration

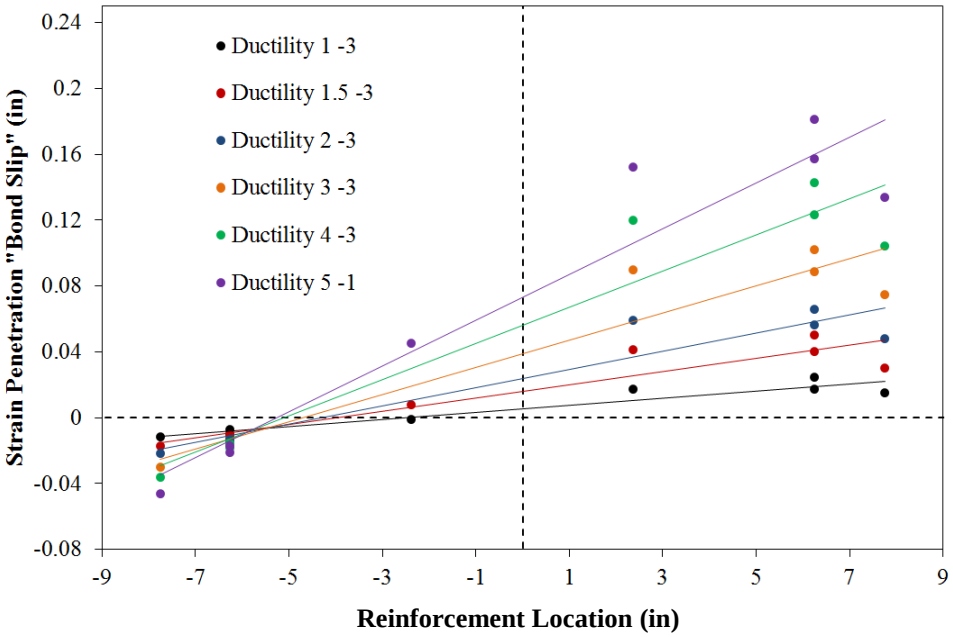

Figure 1.577 T22 – Bond Slip Profiles during Pull Cycles due to Strain Penetration

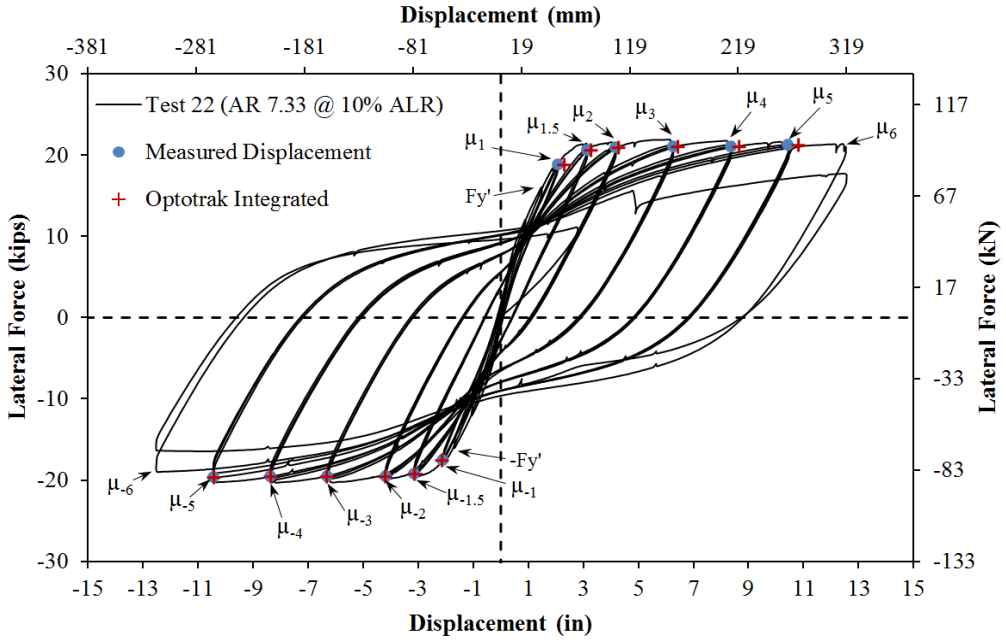

Figure 1.578 T22 – Comparison of Measured and Optotrak Integrated Displacements

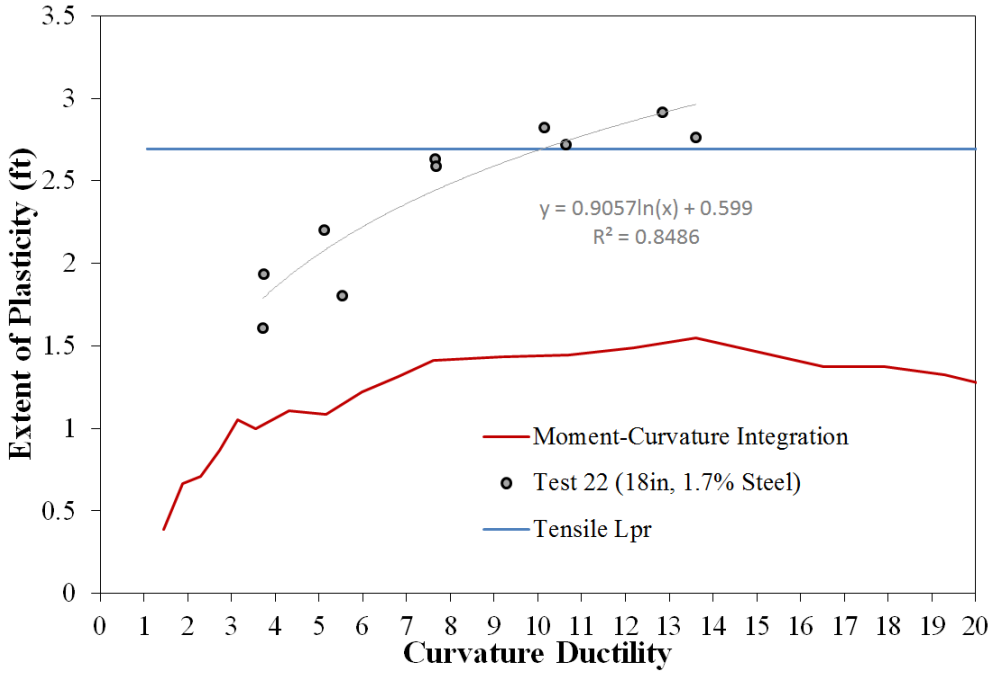

Figure 1.579 T22 – Measured Spread of Plasticity (Circular Data Points)

1.3.5 Test 23 – Aspect Ratio of 8.67 and 5% Axial Load

Table 1.41 Observations for Test 23 – Aspect Ratio of 8.67 and 5% Axial Load

VALUES OF INTEREST:	
Concrete Compressive Strength:	$f_c' = 6606\ psi$
Axial Load:	$P = 75\ kips\ \ (P/(f_c' A_g) = 5\%)$
Column Length and Aspect Ratio:	$13ft\ \ (L/D = 8.67)$
Analytical First Yield Force:	$F_y' = 11.55\ kips$
Experimental First Yield Displacement:	$\Delta_y' = 2.01"$
Analytical Nominal Moment Capacity:	$M_n = 207.1\ kip * ft$
Equivalent Yield Displacement:	$\Delta_y = 2.78"$
Maximum Lateral Force:	$16.26\ kips$
DAMAGE OBSERVATIONS:	
First Cracking North:	$1/2Fy' = 0.63"$
First Cracking South:	$-1/2Fy' = -0.62"$
Cover Concrete Crushing North:	$\mu_3^{-1} = -8.31"$
Cover Concrete Crushing South:	$\mu_3^{+1} = 8.31"$
Transverse Steel Yield North:	At $-9.08"$ during pull to $\mu_4^{-1} = -11.12"$
Transverse Steel Yield South:	At $10.83"$ during push to $\mu_4^{+1} = 11.09"$
Longitudinal Bar Buckling North:	Reversal from $\mu_6^{+1} = 16.65"$
Longitudinal Bar Buckling South:	Reversal from $\mu_6^{-1} = -16.65"$
Longitudinal Bar Fracture North:	At $5.50"$ during push to $\mu_7^{+2} = 19.43"$
Longitudinal Bar Fracture South:	Test Concluded without Fracture of South Bars

$*\mu_6^{-1} = -12.53"$represents the first pull cycle of displacement ductility six

Table 1.42 Strain Data Summary for Test 23 – Aspect Ratio of 8.67 and 5% Axial Load

MATERIAL STRAINS:	
Cover Concrete Crushing North:	$\varepsilon_s = 0.0052\ (compression)\ \ ^*\mu_{\Delta 2} = -5.56"$
Cover Concrete Crushing South:	$\varepsilon_s = 0.0062\ (compression)\ \ ^*\mu_{\Delta 2} = 5.54"$
Transverse Steel Yield North:	$\varepsilon_s = 0.0136\ (compression)$
Transverse Steel Yield South:	$\varepsilon_s = 0.0151\ (compression)$
Longitudinal Bar Buckling North:	$\varepsilon_s = 0.051\ (peak\ tension\ prior\ to\ bb)$
	$\varepsilon_s = 0.022\ (peak\ comp.\ prior\ to\ bb)$
Longitudinal Bar Buckling South:	$\varepsilon_s = 0.048\ (peak\ tension\ prior\ to\ bb)$
	$\varepsilon_s = 0.031\ (peak\ comp.\ prior\ to\ bb)$
Mander (1988) Ultimate Concrete Compression Strain, $\varepsilon_{cu} = 0.0199$	

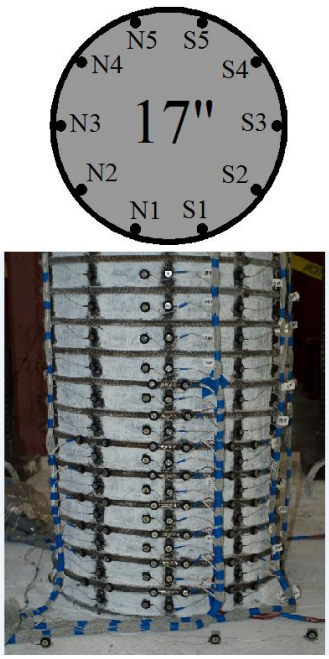

Name	x [mm]	y [mm]	z [mm]
Marker_1	169.570	-694.910	-2611.062
Marker_2	170.205	-641.193	-2611.110
Marker_3	171.597	-594.726	-2611.574
Marker_4	169.156	-544.798	-2610.561
Marker_5	170.116	-492.121	-2611.579
Marker_6	169.271	-443.175	-2611.191
Marker_7	168.224	-396.535	-2610.618
Marker_8	169.438	-347.709	-2611.148
Marker_9	169.582	-297.839	-2610.950
Marker_10	168.936	-246.482	-2610.402
Marker_11	169.689	-197.529	-2610.705
Marker_12	169.091	-147.943	-2610.051
Marker_13	169.744	-99.317	-2609.968
Marker_14	169.118	-49.669	-2609.104
Marker_15	170.481	-0.909	-2609.341
Marker_16	168.753	47.445	-2608.111
Marker_17	168.479	95.395	-2608.178
Marker_18	168.429	146.672	-2607.526
Marker_19	168.986	196.411	-2607.677
Marker_20	168.108	245.567	-2606.926
Marker_21	168.601	292.830	-2606.560
Marker_22	168.001	341.971	-2605.898
Marker_23	169.099	392.564	-2606.259
Marker_24	168.392	441.807	-2605.823
Marker_25	167.860	488.106	-2605.056
Marker_26	168.529	535.798	-2605.452
Marker_27	168.938	587.084	-2605.602
Marker_28	169.293	636.853	-2606.118
Marker_29	169.018	686.467	-2606.140
Marker_30	167.608	736.931	-2605.678
Marker_31	169.973	790.430	-2606.796

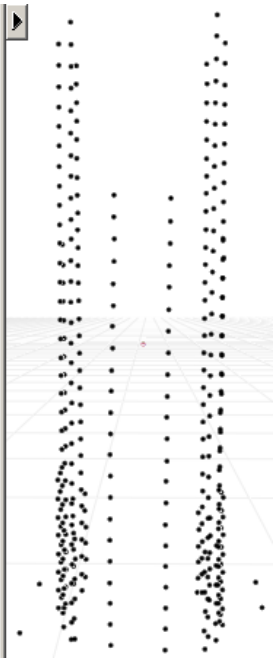

Figure 1.580 T23 – Cross Section Bar Designation and Target Marker Application

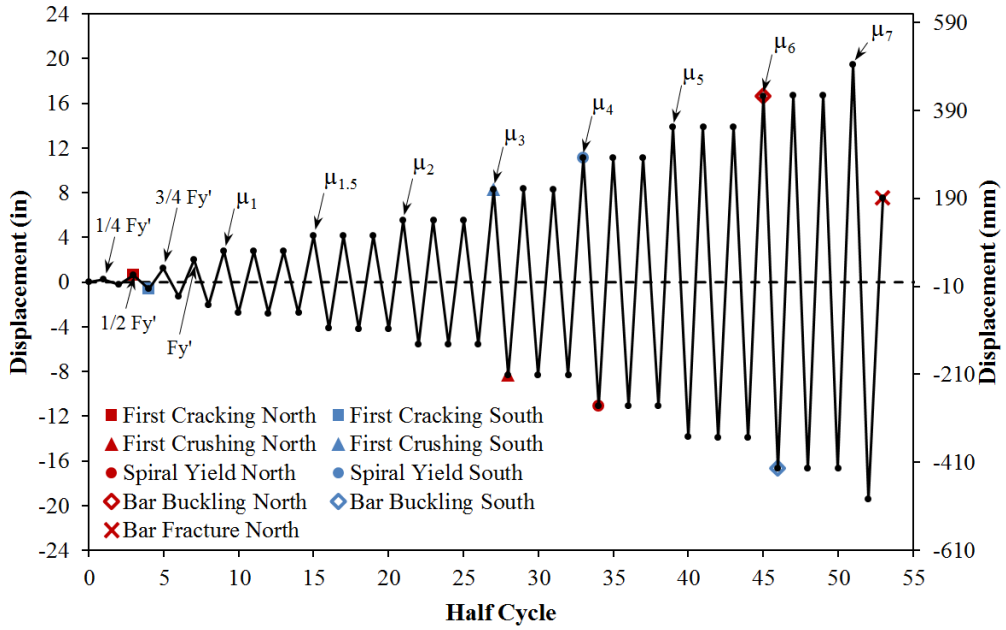

Figure 1.581 T23 – Symmetric Three Cycle Set Load History

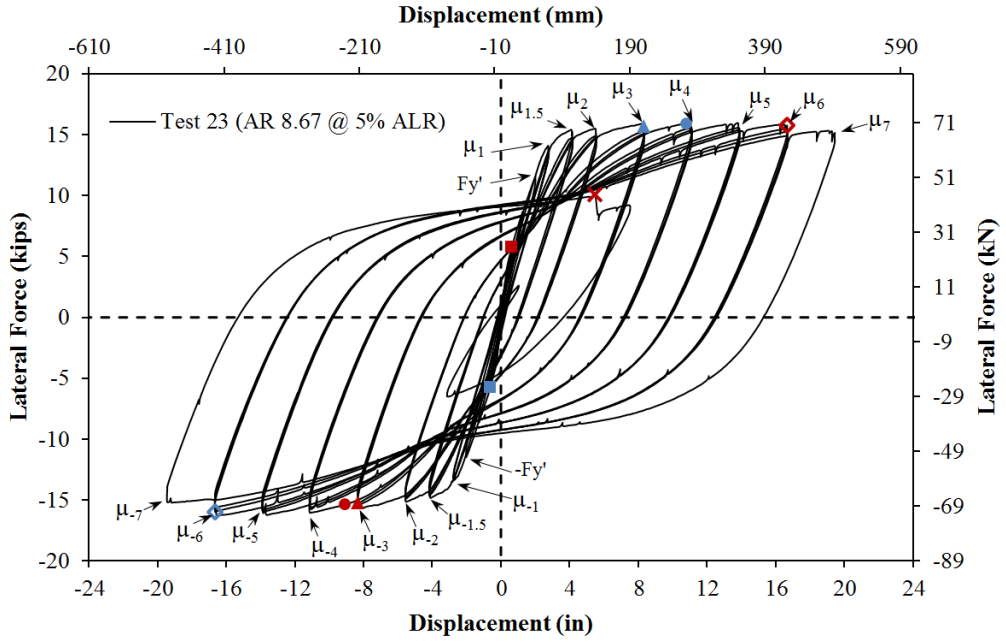

Figure 1.582 T23 – Lateral Force vs. Displacement Response

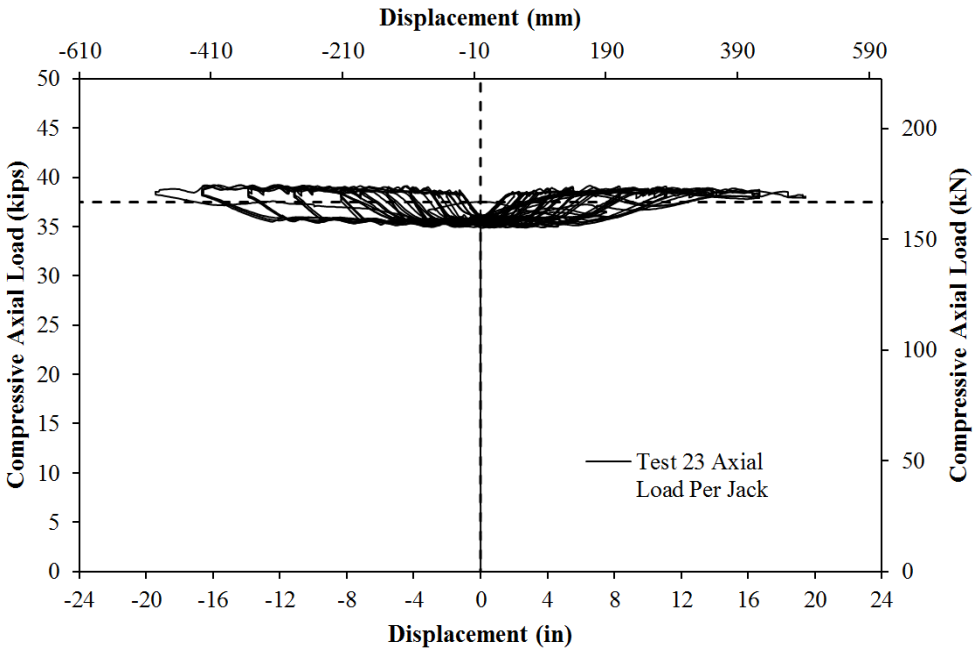

Figure 1.583 T23 – Compressive Axial Load from One Jack (Total = 2*Value)

Figure 1.584 T23 – Test Setup for the Largest Aspect Ratio Specimens

Test 23 Aspect Ratio of 8.67 and 5% Axial Load – Experimental Observations

The symmetric three-cycle-set laboratory load history is typically used to evaluate the seismic performance of structural components. The load history begins with elastic cycles to the following increments of the analytically predicted first yield force: ¼ Fy', ½ Fy', ¾ Fy', and Fy'. The first yield force for the tested material and geometric properties was determined using moment-curvature analysis (Test 23: Cumbia Fy' = 11.55 kips with f'c = 6606 psi). The first yield displacement was obtained as an average for the experimental first yield push and pull cycles ($\Delta'_y = 2.01$"). Vertical strain profiles for both push and pull cycles up to the first yield force appear in Figure 1.585 with a dashed line representing the yield strain of the longitudinal reinforcement. The equivalent yield displacement, used to determine the displacement ductility levels ($\mu_{\Delta 1} = 1 * \Delta_y$), is then calculated as $\Delta_y = \Delta'_y(M_n/M'_y) = 2.78$" for Test 23. The symmetric three-cycle-set load history resumes with three balanced cycles at each of the following displacement ductility levels: 1, 1.5, 2, 3, 4, 5, 6, 7, 8, etc. The full symmetric three-cycle-set load history appears in Figure 1.581, and the resulting lateral force versus top column displacement hysteresis is shown in Figure 1.582.

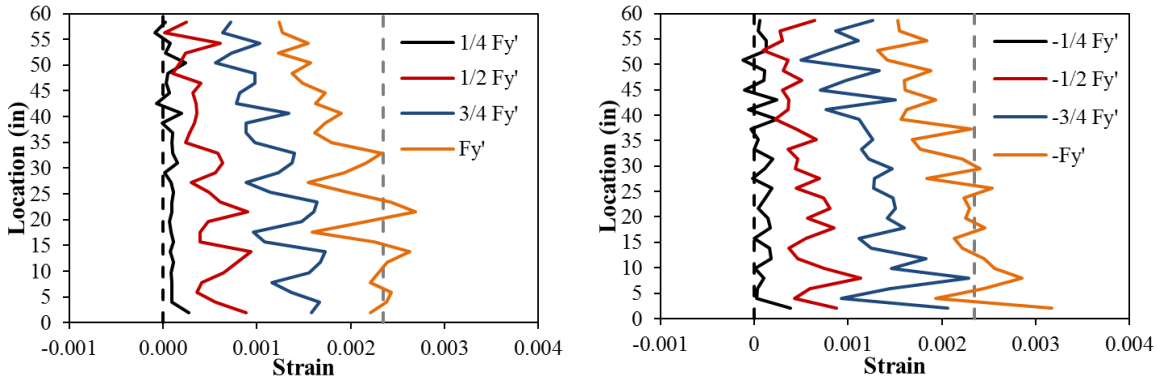

Figure 1.585 T23 – Strain Profiles before Yield (Left) Bar N3 and (Right) Bar S3

The test began with cycles in ¼ Fy' (first yield force) increments in each direction of loading until the first yield force was reached. The first cracks on the North and South sides of the specimen were observed during $(1/2Fy' = 0.63")$ and $(-1/2Fy' = -0.62")$ respectively. The crack distribution on all sides of the specimen at first yield, $(Fy' = 2.00")$ and $(-Fy' = -2.02")$, appears in Figure 1.586. The crack progression at displacement ductility 1, 1.5, and 2 appear in Figure 1.587, Figure 1.588, and Figure 1.589 respectively. During these cycles the cracks became more numerous and increased in inclination on the shear faces of the specimen. A small amount of core concrete crushed on the South side of the specimen during $(\mu_3^{+1} = 8.31")$, Figure 1.590. A similar observation was made on the North side of the specimen during $(\mu_3^{-1} = -8.31")$, Figure 1.590. The crushing on each side of the specimen during ductility three was not severe, and it appeared that only a thin layer of concrete flaked off between spiral layers. Photos of the crack distributions during displacement ductility 3, 4, and 5 appear in Figure 1.591, Figure 1.592, and Figure 1.593 respectively.

The North extreme fiber bar N3 visibly buckled after reversal from $(\mu_6^{+1} = 16.65")$, as shown in Figure 1.594. The South extreme fiber bar S3 showed signs of measurable deformation after reversal from $(\mu_6^{-1} = -16.65")$, see Figure 1.595. A definitive visible buckling observation could not be made at this time because the outward deformation was small. Figure 1.596 depicts additional deformation in previously buckled bar N3 at $(\mu_6^{-2} = -16.66")$ and bar S3 at $(\mu_6^{+3} = 16.67")$. It is clear that visible buckling occurred over the same region (6.5" above the footing) where measurable deformation was observed in bar S3. A second outward buckled region was observed 10.5" above the footing on buckled bar S3. The buckled deformation in bars S3 and N3 became worse during $(\mu_7^{+1} = 19.43")$ and $(\mu_7^{-1} = -19.44")$ respectively, see Figure 1.597. Adjacent bars N2 and N4 buckled during $(\mu_7^{-1} = -19.44")$. Previously buckled bar N3 ruptured at 5.50" during the push cycle to μ_7^{+2}, Figure 1.598. The test was concluded after bar fracture occurred, and photos of the specimen after removal of the instrumentation appear in Figure 1.599.

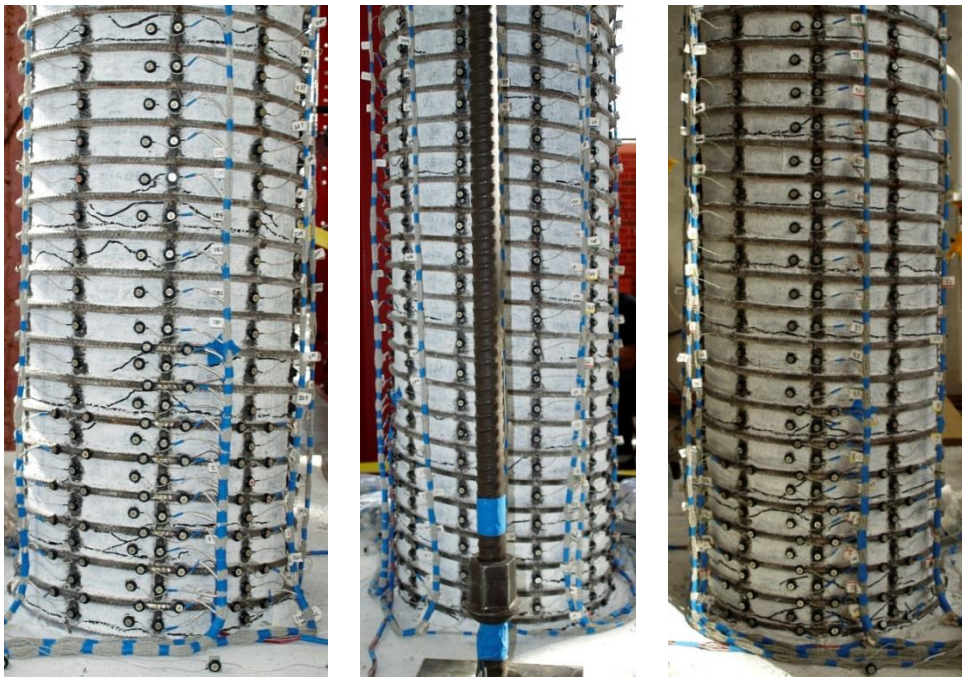

Figure 1.586 T23 – (Left) North at Fy', (Mid) Front at -Fy', and (Right) South at -Fy'

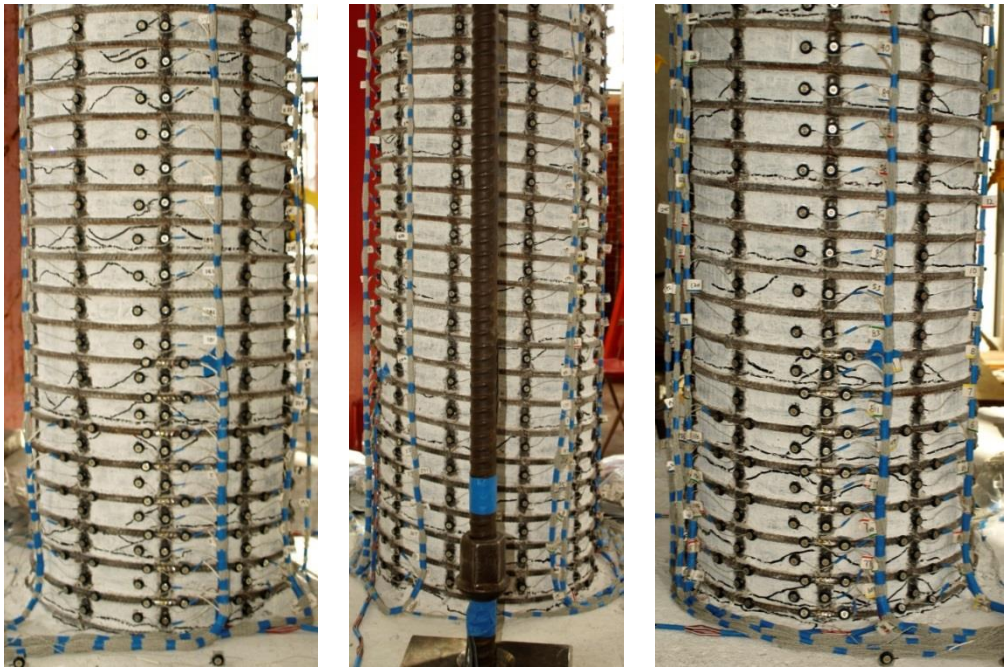

Figure 1.587 T23 – (Left) North at μ_1^{+3}, (Mid) Front at μ_1^{-3}, and (Right) South at μ_1^{-3}

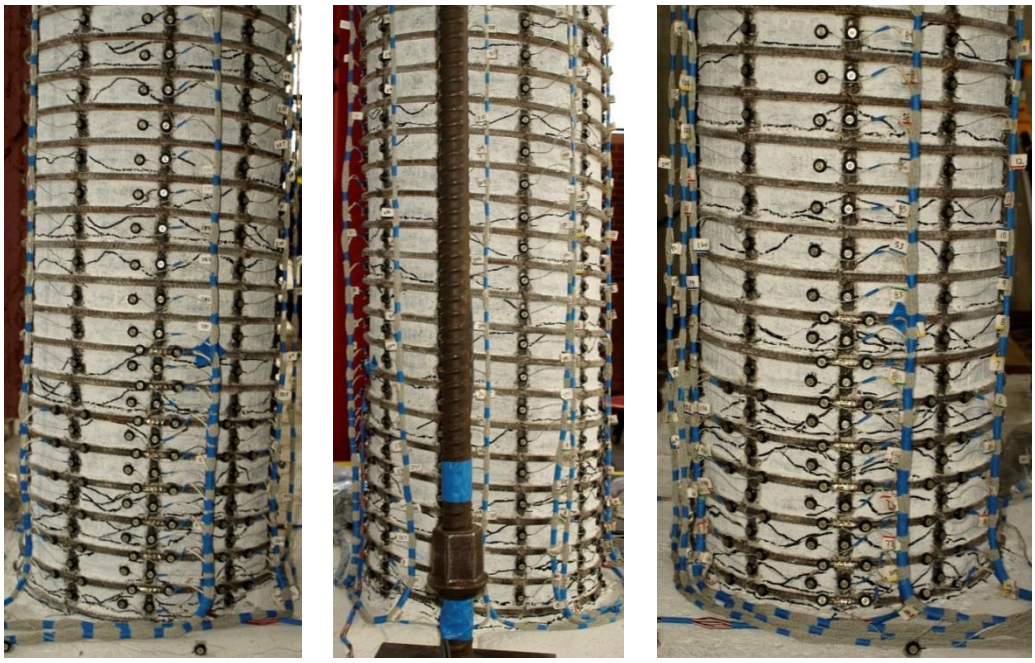

Figure 1.588 T23 – (Left) North at $\mu_{1.5}^{+3}$, (Mid) Front at $\mu_{1.5}^{-3}$, and (Right) South at $\mu_{1.5}^{-3}$

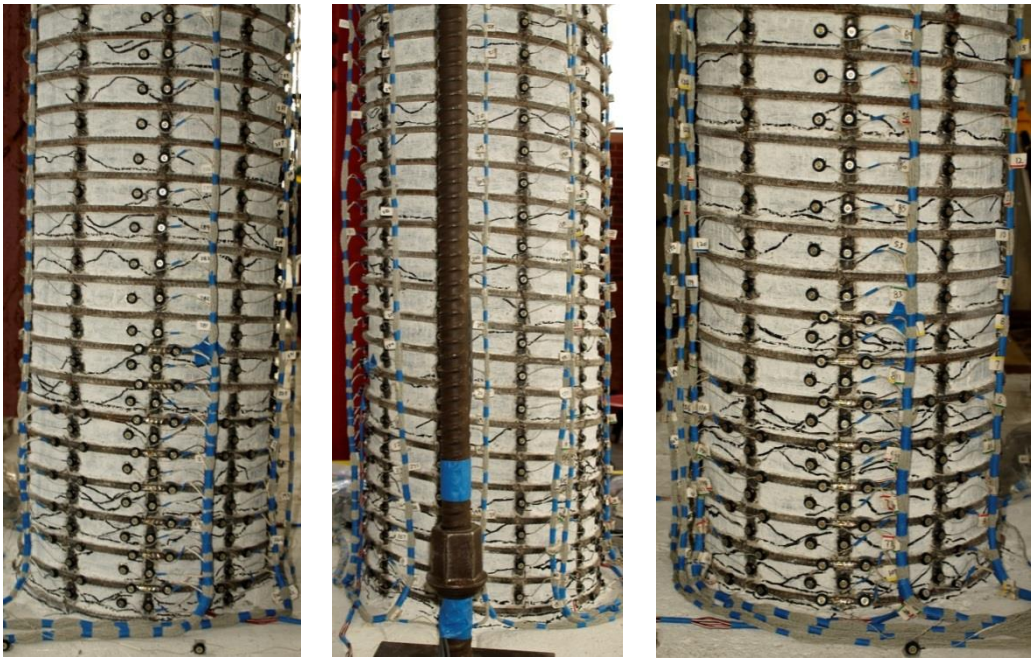

Figure 1.589 T23 – (Left) North at μ_{2}^{+3}, (Mid) Front at μ_{2}^{-3}, and (Right) South at μ_{2}^{-3}

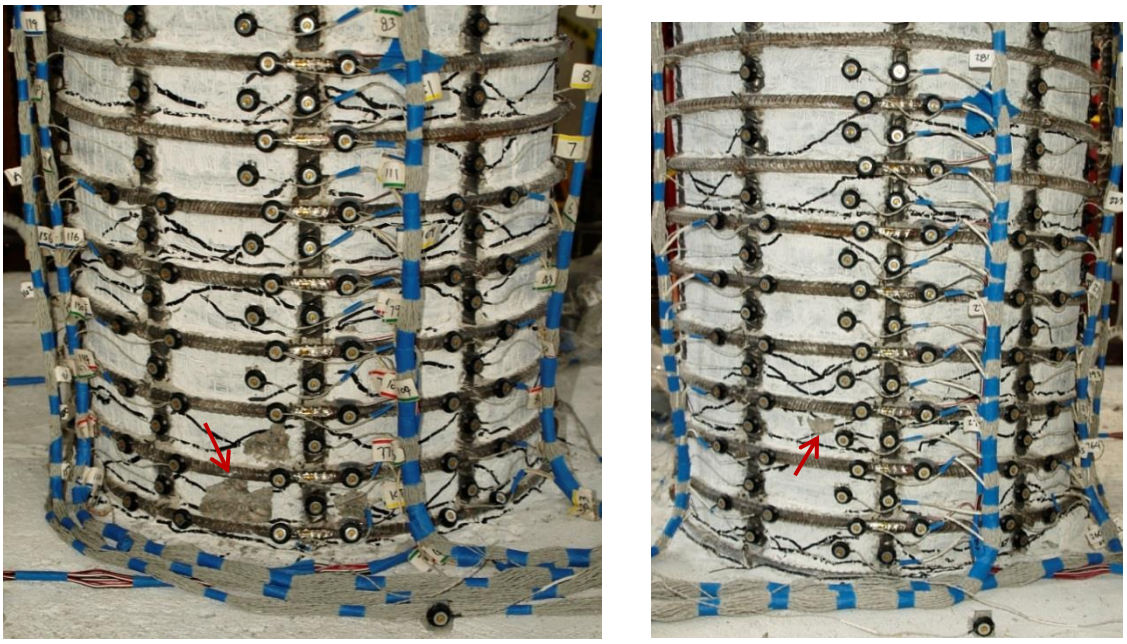

Figure 1.590 T23 – (Left) Concrete Crushing on the South Side at μ_3^{+1} and (Right) Concrete Crushing on the North Side at μ_3^{-1}

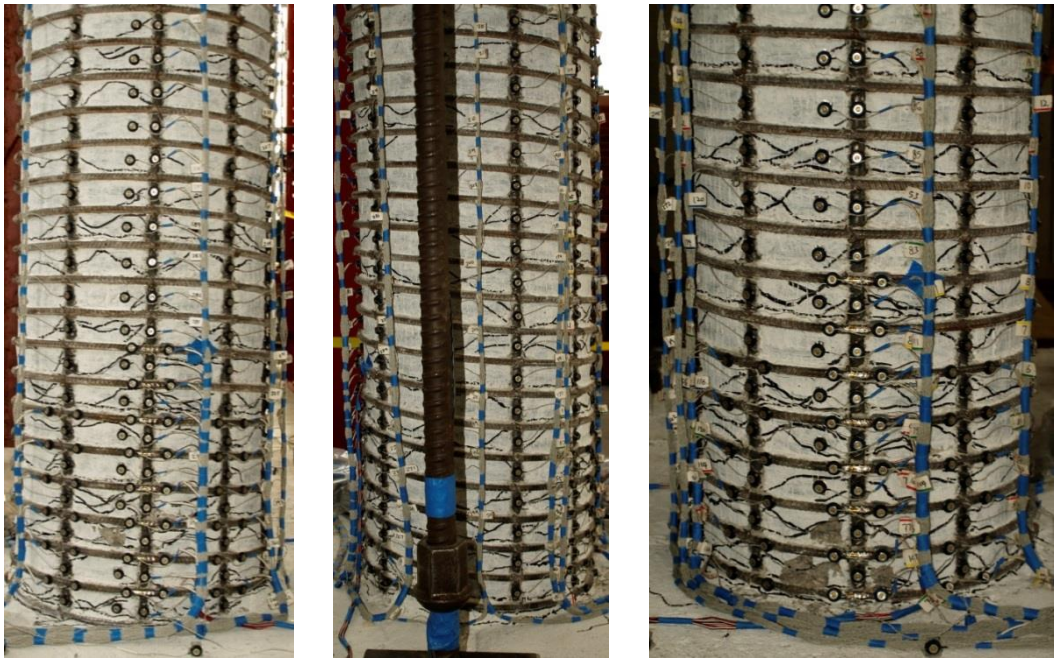

Figure 1.591 T23 – (Left) North at μ_3^{+3}, (Mid) Front at μ_3^{-3}, and (Right) South at μ_3^{-3}

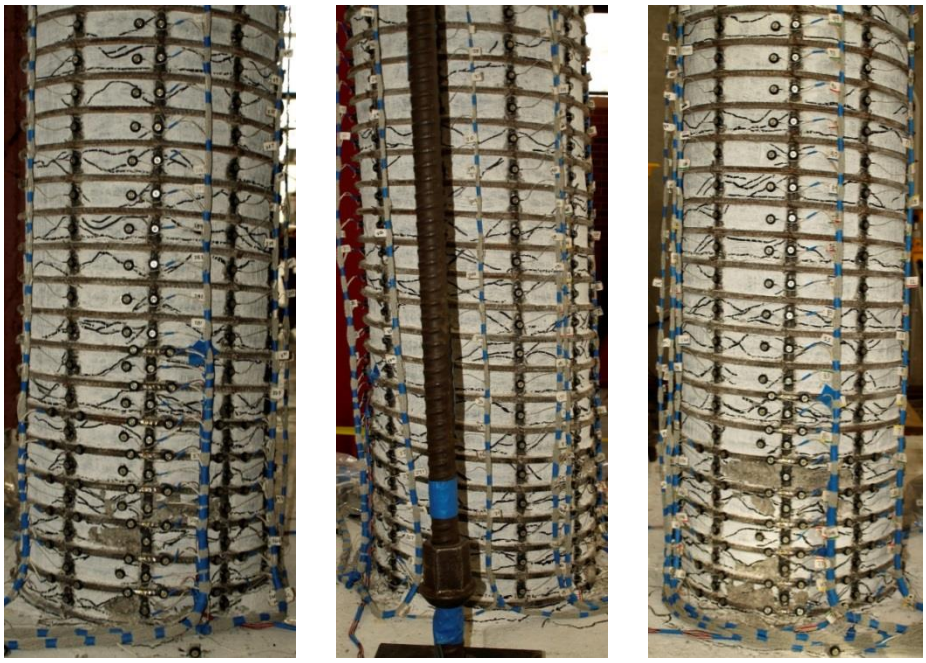

Figure 1.592 T23 – (Left) North at μ_4^{+3}, (Mid) Front at μ_4^{-3}, and (Right) South at μ_4^{-3}

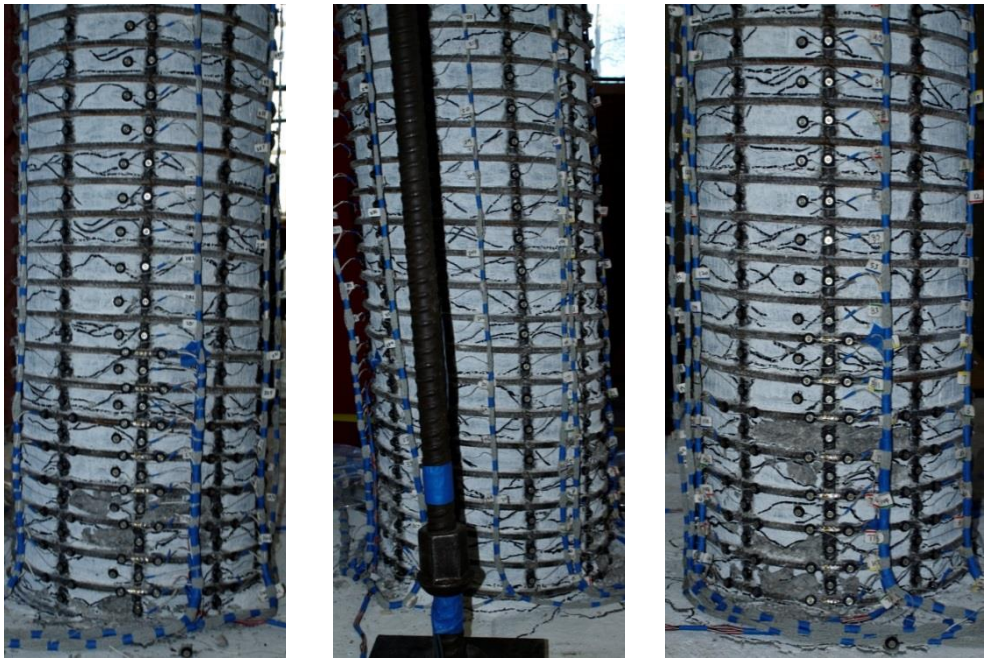

Figure 1.593 T23 – (Left) North at μ_5^{+3}, (Mid) Front at μ_5^{-3}, and (Right) South at μ_5^{-3}

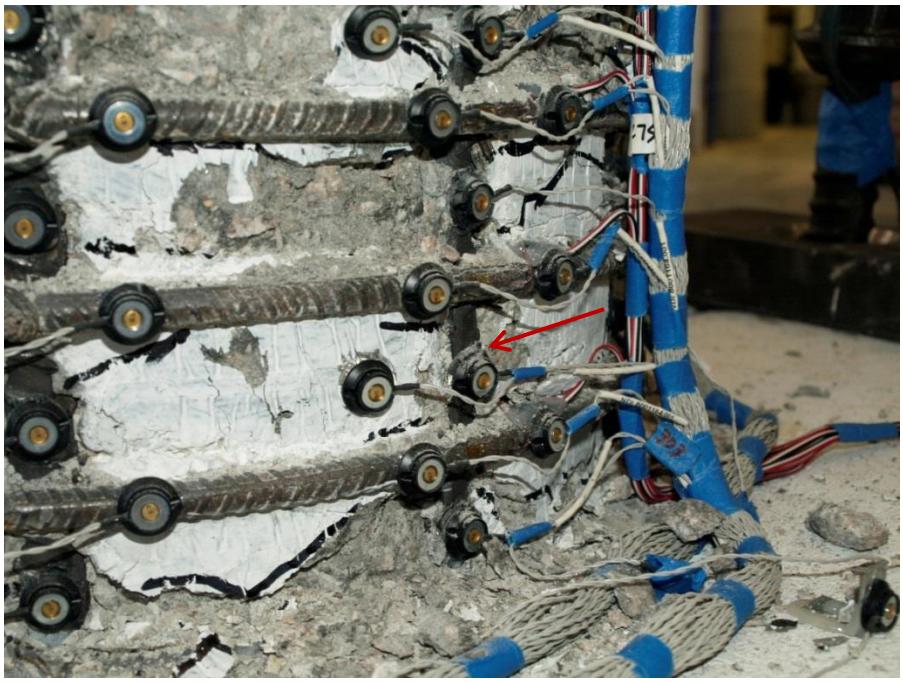

Figure 1.594 T23 – Buckling of Bar N3 after Reversal from ($\mu_6^{+1} = 16.65$")

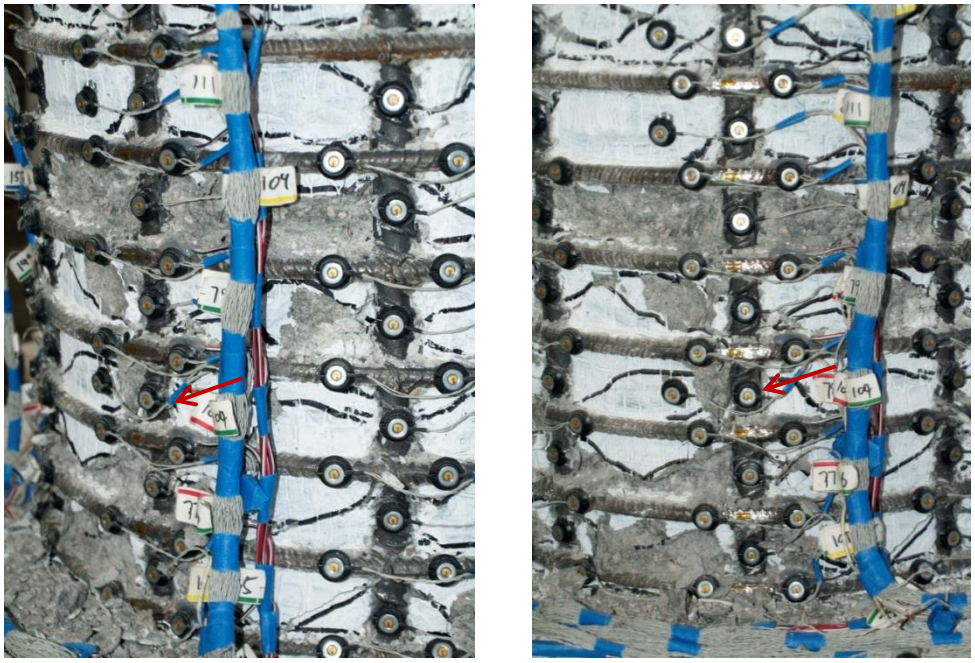

Figure 1.595 T23 – Measurable Deformation of Bar S3 during ($\mu_6^{+2} = 16.65$")

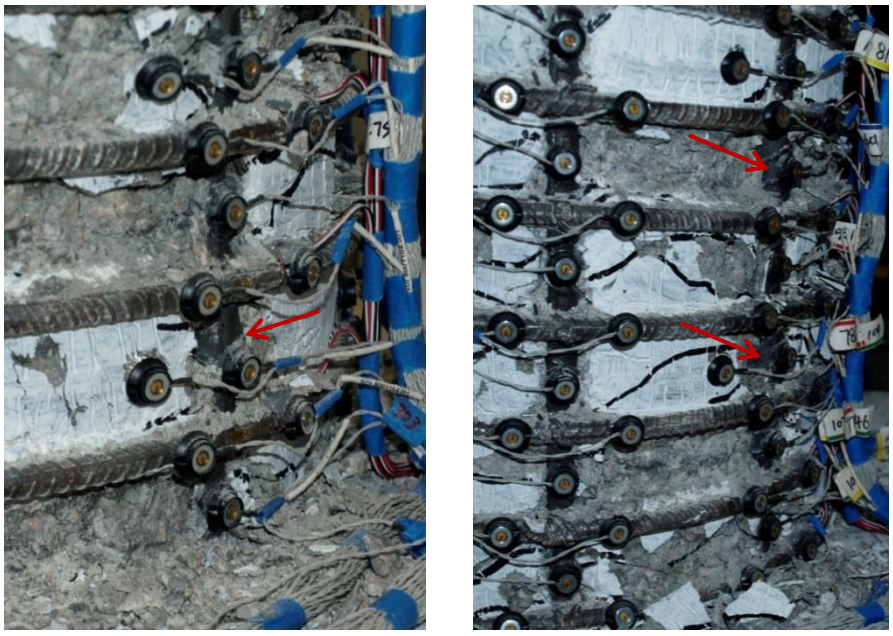

Figure 1.596 T23 – (Left) Additional Deformation in Buckled Bar N3 at ($\mu_6^{-2} = -16.66$") and (Right) Additional Deformation in Buckled Bar S3 at ($\mu_6^{+3} = 16.67$")

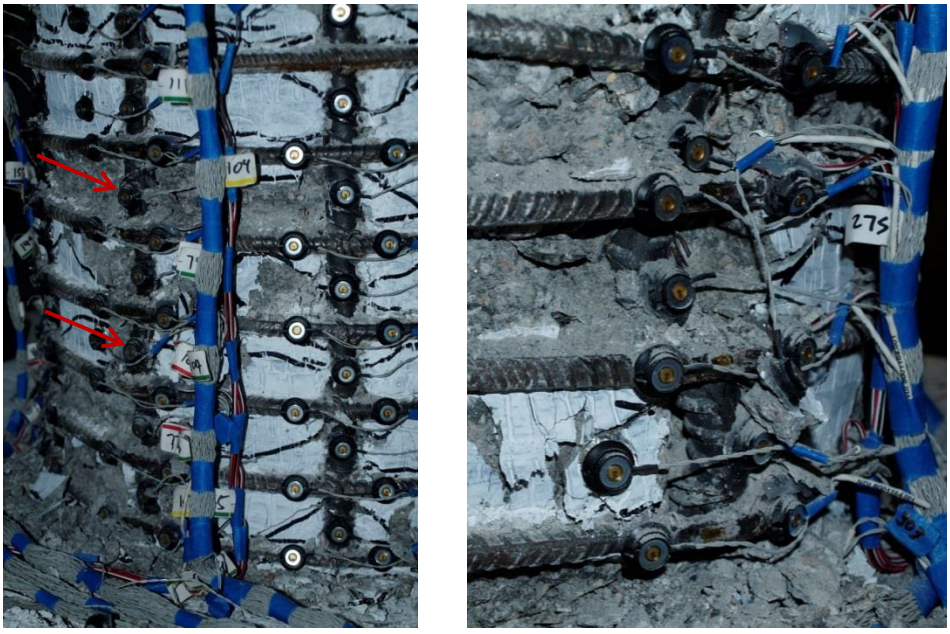

Figure 1.597 T23 – (Left) Additional Deformation in Buckled Bar S3 at ($\mu_7^{+1} = 19.43$") and (Right) Additional Deformation in Buckled Bar N3 at ($\mu_7^{-1} = -19.44$")

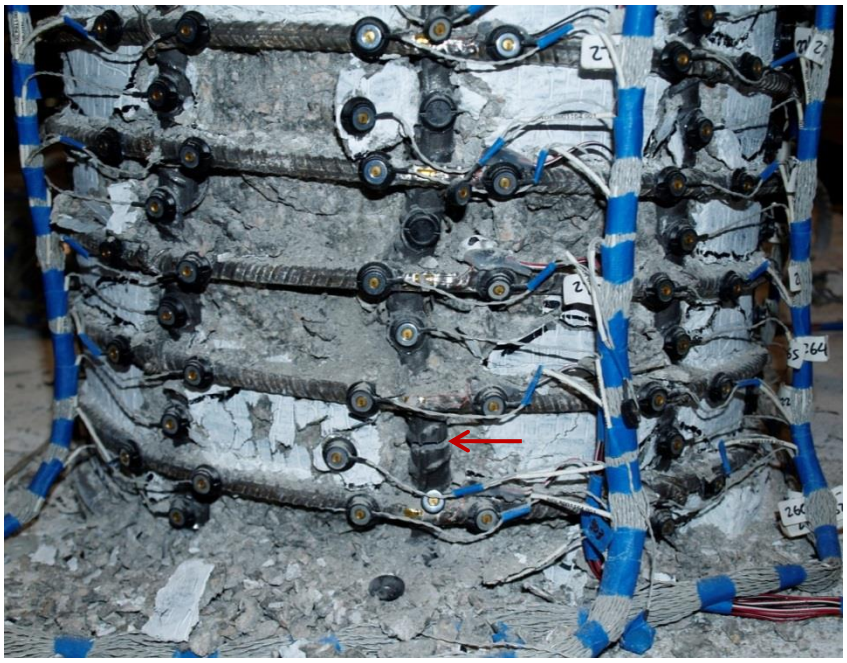

Figure 1.598 T23 – Fracture of Previously Buckled Bar N3 at 5.50" during μ_7^{+2}

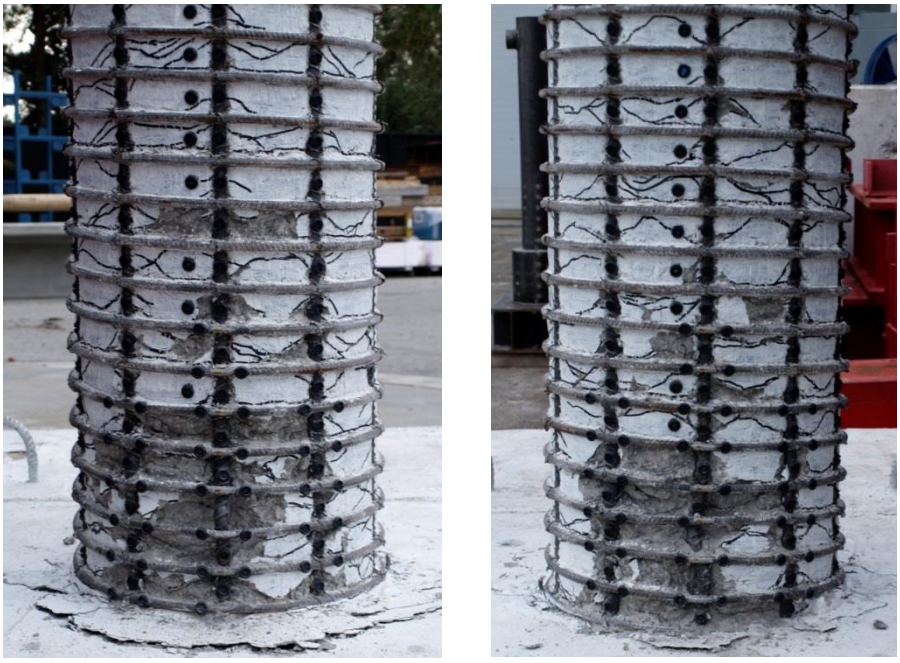

Figure 1.599 T23 – After the Test (Left) South Side and (Right) North Side

Test 23 Aspect Ratio of 8.67 and 5% Axial Load – Strain Data Analysis

North Reinforcement

Vertical strain profiles for the North extreme fiber bar N3 placed into tension during push cycles appear in the right half of Figure 1.600. This figure shows both extreme fiber bars on the same graph to illustrate the effects of tension shift on strain profiles. Compressive vertical strain profiles for North extreme fiber bar N3 during pull cycles appear in the left half of Figure 1.601. A peak tensile strain of 0.0514, located 3.95" above the footing, was measured for North extreme fiber bar N3 during ($\mu_6^{+1} = 16.65"$). The bar visibly buckled under compressive stress during the following reversal of load. The relationship between tensile strain and displacement for this gage length appears in Figure 1.604. The solid line contains data during the push cycle loading up to the peak displacement, and the dashed line represents the subsequent reversal of load. The monotonic moment-curvature prediction with the PCK (2007) Lp Hinge Method matches well until displacement ductility three, when it begins to over predict the measured tensile strains.

A peak compressive strain of -0.0224 was measured 7.82" above the footing during ($\mu_5^{-2} = -13.90"$). This value exceeds the Mander ultimate concrete compressive strain of 0.0199. The relationship between compressive strain and displacement for this gage length appears in Figure 1.605. The measured compressive strains begin to exceed the moment-curvature prediction with the PCK (2007) Lp Hinge Method after displacement ductility two. Spiral strains measured in the first eight layers about the footing on the North side of the specimen appear in Figure 1.603 for compressive pull cycles. The spiral layer 5.69" above the footing entered the inelastic range at -9.08" during the pull cycle to ($\mu_4^{-1} = -11.12"$). A peak spiral strain of 0.0030 was measured over this spiral layer before visible bar buckling.

Strain hystereses for gage lengths 1.94" and 3.95" above the footing on bar N3 appear in Figure 1.608 and Figure 1.609. This region aligns with the outward buckling of bar N3 shown in Figure 1.594. Transverse steel strain hysteresis for spiral layers 1.75" and 3.75" above the footing are shown in Figure 1.610 and Figure 1.611. Bar N3 visibly buckled after

the reversal from ($\mu_6^{+1} = 16.65"$). The outward bar buckling lead to a spike in the transverse steel restraint strains which were previously in the elastic range. It is important to note that a small amount of measurable deformation occurred during compressive cycles of displacement ductility five. Cycle-to-cycle increases in compressive demand in Figure 1.608 during displacement ductility five align with similar increases in spiral demands.

South Reinforcement

Vertical strain profiles for the South extreme fiber bar S3 placed into tension during pull cycles appear in the right half of Figure 1.601. A peak tensile strain of 0.0479, located 2.10" above the footing, was measured during ($\mu_6^{-1} = -16.65"$). The following reversal to ($\mu_6^{+2} = 16.68"$) produced measurable deformation in the region of bar S3 which later visibly buckled. A tensile strain of 0.0506 was measured over the same gage length at ($\mu_6^{-2} = -16.66"$). The relationship between tensile strain and displacement for the gage length 2.10" appears in Figure 1.606. The moment-curvature prediction matches well until displacement ductility three, when the PCK (2007) Lp Hinge Method begins to over predict the measured tensile strains.

Compressive vertical strain profiles for the South extreme fiber bar S3 during push cycles appear in the left half of Figure 1.600. The effect of this compressive demand on spiral strains is shown in Figure 1.602. A peak compressive strain of -0.0305 was measured 5.93" above the footing at ($\mu_6^{+1} = 16.65"$). At this displacement a peak spiral strain of 0.0072 was measured 5.93" above the footing. As previously mentioned, measurable deformation occurred during ($\mu_6^{+2} = 16.65"$). The compressive strain 5.93" above the footing on bar S3 increased to -0.0406 during this cycle, and the spiral strains increased to 0.0083. The relationship between compressive strain and displacement for the gage length 5.93" above the footing appears in Figure 1.607. The measured compressive strains exceed the moment-curvature prediction with the PCK (2007) Lp Hinge Method after displacement ductility 1.5. Spiral yielding on the South side of the specimen occurred at 10.83" above the footing during the push cycle to ($\mu_4^{+1} = 11.09"$).

The strain hysteresis for the outward buckled region of bar S3 appears in Figure 1.612 for the gage length 4.01" above the footing. A picture of the outward buckled region of bar S3 appears in the right photo of Figure 1.596. This strain hysteresis clearly shows that measurable deformation occurred after reversal from ($\mu_6^{-1} = -16.65"$), at the same location where the bar visibly buckled during ($\mu_6^{+3} = 16.67"$). A strain hysteresis for the gage length 5.93" above the footing appears in Figure 1.613. For this gage length, the measurable deformation resulted in additional compressive demand. The transverse steel strain hysteresis for spiral layers 5.78" and 7.75" above the footing appear in Figure 1.614 and Figure 1.615 respectively. The transverse steel layer 5.78" aligns with the lower buckled region of bar S3, while the spiral layer 7.75" overlaid the upper buckled region. The measurable deformation during ($\mu_6^{+2} = 16.68"$) lead to a spike in the measured spiral strains 5.78" above the footing, which caused the strain gage to become debonded. This same cycle only lead to a small increase in the spiral strains measured 7.75" above the footing. For this spiral layer, the large spike in transverse steel strain occurred during ($\mu_6^{+3} = 16.67"$) when visible buckling was observed.

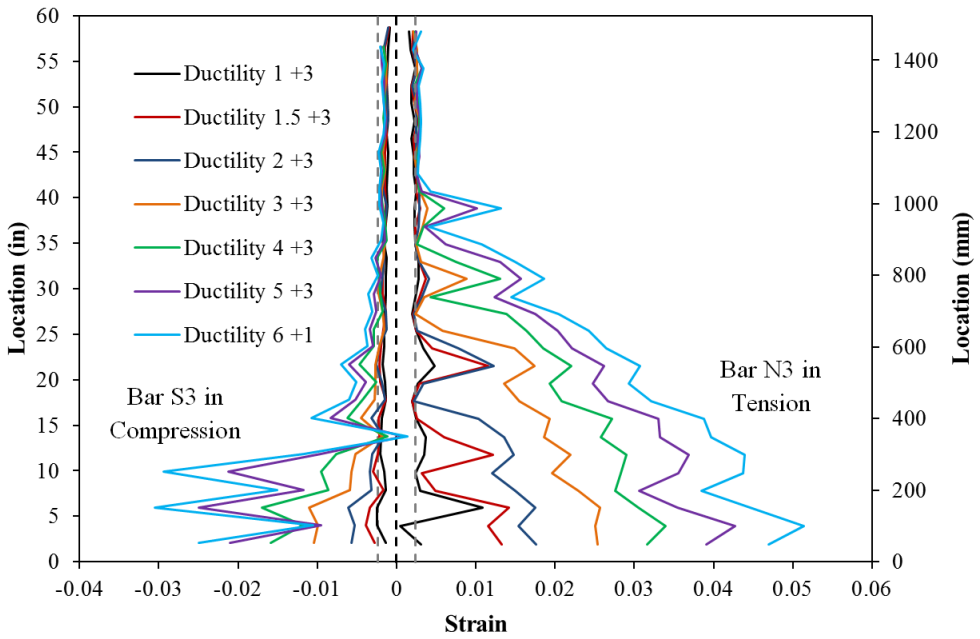

Figure 1.600 T23 – Extreme Fiber Bar Vertical Strain Profiles during Push Cycles

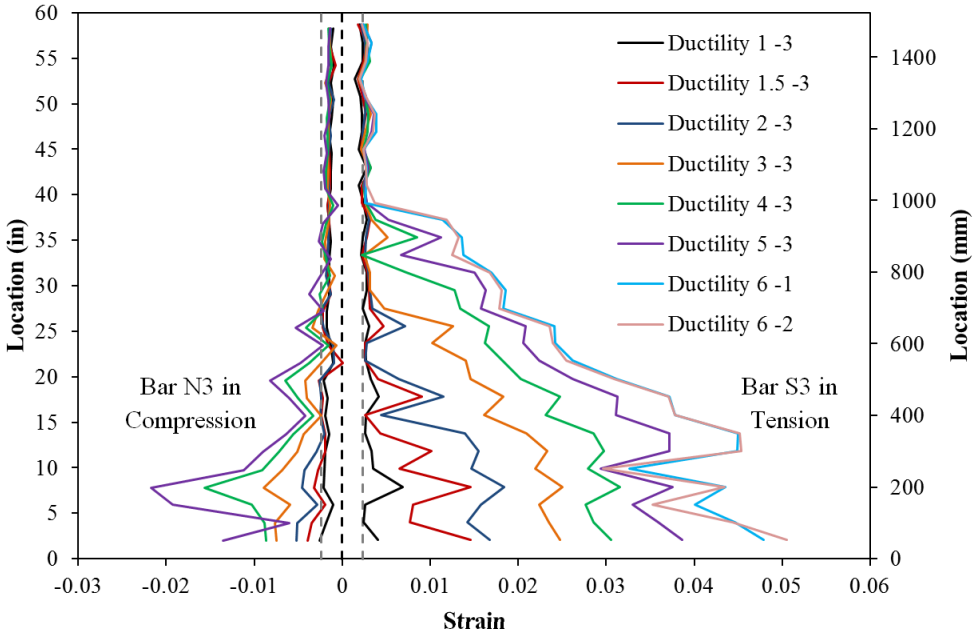

Figure 1.601 T23 – Extreme Fiber Bar Vertical Strain Profiles during Pull Cycles

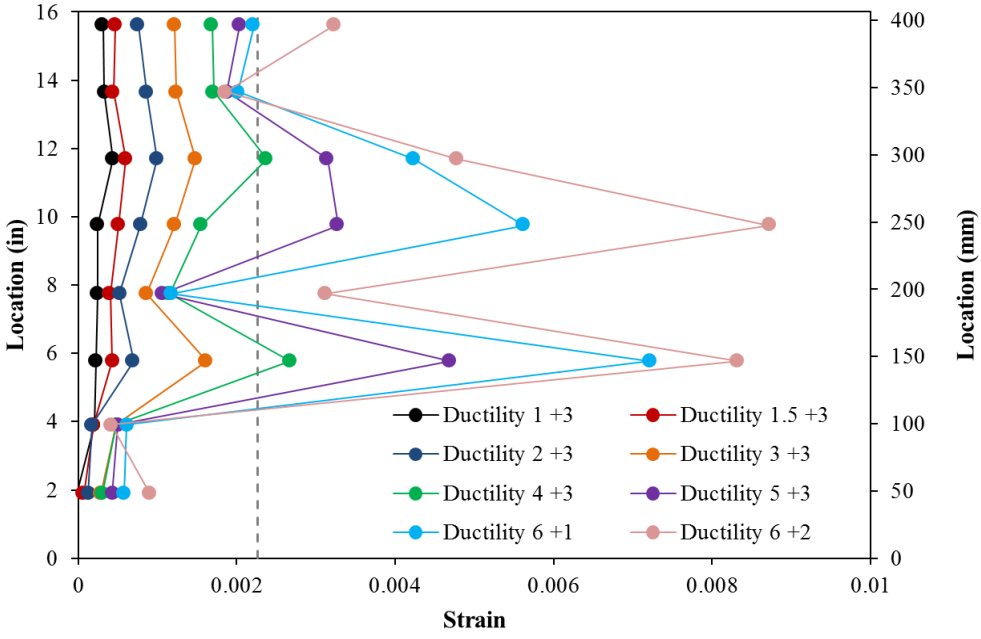

Figure 1.602 T23 – South Spiral Strains during Compressive Push Cycles

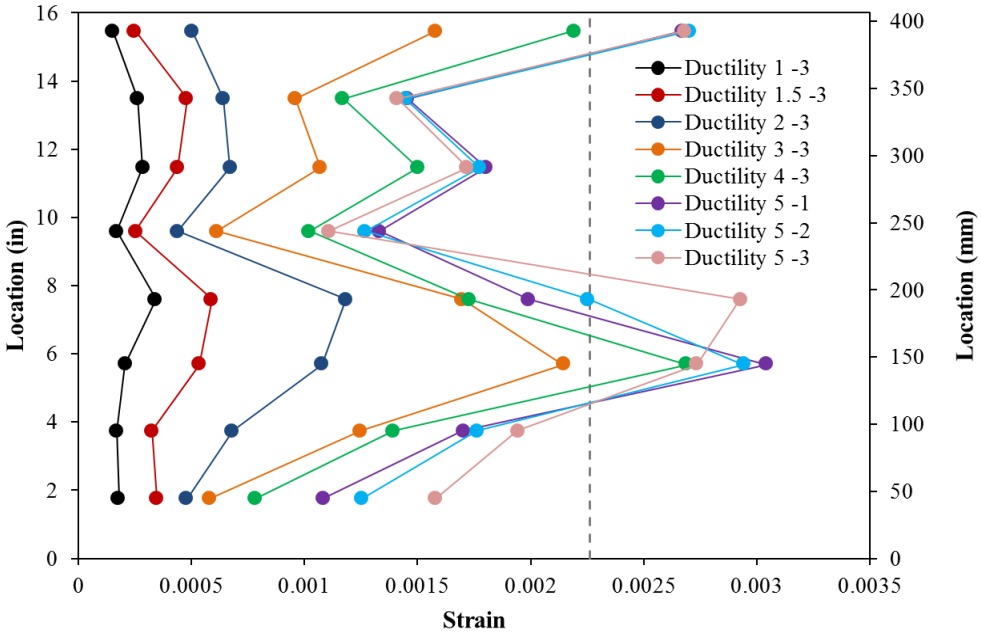

Figure 1.603 T23 – North Spiral Strains during Compressive Pull Cycles

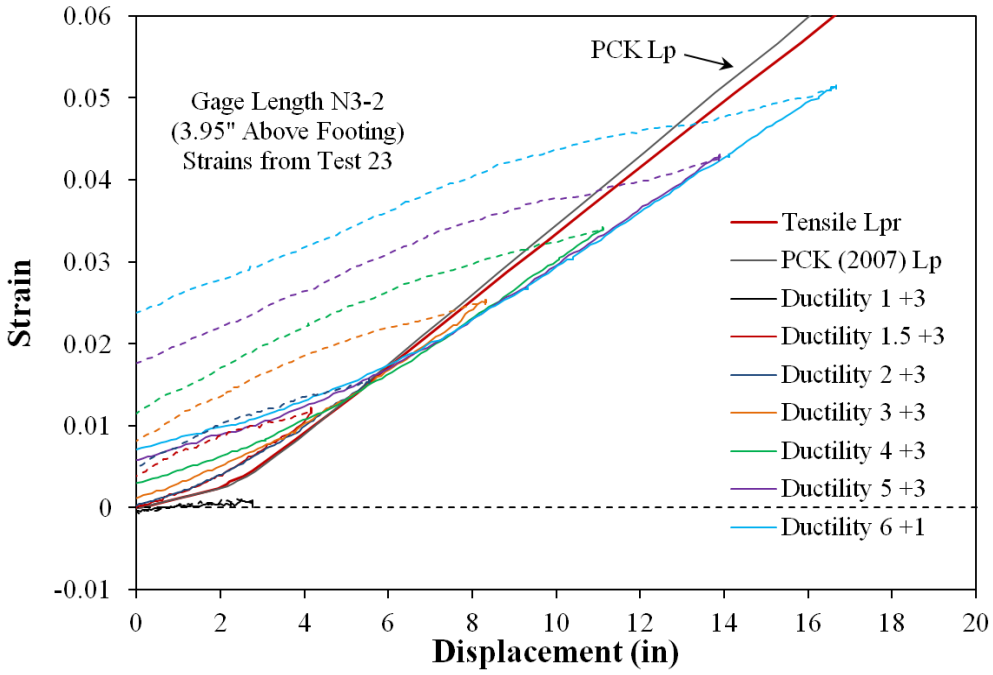

Figure 1.604 T23 – Tensile Strain-Displacement for Bar N3 during Push Cycles

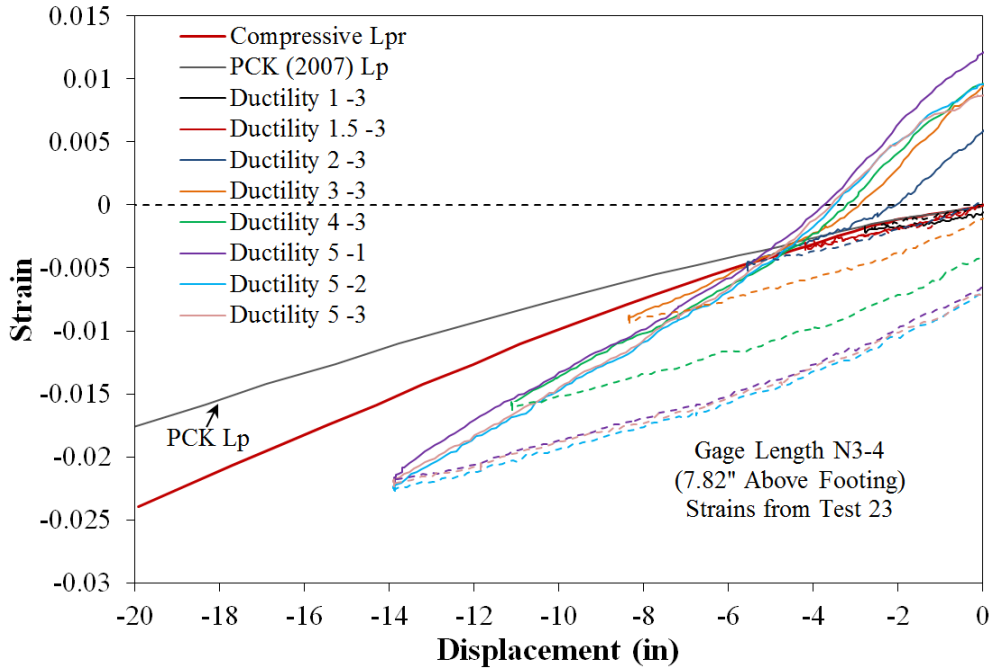

Figure 1.605 T23 – Compressive Strain-Displacement for Bar N3 during Pull Cycles

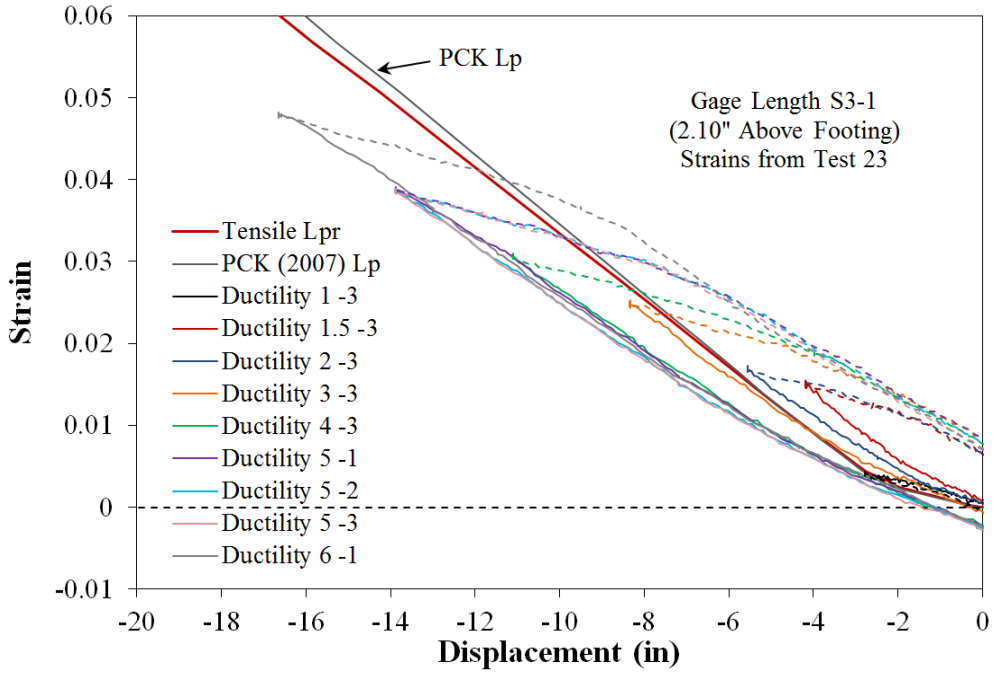

Figure 1.606 T23 – Tensile Strain-Displacement for Bar S3 during Pull Cycles

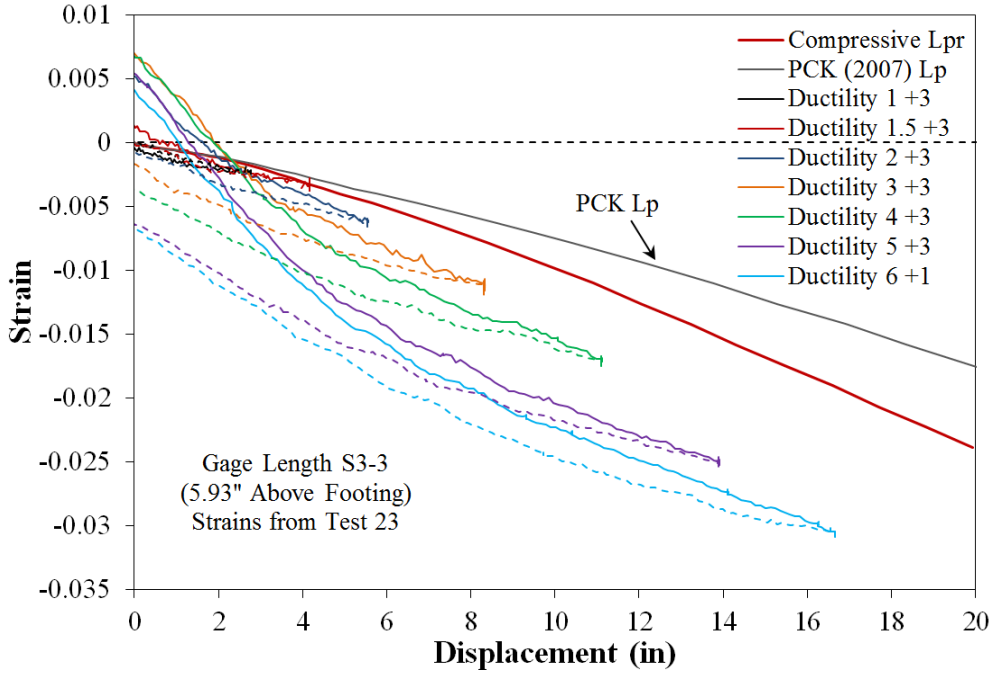

Figure 1.607 T23 – Compressive Strain-Displacement for Bar S3 during Push Cycles

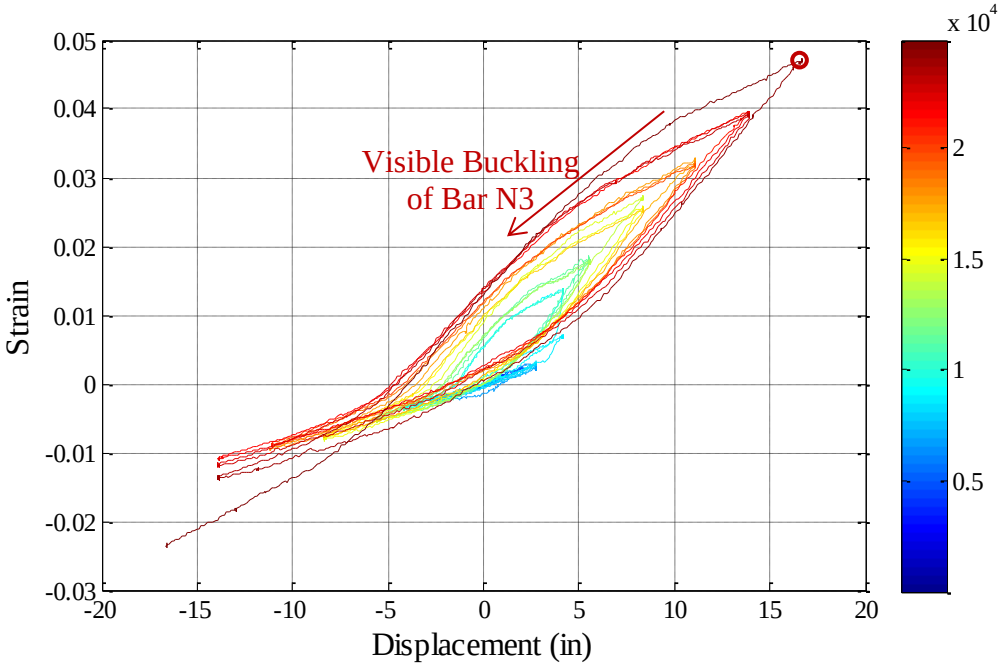

Figure 1.608 T23 – Strain Hysteresis for Bar N3 to Buckling (1.94" Above the Footing)

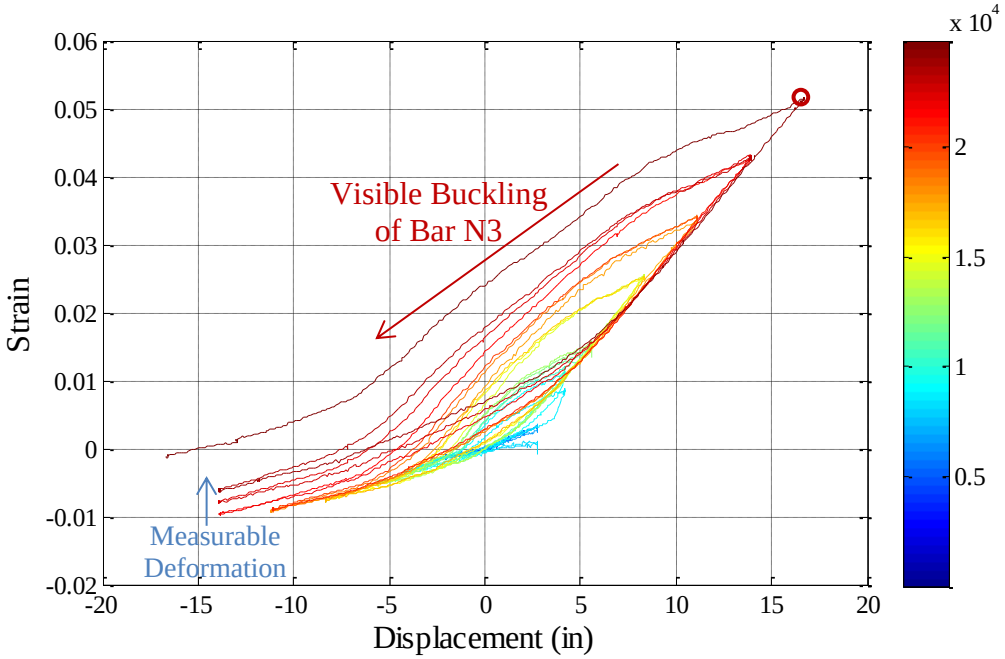

Figure 1.609 T23 – Strain Hysteresis for Bar N3 to Buckling (3.95" Above the Footing)

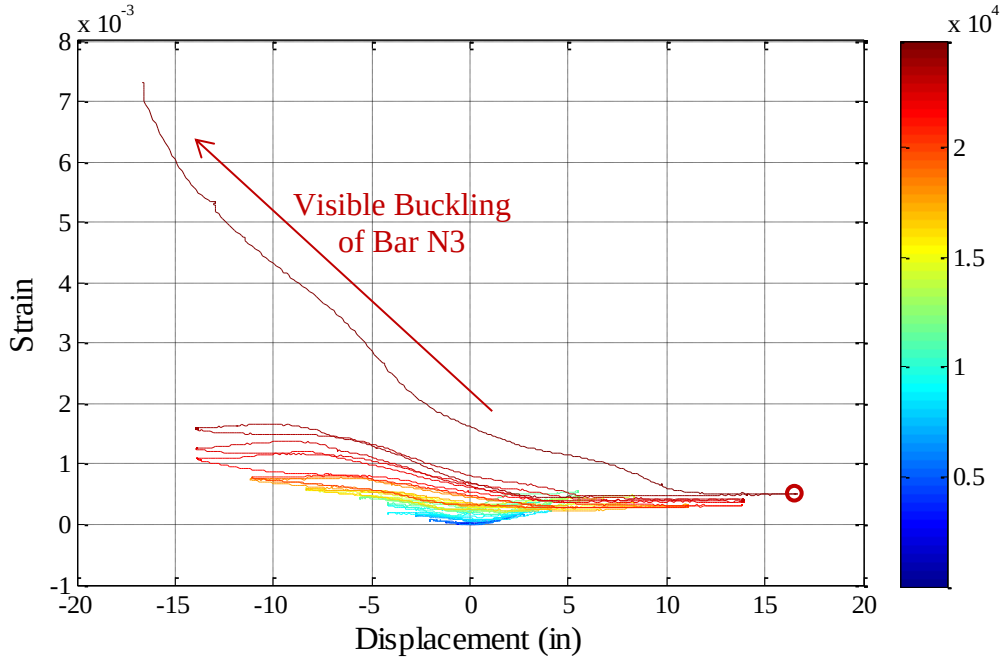

Figure 1.610 T23 – Spiral Strain Hysteresis over North Buckled Region (1.75" Above)

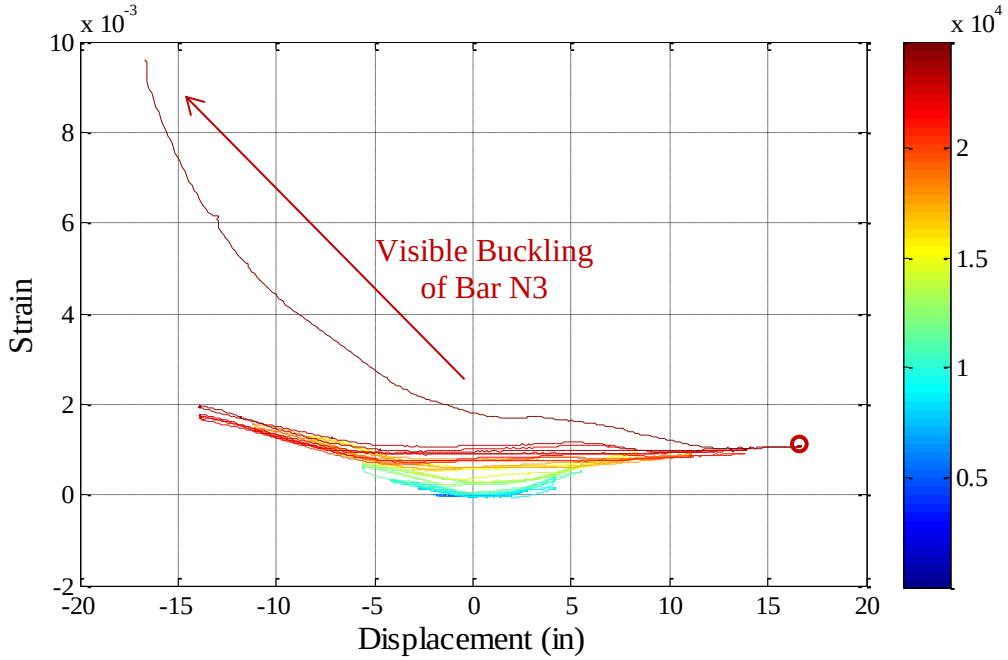

Figure 1.611 T23 – Spiral Strain Hysteresis over North Buckled Region (3.75" Above)

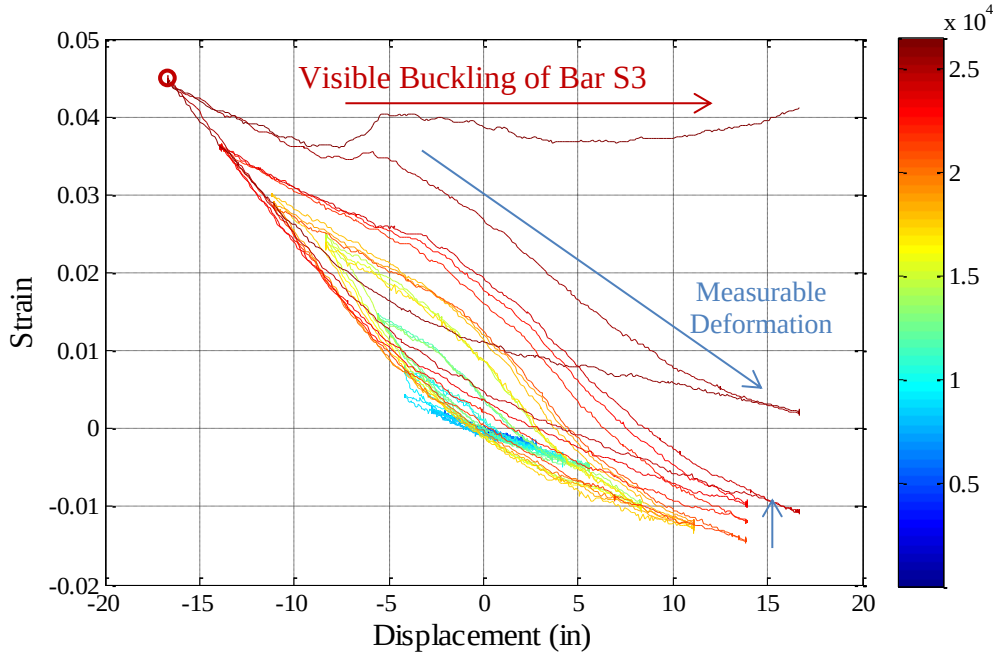

Figure 1.612 T23 – Strain Hysteresis for Bar S3 to Buckling (4.01" Above the Footing)

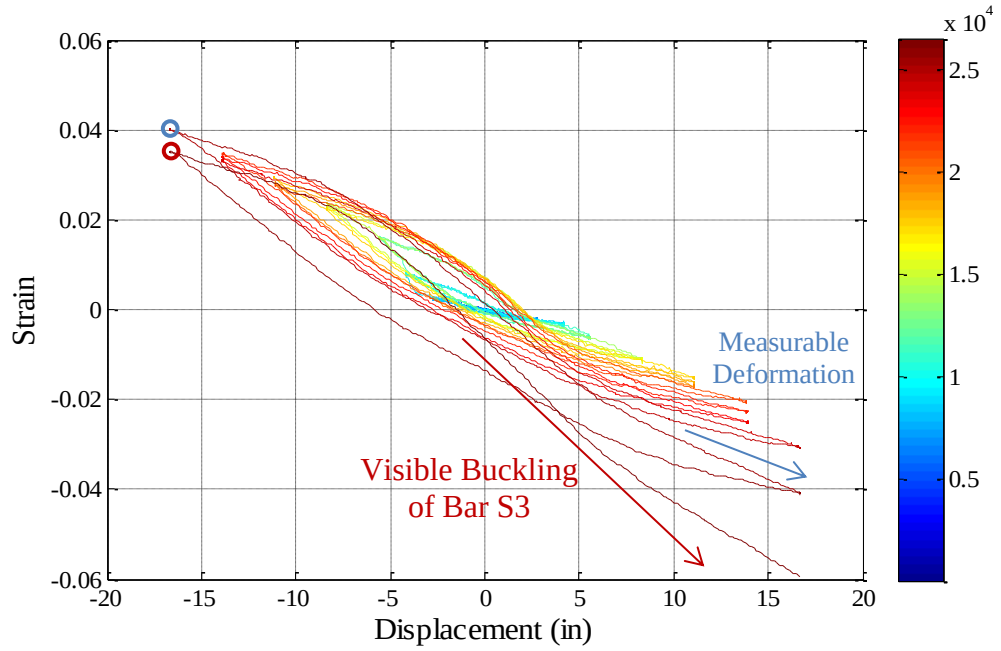

Figure 1.613 T23 – Strain Hysteresis for Bar S3 to Buckling (5.93" Above the Footing)

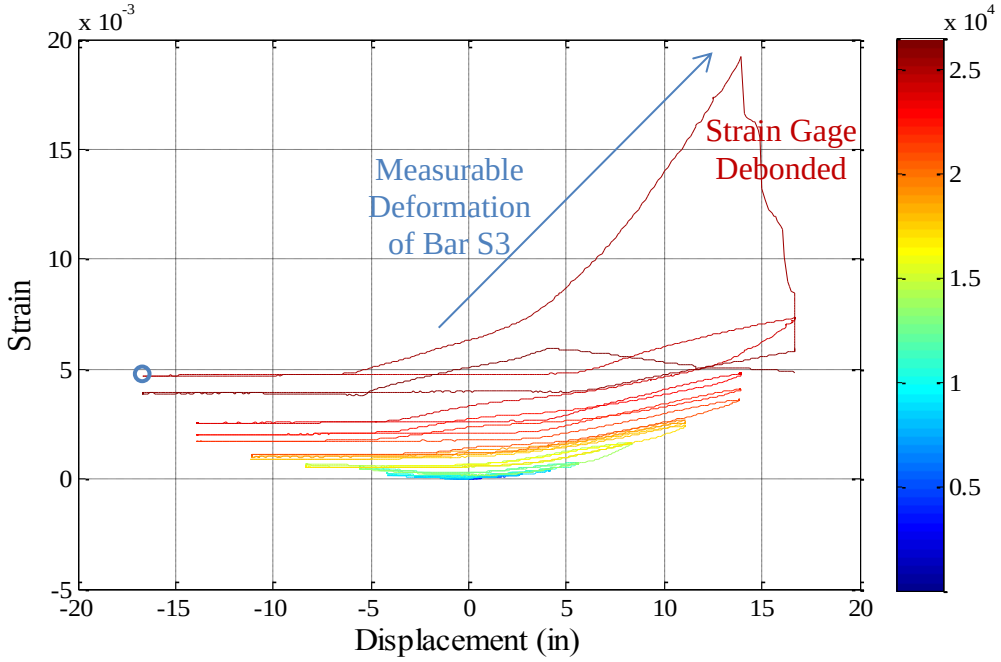

Figure 1.614 T23 – Spiral Strain Hysteresis over South Buckled Region (5.78" Above)

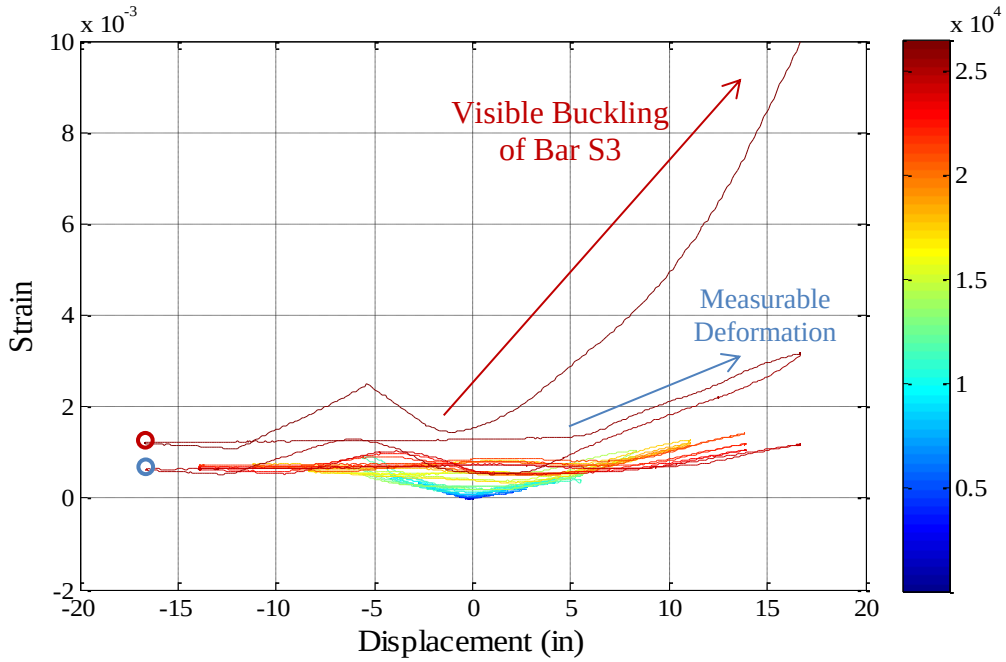

Figure 1.615 T23 – Spiral Strain Hysteresis over South Buckled Region (7.75" Above)

Test 23 Aspect Ratio of 8.67 and 5% Axial Load – Curvature and Strain Penetration

The cross section curvature for each horizontal section above the footing is determined by connecting the strain measurements from all eight instrumented bars with a least squared error line. The curvature is then extracted from the slope of the least squared error line, see Figure 1.616 and Figure 1.617. The cross section curvature profiles in these figures are shown for the first horizontal section above the footing-column interface. For these sections, it appears that the plane sections hypothesis remains appropriate. Vertical curvature profiles are plotted for push and pull cycles in Figure 1.618 and Figure 1.619 respectively. These figures show that plastic curvatures have a linear distribution at higher displacement ductility levels. The extent of plastic curvatures above the footing can be calculated by determining where the linear plastic curvature distribution intersects the triangular yield curvature profile, shown as a grey dashed line. The measured spread of plasticity as a function of base section curvature ductility appears in Figure 1.625.

The target marker on each bar placed closest the footing-column interface can be used to monitor strain penetration behavior. The bond slip hysteresis for bars N3 and S3 appear in Figure 1.620 and Figure 1.621 respectively. If the tensile and compressive bond slips of the instrumented bars are plotted along the cross section depth, the base rotation attributable to strain penetration may be calculated. The slip profiles for push and pull cycles appear in Figure 1.622 and Figure 1.623 respectively. The rotation of the base section can be extracted from the slope of the least squared error line connecting all of the measured bar slips

Combining the curvatures over the instrumented region (5ft above the footing), bond slip profiles, and an elastic curvature assumption above the instrumented region, the top column displacement can be calculated by integrating the curvature distributions and extrapolating the fixed-end rotations to the center of loading. The top column displacements calculated from the Optotrak system are compared to displacements measured with a string potentiometer at the center of loading in Figure 1.624. The Optotrak integrated displacements slightly exceed the measured response in both directions of loading.

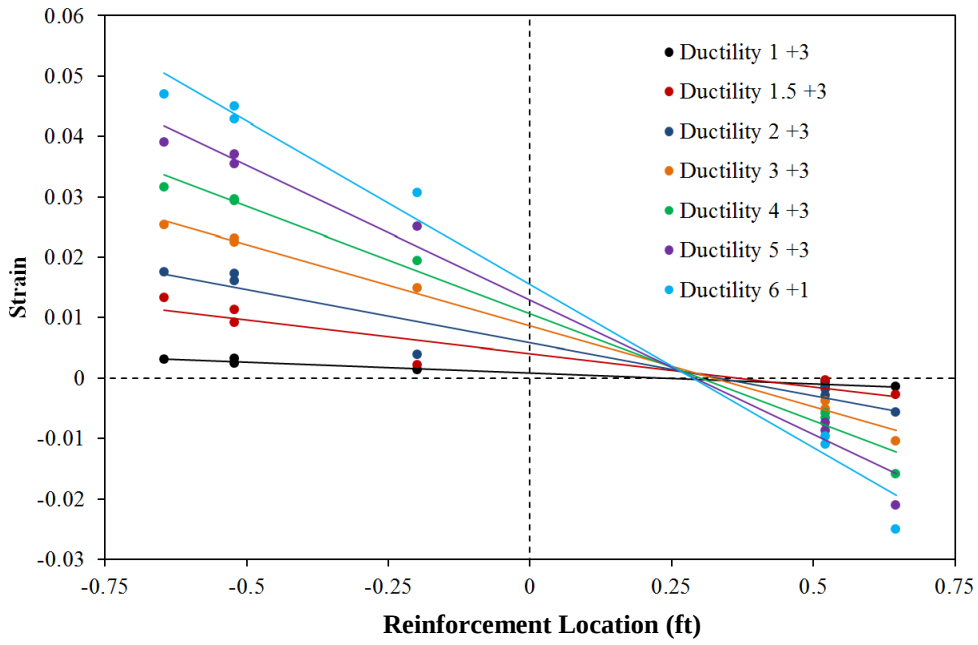

Figure 1.616 T23 – Cross Section Curvatures during Push Cycles (2.02” above Footing)

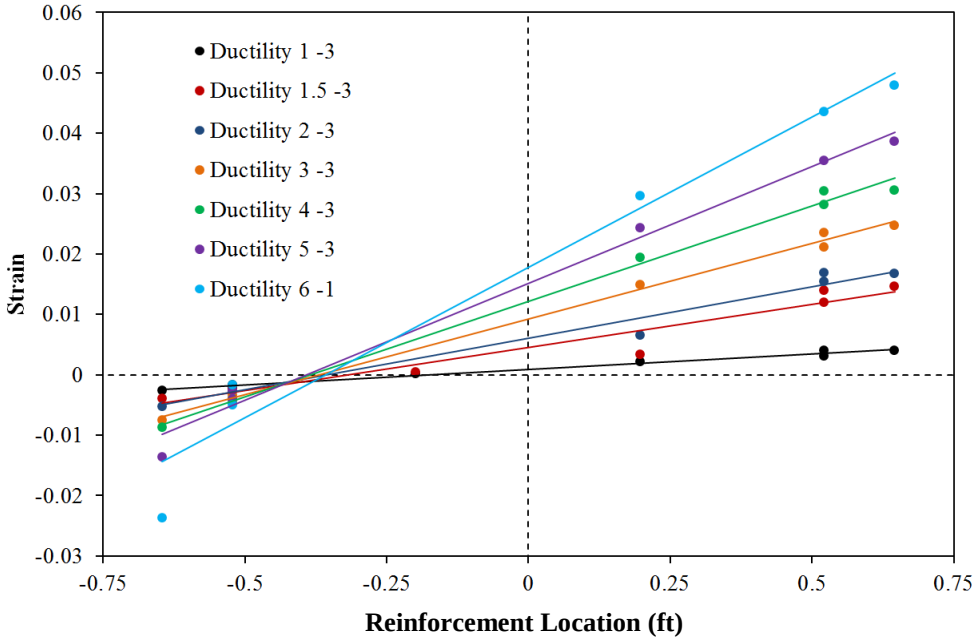

Figure 1.617 T23 – Cross Section Curvatures during Pull Cycles (2.02" above Footing)

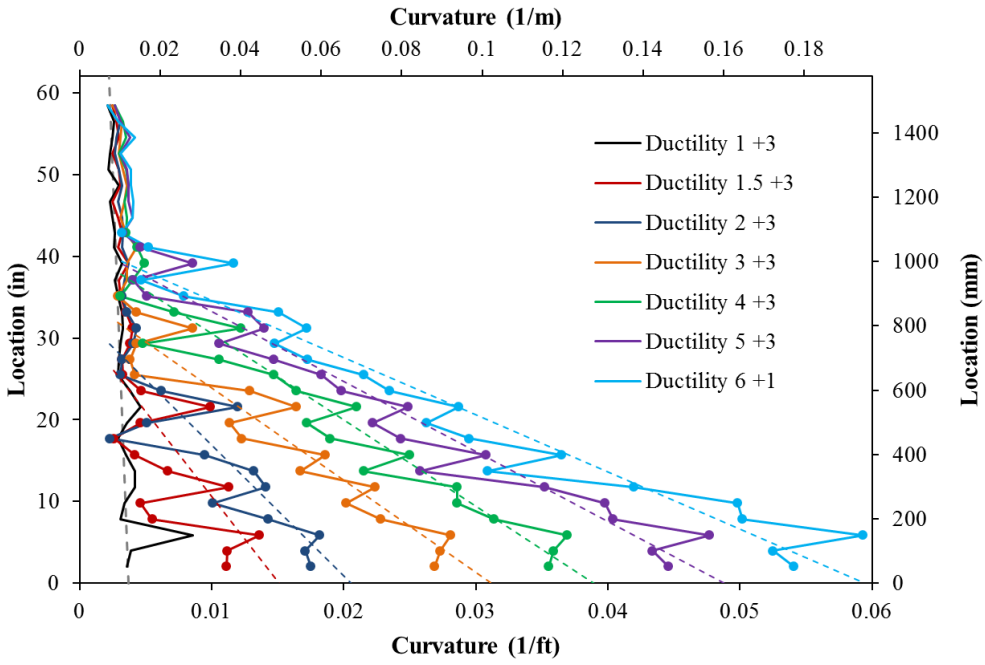

Figure 1.618 T23 – Push Cycle Curvature Profiles with Plastic Regression Lines

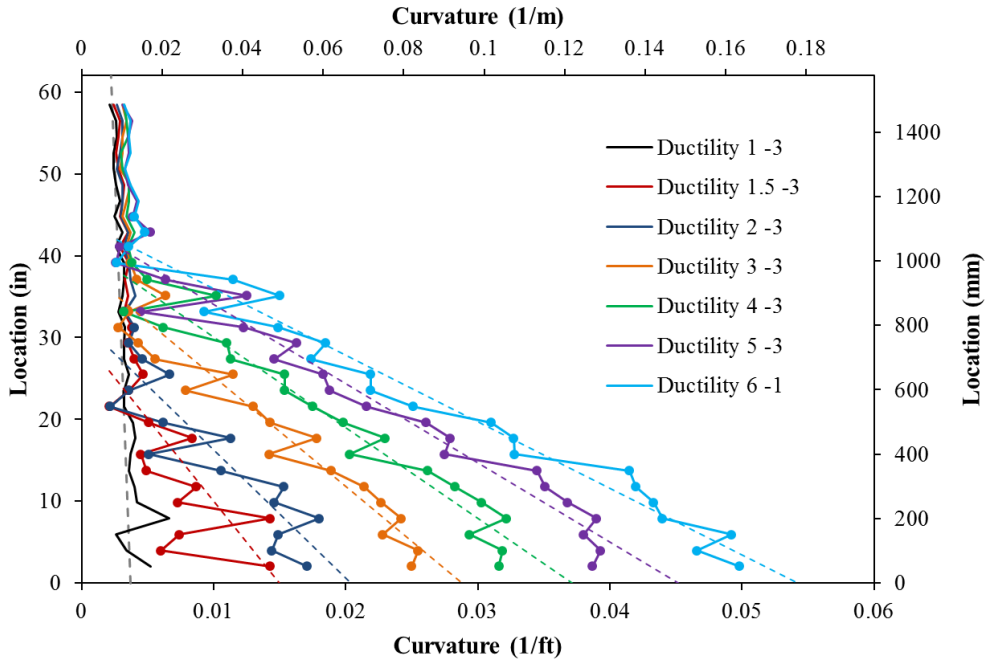

Figure 1.619 T23 – Pull Cycle Curvature Profiles with Plastic Regression Lines

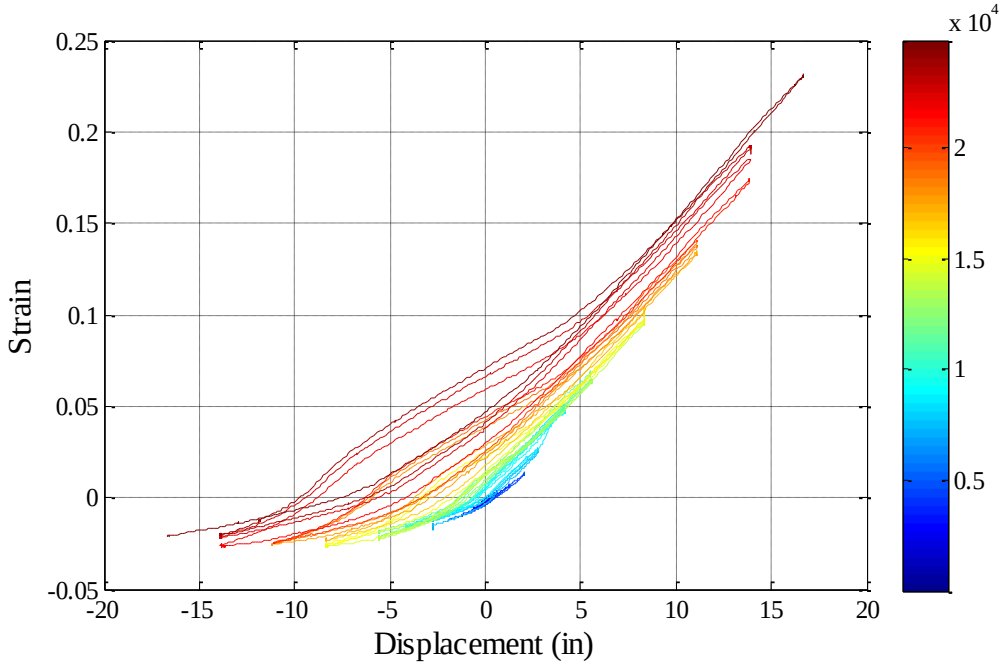

Figure 1.620 T23 – Bar N3 Bond Slip Hysteresis due to Strain Penetration

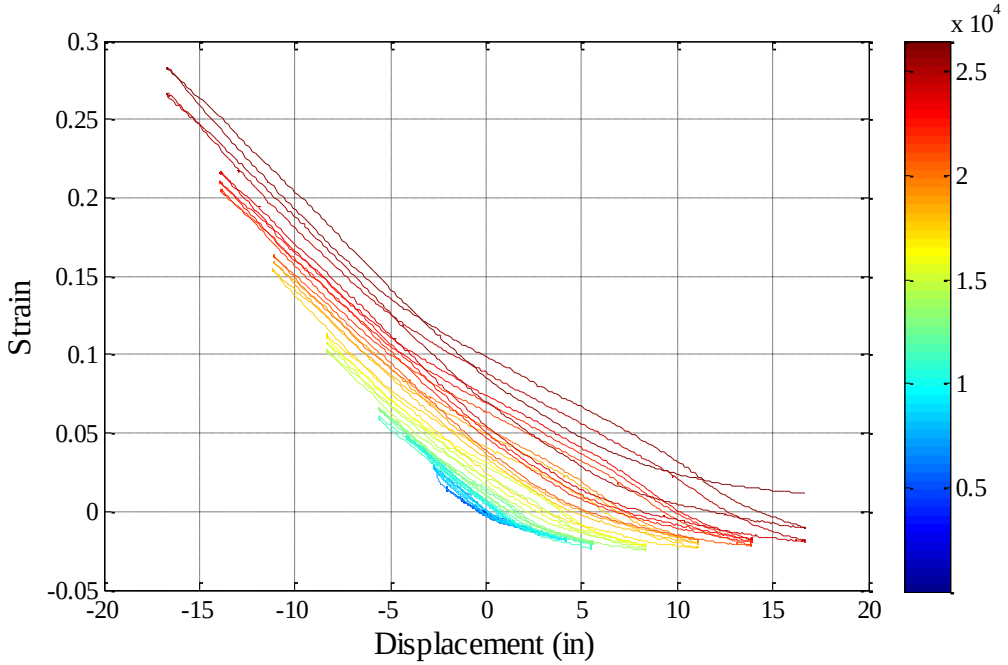

Figure 1.621 T23 – Bar S3 Bond Slip Hysteresis due to Strain Penetration

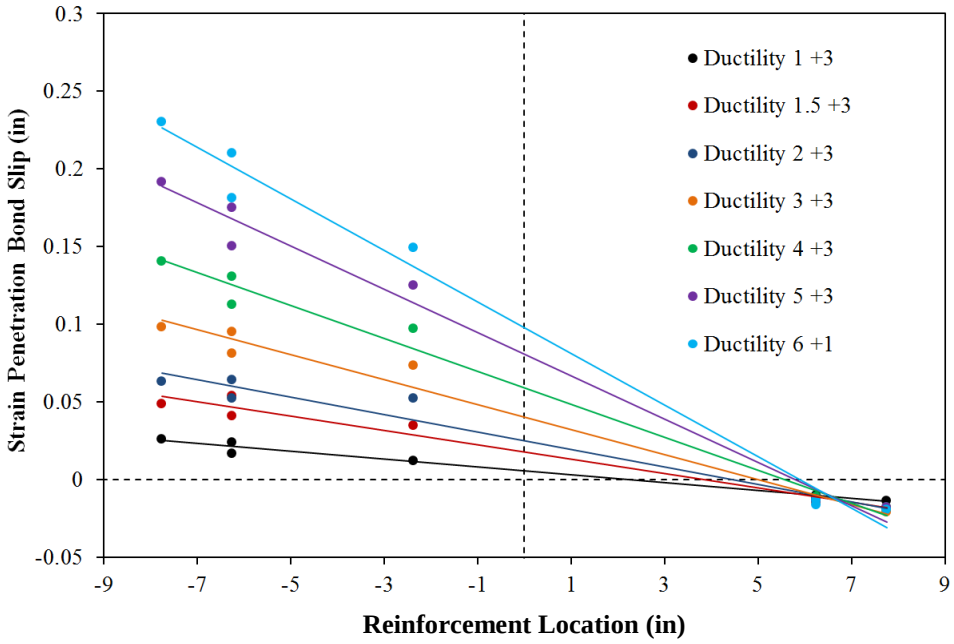

Figure 1.622 T23 – Bond Slip Profiles during Push Cycles due to Strain Penetration

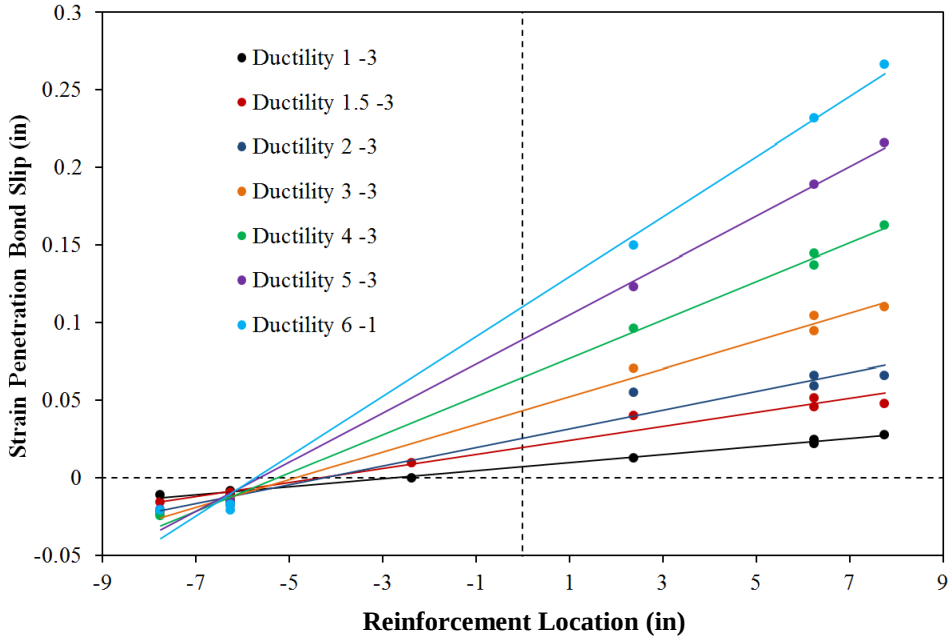

Figure 1.623 T23 – Bond Slip Profiles during Pull Cycles due to Strain Penetration

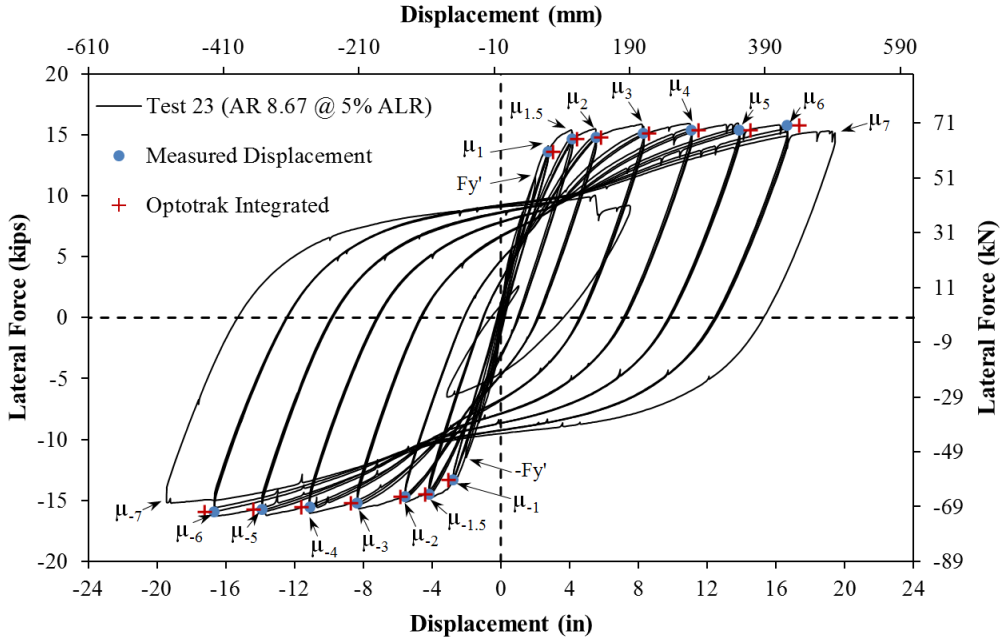

Figure 1.624 T23 – Comparison of Measured and Optotrak Integrated Displacements

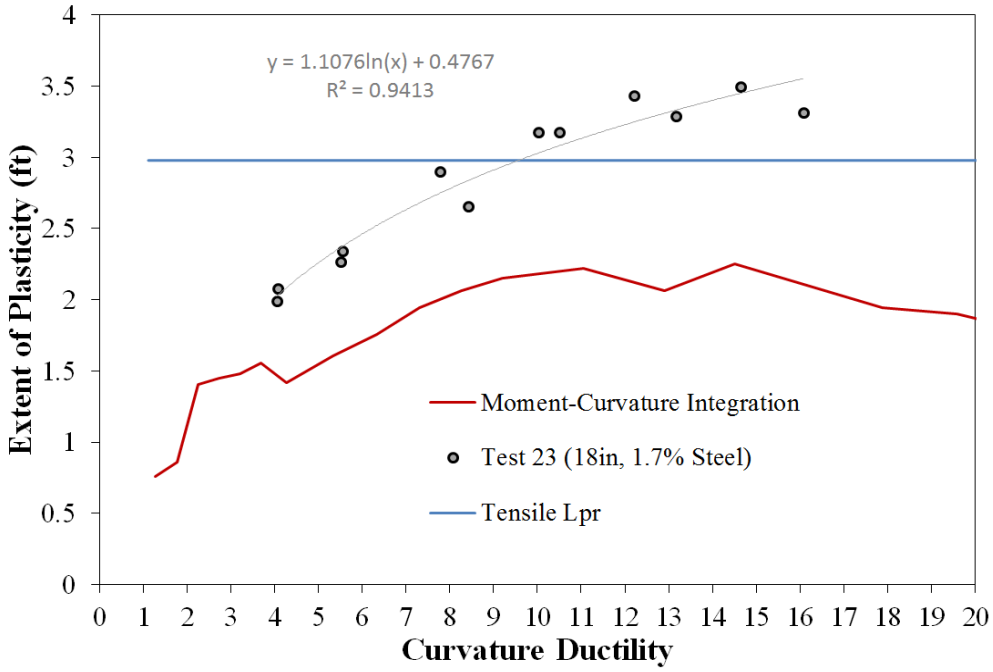

Figure 1.625 T23 – Measured Spread of Plasticity (Circular Data Points)

1.3.6 Test 24 – Aspect Ratio of 8.67 and 10% Axial Load

Table 1.43 Observations for Test 24 – Aspect Ratio of 8.67 and 10% Axial Load

VALUES OF INTEREST:	
Concrete Compressive Strength:	$f_c' = 6473\ psi$
Axial Load:	$P = 147\ kips\ \ (P/(f_c' A_g) = 10\%)$
Column Length and Aspect Ratio:	$13ft\ \ (L/D = 8.67)$
Analytical First Yield Force:	$F_y' = 13.58\ kips$
Experimental First Yield Displacement:	$\Delta_y' = 2.16"$
Analytical Nominal Moment Capacity:	$M_n = 233.7\ kip * ft$
Equivalent Yield Displacement:	$\Delta_y = 2.86"$
Maximum Lateral Force:	$17.92\ kips$
DAMAGE OBSERVATIONS:	
First Cracking North:	$1/2Fy' = 0.63"$
First Cracking South:	$-1/2Fy' = -0.69"$
Cover Concrete Crushing North:	$\mu_2^{-2} = -5.72"$
Cover Concrete Crushing South:	$\mu_3^{+1} = 8.58"$
Transverse Steel Yield North:	At $-6.60"$ during pull to $\mu_3^{-1} = -8.58"$
Transverse Steel Yield South:	At $7.34"$ during push to $\mu_3^{+1} = 8.58"$
Longitudinal Bar Buckling North:	Reversal from $\mu_5^{+1} = 14.29"$
Longitudinal Bar Buckling South:	Reversal from $\mu_5^{-1} = -14.31"$
Longitudinal Bar Fracture North:	At $10.49"$ during push to $\mu_5^{+4} = 14.33"$
Longitudinal Bar Fracture South:	At $-7.71"$ during pull to $\mu_5^{-6} = -14.33"$

*$\mu_5^{-1} = -14.31"$ represents the first pull cycle of displacement ductility five

Table 1.44 Strain Data Summary for Test 24 – Aspect Ratio 8.67 and 10% Axial Load

MATERIAL STRAINS:

Cover Concrete Crushing North:	$\varepsilon_s = 0.0085\ (compression)$
Cover Concrete Crushing South:	$\varepsilon_s = 0.0083\ (compression)\ \ ^*\mu_{\Delta 2} = 5.73"$
Transverse Steel Yield North:	$\varepsilon_s = 0.0155\ (compression)$
Transverse Steel Yield South:	$\varepsilon_s = 0.0131\ (compression)$
Longitudinal Bar Buckling North:	$\varepsilon_s = 0.037\ (peak\ tension\ prior\ to\ bb)$
	$\varepsilon_s = 0.028\ (peak\ comp.\ prior\ to\ bb)$
Longitudinal Bar Buckling South:	$\varepsilon_s = 0.045\ (peak\ tension\ prior\ to\ bb)$
	$\varepsilon_s = 0.020\ (peak\ comp.\ prior\ to\ bb)$

Mander (1988) Ultimate Concrete Compression Strain, $\varepsilon_{cu} = 0.0202$

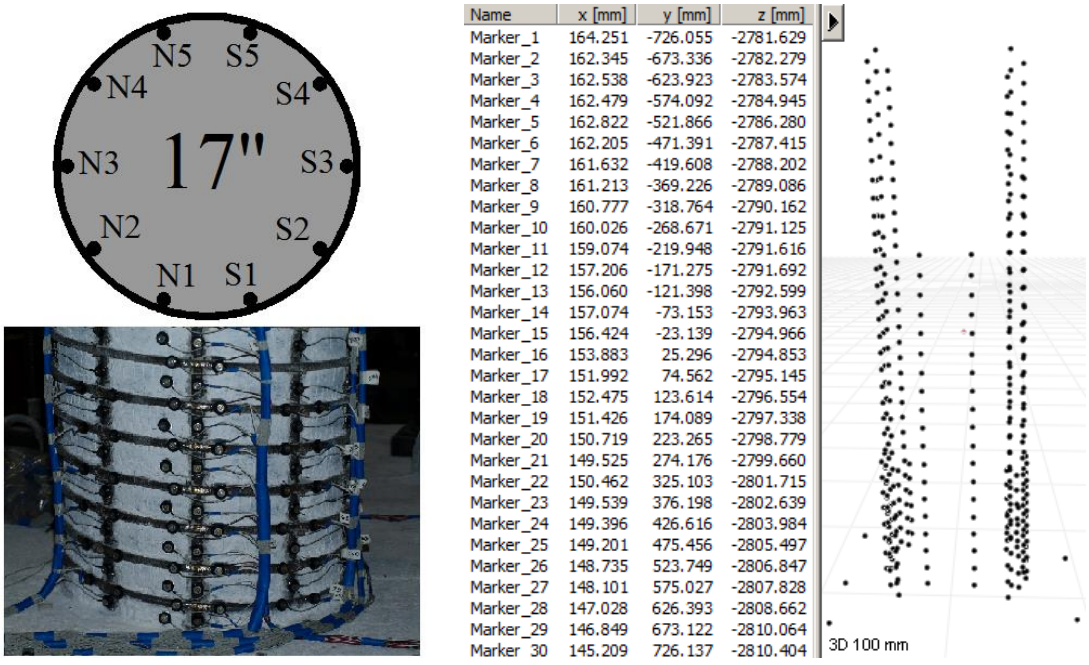

Name	x [mm]	y [mm]	z [mm]
Marker_1	164.251	-726.055	-2781.629
Marker_2	162.345	-673.336	-2782.279
Marker_3	162.538	-623.923	-2783.574
Marker_4	162.479	-574.092	-2784.945
Marker_5	162.822	-521.866	-2786.280
Marker_6	162.205	-471.391	-2787.415
Marker_7	161.632	-419.608	-2788.202
Marker_8	161.213	-369.226	-2789.086
Marker_9	160.777	-318.764	-2790.162
Marker_10	160.026	-268.671	-2791.125
Marker_11	159.074	-219.948	-2791.616
Marker_12	157.206	-171.275	-2791.692
Marker_13	156.060	-121.398	-2792.599
Marker_14	157.074	-73.153	-2793.963
Marker_15	156.424	-23.139	-2794.966
Marker_16	153.883	25.296	-2794.853
Marker_17	151.992	74.562	-2795.145
Marker_18	152.475	123.614	-2796.554
Marker_19	151.426	174.089	-2797.338
Marker_20	150.719	223.265	-2798.779
Marker_21	149.525	274.176	-2799.660
Marker_22	150.462	325.103	-2801.715
Marker_23	149.539	376.198	-2802.639
Marker_24	149.396	426.616	-2803.984
Marker_25	149.201	475.456	-2805.497
Marker_26	148.735	523.749	-2806.847
Marker_27	148.101	575.027	-2807.828
Marker_28	147.028	626.393	-2808.662
Marker_29	146.849	673.122	-2810.064
Marker_30	145.209	726.137	-2810.404

Figure 1.626 T24 – Cross Section Bar Designation and Target Marker Application

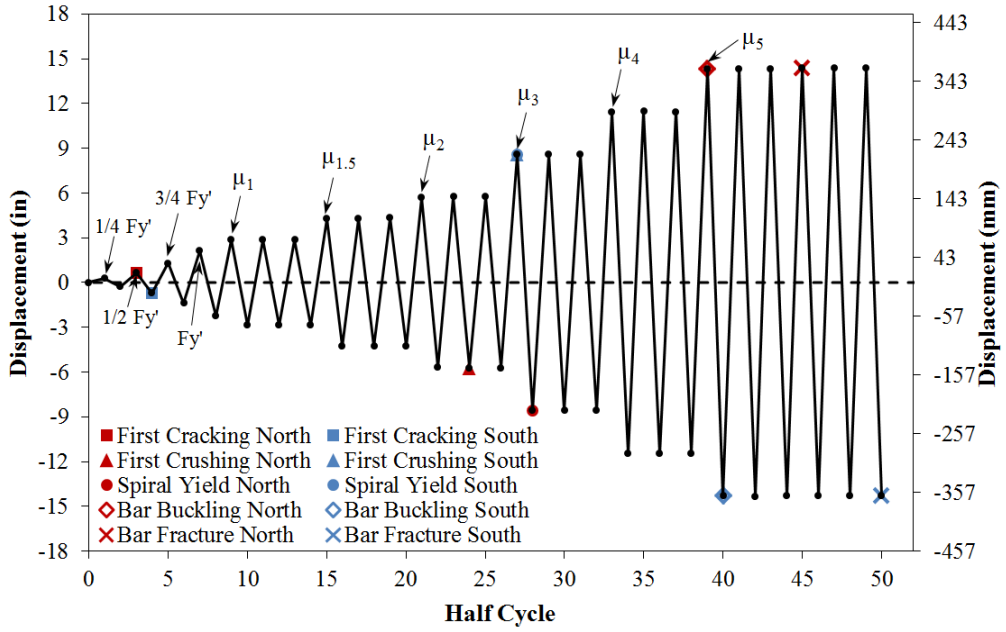

Figure 1.627 T24 – Symmetric Three Cycle Set Load History

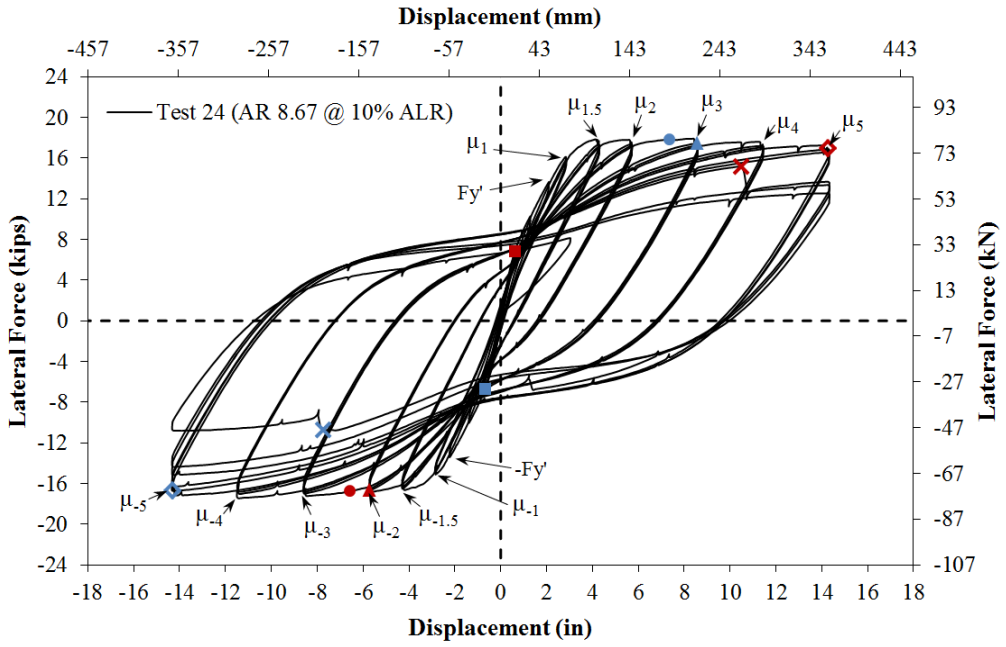

Figure 1.628 T24 – Lateral Force vs. Displacement Response

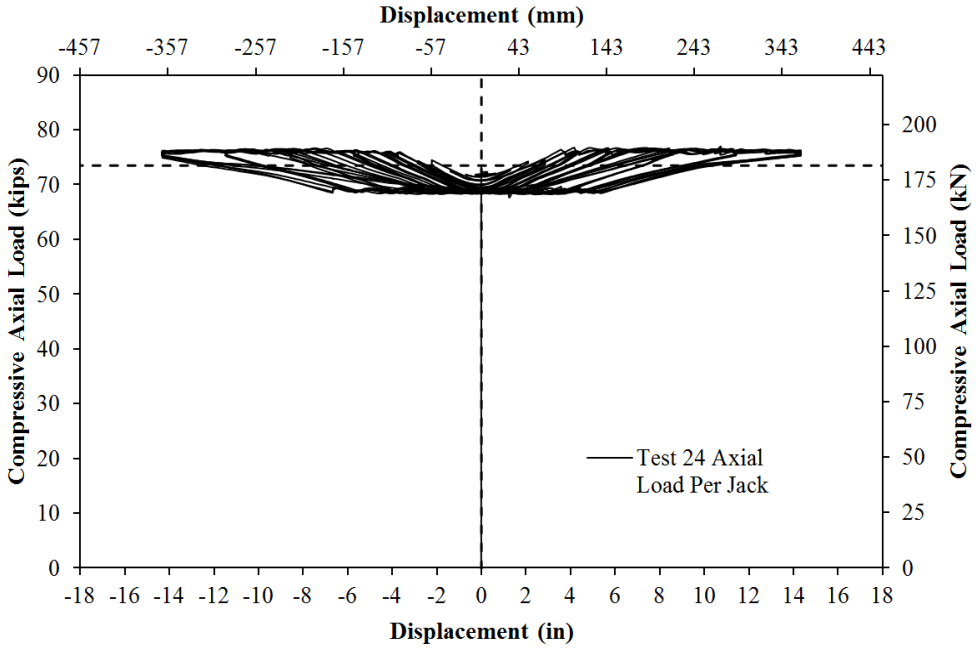

Figure 1.629 T24 – Compressive Axial Load from One Jack (Total = 2*Value)

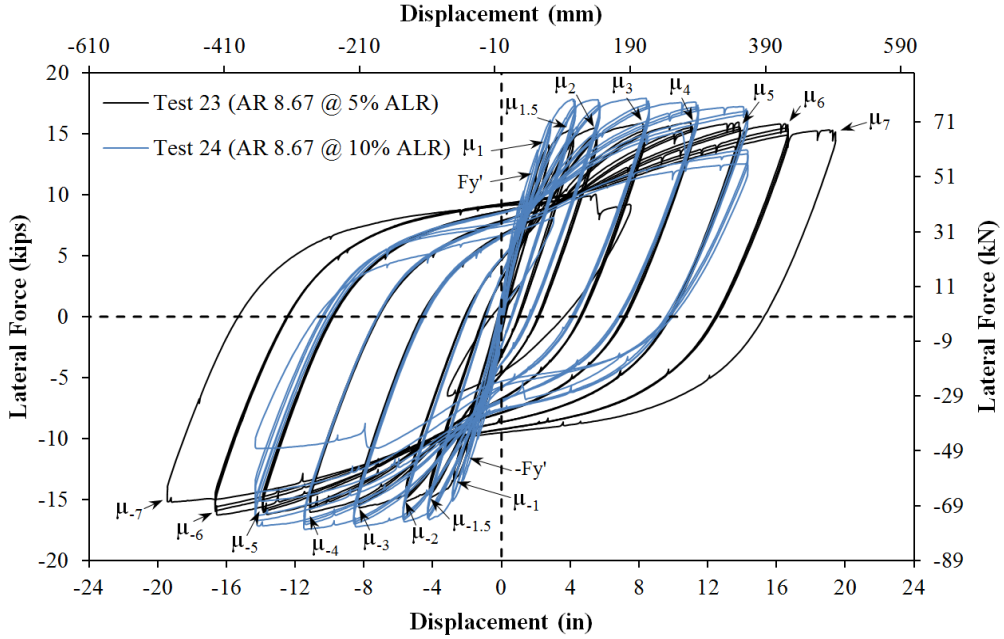

Figure 1.630 Hysteretic Comparison of T23 and T24 with Different Axial Load Levels

Test 24 Aspect Ratio of 8.67 and 10% Axial Load – Experimental Observations

The symmetric three-cycle-set laboratory load history is typically used to evaluate the seismic performance of structural components. The load history begins with elastic cycles to the following increments of the analytically predicted first yield force: ¼ Fy', ½ Fy', ¾ Fy', and Fy'. The first yield force for the tested material and geometric properties was determined using moment-curvature analysis (Test 24: Cumbia Fy' = 13.58 kips with f'c = 6473 psi). The first yield displacement was obtained as an average for the experimental first yield push and pull cycles ($\Delta'_y = 2.16$"). Vertical strain profiles for both push and pull cycles up to the first yield force appear in Figure 1.631 with a dashed line representing the yield strain of the longitudinal reinforcement. The equivalent yield displacement, used to determine the displacement ductility levels ($\mu_{\Delta 1} = 1 * \Delta_y$), is then calculated as $\Delta_y = \Delta'_y(M_n/M'_y) = 2.86$" for Test 24. The symmetric three-cycle-set load history resumes with three balanced cycles at each of the following displacement ductility levels: 1, 1.5, 2, 3, 4, 5, 6, 7, 8, etc. The full symmetric three-cycle-set load history appears in Figure 1.627, and the resulting lateral force versus top column displacement hysteresis is shown in Figure 1.628.

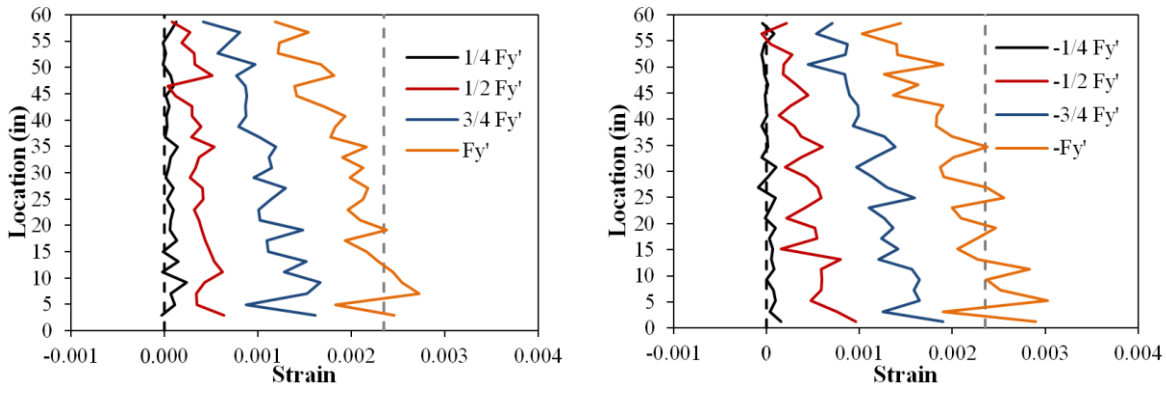

Figure 1.631 T24 – Strain Profiles before Yield, (Left) North and (Right) South

The test began with cycles in ¼ Fy' (first yield force) increments in each direction of loading until the first yield force was reached. The first cracks on the North and South sides of the specimen were observed during $(1/2Fy' = 0.63")$ and $(-1/2Fy' = -0.69")$ respectively. The crack distribution on all sides of the specimen at first yield, $(Fy' = 2.10")$ and $(-Fy' = -2.23")$, appears in Figure 1.632. The crack progression at displacement ductility 1, 1.5, and 2 appear in Figure 1.633, Figure 1.634, and Figure 1.637 respectively. During these cycles the cracks became more numerous and increased in inclination on the shear faces of the specimen.

The first signs of visible flaking of the core concrete, which precedes crushing, occurred on the South side at $(\mu_2^{+1} = 5.71")$ and the North side at $(\mu_2^{-1} = -5.71")$ as shown in Figure 1.635. A small amount of core concrete crushed on the North side of the specimen during the following pull cycle to $(\mu_2^{-2} = -5.72")$, as shown in the left photo of Figure 1.636. A similar observation was made on the South side of the specimen during $(\mu_3^{+1} = 8.58")$. A photo of crushing on the South side of the specimen appears in the right portion of Figure 1.636, a better quality picture is not available. The crushing on each side of the specimen during ductility three was not severe, and it appeared that only a thin layer of concrete flaked off between spiral layers. The crack progression during displacement ductility three and four are shown in Figure 1.638 and Figure 1.639 respectively.

Progressively larger spiral strains were observed on the North side of the specimen during displacement ductility four. In previous tests, this occurred when the extreme fiber longitudinal bar measurably deformed before visible bar buckling. A photo of the North extreme fiber bar N3 at $(\mu_4^{-3} = -11.44")$, in left side of Figure 1.640, shows that visible buckling had not yet occurred over the regions of large inelastic spiral strains. Instead, visible bar buckling of bar N3 occurred under compressive stress during the reversal from $(\mu_5^{+1} = 14.29")$, as shown in the right photo of Figure 1.640. Similarly, the South extreme fiber bar S3 buckled during the reversal from $(\mu_5^{-1} = -14.32")$, as shown in the left photo of Figure 1.641. The first observation of buckling on each side of the specimen occurred when the outward deformation of the bar was still small.

Additional deformation in the previously buckled bar N3 was observed during the subsequent pull cycle to ($\mu_5^{-2} = -14.33$") in Figure 1.642. Similarly, additional deformation in buckled bar S3 was observed during ($\mu_5^{+3} = 14.33$"), see the right photo of Figure 1.641. The outward deformation in buckled bar N3 continued to increase during ($\mu_5^{-3} = -14.33$"), and the bar fractured in tension during the subsequent push cycle to ($\mu_5^{+4} = 14.33$"), as shown in Figure 1.643. Fracture of bar N3 lead to a 24% loss in strength measured at ($\mu_5^{+4} = 14.33$") relative to the peak lateral force measured in the push direction of loading. Adjacent North reinforcing bar N4 buckled during ($\mu_5^{-4} = -14.32$"), see the left photo of Figure 1.644.

The deformation in previously buckled bar S3 became even more severe during ($\mu_5^{+6} = 14.34$") as shown in the right photo of Figure 1.644. Bar S3 fractured in tension during the subsequent reversal to ($\mu_5^{-6} = -14.33$"), see Figure 1.645. Fracture of bar S3 lead to a 39% loss in strength measured at ($\mu_5^{-6} = -14.33$") relative to the peak lateral force measured in the pull direction of loading. At this time the test was concluded with two buckled bars and one fractured bar on the North side of the specimen and one buckled and fractured bar on the South side of the specimen. Photos of all sides of the specimen after removal of the instrumentation appear in Figure 1.646.

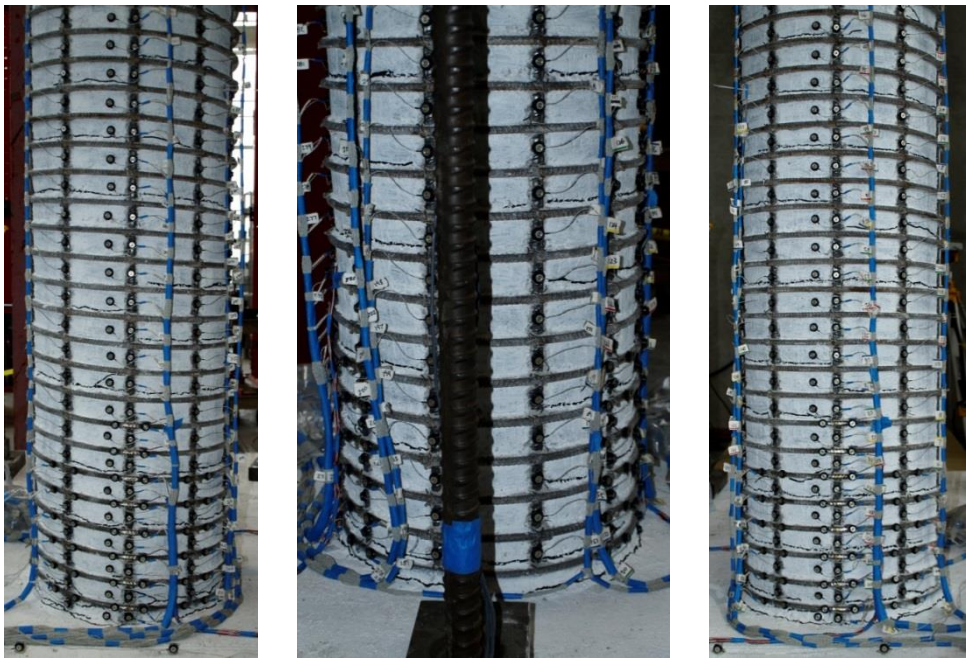

Figure 1.632 T24 – (Left) North at Fy', (Mid) Front at -Fy', and (Right) South at -Fy'

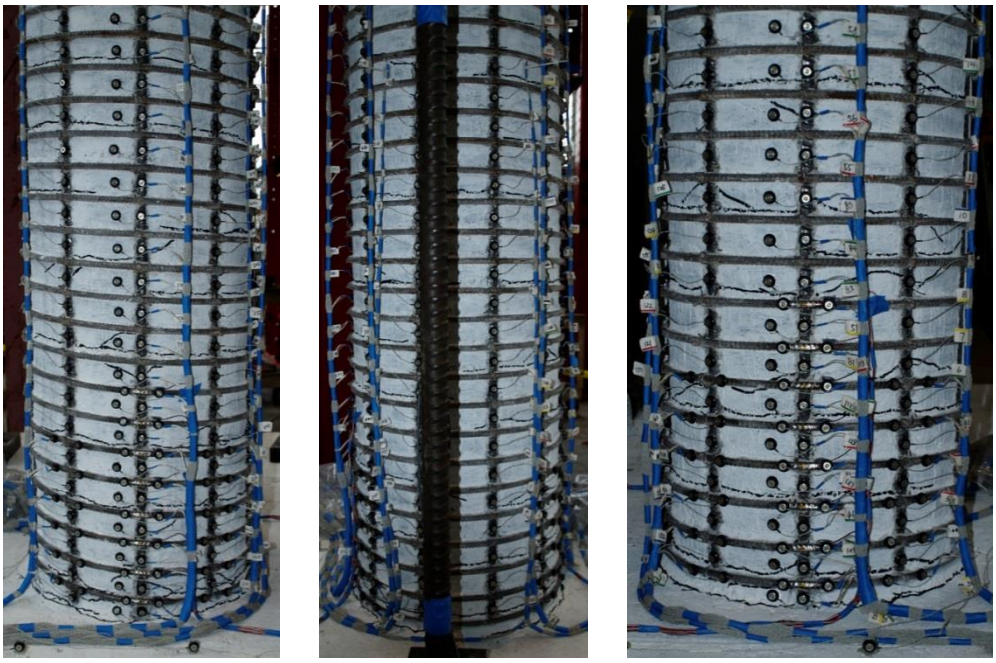

Figure 1.633 T24 – (Left) North at μ_1^{+3}, (Mid) Front at μ_1^{-3}, and (Right) South at μ_1^{-3}

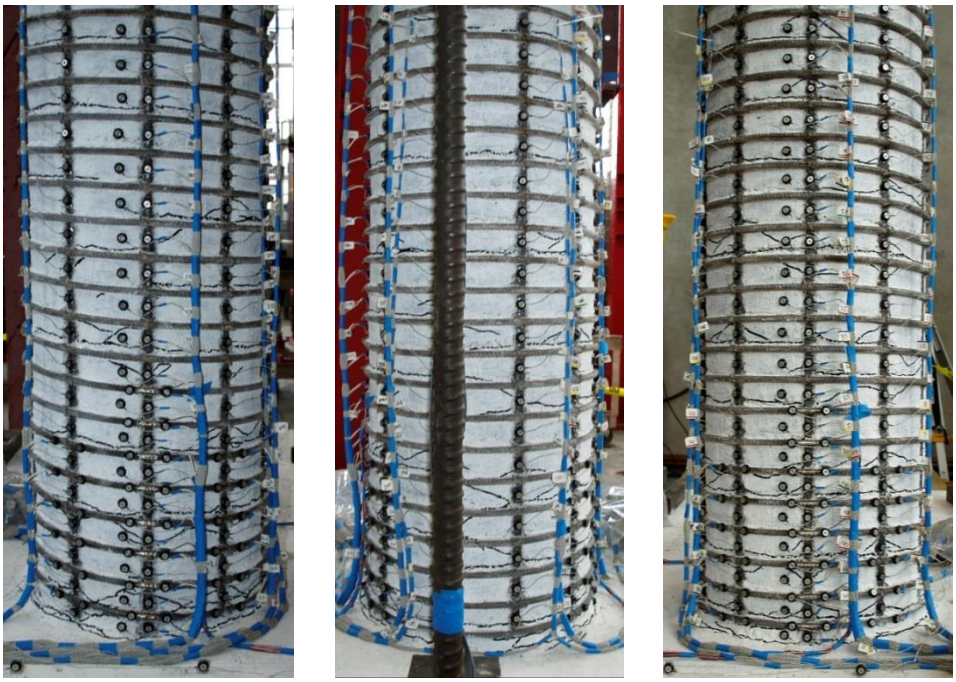

Figure 1.634 T24 – (Left) North at $\mu_{1.5}^{+3}$, (Mid) Front at $\mu_{1.5}^{-3}$, and (Right) South at $\mu_{1.5}^{-3}$

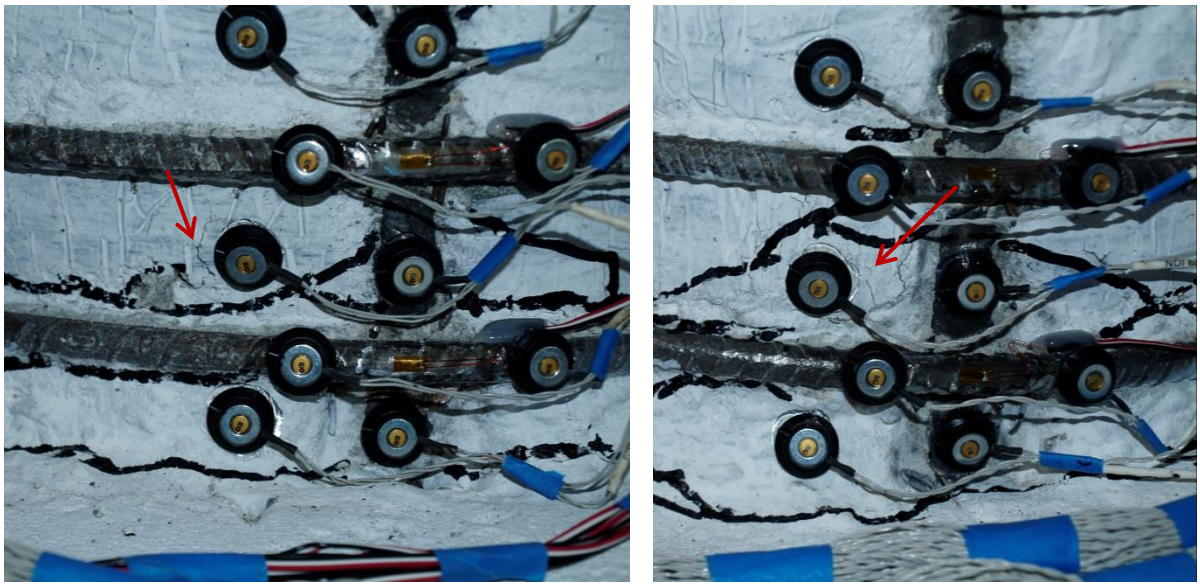

Figure 1.635 T24 – Visible Flaking of Cover Concrete which Precedes Crushing (Left) South Side during μ_2^{+1} and (Right) North Side during μ_2^{-1}

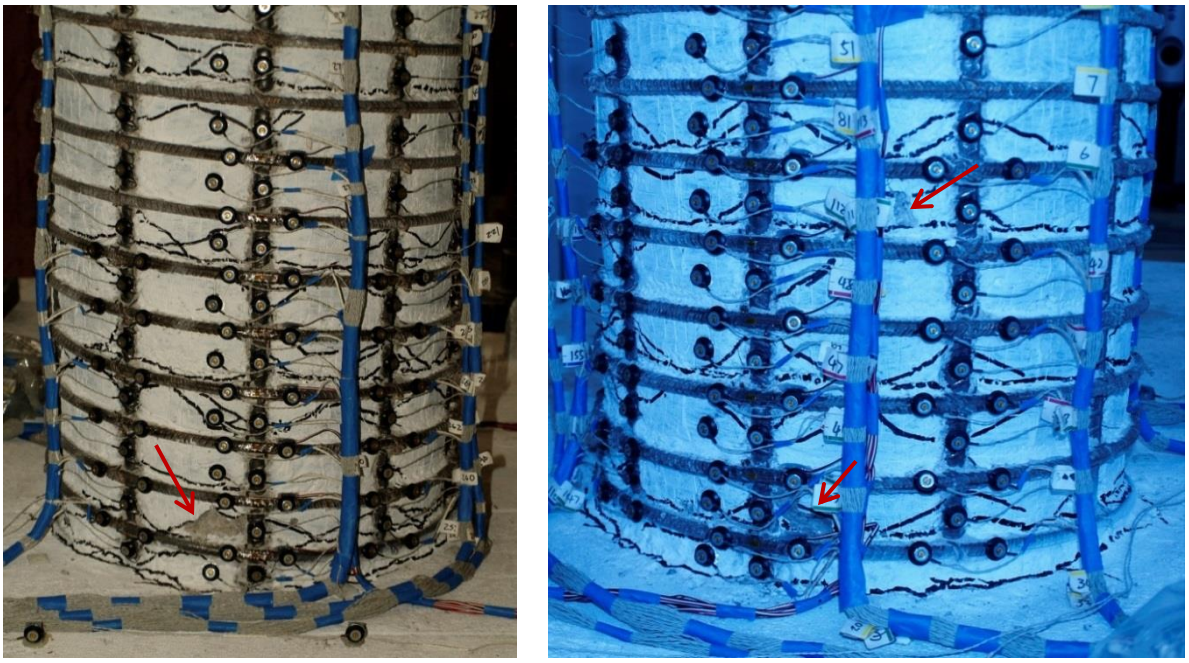

Figure 1.636 T24 – Concrete Crushing on (Left) the North Side during μ_2^{-2} and (Right) the South Side during μ_3^{+1}

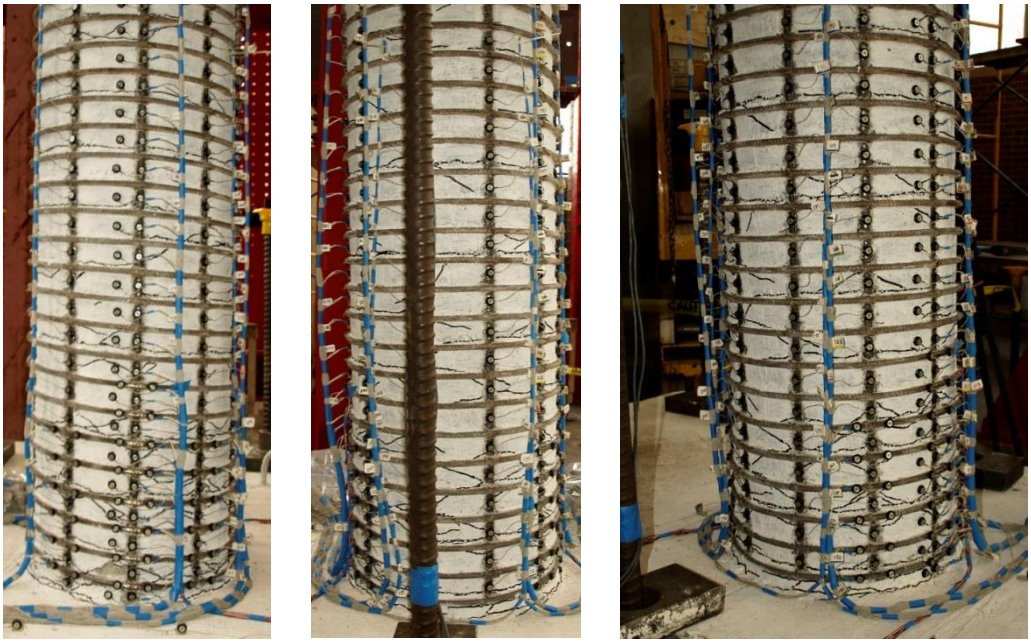

Figure 1.637 T24 – (Left) North at μ_2^{+3}, (Mid) Front at μ_2^{-3}, and (Right) South at μ_2^{-3}

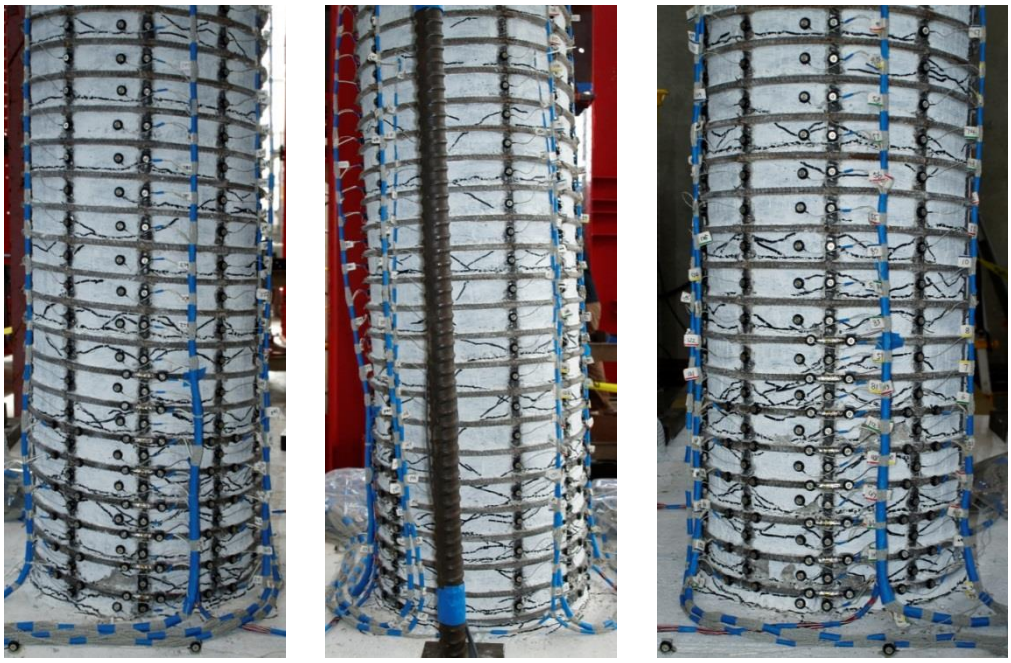

Figure 1.638 T24 – (Left) North at μ_3^{+3}, (Mid) Front at μ_3^{-3}, and (Right) South at μ_3^{-3}

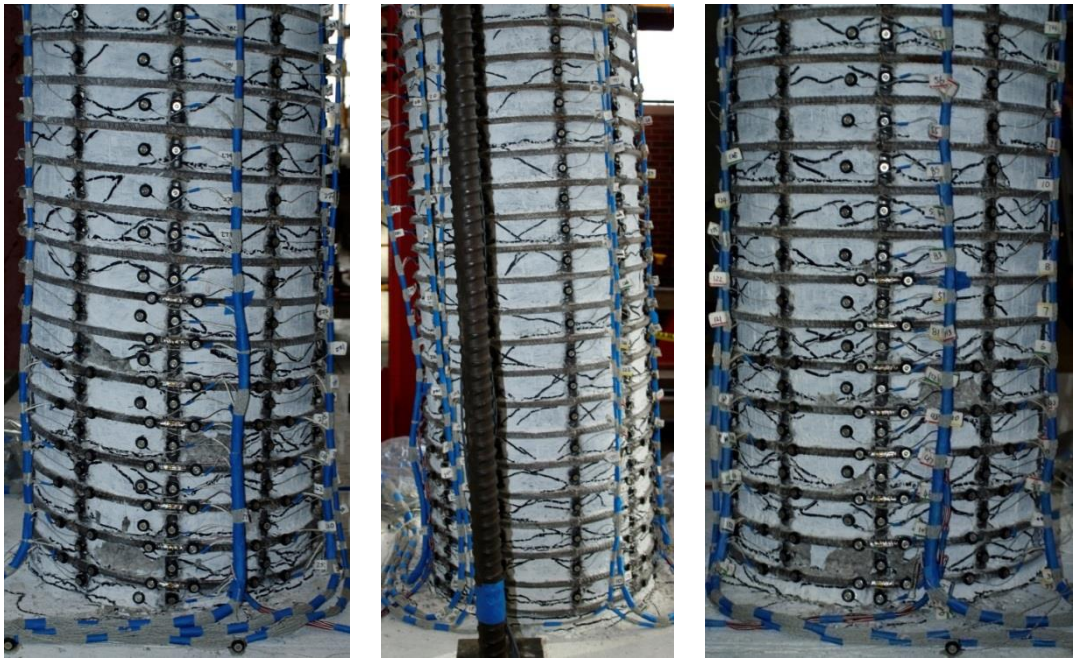

Figure 1.639 T24 – (Left) North at μ_4^{+3}, (Mid) Front at μ_4^{-3}, and (Right) South at μ_4^{-3}

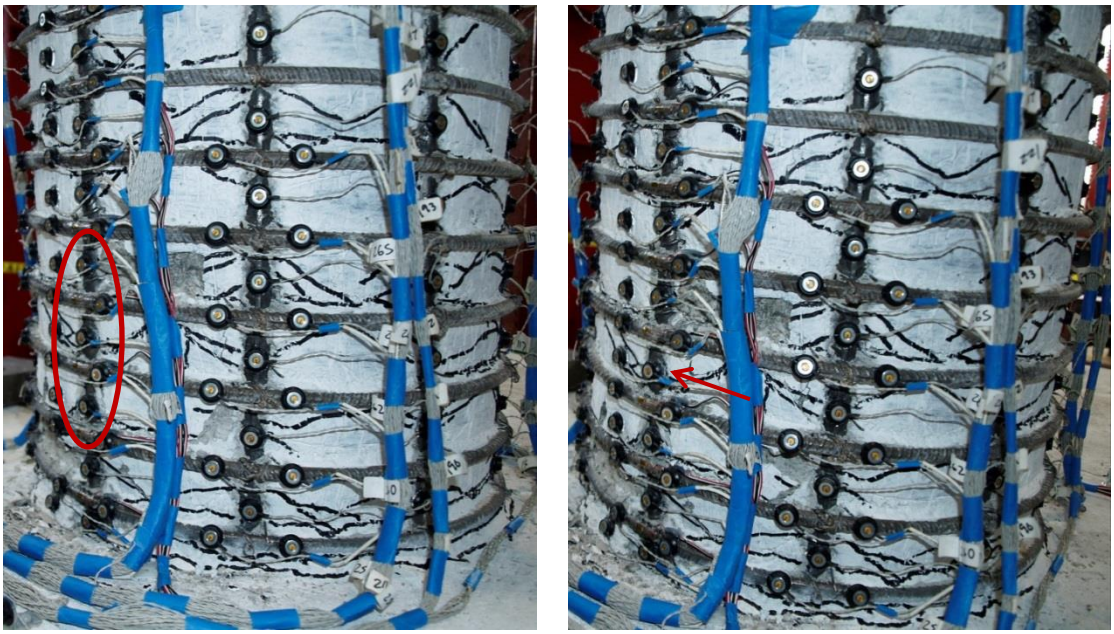

Figure 1.640 T24 – (Left) North Side during μ_4^{-3} without Visible Bar Buckling and (Right) Visible Bar Buckling of N3 during μ_5^{-1}

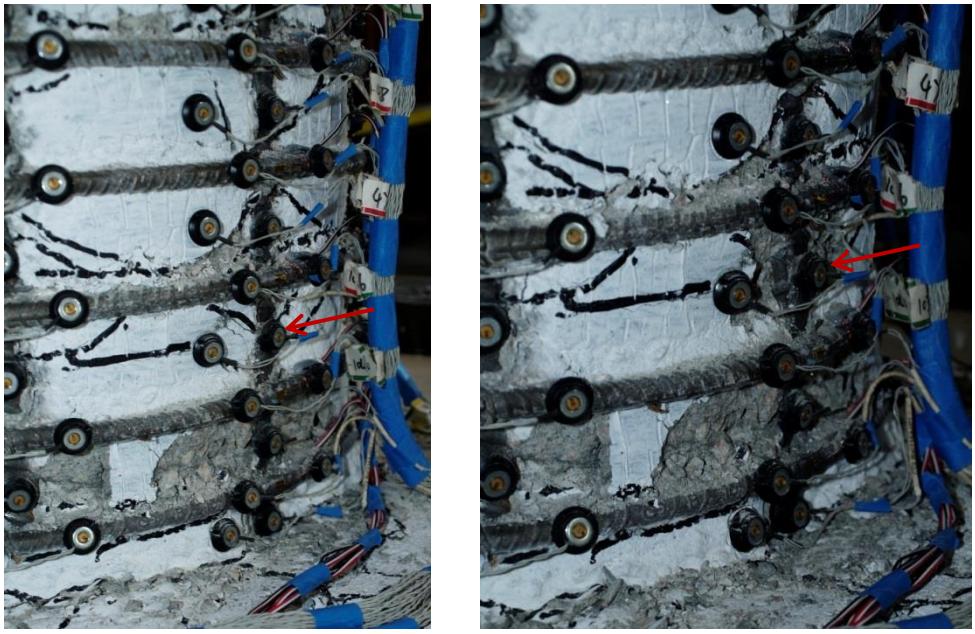

Figure 1.641 T24 – (Left) Visible Bar Buckling of S3 during μ_5^{+2} and (Right) Additional Deformation in Buckled Bar S3 during μ_5^{+3}

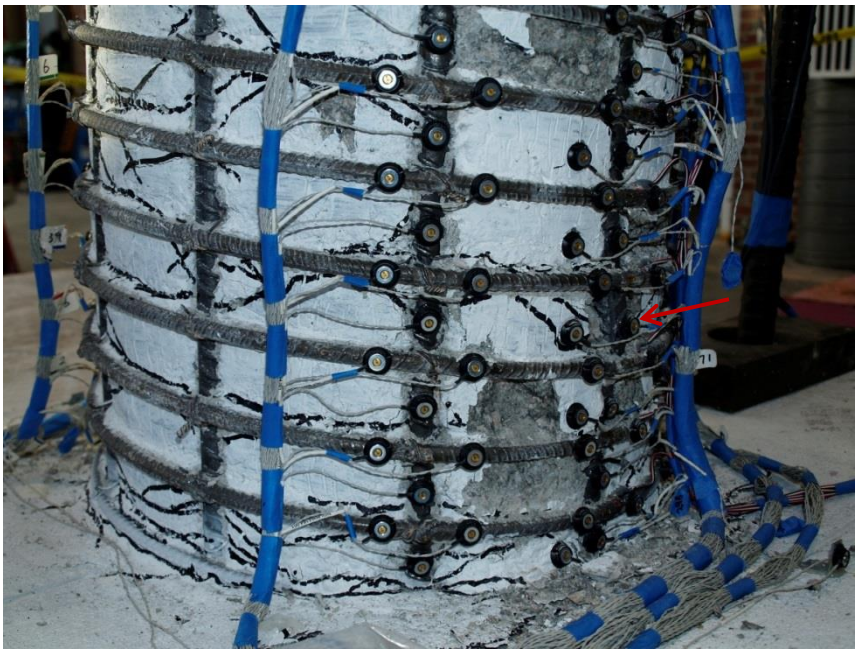

Figure 1.642 T24 – Additional Deformation in Previously Buckled Bar N3 during μ_5^{-2}

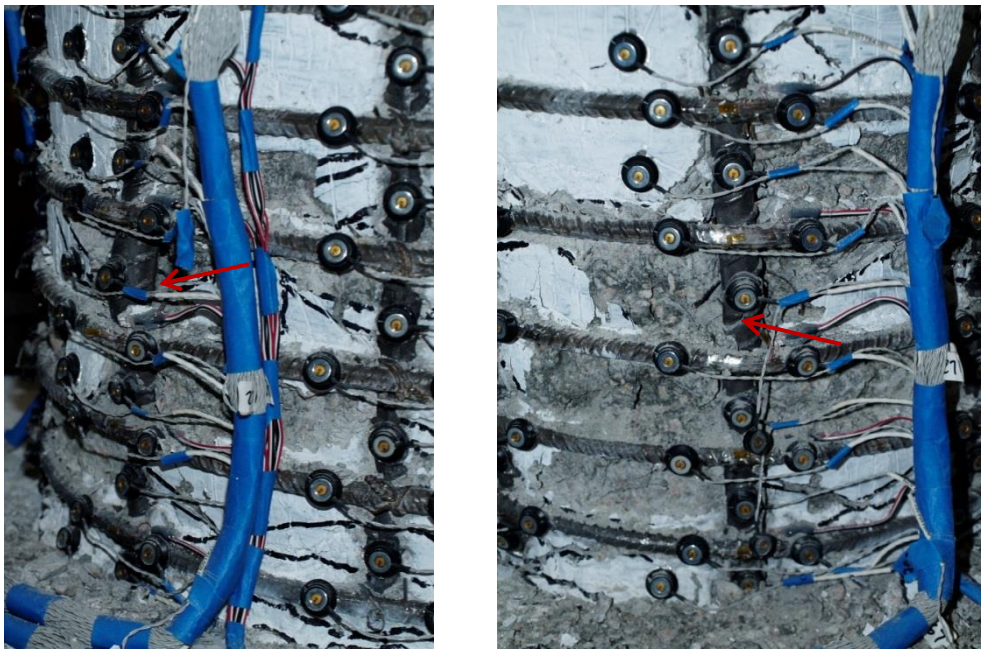

Figure 1.643 T24 – (Left) Additional Deformation in Buckled Bar N3 during μ_5^{-3} and (Right) Fracture of Previously Buckled Bar N3 during μ_5^{+4}

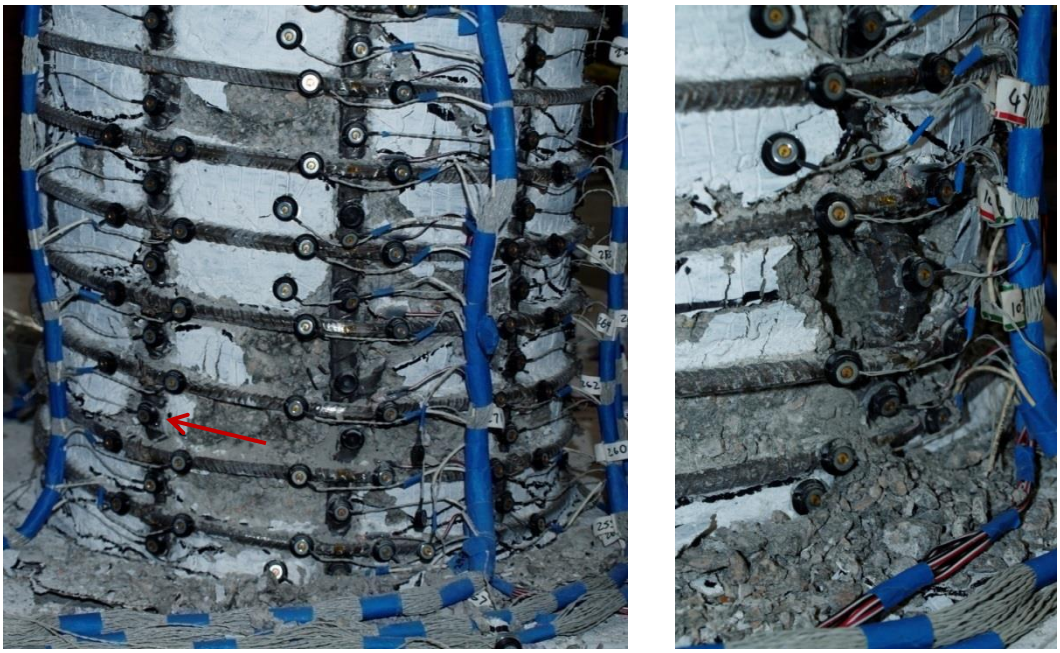

Figure 1.644 T24 – (Left) Buckling of Adjacent Bar N4 during μ_5^{-4} and (Right) Additional Deformation in Bar S3 during μ_5^{+6}

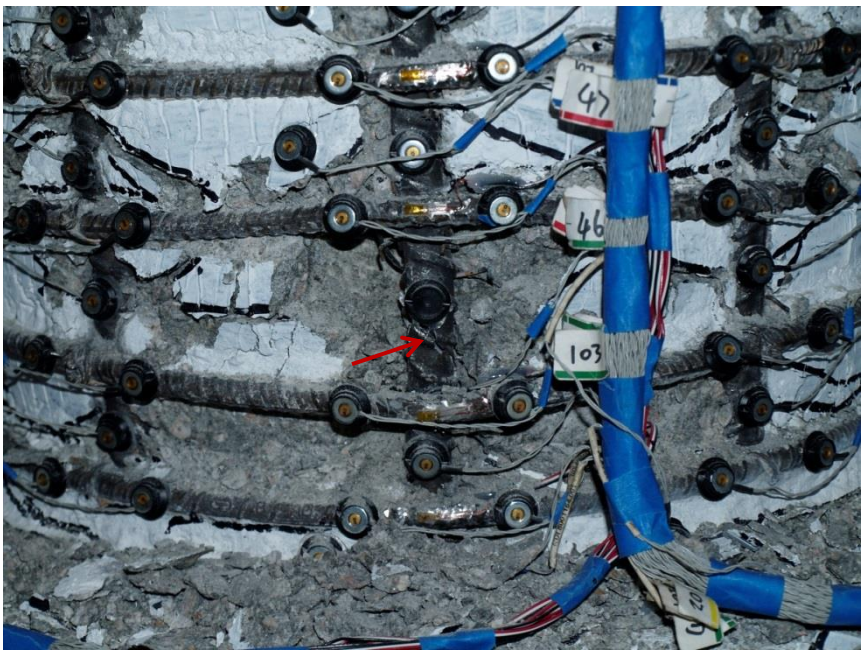

Figure 1.645 T24 – Fracture of Previously Buckled Bar S3 during μ_5^{-6}

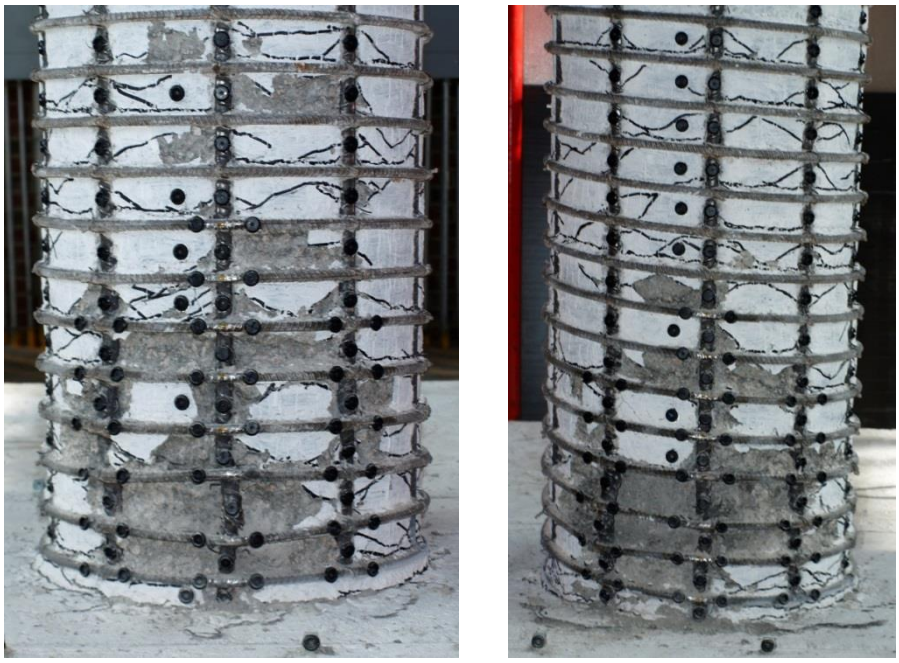

Figure 1.646 T24 – After the Test (Left) South Side and (Right) North Side

Test 24 Aspect Ratio of 8.67 and 10% Axial Load – Strain Data Analysis

North Reinforcement

Vertical strain profiles for the North extreme fiber bar N3 placed into tension during push cycles appear in the right half of Figure 1.647. This figure shows both extreme fiber bars on the same graph to illustrate the effects of tension shift on strain profiles. Compressive vertical strain profiles for North extreme fiber bar N3 during pull cycles appear in the left half of Figure 1.648. A peak tensile strain of 0.0365, located 11.13" above the footing, was measured for North extreme fiber bar N3 during ($\mu_5^{+1} = 14.29"$). A tensile strain of 0.0359 was measured 4.98" above the footing during the same cycle. Extreme fiber bar N3 visibly buckled under compressive stress during the following reversal of load to ($\mu_5^{-1} = -14.32"$). The relationship between tensile strain and displacement for the gage length 4.98" above the footing appears in Figure 1.651. The moment-curvature prediction

with the PCK (2007) Lp Hinge Method begins to overestimate the measured tensile strains after displacement ductility three at an increasing rate. Each line represents a single push cycle which began with the column at zero displacement and ended at the peak of a continuous push cycle. The solid line contains data during the push cycle loading up to the peak displacement, and the dashed line represents the subsequent reversal of load.

A peak compressive strain of -0.0283 was measured 2.97" above the footing during ($\mu_4^{-3} = -11.44"$). This value exceeds the Mander ultimate concrete compressive strain of 0.0202. A second region of large compressive demand produced a strain of -0.0219 for the gage length 7.07" above the footing. The relationship between compressive strain and displacement for the gage length 2.97" above the footing appears in Figure 1.652. The measured compressive strains begin to exceed the moment-curvature prediction with the PCK (2007) Lp Hinge Method after displacement ductility 1.5. Each cycle of displacement ductility four was shown to highlight measurable deformation of bar N3.

The effects of compression on eight spiral layers on the North side of the specimen appear in Figure 1.650. The first spiral layer on the North side of the specimen entered the inelastic range at $-6.60"$ during pull cycle to ($\mu_3^{-1} = -8.58"$). Measureable deformation during displacement ductility four lead to an increase in the spiral strains measured 5.41" above the footing from 0.0074, 0.0124, to 0.0189 during consecutive cycles of displacement ductility four. This measurable deformation aligns with the region of outward visible bar buckling shown in Figure 1.642. Gage lengths above and below the outward deformed region of bar N3 would have apparent larger compressive strains since the target markers are located on the concave side of the buckled bar. Alternatively, the gage lengths located on the convex side of the outward buckled bar increase under compressive demand.

Strain hysteresis for extreme fiber bar N3 up to visible bar buckling are shown in Figure 1.655, Figure 1.656, and Figure 1.657 for gage lengths 2.97", 4.98" and 7.07" above the footing respectively. The gage length 4.98" represents the outward buckled region of bar N3, and aligns with the largest spiral strains measured 5.41" above the footing. The gage lengths 2.97" and 7.07" above the footing appear above and below the outward buckled region.

These gage lengths had significant measurable deformation during successive pull cycles of displacement ductility four. Transverse steel strain hysteresis for spiral layers 5.41" and 7.34" above the footing appear in Figure 1.658 and Figure 1.659 respectively. It is clear that the measurable deformation lead to significant increases in the spiral strains measured during displacement ductility four. The strain gages on each spiral layer debonded, preventing further measurement, during the pull cycle to ($\mu_5^{-1} = -14.32"$) when outward visible bar buckling was observed for bar N3.

South Reinforcement

Vertical strain profiles for the South extreme fiber bar S3 placed into tension during pull cycles appear in the right half of Figure 1.648. A peak tensile strain of 0.0454, located 5.19" above the footing, was measured during ($\mu_5^{-1} = -14.32"$). The South extreme fiber bar S3 buckled under compressive stress during the following reversal to ($\mu_5^{+2} = 14.33"$). The relationship between tensile strain and displacement for the gage length 5.19" above the footing appears in Figure 1.653. For this gage length, the moment-curvature prediction with the PCK (2007) Lp Hinge Method only slightly overestimates the measured tensile strains after displacement ductility three.

Compressive vertical strain profiles for bar S3 appear in the left half of Figure 1.647. A peak compressive strain of -0.02044 was measured 1.30" above the footing during ($\mu_5^{+1} = 14.29"$). Regions of compressive demand 5.19" and 9.29" above the footing produced compressive strains of -0.0176 and -0.0187 respectively. The relationship between compressive strain and displacement for gage length 9.29" above the footing appears in Figure 1.654. The measured compressive strains are underestimated by moment-curvature analysis with the PCK (2007) Lp Hinge Method after displacement ductility 1.5. Measured spiral strains the lowest eight South spiral layers appear in Figure 1.649. A peak spiral strain of 0.0100 was measured 3.06" above the footing during ($\mu_5^{+1} = 14.29"$). Over this same gage length, spiral strains increased from 0.0042, 0.0049, to 0.0057 during successive

compressive cycles of displacement ductility four. Outward visible bar buckling was observed over the gage length 3.14" above the footing as shown in Figure 1.641.

Longitudinal steel strain hysteresis for gage lengths 3.14" and 5.19" above the footing on bar S3 appear in Figure 1.660 and Figure 1.661 respectively. The gage length 3.14" above the footing aligns with the outward buckled region of bar S3, in Figure 1.641, and the largest spiral strains measured 3.06" above the footing. Transverse steel strain hysteresis for spiral layers 3.06" and 5.15" above the footing appear in Figure 1.662 and Figure 1.663 respectively. Visible buckling of bar S3 altered the strain and displacement relationship for the gage length 3.14" above the footing and caused a spike in measured spiral strains 3.06" and 5.15" above the footing. The spiral stain hystereses indicate a small cycle-to-cycle deformation during successive compressive cycles of displacement ductility four.

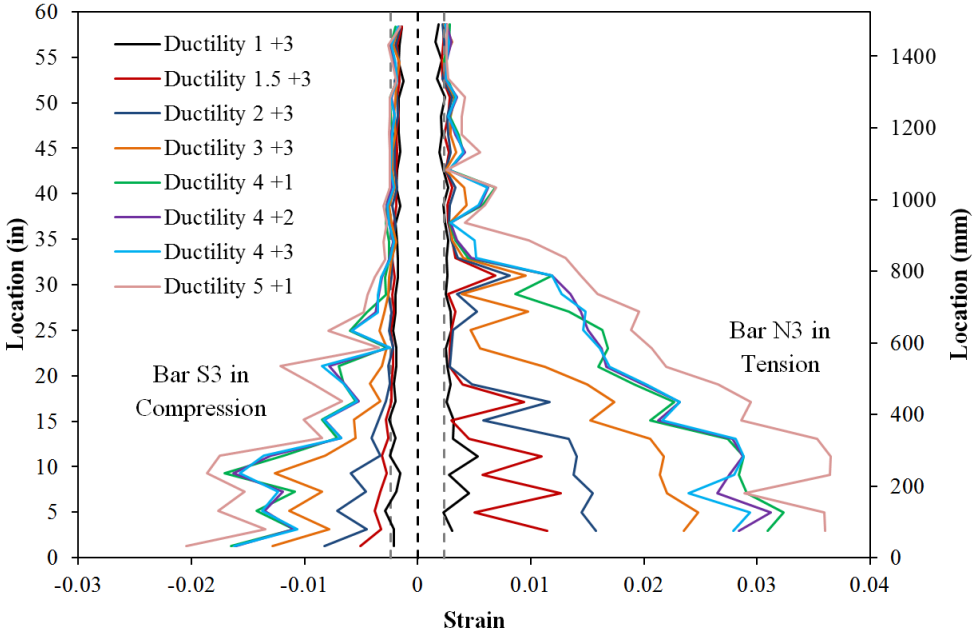

Figure 1.647 T24 – Extreme Fiber Bar Vertical Strain Profiles during Push Cycles

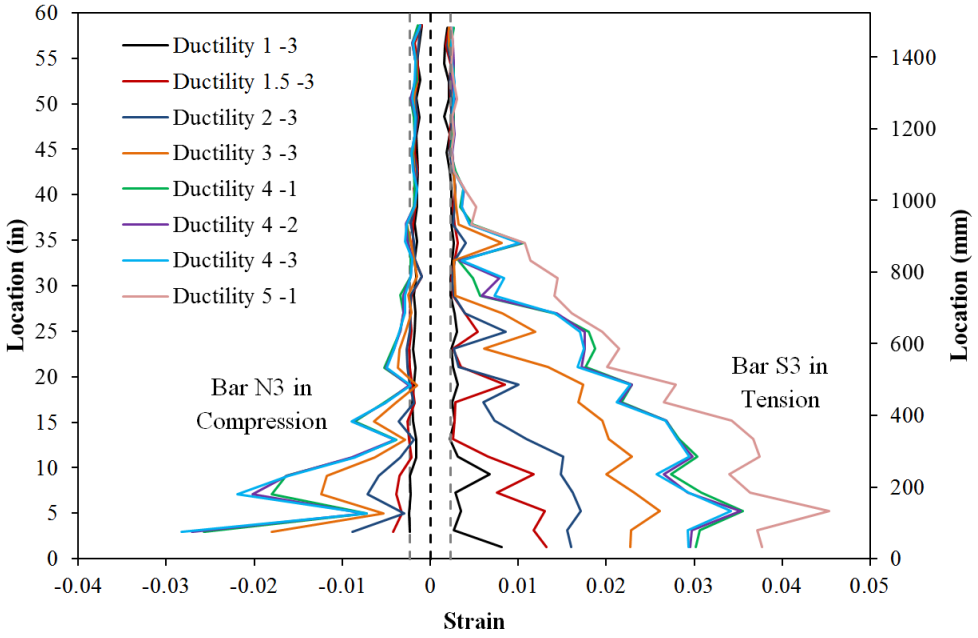

Figure 1.648 T24 – Extreme Fiber Bar Vertical Strain Profiles during Pull Cycles

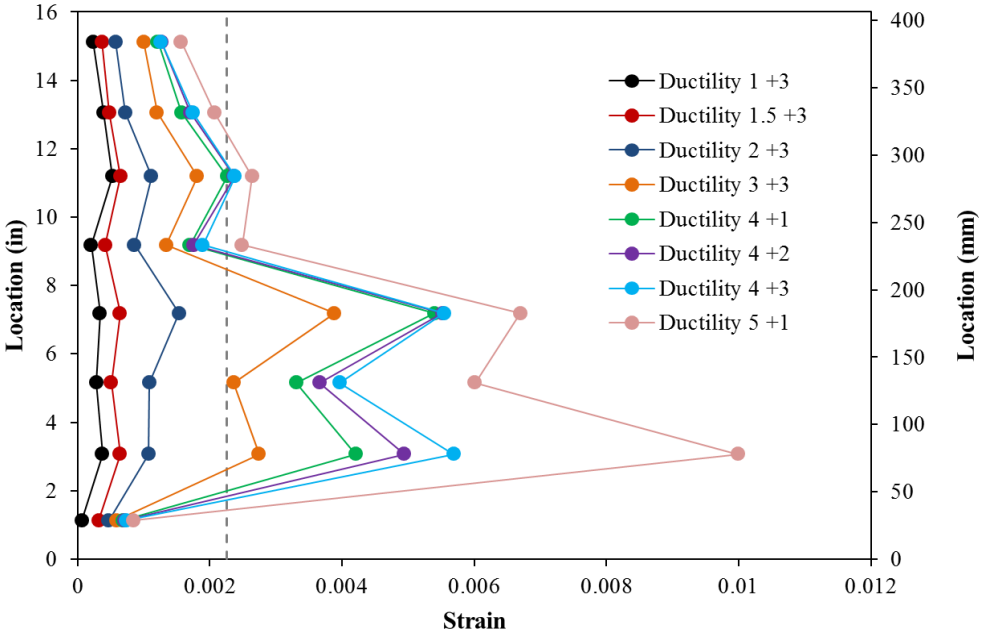

Figure 1.649 T24 – Spiral Strains on the South Side during Push Cycles

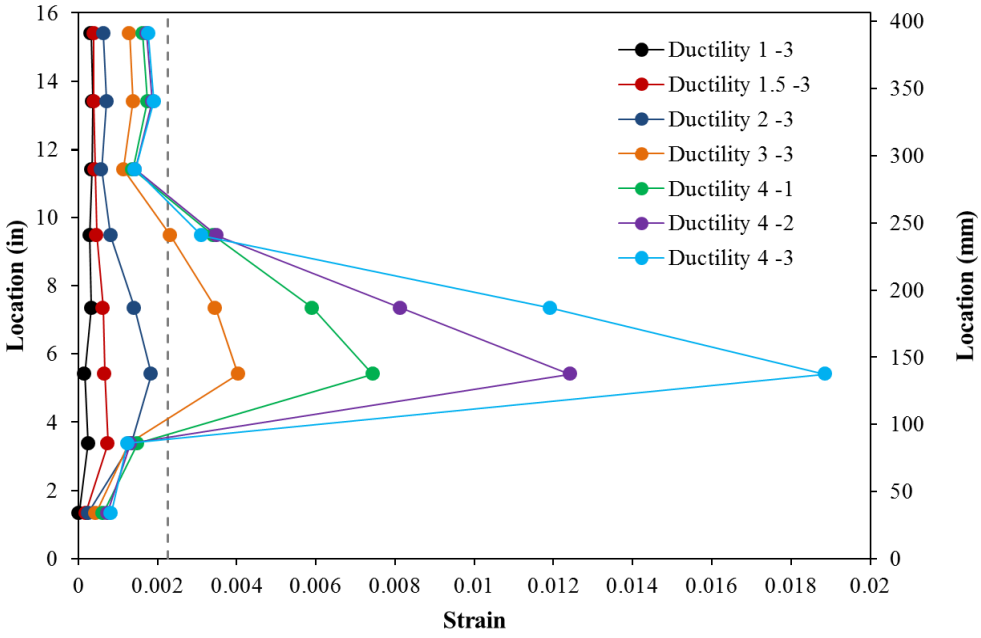

Figure 1.650 T24 – Spiral Strains on the North Side during Pull Cycles

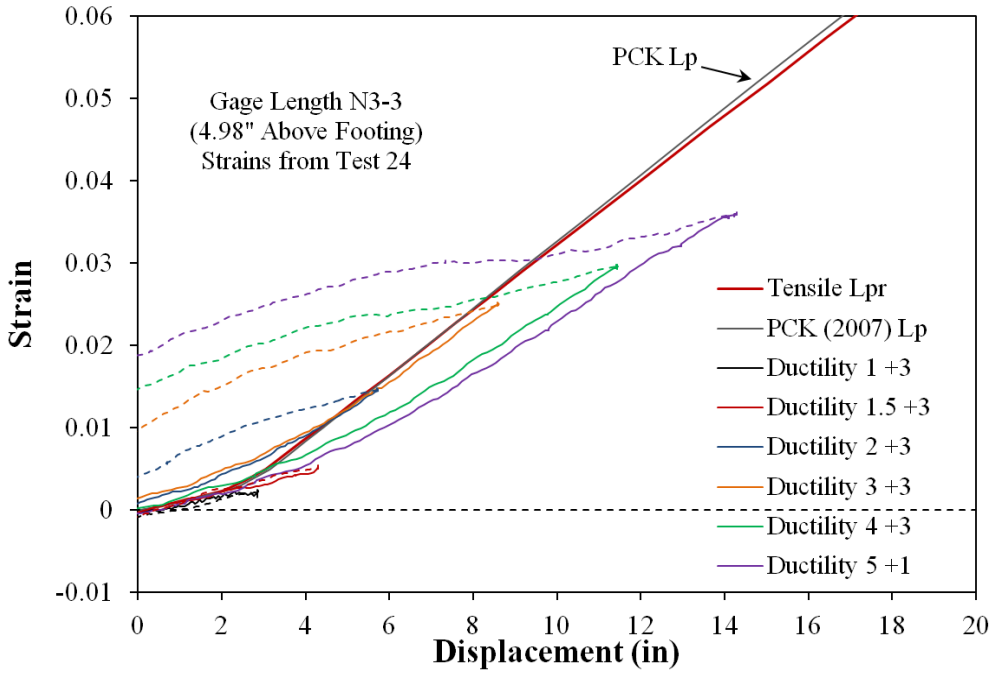

Figure 1.651 T24 – Tensile Strain-Displacement for Bar N3 during Push Cycles

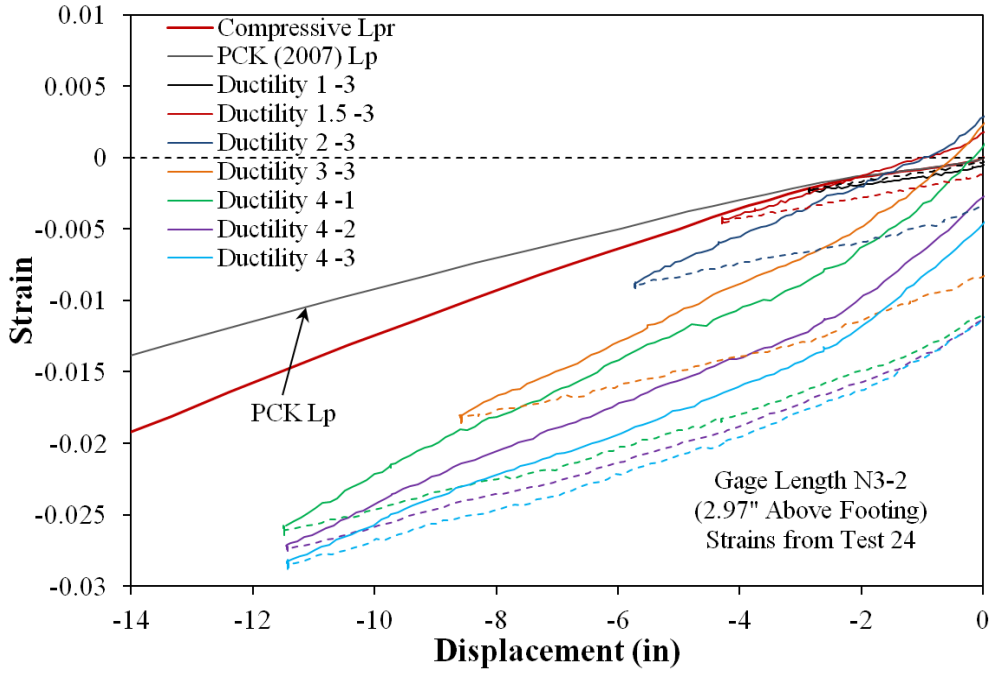

Figure 1.652 T24 – Compressive Strain-Displacement for Bar N3 during Pull Cycles

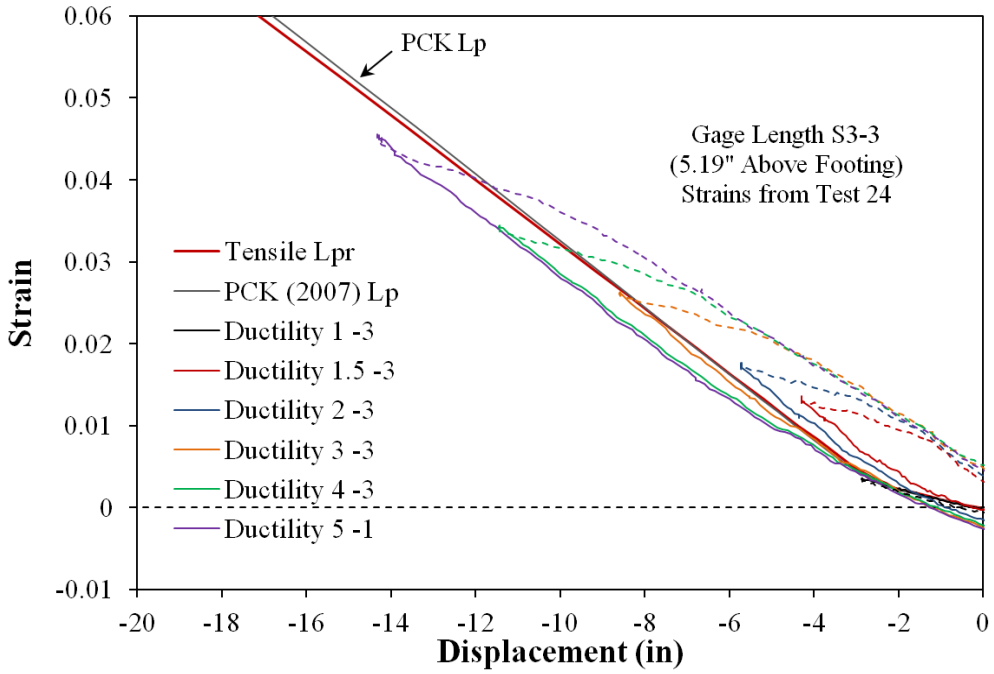

Figure 1.653 T24 – Tensile Strain-Displacement for Bar S3 during Pull Cycles

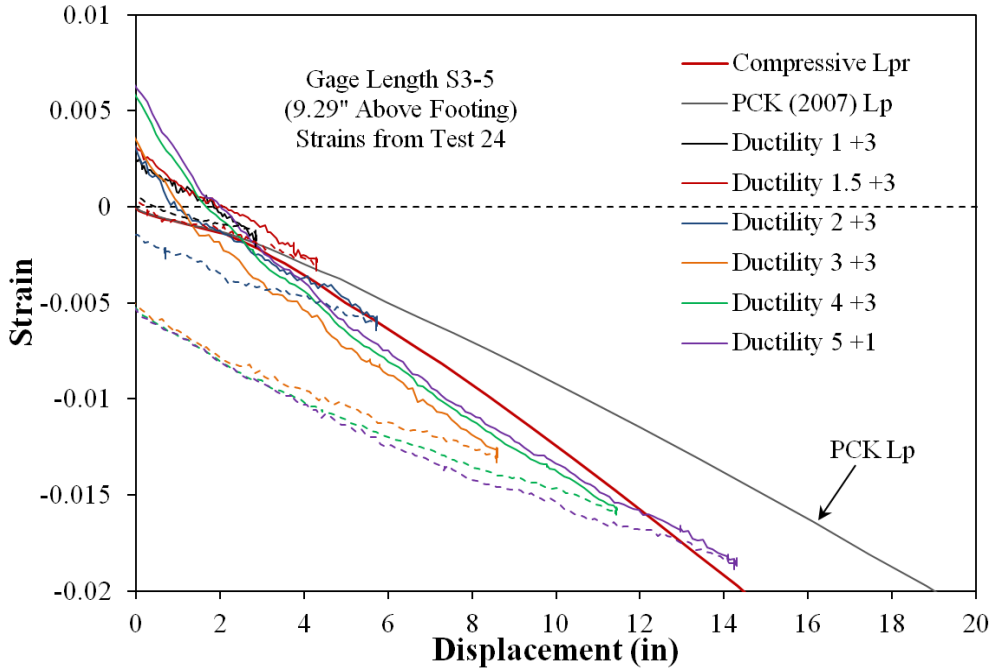

Figure 1.654 T24 – Compressive Strain-Displacement for Bar S3 during Push Cycles

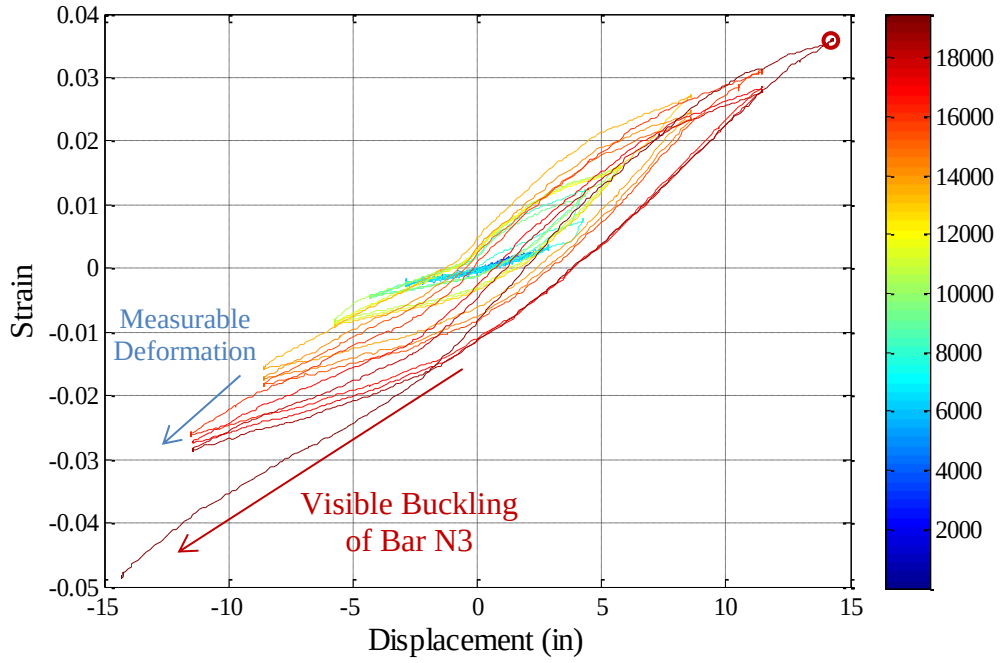

Figure 1.655 T24 – Strain Hysteresis for Bar N3 to Buckling (2.97" Above the Footing)

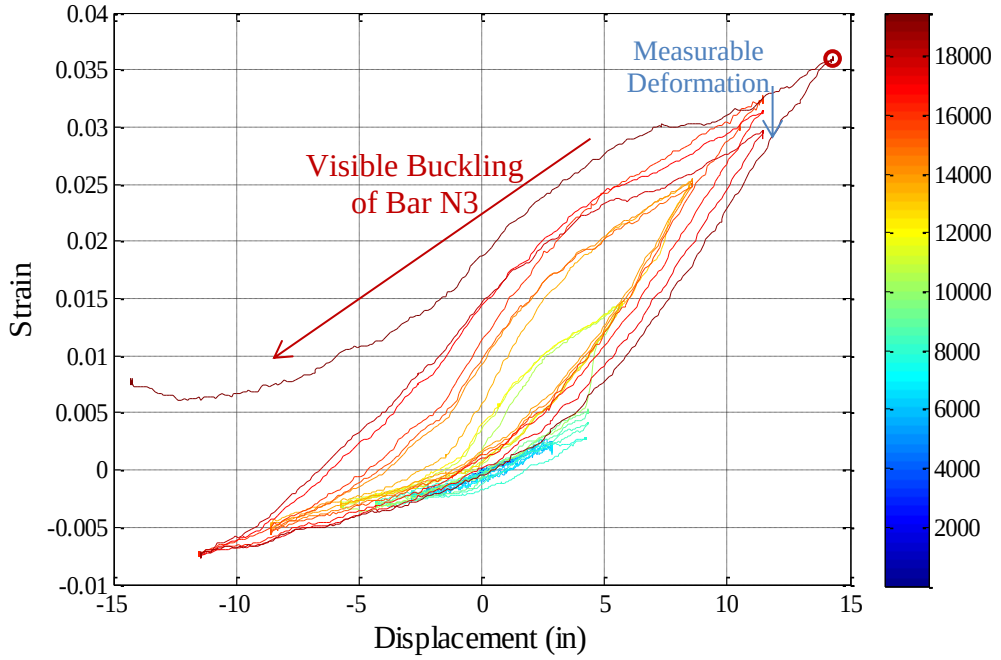

Figure 1.656 T24 – Strain Hysteresis for Bar N3 to Buckling (4.98" Above the Footing)

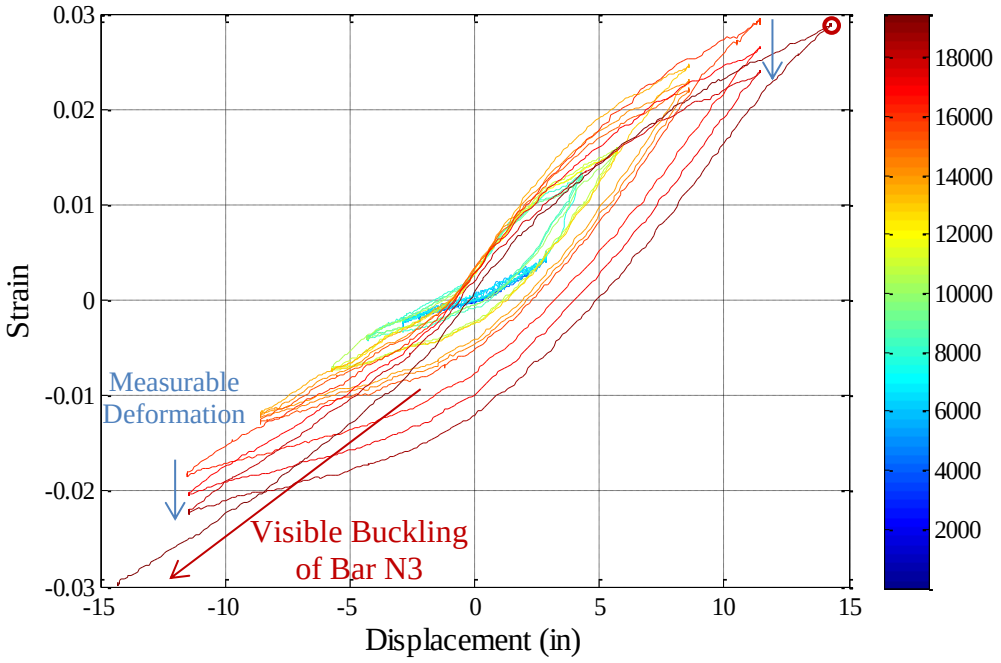

Figure 1.657 T24 – Strain Hysteresis for Bar N3 to Buckling (7.07" Above the Footing)

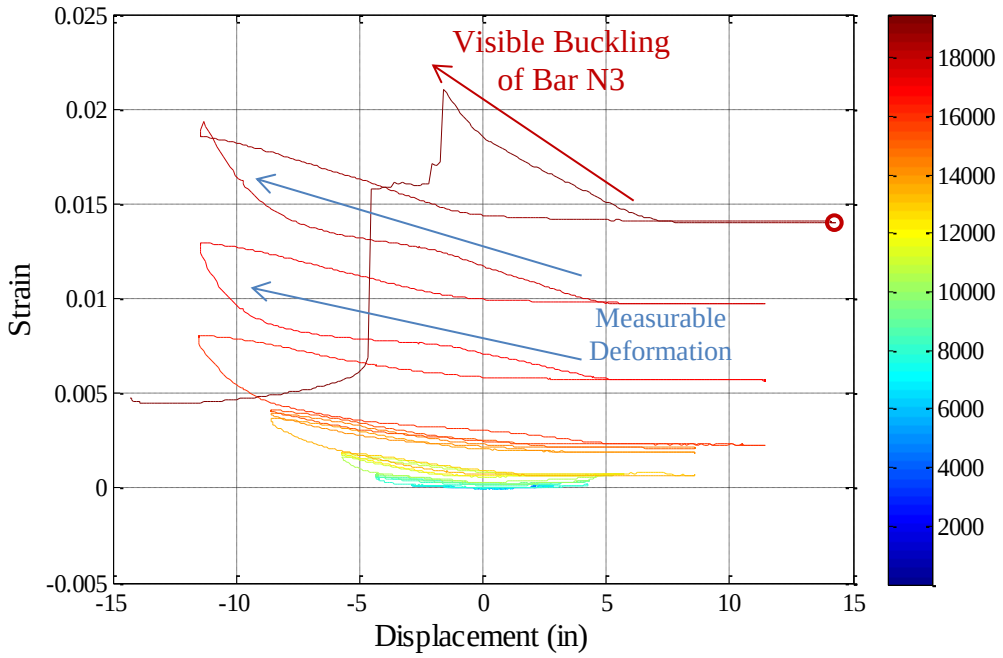

Figure 1.658 T24 – Spiral Strain Hysteresis over North Buckled Region (5.41" Above)

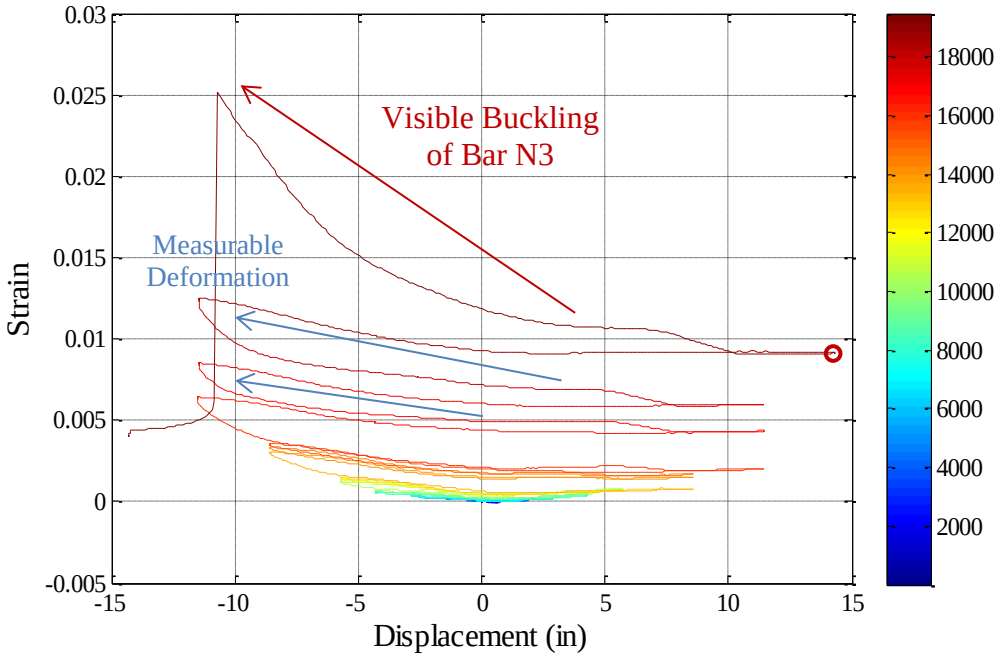

Figure 1.659 T24 – Spiral Strain Hysteresis over North Buckled Region (7.34" Above)

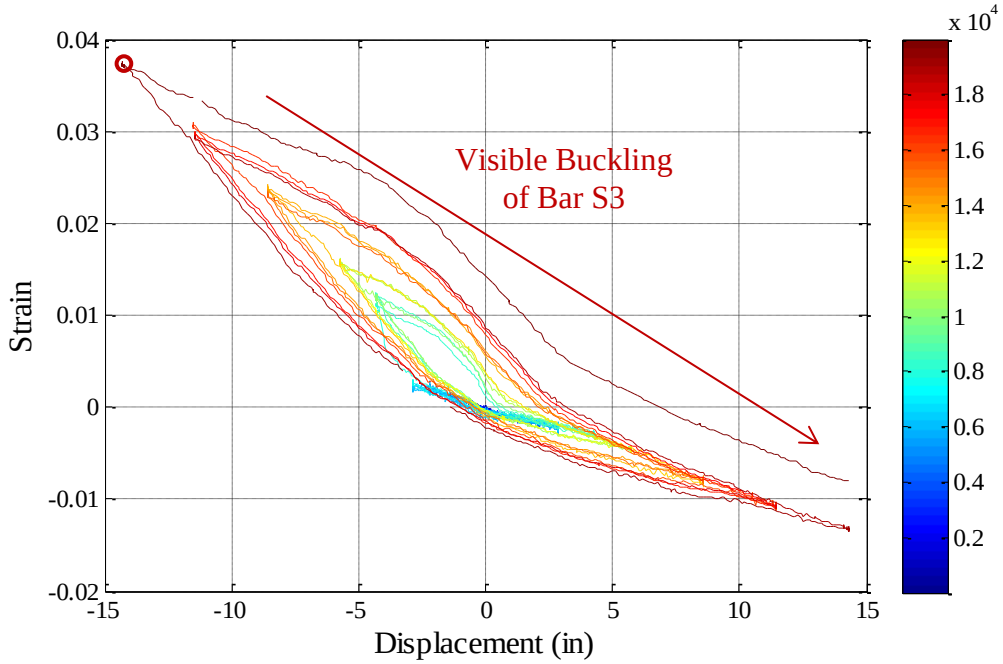

Figure 1.660 T24 – Strain Hysteresis for Bar S3 to Buckling (3.14" Above the Footing)

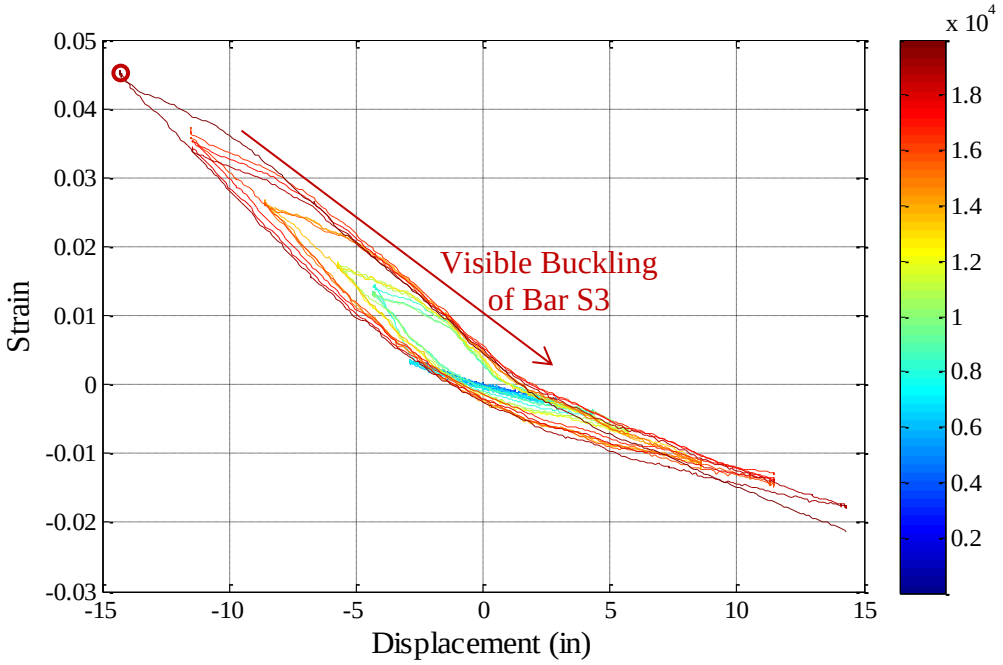

Figure 1.661 T24 – Strain Hysteresis for Bar S3 to Buckling (5.19" Above the Footing)

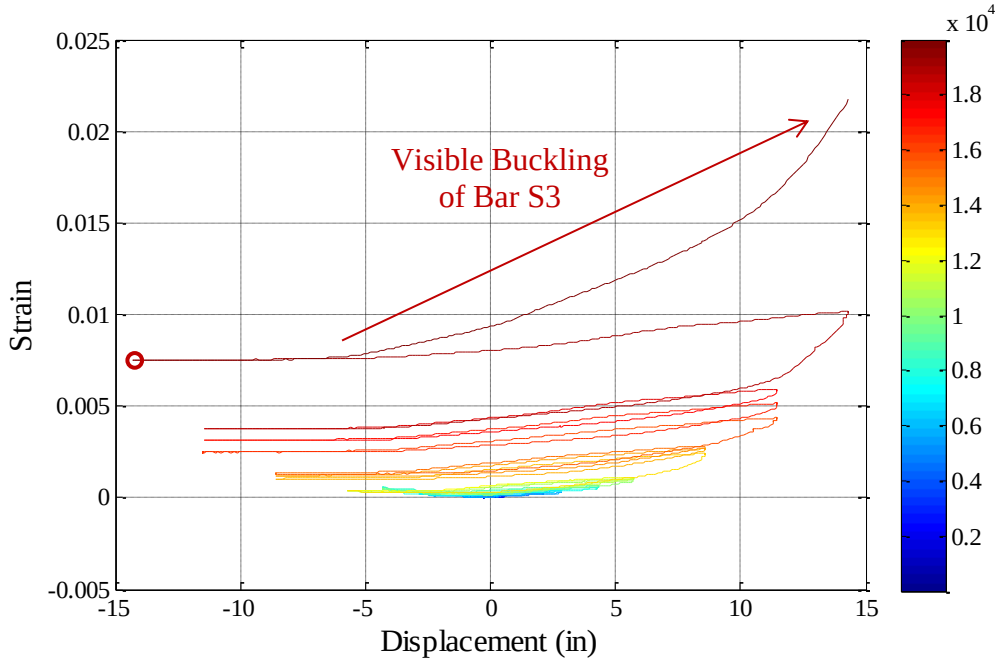

Figure 1.662 T24 – Spiral Strain Hysteresis over South Buckled Region (3.06" Above)

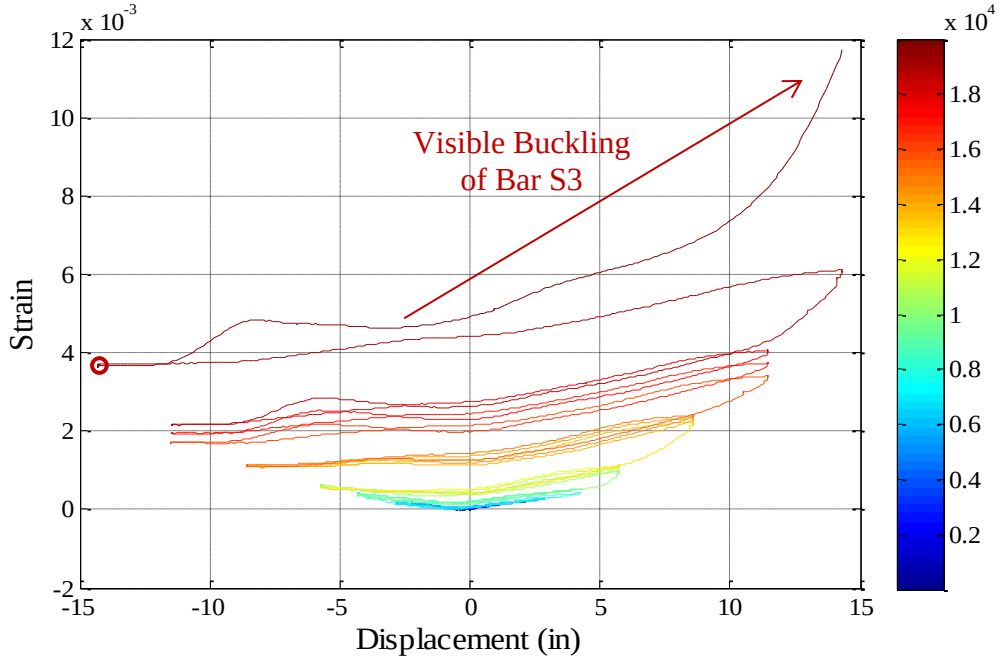

Figure 1.663 T24 – Spiral Strain Hysteresis over South Buckled Region (5.16" Above)

Test 24 Aspect Ratio of 8.67 and 10% Axial Load – Curvature and Strain Penetration

The cross section curvature for each horizontal section above the footing is determined by connecting the strain measurements from all eight instrumented bars with a least squared error line. The curvature is then extracted from the slope of the least squared error line, see Figure 1.664 and Figure 1.665. The cross section curvature profiles in these figures are shown for the third horizontal section above the footing-column interface. For these sections, it appears that the plane sections hypothesis remains appropriate. Vertical curvature profiles are plotted for push and pull cycles in Figure 1.666 and Figure 1.667 respectively. These figures show that plastic curvatures have a linear distribution at higher displacement ductility levels. The extent of plastic curvatures above the footing can be calculated by determining where the linear plastic curvature distribution intersects the triangular yield curvature profile, shown as a grey dashed line. The dashed lines for each curvature distribution represent a least squared error linear fit to the plastic portion of the measured curvatures. The measured spread of plasticity as a function of abase section curvature ductility appears on Figure 1.673.

The target marker on each bar placed closest the footing-column interface can be used to create bond slip hysteresis and horizontal bond slip profiles attributable to strain penetration of reinforcement into the footing. The bond slip hysteresis for bars N4 and S3 appear in Figure 1.668 and Figure 1.669 respectively. The lowest target marker on extreme fiber bar N3 was obstructed by wires during the test preventing bond slip and strain measurements for the lowest gage length. The first spiral layer was located close to the footing-column interface, therefore there was not enough room to place LEDs on many of the other reinforcing bars. If the lowest LEDs on these bars were used they would incorrectly include a large portion of the flexural strains measured between the footing and the next LED above the spiral layer. For this reason, the bond slip profiles for the base section are only measured in terms of bars S3 and N4 in Figure 1.670 and Figure 1.671. The rotation of the base section can is extracted from the slope of the least squared error line for the measured data.

Combining the curvatures over the instrumented region (5ft above the footing), bond slip profiles, and an elastic curvature assumption above the instrumented region, the top column displacement can be calculated by integrating the curvature distributions and extrapolating the fixed-end rotations to the center of loading. The top column displacements calculated from the Optotrak system are compared to displacements measured with a string potentiometer at the center of loading in Figure 1.672. The Optotrak integrated displacements exceed the measured response in the push direction of loading. The calculations have been verified, and it is likely that the strain penetration rotations calculated using only two reinforcing bars contribute to this error. Additionally, any errors in curvatures or base rotations are amplified by the long moment arm to the center of loading for this column with a high aspect ratio.

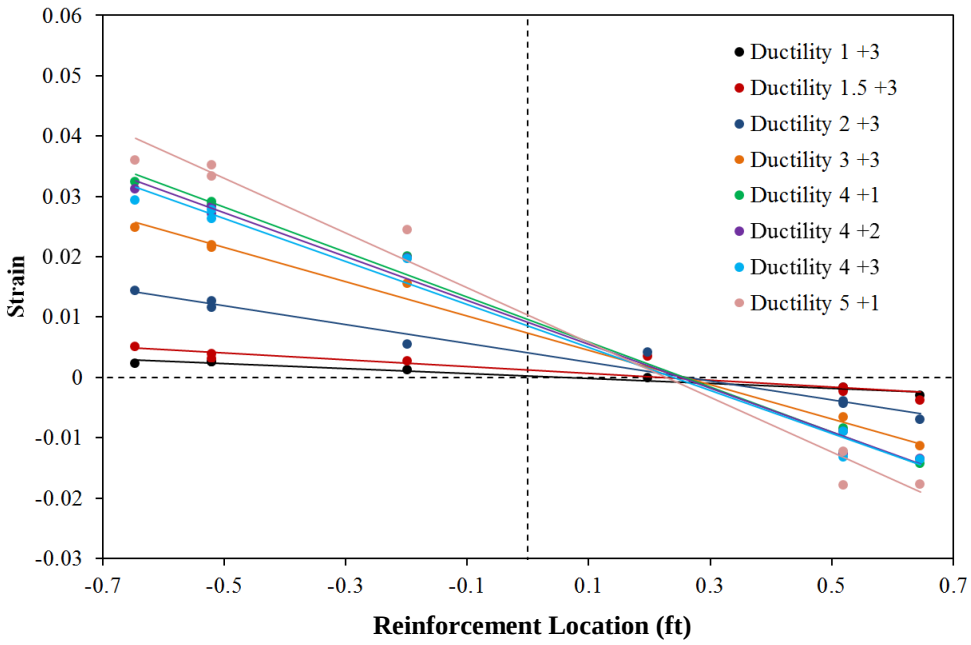

Figure 1.664 T24 – Cross Section Curvatures during Push Cycles (4.97" Above)

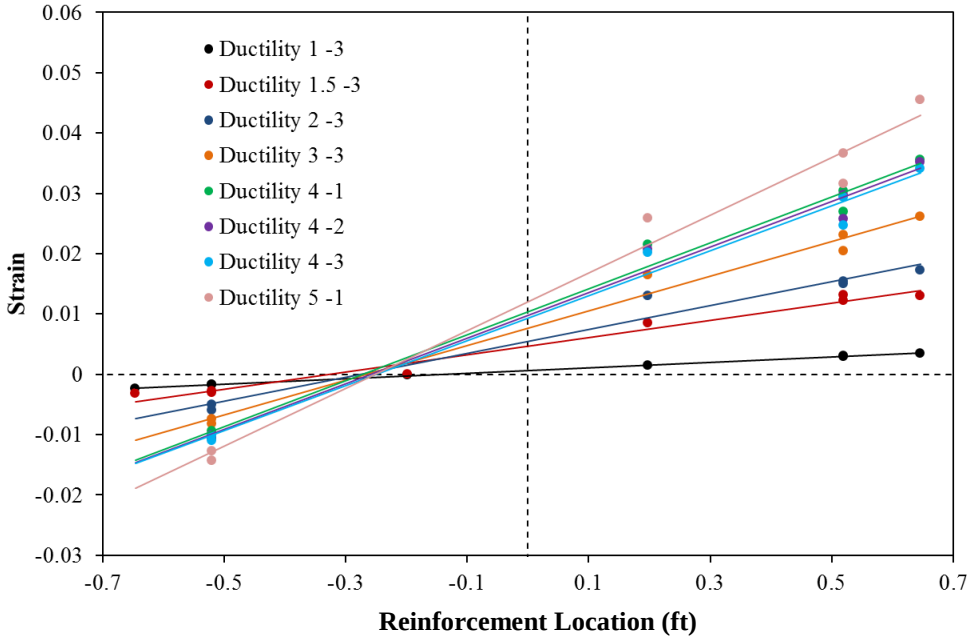

Figure 1.665 T24 – Cross Section Curvatures during Pull Cycles (4.97" Above)

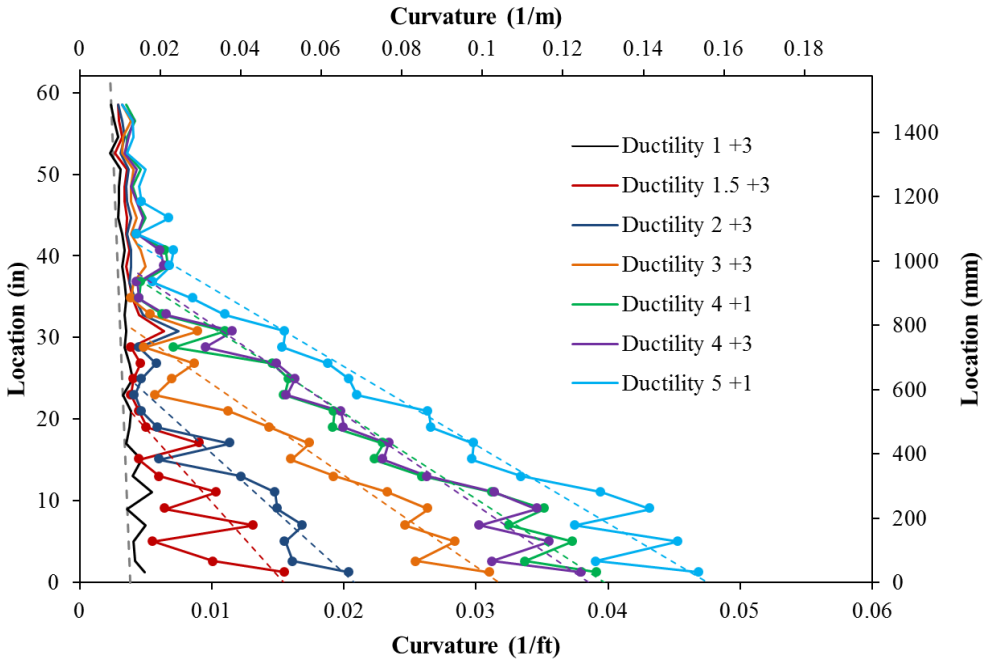

Figure 1.666 T24 – Push Cycle Curvature Profiles with Plastic Regression

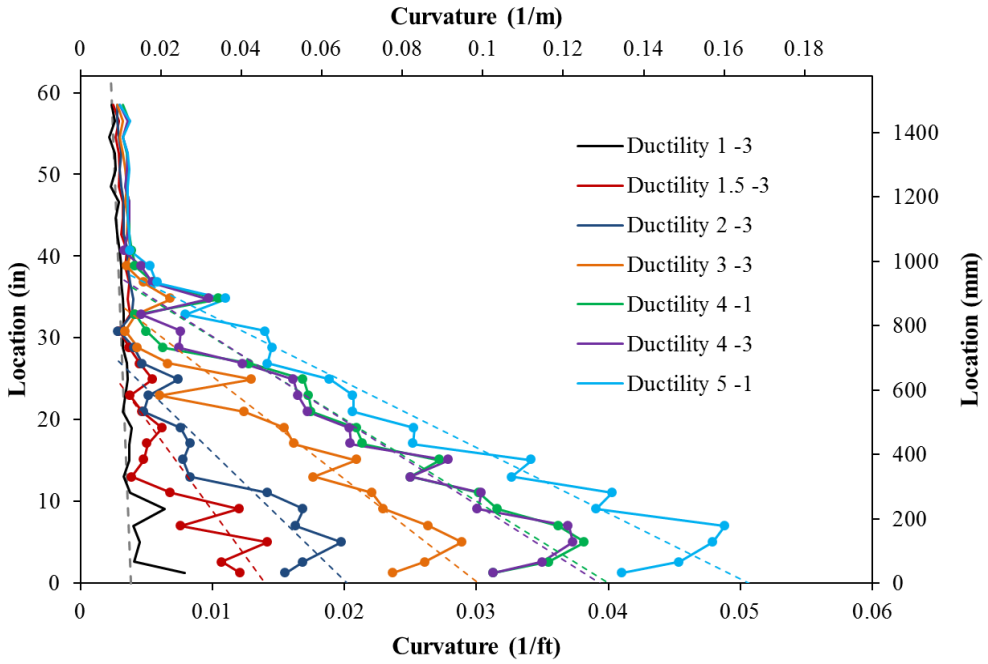

Figure 1.667 T24 – Pull Cycle Curvature Profiles with Plastic Regression

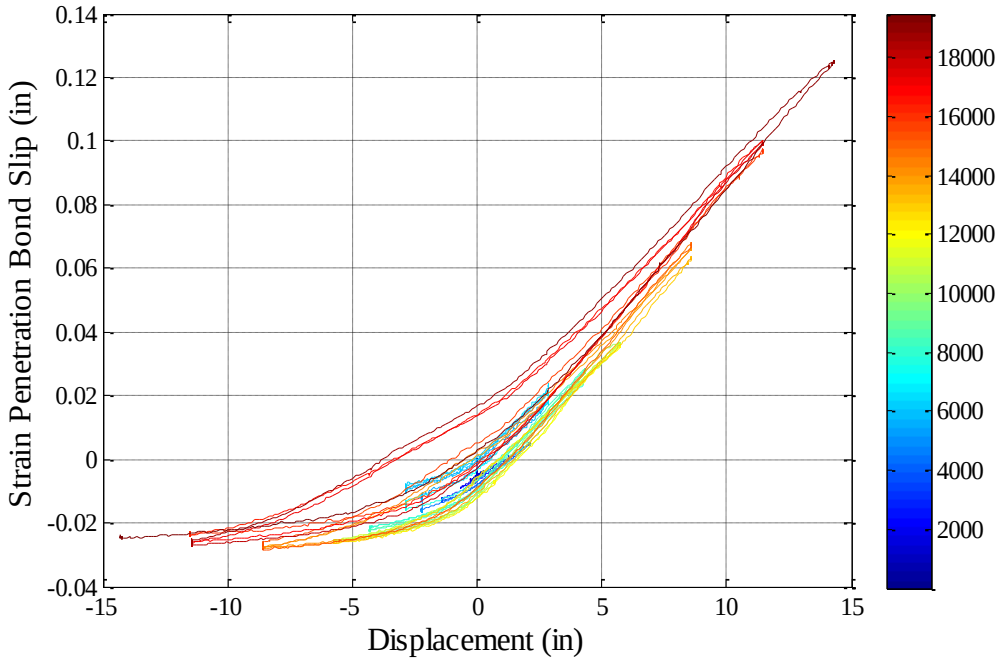

Figure 1.668 T24 – Bar N4 Bond Slip Hysteresis due to Strain Penetration

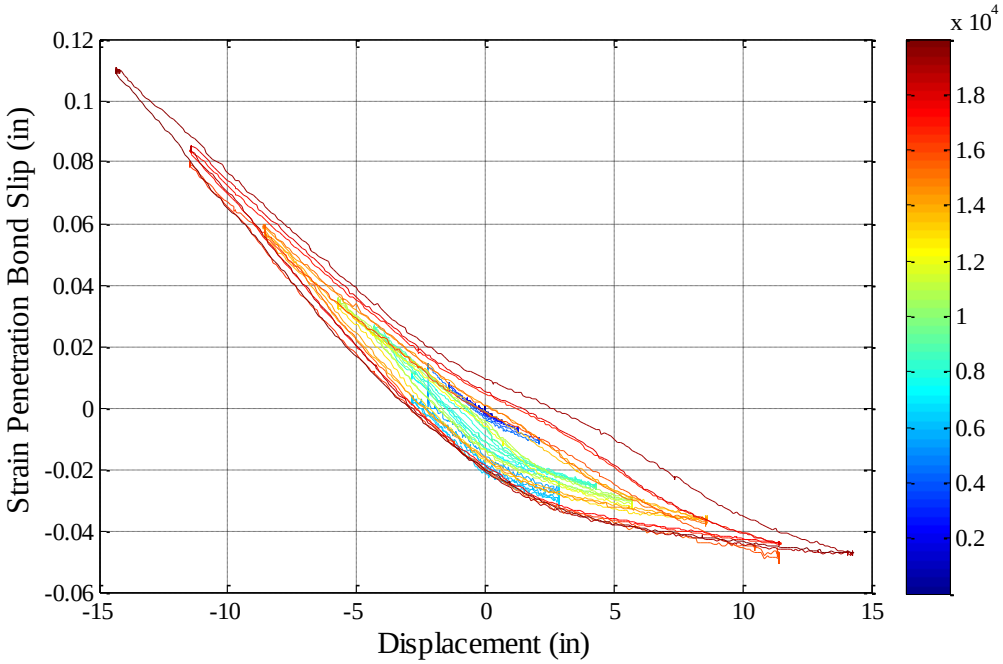

Figure 1.669 T24 – Bar S3 Bond Slip Hysteresis due to Strain Penetration

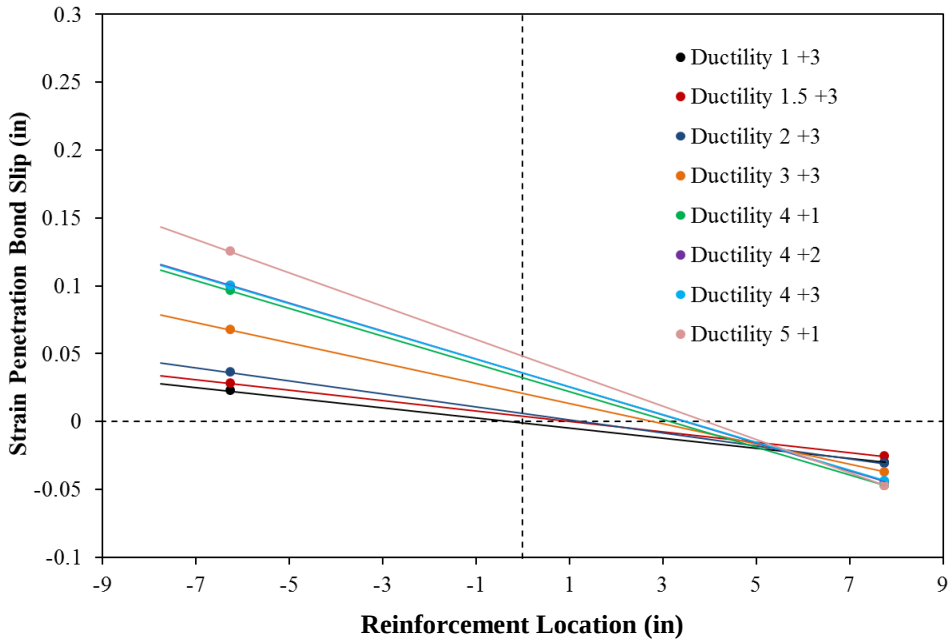

Figure 1.670 T24 – Base Rotation due to Strain Penetration during Push Cycles

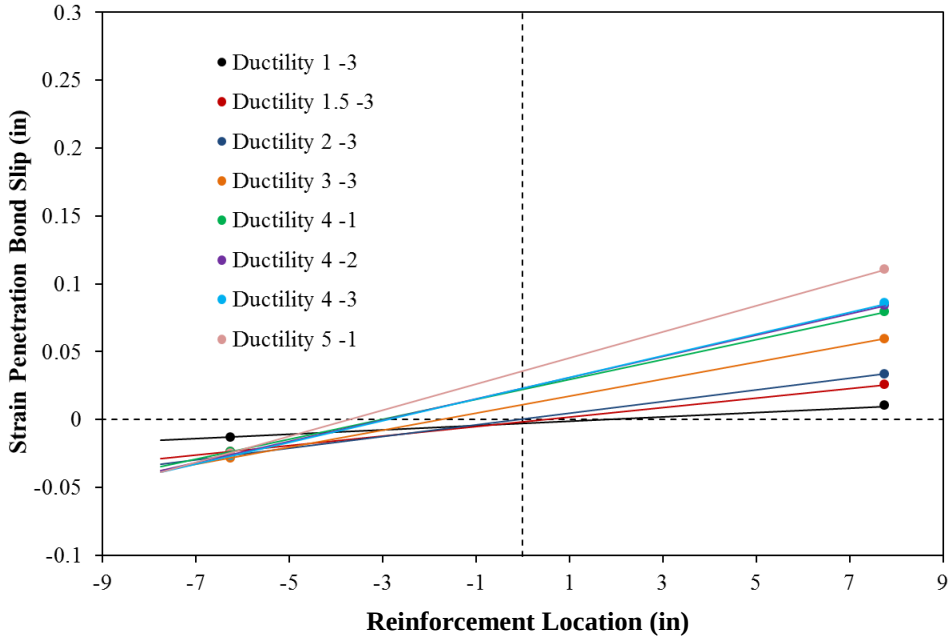

Figure 1.671 T24 – Base Rotation due to Strain Penetration during Pull Cycles

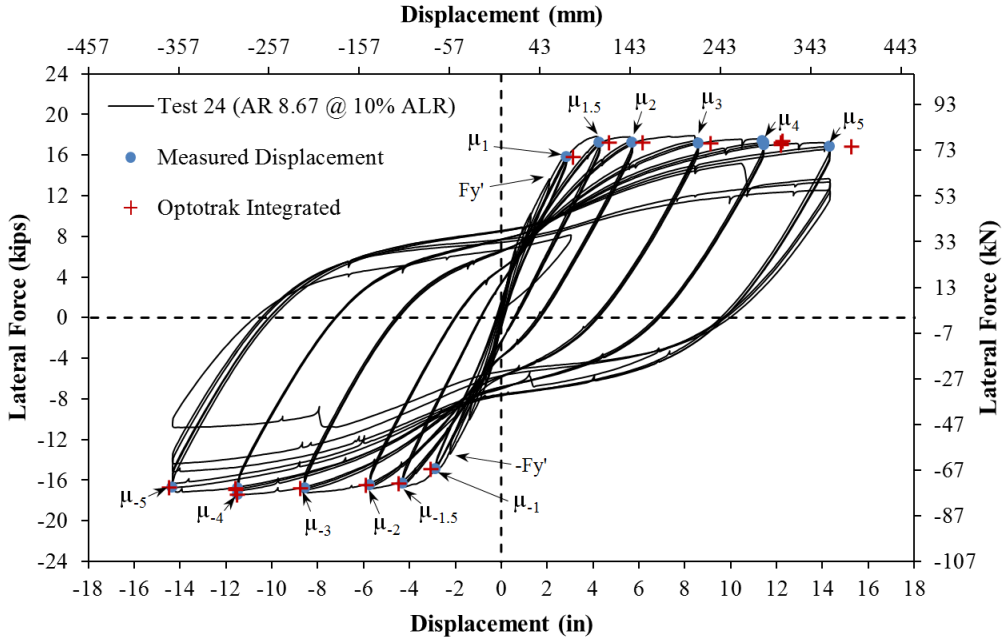

Figure 1.672 T24 – Comparison of Measured and Optotrak Integrated Displacements

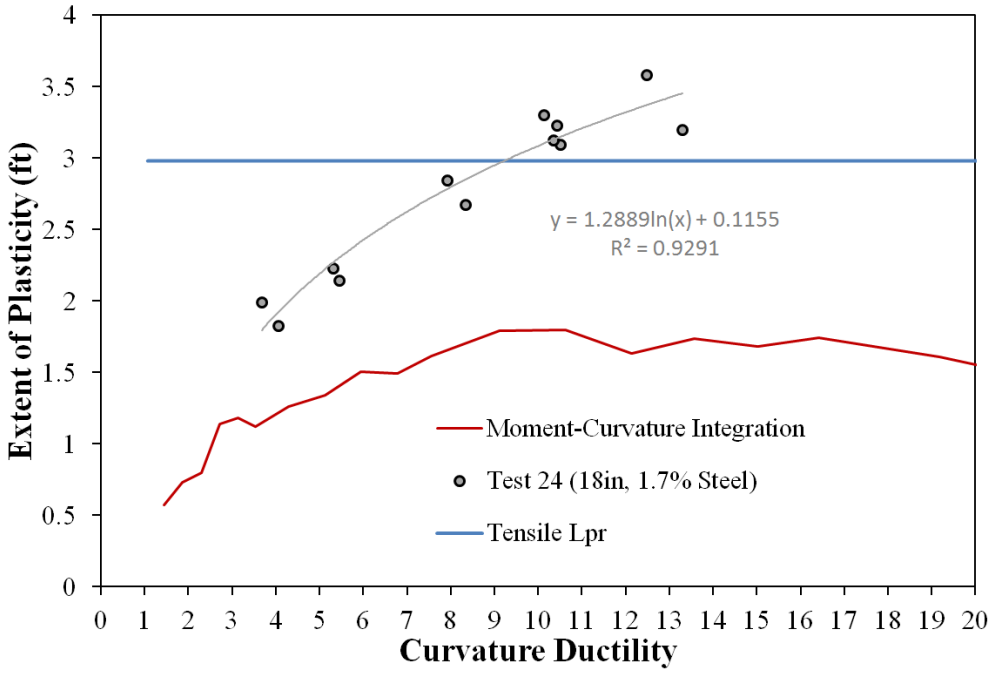

Figure 1.673 T24 – Measured Spread of Plasticity (Circular Data Points)

1.4 Steel Content and Axial Load Variable Tests 25-30

The effects of longitudinal steel content and higher levels of axial load ratio on column performance were the main variables for Tests 25-30. The test matrix for the eight columns is shown in

Table 1.45, and the material properties of the reinforcement appear in Table 1.46. Similar 18" and 24" column configurations were used so that the results could be compared to previous experiments with either different axial load or longitudinal steel content. The shear span for all six cantilever columns was 8ft (244cm). Stress-strain curves for the longitudinal and transverse steel appear in Figure 1.674 and Figure 1.675. The test series used the full cover concrete blockout method with target markers applied to both longitudinal and transverse steel, Figure 1.677.

The 18" (457mm) diameter bridge columns, Figure 1.676, contained either 10 #6 ($A_{st}/A_g = 1.7\%$) or 10 #8 ($A_{st}/A_g = 3.1\%$) A706 bars for longitudinal reinforcement and a #3 (9.5mm) A706 spiral at 2" spacing ($4A_{sp}/D's = 1.3\%$). The 24" (610mm) diameter bridge columns, Figure 1.676, contained either 16 #6 ($A_{st}/A_g = 1.6\%$) or 16 #7 ($A_{st}/A_g = 2.1\%$) A706 bars for longitudinal reinforcement and a #3 (9.5mm) A706 spiral at 2" spacing ($4A_{sp}/D's = 1\%$). Previous 18" diameter specimens were subjected to 5% and 10% axial load. Two specimens, with nominally identical geometry and reinforcement, are subjected to 15% and 20% axial load. Previous 24" diameter specimens utilized approximately 5% axial load, this same test configuration is subjected to 10% axial load here. In addition, the combination of higher steel content and different levels of axial load is investigated.

Table 1.45 Column Summary for Steel Content and Axial Load Variable Tests 25-30

Test	Load History	D (in)	L/D	Long. Steel (ρ_l)	Spiral Detailing (ρ_s)	f'c (psi)	P/f'c*Ag
25	Three Cycle Set	24	4	16 #7 bars (2.1%)	#3 at 2" (1%)	6289	5%
26	Three Cycle Set	24	4	16 #7 bars (2.1%)	#3 at 2" (1%)	5890	10%
27	Three Cycle Set	24	4	16 #6 bars (1.6%)	#3 at 2" (1%)	6149	10%
28	Three Cycle Set	18	5.33	10 #6 bars (1.7%)	#3 at 2" (1.3%)	6239	15%
29	Three Cycle Set	18	5.33	10 #6 bars (1.7%)	#3 at 2" (1.3%)	5912	20%
30	Three Cycle Set	18	5.33	10 #8 bars (3.1%)	#3 at 2" (1.3%)	6050	15%

Table 1.46 Reinforcement Material Property Summary for Columns 25-30

Longitudinal Reinforcement	εy	fy (ksi)	εh	fh (ksi)	εu	fu (ksi)
Tests 25-30 (#6 Bar)	0.00237	68.7	0.01363	68.8	0.11781	93.7
Tests 25-30 (#7 Bar)	0.00240	69.7	0.01261	69.7	0.11440	95.5
Tests 25-30 (#8 Bar)	0.00243	70.5	0.01095	70.5	0.10929	97.7

Transverse Steel	εy (0.2% offset)	fy (ksi)	εu	fu (ksi)
Tests 25-30 (#3 Spiral)	0.00428	63.9	0.11313	95.2

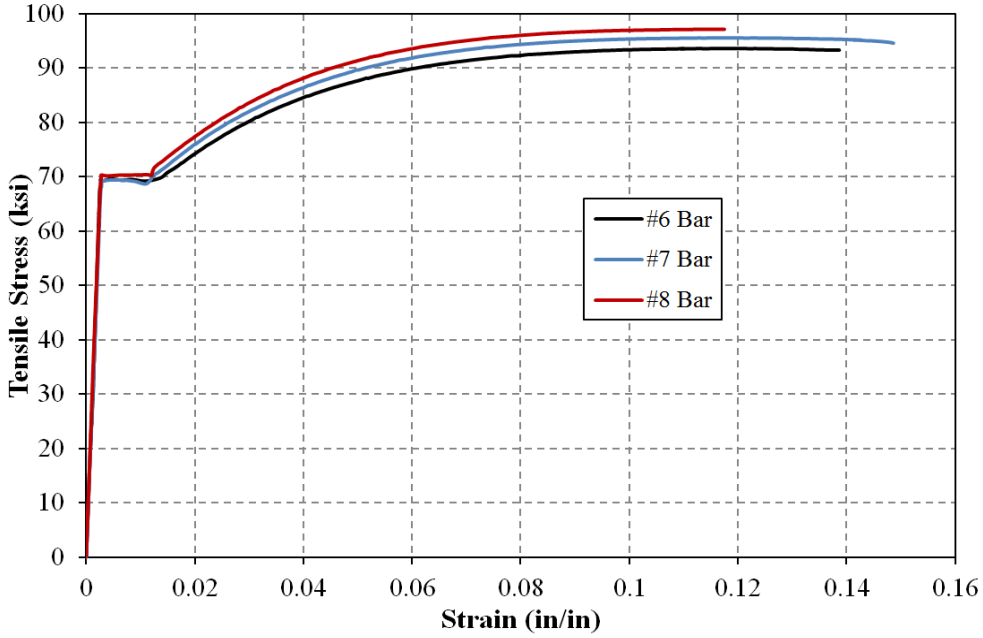

Figure 1.674 Test 25-30 – Longitudinal Steel Tensile Test Results

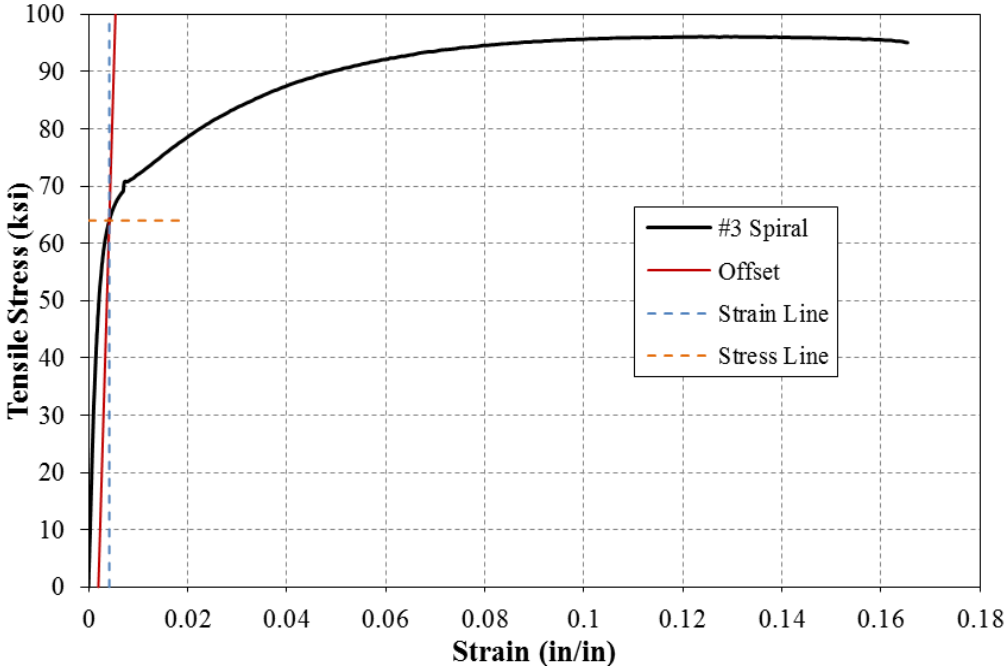

Figure 1.675 Test 25-30 – Transverse Steel Tensile Test Results

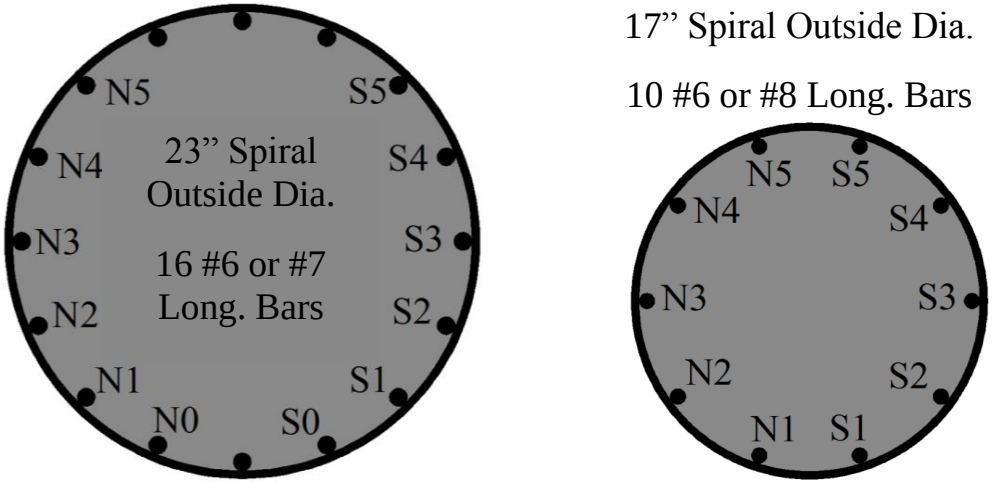

Figure 1.676 Tests 25-30 Cross Section and Bar Designation for Both Diameters

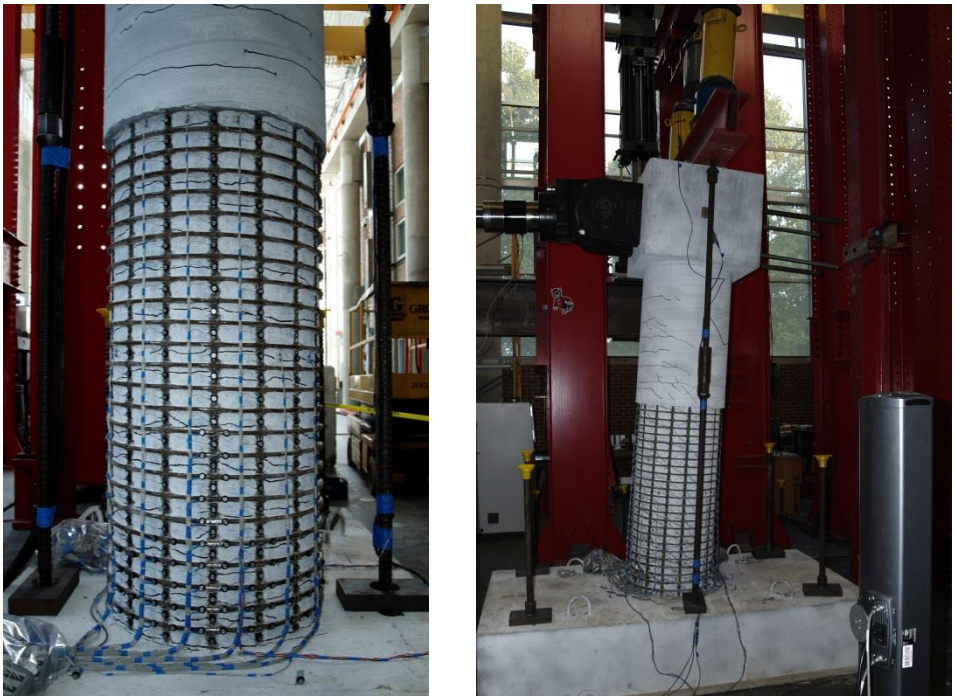

Figure 1.677 Complete Cover Concrete Blockout with Direct Application of Target Markers to Longitudinal and Transverse Steel

1.4.1 Test 25 – 24" Dia. Column with 2.1% Long. Steel and 5% Axial Load

Table 1.47 Observations for Test 25 – 24" Dia. With 2.1% Steel and 5% Axial Load

VALUES OF INTEREST:	
Concrete Compressive Strength:	$f_c' = 6287\ psi$
Axial Load:	$P = 131\ kips\ \ (P/(f_c' A_g) = 5\%)$
Longitudinal Steel Content:	16 #7 $Bars\ \ (A_{st}/A_g = 2.1\%)$
Analytical First Yield Force:	$F_y' = 52.9\ kips$
Experimental First Yield Displacement:	$\Delta_y' = 0.74"$
Analytical Nominal Moment Capacity:	$M_n = 584.2\ kip * ft$
Equivalent Yield Displacement:	$\Delta_y = 1.02"$
Maximum Lateral Force:	$81.1\ kips$
DAMAGE OBSERVATIONS:	
First Cracking North:	$1/2Fy' = 0.21"$
First Cracking South:	$-1/2Fy' = -0.26"$
Cover Concrete Crushing North:	$\mu_{1.5}^{-2} = -1.52"$
Cover Concrete Crushing South:	$\mu_{1.5}^{+3} = 1.53"$
Transverse Steel Yield North:	At $-3.06"$ during pull to $\mu_3^{-3} = -3.06"$
Transverse Steel Yield South:	At 2.44" during push to $\mu_3^{+1} = 3.08"$
Longitudinal Bar Buckling North:	Reversal from $\mu_6^{+2} = 6.14"$
Longitudinal Bar Buckling South:	Reversal from $\mu_5^{-1} = -5.12"$
Longitudinal Bar Fracture North:	At 7.00" during push to $\mu_7^{+2} = 7.17"$
Longitudinal Bar Fracture South:	At 0.50" during pull to $\mu_7^{-1} = -7.17"$

*$\mu_5^{-1} = -5.12"$ represents the first pull cycle of displacement ductility five

Table 1.48 Strain Data Summary for Test 25 – 24" Dia. With 2.1% Steel and 5% Axial

MATERIAL STRAINS:	
Cover Concrete Crushing North:	$\varepsilon_s = 0.0036\ (compression)$
Cover Concrete Crushing South:	$\varepsilon_s = 0.004\ (compression)$
Transverse Steel Yield North:	$\varepsilon_s = 0.0091\ (compression)$
Transverse Steel Yield South:	$\varepsilon_s = 0.0125\ (compression)$
Longitudinal Bar Buckling North:	$\varepsilon_s = 0.042\ (peak\ tension\ prior\ to\ bb)$
	$\varepsilon_s = 0.016\ (peak\ comp.\ prior\ to\ bb)$
Longitudinal Bar Buckling South:	$\varepsilon_s = 0.035\ (peak\ tension\ prior\ to\ bb)$
	$\varepsilon_s = 0.019\ (peak\ comp.\ prior\ to\ bb)$
Mander (1988) Ultimate Concrete Compression Strain, $\varepsilon_{cu} = 0.016$	

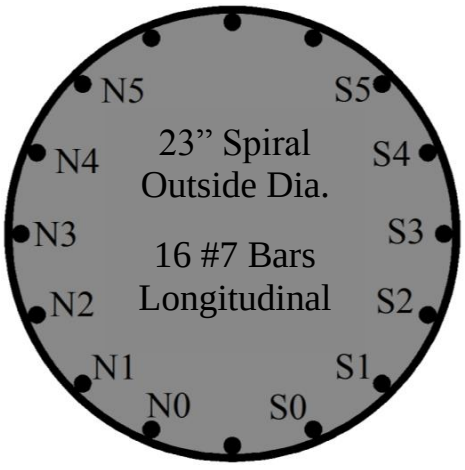

Figure 1.678 T25 – Cross Section Bar Designation

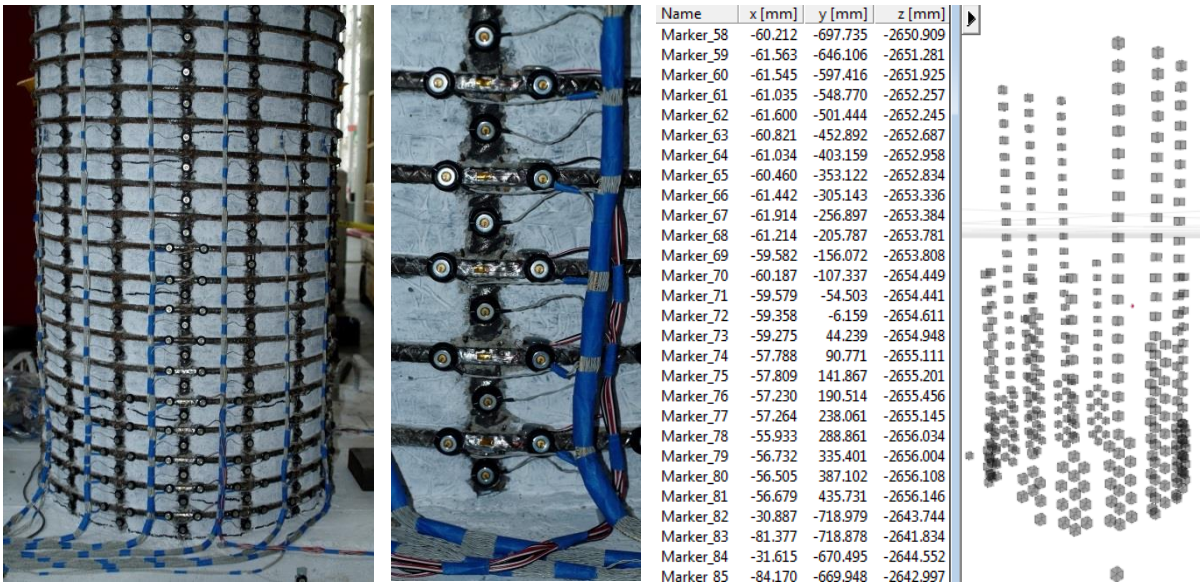

Name	x [mm]	y [mm]	z [mm]
Marker_58	-60.212	-697.735	-2650.909
Marker_59	-61.563	-646.106	-2651.281
Marker_60	-61.545	-597.416	-2651.925
Marker_61	-61.035	-548.770	-2652.257
Marker_62	-61.600	-501.444	-2652.245
Marker_63	-60.821	-452.892	-2652.687
Marker_64	-61.034	-403.159	-2652.958
Marker_65	-60.460	-353.122	-2652.834
Marker_66	-61.442	-305.143	-2653.336
Marker_67	-61.914	-256.897	-2653.384
Marker_68	-61.214	-205.787	-2653.781
Marker_69	-59.582	-156.072	-2653.808
Marker_70	-60.187	-107.337	-2654.449
Marker_71	-59.579	-54.503	-2654.441
Marker_72	-59.358	-6.159	-2654.611
Marker_73	-59.275	44.239	-2654.948
Marker_74	-57.788	90.771	-2655.111
Marker_75	-57.809	141.867	-2655.201
Marker_76	-57.230	190.514	-2655.456
Marker_77	-57.264	238.061	-2655.145
Marker_78	-55.933	288.861	-2656.034
Marker_79	-56.732	335.401	-2656.004
Marker_80	-56.505	387.102	-2656.108
Marker_81	-56.679	435.731	-2656.146
Marker_82	-30.887	-718.979	-2643.744
Marker_83	-81.377	-718.878	-2641.834
Marker_84	-31.615	-670.495	-2644.552
Marker_85	-84.170	-669.948	-2642.997

Figure 1.679 T25 – Target Marker Application and Optotrak Output

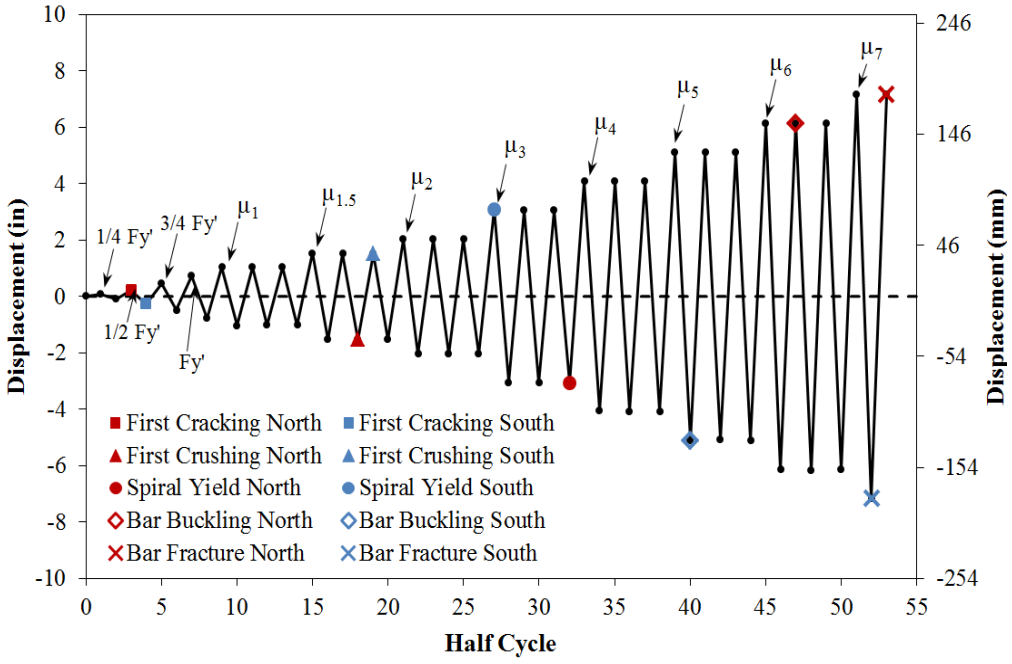

Figure 1.680 T25 – Symmetric Three Cycle Set Load History

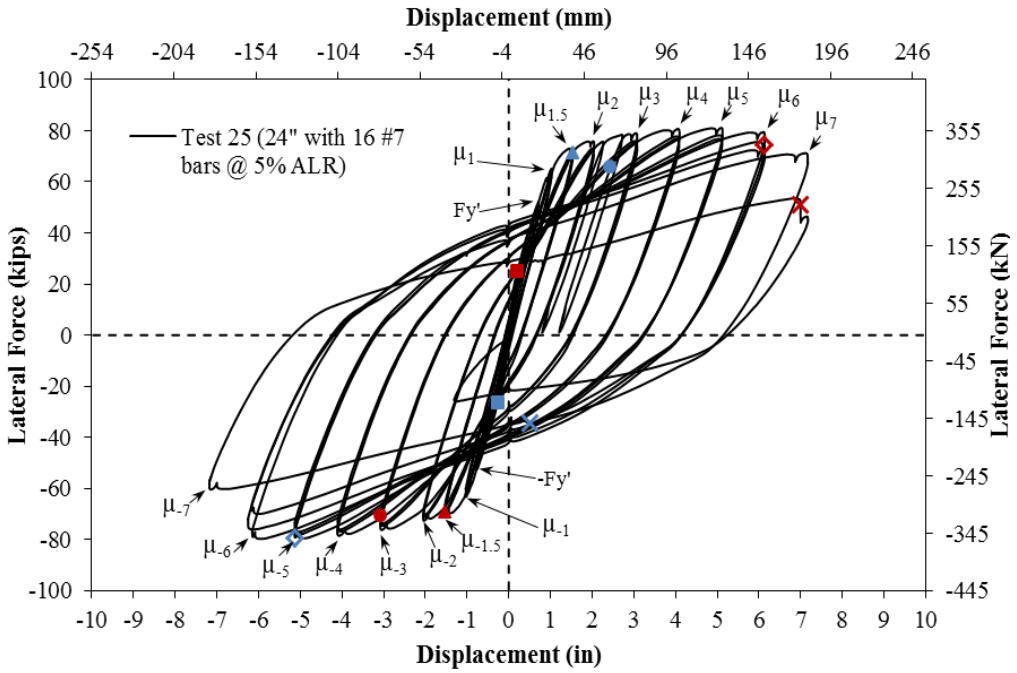

Figure 1.681 T25 – Lateral Force vs. Top Column Displacement Response

Test 25 – 24" Dia. with 2.1% Steel and 5% Axial Load – Experimental Observations

Specimens 25-30 focus on the effects of longitudinal steel content, longitudinal bar diameter, and higher levels of axial load on column behavior. The 24" diameter column contains 16 #7 (A706) bars for longitudinal reinforcement ($A_{st}/A_g = 2.1\%$) and a #3 A706 spiral at 2" on center ($4A_{sp}/(D's) = 1\%$). The specimen had an 8ft cantilever length ($L/D = 4$), and was subjected to ($P/(f_c'A_g) = 5\%$) axial load. The symmetric three-cycle-set load history is commonly used to evaluate the seismic performance of structural components. The load history begins with elastic cycles to the following increments of the analytically predicted first yield force: ¼ F_y', ½ F_y', ¾ F_y', and F_y'. The experimental first yield displacement is then determined by taking the average of the recorded displacements during the first yield push and pulls cycles. The equivalent yield displacement, used to determine the displacement ductility levels ($\mu_{\Delta 1} = 1 * \Delta_y$), is then calculated as $\Delta_y = \Delta_y'(M_n/M_y')$.

The symmetric three-cycle-set load history resumes with three balanced cycles at each of the following displacement ductility levels: 1, 1.5, 2, 3, 4, 5, etc. The imposed displacement history and resulting hysteretic response are shown in Figure 1.680 and Figure 1.681.

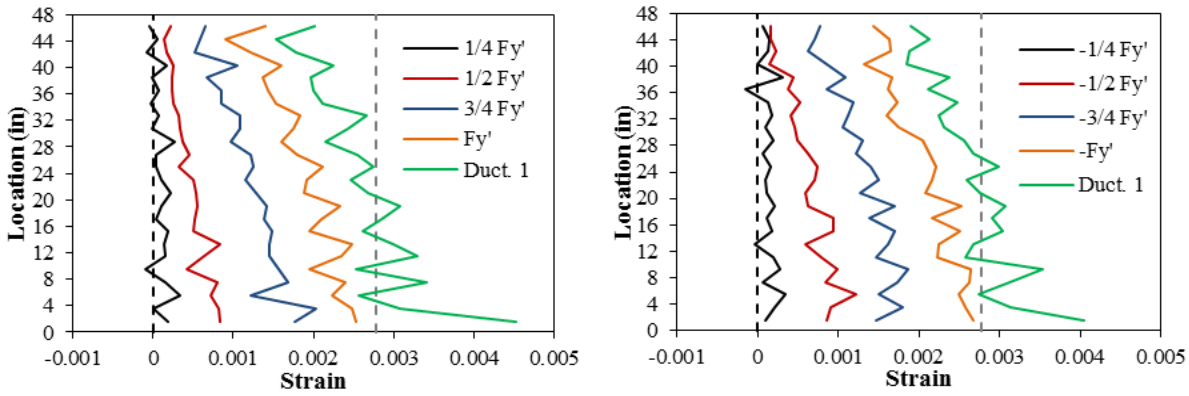

Figure 1.682 T25 – Strain Profiles before Yield, (Left) North and (Right) South

The test began with cycles in ¼ Fy' (first yield force) increments in each direction of loading until the first yield force was reached. The first cracks on the North and South sides of the specimen were observed during $(1/2Fy' = 0.21")$ and $(-1/2Fy' = -0.26")$ respectively, Figure 1.683. The crack distribution on all sides of the specimen at first yield, $(Fy' = 0.71")$ and $(-Fy' = -0.77")$, appears in Figure 1.684. Tensile vertical strain profiles for north and south reinforcing bars during elastic push and pull cycles appear in Figure 1.682. The average experimental first yield displacement was used to calculate the equivalent yield displacement, $\Delta_y = \Delta_y'(M_n/M_y') = 1.02"$, which defined the reversal amplitudes for the remainder of the test.

The crack progression at displacement ductility 1, 1.5, 2, 3, 4, and 5 appear in Figure 1.685, Figure 1.687, Figure 1.688, Figure 1.689, Figure 1.690, and Figure 1.693 respectively. During these cycles the cracks became more numerous and increased in inclination on the shear faces of the specimen. The first signs of concrete crushing on the North side of the

specimen occurred just above the footing during ($\mu_{1.5}^{-2} = -1.52$"), Figure 1.686. To a smaller extent, crushing on the South side of the specimen was observed during ($\mu_{1.5}^{+3} = 1.53$"), Figure 1.686. As compressive demands increased during displacement ductility 1.5 to 5, crushing gradually increased on each side of the specimen without influencing the measured lateral forces. This compressive demand combined with local longitudinal bar restraint demands led to spiral yielding on each side of the specimen during displacement ductility three, Figure 1.689. Although these spiral strains increased during successive cycles of displacement ductility four and during the first cycle at ductility five, the reinforcing bars remained visually straight, Figure 1.691

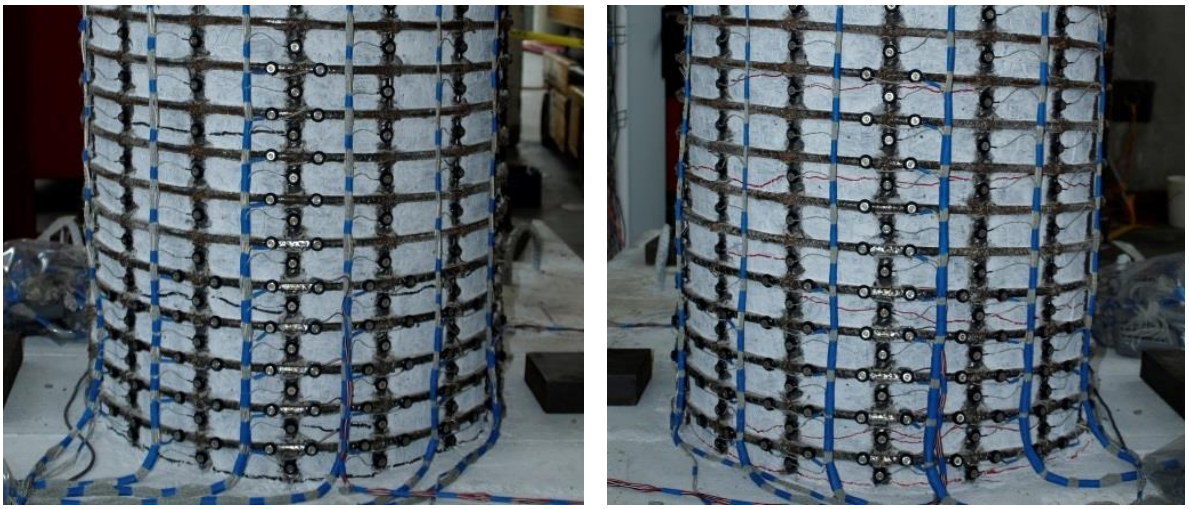

Figure 1.683 T25 – (Left) North 1st Cracking during ($1/2Fy' = 0.21$"), (Right) South 1st Cracking during ($-1/2Fy' = -0.26$")

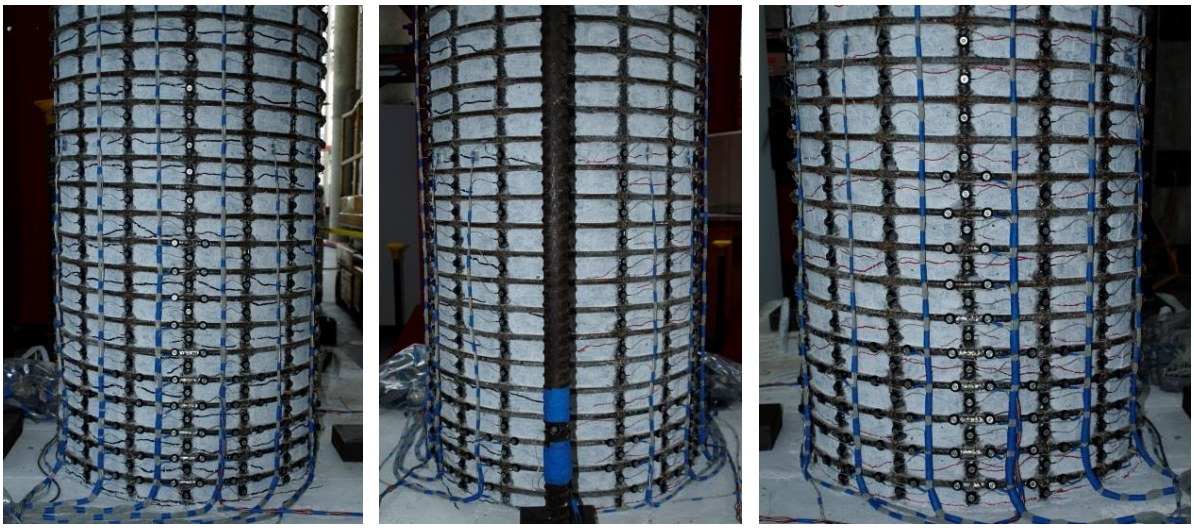

Figure 1.684 T25 – (Left) North Crack Distribution at ($Fy' = 0.71$"), (Middle and Right) Crack Distributions on the Front and Right Sides at ($-Fy' = -0.77$")

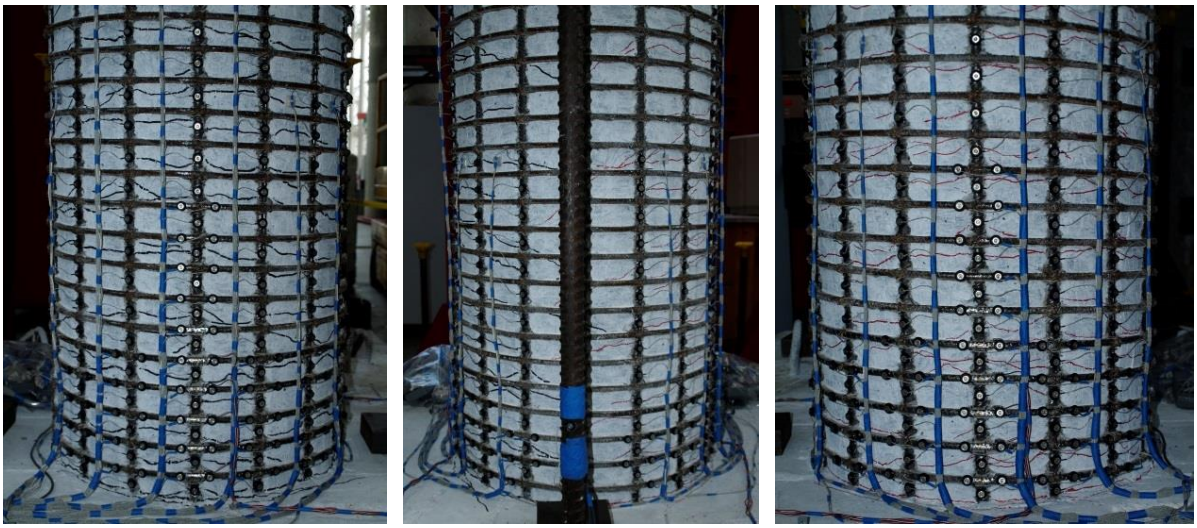

Figure 1.685 T25 – (Left) North Crack Distribution at ($\mu_1^{+3} = 1.02$"), (Middle and Right) Crack Distributions on the Front and Right Sides at ($\mu_1^{-3} = -1.02$")

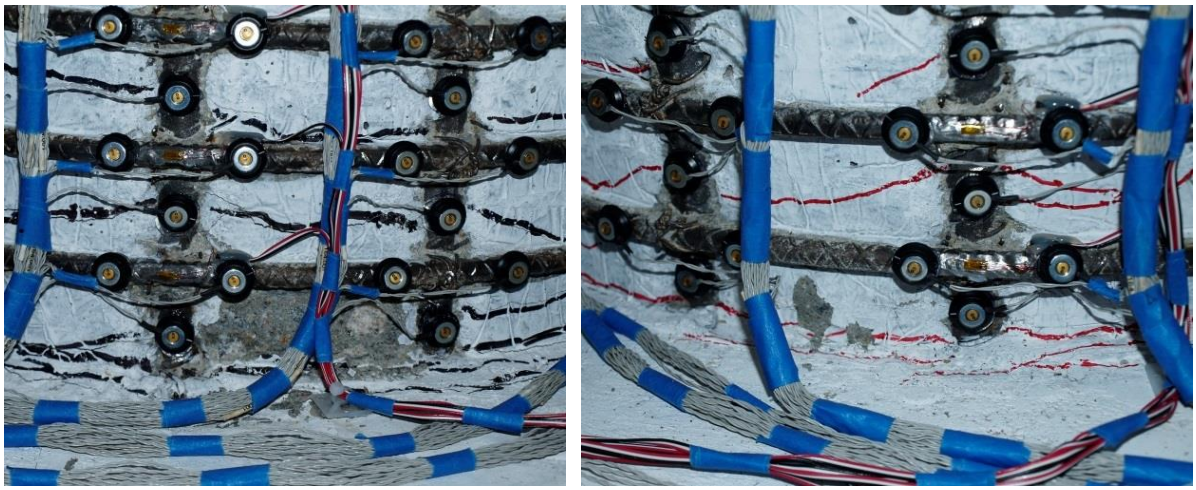

Figure 1.686 T25 – (Left) North 1st Crushing during ($\mu_{1.5}^{-2} = -1.52$"), (Right) South 1st Crushing during ($\mu_{1.5}^{+3} = 1.53$")

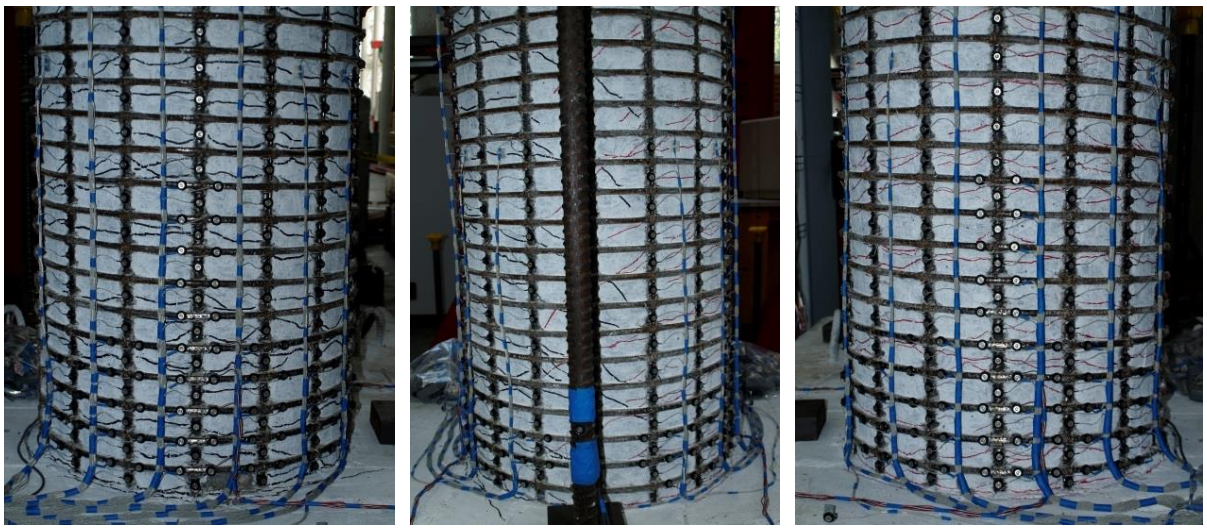

Figure 1.687 T25 – (Left) North Crack Distribution at ($\mu_{1.5}^{+3} = 1.53$"), (Middle and Right) Crack Distributions on the Front and Right Sides at ($\mu_{1.5}^{-3} = -1.53$")

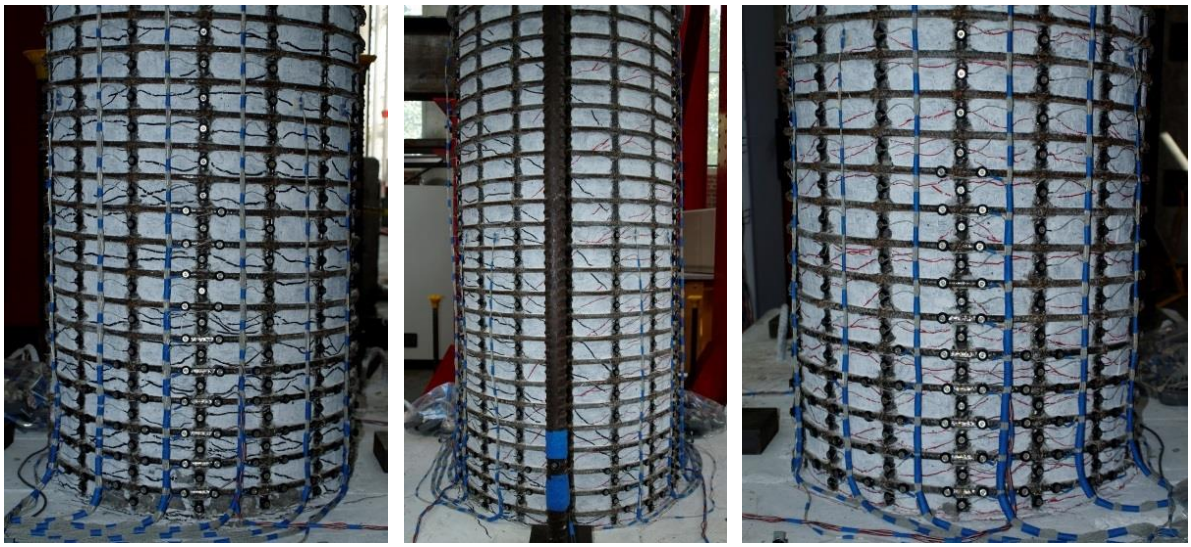

Figure 1.688 T25 – (Left) North Crack Distribution at ($\mu_2^{+3} = 2.04$"), (Middle and Right) Crack Distributions on the Front and Right Sides at ($\mu_2^{-3} = -2.04$")

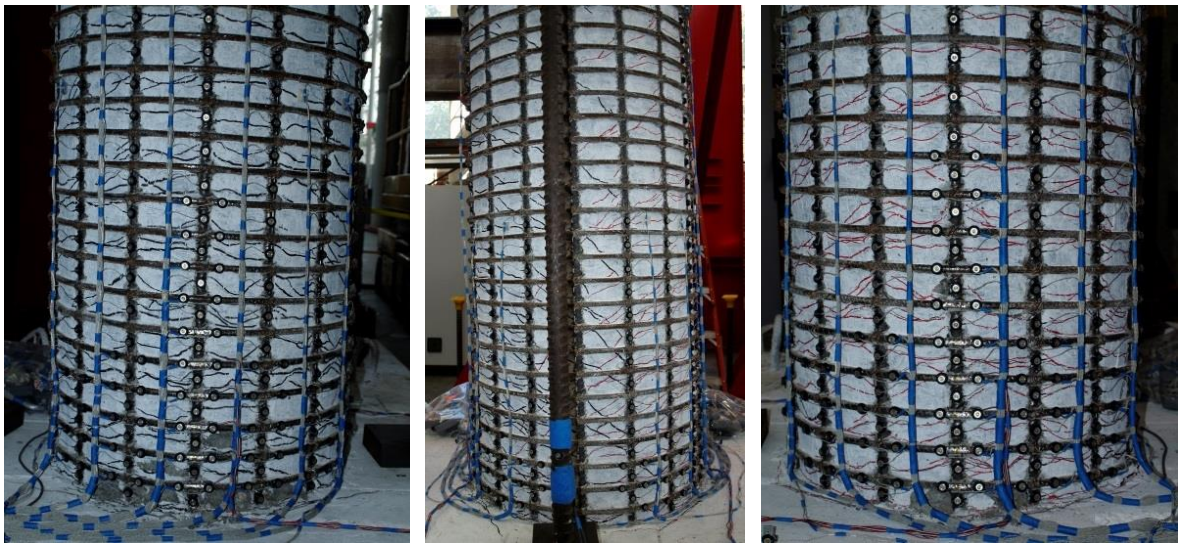

Figure 1.689 T25 – (Left) North Crack Distribution at ($\mu_3^{+3} = 3.06$"), (Middle and Right) Crack Distributions on the Front and Right Sides at ($\mu_3^{-3} = -3.06$")

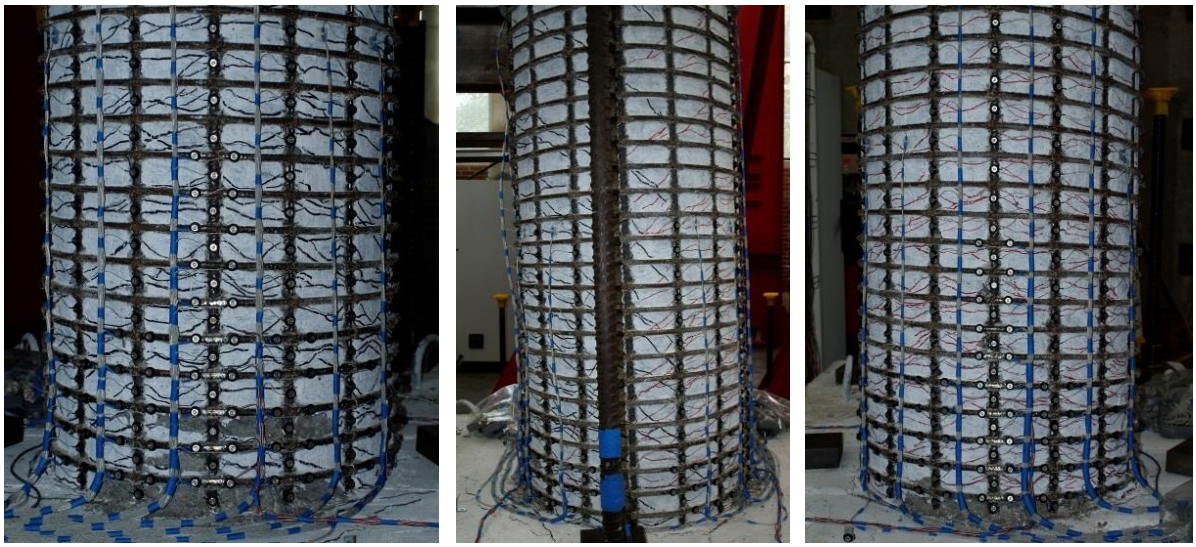

Figure 1.690 T25 – (Left) North Crack Distribution at ($\mu_4^{+3} = 4.08$"), (Middle and Right) Crack Distributions on the Front and Right Sides at ($\mu_4^{-3} = -4.09$")

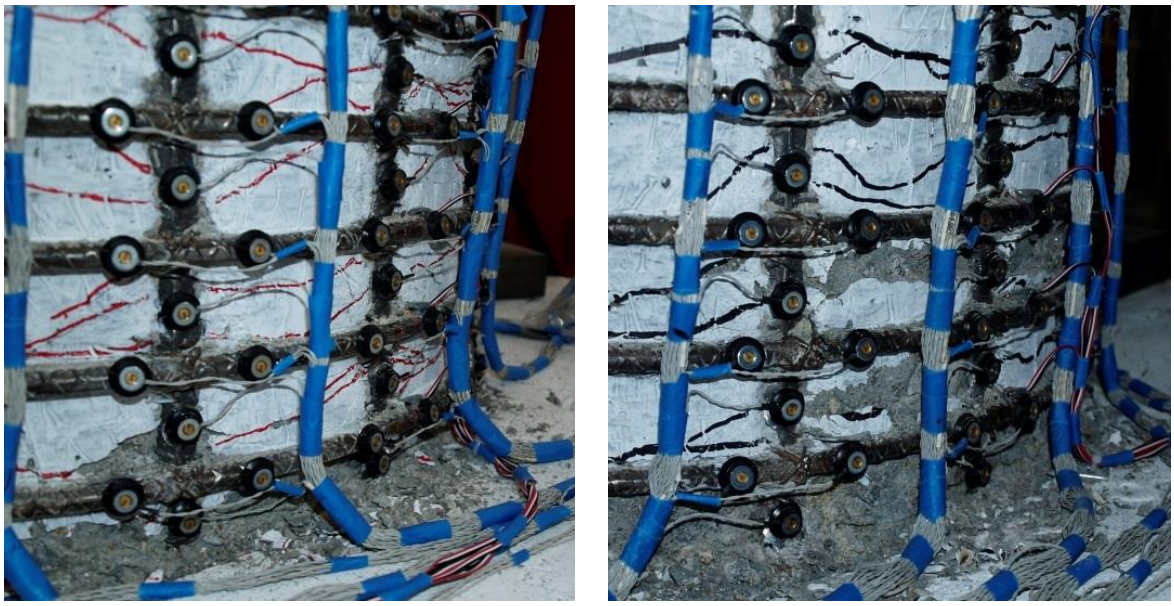

Figure 1.691 T25 – (Left) No Buckling of N3 during ($\mu_5^{+1} = 5.11$"), (Right) No Buckling of S3 during ($\mu_5^{-1} = -5.12$")

The south extreme fiber bar buckled during the subsequent reversal from tensile strains sustained during ($\mu_5^{-1} = -5.12$"), as shown in the left photo of Figure 1.692. The outward buckled region occurred over the second gage length above the footing which encompassed the second spiral layer. The buckled deformation increased during ($\mu_5^{+3} = 5.10$"). Two adjacent south reinforcing bars, S2 and S4, buckled during ($\mu_6^{+2} = 6.14$"), Figure 1.694. Although buckling on the north side of the specimen was delayed by a displacement ductility level, three extreme fiber bars visibly buckled during after reversal from tensile strains sustained during ($\mu_6^{+2} = 6.14$"), Figure 1.694. Two additional north bars, N1 and N5, buckled during ($\mu_6^{-3} = -6.15$"), Figure 1.695, which produced a pronounced outward deformation of the spiral overlaying the five buckled bars on the north side of the specimen. South bar S1 buckled during ($\mu_7^{+1} = 7.16$"), Figure 1.695. The extreme fiber south bar S3 ruptured at 0.50" during the pull cycle to ($\mu_7^{-1} = -7.17$"), Figure 1.696. The north extreme fiber bars N2 and N3 ruptured at 7.00" during the push cycle to ($\mu_7^{+2} = 7.17$"), Figure 1.696. The test was concluded with fractured bars on each side of the specimen, photos of the specimen after removal of the instrumentation appear in Figure 1.697 and Figure 1.698.

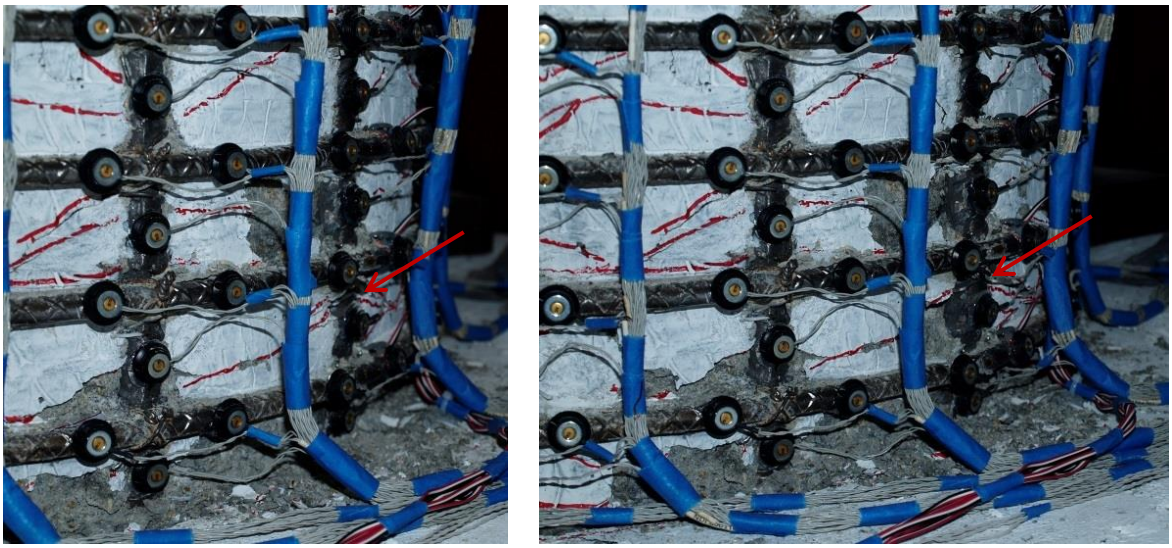

Figure 1.692 T25 – (Left) Buckling of Bar S3 during ($\mu_5^{+2} = 5.10$"), (Right) Increased Buckled Deformation at ($\mu_5^{+3} = 5.10$")

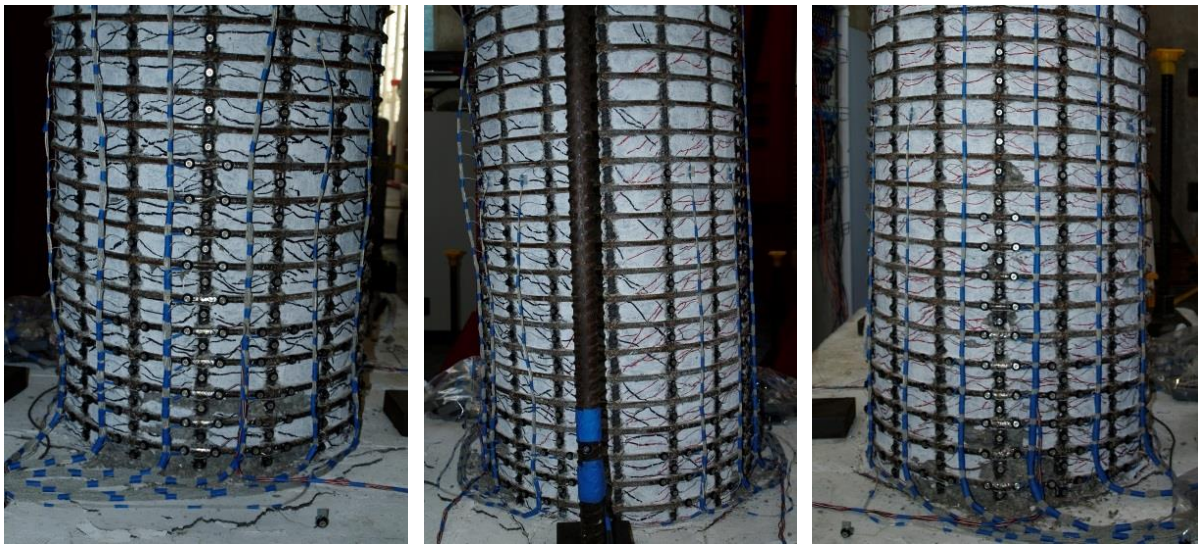

Figure 1.693 T25 – North, Front, and South Sides of the Specimen at ($\mu_5^{-3} = -5.11$")

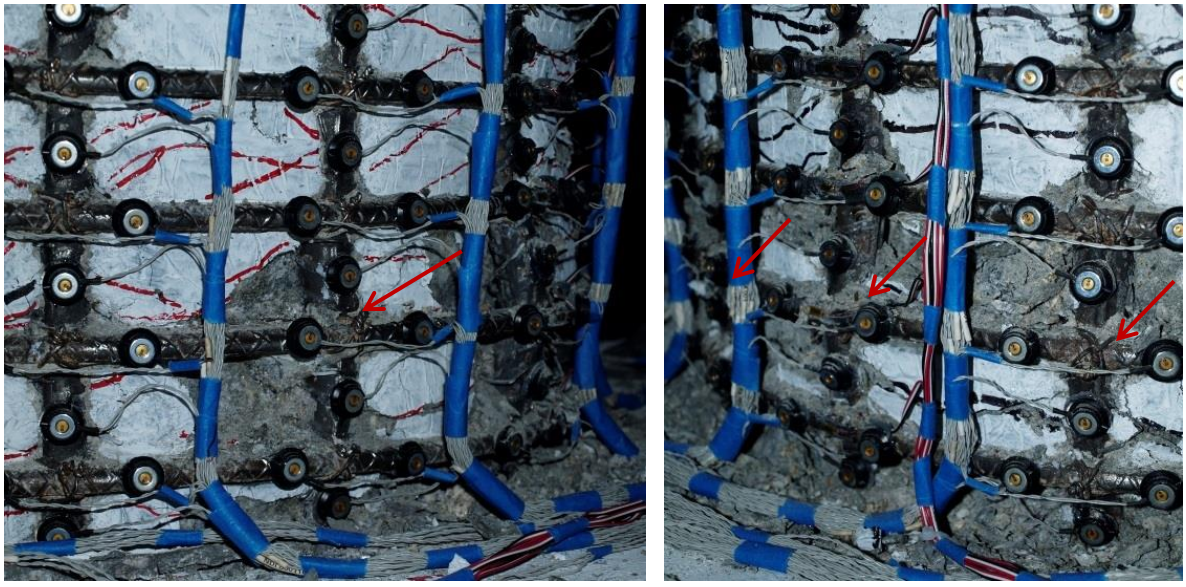

Figure 1.694 T25 – (Left) Buckling of Adjacent South Bars S2 and S4 during ($\mu_6^{+2} = 6.14$"), (Right) Buckling of North Bars N2, N3, and N4 during ($\mu_6^{-2} = -6.17$")

Figure 1.695 T25 – (Left) Buckling of N1 and N5 during ($\mu_6^{-3} = -6.15$"), (Right) Buckling of S1 during ($\mu_7^{+1} = 7.16$")

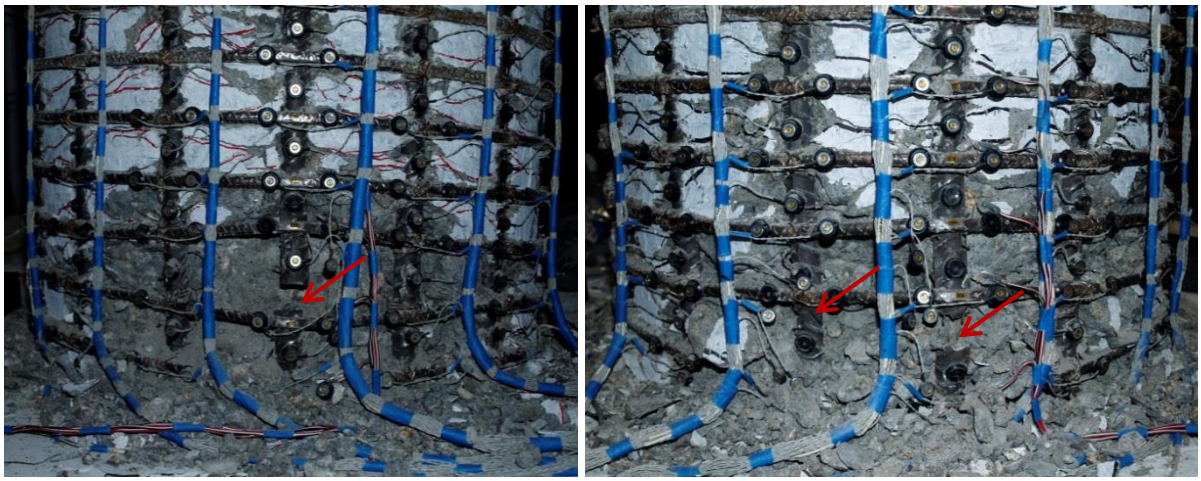

Figure 1.696 T25 – (Left) Fracture of Bar S3 during ($\mu_7^{-1} = -7.17$"), (Right) Fracture of Bars N3 and N4 during ($\mu_7^{+2} = 7.17$")

Figure 1.697 T25 – (Left) North Side of the Specimen after Test, (Right) Front Side

Figure 1.698 T25 – (Left) South Side of the Specimen after Test, (Right) Back Side

Test 25 – 24" Dia. with 2.1% Steel and 5% Axial Load – Strain Data Analysis

North Reinforcement

Vertical strain profiles for the north extreme fiber bar N3, which is placed into tension during push cycles, appear in the right half of Figure 1.699. This figure shows both extreme fiber bars on the same graph to illustrate the effects of tension shift. Compression strains are concentrated near the footing-column interface while tension strains are spread higher above the footing following the inclined flexural-shear crack distribution. Compressive vertical strain profiles for north extreme fiber bar N3 during pull cycles appear in the left half of Figure 1.700. A peak tensile strain of 0.0422 was measured 7.44" above the footing on bar N3 during ($\mu_6^{+2} = 6.14"$), before the bar visibly buckled during the subsequent reversal of load. A compressive strain of -0.0091 was measured 1.63" above the footing on bar N3 during ($\mu_3^{-3} = -3.06"$), when the spiral in the confinement region yielded.

Measured spiral strains in six layers which overlaid the north extreme fiber bar appear in Figure 1.703 for pull cycles which placed the north side in compression. Successive cycles during displacement ductility four and five produced larger inelastic demands on the spiral reinforcement. For the second spiral layer above the footing, inelastic strains decreased the lateral restraint stiffness, which led to measurable outward deformation of the north extreme fiber bar before visible buckling. The measureable deformation formed a convex outward deformed region on the outside surface of the longitudinal bar, and an inward concave region just above the outward deformation. Optotrak gage lengths in the convex outward deformed region would show increased tensile strains during compression cycles which should have resulted in larger levels of compression, Figure 1.708. Similarly, gage lengths on the concave region would show some degree of increased compression due to the deformed geometry, Figure 1.709. As a comparison, the gage length just above the concave and concave regions remained straight and produced stable hysteretic response, Figure 1.710. It is important to note that all three gage lengths on Bar N3 showed rapid increase in the apparent deformation when visible buckling was observed during ($\mu_6^{-2} = -6.17"$), Figure

1.693. Although the measured compression strains in bar N3 may have been influenced by bar deformation, a compression strain of -0.0161 was measured 5.45" above the footing during ($\mu_5^{-3} = -5.11"$). The peak compression strain of -0.0269, measured during ($\mu_6^{-1} = -6.14"$), was likely influence by bar deformation, which is why it has been excluded from Figure 1.705.

Tensile strain in the second spiral layer above the footing, which overlaid the outward deformed region of bar N3, spiked during visible bar buckling, Figure 1.711. The figure contains spiral data obtained from a strain gage and an Optotrak gage length, Figure 1.679. The Optotrak strains were calculated from arc-lengths which utilized the measured 3D distance chord lengths between two adjacent LEDs and the known outside diameter of the spiral reinforcement. It is important to note that arc-length calculations become inaccurate once severe yielding in the spiral leads to the reinforcement straightening out to the left and right of the localized yielding directly over the bar. The arc-strains are still presented because the strain gage debonded, preventing further measurement to the point of visible bar buckling. The distribution of arc-strains measured around the circumference of the second spiral layer above the footing appears in Figure 1.716 and Figure 1.717. The north region is under compression during pull cycles in Figure 1.717. The middle of the section corresponds to zero along the circumference, and negative values wrap around the north side of the specimen. Specifically, measured-arc strains which overlay the three north extreme fiber bars N2, N3, and N4 are shown with vertical dashed lines. The spiral yielding is more evenly distributed along the north circumference, when compared to localized spiral yielding observed on the south side of the specimen in Figure 1.716. Also, yielding along multiple spiral layers above the footing on the north side of the specimen, Figure 1.703, is more evenly distributed than localized yielding on the south side observed in Figure 1.702. These two observations support the fact that bar buckling occurred one displacement ductility level later on the north side when compared to the south side. Furthermore, when the north side did buckle, three bars buckled simultaneously due to the distributed spiral yielding.

The relationship between tensile strain and displacement for the peak tensile gage lengths on bar N3, 7.44" above the footing, appears in Figure 1.704. The gage length centered 3.54" above the footing had slightly lower strain magnitudes, but significantly higher unloading strains. This gage length corresponded to the outward deformed region when the bar buckled, Figure 1.694. The monotonic moment curvature prediction with the PCK (2007) Lp Hinge Method overestimates the measured tension strains at an increasing rate at higher levels of ductility. The relationship between compressive strain and displacement for the gage length 5.45" above the footing on bar N3 appears in Figure 1.705. The measured compressive strains slightly exceed the prediction with the PCK (2007) Lp Hinge Method after transverse steel yielding occurred in the north confinement region during ($\mu_3^{-3} = -3.06"$).

South Reinforcement

Vertical strain profiles for the south extreme fiber bar S3, which is placed into tension during pull cycles, appear in the right half of Figure 1.700. Compressive vertical strain profiles for south extreme fiber bar S3 during push cycles appear in the left half of Figure 1.699. A peak tension strain of 0.0353 was measured 7.36" above the footing on bar S3 during ($\mu_5^{-1} = -5.12"$), before visible bar buckling occurred during the subsequent reversal of load. The tension strains measured in lower gage lengths on bar S3 were smaller, although adjacent bars S2 and S4 had large tensile strains near the footing-column interface, Figure 1.701. A compressive strain of -0.0125 was measured 1.58" above the footing on bar S3 during ($\mu_3^{+1} = 3.08"$), when the spiral in the confinement region yielded. Measured spiral strains in six layers which overlaid the south extreme fiber bar appear in Figure 1.702 for push cycles which placed that side in compression. Successive cycles during displacement ductility four produced large inelastic demands on the second layer of spiral reinforcement. The measured strains obtained from the Optotrak system and a strain gage overlaying the second spiral appear in Figure 1.715. The spiral strains spiked when the bar visibly buckled during ($\mu_5^{+2} = 5.10"$).

Since Optotrak LEDs are placed on the outside surface of the bar, measurable deformation can be monitored in the concave and convex regions of the deformed shape. The outward deformed region (convex) developed in the gage length 3.47" above the footing on bar S3, Figure 1.712. Above the convex region, a concave region developed which increased compression strains 5.44" above the footing, Figure 1.713. The region 7.36" above the footing on bar S3 appears to be unaffected by the measurable deformation which occurred below, Figure 1.714. The concave and convex deformed regions of bar S3 show a sharp deviation when visible bar buckling was observed during ($\mu_5^{+2} = 5.10"$). Spiral strains measured around the circumference of the second spiral layer above the footing depict large localized inelasticity at the location of the extreme fiber bars S3 and S4 during push cycles, Figure 1.716. The magnitude and localized nature of the spiral strains, both around the circumference (Figure 1.716) and vertically above the footing (Figure 1.702), contributed to bar buckling one displacement ductility level earlier than the north side of the specimen.

The relationship between tension strain and displacement for the gage length 7.36" above the footing on bar S3 appear in Figure 1.706. Similar observations to those commented on for north reinforcement apply here as well, the moment curvature analysis overestimated tension strains. The relationship between compressive strain and displacement for the gage length 5.44" above the footing appears in Figure 1.707. The measured compressive strains begin to exceed the moment curvature prediction with the PCK (2007) Lp Hinge Method during ductility three, when the transverse steel entered the inelastic range. A peak compression strain of -0.0190 was measured 5.44" above the footing during ($\mu_5^{+1} = 5.11"$). This gage length was on the concave side of the measurable deformation, so it is difficult to say how much the value may be influenced.

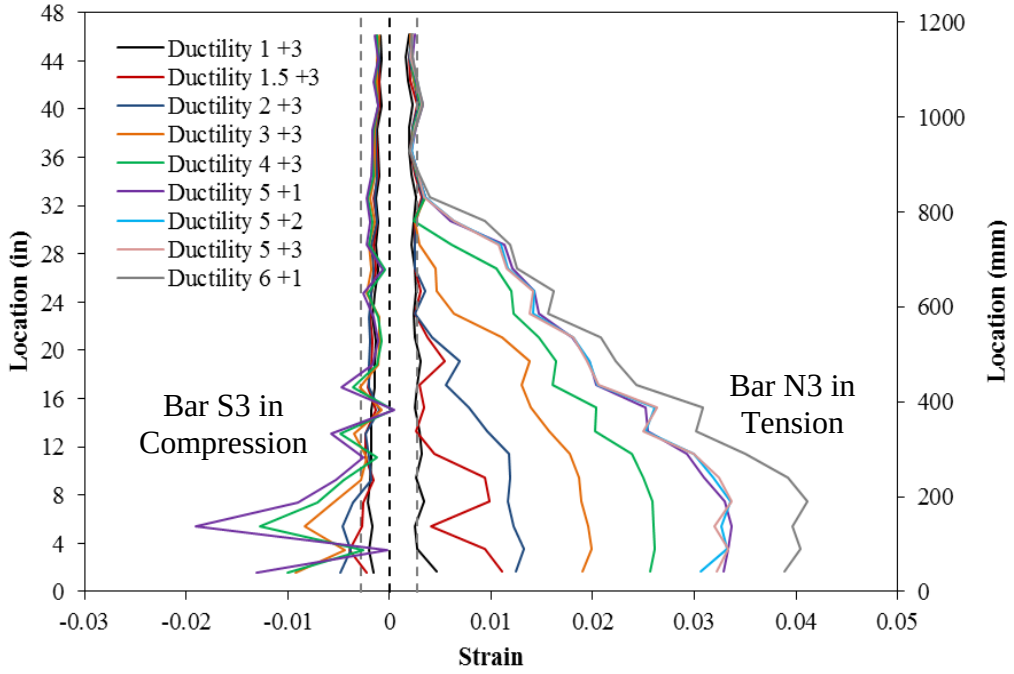

Figure 1.699 T25 – Extreme Fiber Bar Vertical Strain Profiles during Push Cycles

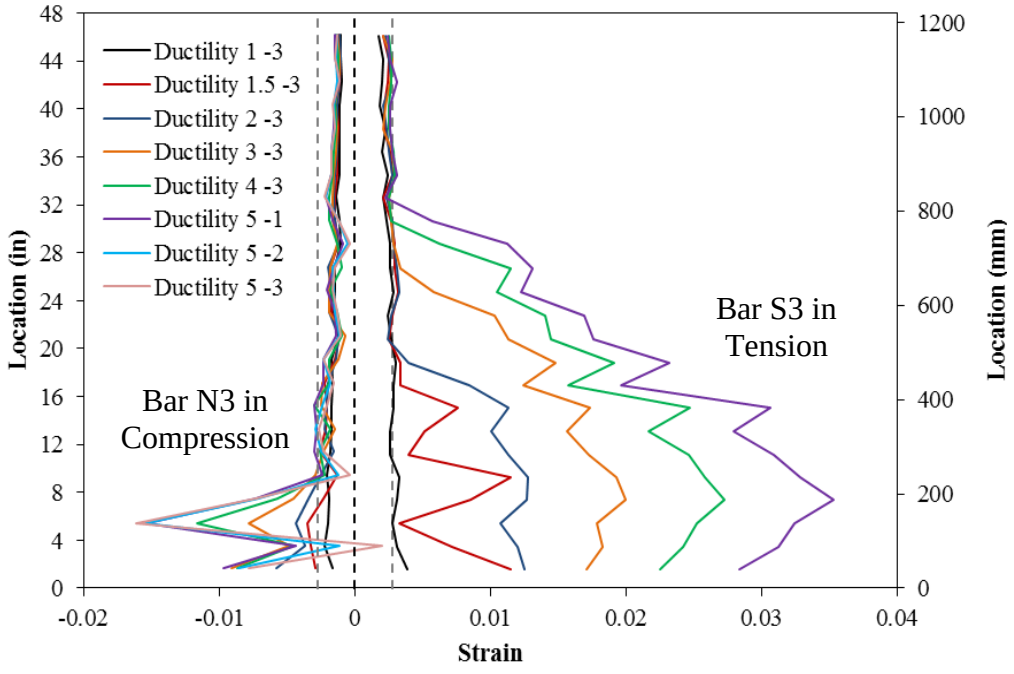

Figure 1.700 T25 – Extreme Fiber Bar Vertical Strain Profiles during Pull Cycles

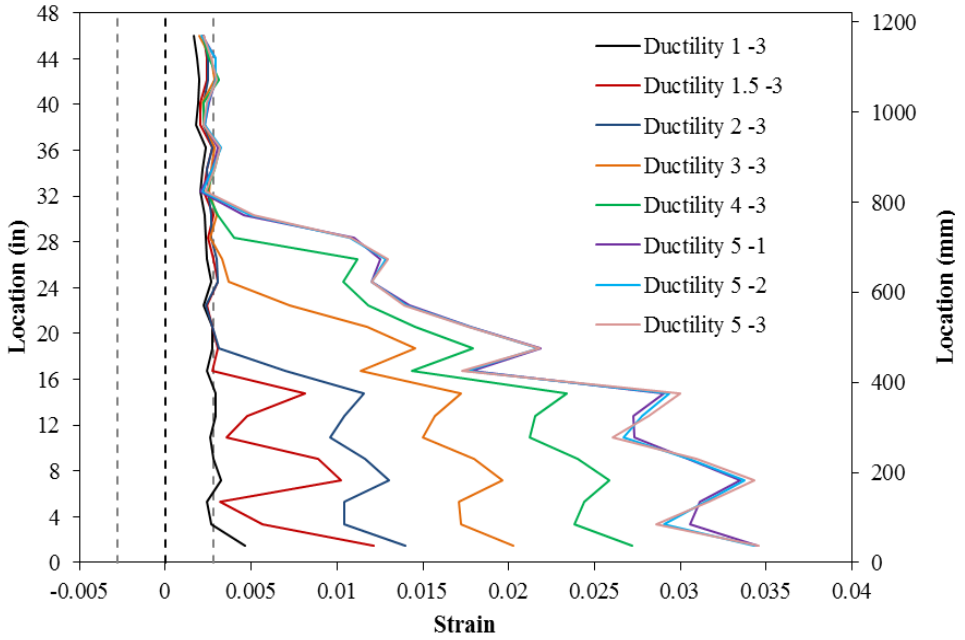

Figure 1.701 T25 – Adjacent South Bar S4 (above) and Bar S2 (not shown) had Large Tension Strains near the Footing

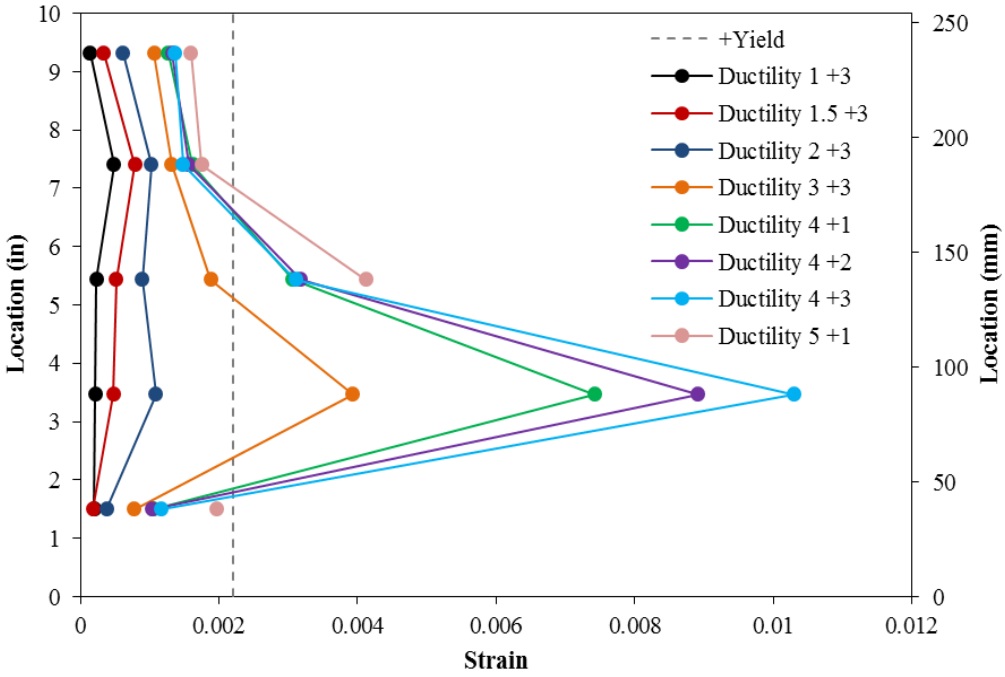

Figure 1.702 T25 – Spiral Strains on the South Side during Push Cycles

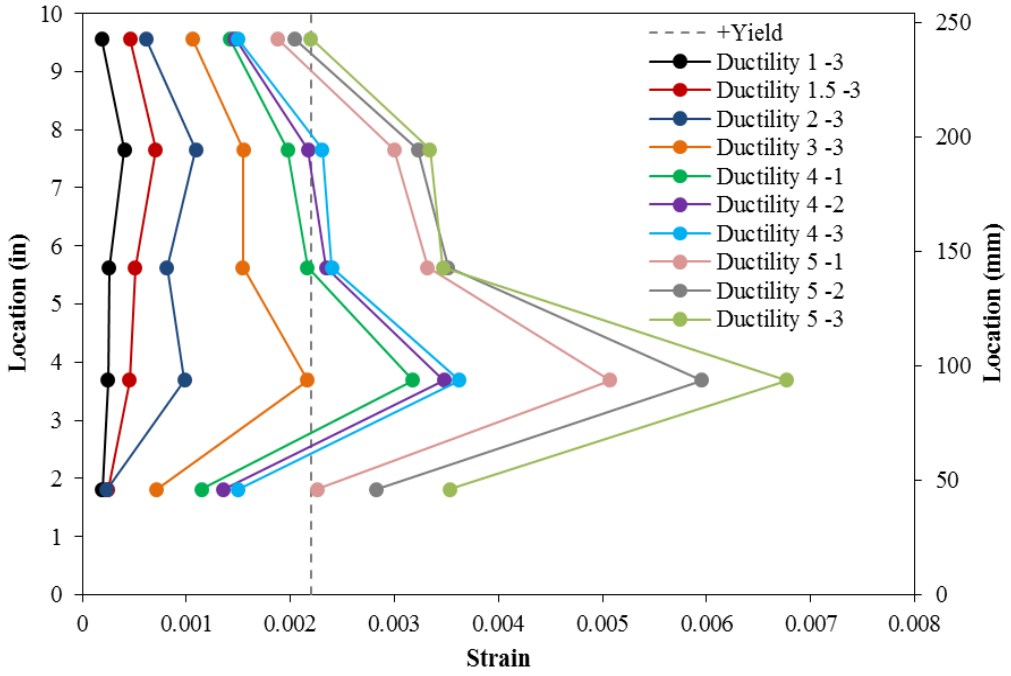

Figure 1.703 T25 – Spiral Strains on the North Side during Pull Cycles

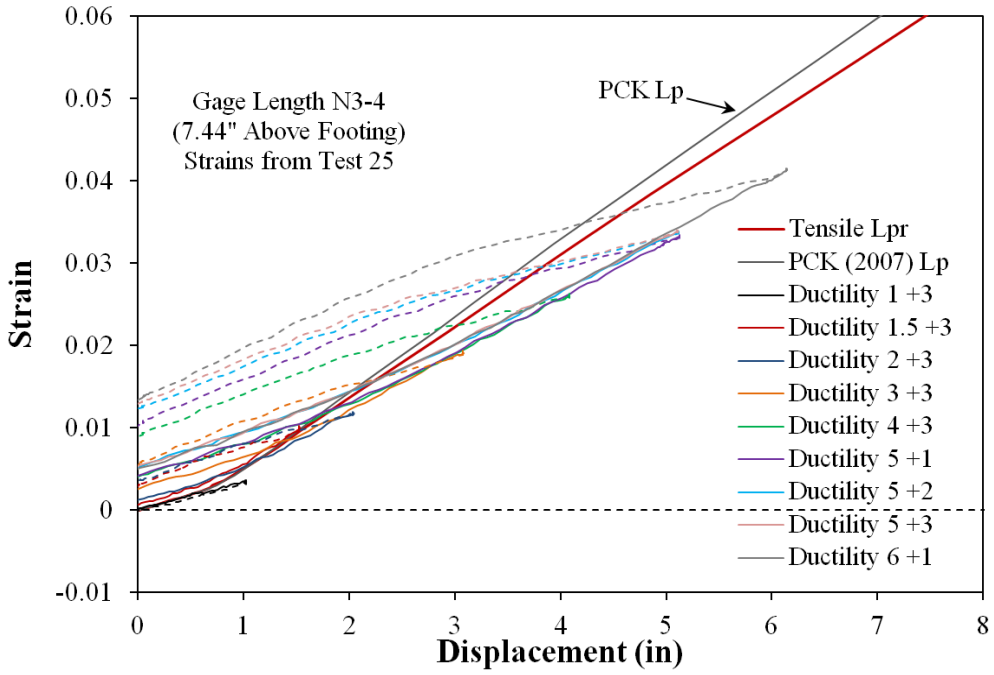

Figure 1.704 T25 – Tension Strain-Displacement for Bar N3 during Push Cycles

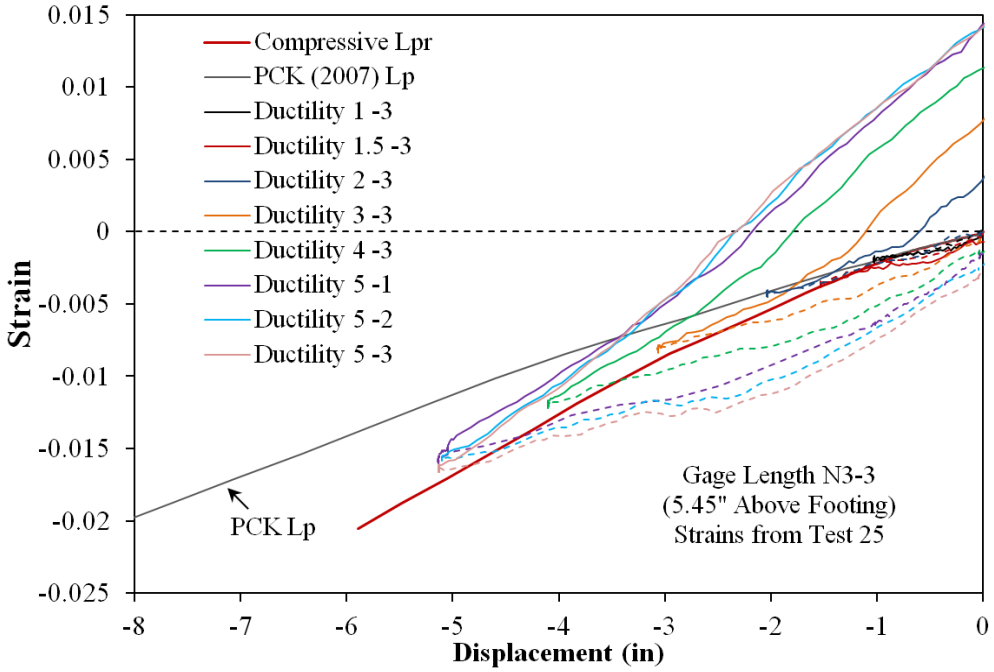

Figure 1.705 T25 – Compressive Strain-Displacement for Bar N3 during Pull Cycles

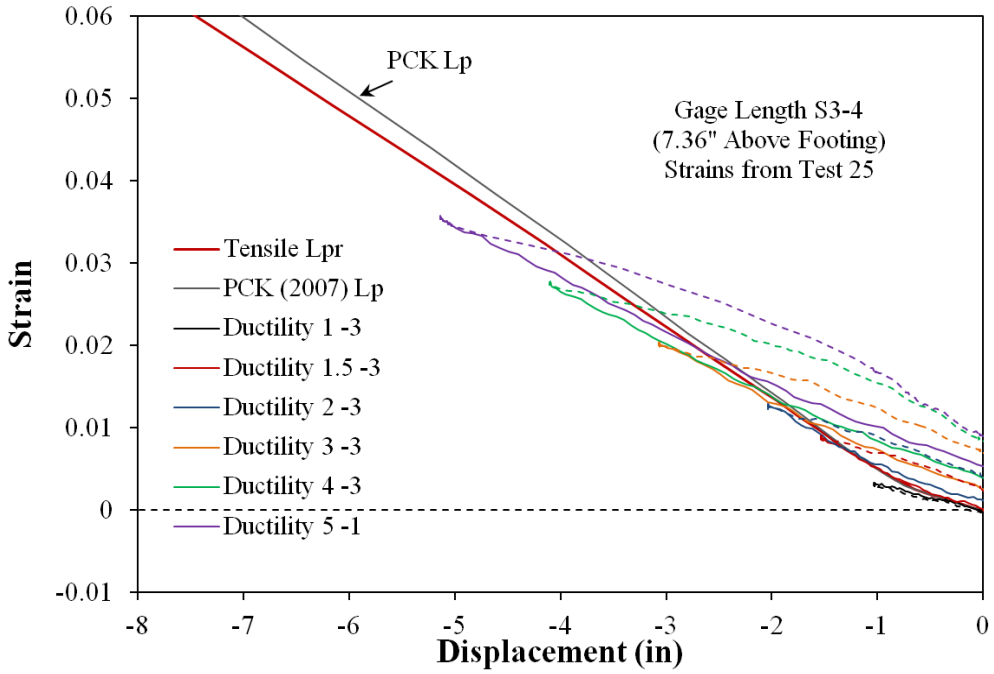

Figure 1.706 T25 – Tensile Strain-Displacement for Bar S3 during Pull Cycles

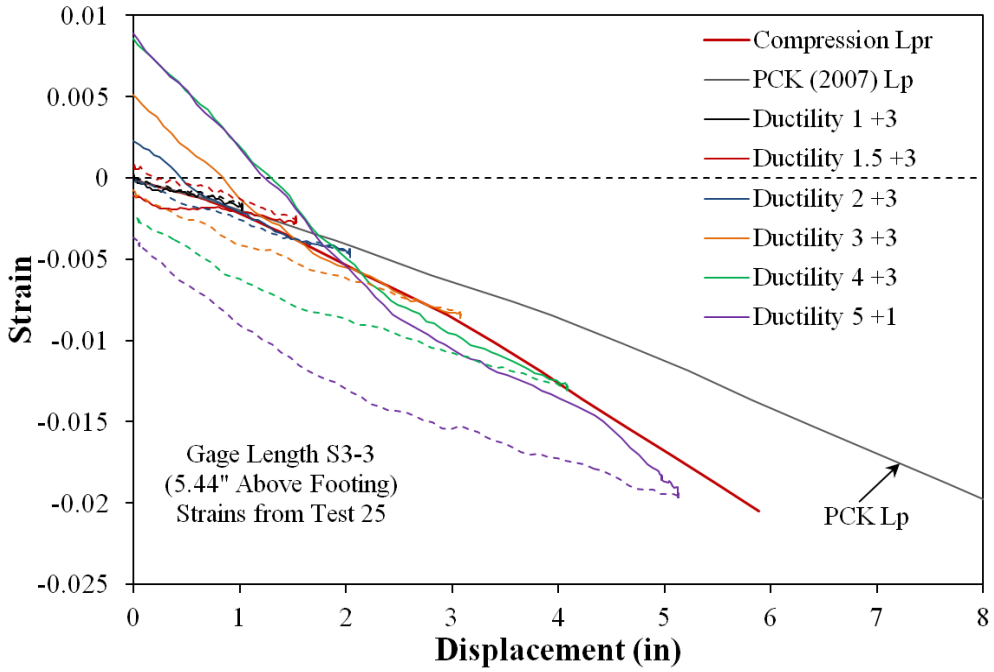

Figure 1.707 T25 – Compressive Strain-Displacement for Bar S3 during Push Cycles

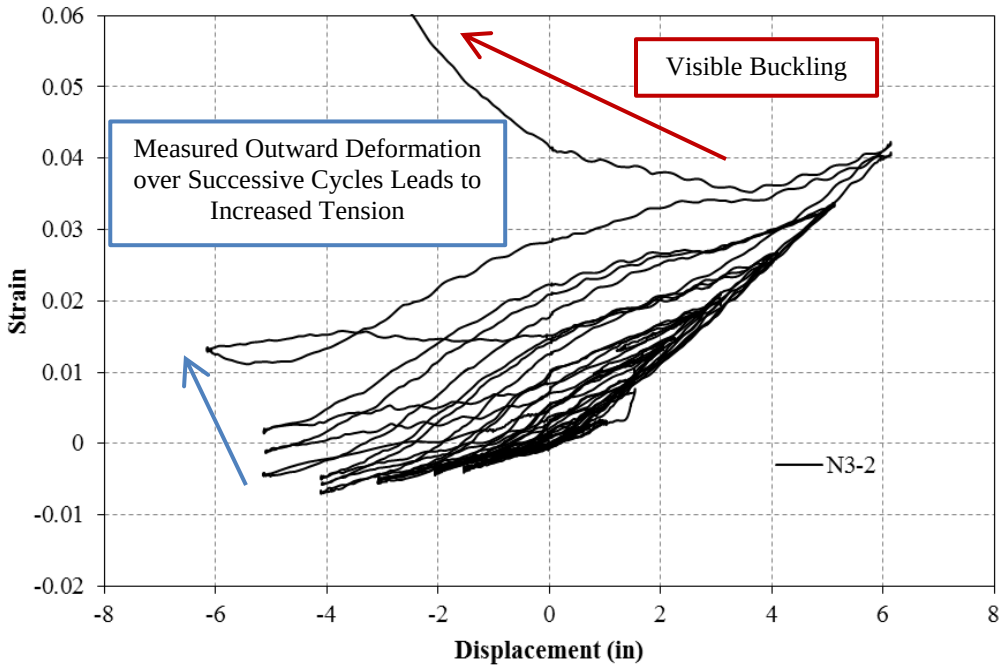

Figure 1.708 T25 – Bar N3 Strain Hysteresis to Buckling (3.53" above the Footing)

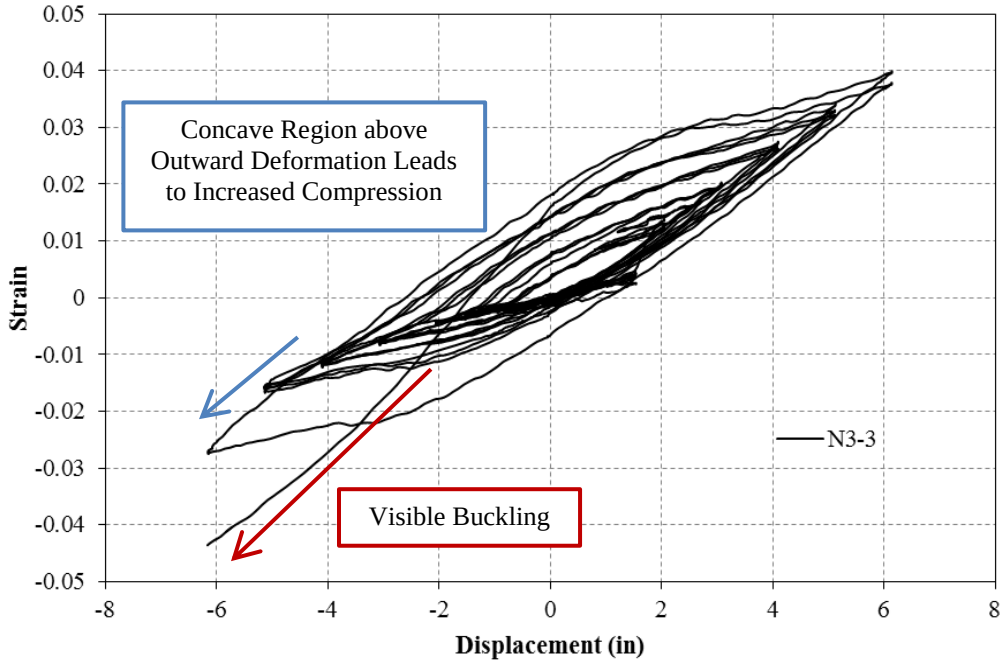

Figure 1.709 T25 – Bar N3 Strain Hysteresis to Buckling (5.45" above the Footing)

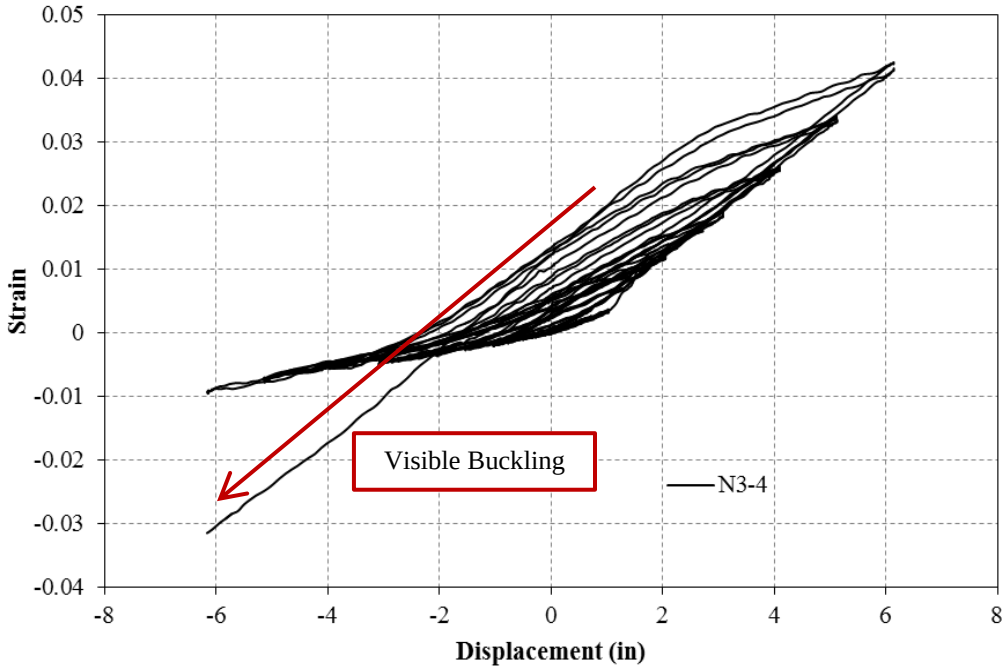

Figure 1.710 T25 – Bar N3 Strain Hysteresis to Buckling (7.44" above the Footing)

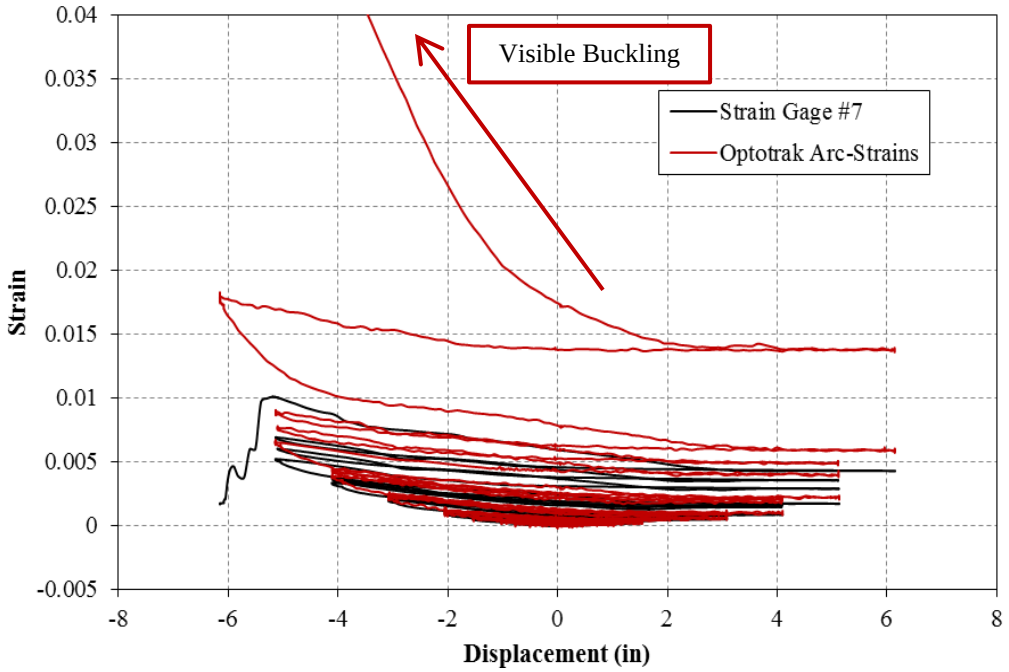

Figure 1.711 T25 – Spiral Strain Hysteresis over North Buckled Region (3.69" Above)

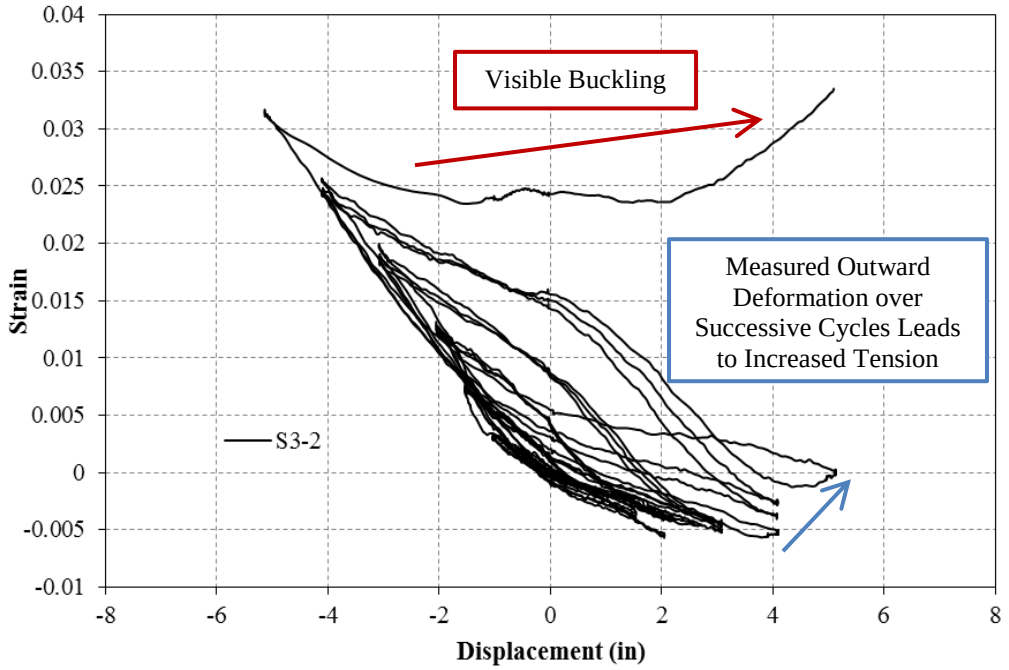

Figure 1.712 T25 – Bar S3 Strain Hysteresis to Buckling (3.47" above the Footing)

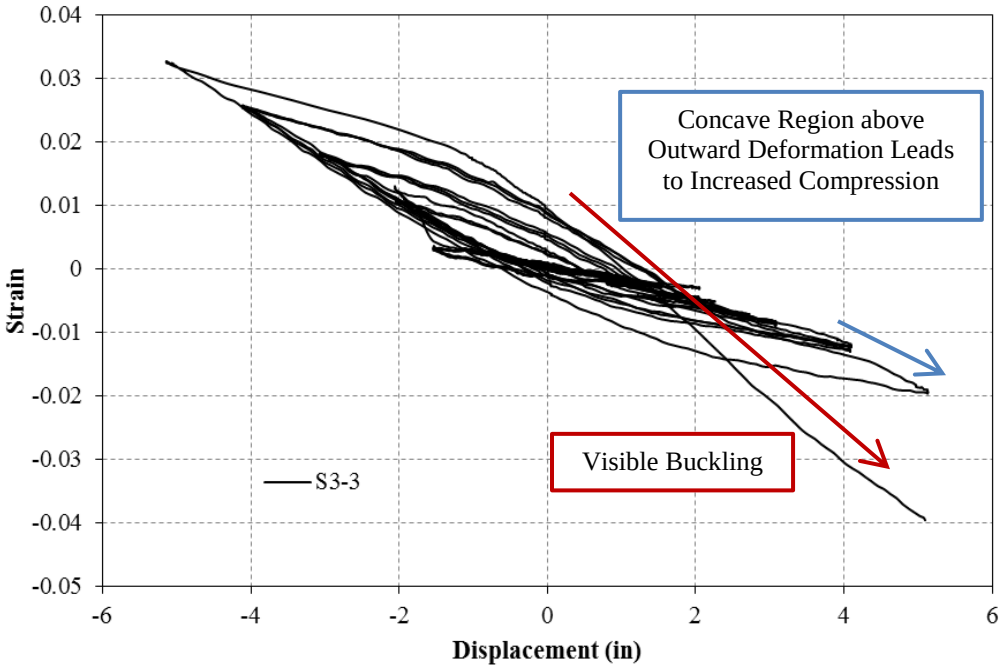

Figure 1.713 T25 – Bar S3 Strain Hysteresis to Buckling (5.44" above the Footing)

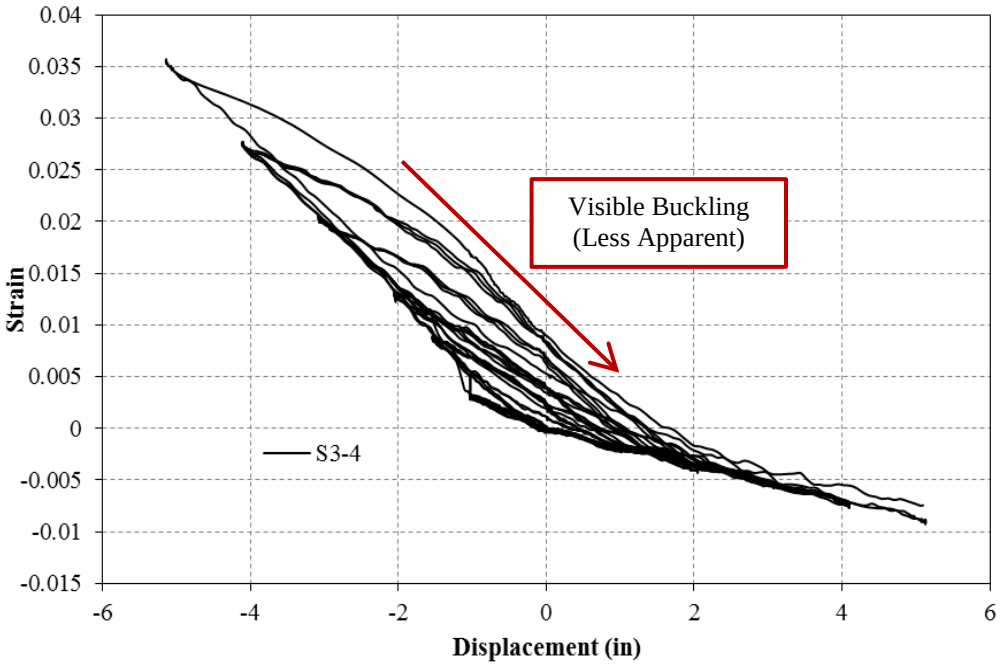

Figure 1.714 T25 – Bar S3 Strain Hysteresis to Buckling (7.36" above the Footing)

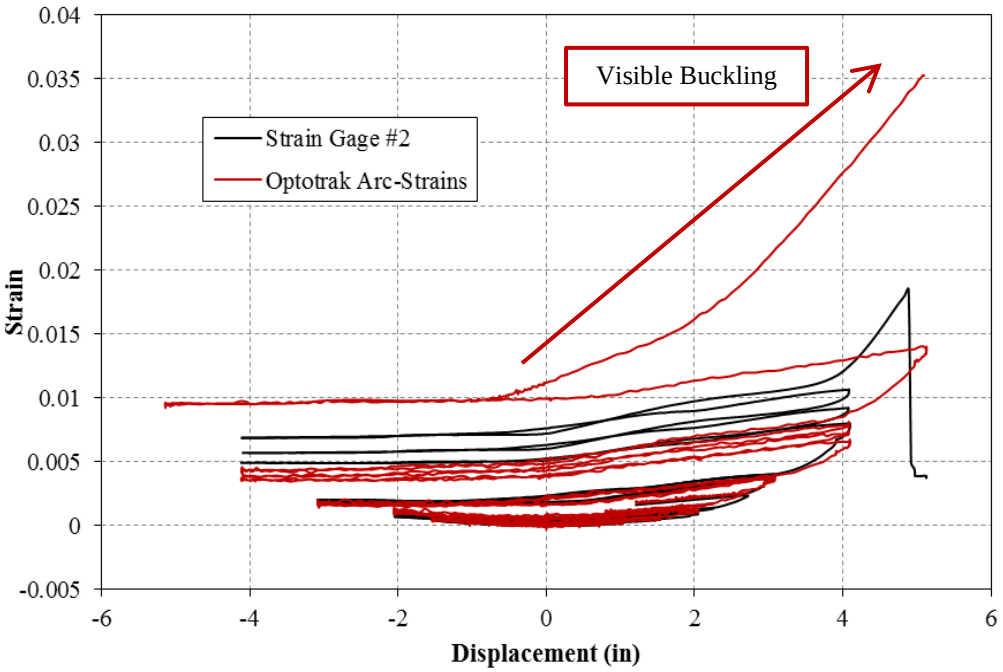

Figure 1.715 T25 – Spiral Strain Hysteresis over South Buckled Region (3.47" Above)

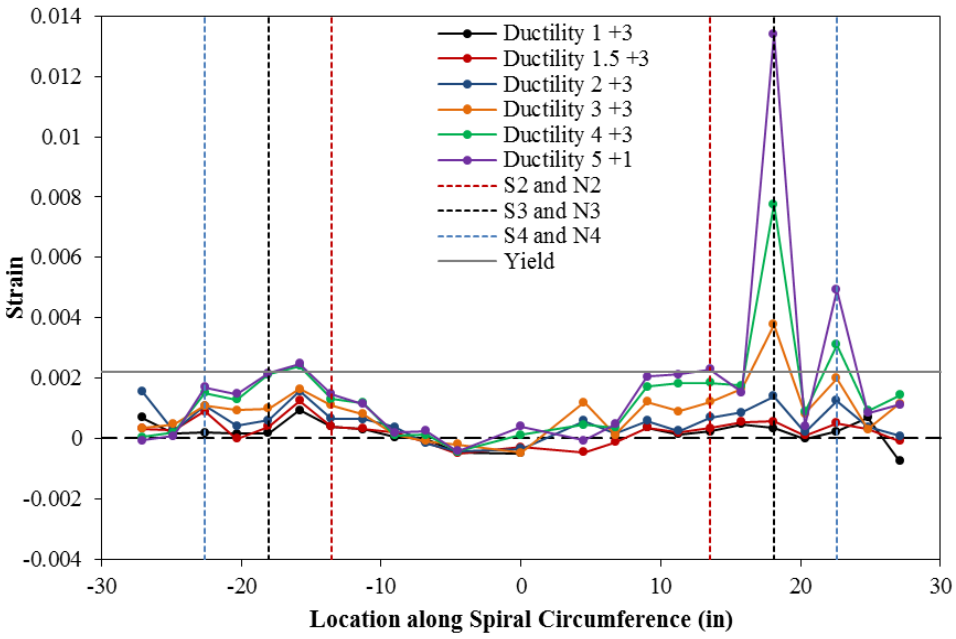

Figure 1.716 T25 – Spiral Strain Distribution for the 2nd Spiral above the Footing during Push Cycles (Positive Location = South)

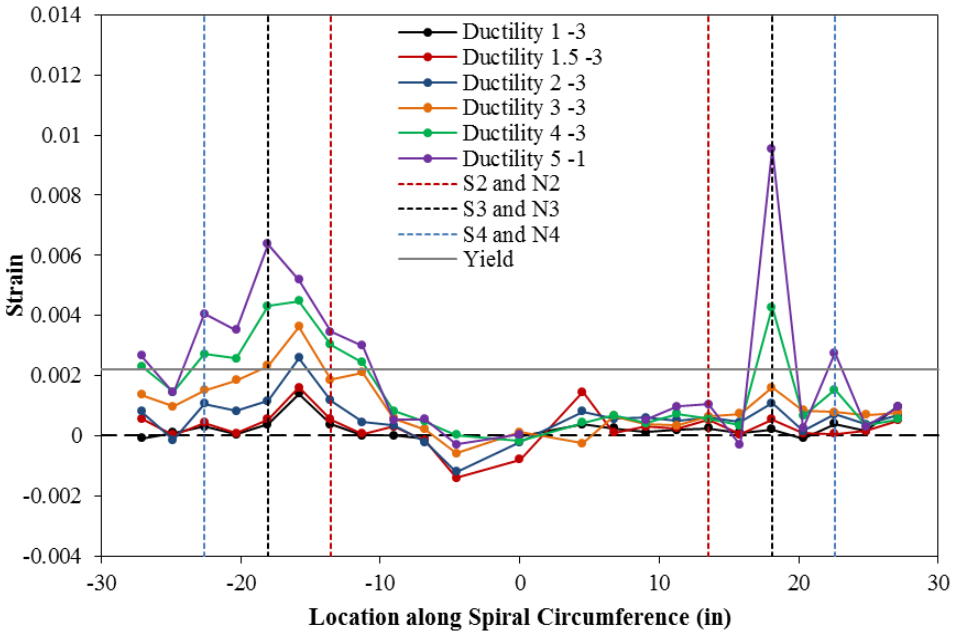

Figure 1.717 T25 – Spiral Strain Distribution for the 2nd Spiral above the Footing during Pull Cycles (Negative Location = North)

Test 25 – Curvature and Strain Penetration Data Analysis

Cross section strain profiles for the third horizontal section above the footing appear in Figure 1.718 and Figure 1.719 for push and pull cycles respectively. This was the first horizontal section in which LEDs for bars instrumented on the shear face of the column were visible to the camera. The third section, 5.36" above the footing, had the largest measured curvatures during pull cycles and the second largest curvatures during push cycles of any horizontal cut through the instrumented region. It appears that reinforcing bars on the shear face of the column have larger tensile strains than those predicted under the plane sections hypothesis. This will continue to be monitored in future tests to investigate the repeatability of such observations. The cross section curvature is calculated by the slope of the least squared line connecting strains measured in twelve reinforcing bars at various locations in the column, Figure 1.679. If the curvatures for many horizontal cross sections are analyzed,

curvature profiles for the plastic hinge region can be constructed; Figure 1.720 and Figure 1.721 for push and pull cycles respectively. Measured curvatures during displacement ductility one closely match the elastic curvature profile, which linearly decreases from yield curvature at the footing-column interface to zero at the center of the applied lateral load.

Plastic curvatures were found to follow a linear distribution. Linear least squared error plastic curvature lines were fit to the plastic portion of the measured curvature profiles. The extrapolation of this linear curvature line with the footing-column interface was taken as the base section curvature, since LEDs are incapable of measuring strains in this region. As the base section curvature ductility increased, the height at which the linear plastic curvature distribution intersected the elastic curvature profile also increased. The height of this intersection is termed the extent of plasticity. The measured spread of plasticity as a function of base section curvature ductility appears as circular data points in Figure 1.725.

Curvature profiles describe the elastic and plastic flexural displacements of the column, but do not address fixed-end rotations which result from strain penetration of longitudinal reinforcement into the footing. The measured vertical displacements of Optotrak LEDs placed closest to the footing column interface can be used to quantify this fixed-end rotation, Figure 1.722 and Figure 1.723. The fixed-end rotation is taken as the slope of the least squared error line connecting the strain penetration bond slip of reinforcement occurs over the partially bonded region over which the bar is being developed in tension or compression. The strain penetration displacement is obtained by multiplying this rotation by the cantilever height of the column. If an elastic curvature profile assumption is made for curvatures higher than those measured with instrumentation, then the entire curvature profile may be integrated to obtain the total column flexural displacement. This column flexural displacement was added to the strain penetration displacement, and compared to the experimentally measured displacements in Figure 1.724.

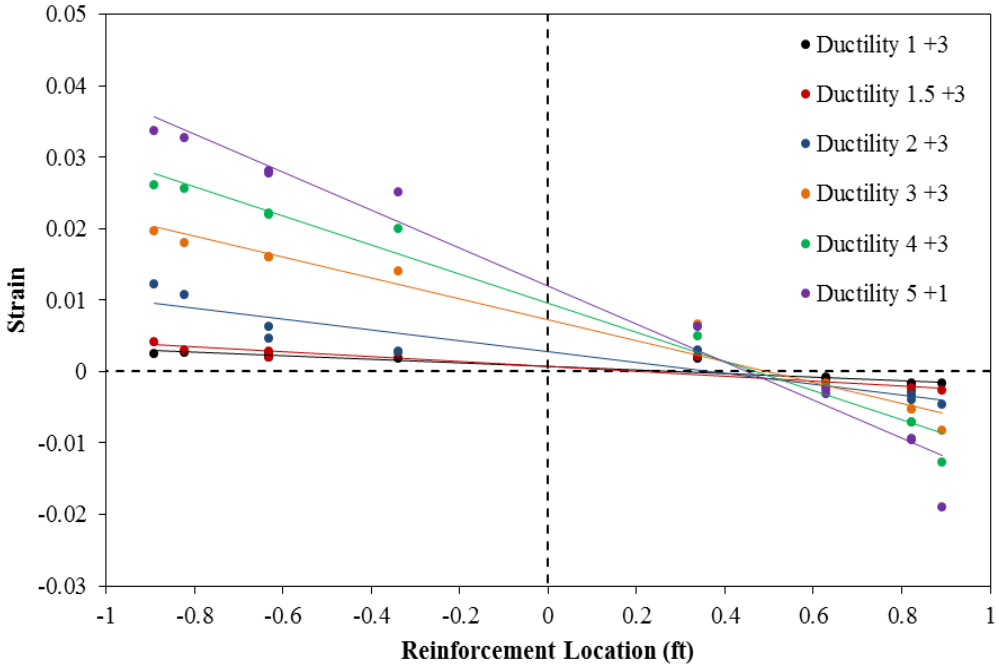

Figure 1.718 T25 – Push Cycle Cross Section Curvature Profiles, 5.36" Above Footing

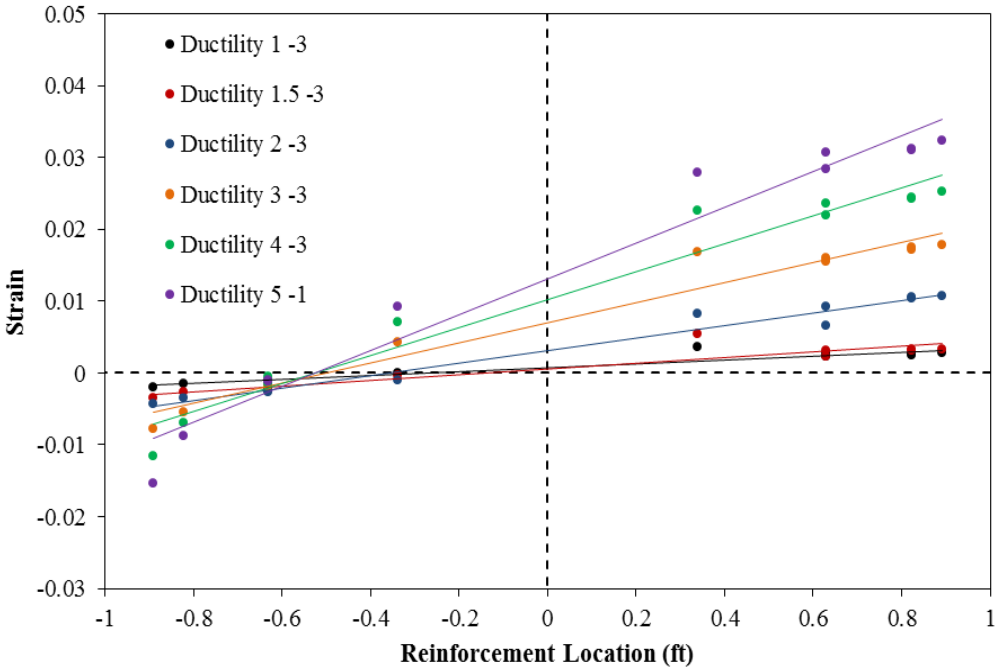

Figure 1.719 T25 – Pull Cycle Cross Section Curvature Profiles, 5.36" Above Footing

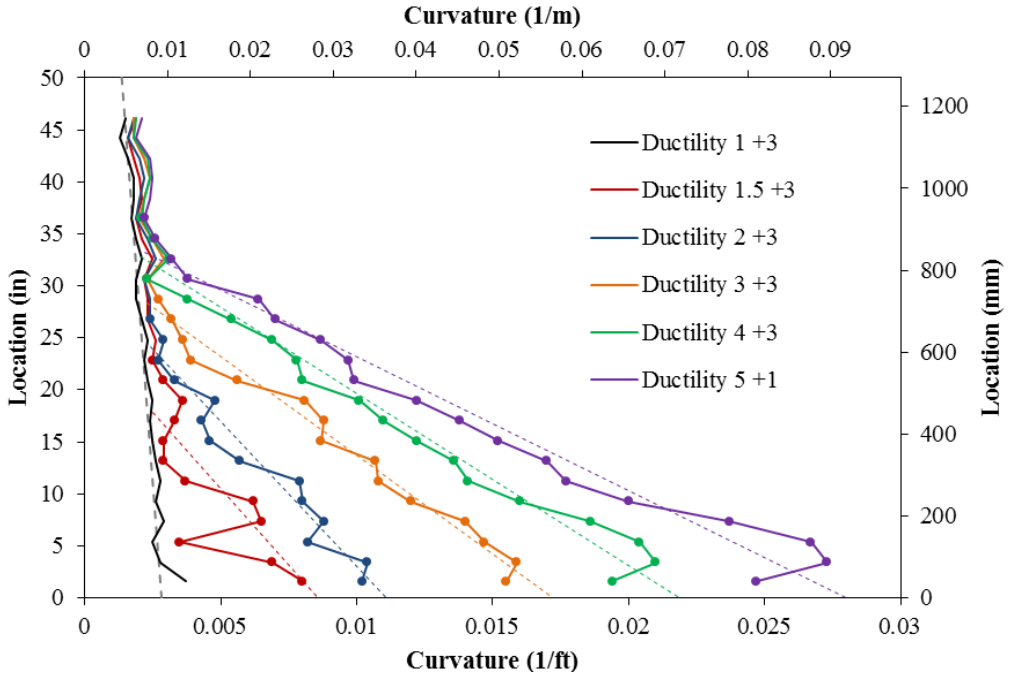

Figure 1.720 T25 – Push Cycle Curvature Distribution with Plastic Regression

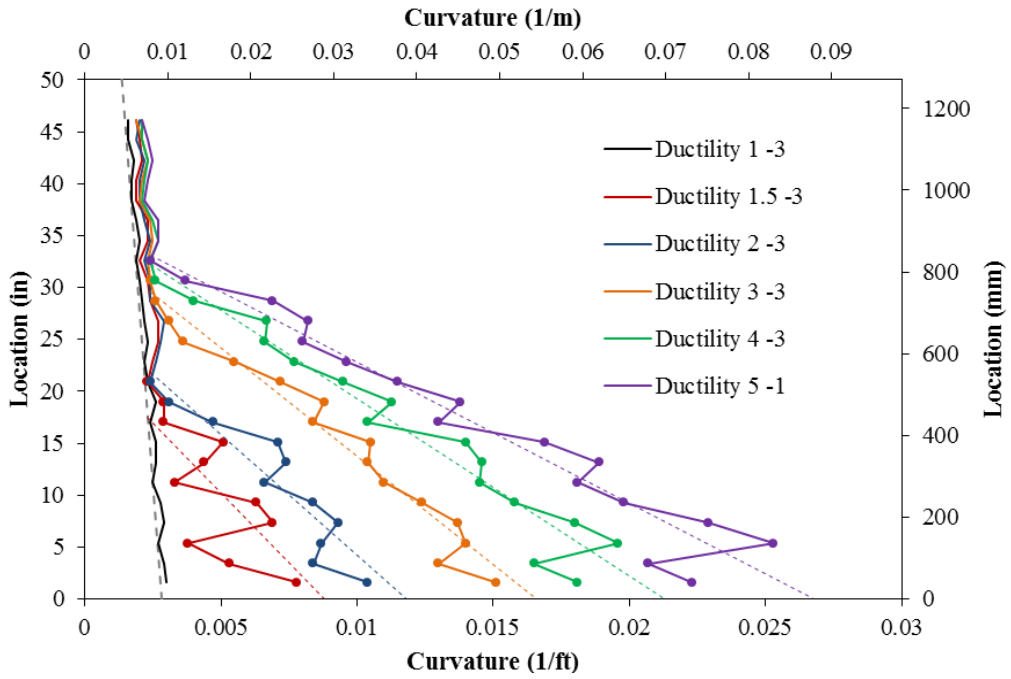

Figure 1.721 T25 – Pull Cycle Curvature Distribution with Plastic Regression

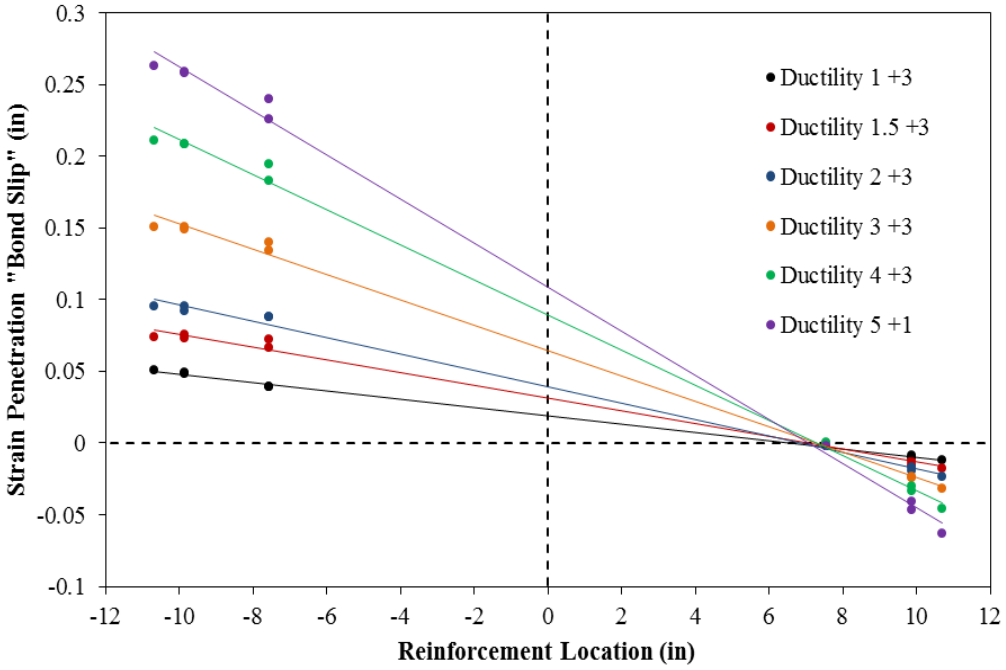

Figure 1.722 T25 – Push Cycle Base Rotations due to Strain Penetration

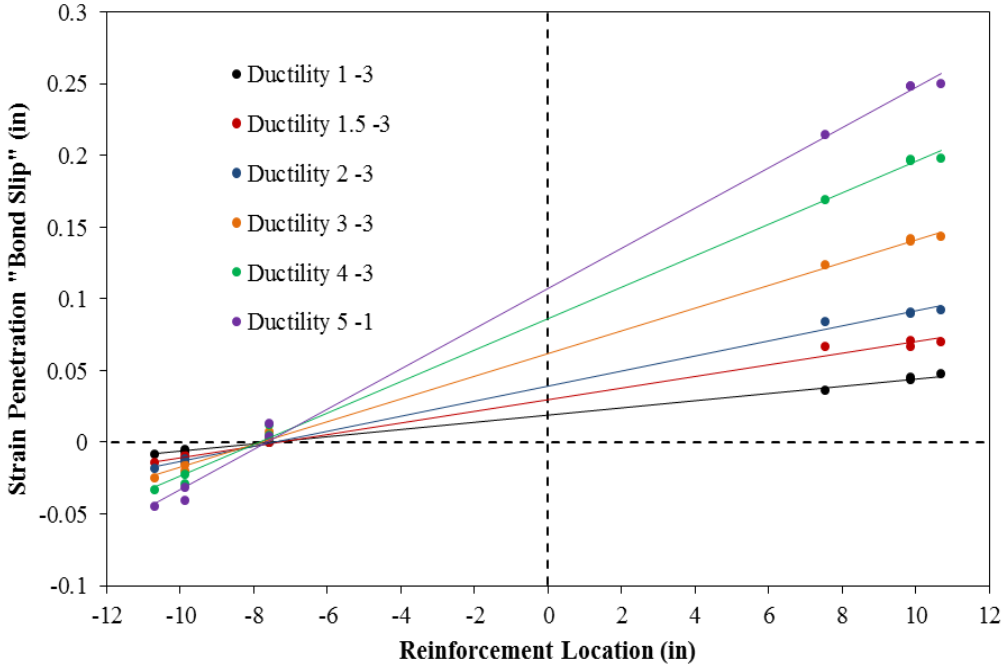

Figure 1.723 T25 – Pull Cycle Base Rotations due to Strain Penetration

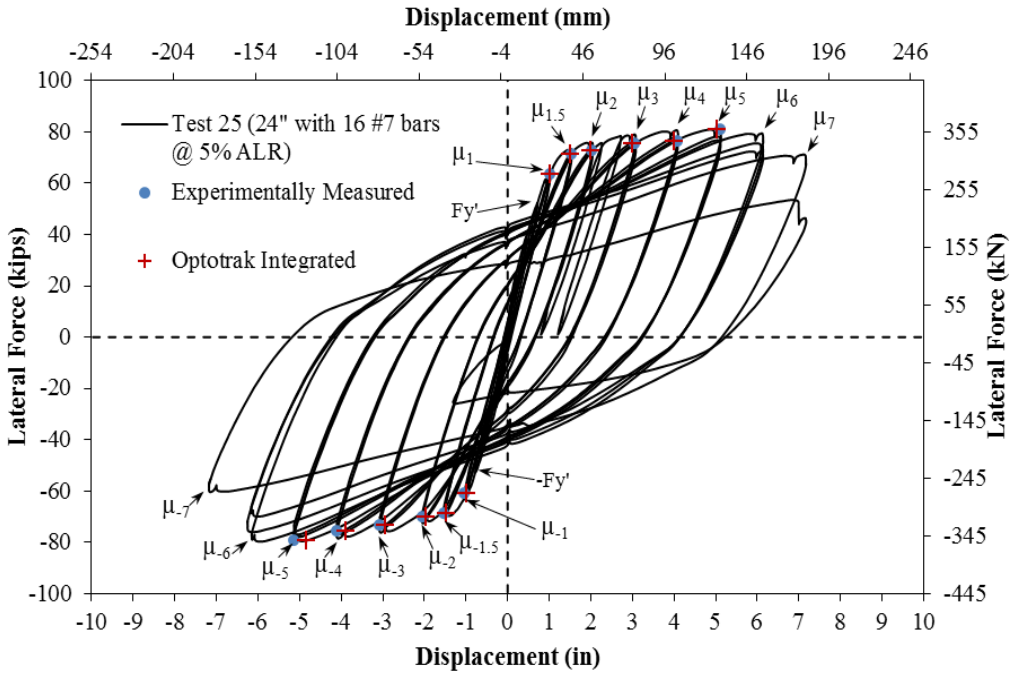

Figure 1.724 T25 – Comparison of Measured and Optotrak Integrated Displacements

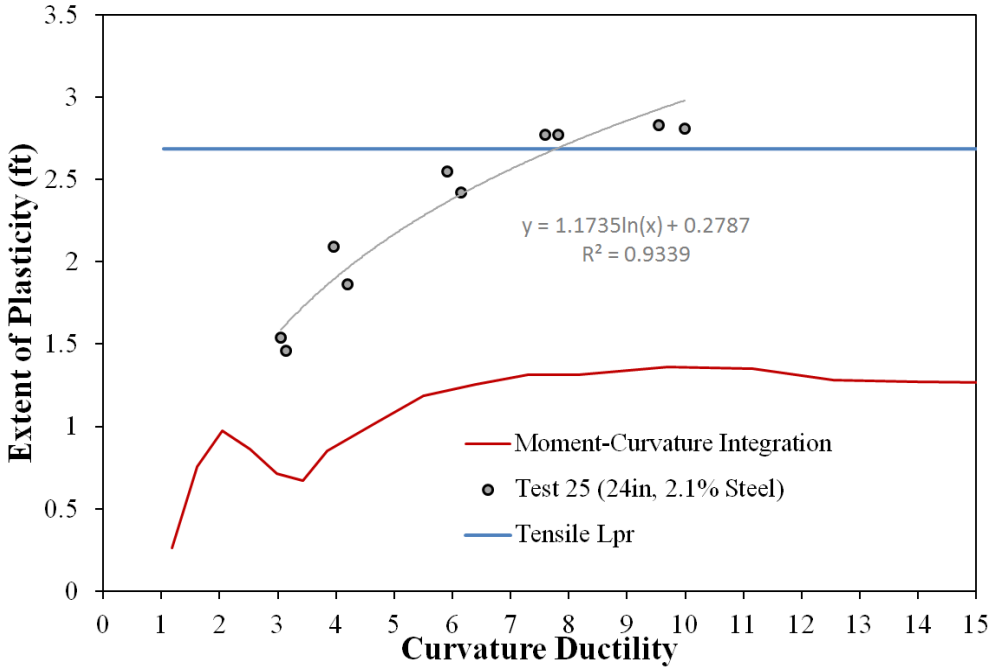

Figure 1.725 T25 – Measured Spread of Plasticity (Circular Data Points)

1.4.2 Test 26 – 24" Dia. Column with 2.1% Long. Steel and 10% Axial Load

Table 1.49 Observations for Test 26 – 24" Dia. With 2.1% Steel and 10% Axial Load

VALUES OF INTEREST:	
Concrete Compressive Strength:	$f_c' = 5890\ psi$
Axial Load:	$P = 244.7\ kips\ \ (P/(f_c' A_g) = 10\%)$
Longitudinal Steel Content:	16 #7 $Bars\ \ (A_{st}/A_g = 2.1\%)$
Analytical First Yield Force:	$F_y' = 59.84\ kips$
Experimental First Yield Displacement:	$\Delta_y' = 0.75"$
Analytical Nominal Moment Capacity:	$M_n = 636.83\ kip * ft$
Equivalent Yield Displacement:	$\Delta_y = 0.99"$
Maximum Lateral Force:	$88.8\ kips$
DAMAGE OBSERVATIONS:	
First Cracking North:	$1/2Fy' = 0.24"$
First Cracking South:	$-1/2Fy' = -0.25"$
Cover Concrete Crushing North:	$\mu_{1.5}^{-2} = -1.49"$
Cover Concrete Crushing South:	$\mu_{1.5}^{+2} = 1.50"$
Transverse Steel Yield North:	At $-2.68"$ during pull to $\mu_3^{-1} = -2.99"$
Transverse Steel Yield South:	At $2.43"$ during push to $\mu_3^{+1} = 2.97"$
Longitudinal Bar Buckling North:	Reversal from $\mu_5^{+2} = 4.98"$
Longitudinal Bar Buckling South:	Reversal from $\mu_4^{-3} = -3.98"$
Longitudinal Bar Fracture North:	At $5.23"$ during push to $\mu_6^{+4} = 5.97"$
Longitudinal Bar Fracture South:	At $-5.90"$ during pull to $\mu_6^{-2} = -5.98"$

*$\mu_5^{+2} = 4.98"$ represents the second push cycle of displacement ductility five

Table 1.50 Strain Data Summary for Test 26 – 24" Dia. with 2.1% Steel and 10% Axial

MATERIAL STRAINS:	
Cover Concrete Crushing North:	$\varepsilon_s = 0.0045\ (compression)$
Cover Concrete Crushing South:	$\varepsilon_s = 0.0046\ (compression)$
Transverse Steel Yield North:	$\varepsilon_s = 0.0089\ (compression)$
Transverse Steel Yield South:	$\varepsilon_s = 0.0121\ (compression)$
Longitudinal Bar Buckling North:	$\varepsilon_s = 0.032\ (peak\ tension\ prior\ to\ bb)$
	$\varepsilon_s = 0.016\ (peak\ comp.\ prior\ to\ bb)$
Longitudinal Bar Buckling South:	$\varepsilon_s = 0.024\ (peak\ tension\ prior\ to\ bb)$
	$\varepsilon_s = 0.027\ (peak\ comp.\ prior\ to\ bb)$
Mander (1988) Ultimate Concrete Compression Strain, $\varepsilon_{cu} = 0.0167$	

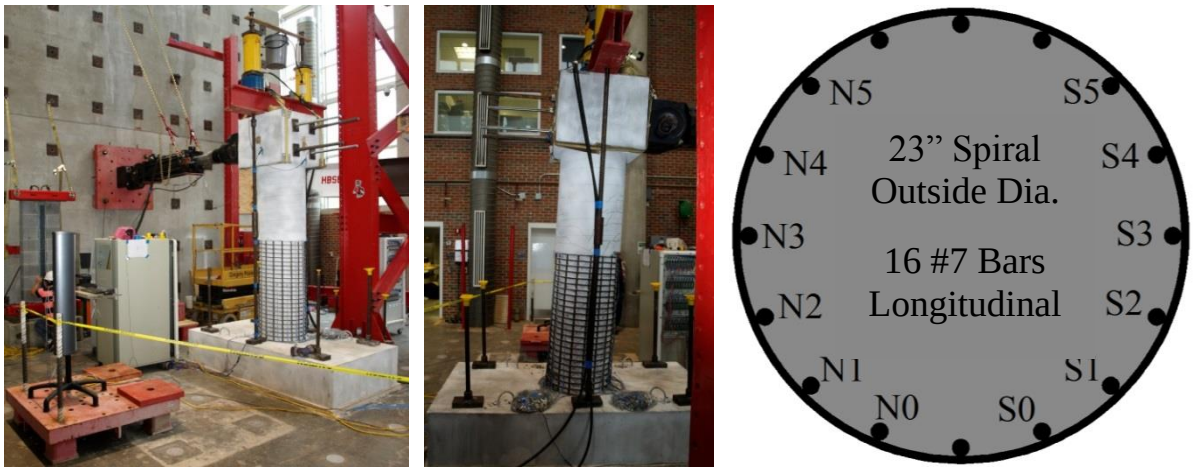

Figure 1.726 T26 – Cross Section Bar Designation

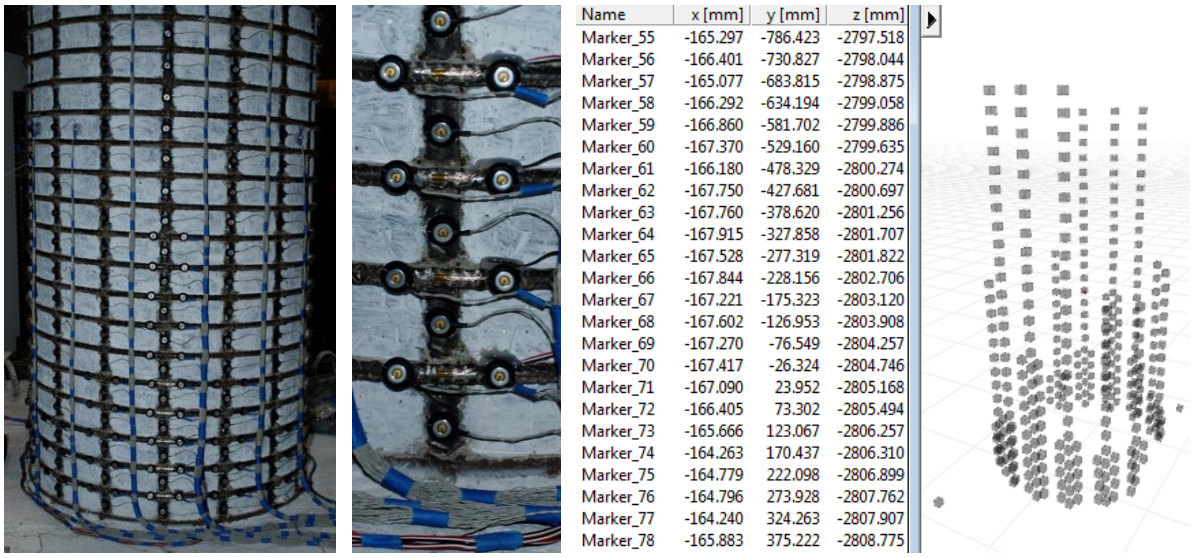

Name	x [mm]	y [mm]	z [mm]
Marker_55	-165.297	-786.423	-2797.518
Marker_56	-166.401	-730.827	-2798.044
Marker_57	-165.077	-683.815	-2798.875
Marker_58	-166.292	-634.194	-2799.058
Marker_59	-166.860	-581.702	-2799.886
Marker_60	-167.370	-529.160	-2799.635
Marker_61	-166.180	-478.329	-2800.274
Marker_62	-167.750	-427.681	-2800.697
Marker_63	-167.760	-378.620	-2801.256
Marker_64	-167.915	-327.858	-2801.707
Marker_65	-167.528	-277.319	-2801.822
Marker_66	-167.844	-228.156	-2802.706
Marker_67	-167.221	-175.323	-2803.120
Marker_68	-167.602	-126.953	-2803.908
Marker_69	-167.270	-76.549	-2804.257
Marker_70	-167.417	-26.324	-2804.746
Marker_71	-167.090	23.952	-2805.168
Marker_72	-166.405	73.302	-2805.494
Marker_73	-165.666	123.067	-2806.257
Marker_74	-164.263	170.437	-2806.310
Marker_75	-164.779	222.098	-2806.899
Marker_76	-164.796	273.928	-2807.762
Marker_77	-164.240	324.263	-2807.907
Marker_78	-165.883	375.222	-2808.775

Figure 1.727 T26 – Target Marker Application and Optotrak Spatial Output

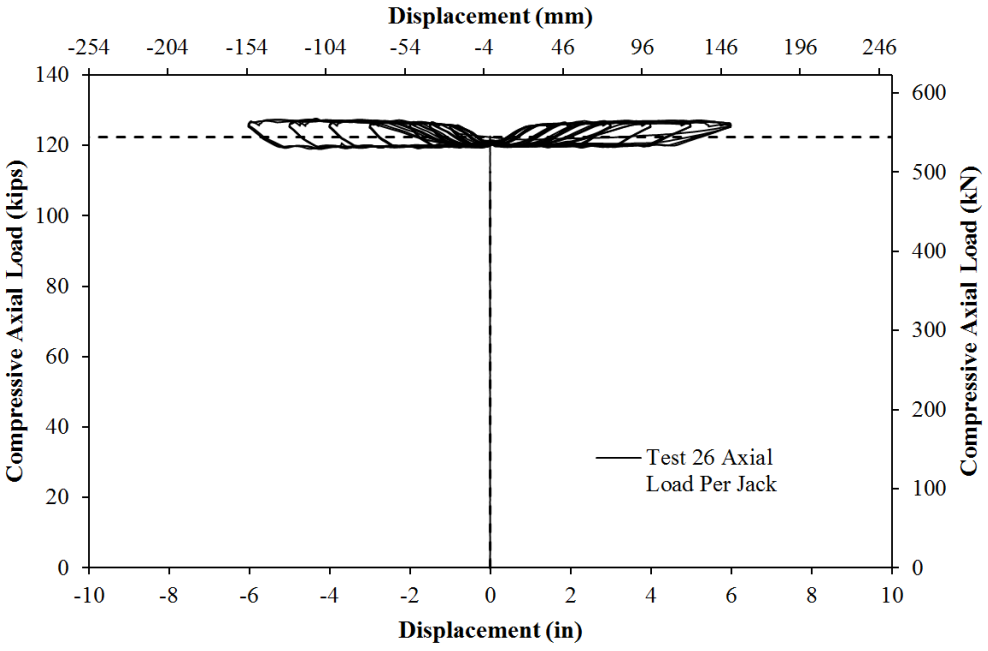

Figure 1.728 T26 – Compressive Axial Load from One Jack (Total = 2*Value)

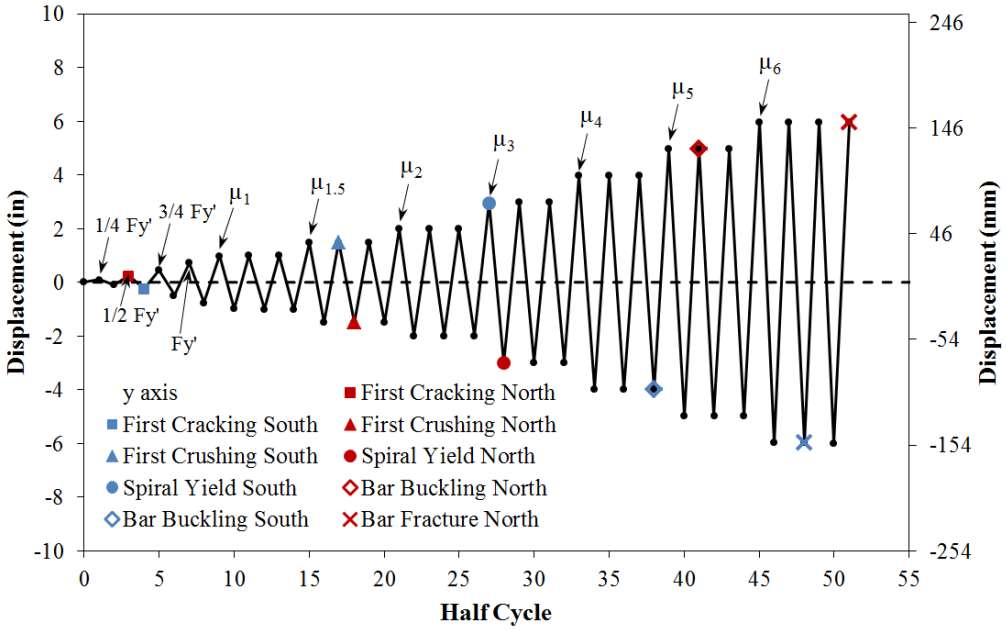

Figure 1.729 T26 – Symmetric Three Cycle Set Load History

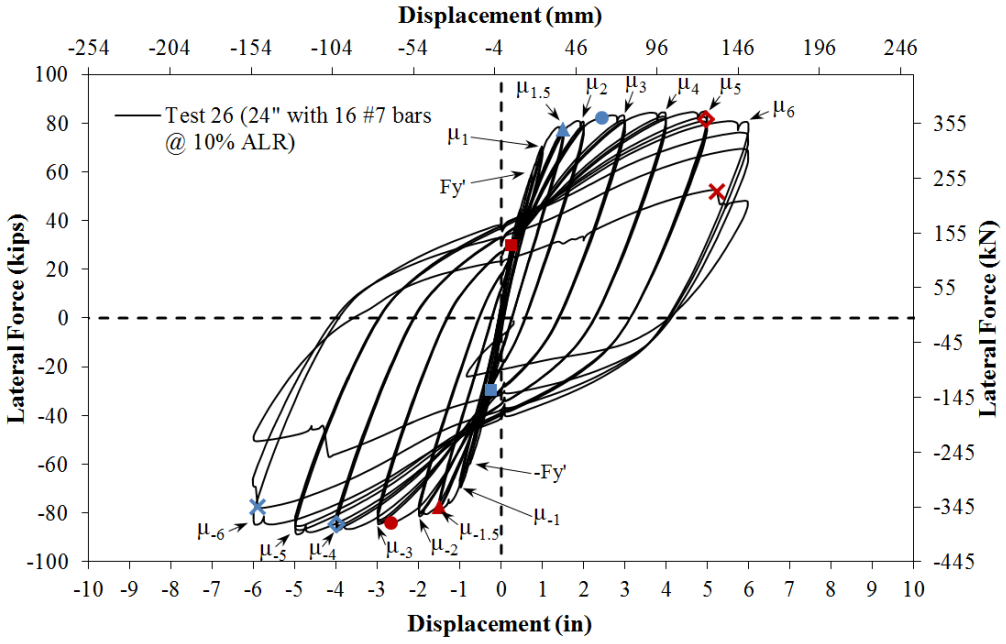

Figure 1.730 T26 – Lateral Force vs. Displacement Response

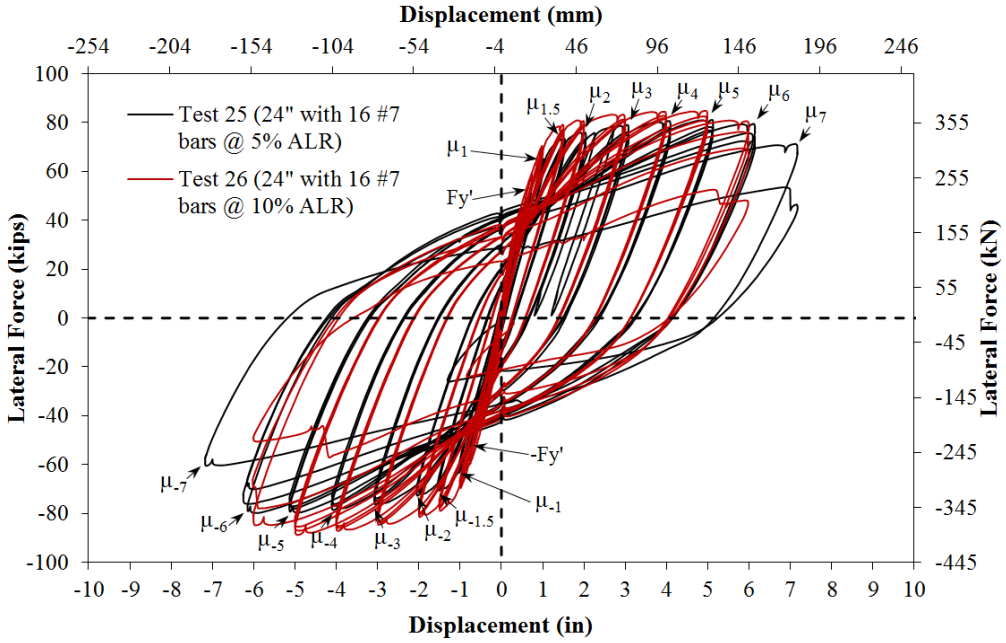

Figure 1.731 Hysteretic Comparison of T25 and T26 with Different Axial Load Levels

Test 26 – 24" Dia. with 2.1% Steel and 10% Axial Load – Experimental Observations

Specimens 25-30 focus on the effects of longitudinal steel content, longitudinal bar diameter, and higher levels of axial load on column behavior. This section summarizes experimental observations and data analysis for column Test 26. The 24" diameter column contains 16 #7 (A706) bars for longitudinal reinforcement ($A_{st}/A_g = 2.1\%$) and a #3 A706 spiral at 2" on center ($4A_{sp}/(D's) = 1\%$). The specimen had an 8ft cantilever length ($L/D = 4$), and was subjected to ($P/(f_c'A_g) = 10\%$) axial load. The symmetric three-cycle-set load history is commonly used to evaluate the seismic performance of structural components. The load history begins with elastic cycles to the following increments of the analytically predicted first yield force: ¼ F_y', ½ F_y', ¾ F_y', and F_y'. The experimental first yield displacement is then determined by taking the average of the recorded displacements during the first yield push and pulls cycles. The equivalent yield displacement, used to determine

the displacement ductility levels ($\mu_{\Delta 1} = 1 * \Delta_y$), is then calculated as $\Delta_y = \Delta'_y(M_n/M'_y)$. The symmetric three-cycle-set load history resumes with three balanced cycles at each of the following displacement ductility levels: 1, 1.5, 2, 3, 4, 5, etc. The imposed displacement history and resulting hysteretic response appears in Figure 1.729 and Figure 1.730.

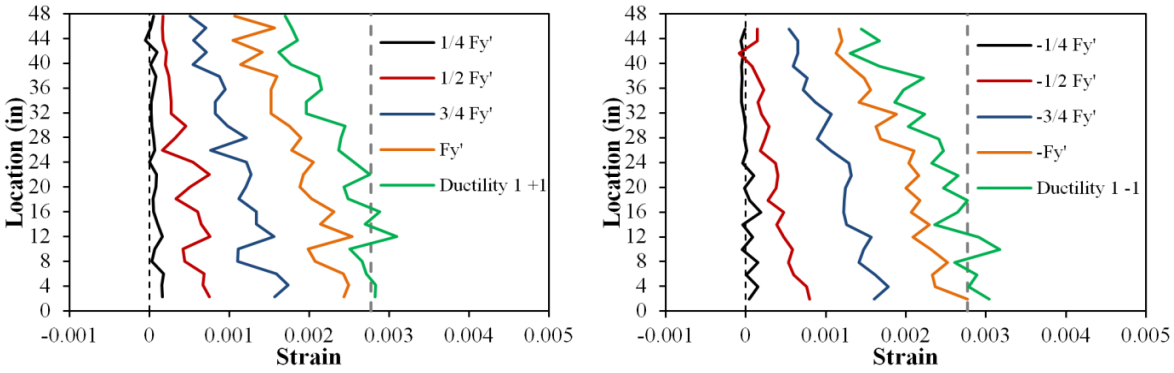

Figure 1.732 T26 – Strain Profiles before Yield, (Left) North and (Right) South

The test began with cycles in ¼ Fy' (first yield force) increments in each direction of loading until the first yield force was reached. A single crack formed at the footing-column interface on the North and South sides of the specimen during $(1/2Fy' = 0.24")$ and $(-1/2Fy' = -0.25")$ respectively. More distributed cracking formed above the base section during $(3/4Fy' = 0.46")$ and $(-3/4Fy' = -0.48")$, Figure 1.733. The crack distribution on all sides of the specimen at first yield, $(Fy' = 0.74")$ and $(-Fy' = -0.76")$, appears in Figure 1.734. Tensile vertical strain profiles for north and south reinforcing bars during elastic push and pull cycles appear in Figure 1.732. The average experimental first yield displacement was used to calculate the equivalent yield displacement, $\Delta_y = \Delta'_y(M_n/M'_y) = 0.99"$, which defined the reversal amplitudes for reminder of the test.

The crack progression at displacement ductility 1, 1.5, 2, 3, and 4 appear in Figure 1.735, Figure 1.737, Figure 1.739, Figure 1.740, and Figure 1.742 respectively. During these cycles the cracks became more numerous and increased in inclination on the shear faces of the specimen. Small amounts concrete flaking was observed on the south and north sides of

the specimen during ($\mu_{1.5}^{+1} = 1.49$") and ($\mu_{1.5}^{-1} = -1.49$"), Figure 1.736. This visible flaking resulted in small amounts of concrete crushing during ($\mu_{1.5}^{+2} = 1.50$") and ($\mu_{1.5}^{-2} = -1.49$"). Crushing on the south and north sides of the specimen increased at ($\mu_{2}^{+1} = 1.99$") and ($\mu_{2}^{-1} = -1.99$"), Figure 1.738. As compressive demands increased during displacement ductility 1.5 to 4, crushing gradually increased on each side of the specimen without influencing the measured lateral forces. Compressive demand during ($\mu_{3}^{+1} = 2.97$") and ($\mu_{3}^{-1} = -2.99$") lead to spiral yielding in confinement regions. Spiral strains on each side of the specimen increased during each successive cycle of ductility four, but the extreme fiber reinforcement remained visibly straight, Figure 1.741.

The south extreme fiber bar visibly buckled during ($\mu_{5}^{+1} = 4.98$"), as shown in the left photo of Figure 1.743. The outward buckled region occurred over the second gage length above the footing which encompassed the second spiral layer. The buckled deformation increased during ($\mu_{5}^{+2} = 4.98$"). The north extreme fiber bar visibly buckled during the reversal from tension strains sustained during ($\mu_{5}^{+2} = 4.98$"), Figure 1.744. Two adjacent south reinforcing bars, S2 and S4, buckled during ($\mu_{5}^{+3} = 4.97$"), Figure 1.745. Two adjacent north reinforcing bars, N2 and N4, buckled during ($\mu_{6}^{-1} = -5.97$"), Figure 1.746. Severe buckling of three bars on the south side of the specimen during ($\mu_{6}^{+2} = 5.97$") led to significant crushing of core concrete, Figure 1.747. Previously buckled south extreme fiber bar S3 ruptured during ($\mu_{6}^{-2} = -5.98$"), Figure 1.747, resulting in the first significant loss in the strength. South reinforcing bars S1 and S5 buckled during ($\mu_{6}^{+3} = 5.97$"), Figure 1.748. Two additional south bars, S2 and S4, ruptured during ($\mu_{6}^{-3} = -5.99$"), Figure 1.748. Previously buckled north reinforcing bars N3 and N4 ruptured during ($\mu_{6}^{+4} = 5.97$"), Figure 1.749. The test was concluded with fractured bars on each side of the specimen, photos of the hinge region after removal of the instrumentation appear in Figure 1.749 and Figure 1.750.

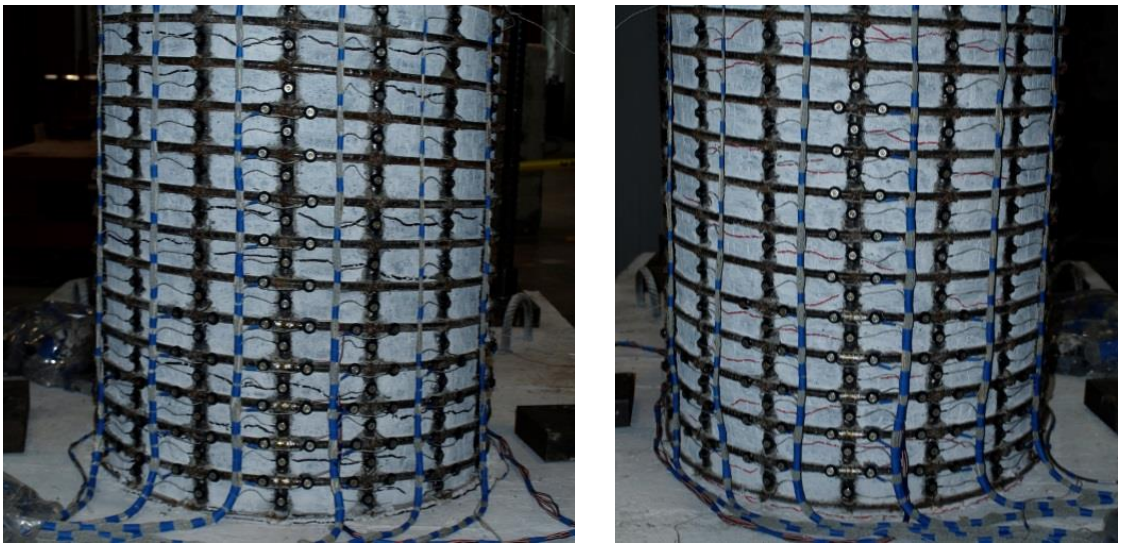

Figure 1.733 T26 – (Left) North Distributed Cracking during ($3/4Fy' = 0.46$"), (Right) South Distributed Cracking during ($-3/4Fy' = -0.48$")

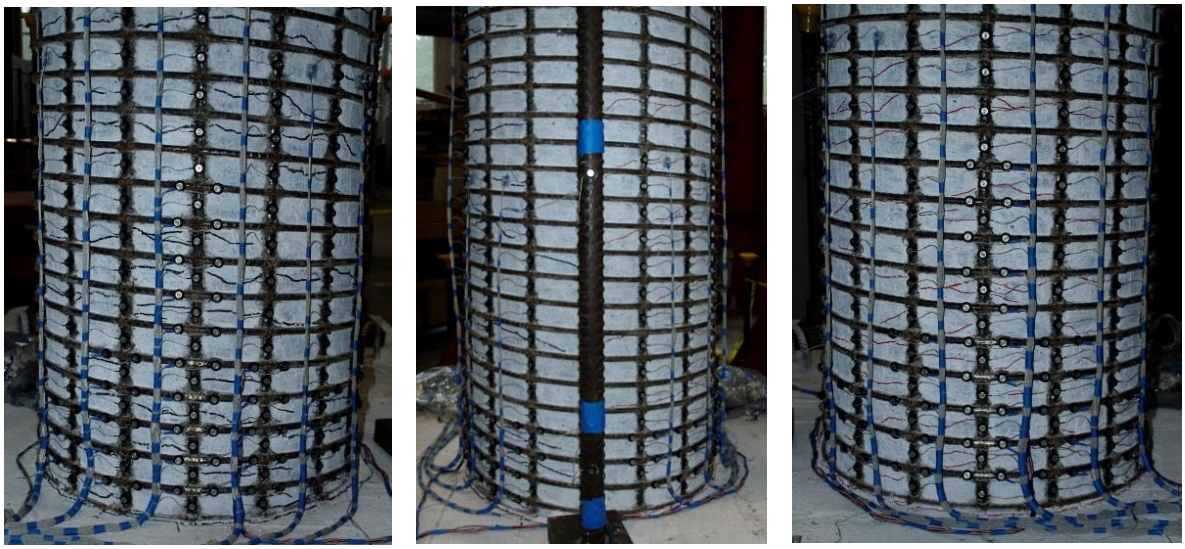

Figure 1.734 T26 – (Left) North Crack Distribution at ($Fy' = 0.74$"), (Middle and Right) Crack Distributions on the Front and Right Sides at ($-Fy' = -0.76$")

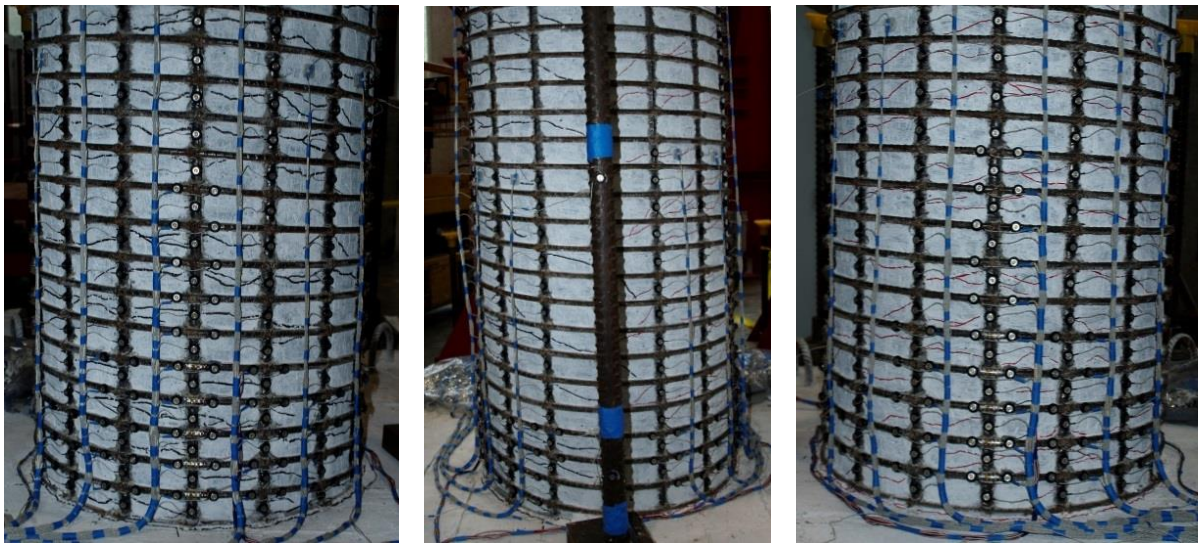

Figure 1.735 T26 – (Left) North Crack Distribution at ($\mu_1^{+3} = 1.00$"), (Middle and Right) Crack Distributions on the Front and Right Sides at ($\mu_1^{-3} = -1.01$")

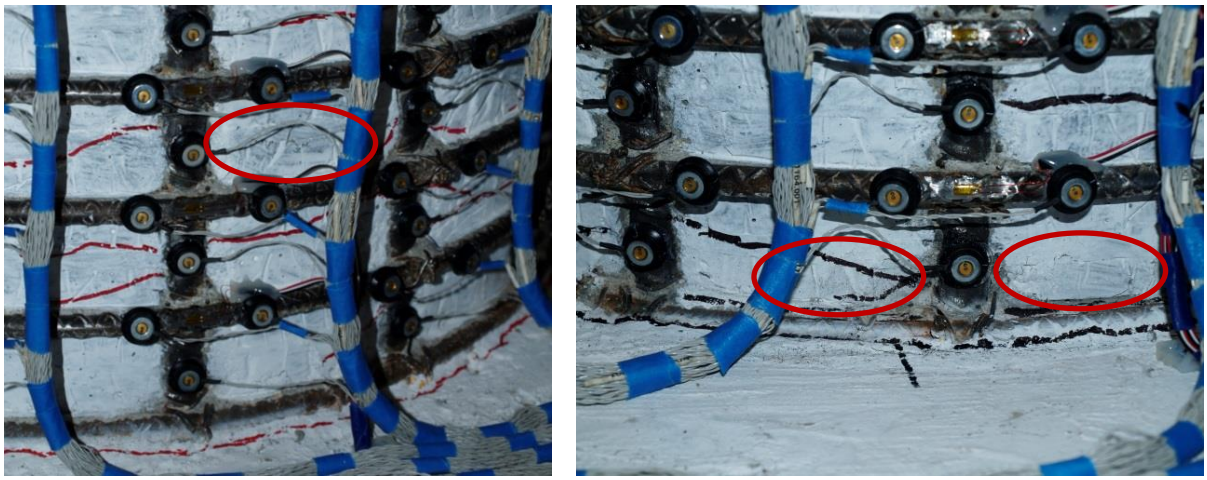

Figure 1.736 T26 – (Left) South Concrete Flaking during ($\mu_{1.5}^{+1} = 1.49$"), (Right) North Concrete Flaking during ($\mu_{1.5}^{-1} = -1.49$")

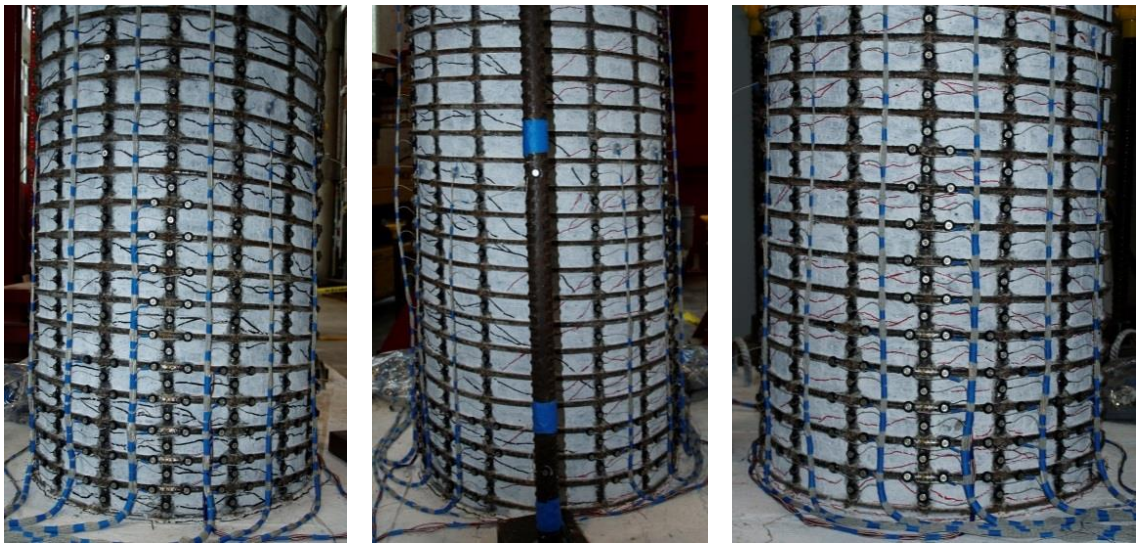

Figure 1.737 T26 – (Left) North Crack Distribution at ($\mu_{1.5}^{+3} = 1.50$"), (Middle and Right) Crack Distributions on the Front and Right Sides at ($\mu_{1.5}^{-3} = -1.50$")

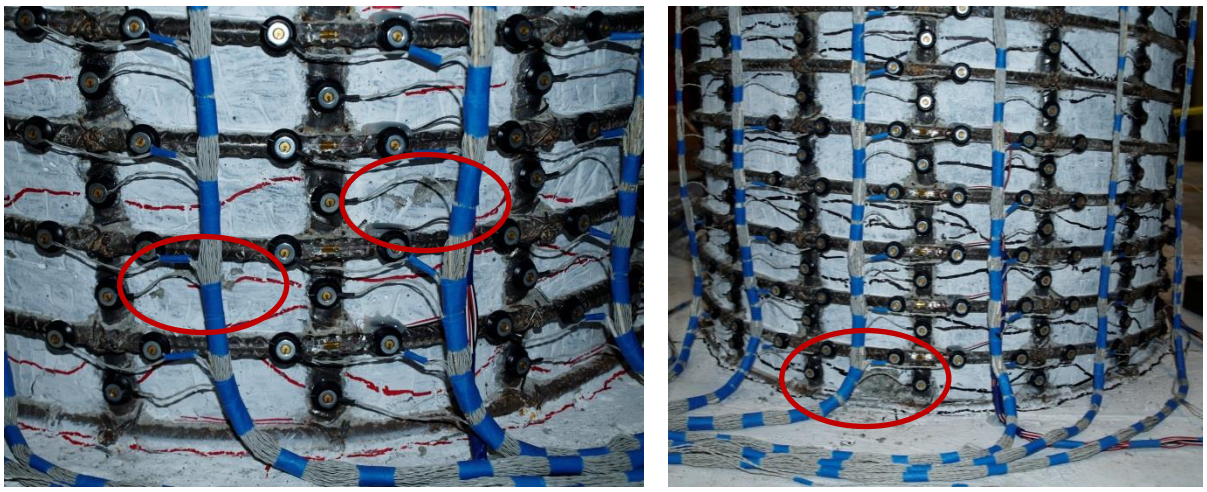

Figure 1.738 T26 – (Left) South Crushing during ($\mu_{2}^{+1} = 1.99$"), (Right) North Crushing during ($\mu_{2}^{-1} = -1.99$")

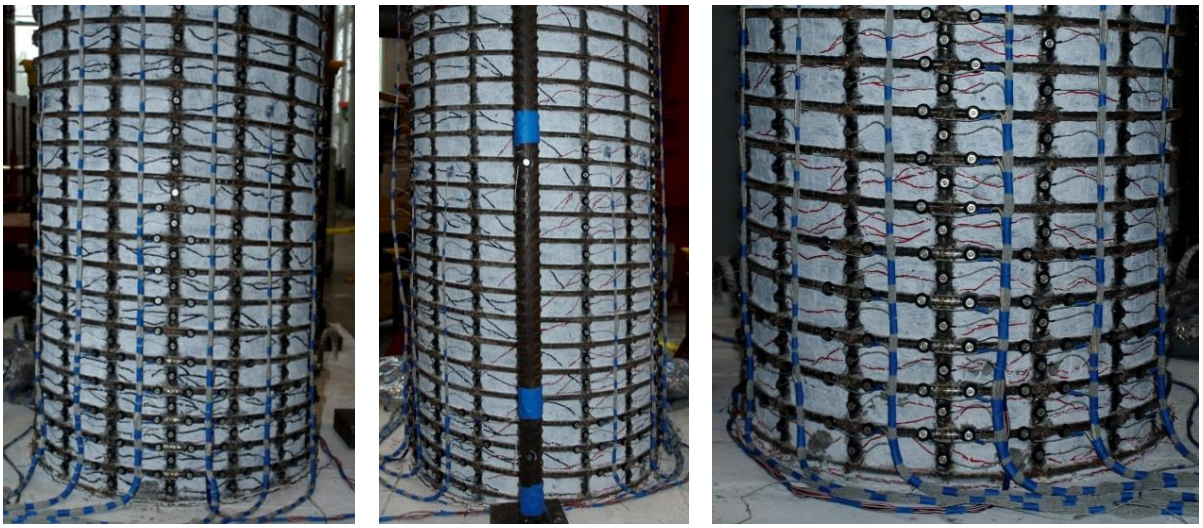

Figure 1.739 T26 – (Left) North Crack Distribution at ($\mu_2^{+3} = 1.99$"), (Middle and Right) Crack Distributions on the Front and Right Sides at ($\mu_2^{-3} = -1.99$")

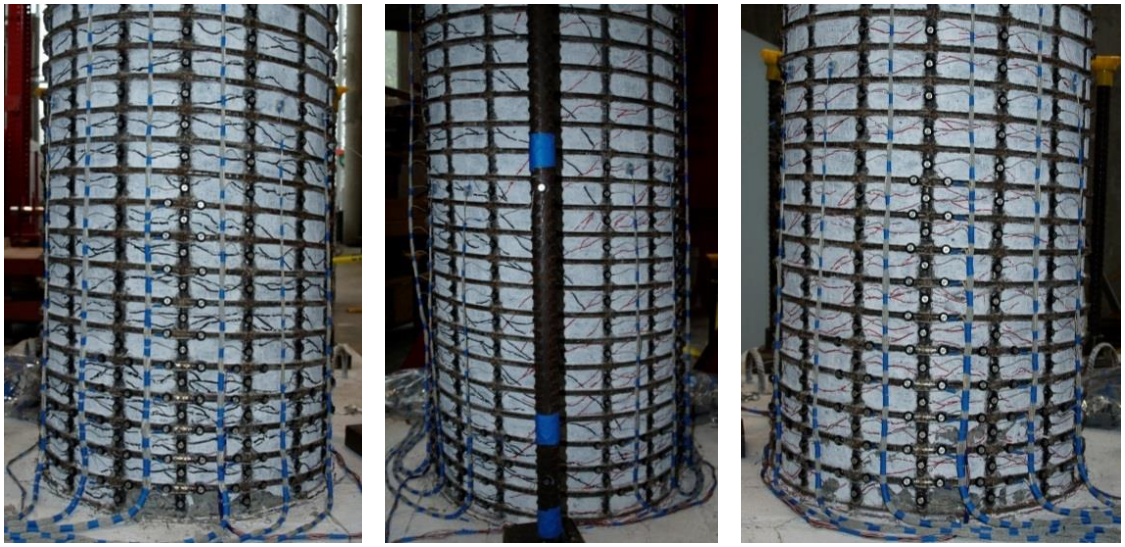

Figure 1.740 T26 – (Left) North Crack Distribution at ($\mu_3^{+3} = 2.98$"), (Middle and Right) Crack Distributions on the Front and Right Sides at ($\mu_3^{-3} = -2.98$")

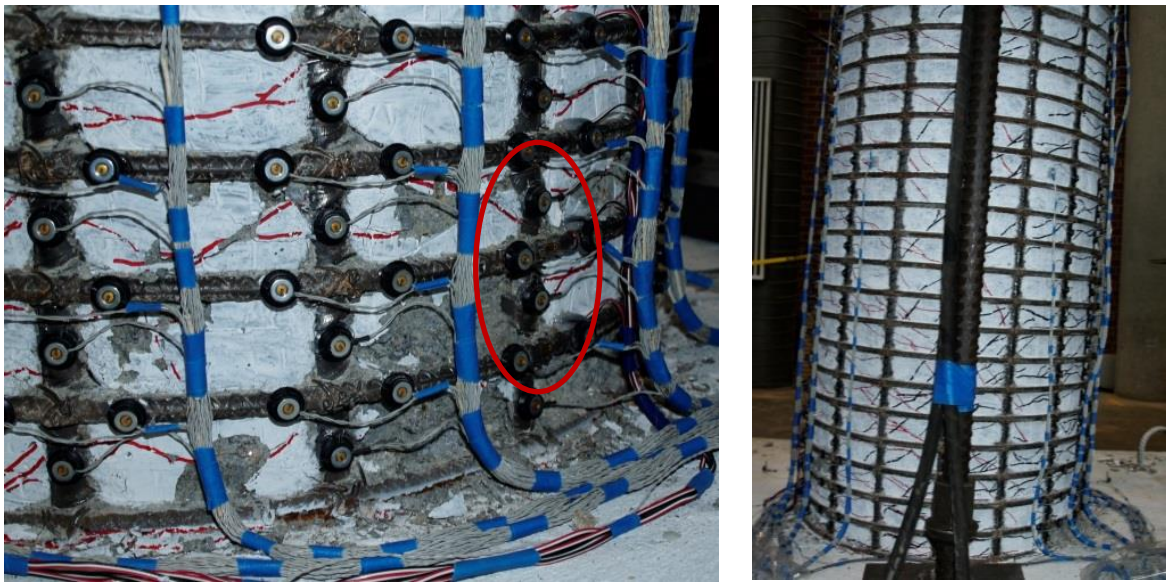

Figure 1.741 T26 – (Left) Bar S3 Remained Visibly Straight during ($\mu_4^{+3} = 3.98$"), (Right) Crack Distribution on the Back Side

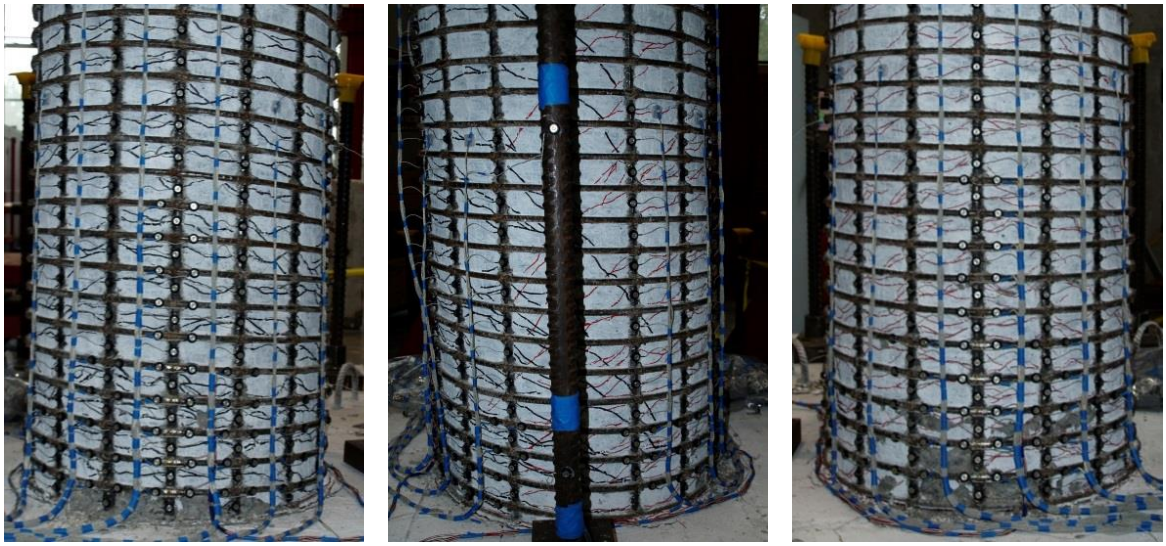

Figure 1.742 T26 – (Left) North Crack Distribution at ($\mu_4^{+3} = 3.98$"), (Middle and Right) Crack Distributions on the Front and Right Sides at ($\mu_4^{-3} = -3.98$")

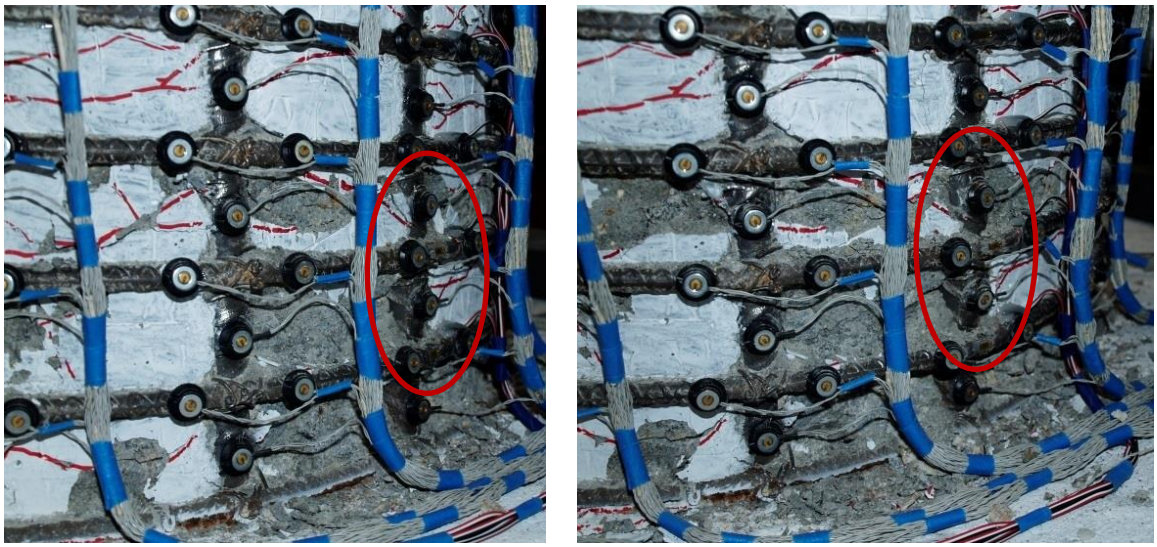

Figure 1.743 T26 – (Left) Slight Visible Buckling of Bar S3 during ($\mu_5^{+1} = 4.98$"), (Right) Increased Deformation in Buckled Bar S3 during ($\mu_5^{+2} = 4.98$")

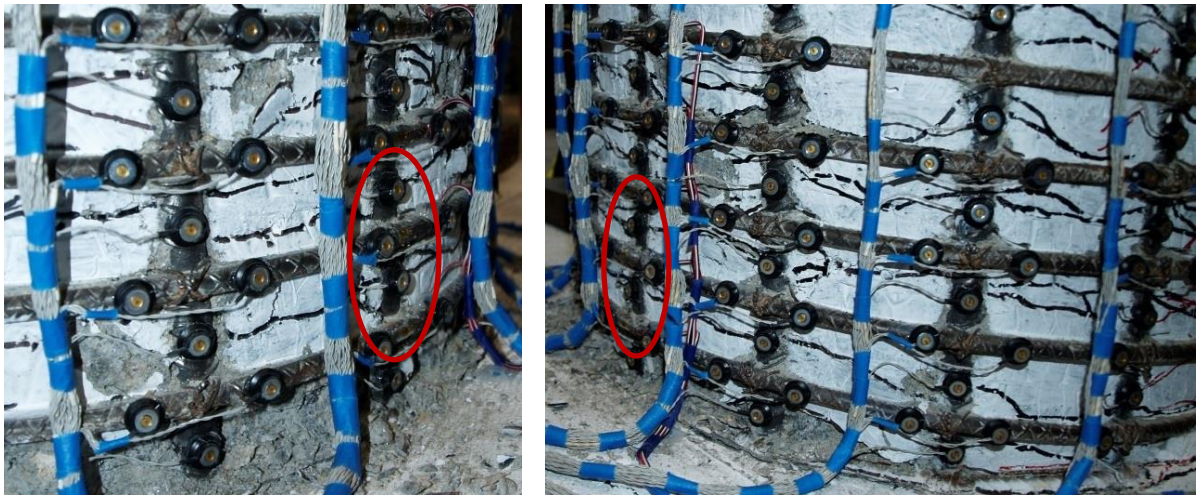

Figure 1.744 T26 – Slight Visible Buckling of Bar N3 during ($\mu_5^{-2} = -4.99$")

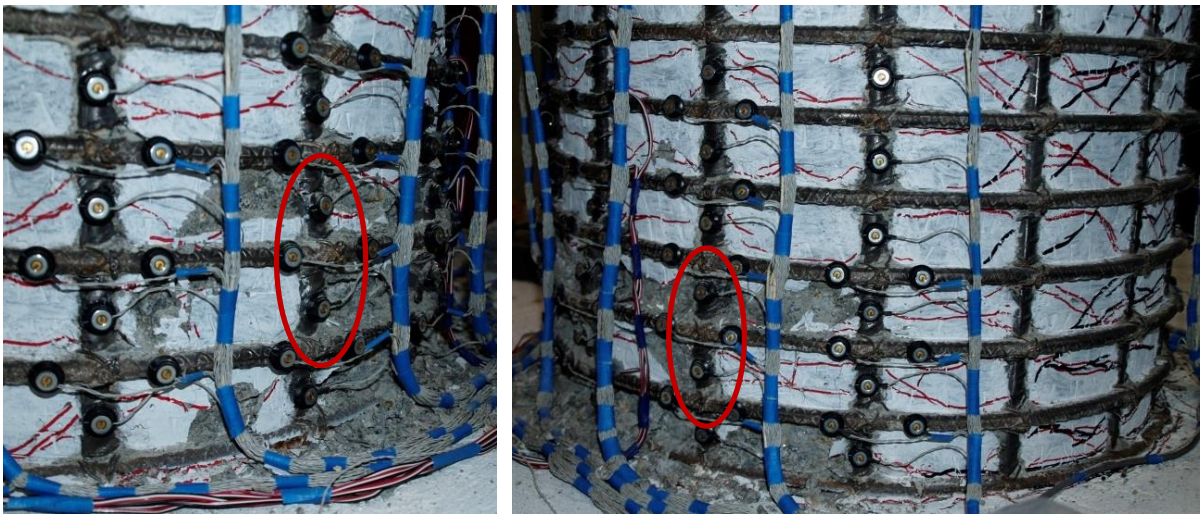

Figure 1.745 T26 – Buckling of Adjacent South Bars S2 and S4 during ($\mu_5^{+3} = 4.97$")

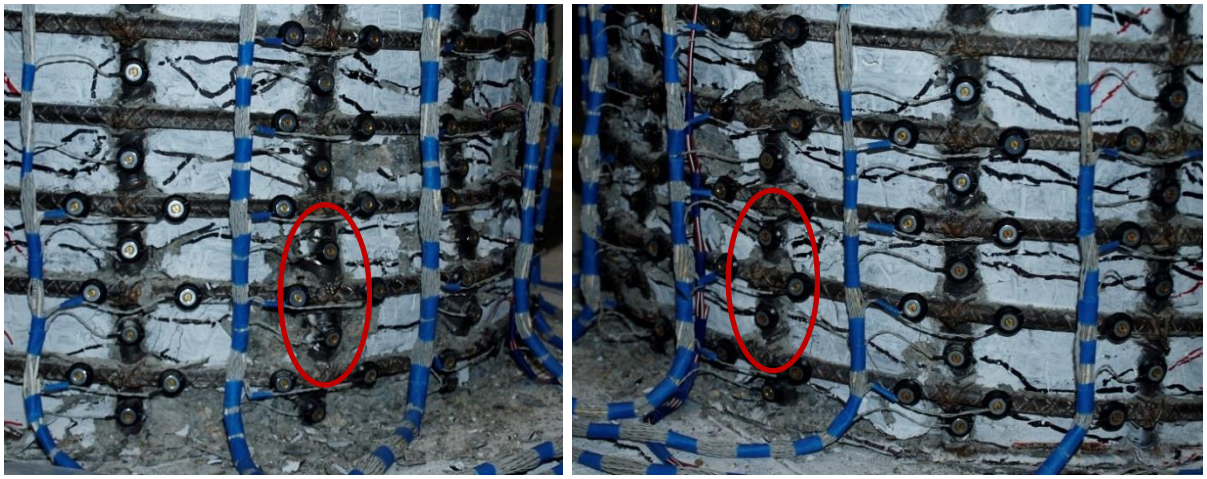

Figure 1.746 T26 – Buckling of North Bars N4 and N2 during ($\mu_6^{-1} = -5.97$")

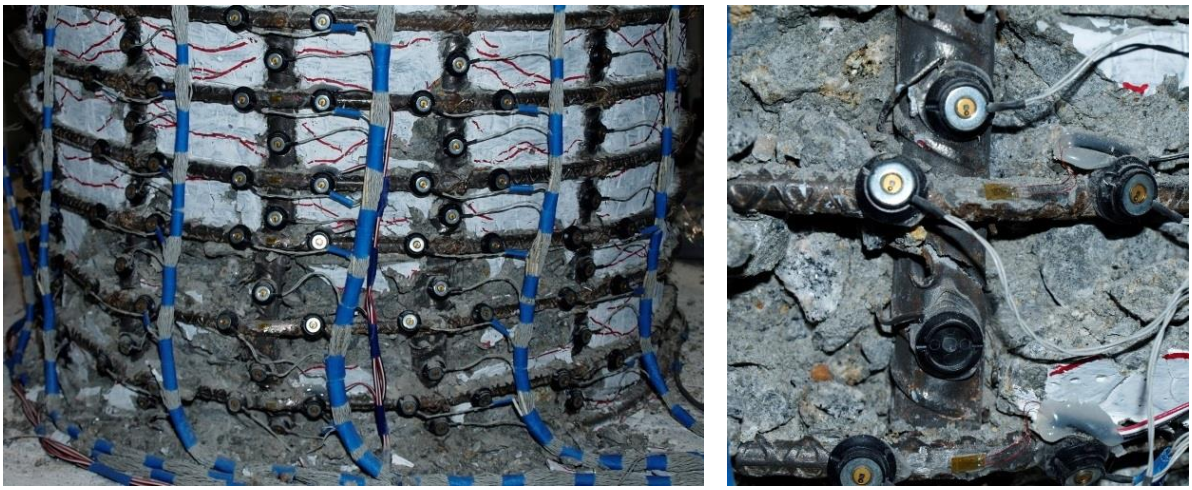

Figure 1.747 T26 – (Left) South Side of the Specimen during ($\mu_6^{+2} = 5.97$"), (Right) Fracture of Previously Buckled Bar S3 during ($\mu_6^{-2} = 5.98$")

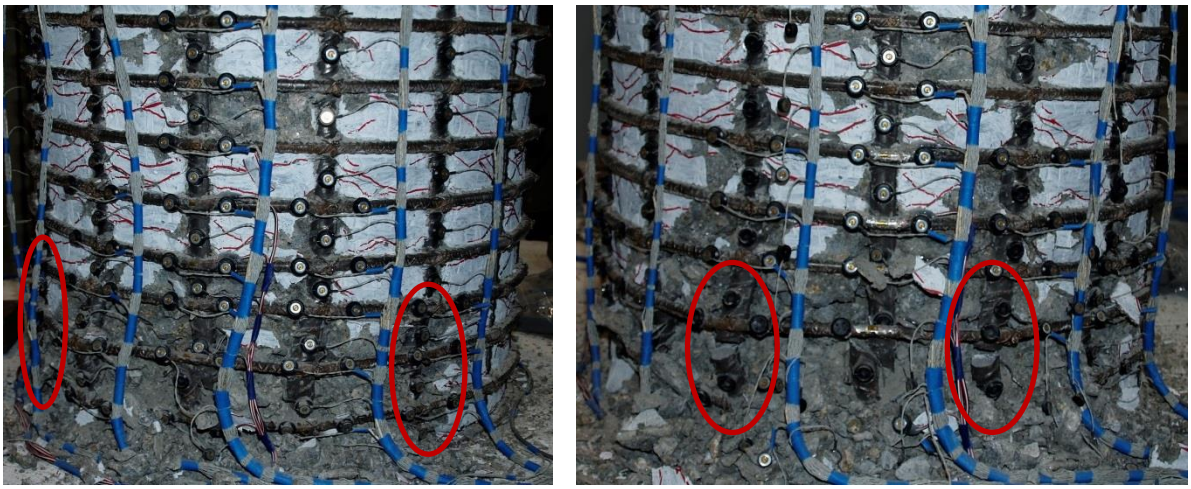

Figure 1.748 T26 – (Left) Buckling of South Bars S1 and S5 during ($\mu_6^{+3} = 5.97$"), (Right) Fracture of Previously Buckled South Bars S2 and S4 during ($\mu_6^{-3} = -5.99$")

Figure 1.749 T26 – (Left) Fracture of Previously Buckled Bars N3 and N4 during ($\mu_6^{+4} = 5.97$"), Front (Middle) and Back (Right) After the Test

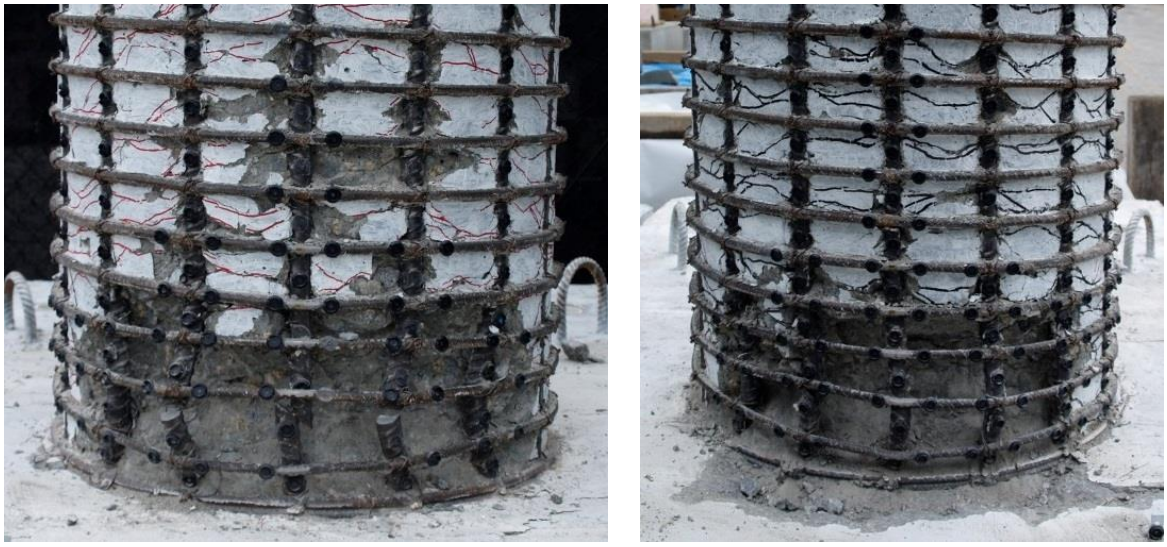

Figure 1.750 T26 – After the Test (Left) South Side and (Right) North Side

Test 26 – 24" Dia. with 2.1% Steel and 10% Axial Load – Strain Data Analysis

North Reinforcement

Vertical strain profiles for the north extreme fiber bar N3, which is placed into tension during push cycles, appear in the right half of Figure 1.751. This figure shows both extreme fiber bars on the same graph to illustrate the effects of tension shift. Compression strains are concentrated near the footing-column interface while tension strains are spread higher above the footing following the inclined flexural-shear crack distribution. Compressive vertical strain profiles for north extreme fiber bar N3 during pull cycles appear in the left half of Figure 1.752. A peak tensile strain of 0.0319 was measured 6.00" above the footing on bar N3 during ($\mu_5^{+1} = 4.98"$), before the bar visibly buckled during ($\mu_5^{-2} = -4.97"$). The relationship between strain and displacement for this gage length appears in Figure 1.756. Moment-curvature analysis with the PCK (2007) Lp Hinge Method begins to over predict the measured tensile strains at an increasing rate beyond displacement ductility two. A compressive strain of –0.0089 was measured 2.24" above the footing on bar N3 during ($\mu_3^{-1} = -2.99"$), when the first spiral in the confinement region yielded. Measured spiral strains in six layers which overlaid the north extreme fiber bar appear in Figure 1.755. Spiral tensions trains increased during each successive pull cycle of displacement ductility four. The relationship between compressive strain and displacement, for the gage length 6.00" above the footing on bar N3, appears in Figure 1.757. The measured compressive strains match the moment-curvature prediction with the PCK (2007) Lp Hinge Method through displacement ductility four. A peak compressive strain of -0.0164 was measured 6.00" above the footing on bar N3 during ($\mu_5^{-1} = -4.98"$).

Strain hysteresis for gage lengths 4.16" and 5.45" above the footing on bar N3 appear in Figure 1.760 and Figure 1.761. Both remained stable until the point of visible bar buckling during ($\mu_5^{-2} = -4.97"$). Tensile strain in the second spiral layer above the footing, which overlaid the outward deformed region of bar N3, spiked during visible bar buckling, Figure 1.762. The figure contains spiral data obtained from a strain gage and an Optotrak gage

length, Figure 1.727. The Optotrak strains were calculated using arc-lengths obtained from measured 3D distance chord lengths and the known outside diameter of the spiral. It is important to note that arc-length calculations become inaccurate once severe yielding in the spiral leads to the reinforcement straightening out to the left and right of the localized yielding directly over the bar where the strain gage is located. The distribution of arc-strains measured around the circumference of the first spiral layer above the footing appears in Figure 1.769. This first spiral layer only encompassed the north region of the column which was under compression during pull cycles. The middle of the section corresponds to zero along the circumference, and negative values wrap around the north side of the specimen. Specifically, measured-arc strains which overlay the three north extreme fiber bars N2, N3, and N4 are shown with vertical dashed lines. The distribution of measured spiral strains for the second and third layers above the footing on the north side appear in Figure 1.771 and Figure 1.773. Inelastic spiral strains were concentrated in the first two spiral layers above the footing in the region between bars N2, N3, and N4.

South Reinforcement

Vertical strain profiles for the south extreme fiber bar S3, which is placed into tension during pull cycles, appear in the right half of Figure 1.752. Compressive vertical strain profiles for south extreme fiber bar S3 during push cycles appear in the left half of Figure 1.751. The compressive vertical strain profiles for bars S2, S3, and S4 had a similar shape for the first three gage lengths above the footing, Figure 1.753. Their measured compressive strains appear to be influenced by measurable deformation which occurred after yielding of the spiral reinforcement. A diagram which shows the location and effect of measurable deformation appears in Figure 1.763. The first and third gage lengths above the footing had increased compression while the gage length had additional tension during pull cycles. This behavior is observable in the measured strain hysteresis 1.96” (Figure 1.764), 3.98” (Figure 1.765), and 5.89” (Figure 1.766) above the footing. As a comparison, the gage length 9.96” above the footing on bar S3, Figure 1.767, appears to be unaffected by measurable deformation.

A peak tension strain of 0.0318 was measured 3.98" above the footing on bar S3 during ($\mu_5^{-1} = -4.98"$). Visible buckling was observed during the previous push cycle, but it is expected that the bar straightened out and produced reliable strains at ($\mu_5^{-1} = -4.98"$). The peak tension strain before bar buckling of 0.0244 was measured 9.96" above the footing on bar S3 during ($\mu_4^{-1} = -3.98"$). The relationship between tension strain and displacement for the gage length 9.96" above the footing appears in Figure 1.758. Moment-curvature analysis with the PCK (2007) Lp Hinge Method begins to over predict the measured tension strains during displacement ductility three. A compressive strain of -0.0121 was measured 1.96" above the footing during ($\mu_3^{-1} = -2.99"$) when first spiral layer in the south confinement region yielded. The peak compression strain of -0.0273, measured 5.88" above the footing on bar S3, is unreliable due to measured deformation. The relationship between compressive strain and displacement for this gage length appears in Figure 1.759. The measurable deformation led to compressive strains which significantly exceed the moment-curvature prediction with the PCK (2007) Lp Hinge Method.

Measured strains in six spiral layers which overlaid the south extreme fiber bar appear in Figure 1.754 for push cycles. Cycles during displacement ductility four produced successively larger inelastic demands on the bottom three layers of spiral reinforcement. Strain gage and Optotrak strain hysteresis for the spiral layer 4.03" above the footing appear in Figure 1.768. The two measurement methods match well until the strain gage debonded during the third push cycle of displacement ductility four. The spiral strains spiked during ($\mu_5^{+1} = 4.98"$) when visible bar buckling was observed, Figure 1.743. Measured arc-strains around the circumference of spirals on the south side of the specimen during push cycles appear in Figure 1.770 and Figure 1.772. Inelastic spiral strains were localized over bars S2, S3, and S4.

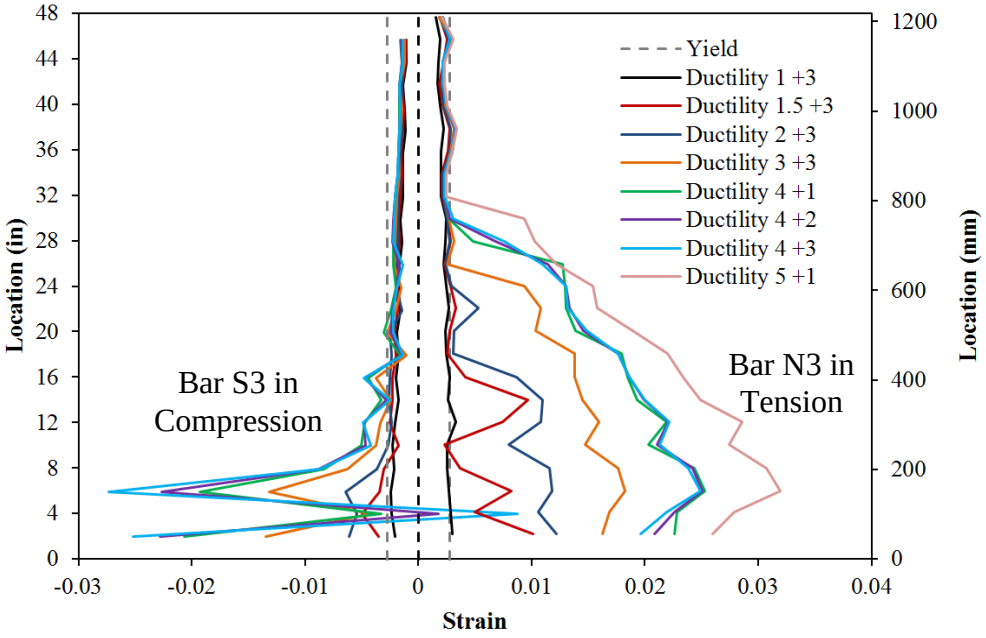

Figure 1.751 T26 – Extreme Fiber Bar Vertical Strain Profiles during Push Cycles

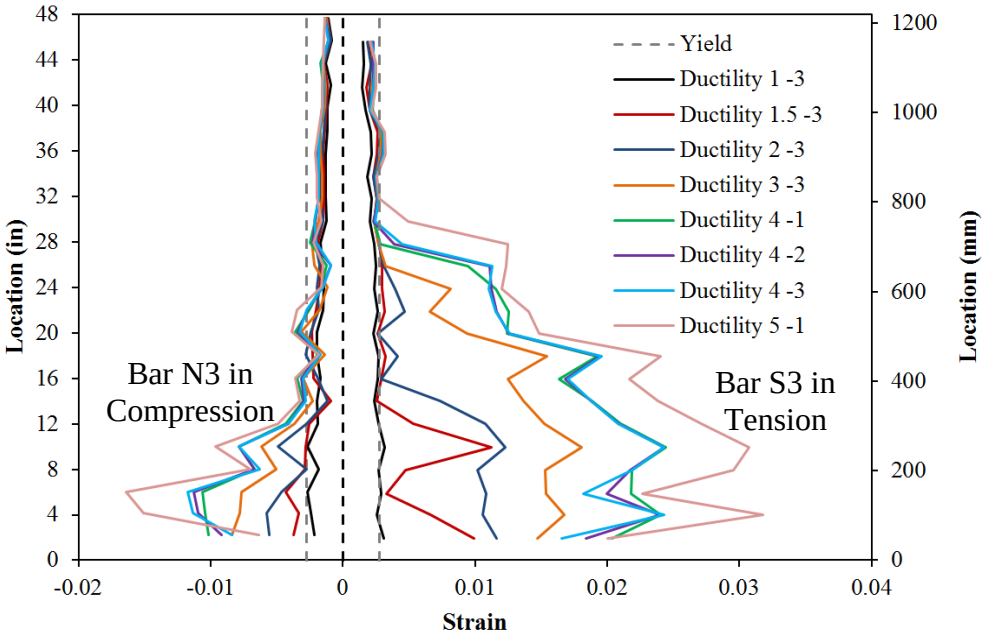

Figure 1.752 T26 – Extreme Fiber Bar Vertical Strain Profiles during Pull Cycles

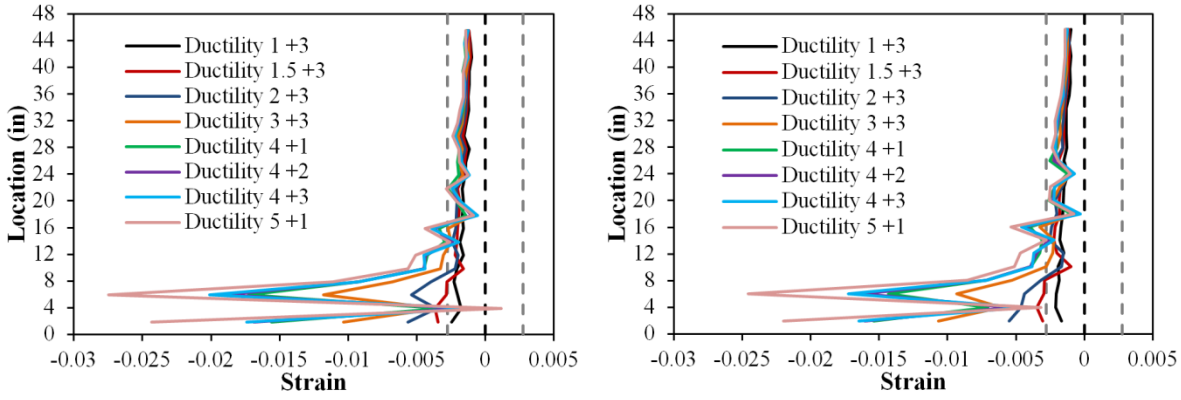

Figure 1.753 T26 – Similar Compressive Strain Profiles Observed in Adjacent South Bars S4 (Left) and S2 (Right)

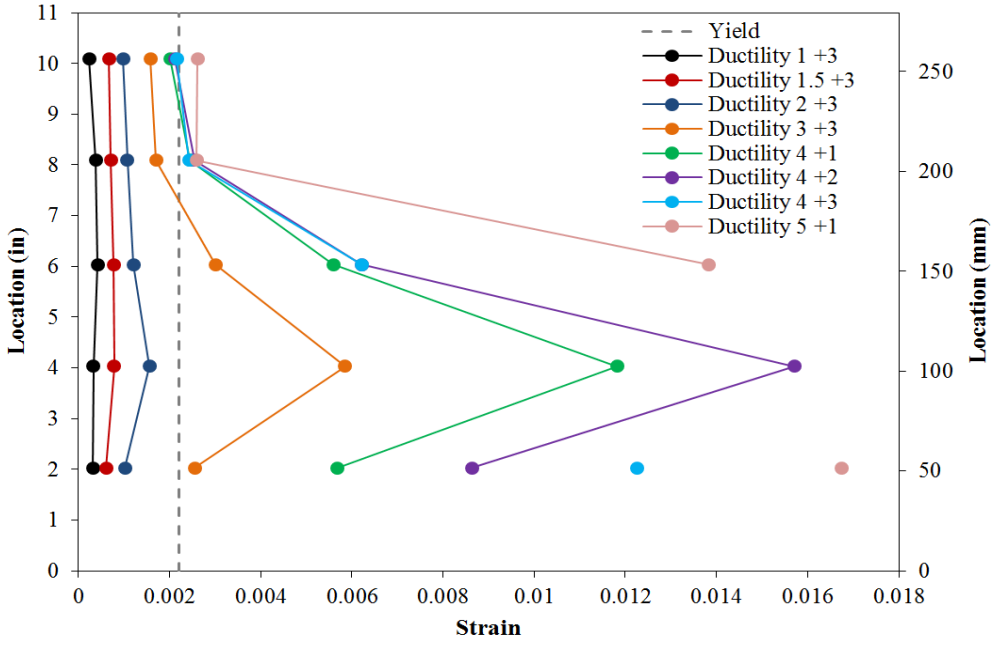

Figure 1.754 T26 – Spiral Strains on the South Side during Push Cycles

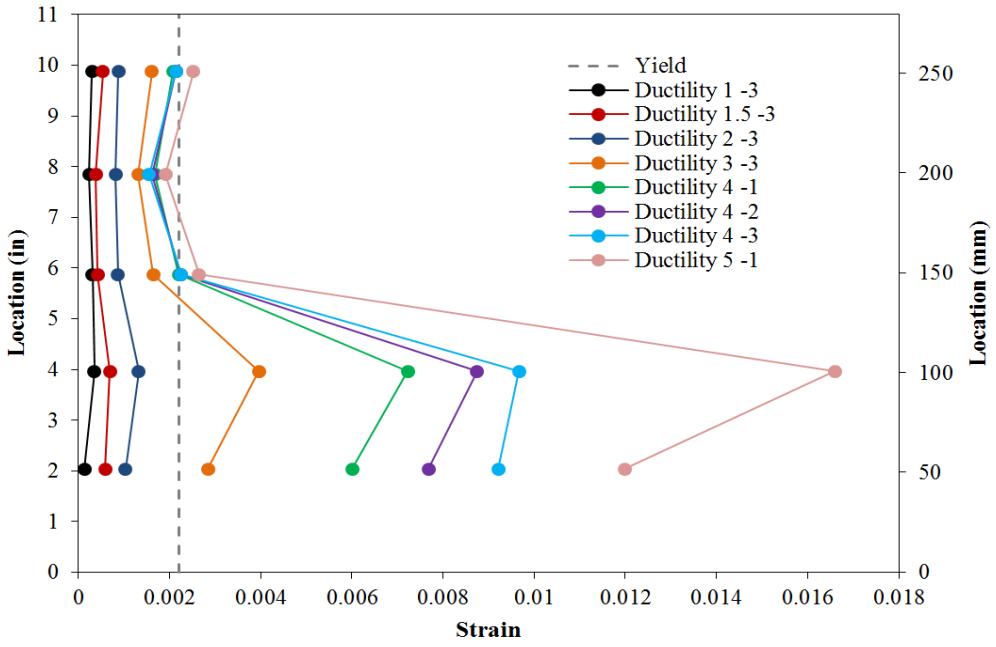

Figure 1.755 T26 – Spiral Strains on the North Side during Pull Cycles

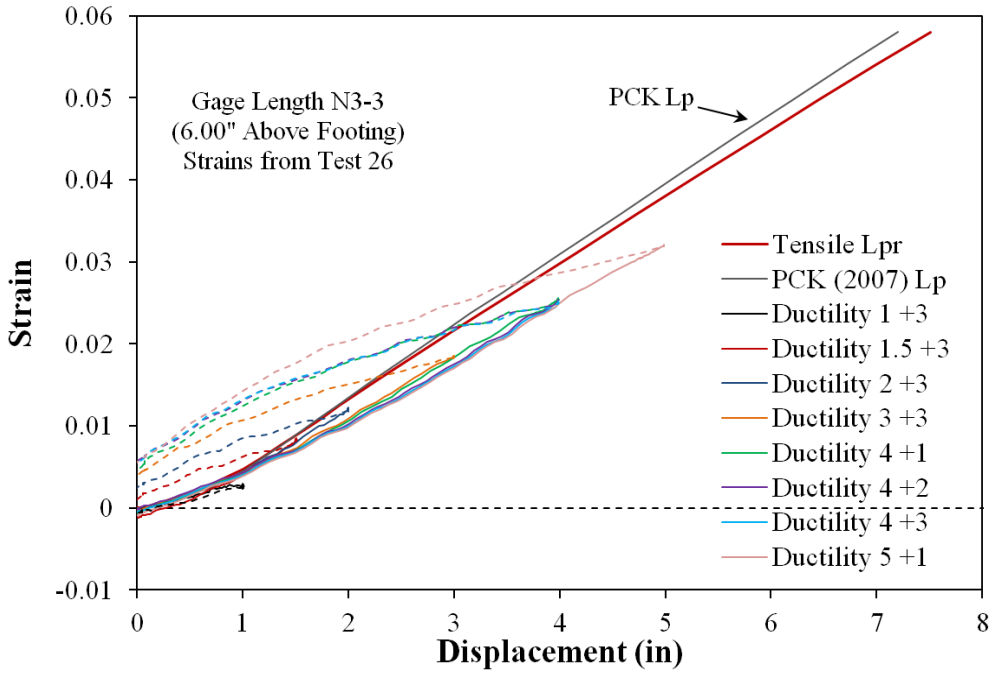

Figure 1.756 T26 – Tensile Strain-Displacement for Bar N3 during Push Cycles

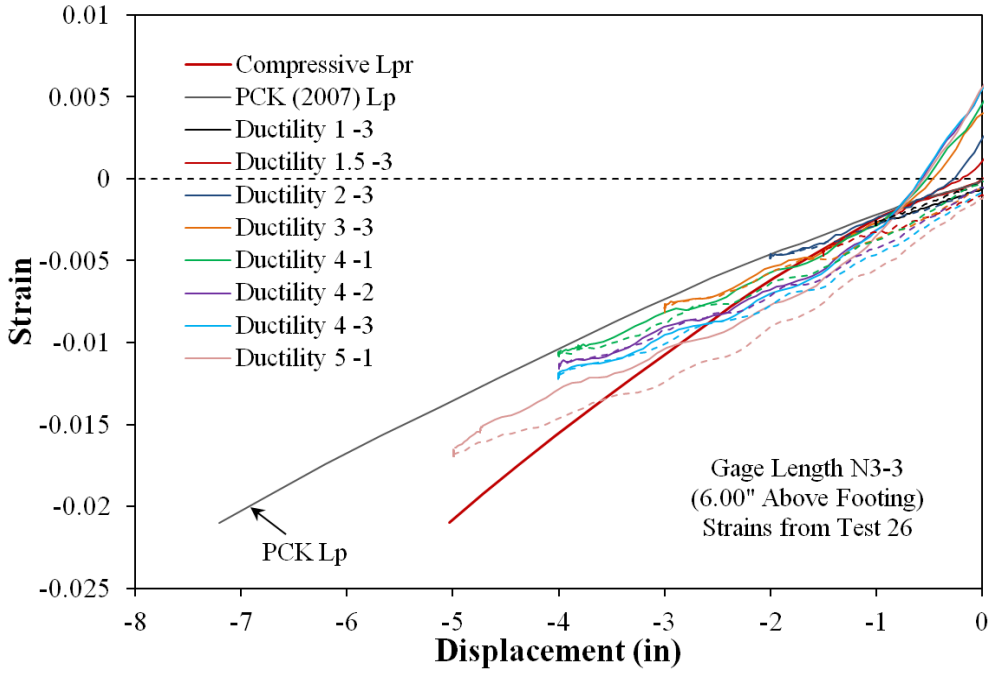

Figure 1.757 T26 – Compressive Strain-Displacement for Bar N3 during Pull Cycles

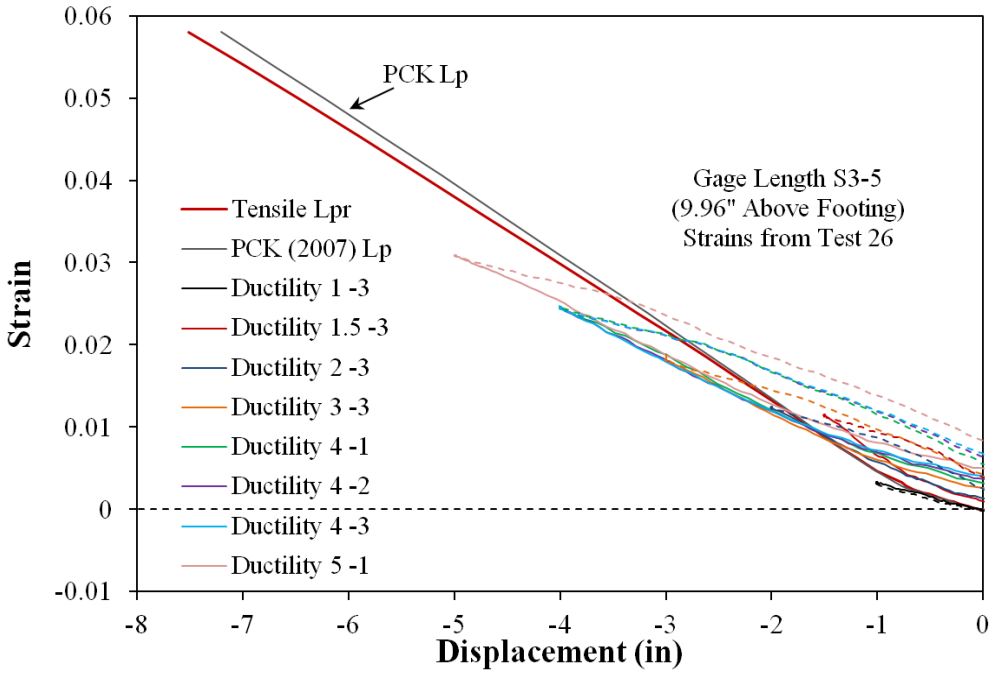

Figure 1.758 T26 – Tensile Strain-Displacement for Bar S3 during Pull Cycles

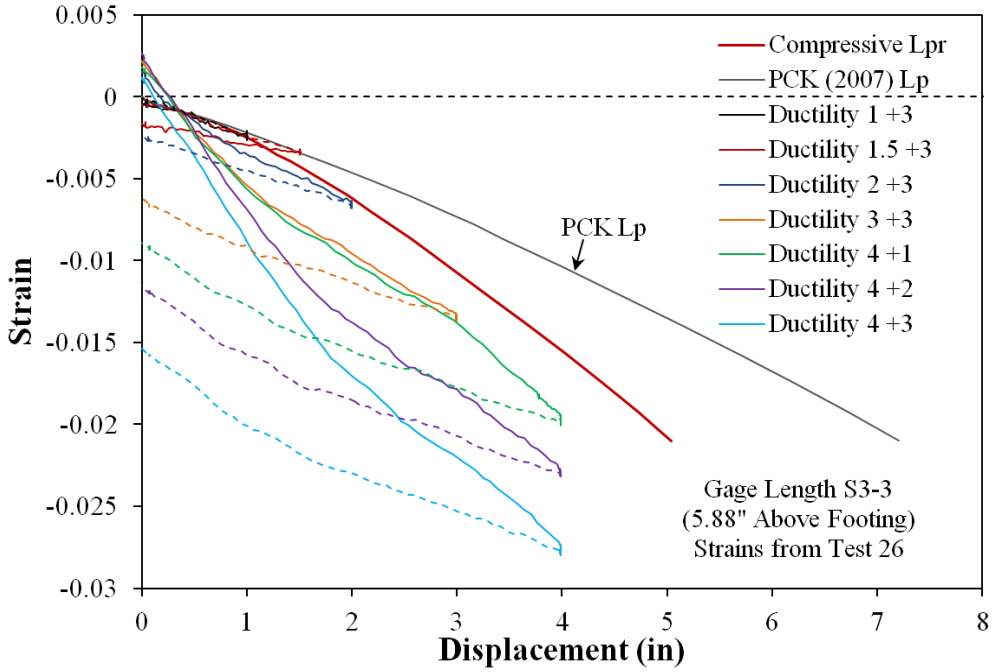

Figure 1.759 T26 – Compressive Strain-Displacement for Bar S3 during Push Cycles

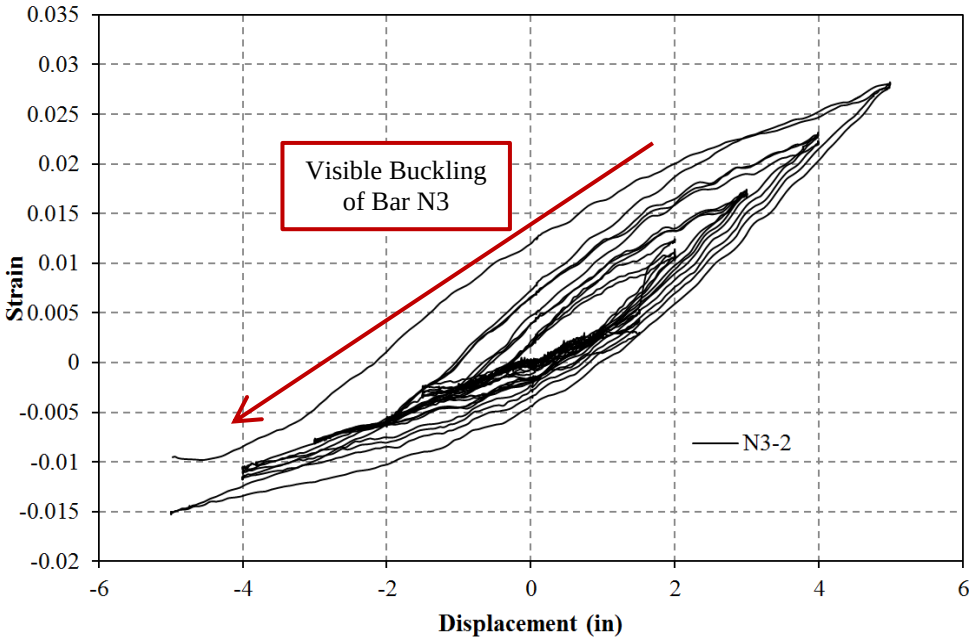

Figure 1.760 T26 – Bar N3 Strain Hysteresis to Buckling (4.16" Above Footing)

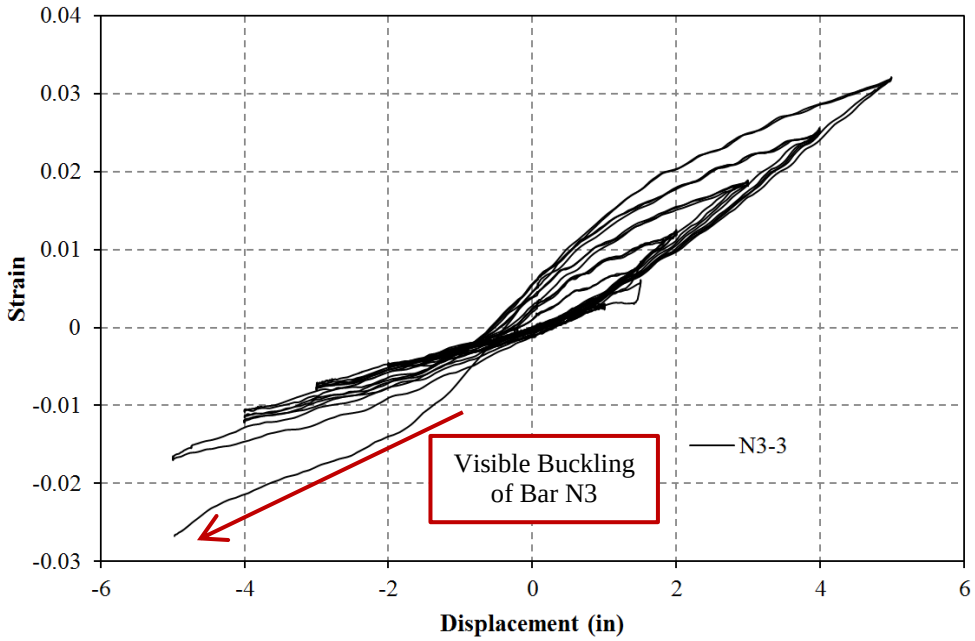

Figure 1.761 T26 – Bar N3 Strain Hysteresis to Buckling (5.45" Above Footing)

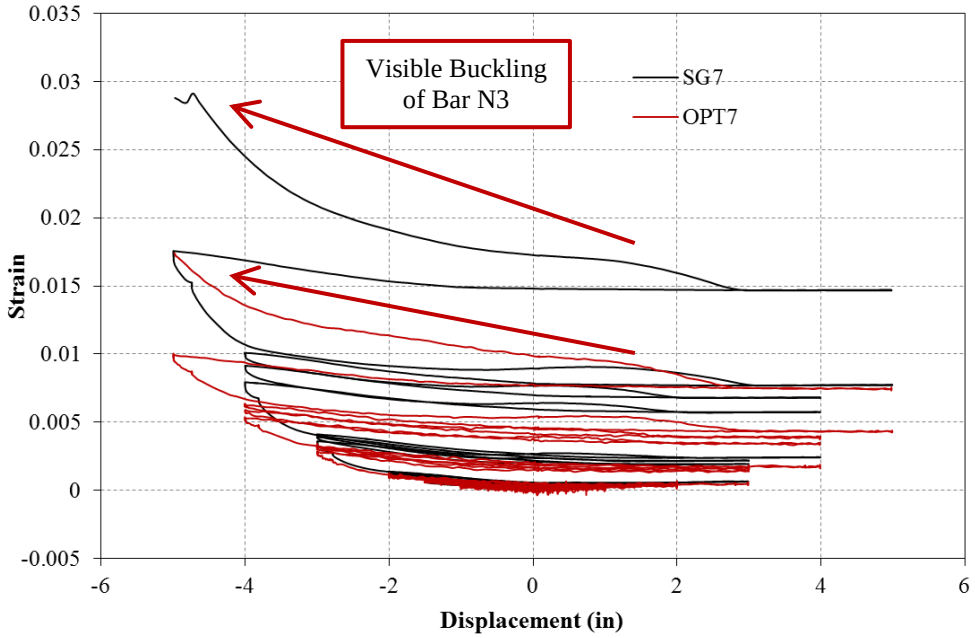

Figure 1.762 T26 – Spiral Strain Hysteresis over North Buckled Region (3.97" Above)

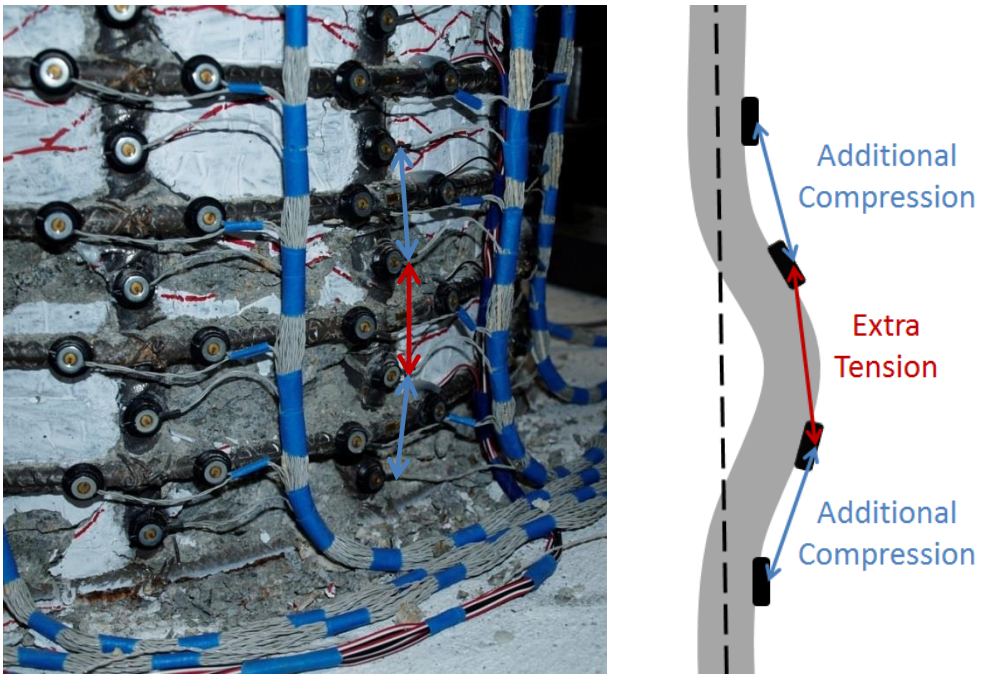

Figure 1.763 T26 – Locations of Measurable Deformation before Visible Buckling

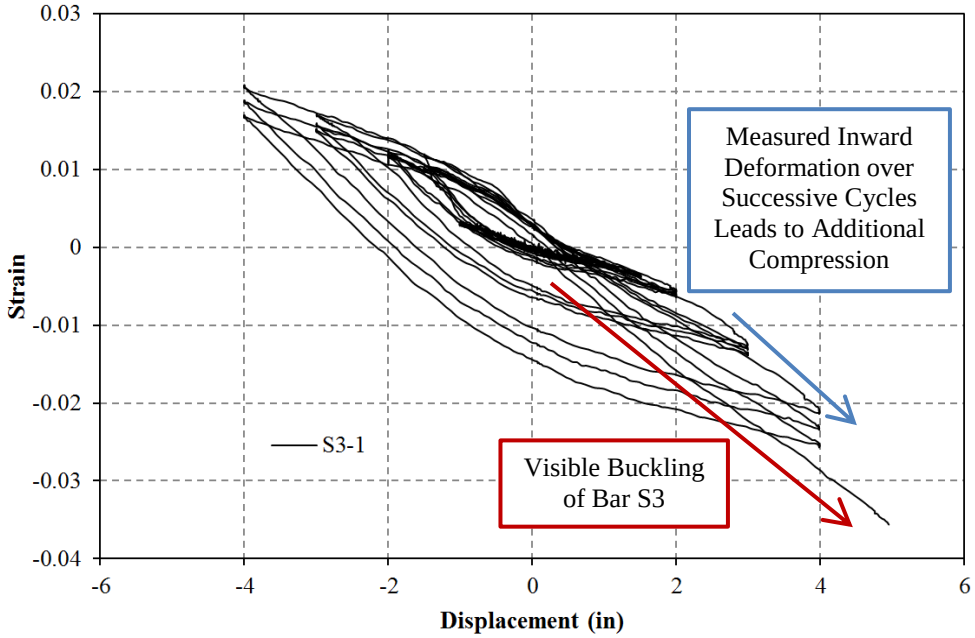

Figure 1.764 T26 – Bar S3 Strain Hysteresis to Buckling (1.96" Above Footing)

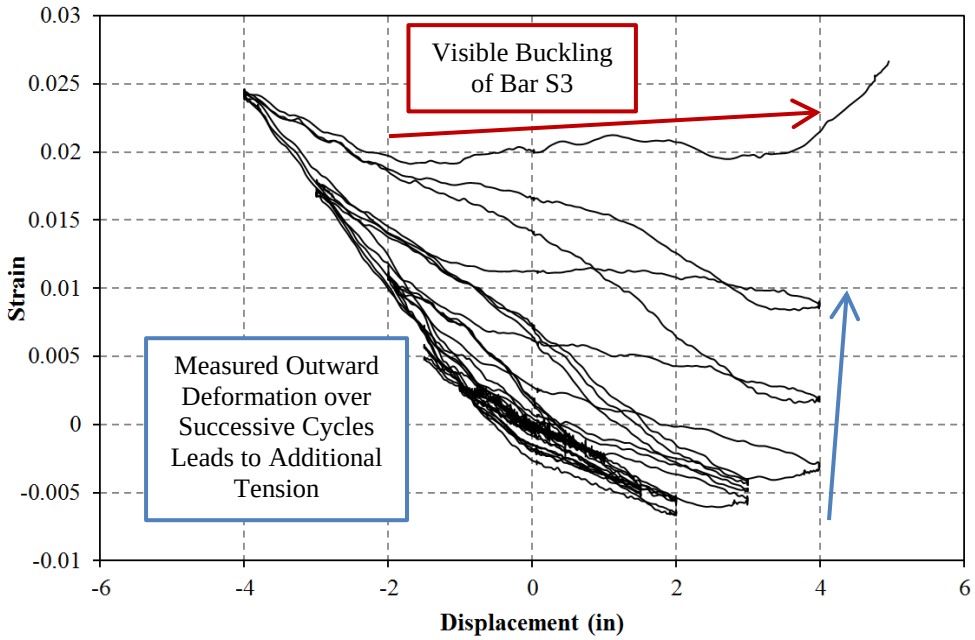

Figure 1.765 T26 – Bar S3 Strain Hysteresis to Buckling (3.98" Above Footing)

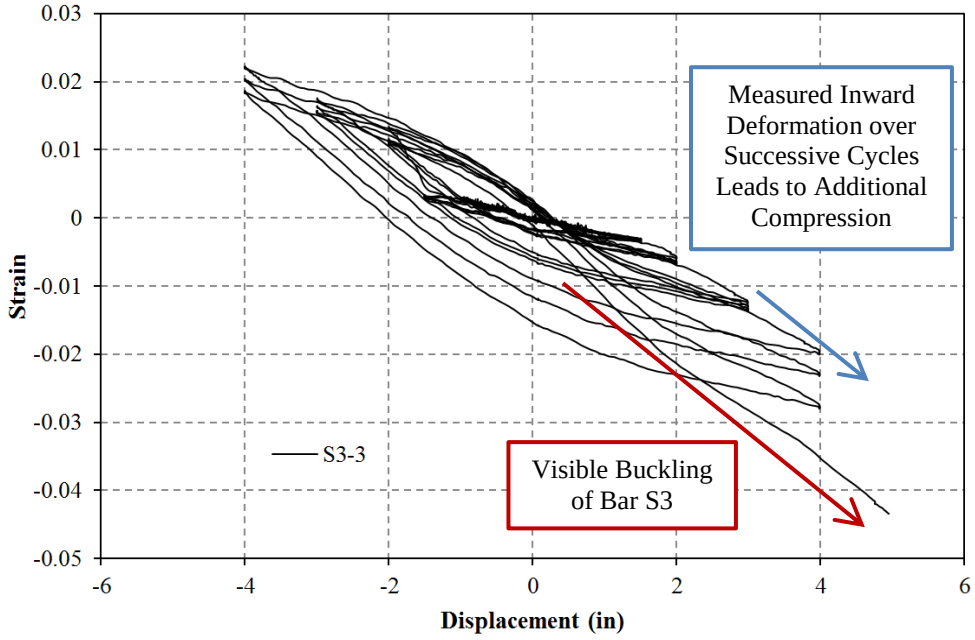

Figure 1.766 T26 – Bar S3 Strain Hysteresis to Buckling (5.89" Above Footing)

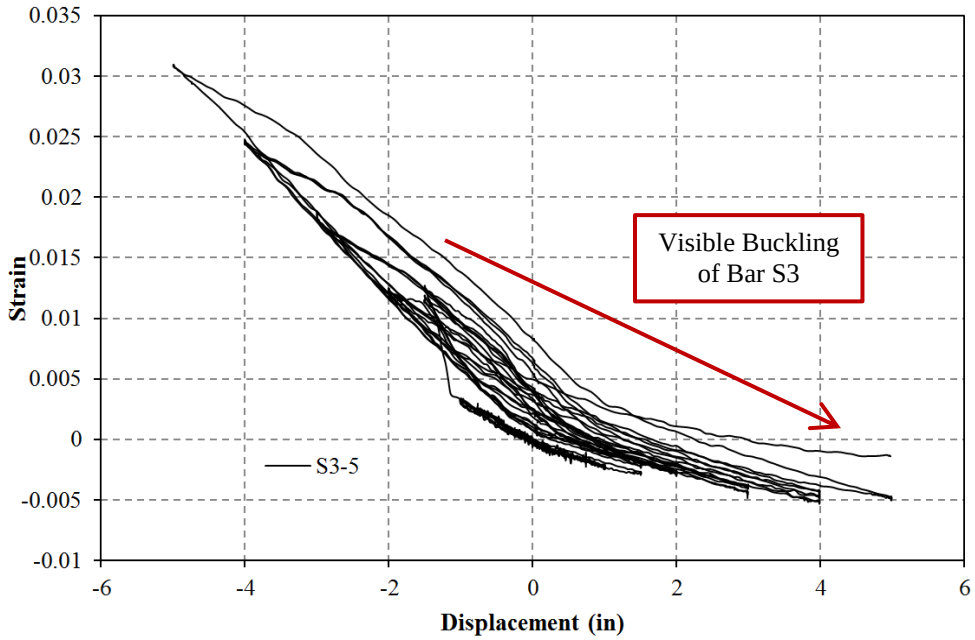

Figure 1.767 T26 – Bar S3 Strain Hysteresis to Buckling (9.96" Above Footing)

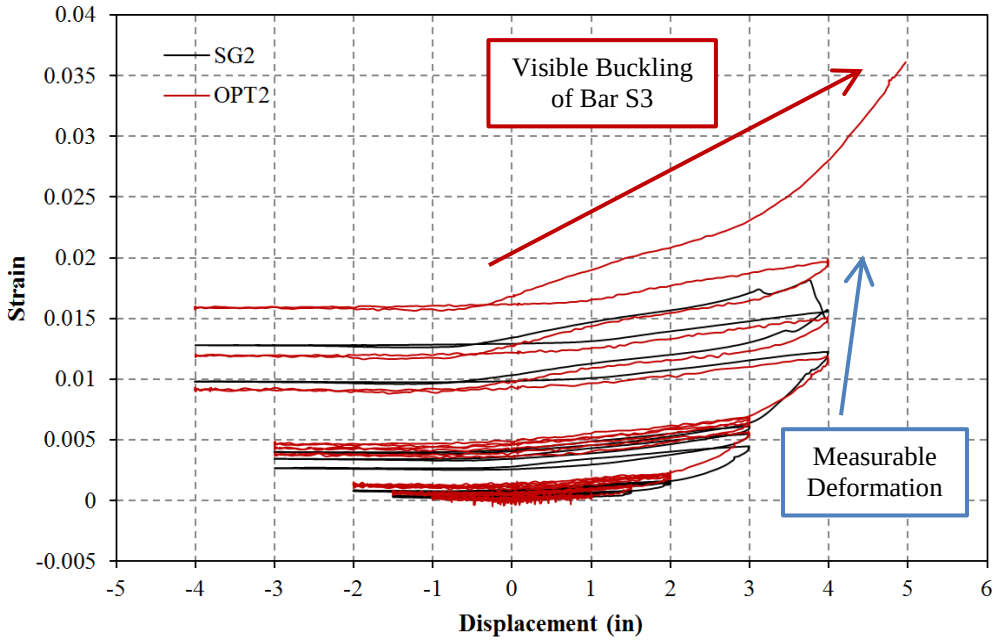

Figure 1.768 T26 – Spiral Strain Hysteresis over South Buckled Region (4.03" Above)

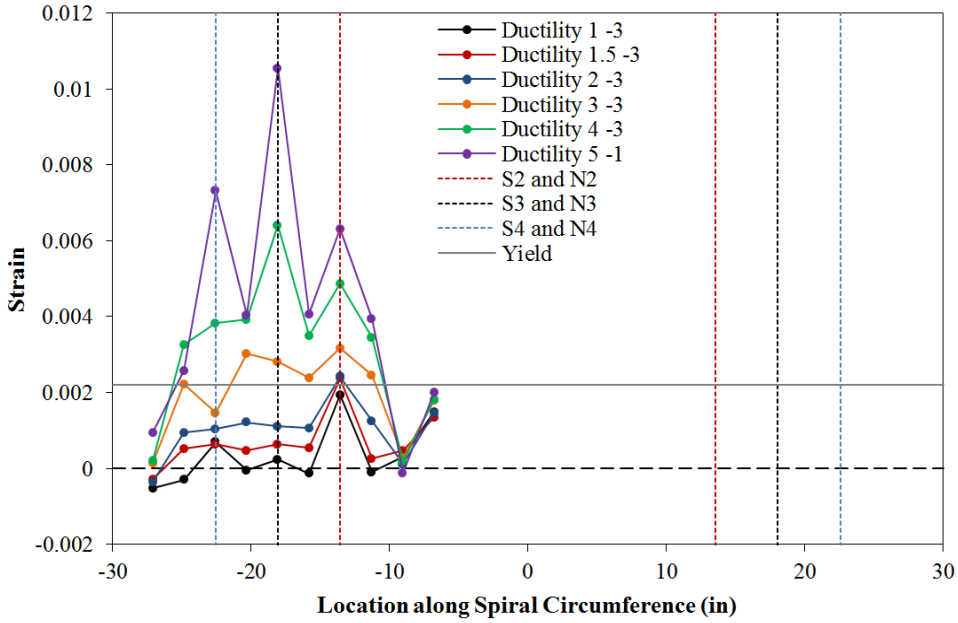

Figure 1.769 T26 – Spiral Strain Distribution for the 1nd Spiral above the Footing during Pull Cycles (Negative Location = North)

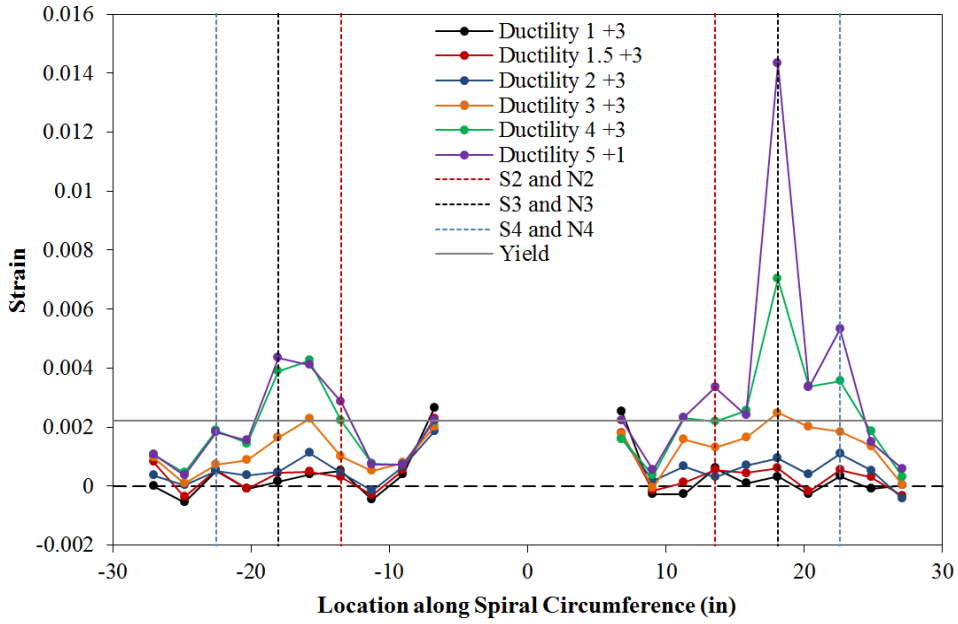

Figure 1.770 T26 – (2nd Spiral Layer North and 1st Spiral Layer South) above the Footing during Push Cycles (Positive = South)

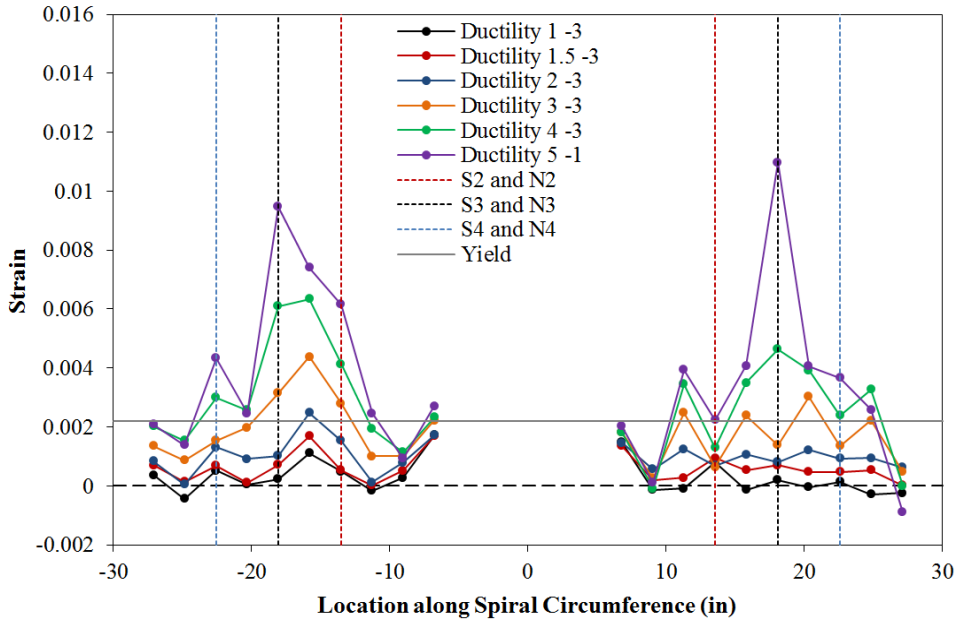

Figure 1.771 T26 – (2nd Spiral Layer North and 1st Spiral Layer South) above the Footing during Pull Cycles (Negative = North)

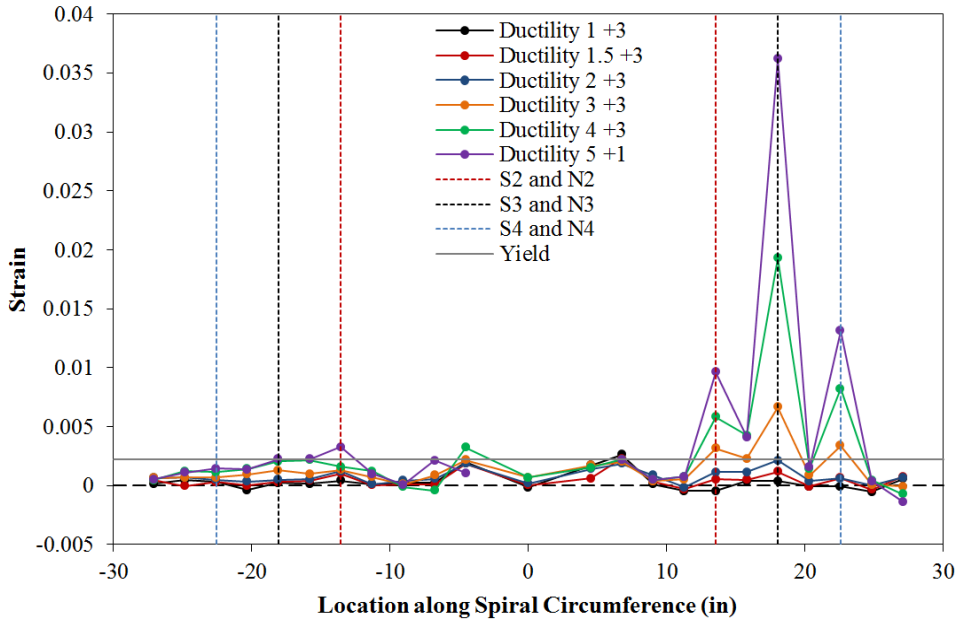

Figure 1.772 T26 – (3rd Spiral Layer North and 2nd Spiral Layer South) above the Footing during Push Cycles (Positive = South)

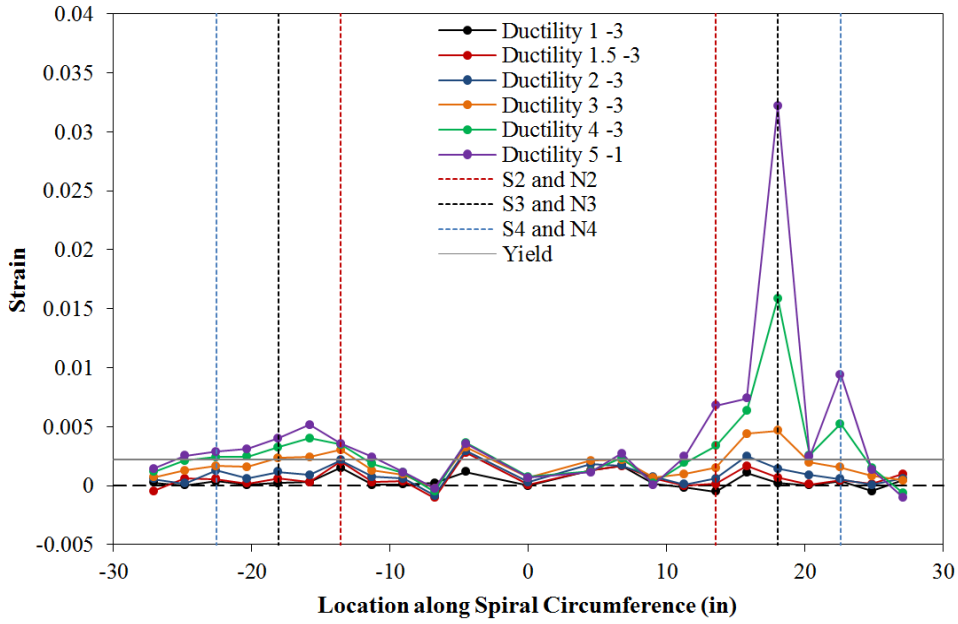

Figure 1.773 T26 – (3rd Spiral Layer North and 2nd Spiral Layer South) above the Footing during Pull Cycles (Negative = North)

Test 26 – Curvature and Strain Penetration Data

Cross section strain profiles for the fourth horizontal section above the footing appear in Figure 1.774 and Figure 1.775 for push and pull cycles respectively. The plane section hypothesis fits the measured strain data well for this section since it lies above the region which was influence by measurable deformation on the south side of the specimen. The curvature is calculated as the slope of the least squared line connecting strains measured in twelve instrumented reinforcing bars in the cross section, Figure 1.727. If the curvatures for many horizontal cross sections are analyzed, curvature profiles for the plastic hinge region can be constructed; Figure 1.776 and Figure 1.777 for push and pull cycles respectively. Measured curvatures during displacement ductility one closely match the elastic curvature profile, which linearly decreases from yield curvature at the footing-column interface to zero at the center of the applied lateral load.

Plastic curvatures were found to follow a linear distribution. Linear least squared error plastic curvature lines were fit to the plastic portion of the measured curvature profiles. The extrapolation of this linear curvature line with the footing-column interface was taken as the base section curvature, since LEDs are incapable of measuring strains in this region. As the base section curvature ductility increased, the height at which the linear plastic curvature distribution intersected the elastic curvature profile also increased. This measured spread of plasticity as a function of base section curvature ductility is plotted in Figure 1.781 with circular data points.

Curvature profiles describe the elastic and plastic flexural displacements of the column, but do not address fixed-end rotations which result from development of longitudinal reinforcement into the footing. The measured vertical displacements of Optotrak LEDs placed closest to the footing column interface can be used to quantify this fixed-end rotation, Figure 1.778 and Figure 1.779. The fixed-end rotation is taken as the slope of the least squared error line fit to the bond slip profile. The strain penetration displacement is obtained by multiplying this rotation by the cantilever height of the column. If an elastic curvature profile assumption is made for curvatures higher than those measured with instrumentation, then the entire curvature profile may be integrated to obtain the total column flexural displacement. This column flexural displacement was added to the strain penetration displacement, and compared to the experimentally measured displacements in Figure 1.780. The Optotrak integrated displacement matches well with those obtained from a string potentiometer placed at the center of the lateral load, which indicates that shear deformation are small.

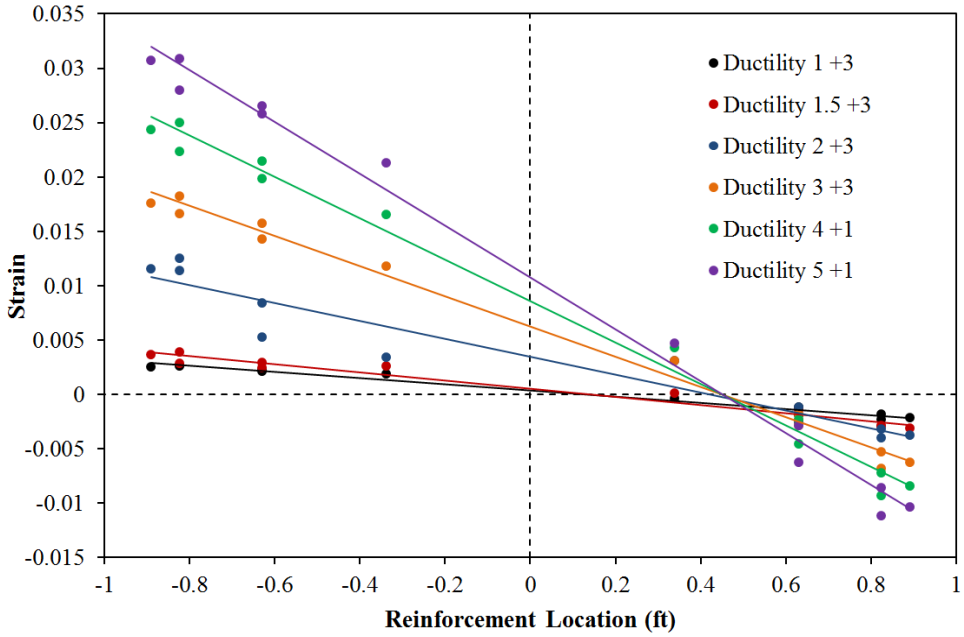

Figure 1.774 T26 – Push Cycle Cross Section Strain Profiles, 7.97" Above Footing

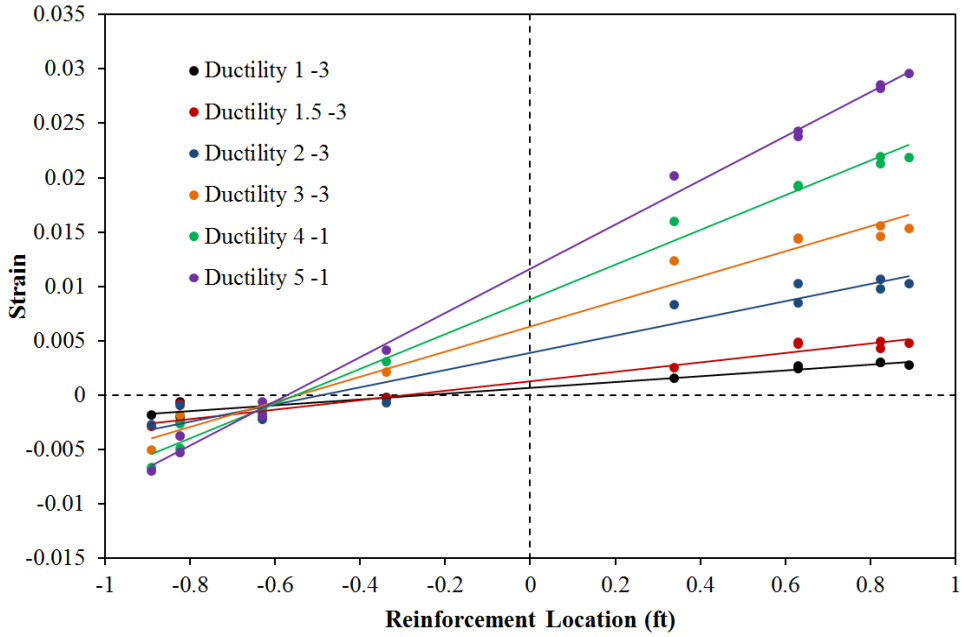

Figure 1.775 T26 – Pull Cycle Cross Section Strain Profiles, 7.97" Above Footing

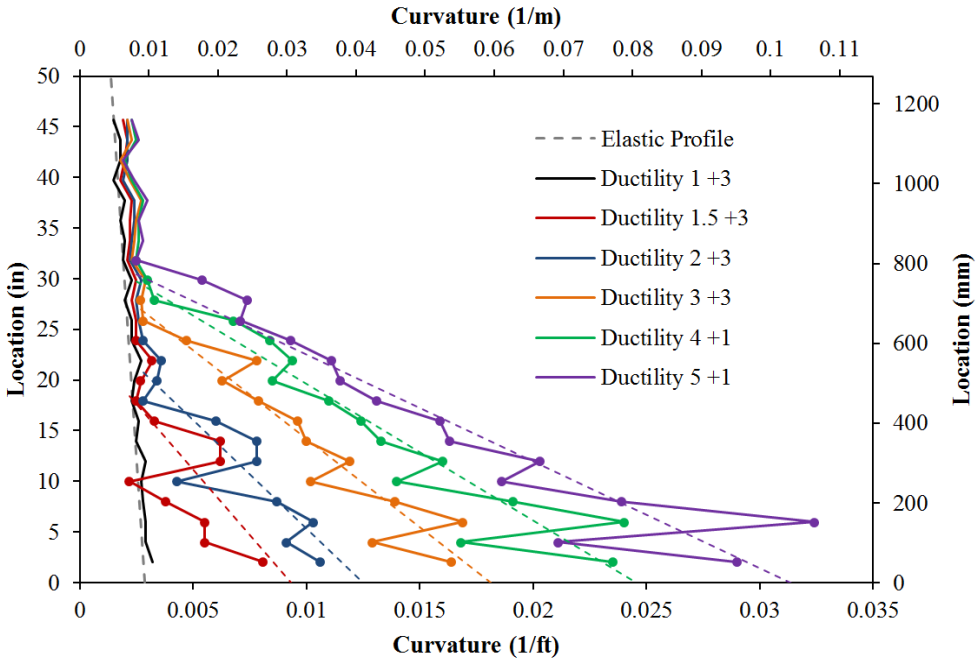

Figure 1.776 T26 – Push Cycle Curvature Profiles with Plastic Regression

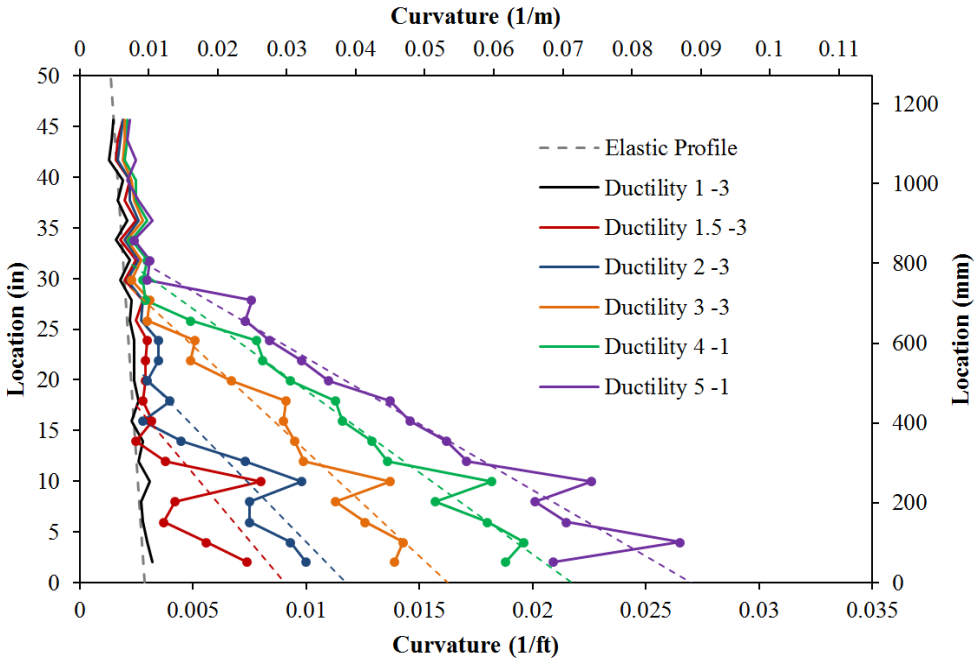

Figure 1.777 T26 – Pull Cycle Curvature Profiles with Plastic Regression

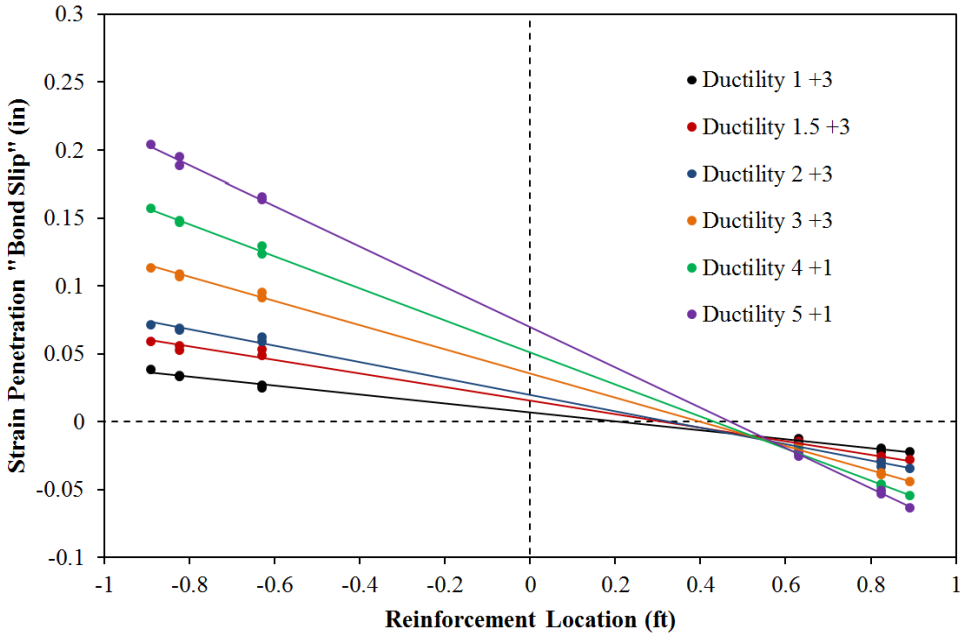

Figure 1.778 T26 – Fixed-End Rotation due to Strain Penetration during Push Cycles

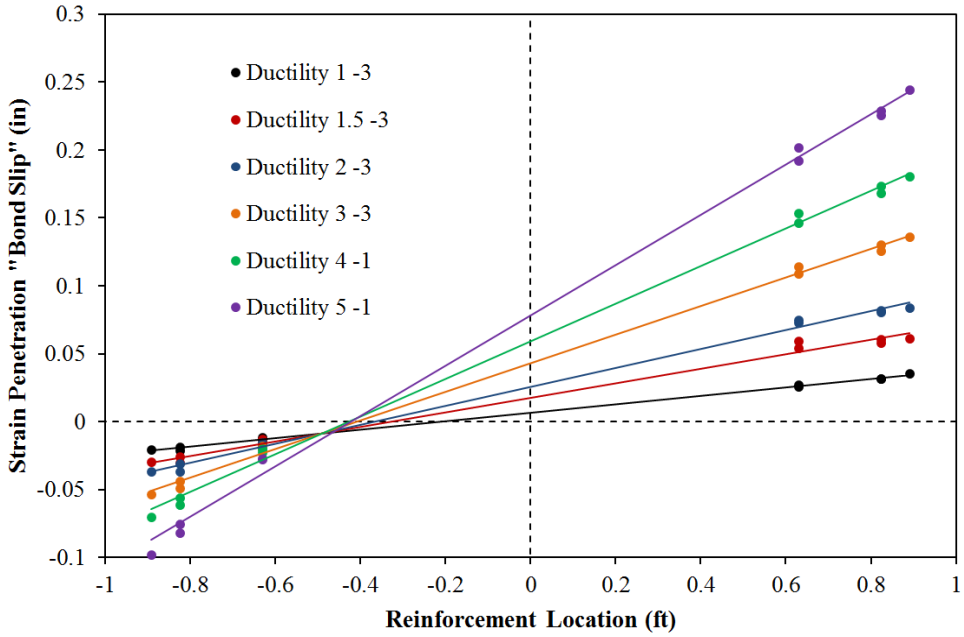

Figure 1.779 T26 – Fixed-End Rotation due to Strain Penetration during Pull Cycles

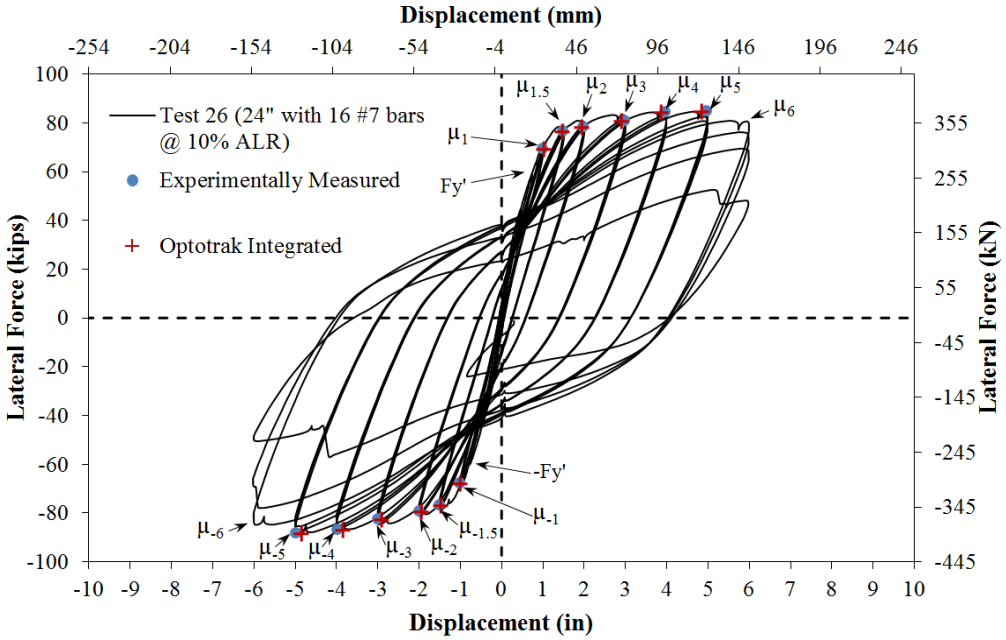

Figure 1.780 T26 – Comparison of Measured and Optotrak Integrated Displacements

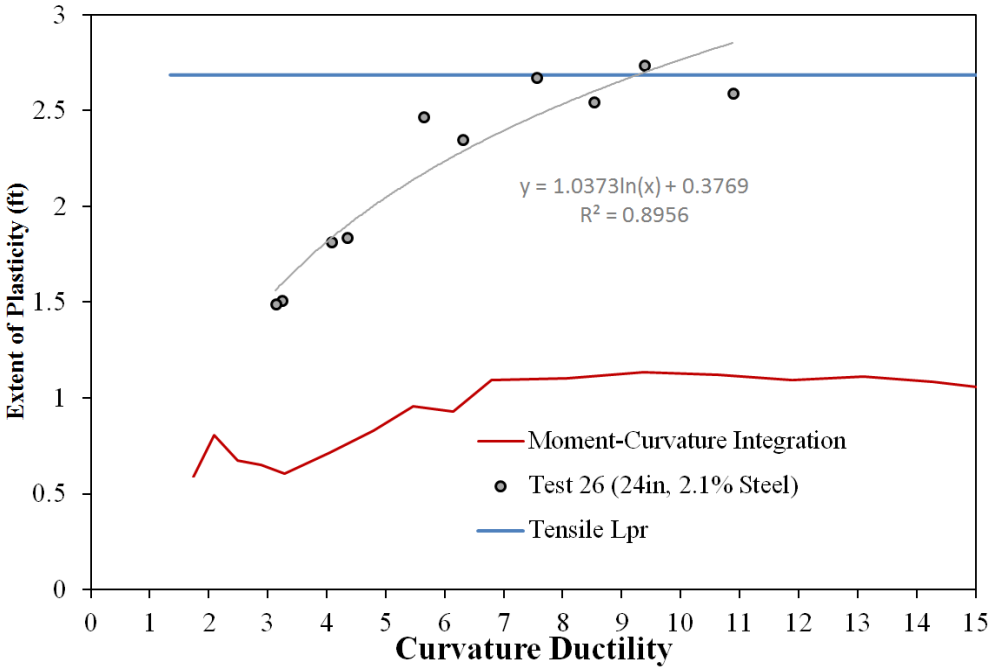

Figure 1.781 T26 – Measured Spread of Plasticity (Circular Data Points)

1.4.3 Test 27 – 24" Dia. Column with 1.6% Long. Steel and 10% Axial Load

Table 1.51 Observations for Test 27 – 24" Dia. With 1.6% Steel and 10% Axial Load

VALUES OF INTEREST:	
Concrete Compressive Strength:	$f_c' = 6149\ psi$
Axial Load:	$P = 255.5\ kips\ \ (P/(f_c' A_g) = 10\%)$
Longitudinal Steel Content:	16 #6 $Bars\ \ (A_{st}/A_g = 1.6\%)$
Analytical First Yield Force:	$F_y' = 50.53\ kips$
Experimental First Yield Displacement:	$\Delta_y' = 0.70"$
Analytical Nominal Moment Capacity:	$M_n = 531.72\ kip * ft$
Equivalent Yield Displacement:	$\Delta_y = 0.92"$
Maximum Lateral Force:	$70.19\ kips$
DAMAGE OBSERVATIONS:	
First Cracking North:	$1/2Fy' = 0.20"$
First Cracking South:	$-1/2Fy' = -0.21"$
Cover Concrete Crushing North:	$\mu_{1.5}^{-1} = -1.38"$
Cover Concrete Crushing South:	$\mu_{1.5}^{+2} = 1.38"$
Transverse Steel Yield North:	At $-2.77"$ during pull to $\mu_3^{-1} = -2.76"$
Transverse Steel Yield South:	At $2.76"$ during push to $\mu_3^{+1} = 2.76"$
Longitudinal Bar Buckling North:	Reversal from $\mu_5^{+1} = 4.60"$
Longitudinal Bar Buckling South:	Reversal from $\mu_4^{-3} = -3.67"$
Longitudinal Bar Fracture North:	At $1.37"$ during push to $\mu_6^{+3} = 5.53"$
Longitudinal Bar Fracture South:	At $-4.94"$ during pull to $\mu_6^{-2} = -5.53"$

*$\mu_5^{+1} = 4.60"$ represents the first push cycle of displacement ductility five

Table 1.52 Strain Data Summary for Test 27 – 24" Dia. with 1.6% Steel and 10% Axial

MATERIAL STRAINS:	
Cover Concrete Crushing North:	$\varepsilon_s = 0.0036\ (compression)$
Cover Concrete Crushing South:	$\varepsilon_s = 0.0038\ (compression)$
Transverse Steel Yield North:	$\varepsilon_s = 0.0168\ (compression)$
Transverse Steel Yield South:	$\varepsilon_s = 0.0124\ (compression)$
Longitudinal Bar Buckling North:	$\varepsilon_s = 0.036\ (peak\ tension\ prior\ to\ bb)$
	$\varepsilon_s = 0.032\ (peak\ comp.\ prior\ to\ bb)$
Longitudinal Bar Buckling South:	$\varepsilon_s = 0.024\ (peak\ tension\ prior\ to\ bb)$
	$\varepsilon_s = 0.023\ (peak\ comp.\ prior\ to\ bb)$
Mander (1988) Ultimate Concrete Compression Strain, $\varepsilon_{cu} = 0.0163$	

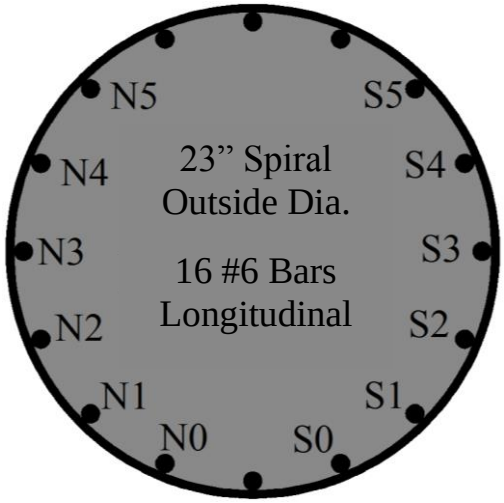

Figure 1.782 T27 – Test Setup and Cross Section Bar Designation

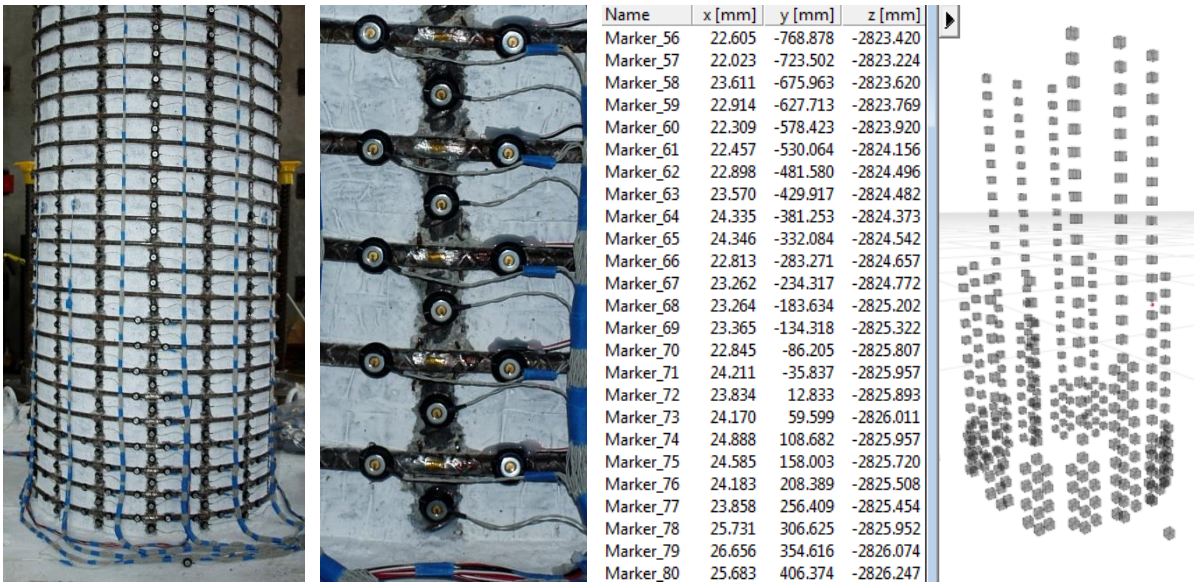

Name	x [mm]	y [mm]	z [mm]
Marker_56	22.605	-768.878	-2823.420
Marker_57	22.023	-723.502	-2823.224
Marker_58	23.611	-675.963	-2823.620
Marker_59	22.914	-627.713	-2823.769
Marker_60	22.309	-578.423	-2823.920
Marker_61	22.457	-530.064	-2824.156
Marker_62	22.898	-481.580	-2824.496
Marker_63	23.570	-429.917	-2824.482
Marker_64	24.335	-381.253	-2824.373
Marker_65	24.346	-332.084	-2824.542
Marker_66	22.813	-283.271	-2824.657
Marker_67	23.262	-234.317	-2824.772
Marker_68	23.264	-183.634	-2825.202
Marker_69	23.365	-134.318	-2825.322
Marker_70	22.845	-86.205	-2825.807
Marker_71	24.211	-35.837	-2825.957
Marker_72	23.834	12.833	-2825.893
Marker_73	24.170	59.599	-2826.011
Marker_74	24.888	108.682	-2825.957
Marker_75	24.585	158.003	-2825.720
Marker_76	24.183	208.389	-2825.508
Marker_77	23.858	256.409	-2825.454
Marker_78	25.731	306.625	-2825.952
Marker_79	26.656	354.616	-2826.074
Marker_80	25.683	406.374	-2826.247

Figure 1.783 T27 – Target Marker Application and Optotrak Spatial Output

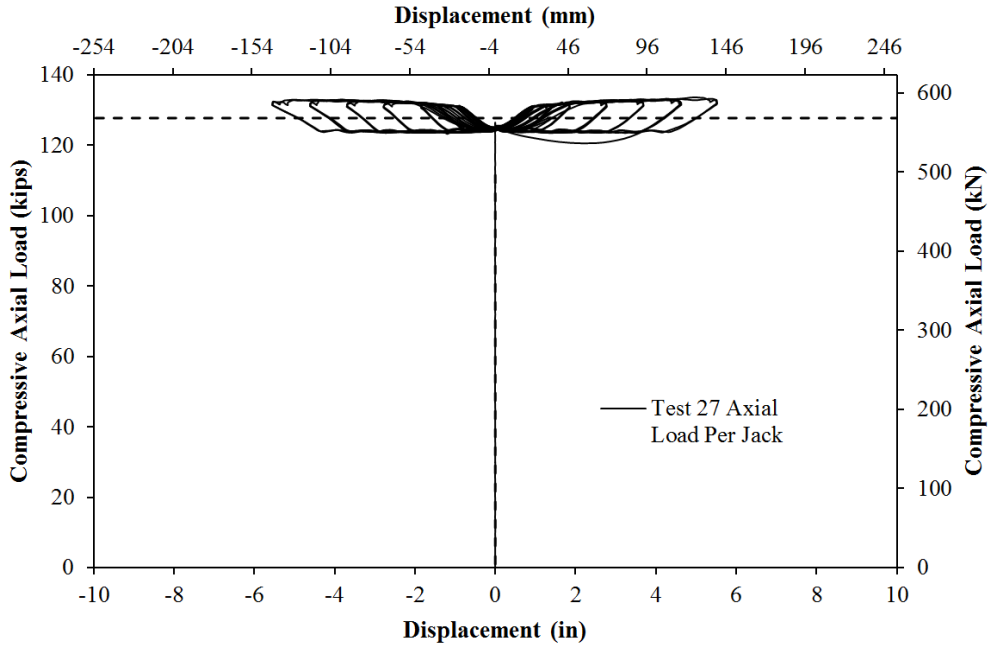

Figure 1.784 T27 – Compressive Axial Load from One Jack (Total = 2*Value)

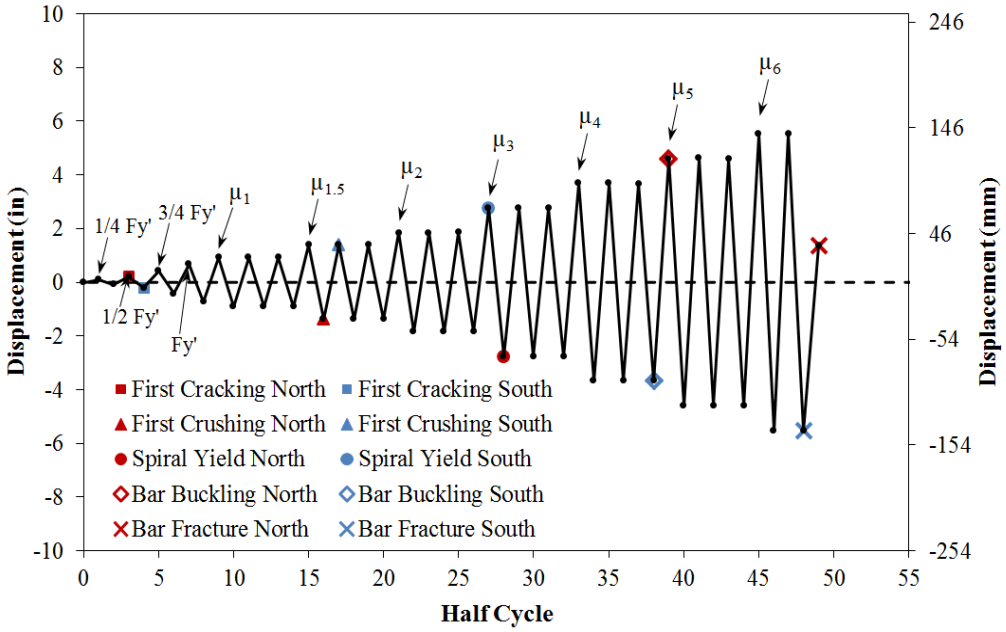

Figure 1.785 T27 – Symmetric Three Cycle Set Load History

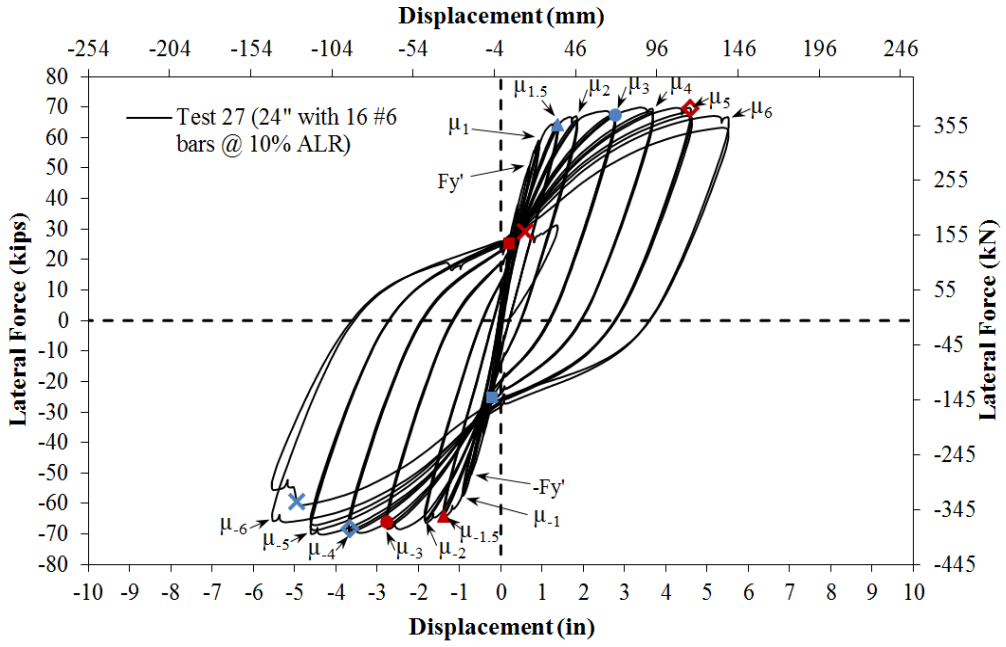

Figure 1.786 T27 – Lateral Force vs. Displacement Hysteretic Response

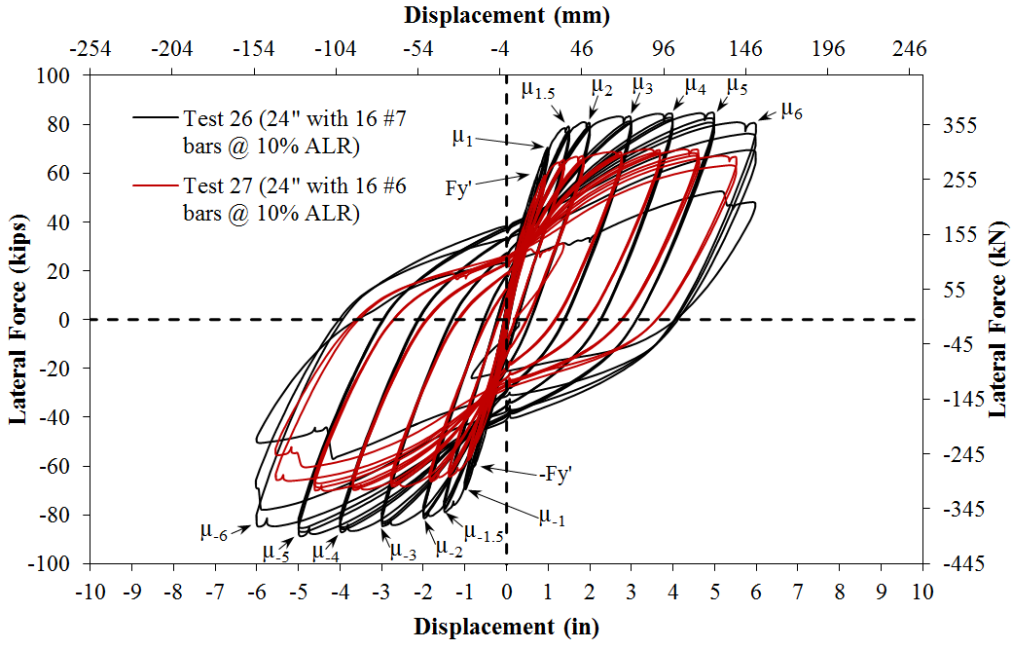

Figure 1.787 T27 – Hysteretic Comparison of T26 and T27 with Different Steel Content

Test 27 – 24" Dia. with 1.6% Steel and 10% Axial Load – Experimental Observations

Specimens 25-30 focus on the effects of longitudinal steel content, longitudinal bar diameter, and higher levels of axial load on column behavior. This report summarizes experimental observations and data analysis for column Test 27. The 24" diameter column contains 16 #6 (A706) bars for longitudinal reinforcement ($A_{st}/A_g = 1.6\%$) and a #3 A706 spiral at 2" on center ($4A_{sp}/(D's) = 1\%$). The specimen had an 8ft cantilever length ($L/D = 4$), and was subjected to ($P/(f_c'A_g) = 10\%$) axial load. The symmetric three-cycle-set load history is commonly used to evaluate the seismic performance of structural components. The load history begins with elastic cycles to the following increments of the analytically predicted first yield force: ¼ F_y', ½ F_y', ¾ F_y', and F_y'. The experimental first yield displacement is then determined by taking the average of the recorded displacements during the first yield push and pulls cycles. The equivalent yield displacement, used to determine

the displacement ductility levels ($\mu_{\Delta 1} = 1 * \Delta_y$), is then calculated as $\Delta_y = \Delta'_y(M_n/M'_y)$. The symmetric three-cycle-set load history resumes with three balanced cycles at each of the following displacement ductility levels: 1, 1.5, 2, 3, 4, 5, etc. The imposed displacement history and resulting hysteretic response appear in Figure 1.785 and Figure 1.786.

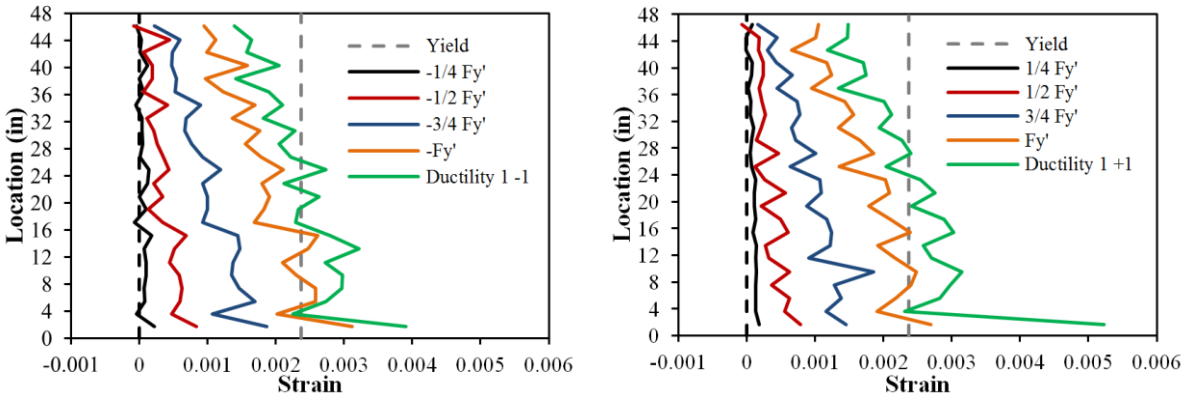

Figure 1.788 T27 – Strain Profiles before Yield, (Left) North and (Right) South

The test began with cycles in ¼ Fy' (first yield force) increments in each direction of loading until the first yield force was reached. The first cracks on the north and south sides of the specimen formed during ($1/2Fy' = 0.20$") and ($-1/2Fy' = -0.21$") respectively, Figure 1.789. The crack distribution on all sides of the specimen at first yield, ($Fy' = 0.68$") and ($-Fy' = -0.72$"), appears in Figure 1.790. Tensile vertical strain profiles for north and south reinforcing bars during elastic push and pull cycles appear in Figure 1.788. The average experimental first yield displacement was used to calculate the equivalent yield displacement, $\Delta_y = \Delta'_y(M_n/M'_y) = 0.92$", which defined the reversal amplitudes for reminder of the test.

The crack progression at displacement ductility 1, 1.5, 2, 3, and 4 appear in Figure 1.791, Figure 1.793, Figure 1.795, Figure 1.797, and Figure 1.799 respectively. During these cycles the cracks became more numerous and increased in inclination on the shear faces of the specimen. Small amounts concrete flaking was observed on the south and north sides of the specimen during ($\mu_{1.5}^{+2} = 1.38$") and ($\mu_{1.5}^{-1} = -1.38$"), Figure 1.792. In previous

tests, this flaking leads to crushing during subsequent cycles, but crushing was not observed until displacement ductility two. Crushing on the south and north sides of the specimen occurred during ($\mu_2^{+1} = 1.84$") and ($\mu_2^{-1} = -1.83$"), Figure 1.794. As compressive demands increased during displacement ductility 1.5 to 4, crushing gradually increased on each side of the specimen. Compressive demand during ($\mu_3^{+1} = 2.76$") and ($\mu_3^{-1} = -2.76$") lead to spiral yielding in confinement regions, Figure 1.796. Spiral strains on each side of the specimen increased during each successive cycle of ductility four, but the extreme fiber reinforcement remained visibly straight, Figure 1.798

The south extreme fiber bar visibly buckled during ($\mu_5^{+1} = 4.60$"), as shown in the left photo of Figure 1.800. The outward buckled region occurred over the second gage length above the footing which encompassed the second spiral layer. The buckled deformation increased during ($\mu_5^{+2} = 4.61$"), Figure 1.800. The north extreme fiber bar visibly buckled during the reversal from tension strains sustained during ($\mu_5^{+1} = 4.60$"), Figure 1.801. An adjacent north reinforcing bar N4 buckled during ($\mu_5^{-2} = -4.59$"), Figure 1.802. Previously buckled north reinforcement placed into tension during ($\mu_5^{+3} = 4.60$") straightened out, showing large amounts of permanent deformation in spirals overlaying the outward buckled region, Figure 1.802. An adjacent north bar N2 buckled during ($\mu_5^{-3} = 4.60$"), Figure 1.803. Two additional south reinforcing bars, S2 and S4, buckled during ($\mu_6^{+1} = 5.52$"), Figure 1.803 and Figure 1.804. Significant core concrete crushing behind three buckled north reinforcing occurred during ($\mu_6^{-1} = -5.54$"), Figure 1.804. The previously buckled extreme fiber south bar S3 ruptured during ($\mu_6^{-2} = -5.53$"), Figure 1.805, leading to a significant loss in strength. Two previously buckled north bars N3 and N4 ruptured before straightening out in tension during the third push cycle of ductility six, Figure 1.805. Photos of the specimen after the instrumentation was removed appear in Figure 1.806 and Figure 1.807.

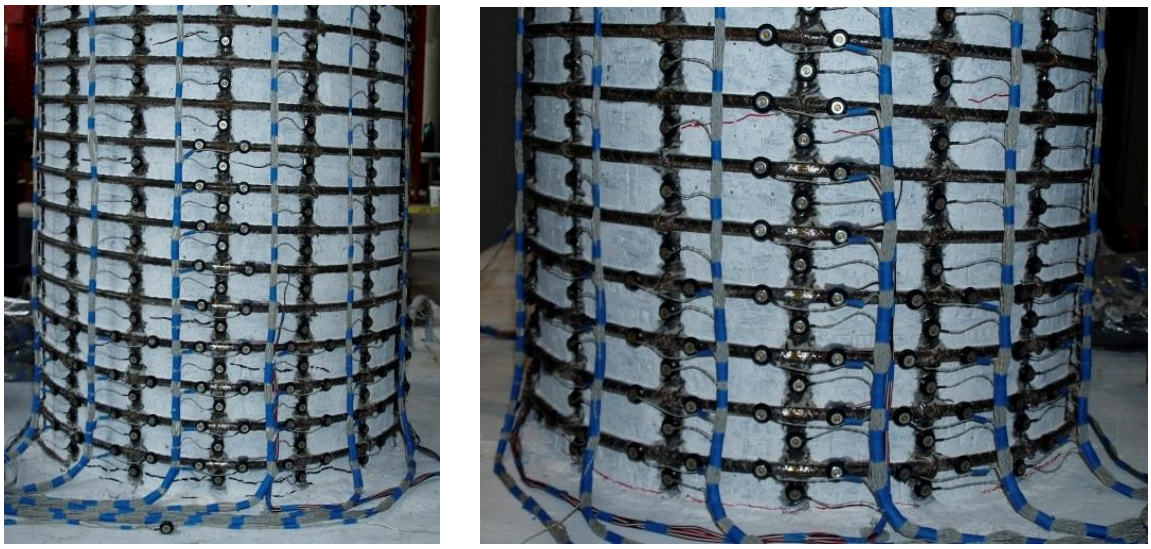

Figure 1.789 T27 – (Left) Cracking on the North Side during ($1/2Fy' = 0.20$"), (Right) South Cracking ($-1/2Fy' = -0.21$")

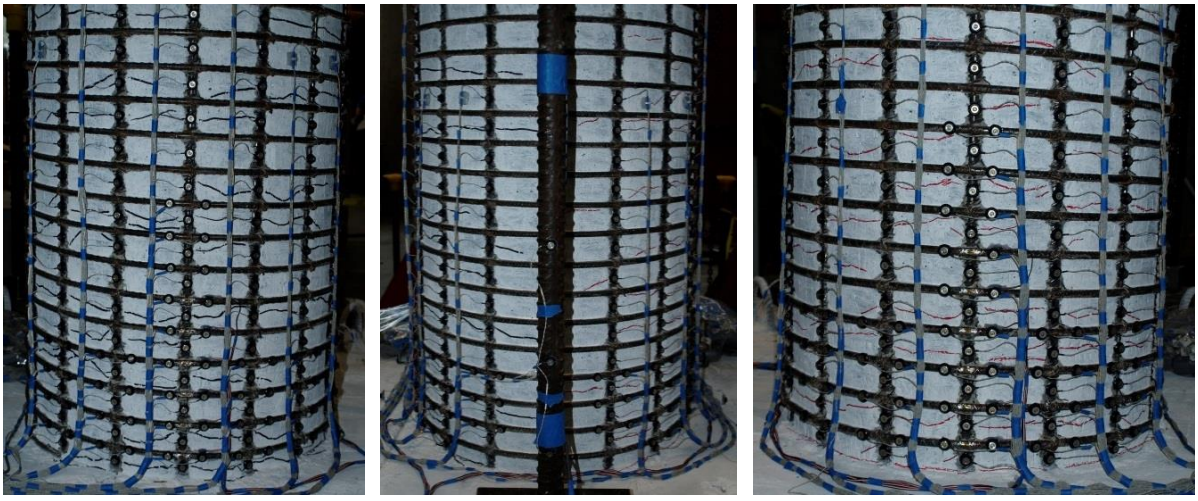

Figure 1.790 T27 – (Left) North Crack Distribution at ($Fy' = 0.68$"), (Middle and Right) Crack Distributions on the Front and Right Sides at ($-Fy' = -0.72$")

Figure 1.791 T27 – (Left) North Crack Distribution at ($\mu_1^{+3} = 0.92$"), (Middle and Right) Crack Distributions on the Front and Right Sides at ($\mu_1^{-3} = -0.92$")

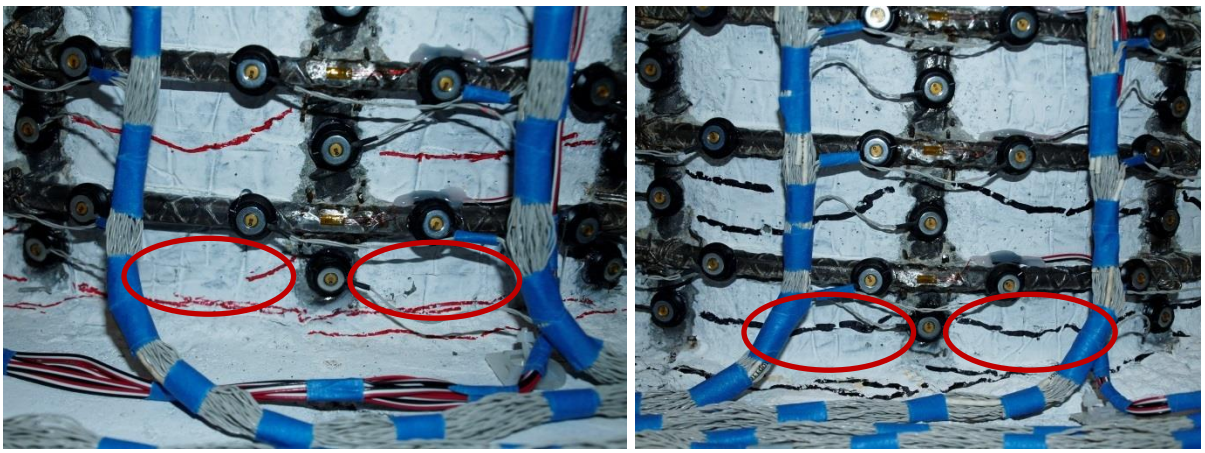

Figure 1.792 T27 – (Left) South Concrete Flaking during ($\mu_{1.5}^{+2} = 1.38$"), (Right) North Concrete Flaking during ($\mu_{1.5}^{-1} = -1.38$")

Figure 1.793 T27 – (Left) North Crack Distribution at ($\mu_{1.5}^{+3} = 1.38$"), (Middle and Right) Crack Distributions on the Front and Right Sides at ($\mu_{1.5}^{-3} = -1.38$")

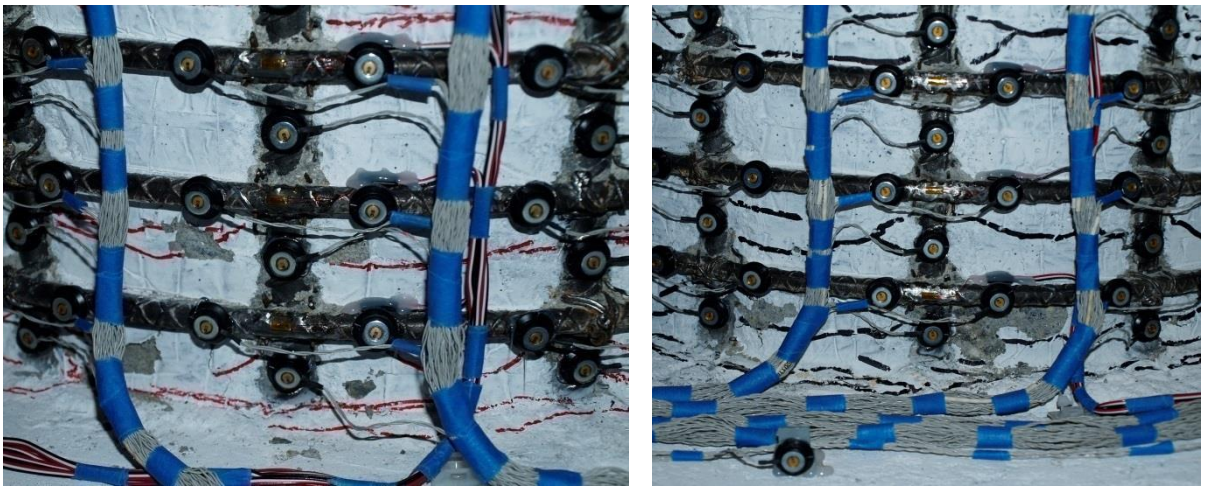

Figure 1.794 T27 – (Left) South Crushing during ($\mu_{2}^{+1} = 1.84$"), (Right) North Crushing during ($\mu_{2}^{-1} = -1.83$")

Figure 1.795 T27 – (Left) North Crack Distribution at ($\mu_2^{+3} = 1.84$"), (Middle and Right) Crack Distributions on the Front and Right Sides at ($\mu_2^{-3} = -1.84$")

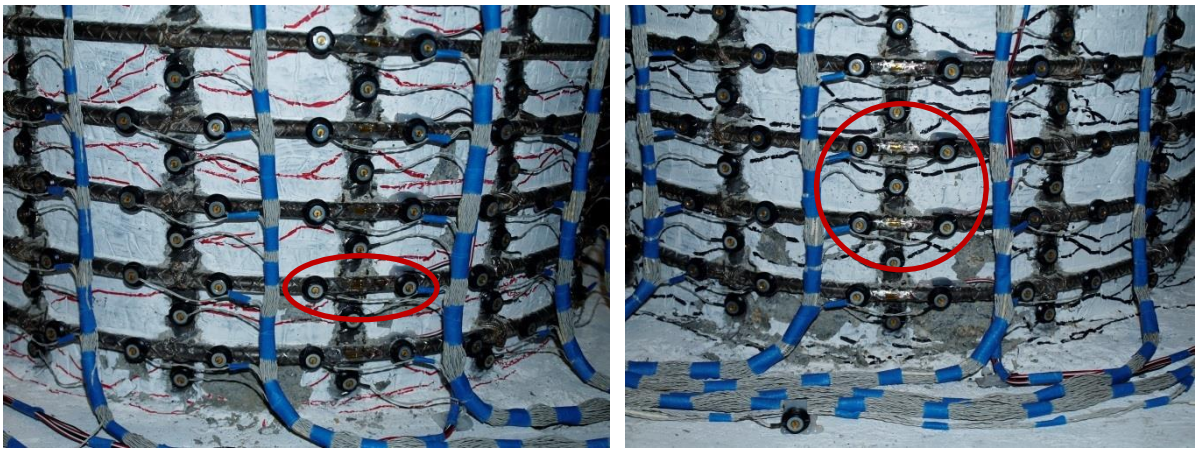

Figure 1.796 T27 – (Left) South Spiral Yield at ($\mu_3^{+1} = 2.76$"), (Right) North Spiral Yield at ($\mu_3^{-1} = -2.76$")

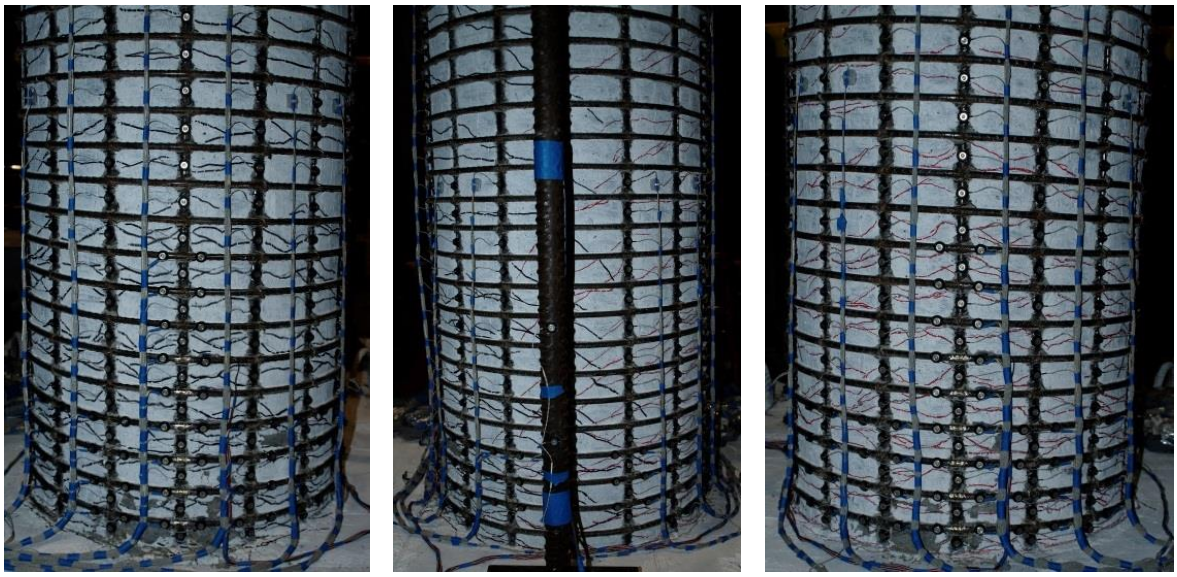

Figure 1.797 T27 – (Left) North Crack Distribution at ($\mu_3^{+3} = 2.76$"), (Middle and Right) Crack Distributions on the Front and Right Sides at ($\mu_3^{-3} = -2.76$")

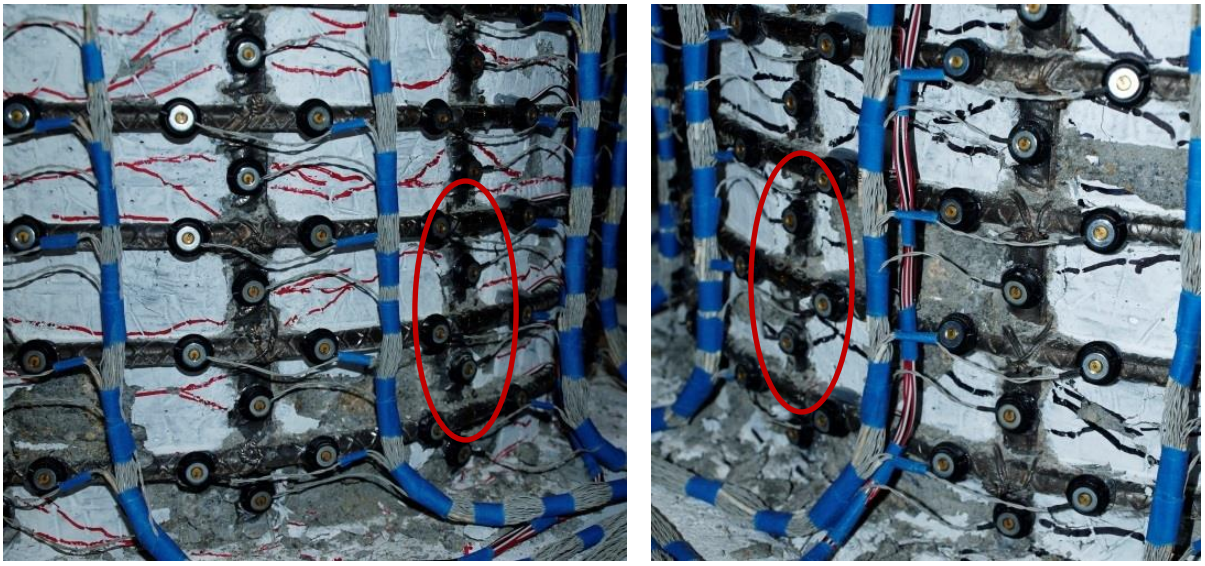

Figure 1.798 T27 – (Left) Bar S3 Remained Visibly Straight during ($\mu_4^{+3} = 3.66$"), (Right) Bar N3 Remained Visibly Straight during ($\mu_4^{-3} = -3.67$")

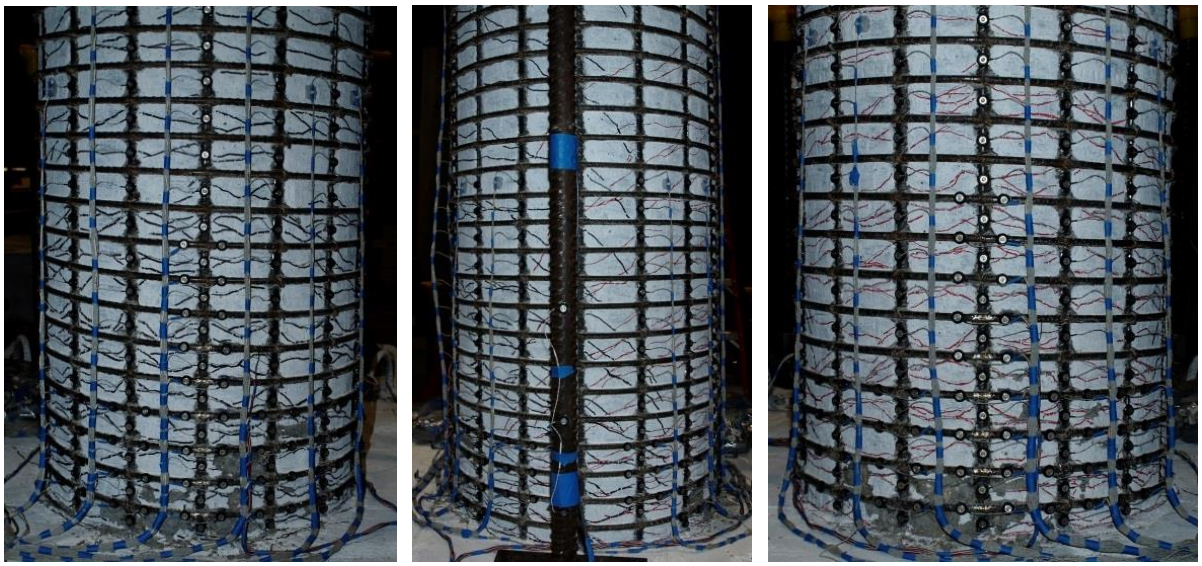

Figure 1.799 T27 – (Left) North Crack Distribution at ($\mu_4^{+3} = 3.66$"), (Middle and Right) Crack Distributions on the Front and Right Sides at ($\mu_4^{-3} = -3.67$")

Figure 1.800 T27 – (Left) Very Slight Visible Buckling of Bar S3 during ($\mu_5^{+1} = 4.60$"), (Right) Increased Deformation in Buckled Bar S3 during ($\mu_5^{+2} = 4.61$")

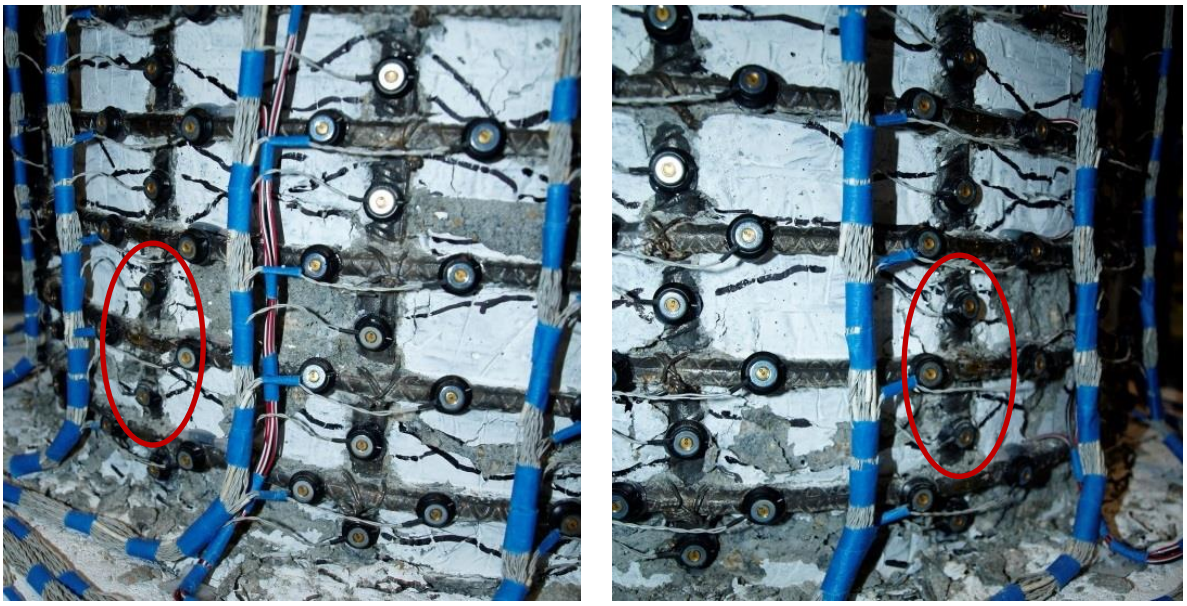

Figure 1.801 T27 – Visible Buckling of Bar N3 during ($\mu_5^{-1} = -4.60$")

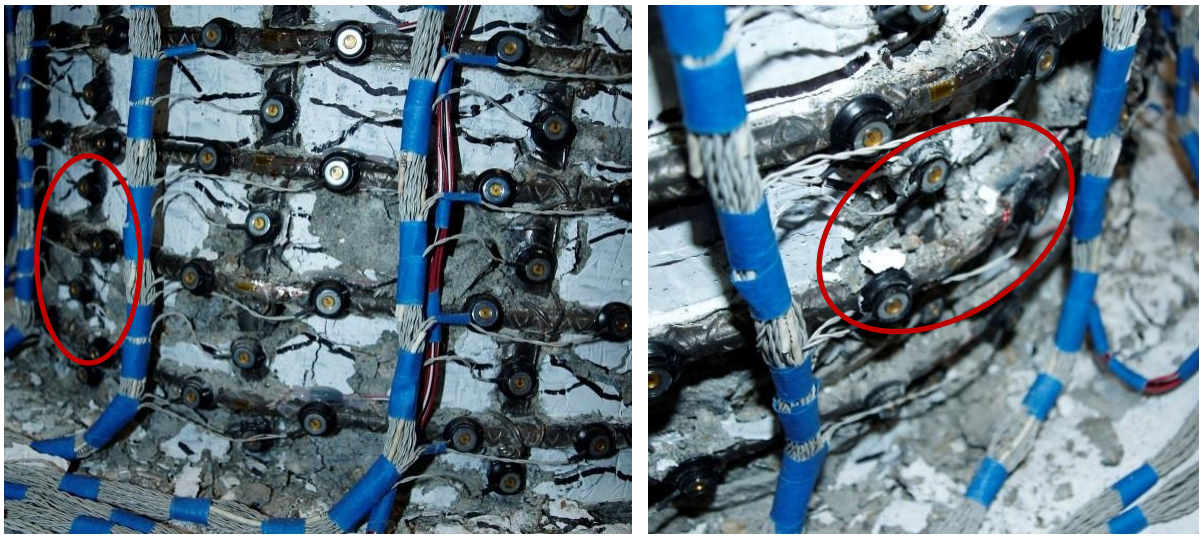

Figure 1.802 T27 – (Left) Buckling of Adjacent Bar N4 ($\mu_5^{-2} = -4.59$"), (Right) North Spiral Deformation at ($\mu_5^{+3} = 4.60$")

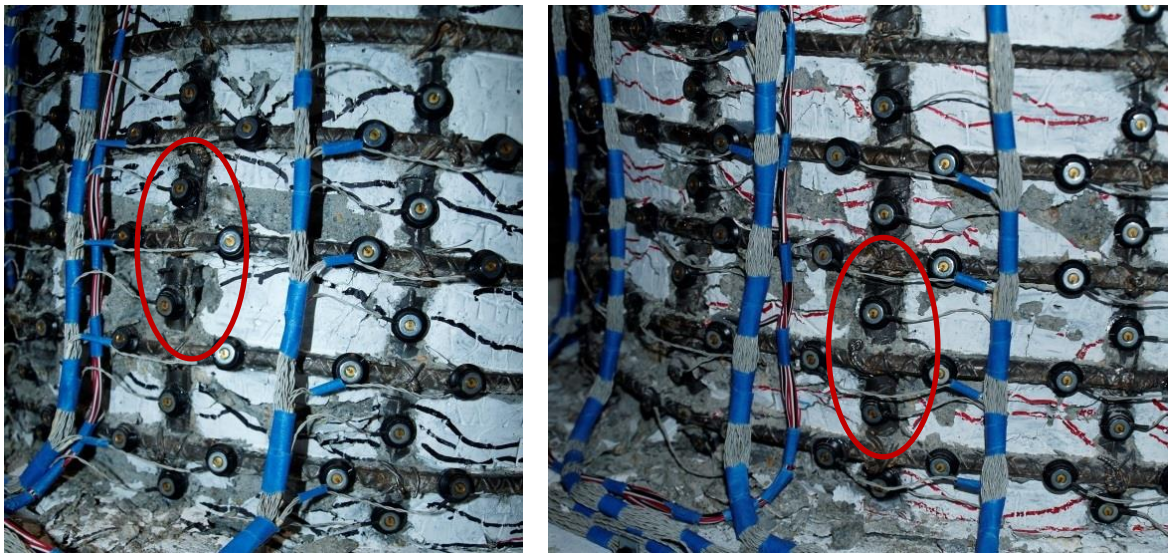

Figure 1.803 T27 – (Left) Buckling of Adjacent Bar N2 during ($\mu_5^{-3} = -4.60$"), (Right) Buckling of Adjacent Bar S4 during ($\mu_6^{+1} = 5.52$")

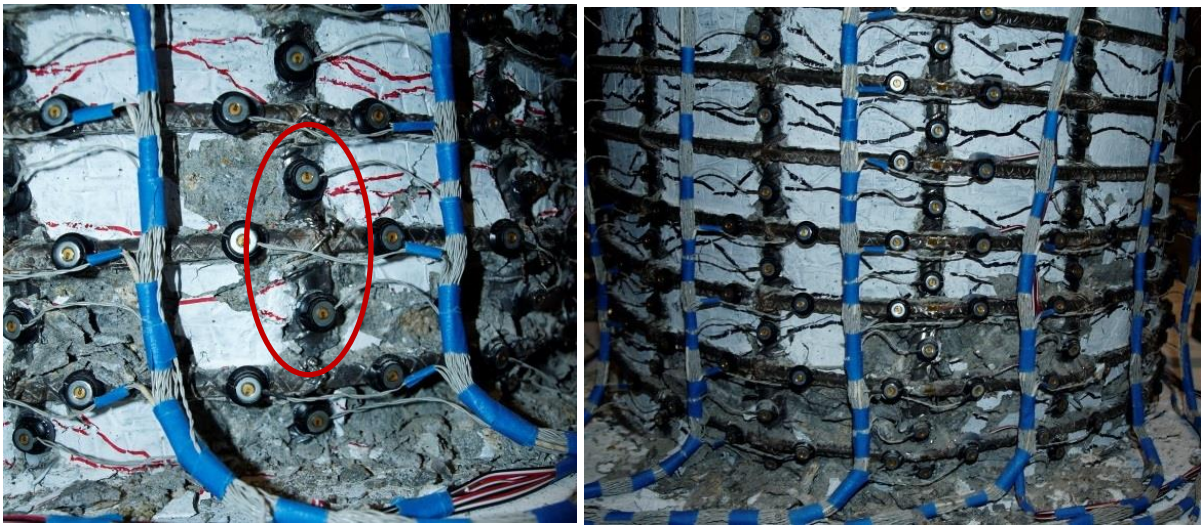

Figure 1.804 T27 – (Left) Buckling of Adjacent Bar S2 during ($\mu_6^{+1} = 5.52$"), (Right) North Side at ($\mu_6^{-1} = -5.54$")

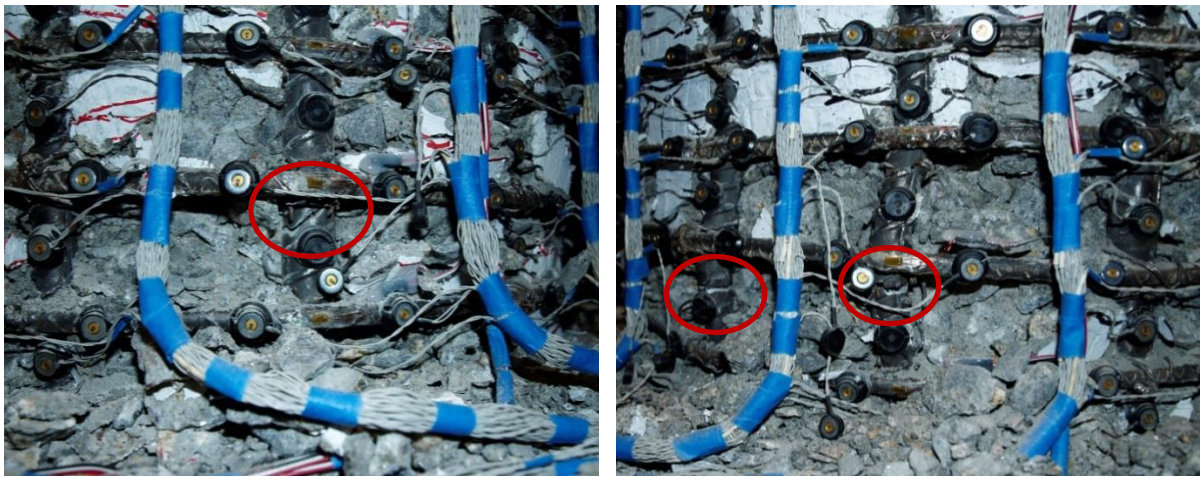

Figure 1.805 T27 – (Left) Fracture of Previously Buckled Bar S3 during ($\mu_6^{-2} = -5.53$"), (Right) Fracture of Previously Buckled South Bars N3 and N4 during (μ_6^{+3})

Figure 1.806 T27 – After the Test (Left) South Side and (Right) North Side

Figure 1.807 T27 – (Left to Right) Front, Back, North, and South Sides after the Test

Test 27 – 24" Dia. with 1.6% Steel and 10% Axial Load – Strain Data Analysis

North Reinforcement

Vertical strain profiles for the north extreme fiber bar N3, which is placed into tension during push cycles, appear in the right half of Figure 1.808. This figure shows both extreme fiber bars on the same graph to illustrate the effects of tension shift. Compression strains are concentrated near the footing-column interface while tension strains are spread higher above the footing following the inclined flexural-shear crack distribution. Compressive vertical strain profiles for north extreme fiber bar N3 during pull cycles appear in the left half of Figure 1.809. A peak tensile strain of 0.0361 was measured 7.56" above the footing on bar N3 during ($\mu_5^{+1} = 4.60"$), before the bar visibly buckled during ($\mu_5^{-1} = -4.60"$). The relationship between tension strain and displacement for this gage length appears in Figure 1.812. Moment-curvature analysis with the PCK (2007) Lp Hinge Method begins to over

predict the measured tensile strains at an increasing rate beyond displacement ductility two. A compressive strain of –0.0168 was measured 1.70" above the footing on bar N3 during ($\mu_3^{-1} = -2.76$"), when the first spiral in the confinement region yielded.

Measured spiral strains in six layers which overlaid the north extreme fiber bar appear in Figure 1.811. Spiral tension strains increased during each successive pull cycle of displacement ductility four. The relationship between compressive strain and displacement for the bar N3 gage length 5.57" above the footing appears in Figure 1.814. The measured compressive strains match the moment-curvature prediction with the PCK (2007) Lp Hinge Method through ($\mu_4^{-1} = -3.67$"), but begin to deviate during the second and third pull cycles. A diagram depicting the influence of measurable outward deformation on three adjacent gage lengths is shown in Figure 1.822. Inspection of compressive strain profiles for bar N3 point out that the first three gage lengths above the footing were influenced by measurable deformation before visible bar buckling, Figure 1.809. A peak compressive strain of -0.0322 was measured 1.70" above the footing on bar N3 during ($\mu_4^{-3} = -3.67$"). It is likely that this compressive strain is influenced by measurable deformation, but it is unclear why the deformation was observed before yielding of the transverse steel, Figure 1.813.

Strain hysteresis for gage lengths 3.59", 5.57" and 7.56" above the footing on bar N3 appear in Figure 1.818, Figure 1.819, and Figure 1.820. The hysteresis remained stable through ($\mu_4^{-1} = -3.67$"), when the peak spiral tension strain measured by a strain gage reached 0.0048 for the layer 3.78" above the footing, Figure 1.821. The hysteresis contains spiral data from a strain gage and an Optotrak gage length, Figure 1.783. The Optotrak strains were calculated using arc-lengths obtained from measured 3D distance chord lengths and the known outside diameter of the spiral. It is important to note that arc-length calculations become inaccurate once severe yielding in the spiral leads to the reinforcement straightening out to the left and right of the localized yielding directly over the bar where the strain gage is located. The bar N3 strain hystereses and the overlaying spiral strain hysteresis show a major deviation during ($\mu_5^{-1} = -4.60$") when visible bar buckling was observed,

Figure 1.801. The distribution of arc-strains measured around the circumference of the second and third spiral layers above the footing during compressive pull cycles appear in Figure 1.829 and Figure 1.831 respectively. The north side of the specimen is on the left side of the graph with negative location values, specific locations of bars N2, N3, and N4 are highlighted with vertical dashed lines. The largest spiral tension strains were measured directly over reinforcing bars, and inelastic spiral strains are concentrated in the compressive zone with elastic strains near the center of the section.

South Reinforcement

Vertical strain profiles for the south extreme fiber bar S3, which is placed into tension during pull cycles, appear in the right half of Figure 1.809. Compressive vertical strain profiles for south extreme fiber bar S3 during push cycles appear in the left half of Figure 1.808. The measured compressive strains for bar S3 appear to be influenced by measurable deformation which occurred after yielding of the transverse steel. A diagram which shows the location and effect of measurable deformation in Bar S3 appears in Figure 1.822. The first and third gage lengths above the footing had increased compression while the second gage length had additional tension during pull cycles. This behavior is observable in the measured strain hysteresis 1.77" (Figure 1.823), 3.60" (Figure 1.824), and 5.48" (Figure 1.825) above the footing. As a comparison, the gage length 7.40" above the footing on bar S3, Figure 1.826, appears to be unaffected by measurable deformation.

The peak tension strain before bar buckling of 0.0243 was measured 3.60" above the footing on bar S3 during ($\mu_4^{-3} = -3.67"$). The relationship between tension strain and displacement for this gage lengths 3.60" and 11.23" above the footing appear in Figure 1.815 and Figure 1.816. Moment-curvature analysis with the PCK (2007) Lp Hinge Method begins to over predict the measured tension strains during displacement ductility two. A compressive strain of -0.0124 was measured 1.77" above the footing during ($\mu_3^{-1} = -2.76"$), when the first spiral layer in the south confinement region yielded. The peak compression strain of -0.0228, measured 1.77" above the footing on bar S3, may be unreliable due to deformation. The relationship between compressive strain and displacement for this gage

length appears in Figure 1.817. The measurable deformation led to compressive strains which significantly exceed the moment-curvature prediction, with the PCK (2007) Lp Hinge Method, in this gage length as well as the one 5.48" above the footing.

Measured strains in six spiral layers which overlaid the south extreme fiber bar appear in Figure 1.810 for push cycles. Cycles during displacement ductility four produced successively larger inelastic demands on the bottom three layers of spiral reinforcement. Strain gage and Optotrak strain hysteresis for the spiral layer 3.63" above the footing appear in Figure 1.827. The two measurement methods match well until ($\mu_4^{+1} = 3.68"$), when the effects of measurable deformation became apparent and presumably the arc-strains no longer represent the geometry of the spiral over bar S3. The spiral strains spiked during ($\mu_5^{+1} = 4.60"$) when visible bar buckling was observed, Figure 1.800, and increased more significantly as the buckled deformation grew during ($\mu_5^{+2} = 4.61"$). Measured arc-strains around the circumference of the second and third spiral layers on the south side of the specimen during push cycles appear in Figure 1.828 and Figure 1.830. The largest inelastic spiral strains were localized over bars S2, S3, and S4 which are shown on the right side of the figures with vertical dashed lines.

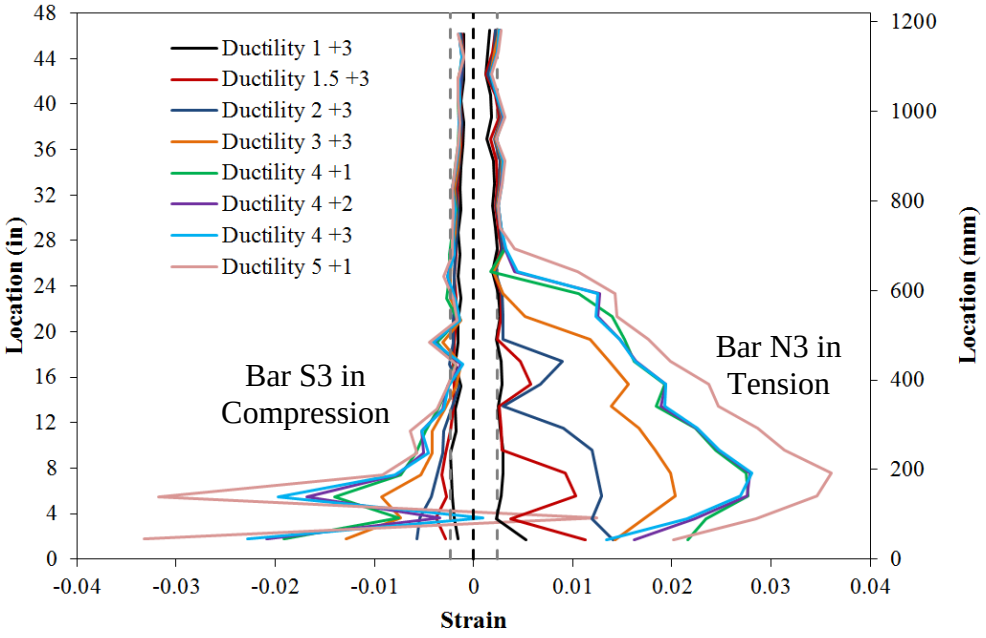

Figure 1.808 T27 – Extreme Fiber Bar Vertical Strain Profiles during Push Cycles

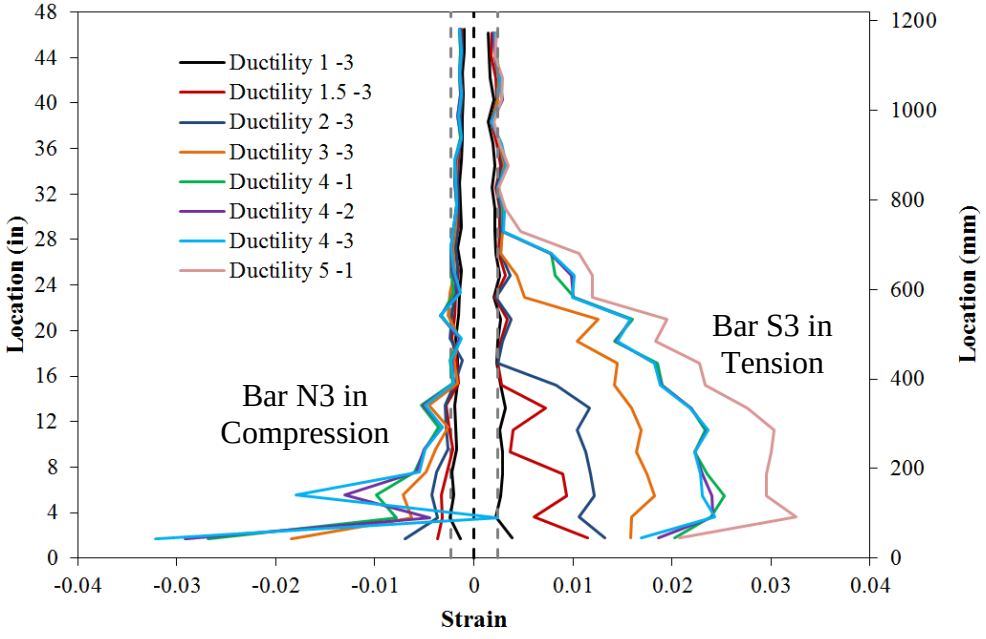

Figure 1.809 T27 – Extreme Fiber Bar Vertical Strain Profiles during Pull Cycles

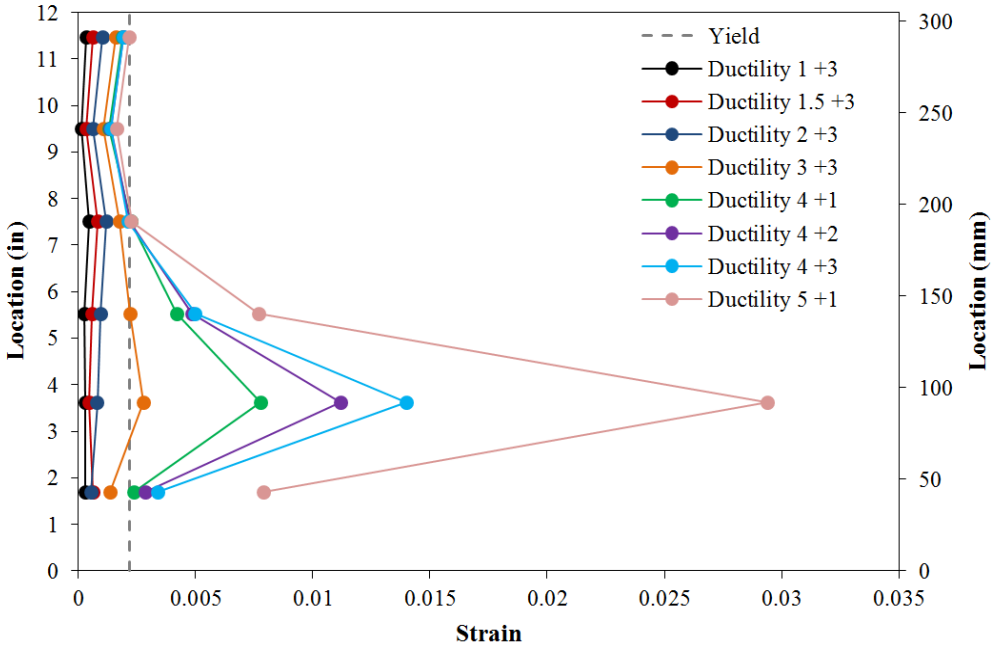

Figure 1.810 T27 – Spiral Strains on the South Side during Push Cycles

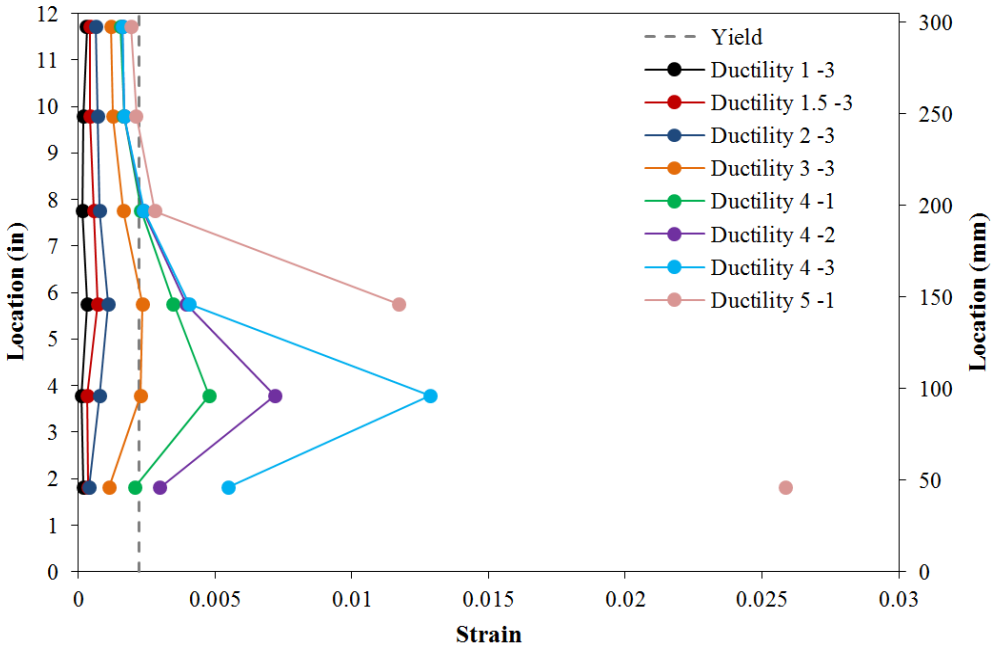

Figure 1.811 T27 – Spiral Strains on the North Side during Pull Cycles

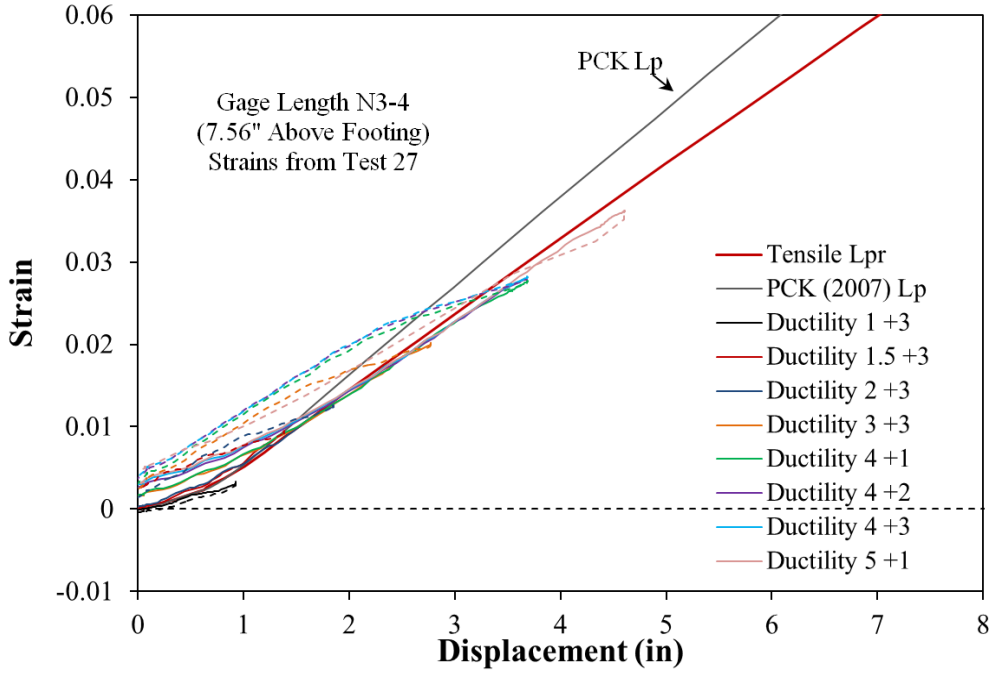

Figure 1.812 T27 – Tensile Strain-Displacement for Bar N3 during Push Cycles

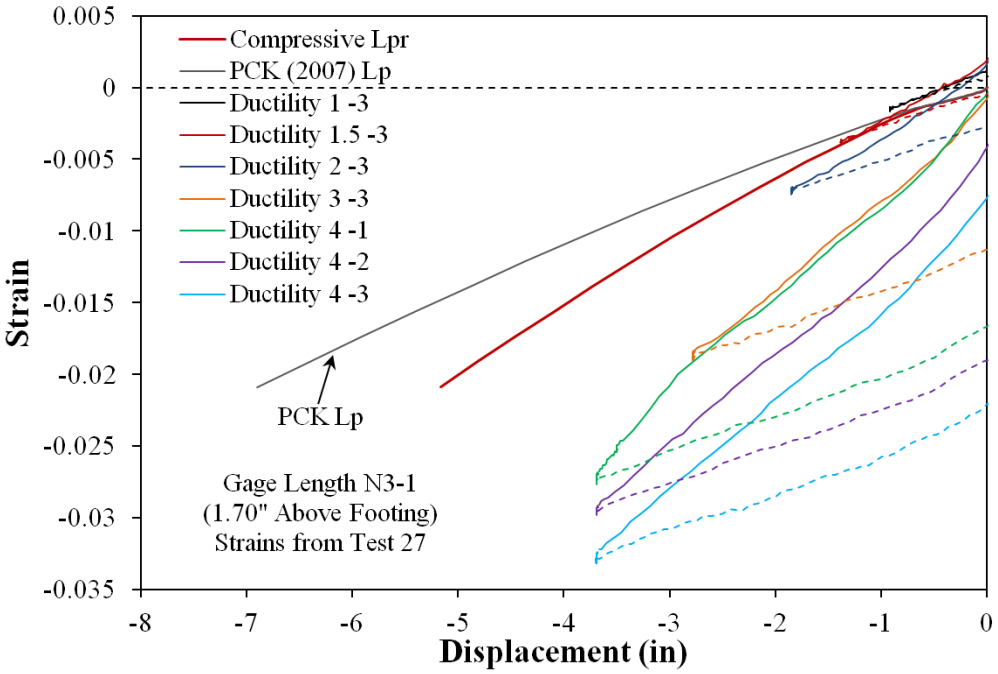

Figure 1.813 T27 – Compressive Strain-Displacement for Bar N3 during Pull Cycles

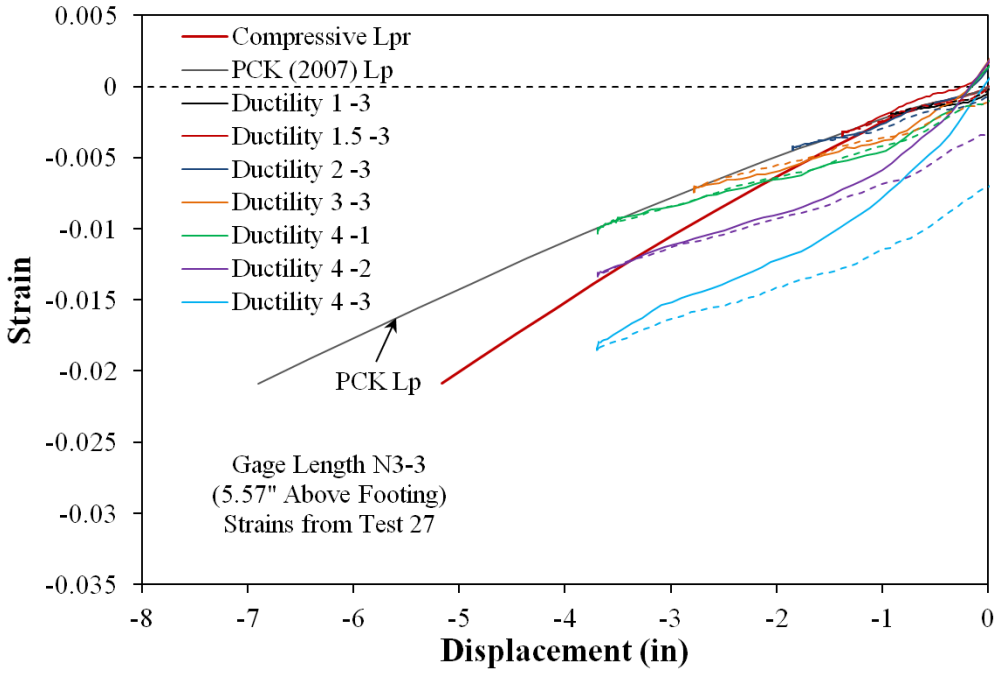

Figure 1.814 T27 – Compressive Strain-Displacement for Bar N3 during Pull Cycles

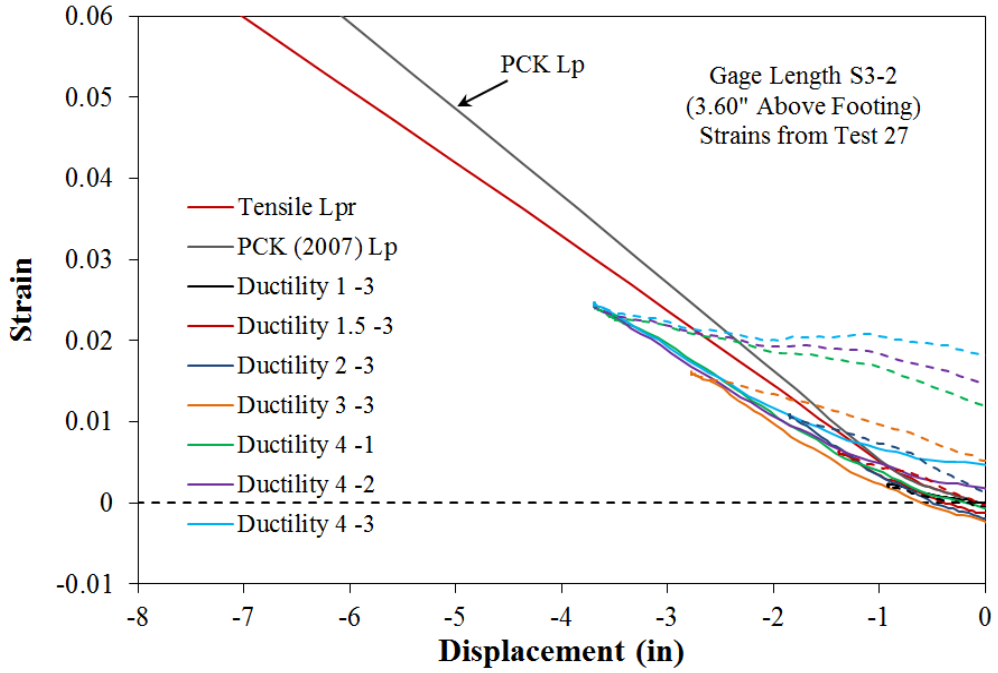

Figure 1.815 T27 – Tensile Strain-Displacement for Bar S3 during Pull Cycles

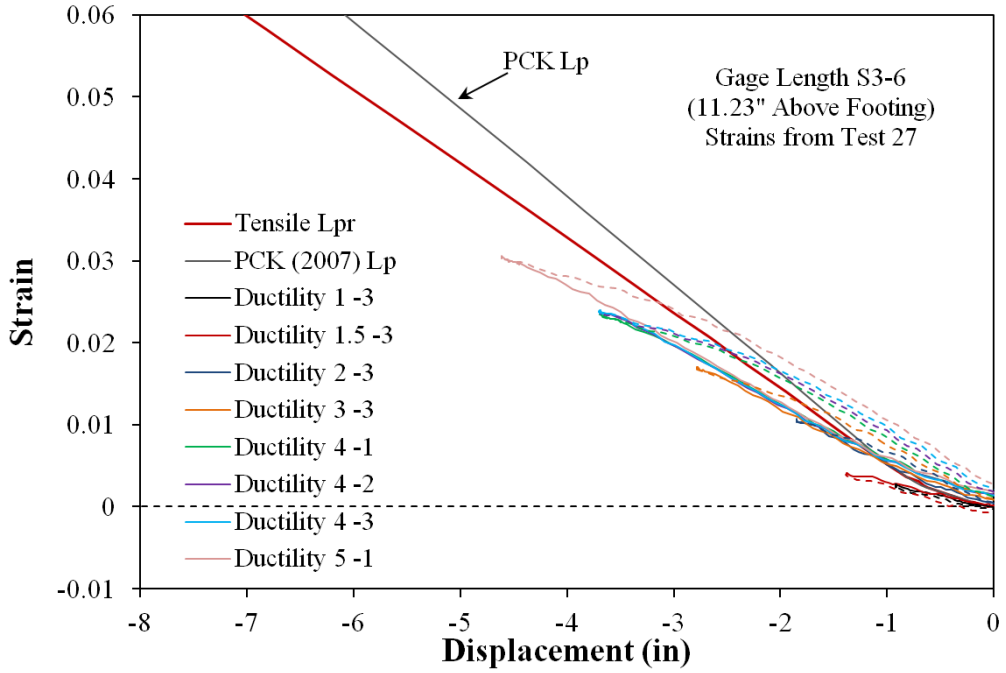

Figure 1.816 T27 – Tensile Strain-Displacement for Bar S3 during Pull Cycles

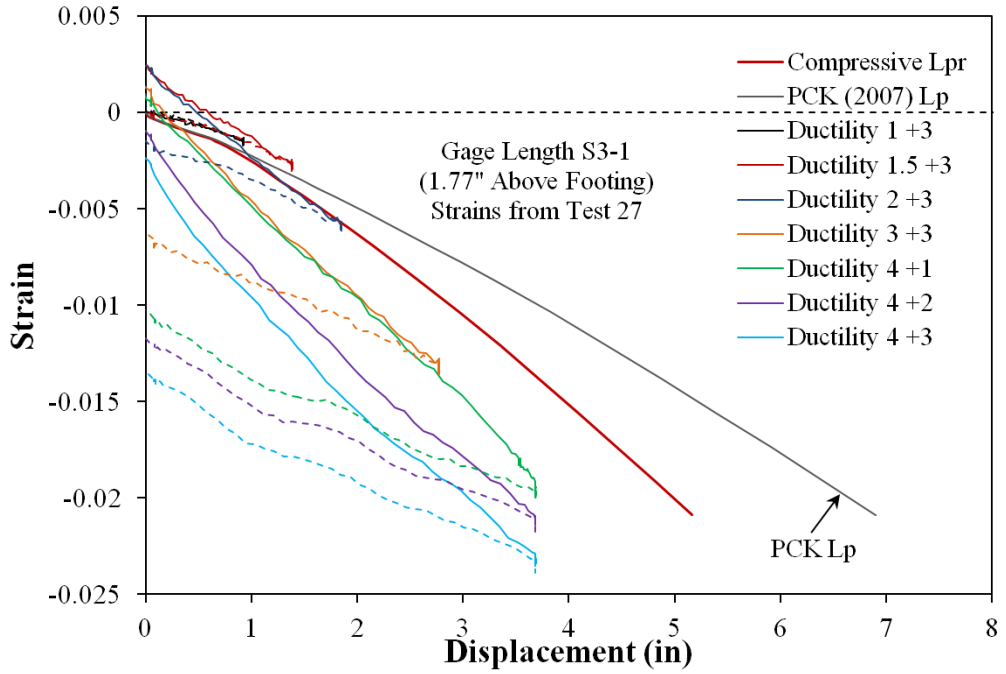

Figure 1.817 T27 – Compressive Strain-Displacement for Bar S3 during Push Cycles

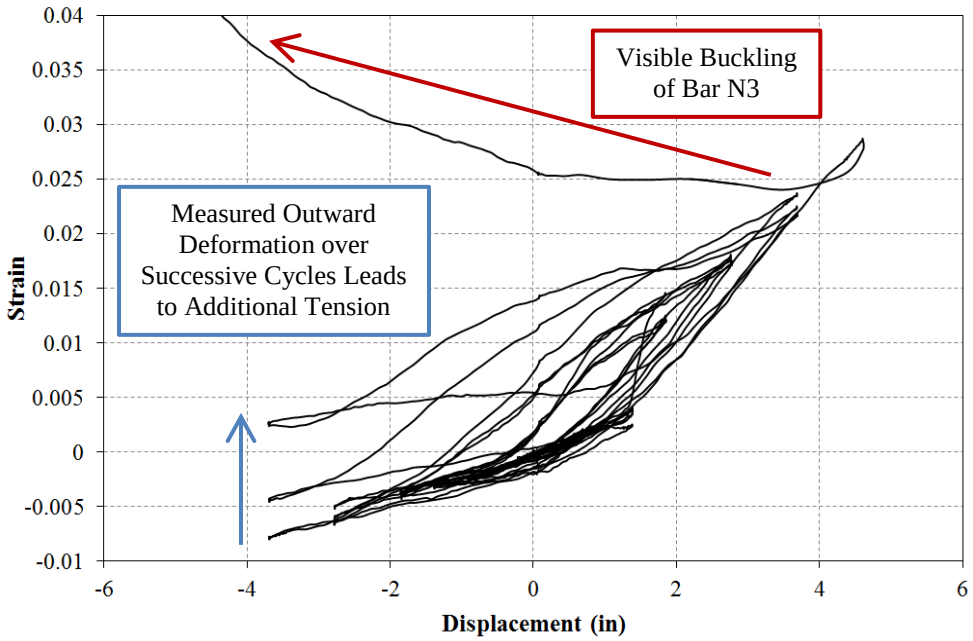

Figure 1.818 T27 – Bar N3 Strain Hysteresis to Buckling (3.59" Above the Footing)

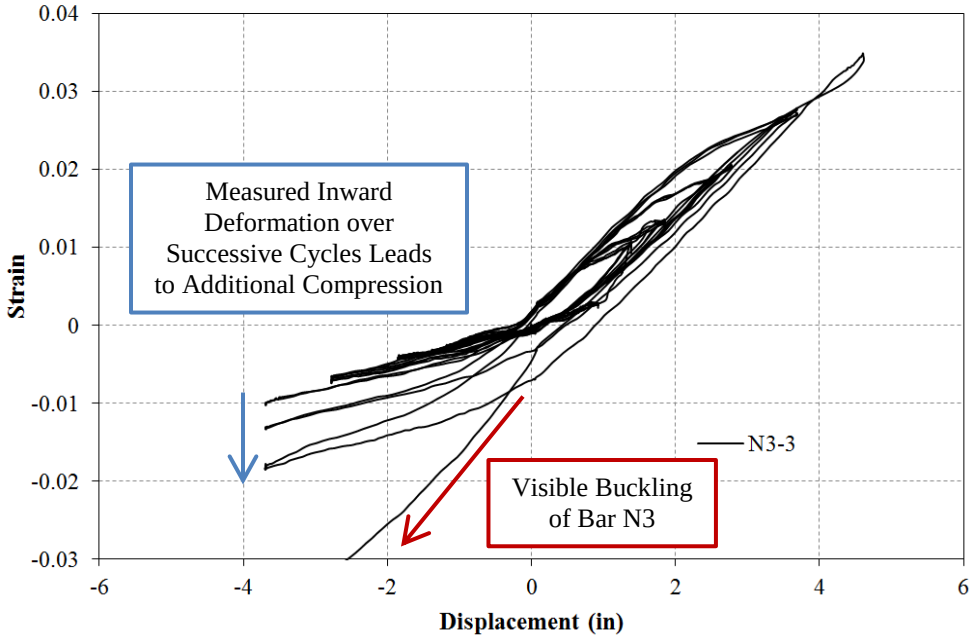

Figure 1.819 T27 – Bar N3 Strain Hysteresis to Buckling (5.57" Above the Footing)

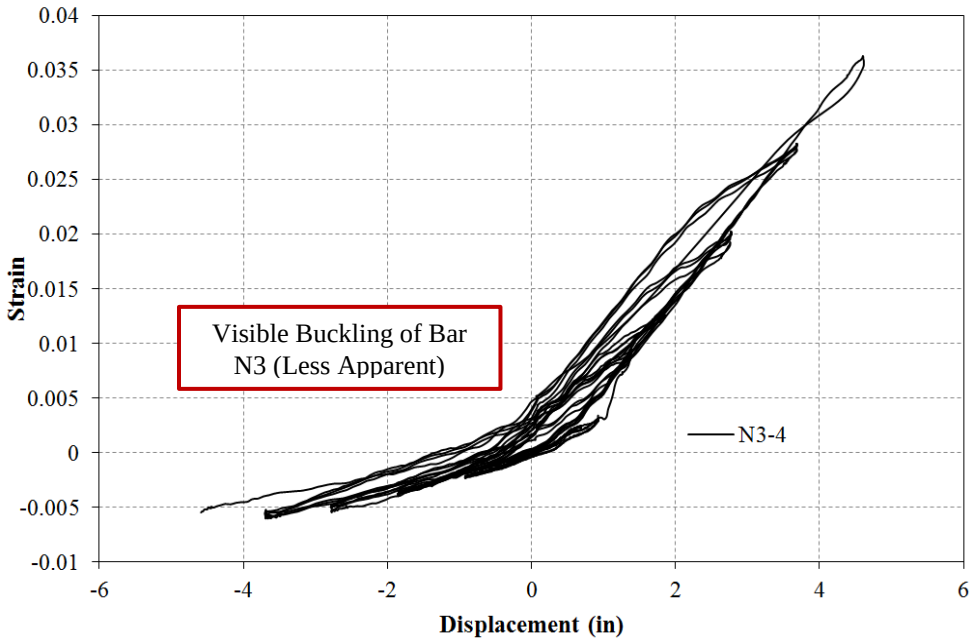

Figure 1.820 T27 – Bar N3 Strain Hysteresis to Buckling (7.56" Above the Footing)

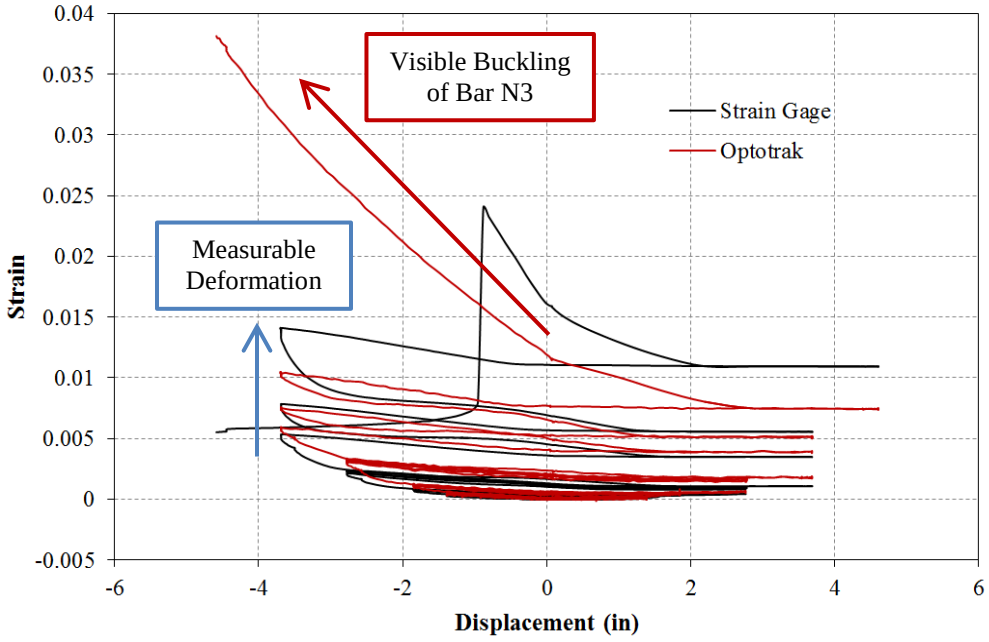

Figure 1.821 T27 – Spiral Strain Hysteresis over North Buckled Region (3.78" Above)

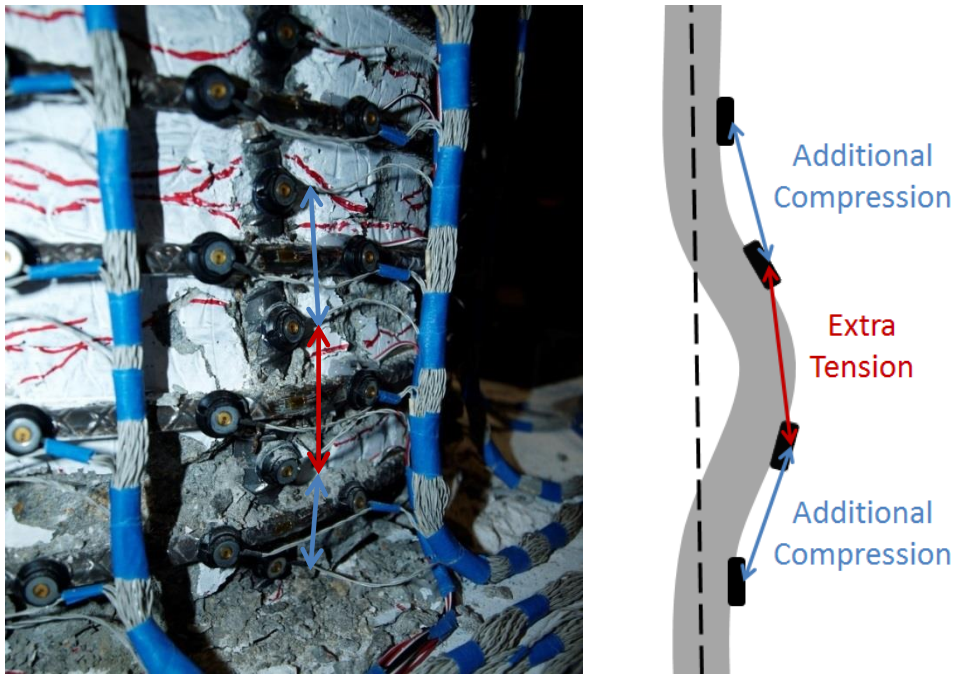

Figure 1.822 T27 – Location of Measurable Deformation and Bar S3 Buckled Shape

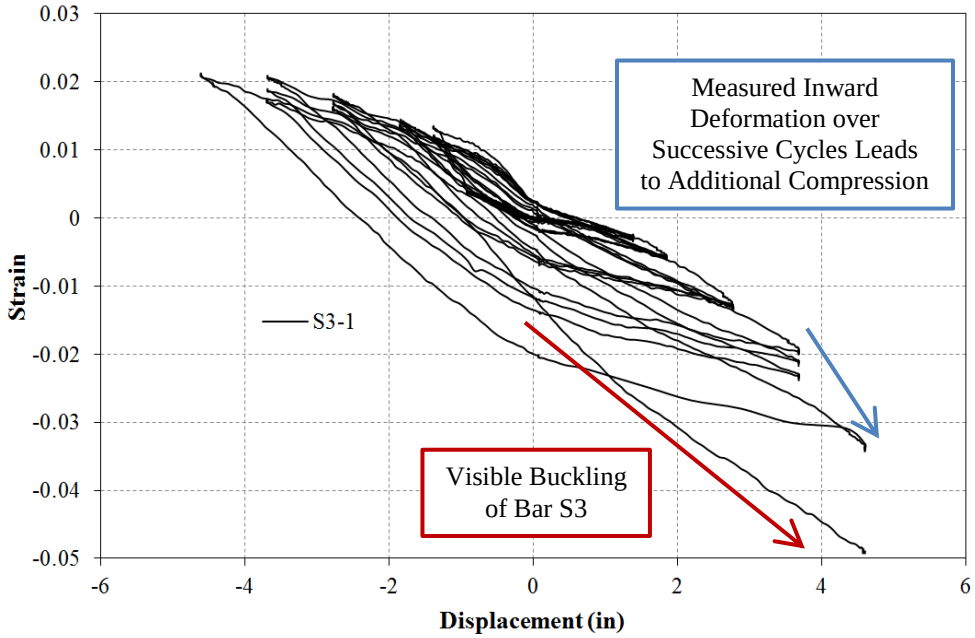

Figure 1.823 T27 – Bar S3 Strain Hysteresis to Buckling (1.77” Above the Footing)

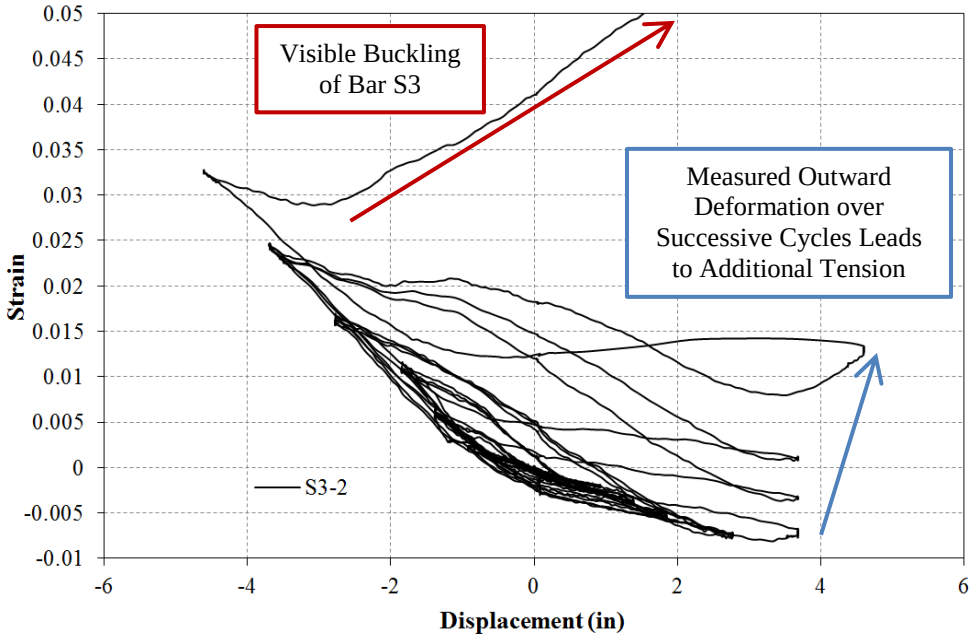

Figure 1.824 T27 – Bar S3 Strain Hysteresis to Buckling (3.60" Above the Footing)

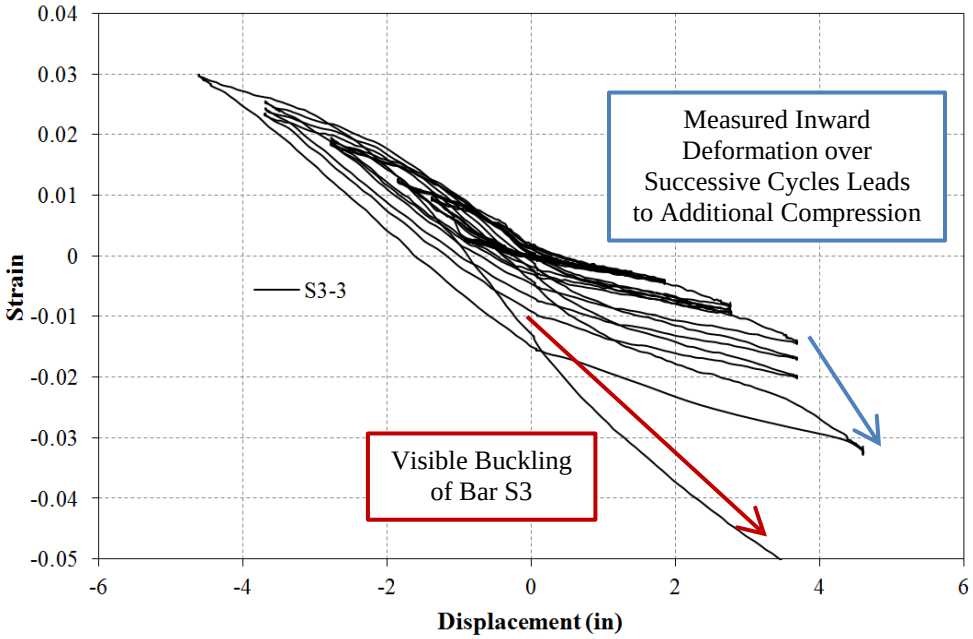

Figure 1.825 T27 – Bar S3 Strain Hysteresis to Buckling (5.48" Above the Footing)

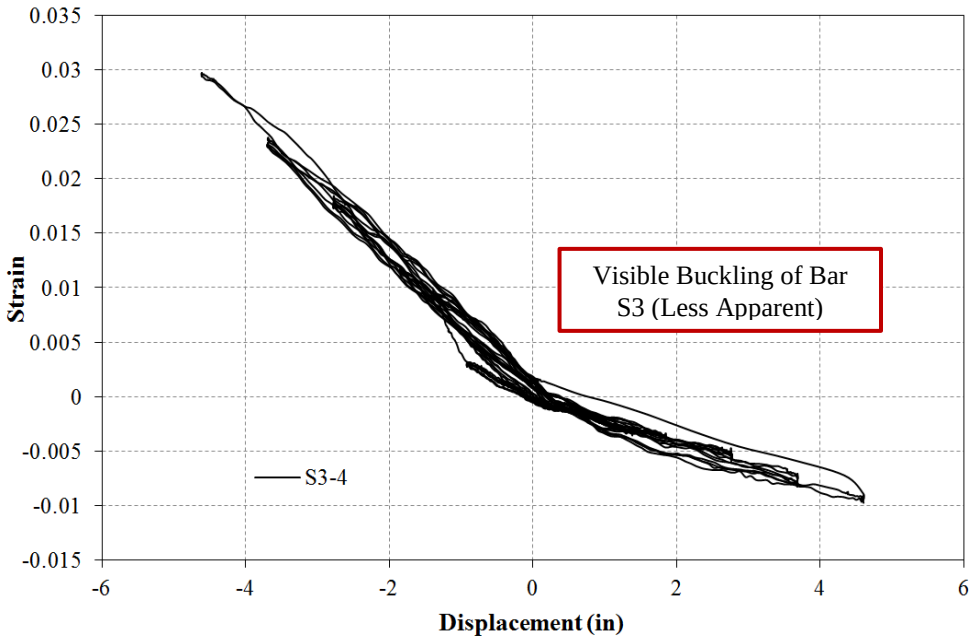

Figure 1.826 T27 – Bar S3 Strain Hysteresis to Buckling (7.40" Above the Footing)

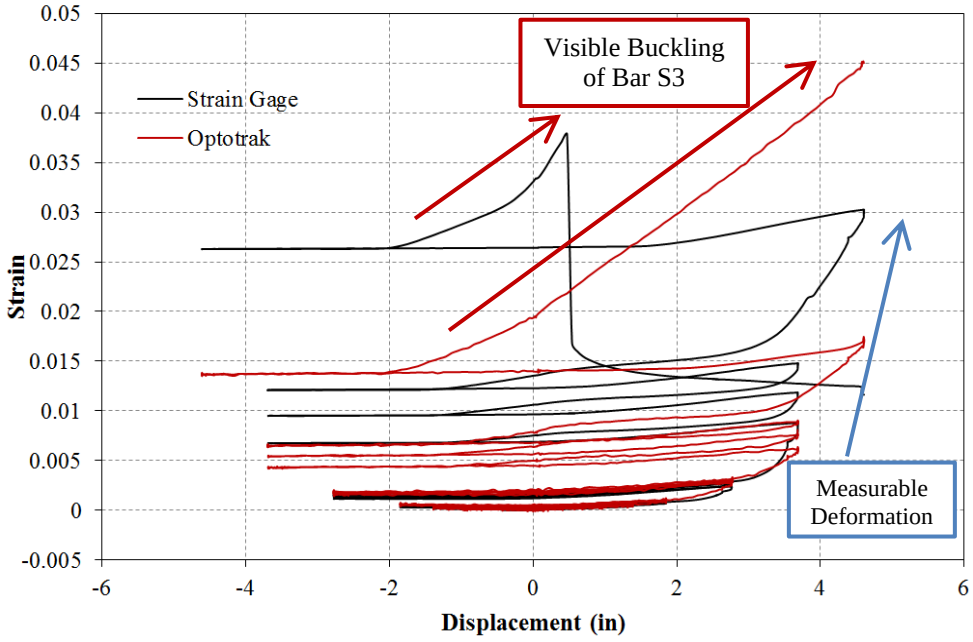

Figure 1.827 T27 – Spiral Strain Hysteresis over South Buckled Region (3.63" Above)

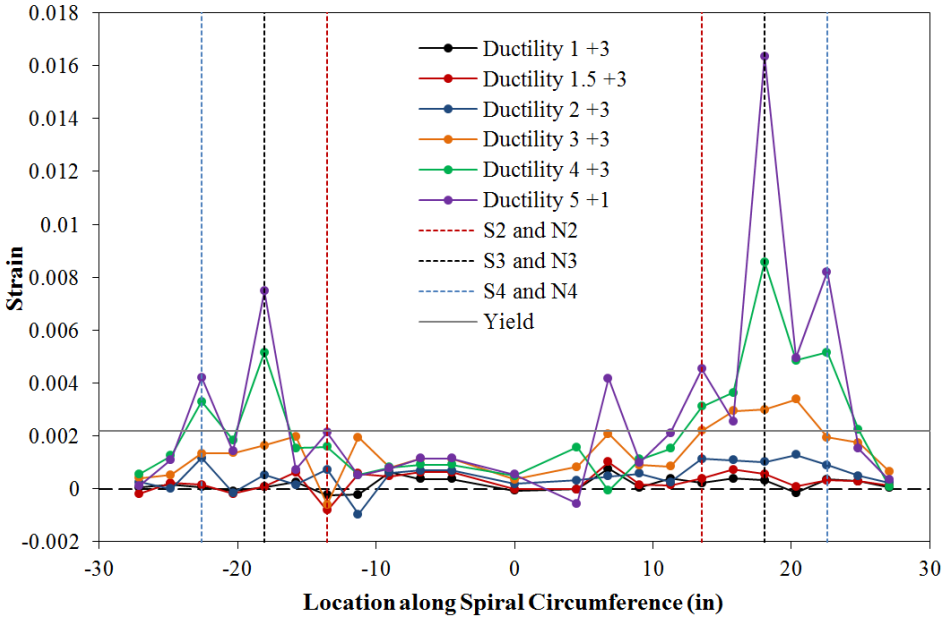

Figure 1.828 T27 – Spiral Strain Distribution for the 2nd Spiral above the Footing during Push Cycles (Positive = South)

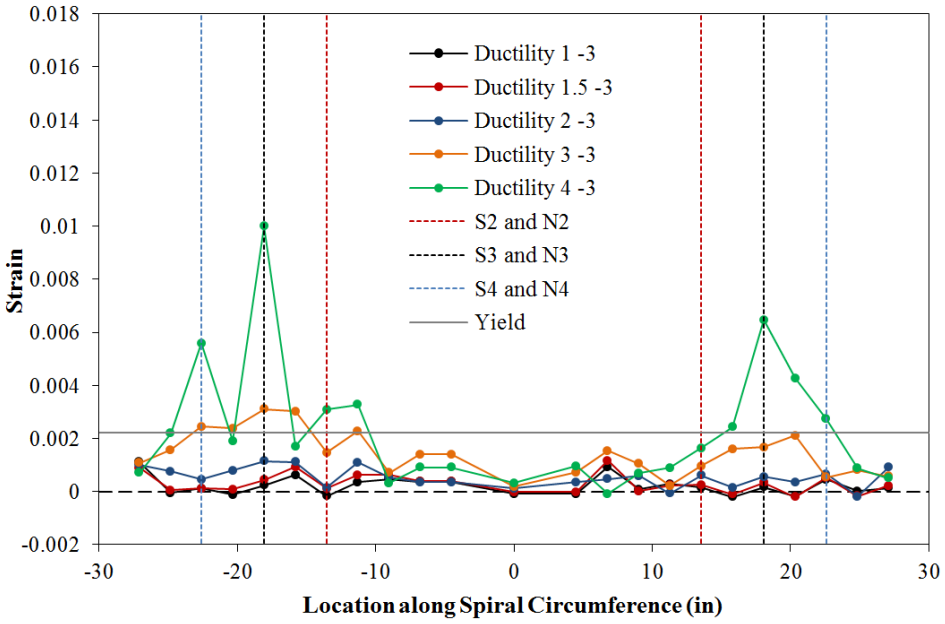

Figure 1.829 T27 – Spiral Strain Distribution for the 2nd Spiral above the Footing during Pull Cycles (Negative = North)

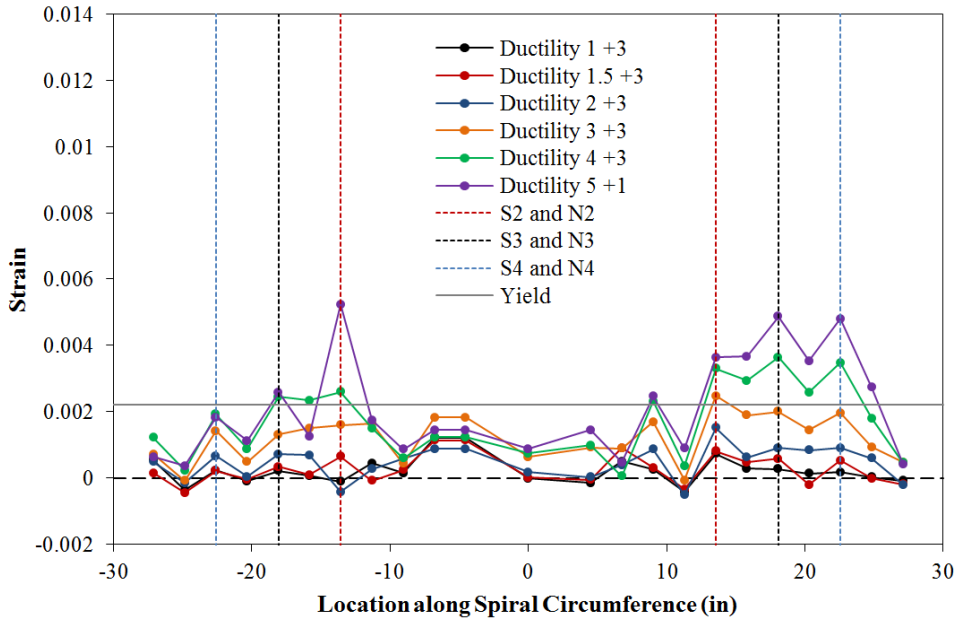

Figure 1.830 T27 – Spiral Strain Distribution for the 3rd Spiral above the Footing during Push Cycles (Positive = South)

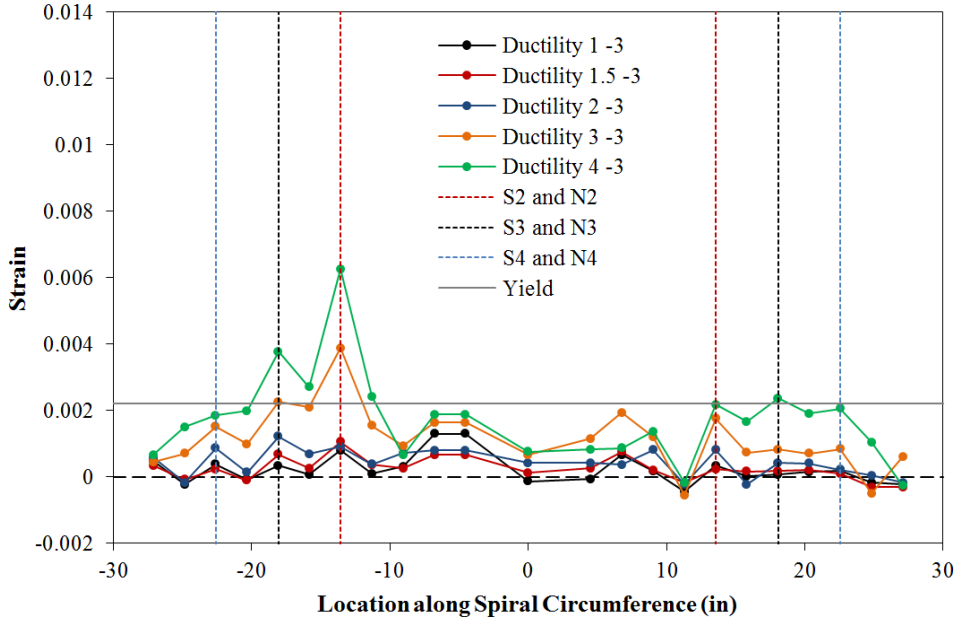

Figure 1.831 T27 – Spiral Strain Distribution for the 3rd Spiral above the Footing during Pull Cycles (Negative = North)

Test 27 – Curvature and Strain Penetration Data

Cross section strain profiles for the second horizontal section above the footing appear in Figure 1.832 and Figure 1.833 for push and pull cycles respectively. This is the first horizontal section above the footing with instrumented gage lengths on bars S0 and N0. The curvature is calculated as the slope of the least squared line connecting strains measured in twelve instrumented reinforcing bars. If the curvatures for many horizontal cross sections are analyzed, curvature profiles for the plastic hinge region can be constructed; Figure 1.834 and Figure 1.835 for push and pull cycles respectively. Plastic curvatures were found to follow a linear distribution. Linear least squared error plastic curvature lines were fit to the plastic portion of the measured curvature profiles. The extrapolation of this linear curvature line with the footing-column interface was taken as the base section curvature. As the base section curvature ductility increased, the height at which the linear plastic curvature distribution intersected the elastic curvature profile also increased. Circular data points in Figure 1.839 plot the measured spread of plasticity as a function of base section curvature ductility.

Curvature profiles describe the elastic and plastic flexural displacements of the column, but do not address fixed-end rotations which result from development of longitudinal reinforcement into the footing. The measured vertical displacements of Optotrak LEDs placed closest to the footing column interface can be used to quantify this fixed-end rotation, Figure 1.836 and Figure 1.837. The fixed-end rotation is taken as the slope of the least squared error line fit to the bond slip profile. If an elastic curvature profile assumption is made for curvatures higher than those measured with instrumentation, then the entire curvature profile may be integrated to obtain the total column flexural displacement. This column flexural displacement was added to the strain penetration displacement, and compared to the experimentally measured displacements in Figure 1.838. The Optotrak integrated displacement matches well with those obtained from a string potentiometer placed at the center of the lateral load, which indicates that shear deformation are small.

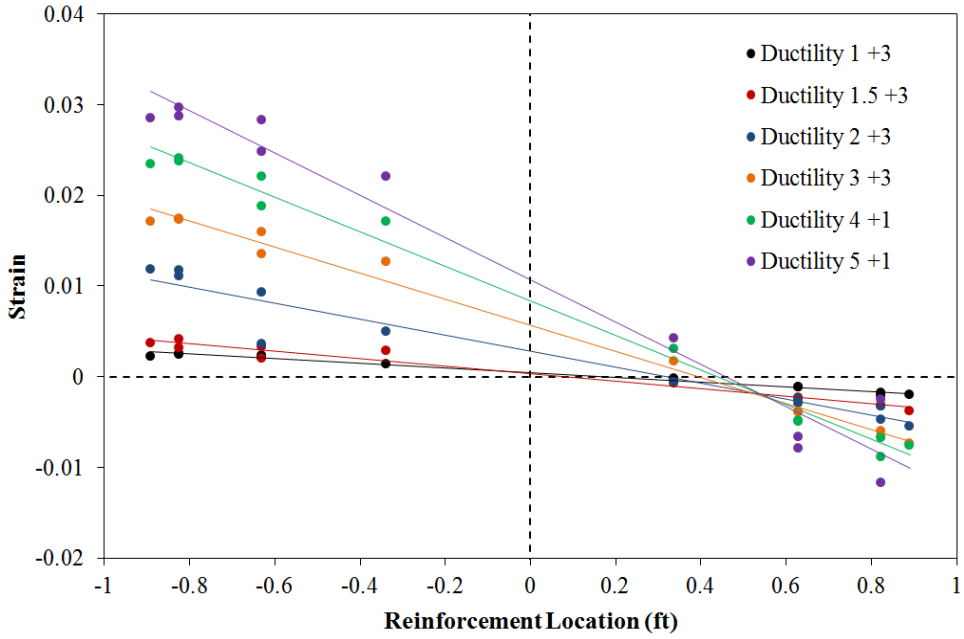

Figure 1.832 T27 – Strain Profiles during Push Cycles for Section 3.58" Above Footing

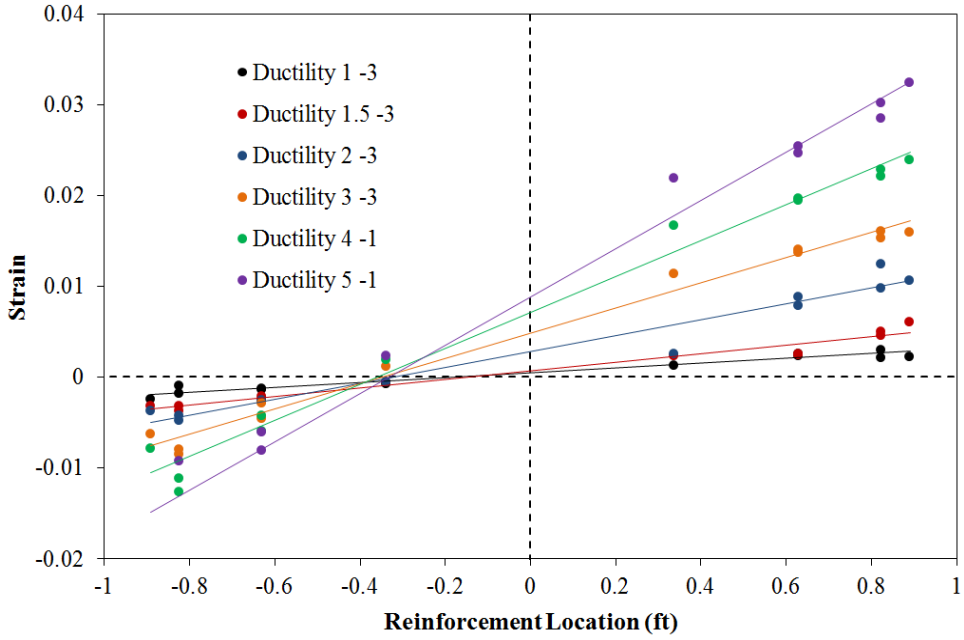

Figure 1.833 T27 – Strain Profiles during Pull Cycles for Section 3.58" Above Footing

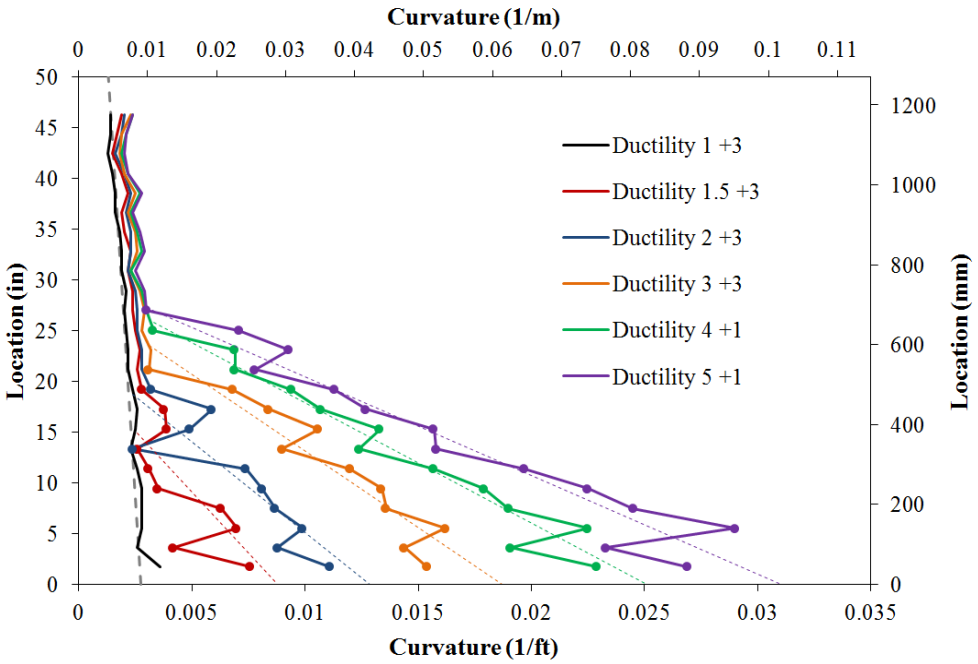

Figure 1.834 T27 – Push Cycle Curvature Profiles with Linear Plastic Regression

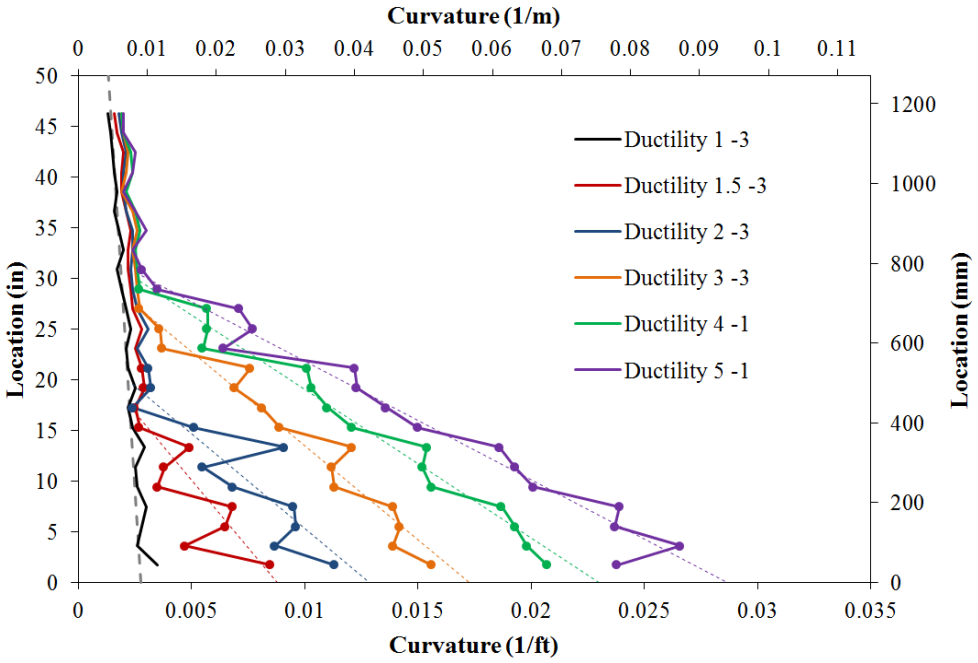

Figure 1.835 T27 – Pull Cycle Curvature Profiles with Linear Plastic Regression

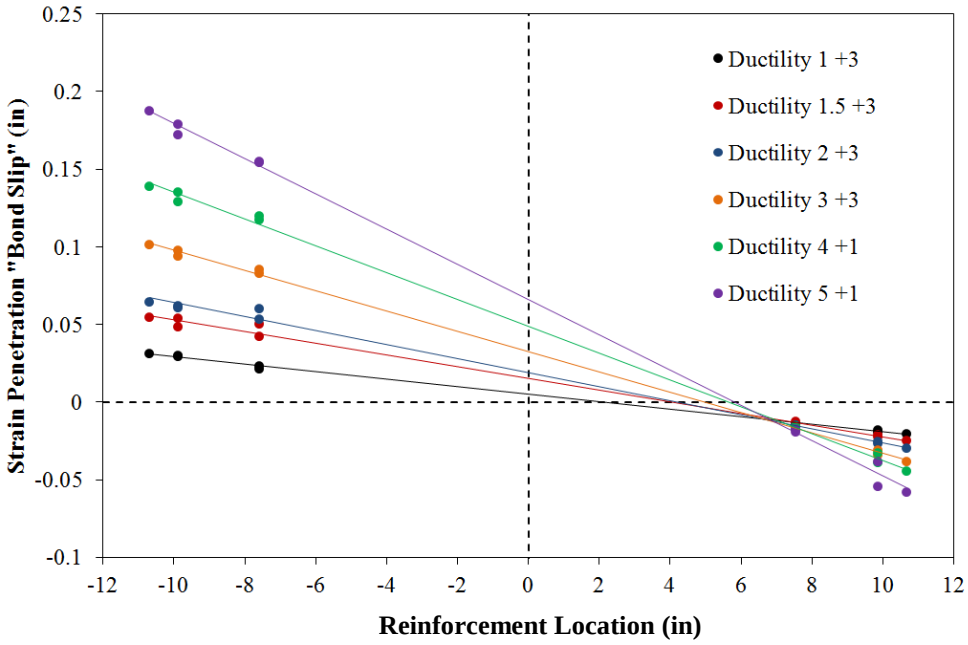

Figure 1.836 T27 – Base Rotation due to Strain Penetration during Push Cycles

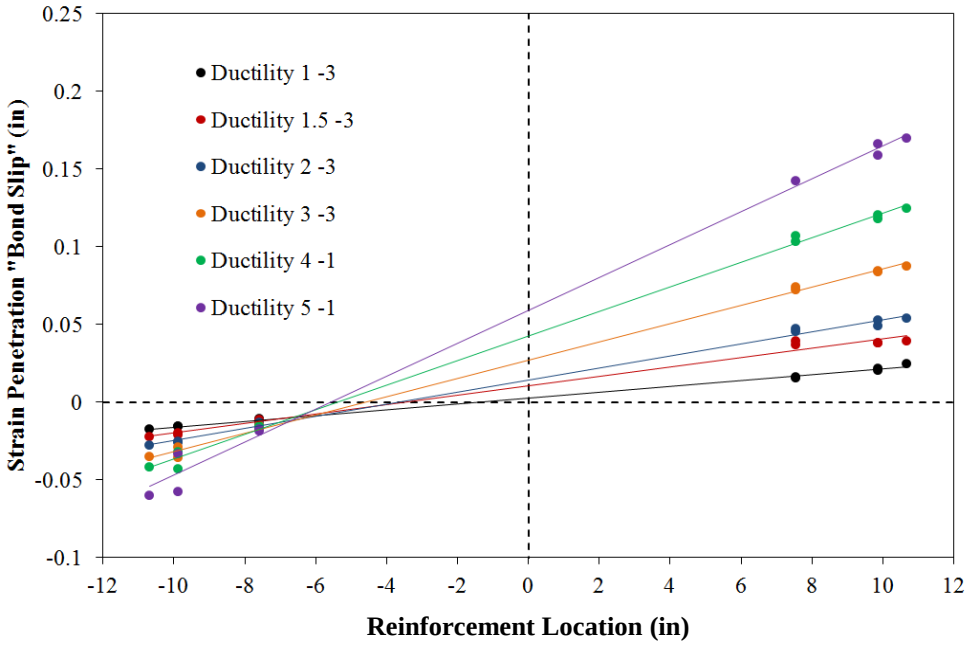

Figure 1.837 T27 – Base Rotation due to Strain Penetration during Pull Cycles

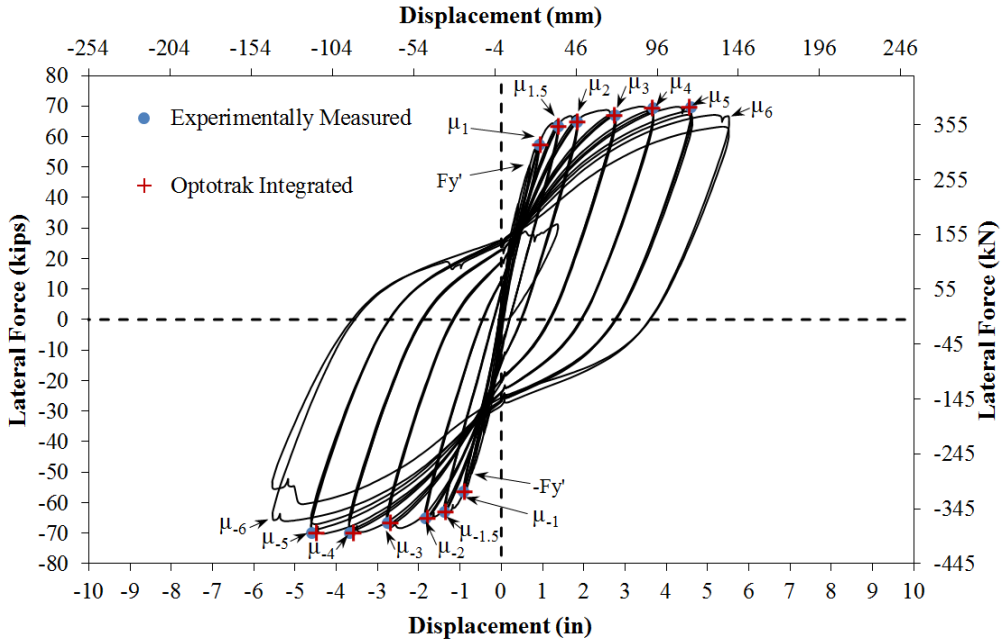

Figure 1.838 T27 – Comparison of Measured and Optotrak Integrated Displacements

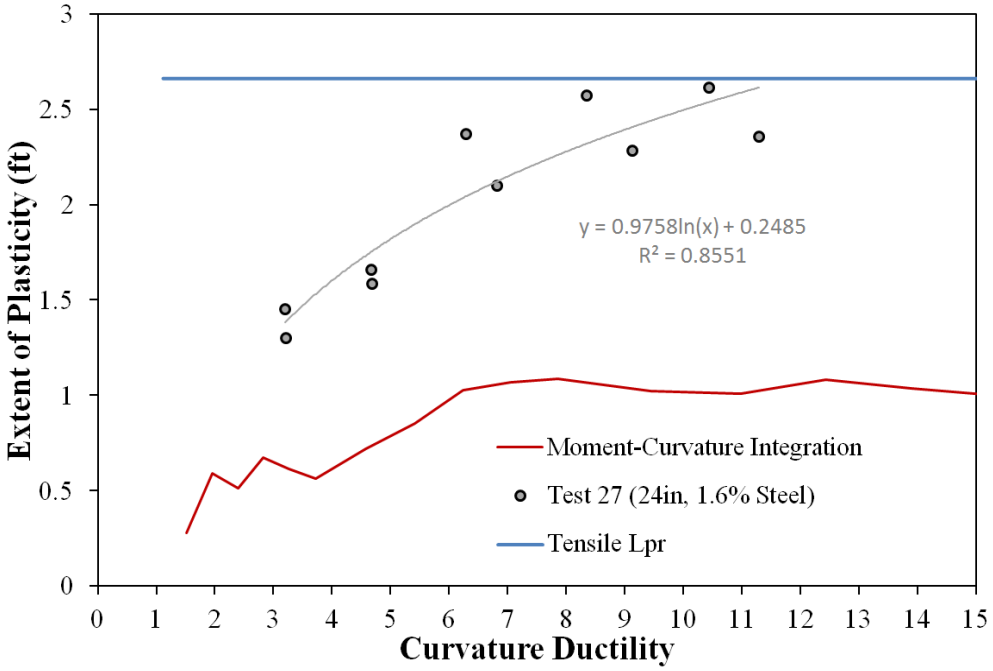

Figure 1.839 T27 – Measured Spread of Plasticity (Circular Data Points)

1.4.4 Test 28 – 18" Dia. Column with 1.7% Long. Steel and 15% Axial Load

Table 1.53 Observations for Test 28 – 18" Dia. With 1.7% Steel and 15% Axial Load

VALUES OF INTEREST:	
Concrete Compressive Strength:	$f_c' = 6239\ psi$
Axial Load:	$P = 212.4\ kips\ \ (P/(f_c' A_g) = 15\%)$
Longitudinal Steel Content:	10 #6 $Bars\ \ (A_{st}/A_g = 1.7\%)$
Analytical First Yield Force:	$F_y' = 25.17\ kips$
Experimental First Yield Displacement:	$\Delta_y' = 1.05"$
Analytical Nominal Moment Capacity:	$M_n = 255.23\ kip * ft$
Equivalent Yield Displacement:	$\Delta_y = 1.34"$
Maximum Lateral Force:	$31.94\ kips$
DAMAGE OBSERVATIONS:	
First Cracking North:	$3/4Fy' = 0.60"$
First Cracking South:	$-1/2Fy' = -0.33"$
Cover Concrete Crushing North:	$\mu_{1.5}^{-3} = -2.00"$
Cover Concrete Crushing South:	$\mu_{1.5}^{+3} = 2.00"$
Transverse Steel Yield North:	At $-3.72"$ during pull to $\mu_3^{-1} = -4.00"$
Transverse Steel Yield South:	At $3.20"$ during push to $\mu_3^{+1} = 4.00"$
Longitudinal Bar Buckling North:	Reversal from $\mu_5^{+2} = 6.68"$
Longitudinal Bar Buckling South:	Reversal from $\mu_4^{-3} = -5.34"$
Longitudinal Bar Fracture North:	At $6.92"$ during push to $\mu_6^{+2} = 8.00"$
Longitudinal Bar Fracture South:	At $-2.94"$ during pull to $\mu_6^{-2} = -8.01"$

*$\mu_5^{+2} = 6.68"$ represents the second push cycle of displacement ductility five

Table 1.54 Strain Data Summary for Test 28 – 18" Dia. with 1.7% Steel and 15% Axial

MATERIAL STRAINS:	
Cover Concrete Crushing North:	$\varepsilon_s = 0.0051\ (compression)$
Cover Concrete Crushing South:	$\varepsilon_s = 0.0055\ (compression)$
Transverse Steel Yield North:	$\varepsilon_s = 0.0123\ (compression)$
Transverse Steel Yield South:	$\varepsilon_s = 0.0143\ (compression)$
Longitudinal Bar Buckling North:	$\varepsilon_s = 0.036\ (peak\ tension\ prior\ to\ bb)$
	$\varepsilon_s = 0.034\ (peak\ comp.\ prior\ to\ bb)$
Longitudinal Bar Buckling South:	$\varepsilon_s = 0.030\ (peak\ tension\ prior\ to\ bb)$
	$\varepsilon_s = 0.024\ (peak\ comp.\ prior\ to\ bb)$
Mander (1988) Ultimate Concrete Compression Strain, $\varepsilon_{cu} = 0.0194$	

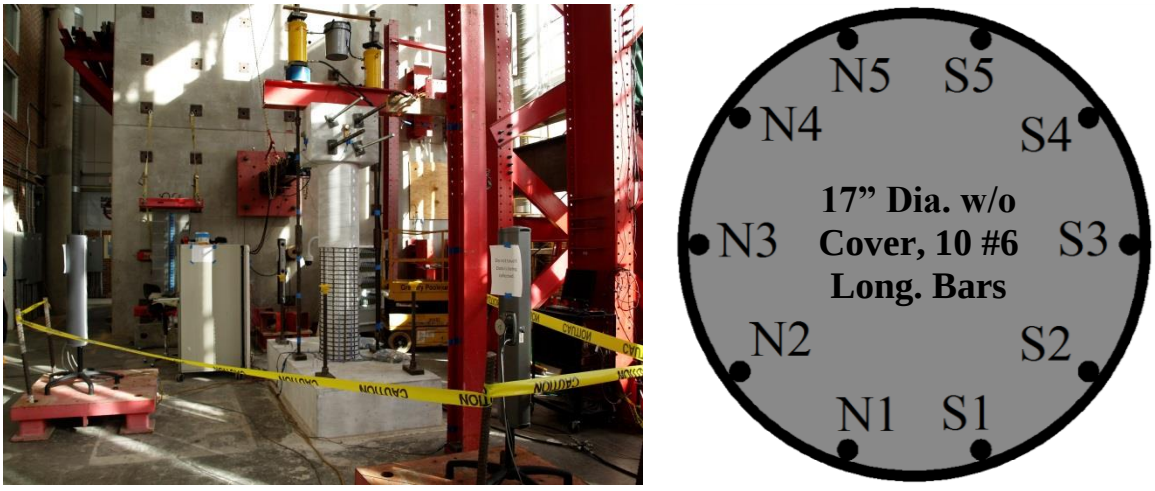

Figure 1.840 T28 – Test Setup and Cross Section Bar Designation

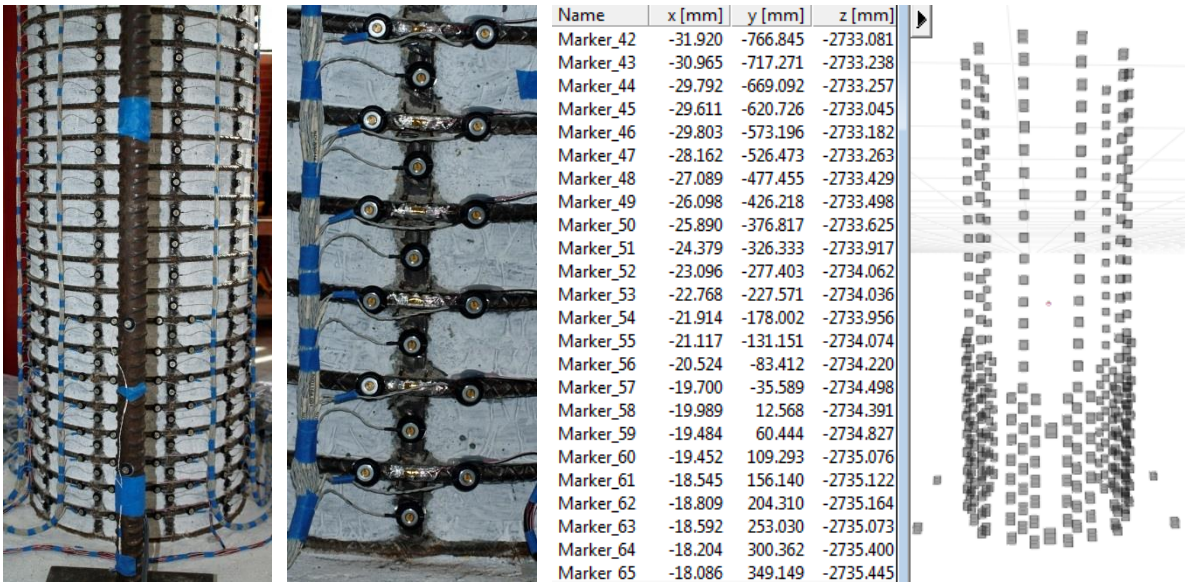

Name	x [mm]	y [mm]	z [mm]
Marker_42	-31.920	-766.845	-2733.081
Marker_43	-30.965	-717.271	-2733.238
Marker_44	-29.792	-669.092	-2733.257
Marker_45	-29.611	-620.726	-2733.045
Marker_46	-29.803	-573.196	-2733.182
Marker_47	-28.162	-526.473	-2733.263
Marker_48	-27.089	-477.455	-2733.429
Marker_49	-26.098	-426.218	-2733.498
Marker_50	-25.890	-376.817	-2733.625
Marker_51	-24.379	-326.333	-2733.917
Marker_52	-23.096	-277.403	-2734.062
Marker_53	-22.768	-227.571	-2734.036
Marker_54	-21.914	-178.002	-2733.956
Marker_55	-21.117	-131.151	-2734.074
Marker_56	-20.524	-83.412	-2734.220
Marker_57	-19.700	-35.589	-2734.498
Marker_58	-19.989	12.568	-2734.391
Marker_59	-19.484	60.444	-2734.827
Marker_60	-19.452	109.293	-2735.076
Marker_61	-18.545	156.140	-2735.122
Marker_62	-18.809	204.310	-2735.164
Marker_63	-18.592	253.030	-2735.073
Marker_64	-18.204	300.362	-2735.400
Marker 65	-18.086	349.149	-2735.445

Figure 1.841 T28 – Target Marker Application and Optotrak Spatial Output

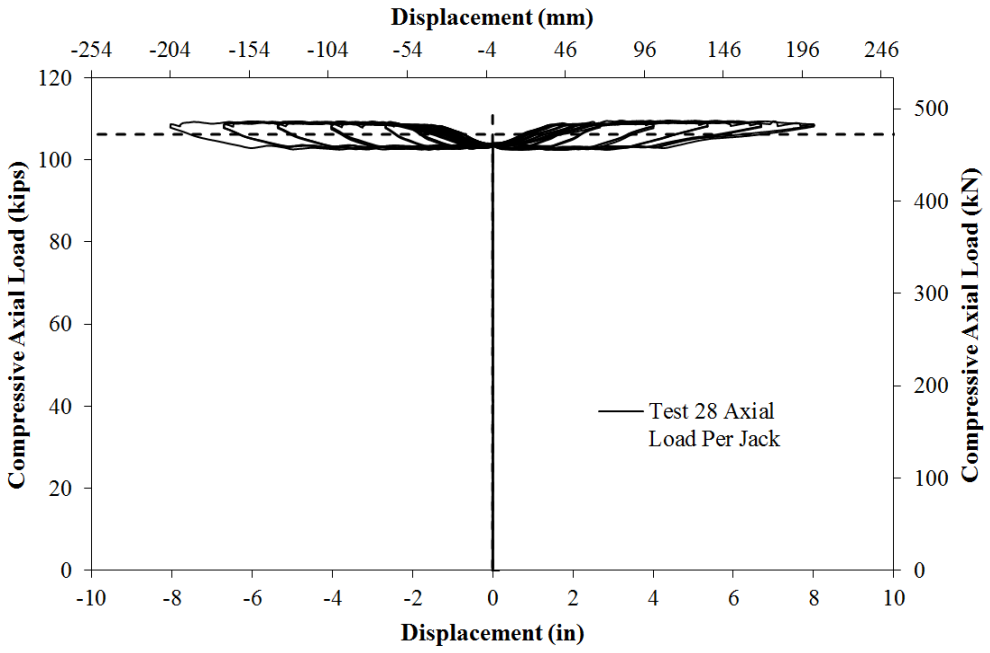

Figure 1.842 T28 – Compressive Axial Load from One Jack (Total = 2*Value)

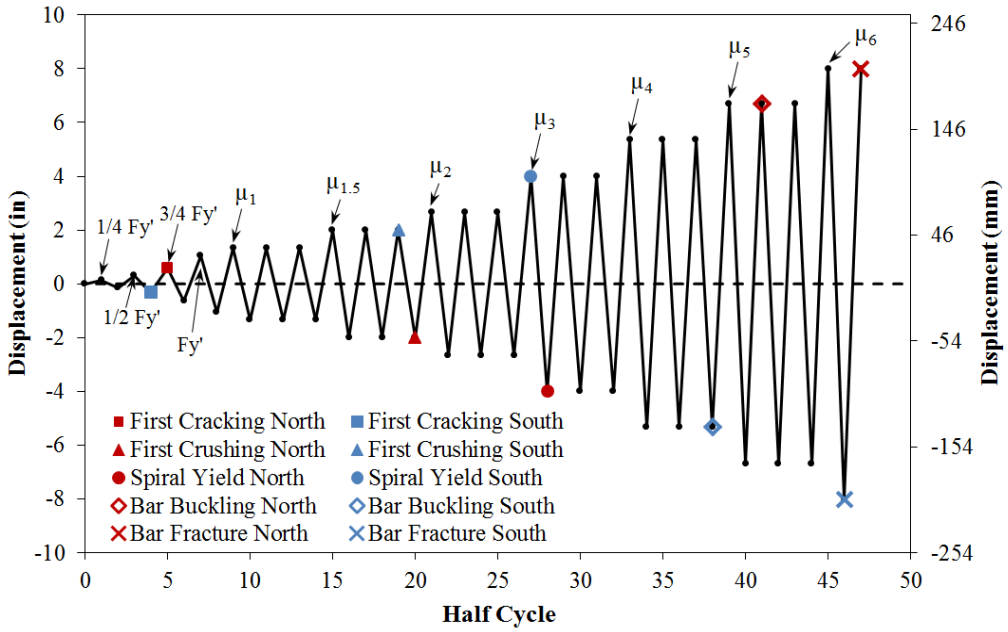

Figure 1.843 T28 – Symmetric Three Cycle Set Load History

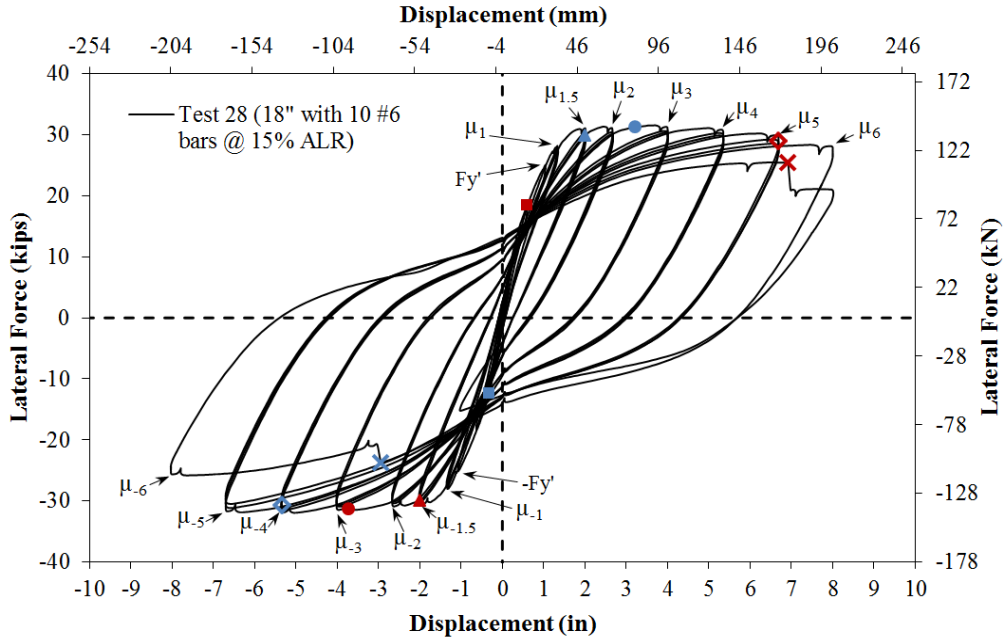

Figure 1.844 T28 – Lateral Force vs. Top Column Displacement Response

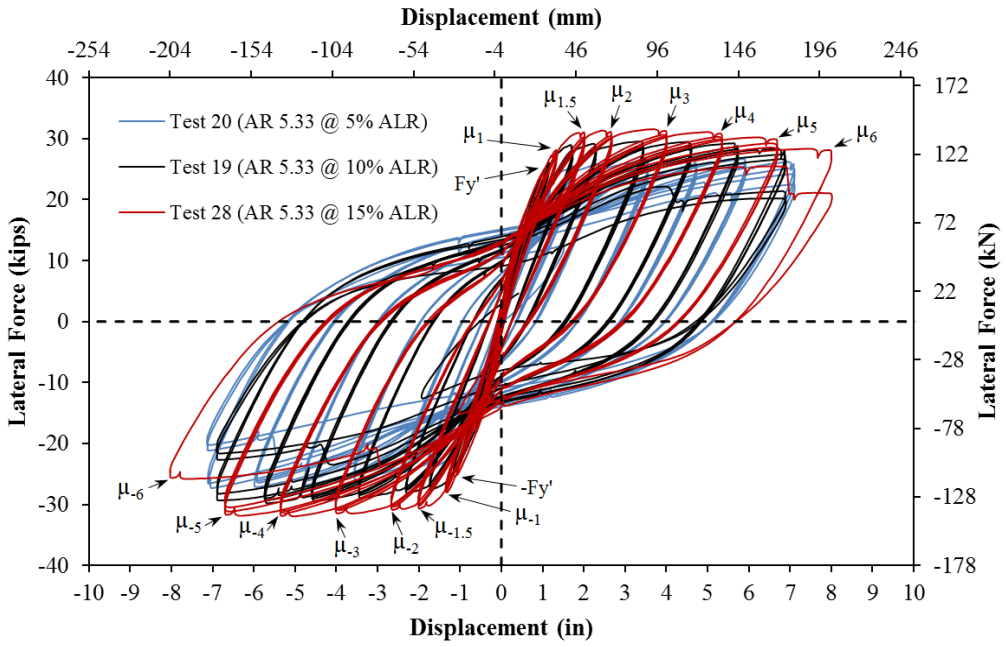

Figure 1.845 T28 – Comparison of T19, T20, and T28 with Different Axial Load Levels

Test 28 – 18" Dia. with 1.7% Steel and 15% Axial Load – Experimental Observations

Specimens 25-30 focus on the effects of longitudinal steel content, longitudinal bar diameter, and higher levels of axial load on column behavior. The 18" diameter column chosen for Test 28 contains 10 #6 (A706) bars for longitudinal reinforcement ($A_{st}/A_g =$ 1.7%) and a #3 A706 spiral at 2" on center ($4A_{sp}/(D's) = 1.3\%$). The specimen had an 8ft cantilever length ($L/D = 5.33$), and was subjected to ($P/(f_c'A_g) = 15\%$) axial load. The experiments utilized a quasi-static displacement controlled loading procedure. The symmetric three-cycle-set load history is commonly used to evaluate the seismic performance of structural components. The load history begins with elastic cycles to the following increments of the analytically predicted first yield force: ¼ F_y', ½ F_y', ¾ F_y', and F_y'. The experimental first yield displacement is then determined by taking the average of the recorded displacements during the first yield push and pulls cycles. The equivalent yield

displacement, used to determine the displacement ductility levels ($\mu_{\Delta 1} = 1 * \Delta_y$), is then calculated as $\Delta_y = \Delta'_y(M_n/M'_y)$. The symmetric three-cycle-set load history resumes with three balanced cycles at each of the following displacement ductility levels: 1, 1.5, 2, 3, 4, 5, etc. The lateral displacement history and resulting hysteretic response for Test 28 appear in Figure 1.843 and Figure 1.844. Previous Tests 19 and 20 contained similar geometry and detailing, but had 10% and 5% axial load. A hysteretic comparison of the Tests 19, 20 and 28 is shown in Figure 1.845.

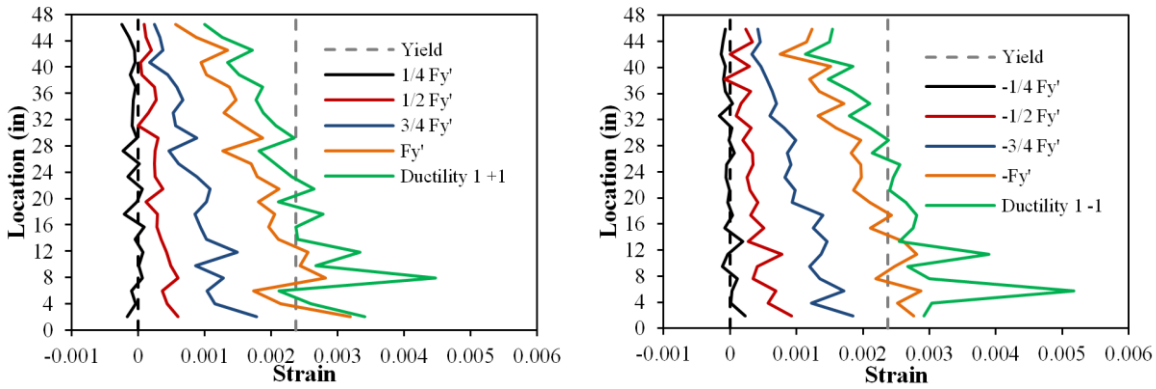

Figure 1.846 T28 – Strain Profiles before Yield, (Left) North and (Right) South

The test began with cycles in ¼ Fy' (first yield force) increments in each direction of loading until the first yield force was reached. The first cracks on the north and south sides of the specimen formed during ($3/4Fy' = 0.60$") and ($-1/2Fy' = -0.33$") respectively, Figure 1.847. The crack distribution on all sides of the specimen at first yield, ($Fy' = 1.04$") and ($-Fy' = -1.07$"), appears in Figure 1.848. Tensile vertical strain profiles for north and south reinforcing bars during elastic push and pull cycles appear in Figure 1.846. The average experimental first yield displacement was used to calculate the equivalent yield displacement, $\Delta_y = \Delta'_y(M_n/M'_y) = 1.05$", which defined the reversal amplitudes for reminder of the test.

The crack progression at displacement ductility 1, 1.5, 2, 3, and 4 appear in Figure 1.849, Figure 1.851, Figure 1.853, Figure 1.855, and Figure 1.857 respectively. During these

cycles the cracks became more numerous and increased in inclination on the shear faces of the specimen. Small amounts concrete flaking was observed on the south and north sides of the specimen during ($\mu_{1.5}^{+3} = 2.00$") and ($\mu_{1.5}^{-3} = -2.00$"), Figure 1.850. In previous tests, this flaking leads to crushing during subsequent cycles, but crushing was not observed until displacement ductility two. Crushing on the south and north sides of the specimen increased at ($\mu_{2}^{+1} = 2.66$") and ($\mu_{2}^{-1} = -2.65$"), Figure 1.852. As compressive demands increased during displacement ductility 1.5 to 4, crushing gradually increased on each side of the specimen. Compressive demand during ($\mu_{3}^{+1} = 4.00$") and ($\mu_{3}^{-1} = -4.00$") led to spiral yielding in confinement regions, Figure 1.854. Spiral strains on each side of the specimen increased during each successive cycle of ductility four, but the extreme fiber reinforcement remained visibly straight, Figure 1.856.

The south extreme fiber bar S3 visibly buckled during ($\mu_{5}^{+1} = 6.68$"), as shown in the left photo of Figure 1.858. The outward buckled region occurred over the second and third gage lengths above the footing. The buckled deformation of bar S3 increased during ($\mu_{5}^{+2} = 6.68$"), Figure 1.859. The north extreme fiber bar visibly buckled after reversal from ($\mu_{5}^{+2} = 6.68$"), Figure 1.860. The buckled deformation of bar N3 increased over the fourth gage length above the footing during ($\mu_{5}^{-3} = -6.69$"), Figure 1.860. The previously buckled south extreme fiber bar ruptured during ($\mu_{6}^{-1} = -8.01$"), Figure 1.861. Bar S3 ruptured at the same location where the outward deformation was the largest during ($\mu_{6}^{+1} = 8.00$"). An additional north reinforcing bar, N2, buckled during ($\mu_{6}^{-1} = -8.01$"), Figure 1.862. The previously buckled north extreme fiber bar N3 ruptured during ($\mu_{6}^{+2} = 8.00$"), Figure 1.863. Two additional south reinforcing bars, S2 and S4, buckled during ($\mu_{6}^{+2} = 8.00$"), Figure 1.863. At this time the test was concluded with ruptured reinforcement on each side of the specimen which led to significant losses in strength in each direction of loading. Photos of the specimen after the instrumentation was removed appear in Figure 1.864 and Figure 1.865.

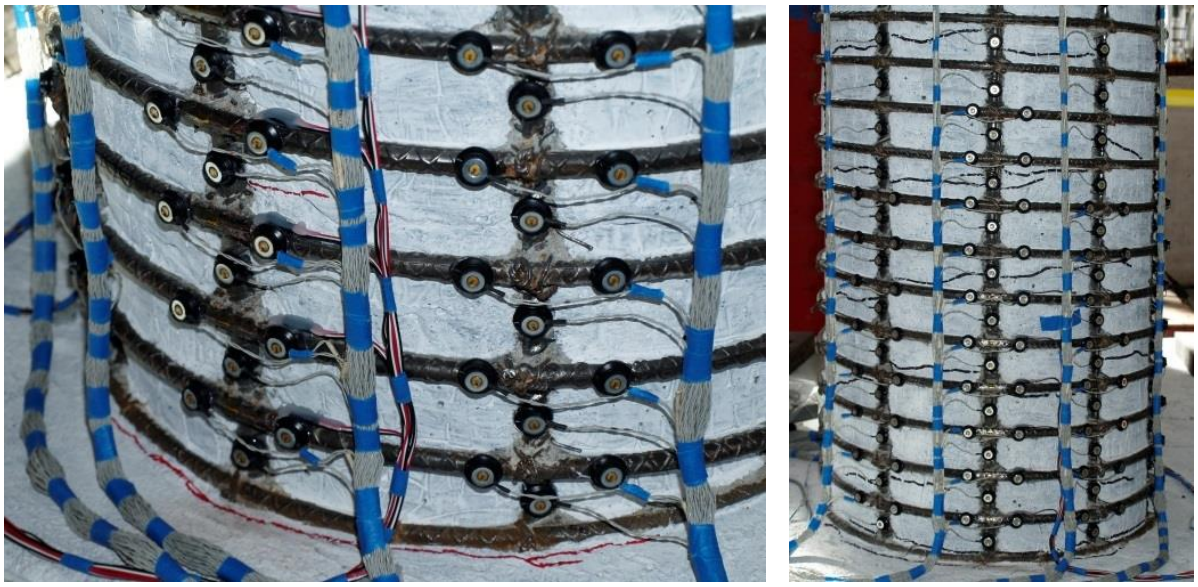

Figure 1.847 T28 – (Left) Cracking on the South Side during ($-1/2Fy' = -0.33$"), (Right) North Cracking ($3/4Fy' = 0.60$")

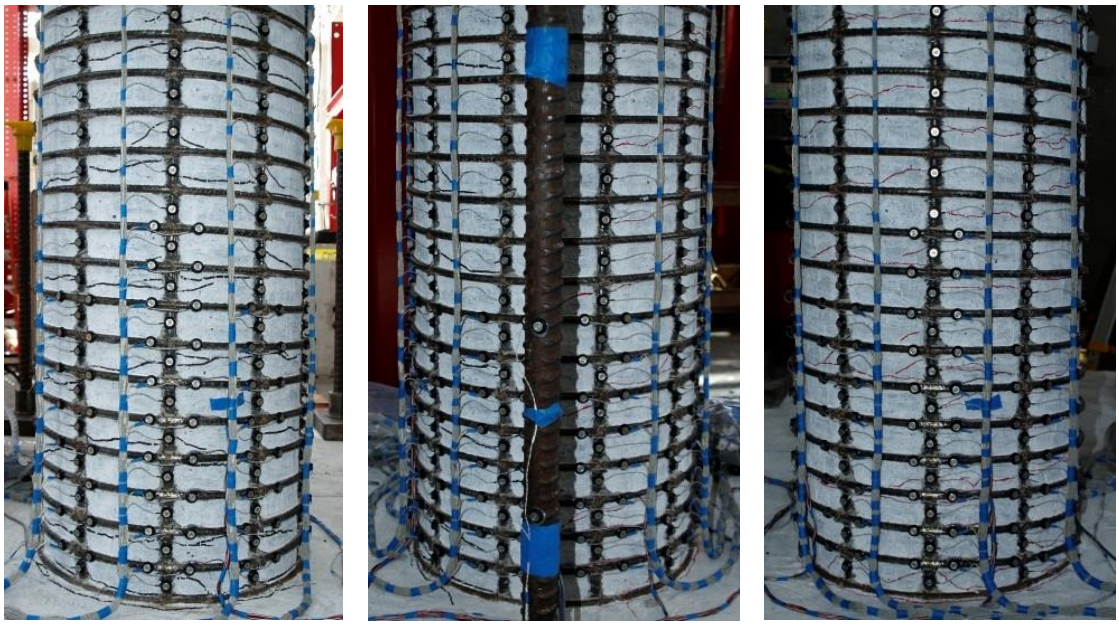

Figure 1.848 T28 – (Left) North Crack Distribution at ($Fy' = 1.04$"), (Middle and Right) Crack Distributions on the Front and Right Sides at ($-Fy' = -1.07$")

Figure 1.849 T28 – (Left) North Crack Distribution at ($\mu_1^{+3} = 1.34$"), (Middle and Right) Crack Distributions on the Front and Right Sides at ($\mu_1^{-3} = -1.34$")

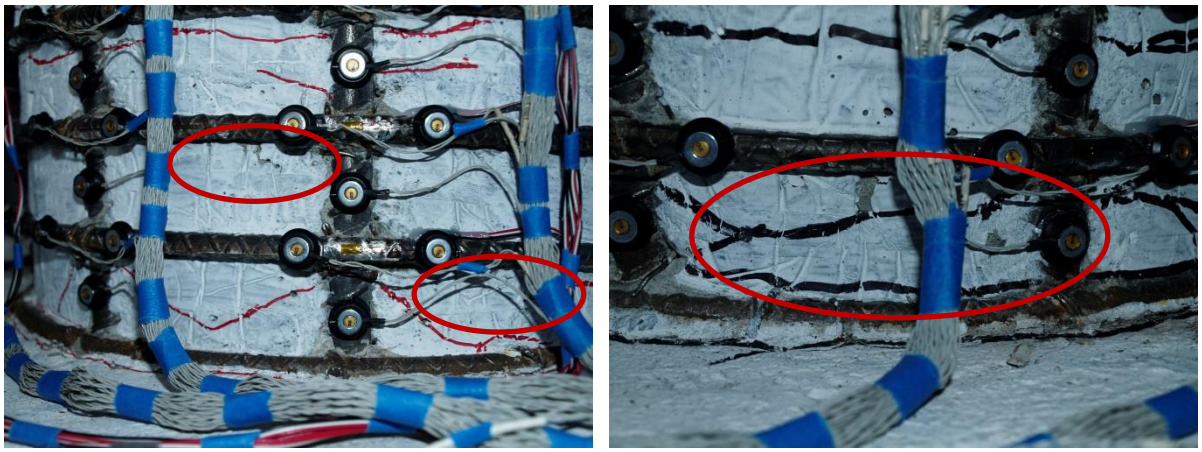

Figure 1.850 T28 – (Left) South Concrete Flaking during ($\mu_{1.5}^{+3} = 2.00$"), (Right) North Concrete Flaking during ($\mu_{1.5}^{-3} = -2.00$")

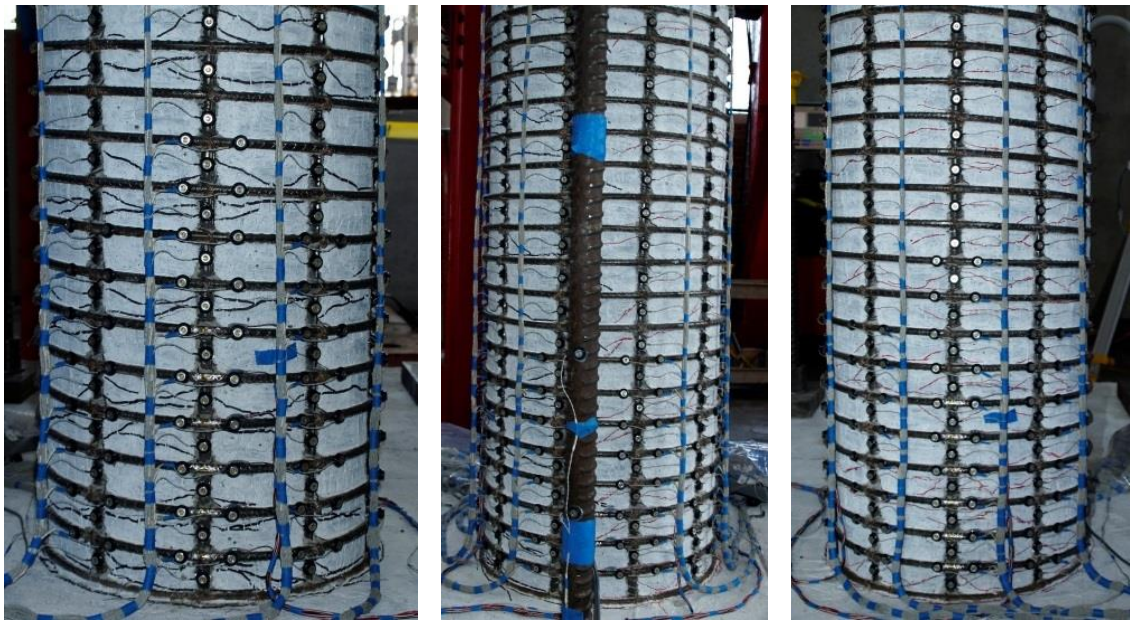

Figure 1.851 T28 – (Left) North Crack Distribution at ($\mu_{1.5}^{+3} = 2.00$"), (Middle and Right) Crack Distributions on the Front and Right Sides at ($\mu_{1.5}^{-3} = -2.00$")

Figure 1.852 T28 – (Left) South Crushing during ($\mu_{2}^{+1} = 2.66$"), (Right) North Crushing during ($\mu_{2}^{-1} = -2.65$")

Figure 1.853 T28 – (Left) North Crack Distribution at ($\mu_2^{+3} = 2.67$"), (Middle and Right) Crack Distributions on the Front and Right Sides at ($\mu_2^{-3} = -2.66$")

Figure 1.854 T28 – (Left) South Spiral Yield at ($\mu_3^{+1} = 4.00$"), (Right) North Spiral Yield at ($\mu_3^{-1} = -4.00$")

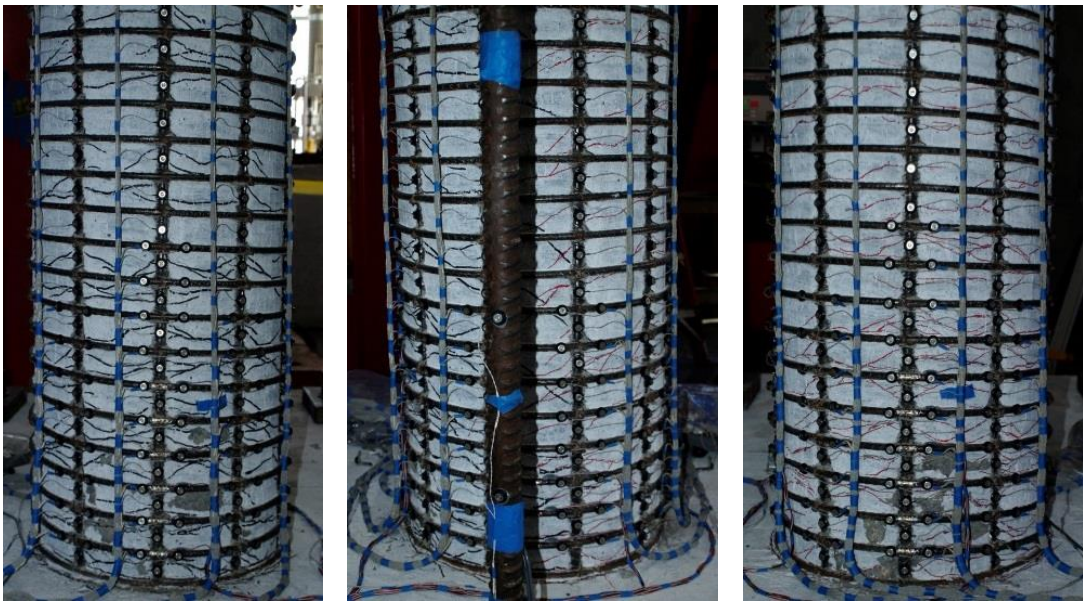

Figure 1.855 T28 – (Left) North Crack Distribution at ($\mu_3^{+3} = 4.00$"), (Middle and Right) Crack Distributions on the Front and Right Sides at ($\mu_3^{-3} = -4.00$")

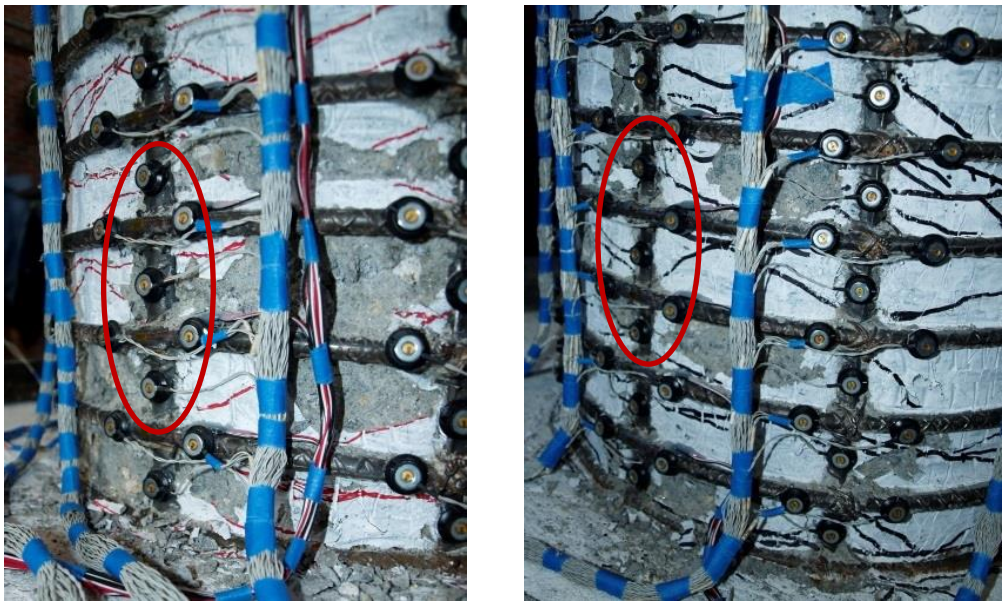

Figure 1.856 T28 – (Left) Bar S3 Remained Visibly Straight during ($\mu_4^{+3} = 5.34$"), (Right) Bar N3 Remained Visibly Straight during ($\mu_4^{-3} = -5.34$")

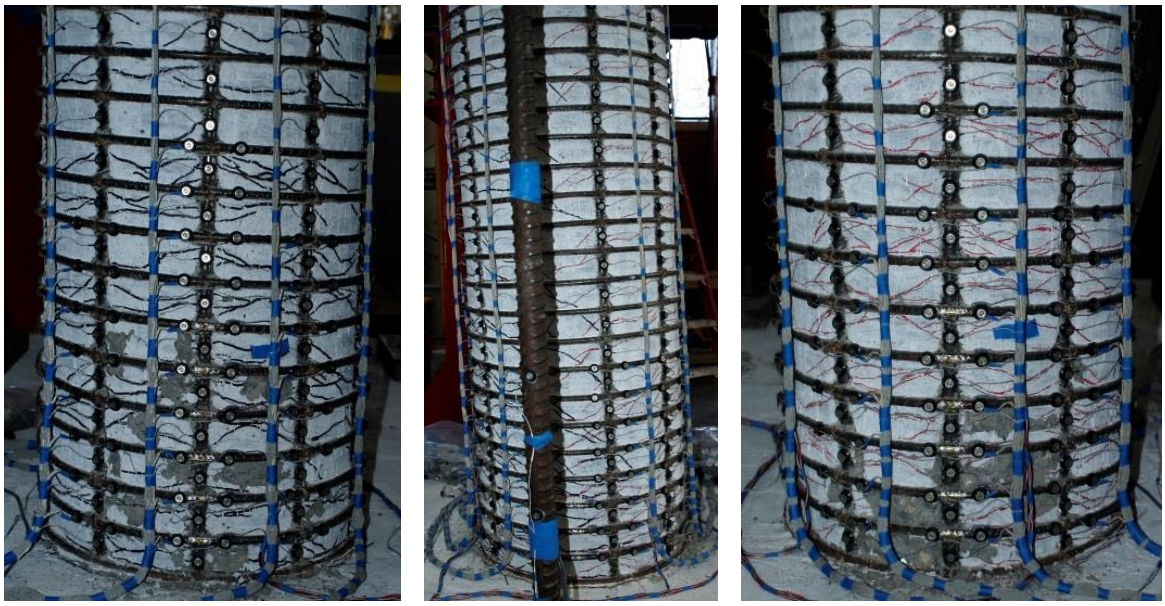

Figure 1.857 T28 – (Left) North Crack Distribution at ($\mu_4^{+3} = 5.34$"), (Middle and Right) Crack Distributions on the Front and Right Sides at ($\mu_4^{-3} = -5.34$")

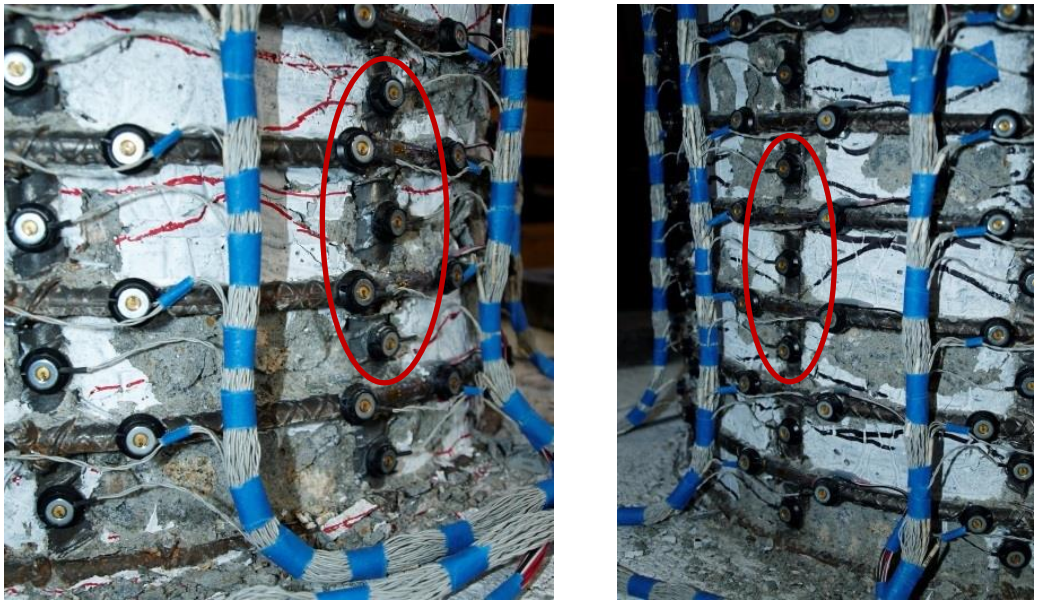

Figure 1.858 T28 – (Left) Visible Buckling of Bar S3 during ($\mu_5^{+1} = 6.68$"), (Right) Bar N3 Remained Visibly Straight during ($\mu_5^{-1} = -6.68$")

Figure 1.859 T28 – (Left) Lateral Deformation and (Right) Increased Deformation in Bar S3 during ($\mu_5^{+2} = 6.68$")

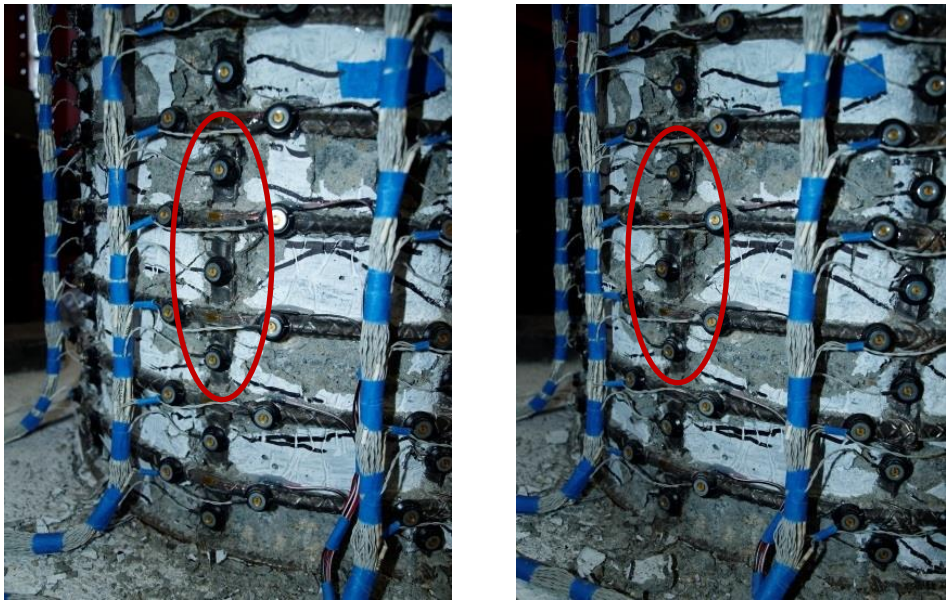

Figure 1.860 T28 – (Left) Visible Buckling of Bar N3 during ($\mu_5^{-2} = -6.69$"), (Right) Increased Deformation in Bar N3 during ($\mu_5^{-3} = -6.69$")

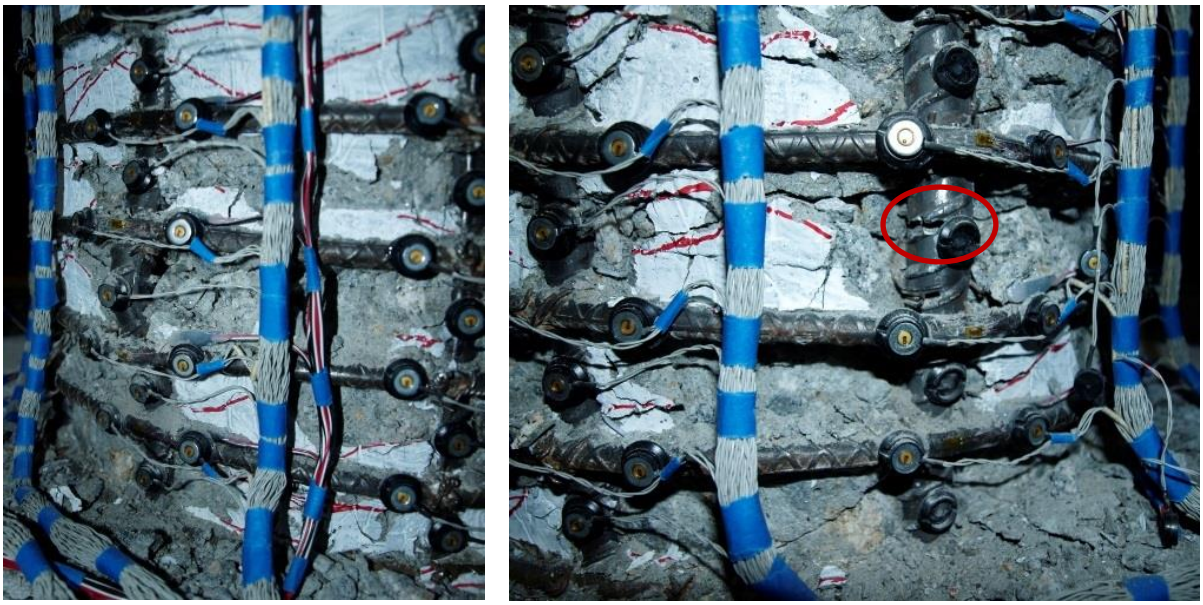

Figure 1.861 T28 – (Left) Increased Deformation in Bar S3 ($\mu_6^{+1} = 8.00$"), (Right) Fracture of Bar S3 during ($\mu_6^{-1} = -8.01$")

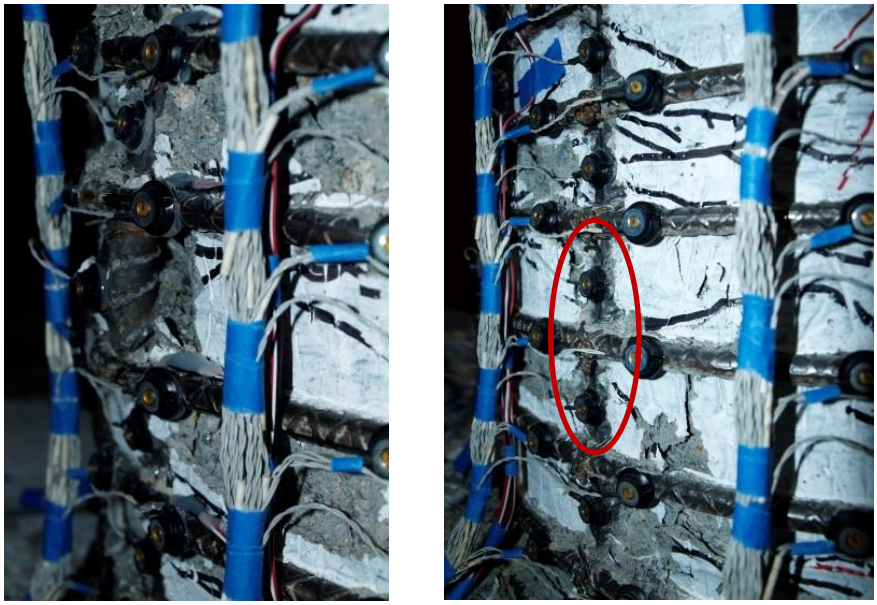

Figure 1.862 T28 – (Left) Increased Deformation in Bar N3 during ($\mu_6^{-1} = -8.01$"), (Right) Buckling of Adjacent Bar N2 during ($\mu_6^{-1} = -8.01$")

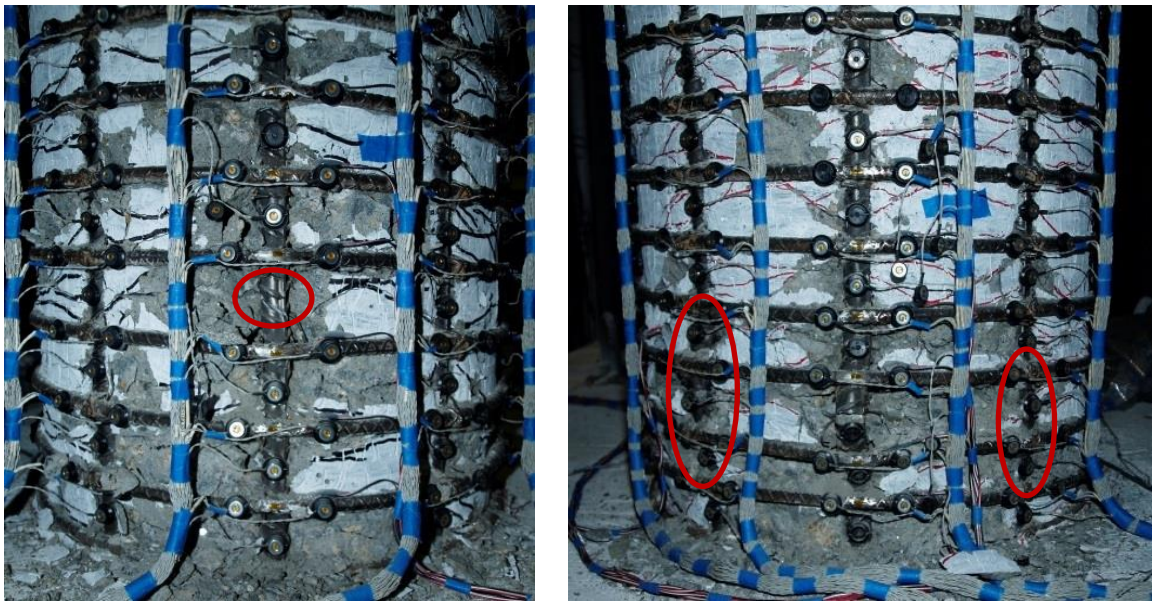

Figure 1.863 T28 – (Left) Fracture of Bar N3 during ($\mu_6^{+2} = 8.00$"), (Right) Buckling of Adjacent Bars S2 and S4 during ($\mu_6^{+2} = 8.00$")

Figure 1.864 T28 – After the Test (Left) South Side and (Right) North Side

Figure 1.865 T28 – After the Test (Left) Front Side and (Right) Back Side

Test 28 – 18" Dia. with 1.7% Steel and 15% Axial Load – Strain Data Analysis

North Reinforcement

Vertical strain profiles for the north extreme fiber bar N3, which is placed into tension during push cycles, appear in the right half of Figure 1.866. This figure shows both extreme fiber bars on the same graph. Compressive vertical strain profiles for north extreme fiber bar N3 during pull cycles appear in the left half of Figure 1.867. A peak tensile strain of 0.0362 was measured 3.99" above the footing on bar N3 during ($\mu_5^{+2} = 6.68"$), before bar buckling was observed during ($\mu_5^{-2} = -6.69"$). The relationship between tension strain and displacement for the gage lengths 2.04" and 5.92" above the footing appear in Figure 1.870 and Figure 1.871. Moment-curvature analysis with the PCK (2007) Lp Hinge Method begins to over predict the measured tensile strains at an increasing rate beyond displacement ductility two for both gage lengths. A compressive strain of –0.012 was measured 3.99" and 9.83" above the footing on bar N3 during ($\mu_3^{-1} = -4.00"$), when the first spiral in the confinement region yielded. The relationship between compressive strain and displacement

for the bar N3 gage length 9.83" above the footing appears in Figure 1.872. The measured compressive strains exceed the moment-curvature prediction with the PCK (2007) Lp Hinge Method beyond displacement ductility two. Successive pull cycles during displacement ductility four produced larger compressive strains. The gage length 9.83" above the footing was located just above the outward buckled deformation, Figure 1.860, suggesting that the measured strains may have been influenced by deformation before visible buckling.

Measured spiral strains in six layers which overlaid the north extreme fiber bar appear in Figure 1.869. Spiral tension strains in the third and fourth layers above the footing increased during each successive pull cycle of displacement ductility four. A spiral strain hysteresis for the layer 7.97" above the footing which overlaid the outward deformed region of bar N3 appears in Figure 1.878. The hysteresis contains spiral data from a strain gage and an Optotrak gage length, Figure 1.841. The Optotrak strains were calculated using arc-lengths obtained from measured 3D distance chord lengths and the known outside diameter of the spiral. It is important to note that arc-length calculations become inaccurate once severe yielding in the spiral leads to the reinforcement straightening out to the left and right of the localized yielding directly over the bar where the strain gage is located. Each consecutive pull cycle of displacement ductility four led to larger inelastic spiral strains, which indicates that measurable outward deformation occurred before visible bar buckling. The sharpest increase in measured spiral strains occurred during ($\mu_5^{-2} = -6.69"$), when visible bar buckling was observed and the strain gage debonded preventing further measurement. The distribution of arc-strains measured around the circumference of the third and fourth spiral layers above the footing during pull cycles appear in Figure 1.887 and Figure 1.888 respectively. The north side of the specimen is on the left side of the graph with negative location values and specific locations of bars N2, N3, and N4 are highlighted with vertical dashed lines.

Strain hysteresis for gage lengths 5.92", 7.87" and 9.83" above the footing on bar N3 appear in Figure 1.875, Figure 1.876, and Figure 1.877. The gage lengths 5.92" and 7.87" above the footing overlaid the region which outwardly deformed during ($\mu_5^{-2} = -6.69"$),

Figure 1.860. The diagram in Figure 1.879 depicts the effect of buckled deformation on strains measured by LEDs attached to the outside surface of reinforcing bars. Gage lengths in the outward deformed region show increased tension during compressive cycles and gage lengths just above show additional compression. The hysteresis 7.87" above the footing remained stable until ($\mu_5^{-1} = -6.69"$) when measured compressive strains deviated from previous trends. By contrast, measurable deformation in the gage length 9.83" above the footing, Figure 1.877, started during displacement ductility three, increased during successive cycles of ductility four, and spiked as the bar buckled during ($\mu_5^{-2} = -6.69"$). The compressive strain values for this gage length may be influenced by measurable deformation, and may not represent the actual level of compression since similar spikes were not observed in adjacent bars N2 and N4.

South Reinforcement

Vertical strain profiles for the south extreme fiber bar S3, which is placed into tension during pull cycles, appear in the right half of Figure 1.867. Compressive vertical strain profiles for south extreme fiber bar S3 during push cycles appear in the left half of Figure 1.866. The peak tension strain of 0.0358 was measured 9.50" above the footing on bar S3 during ($\mu_5^{-1} = -6.68"$). It is important to note that visible bar buckling was observed during ($\mu_5^{+1} = 6.68"$), Figure 1.858. The buckled deformation was small, and the bar was expected to straighten out during ($\mu_5^{-1} = -6.68"$). The peak tension strain prior to visible bar buckling of 0.0299 was measured 5.76" above the footing during ($\mu_4^{-1} = -5.34"$). The relationship between tension strain and displacement for the gage length 7.65" above the footing appears in Figure 1.873. Moment-curvature analysis with the PCK (2007) Lp Hinge Method begins to over predict the measured tension strains at an increasing rate beyond displacement ductility two. A compressive strain of -0.0143 was measured 1.93" above the footing when the first confinement steel yielded on the south side of the specimen during ($\mu_3^{+1} = 4.00"$). A peak compressive strain of -0.0243 was measured over this same gage length during ($\mu_4^{+3} = 5.34"$). Moment-curvature analysis with the PCK (2007) Lp Hinge

Method under predicts the measured compressive strains in the gage length 1.93" above the footing, Figure 1.874.

Measured strains in six spiral layers which overlaid the south extreme fiber bar appear in Figure 1.868 for push cycles. Cycles during displacement ductility four produced successively larger inelastic demands on the second and third spiral layers. Strain gage and Optotrak strain hysteresis for the spiral layer 3.89" and 5.84" above the footing appear in Figure 1.883 and Figure 1.884 respectively. The two measurement methods match well until ($\mu_4^{+1} = 5.35"$), when the effects of measurable deformation became apparent and presumably the arc-strains no longer represent the geometry of the spiral over bar S3. The spiral strains increased during ($\mu_5^{+1} = 4.60"$) when visible bar buckling was observed, Figure 1.858, and increased more significantly as the buckled deformation grew during ($\mu_5^{+2} = 6.68"$). Measured arc-strains around the circumference of the second and third spiral layers on the south side of the specimen during push cycles appear in Figure 1.885 and Figure 1.886. The largest inelastic spiral strains were localized over bars S2, S3, and S4 which are shown on the right side of the figures with vertical dashed lines.

The influence of measurable deformation before bar buckling becomes easier to understand when the specific gage lengths in question are located on buckled bar, Figure 1.879. The second and third gage lengths above the footing overlay the outward deformed region. The strain hysteresis for the gage length 5.76" above the footing, Figure 1.881, shows a significant deviation during ($\mu_5^{+2} = 6.68"$), but not during ($\mu_5^{+1} = 6.68"$) when visible bar buckling was first observed. The gage lengths 1.93" (Figure 1.880) and 7.65" (Figure 1.882) above the footing show additional compression during push cycles for the regions just above and below the outward deformation observed during bar buckling. The largest spiral strains are not measured in layers overlaying the peak compressive gage lengths, but rather the second and third spiral layers which encompassed the outward deformed region, Figure 1.868.

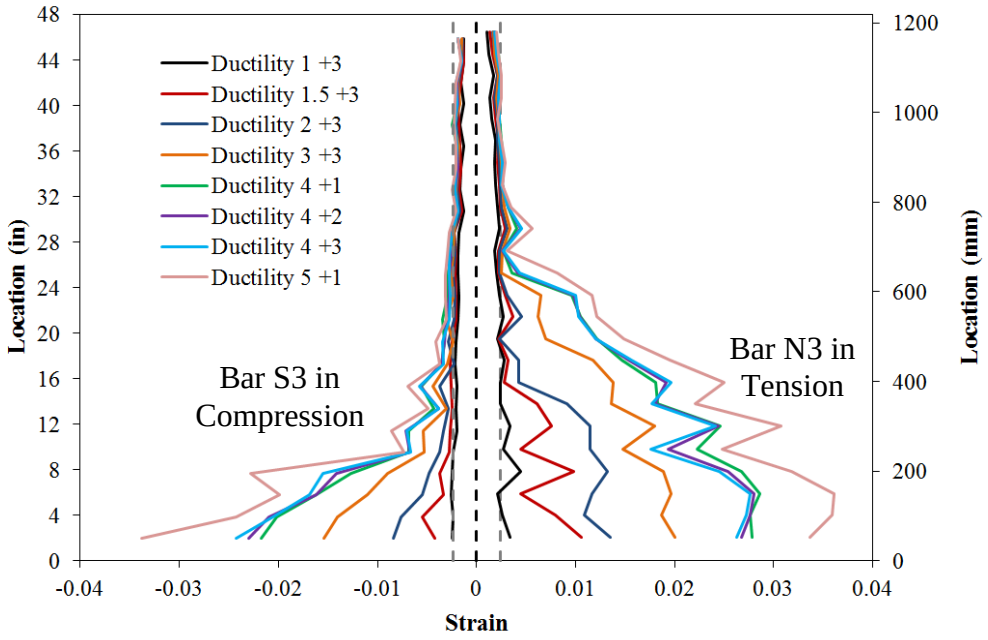

Figure 1.866 T28 – Extreme Fiber Bar Vertical Strain Profiles during Push Cycles

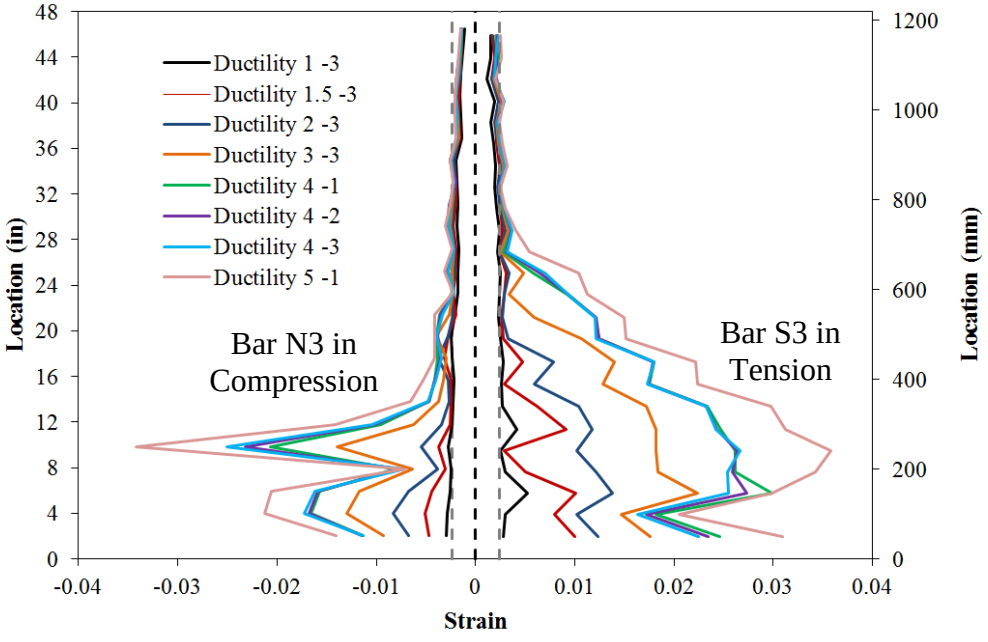

Figure 1.867 T28 – Extreme Fiber Bar Vertical Strain Profiles during Pull Cycles

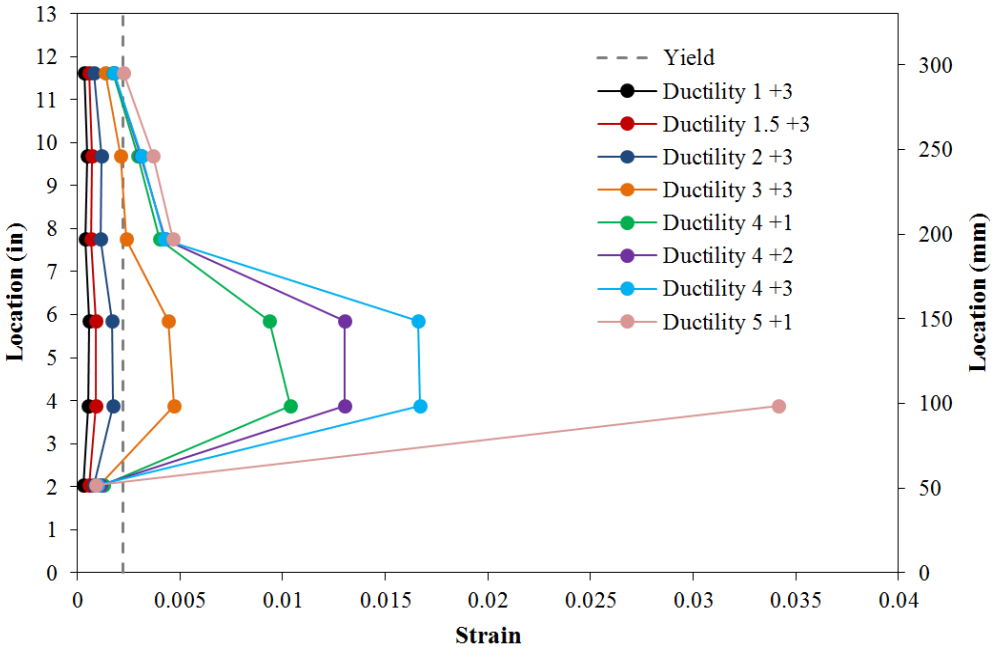

Figure 1.868 T28 – Spiral Strains on the South Side during Push Cycles

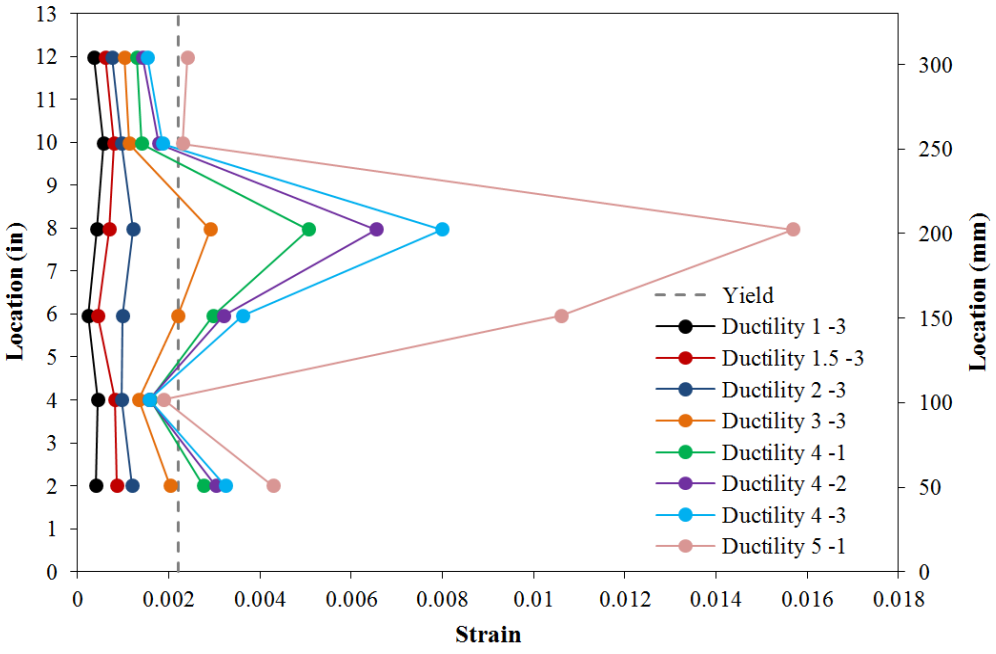

Figure 1.869 T28 – Spiral Strains on the North Side during Pull Cycles

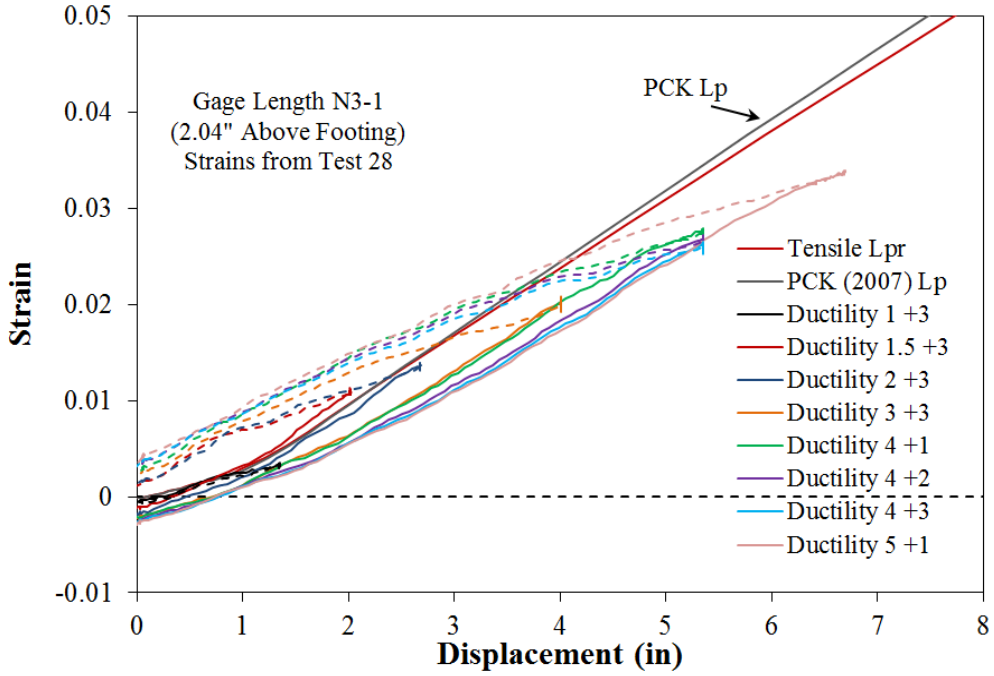

Figure 1.870 T28 – Tensile Strain-Displacement for Bar N3 during Push Cycles

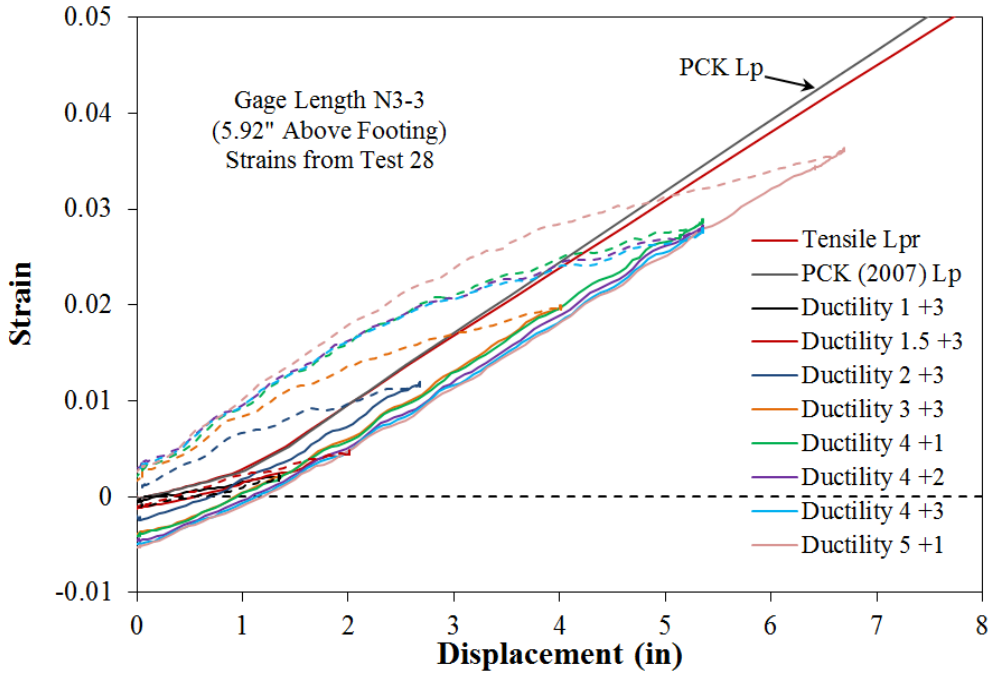

Figure 1.871 T28 – Tensile Strain-Displacement for Bar N3 during Push Cycles

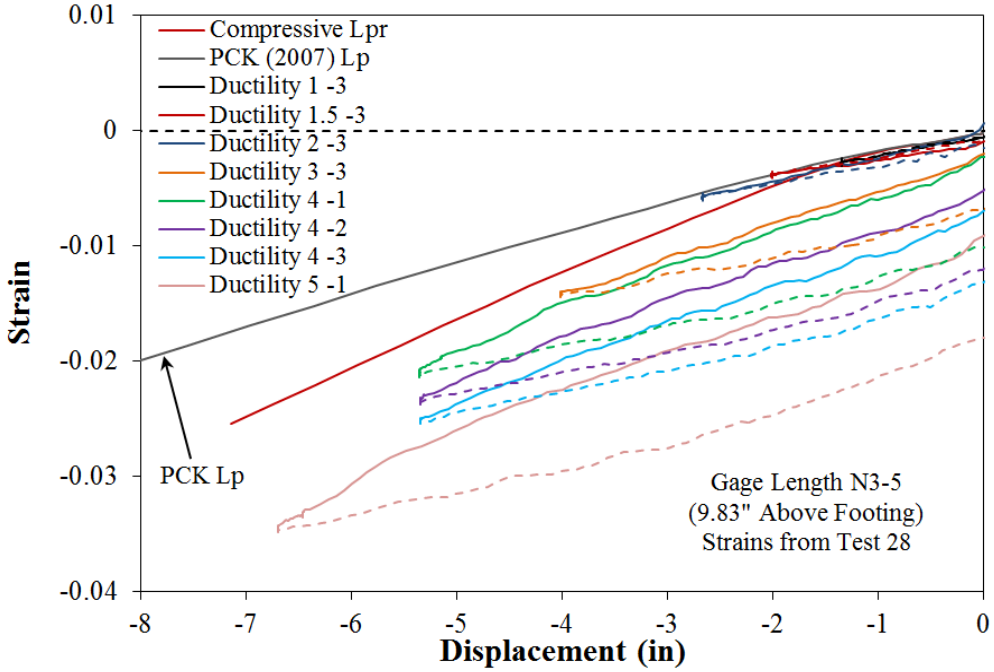

Figure 1.872 T28 – Compressive Strain-Displacement for Bar N3 during Pull Cycles

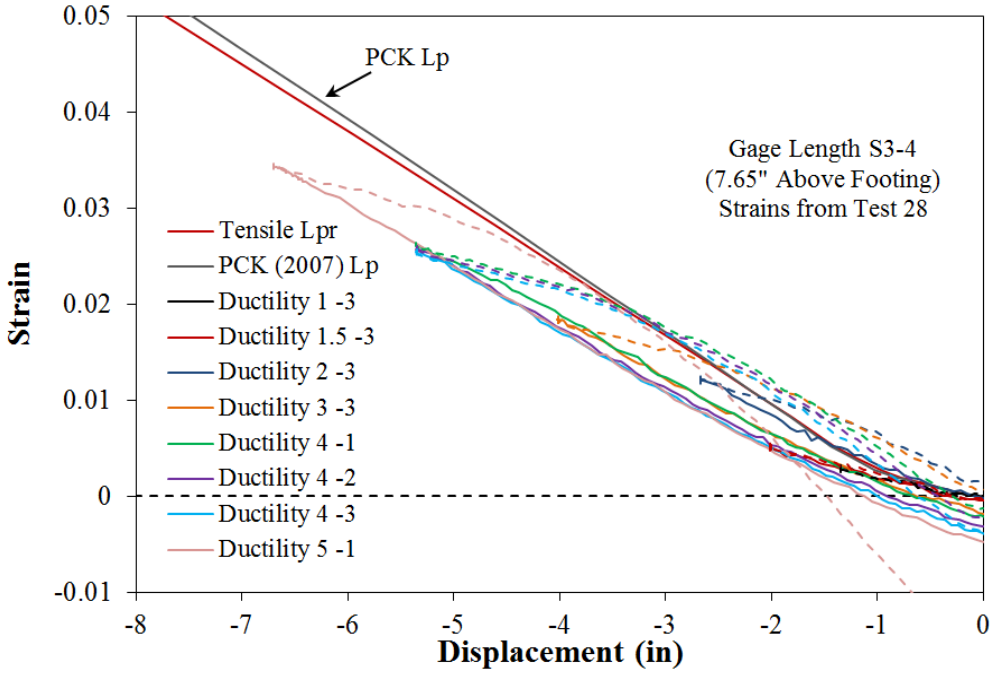

Figure 1.873 T28 – Tensile Strain-Displacement for Bar S3 during Pull Cycles

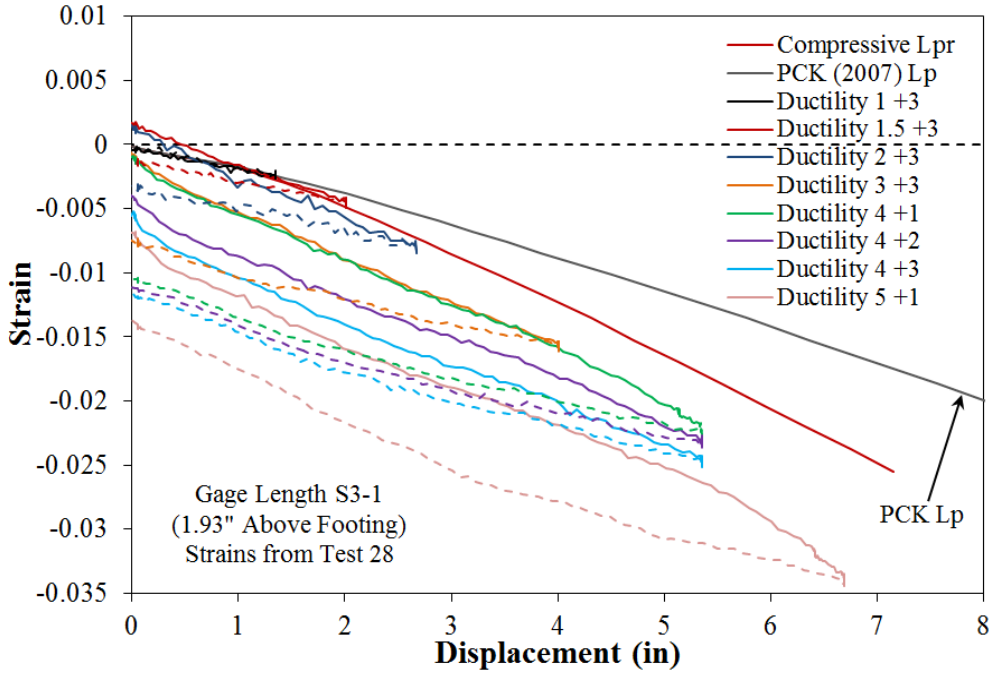

Figure 1.874 T28 – Compressive Strain-Displacement for Bar S3 during Push Cycles

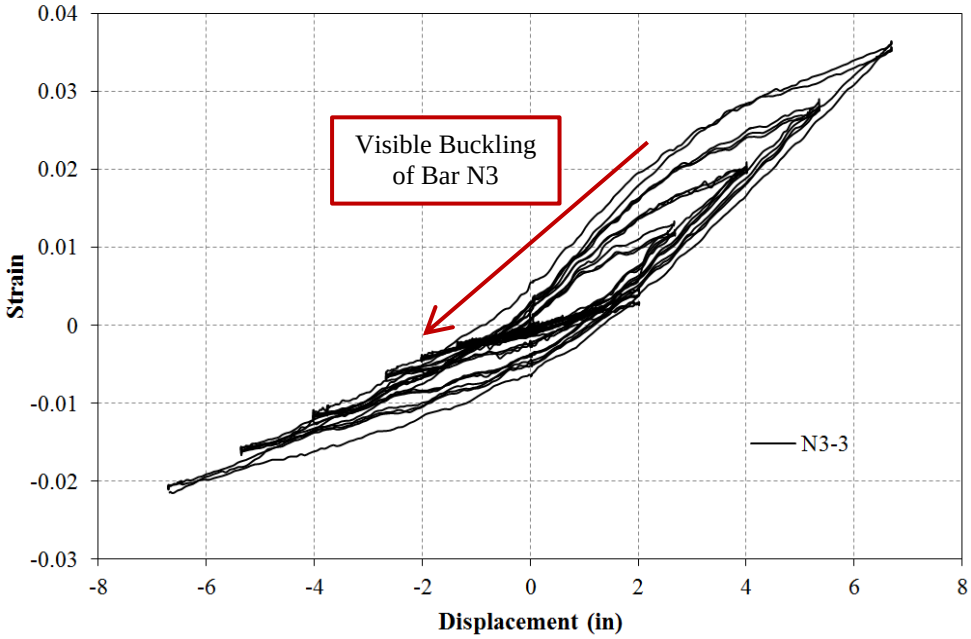

Figure 1.875 T28 – Strain Hysteresis for Bar N3 to Buckling (5.92" Above the Footing)

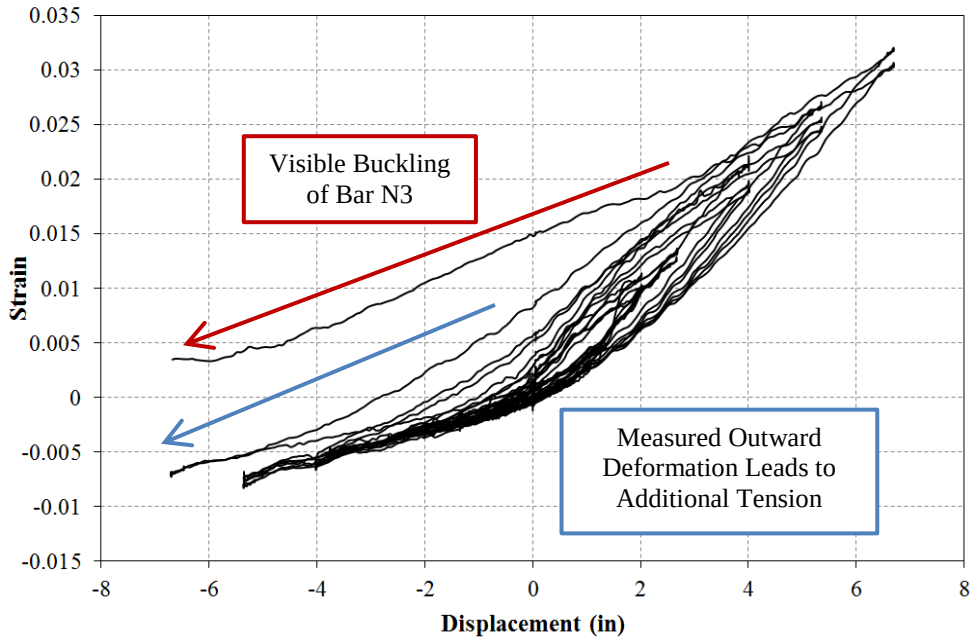

Figure 1.876 T28 – Strain Hysteresis for Bar N3 to Buckling (7.87" Above the Footing)

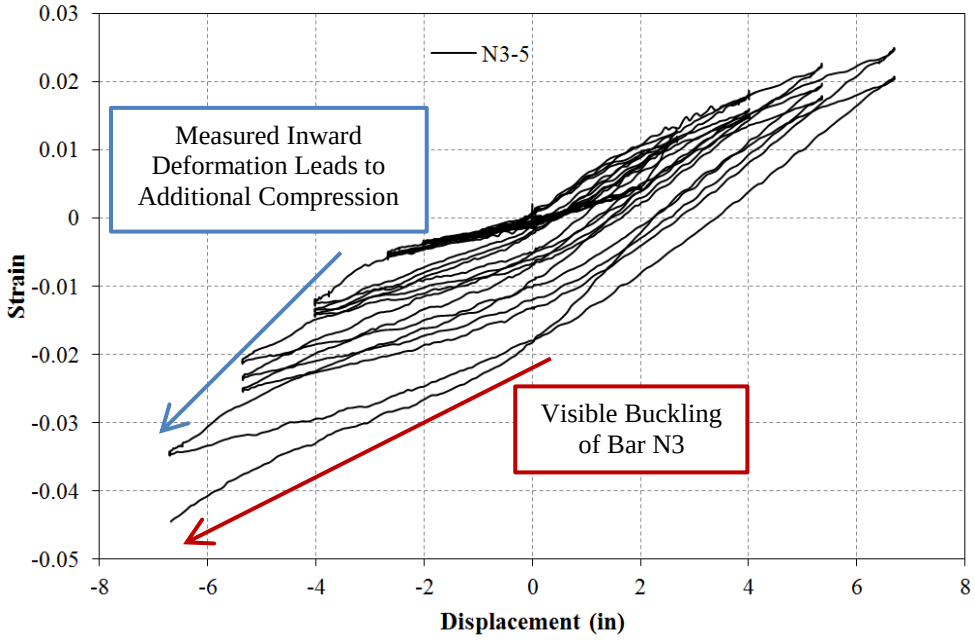

Figure 1.877 T28 – Strain Hysteresis for Bar N3 to Buckling (9.83" Above the Footing)

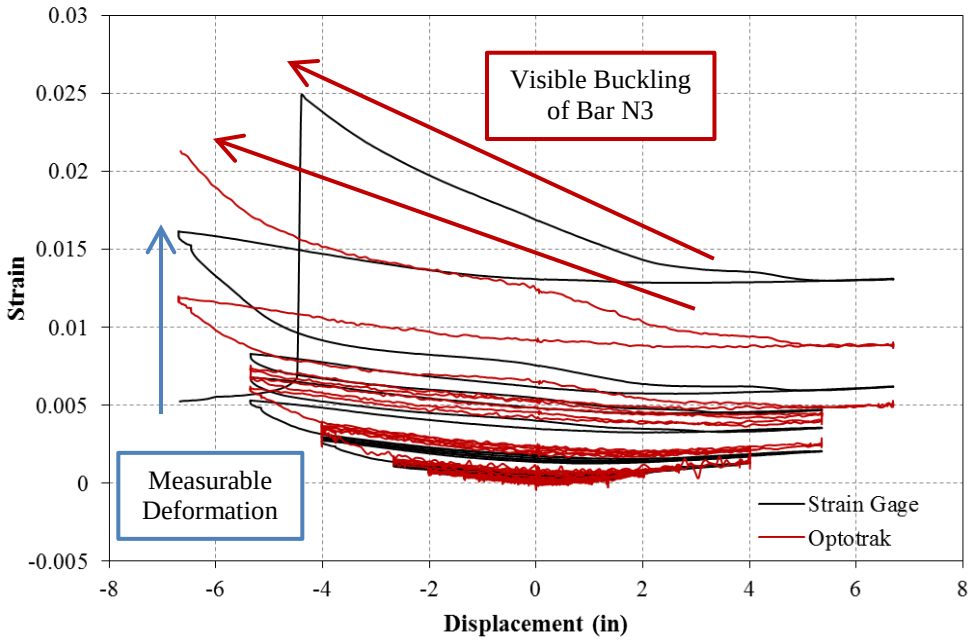

Figure 1.878 T28 – Spiral Strain Hysteresis over North Buckled Region (7.97" Above)

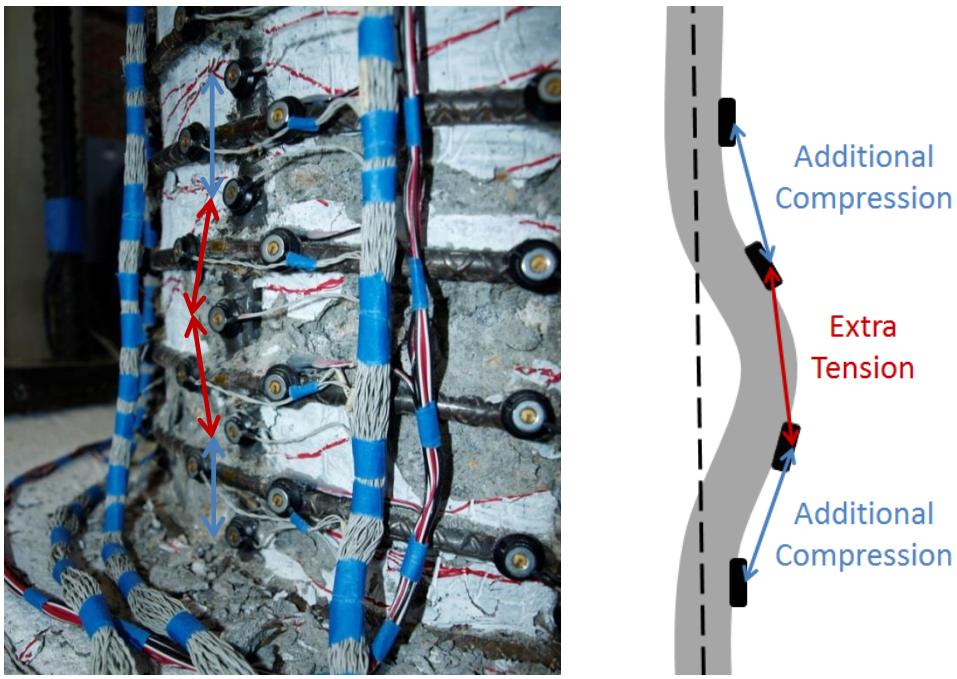

Figure 1.879 T28 – Measureable Deformation Matches Buckled Shape of Bar S3

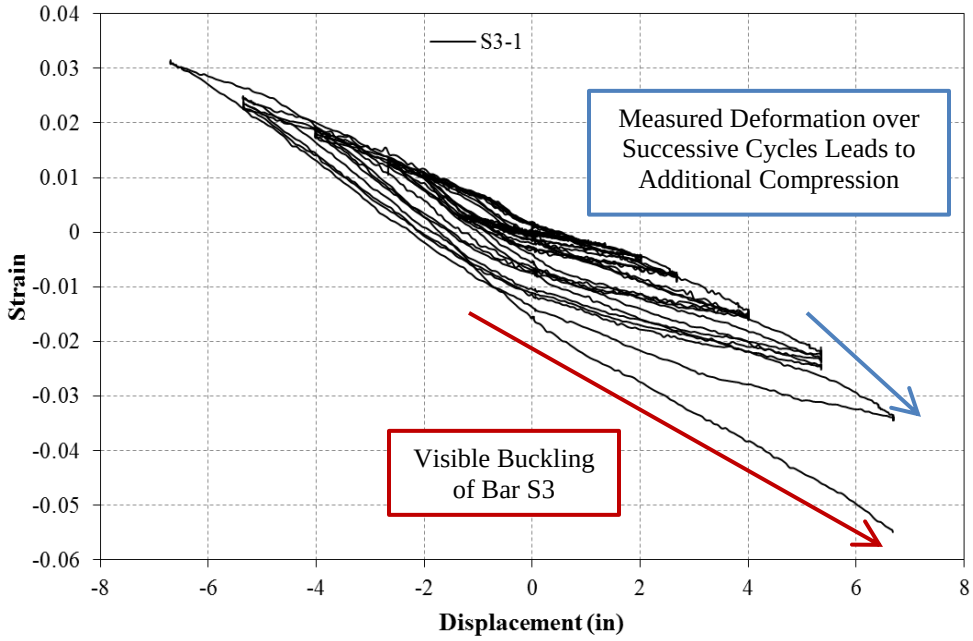

Figure 1.880 T28 – Strain Hysteresis for Bar S3 to Buckling (1.93" Above the Footing)

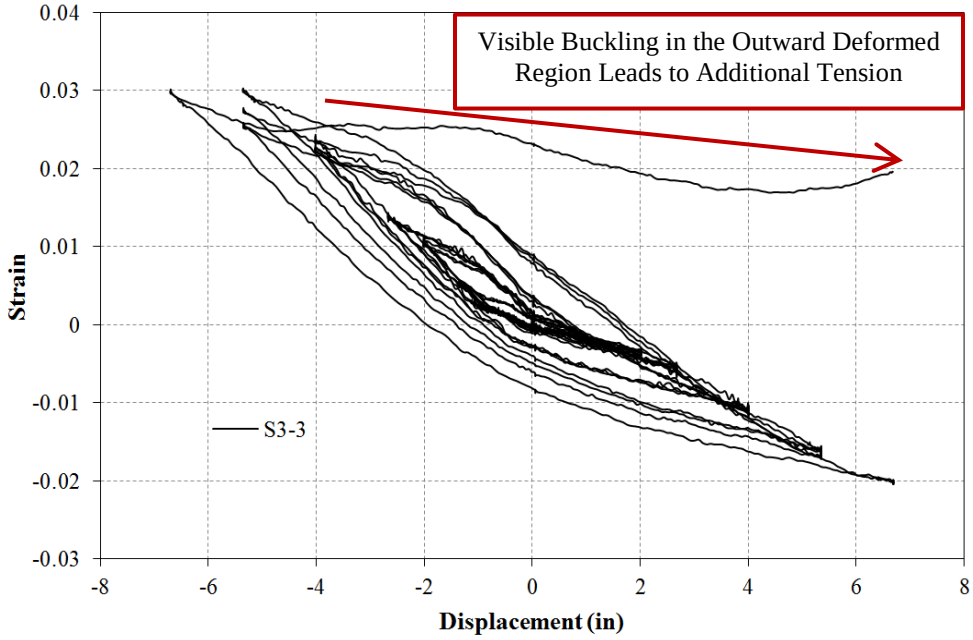

Figure 1.881 T28 – Strain Hysteresis for Bar S3 to Buckling (5.76" Above the Footing)

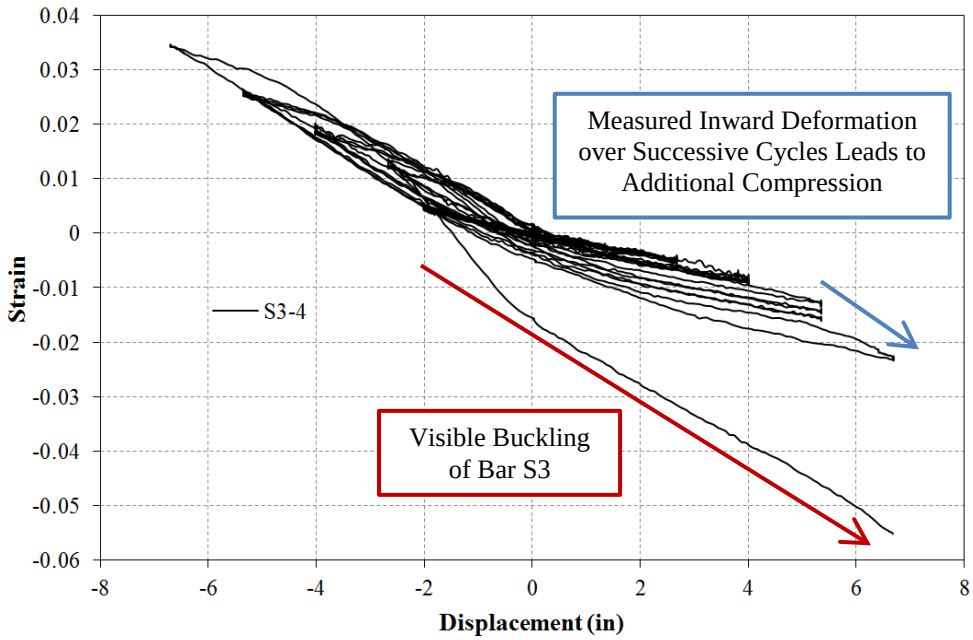

Figure 1.882 T28 – Strain Hysteresis for Bar S3 to Buckling (7.65" Above the Footing)

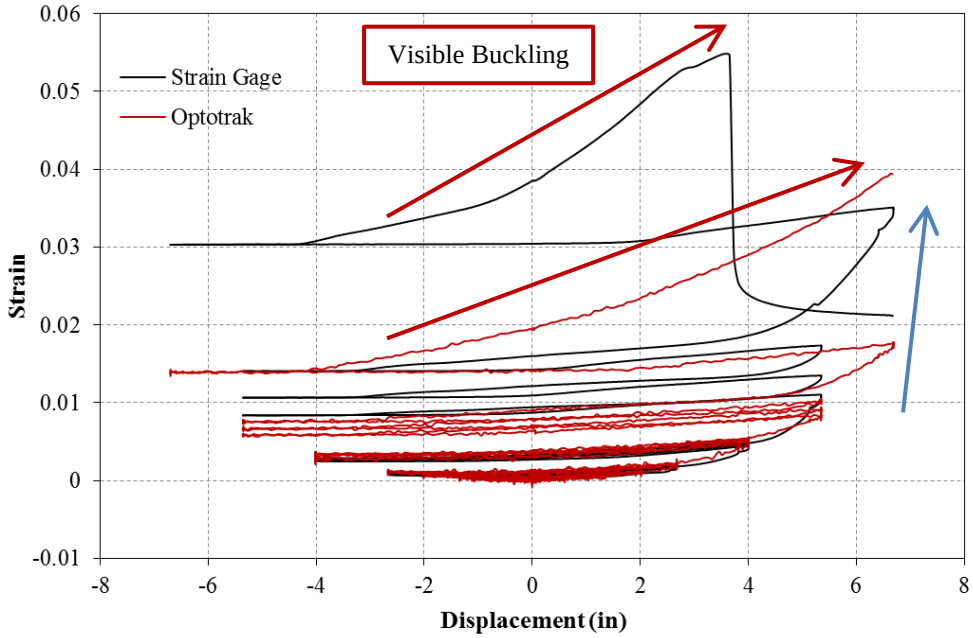

Figure 1.883 T28 – Spiral Strain Hysteresis over South Buckled Region (3.89" Above)

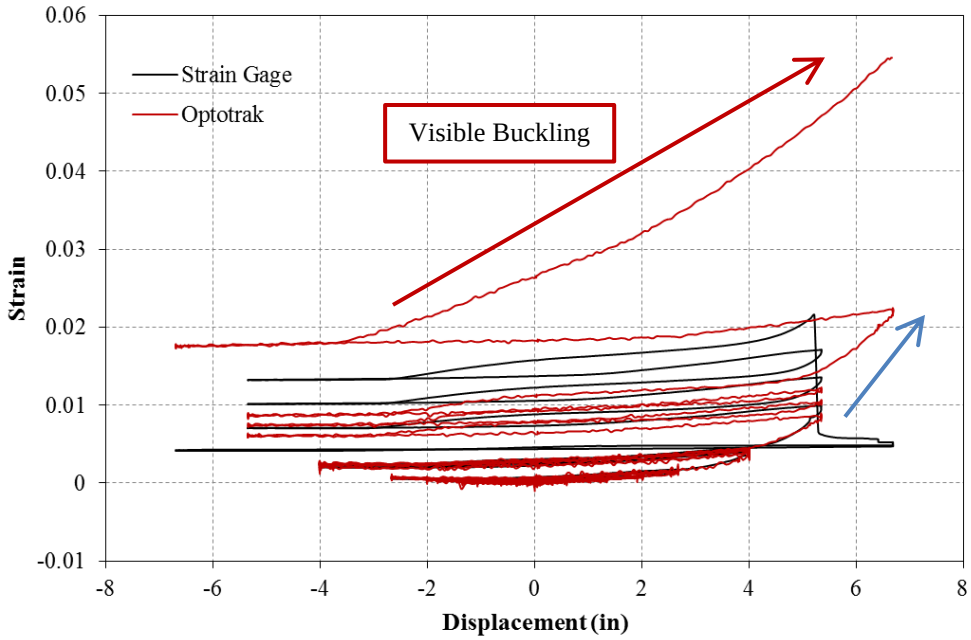

Figure 1.884 T28 – Spiral Strain Hysteresis over South Buckled Region (5.84" Above)

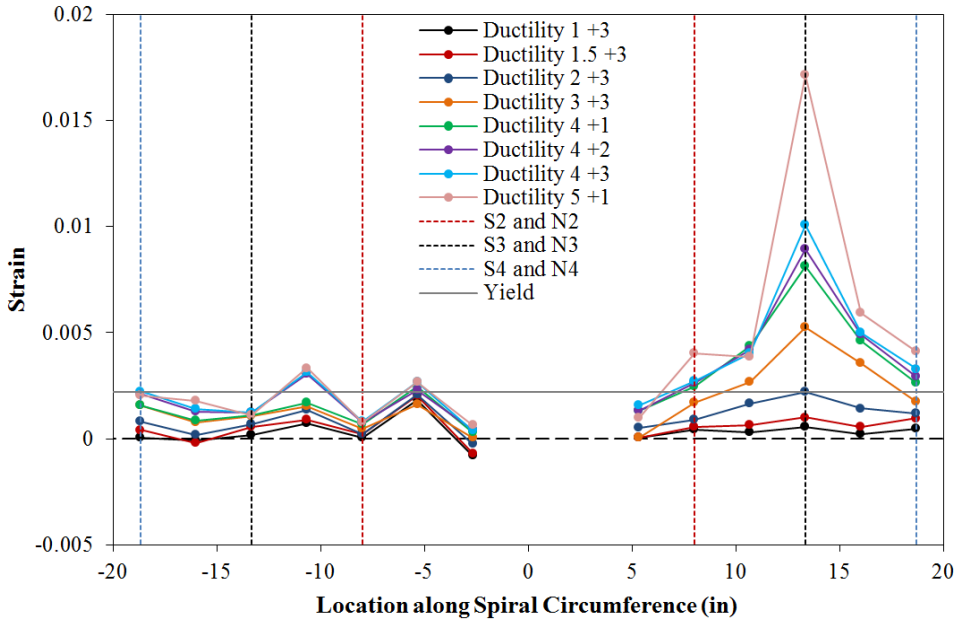

Figure 1.885 T28 – Spiral Strain Distribution for the 2nd Spiral above the Footing during Push Cycles (Positive = South)

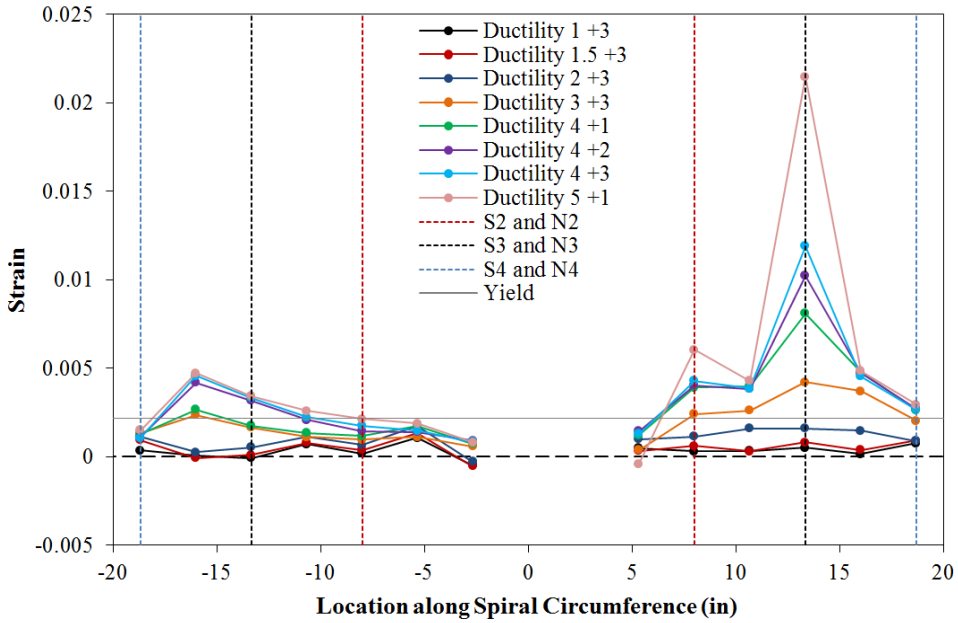

Figure 1.886 T28 – Spiral Strain Distribution for the 3nd Spiral above the Footing during Push Cycles (Positive = South)

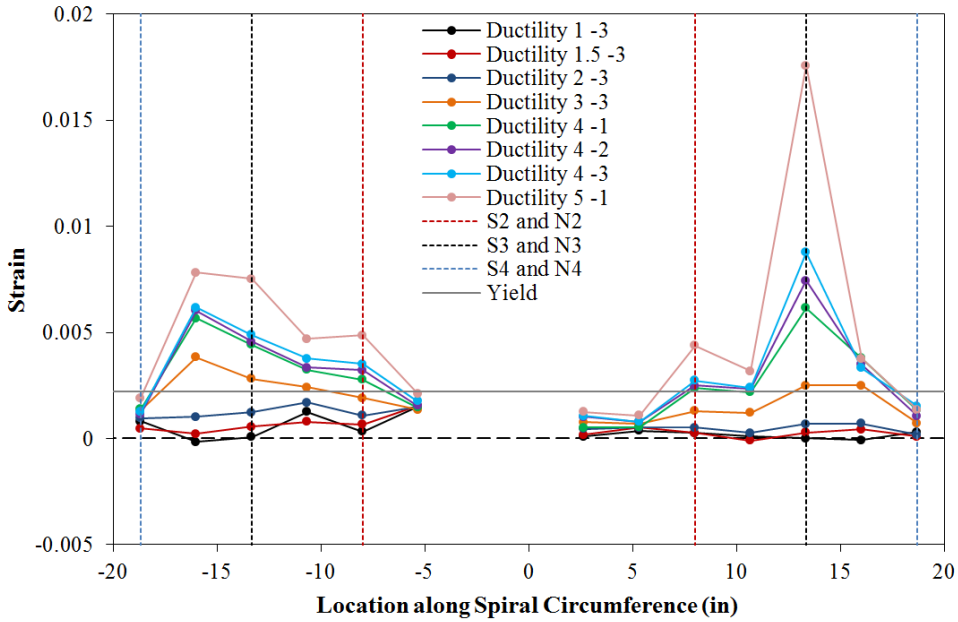

Figure 1.887 T28 – Spiral Strain Distribution for the 3rd Spiral above the Footing during Pull Cycles (Negative = North)

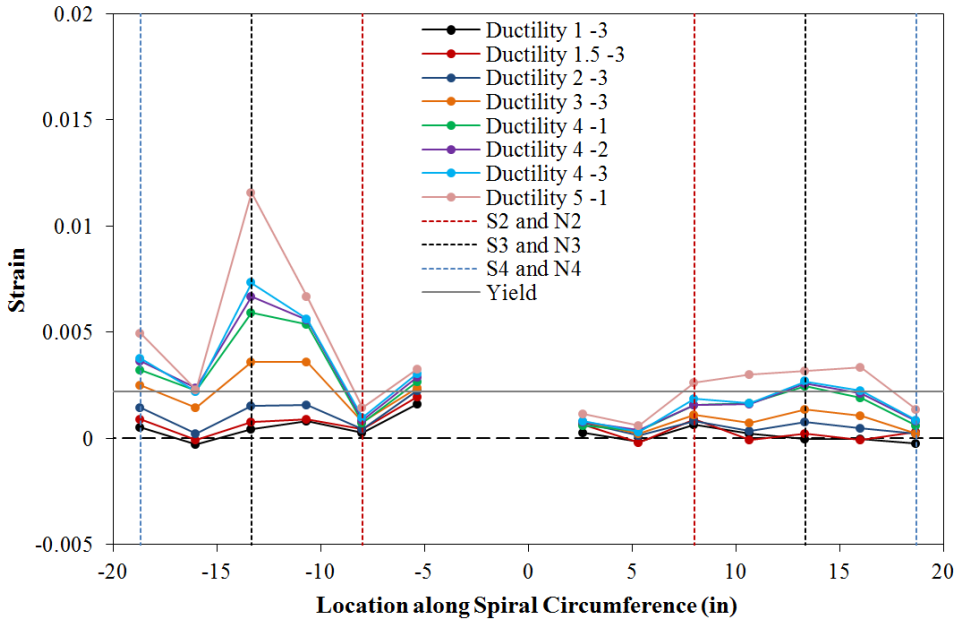

Figure 1.888 T28 – Spiral Strain Distribution for the 4th Spiral above the Footing during Pull Cycles (Negative = North)

Test 28 – Curvature and Strain Penetration Data

Cross section strain profiles for the third horizontal section above the footing appear in Figure 1.889 and Figure 1.890 for push and pull cycles respectively. The curvature is calculated as the slope of the least squared line connecting strains measured in eight instrumented reinforcing bars. If the curvatures for many horizontal cross sections are analyzed, curvature profiles for the plastic hinge region can be constructed; Figure 1.891 and Figure 1.892 for push and pull cycles respectively. Linear least squared error regression lines were fit to the plastic portion of the measured curvature profiles. The extrapolation of this linear curvature line with the footing-column interface was taken as the base section curvature. As the base section curvature ductility increased, the height at which the linear plastic curvature distribution intersected the elastic curvature profile also increased. Circular data points in Figure 1.896 plot the measured spread of plasticity as a function of base section curvature ductility.

Curvature profiles describe the elastic and plastic flexural displacements of the column, but do not address fixed-end rotations which result from development of longitudinal reinforcement into the footing. The measured vertical displacements of Optotrak LEDs placed closest to the footing column interface can be used to quantify this fixed-end rotation, Figure 1.893 and Figure 1.894. The fixed-end rotation is taken as the slope of the least squared error line fit to the bond slip profile. The strain penetration displacement is obtained by multiplying this rotation by the cantilever height of the column. If an elastic curvature profile assumption is made for curvatures higher than those measured with instrumentation, then the entire curvature profile may be integrated to obtain the total column flexural displacement. This column flexural displacement was added to the strain penetration displacement, and compared to the experimentally measured displacements in Figure 1.895. The Optotrak integrated displacement matches well with those obtained from a string potentiometer placed at the center of the lateral load, which indicates that shear deformation are small.

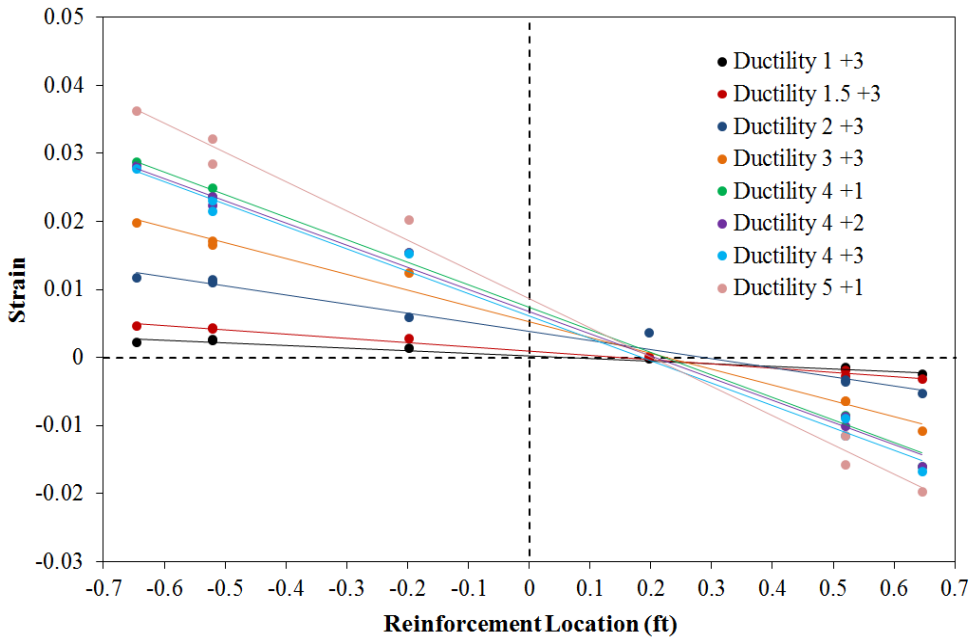

Figure 1.889 T28 – Push Cycle Strain Profiles for Section 5.86" Above the Footing

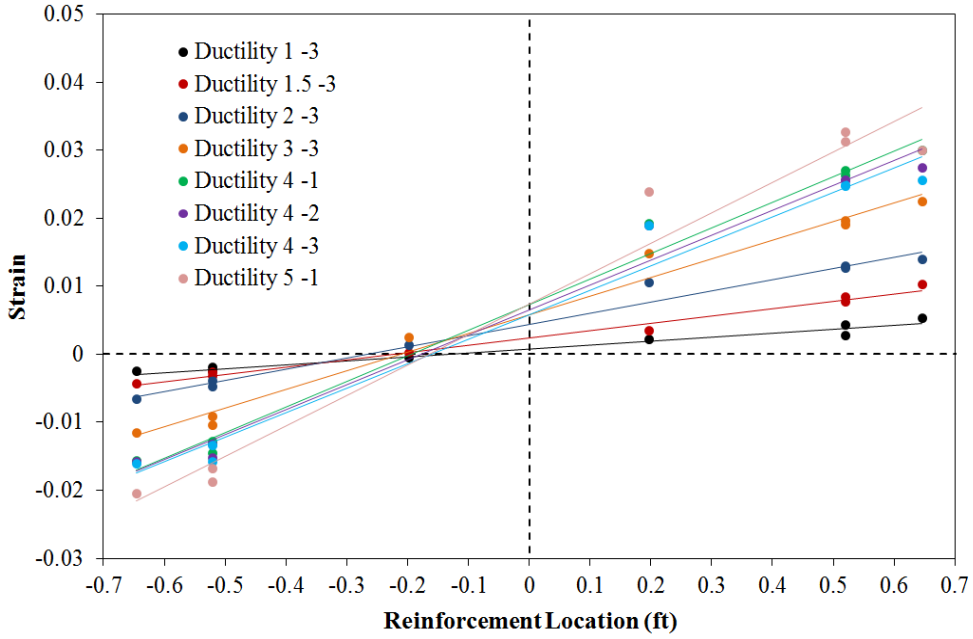

Figure 1.890 T28 – Pull Cycle Strain Profiles for Section 5.86" Above the Footing

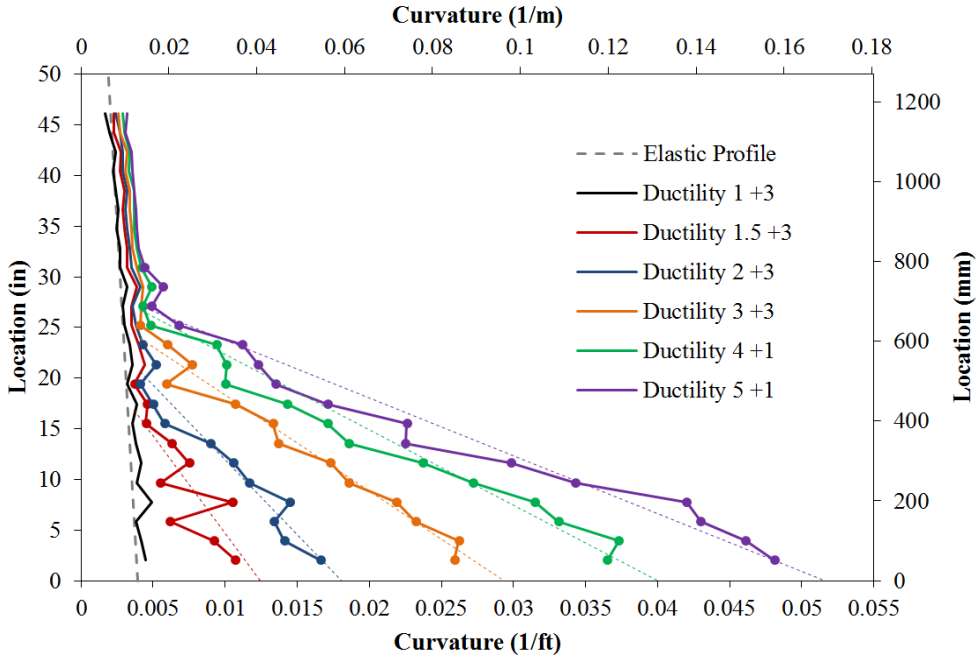

Figure 1.891 T28 – Push Cycle Curvature Profiles with Linear Plastic Regression

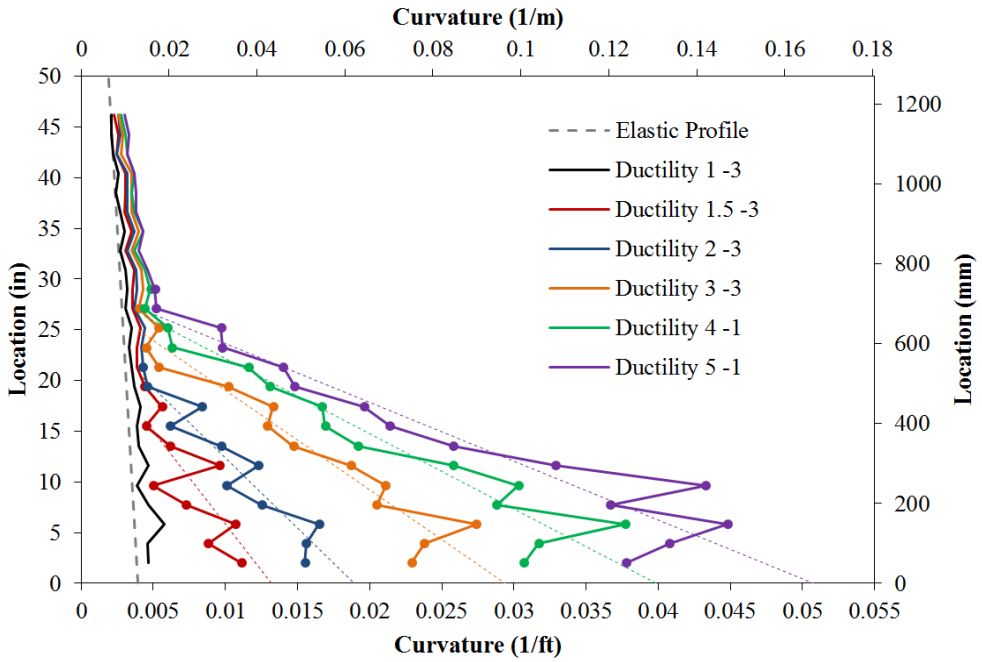

Figure 1.892 T28 – Pull Cycle Curvature Profiles with Linear Plastic Regression

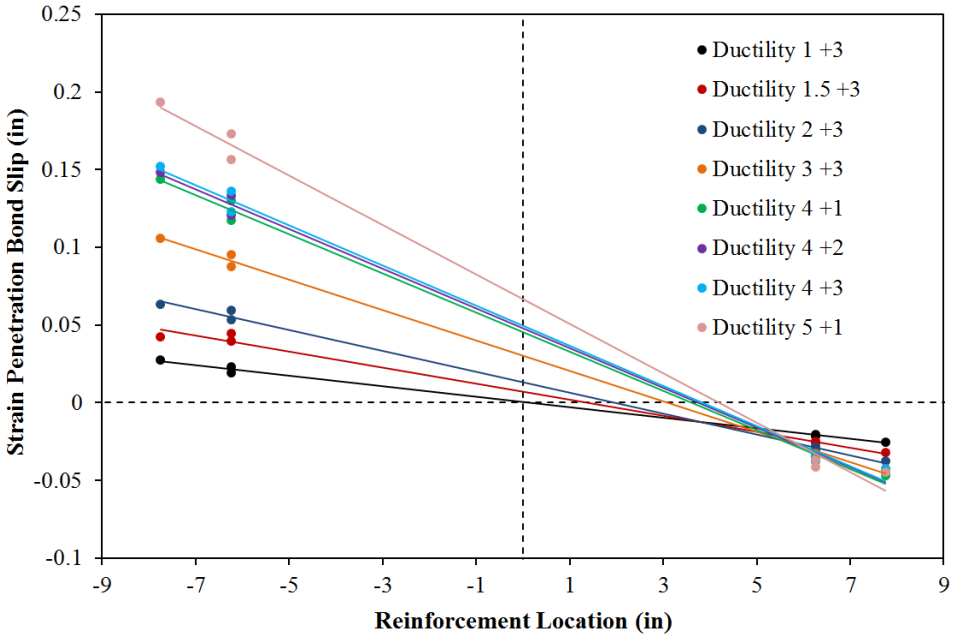

Figure 1.893 T28 – Base Rotation due to Strain Penetration during Push Cycles

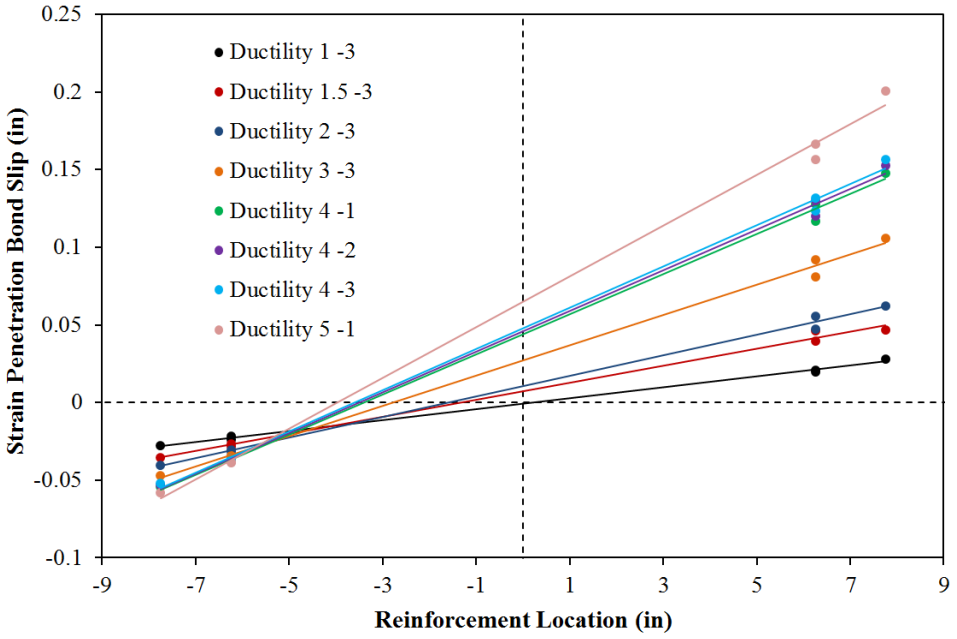

Figure 1.894 T28 – Base Rotation due to Strain Penetration during Pull Cycles

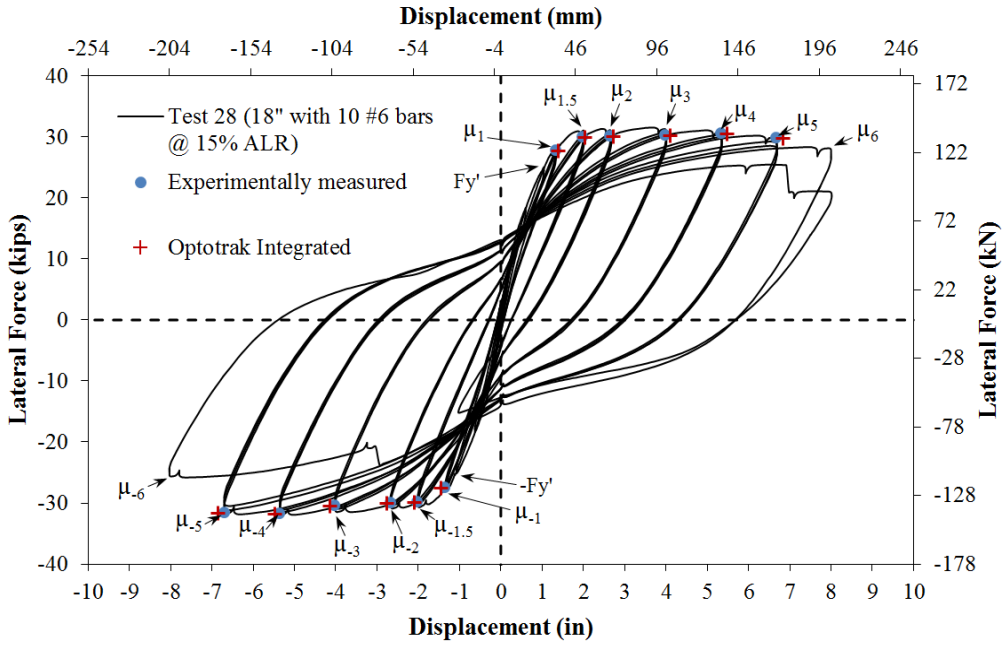

Figure 1.895 T28 – Comparison of Measured and Optotrak Integrated Displacements

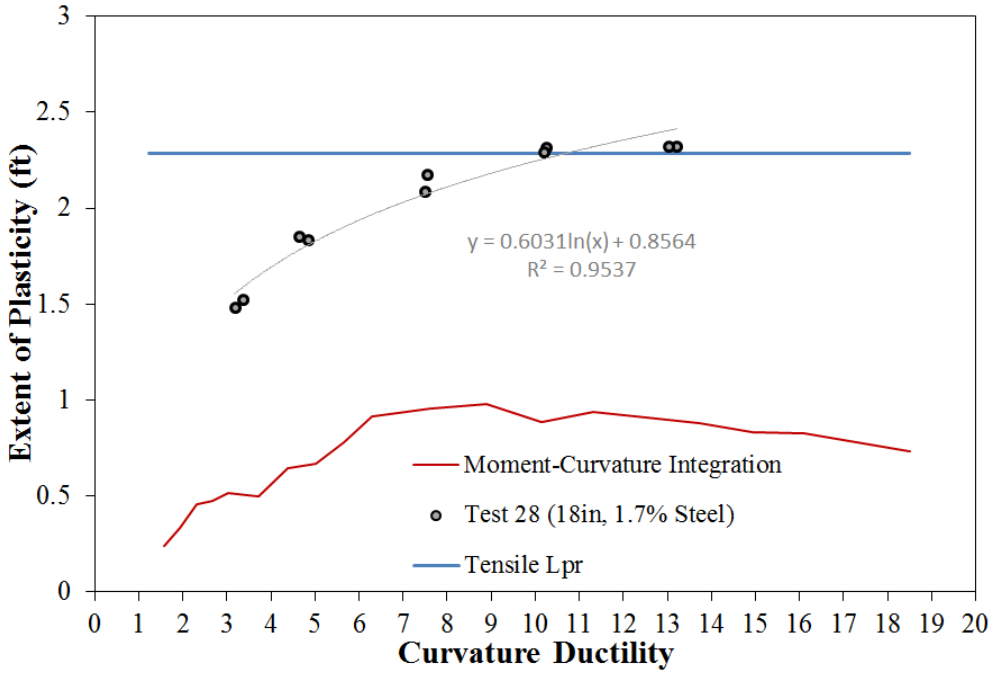

Figure 1.896 T28 – Measured Spread of Plasticity (Circular Data Points)

1.4.5 Test 29 – 18" Dia. Column with 1.7% Long. Steel and 20% Axial Load

Table 1.55 Observations for Test 29 – 18" Dia. With 1.7% Steel and 20% Axial Load

VALUES OF INTEREST:	
Concrete Compressive Strength:	$f_c' = 5911\ psi$
Axial Load:	$P = 268.4\ kips\ \ (P/(f_c' A_g) = 20\%)$
Longitudinal Steel Content:	10 #6 $Bars\ \ (A_{st}/A_g = 1.7\%)$
Analytical First Yield Force:	$F_y' = 27.13\ kips$
Experimental First Yield Displacement:	$\Delta_y' = 1.08"$
Analytical Nominal Moment Capacity:	$M_n = 269.95\ kip * ft$
Equivalent Yield Displacement:	$\Delta_y = 1.34"$
Maximum Lateral Force:	$33.81\ kips$
DAMAGE OBSERVATIONS:	
First Cracking North:	$3/4Fy' = 0.60"$
First Cracking South:	$-3/4Fy' = -0.62"$
Cover Concrete Crushing North:	$\mu_{1.5}^{-1} = -2.02"$
Cover Concrete Crushing South:	$\mu_{1.5}^{+1} = 2.01"$
Transverse Steel Yield North:	At $-2.89"$ during pull to $\mu_3^{-1} = -4.03"$
Transverse Steel Yield South:	At $2.69"$ during push to $\mu_2^{+3} = 2.69"$
Longitudinal Bar Buckling North:	Reversal from $\mu_6^{+1} = 8.06"$
Longitudinal Bar Buckling South:	Reversal from $\mu_5^{-1} = -6.72"$
Longitudinal Bar Fracture North:	Test Concluded Before North Bar Fractured
Longitudinal Bar Fracture South:	At $-1.62"$ during pull to $\mu_6^{-1} = -8.06"$

*$\mu_5^{-1} = -6.72"$ represents the first pull cycle of displacement ductility five

Table 1.56 Strain Data Summary for Test 29 – 18" Dia. with 1.7% Steel and 20% Axial

MATERIAL STRAINS:	
Cover Concrete Crushing North:	$\varepsilon_s = 0.0055$ $(compression)$
Cover Concrete Crushing South:	$\varepsilon_s = 0.0054$ $(compression)$
Transverse Steel Yield North:	$\varepsilon_s = 0.0142$ $(compression)$
Transverse Steel Yield South:	$\varepsilon_s = 0.0103$ $(compression)$
Longitudinal Bar Buckling North:	$\varepsilon_s = 0.055$ $(peak\ tension\ prior\ to\ bb)$
	$\varepsilon_s = 0.044$ $(peak\ comp.\ prior\ to\ bb)$
Longitudinal Bar Buckling South:	$\varepsilon_s = 0.036$ $(peak\ tension\ prior\ to\ bb)$
	$\varepsilon_s = 0.032$ $(peak\ comp.\ prior\ to\ bb)$
Mander (1988) Ultimate Concrete Compression Strain, $\varepsilon_{cu} = 0.020$	

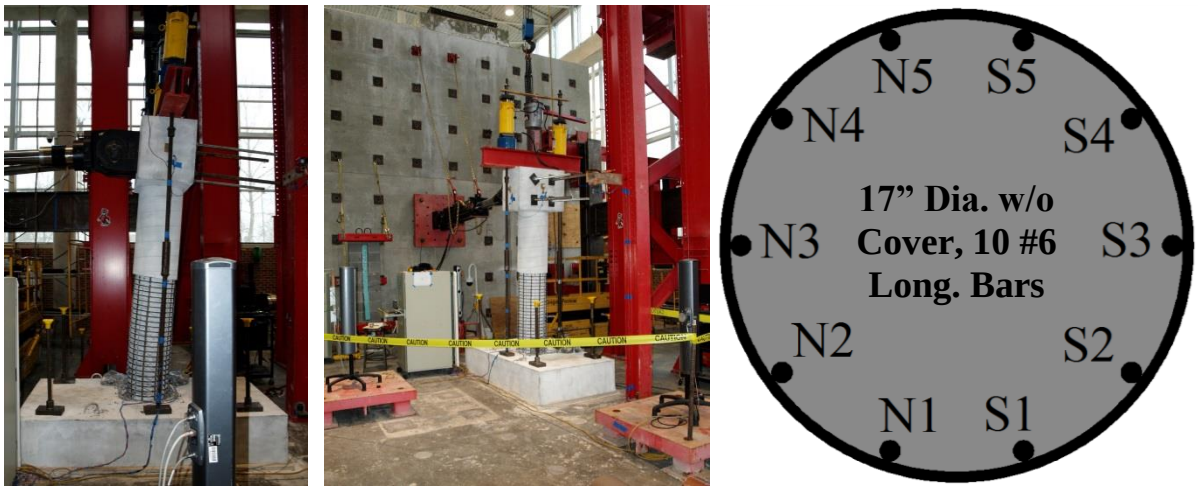

Figure 1.897 T28 – Test Setup and Cross Section Bar Designation

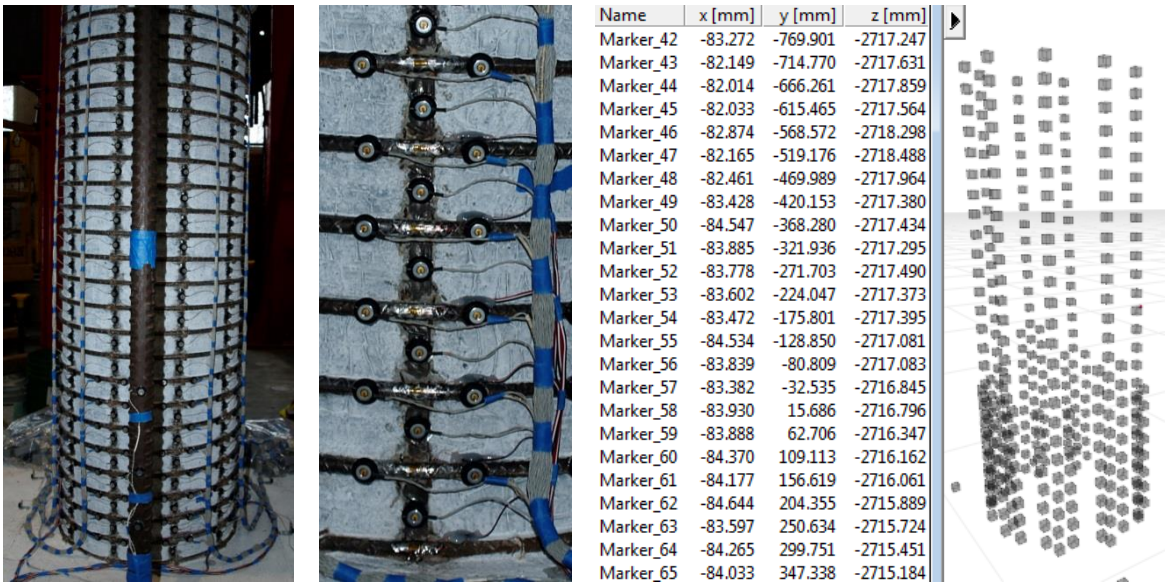

Name	x [mm]	y [mm]	z [mm]
Marker_42	-83.272	-769.901	-2717.247
Marker_43	-82.149	-714.770	-2717.631
Marker_44	-82.014	-666.261	-2717.859
Marker_45	-82.033	-615.465	-2717.564
Marker_46	-82.874	-568.572	-2718.298
Marker_47	-82.165	-519.176	-2718.488
Marker_48	-82.461	-469.989	-2717.964
Marker_49	-83.428	-420.153	-2717.380
Marker_50	-84.547	-368.280	-2717.434
Marker_51	-83.885	-321.936	-2717.295
Marker_52	-83.778	-271.703	-2717.490
Marker_53	-83.602	-224.047	-2717.373
Marker_54	-83.472	-175.801	-2717.395
Marker_55	-84.534	-128.850	-2717.081
Marker_56	-83.839	-80.809	-2717.083
Marker_57	-83.382	-32.535	-2716.845
Marker_58	-83.930	15.686	-2716.796
Marker_59	-83.888	62.706	-2716.347
Marker_60	-84.370	109.113	-2716.162
Marker_61	-84.177	156.619	-2716.061
Marker_62	-84.644	204.355	-2715.889
Marker_63	-83.597	250.634	-2715.724
Marker_64	-84.265	299.751	-2715.451
Marker_65	-84.033	347.338	-2715.184

Figure 1.898 T28 – Target Marker Application and Optotrak Spatial Output

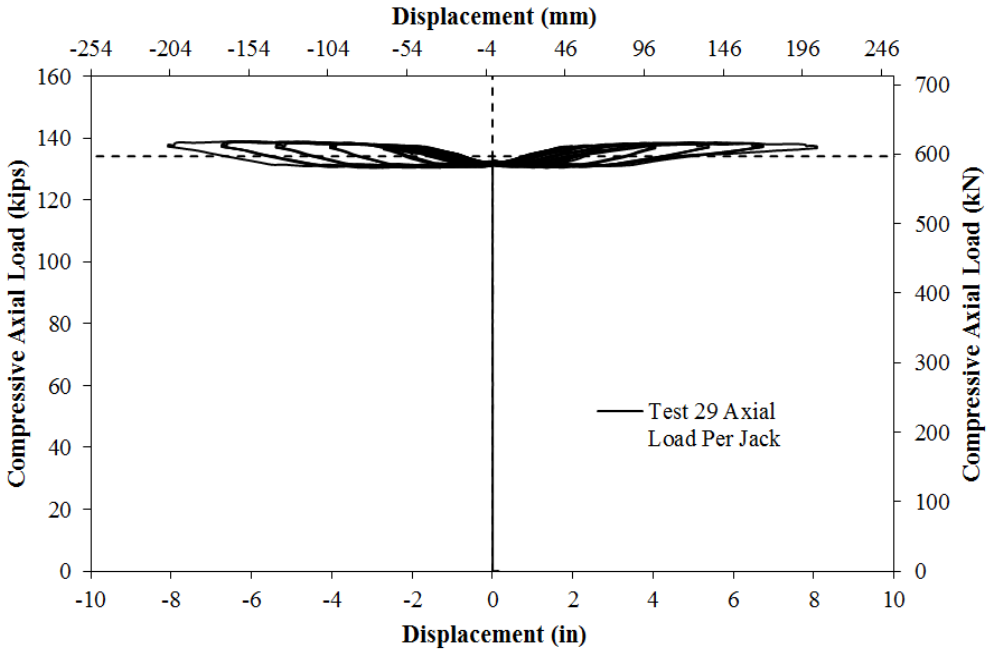

Figure 1.899 T28 – Compressive Axial Load from One Jack (Total = 2*Value)

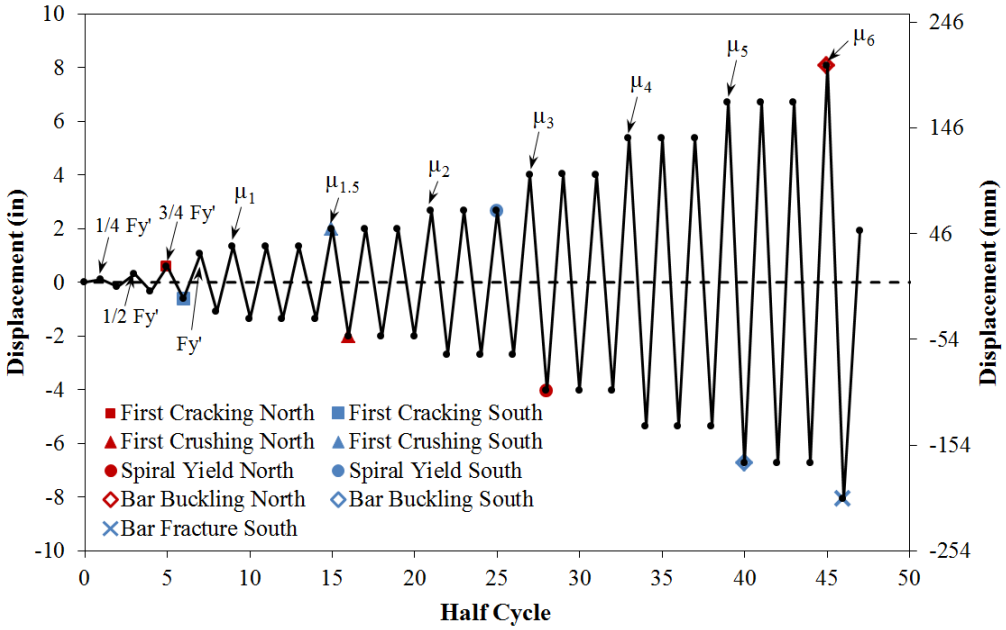

Figure 1.900 T29 – Symmetric Three Cycle Set Load History

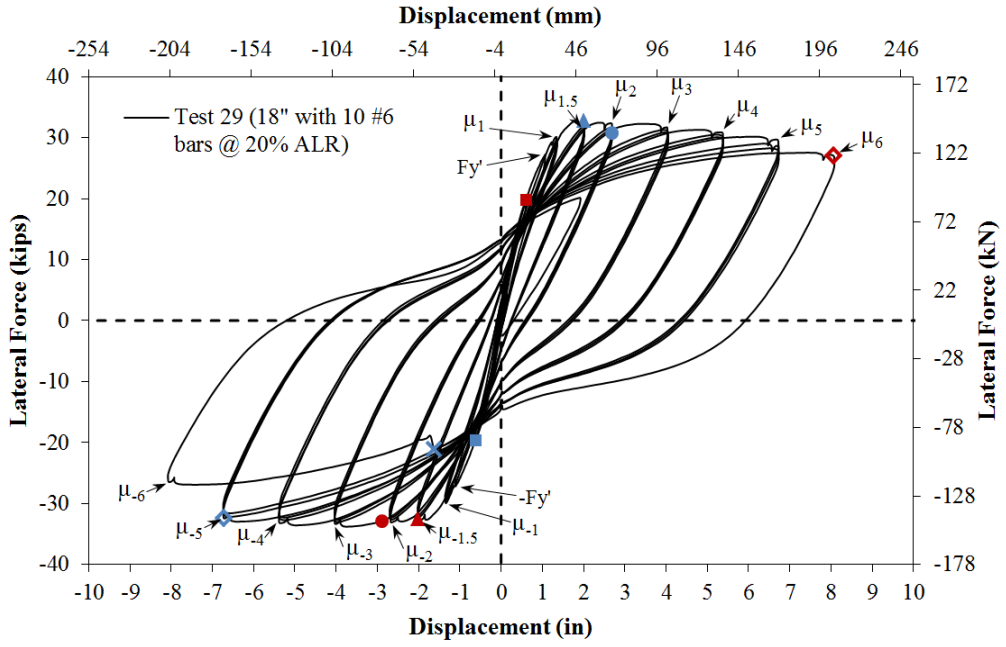

Figure 1.901 T29 – Lateral Force vs. Top Column Displacement Response

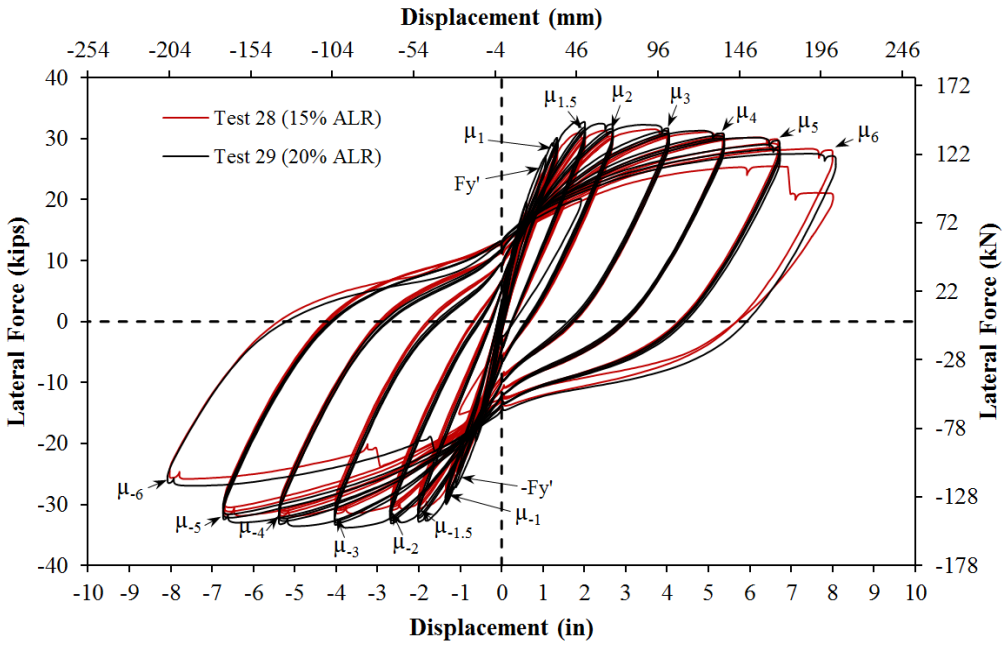

Figure 1.902 T29 – Comparison for T28 and T29 with Different Axial Load Levels

Test 29 – 18" Dia. with 1.7% Steel and 20% Axial Load – Experimental Observations

Specimens 25-30 focus on the effects of longitudinal steel content, longitudinal bar diameter, and higher levels of axial load on column behavior. This report summarizes experimental observations and data analysis for column Test 29. The 18" diameter column contains 10 #6 (A706) bars for longitudinal reinforcement ($A_{st}/A_g = 1.7\%$) and a #3 A706 spiral at 2" on center ($4A_{sp}/(D's) = 1.3\%$). The specimen had an 8ft cantilever length ($L/D = 5.33$), and was subjected to ($P/(f_c'A_g) = 20\%$) axial load. The experiments utilized a quasi-static displacement controlled loading procedure. The symmetric three-cycle-set load history is commonly used to evaluate the seismic performance of structural components. The load history begins with elastic cycles to the following increments of the analytically predicted first yield force: ¼ F_y', ½ F_y', ¾ F_y', and F_y'. The experimental first yield displacement is then determined by taking the average of the recorded displacements during

the first yield push and pulls cycles. The equivalent yield displacement, used to determine the displacement ductility levels ($\mu_{\Delta 1} = 1 * \Delta_y$), is then calculated as $\Delta_y = \Delta'_y(M_n/M'_y)$. The symmetric three-cycle-set load history resumes with three balanced cycles at each of the following displacement ductility levels: 1, 1.5, 2, 3, 4, 5, etc. The displacement history and resulting hysteretic response for Test 29 appears in Figure 1.900 and Figure 1.901. Previous Tests 20, 19, and 28 contained similar geometry and detailing, but had 5, 10, and 15% axial load. A hysteretic comparison of Tests 28 and 29 appears in Figure 1.902.

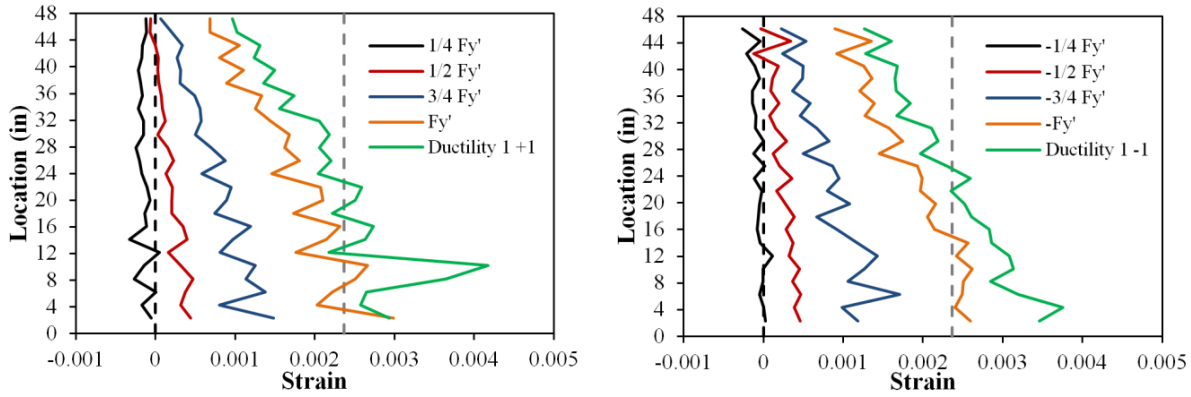

Figure 1.903 T29 – Strain Profiles before Yield, (Left) North and (Right) South

The test began with cycles in ¼ Fy' (first yield force) increments in each direction of loading until the first yield force was reached. The first cracks on the north and south sides of the specimen formed during ($3/4Fy' = 0.60$") and ($-3/4Fy' = -0.62$") respectively, Figure 1.904. The crack distribution on all sides of the specimen at first yield, ($Fy' = 1.07$") and ($-Fy' = -1.10$"), appears in Figure 1.905. Tensile vertical strain profiles for north and south reinforcing bars during elastic push and pull cycles appear in Figure 1.903. The average experimental first yield displacement was used to calculate the equivalent yield displacement, $\Delta_y = \Delta'_y(M_n/M'_y) = 1.08$", which defined the reversal amplitudes for reminder of the test.

The crack progression at displacement ductility 1, 1.5, 2, 3, and 4 appear in Figure 1.906, Figure 1.908, Figure 1.910, Figure 1.912, and Figure 1.914 respectively. During these

cycles the cracks became more numerous and increased in inclination on the shear faces of the specimen. Small amounts concrete crushing was observed on the south and north sides of the specimen during ($\mu_{1.5}^{+1} = 2.01$") and ($\mu_{1.5}^{-1} = -2.02$"), Figure 1.907. This crushing increased during the next two cycles of displacement ductility 1.5, Figure 1.908. As compressive demands increased during displacement ductility 1.5 to 4, crushing gradually increased on each side of the specimen. Compressive demand during ($\mu_3^{+1} = 4.03$") and ($\mu_3^{-1} = -4.03$") led to spiral yielding in confinement regions, Figure 1.911. Spiral strains on each side of the specimen increased during each successive cycle of ductility four, but the extreme fiber reinforcement remained visibly straight, Figure 1.913.

Even though spiral strains in confinement regions increased, the south extreme fiber bar remained visibly straight during ($\mu_5^{+1} = 6.72$") and similarly the north bar during ($\mu_5^{-1} = -6.72$"), Figure 1.915. The south extreme fiber bar visibly buckled during ($\mu_5^{+2} = 6.72$"), Figure 1.916. The outward buckled region occurred over the third and fourth gage lengths above the footing. Adjacent south reinforcing bars S2 and S4 buckled during ($\mu_6^{+1} = 8.06$") and the buckled deformation in bar S3 significantly increased, Figure 1.917. The south bar fractured during ($\mu_6^{-1} = -8.06$"), Figure 1.918, resulting in the first significant loss in strength. Visible buckling of north extreme fiber bar N3 and adjacent bar N2 was observed during ($\mu_6^{-1} = -8.06$"), Figure 1.918. At this point the test was concluded without fracturing north reinforcement, since it was clear that multiple cycles would be needed with a south extreme fiber region which already had significant damage. Photos of the specimen after the instrumentation was removed appear in Figure 1.919 and Figure 1.920.

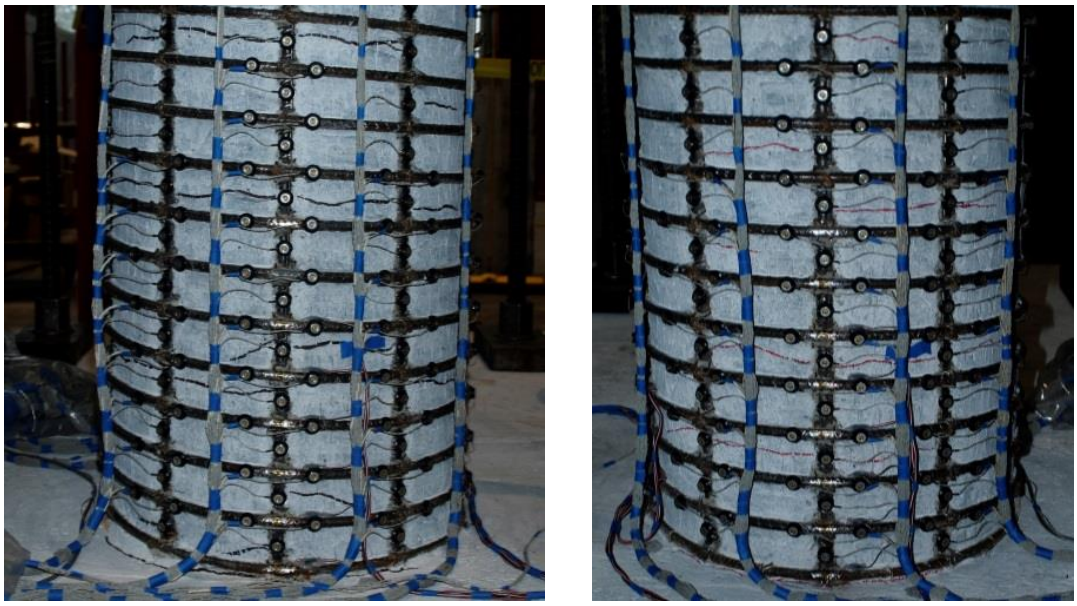

Figure 1.904 T29 – (Left) Cracking on the North Side during ($3/4Fy' = 0.60$"), (Right) South Cracking ($-3/4Fy' = -0.62$")

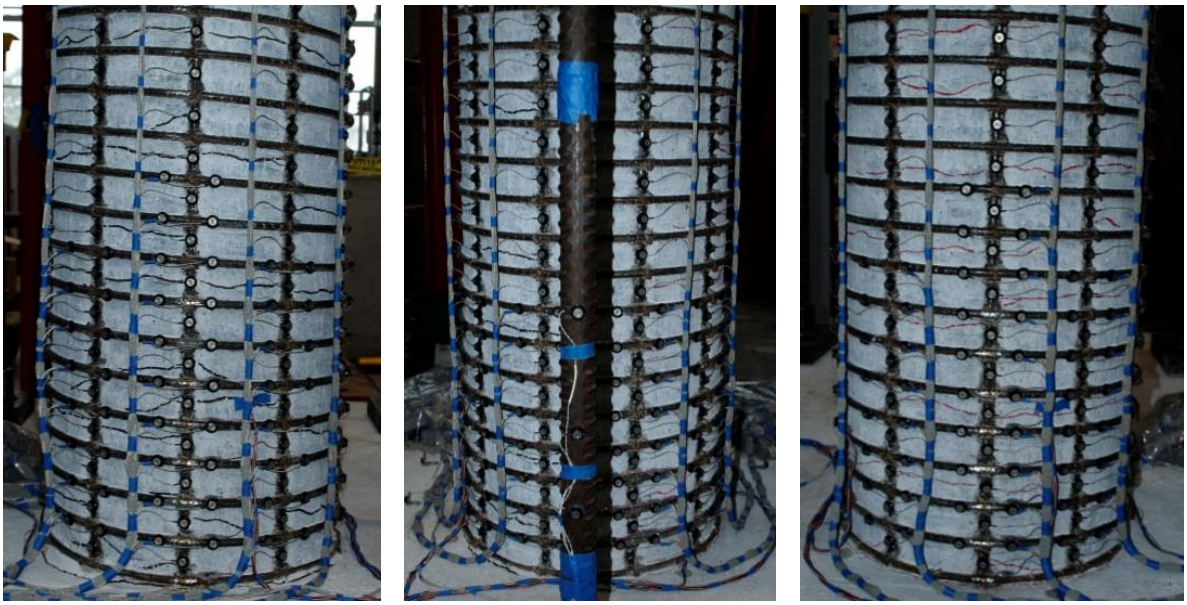

Figure 1.905 T29 – (Left) North Crack Distribution at ($Fy' = 1.07$"), (Middle and Right) Crack Distributions on the Front and Right Sides at ($-Fy' = -1.10$")

Figure 1.906 T29 – (Left) North Crack Distribution at ($\mu_1^{+3} = 1.35$"), (Middle and Right) Crack Distributions on the Front and Right Sides at ($\mu_1^{-3} = -1.35$")

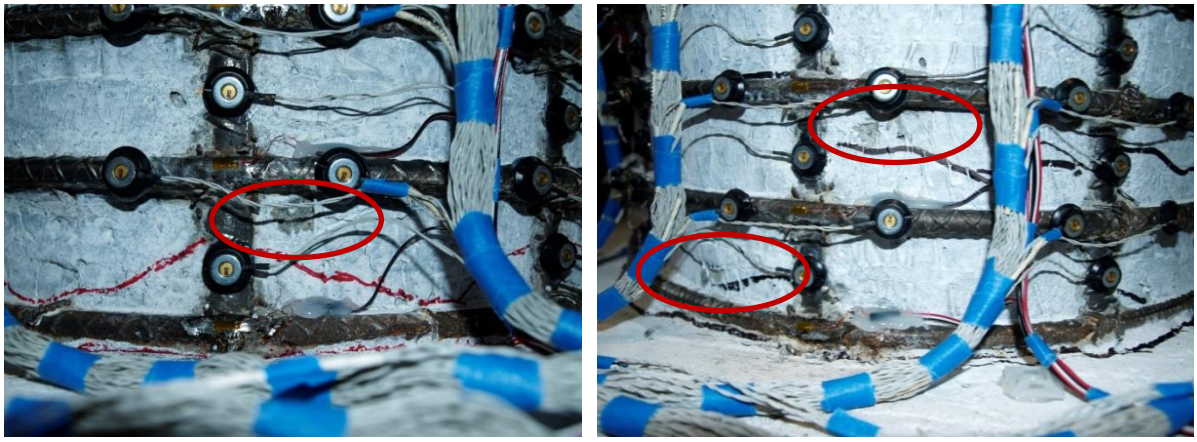

Figure 1.907 T29 – (Left) South Concrete Crushing during ($\mu_{1.5}^{+1} = 2.01$"), (Right) North Crushing during ($\mu_{1.5}^{-1} = -2.02$")

Figure 1.908 T29 – (Left) North Crack Distribution at ($\mu_{1.5}^{+3} = 2.01$"), (Middle and Right) Crack Distributions on the Front and Right Sides at ($\mu_{1.5}^{-3} = -2.01$")

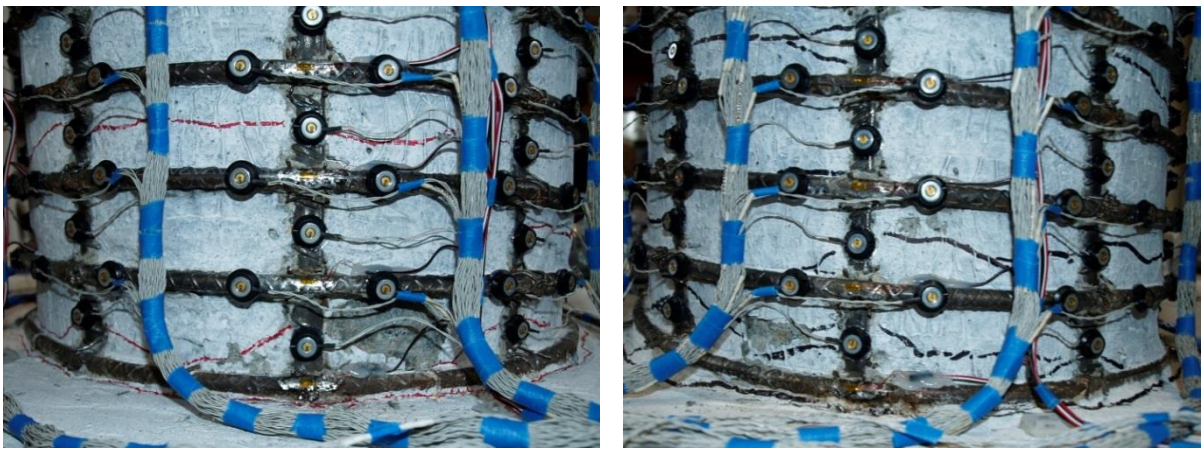

Figure 1.909 T29 – Extent of Crushing during Displacement Ductility 1.5, (Left) South and (Right) North

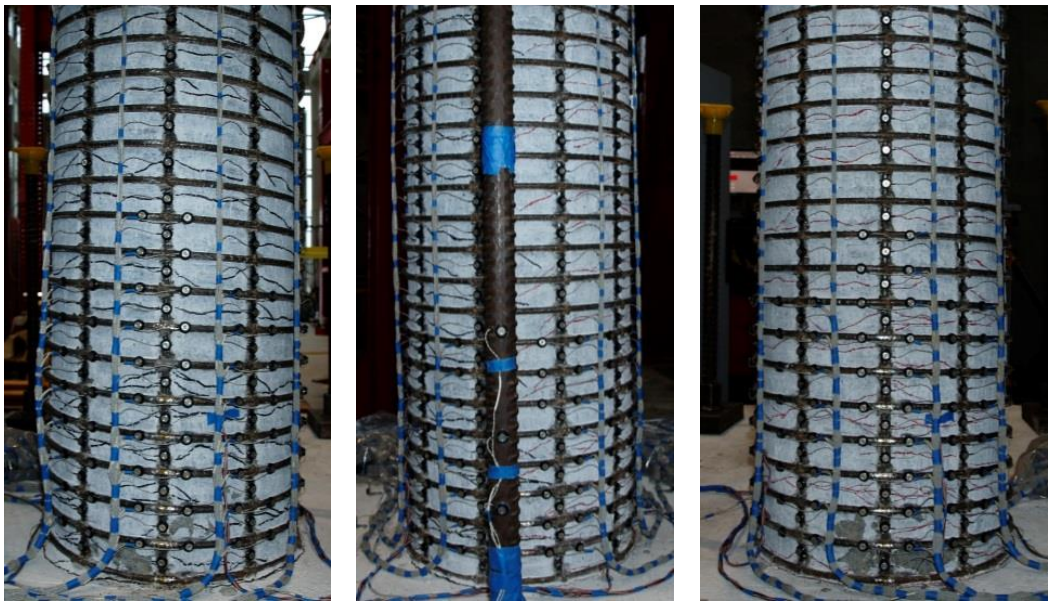

Figure 1.910 T29 – (Left) North Crack Distribution at ($\mu_2^{+3} = 2.69$"), (Middle and Right) Crack Distributions on the Front and Right Sides at ($\mu_2^{-3} = -2.69$")

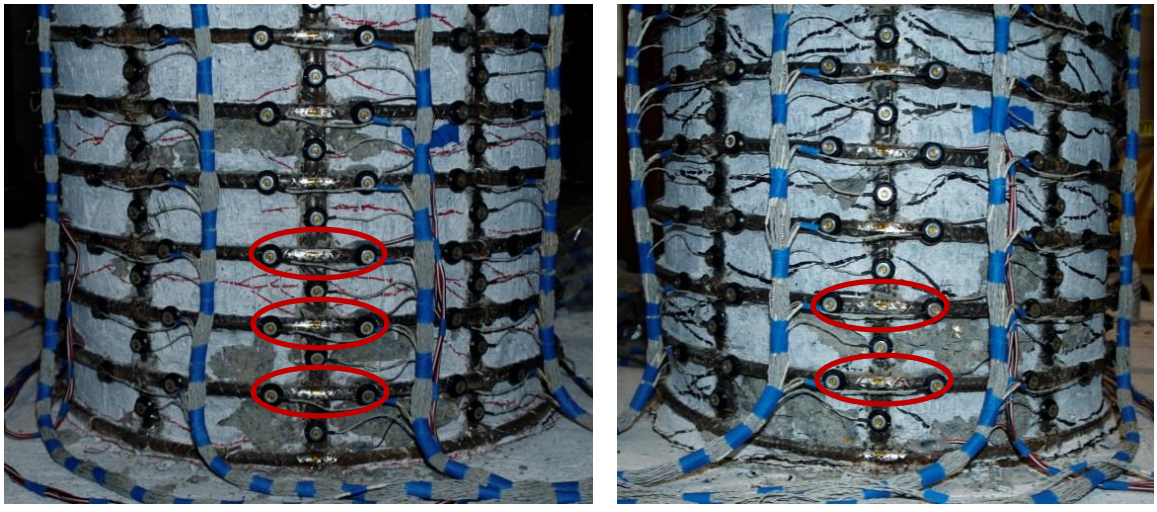

Figure 1.911 T29 – Spiral Layers which Yielded during Displacement Ductility Three, (Left) South and (Right) North

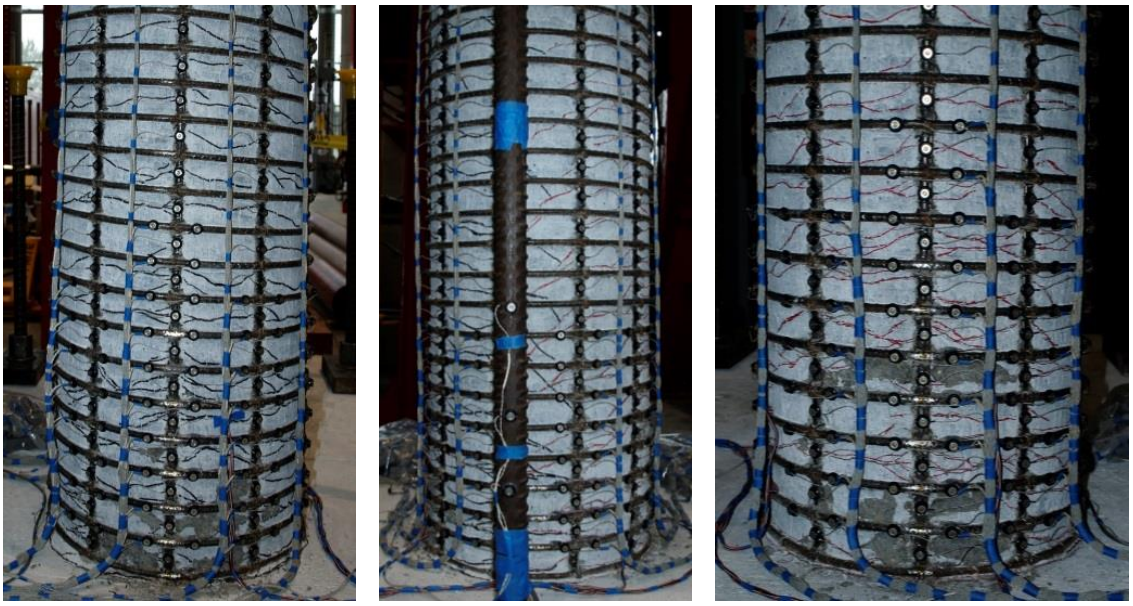

Figure 1.912 T29 – (Left) North Crack Distribution at ($\mu_3^{+3} = 4.02$"), (Middle and Right) Crack Distributions on the Front and Right Sides at ($\mu_3^{-3} = -4.03$")

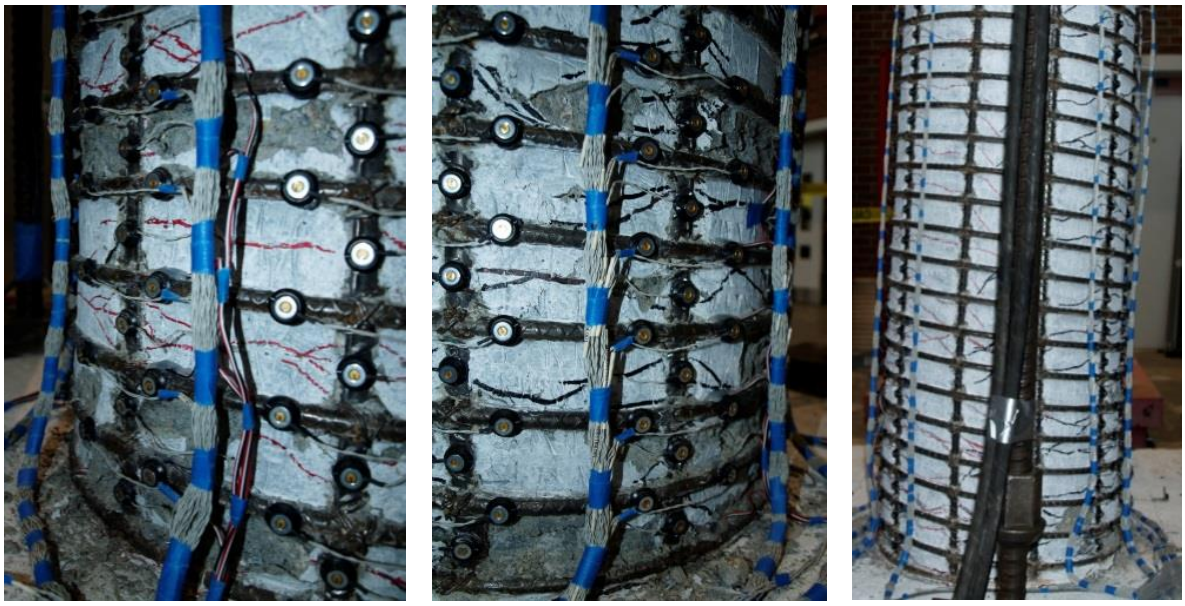

Figure 1.913 T29 – (Left) Bar S3 Remained Visibly Straight during ($\mu_4^{+3} = 5.37$"), (Middle) Bar N3 Remained Visibly Straight during ($\mu_4^{-3} = -5.37$"), (Right) Back of the Specimen at ($\mu_4^{-3} = -5.37$")

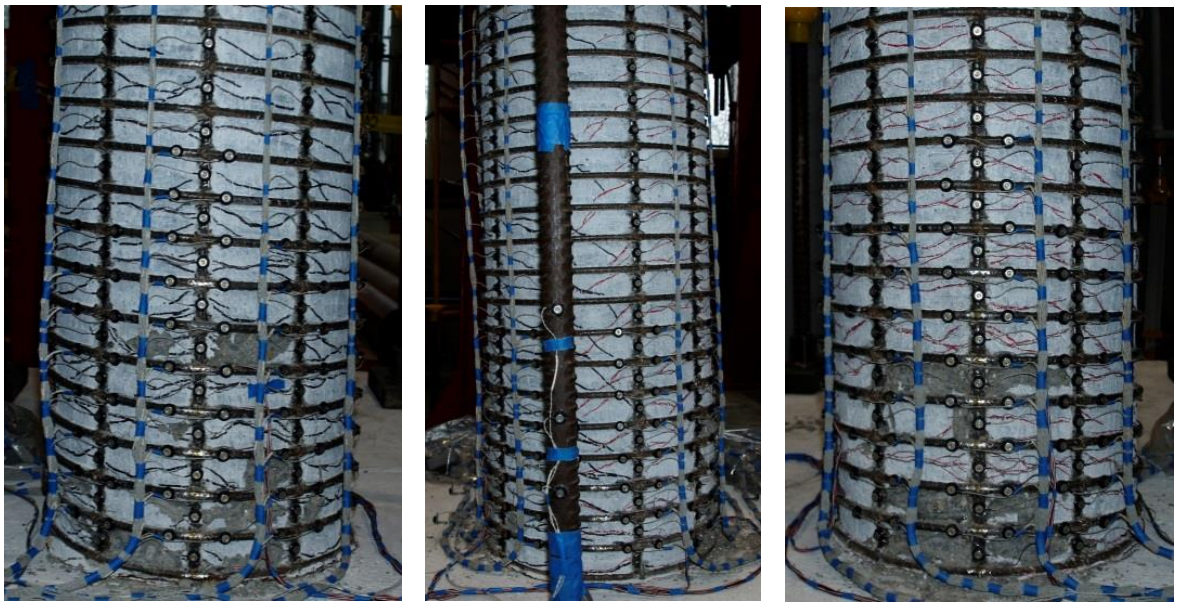

Figure 1.914 T29 – (Left) North Crack Distribution at ($\mu_4^{+3} = 5.37$"), (Middle and Right) Crack Distributions on the Front and Right Sides at ($\mu_4^{-3} = -5.37$")

Figure 1.915 T29 – (Left) Bar S3 Remained Visibly Straight during ($\mu_5^{+1} = 6.72$"), (Middle) Lateral Deformation at ($\mu_5^{-1} = -6.72$"), (Right) Bar N3 Remained Visibly Straight during ($\mu_5^{-1} = -6.72$")

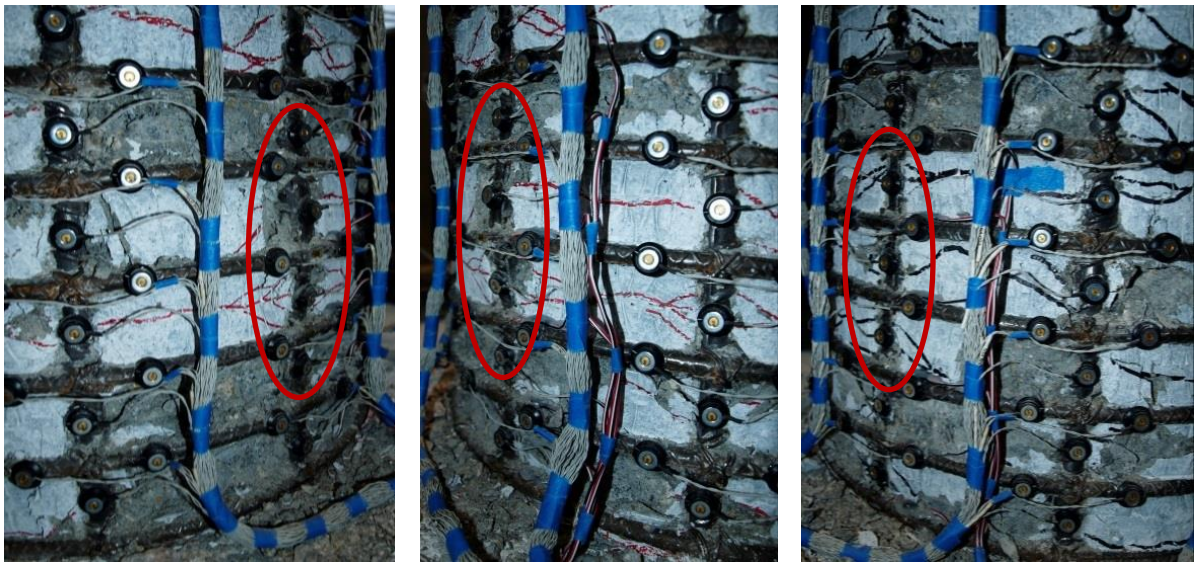

Figure 1.916 T29 – (Left and Middle) Visible Buckling of Bar S3 during ($\mu_5^{+2} = 6.72$"), (Right) Bar N3 Remained Visibly Straight during ($\mu_5^{+3} = 6.72$")

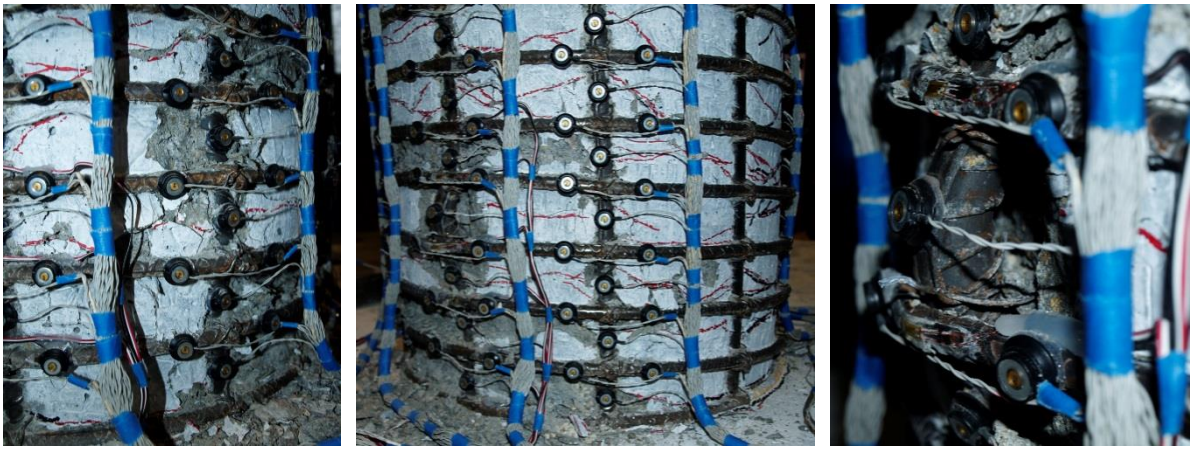

Figure 1.917 T29 – (Left) Buckling of Adjacent Bars S2 and S4 during ($\mu_6^{+1} = 8.06$"), (Middle and Right) Increase in the Buckled Deformation of Bar S3 during ($\mu_6^{+1} = 8.06$")

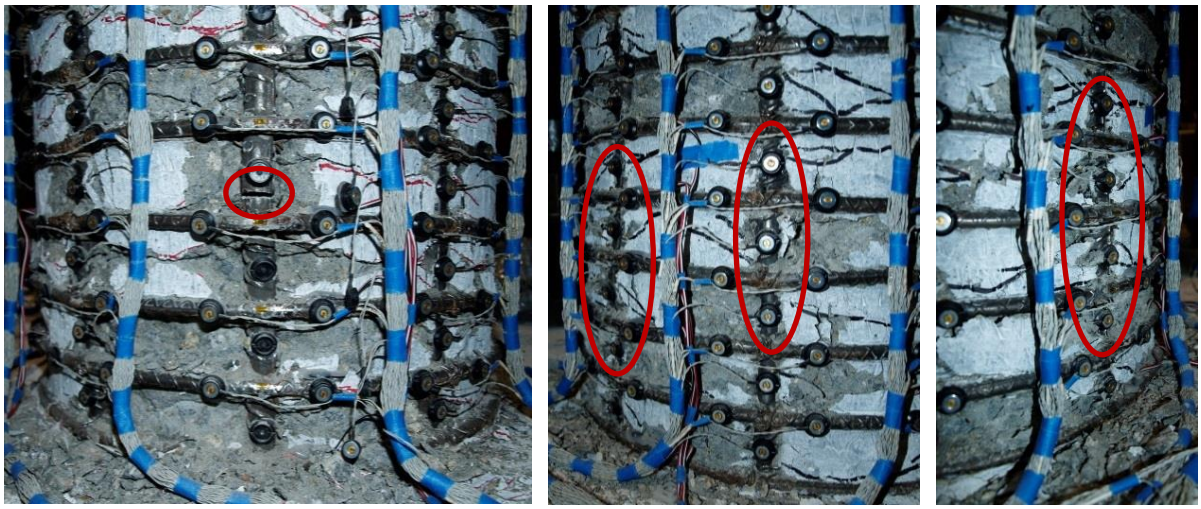

Figure 1.918 T29 – (Left) Fracture of Bar S3 during ($\mu_6^{-1} = -8.06$"), (Middle and Right) Buckling of Bars N2 and N3 during ($\mu_6^{-1} = -8.06$")

Figure 1.919 T29 – After the Test (Left) North Side and (Right) South Side

Figure 1.920 T29 – (Left to Right) North, Front, South, and Back Sides after the Test

Test 29 – 18" Dia. with 1.7% Steel and 20% Axial Load – Strain Data Analysis

North Reinforcement

Vertical strain profiles for the north extreme fiber bar N3, which is placed into tension during push cycles, appear in the right half of Figure 1.921. This figure shows both extreme fiber bars on the same graph. Compressive vertical strain profiles for north extreme fiber bar N3 during pull cycles appear in the left half of Figure 1.922. Strain profiles for additional cycles of displacement ductility five appear in Figure 1.923 and Figure 1.924, since bar buckling was delayed by one ductility level on the north side of the specimen. A peak tensile strain of 0.0549 was measured 6.27" above the footing on bar N3 during ($\mu_6^{+1} = 8.06"$), before bar buckling was observed during ($\mu_6^{-1} = -8.06"$). The relationship between tension strain and displacement for this gage length appears in Figure 1.927. The measured tension strains for this gage length are predicted well by monotonic moment-curvature analysis with the PCK (2007) Lp Hinge Method. A compressive strain of –0.0142 was measured 4.33"

above the footing on bar N3 during ($\mu_3^{-1} = -4.03$"), when the first spiral in the confinement region yielded. The relationship between compressive strain and displacement for this gage length appears in Figure 1.928. The measured compressive strains exceed the moment-curvature prediction beyond displacement ductility two.

Measured spiral strains in six layers which overlaid the north extreme fiber bar appear in Figure 1.926. Spiral tension strains in the second and third layers above the footing increased during each successive pull cycle of displacement ductility four and five. A spiral strain hysteresis for the layer 6.41" above the footing which overlaid the outward deformed region of bar N3 appears in Figure 1.934. The hysteresis contains spiral data from a strain gage and an Optotrak gage length, Figure 1.898. The Optotrak strains were calculated using arc-lengths obtained from measured 3D distance chord lengths and the known outside diameter of the spiral. It is important to note that arc-length calculations become inaccurate once severe yielding in the spiral leads to the reinforcement straightening out to the left and right of the localized yielding directly over the bar where the strain gage is located. Each consecutive pull cycle of displacement ductility five led to larger inelastic spiral strains, which indicates that measurable outward deformation occurred before visible bar buckling. The strain gage debonded during ($\mu_5^{-3} = -6.72$"), preventing further measurement. The sharpest increase in measured spiral strains occurred during ($\mu_6^{-1} = -8.06$"), when visible bar buckling was observed. The distribution of arc-strains measured around the circumference of the second, fourth, and fifth spiral layers above the footing during pull cycles appear in Figure 1.940, Figure 1.941, and Figure 1.942. The north side of the specimen is on the left side of the graph with negative location values and specific locations of bars N2, N3, and N4 are highlighted with vertical dashed lines.

Strain hysteresis for gage lengths 4.33", 6.27", and 8.22" above the footing on bar N3 appear in Figure 1.931, Figure 1.932, and Figure 1.933. The effect of measurable deformation on recorded strains can be visualized when comparing the location of the gage lengths with the deformed regions of the buckled extreme fiber bar, Figure 1.935. The gage length 6.27" above the footing overlaid the outward deformed region of bar N3, Figure

1.918. This gage length experienced additional tension during successive pull cycles of displacement ductility five as a result of measurable outward deformation. This deformation rapidly increased during ($\mu_6^{-1} = -8.06"$), when visible buckling was observed. The gage lengths 4.33" and 8.22" lie just below and above the outward deformed region. These gage lengths experience additional compression due to measurable deformation, as shown in Figure 1.931. Larger compressive strains were measured during each successive cycle of displacement ductility four and five, but the exact strain magnitudes may be influenced by the measurable deformation. The effect of this deformation is less apparent in the hysteresis 8.22" above the footing, Figure 1.933.

South Reinforcement

Vertical strain profiles for the south extreme fiber bar S3, which is placed into tension during pull cycles, appear in the right half of Figure 1.922. Compressive vertical strain profiles for south extreme fiber bar S3 during push cycles appear in the left half of Figure 1.921. A peak tension strain of 0.0357 was measured 6.30" above the footing on bar S3 at ($\mu_5^{-1} = -6.72"$), before the bar visibly buckled during ($\mu_5^{+2} = 6.72"$). A tension strain of 0.0342 was measured 12.05" above the footing during ($\mu_5^{-1} = -6.72"$). The relationship between tension strain and displacement for the gage length 6.30" above the footing appears in Figure 1.929. Moment-curvature analysis with the PCK (2007) Lp Hinge Method begins to over predict measured tension strains at an increasing rate beyond displacement ductility two. A compressive strain of -0.0156 was measured 2.03" above the footing when the first confinement steel yielded on the south side of the specimen during ($\mu_3^{+1} = 4.03"$). A peak compressive strain of -0.0316 was measured 12.05" above the footing during ($\mu_5^{+1} = 6.72"$). The relationship between compressive strain and displacement for the gage length 8.22" above the footing appears in Figure 1.930. The measured compressive strains exceed the moment-curvature prediction with the PCK (2007) Lp Hinge Method beyond displacement ductility two.

Measured strains in six spiral layers which overlaid the south extreme fiber bar appear in Figure 1.925 for push cycles. Cycles during displacement ductility four produced successively larger inelastic demands on the third and fourth spiral layers. Strain gage and Optotrak strain hysteresis for the spiral layer 6.28" above the footing appears in Figure 1.939. The two measurement methods begin the deviate during displacement ductility three and four, when the effects of measurable deformation became apparent and presumably the arc-strains no longer represent the geometry of the spiral over bar S3. The spiral strains increased during ($\mu_5^{+2} = 6.72"$) when visible bar buckling was observed. Measured arc-strains around the circumference of the fourth and fifth spiral layers on the south side of the specimen during push cycles appear in Figure 1.943 and Figure 1.944.

The influence of measurable deformation before bar buckling becomes easier to understand when the specific gage lengths in question are located on buckled bar, Figure 1.935. Bar S3 strain hysteresis for gage lengths 4.34", 6.30" and 8.22" above the footing appear in Figure 1.936, Figure 1.937, and Figure 1.938. The gage length 6.30" above the footing overlaid the outward buckled region, Figure 1.916. The hysteresis remained stable until visible bar buckling occurred during ($\mu_5^{+2} = 6.72"$). The gage lengths 4.34" and 8.22" above the footling were just below and above the outward buckled region. Significantly larger compressive strains were measured 8.22" above the footing, Figure 1.938, after confinement steel yielded during ($\mu_3^{+1} = 4.03"$).

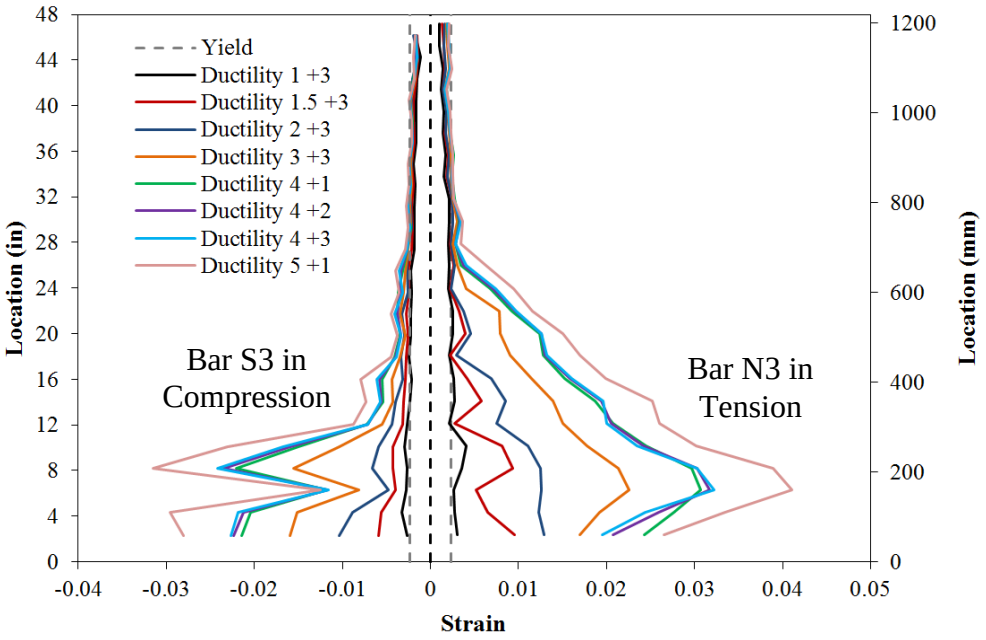

Figure 1.921 T29 – Extreme Fiber Bar Vertical Strain Profiles during Push Cycles

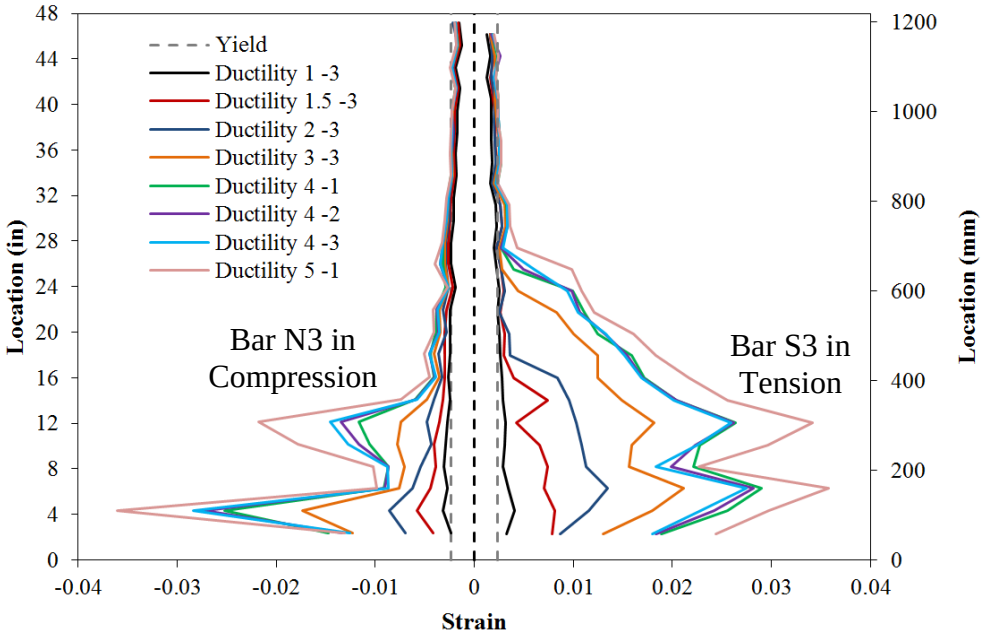

Figure 1.922 T29 – Extreme Fiber Bar Vertical Strain Profiles during Pull Cycles

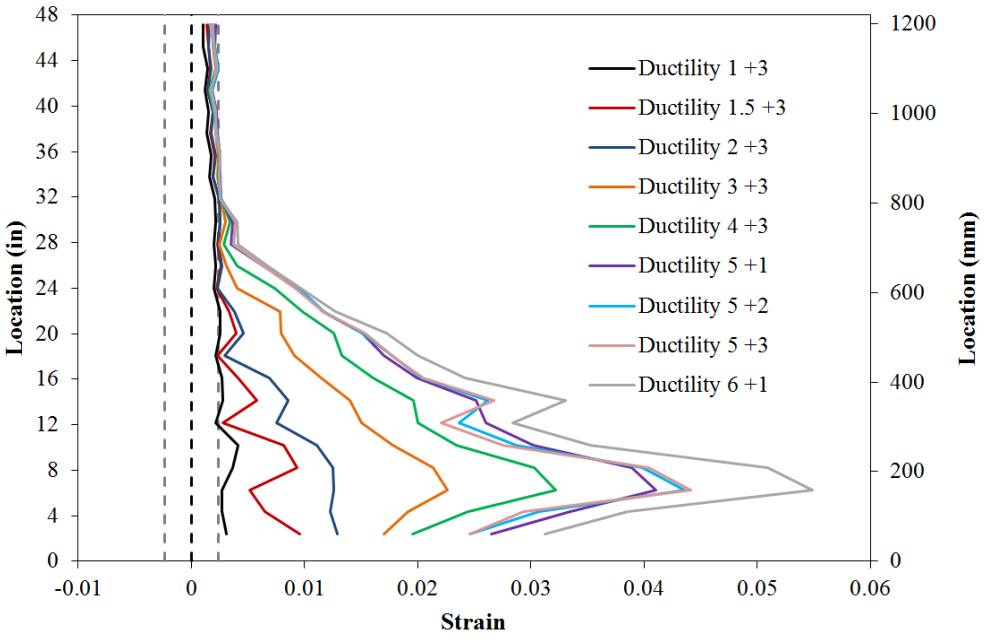

Figure 1.923 T29 – Extreme Fiber Bar N3 Tension Strain Profiles for Push Cycles

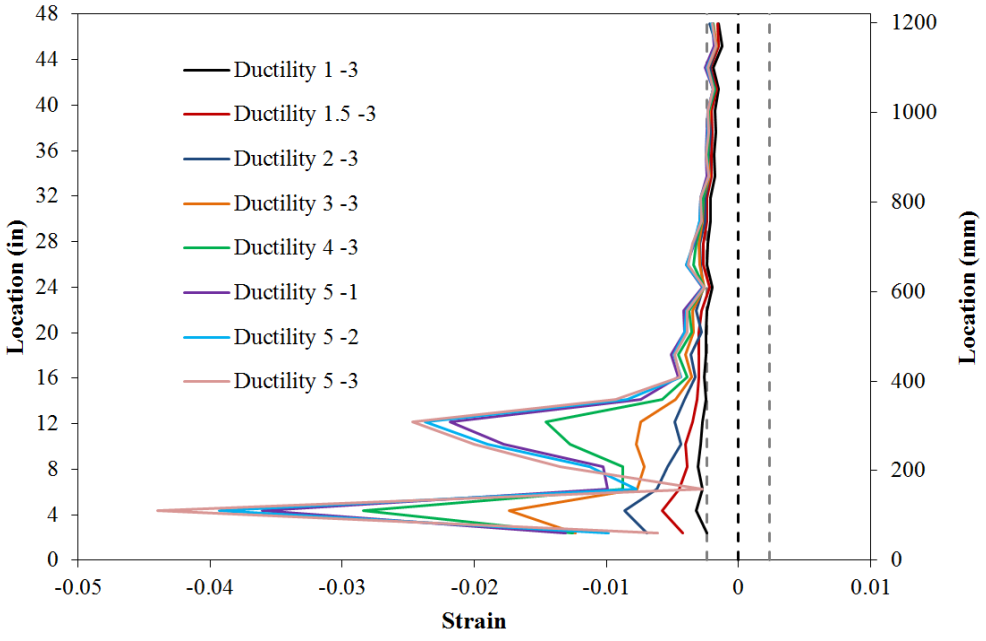

Figure 1.924 T29 – Extreme Fiber Bar N3 Compression Strain Profiles for Pull Cycles

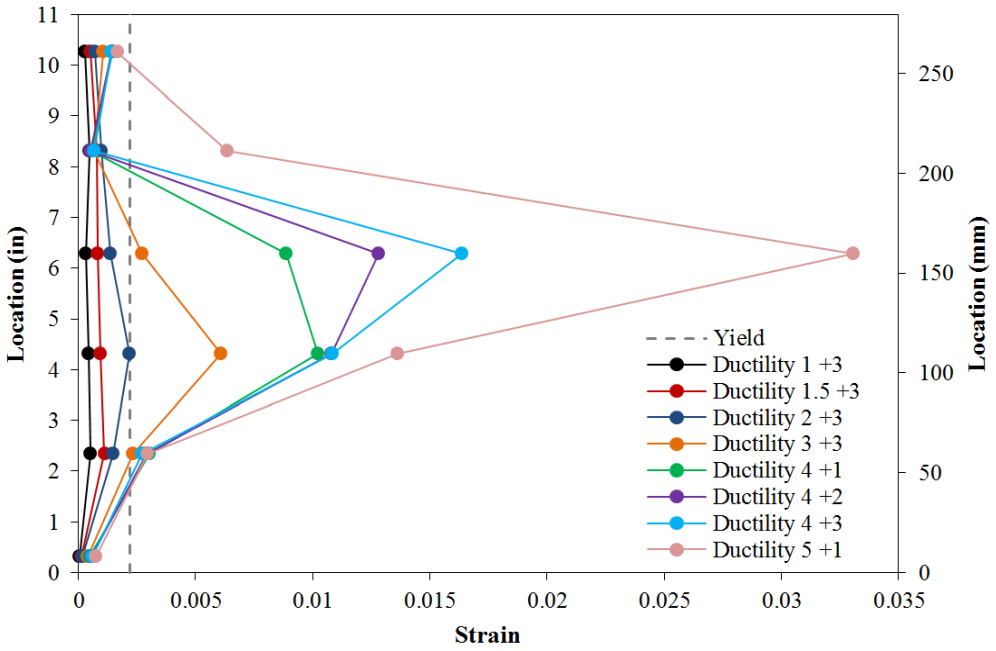

Figure 1.925 T29 – Spiral Strain on the South Side of the Specimen during Push Cycles

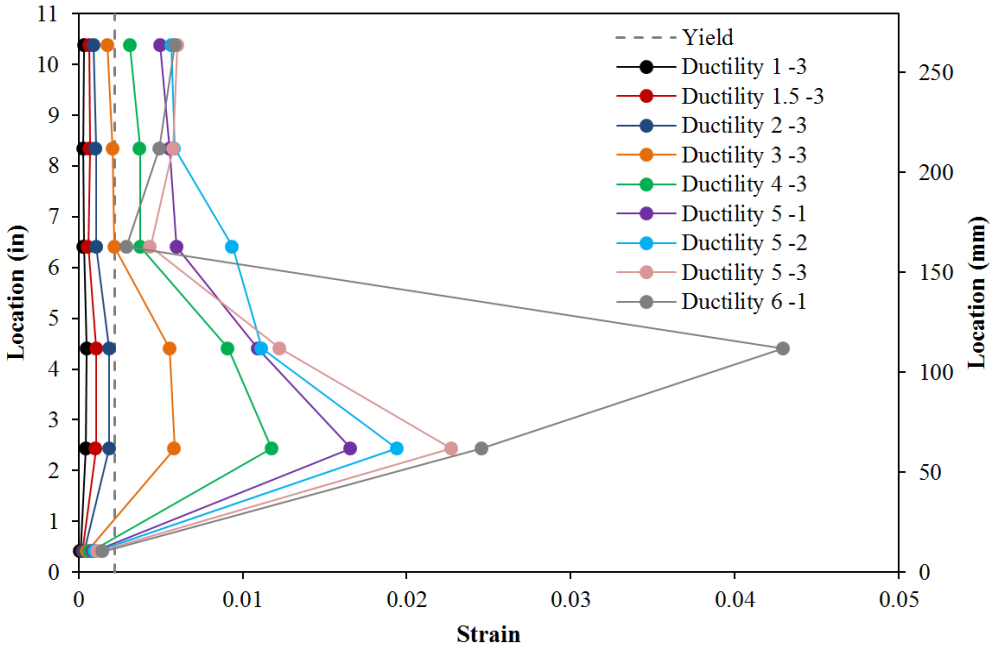

Figure 1.926 T29 – Spiral Strain on the North Side of the Specimen during Pull Cycles

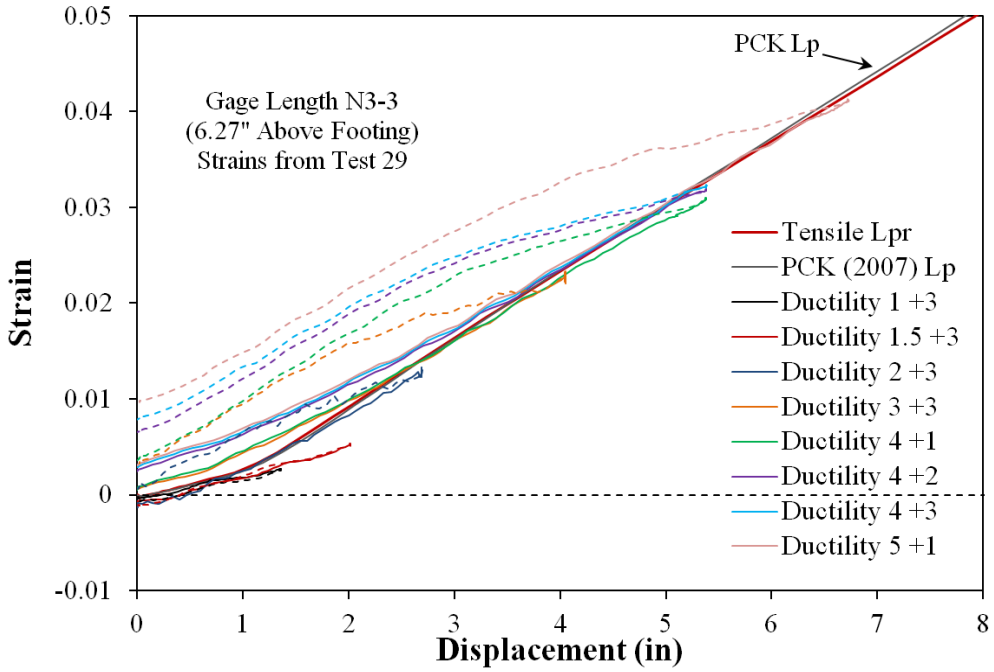

Figure 1.927 T29 – Tensile Strain-Displacement for Bar N3 during Push Cycles

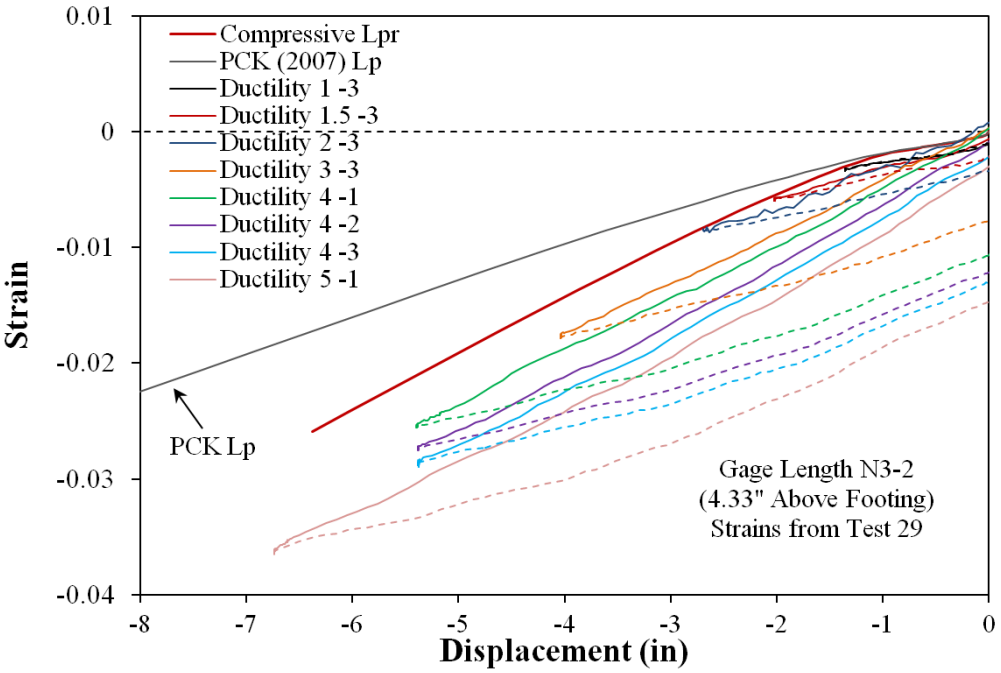

Figure 1.928 T29 – Compressive Strain-Displacement for Bar N3 during Pull Cycles

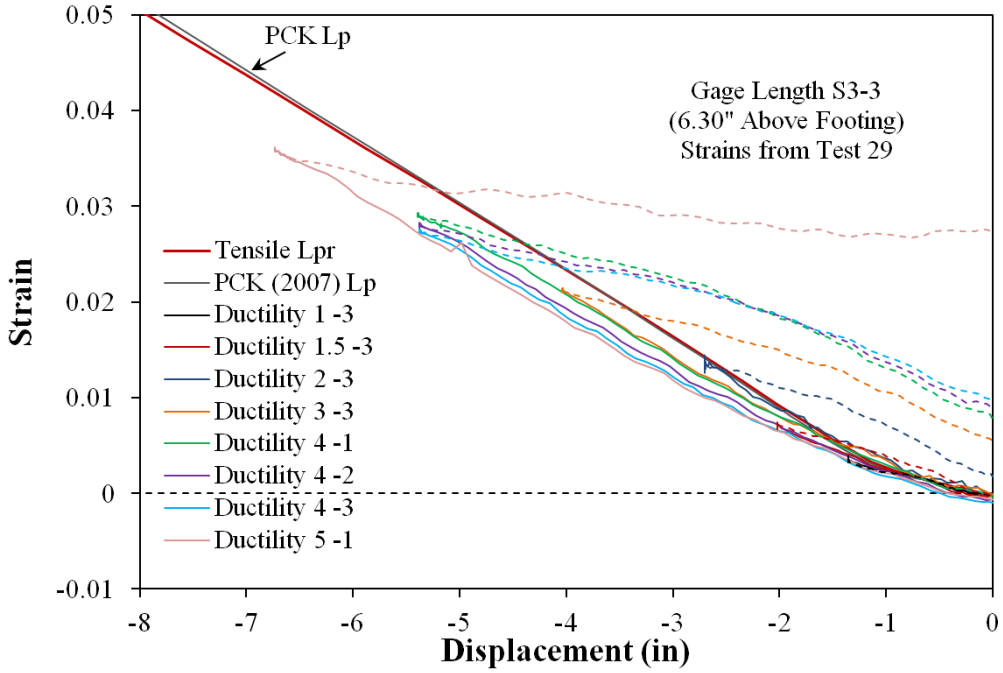

Figure 1.929 T29 – Tensile Strain-Displacement for Bar S3 during Pull Cycles

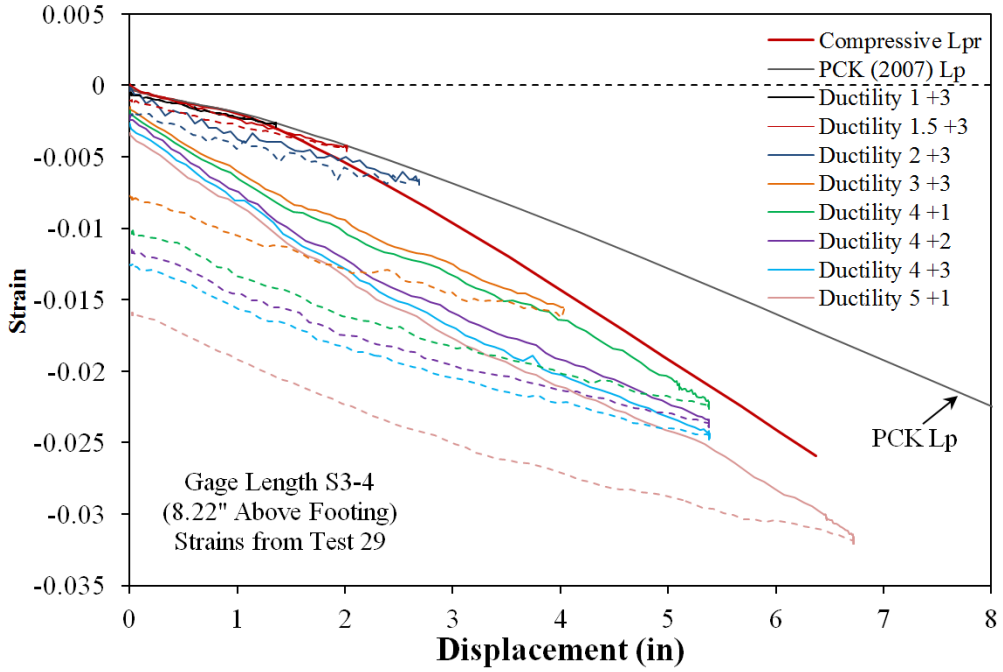

Figure 1.930 T29 – Compressive Strain-Displacement for Bar S3 during Push Cycles

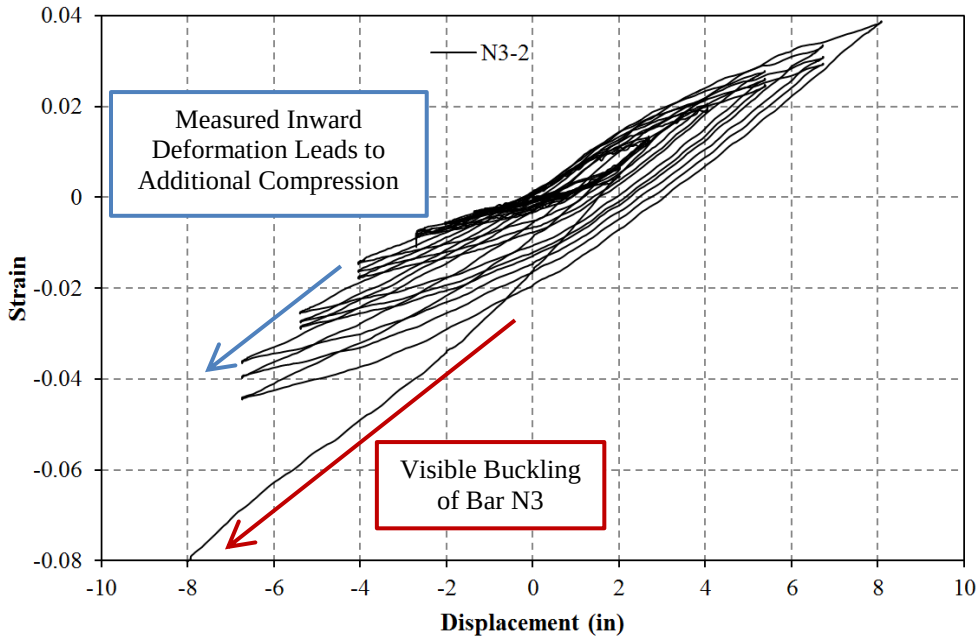

Figure 1.931 T29 – Bar N3 Strain Hysteresis to Buckling (4.33" Above the Footing)

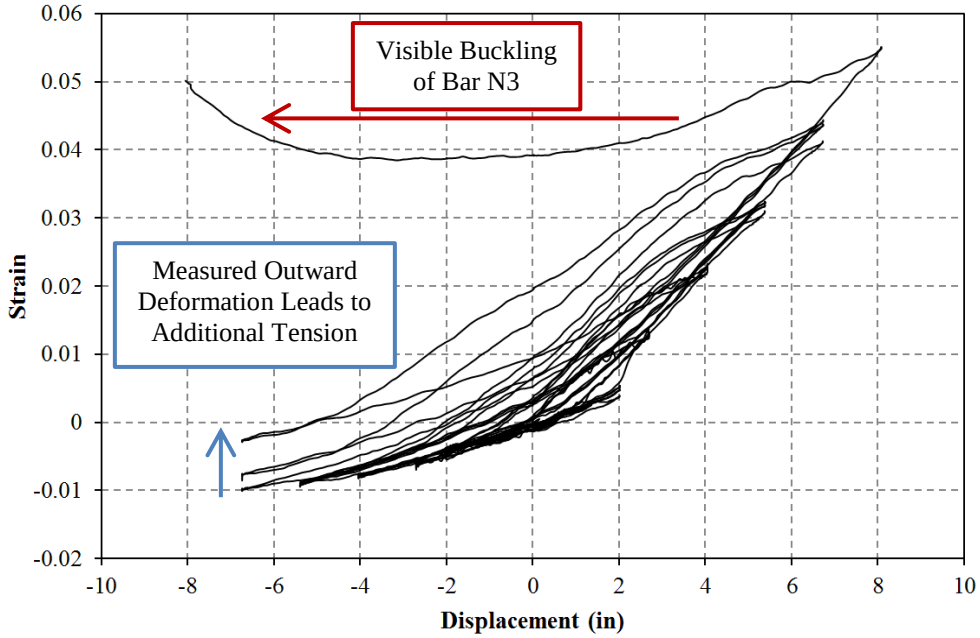

Figure 1.932 T29 – Bar N3 Strain Hysteresis to Buckling (6.27" Above the Footing)

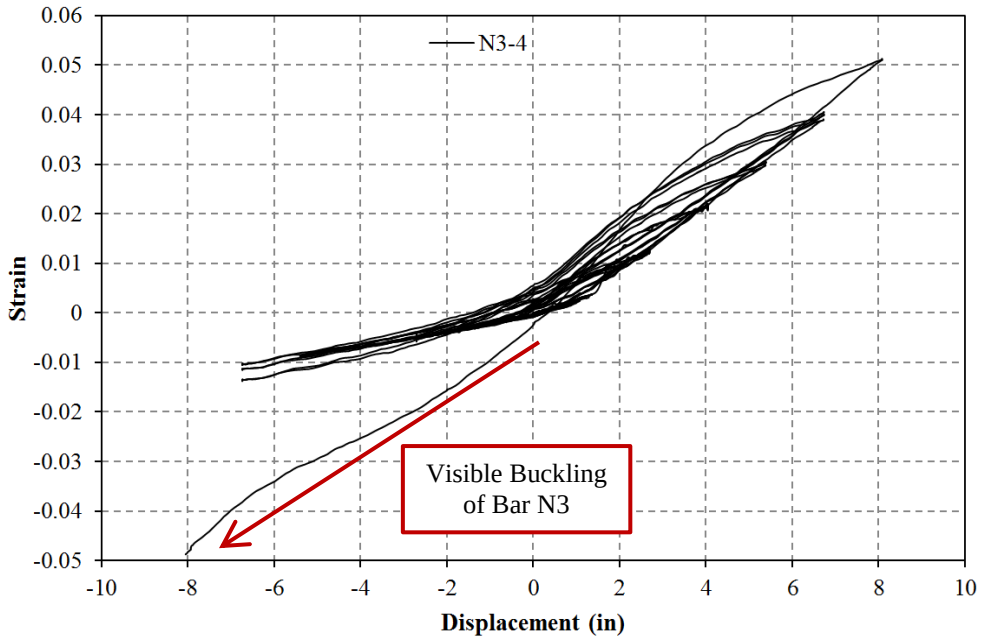

Figure 1.933 T29 – Bar N3 Strain Hysteresis to Buckling (8.22" Above the Footing)

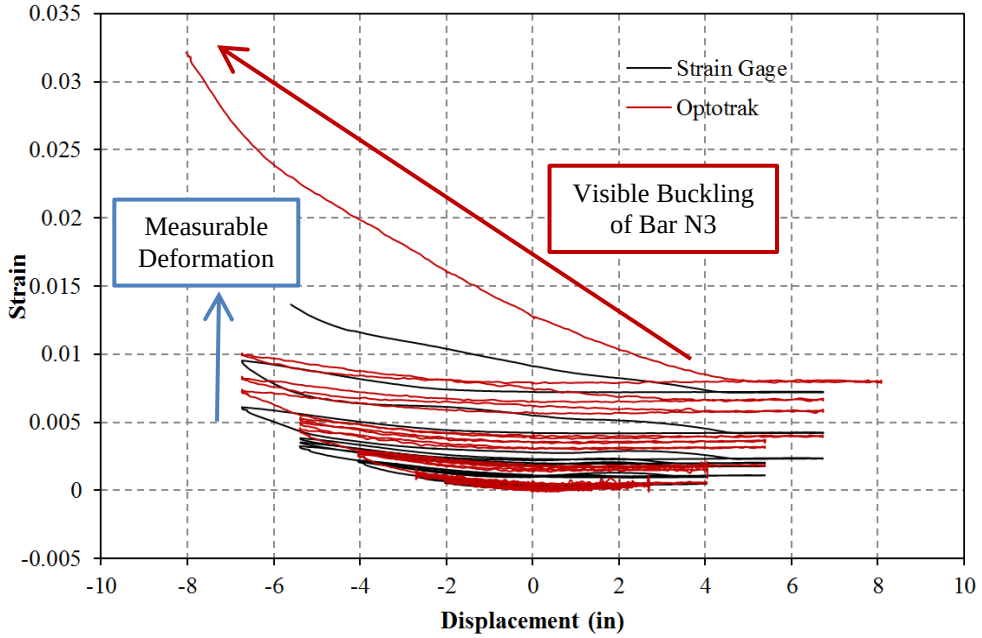

Figure 1.934 T29 – Spiral Strain Hysteresis over North Buckled Region (6.41" Above)

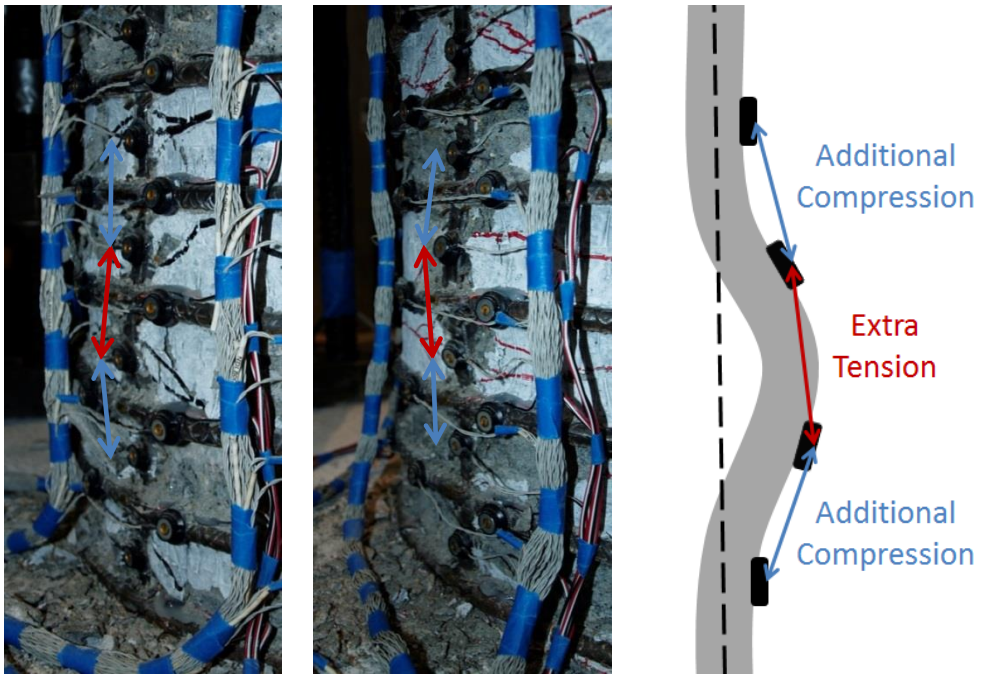

Figure 1.935 T29 – Buckled Shape of Bar N3 (Left) and Bar S3 (Middle)

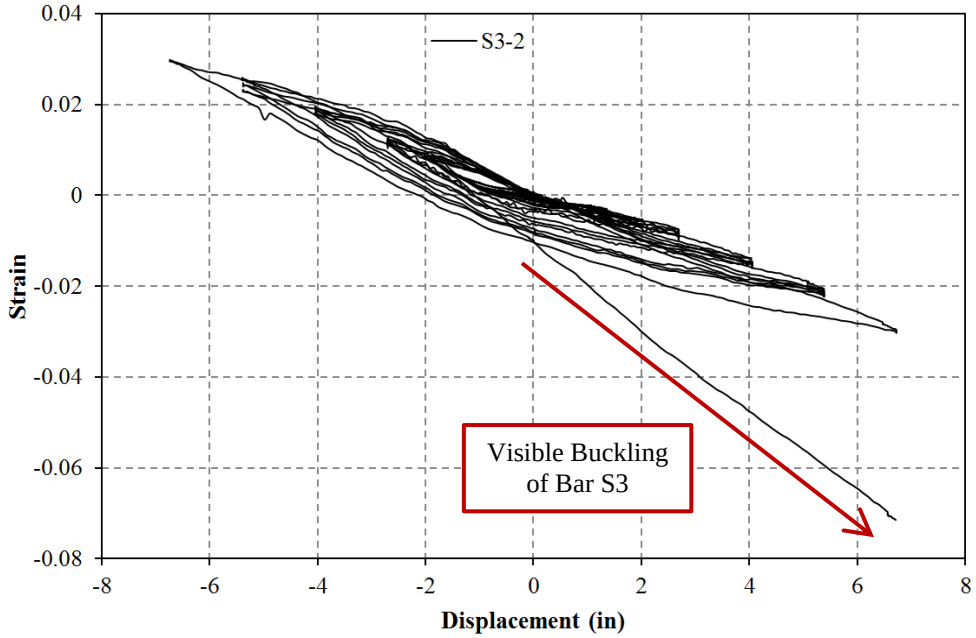

Figure 1.936 T29 – Bar S3 Strain Hysteresis to Buckling (4.34" Above the Footing)

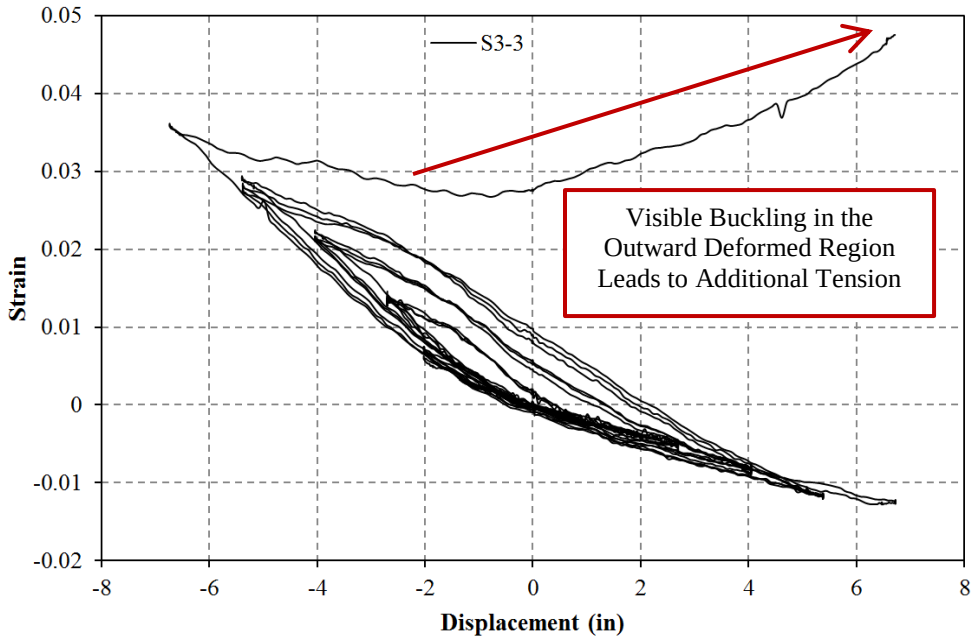

Figure 1.937 T29 – Bar S3 Strain Hysteresis to Buckling (6.30" Above the Footing)

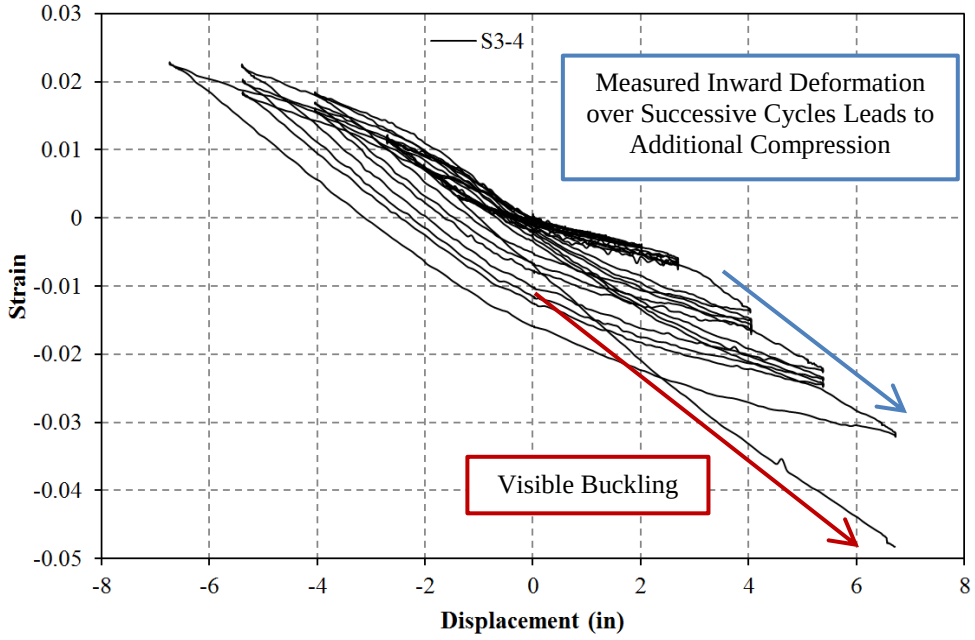

Figure 1.938 T29 – Bar S3 Strain Hysteresis to Buckling (8.22" Above the Footing)

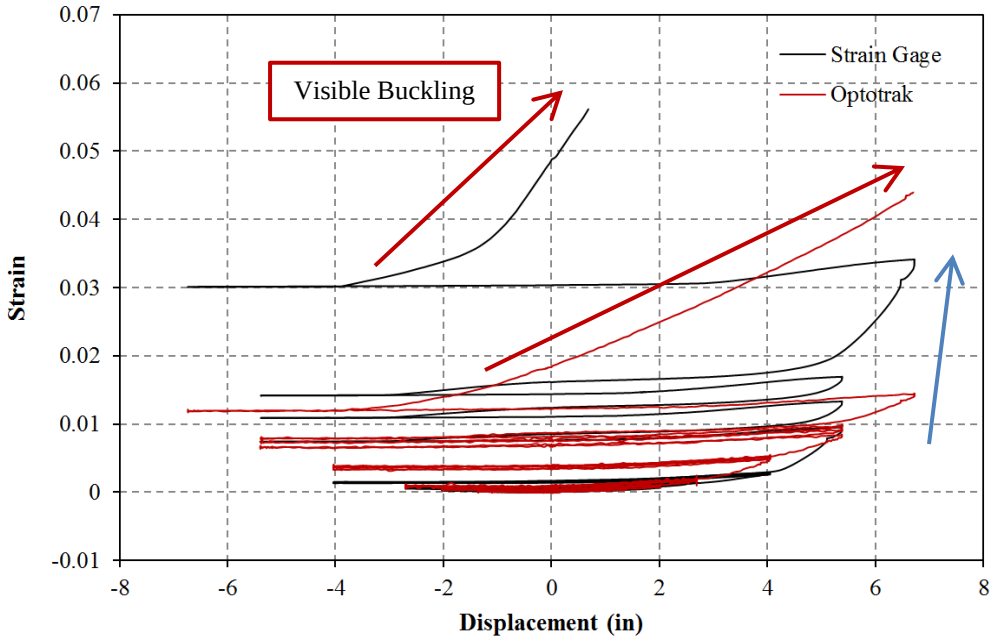

Figure 1.939 T29 – Spiral Strains over the North Buckled Region (6.28" Above)

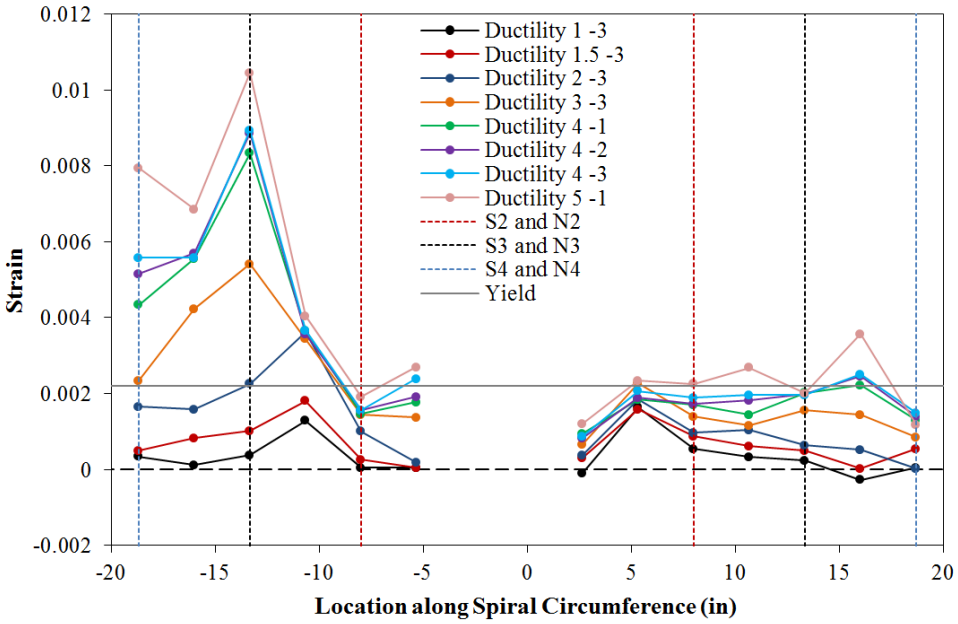

Figure 1.940 T29 – Spiral Strain Distribution for the 2nd Spiral above the Footing during Pull Cycles (Negative = North)

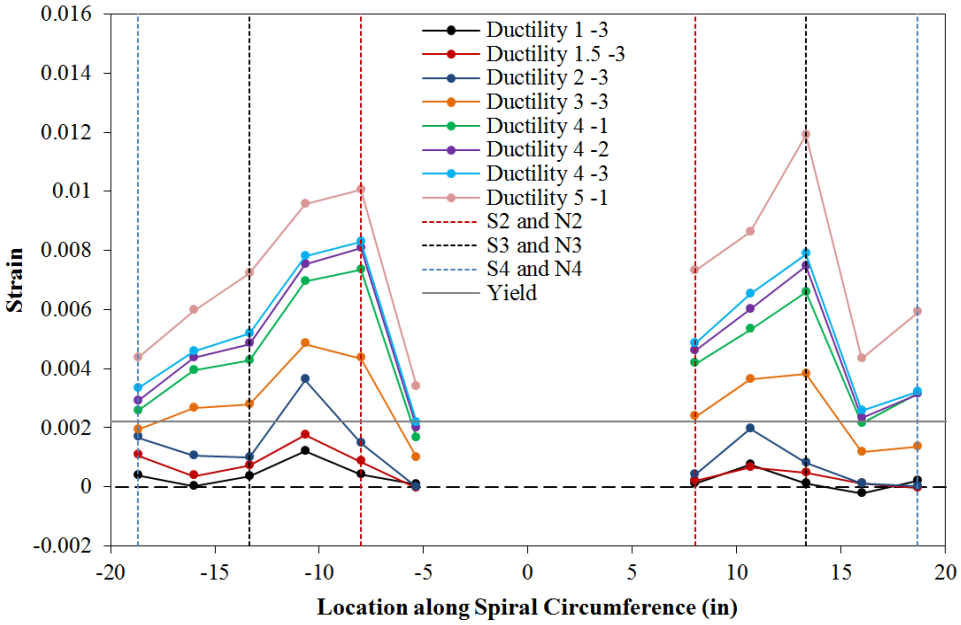

Figure 1.941 T29 – Spiral Strain Distribution for the 4th Spiral above the Footing during Pull Cycles (Negative = North)

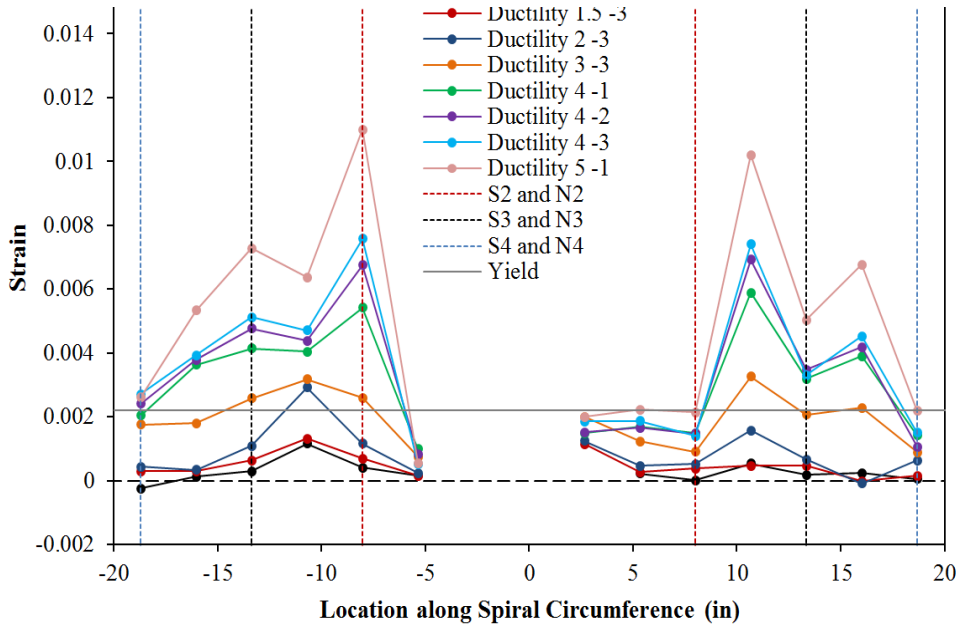

Figure 1.942 T29 – Spiral Strain Distribution for the 5th Spiral above the Footing during Pull Cycles (Negative = North)

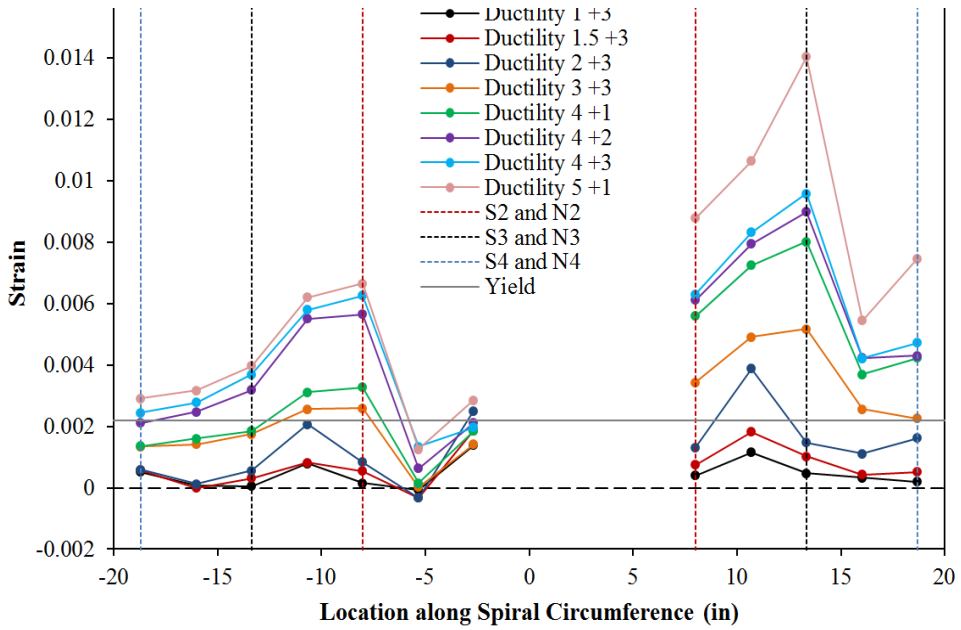

Figure 1.943 T29 – Spiral Strain Distribution for the 4th Spiral above the Footing during Push Cycles (Positive = South)

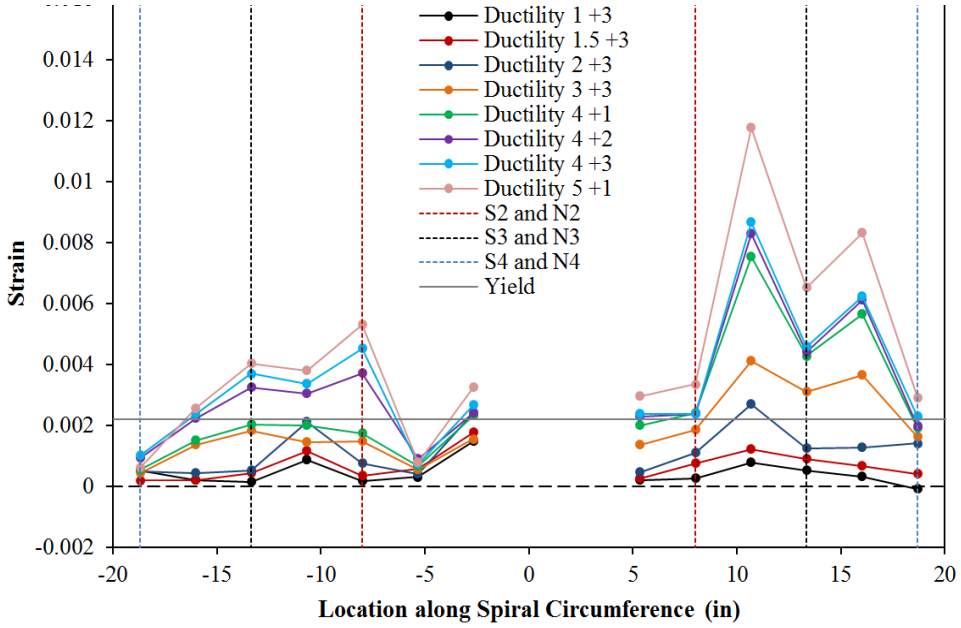

Figure 1.944 T29 – Spiral Strain Distribution for the 5th Spiral above the Footing during Push Cycles (Positive = South)

Test 29 – Curvature and Strain Penetration Data

Cross section strain profiles for the second horizontal section above the footing appear in Figure 1.945 and Figure 1.946 for push and pull cycles respectively. Individual bar strains appear to deviate from the planes section hypothesis for this section. The curvature is calculated as the slope of the least squared line connecting strains measured in eight instrumented reinforcing bars, Figure 1.897. If the curvatures for many horizontal cross sections are analyzed, curvature profiles for the plastic hinge region can be constructed; Figure 1.947 and Figure 1.948 for push and pull cycles respectively. Measured curvatures during displacement ductility one closely match the elastic curvature profile, which linearly decreases from yield curvature at the footing-column interface to zero at the center of the applied lateral load. Linear least squared error plastic curvature lines were fit to the plastic portion of the measured curvature profiles. The extrapolation of this linear curvature line with the footing-column interface was taken as the base section curvature. As the base section curvature ductility increased, the height at which the linear plastic curvature distribution intersected the elastic curvature profile also increased. Circular data points in Figure 1.952 plot the measured spread of plasticity as a function of base section curvature ductility.

Curvature profiles describe the elastic and plastic flexural displacements of the column, but do not address fixed-end rotations which result from development of longitudinal reinforcement into the footing. The measured vertical displacements of Optotrak LEDs placed closest to the footing column interface can be used to quantify this fixed-end rotation, Figure 1.949 and Figure 1.950. The fixed-end rotation is taken as the slope of the least squared error line fit to the bond slip profile. If an elastic curvature profile assumption is made for curvatures higher than those measured with instrumentation, then the entire curvature profile may be integrated to obtain the total column flexural displacement. This column flexural displacement was added to the strain penetration displacement, and compared to the experimentally measured displacements in Figure 1.951.

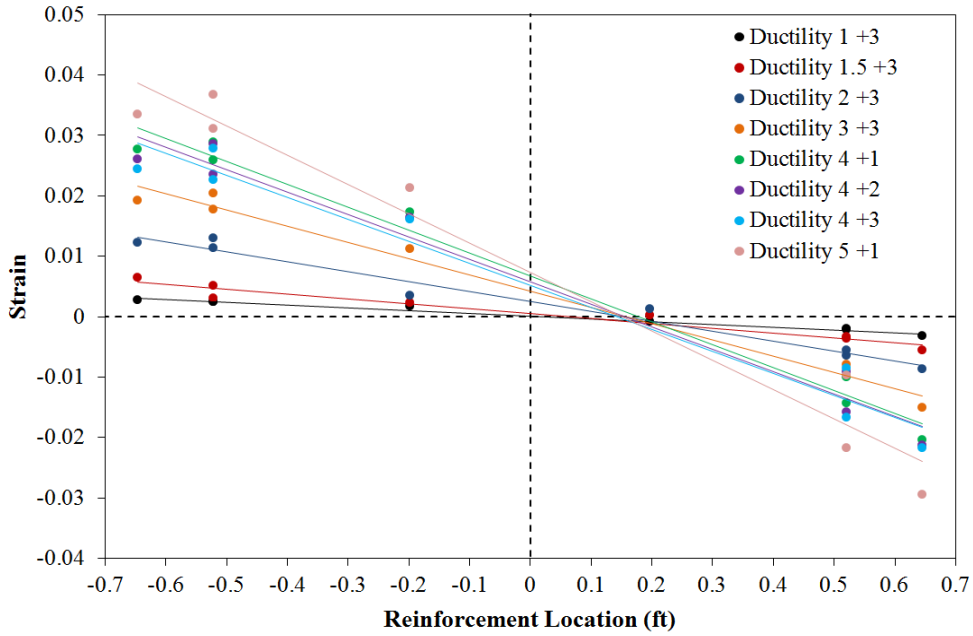

Figure 1.945 T29 – Push Cycle Strain Profiles for Section 4.31" Above the Footing

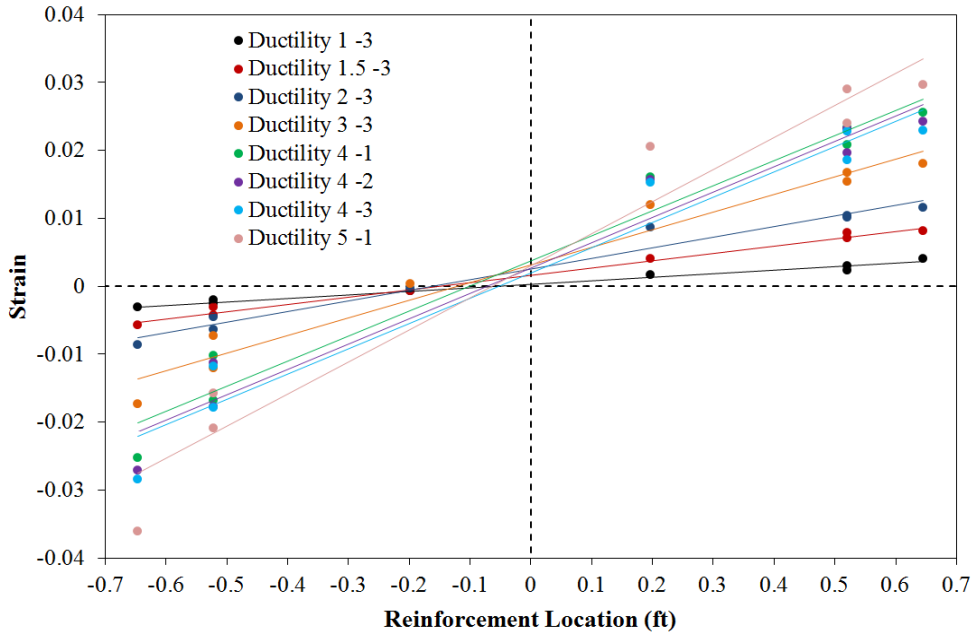

Figure 1.946 T29 – Pull Cycle Strain Profiles for Section 4.31" Above the Footing

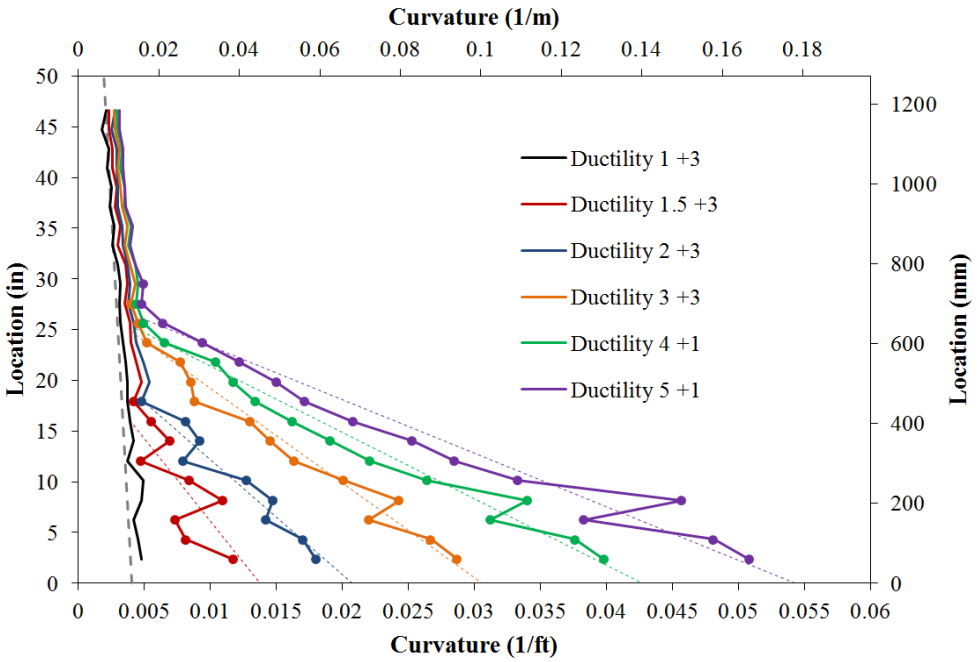

Figure 1.947 T29 – Push Cycle Curvature Profiles with Linear Plastic Regression

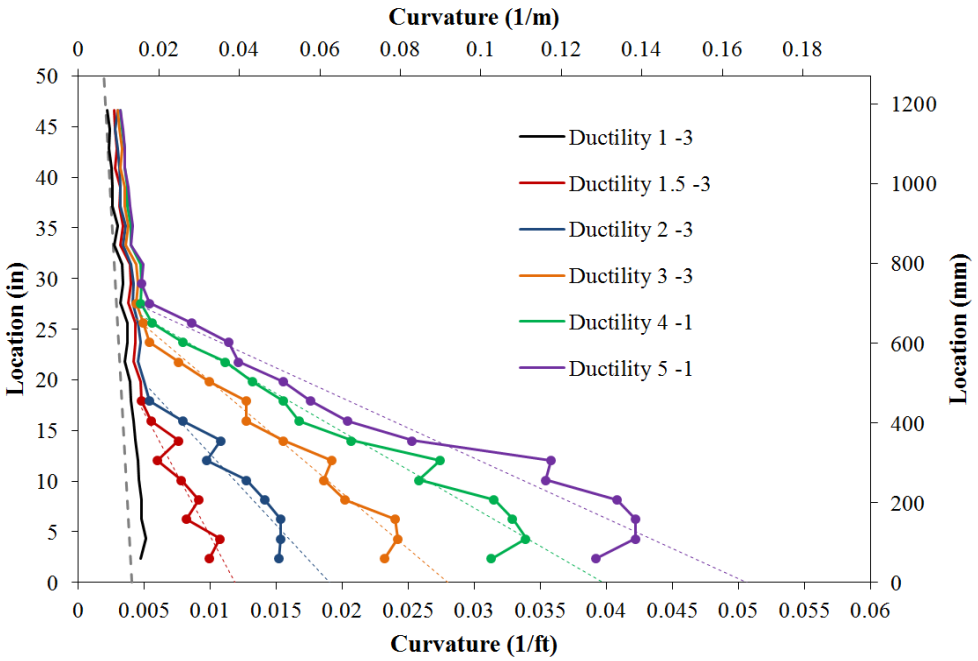

Figure 1.948 T29 – Pull Cycle Curvature Profiles with Linear Plastic Regression

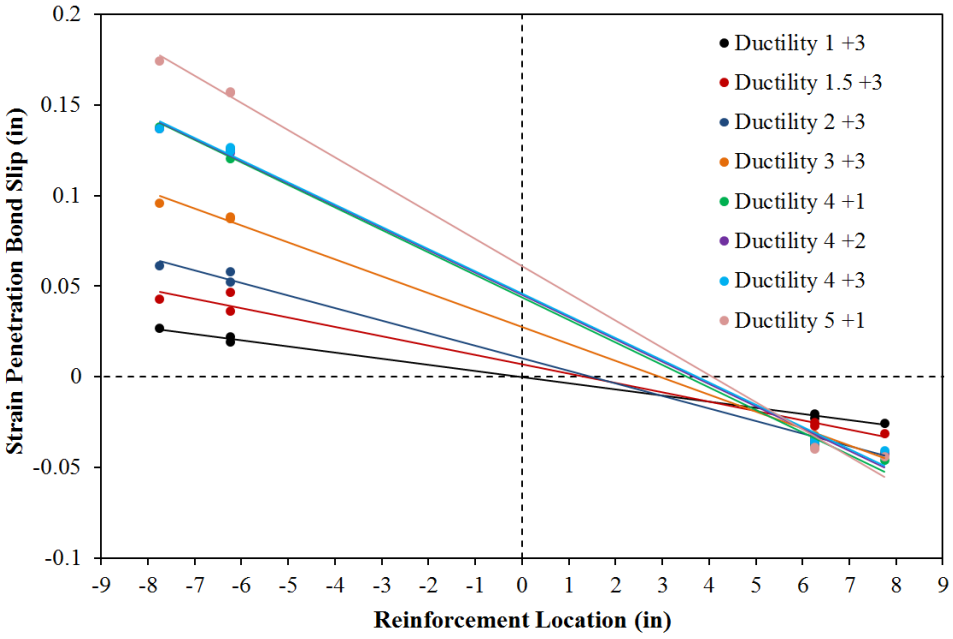

Figure 1.949 T29 – Base Rotation due to Strain Penetration during Push Cycles

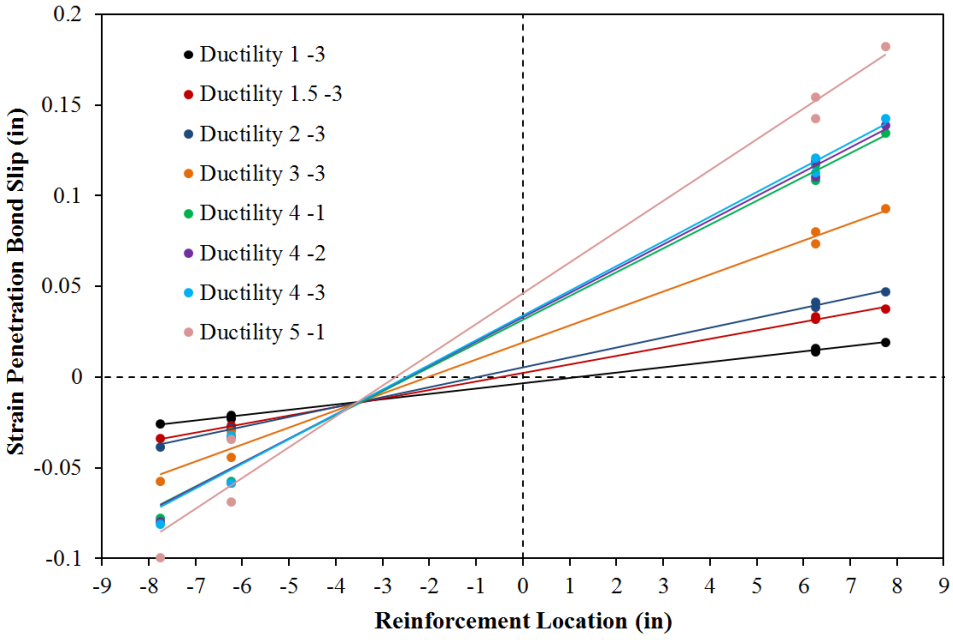

Figure 1.950 T29 – Base Rotation due to Strain Penetration during Pull Cycles

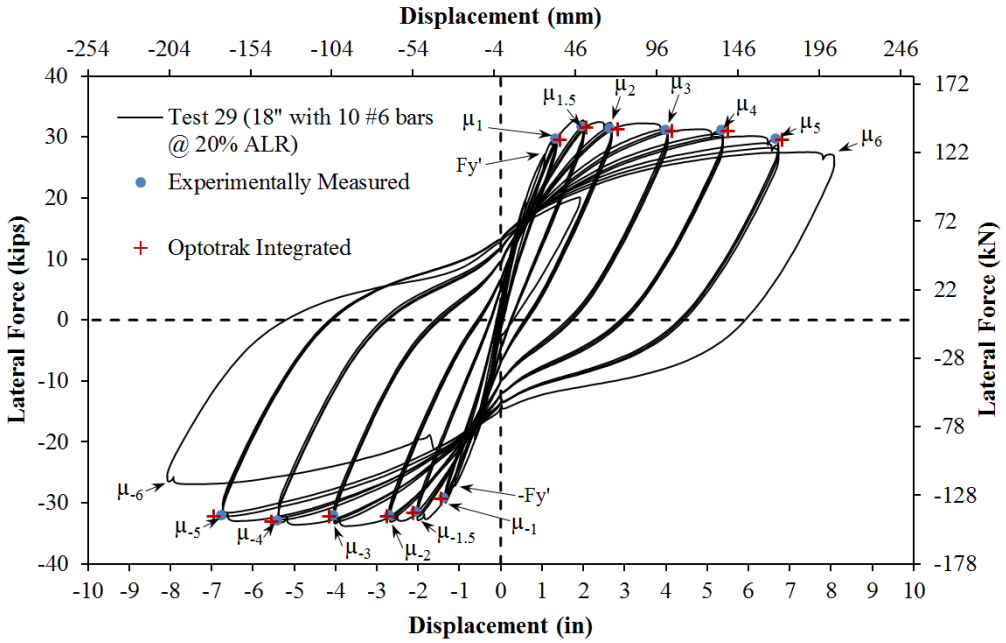

Figure 1.951 T29 – Comparison of Measured and Optotrak Integrated Displacements

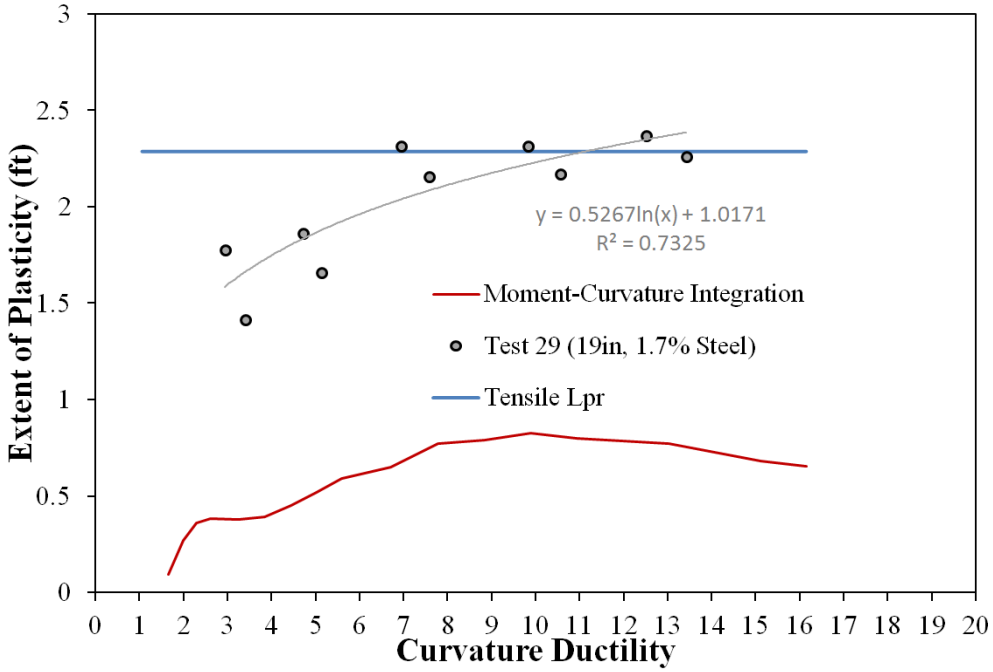

Figure 1.952 T29 – Measured Spread of Plasticity (Circular Data Points)

1.4.6 Test 30 – 18" Dia. Column with 3.1% Long. Steel and 15% Axial Load

Table 1.57 Observations for Test 30 – 18" Dia. With 3.1% Steel and 15% Axial Load

VALUES OF INTEREST:	
Concrete Compressive Strength:	$f_c' = 6050\ psi$
Axial Load:	$P = 206\ kips\ \ (P/(f_c' A_g) = 15\%)$
Longitudinal Steel Content:	10 #8 $Bars\ \ (A_{st}/A_g = 3.1\%)$
Analytical First Yield Force:	$F_y' = 34.61\ kips$
Experimental First Yield Displacement:	$\Delta_y' = 1.15"$
Analytical Nominal Moment Capacity:	$M_n = 356.35\ kip * ft$
Equivalent Yield Displacement:	$\Delta_y = 1.48"$
Maximum Lateral Force:	$47.48\ kips$
DAMAGE OBSERVATIONS:	
First Cracking North:	$3/4Fy' = 0.69"$
First Cracking South:	$-3/4Fy' = -0.76"$
Cover Concrete Crushing North:	$\mu_{1.5}^{-1} = -2.21"$
Cover Concrete Crushing South:	$\mu_{1.5}^{+1} = 2.21"$
Transverse Steel Yield North:	At $-2.74"$ during pull to $\mu_2^{-1} = -2.95"$
Transverse Steel Yield South:	At $2.74"$ during push to $\mu_2^{+1} = 2.95"$
Longitudinal Bar Buckling North:	Reversal from $\mu_5^{+1} = 7.39"$
Longitudinal Bar Buckling South:	Reversal from $\mu_5^{-1} = -7.39"$
Longitudinal Bar Fracture North:	At $8.75"$ during push to $\mu_6^{+1} = 8.88"$
Longitudinal Bar Fracture South:	At $-3.27"$ during the final pull cycle of the test

*$\mu_5^{-1} = -7.39"$ represents the first pull cycle of displacement ductility five

Table 1.58 Strain Summary for Test 30 – 18" Dia. With 3.1% Steel and 15% Axial

MATERIAL STRAINS:	
Cover Concrete Crushing North:	$\varepsilon_s = 0.0052\ (compression)$
Cover Concrete Crushing South:	$\varepsilon_s = 0.0059\ (compression)$
Transverse Steel Yield North:	$\varepsilon_s = 0.0095\ (compression)$
Transverse Steel Yield South:	$\varepsilon_s = 0.0094\ (compression)$
Longitudinal Bar Buckling North:	$\varepsilon_s = 0.036\ (peak\ tension\ prior\ to\ bb)$
	$\varepsilon_s = 0.022\ (peak\ comp.\ prior\ to\ bb)$
Longitudinal Bar Buckling South:	$\varepsilon_s = 0.033\ (peak\ tension\ prior\ to\ bb)$
	$\varepsilon_s = 0.026\ (peak\ comp.\ prior\ to\ bb)$
Mander (1988) Ultimate Concrete Compression Strain, $\varepsilon_{cu} = 0.0197$	

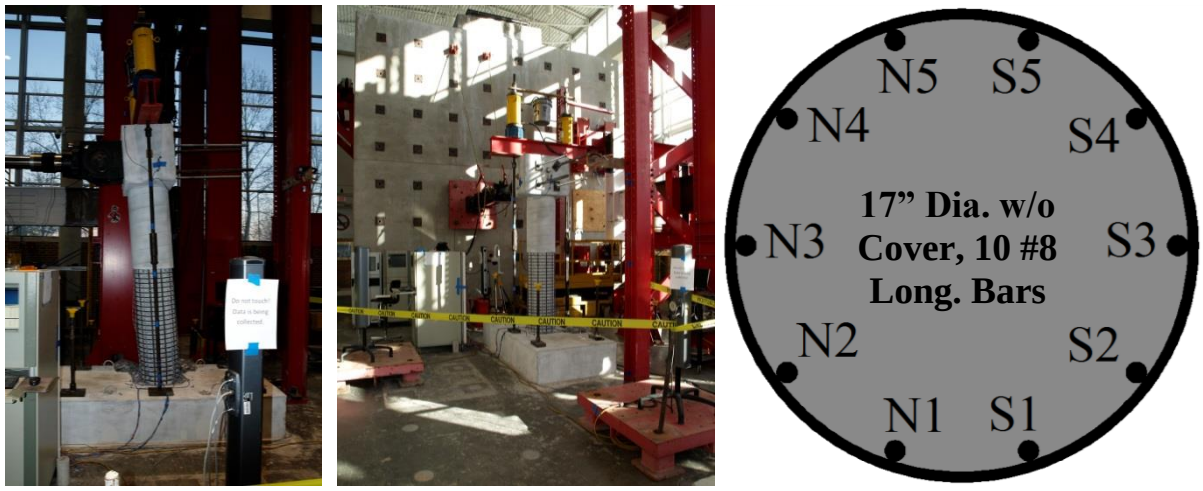

Figure 1.953 T30 – Test Setup and Cross Section Bar Designation

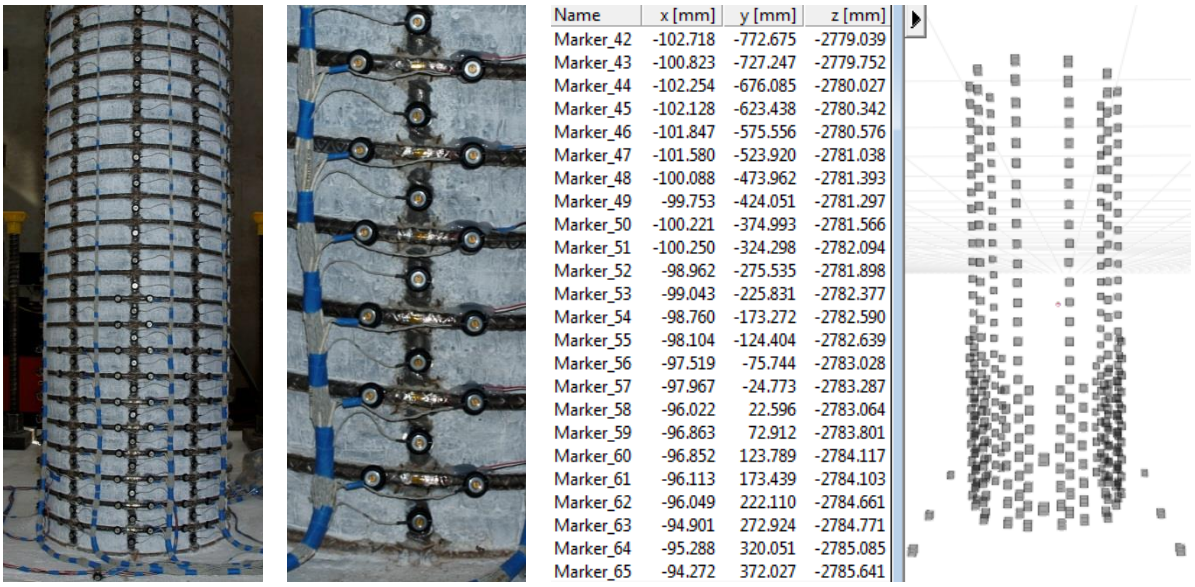

Name	x [mm]	y [mm]	z [mm]
Marker_42	-102.718	-772.675	-2779.039
Marker_43	-100.823	-727.247	-2779.752
Marker_44	-102.254	-676.085	-2780.027
Marker_45	-102.128	-623.438	-2780.342
Marker_46	-101.847	-575.556	-2780.576
Marker_47	-101.580	-523.920	-2781.038
Marker_48	-100.088	-473.962	-2781.393
Marker_49	-99.753	-424.051	-2781.297
Marker_50	-100.221	-374.993	-2781.566
Marker_51	-100.250	-324.298	-2782.094
Marker_52	-98.962	-275.535	-2781.898
Marker_53	-99.043	-225.831	-2782.377
Marker_54	-98.760	-173.272	-2782.590
Marker_55	-98.104	-124.404	-2782.639
Marker_56	-97.519	-75.744	-2783.028
Marker_57	-97.967	-24.773	-2783.287
Marker_58	-96.022	22.596	-2783.064
Marker_59	-96.863	72.912	-2783.801
Marker_60	-96.852	123.789	-2784.117
Marker_61	-96.113	173.439	-2784.103
Marker_62	-96.049	222.110	-2784.661
Marker_63	-94.901	272.924	-2784.771
Marker_64	-95.288	320.051	-2785.085
Marker_65	-94.272	372.027	-2785.641

Figure 1.954 T30 – Target Marker Application and Optotrak Spatial Output

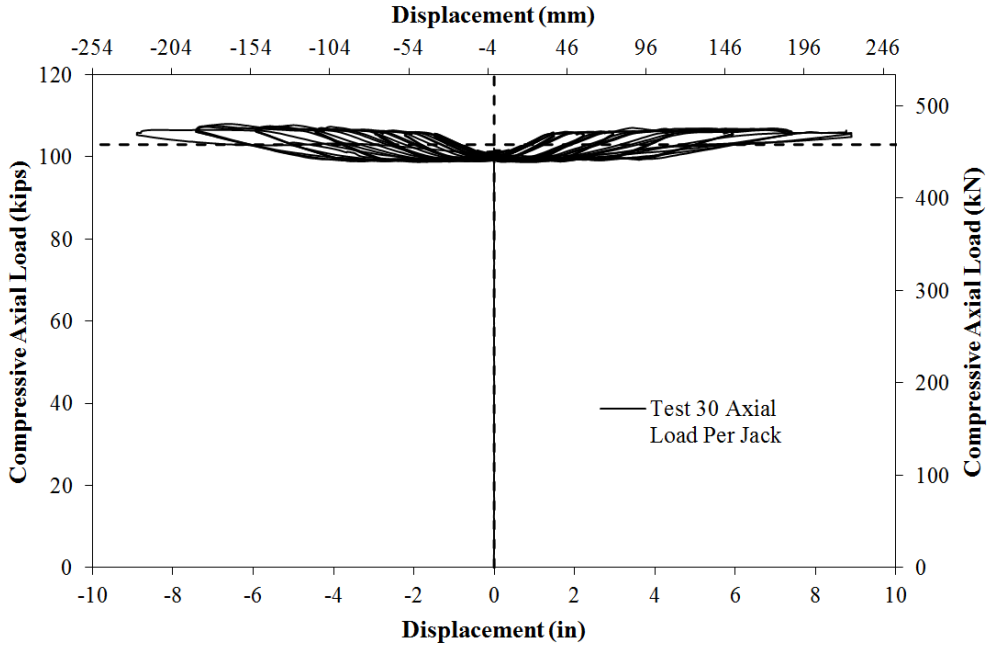

Figure 1.955 T30 – T28 – Compressive Axial Load from One Jack (Total = 2*Value)

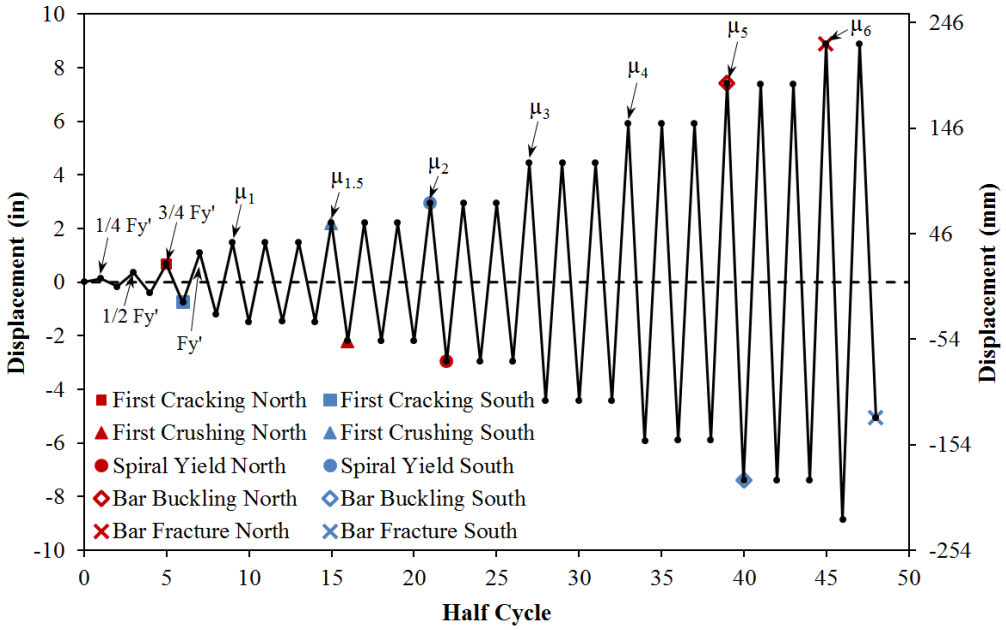

Figure 1.956 T30 – Symmetric Three Cycle Set Load History

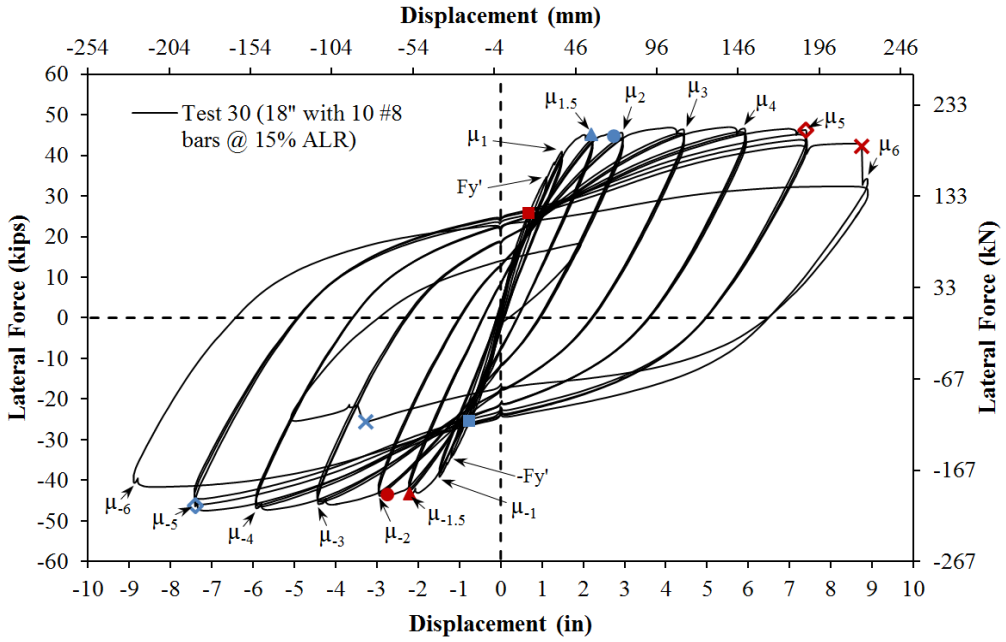

Figure 1.957 T30 – Lateral Force vs. Top Column Displacement Response

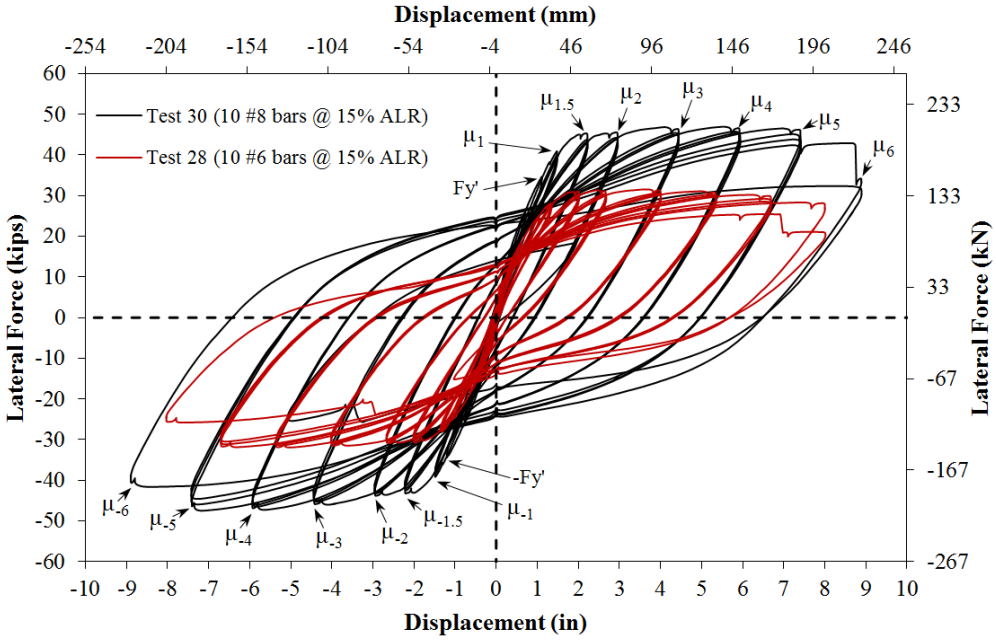

Figure 1.958 Hysteretic Comparison for T28 and T30 with Different Steel Content

Test 30 – 18" Dia. with 3.1% Steel and 15% Axial Load – Experimental Observations

Specimens 25-30 focus on the effects of longitudinal steel content, longitudinal bar diameter, and higher levels of axial load on column behavior. This section summarizes experimental observations and data analysis for Test 30. The 18" diameter column contains 10 #8 (A706) bars for longitudinal reinforcement ($A_{st}/A_g = 3.1\%$) and a #3 A706 spiral at 2" on center ($4A_{sp}/(D's) = 1.3\%$). The specimen had an 8ft cantilever length ($L/D = 5.33$), and was subjected to ($P/(f_c'A_g) = 15\%$) axial load. Previous Test 28 was nominally identical, except it was reinforced with 10 #6 longitudinal bars (1.7%). The symmetric three-cycle-set load history is commonly used to evaluate the seismic performance of structural components. The load history begins with elastic cycles to the following increments of the analytically predicted first yield force: ¼ F_y', ½ F_y', ¾ F_y', and F_y'. The experimental first yield displacement is then determined by taking the average of the

recorded displacements during the first yield push and pulls cycles. The equivalent yield displacement, used to determine the displacement ductility levels ($\mu_{\Delta 1} = 1 * \Delta_y$), is then calculated as $\Delta_y = \Delta'_y(M_n/M'_y)$. The symmetric three-cycle-set load history resumes with three cycles at each of the following displacement ductility levels: 1, 1.5, 2, 3, 4, 5, etc.

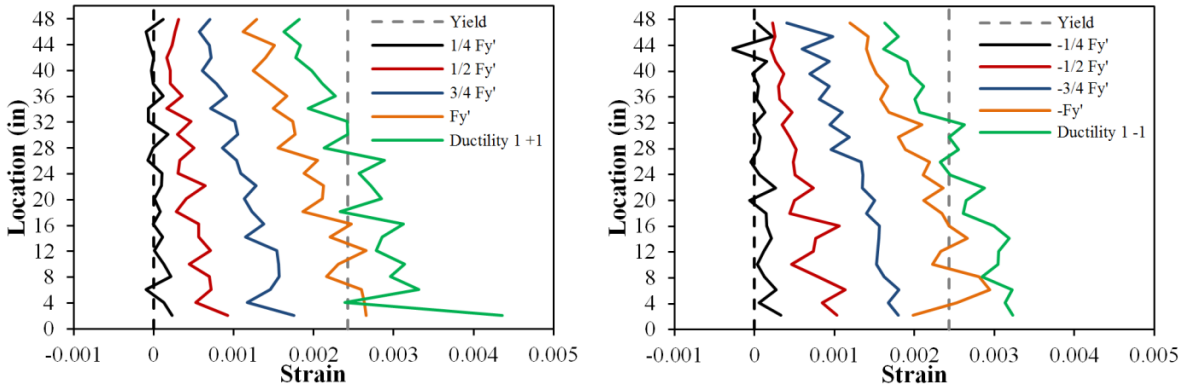

Figure 1.959 T30 – Strain Profiles before Yield, (Left) North and (Right) South

The test began with cycles in ¼ Fy' (first yield force) increments in each direction of loading until the first yield force was reached. The first cracks on the north and south sides of the specimen formed during ($3/4Fy' = 0.69$") and ($-3/4Fy' = -0.76$") respectively, Figure 1.960. The crack distribution on all sides of the specimen at first yield, ($Fy' = 1.10$") and ($-Fy' = -1.20$"), appears in Figure 1.961. Tensile vertical strain profiles for north and south reinforcing bars during elastic push and pull cycles appear in Figure 1.959. The average experimental first yield displacement was used to calculate the equivalent yield displacement, $\Delta_y = \Delta'_y(M_n/M'_y) = 1.15$", which defined the reversal amplitudes for reminder of the test.

The crack progression at displacement ductility 1, 1.5, 2, and 3 appear in Figure 1.962, Figure 1.964, Figure 1.966, and Figure 1.967 respectively. During these cycles the cracks

became more numerous and increased in inclination on the shear faces of the specimen. Small amounts concrete crushing was observed on the south and north sides of the specimen during ($\mu_{1.5}^{+1} = 2.21"$) and ($\mu_{1.5}^{-1} = -2.21"$), Figure 1.963. As compressive demands increased during displacement ductility 1.5 to 4, crushing gradually increased on each side of the specimen. Compressive demand during ($\mu_{2}^{+1} = 2.95"$) and ($\mu_{2}^{-1} = -2.95"$) led to spiral yielding in confinement regions, Figure 1.965. Spiral strains on each side of the specimen increased during successive cycles of ductility four, but the extreme fiber reinforcement remained visibly straight, Figure 1.968.

Even though spiral strains in confinement regions increased, the south extreme fiber bar remained visibly straight during ($\mu_{5}^{+1} = 7.39"$), Figure 1.969. The north extreme fiber bar visibly buckled during ($\mu_{5}^{-1} = -7.39"$), Figure 1.969. Visible buckling of the south extreme fiber bar was observed during the subsequent reversal to ($\mu_{5}^{+2} = 7.38"$), Figure 1.970. The buckled deformation in the north (Figure 1.970) and south (Figure 1.971) extreme fiber bars increased during ($\mu_{5}^{-2} = -7.40"$) and ($\mu_{5}^{+3} = 7.39"$) respectively. The extent of spiral deformation over the south buckled bar during ($\mu_{5}^{-3} = -7.39"$) is shown in Figure 1.971. The previously buckled north extreme fiber bar fractured during ($\mu_{6}^{+1} = 8.88"$), Figure 1.972, resulting in the first significant loss in strength. Two adjacent north reinforcing bars, N2 and N4, buckled during ($\mu_{6}^{-1} = -8.88"$), Figure 1.972. Two adjacent south reinforcing bars, S2 and S4, buckled during ($\mu_{6}^{+2} = 8.87"$), Figure 1.973. The south extreme fiber bar fractured at -3.27" during μ_{6}^{-2}, Figure 1.973. At this point the test was concluded with fractured reinforcement on each side of the specimen and severe strength loss. Photos of the specimen after the instrumentation was removed appear in Figure 1.974 and Figure 1.975. Crushed concrete behind buckled bars in extreme fiber regions was removed, highlighting the effect confinement loss behind deformed transverse steel.

Figure 1.960 T30 – (Left) Cracking on the North Side during ($3/4Fy' = 0.69$"), (Right) South Cracking ($-3/4Fy' = -0.76$")

Figure 1.961 T30 – (Left) North Crack Distribution at ($Fy' = 1.10$"), (Middle and Right) Crack Distributions on the Front and Right Sides at ($-Fy' = -1.20$")

Figure 1.962 T30 – (Left) North Crack Distribution at ($\mu_1^{+3} = 1.48$"), (Middle and Right) Crack Distributions on the Front and Right Sides at ($\mu_1^{-3} = -1.48$")

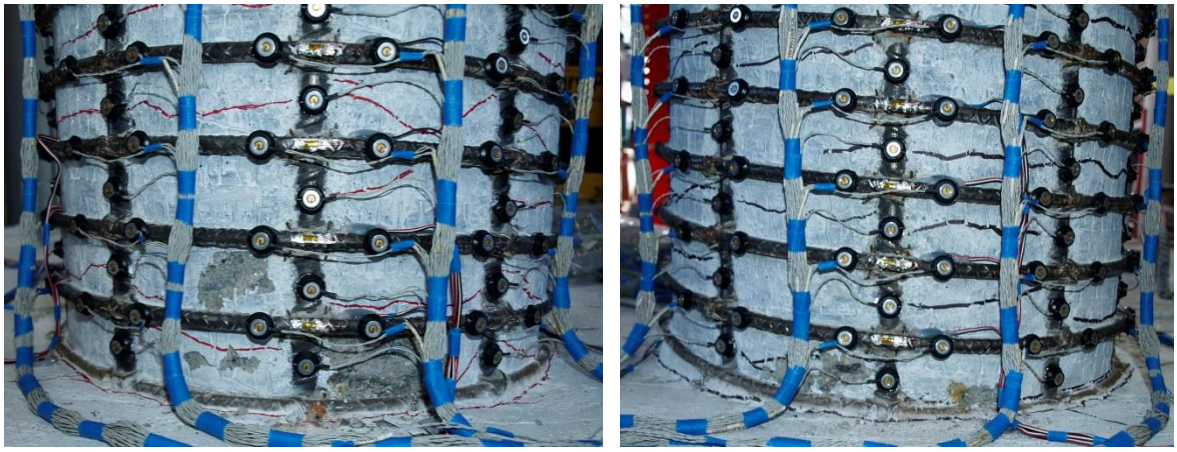

Figure 1.963 T30 – (Left) South Concrete Crushing during ($\mu_{1.5}^{+1} = 2.21$"), (Right) North Crushing during ($\mu_{1.5}^{-1} = -2.21$")

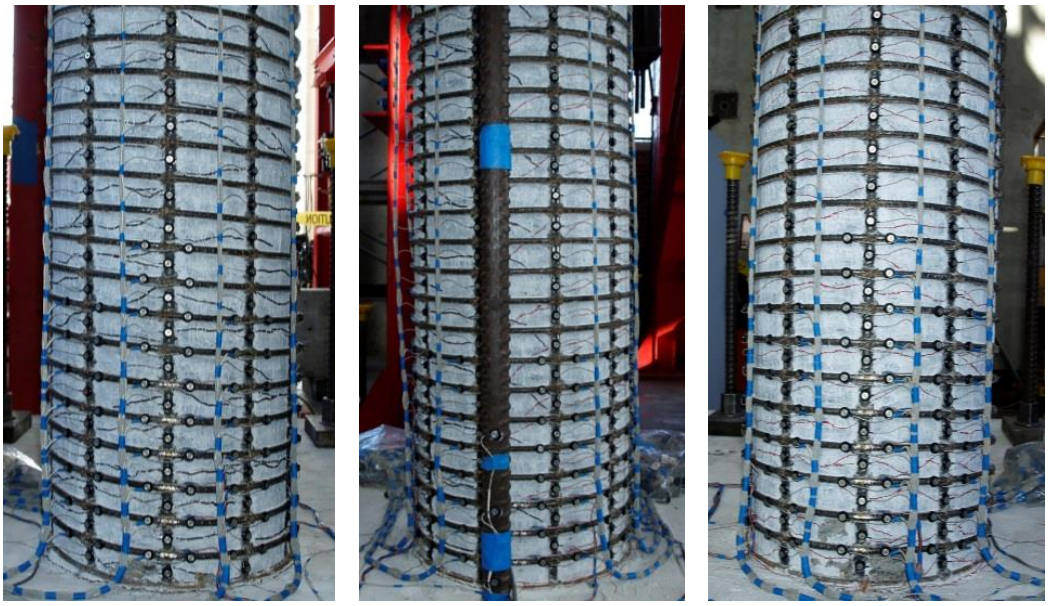

Figure 1.964 T30 – (Left) North Crack Distribution at ($\mu_{1.5}^{+3} = 2.01$"), (Middle and Right) Crack Distributions on the Front and Right Sides at ($\mu_{1.5}^{-3} = -2.01$")

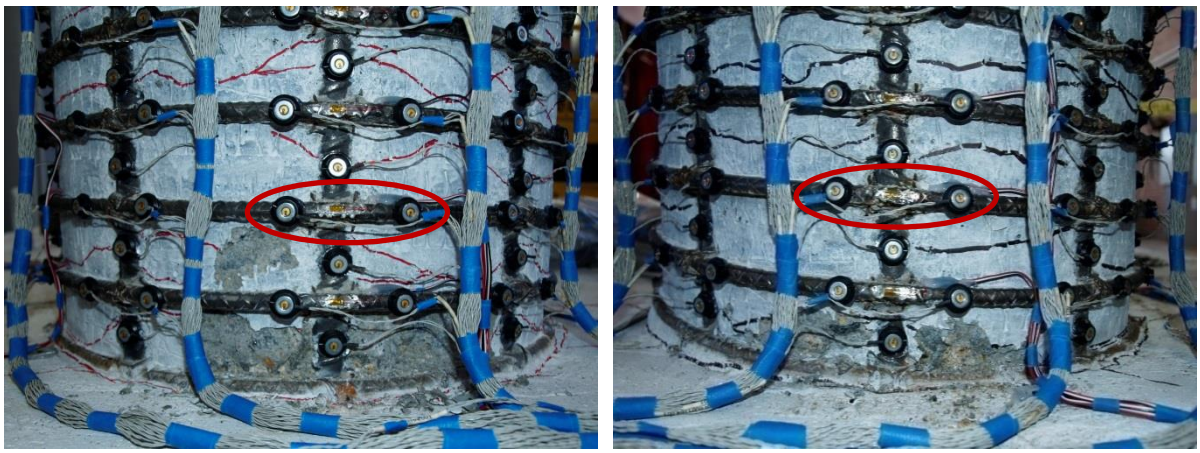

Figure 1.965 T30 – Spiral Layers which Yielded during Displacement Ductility Two, (Left) South and (Right) North

Figure 1.966 T30 – (Left) North Crack Distribution at ($\mu_2^{+3} = 2.95$"), (Middle and Right) Crack Distributions on the Front and Right Sides at ($\mu_2^{-3} = -2.95$")

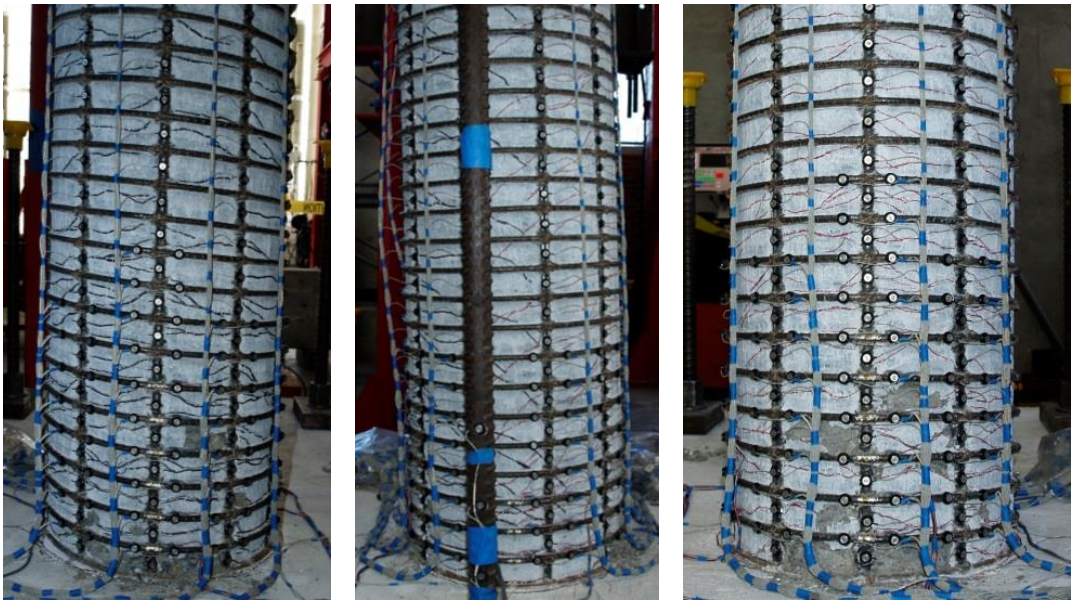

Figure 1.967 T30 – (Left) North Crack Distribution at ($\mu_3^{+3} = 4.43$"), (Middle and Right) Crack Distributions on the Front and Right Sides at ($\mu_3^{-3} = -4.43$")

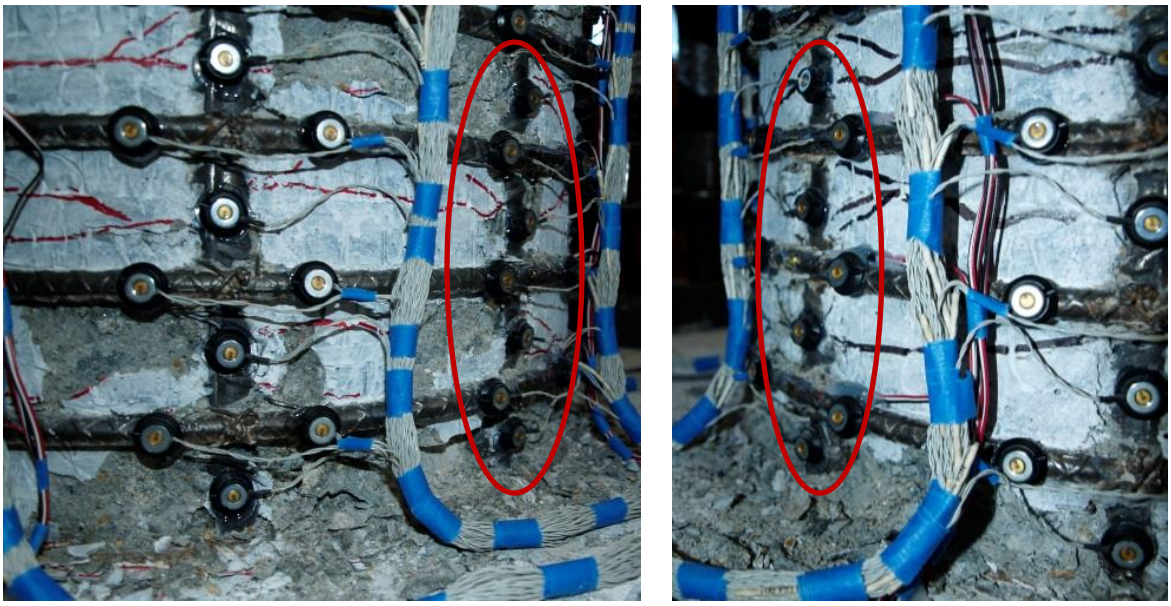

Figure 1.968 T30 – (Left) Bar S3 Remained Visibly Straight during ($\mu_4^{+3} = 5.92$") and (Right) Bar N3 Remained Visibly Straight during ($\mu_4^{-3} = -5.91$")

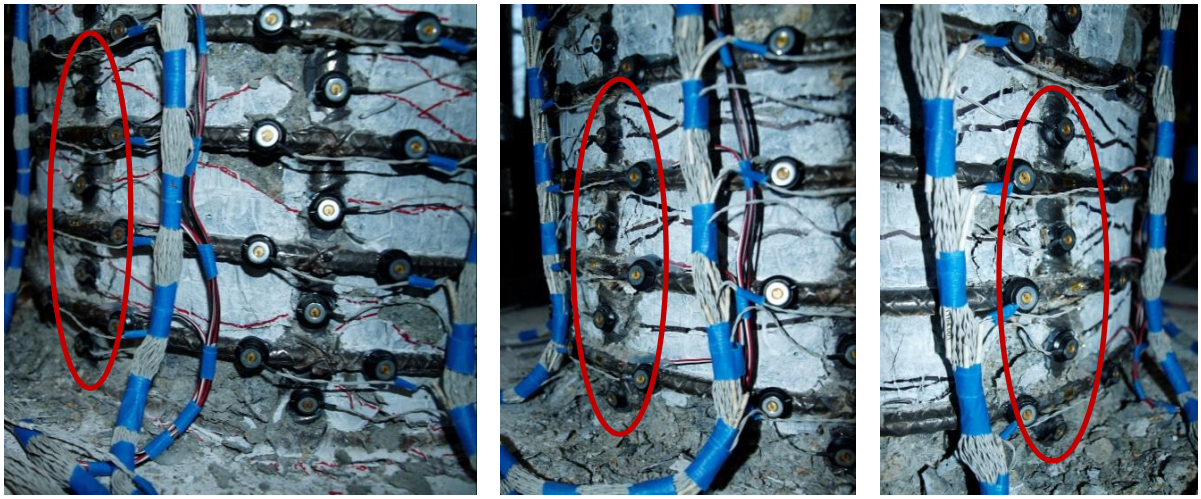

Figure 1.969 T30 – (Left) Bar S3 Remained Visibly Straight during ($\mu_5^{+1} = 7.39$"), (Middle and Right) Visible Buckling of Bar N3 during ($\mu_5^{-1} = -7.39$")

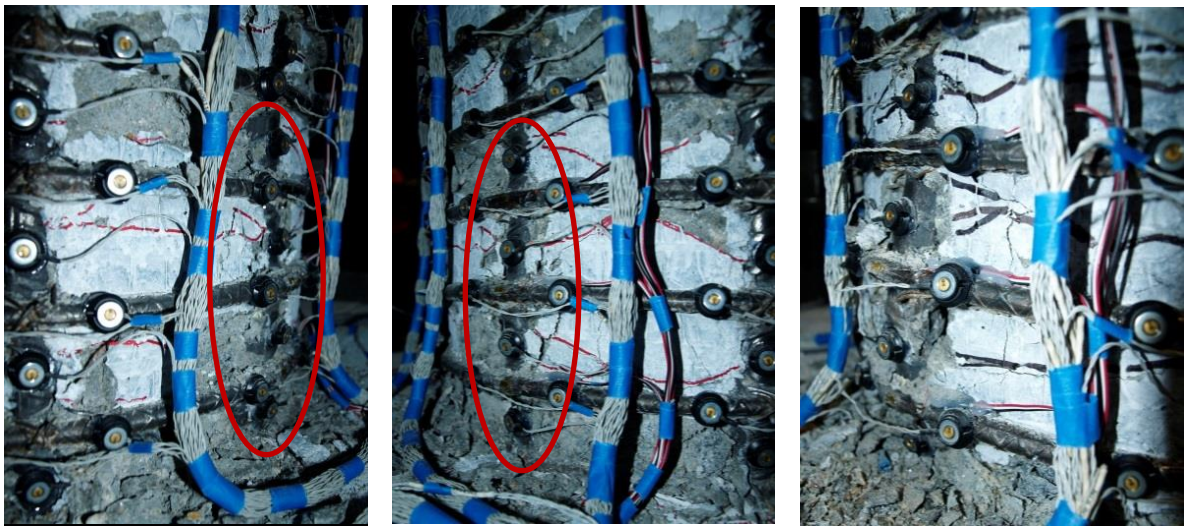

Figure 1.970 T30 – (Left and Middle) Visible Buckling of Bar S3 during ($\mu_5^{+2} = 7.38$"), (Right) Increased Deformation in Bar N3 during ($\mu_5^{-2} = -7.40$")

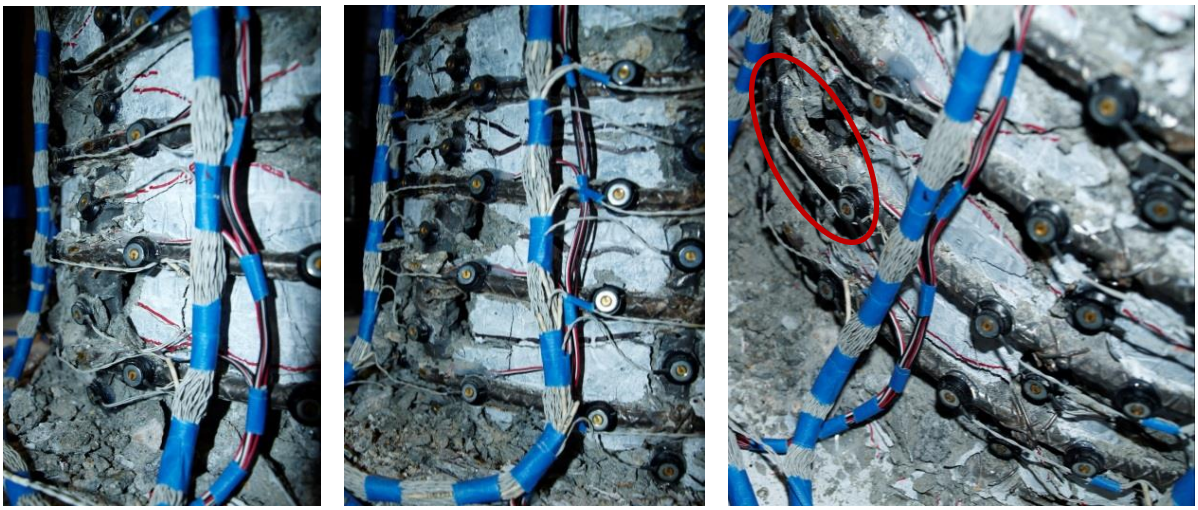

Figure 1.971 T30 – (Left) Increased Deformation in Bar S3 during ($\mu_5^{+3} = 7.39$"), (Middle) Increased Deformation in Bar N3 during ($\mu_5^{-3} = -7.39$"), (Right) South Spiral Deformation during ($\mu_5^{-3} = -7.39$")

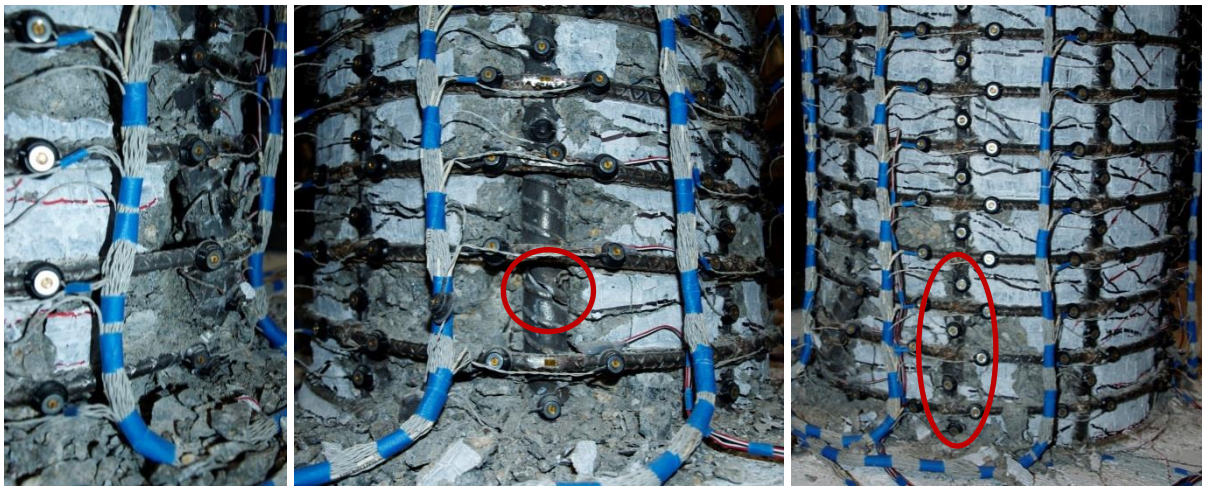

Figure 1.972 T30 – (Left) Increased Deformation in Bar S3 during ($\mu_6^{+1} = 8.88$), (Middle) Fracture of Bar N3 during ($\mu_6^{+1} = 8.88$"), Buckling of Adjacent Bars N2 and N4 during ($\mu_6^{-1} = -8.88$")

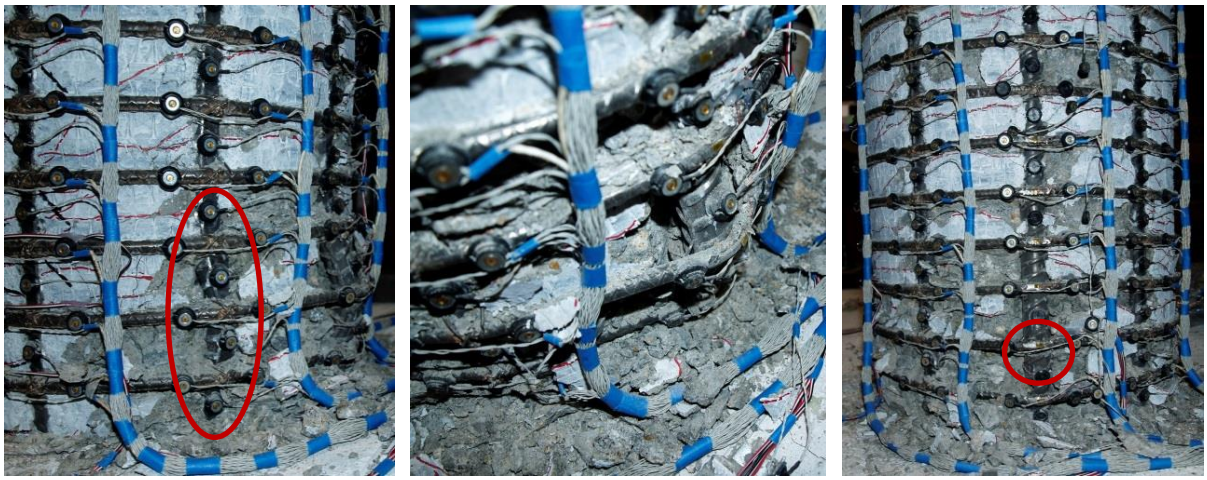

Figure 1.973 T30 – (Left) Buckling of Adjacent Bars S2 and S4 during ($\mu_6^{+2} = 8.87$), (Middle) South Spiral Deformation during ($\mu_6^{+2} = 8.87$), (Right) Fracture of Bar S3 during (μ_6^{-2})

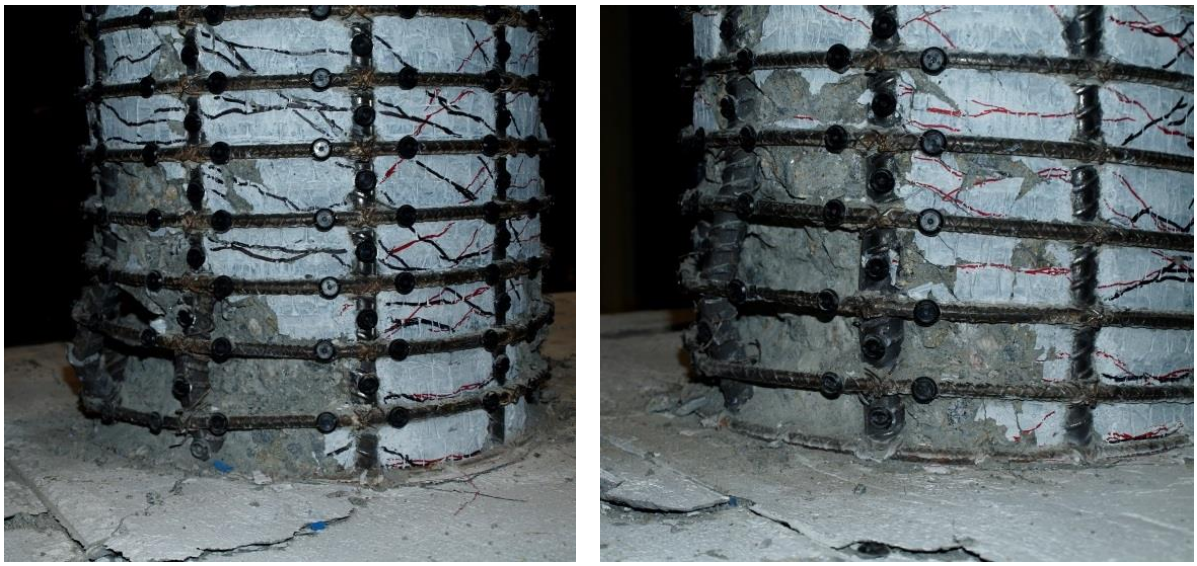

Figure 1.974 T30 – After the Test (Left) North and (Right) South Side of the Specimen

Figure 1.975 T30 – (Left to Right) North, Front, South, and Back Sides after the Test

Test 30 – 18" Dia. with 3.1% Steel and 15% Axial Load – Strain Data Analysis

North Reinforcement

Vertical strain profiles for the north extreme fiber bar N3, which is placed into tension during push cycles, appear in the right half of Figure 1.976. This figure shows both extreme fiber bars on the same graph. Compressive vertical strain profiles for north extreme fiber bar N3 during pull cycles appear in the left half of Figure 1.977. Tension strain profiles for adjacent north reinforcing bars N2 and N4 appear in Figure 1.979. By comparison, these bars do not show as large of a decrease in tension strain measured over the first gage length above the footing. A peak tensile strain of 0.0362 was measured 4.07" above the footing on bar N3 during ($\mu_5^{+1} = 7.39"$), before bar buckling was observed during ($\mu_5^{-1} = -7.39"$). The relationship between tension strain and displacement for this gage length appears in Figure 1.981. The measured tension strains for this gage length are predicted well by monotonic moment-curvature analysis with the PCK (2007) Lp Hinge Method. Prior to displacement ductility five, the peak tensile gage length was centered 6.08" above the footing. Tension strains measured in this gage length, Figure 1.982, slightly exceed the prediction. A compressive strain of –0.0095 was measured 2.09" above the footing on bar N3 during ($\mu_2^{-1} = -2.95"$), when confinement steel yielded on the north side of the specimen. A compressive strain of –0.0210 was measured 2.09" above the footing on bar N3 during ($\mu_4^{-1} = -5.92"$). It appears that measurable deformation occurred in the North bar during μ_4^{-2} and μ_4^{-3}, resulting in smaller compressive strains in the gage length 4.07" above the footing and larger strains measured 6.08" above the footing. A peak compressive strain prior to buckling of -0.0222 was measured 6.08" above the footing during ($\mu_4^{-3} = -5.91"$). The relationship between compressive strain and displacement for gage length 2.09" above the footing on bar N3 appears in Figure 1.983. The measured compressive strains exceed the moment-curvature prediction with the PCK (2007) Lp Hinge Method.

Measured spiral strains in six layers which overlaid the north extreme fiber bar appear in Figure 1.980. The first spiral layer was located at the footing-column interface, and was not

instrumented with a strain gage or LEDs. Spiral tension strains in the second and third layers above the footing increased during each successive pull cycle of displacement ductility four. A spiral strain hysteresis for the layer 4.19" above the footing, which overlaid the outward deformed region of bar N3, appears in Figure 1.989. The hysteresis contains spiral data from a strain gage and an Optotrak gage length, Figure 1.954. The Optotrak strains were calculated using arc-lengths obtained from measured 3D distance chord lengths and the known outside diameter of the spiral. It is important to note that arc-length calculations become inaccurate once severe yielding in the spiral leads to the reinforcement straightening out to the left and right of the localized yielding directly over the bar where the strain gage is located. Each consecutive pull cycle of displacement ductility four led to larger inelastic spiral strains, which indicates that measurable outward deformation occurred before visible bar buckling. The sharpest increase in measured spiral strains occurred during ($\mu_5^{-1} = -7.39"$), when visible bar buckling was observed. The distribution of arc-strains measured around the circumference of the second and third spiral layers above the footing during pull cycles appears in Figure 1.995 and Figure 1.997. The north side of the specimen is on the left side of the graph with negative location values and specific locations of bars N2, N3, and N4 are highlighted with vertical dashed lines.

Strain hysteresis for gage lengths 4.07" and 6.08" above the footing on bar N3 appear in Figure 1.987 and Figure 1.988. The effect of measurable deformation on recorded strains can be visualized when comparing the location of the gage lengths with the deformed regions of the buckled extreme fiber bar, Figure 1.990. The gage length 4.07" above the footing overlaid the outward deformed region of bar N3, Figure 1.969. This gage length experienced additional tension during successive pull cycles of displacement ductility four as a result of measurable outward deformation. This deformation rapidly increased during ($\mu_5^{-1} = -7.39"$), when visible buckling was observed. The gage length 6.08" was located just above the outward deformed region of bar N3. This gage length experience additional compression due to measurable deformation, as shown in Figure 1.988. Larger compressive strains were measured during each successive cycle of displacement ductility four.

South Reinforcement

Vertical strain profiles for the south extreme fiber bar S3, which is placed into tension during pull cycles, appear in the right half of Figure 1.977. Tension strain profiles for adjacent south reinforcing bars S2 and S4 appear in Figure 1.978. Compressive vertical strain profiles for south extreme fiber bar S3 during push cycles appear in the left half of Figure 1.976. A peak tension strain of 0.0329 was measured 8.18" above the footing on bar S3 at ($\mu_5^{-1} = -7.39"$), before the bar visibly buckled during ($\mu_5^{+2} = 7.38"$). Similar peak tension strains of 0.0315 and 0.0327 were measured 4.16" and 12.14" above the footing during ($\mu_5^{-1} = -7.39"$). The relationship between tension strain and displacement for the gage length 12.14" above the footing on bar S3 appears in Figure 1.984. The measured tension strains match the moment-curvature prediction well when the PCK (2007) Lp Hinge Method is used. A compressive strain of -0.0094 was measured 2.25" above the footing when the first confinement steel layer yielded on the south side of the specimen during ($\mu_2^{+1} = 2.25"$). A peak compressive strain of -0.0263 was measured 2.25" above the footing during ($\mu_5^{+1} = 7.39"$). During the same cycle, a compression strain of -0.0260 was measured 6.20" above the footing. The relationship between compressive strain and displacement for the gage lengths 2.25" and 6.20" above the footing appears in Figure 1.985 and Figure 1.986. The measured compressive strains exceed the moment-curvature prediction with the PCK (2007) Lp Hinge Method beyond displacement ductility 1.5 for the gage length 2.25" above the footing.

Measured strains in six spiral layers which overlaid the south extreme fiber bar appear in Figure 1.980 for push cycles. Cycles during displacement ductility four produced successively larger inelastic demands on the second and third spiral layers. Strain gage and Optotrak strain hysteresis for the spiral layer 6.28" above the footing appears in Figure 1.993. The two measurement methods begin the deviate during displacement ductility three and four. The spiral strains increased significantly during ($\mu_5^{+2} = 7.38"$) when visible bar buckling was observed. Measured arc-strains around the circumference of the second and third spiral layers on the south side of the specimen during push cycles appear in Figure

1.994 and Figure 1.996. Spiral strain hystereses for stain gages placed at mid-section (Diameter/2) appear in Figure 1.998 and Figure 1.999. The spiral layer 2.16" above the footing, Figure 1.998, was not crossed by inclined flexural-shear cracks. The spiral layer 6.22" above the footing was crossed by only mildly inclined flexural-shear cracks. The three spiral layers instrumented on the shear face of the column did not yield before bar buckling.

The influence of measurable deformation before bar buckling becomes easier to understand when the specific gage lengths in question are located on buckled bar, Figure 1.990. Bar S3 strain hysteresis for gage lengths 4.16" and 6.20" above the footing on bar S3 appear in Figure 1.991 and Figure 1.992. The gage length 4.16" above the footing, Figure 1.991, overlaid the outward buckled region. Smaller compressive strain magnitudes were measured during μ_4^{+2}, μ_4^{+3}, and μ_5^{+1} due to small amounts of outward deformation prior to visible bar buckling during ($\mu_5^{+2} = 7.38"$). The gage length 6.20" above the footing was located just above the outward buckled region. Successively larger compressive strains were measured during μ_4^{+2}, μ_4^{+3}, and μ_5^{+1}, Figure 1.992.

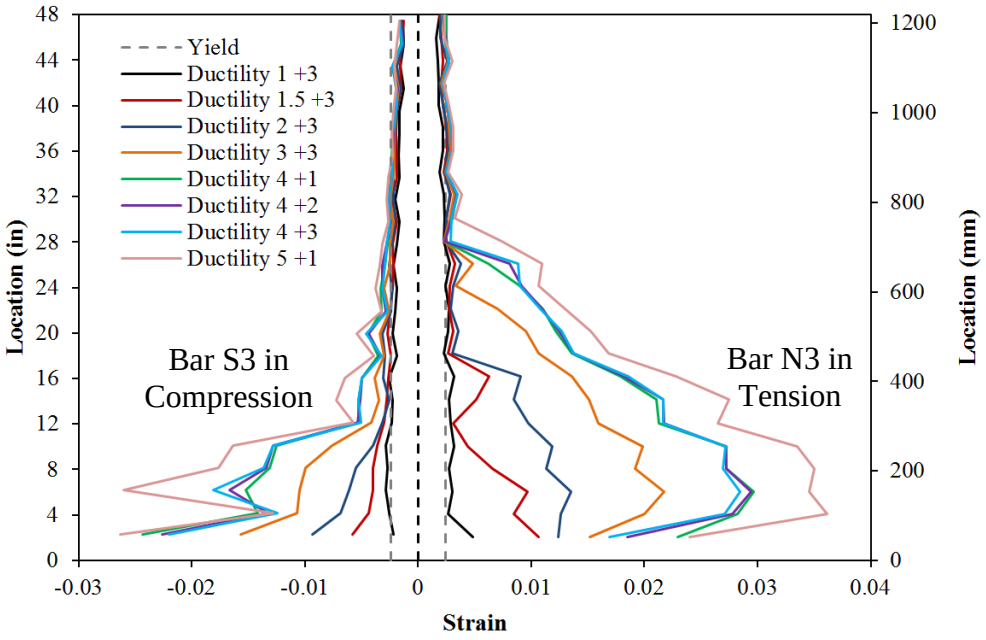

Figure 1.976 T30 – Extreme Fiber Bar Vertical Strain Profiles during Push Cycles

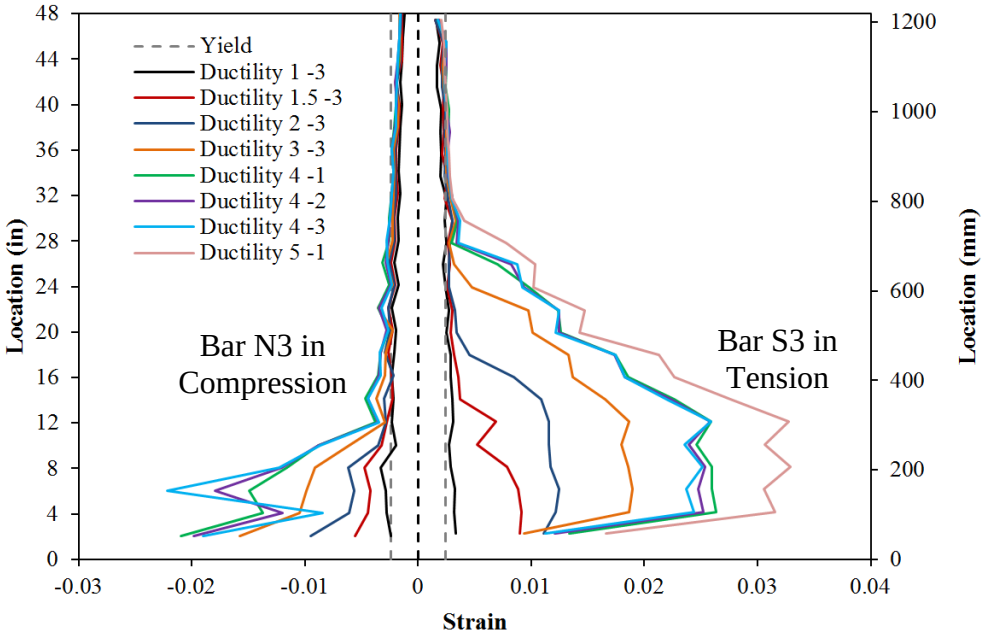

Figure 1.977 T30 – Extreme Fiber Bar Vertical Strain Profiles during Pull Cycles

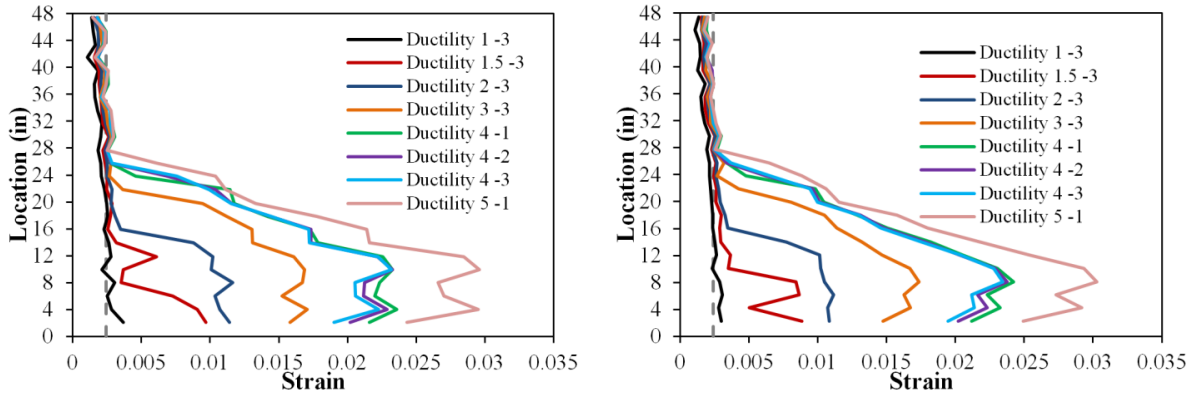

Figure 1.978 T30 – (Left) Bar S4 and (Right) Bar S2 Tensile Strain Profiles

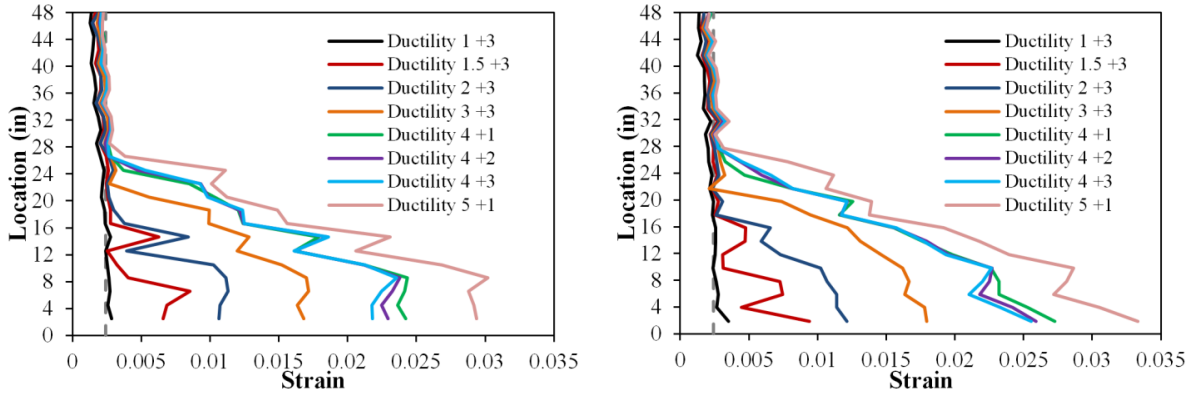

Figure 1.979 T30 – (Left) Bar N4 and (Right) Bar N2 Tensile Strain Profiles

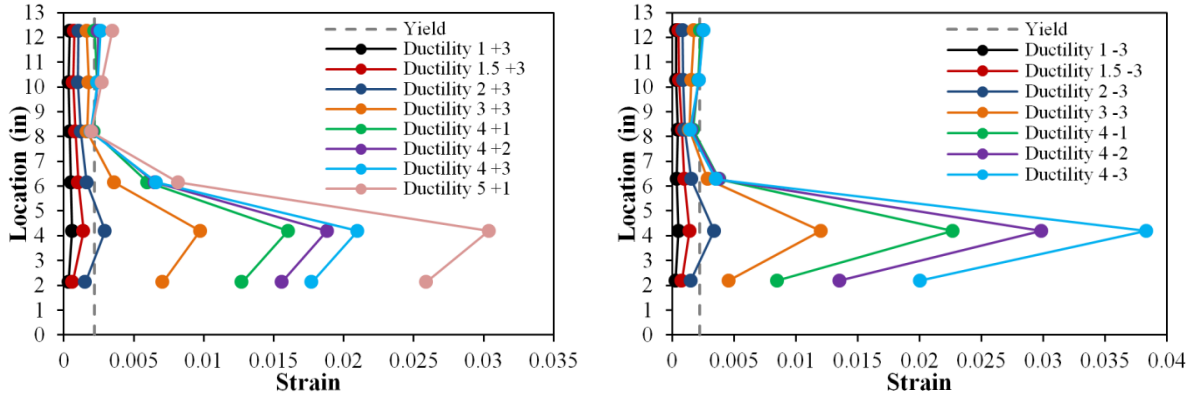

Figure 1.980 T30 – Spiral Strains for Compressive Cycles (Left) South, (Right) North

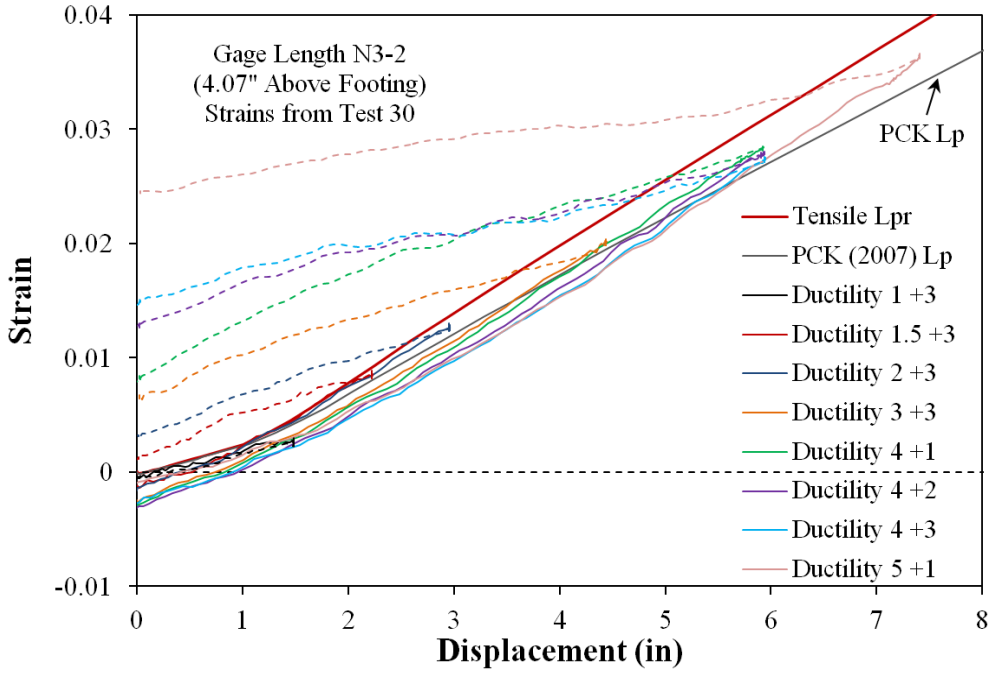

Figure 1.981 T30 – Tensile Stain-Displacement for Bar N3 during Push Cycles

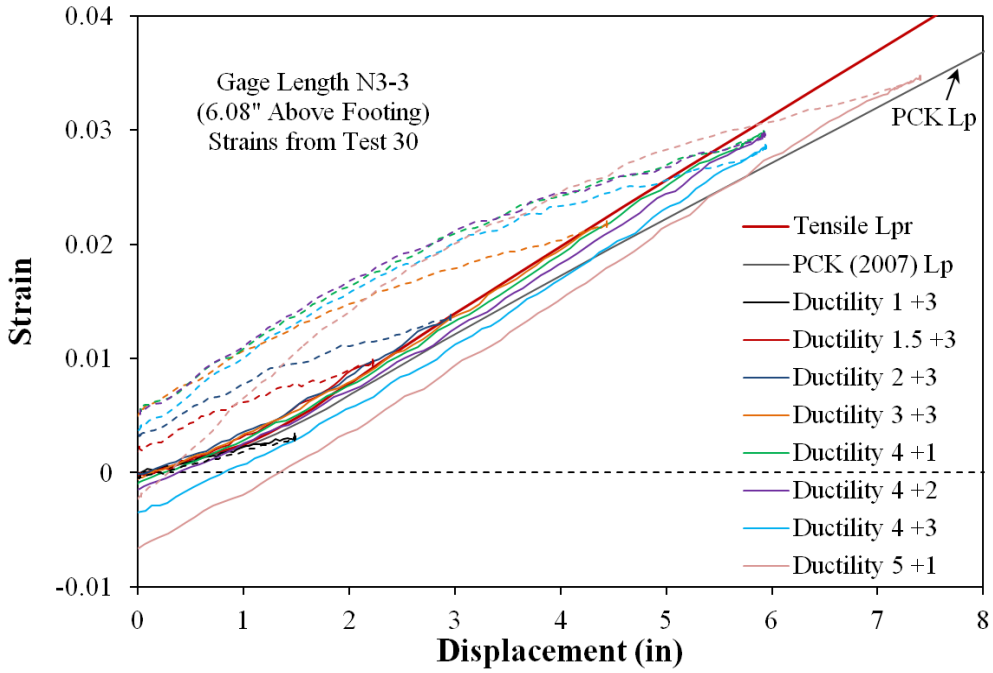

Figure 1.982 T30 – Tensile Stain-Displacement for Bar N3 during Push Cycles

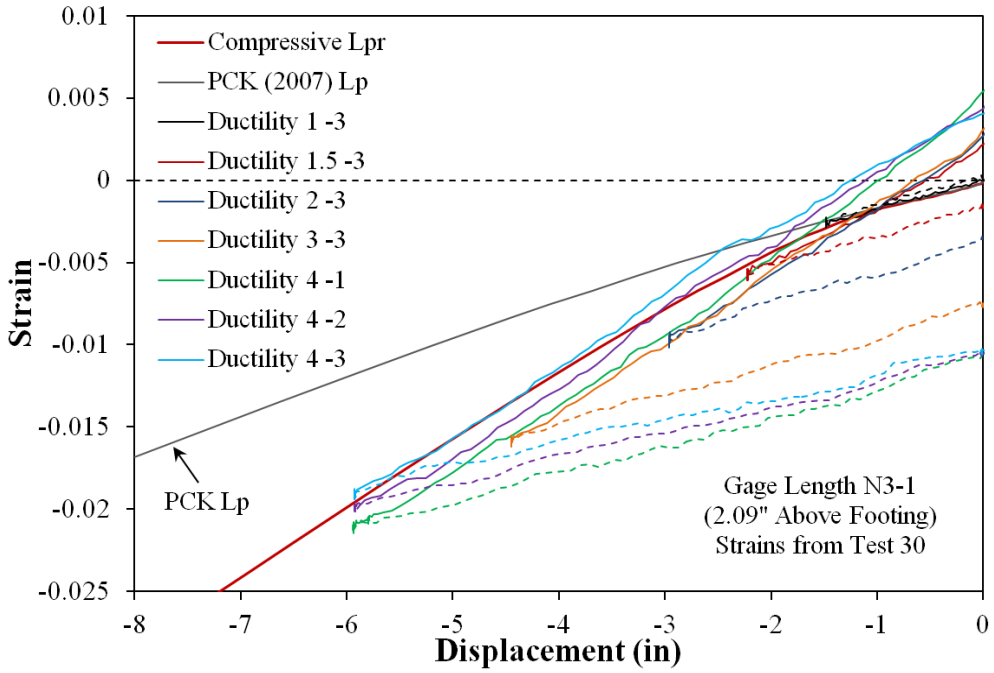

Figure 1.983 T30 – Compressive Strain-Displacement for Bar N3 during Pull Cycles

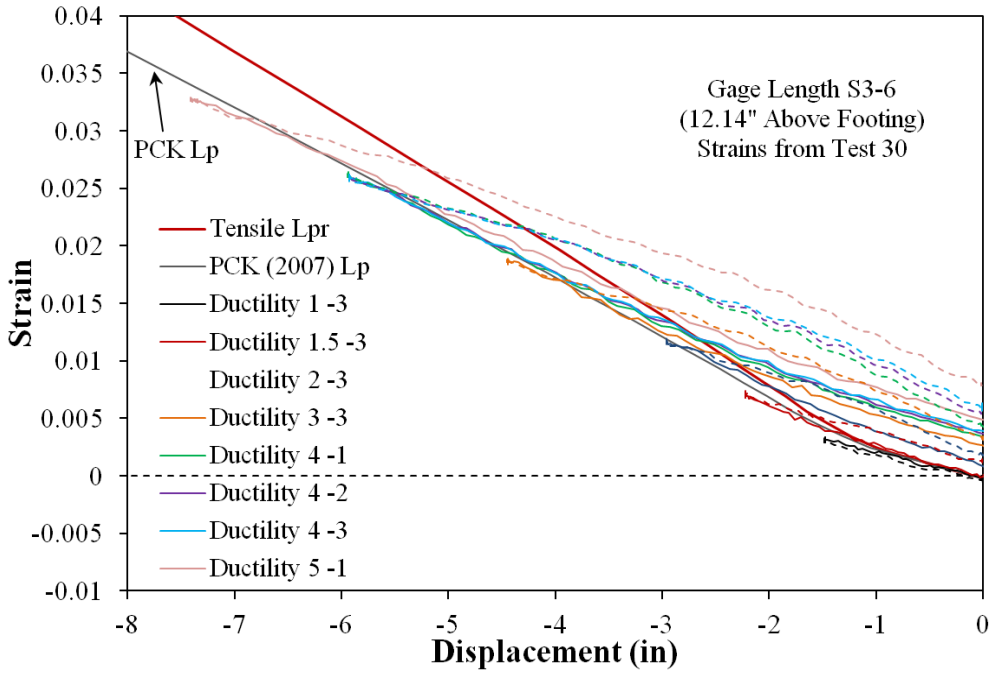

Figure 1.984 T30 – Tensile Strain-Displacement for Bar S3 during Pull Cycles

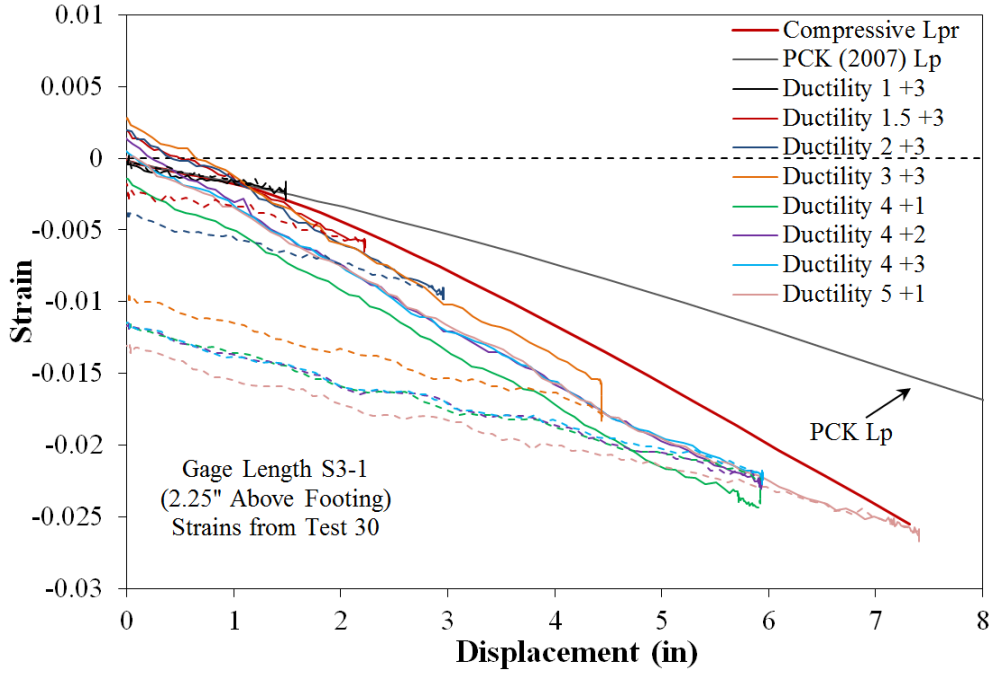

Figure 1.985 T30 – Compressive Strain-Displacement for Bar S3 during Push Cycles

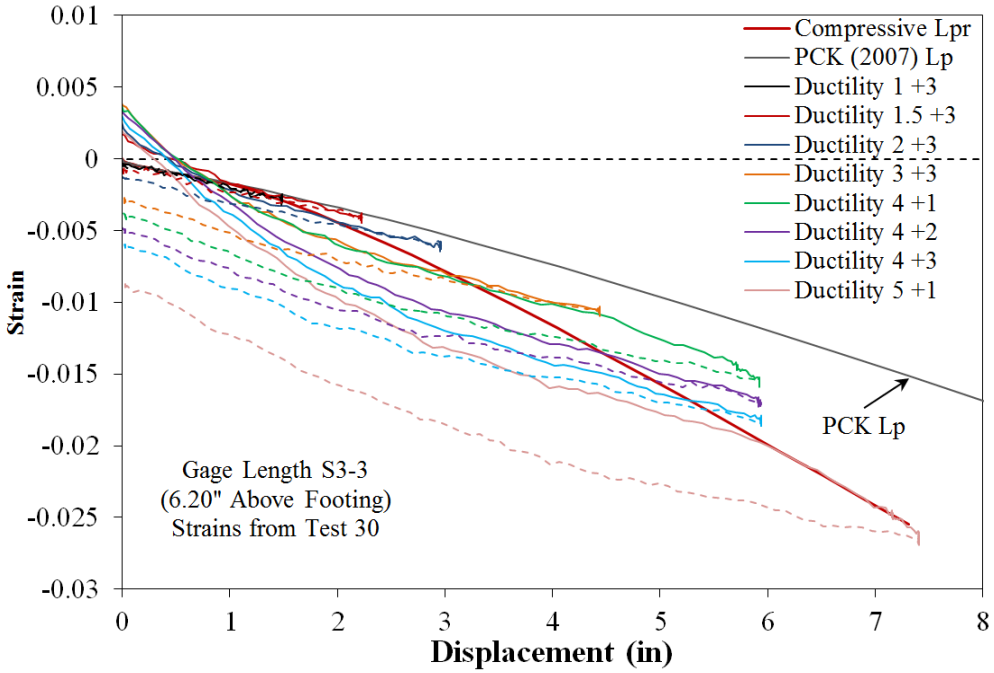

Figure 1.986 T30 – Compressive Strain-Displacement for Bar S3 during Push Cycles

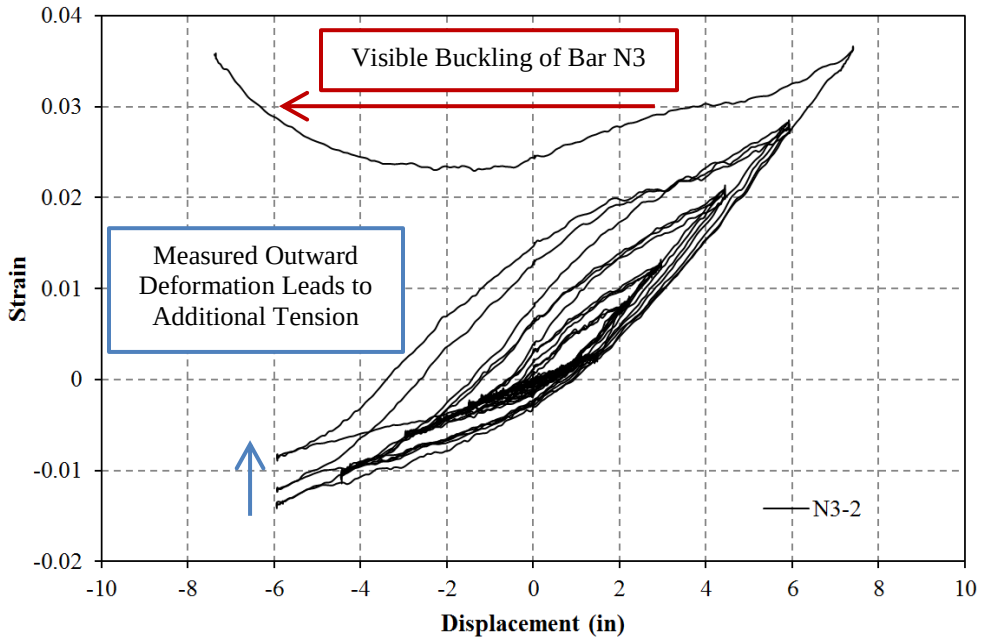

Figure 1.987 T30 – Bar N3 Strain Hysteresis to Buckling (4.07" Above the Footing)

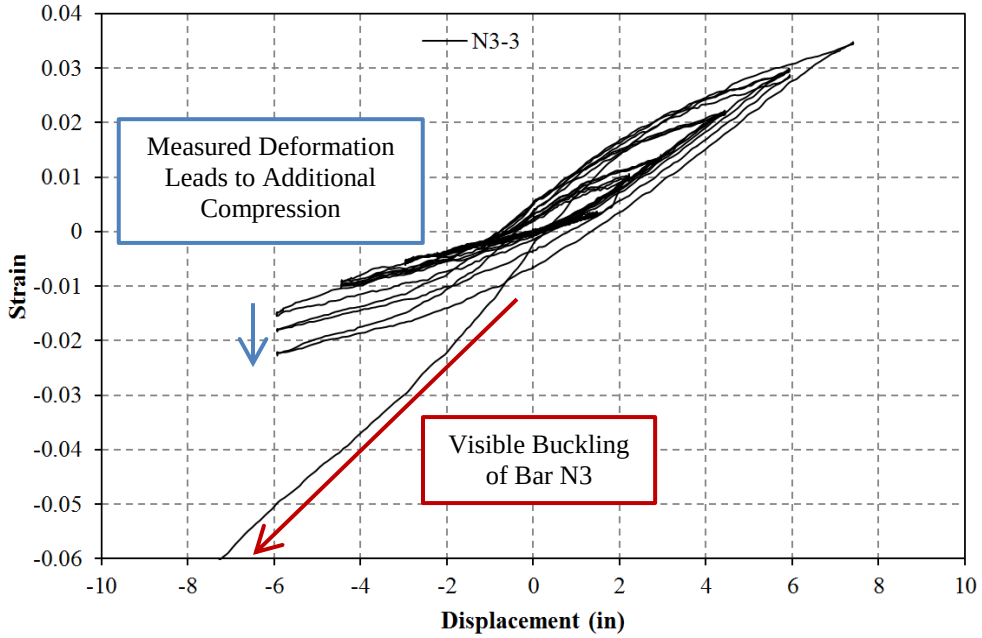

Figure 1.988 T30 – Bar N3 Strain Hysteresis to Buckling (6.08" Above the Footing)

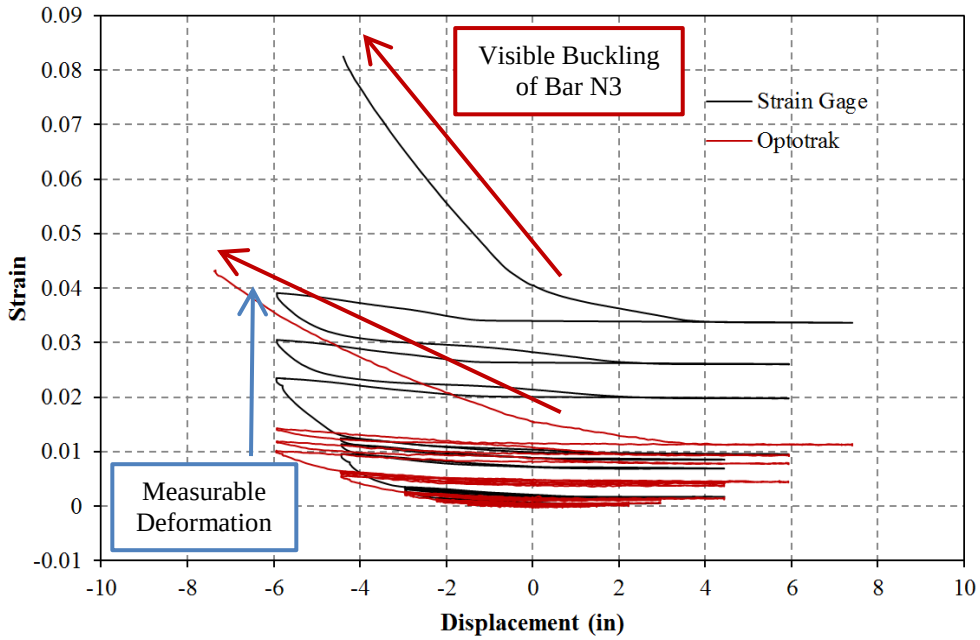

Figure 1.989 T30 – Spiral Strains over the North Buckled Region (4.19" Above)

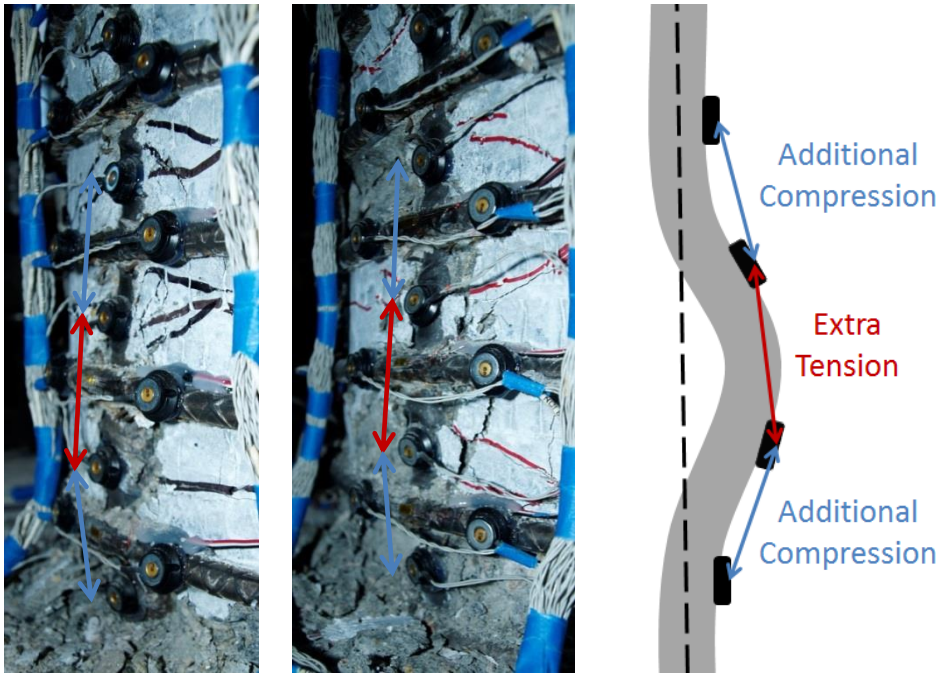

Figure 1.990 T30 – Buckled Shape of Bar N3 (Left) and Bar S3 (Middle)

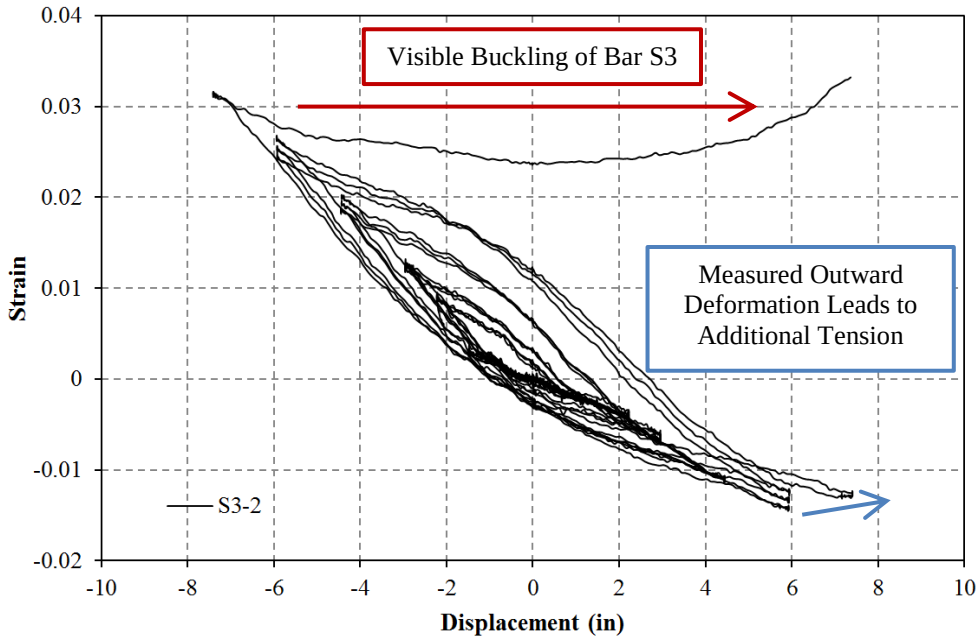

Figure 1.991 T30 – Bar S3 Strain Hysteresis to Buckling (4.16" Above the Footing)

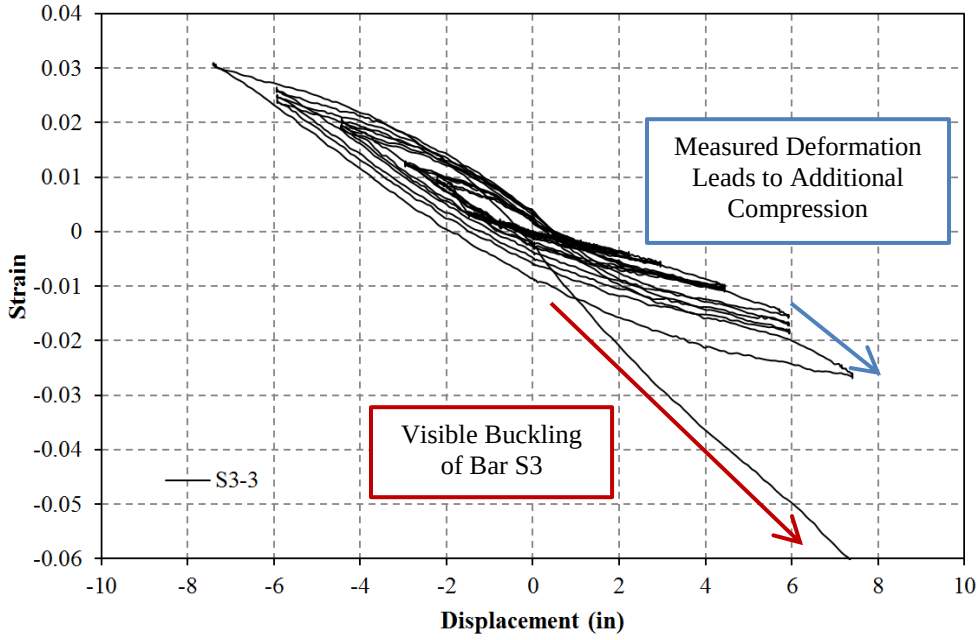

Figure 1.992 T30 – Bar S3 Strain Hysteresis to Buckling (6.20" Above the Footing)

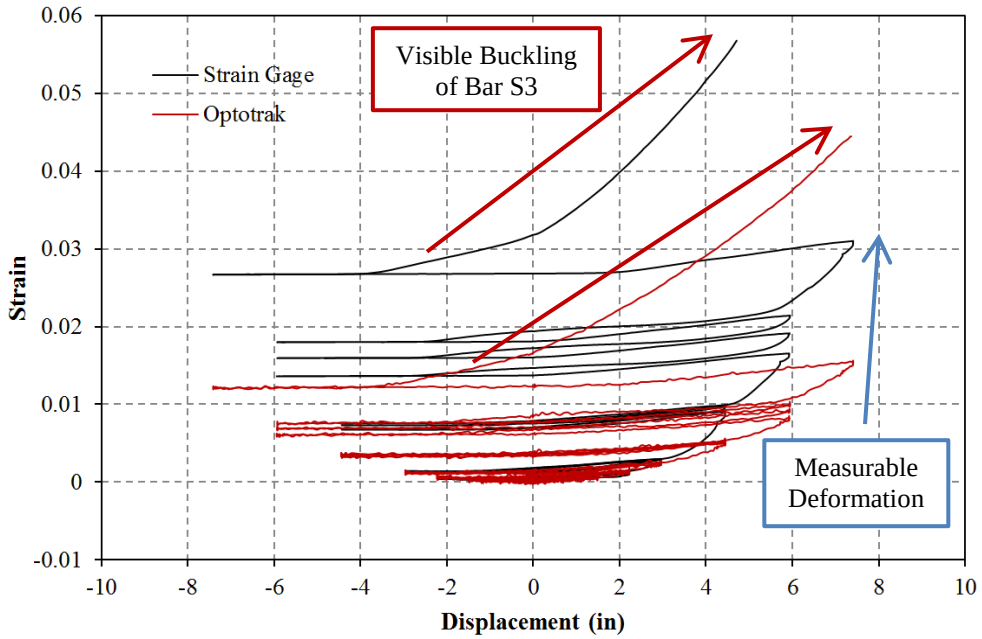

Figure 1.993 T30 – Spiral Strains over the South Buckled Region (6.28" Above)

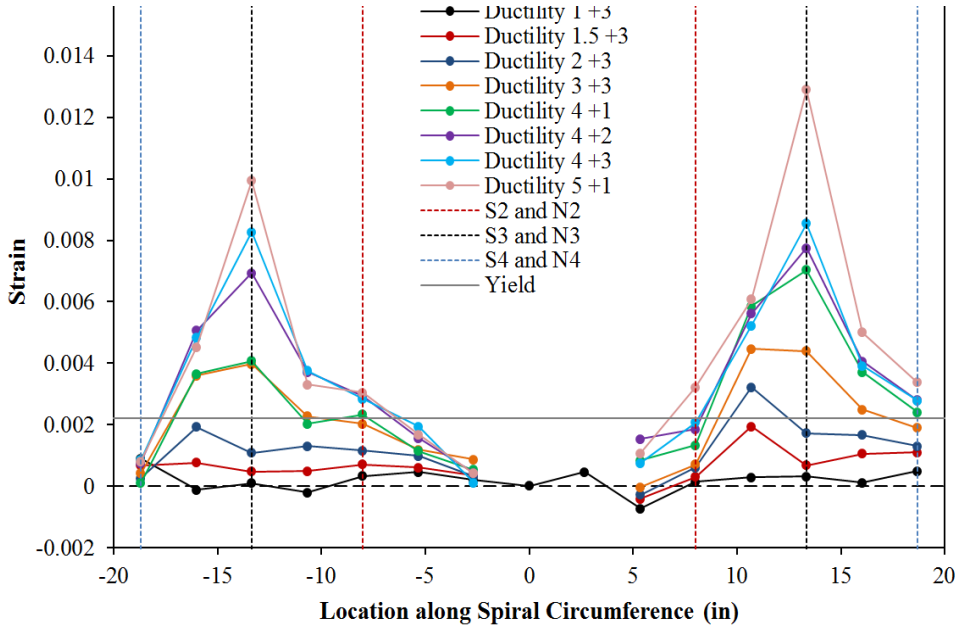

Figure 1.994 T30 – Spiral Strain Distribution for the 2nd Spiral above the Footing during Push Cycles (Positive= South)

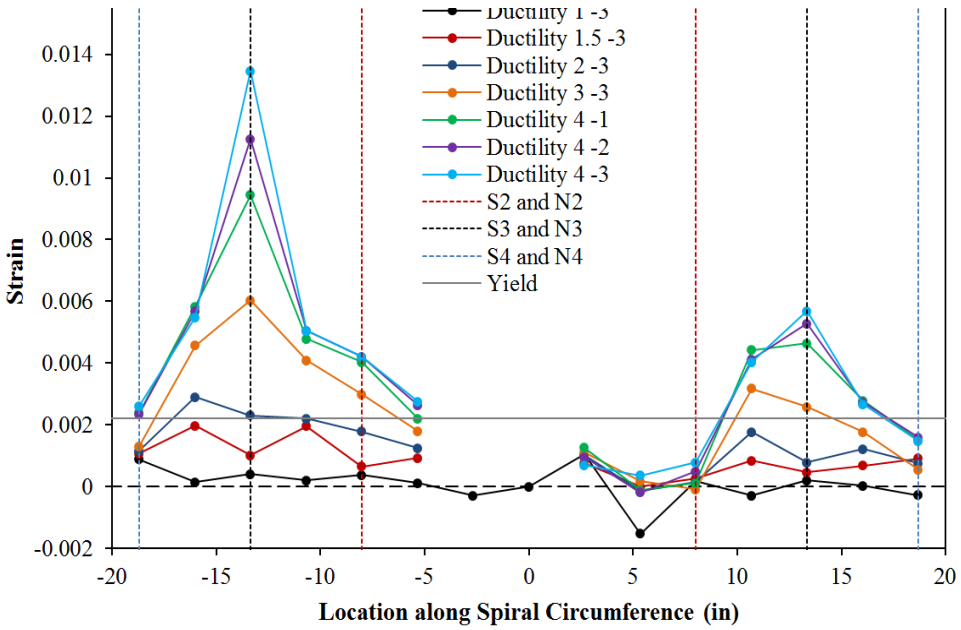

Figure 1.995 T30 – Spiral Strain Distribution for the 2nd Spiral above the Footing during Pull Cycles (Negative = North)

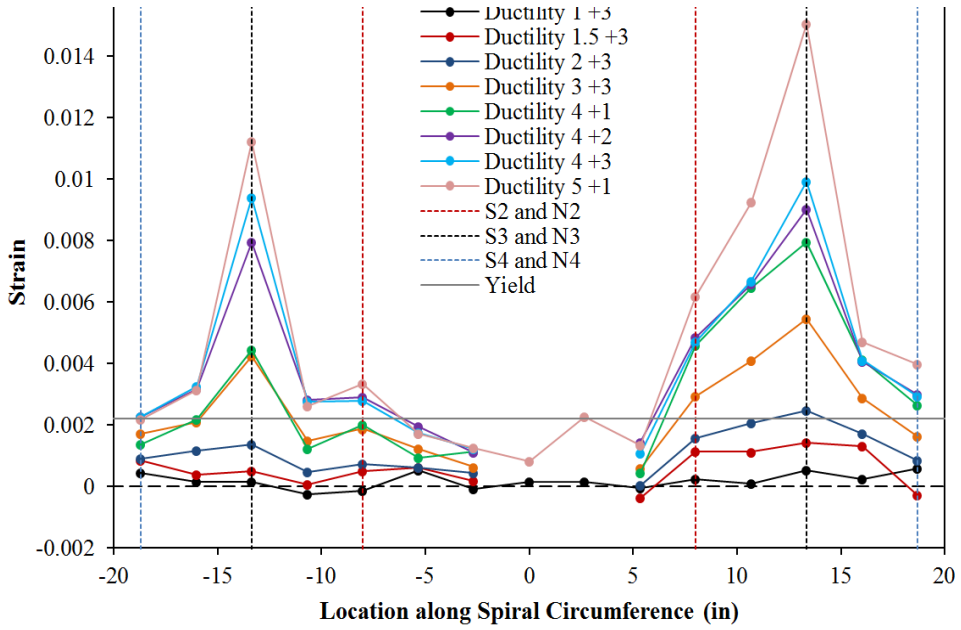

Figure 1.996 T30 – Spiral Strain Distribution for the 3rd Spiral above the Footing during Push Cycles (Positive= South)

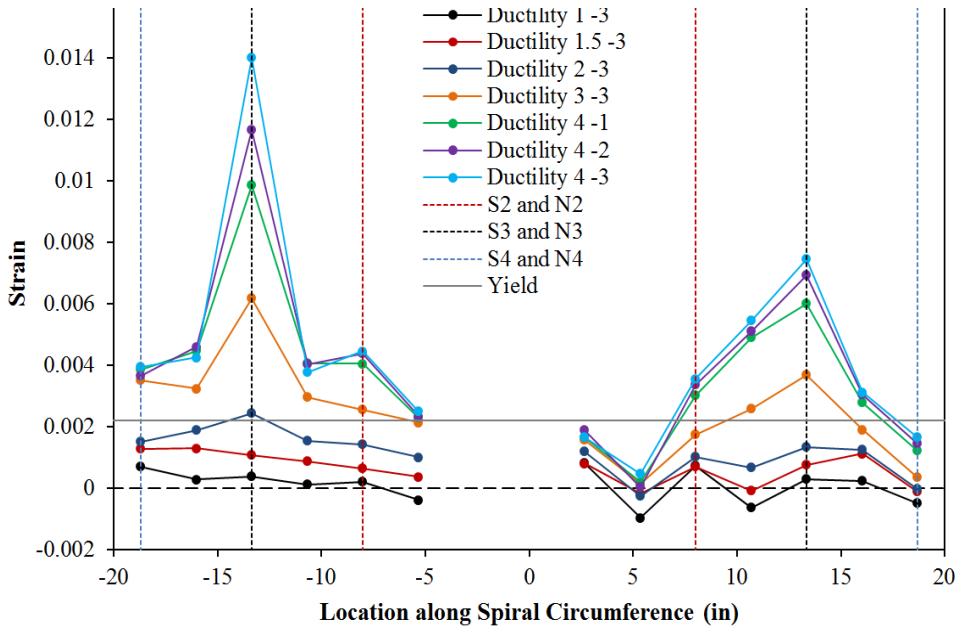

Figure 1.997 T30 – Spiral Strain Distribution for the 3rd Spiral above the Footing during Pull Cycles (Negative = North)

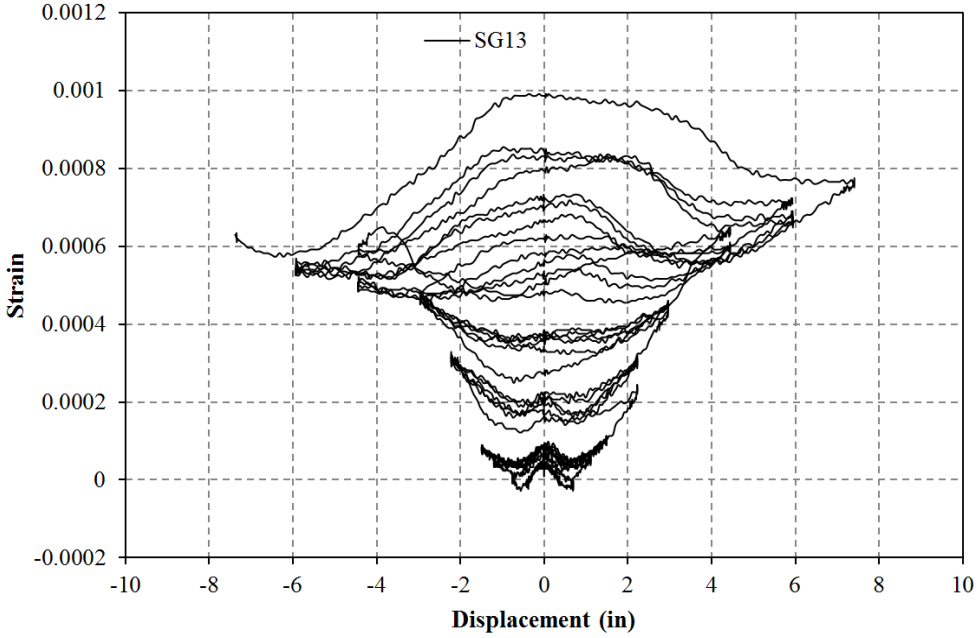

Figure 1.998 T30 – Second Spiral Layer Strain Hysteresis at Midsection (2.16" Above)

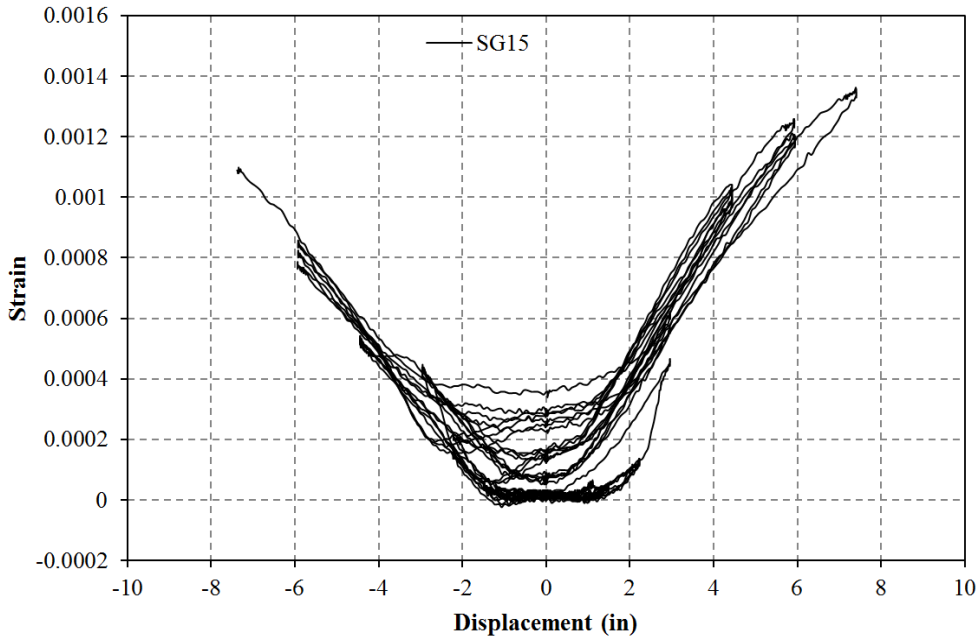

Figure 1.999 T30 – Second Spiral Layer Strain Hysteresis at Midsection (6.22" Above)

Test 30 – Curvature and Strain Penetration Data

Cross section strain profiles for the second horizontal section above the footing appear in Figure 1.1000 and Figure 1.1001 for push and pull cycles respectively. This is the first horizontal section above the footing which included strain measurements for bars S1 and N1. Individual bar strains appear to deviate from the planes section hypothesis for this section, but the overall trend is captured well. The curvature is calculated as the slope of the least squared line connecting strains measured in eight instrumented reinforcing bars. If the curvatures for many horizontal cross sections are analyzed, curvature profiles for the plastic hinge region can be constructed; Figure 1.1002 and Figure 1.1003 for push and pull cycles respectively. Measured curvatures during displacement ductility one closely match the elastic curvature profile, which linearly decreases from yield curvature at the footing-column interface to zero at the center of the applied lateral load. Plastic curvatures were found to follow a linear distribution. Linear least squared error plastic curvature lines were fit to the

plastic portion of the measured curvature profiles. The extrapolation of this linear curvature line with the footing-column interface was taken as the base section curvature. As the base section curvature ductility increased, the height at which the linear plastic curvature distribution intersected the elastic curvature profile also increased. Circular data points in Figure 1.1007 plot the measured spread of plasticity as a function of base section curvature ductility.

Curvature profiles describe the elastic and plastic flexural displacements of the column, but do not address fixed-end rotations which result from development of longitudinal reinforcement into the footing. The measured vertical displacements of Optotrak LEDs placed closest to the footing column interface can be used to quantify this fixed-end rotation, Figure 1.1004 and Figure 1.1005. The fixed-end rotation is taken as the slope of the least squared error line fit to the bond slip profile. The strain penetration displacement is obtained by multiplying this rotation by the cantilever height of the column. If an elastic curvature profile assumption is made for curvatures higher than those measured with instrumentation, then the entire curvature profile may be integrated to obtain the total column flexural displacement. This column flexural displacement was added to the strain penetration displacement, and compared to the experimentally measured displacements in Figure 1.1006. The Optotrak integrated displacements slightly exceed those obtained from a string potentiometer placed at the center of the lateral load.

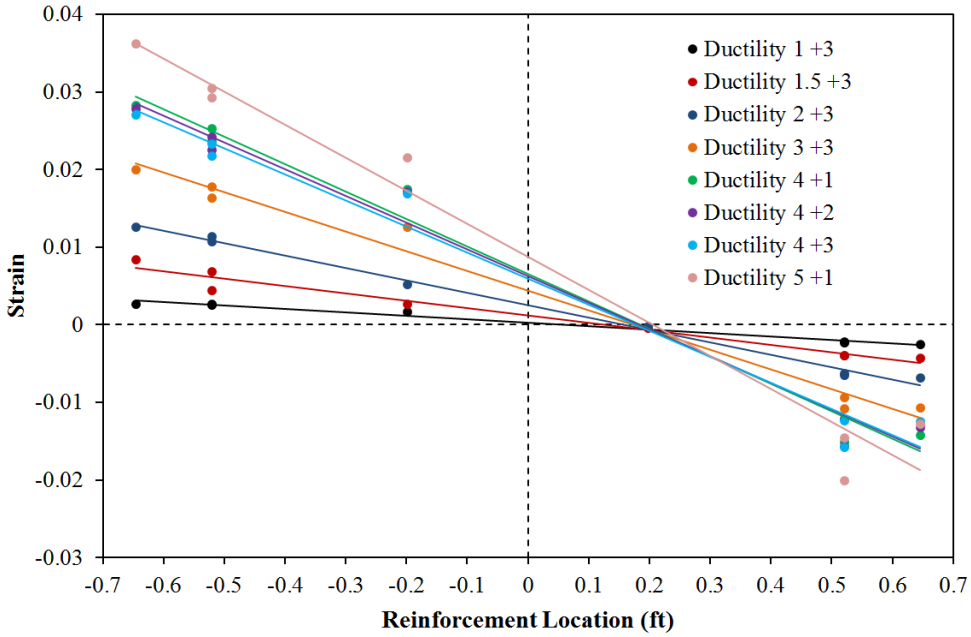

Figure 1.1000 T30 – Push Cycle Strain Profiles for the Section 4.11" Above the Footing

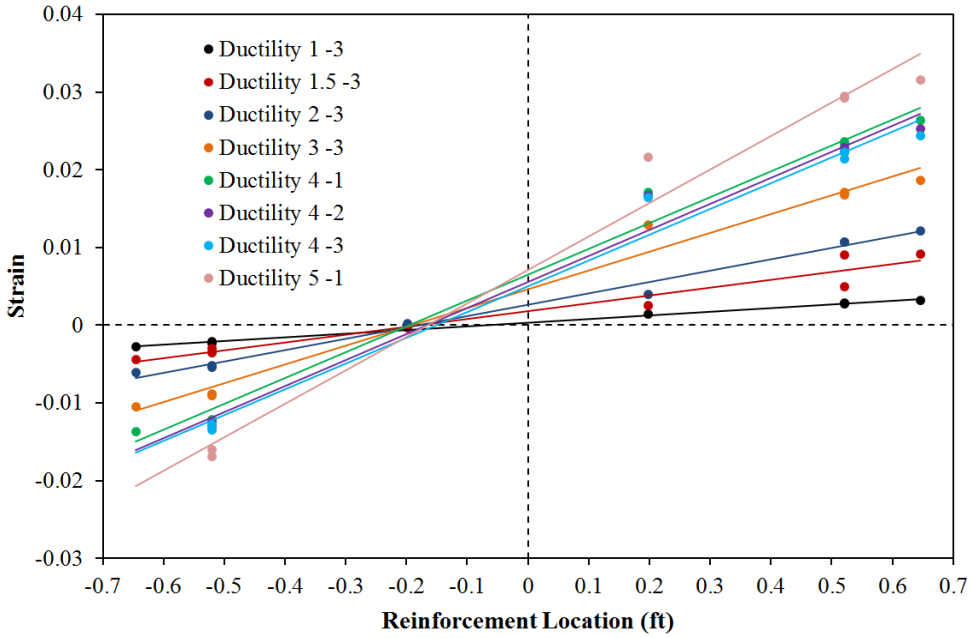

Figure 1.1001 T30 – Pull Cycle Strain Profiles for the Section 4.11" Above the Footing

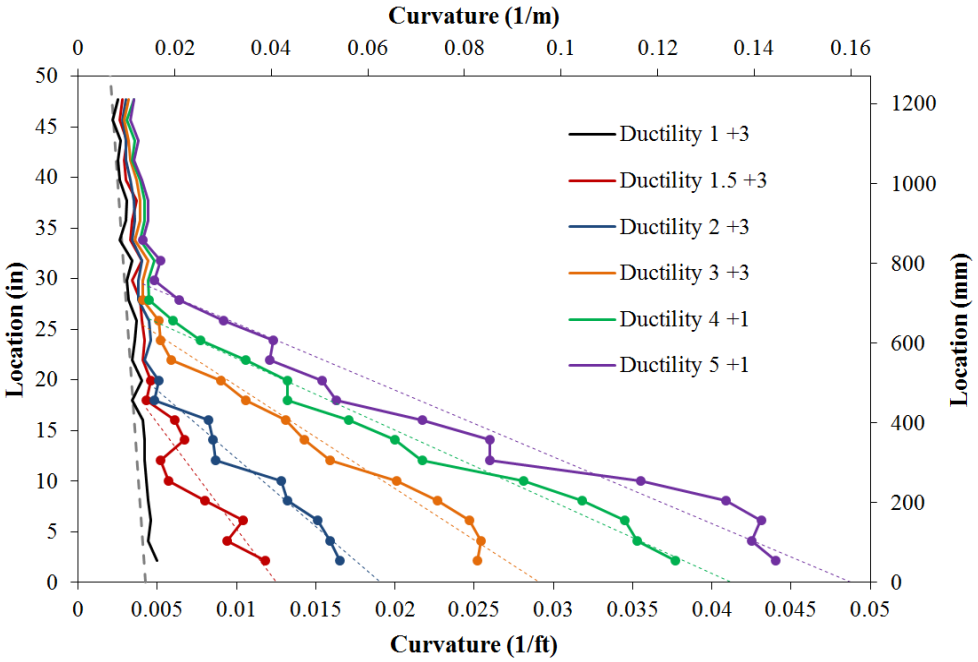

Figure 1.1002 T30 – Push Cycle Curvature Profiles with Plastic Regression Lines

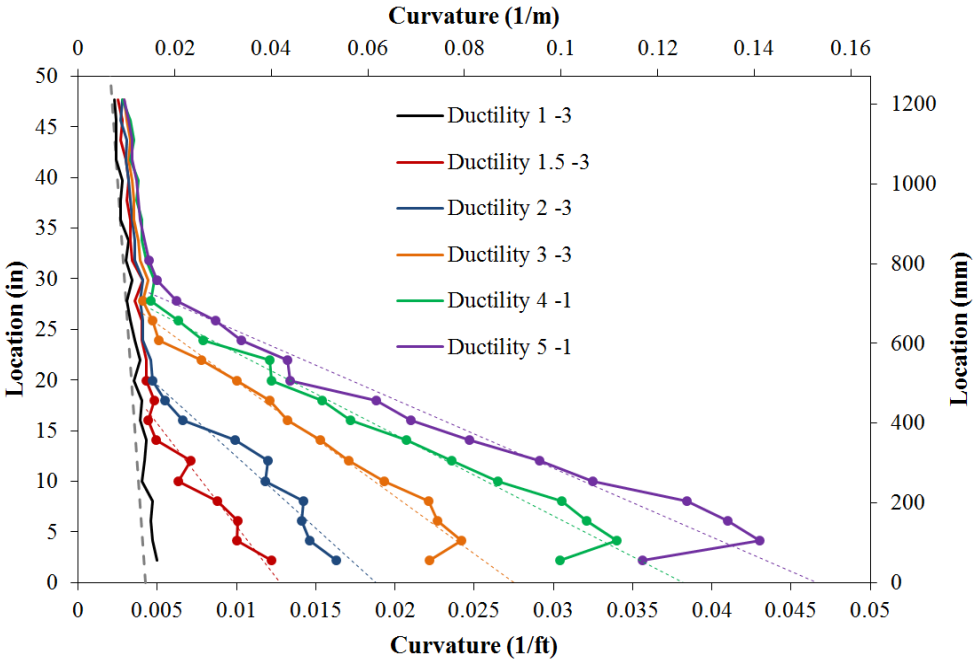

Figure 1.1003 T30 – Pull Cycle Curvature Profiles with Plastic Regression Lines

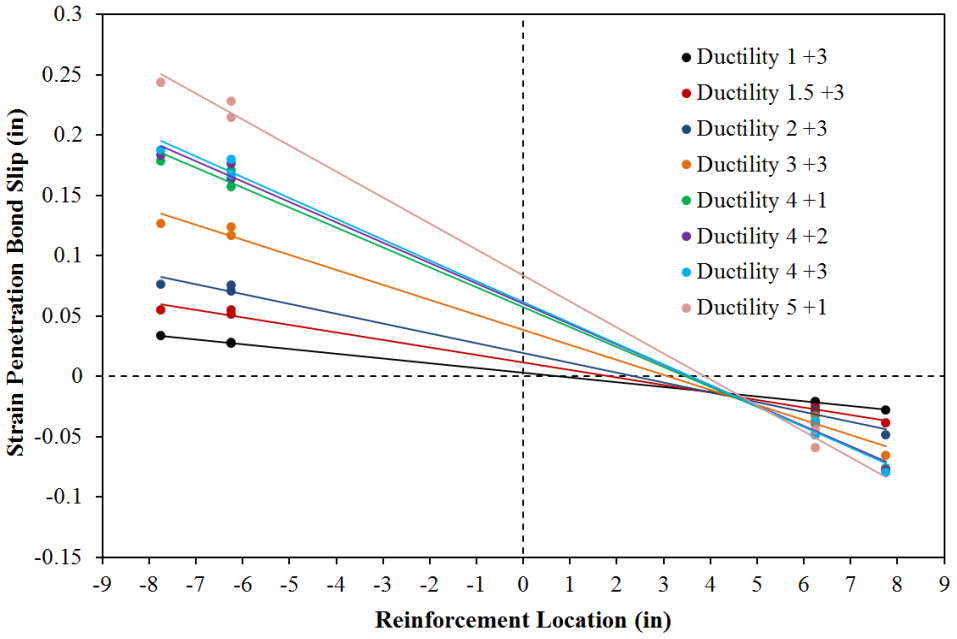

Figure 1.1004 T30 – Base Rotation due to Strain Penetration during Push Cycles

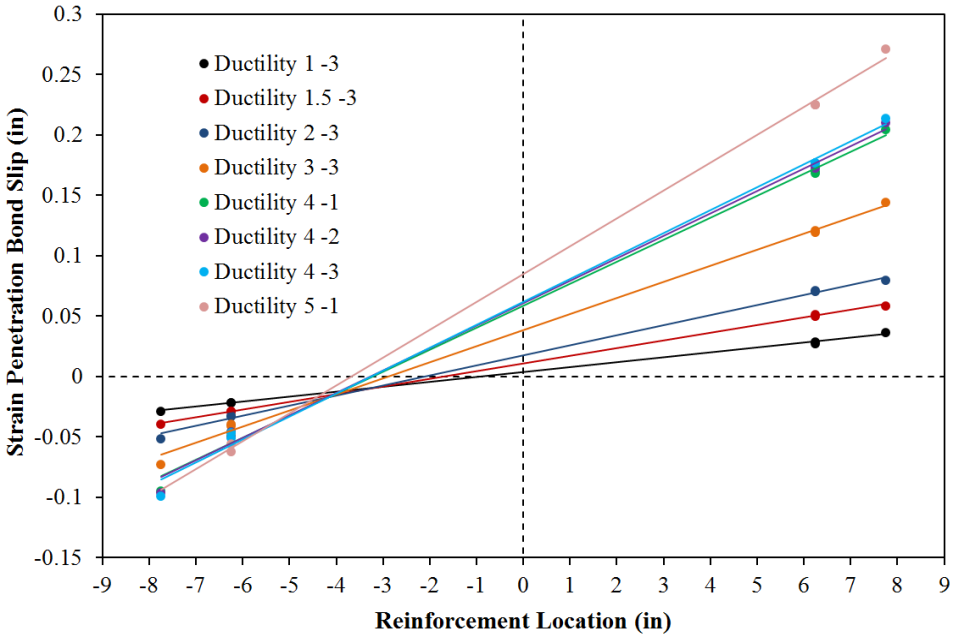

Figure 1.1005 T30 – Base Rotation due to Strain Penetration during Pull Cycles

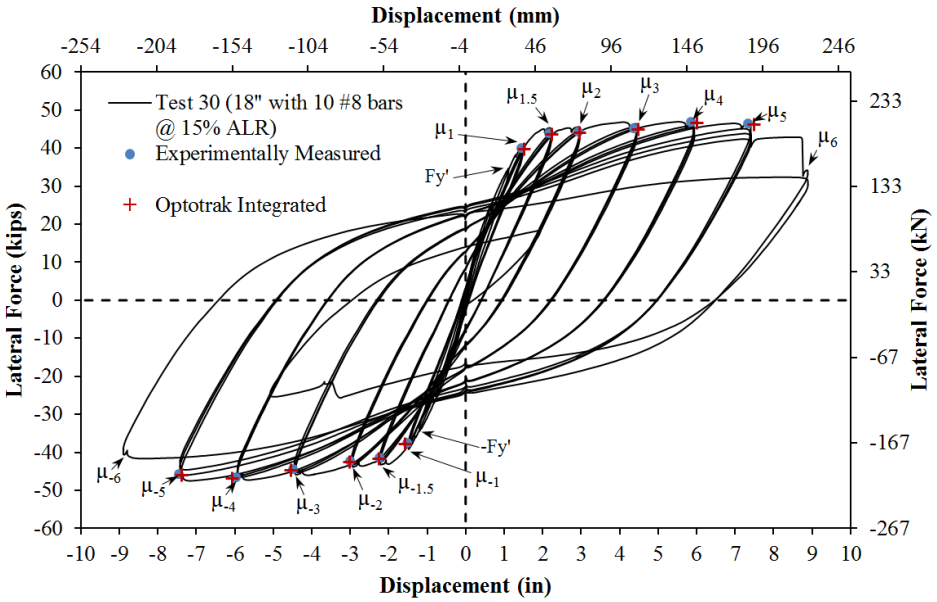

Figure 1.1006 T30 – Comparison of Measured and Optotrak Integrated Displacements

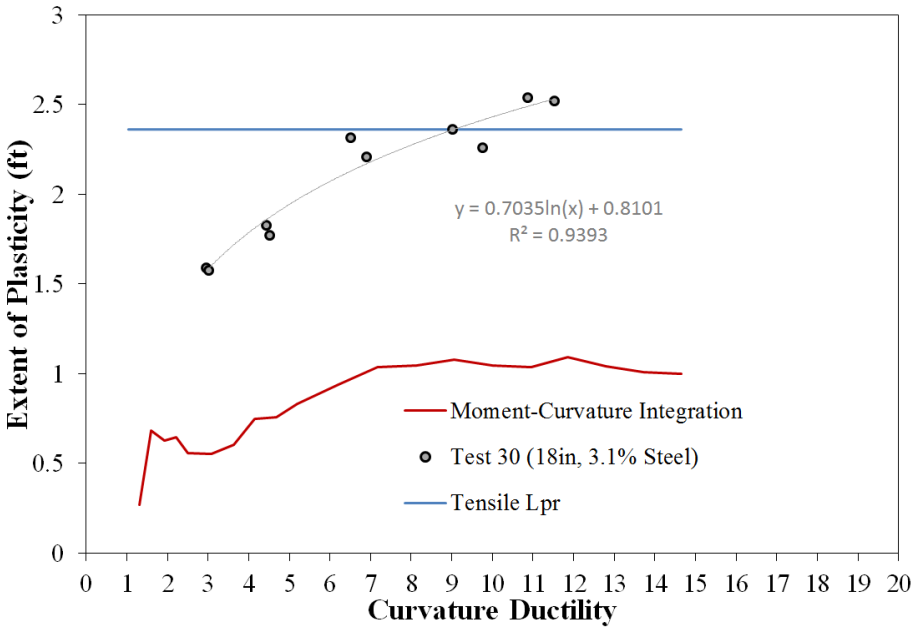

Figure 1.1007 T30 – Measured Spread of Plasticity (Circular Data Points)

Chapter 2: Weldability of A706 Reinforcing Steel

An experimental study was carried out to assess the performance of thirty circular, well-confined, bridge columns with varying lateral displacement history, transverse reinforcement detailing, axial load, aspect ratio, and longitudinal steel content. A key feature of the experiments is the high fidelity strain data obtained through the use of an optical 3D position measurement system. Over the course of the study three different techniques were used to monitor material strains with the Optotrak system: (1) a single positon monitor with steel post extensions, (2) two position monitors with vertical cover concrete blockouts, and (3) three position monitors with a complete cover blockout.

2.1 Test 7 and Weldability of A706 Reinforcing Steel

The single position monitor method was used for the first seven specimens, which were ultimately excluded from design recommendations in this report. This instrumentation technique, shown in Figure 2.3, had target markers applied to the ends of tack welded steel posts. Vertical cover concrete blockout strips over six extreme fiber bars were created by blocking out the cover concrete with insulation foam during casting. The measured strains from the target markers at the ends of the post extensions suffer from the same issues of the traditional curvature rod method. Strains are not measured at the location of interest; therefore the recorded values are influenced by rotations of the rods themselves. This was however not the biggest problem with this instrumentation method, since it was found that the ASTM A706 longitudinal steel utilized in Tests 7-12 had a reduced strain capacity under the influence of the surface tack welds. Ultimately, the single position monitor technique was abandoned, and Tests 8-30 utilized multiple position monitors with direct application of target markers to the reinforcing steel.

In the following section, experimental observations for nominally identical Tests 7 and 9 are compared. The 24” diameter bridge columns contained 16 #6 A706 bars for longitudinal

reinforcement ($A_{st}/A_g = 1.6\%$) and a #3 A706 spiral at 2" pitch ($4A_{sp}/(D's) = 1\%$). Both columns were subjected to symmetric three-cycle-set load histories, Figure 2.2, and a constant compressive axial load of 170 kips ($P/(f_c'A_g) = 5.5\%$). The cantilever specimens had an aspect ratio ($L/D = 4$). The only difference is that column Test 7 utilized a single Optotrak position monitor and tack welded steel post extensions, while Test 8 had multiple position monitors and direct application of target markers to the reinforcing steel. A comparison of the resulting force versus deformation response for the two tests appears in Figure 2.1. In Test 7 rupture of longitudinal reinforcement occurred prior to longitudinal bar buckling. In the other cyclically loaded experiments, bar buckling always occurred prior to rupture. Three south reinforcing bars fractured during pull cycles of displacement ductility six, and two north reinforcing bars fractured during the first push cycle of displacement ductility eight.

The first yield force for the tested material and geometric properties was determined using moment curvature analysis ($F_y' = 46.85\ kips\ with\ f_c' = 6545\ psi$). The initial part of the symmetric three cycle set load history contains reversals of loading at ¼ Fy', ½ Fy', ¾ Fy', and Fy'. After the specimen has reached the first yield force in each direction, the first yield displacement is obtained as an average ($\Delta_y' = 0.62"$). The equivalent yield displacement, used to determine the displacement ductility levels ($\mu_{\Delta 1} = 1 * \Delta_y$), is then calculated as $\Delta_y = \Delta_y'(M_n/M_y') = 0.83"$. The symmetric three-cycle-set load history then resumes with three complete cycles of loading at each displacement ductility level shown in Figure 2.2.

Concrete cracking occurred during push and pull cycles of ¾ Fy' on the north and south sides of the specimen respectively. The first signs of cover concrete crushing were observed at ($\mu_{1.5}^{+3} = 1.26"$) on the south side of the specimen, Figure 2.4. Cover concrete on the north side of the specimen did not begin to crush until ($\mu_2^{-1} = -1.66"$). Additional cracks formed and the extent of cover concrete crushing increased while the test proceeded without incident through displacement ductility four, Figure 2.4. During the first pull cycle of displacement ductility six ($\mu_6^{-1} = -4.97"$), south reinforcing bar S2 fractured, resulting in a significant

loss in strength. This observation was unexpected, since fracture never occurred prior to visible buckling in any of the cyclically loaded experiments and the strain demand should not have exceeded the strain at maximum stress for the plain reinforcing bars. Also, Bar S2 is adjacent to the extreme fiber bar and should experience smaller strain demands. Ultimately, this early fracture is attributed to embrittlement of the A706 reinforcing steel through the heat effects of welding the steel post extensions utilized in the instrumentation system. This was also unexpected, since the reinforcing steel in the first six specimens was unaffected by the surface tack welds.

The load history was continued to evaluate the degradation behavior of the specimen, and to see if a similar observation would occur on the north side of the specimen. The extreme fiber south reinforcing Bar S3 buckled during the third push cycle of displacement ductility six ($\mu_6^{+3} = 4.99"$). Since Bar S2 fractured prior to this observation, the peak tensile strain has little relevance due to the distortion of equilibrium in the cross section. Bar S3 was the first and only bar to buckle during the symmetric three-cycle-set load history which highlights the change in failure mechanism due to the weld process lowering the strain capacity of the steel.

During the third pull cycle of ductility six ($\mu_6^{-3} = -4.98"$), Bars S3 and S4 ruptured, resulting in a significant loss in strength. Three cycles at displacement ductility six were concluded without buckling or rupture of north reinforcement. North Bars N2 and N3 ruptured during the first push cycle of ductility eight ($\mu_8^{+1} = 6.65"$). The fractures occurred roughly ten inches above the footing at the location of the largest crack throughout the test. With large losses in strength on both sides of the column the test was concluded.

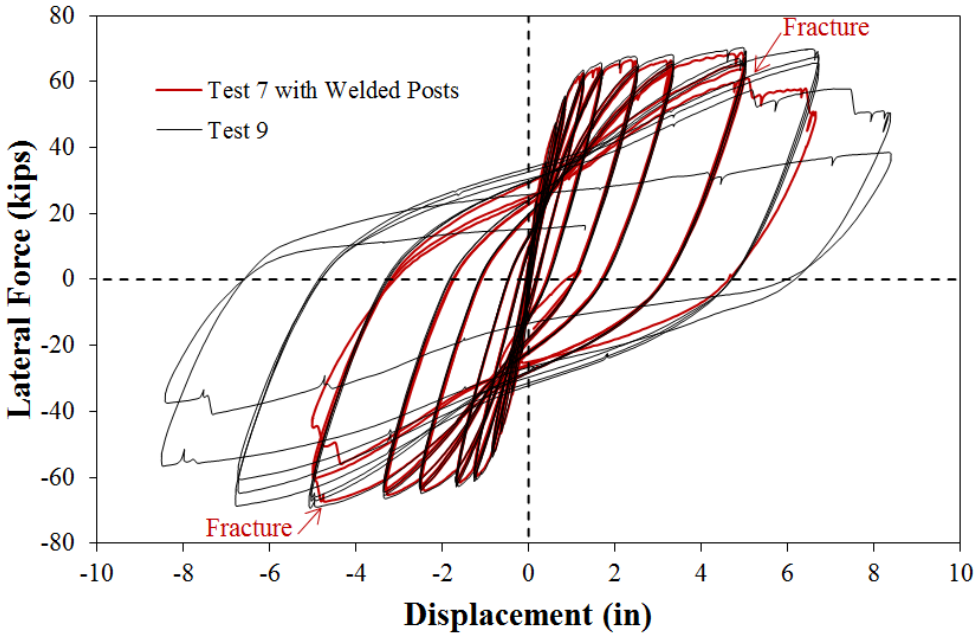

Figure 2.1 Tig-Welded Steel Posts Reduced Deformation Capacity in One Column

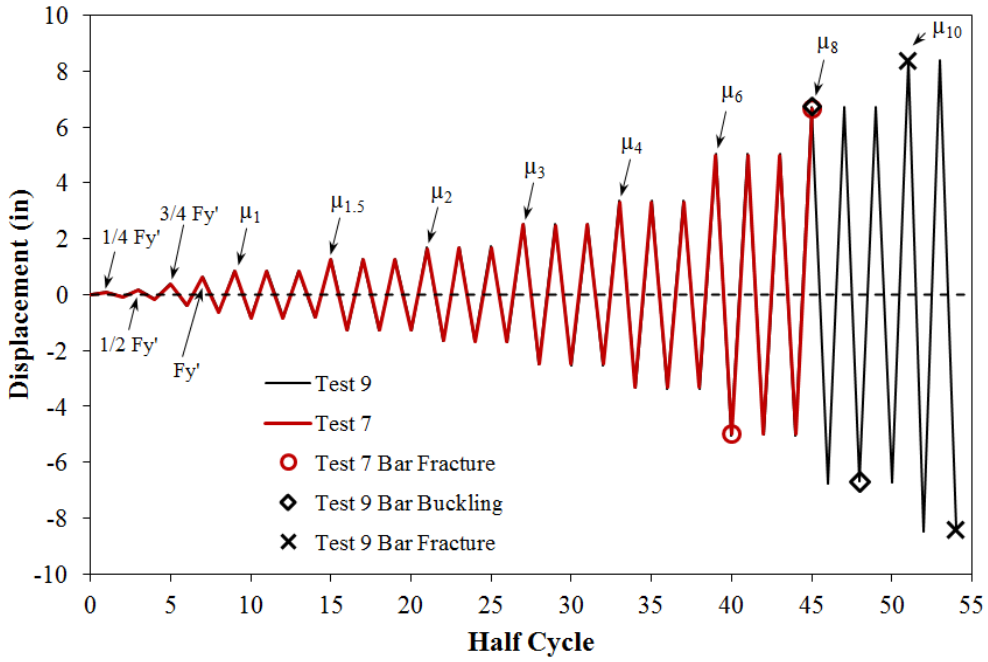

Figure 2.2 Symmetric Three-Cycle-Set Load History for Tests 7 and 9

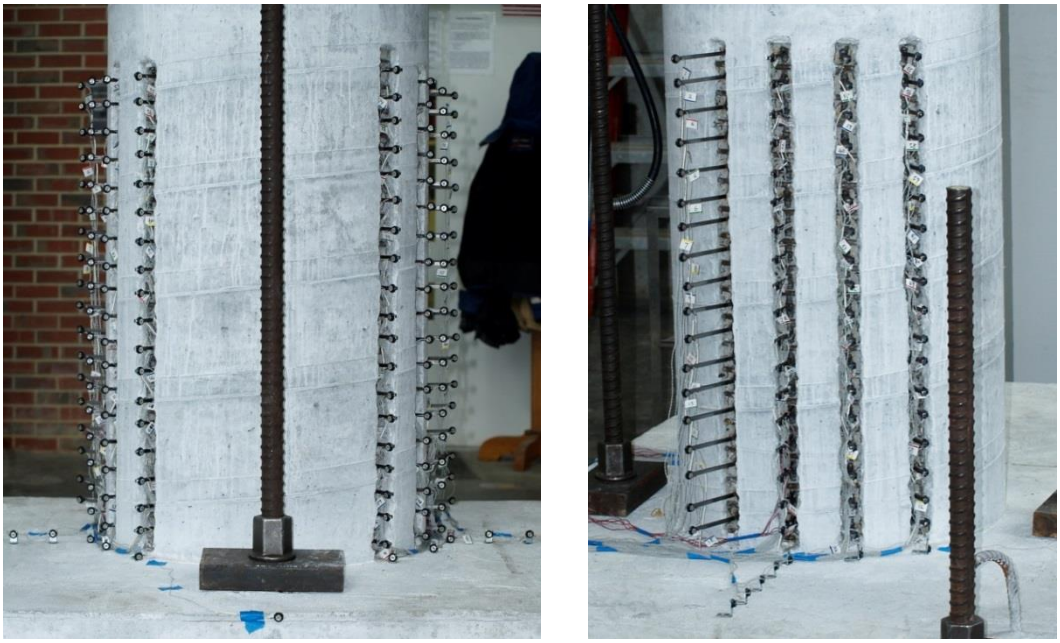

Figure 2.3 Single Optotrak Method Utilizing Post Extensions (Ultimately Abandoned)

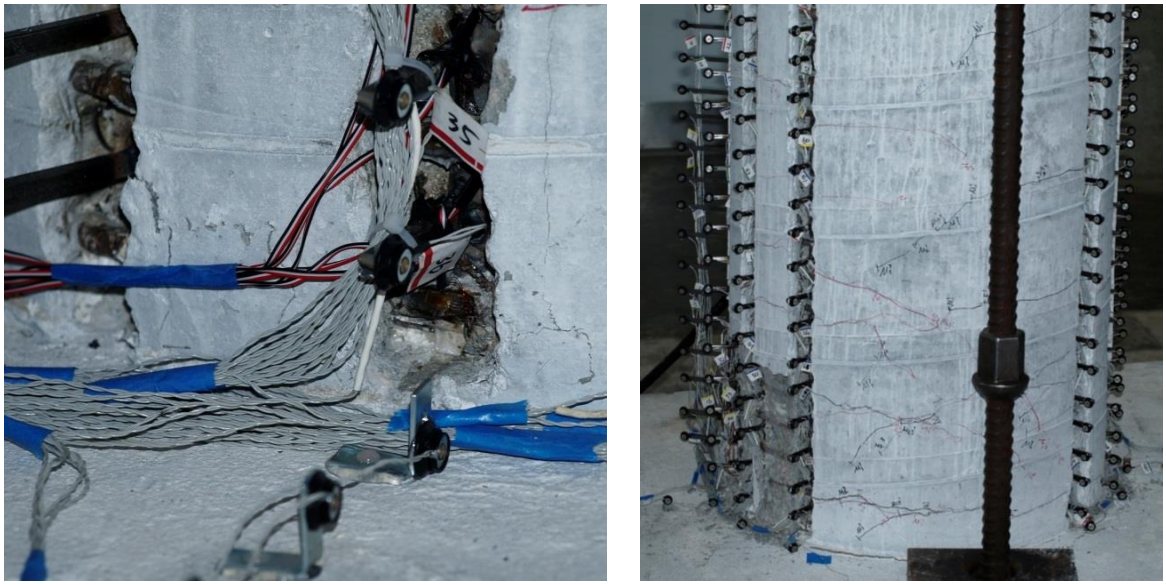

Figure 2.4 (Left) Crushing at $\mu_{1.5}^{+3}$ on South Side and (Right) Crack Distribution at μ_{4}^{-3}

Figure 2.5 (Left) Early Fracture of Bar S2 during μ_6^{-1} and (Right) Buckling of Bar S3 during μ_6^{+3}

2.2 A706 Steel Properties and Weldability for Tests 1-6 and 7-12

Additional material tests were carried out on A706 longitudinal reinforcement from Tests 1-6 and 7-12 to determine why one batch had reduced strain at maximum stress, but the other was not influenced by the surface tack welds utilized in the instrumentation technique. A summary of material properties for seven plain reinforcing bars and four bars with tack welded posts at 2" spacing appears in Table 2.1 for Tests 7-12. For each tension test, the following data appears in the table: (1) stress and strain at yield; (2) stress and strain at the beginning of strain hardening (end of yield plateau); and (3) stress and strain at maximum stress (ultimate condition). The average strain at maximum stress for the plain bars was 0.1331, while the ultimate strain was reduced for the tack welded bars to 0.0938. The effects of welding on this batch of steel are evident in the stress-strain response for the fourth bar test, Figure 2.6, which had a strain at maximum stress of only 0.0731. The material tests confirm the observations of early fracture of longitudinal reinforcement in Test 7. To highlight the fact that welding was not an issue for reinforcing bars in Tests 1-6, additional

material tests on plain reinforcing bars and steel with both 2" and 4" tack welded post spacings were tested. The strain at maximum stress for the three groups of bar tests remained comparable, without a significant reduction in the presence of welds, Table 2.2.

To further investigate the impact of welding on the longitudinal reinforcement, the metallurgical content of both batches were compared to allowable limits in the ASTM A706 standard. All of the welded post specimens utilized the same tungsten inert gas (TIG) welder technique, filler material, and maximum input amperage that controls the level of heat applied when the pedal is fully compressed. The duration of applied heat should not have changed significantly between testing series. Relevant sections of the ASTM standard for A706 reinforcing bars appear in Figure 2.7. Section 1.5 of the ASTM standard states that the chemical composition and carbon equivalent of A706 steel are limited to enhance the weldability of the steel. The standard recommends structural welding procedures that appear in AWS D1.4/D1.4M, the structural welding code for reinforcing steel. The tested material properties and chemical composition from heat analysis obtained from the mill test certification for all of the A706 steel was within the allowable range forth both batches of steel, Figure 2.7.

2.3 Conclusion

The failure mechanism for one column experiment was shifted from fracture of previously buckled bars to early brittle fracture of reinforcement for a batch of steel with surface tack welded posts utilized for instrumentation. The stress and strain at initial yielding and strain hardening were not influenced by the surface tack welds. The maximum stress in the presence of the tack welds was not influenced, but the strain capacity was reduced in the presence of welds. In large bridge columns, individual circular butt welded hoops are commonly utilized instead of spiral reinforcement. This test highlights the need to quality control of welded A706 reinforcement. The strain at maximum stress, and not the value of the stress itself, is the critical parameter in defining the influence of welding on the reinforcement behavior.

Table 2.1 Reinforcement Material Properties for Tests 7-12, Influenced by Welding

Test Series	Bar Number	ε_y	f_y (ksi)	ε_h (hardening)	f_h (ksi)	ε_u (max stress)	f_u (ksi)
Plain Bar	1	0.00231	67.0	0.0148	67.0	0.1597	94.3
	2	0.00232	67.4	0.0155	67.9	0.1334	94.3
	3	0.00232	67.4	0.0145	67.4	0.1503	94.4
	4	0.00234	68.0	0.0135	68.0	0.1213	95.2
	5	0.00238	69.0	0.0135	69.0	0.1249	95.5
	6	0.00238	69.0	0.0153	69.0	0.1288	94.9
	7	0.00237	68.8	0.0150	68.8	0.1133	95.1
Welded Posts at 2”	1	0.00233	67.5	0.0125	67.8	0.1049	94.7
	2	0.00233	67.5	0.0130	67.5	N/A	N/A
	3	0.00237	68.7	0.0130	68.7	0.0731	93.4
	4	0.00236	68.3	0.0141	68.7	0.1034	94.9

Test Series	ε_y	f_y (ksi)	ε_h (hardening)	f_h (ksi)	ε_u (max stress)	f_u (ksi)
Plain Bar Averages	0.00235	68.1	0.0146	68.2	0.1331	94.8
Welded Posts at 2”	0.00234	68.0	0.0132	68.2	0.0938	94.3

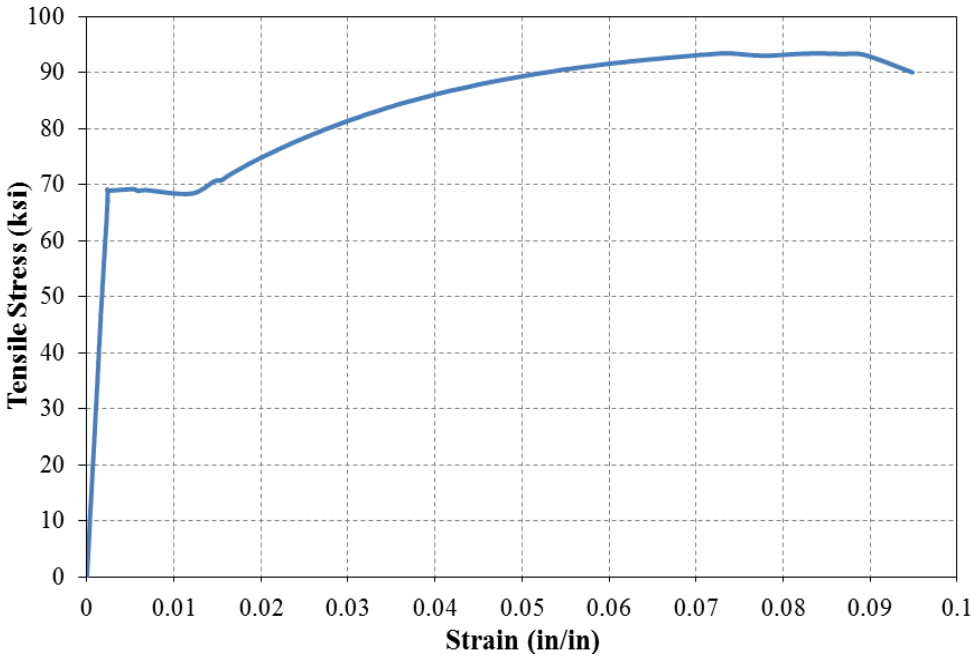

Figure 2.6 Longitudinal Steel from Tests 7-12 with Reduced Strain at Maximum Stress

Table 2.2 Reinforcement Material Properties for Tests 1-6, Not Influenced By Welds

Test Series	Bar Number	ε_y	f_y (ksi)	ε_h (hardening)	f_h (ksi)	ε_u (max stress)	f_u (ksi)
Plain Bar	1	0.00211	61.2	0.0144	61.2	0.1196	85.4
	2	0.00226	65.5	0.0145	65.5	0.1213	89.4
	3	0.00222	64.5	0.0140	64.5	0.1246	89.7
Welded Posts at 4”	1	0.00210	60.8	0.0133	60.8	0.1193	85.2
	2	0.00221	64.0	0.0131	64.0	N/A	88.6
	3	0.00220	63.8	0.0130	63.8	0.1028	88.0
	4	0.00219	63.5	0.0130	63.5	0.1291	88.2
	5	0.00221	64.0	0.0130	64.0	0.1293	88.6
Welded Posts at 2”	1	0.00224	65.0	0.0140	65.3	0.1144	88.6
	2	0.00225	65.3	0.0140	65.3	0.1060	88.3
	3	0.00224	65.0	0.0153	66.0	0.1102	88.3
	4	0.00225	65.3	0.0140	65.3	0.1115	87.8

Test Series	ε_y	f_y (ksi)	ε_h (hardening)	f_h (ksi)	ε_u (max stress)	f_u (ksi)
Plain Bar Averages	0.00220	63.7	0.0143	63.7	0.1218	88.1
Welded Posts at 4”	0.00218	63.2	0.0131	63.2	0.1201	87.7
Welded Posts at 2”	0.00225	65.2	0.0143	65.5	0.1105	88.2

TABLE 2 Tensile Requirements

	Grade 60 [420]	Grade 80 [5
ile strength, min, psi [MPa]	80 000 [550][A]	100 000 [69
strength, min, psi [MPa]	60 000 [420]	80 000 [55(
strength, max, psi [MPa]	78 000 [540]	98 000 [67
gation in 8 in. [200 mm], min, %		
Designation Nos.		
4, 5, 6 [10, 13, 16, 19]	14	12
8, 9, 10, 11 [22, 25, 29, 32, 36]	12	12
, 18 [43, 57]	10	10

ısile strength shall not be less than 1.25 times the actual yield strer

1.5 *Welding*—This specification limits chemical composition (6.2) and carbon equivalent (6.4) to enhance the weldability of the material. When steel is to be welded, a welding procedure suitable for the chemical composition and intended use or service should be used. The use of the latest edition of AWS D1.4/D1.4M is recommended. This document describes the proper selection of the filler metals, preheat/interpass temperatures, as well as, performance and procedure qualification requirements.

6.2 The chemical composition as shown by heat analysis shall be limited by the following:

Element	max, %
Carbon	0.30
Manganese	1.50
Phosphorus	0.035
Sulfur	0.045
Silicon	0.50

6.4 The heat analysis shall be such as to provide a carbon equivalent (C.E.) not exceeding 0.55 % as calculated by the following formula:

$$\text{C.E.} = \%\,\text{C} + \frac{\%\,\text{Mn}}{6} + \frac{\%\,\text{Cu}}{40} + \frac{\%\,\text{Ni}}{20} + \frac{\%\,\text{Cr}}{10} - \frac{\%\,\text{Mo}}{50} - \frac{\%\,\text{V}}{10} \quad (1)$$

Figure 2.7 ASTM A706 Specification for Reinforcing Steel

Table 2.3 Mill Specification Reports for Longitudinal Steel from Tests 1-6 and 7-12

Tests	C	Mn	P	S	Si	Cu	Ni	Cr
1-6	0.30	0.85	0.012	0.027	0.24	0.35	0.15	0.19
7-12	0.28	1.14	0.006	0.035	0.21	0.28	0.12	0.12

Tests	Mo	V	Nb	N	Sn	Al	Ti	C Eqv
1-6	0.05	0.028	0.002	0.009	0.016	0.001	0.001	0.472
7-12	0.02	0.033	N/A	N/A	0.010	N/A	N/A	0.490

Chapter 3: Summary of Column Tests 1-6

The initial six columns for the Load History research program were constructed by a local contractor. Although the need for accurate detailing was expressed and tolerances were specified, the resulting specimens had discrepancies in transverse steel spacings in the plastic hinge region. This influenced the restraint of longitudinal reinforcing bars and significantly impacted the performance of these specimens. Furthermore, these tests utilized the single position monitor and welded steel post extension instrumentation technique discussed in Chapter 2. The strain capacity reinforcing steel was not influenced by the surface tack welded posts, but the technique produced less reliable strains when compared to the use of multiple position monitors and direct application of target markers to the longitudinal reinforcement. The strains measured at the ends of the welded post extensions are influenced by rotations of the posts themselves which arise due to the curvature gradient over the gage length. For this reason, as well as the detailing errors mentioned, the occurrence of limit states in Tests 1-6 were not included in the formulation of design recommendations. A brief summary of each test is included in this section to highlight the observed behavior.

3.1 Test Setup and Instrumentation for Specimens 1-6

The 24" diameter bridge columns contained 16 #6 A706 bars for longitudinal reinforcement ($A_{st}/A_g = 1.6\%$) and a #3 A706 spiral at 2" pitch ($4A_{sp}/(D's) = 1\%$). The columns were subjected to a constant compressive axial load of 170 kips ($P/(f'_c A_g) \approx 5\%$). The cantilever specimens had an aspect ratio ($L/D = 4$). The main variable for the first six expeirments was the lateral displacement history employed in the test. Due to the detailing errors, the spacing of transverse steel in regions of the column critical to bar buckling was also variable. In the following section, the load history for each experiment and a brief summary of the observed damage is summarized for Tests 1-6. The cross section and instrumentation system utilized in Tests 1-6 appears in Figure 3.1 and Figure 3.2. Tests 1 and 3-6 had vertical cover concrete blockout strips and tack welded steel post extensions.

For comparison, Test 2 was conducted with a full cover concrete to verify that the blockout strips did not influence the performance of the column after initial crushing. A summary of reinforcement material properties for both longitudinal and transverse steel appears in Table 3.1. The material properties for the longitudinal reinforcement were not influenced by surface tack welds. The tested material properties for the column concrete in Tests 1-6 appear in Table 3.1. Since the columns were constructed by a contractor it is unknown why there is such disparity in the column concrete strength and associated axial load ratios under the constant applied compressive load of 170 kips.

Table 3.1 Material Properties for Tests 1-6

Longitudinal Steel	ε_y	f_y (ksi)	ε_h (hardening)	f_h (ksi)	ε_u (max stress)	f_u (ksi)
Plain Bar Averages	0.00220	63.7	0.0143	63.7	0.1218	88.1
Welded Posts at 4”	0.00218	63.2	0.0131	63.2	0.1201	87.7
Welded Posts at 2”	0.00225	65.2	0.0143	65.5	0.1105	88.2

Transverse Steel	f_y (ksi)	f_u (ksi)
#3 A706 Spiral	64.0	101.1

Test #	**1**	**2**	**3**	**4**	**5**	**6**
Concrete $(f_c' \; in \; MPa)$	7.40	5.06	7.50	7.93	8.40	10.18
Axial $\left(P/f_c'A_g \; in \; \%\right)$	5.1	7.4	5.0	4.7	4.5	3.69

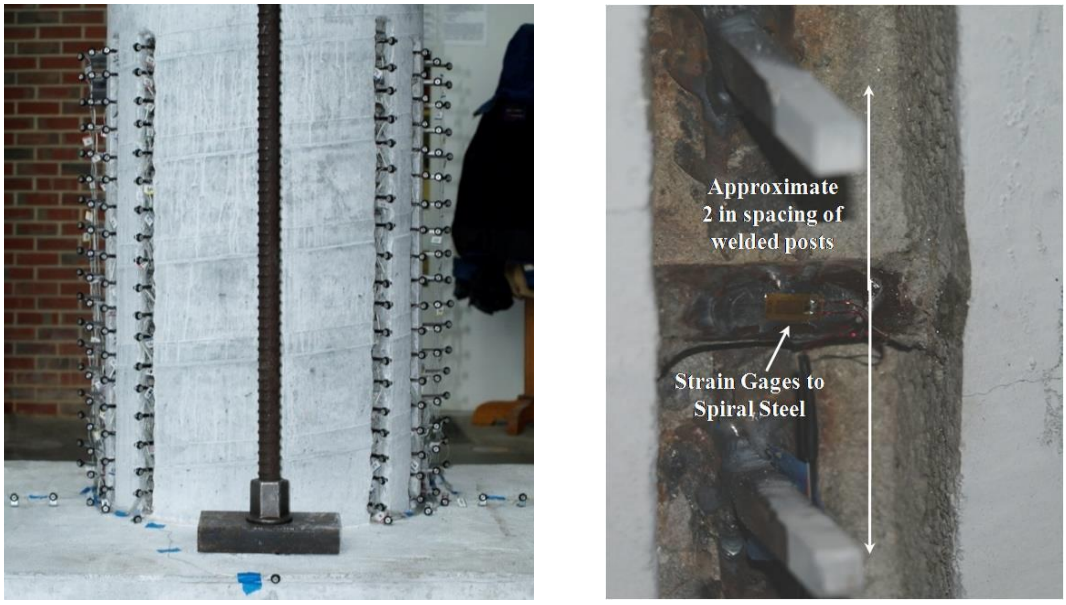

Figure 3.1 Single Optotrak Method Utilizing Post Extensions (Ultimately Abandoned)

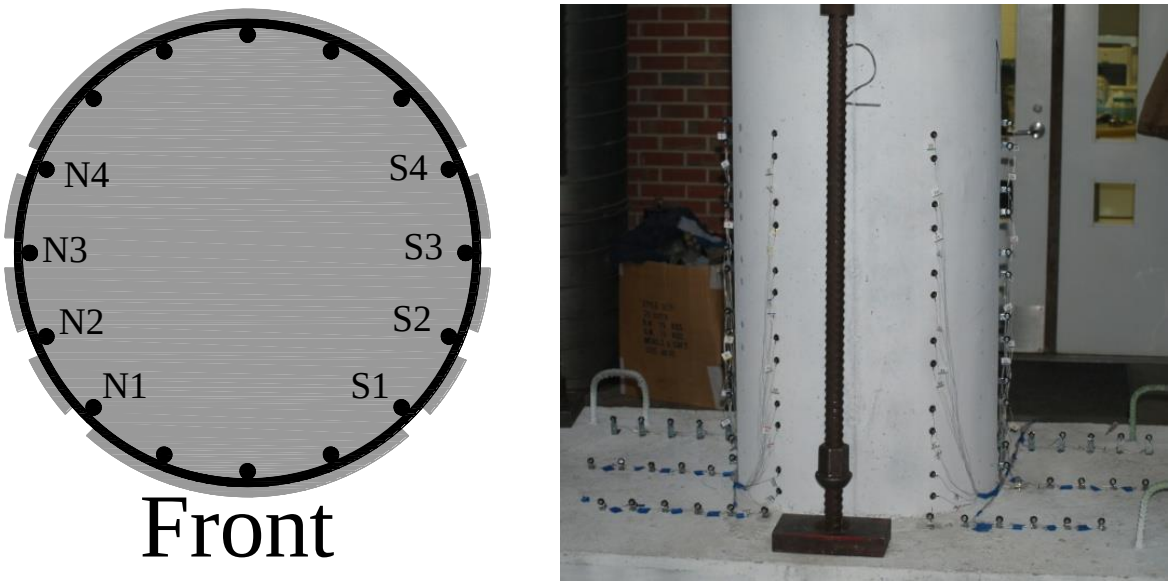

Figure 3.2 (Left) Cross Section with Blockouts and (Right) Test 2 with Full Cover

3.2 Test 1: Pushover Load History

To evaluate the tensile bar buckling mechanism, a pushover load history was utilized for Test 1. In a cyclic load history bar buckling is expected to occur after reversal from a peak tensile strain while the bar is under net elongation, but compressive stress. During the subsequent reversal while the cracks are still closing, the longitudinal reinforcement is the sole source of compression zone stability. Furthermore, the tangent modulus for the reinforcing bar is reduced during reversals from lager values of tensile strain, which influences buckling behavior. For these reasons, bar buckling was not expected to occur under direct compression alone for the well confined bridge column. As the load increased, the test was paused for observation at each of the labeled observation points below in the resulting hysteretic response, Figure 3.3. The small drops in force resulted from relaxation at observation displacements. The specimen was briefly unloaded and reloaded after displacement ductility eight.

The recorded displacement at the analytical first yield force of $\left(\mathrm{F}'_y = 43.84\ kips\right)$ was $\left(\Delta'_y = 0.48"\right)$. The equivalent yield displacement, used to determine the displacement ductility levels $\left(\mu_{\Delta 1} = 1 * \Delta_y\right)$, is then calculated as $\Delta_y = \Delta'_y\left(M_n/M'_y\right) = 0.65"$. Concrete cracking was first observed at ¾ Fy'. Displacement ductility two marked the onset of cover concrete crushing, while the cracks on the tension side measured 1.25 mm in width. At the base of the column, ¼" cracks widths were measured at ductility twelve ($\mu_{\Delta 12} = 7.74"$). There was no loss in strength through displacement ductility eighteen ($\mu_{\Delta 18} = 11.57"$). At 12.5", two longitudinal bars on the tension side ruptured causing an 18% loss in strength. The bars ruptured at the location of the largest crack on the tension side, Figure 3.5. The displacement was increased to ductility twenty-two ($\mu_{\Delta 22} = 14.20"$) without further strength loss or rupture of reinforcement. This concluded the monotonic portion of the test. Upon reversal of loading all of the bars previously exposed to tension buckled and a residual displacement over twelve inches was observed.

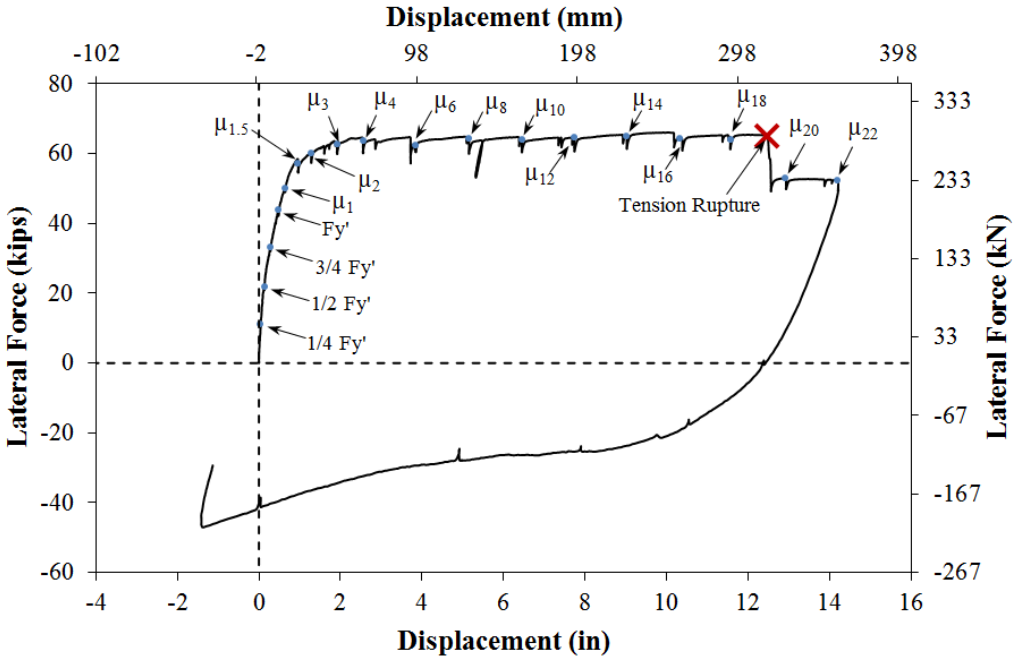

Figure 3.3 Test 1 – Hysteretic Response for Pushover Load History

Figure 3.4 Test 1 – (Left) Compressive and (Right) Tensile Sides at $\mu_{\Delta 18} = 11.57$"

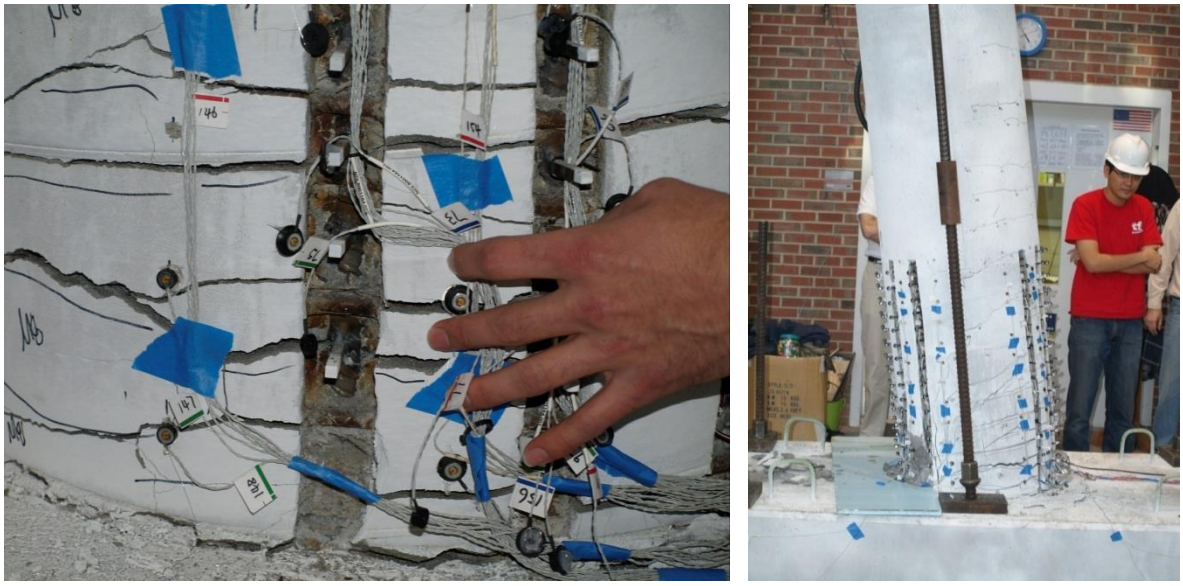

Figure 3.5 Test 1 – (Left) Fracture of Two North Bars at 12.5" and (Right) Lateral Displacement at $\mu_{\Delta 22} = 14.22"$

3.3 Test 2: Three-Cycle-Set with Full Cover Concrete

The second test utilized a column with full cover concrete to determine the effect, if any, of longitudinal cover blockouts and welded posts used in other specimens to determine steel strains in the inelastic range. The specimen was subjected to a symmetric three-cycle-set load history, which is commonly used to evaluate the seismic performance of structural components. Since the symmetric three-cycle-set load history is considered as more severe than the demands produced by real earthquakes, the force displacement response can be used for comparison to other tests.

The first yield force for the tested material and geometric properties was determined using moment curvature analysis $\left(F_y' = 42.69\ kips\ for\ f_c' = 5.06\ ksi\right)$. The initial portion of the symmetric three cycle set load history contains reversals of loading at ¼ Fy', ½ Fy', ¾ Fy', and Fy'. After the specimen has reached the first yield force in each direction, the first yield displacement is obtained as an average $\left(\Delta_y' = 0.51"\right)$. The equivalent yield

displacement, used to determine the displacement ductility levels $(\mu_{\Delta 1} = 1 * \Delta_y)$, is then calculated as $\Delta_y = \Delta'_y(M_n/M'_y) = 0.83"$. The symmetric three-cycle-set load history then resumes with three complete cycles of loading at each displacement ductility level shown in Figure 2.2. The resulting hysteretic response for Test 2 appears in Figure 3.7. A hysteretic comparison of the monotonic and cyclic response from Tests 1 and 2 is shown in Figure 3.8.

The first cracks on the north and south sides of the specimen were observed during ¾ Fy' push and pull cycles respectively. Cover concrete crushing was first observed on the south side of the specimen, Figure 3.9, during the first push cycle of displacement ductility three $(\mu_3^{+1} = 1.72")$. The north extreme fiber bar buckled after reversal from $(\mu_8^{+1} = 5.27")$, Figure 3.10. Buckled occurred over adjacent ≈2.5" transverse steel spacings, which is larger than the specified 2" spacing in construction of the specimens. Adjacent north bars N2 and N4 buckled during ductility eight, resulting in the buckled deformation shown in Figure 3.10. The previously buckled north extreme fiber bar N3 ruptured during $(\mu_{10}^{+1} = 6.60")$, resulting in the first notable loss in strength.

The spacing of transverse steel is critical to the location and deformation at the initiation of bar buckling. The south side of the specimen, with an average 2" spacing of transverse steel, had bar buckling delayed until $(\mu_{10}^{+2} = 6.59")$. During $(\mu_{10}^{+2} = 6.59")$, two additional north reinforcing bars N2 and N4 ruptured. During $(\mu_{10}^{+3} = 6.56")$, an additional north bar fractured and an adjacent south bar buckled. During $(\mu_{10}^{-3} = -6.77)$, three previously buckled bars on the south side of the specimen ruptured resulting in a significant loss in strength. A full cycle was completed at $\mu_{\Delta 12}$ to evaluate further strength degredation even though significant strength loss had already occurred in both directions of loading.

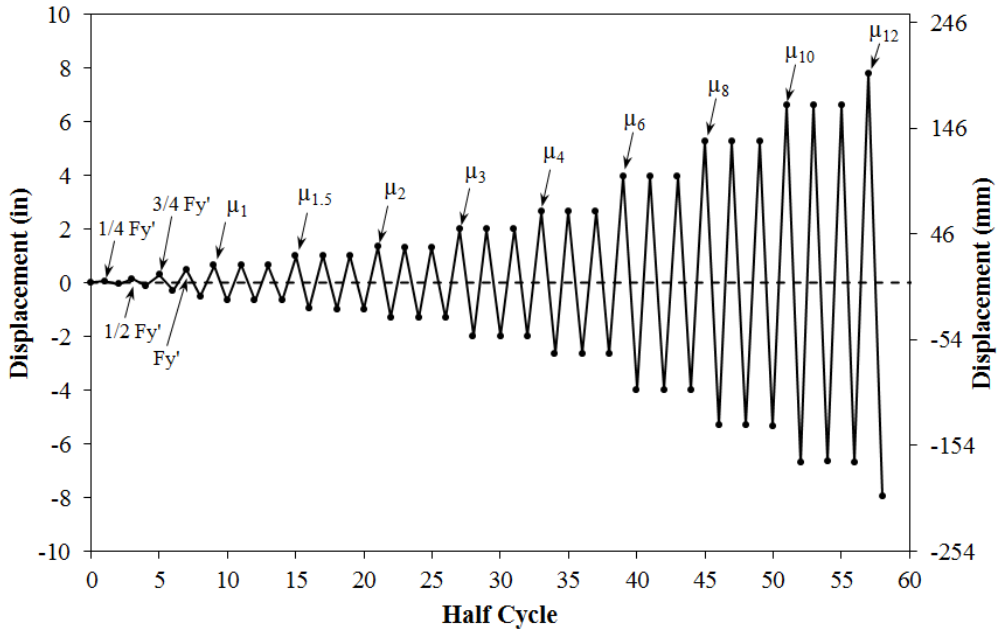

Figure 3.6 Test 2 – Symmetric Three-Cycle-Set Load History

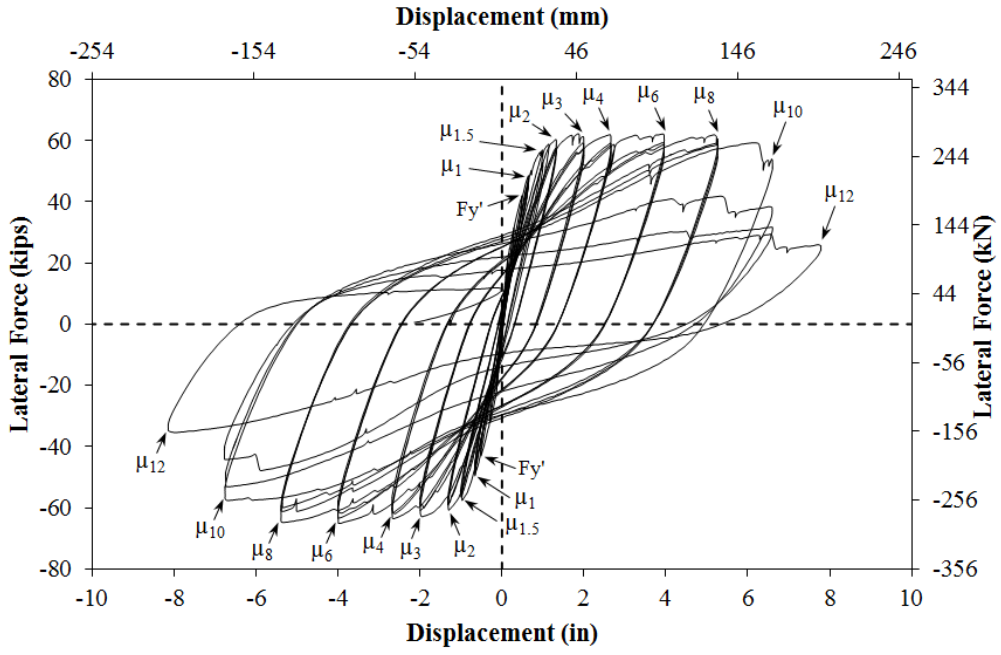

Figure 3.7 Test 2 – Hysteretic Response

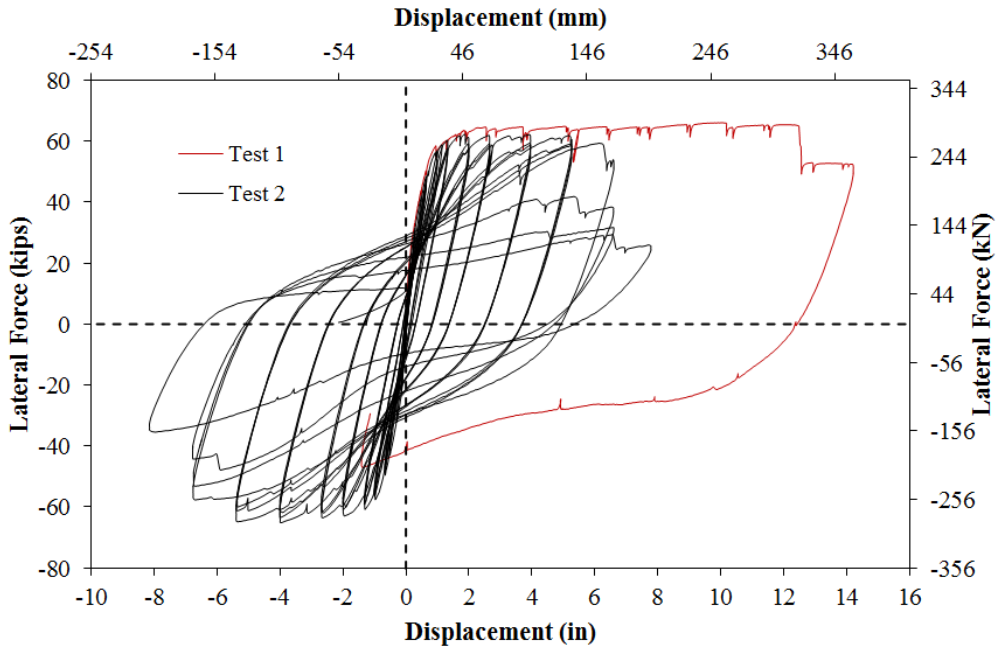

Figure 3.8 Hysteretic Comparison of Monotonic Test 1 and Cyclic Test 2

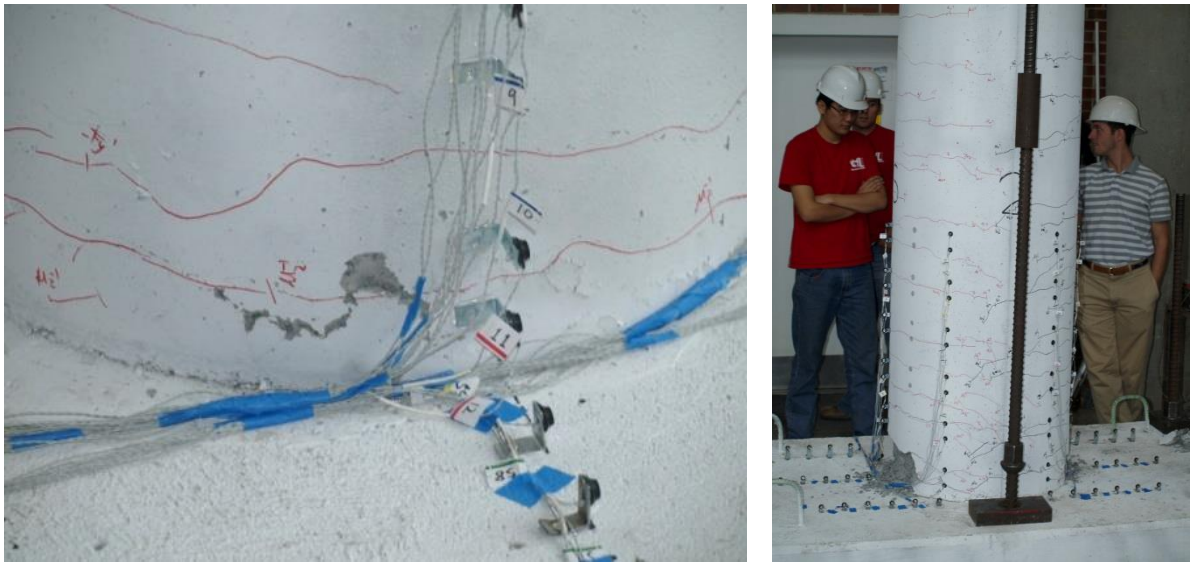

Figure 3.9 Test 2 – (Left) Initial Crushing on the South Side during $\left(\mu_3^{+1} = 1.72"\right)$ and (Right) Crack Distriubtion at $\left(\mu_4^{-3} = -2.68"\right)$

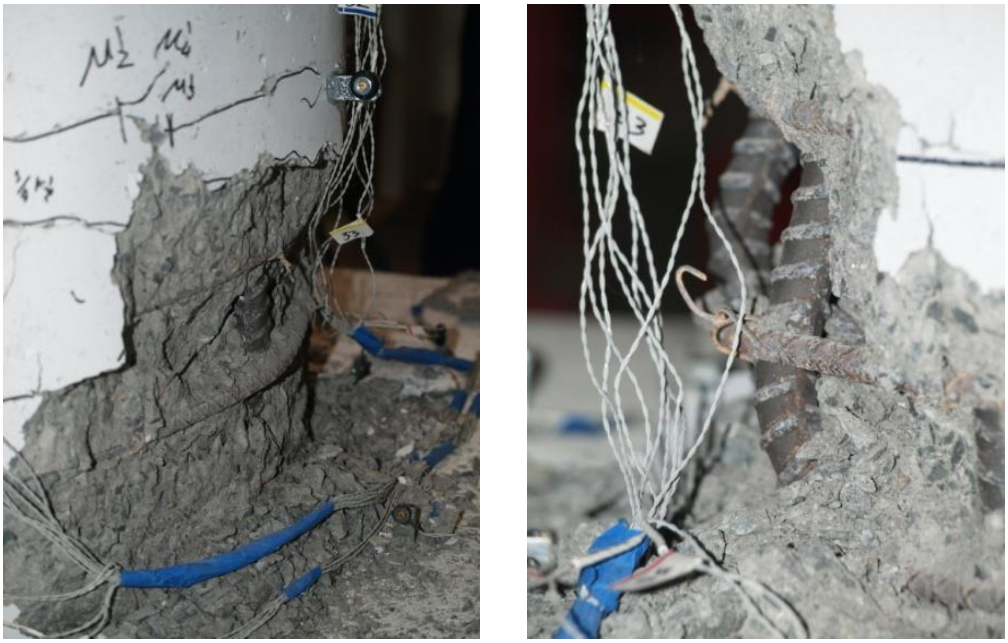

Figure 3.10 Test 2 – (Left) Buckling of Bar N3 during $\left(\mu_8^{-1} = -5.39"\right)$ and (Right) Deformation in Multiple Buckled North Bars at $\left(\mu_8^{-3} = -5.36"\right)$

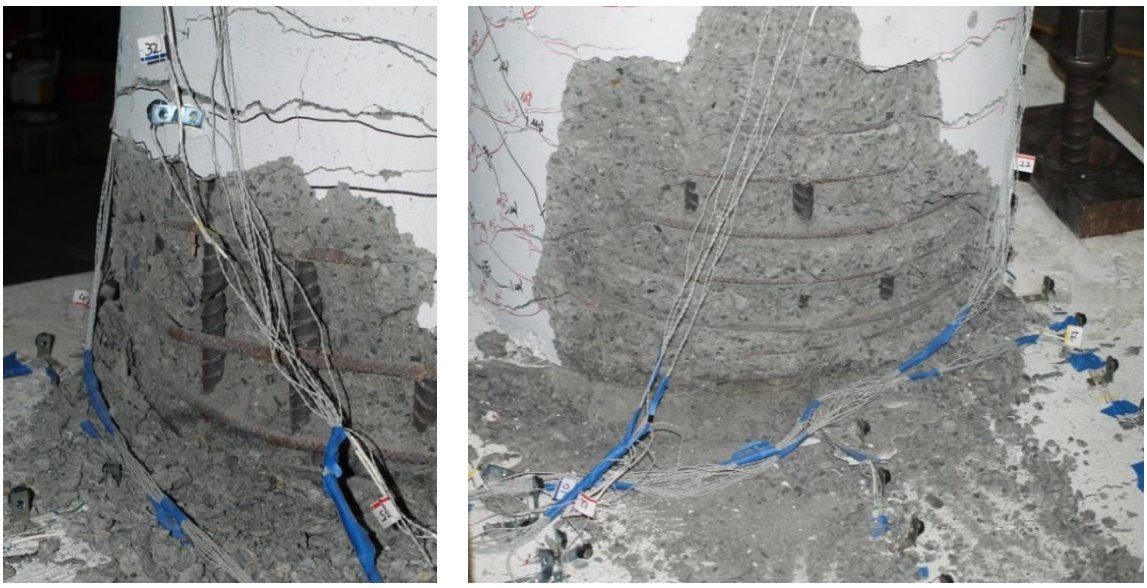

Figure 3.11 Test 2 – (Left) Fracture of Previously Buckled Bar N3 during $\left(\mu_{10}^{+1} = 6.60"\right)$ and (Right) Buckling of South Extreme Fiber Bar S3 during $\left(\mu_{10}^{+2} = 6.59"\right)$

3.4 Test 3: Three-Cycle-Set with Cover Blockouts

The third specimen was nominally identical to the second, except vertical cover concrete blockout strips were installed over extreme fiber reinforcement during construction for the instrumentation system. The first yield force for the tested material and geometric properties was determined using moment curvature analysis $\left(F_y' = 44.20\ kips\ for\ f_c' = 7.50\ ksi\right)$. The initial portion of the symmetric three cycle set load history contains reversals of loading at ¼ Fy', ½ Fy', ¾ Fy', and Fy'. After the specimen has reached the first yield force in each direction, the first yield displacement is obtained as an average $\left(\Delta_y' = 0.47"\right)$. The equivalent yield displacement, used to determine the displacement ductility levels $\left(\mu_{\Delta 1} = 1 * \Delta_y\right)$, is then calculated as $\Delta_y = \Delta_y'\left(M_n/M_y'\right) = 0.67"$. The symmetric three-cycle-set load history then resumes with three complete cycles of loading at each displacement ductility level shown in Figure 3.12. The resulting hysteretic response for Test 3 and a comparison of the response of Test 2 appears in Figure 3.13 and Figure 3.14 respectively.

The first cracks on the south side of the specimen were observed during the -½ Fy' pull cycle. Cover concrete crushing was observed on the north side of the specimen during $(\mu_3^{-1} = -2.05")$, Figure 3.15. The crack distriubtion on the front of the specimen during $(\mu_3^{-3} = -2.02")$ is also shown in Figure 3.15. A bar on the north side fo the speicmen visibly buckled duirng $(\mu_6^{-1} = -4.07")$, Figure 3.16, at the location of the largest transverse steel sapcing of 3" above the column base. Since the specified transverse steel spacing was only 2", the detailing error led to a reduction in the deformation capacity of the column. Three additional north reinforcing bars buckled during $(\mu_8^{-1} = -5.45")$, before any south reinforcement showed signs of buckling. Two perviously buckled north reinforcing bars fratured during $(\mu_8^{+3} = 5.37")$, Figure 3.17, resulting in the first significant loss in strength. A third north bar fractured during $(\mu_{10}^{+1} = 6.67")$, followed by a fourth during $(\mu_{10}^{+2} = 6.65")$.

Compare this to the south side of the specimen, Figure 3.16, where the critical transverse steel spacing above the footing was only 1.5" on center. Visible buckling of two south

reinforcing bars was delayed until ($\mu_{10}^{+2} = 6.65$"), when cross section equilibrium had already been influenced by fractured north reinforcing bars. One of these south buckled bars ruptured during ($\mu_{10}^{-2} = -6.70$"), followed by the second during ($\mu_{10}^{-3} = -6.70$"). This test exemplifies the need for consistent transverse steel detailing, and shows ultimately why the results from Tests 1-6 were not included in the formulation of design recommendations for this research program.

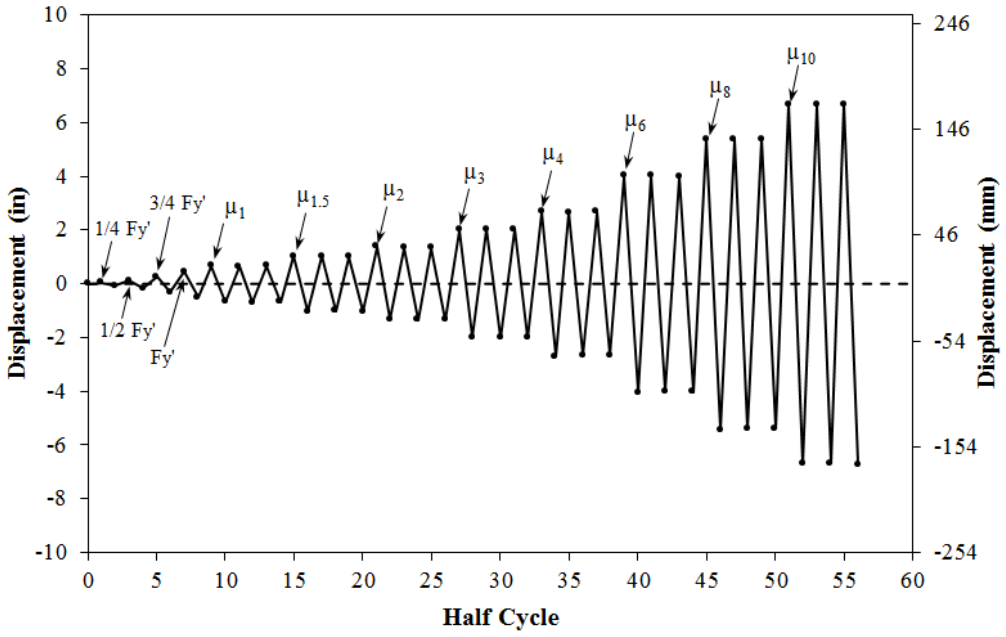

Figure 3.12 Test 3 – Symmetric Three-Cycle-Set Load History

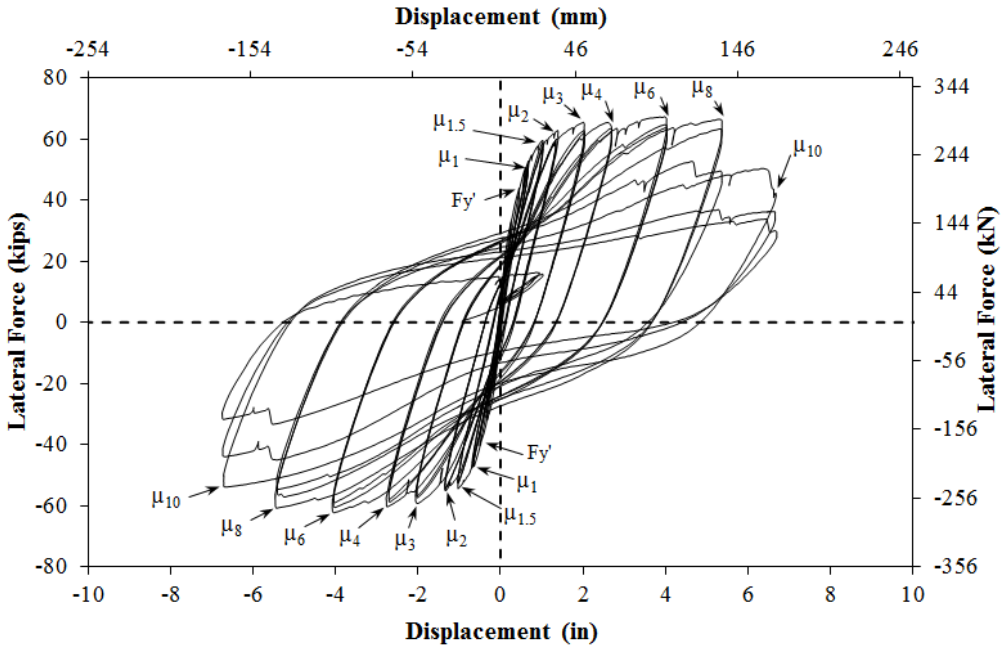

Figure 3.13 Test 3 – Hysteretic Response

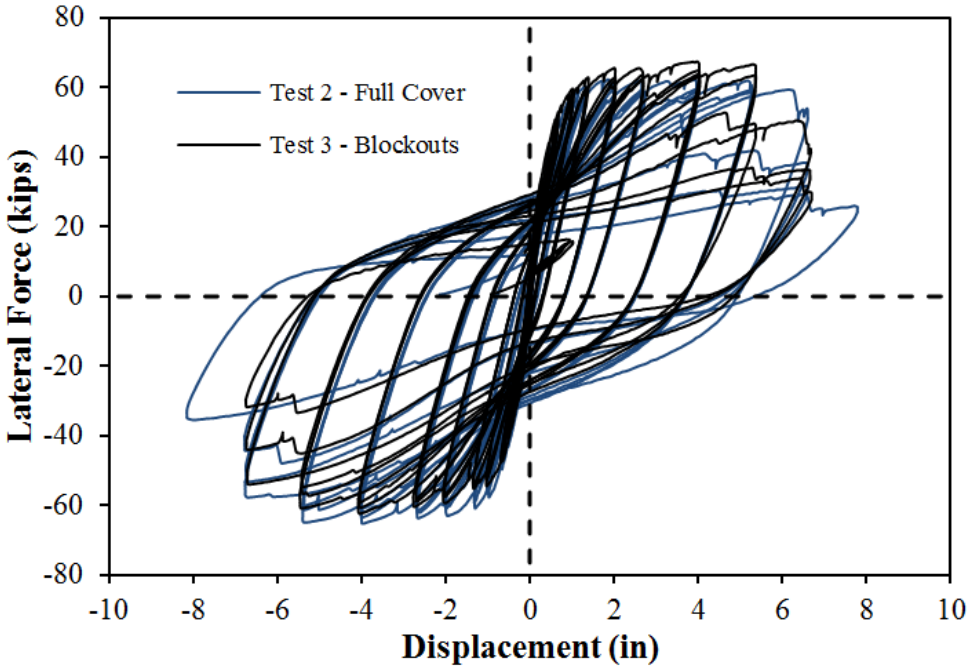

Figure 3.14 Hysteretic Comparison of Tests 2 and 3

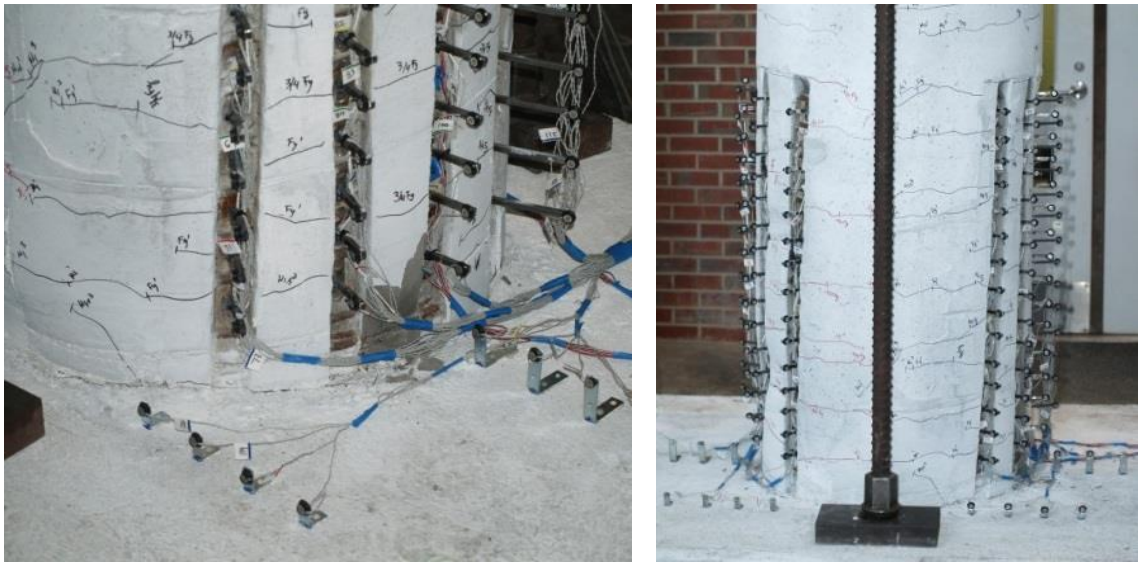

Figure 3.15 Test 3 – (Left) North Concrete Crushing during $\left(\mu_3^{-1} = -2.05"\right)$ and (Right) Crack Distribution on the Front of the Specimen during $\left(\mu_3^{-3} = -2.02"\right)$

Figure 3.16 Test 3 – (Left) Buckling of North Reinforcement during $\left(\mu_6^{-1} = -4.07"\right)$ and (Right) Buckling of South Reinforcement during $\left(\mu_{10}^{+2} = 6.65"\right)$

Figure 3.17 Test 3 – Fracture of Bars N2 and N3 during $\left(\mu_8^{+3} = 5.37"\right)$

3.5 Test 4: 1940 El Centro Earthquake Load History

The goal of the physical tests in the research program is to investigate the impact of load history on the relationship between strain and displacement and the performance strain limits. Tests one through three focused on monotonic and symmetric three-cycle-set load histories. The displacement input for Tests 4-6 is determined using acceleration time histories from recorded earthquakes and non-linear time history analysis. Test four was subjected to an analytical load history obtained from the north-south component of the 1940 El Centro earthquake. The top column displacement history in Figure 3.18 was determined using Ruaumoko inelastic time history analysis with a viscous damping ratio of 5.7% based on tangent stiffness and a thin Takeda hysteretic rule. A scale of three times the original acceleration values in the El Centro time history was chosen to produce buckling on both sides of the specimen. The scale was chosen based on the amplitude of the resulting peak displacements in the load history for the push and pull directions of loading. The maximum spacing of the transverse steel in the plastic hinge region on the North and South sides of the column was 3" and 2" respectively. The load history was oriented such that the south side

would experience tension under displacement ductility ten, corresponding the deformation which induced bar buckling for a similar transverse steel spacing in prior experiments. In the cycle naming system, ($\mu_{-10.0}^{3.00\,sec} = -6.71"$) represents a pull cycle to displacement ductility 10 which occurred 3.00 seconds into the analytical 1940 El Centro load history. The time axis in Figure 3.18 is a reference to the peak cycles in the analytical load history, in the experiment the load was applied in a quasi-static manner.

The fourth test began with the application of 170 kips of axial load, which is an axial load ratio of 5% for the tested cylinder strength ($f_c' = 7.93ksi$). During the fourth half cycle of load the specimen was held at the analytical first yield force of 44.02 kips to determine the first yield displacement for ductility calculations ($\Delta_y' = 0.50"$). The push cycle then resumed until the target displacement of ($\mu_{1.0}^{1.00\,sec} = 0.67"$) was readed. The crack distribution on the north side of the specimen during this cycle, and the south side during the subsequent cycle to ($\mu_{-1.0}^{1.32\,sec} = -0.66"$) is shown in Figure 3.22. Concrete crushing was observed on the south side of the specimen during the push cycle to ($\mu_{5.9}^{1.67\,sec} = 3.96"$), Figure 3.23. Crushing on the north side of the specimen was observed during ($\mu_{-6.4}^{2.03\,sec} = -4.40"$).

Longitudinal steel buckling was observed during the reversal from ($\mu_{5.8}^{2.44\,sec} = 3.91"$), during the pull cycle to ($\mu_{-10.0}^{3.00\,sec} = -6.71"$), when the extreme fiber north Bar N3 visibly deformed as shown in Figure 3.24. On the South side of the column, bar buckling was observed after reversal from ($\mu_{-4.3}^{3.86\,sec} = -2.95"$), while on the way to ($\mu_{5.7}^{4.45\,sec} = 3.81"$) as shown in Figure 3.24. Two additional bars on the north side of the specimen buckled during the pull cycle to ($\mu_{-2.6}^{4.78\,sec} = -1.77"$). An additional south reinforcing bar buckled during the push cycle to ($\mu_{-0.2}^{4.97\,sec} = -0.11"$). The previously buckled south reinforcing bar ruptured during the pull cycle to ($\mu_{-2.6}^{8.36\,sec} = -1.80"$). The remainder of the load history consisted of small inelastic cycles which did not produce further notable damage.

The scale chosen for the 1940 El Centro acceleration time history produced buckling on each side of the specimen, and a single fractured reinforcing bar. The reinforcing bars did not immediately buckle upon reversal from the first inelastic peak matching the predicted

buckling displacements for the given spiral spacing from previous tests, which indicates that the displacement amplitudes in the load history were properly scaled to produce bar buckling.

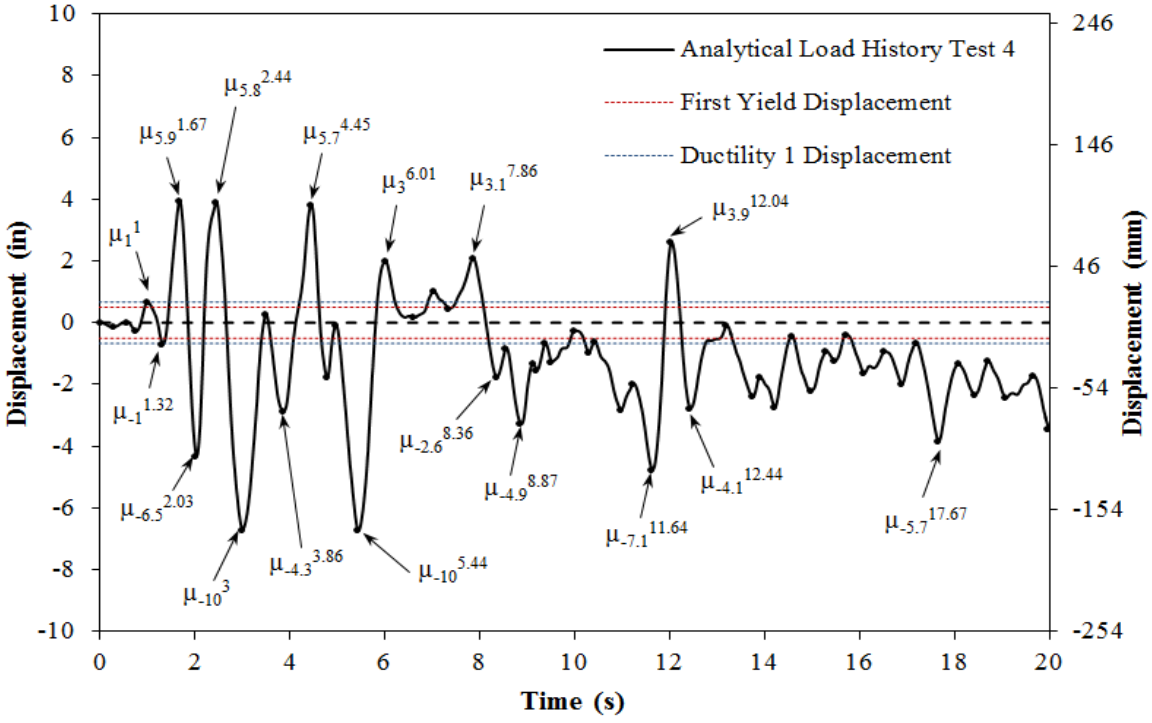

Figure 3.18 Test 4 – Analytical Lateral Displacement History for 1940 El Centro EQ

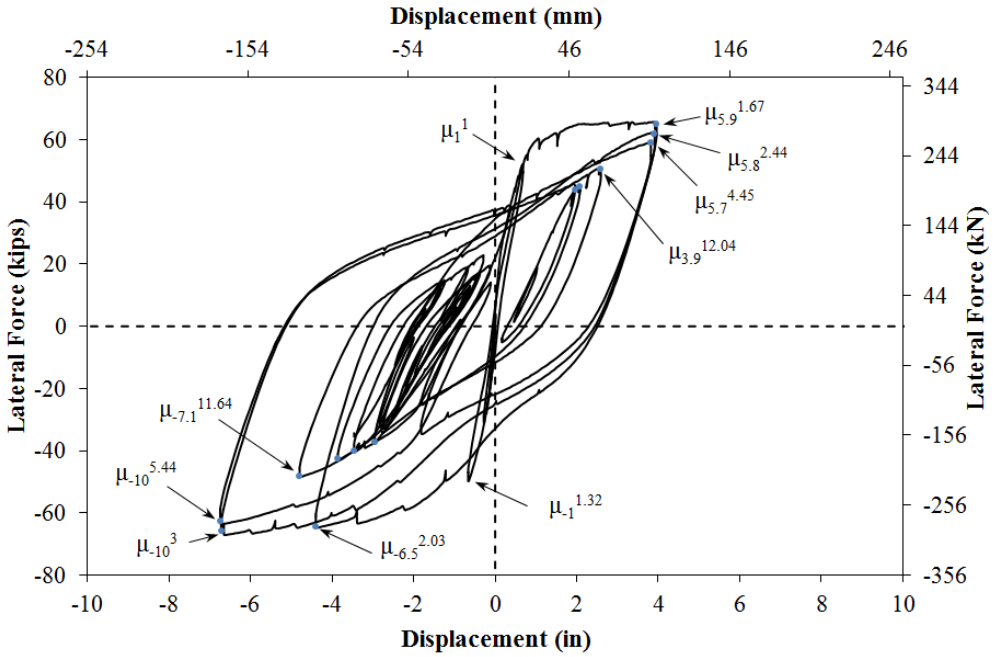

Figure 3.19 Test 4 – Hysteretic Response for the 1940 El Centro EQ

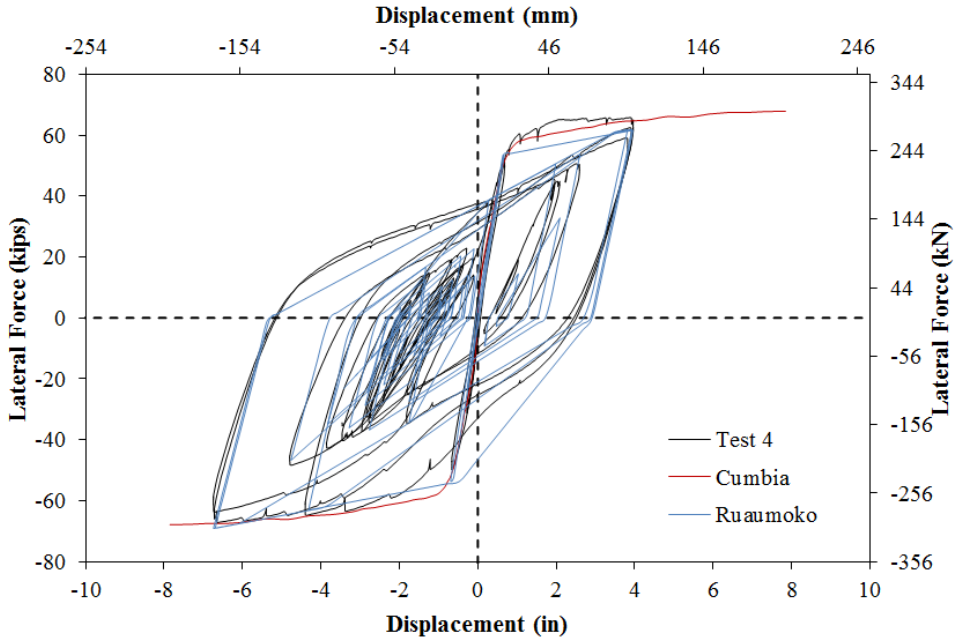

Figure 3.20 Test 4 – Comparison of Analytical and Experimental Hysteretic Response

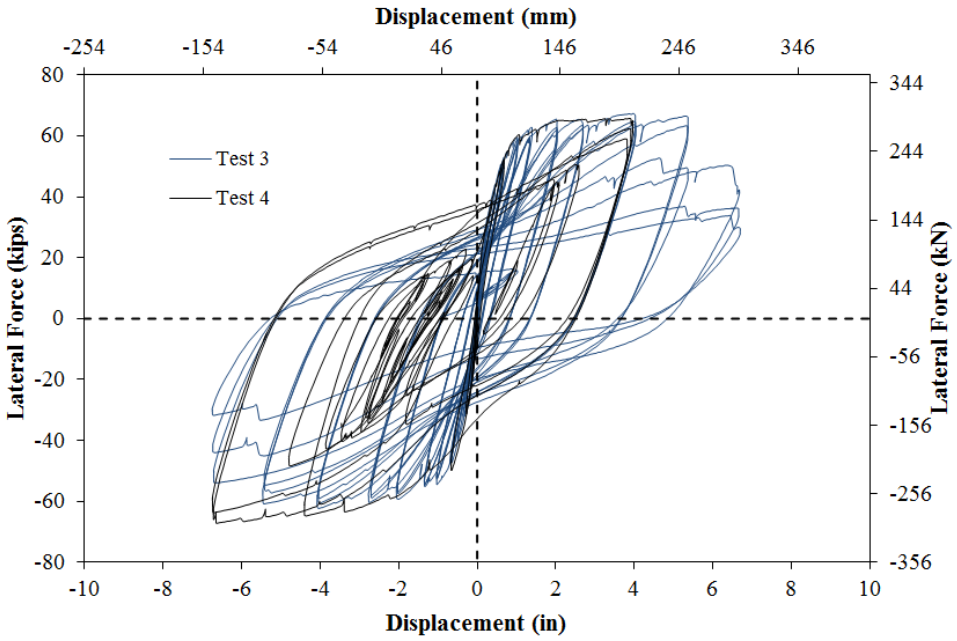

Figure 3.21 Comparison of Cyclic Test 3 and 1940 El Centro EQ Load History

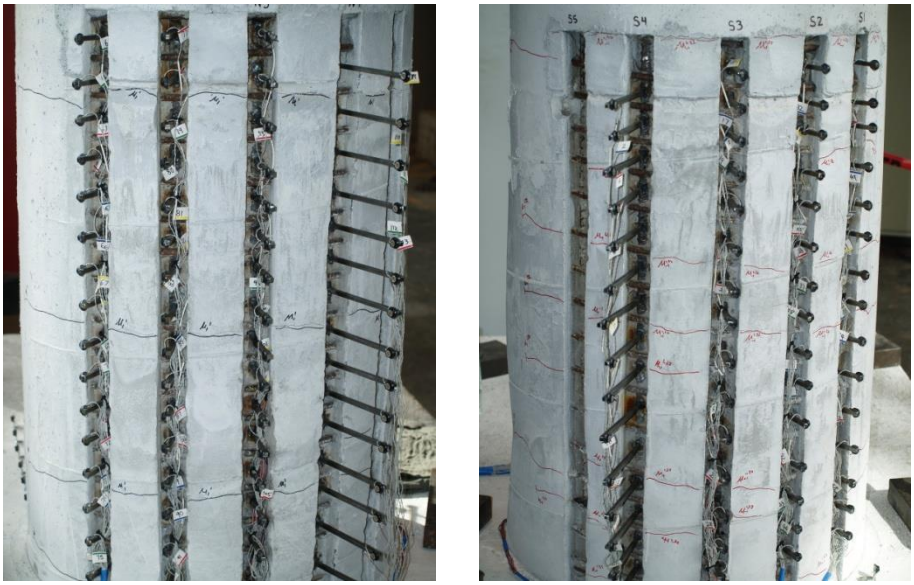

Figure 3.22 Test 4 – (Left) Crack distribution at $\left(\mu_{1.0}^{1.00sec} = 0.67"\right)$ and (Right) Crack Distribution at $\left(\mu_{-1.0}^{1.32sec} = -0.66"\right)$

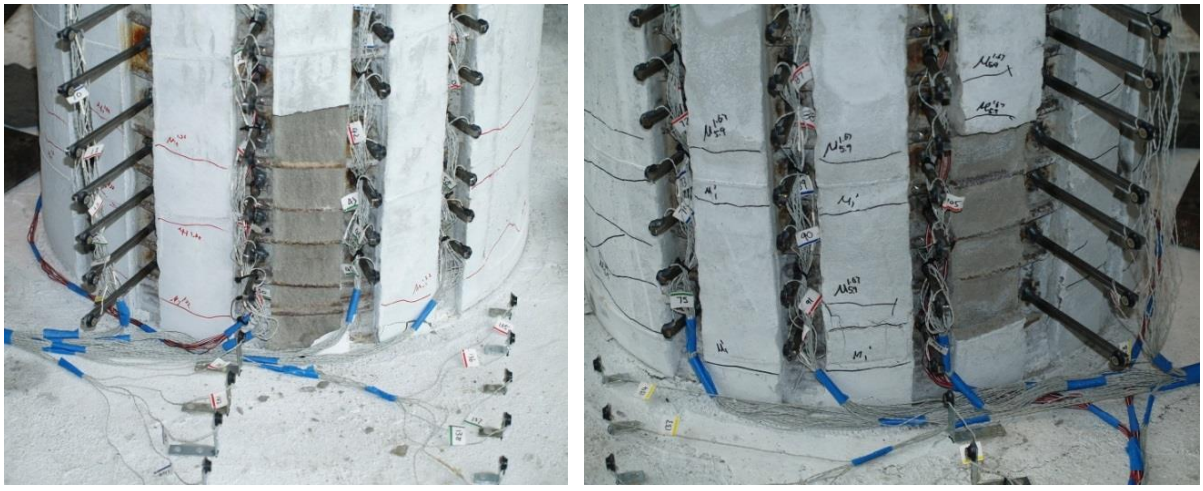

Figure 3.23 Test 4 – (Left) Crushing on the South during $\left(\mu_{5.9}^{1.67sec} = 3.96"\right)$ and (Right) Crushing on the North during $\left(\mu_{-6.4}^{2.03sec} = -4.40"\right)$

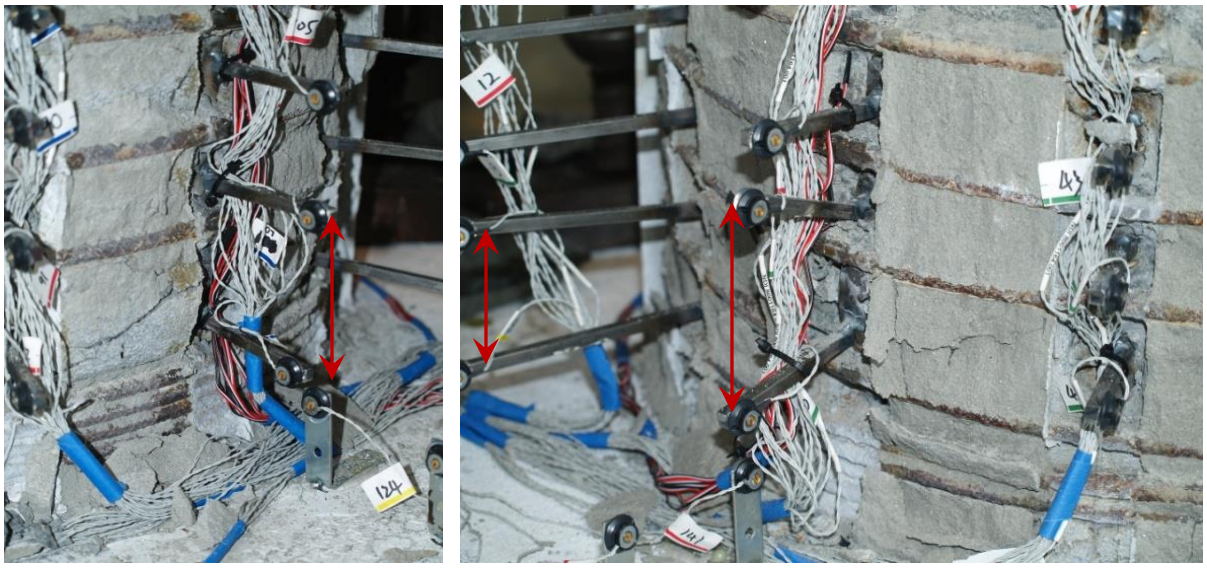

Figure 3.24 Test 4 – (Left) Buckling of North Bar N3 at $\left(\mu_{-10.0}^{3.00\,sec} = -6.71"\right)$ and (Right) Buckling of South Bar S3 and S4 at $\left(\mu_{5.7}^{4.45\,sec} = 3.81"\right)$

3.6 Test 5: 1978 Tabas Earthquake Load History

The first three tests focused on monotonic and symmetric three-cycle-set load histories. The displacement input for Tests 4-6 is determined using acceleration time histories from recorded earthquakes and non-linear time history analysis. Test five was subjected to an analytical load history obtained from the 1978 Tabas earthquake in Iran. The top column displacement history in Figure 3.25 was determined using Ruaumoko inelastic time history analysis with a viscous damping ratio of 5.7% based on tangent stiffness and a thin Takeda hysteretic rule. The scale factor for the acceleration values in the Tabas load history was chosen based on displacements that caused buckling in previous tests with similar transverse steel spacing in the plastic hinge. The resulting hysteretic response for the Tabas load history is shown in Figure 3.26.

The fifth test began with the application of 170 kips of axial load, which is an axial load ratio of 5% for the tested cylinder strength ($f_c' = 8.4\ ksi$). During the first half cycle of load the specimen was held at the analytical first yield force of 44 kips to determine the first yield displacement for ductility calculations ($\Delta_y' = 0.55"$). To allow for direct comparison to previous tests, the ductility levels for Test 5 were based on a first yield displacement of 0.50" and corresponding ductility one displacement of 0.67". Previous tests results with a maximum transverse steel spacing of 3" (north) and 2" (south) in the plastic hinge region have shown that buckling occurs upon reversal from ($\mu_{\Delta 6} = 4.04"$) and ($\mu_{\Delta 10} = 6.72"$) accordingly. In Figure 3.25, the peak displacements from the analytical load history are highlighted, ($\mu_{7.7}^{11.38\ sec} = 5.20"$) or ($\mu_{7.5}^{11.98\ sec} = 5.07"$) to buckle the North reinforcement upon reversal and ($\mu_{-10.0}^{14.26\ sec} = -6.68"$) for the South. First crushing of cover concrete on the north and south sides of the specimen were observed at ($\mu_{2.4}^{5.08\ sec} = 1.59"$) and ($\mu_{-2.1}^{5.4\ sec} = -1.57"$) respectfully, Figure 3.27. In the physical test, bar buckling was not observed during the Tabas load history. Photos of the north and south sides of the specimen at the conclusion of the Tabas load history appear in Figure 3.28.

The post-earthquake capacity of the column was investigated by subjecting the same specimen to a symmetric three-cycle-set load history identical to Tests 2 and 3, Figure 3.29. The resulting hysteretic response appears in for the cyclic aftershock load history appears in Figure 3.30 and Figure 3.31. The cyclic aftershock hysteretic response is compared to that of an initially undamaged column from Test 3 in Figure 3.32.

The first sign of reinforcement buckling occurred during the first pull cycle of ductility six ($\mu_6^{-1} = -4.07"$), when the North extreme fiber bar began to visible deform in two separate locations as shown in Figure 3.33. During ($\mu_8^{-1} = -5.46"$), Bar S1 ruptured in tension without previous signs of buckling and Bar N4 buckled at the same location as the upper buckled region Bar N3. The rupture of Bar S1 was not expected, since it is not an extreme fiber experiencing the largest demands. The early fracture is attributed to the effects of welding on the strain capacity of the base material, but it is unclear why this was only observed in a single experiment and not at the location of the largest demands. The influence of welding on the steel material properties from reinforcing bar tensile tests is the topic of the previous chapter of this report.

On the way to ($\mu_8^{+2} = 5.35"$), Bar S3 became the first bar to buckle on the South side of the column and previously buckled bar N3 ruptured in tension. Other notable events occurred as follows: Bars S2 and S4 buckled during μ_8^{+3}; Bar S4 ruptured during μ_{10}^{-1}; Bar N4 ruptured during μ_{10}^{+2}; and Bar N2 ruptured during μ_{10}^{+3}. Envelope curves connecting the peaks of the third cycle of each ductility level in Tests 2, 3, and 5b appear in Figure 3.34. This figure illustrates the degree of stiffness degradation in the cyclic aftershock load history caused by the prior Tabas earthquake record. The degradation behavior at the ultimate level appears to be similar between the three experiments.

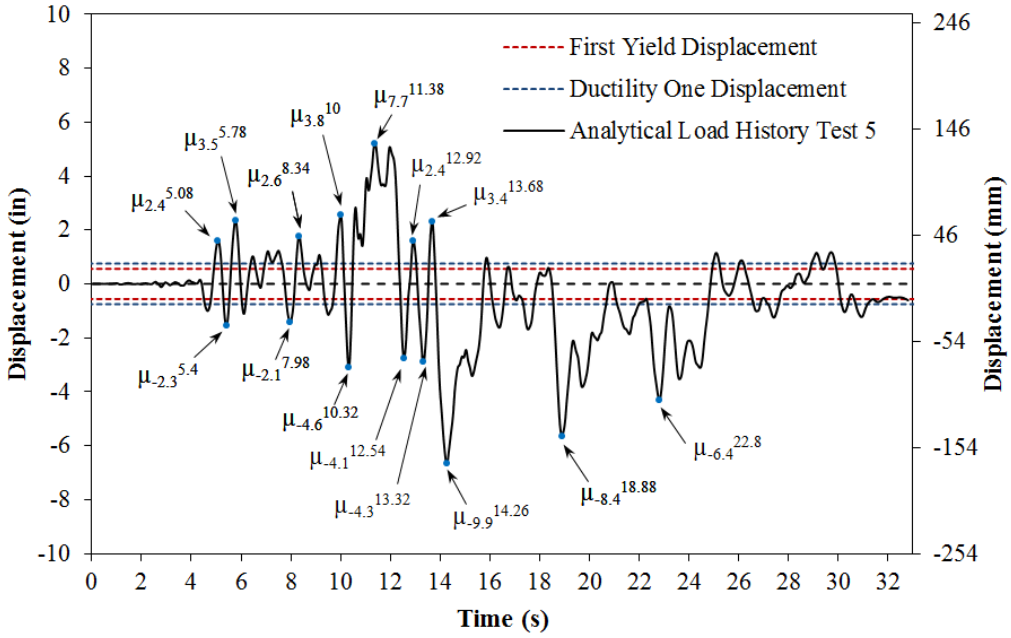

Figure 3.25 Test 5 – Analytical 1978 Tabas Earthquake Load History

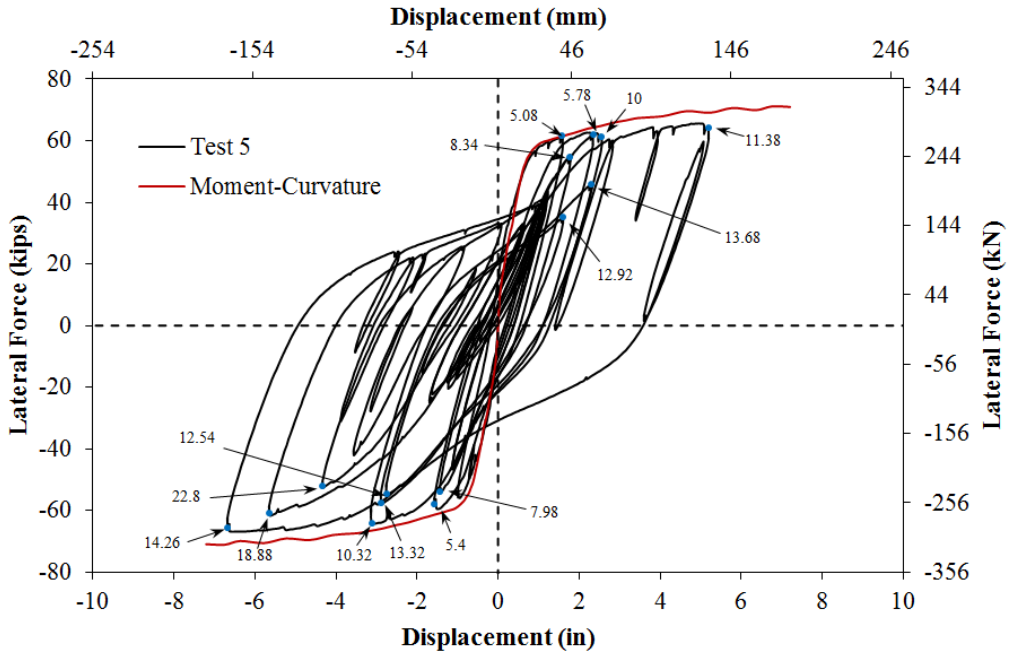

Figure 3.26 Test 5 – Hysteretic Response for 1978 Tabas EQ Load History

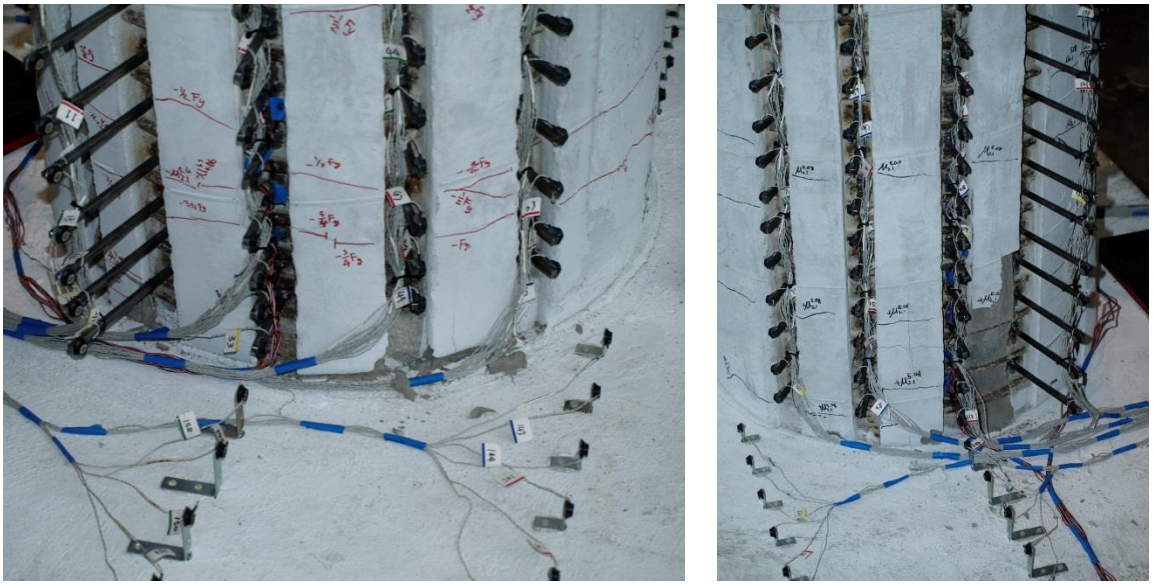

Figure 3.27 Test 5 – (Left) North Concrete Crushing at $\left(\mu_{2.4}^{5.08\,sec} = 1.59"\right)$ and (Right) South Concrete Crushing at $\left(\mu_{-2.1}^{5.4\,sec} = -1.57"\right)$

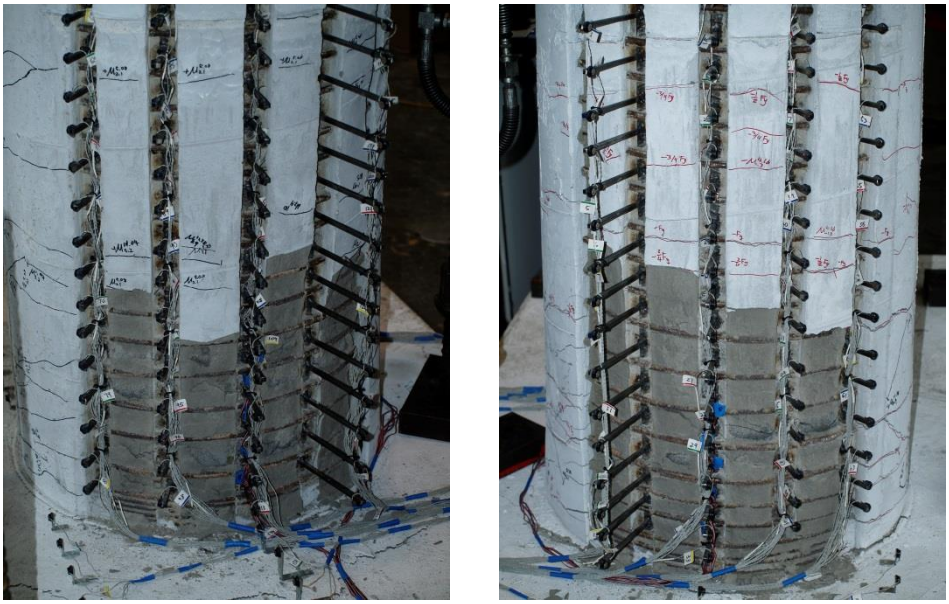

Figure 3.28 Test 5 – (Left) North and (Right) South Sides after Tabas EQ LH

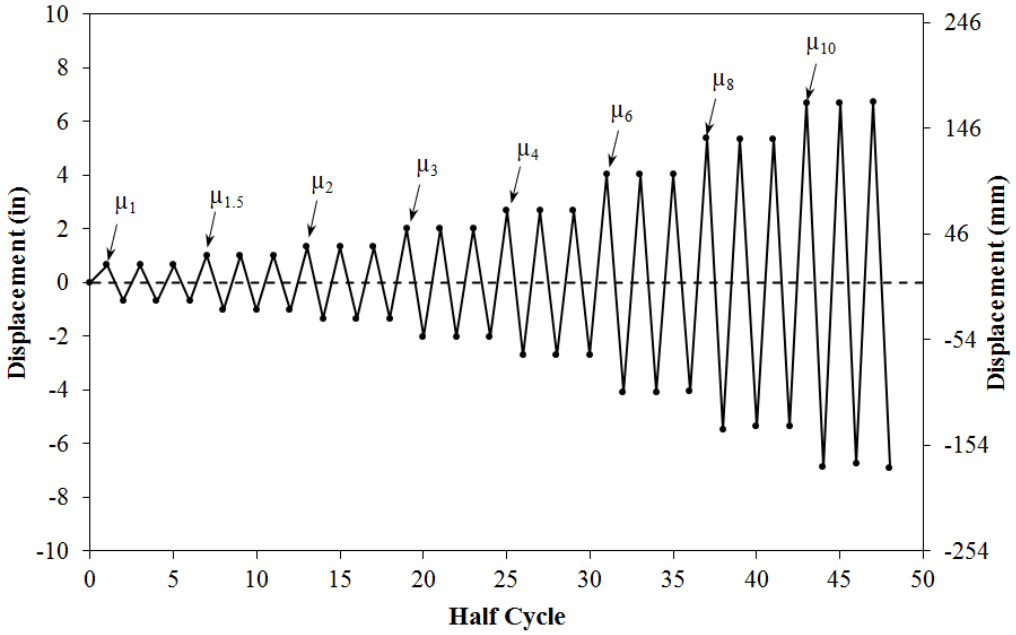

Figure 3.29 Test 5b – Symmetric Three-Cycle-Set Aftershock Load History

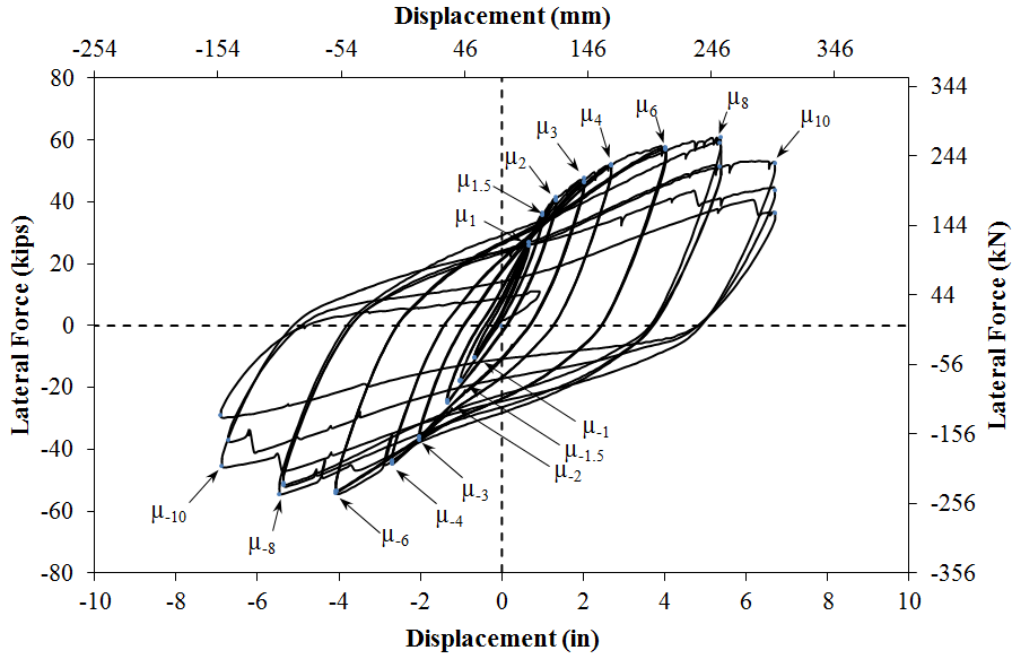

Figure 3.30 Test 5b – Hysteretic Response for Cyclic Aftershock Load History

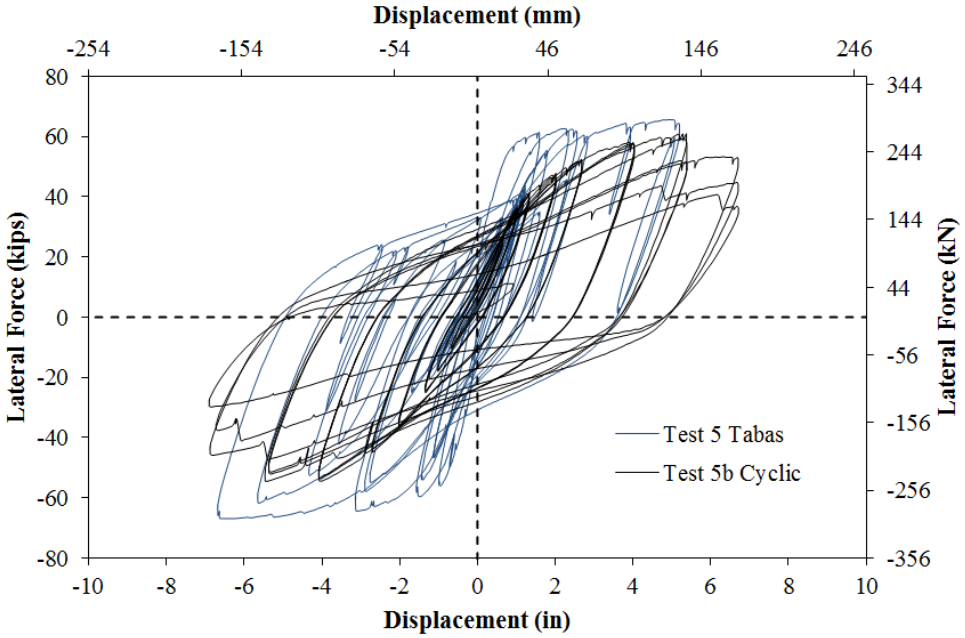

Figure 3.31 Tests 5 and 5b – Comparison of Tabas EQ LH and Cyclic Aftershock

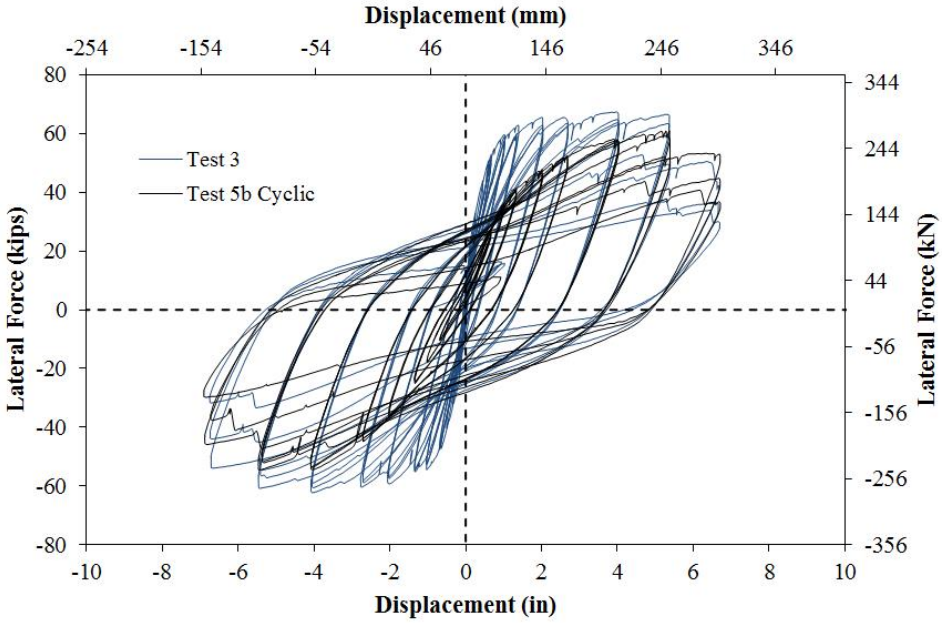

Figure 3.32 Tests 3 and 5b – Hysteretic Comparison for Initially Undamaged Symmetric Three-Cycle-Set and Cyclic Aftershock Load Histories

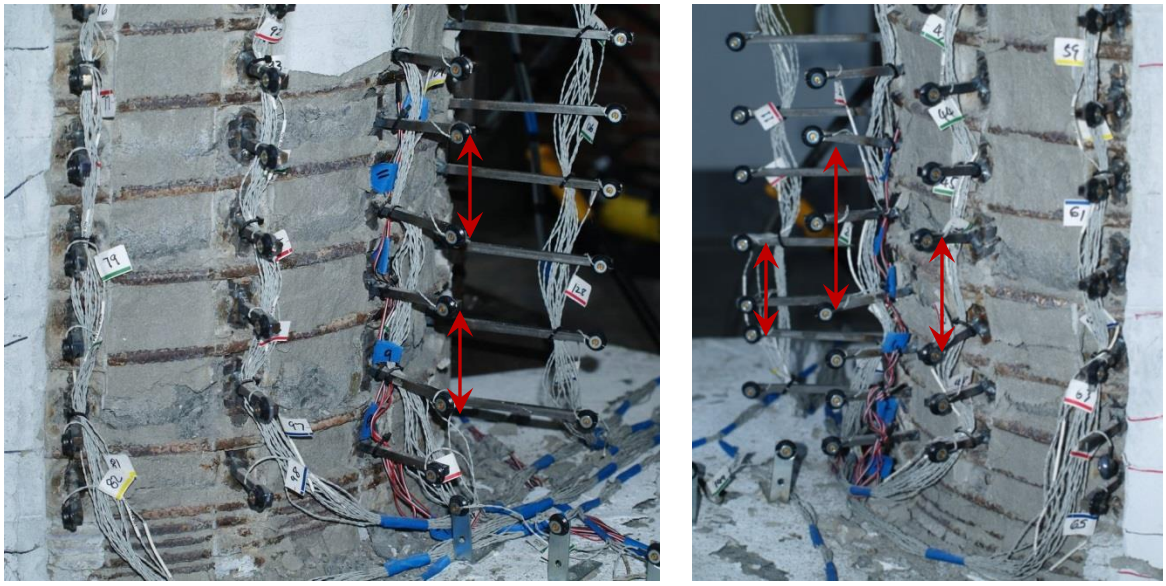

Figure 3.33 Test 5b – (Left) Buckling of Bar N3 during $\left(\mu_6^{-1} = -4.07"\right)$ and (Right) Three South Buckled Bars at $\left(\mu_8^{+3} = 8.35"\right)$

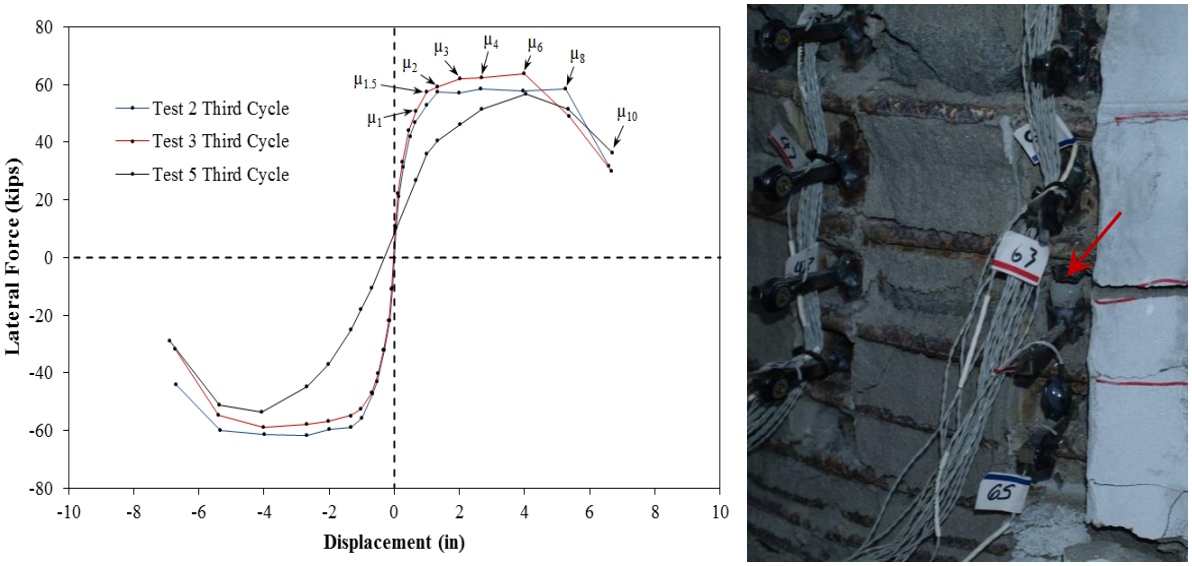

Figure 3.34 Test 5b – (Left) Third Cycle Envelope Curves for Tests 2, 3, and 5b (Right) Fracture of Bar S1 during $\left(\mu_8^{-1} = -5.46"\right)$

3.7 Test 6: 1978 Tabas Earthquake Load History

The first three tests focused on monotonic and symmetric three-cycle-set load histories. The displacement input for Tests 4-6 is determined using acceleration time histories from recorded earthquakes and non-linear time history analysis. Test five was subjected to an analytical load history obtained from the 1978 Tabas earthquake in Iran. The top column displacement history in Figure 3.35 was determined using Ruaumoko inelastic time history analysis with a viscous damping ratio of 5.7% based on tangent stiffness and a thin Takeda hysteretic rule. The Tabas load history utilized in Test 6 was an exact inverse of the displacement history from Test 5. The resulting hysteretic response for the Tabas load history is shown in Figure 3.36. A hysteretic comparison of the inverted response from Test 5 and the measured response from Test 6 appears in Figure 3.37.

The sixth test began with the application of 170 kips of axial load, which is an axial load ratio of 3.7% for the tested cylinder strength ($f_c' = 10.2\ ksi$). During the first half cycle of load the specimen was held at the analytical first yield force of 44 kips to determine the first yield displacement for ductility calculations ($\Delta_y' = 0.53"$). To allow for direct comparison to previous tests, the ductility levels for Test 6 were based on a first yield displacement of 0.50" and corresponding ductility one displacement of 0.67". Cover concrete crushing was observed on the north side of the specimen during ($\mu_{-2.4}^{5.08\ sec} = -1.59"$), Figure 3.38. A photo depicting crushing on the south side of the specimen at ($\mu_{4.6}^{10.32\ sec} = 3.11"$) appears in Figure 3.38.

The extent of crushing on the north and south sides of the column at ($\mu_{-7.8}^{11.38\ sec} = -5.24"$) and ($\mu_{10.0}^{14.26\ sec} = 6.70"$) respectively appear in Figure 3.39. The north extreme fiber bars N2 and N3 during the reversal from the peak displacement of ($\mu_{10.0}^{14.26\ sec} = 6.70"$) as shown in Figure 3.40. The photo of the buckled deformation was taken at ($\mu_{-1.5}^{15.86\ sec} = -0.98"$). An additional north reinforcing bar buckled, and the deformation in the two previously buckled bars increased during ($\mu_{-0.1}^{20.90\ sec} = -0.06"$), Figure 3.40.

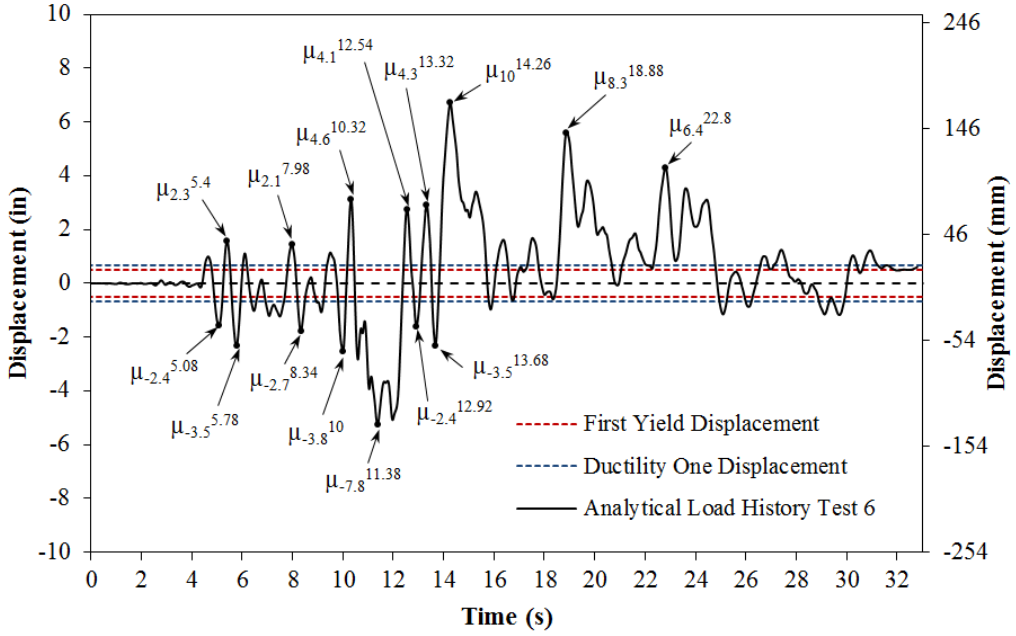

Figure 3.35 Test 6 – 1978 Tabas Earthquake Load History (Inverse of LH from T5)

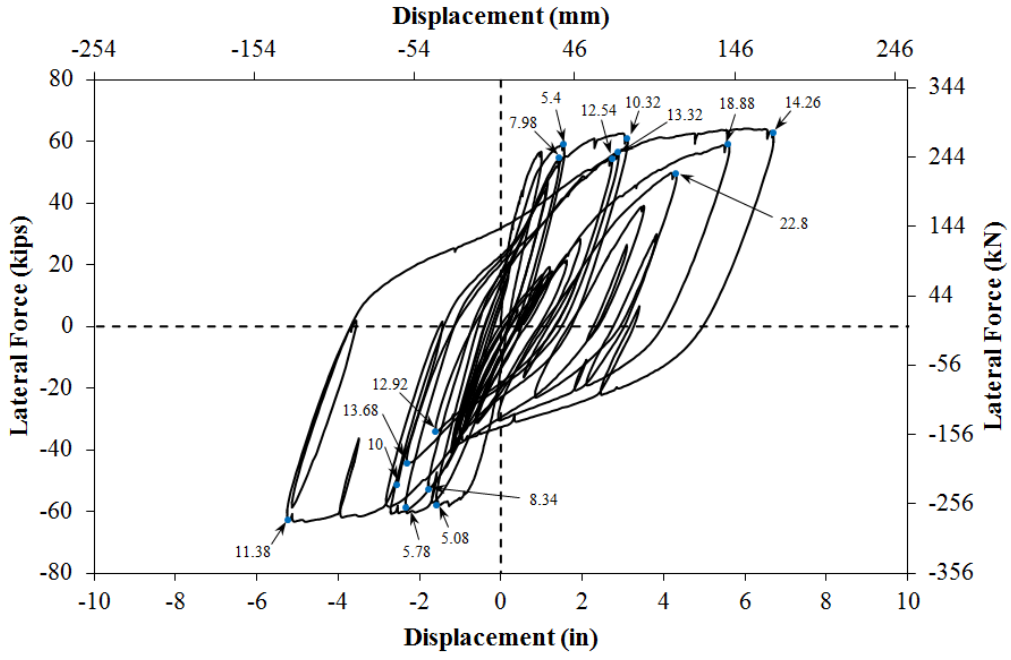

Figure 3.36 Test 6 – Hysteretic Response for Tabas Load History

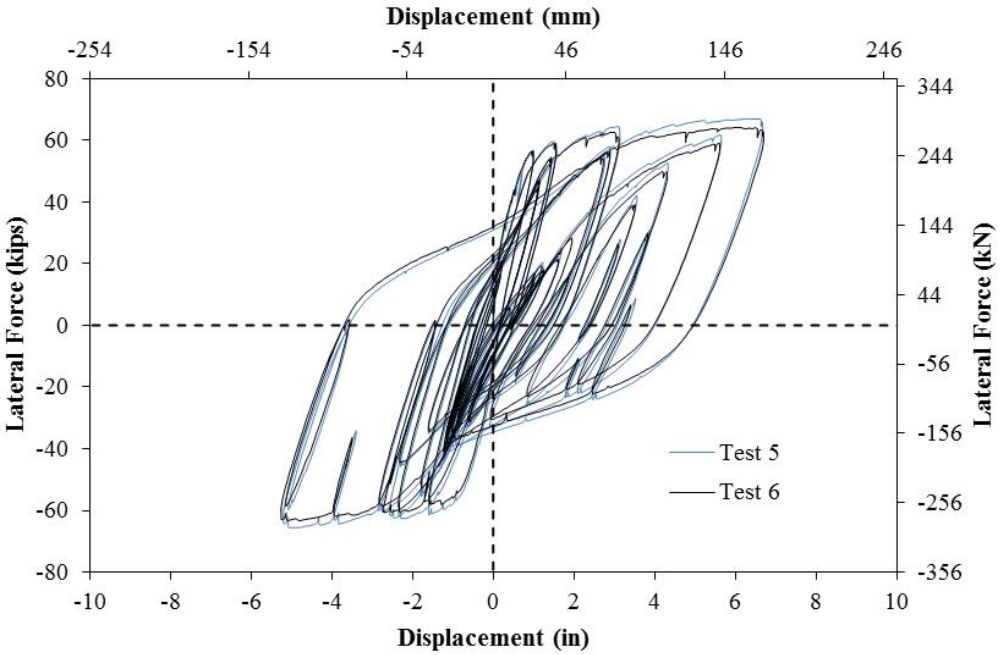

Figure 3.37 Comparison of Test 6 Response and Inverse of Test 5 Response

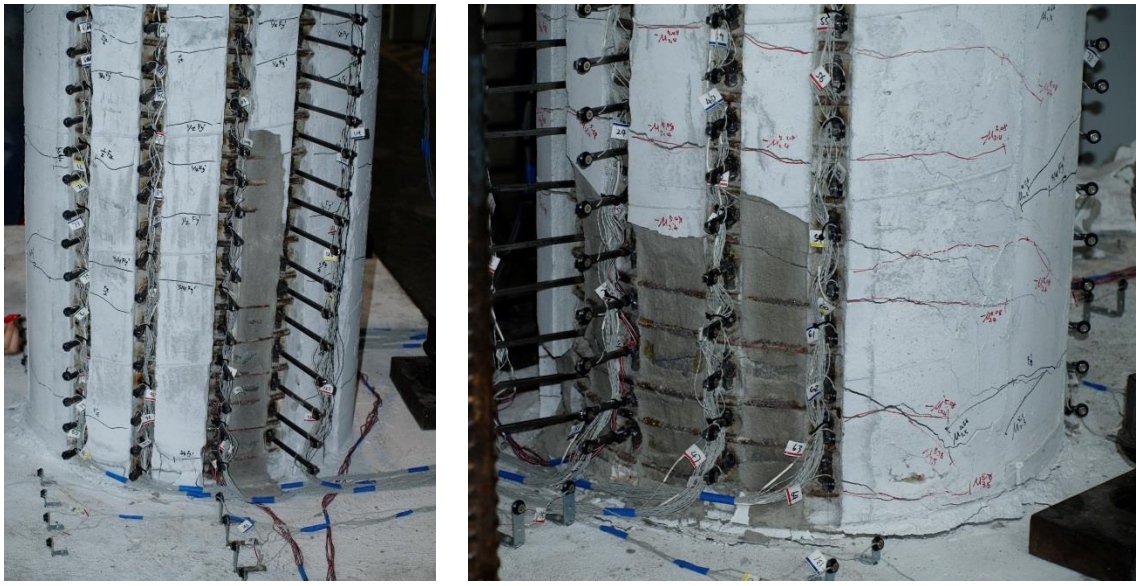

Figure 3.38 Test 6 – (Left) North Crushing observed during $\left(\mu_{-2.4}^{5.08\,sec} = -1.59"\right)$ and (Right) Extent of South Crushing at $\left(\mu_{4.6}^{10.32\,sec} = 3.11"\right)$

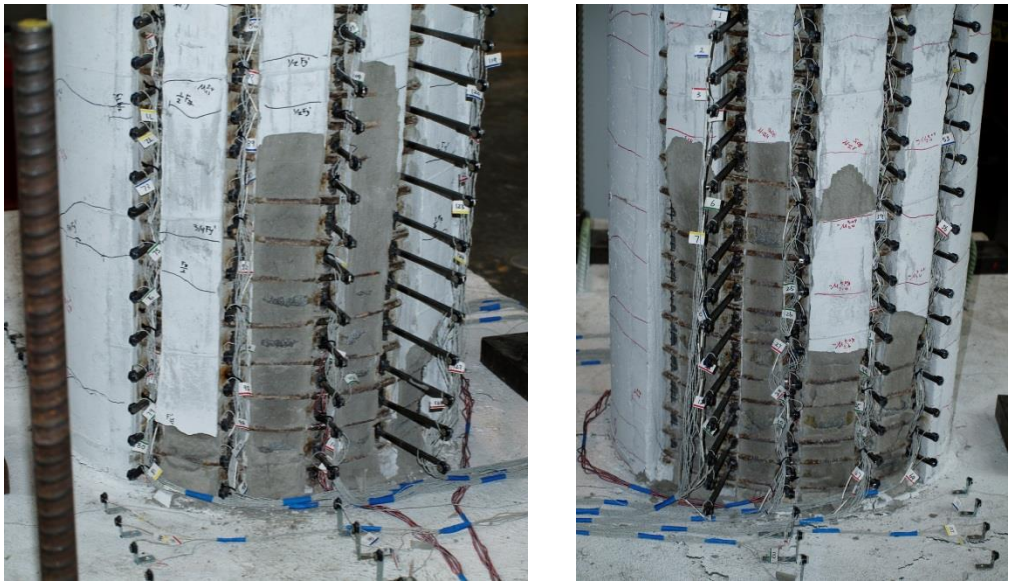

Figure 3.39 Test 6 – (Left) Extent of North Crushing during $\left(\mu_{-7.8}^{11.38\,sec} = -5.24"\right)$ and (Right) Extent of South Crushing during $\left(\mu_{10.0}^{14.26\,sec} = 6.70"\right)$

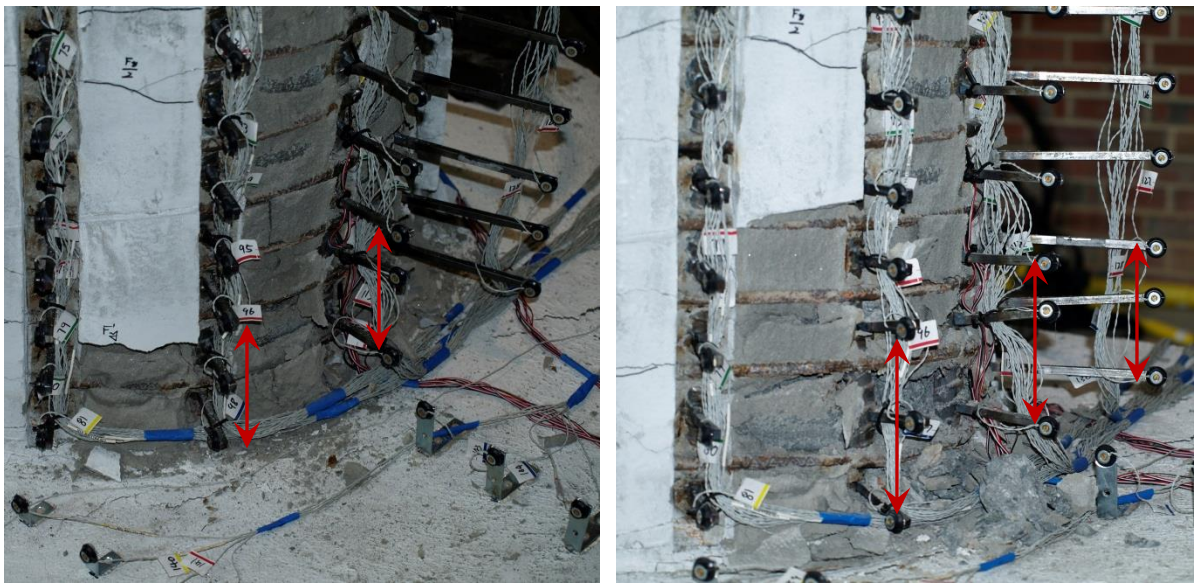

Figure 3.40 Test 6 – (Left) Initial Buckling of Bars N2 and N3 at $\left(\mu_{-1.5}^{15.86\,sec} = -0.98"\right)$ during Reversal from $\left(\mu_{10.0}^{14.26\,sec} = 6.70"\right)$ and (Right) Buckled Deformation in North Bars during $\left(\mu_{-0.1}^{20.90\,sec} = -0.06"\right)$

REFERENCES

Hines, E. M. and Seible F. (2001) Experimental Spread of Plasticity in Reinforced Concrete Bridge Piers. Structural Systems Research Project 2001/08, University of California, San Diego, La Jolla, California, 196 pp.

Hines, E.M., Restrepo, J.I., and Seible, F. (2004). "Force-Displacement Characterization of Well Confined Bridge Piers." *ACI Structural Journal* 101(4), 537-548.

Mander, J. B., Priestley, M. J. N., and Park R. (1988). "Theoretical Stress-Strain Model for Confined Concrete." *ASCE Journal of Structural Engineering* 114(8), 1804-1826.

Montejo, L. A. and Kowalsky, M. J. (2007). "CUMBIA – Set of Codes for the Analysis of Reinforced Concrete Members." Technical Report No. IS-07-01, North Carolina State University, Raleigh, NC.

Northern Digital Inc. "OPTOTRAK Certus HD Dynamic Measuring Machine." Products, <http://www.ndigital.com/industrial/certushd.php> (Jan. 14, 2013)

Priestley, M. J. N., Seible, F., and Calvi, G. M. (1996). Seismic Design and Retrofit of Bridges. John Wiley & Sons, New York.

Priestley, M. J. N., Calvi, G. M., and Kowalsky, M. J. (2007). "Displacement-Based Seismic Design of Structures." IUSS Press, Pavia, Italy.

Zhao, J. and Sritharan, S. (2007). "Modeling of Strain Penetration Effects in Fiber-Based Analysis of Reinforced Concrete Structures." *ACI Structural Journal.* 104(2), 133-141.